NASA/TP—1998–206861

The Development of the Joint NASA GSFC and the National Imagery and Mapping Agency (NIMA) Geopotential Model EGM96

F.G. Lemoine, S.C. Kenyon, J.K. Factor, R.G. Trimmer, N.K. Pavlis, D.S. Chinn, C.M. Cox,
S.M. Klosko, S.B. Luthcke, M.H. Torrence, Y.M. Wang, R.G. Williamson, E.C. Pavlis, R.H. Rapp,
and T. R. Olson

National Aeronautics and
Space Administration

Goddard Space Flight Center
Greenbelt, Maryland 20771

July 1998

The Development of the Joint NASA GSFC and the National Imagery and Mapping Agency (NIMA) Geopotential Model EGM96

F.G. Lemoine, Laboratory for Terrestrial Physics, NASA Goddard Space Flight Center, Greenbelt, MD

S.C. Kenyon, J.K. Factor, and R.G. Trimmer, National Imagery and Mapping Agency, St. Louis, MO

N.K. Pavlis, D.S. Chinn, C.M. Cox, S.M. Klosko, S.B. Luthcke, M.H. Torrence, Y.M. Wang, and R.G. Williamson, Raytheon STX Corporation, Lanham, MD

E.C. Pavlis, Joint Center for Earth Systems Technology, University of Maryland, Baltimore County, and NASA Goddard Space Flight Center, Greenbelt, MD

R.H. Rapp, Department of Civil and Environmental Engineering and Geodetic Science, The Ohio State University, Columbus, OH

T.R. Olson, Colorado Center for Astrodynamics Research, University of Colorado, Boulder, CO

ABSTRACT

The NASA Goddard Space Flight Center (GSFC), the National Imagery and Mapping Agency (NIMA), and The Ohio State University (OSU) have collaborated to develop an improved spherical harmonic model of the Earth's gravitational potential to degree 360. The new model, Earth Gravitational Model 1996 (EGM96), incorporates improved surface gravity data, altimeter-derived gravity anomalies from ERS–1 and from the GEOSAT Geodetic Mission (GM), extensive satellite tracking data—including new data from Satellite Laser Ranging (SLR), the Global Postioning System (GPS), NASA's Tracking and Data Relay Satellite System (TDRSS), the French DORIS system, and the US Navy TRANET Doppler tracking system—as well as direct altimeter ranges from TOPEX/POSEIDON (T/P), ERS-1, and GEOSAT. The final solution blends a low-degree combination model to degree 70, a block-diagonal solution from degree 71 to 359, and a quadrature solution at degree 360. The model was used to compute geoid undulations accurate to better than one meter (with the exception of areas void of dense and accurate surface gravity data) and realize WGS84 as a true three-dimensional reference system. Additional results from the EGM96 solution include models of the dynamic ocean topography to degree 20 from T/P and ERS–1 together, and GEOSAT separately, and improved orbit determination for Earth-orbiting satellites.

The Development of the Joint NASA GSFC and National Imagery and Mapping Agency (NIMA) Geopotential Model EGM96

Key to Authors

Initials	Author	Affiliation
CMC	Christopher M. Cox	Raytheon STX
DSC	Douglas S. Chinn	Raytheon STX
ECP	Erricos C. Pavlis	University of Maryland
FGL	Frank G. Lemoine	NASA Goddard Space Flight Center
JKF	John K. Factor	National Imagery and Mapping Agency
MHT	Mark H. Torrence	Raytheon STX
NKP	Nikolaos K. Pavlis	Raytheon STX
RGT	Ronald G. Trimmer	National Imagery and Mapping Agency
RGW	Ronald G. Williamson	Raytheon STX
RHR	Richard H. Rapp	The Ohio State University
SBL	Scott B. Luthcke	Raytheon STX
SCK	Steve C. Kenyon	National Imagery and Mapping Agency
SMK	Steven M. Klosko	Raytheon STX
TRO	T. Rob Olson	University of Colorado, Boulder
YMW	Yan Ming Wang	Raytheon STX

# 1.	INTRODUCTION

For many applications, the Earth's gravitational potential, *V*, is represented by a spherical harmonic expansion, where the potential coefficients in this expansion have been determined by various techniques. Significant improvement in the estimation of the potential coefficients has taken place over the past 35 years [*Nerem, Jekeli, and Kaula,* 1995], in two general ways. First, the highest degree in the expansion has been extended to increasingly higher degree through the use of additional satellite data and terrestrial gravity data, thereby improving the resolution of the models. Second, the accuracy of the coefficients has been continually improved through the inclusion of additional data that improve in geographic coverage and accuracy over time.

For satellite orbit determination, a spherical harmonic expansion to degree 70 using the heretofore available data has been sufficient for all current applications. However, new geopotential-sensing missions such as GRACE [*Bettadpur and Tapley*, 1996] will require consideration of a better resolved field. Likewise, detailed geoid models require a resolution better than that available from the present satellite-based models. In the 1970's, spherical harmonic representations to degree 180 were estimated. In the 1980's, expansions to degree 360 became available. In 1991, *Rapp, Wang, and Pavlis* [1991] reported a degree 360 model that was based on the satellite-derived model GEM–T2 [*Marsh et al.,* 1990], sea-surface heights from GEOSAT altimeter data, gravity anomalies derived from satellite altimeter data, surface gravity data, and topographic information. Although a simultaneous solution to degree 360 was described in this report, the final model released, OSU91A, was a blend of a low-degree (50) combination model (including satellite tracking and altimetry data and surface gravity data) and the expansion from degree 51 to 360 from the simultaneous solution. The rationale for such a procedure was described in the cited report. The major limitation in OSU91A stemmed from the lack of precise surface gravity data over large continental regions—for instance, most of Asia.

Since 1991, improvements have continued in the development of "low degree" (to 70) combination models using primarily satellite tracking data and surface gravity data. Examples of this type of solution are the JGM–1 and –2 geopotential models developed to aid the orbit determination of the TOPEX/POSEIDON (T/P) satellite [*Nerem et al.,* 1994]. The JGM–2 model, complete to degree 70, was a postlaunch model incorporating T/P laser ranging data and DORIS tracking data. The low-degree combination model development continued, with the determination of an improvement to the JGM–1 model called JGM–3 [*Tapley et al.,* 1996], using additional laser tracking data, DORIS data, and, for the first time, GPS tracking of the TOPEX/POSEIDON satellite. Degree 360 models were reported by *Gruber and Anzenhofer* [1993] and *Gruber, Anzenhofer, and Rentsch* [1995]. The basis for these models was the GRIM4–C4 geopotential model [*Schwintzer et al.*, 1997].

In 1993, the need for improved geoid undulation determinations was becoming increasingly apparent. The primary need was related to the conversion of ellipsoidal height information from GPS determinations to orthometric heights. A related goal for an improved geoid was the establishment of a globally defined geoid that could form the reference surface for a global vertical datum. At this time, the OSU91A model [*Rapp, Wang, and Pavlis*, 1991] was being

widely used for many applications with a known weakness related to using an older generation satellite model as a base, and poor or no surface gravity data in many regions of the world.

A preliminary meeting was held at the 1993 Spring AGU meeting involving Dr. David Smith (National Aeronautics and Space Administration, Goddard Space Flight Center [NASA GSFC]), Muneendra Kumar (Defense Mapping Agency [DMA], which later became the National Imagery and Mapping Agency [NIMA]), and Richard Rapp (The Ohio State University [OSU]) to discuss a possible cooperation between the groups to leverage their long history of research in satellite geopotential recovery and the processing of terrestrial gravity data. Following this positive meeting, followup meetings were held in July and September 1993 at GSFC. With a tentative understanding of mutual interest, a more formal meeting was held at GSFC on October 14, 1993, with presentations by GSFC and NIMA personnel. A discussion took place to draft a Memorandum of Understanding (MOU) between NASA and DMA. The MOU was between the DMA and NASA, on the "Joint Gravity Field and Geoid Improvement Project." As stated in the MOU, "the primary goal is to improve the Earth Gravity Model (EGM), and its associated global geoid, to support terrestrial and extraterrestrial scientific endeavors, as well as to meet the mapping, charting and navigation requirements of both the civil and military sectors." The MOU was signed by NASA on March 11, 1994, and by DMA on April 1, 1994.

The October meeting developed the organization of the joint project through a science working group. To facilitate the activities of the project, four working groups were established: Working Group I, Combination Methods and High Degree Expansions (Chair: Nikolaos Pavlis), Working Group II, Surface Gravity Data Preparations (Chair: Richard Salman), Working Group III, Evaluation of Altimeter Implied Gravity Anomalies (Chair: Ronald Trimmer), and Working Group IV, Satellite Gravity Model Development (Chair: R. Steven Nerem). The chairperson of each working group initially developed the plans and data needed for each area of interest. As the project progressed, personnel and responsibility changes took place. Steve Kenyon from NIMA became involved in the detailed computations with the terrestrial gravity anomaly data, and Frank Lemoine at GSFC continued the direction of the satellite model development after R.S. Nerem accepted a position at the University of Texas at Austin in January 1996.

The overall responsibility for the joint project development was given to the Project Steering Committee. The representatives to the committee were Dr. David Smith from NASA GSFC and Dr. Randall Smith from NIMA. Professor Rapp also served on the Steering Committee.

The next meetings of the science working group took place on January 19, 1994, where the emphasis was on data availability and data needs, and April 5, 1994, where progress reports were given and a milestone plan for overall project deliverables was drafted. This plan called for the delivery of the final potential coefficient model in March 1996. Additional meetings were held throughout 1995 and 1996 to discuss progress and challenges to meeting the agreed-upon goals.

Early in the project planning, it was recognized that international participation in project activities was desirable. A key component in the project was the evaluation of candidate geopotential models. The evaluation of preliminary models through various global and regional tests such as satellite tracking data fits and GPS/leveling undulation comparisons was desired. In November 1994, Professor Rapp, on behalf of the joint project, wrote to Professor Fernando

Sansò, Director of the International Geoid Service, asking if this organization would be willing to establish a Special Working Group (SWG) to evaluate the preliminary geopotential models produced by the joint project. These evaluations would be used to aid in the evaluation and selection of the final geopotential model. Professor Sansò kindly agreed to the request and asked Professor Michael Sideris, of the University of Calgary, to chair the SWG subcommittee that took on this role. Professor Sideris agreed and issued the first circular letter to the members of the SWG on January 17, 1995, requesting their support for the effort. With significant SWG-sponsored international participation, a valuable insight into the models was provided, leading to significant help in the selection of the final model.

1.1　References

Bettadpur, S.V., and B.D. Tapley, Assessments of Future Geopotential Mapping Missions, Abstract U22A-2, *Eos Trans. AGU Suppl.*, 77, 17, AGU Spring Meeting, Baltimore, 1996.

Gruber, T., and M. Anzenhofer, The GFZ 360 gravity field model, in *Proc. of Session G3— European Geophysical Society XVIII General Assembly*, R. Forsberg, H. Denker (eds), 13–18, Geodetic Division, Kort–og Matrikelstyrelsen, Copenhagen, 1993.

Gruber, T., M. Anzenhofer, and M. Rentsch, The 1995 GFZ high resolution gravity model, in: *Global Gravity Field, and Its Temporal Variations*, Rapp, Cazenave, Nerem (eds), 61–70, IAG Symposium 116, Springer–Verlag, Berlin, 1995.

Marsh, J.G., F.J. Lerch, B.H. Putney, T.L. Felsentreger, B.V. Sanchez, S.M. Klosko, G.B. Patel, J.R. Robbins, R.G. Williamson, T.E. Engelis, W.F. Eddy, N.L. Chandler, D.S. Chinn, S. Kapoor, K.E. Rachlin, L.E. Braatz, and E.C. Pavlis, The GEM–T2 gravitational model, *J. Geophys. Res., 95*, B13, 22043–22070, 1990.

Nerem, R.S., C. Jekeli, and W.M. Kaula, Gravity field determination and characteristics retrospective and prospective, *J. Geophys. Res., 100*, B8, 15053–15074, 1995.

Nerem, R.S., F.J. Lerch, J.A. Marshall, E.C. Pavlis, B.H. Putney, B.D. Tapley, R.J. Eanes, J.C. Ries, B.E. Schutz, C.K. Shum, M.M. Watkins, S.M. Klosko, J.C. Chan, S.B. Luthcke, G.B. Patel, N.K. Pavlis, R.G. Williamson, R.H. Rapp, R. Biancle, and F. Noule, Gravity Model Development for TOPEX/POSEIDON: Joint Gravity Models 1 and 2, *J. Geophys. Res.*, 24421–24447, 1994.

Rapp, R.H., Y.M. Wang, and N.K. Pavlis, The Ohio State 1991 Geopotential and Sea Surface Topography Harmonic Coefficient Models, *Rept. 410*, Dept. of Geod. Sci. and Surv, Ohio State University, Columbus, August 1991.

Schwintzer, P., C. Reigber, A. Bode, Z. Kang, S.Y. Zhu, F.H. Massmann, J.C. Raimondo, R. Biancale, G. Balmino, J.M. Lemoine, B. Moynot, J.C. Marty, F. Barlier, and Y. Boudon, Long-wavelength global gravity field models: GRIM4–S4, GRIM4–C4, *J. of Geod., 71*, 189–208, 1997.

Tapley, B.D., M.M Watkins, J.C. Ries, G.W. Davis, R.J. Eanes, S.R. Poole, H.J. Rim, B.E. Schutz, C.K. Shum, R.S. Nerem, F.J. Lerch, J.A. Marshall, S.M. Klosko, N.K. Pavlis, and R.G. Williamson, The Joint Gravity Model 3, *J. Geophys. Res., 101* (B12), 28029–28049, 1996.

2. THE DEVELOPMENT OF THE GLOBAL TOPOGRAPHIC DATA BASE JGP95E

2.1 Introduction

The development of a global, high-degree ($N_{max} = 360$) gravitational model requires the incorporation of surface gravity information into the solution, to determine the fine structure of the field. Elevation information is of critical importance to the processing of surface (and airborne) gravity data, particularly over land areas. First of all, a (point value) Molodensky free-air gravity anomaly on the Earth's surface is defined as [*Heiskanen and Moritz*, 1967, eq. 8–9]:

$$\Delta g_{FA} = g_{obs} - \gamma_{ell} \left[1 - 2 \left(1 + f + m - 2f \sin^2 \phi \right) \left(H^*/a \right) + 3 \left(H^*/a \right)^2 \right] \tag{2.1-1}$$

and therefore its evaluation requires knowledge of the normal height H^* of the gravity station (H^* is generally unavailable, so the orthometric height H is used instead). As it will be discussed in detail in following sections, elevation information is also required during several pre-processing steps related to the mean anomaly estimation, and to the geopotential model development and use, including [*Kenyon and Pavlis*, 1996]:

1. Computation of terrain corrections required in order to form point values of refined Bouguer gravity anomalies [*Heiskanen and Moritz*, 1967, p. 131–133].

2. Computation of Residual Terrain Model (RTM) effects applied to point free-air gravity anomalies.

3. Spherical harmonic representation of the elevation to create reference Bouguer anomalies used in the remove-restore process of Least Squares Collocation (LSC).

4. Computation of g_1 analytical continuation terms.

5. Computation of topographic-isostatic anomalies.

6. Computation of height anomaly to geoid undulation conversion terms.

Topographic information is critical for the estimation of area-mean gravity anomalies primarily because the available point gravity measurements do not cover the surface of the Earth uniformly and with infinitely high density (this latter requirement can never be met in practice). Gravity observations are usually made along roads and are sparser over mountainous terrain. The accuracy of mean anomaly predictions can be improved significantly by exploiting the high (positive) correlation between free-air anomalies and elevations [*Uotila*, 1967]. Local (high-frequency) topographic effects are numerically removed from the point free-air anomalies. The estimation of area-mean values is then performed over a much smoother residual anomaly field. This reduces significantly errors arising from the sparseness of the point data, especially over areas of mountainous terrain. Area-mean values of the topographic effects are then restored to the predicted mean residual anomaly value, producing the final estimate of the mean free-air anomaly. Items 1, 2, and 3 above are related to this mean anomaly prediction scheme (see Section 3). Items 4 and 5 are related to the modeling and estimation algorithm applied to derive

potential coefficient information from terrestrial gravity anomaly data (see Sections 7.2 and 8). Item 6 relates to studies discussed by *Rapp* [1997] (see also Section 5.2.1).

It becomes clear from the above that the elevation and the gravity anomaly information to be used in a global geopotential modeling effort are inter-related. Proper development of a global mean free-air anomaly data base, requires the availability of a global high-resolution elevation data base. The elevation information which accompanies the point free-air gravity anomalies should be consistent with corresponding information in the global elevation data base. The absolute accuracy of the elevations in these two sources is obviously important. However, reliable error estimates for either source of elevation data is seldom available. Assessment of the accuracy of elevation data is quite challenging (especially at very long wavelengths), given the significant heterogeneity of the information used to compile global data bases. A more manageable task is to try to verify at least the consistency between elevations in the gravity records and in the global elevation file. To accomplish this task requires access to both the point gravity anomaly data base and the global high-resolution elevation data base. Such access was only available within NIMA, and therefore the task of checking and verifying the consistency of the elevations in the two data bases was conducted within that agency.

During the gravity anomaly evaluation process and before data is entered into NIMA's Point Gravity Anomaly (PGA) file, the elevation values in the gravity records are quality controlled. Each elevation value is checked against detailed contour plots from Digital Terrain Elevation Data (DTED) or other map sources that are available over the anomaly coverage area. If the elevation of the anomaly does not match detailed local contour maps then an assessment of the anomaly is made. Occasionally, elevation blunders are found and corrected. Other elevation problems may exist that require the gravity source to be re-evaluated with additional sources of information. A few rare cases exist where gravity sources may not even have elevations initially as part of the data records and elevation values from the best available sources must be assigned to them. Significant effort was made by NIMA to ensure the consistency of the elevations used throughout the joint project. These include the elevations in NIMA's PGA file, 1´ local elevation files used in development of Terrain Corrections (TC) and Residual Terrain Model (RTM) effects (Section 2.4), and the 5´ values which are part of the global topographic data base JGP95E (JGP stands for <u>J</u>oint <u>G</u>ravity <u>P</u>roject), whose development will be described in the following sections. The development of JGP95E was a cooperative effort between Hughes STX and NIMA personnel. The Hughes STX organization is now Raytheon STX and will be abbreviated hereafter as RSTX.

2.2   Data Requirements and Data Availability

We begin with two definitions. The term Digital Elevation Model (DEM) will be used here to identify a data set that provides a single piece of information pertaining to any given cell on the surface of the ellipsoid: the (mean) orthometric height (or depth) over the cell in question. This information defines the location of the surface of interface between atmospheric air and the Earth, over non-oceanic areas, continuing as the ocean bottom, over oceanic areas. In contrast, the term Digital Topographic Model (DTM) will be used here to identify data sets providing additional information pertaining to different terrain types (ice caps, ice shelves, lakes, etc.), and

the associated thickness of ice, or lake depth information. For gravity modeling purposes, one would ideally like to have available a global DTM at very high-resolution accompanied by a global crustal density data set. This was discussed during early meetings of the joint project, and it was recognized that global crustal density information was not readily available. Compilation of such a file would have required resources not available to the Project, and therefore the compilation of an updated and improved 5′ global DTM was identified as the next best goal which was within the joint project's reach.

For gravity modeling purposes it is also important to know the vertical (and horizontal) datum to which each elevation (and gravity anomaly) value refers [*Heck*, 1990]. This issue was also considered during early meetings of the Project. Unfortunately, information pertaining to vertical datums is not always known or available in NIMA's PGA or elevation files, and such identification of the data was impossible.

At the onset of the joint project (early 1994) the following topographic information was available to the wider science community:

1. The TUG87 global DEM compiled at the Technical University of Graz [*Wieser*, 1987]. This DEM exists in 5′, 30′ and 1° resolution. RSTX acquired these three versions of the TUG87 file from OSU [*Rapp, private communication*, 1994].

2. The ETOPO5U global DEM compiled at the National Geophysical Data Center in Boulder, Colorado [*NGDC*, 1988], which exists in 5′ resolution. ETOPO5U is an updated and improved version of ETOPO5 [*NGDC*, 1986].

3. The GGTOPO global DTM compiled at Trent University in Peterborough, Ontario, Canada [*Cogley*, 1987]. GGTOPO exists in 1° resolution.

Pavlis [1989] had examined the GGTOPO data and produced a slightly modified version of that file designated GGTOPO.MOD. He then used GGTOPO.MOD in combination with TUG87, to compile a global DTM designated OSUJAN89. This file was created in 30′ and 1° resolution (although the ice thickness and lake depth information was only available at the 1° level). The 30′ version was used to develop the degree 360 topographic-isostatic gravitational models described by *Pavlis and Rapp* [1990]. RSTX personnel acquired from OSU the 30′ and 1° versions of the OSUJAN89 file in August 1994 and the GGTOPO.MOD file in November 1994.

During one of the early meetings (on January 19, 1994), R.H. Rapp brought to the attention of the joint project the availability of an improved (over ETOPO5U) global 5′ DEM developed at the NGDC and designated TerrainBase. RSTX personnel acquired from R.H. Rapp the TerrainBase file, version 1.0 (v1.0), in August 1994. This 5′ DEM is documented in [*Row, Hastings and Dunbar*, 1995], and is sometimes referred to as "TerrainBase Beta version 1.0."

It is important to note here that none of the publicly available DEMs and DTMs discussed above contains any information related to the accuracy of the elevation or ice thickness and lake depth data.

2.3   The 5´x5´ Global Digital Topographic Model Development

From early discussions, the goal was set to develop as part of the gravity modeling effort, a global DTM at 5´ resolution, based on the best topographic information that could be made available within the joint project. In addition, the requirement was imposed that this 5´ DTM be made available to the community, without any classification restrictions. It was understood early on that to accomplish this would require the release of NIMA's DTED file at 5´ resolution. The DTED would provide the best elevation estimates over land, while TerrainBase v1.0 would provide the bathymetric information. Updated (over GGTOPO) ice thickness and lake depth information was sought by R.H. Rapp who contacted G. Cogley in June 1994, but unfortunately no updates to the GGTOPO file were available. Therefore, GGTOPO would be used to provide ice thickness and lake depth information, interpolated from the 1° to the 5´ resolution.

A significant obstacle towards meeting the above goal was the classified status of the DTED information globally and at 5´ resolution. While NIMA concentrated its efforts in accomplishing the release of this file, RSTX personnel begun the compilation of a global 5´ DTM (JGP95A), based on TerrainBase v1.0, TUG87, the GGTOPO.MOD file, and ice surface elevations obtained from satellite altimetry. NIMA provided RSTX with preliminary 15´ and 30´ releases of DTED, which RSTX used in various comparisons. The release of the 5´ DTED file in February 1995, enabled the first merging of this information into JGP95A. Further improvements and corrections were subsequently made to this file, through coordinated analyses and comparisons made by both the NIMA and the RSTX groups. These resulted in the development of the final 5´ DTM (JGP95E) which was created in November 1995. The steps leading to the development of JGP95E are discussed next in some detail.

2.3.1   Data Base Development Activities at NIMA

NIMA's DTED High Resolution Point Value File

The primary source of elevation information used to develop 5´, 15´ and 30´ global DEMs at NIMA is the DTED file which NIMA maintains. DTED is a digitized point value file compiled based on photographic and cartographic sources. The file is largely derived by photogrammetric methods; approximately five percent of its data are from map sources. The latitudinal spacing of the data is constant, equal to 3" (arcseconds). The longitudinal spacing varies with absolute latitude: it is 3" for $|\varphi| \leq 50°$, 6" for $50° < |\varphi| \leq 70°$, 9" for $70° < |\varphi| \leq 75°$, 12" for $75° < |\varphi| \leq 80°$, and 18" for $80° < |\varphi| \leq 90°$. DTED is vertically referenced to Mean Sea Level (MSL) and horizontally to WGS84. The high resolution DTED data are organized in files covering 1°x1° cells. A uniform error estimate is assigned to all point elevation values within a 1° cell. If multiple sources of elevation information exist within a 1° cell, the error associated with the least accurate source is assigned to all the data within that cell. This can reach ±200 m. For DTED data derived using photogrammetric techniques, the vertical error can reach ±30 m relative to MSL, and is expressed as a linear error at the 90 percent confidence level. The horizontal error can reach ±50 m relative to WGS84 and is expressed as a circular error at the 90 percent confidence level.

The DTED file goes through an extensive quality review. Its elevations are contoured and compared to existing maps to ensure proper modeling of elevations. Profile plots are used to identify abnormal slopes, spikes or depressions. Examination of sharp peaks, cliffs and other natural features is accomplished to account for naturally occurring topographic contrasts. Lake shorelines are overlaid and adjusted to the surrounding terrain. No elevations on the lake shores are allowed to be below the elevation of the lake. Shallow land areas just inside coastlines must have elevations equal to 1 m to define land boundaries. In areas where map and photogrammetricaly derived elevations are merged, ramp feathering is performed along common boundaries. The map source is always feathered into the photogrammetricaly derived source. In areas where maps are used from bordering nations and ramp feathering is needed, cartographic judgment is imposed.

The DTED file does contain most inland water elevations, but contains *no* ocean depths. There are land areas however, where elevations below MSL can occur. The *only* negative elevations occurring in the NIMA DTED file are where landforms and bodies of water are known to be below MSL. These areas are listed in Table 2.3.1–1.

Table 2.3.1–1. Areas below Mean Sea Level identified in the NIMA DTED file.

Name	Coverage Area
Caspian/Aral Sea	35–50° N, 43–65° E
Tunisia Depression	32–35° N, 5–9.5° E
Qattara Depression	27–30.75° N, 25–30° E
Death Valley	35–37° N, 118–116° W
Salton Sea	32.5–34° N, 117.25–115° W
Lake Eyre	30–26° S, 135–140° E
Lake Tiberias	32–33° N, 35.25–35.75° E
Turfan Depression	40–45° N, 87–92° E
Dead Sea	29.75–32° N, 35–36° E

NIMA's 5´, 15´ and 30´ Mean Elevation DEMs

During the summer of 1994, NIMA developed a preliminary global 5´ DEM. This file took into consideration NIMA's best 5´ mean elevation data and other available worldwide elevation sources. NIMA 5´ map-derived and NIMA 5´ DTED values were extracted and merged with the "Alpha version" of NGDC's TerrainBase global DEM. If the NGDC 5´ elevation data were based on larger scale map sources than overlapping NIMA map-derived data, the NGDC data were preferred over NIMA's map source data. Land boundaries between different merged elevation sources were checked using detailed contour plots. In some places, such as the Northwest Territories, Canada, Mexico, Poland, and Turkey, a 5´ shift in longitude was made from East to West relative to the NIMA 5´ DTED to merge the NGDC TerrainBase sources properly. The 5´ mean elevations computed from the DTED data were calculated using a weighted average over all points on or within each 5´x5´ cell.

As mentioned before, the high resolution DTED data are organized in files covering 1°x1° cells. Over those 1° cells that are not entirely composed of land areas, the 5´ mean elevations of their oceanic regions were initially filled with zero values. These erroneous zero values were subsequently screened out and overwritten with the TerrainBase bathymetric data. In lake regions, such as the Great Lakes and the Caspian Sea, the 5´ DTED showed some unrealistic variations of the lake surface elevations. Constant lake surface elevation values were subsequently imposed on the 5´ cells within each lake boundary.

Software was developed to check for possible spikes (program SPIKE) in the elevation file. Elevation spikes were only checked over land areas. The four surrounding elevation values were subtracted from each 5´ elevation and if all differences exceeded 500 m, the elevation point being evaluated was identified as a possible problem (spike). Five large elevation spikes, with differences exceeding 2000 m, were identified by SPIKE. These five spikes were examined in detail to determine the cause of the problem. Of the 5 spikes, 2 were near the coastline of Alaska, 1 in Canada and 2 in South America. The method for correcting spikes was to look for blunders, i.e., decimal point problems and transposed digits. No averaging of the spikes was performed. Fifty-two smaller possible elevation errors ranging from 500 to 2000 m were also identified by SPIKE. These smaller spikes were also examined for decimal point and transposed digit errors.

Elevation data over Antarctica and Greenland were found to have errors, detected through the use of detailed contour plots, where stair stepping features could be seen. Some of these elevation problems were not corrected in the development of NIMA's 5´ file.

NIMA also developed global DEMs containing 15´x15´ and 30´x30´ mean elevation values. Two such files, designated "dmatopo.min15.v082994" and "dmatopo.min30.v082994" were released by NIMA on August 29, 1994 [*Kenyon, private communication*, 1994]. These DEMs were used at RSTX for some of the preliminary comparisons discussed in the next section. However, the 5´ mean elevation file underlying these DEMs was still unavailable to the project at that time.

2.3.2 Data Base Development Activities at RSTX

The objective of the topographic data base development activities at RSTX was to compile a global 5´ DTM using the best data that were publicly available at that time (mid 1994). To accomplish this we decided to follow the same general procedures that were implemented in the development of the OSUJAN89 global DTM [*Pavlis*, 1989]. Specifically, we sought the best available 5´ DEM which could define the surface elevations and the ocean depths, while the GGTOPO.MOD file (interpolated to the 5´ level) would define ice thickness and lake depth information. According to the terrain classification in GGTOPO.MOD, the resulting global DTM would contain information pertaining to six terrain types: dry land below MSL, lake, oceanic ice shelf, ocean, grounded glacier and dry land above MSL. The compilation of the new 5´ DTM would rely on the merging and combination of information from the following sources:

1. TerrainBase (Beta) Version 1.0: This DEM was considered to be the best publicly available source of surface elevation and ocean depth information, in general. This file is based on the merging of information from 18 different sources [*Row, Hastings and Dunbar*, 1995]. These

are listed in Table 2.3.2–1. The file, as acquired from OSU, did not contain the source identification information for each 5´ cell.

Table 2.3.2–1. Elevation data by source, present in TerrainBase (Beta) version 1.0.

Source ID	Source Description	Num. of 5´ cells
0	Bathymetry gaps / 0 values on land	78916
2	Africa 5´ DEM	359280
5	North America 5´ DEM	202828
6	Andes Mountains 3´ DEM	44552
8	Australia 5´ DEM	99276
9	Austria 1.5´x2.5´ DEM	3252
10	Brazil Cerrados 2´ DEM	74484
11	Europe 5´ DEM	205880
12	Global FNOC 10´ DEM	1984240
13	Greenland 5´x10´ DEM	94984
16	Haiti 30” DEM	1068
17	Italy 30” DEM	5428
18	Japan 5´ DEM	13940
19	Madagascar 30” DEM	7312
20	Netherlands 3´x5´ DEM	376
21	Northwest Territories 5´ DEM	23312
22	Global Bathymetry 5´ DBM	5987788
26	United States 30” DEM	144284
	TOTAL	9331200

For various comparisons and analyses discussed next, a 30´ and 1° version of this file were developed, by area-weighted averaging of the 5´ values.

2. TUG87: TUG87 (in its 30´ version) was used originally in various comparisons with the file "dmatopo.min30.v082994." It was included in the current DTM development, as a "second best" (with respect to TerrainBase) source of surface elevation information.

3. GGTOPO.MOD: This was the main source of terrain classification, as well as information pertaining to ice thicknesses and lake depths. The original 1° file was "split-up" into 30´ and 5´ versions. This was done by assigning identical information to all 4 30´ cells within a given 1° cell (and similarly for the 144 5´ cells).

4. ALTIM94: One of the most problematic areas in terms of accurate elevation information is the Antarctic continent. Ambiguities related to the actual surface represented in various DEMs (ice surface, equivalent rock topography, or "bedrock" topography) have been reported in previous studies [*Laskowski*, 1984; *Pavlis*, 1989]. This situation had been hardly improved with the TerrainBase DEM, whose data over this area were obtained from the Fleet Numerical Oceanography Center (FNOC) global 10´ DEM. Height "terracing" and variations in grid detail were still identified by *Row, Hastings and Dunbar* [1995, page 5–12] to be common problems over Antarctica.

Development of ALTIM94

To improve the DEM quality over Antarctica, we decided to investigate the possibility of using ice surface orthometric heights, computed from ellipsoidal heights derived from satellite radar altimetry and geoid undulation information implied by a high-degree global geopotential model. To this end, we acquired a gridded data set of altimetry-derived ellipsoidal heights from J. Zwally (NASA GSFC) [*private communication*, 1994]. The original data set was given on a 10 km equidistant grid, covering the continental and ice shelf areas within the window $-81.5° \leq \varphi \leq -60°$, $0° \leq \lambda < 360°$. These values were derived from re-tracked ERS–1 altimetry. This data set was used to compute a corresponding 5′ equiangular grid of area-mean values. Details on the data processing and the re-tracking algorithm used to derive the ellipsoidal elevations can be found in [*Zwally et al.*, 1994], which describes a preliminary version of the data set that we acquired. An equiangular 5′ grid of mean values of geoid undulations was computed from the composite model JGM–2/OSU91A to degree 360. These values were subtracted from the ellipsoidal heights, thus providing estimates of 5′ mean orthometric heights over the area of altimetric coverage. This orthometric height data set is designated ALTIM94. It represents unambiguously a mapping of the surface elevations.

Several comparisons were made between the elevations from various DEMs over Antarctica. Results from one set of such comparisons are summarized in Table 2.3.2–2. These particular comparisons considered 30′ mean values. Only those 30′ cells which are within $-81.5° \leq \varphi \leq -60°$ and whose surface elevation in TerrainBase is greater than zero were involved in the comparisons of Table 2.3.2–2. Figure 2.3.2–1 shows the differences between the TerrainBase and the ALTIM94 DEMs over the 13116 30′ cells which were compared.

Table 2.3.2–2. Statistics of surface elevations and surface elevation differences implied by various DEMs over parts of Antarctica. 13116 30′ cells compared. Mean and RMS values are area-weighted estimates. Units are m.

DEM(s) Compared	Minimum	Maximum	Mean	RMS
TBase	.3	4017.4	2051.5	2317.6
TBase - ALTIM94	−962.1	1555.1	−1.4	266.3
TUG87 - ALTIM94	−984.8	1462.7	16.1	264.9
NIMA94 - ALTIM94	−984.8	1465.7	13.8	262.1

TBase = TerrainBase v1.0, NIMA94 = dmatopo.min30.v082994
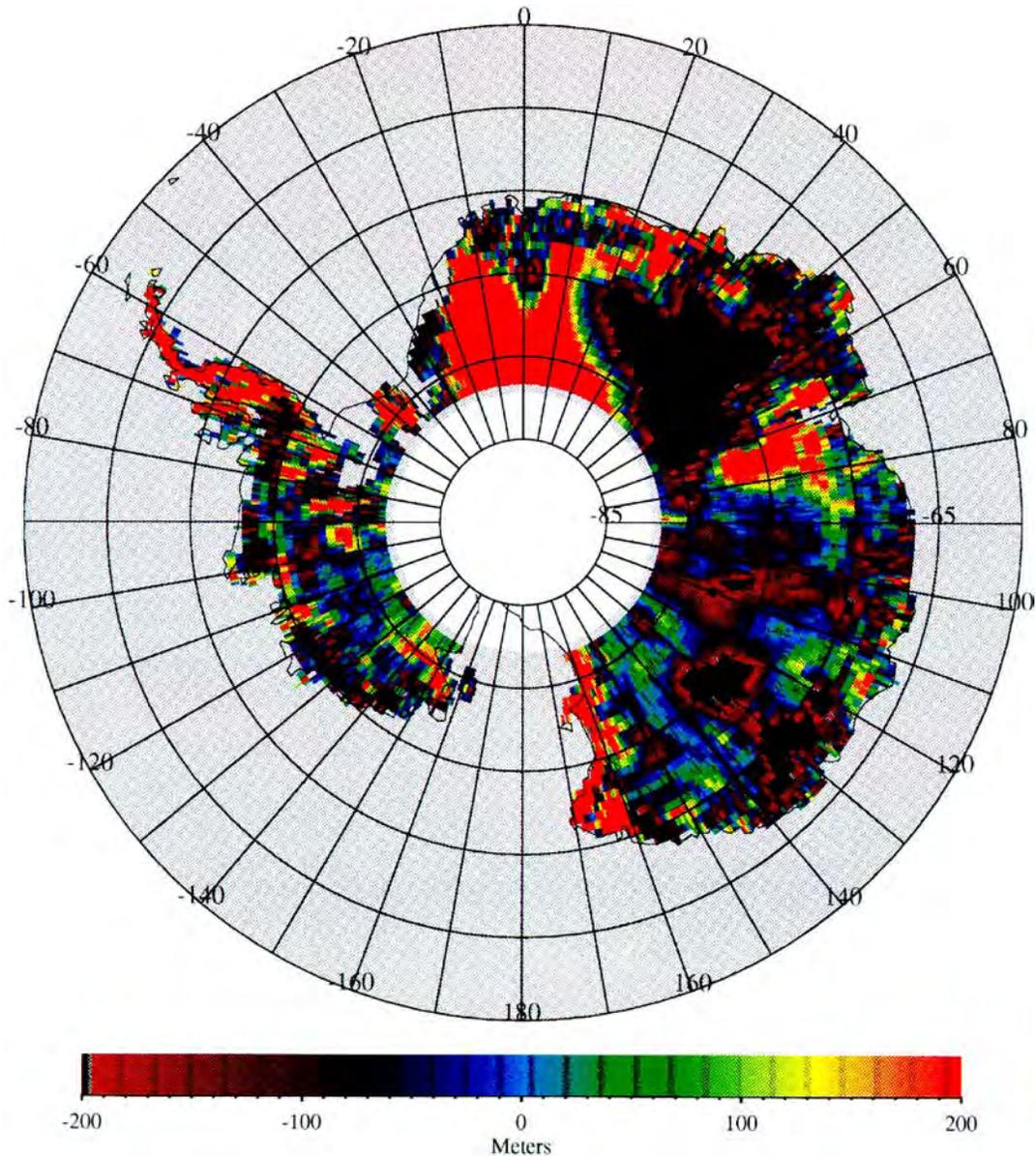
Figure 2.3.2–1. Orthometric height differences over Antartica in terms of 30´x30´ mean values. TerrainBase v1.0 minus ALTIM94 (see text).

The orthometric heights in ALTIM94 are subject to radial orbit errors, altimeter data errors, surface slope-induced errors, as well as errors (commission and omission) of the model undulations. Radial orbit errors had been reduced through cross-over adjustment techniques, prior to the estimation of ellipsoidal heights. The slope-induced errors can reach tens of meters over crevasses and terminus areas of the ice cap. These were reduced using the algorithm described in [*Brenner et al.*, 1983]. Over flat ice surfaces with good altimeter coverage, the 5´ mean ellipsoidal heights can reach accuracy of ±2 m or better. Geoid undulation errors over the area in question can be quite large, given its poor surface gravity data coverage. *Rapp* [1996]

reported geoid undulation errors reaching 9 m in some areas around 78° S latitude (Weddell Sea), for the OSU91A model (to degree 360). He also suggested a ±2 m geoid undulation error for the same model, as a representative estimate applicable to "land areas with no surface gravity data" (as is the case for the most part of Antarctica). With these considerations in mind, one may assign conservative estimates of the total error in the 5′ mean orthometric heights of ALTIM94 that range from ±5 m (flat ice surface) to ±20 m (steep sloping surface). The RMS differences in Table 2.3.2–2 exceed the expected errors of the ALTIM94 elevations by more than an order of magnitude. Several extended regions can be seen in Figure 2.3.2–1, where the differences TBase-ALTIM94 exceed 200 m in absolute value. These large differences should be attributed (primarily) to gross errors in the "terrestrial" DEMs, which also implies that ALTIM94 should be the preferred source of surface elevation information over this area. Maps of the differences TUG87-ALTIM94 and NIMA94-ALTIM94 (not shown here) were practically identical to the map of Figure 2.3.2–1. This is not surprising since the terrestrial DEMs most probably share the same data over the area in question. The altimetric file represents information independent from these DEMs.

The Development of the JGP95A DTM

By design, the development of JGP95A followed closely the general procedures used in the development of the OSUJAN89 file [*Pavlis*, 1989]. According to the terrain classification used in the GGTOPO DTM, JGP95A would consider six terrain types, as illustrated schematically in Figure 2.3.2–2 (adapted from [*Pavlis and Rapp*, 1990]). The parameters S_h, L_d, O_d, and I_t represent surface elevation, lake depth, ocean depth and ice thickness, respectively. According to this terrain classification, a global DTM must provide all the necessary information in order to define these parameters, for every equiangular cell on the ellipsoid. Figure 2.3.2–2 also lists certain constraints that the data associated with each terrain type must fulfill, in order to be physically meaningful. When topographic data from different sources are merged together to produce a DTM (as was the case here), it is possible to encounter violations of these constraints in the resulting file. For example, a cell identified as "ocean" in one source, may have positive surface elevation in another. It is therefore mandatory that any existing violations of these constraints in the merged DTM be identified, examined carefully and somehow resolved, if one wishes to produce a DTM that would be at least self-consistent.

The development of the merged DTM requires also the design of some merging algorithm, which would select the "best" topographic information among multiple, overlapping sources that may be available regionally or globally. Quantitative measures of what is "best", are difficult to derive in most cases, so our merging algorithm gave preference (in general) to the most recent elevation information available. Our decisions were influenced also by the documentation accompanying various elevation sources. Numerous statistics were computed and maps illustrating elevation differences between different sources were examined in an attempt to identify problems and exclude spurious data. We summarize next the results of certain comparisons, which guided the design of the merging algorithm used to develop JGP95A.
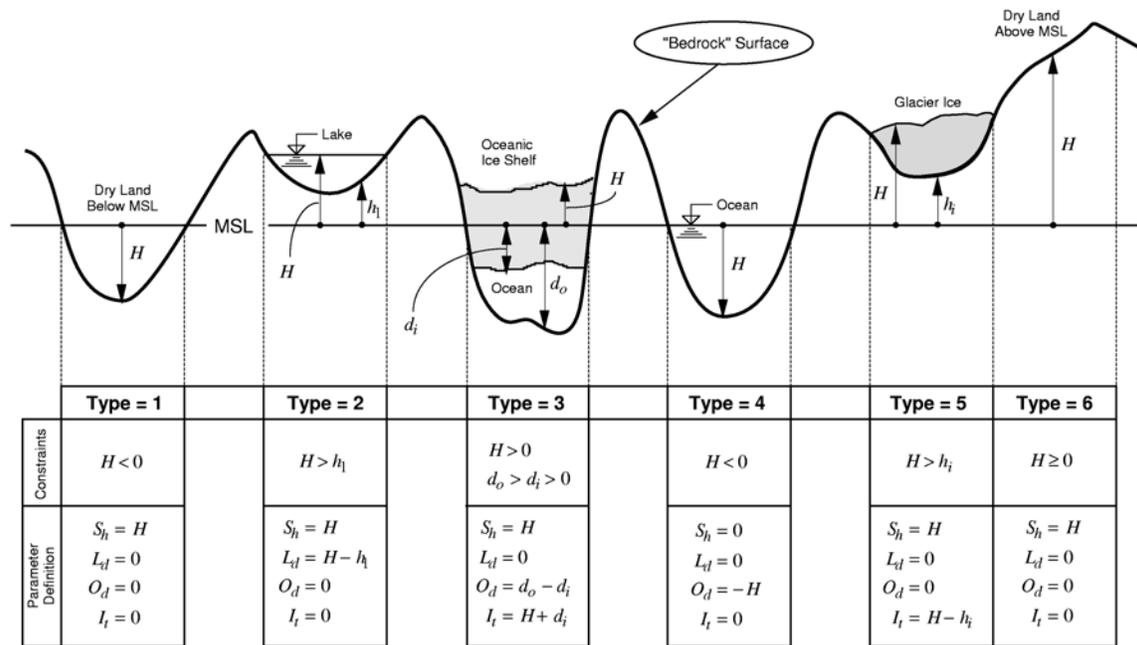
Figure 2.3.2–2. Terrain classification and associated notation (adapted from [*Pavlis and Rapp*, 1990]).

	Type = 1	Type = 2	Type = 3	Type = 4	Type = 5	Type = 6
Constraints	$H < 0$	$H > h_l$	$H > 0$ $d_o > d_i > 0$	$H < 0$	$H > h_i$	$H \geq 0$
Parameter Definition	$S_h = H$ $L_d = 0$ $O_d = 0$ $I_t = 0$	$S_h = H$ $L_d = H - h_l$ $O_d = 0$ $I_t = 0$	$S_h = H$ $L_d = 0$ $O_d = d_o - d_i$ $I_t = H + d_i$	$S_h = 0$ $L_d = 0$ $O_d = -H$ $I_t = 0$	$S_h = H$ $L_d = 0$ $O_d = 0$ $I_t = H - h_i$	$S_h = H$ $L_d = 0$ $O_d = 0$ $I_t = 0$

Global elevation comparisons using 30´ mean values were made between the files TUG87, TerrainBase v1.0, ETOPO5U and "dmatopo.min30.v082994" (hereon designated NIMA94). These comparisons indicated that:

1. The bathymetric data of NIMA94, TerrainBase and ETOPO5U are essentially identical over most ocean areas. TerrainBase differs from NIMA94 and ETOPO5U over a limited area off the coast of Peru-Chile, in some areas of the Mediterranean and in some coastal regions around Japan. The bathymetric data of TUG87 however were systematically different from the corresponding data of the other three files. These differences were found to be correlated with depth.

2. The comparisons over land areas indicated that TerrainBase and NIMA94 agreed well over most of N. America (except for some areas in Alaska and Yukon, and areas in Mexico and Central America). TerrainBase and NIMA94 contained approximately the same values over Europe and (to a lesser extent) over Australia. The largest differences between TerrainBase and NIMA94 were found over Asia (particularly China and Tibet). Large differences between these two files exist also over S. America (especially the Andes Mountains) and over regions of Africa. Over S. America and Africa, the differences NIMA94 minus TUG87 were (in general) smaller that the differences TerrainBase minus TUG87. Over the ice covered regions of Greenland and Antarctica, NIMA94 and TUG87 were practically identical. The surface elevations from TerrainBase differed significantly from the corresponding values of the NIMA94 and TUG87 files. A closer examination of the data over these regions, employing

also altimetry-derived estimates of the surface elevations, was necessary to clarify the situation over these areas.

Comparisons of the ice surface elevations of various files, over areas classified as "grounded glacier terrain" (type 5), were made over both Greenland and Antarctica. Over Greenland, we constructed again a file of 5´x5´ ice surface elevations derived from altimetry (GEOSAT and ERS–1 data) and the JGM–2/OSU91A geoid model. This file was compared to the TerrainBase 5´ file. Over the relatively smooth, inland areas of the ice cap, the two elevation sources agreed to better than ±20 m. Differences exceeding ±200 m were identified near the coast. The TerrainBase data over Greenland were contributed by S. Ekholm of Kort-og Matrikelstyrelsen (KMS), Denmark. These data were derived from GEOSAT and ERS–1 altimetry and airborne altimetry acquired during the Greenland Aerogeophysics Project (GAP), among other sources [*Row, Hastings and Dunbar*, 1995, p. 4–32]. Based on the documentation, the TerrainBase data over Greenland were considered preferable over our own altimetric estimates of the ice surface elevations (which did not include any GAP data).

The situation over Antarctica is more complicated. Due to the inclination of ERS–1, ice surface elevations derived from altimetry were not available south of 81.5° S. Therefore, to cover the entire continent, the altimetry-derived elevations need to be "patched" with some terrestrial source south of 81.5° S. In order to avoid large step discontinuities at the border of the two sources, we decided to proceed as follows. We compared the altimetric estimates of the ice surface elevations with those from various DEMs, over their area of overlap. This was done in order to identify which terrestrial DEM was closer to the altimetric estimate. This comparison was performed in terms of 1° mean values, over 3045 1° cells classified as "grounded glacier" in the GGTOPO.MOD DTM, and located south of 60° S latitude. The results of these comparisons are summarized in Table 2.3.2–3. NIMA94 was not included in these tests, since it had been verified already that NIMA94 is practically identical to TUG87 over this area, and furthermore NIMA94 contained an erroneous set of data along the parallel of approximately 82° S latitude (TUG87 was free of this problem). Based on the results of Table 2.3.2–3, the best candidate to provide the ice surface elevations south of 81.5° S was TUG87, considering especially the very small overall bias (–2.1 m) between TUG87 and ALTIM94.

Table 2.3.2–3. Statistics of surface elevation differences between various DEMs over grounded glacier (type 5) terrain south of 60° South latitude. 3045 1° cells compared. Mean and RMS values are area-weighted estimates. Units are m.

DEMs Compared	Minimum	Maximum	Mean	RMS
GGTOPO - ALTIM94	−1164.0	2542.0	76.1	354.9
TBase - ALTIM94	−800.8	1184.8	−20.4	256.7
TUG87 - ALTIM94	−745.2	1199.7	−2.1	253.9

TBase = TerrainBase v1.0, GGTOPO = GGTOPO .MOD

An additional consideration related to the ice surface elevations south of 81.5° S latitude was related to "terracing" problems that existed in the TUG87 file. These were mostly visible in plots of the meridional slopes of the ice surface, where they manifested their presence as concentric circles of constant latitude. To reduce these discontinuities and also provide a smooth transition from the ALTIM94 to the TUG87 elevations, we decided to form a smoothed version of the ice surface elevations over Antarctica as follows. We constructed a file of 5´x5´ ice surface elevations extending from 78° S to the South Pole. Between 78° S and 81.5° S the data consisted of ALTIM94 values, while south of 81.5° S the data were taken from TUG87. We then performed a moving average smoothing of these data, using a moving "window" extending 100 km in the N-S and 50 km in the E-W directions and centered at the center of each 5´ cell. The 78° S to 81.5° S coverage with ALTIM94 data was introduced to provide a "tie" between the TUG87 and the ALTIM94 data sets. However, smoothed ice surface elevations were only used south of 80° S latitude when forming JGP95A. This smoothing procedure reduced significantly the "terracing" effects observed in the output data set, which was designated "Smoothed Antarctica."

Another terrain type that required special consideration was the "oceanic ice shelf" (type 3). Preliminary comparisons demonstrated that TerrainBase contained identically zero values for the ice surface elevation over most of the area covered by the Ross and Ronne ice shelves. Over the Ross ice shelf, TerrainBase, TUG87 and NIMA94 contained practically the same data. Over the Ronne ice shelf, NIMA94 and TUG87 were found to be identical, while TerrainBase contained slightly different elevations from NIMA94 (or TUG87). These comparisons indicated that TerrainBase, TUG87 and NIMA94 do not contain reliable values for the ice surface elevations over ice shelf areas. GGTOPO.MOD and ALTIM94 were therefore considered as candidates for providing the ice surface elevations over these areas. Over the Ross ice shelf, GGTOPO.MOD minus ALTIM94 surface elevations had a mean difference of 1.2 m and an RMS difference of 21.7 m. The corresponding statistics over the Ronne ice shelf were –21.8 m and 75.5 m. The differences TerrainBase minus ALTIM94 over the Ronne ice shelf had a mean value of –101.0 m and an RMS value of 225.1 m. Based on these comparisons, we considered ALTIM94 to be the best candidate source of the ice surface elevations over the ice shelf areas, and GGTOPO.MOD to be the second best alternative source.

The conclusions drawn from the comparisons of the various DEMs guided the design of a merging procedure which was used to develop JGP95A. We outline this procedure in brief next.

A. Globally: TerrainBase determines the coastline, i.e., is used to distinguish cells representing dry land above MSL from those representing ocean areas. TerrainBase also provides the surface elevation and ocean depth values and can change the terrain type from that specified in GGTOPO.MOD (5´ split-up version). GGTOPO.MOD exclusively defines cells classified as lake and provides the lake depth and ice thickness information.

B. Areas of $\varphi < -60°$: TerrainBase determines the coastline and the ocean depth. However, different considerations apply here to different terrain types. Over grounded glacier or dry land above MSL, the surface elevation is taken from ALTIM94. If ALTIM94 value is not available, TUG87 value is used. For grounded glacier the ice thickness is taken from

GGTOPO.MOD. Over oceanic ice shelf, the surface elevation is taken from ALTIM94. If ALTIM94 value is not available, GGTOPO.MOD value is used. The ice thickness and ocean depth information is taken from GGTOPO.MOD. Over the Ross and Ronne ice shelves, in cases where the ice thickness, ocean depth and surface elevation values are causing inconsistencies (i.e., intermixing layers), we maintain the GGTOPO.MOD ice thickness and ocean depth values, and set the surface elevation equal to its average value over the corresponding ice shelf (only eight 5´ cells over the Ronne ice shelf required such action to be taken).

C. Areas of $\varphi < -80°$: The surface elevations here were taken from the "Smoothed Antarctica" data set. GGTOPO.MOD defined the ice thickness and ocean depth values.

This merging procedure created the JGP95A 5´ DTM on February 13, 1995. This file was subsequently checked to verify its internal consistency. It was verified that only one type of constraint violation was present in the JGP95A DTM data. There were 2736 5´ cells identified as "lake", but having a lake depth value of zero. Further investigation showed that this problem originated from the 1° version of GGTOPO.MOD, where 19 1° cells with this problem were identified. The zero values for the lake depth over these 19 1° cells may also be due to the format used in the original GGTOPO file, where data are rounded off to the nearest 10 m. The split-up of GGTOPO.MOD into 5´ cells transferred this problem into the corresponding 2736 (=19x12x12) cells of JGP95A (since GGTOPO.MOD 5´ version exclusively defined lake areas in our merging algorithm). Anticipating the release of the 5´ NIMA DTED file (which would provide terrain information in original 5´ resolution without any need for split-up), we left the 2736 problematic cells in JGP95A uncorrected at that point. Of the total 9331200 5´ cells, the surface elevation (or depth) in JGP95A originates from TerrainBase in 8395889 cells, from TUG87 in 4013 cells, from ALTIM94 in 411617 cells, from GGTOPO.MOD in 1273 cells, from "Smoothed Antarctica" in 518400 cells, and from the average over the Ronne ice shelf in 8 cells.

2.3.3 The Merging of the NIMA and RSTX Data Bases

The development and verification of the JGP95A 5´ DTM was presented during a meeting of the joint project held on February 27, 1995. Several problems associated with its data were identified by the RSTX team, including the presence of "spikes" and "terraces", and the misidentification of lakes and in some areas of dry land below MSL. The RSTX team recommended that further improvements over JGP95A were necessary. These could be facilitated significantly by: a) the release of the 5´ NIMA DTED file, and b) the acquisition from NGDC of source code information identifying the specific origin of each 5´ elevation value in TerrainBase.

During the same meeting, NIMA released to the joint project the 5´ DTED information. Therefore, it became possible to proceed with the development of a 5´ global DTM which would incorporate the best elevation information available within NIMA. It was recognized at that meeting that the merging of DTED and JGP95A data could be significantly expedited if NIMA and RSTX personnel were to work together at the same site. This was indeed done and the combined effort led to the development of the JGP95B 5´ DTM.

The Development of the JGP95B DTM

The 5′ DTED file received from NIMA was designated "dmatopo.min05.v022795," and for brevity will be referred to as NIMA95. The original file contained six pieces of information associated with each 5′ cell. These were the latitude and longitude of the cell's center, the cell's mean elevation (in meters), a code for NIMA's internal use, an elevation type and a source code. Six possible elevation types were present in the file: ocean (5783 5′ cells), mixed land and ocean (29485 cells), land possibly negative (11425 cells), land positive (1760717 cells), large lake included (8657 cells), and unknown (7515133 cells). Five possible source codes were present in the NIMA95 file: WGS72 DTED (4136 cells), WGS84 DTED (1471546 cells), mixed DTED (42360 cells), map derived (298025 cells), and NGDC TerrainBase (7515133 cells; it is not always clear which version of TerrainBase was used here). The geographic distribution of elevation types and source codes in the NIMA95 file are shown in Figures 2.3.3–1 and 2.3.3–2, respectively. Later on, NIMA informed the project that the WGS72 source code identification was incorrect, and should have been WGS84 DTED instead (i.e., all DTED data were horizontally referenced to WGS84).
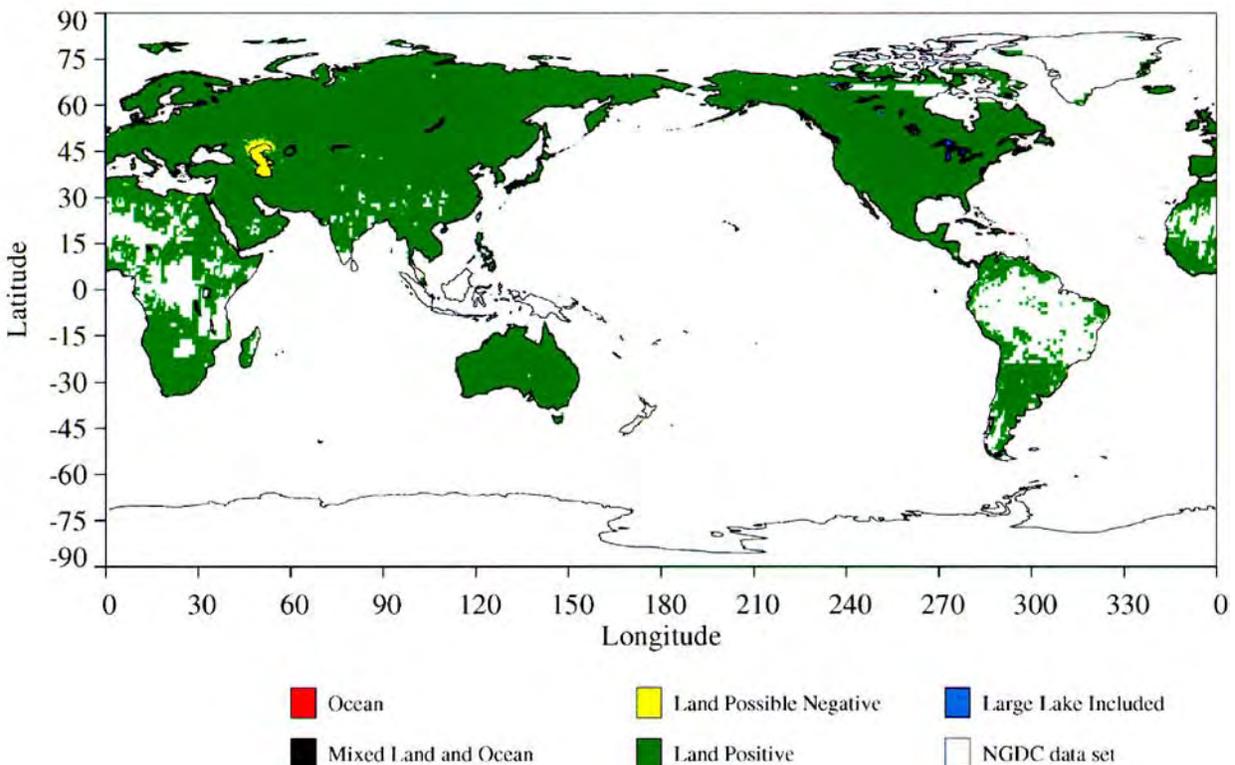
Figure 2.3.3-1. Geographic distribution of elevation types present in the NIMA95 5′x5′ elevation file
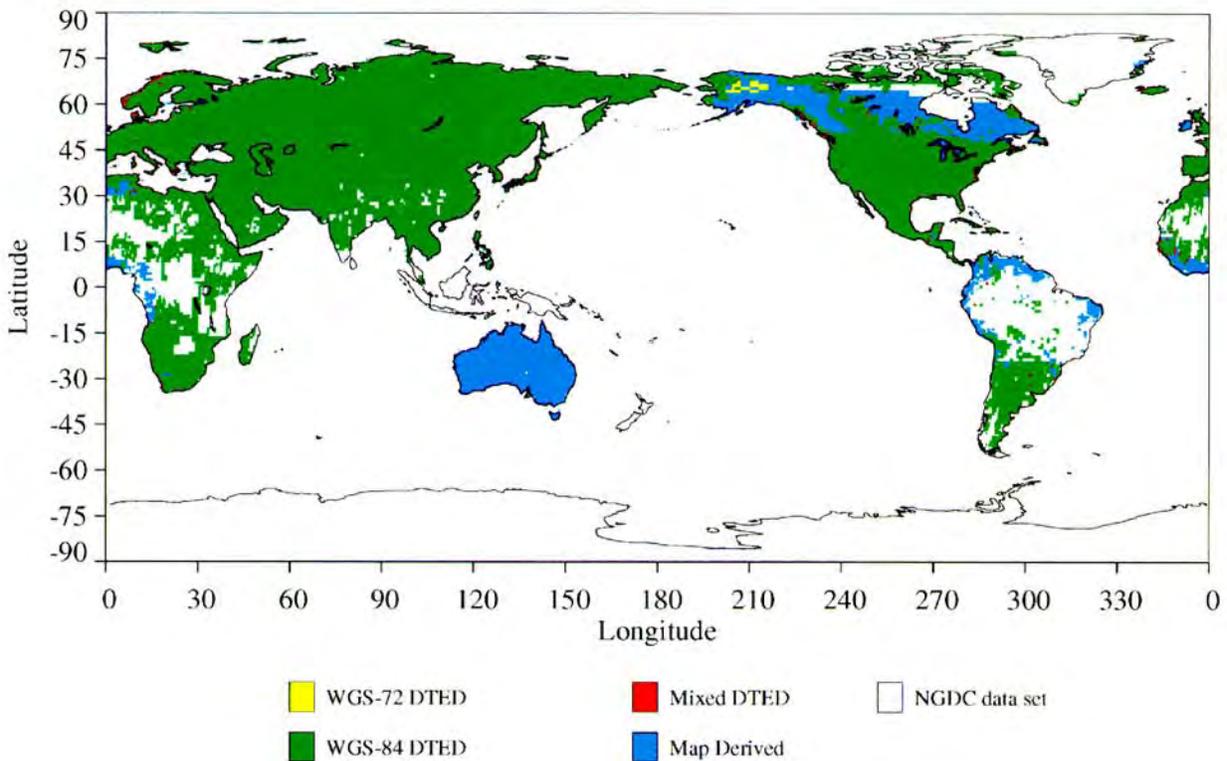
Figure 2.3.3-2. Geographic distribution of elevation source codes present in the NIMA95 5´x5´ elevation file

NIMA recommended that DTED surface elevations, where available, were to be preferred over any other elevation source. However, it was not always clear if the same was applicable for "mixed DTED" or "map derived" data in the NIMA95 file. The latter was a collection of 5´ mean DEMs assembled to support various projects within NIMA. These data were determined from 1:100000 or larger series charts, and were used mostly in Canada, Africa, and the northern regions of South America. In the South American regions of Peru and Columbia the map source data were derived mostly by visual interpolation of point values from topographic contours and simply averaged to 5´ mean elevations. The contour frequency dictated the number of points to average as either one, four, or nine. These 5´ DEMs were considered more accurate than the TerrainBase, US Navy Fleet Numerical Oceanography Center, and 10´ DEM sources over these South American regions.

To enable somewhat more informed decisions to be made regarding the merging of the DTED and the TerrainBase data, RSTX personnel requested and received from NGDC [*Hastings, private communication*, 1995] the source codes identifying the origin of the TerrainBase data (see Table 2.3.2–1). Figure 2.3.3–3 shows the geographic distribution of the (18) elevation sources that comprise TerrainBase v1.0. With the information available at that point, we decided to compare the NIMA95 and TerrainBase surface elevation data, considering each source identified within TerrainBase separately. We excluded from this differencing the cells in

NIMA95 whose source was NGDC, to prevent possible identical values from participating in the comparisons. Statistics from these comparisons are given in Table 2.3.3–1.
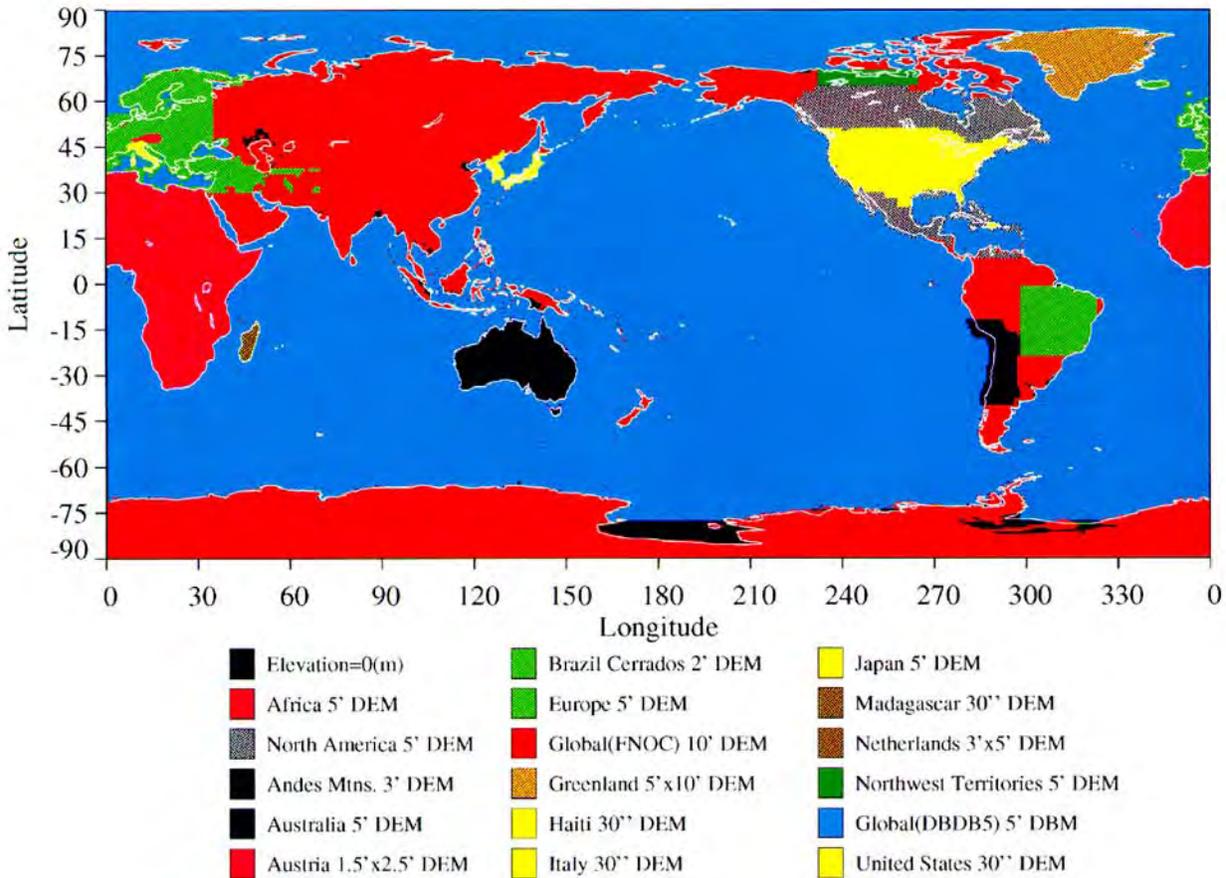
Figure 2.3.3-3. Geographic distribution of elevation source codes present in the TerrainBase v1.0 5´x5´ elevation file

Table 2.3.3–1 should be examined with due consideration to the fact that in many areas the overlapping portion of NIMA95 and TerrainBase, covered by data of different origin, represents only a small portion of the entire area covered by the corresponding TerrainBase source. Such examples are the "Global Bathymetry 5´ DBM" and the "Greenland 5´x10´ DEM." Table 2.3.3–1 provides the total number of 5´ cells within a given TerrainBase source, as well as the number of the 5´ cells involved in each comparison. This enables one to assess how representative are the statistics of the differences given in Table 2.3.3–1, over the entire extent of a given TerrainBase source. TerrainBase sources that are well represented in this regard include the "United States 30" DEM," the "Europe 5´ DEM," and the "Australia 5´ DEM." It is noteworthy that even over these three areas (which are probably among the best surveyed areas of the Earth), there are significant differences between the two data bases. Even more disconcerting is the fact that both the "United States 30" DEM" and the "Europe 5´ DEM" in TerrainBase were developed and contributed by NIMA [*Row, Hastings and Dunbar*, 1995], although it is not clear if the

contributed data were based on DTED information. The comparison over the TerrainBase source designated "Global FNOC 10´ DEM" covers primarily Asia (and some regions in S. America and Alaska—see Figures 2.3.3–2 and 2.3.3–3). Over these regions, some of the largest differences between the two data bases exist. The large relative bias (–26 m) is particularly alarming. In lieu of a third independent data set for comparison, we generally accepted DTED as the most accurate source of surface elevation information.

Table 2.3.3–1. Statistics of the 5´ elevation differences NIMA95 minus TerrainBase (Beta) version 1.0, by source present in TerrainBase (Beta) version 1.0. Mean and RMS differences are area-weighted estimates.

TerrainBase Source Description	Number of 5´ cells		Mean Diff. (m)	RMS Diff. (m)
	Total	Compared		
Bathymetry gaps / 0 values on land	78916	12937	2.8	50.0
Africa 5´ DEM	359280	232413	-0.3	113.7
North America 5´ DEM	202828	162726	–2.9	88.9
Andes Mountains 3´ DEM	44552	27773	–5.0	156.7
Australia 5´ DEM	99276	98832	1.6	57.0
Austria 1.5´x2.5´ DEM	3252	3252	–3.6	24.6
Brazil Cerrados 2´ DEM	74484	12688	–25.4	100.8
Europe 5´ DEM	205880	162138	–2.9	43.4
Global FNOC 10´ DEM	1984240	907005	–25.7	198.9
Greenland 5´x10´ DEM	94984	4227	–67.1	234.4
Haiti 30" DEM	1068	1059	–39.9	103.9
Italy 30" DEM	5428	5114	–8.4	42.5
Japan 5´ DEM	13940	10123	–6.9	39.1
Madagascar 30" DEM	7312	5229	–7.0	46.1
Netherlands 3´x5´ DEM	376	373	-0.1	1.6
Northwest Territories 5´ DEM	23312	13753	-0.4	34.6
Global Bathymetry 5´ DBM	5987788	12287	38.5	197.3
United States 30" DEM	144284	144138	0.7	14.8

J. Factor (NIMA) visited RSTX during March 20–24, 1995. He provided statistics of some comparisons performed earlier at NIMA, where the preliminary (Alpha) version of TerrainBase was compared to the DTED data. His results indicated that the TerrainBase Alpha version data in some areas (i.e. Europe and North America) were shifted (mis-registered) by 5´ in longitude to the west, relative to DTED. It was important to verify that this shift was not also present in the TerrainBase (Beta) v1.0 data. Comparison of the statistics given in Table 2.3.3–1, with corresponding statistics computed earlier at NIMA, verified that TerrainBase v1.0 had indeed corrected this shift, at least over the areas identified previously by NIMA.

Next, we designed a selection algorithm that would merge the DTED data with TerrainBase, ALTIM94, TUG87 and the rest of the files used to develop JGP95A. This merging procedure took into account the results from the comparisons given in Table 2.3.3–1, and recommendations made by J. Factor based on his insight regarding DTED. In general, the selection algorithm gave

preference to NIMA95 information. However, five TerrainBase sources were identified whose data were considered more reliable than the corresponding NIMA95 data. These were: the "Australia 5′ DEM," the "Brazil Cerrados 2′ DEM," the "Greenland 5′x10′ DEM," the "Northwest Territories 5′ DEM" and the "Global Bathymetry 5′ DBM." Over the corresponding areas, the NIMA95 file contains (primarily) either "map derived" elevations, or elevations which originated from earlier NGDC compilations (see Figure 2.3.3–2). The existing documentation [*Row, Hastings and Dunbar*, 1995] gave some supporting arguments for our selections. The merging procedure over areas with $\varphi < -60°$ and $\varphi < -80°$ was the same as discussed previously for JGP95A, since the NIMA95 file contains only NGDC data over these areas (see Figure 2.3.3–2). Application of this merging procedure produced on April 9, 1995 the 5′ global DTM designated JGP95B. This file incorporated elevation data from 28 sources. NIMA's DTED was the predominant source over areas of "dry land above MSL." JGP95B used DTED values for 1481629 5′ cells out of the 1518042 cells where such values were available, i.e., 97.6 percent of the available DTED data were selected by the merging process. JGP95B went through the same verification process as JGP95A. 1820 5′ cells were identified here, classified as "lake" but having the problematic zero lake depth values. Thus the more detailed (over GGTOPO.MOD) NIMA95 5′ terrain classification (where available) did help resolve 916 of the occurrences of this conflict, out of the 2736 identified previously in JGP95A. Over the Caspian Sea, a constant -27 m surface elevation was assigned (treated as a separate source).

During the above merging procedure we allowed TerrainBase to be the source determining the coastline. This resulted in 12287 5′ cells where a DTED positive surface elevation existed, while JGP95B was classifying the cells to be oceanic. These cells were (obviously) located near coastal areas, and manifested a conflict between the TerrainBase and the DTED realizations of the coastline. This problem will be revisited in Section 2.3.4.

Using program SPIKE (which was made available to RSTX by NIMA), we identified (based on a 500 m criterion) 1700 possible "spikes" present in JGP95B. Of these, 388 occurred over land areas. The JGP95B DTM and a file containing the locations of the possible "spikes" was then transferred to NIMA for further analysis and evaluation.

2.3.4 The Evolution of the JGP95 Data Bases

The analysis and evaluation of JGP95B at NIMA identified certain problems which necessitated that modifications be made to this file. As the joint project work continued, further analyses revealed some additional problems. The various modifications that were gradually made on the DTM are documented next.

JGP95C

Due to time constraints NIMA decided to concentrate on the investigation of only the 388 possible "spikes" that were identified over land in the JGP95B file. Contour plots were created for evaluation, and "spikes" outside the areas of DTED coverage were checked. Since DTED undergoes an extensive evaluation process within NIMA, only those "spikes" where NIMA 5′ DTED and TerrainBase data merged were examined. If an elevation trend in any way showed

similar behavior near the "spike" as over it, the "spike" was considered to be a valid elevation. In this fashion, only 14 erroneous elevations were finally identified. NIMA provided the recommended elevation information for these 14 cells, and suggested some additional changes over other geographic regions. These recommendations were reviewed by RSTX personnel and finally the two teams agreed to make the following three types of modifications (in addition to the 14 "spike" cells) to the JGP95B DTM.

1. Coastlines: As it was mentioned previously, 12287 (coastal) 5´ cells were identified during the development of JGP95B, where TerrainBase provides a depth (from the "Global Bathymetry 5´ DBM" source), while NIMA95 provides a positive DTED 5´ mean elevation. NIMA indicated that the coastal information from DTED was more reliable than the corresponding TerrainBase information. We modified our merging procedure accordingly, so that DTED information (wherever available), would discriminate between land and ocean 5´ cells, effectively defining a 5´ realization of the coastline.

2. Thule, Greenland (76° N - 78° N, 286° E - 300° E): Over Greenland, the "Greenland 5´x10´ DEM" in TerrainBase was preferred over the DTED data, during the development of JGP95B. This was due to minimal DTED coverage over Greenland. Based on contour plots, NIMA felt that the DTED elevations over Thule, Greenland, provided more detail than the TerrainBase data and that they should be used instead of the values found in TerrainBase. This affected 2054 5´ cells in total, 445 of which were already considered in the coastline modification discussed above. Therefore, 1609 5´ cells were modified here.

3. Northwest (NW) Territories: The TerrainBase documentation stated that "spikes" had been identified in this area which NGDC had already resolved. The mean and RMS difference in the surface elevations between the "Northwest Territories 5´ DEM" and the NIMA95 5´ DEM were -0.4 m and 34.6 m, respectively. Since the differences between the two data sets were relatively small and the NGDC documentation indicated that this area was examined carefully during the TerrainBase development, we had decided to give preference to the "Northwest Territories 5´ DEM," over NIMA95, during the development of JGP95B. NIMA however reported that the DTED data (which cover approximately half of the area in question) should have been preferred. A total of 13507 5´ elevations within the NW Territories were replaced here.

In addition to the above modifications, RSTX personnel decided to modify the elevations of 5 cells on the coast of Antarctica. Based on a similar "spike" evaluation, it was decided that the TUG87 5´ mean elevation over these 5 cells, was more reliable than the elevation information deduced from satellite altimetry. These 5 cells were located over very steep slopes of the Antarctic coast.

Application of the above modifications to the JGP95B file produced the JGP95C 5´ DTM, which was finalized in May 15, 1995. All the intended modifications to JGP95B were also collected in separate files, and during the development of JGP95C, it was verified that these modifications (and these only) were accurately implemented. JGP95C contained in total 1506832 5´ cells whose surface elevation originated from NIMA's DTED file (i.e., 99.3 percent of all the available DTED data were used in JGP95C). At that time, the joint project agreed that JGP95C

would be the fundamental DTM providing elevation information necessary during the various steps of the prediction of 30′ mean gravity anomalies, and their subsequent analysis for the development of the geopotential models.

JGP95D and JGP95E

The JGP95C DTM was used by NIMA during a comprehensive re-evaluation of the 30′ mean gravity anomaly predictions (primarily over land areas). The resulting gravity anomaly file from this prediction was released to the joint project in September 1995. Combination solutions developed using this gravity anomaly file (see Section 8.5), demonstrated some degradation of the results over the eastern part of Australia, as compared to solutions based on a previous 30′ mean anomaly compilation. Examination of gravity anomaly residuals showed that these were highly correlated with the differences between the NIMA95 ("map derived") elevations and the TerrainBase ("Australia 5′ DEM") values over this area. Additional tests were carried out, using also comparisons with independent geoid undulation information from GPS and leveling. The gravity anomaly predictions which were based on the NIMA "map derived" elevations, were found to produce smaller gravity anomaly residuals in the combination solution (i.e., they agreed better with the satellite-only model). Also, the combination solution which was based on them, agreed better with the GPS/leveling information, than the corresponding solution employing anomalies based on the JGP95C file. These results indicated that the NIMA "map derived" elevations were preferable to the TerrainBase values, over the land areas of Australia and Tasmania east of longitude 140° E. This modification affected 36047 5′ cells of the JGP95C file and produced the JGP95D DTM on October 23, 1995.

A final verification of the JGP95D DTM performed at NIMA indicated that an additional minor modification was necessary. This affected the 5′ mean elevations within a 30′x30′ cell centered at 35.25° S latitude, 150.25° E longitude. NIMA provided the (36) recommended 5′ mean elevation values over this 30′ cell, which were enforced onto the JGP95D DTM. The resulting file, designated JGP95E, constitutes the final 5′ global DTM adopted by the joint project. JGP95E was finalized on November 6, 1995, and was made available to the wider scientific community in January 1996.

Table 2.3.4–1 provides the number of 5′ cells and the percentage of the Earth's area, covered by each terrain type in the JGP95E 5′ global DTM. Table 2.3.4–2 provides the number of 5′ cells originating from each of the 29 sources which contributed data to the development of JGP95E. The geographic distribution of the terrain type and source information is displayed in Figures 2.3.4–1 and 2.3.4–2. The primary source of elevation information over land areas was NIMA's 5′ DTED which provided 1484976 5′ cells covering 66.01 percent of the Earth's land surface area for dry land below and above MSL.

Table 2.3.4–1. Terrain classification by type in the JGP95E 5´ global DTM.

Terrain Type	Num. of 5´ cells	Percentage Area
Dry Land below MSL	6659	0.08
Lake	12790	0.16
Oceanic Ice Shelf	65088	0.20
Ocean	6142527	70.70
Grounded Glacier	968022	2.81
Dry Land above MSL	2136114	26.05
TOTAL	9331200	100.00

Table 2.3.4–2. Elevation data by source, present in the JGP95E 5´ global DTM (TB = TerrainBase).

Source ID	Source Description	Num. of 5´ cells
0	TB, Bathym. gaps / 0 values on land	7792
2	TB, Africa 5´ DEM	125937
5	TB, North America 5´ DEM	40102
6	TB, Andes Mountains 3´ DEM	16779
8	TB, Australia 5´ DEM	63057
10	TB, Brazil Cerrados 2´ DEM	74484
11	TB, Europe 5´ DEM	43742
12	TB, Global FNOC 10´ DEM	194914
13	TB, Greenland 5´x10´ DEM	93375
16	TB, Haiti 30” DEM	9
17	TB, Italy 30” DEM	314
18	TB, Japan 5´ DEM	3817
19	TB, Madagascar 30” DEM	2083
20	TB, Netherlands 3´x5´ DEM	3
21	TB, Northwest Territories 5´ DEM	9373
22	TB, Global Bathymetry 5´ DBM	5969275
26	TB, United States 30” DEM	146
41 & 42	NIMA 5´ DTED	1465209
43	NIMA 5´ DTED and Map Source Mixed	41623
48	NIMA Map Source	224782
50	ETOPO5, 5´ DEM	3805
51	TUG87	4016
52	ALTIM94	418900
53	Smoothed Antarctic	518400
54	GGTOPO.MOD	9073
55	Avg. Ross Ice Shelf	2
56	Avg. Ronne Ice Shelf	8
57	Caspian Sea (surf. elevation = –27 m)	144
58	TB, Alpha version	36
	TOTAL	9331200
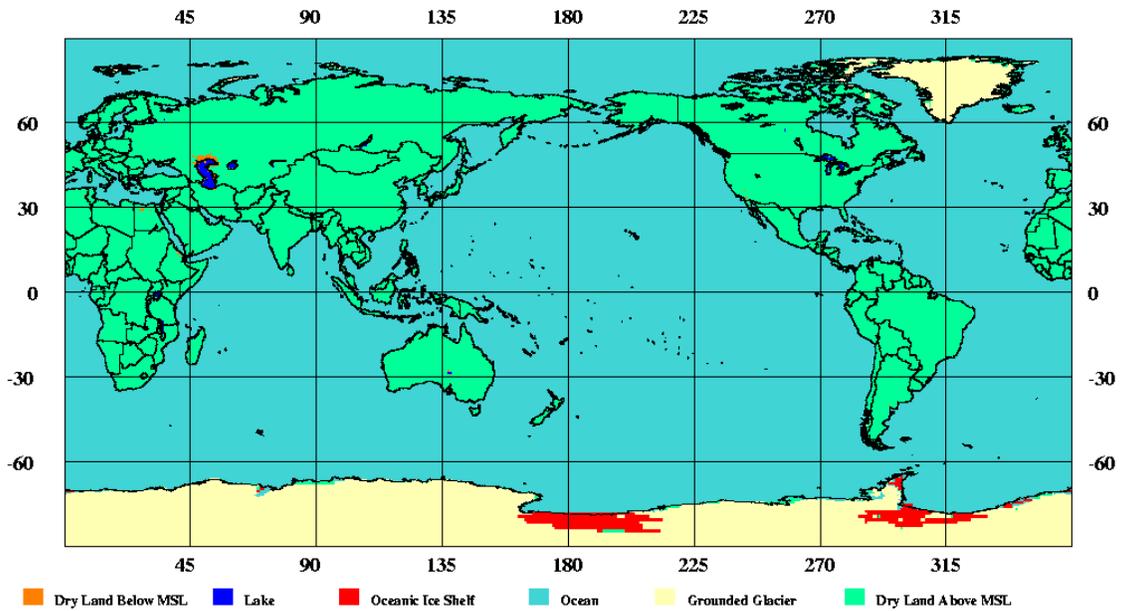
Figure 2.3.4-1. Geographic distribution of terrain types identified in the JGP95E 5´x5´ global elevation file.
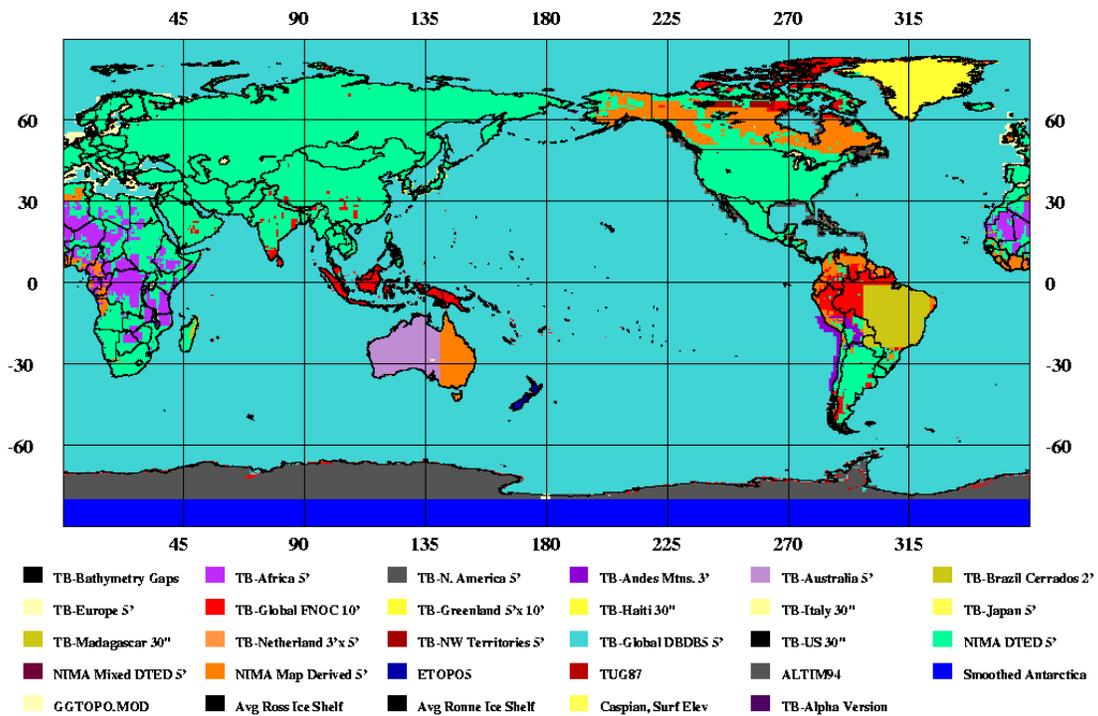
Figure 2.3.4-2. Geographic distribution of elevation source codes identified in the JGP95E 5´x5´ global elevation file.

2–23

2.4　Local Elevation Grids For Terrain Corrections and Residual Terrain Model Effects

JGP95E was instrumental for the computation of Terrain Corrections (TC) and Residual Terrain Model (RTM) effects. These quantities require high resolution elevation surfaces in order to be computed accurately. NIMA DTED data averaged to 1′ mean values, in combination with JGP95E data, were used to evaluate these quantities. In areas where 1′ NIMA DTED data was partially or totally unavailable for the construction of high resolution terrain grids, JGP95E was interpolated (bi-linearly) to the 1′ locations as a supplement. Local terrain surfaces, an inner high resolution, an outer coarser resolution, and a reference elevation surface h_{ref} were needed for input to the programs used to evaluate TC effects and RTM anomalies.

A terrain correction (which is always positive) may be used to form a refined Bouguer gravity anomaly using the formula:

$$\Delta g_B = \Delta g_{FA} - 2\pi G\rho H + C \tag{2.4–1}$$

where:

Δg_B is the refined Bouguer gravity anomaly,

Δg_{FA} is the free-air gravity anomaly,

C is the terrain correction,

H is the orthometric height,

ρ is the (uniform) crustal density, and

G is the universal Gravitational constant.

The terrain correction at a point P, (C_P), can be written as:

$$C_P = G\rho \int_{-\infty}^{\infty} \int_{-\infty}^{\infty} \int_{z=H_P}^{z=H(x,y)} \frac{z - H_P}{\left[(x - x_P)^2 + (y - y_P)^2 + (z - H_P)^2\right]^{3/2}} dx\,dy\,dz \tag{2.4–2}$$

A reference elevation surface h_{ref} can be derived (in principle) by using a low-pass filtering of the local elevation grids. One aims to produce a reference topographic surface whose effects on gravity would be consistent with the topographic gravity effects already included in the reference geopotential model that is used in the remove and restore steps of the mean anomaly prediction (up to the specific degree and order to which the reference model is used) [*Forsberg*, 1994]. This type of "long wavelength" reference elevation surface may be used with a "short wavelength" high resolution elevation surface to produce an RTM gravity anomaly, Δg_{RTM}. An RTM gravity anomaly at a point P is given by:

$$\Delta g_{RTM_P} = G\rho \int_{-\infty}^{\infty} \int_{-\infty}^{\infty} \int_{z=h_{ref}(x,y)}^{z=h(x,y)} \frac{z - h_P}{\left[(x - x_P)^2 + (y - y_P)^2 + (z - h_P)^2\right]^{3/2}} dx\,dy\,dz \tag{2.4–3}$$

where $h(x,y)$ is the elevation from a high resolution terrain model and $h_{ref}(x,y)$ is the elevation from the filtered reference elevation surface. The Δg_{RTM} anomalies fluctuate from negative to

positive, since topographic areas are either above or below the reference elevation surface. A constant (average) crustal density value, $\rho = 2670$ kg/m^3, was used in the implementation of equations (2.4–1), (2.4–2), and (2.4–3) above.

NIMA calculated terrain corrections for Bouguer gravity anomalies and RTM effects for free-air gravity anomalies to be used in the joint project. The basic procedure was to calculate terrain corrections and RTM effects for each individual point gravity anomaly location. This helped define a residual gravity anomaly field needed for the prediction of the 30´ area-mean values. A 2-D Fast Fourier Transform program called TCFOUR and a prism integration program called TC, available from the GRAVSOFT package [*Tscherning, Forsberg, and Knudsen*, 1992], were used to perform these calculations.

In program TC, approximate prism integration equations are used out to large distances from the computation point, to evaluate the anomalous potential effects on the (point) gravity anomaly [*Forsberg*, 1984]. A dense grid of 1´ mean elevations out to a radial distance (R$_1$) of 22 km and a coarser grid of 5´ mean elevations out to a radial distance (R$_2$) of 200 km were used in the computation of RTM effects and terrain corrections. A densification of the inner, high resolution terrain model was performed to eliminate prism edge effects at the computation point [*Forsberg*, 1994]. This densification is essential in order to avoid a computation point P being located at the edge of a prism, giving rise to artificial terrain effects from the prism's "edges" [*ibid*., 1994, page 119]. Figure 2.4–1 [from *Forsberg*, 1994, p. 120] illustrates the densified (defined using a parabolic hyperboloid interpolation scheme with closer grid spacing near the center), inner (1´) and outer (5´) zone elevation grids around the computation point. For the densification, a bi-cubic spline was used to smoothly interpolate the high resolution (1´) mean elevation data within a 3´x3´ grid surrounding the computation point. Special attention is needed to circumvent the (unavoidable) mismatch between the elevation at the computation point (obtained from the gravity anomaly record) and the corresponding interpolated value from the densified inner zone grid. Program TC implements a "smooth" modification of the inner zone gridded elevations, so that they match the point elevation value at the gravity station [*ibid*., 1994, page 120].

1° caps filled with 1´ mean elevation data were centered around each computation point. Although the inner (1´) grid extends only up to 22 km from the computation point, the 1° caps were introduced to reduce discontinuities at the boundaries with neighboring points. In areas where $|\varphi| > 55°$, 2° caps of 1´ mean elevations were used. These 1´ grids determined the 1´ elevation values of the inner zone (22 km) and part of the 5´ mean values of the outer zone area. The latter were created by averaging of the 1´ values. For RTM effects only, the 5´ grid was averaged to produce a 10´ reference elevation grid. This was performed by averaging 5´ elevations to 10´, averaging the central 10´ cell with all the surrounding 10´ cells and assigning this mean to the central 10´ cell. This has the effect of creating a 30´ mean elevation and assigning it to the central 10´ elevation location. The 1´, 5´ and 10´ elevation grids were used for RTM computations. For terrain correction computations, the densified, inner (1´) and outer (5´) grids were used.
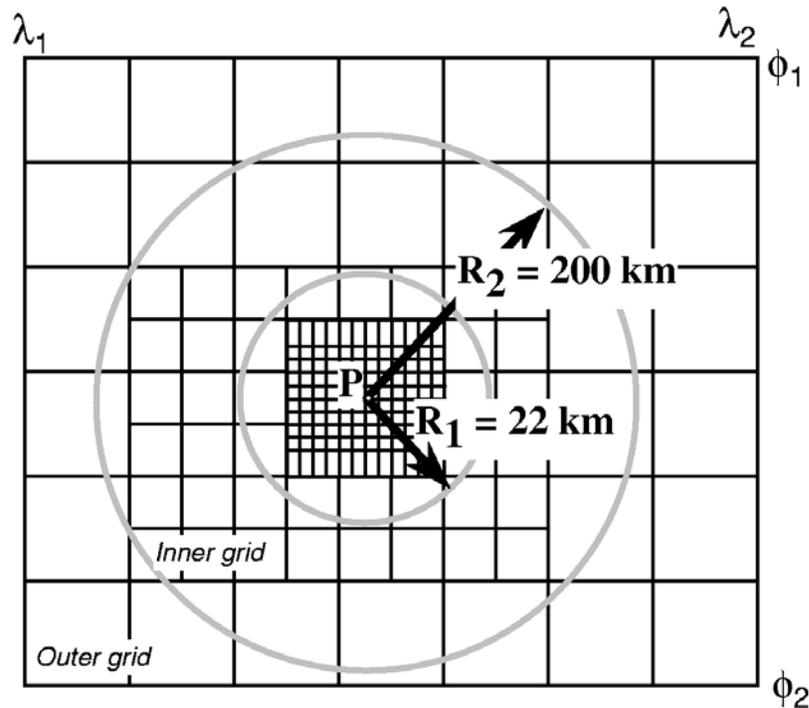
Figure 2.4–1. Use of densified, inner and outer zone elevation grids in program TC (from [*Forsberg,* 1994]).

To facilitate use of equidistant grids needed for the programs, in areas of higher latitudes ($|\varphi| > 55°$), instead of using a 1´ inner zone mean elevation grid, the 1´ values were interpolated to a 2 km inner grid. Instead of a 5´ outer zone grid, a 10 km outer grid was created. For the reference elevation field, a 20 km grid was built in the same manner as the 10´ equiangular grid.

Program TC was used to produce RTM and terrain corrections for reduction of free-air and Bouguer point gravity anomalies, respectively. After LSC was used to predict the 30´ mean gravity anomalies, program TCFOUR was used with the same elevation files as input, to create a grid of 1´ corrections. These values were averaged to the 30´ mean equiangular cell size to produce the mean RTM anomaly values or the mean terrain correction effects, for the "restore" step in the prediction algorithm.

2.5 Development of Spherical Harmonic Coefficient Sets Related to the Topography

The topographic information of the JGP95E DTM was used to compute two sets of spherical harmonic coefficients related to the Earth's topography. For the present applications these sets were required to be complete to degree and order 360. To minimize computational effort, a 30´x30´ version of the JGP95E DTM was developed and was subsequently used to compute the spherical harmonic coefficient sets.

Spherical Harmonic Coefficients of the Earth's Topography

The Earth's topography, i.e., positive heights for land areas above MSL and negative depths for ocean areas (or land areas below MSL), can be expanded in surface spherical harmonics as:

$$H(\theta, \lambda) = \sum_{n=0}^{\infty} \sum_{m=-n}^{n} \overline{H}_{nm} \cdot \overline{Y}_{nm}(\theta, \lambda) \tag{2.5-1}$$

where (θ, λ) are geocentric co-latitude and longitude and $\overline{Y}_{nm}$ is the fully-normalized surface spherical harmonic function of degree n and order m. We seek the fully-normalized coefficients $\overline{H}_{nm}$ (which have units of length). The discretized area-mean value version of equation (2.5-1), truncated to maximum degree 360, takes the form:

$$H_{ij} = \frac{1}{\Delta\sigma_i} \sum_{n=0}^{360} \sum_{m=-n}^{n} \overline{H}_{nm} \cdot \overline{IY}_{nm}^{ij} \tag{2.5-2}$$

where the subscripts (i, j) identify the location of a 30´x30´ cell (whose area is $\Delta\sigma_i$) in a two-dimensional array with i = 0, 1, ..., 359 and j = 0, 1, ..., 719. H_{ij} is now the *mean* elevation over the (i, j) cell, and $\overline{IY}_{nm}^{ij}$ is the integrated value of the surface spherical harmonic function over the same cell. The coefficients $\overline{H}_{nm}$ were computed by:

$$\overline{H}_{nm} = \frac{1}{4\pi q_n} \sum_{i=0}^{N-1} \sum_{j=0}^{2N-1} H_{ij} \cdot \overline{IY}_{nm}^{ij} \tag{2.5-3}$$

where $N = 360$. For the numerical evaluation of equation (2.5-3), *Colombo's* [1981] harmonic analysis algorithm was used (and his proposed quadrature weights q_n). The harmonic coefficients of the topography enable one to compute (point or mean) elevation estimates, band-limited by the frequency content of the degree 360 expansion, through harmonic synthesis. Among other uses, this is helpful when one wants to compute estimates of Bouguer gravity anomalies Δg_B, by:

$$\Delta g_B(mGal) = \Delta g_{FA}(mGal) - 0.1119 \cdot H(m) \tag{2.5-4}$$

Notice that *only* non-negative values of H are applicable in equation (2.5-4). This application of the spherical harmonic coefficients $\overline{H}_{nm}$ was used in the computation of reference Bouguer gravity anomaly values (Section 3.3.2), and in the development of the height anomaly to geoid undulation conversion terms (Section 5.2.1).

Spherical Harmonic Coefficients of the Topographic-Isostatic Potential

We implemented the rigorous formulation described in detail by *Pavlis and Rapp* [1990, Section 3.1], and computed a spherical harmonic coefficient representation of the gravitational potential implied by the topography and its isostatic compensation. Complete local isostatic compensation was assumed. It was modeled according to the Airy-Heiskanen isostatic hypothesis, using a constant depth of compensation of 30 km. The topographic-isostatic coefficients were computed to degree and order 360.

From a geophysicist's point of view our assumed isostatic mechanism would appear rather oversimplified. Among other simplifications, it does not account for the flexural rigidity of the lithosphere, local or regional density variations, or variations in crustal thickness. These limitations were duly recognized by *Pavlis and Rapp* [1990, Section 3.3]. Although more sophisticated isostatic modeling would be desirable, one should bear in mind the purpose of the present development. It is to aid the estimation of gravity anomalies over unsurveyed areas. This is accomplished by combining the low-degree part of a satellite-only model, with the higher degree coefficients of the topographic-isostatic potential (see Section 7.2.2). As it will be discussed in Section 3, unsurveyed areas are mostly concentrated over Antarctica and the northern polar cap, with some additional remaining areas in South America and Africa. Over the majority of the ocean areas, satellite altimetry (either in the form of "direct" tracking or in the form of gravity anomalies) provides a highly accurate mapping of the gravity field. Completely unsurveyed areas at present account for (approximately) 2.3 percent of the total area of the Earth (see Section 8.3). Therefore, the effort required to refine our isostatic formulation, could not be justified given the limited resources of this project. In any event, the ultimate goal remains to be the complete independence of the gravitational model from any isostatic assumptions. This could be achieved in the future, provided that gravity data collection efforts are undertaken over the remaining unsurveyed regions of the Earth (e.g., using airborne gravity surveys). The resulting gravitational models would then be free of any isostatic hypotheses, and thus could provide truly independent boundary conditions to the geophysicist who aims to infer the underlying isostatic mechanisms at work.

2.6 Summary

This section described the development of a global 5´x5´ Digital Topographic Model (DTM) designated JGP95E. This model was compiled by merging topographic information from 29 different sources. The major improvement in JGP95E, as compared to pre-existing DTMs, comes from the release of NIMA's 5' DTED data. These data have now become available to the wider scientific community. In JGP95E, the DTED information covers 66 percent of all land areas. Over areas not covered by DTED, JGP95E used primarily elevation information from TerrainBase version 1.0. Improved (over TerrainBase) estimates of the orthometric elevations of the ice surface over parts of Antarctica were incorporated into JGP95E. These were derived from ERS-1 altimetry and the composite JGM–2/OSU91A gravitational model to degree 360. Significant effort was made by NIMA to verify the consistency of the JGP95E elevations and those elevations associated with the point gravity data records. In this manner, the point gravity data processing, the prediction of 30´ mean anomalies, and other aspects of the geopotential model development process (Bouguer anomaly computation, topographic-isostatic coefficients), were all performed based on a consistent elevation data base.

The JGP95E model classifies terrain into six different types, and provides lake depth and ice thickness information. However, this information was available originally only in 1° resolution. Future DTM compilations would benefit significantly from such information available in finer resolution and with higher accuracy.

Although significant progress has been made here with the development of JGP95E, there are also serious shortcomings with this DTM, which require additional work. JGP95E does not provide any estimate of the accuracy of its topographic data (this is also true for any other DTM or DEM which was freely available at the time that JGP95E was developed). The bathymetric information in JGP95E originates (with few exceptions) from ETOPO5U. Primarily because of the intended use of the DTM in this investigation, there has been little (if any) improvement of the bathymetric data here. Furthermore, it is desirable to compile in the future a global data base of crustal density and crustal thickness. This data base could support more refined formulations for the evaluation of the height anomaly to geoid undulation conversion terms and of the topographic-isostatic potential coefficients.

The near future promises significant advances with respect to the geometric mapping of the surface of the Earth. Satellite missions such as the Geoscience Laser Altimeter System (GLAS) and the Vegetation Canopy Lidar (VCL) mission, are expected to provide (in combination) complete coverage of the Earth's surface with dense and (more or less) uniformly accurate estimates of its ellipsoidal height. In combination with dedicated geopotential mapping missions such as GRACE and GOCE, these data could provide significantly improved estimates of orthometric heights over long and medium wavelengths. Over shorter wavelengths one could envision VCL and GLAS data, in combination with regional and local high-resolution geoid models, as a means of deriving orthometric heights without leveling, over extended areas. VCL and GLAS data however will not provide bathymetric information. At present, the combination of satellite radar altimeter data and *in situ* bathymetric data [*Smith and Sandwell*, 1994] appears to be the most promising and cost effective technique for improving ocean-wide bathymetric data bases.

2.7　References

Brenner, A.C., R.A. Bindschadler, R.H. Thomas, and H.J. Zwally, Slope-induced errors in radar altimetry over continental ice sheets, *J. Geophys. Res., 88,* C3, 1617–1623, 1983.

Cogley, J.G., GGTOPO–Global Terrain Heights, GGDATA Product Description, Trent Univ., Peterborough, Ontario, Canada, 1987.

Colombo, O.L., Numerical methods for harmonic analysis on the sphere, *Rep. 310*, Dept. of Geod. Sci. and Surv., Ohio State Univ., Columbus, 1981.

Forsberg, R., A study of Terrain Reductions, Density Anomalies and Geophysical Inversion Methods in Gravity Field Modeling, *Rep. 355*, Dept. of Geod. Sci. and Surv., Ohio State Univ., Columbus, 1984.

Forsberg, R., Terrain Effects in Geoid Computations, in *Lecture Notes from the International School for the Determination and Use of the Geoid*, pp. 101–134, Milan, Italy, 1994.

Heck, B., An evaluation of some systematic error sources affecting terrestrial gravity anomalies, *Bull. Geod.*, 64, 88–108, 1990.

Heiskanen, W.A., and H. Moritz, *Physical Geodesy*, W.H. Freeman and Co., San Francisco, 1967.

Kenyon, S.C., and N.K. Pavlis, The Development of a Global Surface Gravity Data Base to be Used in the Joint DMA/GSFC Geopotential Model, in: *Global Gravity Field and Its Temporal Variations*, R.H. Rapp, R.S. Nerem and A.A. Cazenave (eds.), IAG Symposia, Vol. 116, Springer–Verlag, Berlin, Heidelberg, 1996.

Laskowski, P., Problems with the OSU mean elevation tape in polar regions, *Internal Rep.*, Dept. of Geod. Sci. and Surv., Ohio State Univ., Columbus, 1984.

NGDC, ETOPO5, Digital Relief of the Surface of the Earth, National Geophysical Data Center Data Announcement 86–MGG–07, Boulder, CO, 1986.

NGDC, ETOPO5U, Digital Relief of the Surface of the Earth, National Geophysical Data Center Data Announcement 88–MGG–02, Boulder, CO, 1988.

Pavlis, N.K., The OSUJAN89 global topographic database—origin, set–up and characteristics, *Internal Rep.*, Dept. of Geod. Sci. and Surv., Ohio State Univ., Columbus, 1989.

Pavlis, N.K., and R.H. Rapp, The development of an isostatic gravitational model to degree 360 and its use in global gravity modelling, *Geophys. J. Int.*, *100*, 369–378, 1990.

Rapp, R.H., Global models for the 1 cm geoid—Present status and near term prospects, *International Summer School of Theoretical Geodesy: Boundary Value Problems and the Modeling of the Earth's Gravity Field in View of the one Centimeter Geoid*, Como, Italy, May 26 – June 7, 1996.

Rapp, R.H., Use of potential coefficient models for geoid undulation determinations using a spherical harmonic representation of the height anomaly/geoid undulation difference, *J. Geod.*, *71*, 282–289, 1997.

Row, L.W., D.A. Hastings, and P.K. Dunbar, TerrainBase Worldwide Digital Terrain Data, Documentation Manual, CD–ROM Release 1.0, NGDC, Boulder, CO, April 1995.

Smith, W.H.F., and D.T. Sandwell, Bathymetry prediction from dense satellite altimetry and sparse shipborne bathymetry, *J. Geophys. Res., 99*, 21803–21824, 1994.

Tscherning, C.C., R. Forsberg, and P. Knudsen, The GRAVSOFT package for geoid determination, *Proc. 1st continental workshop on the geoid in Europe*, p. 327–334, Prague 1992.

Uotila, U.A., Analysis of correlation between free–air gravity anomalies and elevations, *Rep. 94* Dept. of Geod. Sci. and Surv., Ohio State Univ., Columbus, 1967.

Wieser, M., The Global Digital Elevation Terrain Model TUG87, *Internal Report* on Set–up, Origin and Characteristics, Institute of Mathematical Geodesy, Technical University of Graz, Austria, 1987.

Zwally, H.J., A.C. Brenner, J. DiMarzio, and T. Seiss, Ice sheet topography from retracked ERS-1 altimetry, in *Proc. of the Second ERS–1 Symposium—Space at the Service of our Environment*, Hamburg, Germany, 11–14 October 1993, ESA SP–361, 1994.

3. THE SURFACE GRAVITY DATA

3.1 Introduction

The need for an updated and expanded compilation of all available surface gravity information worldwide, was identified early on to be critical for the success of the joint project. In fact, the availability of surface gravity data over extended areas of Asia and eastern Europe, which was brought about by recent international political changes, was one of the main motivations for undertaking this project in the first place.

The gravitational model development (to degree 360) required three specific surface gravity data sets to be developed. Two of them were to include surface (and airborne) gravity data only, while the third would include only the altimetry-derived anomalies. One surface gravity data set would contain 30´ mean values, the other 1° mean values (obviously these two data sets are expected to be consistent over their overlapping areas of coverage). The altimetry-derived anomalies were only required in terms of 30´ mean values. These requirements stemmed from model development considerations. Following the design of OSU91A [*Rapp, Wang and Pavlis*, 1991], the intention here was to use the 1° surface gravity anomalies to form normal equations to degree 70. These would be combined with satellite-only normal equations and with normal equations from "direct" altimeter data, to determine the degree 70 part of the final model. The 30´ surface gravity anomalies and the 30´ altimetry-derived values, would be used along with the satellite-only model to develop the higher than degree 70 part of the final model. This section describes the development of the 30´ and 1° surface gravity data sets. The development of the 30´ altimetric anomalies is described in Section 4. The mean values in all three data sets were to be computed over equi-angular grids on the ellipsoid.

The validation and preprocessing of the detailed gravity anomaly data and the estimation of area-mean values from these data was performed within NIMA. During the planning stages of this task, R.H. Rapp (OSU) prepared a brief paper defining the mean anomaly estimation problem and outlining some solutions which have been proposed in the literature. S.C. Kenyon (NIMA) prepared a corresponding paper where NIMA's proposed approach to the solution of this problem was documented. NIMA proposed to use Least Squares Collocation (LSC) for the estimation of mean anomalies from surface, airborne and altimetric measurements. Kenyon's documentation provided additional details pertaining to the various processing steps. NIMA's proposal was reviewed and discussed by the members of the working groups, and the computational methodology which will be described in Section 3.3 was finally adopted by the project. LSC is an optimal estimation method, well appreciated for its flexibility in terms of data input and for its capability to provide estimates of the errors of the output (predicted) values. The rigor with which LSC treats the problem has a direct impact on its computational requirements. However, given the central importance of the anomaly estimation for this project, it was decided that the effort required for the implementation of LSC was well justified.

The following sections describe the data used and the computational procedures applied in the estimation of surface mean gravity anomalies, and document the final data sets that were developed.

3.2 Detailed Surface Gravity Files

The surface gravity data used in this project have come predominately from data held in NIMA's Point Gravity Anomaly (PGA) file. This file contains in excess of 30 million point values collected and processed by NIMA during the last three decades through its independent collection efforts, reciprocal data arrangements, and cooperative agreements with foreign governments, academic institutions, and private concerns. The PGA file is the primary source of gravity anomalies used in statistical techniques that estimate the 30′ mean terrestrial gravity anomalies directly.

Major terrestrial gravity acquisitions since 1990 include aerogravity over Greenland and parts of the Arctic and Antarctica, surveyed by the Naval Research Laboratory (NRL), and cooperative gravity collection projects, several of which were undertaken in conjunction with the University of Leeds (hereafter GETECH). These collection efforts have improved and densified data holdings over many of the world's land areas. Some of the notable geographic regions include Alaska, Canada, parts of South America and Africa, Southeast Asia, Eastern Europe, and former Soviet Union (FSU). In addition to the above gravity collections, there have been major efforts to improve NIMA's existing 30′ mean anomaly data base by mean anomaly contributions over various countries in Asia. There have also been 30′ mean anomaly contributions by the National Survey and Cadastre, Denmark (Kort–og Matrikelstyrelsen, abbreviated KMS), over the Gulf of Bothnia and the Baltic. A.N. Marchenko [*private communication*, 1996] contributed anomalies over the FSU.

The details of two major NIMA data acquisitions illustrate the significance of the improved gravity coverage over previously void areas. The former Soviet Union is now covered by a set of 8 km x 8 km refined Bouguer anomalies, and the Greenland Aerogeophysics Project resulted in complete aerial gravity coverage (200000 km of flight lines) at 4 kilometers elevation. The Greenland Aerogeophysics Project was also supplemented with new ground surveys by KMS to provide densification along many of the coastal regions for downward continuation and evaluations of the aerogravity.

The gravity data used by NIMA in these surface computations are contained in over 10000 individual sources worldwide. NIMA's first major objective in utilizing the gravity data was to reference all the point gravity anomalies to the WGS84 horizontal datum. Each gravity source was evaluated to determine its geodetic datum and reference system. The majority of gravity sources in the NIMA PGA file are referenced to WGS84. For the gravity sources that were not referenced to WGS84, the appropriate datum transformation from the local geodetic datum of the source to WGS84 was determined. NIMA used the standard datum transformation software MADTRAN [*NIMA,* 1997] for all the local geodetic datum to WGS84 transformations performed in this project except in Australia, as will be explained in Section 3.2.6. The MADTRAN software uses the Standard Molodensky Datum Transformation Formulas in its

local geodetic datum to WGS84 calculations using the changes in ellipsoidal semimajor axis (Δa) and flattening (Δf) between the WGS84 ellipsoid (a = 6378137.0 m, f = 1/298.257223563) and the associated reference ellipsoid of each local geodetic datum, and mean datum shifts in the x, y, and z directions [*DMA,* 1991].

The main approach in the 30´x30´ surface gravity development was to begin with the NIMA PGA file, calculate normal gravity with the mean Earth ellipsoid parameters adopted for this project, reference if necessary the point gravity anomalies to the WGS84 horizontal datum, and then use the most accurate gravitational and elevation models to reduce the data for long- and short-wavelength gravity effects. The LSC procedure implemented at NIMA was then used to directly estimate the 30´x30´ anomalies and their associated error estimates. This was done for all of North America, South America, Europe, Africa, and Australia, and the majority of Asia. The regions of the world where terrestrial 30´ gravity anomalies were not estimated directly by LSC used 30´x30´ gravity anomaly contributions, the averaging of smaller sized mean anomalies to create the 30´ anomalies, or the use of "fill in" anomalies.

The 30´x30´ computational methodology using the PGA file in the NIMA LSC process is described in Sections 3.3.2 and 3.3.3.

The following sections on North America, South America, Europe, Africa, Asia, Australia, and Greenland highlight some of the important gravity sources collected and acquired by NIMA for EGM96. The list of gravity sources for each continent is only a summary of the tremendous volume of gravity information from NIMA that entered into the EGM96 surface gravity computations.

3.2.1 North America

The gravity data used in North America for EGM96 came primarily from NIMA collection efforts. There were 2052 terrestrial gravity sources over North America, totaling approximately 2.4 million point gravity values. These point gravity values were collected by NIMA from sources surveyed between the years 1930 and 1995.

The gravity coverage provided by NIMA over the United States was of high quality and very dense. NIMA used a gravity selection interval of 2´x2´ over the U.S. with an accuracy range of 1 to 10 mGal (1 mGal = 10^{-5} ms^{-2}), with the majority of the point gravity data between 1 to 3 mGal when used in the final 30´ computations. The sources of gravity data in the U.S. were referenced primarily to the NAD27 horizontal datum, and a transformation was needed to shift the data from NAD27 to the WGS84 reference system. Other datums for the point gravity data included WGS84 and WGS72. For NAD27, the transformation parameters used in MADTRAN for the Continental United States were: Δa = -69.4 m, Δf x 10^4 = -0.37264639, Δx = -8 m, Δy = 160 m, and Δz = 176 m using the Clarke 1866 reference ellipsoid and 405 Doppler stations to determine the mean coordinate shifts. Different transformation parameters (Δx, Δy, Δz) were used in Alaska and other parts of the Caribbean and North America [*DMA*, 1991].

The 30´ mean gravity anomaly computations (detailed in Section 3.3) for the United States on average used over 1000 points, with many regions such as the Midwest and Southwest using over 2000 points. These intense concentrations of data were primarily the result of oil exploration in

states such as Texas and Louisiana. In the 30´ mean gravity anomaly computations, the resultant prediction accuracy of the 30´ mean gravity values was approximately 1 mGal over most of the United States.

The gravity coverage over Canada was less dense than over the U.S., reflecting the remoteness of the northern regions. The Canadian gravity collections by NIMA have benefited from an international Mapping, Charting, and Geodesy (MC&G) agreement and exchange program between Canada and the U.S., by which regular updates are made to each country's existing gravity files. Most of the data collected were referenced to NAD27 and required transformation to WGS84. The MADTRAN transformations for the NAD27 Canadian gravity data used mean shifts of $\Delta x = 10$ m, $\Delta y = 158$ m, and $\Delta z = 187$ m. Along the United States border the coverage is more dense, with over 2000 points included in the 30´x30´ computations for border regions in Saskatchewan and Ontario. The 30´ mean gravity anomaly computations over the rest of Canada used data files of lower density and averaged less than 500 point gravity anomalies in the calculation of each individual 30´ mean gravity anomaly. The Hudson Bay area used slightly more data (~1000 gravity points) because of the accessibility of shipborne surveys in this area. The Geological Survey of Canada and the Saskatchewan Energy and Mines were the largest contributors of gravity sources over Canada.

The gravity coverage over Mexico was also less dense than over the United States. The highest density of data is along the Texas border, with southern Mexico having sparse and even void areas. The variable quality and density of the gravity data are very evident when analyzing the accuracies of the estimated 30´ anomalies. The 30´ gravity anomalies for the southern region have higher uncertainties (> 6 mGal), while the northern border region has lower errors (<1.5 mGal). The NAD27 transformation using MADTRAN was performed on sources in Mexico identified as belonging to that local geodetic system with transformation parameters $\Delta x = -12$ m, $\Delta y = 130$ m, and $\Delta z = 190$ m.

3.2.2 South America

The gravity collections for South America that were used in EGM96 came from a variety of sources. NIMA historically has maintained a strong gravity collection effort and association with many of the universities, oil companies, and foreign governments of this continent. This has included a long-time gravity meter loan program to many South American organizations whereby NIMA gravity meters were provided in exchange for the data surveyed with those meters. The majority of gravity information came from the Defense Mapping Agency (DMA) Inter-American Geodetic Survey (IAGS) that was located in Panama and later in San Antonio, Texas, which maintained liaisons in many of the South American countries through MC&G agreements during the 1980's and early 1990's. These cooperative international agreements, along with NIMA's support of various gravity surveys in South America, resulted in the collection of approximately 350000 total gravity points over the continent.

NIMA was also a major participant in the South American Gravity Project (SAGP), which also provided important sources of gravity information over South America [*Green and Fairhead*, 1993] for the EGM96 computations. The SAGP was a 3-year project that used data from NIMA

and 14 other oil industry sponsors and was completed in April 1991 with gravity coverage including Central and South America. There were 244 total gravity sources in the SAGP, with the Bouguer accuracy on land ranging from 1–8 mGal and the free-air accuracy over the oceans ranging from 5–15 mGal. Approximately 330000 land stations and 481000 total ocean gravity stations were included in the SAGP. The major point of contact in South America for the SAGP was Professor Denizar Blitzkow at the University of Sao Paulo, Brazil, who made possible the release of gravity data throughout South America to the SAGP.

There are many difficulties in the collection of gravity data in South America. The mountainous Andes and impenetrable Amazon basin were the major remote areas presenting obstacles to the surveying and gravity collection activities, and many voids occur in the NIMA South American point gravity anomaly data set as a result. In the Andes, many of the gravity surveys followed the road networks through the mountains and missed the high mountainous regions. Therefore, the density and distribution of gravity and the variable quality of elevation models all played a role in the quality of the final 30´ mean gravity anomaly predictions for South America.

The varying quality of elevation models greatly affected the terrain reductions in the development of the 30´x30´ gravity anomalies in South America. The southern one-third of South America benefited from the higher quality WGS84 Digital Terrain Elevation Data (DTED), compared to other available elevation sources. The elevation models for the northern part of South America consisted primarily of NIMA Map Derived 5´ Terrain Data, TerrainBase 10´ U.S. Navy Fleet Numerical Oceanography Center (FNOC) Sources, and the Brazil Cerrados 2´ DEM (see Section 2). The most accurate terrain corrections to support the 30´ Bouguer gravity anomaly predictions are calculated from more detailed terrain models (1´) than these larger spaced, 5´ and 10´ elevation sources. Given the lack of more detailed elevation information, the quality of the NIMA terrain reductions suffered in northern South America.

3.2.3 Europe

The European gravity data used in EGM96 were obtained from NIMA collection activities involving numerous sources, and included a major NIMA acquisition in 1994 of the West–East European Gravity Project (WEEGP) 1991–1994 data. The WEEGP acquisition by NIMA in collaboration with GETECH [*Green and Fairhead*, 1994] contributed unique data and helped fill important voids in the NIMA gravity coverage. The WEEGP objective was to obtain and combine in a comprehensive fashion the extensive individual gravity data sets of all the European nations, including those of Eastern Europe, which had previously been considered State secrets. The WEEGP data consisted of a gridded 8 km x 8 km terrain corrected Bouguer and free-air anomaly set for use west of the Urals (60° to 24° E) in Eastern Europe, of which NIMA used the terrain-corrected Bouguer set in EGM96. The accuracy of the WEEGP gridded point gravity anomaly set was determined to be 7 mGal over Eastern Europe and the FSU.

WEEGP supplemented the already extensive NIMA gravity archive in Western Europe. The amount of gravity data used throughout Europe for the 30´x30´ mean free-air gravity anomalies was substantial; most of the 30´ anomalies were computed with more than 1200 points (see Section 3.3). The amount of data for areas such as Great Britain was aided by international

MC&G agreements with NIMA, whereby data exchanges between the U.S. and Great Britain are made on a routine basis. The 30´ mean gravity anomaly computations over Great Britain were greatly aided by these exchanges, with more than 2000 point gravity anomalies used in the NIMA computational process. Overall, the quality and quantity of the point gravity anomaly data over Europe were excellent and were further supported by the availability of quality DTED over much of the continent. NIMA has collected over 220 individual gravity sources over Europe, with a total of approximately 710000 point gravity values used in EGM96. These collections spanned the years 1951–1997, and have benefited from the association of NIMA with organizations such as the Bureau Gravimetrique International (BGI), GETECH, and KMS. A majority of the European gravity data were referenced to the European Datum 1950 (ED 50); this required NIMA to transform the data to the WGS84 datum [*DMA*, 1991]. The European Datum 1950 uses the International Ellipsoid, with transformation parameters $\Delta x = -87$ m, $\Delta y = -98$ m, and $\Delta z = -121$ m.

Other specific 30´ contributions by KMS filled in voids in the NIMA coverage over the Gulf of Bothnia and the Baltic region. Another contribution, by A.N. Marchenko, then at the Technical University of Graz (Austria) [*private communication*, 1996] also filled in an important void in the former Soviet Union that was not covered by the WEEGP.

3.2.4 Africa

NIMA has maintained a strong collection effort in Africa by cooperating in major land surveys and obtaining data from national data banks, private concerns, universities, and oil companies. A coordinated effort by NIMA and individuals, including Dr. Charles Merry of South Africa and organizations such as the Office De La Recherche Scientifique et Technique Outre-Mer (ORSTOM) facilitated data collection activities over the continent. ORSTOM was a major contributor to NIMA with data in Cameroon, Central African Republic, Niger, Gabon, Chad, Congo, and the Ivory Coast. In 1985, NIMA and the French "Institute Geographique National" cooperated to survey gravity in the former French colonial areas. Fairly dense gravity coverage from these surveys and joint gravity collection projects exists for the countries of Namibia, Botswana, South Africa, Niger, Chad, and the Central African Republic, and was made available for EGM96. Problem areas in the gravity coverage include sparsely covered regions in Libya, Sudan, Egypt, and Angola. These NIMA sources were individually identified for original datum specifications and then transformed to WGS84 before the 30´ computations.

Along with the NIMA collections, the African Gravity Project (AGP) was one of the primary sources of gravity information over Africa. In 1986, the AGP began with GETECH [*Fairhead and Watts*, 1989], lining up support with 16 sponsors, including major contributions from NIMA. The objective of AGP was to collect all the available gravity data over Africa in an organized manner rather than on a country-by-country basis for oil exploration and scientific investigations. A tremendous amount of effort went into the editing, adjustment, and compilation of the gravity data in AGP. The final published report was produced by GETECH in 1988 with the distribution to the sponsors of free-air and Bouguer gravity files and maps, together with detailed documentation on the gravity processing, map details, and survey specifications. The AGP included 389 sources, with a total of approximately 770000 land stations and 1600000 marine

gravity values. The accuracy of the land gravity values, which are controlled by the positioning and elevations of the gravity stations, ranged from 1 to 5 mGal. The uncertainty in height for the land gravity sources in AGP was due to errors in leveling or barometric techniques (for example, a ±5 m error in the barometric method equates to ±1.0 mGal for the point Bouguer anomalies), while a horizontal uncertainty of 1 km adds approximately 0.76 mGal of error in the gravity value. The marine gravity accuracy, which is highly dependent on the ship's navigation, ranged from 3 to 15 mGal and was supplemented by the Digital Bathymetric Data Base 5 (DBDB5). The majority of the gravity data was acquired by actual field surveys, while some of the gravity was derived from maps. A gridded 5´x5´ set of the gravity data was also included over the continent for the AGP. The gravity data were referenced to the International Gravity Standardization Network 1971 (IGSN71) and the WGS84 reference system. All of the AGP data were made available by NIMA for the 30´x30´ mean anomaly computations.

An additional benefit to the processing of the African data was the availability of the NIMA DTED, which covered approximately one-half of the continent, with almost continuous coverage over the southern one-third and northeast regions. The high quality of the 1´ DTED aided all the terrain modeling associated with the gravity computations. The less detailed National Geophysical Data Center (NGDC) 5´ TerrainBase and NIMA 5´ Map Derived Elevation Sources were the other elevation sources that completed the African coverage.

3.2.5 Asia

Until recently, since the Soviet Union did not support gravity data exchanges, topographic–isostatic anomalies or other fill-in gravity anomalies had to be used in Earth gravity models. This situation changed with the availability of a set of 8 km x 8 km refined Bouguer anomalies over the FSU acquired by NIMA in 1995 [*Fairhead and Makedonskii*, 1996] through the North Central Asia Gravity Project (NCAGP, 1993–1995), which complemented WEEGP as discussed earlier in Section 3.2.3.

The WEEGP and NCAGP international gravity compilation projects over the FSU were initially the result of a collaboration between GETECH, the International Scientific Environmental Center (ISEC) of the Russian Academy of Sciences, and BGI. Historically, the FSU conducted gravity surveys over the entire country with over 10 million gravity measurements collected between 1952 and 1985. These gravity surveys formed the WEEGP and NCAGP data bases that were acquired by NIMA after the easing of Cold War tensions.

The objective of NCAGP was to extend the release of gravity data east of the Urals (the limit of WEEGP) to link with gravity coverage of the South East Asia Gravity Project. The NCAGP encompasses the area between the Urals (60°E) and the Pacific Ocean in the east (195°E); the southern boundaries of the FSU and Mongolia (35°N), forming the southern limit; and the Arctic Ocean at 83°N, forming the northern limit. The original NCAGP data were provided on a 8 km x 8 km grid, which provided sufficient resolution to prepare the final 30´ mean gravity anomalies over this region. The NCAGP data were adjusted to IGSN71 and referenced to WGS84. The accuracy of the NCAGP point gravity anomaly data was assigned a value of 7 mGal after NIMA performed an error analysis against other independent source data.

In addition to the land areas over the FSU, ERS–1 altimeter data from the two 168-day Geodetic Missions (GM) were used to derive the gravity field over the open oceanic regions of the Arctic and NW Pacific for the NCAGP.

The NCAGP gravity data collection of refined Bouguer anomalies required some special considerations. A refined Bouguer anomaly is defined as an anomaly with the Bouguer and terrain corrections applied to the free-air anomaly. NIMA did not have access to the terrain correction and elevation files associated with this refined Bouguer data set. This caused NIMA to utilize its DTED file as a replacement over this region for all terrain correction, spherical harmonic modeling of the topography, and Bouguer to free-air anomaly computations. Covariances between the refined Bouguer anomalies were developed using the Forsberg covariance model [*Forsberg*, 1987], and then LSC was applied using these covariances and the refined Bouguer anomalies. The resultant predicted residual anomaly set had 30´ mean terrain corrections applied from the DTED file; the calculation of the surface free-air anomalies again utilized the NIMA 30´ elevation (*H*) file derived from JGP95E by using the factor (0.1119*H*) added to the 30´ Bouguer anomalies.

The Southeast Asia Gravity Project (SEAGP) was another major NIMA acquisition, which was originally sponsored by an oil consortium of 11 companies and NIMA in coordination with GETECH [*Fairhead, Campbell*, *and Williams* 1996]. SEAGP dramatically improved NIMA's gravity holdings in this region and resulted in the collection of nearly 675000 total gravity values over the land and oceanic areas of Southeast Asia. SEAGP also provided an important link with the other large NIMA acquisitions, providing continuity from Western Europe starting with the WEEGP data through central Asia with NCAGP to the Pacific Ocean. All of the data from SEAGP were adjusted to the IGSN71 system and referenced to WGS84. This Southeast Asian region includes the Philippines, East Pakistan, India, Indonesia, Japan, Korea, Malaysia, New Britain, New Guinea, Thailand, the Fiji Islands, and West Pakistan. The collection of ocean sources throughout Indonesia was of particular importance because it filled in previously void regions in the NIMA coverage. There were 322 oceanic sources and 93 individual land sources, with nearly 500000 ocean gravity values and approximately 175000 terrestrial point gravity anomalies. The Indonesian regions of Sumatra and Borneo were completely densified with SEAGP data, with major improvements also in western New Guinea. The density of shipborne gravity data was very high throughout the Indonesia islands and off the northern coast of Australia. This was extremely beneficial to the land–water interface problems encountered in very anomalous regions such as Indonesia, where extreme bathymetry and elevation ranges can exist over limited spatial distances. As an example, for many of the islands in Indonesia it is not uncommon for a 2500 m coastal bathymetry depth to transition abruptly to a 2500 m mountain top over a distance of 50 km.

There was a tremendous need in the EGM96 computations to complement the SEAGP and other NIMA data collections in Southeast Asia with 30´x30´ gravity coverage over China. Previous Earth gravity models such as OSU91A [*Rapp, Wang, and Pavlis*, 1991], complete to degree and order 360, unfortunately had to use larger sized 1° x 1° mean gravity anomaly coverage over China in their development. NIMA recognized this need for 30´x30´ China gravity for EGM96 and collected the best data available. The China 30´x30´ gravity anomaly set was developed from

two main sources of information. East of 104° longitude, the 30´x30´ gravity anomaly set (referred to as China–A) was provided directly by NIMA through international agreements. This geographical region is not extremely mountainous, and the NIMA analysis on this gravity data set showed that an accuracy of 4 mGal was realistic. The geographical area west of longitude 104° (referred to as China–B) contained the Himalayas and required special processing. NIMA has a 5´x5´ terrain-corrected Bouguer gravity anomaly source that was averaged to 30´x 30´ by simple averaging. The DTED file was then used to create the 30´ terrain corrections necessary to convert the terrain corrected Bouguer to a simple Bouguer anomaly. The final 30´x30´ free-air gravity anomaly set west of longitude 104° was then calculated from the 30´x30´ Bouguer anomalies using the JGP95E 5´ elevations averaged to 30´ and the Bouguer plate reduction 0.1119H. The accuracy assigned to the China–B set was 19 mGal, which accounts for the sparseness of data and the mountainous terrain of the Himalayas.

3.2.6 Australia

The data acquired by NIMA covering Australia were supplied by the Australian Geological Survey Organization (AGSO) in 1994. The Australian data collection efforts are supported by an international MC&G agreement and exchange program between the U.S. and Australia that provides regular data updates. The total point gravity data base supplied by AGSO was approximately 670000 values from 383 individual land sources and 2 marine sources, and consisted of observed gravity, meter height, and free-air anomalies in the IGSN71 system. The anomalies were referenced to the Australian Geodetic Datum 1984 and required transformation to WGS84 by NIMA. For this transformation, multiple regression equations [*DMA*, 1991] were developed to transform all the Australian land anomalies from the Australian Geodetic Datum 1984 to WGS84. Where elevations could be provided with the observed gravity, Bouguer anomalies and terrain corrections were also supplied by AGSO, with the heights of the anomalies based on the Australian Height Datum. The accuracy of the Australian point data supplied by AGSO was very good, with most values ranging between 1 and 3 mGal. The JGP95E elevation data base used the Australian 5´ DEM west of 140°E longitude, while NIMA 5´ map derived elevation data were used east of 140°E for the associated terrain reductions over Australia. The computations along the coastline of Australia used point free-air gravity anomalies, while the interior regions were computed with Bouguer anomalies. The amount of gravity information used in the 30´x30´ gravity anomaly computations ranged from a low of approximately 150 points in the southwestern regions to 1300 points in the south-central part of the continent.

3.2.7 Greenland

The Greenland subcontinent was one of the largest voids in gravity coverage for the Northern Hemisphere until 1991. The Greenland Aerogeophysics Project (GAP) was carried out in 1991–1992 by the NRL in cooperation with NIMA, the Naval Oceanographic Office, and Denmark's KMS. This airborne survey was carried out at an altitude of 4.1 km, with a filtering corresponding to a spatial resolution of approximately 15–20 km and an RMS crossover accuracy of 4.6 mGal for the 1991 surveys and 3.4 mGal for the 1992 surveys. More than 200000 line-km of data were collected using two different gravimeters (a Lacoste & Romberg "S" system and the

Bell BGM series) on the same aircraft. These two gravimeters are basically marine gravimeters using rather crude—as compared to modern—inertial technology, gyro-stabilized platform systems that had slight modifications for airborne use. Using these gravimeter data sets, a composite merged data set was created by H. Small of NIMA, preferentially using the Lacoste & Romberg meter data in most cases over the Bell data in the final selection. The Bell airborne gravity data were used in void areas of the Lacoste & Romberg lines, and they were also averaged over 13 selected Lacoste & Romberg lines over the 1992 northern Greenland surveying campaign, where continuity between the two data sets needed to be maintained because of overlap considerations.

The gravity field model over Greenland is based on approximately 31000 airborne gravity data values (at 30 second along-track intervals), and approximately 36000 surface gravity values surveyed by KMS covering the ice-free areas and the ocean. The surface and airborne gravity data have been merged in a blockwise collocation solution, as described in Section 3.3.3, using the Forsberg planar logarithmic covariance functions to generate a consistent 5′ gravity anomaly grid of the Greenland region (59°–84° N, 75°–10° W). Terrain and reference fields have been handled by remove–restore methods. A 2-km height grid of Greenland and surrounding regions has been used for basic Residual Terrain Model (RTM) effects, together with gridded radar echo sounding data for ice sheet thicknesses. Due to the lack of ice depth information near the margins of the ice sheet, systematic errors in the derived gravity field models will be large in these regions. A major cause of error in the Greenland 30′ gravity anomalies is the lack of sufficiently accurate terrain models for rock and ice, which creates problems when the surface and airborne gravity data are combined in LSC. Terrain effects [*Forsberg*, 1984] were computed by prism integration using an averaged 5 km x 5 km digital terrain model, constructed from a heterogeneous mix of different sources (GEOSAT and ERS–1 altimetry, Greenland Aerogeophysics Project (GAP) radar altimetry data [*Ekholm*, 1996], digital mapping projects, and manually scanned maps), with an ice thickness model from radar echo soundings. The RTM terrain model was defined as mass residuals relative to a mean height surface of approximately 90 km resolution. The overall statistics of the Greenland aerogravity after all the mergers and crossover adjustments are shown in Table 3.2.7–1.

Table 3.2.7–1. Statistical summary of the Greenland Aerogeophysics Project, 1991–1992, gravity data.

Total Number of Airborne Points Used	31808
Number of Crossover Gravity Points	1426
Mean (mGal)	0.23
Standard Deviation (mGal)	7.63
RMS (mGal)	7.63
Minimum (mGal)	–32.33
Maximum (mGal)	44.34

The basic computed 5´ free-air gravity anomaly grid has been averaged into the final 30´x30´ mean gravity anomalies by simple averaging techniques. A plot of the Greenland anomalies is shown in Figure 3.2.7–1.

The collocation solution for the calculation of the Greenland 5´ free-air gravity anomalies was carried out using the Forsberg planar logarithmic model using a single covariance model for the entire Greenland area (with parameters of $C0 = 225$ mGal^2, $D = 6$ km, $T = 120$ km, corresponding to a correlation length of 29 km, described in Section 3.3). Terrain effects were restored from an averaged 2.5´ gravity terrain effect grid, and spherical harmonic effects (discussed in Section 3.3) added for the final product. The downward continuation level selected was the surface of the topography (not the geoid) for consistency with the other worldwide surface 30´x30´ anomalies calculated for EGM96. The ice sheet in central Greenland is at 3.3 km altitude, so the effects of downward continuation are small but the effects along the coastline are large (up to 60 mGal or more) where the topography is rugged, ranging from sea level up to 3700 m.

The collocation solution was carried out in 1° blockwise cells with overlaps according to the latitude of the calculations. The overlap north–south around the 1° cells was consistently 1°, but the east–west overlap between 75° and 84° N was 6° in longitude, whereas between 66° and 75° it was 4° in longitude, and between 59° and 66° it was 2° in longitude. These overlaps were based on the convergence of meridians at the high latitudes.
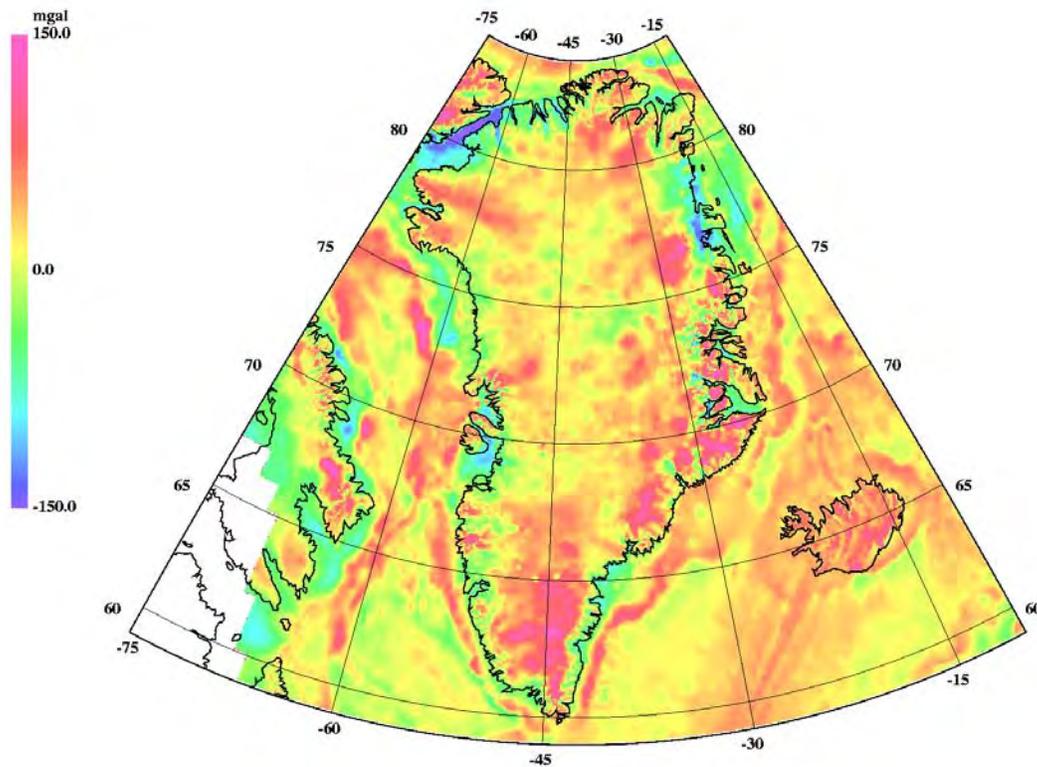
Figure 3.2.7–1. Greenland 30´x30´ mean free-air gravity anomalies.

3.3   Computational Methodology

The optimal calculation of 30´ mean free-air gravity anomalies is based on a infinite number of point gravity anomalies in any specified cell. This definition cannot be realized because the density and distribution of point gravity anomalies vary by geographic region and elevation over the Earth's surface. NIMA has a worldwide requirement to acquire point or mean gravity information at required spacings, but many regions still need additional coverage or densification. NIMA has applied LSC using the Forsberg covariance model [*Forsberg*, 1987] to estimate the 30´ mean gravity anomalies directly using the PGA file. The Forsberg covariance model contains simple, closed formulas for quantities related to the Earth's anomalous potential using a planar approximation. The power spectral decay of the self-consistent Forsberg model closely approximates Kaula's rule, and three parameters (*D*, *T*, and *C0*) characterize the correlation and power of gravity anomalies in a local area. The three parameters are defined as *D*, high-frequency attenuation factor; *T,* low-frequency attenuation factor; and *C0,* the variability of the gravity field.

NIMA selects the most accurate gravity data at appropriate spacing from the PGA file and then reduces the anomaly data for the effects of terrain (high-frequency effects), if necessary, and for long wavelength effects. After these reductions, analytical covariance functions are closely fitted to empirical functions based on the three parameters of Forsberg's model. The local covariance parameters are then used in an LSC algorithm that uses the Forsberg closed expressions for gravimetric quantities, integral formulas for the mean representation of the gravimetric quantities, and Cholesky decomposition to efficiently and accurately calculate the mean gravity anomalies and their predicted errors from available PGA data in a specified cell.

There are two techniques to estimate 30´ free-air gravity anomalies. Section 3.3.2 describes the Bouguer anomaly methodology, and Section 3.3.3 describes the use of free-air anomalies in the computations. Greenland and the coastlines of all continental areas were computed from Molodensky free-air gravity anomalies as defined in eq. (3.3.1–1). The free-air gravity anomaly estimation technique is used along the coastlines to incorporate all of the shipborne free-air anomalies in the water. For all interior continental areas and islands, Bouguer anomalies were used in the computations. The Bouguer anomalies are regionally correlated with elevation, being much smoother than the free-air gravity anomalies, with detrending using topographic information. In high mountain areas, the Bouguer anomaly can easily be highly negative by hundreds of mGal. Since the Bouguer anomaly provides a much smoother anomaly, it provides excellent input to the estimation process of LSC. The main difference in the two methods of computing mean anomalies is the terrain reductions performed.

The 30´ free-air gravity anomaly predictions were performed at the 30´ mean elevation of the cell (from JGP95E) using LSC. The 30´ Bouguer predictions were referred to the geoid (at orthometric elevation $H = 0$) and then restored to the 30´ mean elevation of the cell using the Bouguer reduction of $0.1119\,\overline{H}_{30´}$ (also from JGP95E).

The use of an accurate long-wavelength geopotential spherical harmonic model is critical to the proper reduction of the free-air and Bouguer anomalies and restoration of the predicted 30´

anomalies. For this project, the use of the JGM–2 ($n \leq 70$) model [*Nerem et al.*, 1994] augmented by the OSU91A ($70 < n \leq 360$) model was selected as the most accurate geopotential model available at the processing time.

3.3.1 Preprocessing of Detailed Gravity Anomaly Data

Important steps in NIMA's gravity anomaly preprocessing algorithm include:

1. Gravity anomalies adjusted to IGSN71 system.

2. Major effort to reference all point gravity anomalies to the WGS84 horizontal datum.

3. Molodensky free-air gravity anomalies defined on the Earth's surface. The formula used to compute these anomalies is given by *Heiskanen and Moritz* [1967], eq. (8–9):

$$\Delta g_{FA} = g - \gamma_{ell} \left[1 - 2\left(1 + f + m - 2f\sin^2\varphi\right)\frac{H^*}{a} + 3\left(\frac{H^*}{a}\right)^2 \right] \qquad (3.3.1\text{–}1)$$

where g is the observed value of gravity on the Earth's surface and γ_{ell} is the value of normal gravity on the surface of the reference ellipsoid.

The normal height H^* of the gravity station is generally unavailable, so the orthometric height H is used instead. For the definitions of quantities appearing in (3.3.1–1), see *Heiskanen and Moritz* [1967]. To calculate the normal gravity on the ellipsoid in eq. (3.3.1–1), the closed gravity formula of Somigliana [*DMA*, 1991] is used:

$$\gamma_{ell} = \gamma_e \frac{(1 + k\sin^2\varphi)}{(1 - e^2\sin^2\varphi)^{1/2}} \qquad (3.3.1\text{–}2)$$

An atmospheric correction is necessary in eq. (3.3.1–1) because the WGS84 Earth *GM* value includes the mass of the atmosphere and is used in formulas to calculate the normal gravity in equations 3.3.1–1 and 3.3.1–2 [*DMA*, 1987]. The atmosphere is incorporated to be consistent with the need for having no mass external to the Earth in the solution of the gravimetric boundary value problem. These corrections are [*Dimitrijevich*, 1987, p. 4]:

$$\delta g = 0.87 \cdot e^{-0.116 \cdot H^{1.047}} \qquad \text{mGal if } H \geq 0$$
$$\delta g = 0.87 \qquad\qquad\quad \text{mGal if } H < 0$$

where the orthometric elevation H is in kilometers. The atmospheric correction decreases with altitude and ranges from 0.87 mGal at $H = 0$ to 0.0 mGal for $H \geq 34$ km. The NIMA Bouguer computations on land use the formula:

$$\Delta g_B = \Delta g_{FA} - 0.1119H \qquad \text{(mGal, m)} \qquad (3.3.1\text{–}3)$$

4. The geometry and the gravitational potential of the reference ellipsoid adopted for this project are based on the following:

The second degree zonal coefficient of the JGM–2 model is:

$$(\overline{C}_{2,0})_{JGM-2}^{tide-free} = -484.1654767 \times 10^{-6} \qquad (3.3.1\text{–}4)$$

and the transformation:

$$(J_2)^{zero} = -(\overline{C}_{2,0})^{tide-free}_{JGM-2} \cdot \sqrt{5} - (-3.11080 \times 10^{-8} \cdot 0.3) \tag{3.3.1–5}$$

yields the "zero" (permanent tide) J_2 value adopted for this project. This value, along with:

Semimajor axis, $a = 6378136.3$ m $\hspace{2cm}$ (3.3.1–6)

Geocentric gravitational constant, $GM = 3986004.415 \times 10^8$ m^3 s^{-2} $\hspace{1cm}$ (3.3.1–7)

Mean Earth rotation rate, $\omega = 7292115 \times 10^{-11}$ rad s^{-1} $\hspace{1.5cm}$ (3.3.1–8)

uniquely define the "zero" reference ellipsoid used in this project (GM includes the mass of the atmosphere). All derived geometric and physical constants of the reference ellipsoid were computed in accordance with the recommendations of H. Moritz in *Bulletin Géodésique Vol. 58*, No. 3, 1984, and some of these derived constants are shown in Table 3.3.1–1.

The normal gravity transformation from WGS84 to the formula implied by the above constants was performed on the NIMA PGA data base by differencing precise equations for normal gravity for the two reference systems.

Table 3.3.1–1. Numerical values of some derived parameters of the adopted reference ellipsoid.

Symbol	Parameter	Numerical Value	Units
f^{-1}	reciprocal flattening	0.298256415099D+03	–
b	semiminor axis	0.635675155863D+07	m
e^2	e = first eccentricity	0.669439810568D–02	–
γ_e	normal gravity at Equator	0.978032758157D+06	mGal
γ_P	normal gravity at poles	0.983218707745D+06	mGal
k	$k=(b\gamma_P - a\gamma_e)/a\gamma_e$	0.193183149272D–02	–
m	$m=\omega^2 a^2 b/GM$	0.344978534214D–02	–
$\overline{C}_{2,0}$	second-degree zonal	–0.484169650276D–03	–
$\overline{C}_{4,0}$	fourth-degree zonal	0.790314704521D–06	–
$\overline{C}_{6,0}$	sixth-degree zonal	–0.168729437964D–08	–
$\overline{C}_{8,0}$	eighth-degree zonal	0.346071647263D–11	–
$\overline{C}_{10,0}$	tenth-degree zonal	–0.265086254269D–14	–

$$\Delta g_{EGM96} = \Delta g_{WGS84} + \gamma_{ell}\left[1 - 2\left(1+f+m-2f\sin^2\varphi\right)\frac{H^*}{a} + 3\left(\frac{H^*}{a}\right)^2\right]_{WGS84} -$$

$$\gamma_{ell}\left[1 - 2\left(1+f+m-2f\sin^2\varphi\right)\frac{H^*}{a} + 3\left(\frac{H^*}{a}\right)^2\right]_{EGM96} \tag{3.3.1–9}$$

After all of the above steps are completed, the final formula for the NIMA free-air anomalies is:

$$\Delta g_{EGM96} = g - \gamma_{ell}\left[1 - 2\left(1 + f + m - 2f \sin^2 \varphi\right)\frac{H^*}{a} + 3\left(\frac{H^*}{a}\right)^2\right]_{EGM96} + \delta g \qquad (3.3.1\text{--}10)$$

where:

$$\delta g = 0.87 \cdot e^{-0.116 \cdot H^{1.047}} \qquad (3.3.1\text{--}11)$$

The steps (1–4) are important in reducing some long-wavelength systematic errors present when calculating gravity anomalies [*Heck,* 1990].

3.3.2 Methodology for 30′ Mean Free-Air Anomaly Computation From Point Bouguer Gravity Anomalies

To perform LSC using Bouguer anomalies, the following formulas are used to predict the 30′ mean anomalies and their associated errors:

$$\overline{\Delta g}_{30'} = C_{\overline{\Delta g}\Delta g} \cdot \left(C_{\Delta g \Delta g} + V\right)^{-1} \cdot L + \left(\overline{\Delta g}_B(SH) - \overline{TC} + \Delta g(mean)\right) \qquad (3.3.2\text{--}1)$$

$$M^2\left(\overline{\Delta g}_{30'}\right) = C_{\overline{\Delta g}\,\overline{\Delta g}} - C_{\overline{\Delta g}\Delta g} \cdot \left(C_{\Delta g \Delta g} + V\right)^{-1} \cdot C_{\Delta g \overline{\Delta g}} \qquad (3.3.2\text{--}2)$$

where:

$\overline{\Delta g}_{30'}$ = 30′ mean Bouguer gravity anomaly

$L = \Delta g_B - \Delta g_B(SH) + TC - \Delta g(mean)$

V = noise covariance matrix (diagonal) of point Bouguer gravity anomalies

$C_{\Delta g \Delta g}$ = signal covariance matrix of point Bouguer gravity anomalies

$C_{\overline{\Delta g}\Delta g}$ = signal cross-covariance matrix between 30′ mean and point Bouguer anomalies

TC = point terrain correction

$\Delta g_B(SH)$ = spherical harmonic point Bouguer anomaly

$\Delta g(mean)$ = average of reduced point Bouguer anomalies over the computational area

Δg_B = point Bouguer anomaly

$M^2\left(\overline{\Delta g}_{30'}\right)$ = error variance of 30′ mean gravity anomaly

$C_{\overline{\Delta g}\,\overline{\Delta g}}$ = signal covariance between 30′ mean gravity anomalies

$\overline{\Delta g}_B(SH), \overline{TC}$ = area-mean values of $\Delta g_B(SH)$ and TC.

The steps to prepare the point Bouguer gravity anomalies for LSC consist of:

1. Select point gravity data (Bouguer anomalies) for a 2´x2´ cell size. If point data cannot be obtained at 2´x2´, then larger cell sizes must be used (i.e., 6´x6´).

2. Calculate terrain corrections for the point Bouguer anomalies and add this terrain correction to obtain refined Bouguer anomalies. The terrain correction is the vertical component of the gravitational attraction from the Bouguer plate to the actual topography [*Heiskanen and Moritz,* 1967, eq. 3–21]. NIMA calculated terrain corrections for all terrestrial Bouguer anomalies, as it was explained in detail in Section 2.4, and then added this correction to the point data. The magnitude of the terrain corrections can reach 225 mGal for point values and 50 mGal for 30´ mean values.

3. Remove a long-wavelength spherical harmonic Bouguer field from the point Bouguer anomalies. This step was performed by creating a synthetic 2´x2´ set of free-air anomalies from the JGM–2/OSU91A model (to $N_{max} = 360$). A set of harmonic coefficients of the Earth's topography (to $N_{max} = 360$) was developed using the JGP95E 30´ mean elevation file (see Section 2.5). Then, 2´x2´ elevations $H(SH)$ were synthesized from these coefficients for all land areas. The 2´ synthetic Bouguer anomalies were obtained from the formula:

$$\Delta g_B(SH) = \Delta g_{FA}(SH) - 0.1119 \cdot H(SH) \qquad\qquad (3.3.2\text{--}3)$$

where H is in meters and anomalies are in mGal (*SH* indicates a quantity synthesized from spherical harmonic coefficients and for this project always refers to degree and order 360). These 2´x2´ spherical harmonic Bouguer files were then used to reduce the point Bouguer anomalies by linear interpolation methods.

4. The mean of the reduced gravity data (steps 1–3) is then subtracted to center the data for each computational cell before covariance and mean anomaly calculations.

After these four steps, the L vector in (3.3.2–1) is complete.

5. Develop accurate covariance models of local, reduced gravity fields in 1°x1° cells with a 30´ overlap. The convergence of the meridians in high latitudes is compensated for by extending the east–west overlap around each 1°x1° cell using the cosine of the latitude. Table 3.3.2–1 gives the values used for the overlap.

Table 3.3.2–1. East–west cell overlap used to account for convergence of the meridians.

Absolute Latitude	East–West Overlap
0° to 50°	30´
50° to 60°	45´
60° to 70°	60´
70° to 80°	90´
80° to 90°	180´

The covariance defines the statistical correlation of gravity anomalies and the average product of the anomalies at constant distances of 0´, 2´, 4´, etc. The covariance modeling consists of calculating empirical covariances from the reduced anomaly data and then fitting the Forsberg analytical covariance model parameters ($C0$, D, and T) to the empirical covariance. The anomaly data used for the empirical covariance function should be based on the same reductions applied to the L vector in the collocation equation (3.3.2–1).

The parameter D is chosen to satisfy the curvature of the empirical covariance near the origin. D corresponds to twice the Bjerhammar sphere depth of spherical harmonic analysis [*Forsberg*, 1987]. Also, the Poisson covariance model may be viewed as being generated by a mass layer at depth $D/2$, with a white noise random density distribution [*Forsberg*, 1984]. *Forsberg* [1987, Section 5], showed that for large spherical harmonic degrees, the parameter D is asymptotically related to the parameter s of the Tscherning-Rapp covariance model [*Tscherning and Rapp*, 1974], by $D = R \cdot (1 - s)$, where R ($= 6371$ km) is the radius of the mean-Earth sphere. The parameter T is chosen to satisfy the correlation length of the model. $C0$, the variance of the gravity anomaly, is used to scale the analytical covariance.

The idea behind fitting the above three analytical parameters is to store all the empirical covariances up to 1.5 times the correlation length (the distance where the value of the covariance equals half the value of the variance) and then rigorously hold $C0$ fixed and fit each D parameter from 63.0729 km ($s = 0.9901$) to 0.6371 km ($s = 0.9999$) to the proper T parameter based on the correlation length. The file that holds the T parameters has been developed as a direct-access file and is quickly accessed for each D value and correlation length. For each set of $C0$, D, and T parameters, an analytical covariance is created and compared to the empirical gravity covariance. The optimal set of D and T parameters selected provides the smallest RMS of fit when differenced with the empirical covariance file. This ensures accurate covariance modeling, which is critical for accurate predictions and especially for error estimation [*Moritz*, 1980]. The autocovariance between gravity anomalies in the *Forsberg* [1987] model is:

$$C_{\Delta g \Delta g} = -\log(z + r) \tag{3.3.2–4}$$

where: $z = z1 + z2 + D$ and $r = \sqrt{dx^2 + dy^2 + z^2}$ and $z1$ and $z2$ are the elevations of two points in km; dx and dy are planar coordinate differences between two points in km; and D is defined above.

6. The least-squares collocation step:

The Forsberg covariances are used in the LSC algorithm implementing equations (3.3.2–1) and (3.3.2–2) after steps (1–5) are performed. The V parameter in equations (3.3.2–1) and (3.3.2–2) defines the error variances of the point gravity anomalies going into the collocation formulas. The errors of the gravity data in the PGA file are assigned based on a rigorous analysis of comparable existing sources, quality of equipment used to perform the measurements, terrain models, and datum errors.

The computational scheme is to select the location where the 30´ mean anomaly is predicted (1° cell with the same overlap depending on latitude as performed in calculating the

covariances, with four 30´ mean anomalies computed for each 1° cell). The latitude-dependent overlaps used are given in Table 3.3.2–1. This overlap scenario was also used in the Southern Hemisphere. The only exception to this overlap criterion was for the airborne missions over Greenland and the high Arctic, where different overlaps were used because of the downward continuation solutions being used.

Individual covariances for each 1°x1° cell consist of analytical Forsberg parameters *C0*, *D*, *T*, and the correlation length. For all the reduced anomalies in a 1° cell (including overlap), the planar closed expression for gravity anomalies (eq. 3.3.2–4) is used to develop point covariances depending on the distance in kilometers between them.

The method for computing the covariance between the mean anomalies and all the point anomalies is developed from eq. (7–83) in *Heiskanen and Moritz* [1967]:

$$C_{\overline{\Delta g} \Delta g} = \frac{1}{ab} \int \int C\left(\sqrt{(x - x_i)^2 + (y - y_i)^2}\right) dxdy \qquad (3.3.2–5)$$

where (x_i, y_i) are the coordinates of point anomalies inside a 30´ cell whose sides have length *a* and *b*, respectively. Integration is over all (x, y) in a 30´ cell, and the covariance function being integrated is from eq. (3.3.2–4). To compute the covariances between the mean anomalies, eq. (7–82) from *Heiskanen and Moritz* [1967] is used:

$$C_{\overline{\Delta g} \overline{\Delta g}} = \frac{1}{a^2 b^2} \int \int C\left(\sqrt{(x - x')^2 + (y - y')^2}\right) dxdydx' dy' \qquad (3.3.2–6)$$

The NIMA collocation algorithm uses efficient Cholesky decomposition for the most computationally intensive part of eq. (3.3.2–1), namely $(C_{\Delta g \Delta g} + V)^{-1} \cdot L$. This can be evaluated as the solution of a positive definite symmetric linear system, which may contain up to 5000 equations. For each 30´ prediction, all the data in the 1° cell (plus overlap) are used in the calculation. There must be a minimum of five gravity values in each 1° cell (plus overlap) for the computation to be performed. If this criterion is not met, then the 1° cell and the four 30´ predictions are excluded from the process.

7. The NIMA collocation program estimates four 30´ mean anomalies. The next step required is to restore all of the removed gravitational effects. The last part of eq. (3.3.2–1) defines the quantities that are now necessary to create the final 30´ Bouguer anomaly. From equation (3.3.2–1) we have the restored values ($\overline{\Delta g}_B(SH) - \overline{TC} + \Delta g(\text{mean})$) that represent the mean spherical harmonic Bouguer anomaly, the mean terrain correction calculated from 1´ terrain correction grids, and the reduced mean of the point Bouguer anomalies in the computational area.

8. The final step in the preparation of the 30´ mean gravity anomaly files is the calculation of the 30´ free-air anomaly $\overline{\Delta g}_{FA}$ from the 30´ Bouguer anomaly $\overline{\Delta g}_B$ estimated from eq. (3.3.2–1) and steps 1–7 above.

$$\overline{\Delta g}_{FA}(\text{mGal}) = \overline{\Delta g}_B(\text{mGal}) + 0.1119 \cdot H(\text{m}) \qquad (3.3.2–7)$$

where *H* is the 30´ mean orthometric height created from the 5´ JGP95E elevation file.

3.3.3 Methodology for 30´ Mean Free-Air Anomaly Computation From Point Free-Air Gravity Anomalies

The fundamental formula for using collocation to predict 30´ mean free-air gravity anomalies using point free-air gravity anomalies as input is:

$$\overline{\Delta g}_{30'} = C_{\overline{\Delta g}\Delta g} \cdot \left(C_{\Delta g \Delta g} + V \right)^{-1} \cdot L + RES(mean) \tag{3.3.3--1}$$

where all covariances are defined the same as for the Bouguer anomaly process and:

$L = \Delta g_{FA} - \Delta g_{FA}(SH) - \Delta g_{RTM} - \Delta g(mean)$

Δg_{FA} = point free-air gravity anomaly

$\Delta g_{FA}(SH)$ = spherical harmonic (synthetic) free-air gravity anomaly

Δg_{RTM} = RTM effect on point free-air anomaly

$\Delta g(mean)$ = average of reduced point free-air anomalies over the computational area

V = noise covariance matrix (diagonal) of point free-air gravity anomalies

$RES(mean) = \overline{\Delta g}_{FA}(SH) + \overline{\Delta g}_{RTM} + \Delta g(mean)$ where overbars denote 30´ mean values of the corresponding quantity

The 30´ free-air gravity anomaly estimation process to fit the covariances and perform Least-Squares Collocation is as described in steps (1–7) previously for Bouguer anomaly predictions. The two main differences in the estimation process compared to the Bouguer anomaly estimations are the use of RTM effects to reduce the free-air anomalies for the effects of terrain [*Forsberg*, 1984] and the use of the $N_{max} = 360$ spherical harmonic free-air anomaly to subtract the longer wavelength effects.

3.3.4 Downward Continuation of Airborne Gravity Data Over the Arctic and Antarctica

Previous Earth gravity models over the Arctic and Antarctica have not been able to use actual gravity information due to their inaccessibility and the lack of reliability in airborne gravity. This situation changed with the advent of improved airborne gravity systems that could be carried by P–3 or Twin-Otter aircraft over these remote areas and through the use of kinematic GPS, making the separation of fictitious and gravitational accelerations possible in flight. These systems were used in airborne surveys performed by NRL between 1991–1995 with kinematic GPS and the Lacoste and Romberg "S" system, as in the Greenland project, and covered previously void regions of the high Arctic and Antarctica. The use of kinematic GPS as well as aircraft laser (or radar) altimeters permitted the creation of accurate airborne gravity data, which were subsequently validated after downward continuation by comparison with surface gravity measurements [*Forsberg and Kenyon*, 1995]. The airborne surveys in Greenland had the additional problem of extremely rough topography along the coastlines, while the Arctic and Antarctica were handled in the downward continuation processes similarly to the Greenland data but without any of the associated terrain problems. Therefore, the flight altitudes for the

aerogravity missions over the Arctic and Antarctica were much lower than the 4.1 km flight altitude of Greenland. For example, the Antarctica Corridor Aerogeophysics of the South East Ross Transect Zone (CASERTZ) airborne survey using a Twin-Otter aircraft flew at an average height of 2600 meters over the ellipsoid and between 800 and 1600 meters above the ice surface. The various NRL Arctic airborne surveys using a P–3 aircraft flew at a range of 600 meters to approximately 1000 meters over the ice cap.

To achieve the best possible gravity recovery from airborne sensors, the aircraft must fly long, straight, constant, low-altitude, low-speed, and low-turbulence tracks with line spacing appropriate to the resolution achievable by the airborne gravity system. Because the gravity measurement is critically dependent on the kinematic GPS, it is also important to have good satellite coverage. In addition, radio-frequency sensitivity must be accounted for, and the aircraft must make gentle turns and maneuvers. These are survey design considerations that NRL took into account for each of its Arctic and Antarctica airborne missions. The CASERTZ survey during the austral summer of 1991–1992 surveyed a region of approximately 50000 km^2 covered by 25000 km of airborne track data developed on a 5 km x 5 km grid. The NRL radar altimeter onboard the aircraft was able to make accurate measurements to the sea-ice surface for both the Arctic and Antarctica surveys. The RMS measurement error of the topography was ±0.85 meters for the CASERTZ survey based on all airborne crossovers, while the Arctic topographic surveys provided better than ±10 cm accuracy to the sea-ice surface [*Brozena and Peters*, 1994]. General information about the NRL Arctic 1992–1994 and Antarctica CASERTZ 1991–1992 aerogravity data is compiled in Table 3.3.4–1.

NRL surveyed another adjacent Arctic region in 1995, with support from NIMA, which collected 4693 points and filled in another large void in the Arctic gravity coverage. In the spring of 1996, this airborne survey was processed and provided to NIMA, and the 30´ mean anomalies were calculated and included in EGM96.

Table 3.3.4–1. Statistics of Arctic 1992–1994 and Antarctic 1991–1992 aerogravity data.

	Arctic	Antarctica
Number of Points	10430	6868
Number of Crossover Points	379	1019
Mean (mGal)	0.04	0.07
Standard Deviation (mGal)	3.35	4.05
RMS (mGal)	3.35	4.05
Minimum (mGal)	−11.99	−16.84
Maximum (mGal)	11.61	15.67

A general summary of the information obtained from NRL and used by NIMA concerning these Arctic and Antarctic airborne surveys is as follows:

1. Julian day.

2. Time (day:hour:minute:second) of measurement.

3. Latitude of gravity measurement (decimal degree).

4. Longitude of gravity measurement (decimal degree).

5. Gravity meter measurement at altitude (mGal), corrected for:

    —aircraft vertical acceleration

    — Eötvos and meter platform off-level.

6. GPS altitude (h) in meters with respect to the WGS84 ellipsoid.

7. Radar altimetry height measurement of gravimeter above sea-ice, if available (0.0 otherwise).

8. WGS84 geoid height (N) (meters).

9. Normal gravity γ (mGal).

10. Free-air gravity anomaly $= g - \gamma + 0.3086 \cdot$ (GPS height (h) – WGS84 geoid height (N)) (not used, as explained in step d, below).

11. Regional Arctic geoid heights (meters).

The information from NRL over the Arctic was then analyzed and prepared for use in the NIMA Least-Squares Collocation process, using the following steps:

a) Time filtered the gravity observations (selected measurements at approximately 30 second intervals along a flight line) for use in LSC

b) Applied an impulse response filter function [*Forsberg and Kenyon*, 1995] corresponding to the Lacoste and Romberg instrument

c) Crossover adjusted the gravity track data

d) Computed the airborne free-air gravity anomaly in the above step 10 according to eq. (3.3.1– 10) using for H^* the height from the airborne measurement: $H^* =$ GPS height (h) – WGS84 geoid height (N).

The airborne gravity over the Arctic and Antarctica was reduced with the JGM–2/OSU91A model for the long-wavelength gravity anomaly effects at the altitude of flight. The reduced point gravity anomaly data from the airborne missions were then used in LSC using the Forsberg covariance model. The Forsberg covariance parameters selected for both the Arctic and Antarctica project were $C0 = 225$ mGal^2, $D = 6$ km, $T = 120$ km, corresponding to a correlation length of 29 km. The east–west overlaps for each 1°x1° computational cell at these high latitudes were 180 arc minutes above 80° N or below 80° S; from 70° to 80° N and 70° to 80° S, the overlap was 90 arc minutes. The downward continuation process for the airborne gravity anomaly data set was ideally suited for LSC because existing surface data could be merged into the aerogravity solution, as was done in the case of Greenland. The 30´ mean free-air gravity anomalies were computed directly by LSC at the height of the 30´ mean topographic surface computed from the JGP95E elevation file. The JGM–2/OSU91A spherical harmonic 30´ free-air gravity anomalies were then restored to the predicted anomalies to create the final data sets. The accuracy assigned to much of the Arctic 30´ mean gravity anomalies was between 4 and 6 mGal,

which reflects the initial accuracy of the input data and the error associated with downward continuation.

3.4   Final 30´ Mean Gravity Anomalies Over Land Areas

The preparation of the final 30´x30´ mean gravity anomalies was a monumental effort by NIMA. The analysis of the NIMA point anomaly archives was the first step in the process of creating a worldwide 30´ data base. Every area of the world was scrutinized to determine if improvements could be made or voids filled. If improvements or voids could be filled within the timeframe of the project, every effort was made to make these additions. Many collections of contributed 30´ gravity anomaly data from foreign governments or universities were checked against the NIMA 30´ gravity anomalies computed from the point gravity anomaly data base. The preprocessing steps described in Section 3.3.1 were followed for all point gravity anomalies to minimize long-wavelength systematic errors and other problems in the final 30´ anomalies. NIMA's analysis included checking each individual source of gravity information and then performing the appropriate datum transformation from the local geodetic system to WGS84. The normal gravity for each point gravity anomaly was calculated using the mean Earth ellipsoid constants adopted for the EGM96 project and then differenced with the WGS84 normal gravity to create the point gravity anomaly input files for LSC. All Bouguer anomalies were terrain corrected, and free-air gravity anomalies were all reduced by Residual Terrain Model anomalies as described in Sections 3.3.2 and 3.3.3 before LSC. In addition, the elevation files associated with the gravity anomaly computations were analyzed and compared with the global 5´ DTM JGP95E (described in Section 2), to ensure the consistency of the detailed elevation data associated with the gravity records, and the JGP95E 5´ mean values.

The source codes for the NIMA worldwide terrestrial 30´ mean gravity anomalies are defined by nine individual methods of computation or acquisition. Other sources of 30´ gravity anomaly information came directly from international agreements or internal requests. These acquisitions include 30´ free-air gravity anomaly data from Taiwan by Tsuei Gwo–Chyang [*private communication*, 1994]. Other data acquisitions include 30´ gravity anomalies acquired over the Baltic and Gulf of Bothnia where voids or erroneous gravity anomaly information existed in the NIMA gravity anomaly data base. The KMS 30´ mean free-air gravity anomaly information came from simple averaging of smaller size mean free-air gravity anomalies. There were 35860 30´ terrestrial free-air gravity anomalies and 47087 30´ terrestrial Bouguer anomalies directly computed by NIMA using the LSC process. Table 3.4–1 lists the sources used in the development of the final 30´ terrestrial gravity anomaly file. These free-air and Bouguer anomalies are listed as NIMA (surface gravity data) in Table 3.4–1. A total of 97250 terrestrial 30´x30´ mean free-air gravity anomalies were compiled for this project. Additional statistical information on the NIMA 97250 surface 30´x30´ mean free-air gravity anomalies is given in Table 3.4–2.

Table 3.4–1. Data sources for the terrestrial NIMA 30´x30´ mean gravity anomaly file.

Source	Number
NIMA (surface gravity data)	82947
NIMA (airborne gravity data)	10369
China-A data	2048
China-B data	1766
Taiwan data from Tsuei Gwo-Chyang	40
Baltic data from KMS	4
FSU data from A. Marchenko	4
Gulf of Bothnia data from KMS	72

Table 3.4–2. Statistics on the NIMA 97250 surface 30´ mean free-air gravity anomalies (mGal).

Statistic	Value
Number of Values	97250
Percentage of the Earth's area	35.53
Minimum value (φ,λ)	–251.11 (5.75°, 127.25°)
Maximum value (φ,λ)	399.47 (28.25°, 343.25°)
Mean value	2.26
RMS value	36.92
Minimum σ	0.07
Maximum σ	59.79
RMS σ	5.50

The Ohio State University (OSU) terrestrial 30´x30´ mean free-air gravity anomaly data base [*Kim and Rapp*, 1990] was also used, since it covers a significant amount of oceanic areas not covered by the NIMA 30´ terrestrial anomaly file. Overall statistics of the OSU data base are given in Table 3.4–3. The background on the preprocessing of the 30´x30´ OSU gravity anomaly data base is:

a) OSU 30´ gravity anomalies were converted from the Geodetic Reference System 1967 (GRS67) gravity formula to the one implied by the constants in Section 3.3.1.

b) Gravity anomalies were corrected for the second-order vertical gradient of normal gravity [*Pavlis*, 1988].

c) Gravity anomalies were corrected for the atmospheric effect (eq. 3.3.1–11).

d) The mean elevations in this data base refer to JGP95E.

A comparison was performed between the NIMA and OSU terrestrial 30´x30´ gravity anomalies as one of the quality checks in developing the final NIMA 30´ gravity data base. These statistics are summarized in Table 3.4–4.

Table 3.4–3. Statistics of the OSU terrestrial 30´x30´ mean gravity anomalies (mGal).

Statistic	Value
Number of values	66990
Percentage of the Earth's area	27.71
Minimum value (φ,λ)	−283.56 (34.25°, 141.75°)
Maximum value (φ,λ)	381.76 (19.75°, 204.75°)
Mean value	0.20
RMS value	32.13
Minimum σ	1.00
Maximum σ	46.00
RMS σ	8.36

Table 3.4–4. Statistics of the differences in 30´x30´ mean gravity anomalies
OSU - NIMA (mGal).

Statistic	Value
Number of values compared	45641
Mean difference	−0.52
Standard deviation	12.11
Minimum difference (φ, λ)	−185.93 (28.25°, 343.25°)
Maximum difference (φ, λ)	174.00 (57.75°, 228.25°)

There are certain areas of the world where gravity data are sparse or nonexistent, and the creation of 30´ mean anomalies from the PGA file was impossible. These areas include parts of the Amazon region in South America, Africa, Antarctica, and the Arctic. Over regions void of any terrestrial or altimetry-derived gravity anomalies, "fill-in" values had to be used, as discussed in Sections 7.2.2 and 8.3.

The sources of the data used in the calculation of the 30´ mean surface gravity anomaly file are shown in Figure 3.4–1, the standard deviations of the 30´ mean surface gravity anomalies are shown in Figure 3.4–2, and the number of point gravity anomalies used in the NIMA computations of the 30´ mean gravity anomalies are shown in Figure 3.4–3.
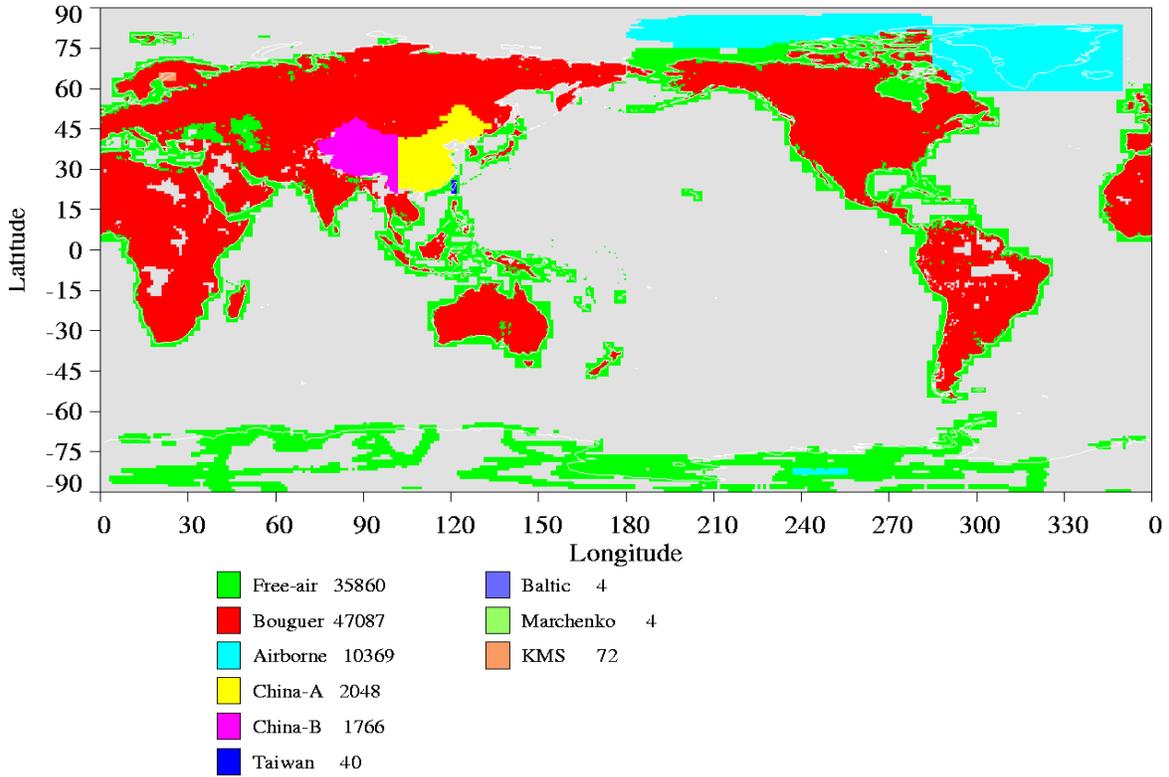
Figure 3.4–1. Sources of the 30´ mean surface gravity anomalies.
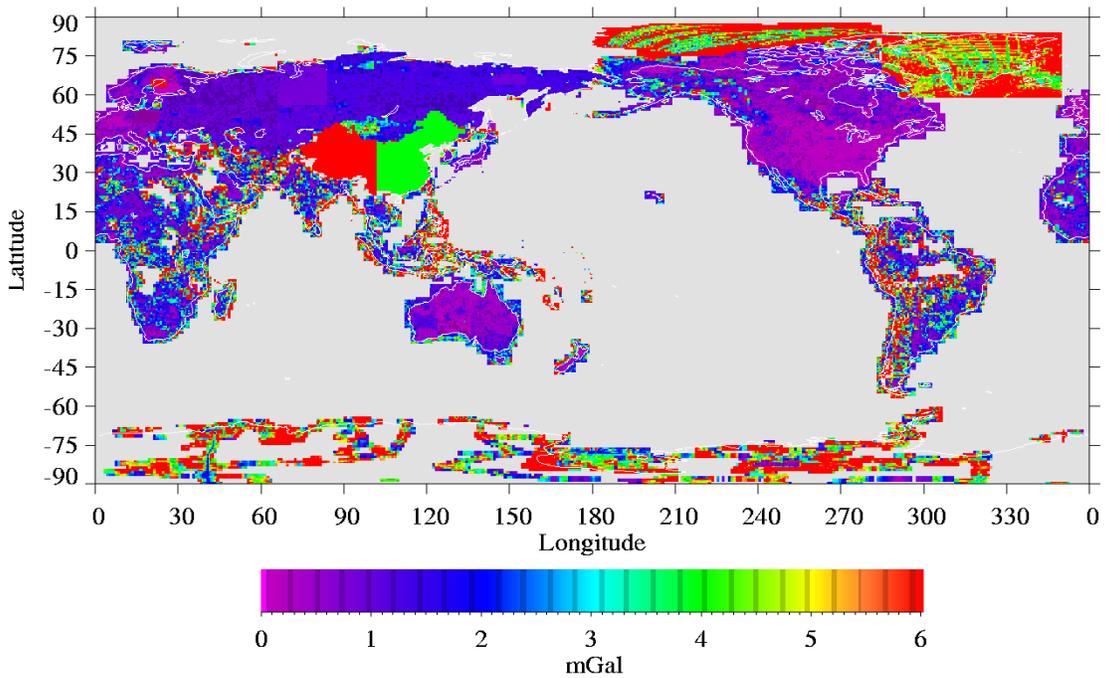
Figure 3.4–2. Standard deviation of 30´ mean surface gravity anomalies.
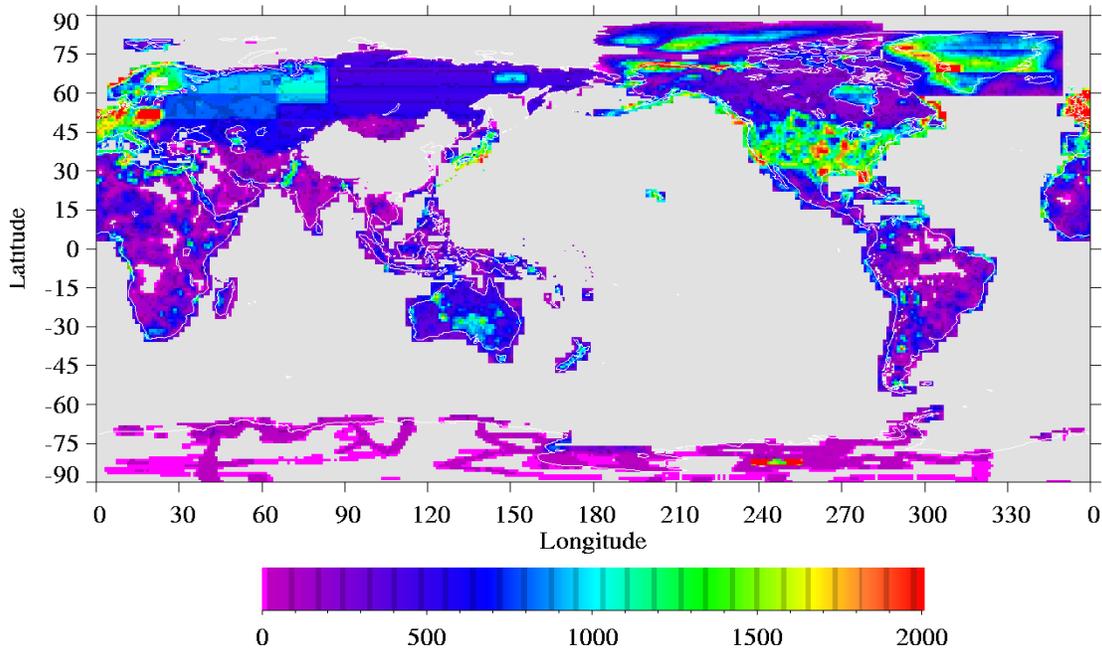
Figure 3.4–3. Number of point gravity anomalies used to calculate the 30´ mean gravity anomalies.

3.5   Final 1° Mean Gravity Anomalies

The final 1° mean gravity anomalies were merged from the NIMA 1° mean surface gravity anomalies over land areas, NIMA 1° mean surface gravity anomalies over ocean areas, and the OSU 1° mean surface gravity anomalies over both land and ocean areas. The NIMA 1° anomalies refer to the project gravity formula with the atmospheric correction applied and were derived primarily from the NIMA 30´ terrestrial gravity anomaly data base used in this project. The number of 30´ mean anomalies used to compute each 1° anomaly was checked when eq. (3.5.1–1) was applied to form the 1° mean anomaly file. There had to be at least one 30´ free-air gravity anomaly in each 1° cell to create the 1° free-air gravity anomalies from any 30´ source available. There were 19605 1° cells that had four 30´ NIMA anomalies, and 2014 1° cells that had four 30´ OSU anomalies. From these, there was a total of 21619 1° cells with four anomalies from either NIMA or OSU out of the total of 52271 1° values. The rest of the 1° gravity anomaly file had a mixture of NIMA and OSU 30´ gravity anomalies or were acquired directly by NIMA or OSU as a 1° anomaly.

For the OSU 1° and 30´ gravity anomaly files, special considerations had to be applied before merging into the 1° global surface anomaly file:

a) The OSU anomalies refer to the GRS67 gravity formula.

b) The OSU anomalies do not have the atmospheric correction applied.

3–26

c) The OSU anomalies do not have the second-order normal gravity gradient correction applied.

Therefore, to process the OSU anomalies and merge them into the 1° global file, NIMA needed to perform the following steps [*Pavlis*, *private communication*, 1995]:

i) Convert the OSU gravity anomalies from GRS67 to the EGM96 gravity formula by:

$$\Delta g(EGM96) = \Delta g(GRS67) + \delta a_0 + \delta a_2 \sin^2(\phi) + \delta a_4 \sin^4(\phi) + \delta a_6 \sin^6(\phi) + \delta a_8 \sin^8(\phi) \qquad (3.5{-}1)$$

where the numerical values are:

$\delta a_0 = -.91257E + 00$
$\delta a_2 = -.67899E - 01$
$\delta a_4 = 0.64176E - 03$
$\delta a_6 = 0.56112E - 10$
$\delta a_8 = 0.54620E - 14$

ii) Apply the atmospheric correction $\delta g = 0.87e^{-0.116H^{1.047}}$ mGal for $H \geq 0$ and $\delta g = 0.87$ mGal for $H < 0$, where H is in km.

iii) Apply the second-order normal gravity gradient correction $\dfrac{\partial^2 \gamma}{\partial h^2}$.

The source codes for the 1° mean gravity anomaly file, which contains a total of 52271 values, are described in Table 3.5–1. The data sources are shown in Figure 3.5–1, and the 1°x1° anomaly standard deviations are illustrated in Figure 3.5–2. Additional statistical information on the terrestrial 1°x1° mean gravity anomalies is given in Table 3.5–2.

Table 3.5–1. Source list for the 1° mean gravity anomaly file.

Source	Number
OSU (October 1990) 1° $\overline{\Delta g}$	14055
NIMA oceanic 1° $\overline{\Delta g}$	18058
NIMA 1° average from surface 30´ data	16505
NIMA 1° average from airborne data	2636
China–A data (1° average)	523
China–B data (1° average)	468
Taiwan data from Tsuei Gwo–Chyang (1° average)	4
Baltic data from KMS (1° average)	1
FSU data from A. Marchenko (1° average)	3
Gulf of Bothnia data from KMS (1° average)	18
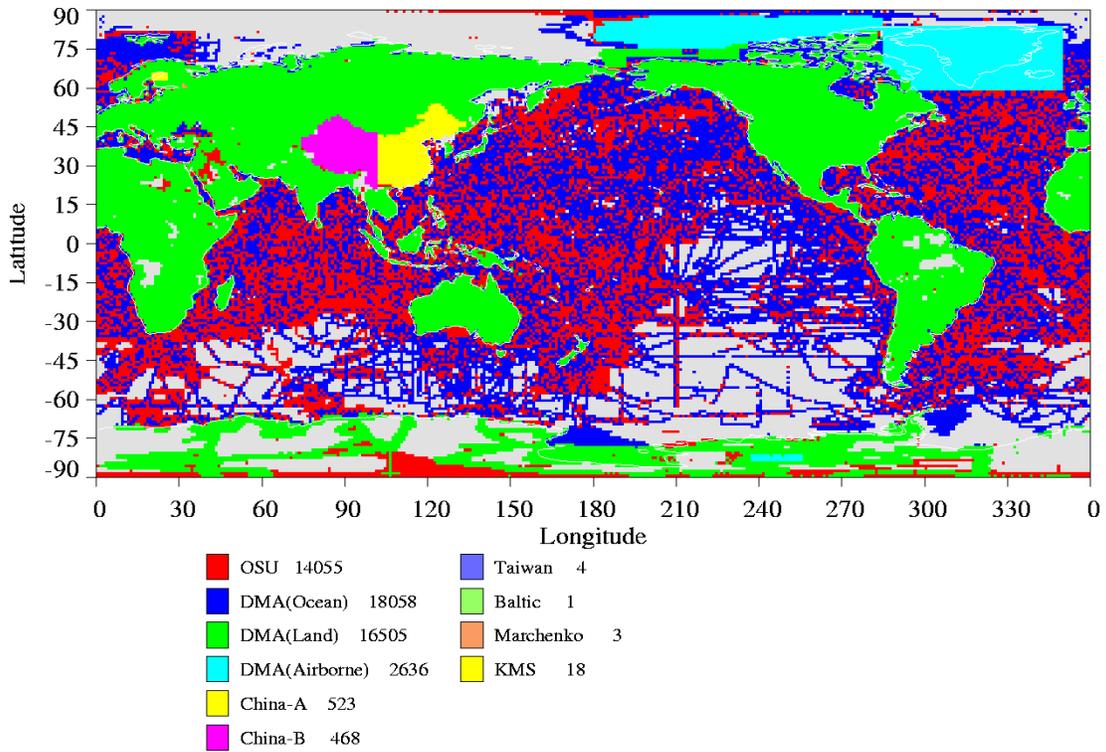
Figure 3.5–1. Sources of the 1° mean gravity anomaly data.

■ OSU 14055			■ Taiwan 4	
■ DMA(Ocean) 18058			■ Baltic 1	
■ DMA(Land) 16505			■ Marchenko 3	
■ DMA(Airborne) 2636			■ KMS 18	
■ China-A 523				
■ China-B 468				
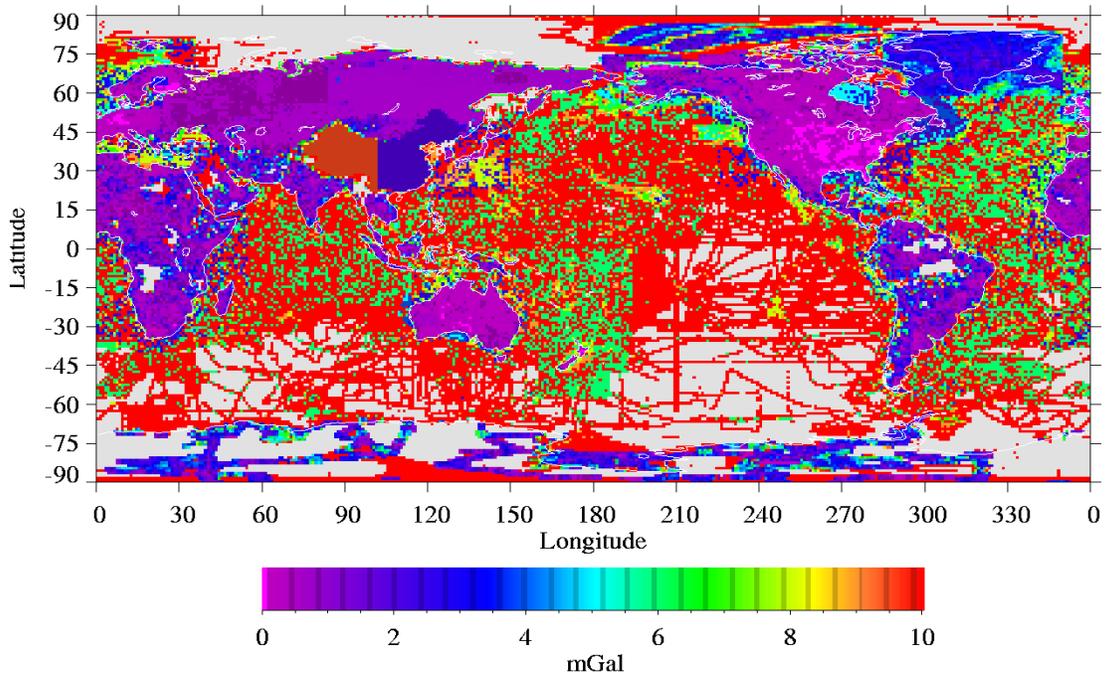
Figure 3.5–2. Standard deviation of the 1° mean gravity anomalies.

Table 3.5–2. Statistics on the terrestrial 1° mean gravity anomalies (mGal).

Statistic	Value
Number of values	52271
Percentage of the Earth's area	87.10
Minimum value (φ, λ)	−282.00 (19.50°, 293.50°)
Maximum value (φ, λ)	336.54 (19.50°, 204.50°)
Mean value	−0.24
RMS value	27.62
Minimum value σ	0.04
Maximum value σ	47.00
RMS σ	11.83

3.5.1 1° Mean Surface Gravity Anomalies Over Land Areas

The 1°x1° mean gravity anomalies calculated over land areas used the 30´x30´ mean terrestrial gravity anomaly file and the OSU "October 1990" 1° mean terrestrial gravity anomaly data [*Yi and Rapp*, 1991]. To calculate the 1°x1° mean gravity anomalies, we used the simple averaging formula:

$$\overline{\Delta g}(1°) = \frac{\sum_{k=1}^{N} \overline{\Delta g}(30')_k}{N} \tag{3.5.1-1}$$

To calculate the standard deviation of the 1° mean value $\sigma(1°)$, we used the formula:

$$\sigma(1°) = \frac{\sqrt{\sum_{k=1}^{N} \sigma^2(30')_k}}{N} + (4 - N) \cdot 3 \quad \text{mGal} \tag{3.5.1-2}$$

where N is the numer of 30´ mean values available within a 1° cell.

3.5.2 1° Mean Surface Gravity Anomalies Over Ocean Areas

The surface gravity data for ocean areas were compiled at the 1° level using the 1° OSU "October 1990" mean anomaly data [*Yi and Rapp*, 1991] that was used for the OSU91A geopotential model [*Rapp, Wang, and Pavlis*, 1991] and the ocean gravity sources collected by NIMA. Accuracy estimates reflecting the number of point anomalies within the 1° cells, and comparisons with altimeter-derived 1° values from the GEOSAT GM data were used to determine the most representative surface values. The method of computation consisted of using simple averaging technique called the "modified average free-air" procedure [*Uotila*, 1967], which divides each 1° cell into smaller cells, i.e., 10´x10´ cells, computes the average gravity anomaly for each smaller cell, and then averages the smaller cell values to the 1° cell size.

3.6 Summary

The development of the final global surface gravity data base has paralleled the computation of the oceanwide altimetry-derived anomaly file used in this project. The formation of these data bases represents the largest geodetic computer project ever attempted at NIMA. Preliminary models [*Nerem et al., 1996; Pavlis et al., 1996*] (and the EGM96 geopotential model) that employed these data have demonstrated significant improvements over preexisting models in areas such as the FSU, Greenland, Canada, Scandinavia, Africa, China, and South America. The major re-computation of the 30′ and 1° surface mean free-air gravity anomalies was completed in October 1995 at NIMA. Certain modifications and improvements were made to these files and the final shipment of the global surface gravity data bases was delivered to GSFC on September 12, 1996. Table 3.6–1 is included to detail the anomaly counts and the percentage of area covered as a function of geographic region for the three data sets, the NIMA terrestrial 30′ anomalies, the OSU terrestrial 30′ anomalies, and the NIMA terrestrial 1° anomalies.

Table 3.6–1. Gravity anomaly count and percentage of area covered by the NIMA 30′ Δg, OSU 30′ Δg , and NIMA 1° Δg data sets as a function of geographic region.

Geographic Area	NIMA 30′ Δg		OSU 30′ Δg		NIMA 1° Δg	
	Num	% area	Num	% area	Num	% area
Land N. Hemisp.	48148	95.12	22101	46.78	12341	97.71
Land S. Hemisp.	21849	80.31	10124	49.95	6456	83.29
Land	69997	90.38	32225	47.79	18797	93.12
Ocean N. Hemisp.	19078	19.84	20729	24.66	16602	94.65
Ocean S. Hemisp.	8175	7.97	14036	15.62	16872	77.21
Ocean	27253	13.03	34765	19.47	33474	84.64
N. Hemisphere	67226	49.65	42830	33.42	28943	95.86
S. Hemisphere	30024	21.42	24160	22.01	23328	78.33
Globe	97250	35.53	66990	27.71	52271	87.10

3.7 References

Brozena, J., and M. Peters, Airborne Gravity Measurement at NRL, *Proceedings of the International Symposium on Kinematic Systems in Geodesy, Geomatics and Navigation*, The University of Calgary, Banff, Canada, August 30–September 2, 1994.

Defense Mapping Agency, Supplement to Department of Defense World Geodetic System 1984 Technical Report, Part 1, *DMA Technical Report 8350.2-A*, December 1, 1987.

Defense Mapping Agency, Department of Defense World Geodetic System 1984, *DMA Technical Report 8350.2*, Second Edition, September 1, 1991.

Dimitrijevich, I., WGS84 Ellipsoidal Gravity Formula and Gravity Anomaly Conversion Equations, Defense Mapping Agency Aerospace Center, 1987.

Ekholm, S., A Full-Coverage High-Resolution Topographic Model of Greenland Computed From a Variety of Digital Elevation Data, *J. Geophys. Res.*, *101*, B10, 21961–21972, 1996.

Fairhead, J.D., and A.B. Watts, The African Gravity Project: Academic, Government and Commercial Data Integrated for New Map of Continent and Margins, *Lamont News Letter,* Vol. 21:6–7, Columbia University, 1989.

Fairhead, J.D., and E.L. Makedonskii, *Gravity Studies of the Former Soviet Union*, European Association of Geoscientists and Engineers, Annual Meeting, Amsterdam, The Netherlands, June 3–7, 1996.

Fairhead J.D., S.J. Campbell, and J.S. Williams, *Regional Gravity: Continental scale compilations in South East Asia*, KG–5:132–136, Society of Exploration Geophysicists, Jakarta, 1996.

Forsberg, R., A Study of Terrain Reductions, Density Anomalies and Geophysical Inversion Methods in Gravity Field Modeling, *Rep. 355*, Dept. of Geod. Sci. and Surv., Ohio State Univ., Columbus, 1984.

Forsberg, R., A New Covariance Model for Inertial Gravimetry and Gradiometry, *J. Geophys. Res., 92*, B2, 1305–1310, 1987.

Forsberg, R., and S. Kenyon, Downward Continuation of Airborne Gravity Data, *Proceedings of IAG Symposium G4, IUGG XXI General Assembly*, Boulder, Colorado, July 2–14, 1995.

Green, C.M., and J.D. Fairhead, The South American Gravity Project, in *Recent Geodetic and Gravimetric Research in Latin America*, IAG Symposium III, Springer–Verlag, 82–95, 1993.

Green, C.M., and J.D. Fairhead, The European Gravity Database: A Tool for Continental Scale Basin Analysis, Abstract KO25, European Association of Petroleum Geoscientists, 1994.

Gwo–Chyang, T., Dept. of Surveying and Mapping Engr. Chung Cheng Institue of Technology, Taiwan, private communication, 1994.

Heck, B., An evaluation of some systematic error sources affecting terrestrial gravity anomalies, *Bull. Geod., 64*, 88–108, 1990.

Heiskanen, W.A., and H. Moritz, *Physical Geodesy*, W.H. Freeman, San Francisco, 1967.

Kim, J., and R.H. Rapp, The development of the July 1989 1°x1° and 30´x30´ terrestrial mean free-air anomaly data bases, *Rep. 403,* Dept. of Geod. Sci. and Surv., Ohio State Univ., Columbus, 1990.

Marchenko, A.N., Technical University of Graz (Austria), private communication, 1996.

Moritz, H., *Advanced Physical Geodesy*, Herbert Wichmann Verlag, Karlsruhe, Germany, 1980.

Nerem, R.S., F.J. Lerch, J.A. Marshall, E.C. Pavlis, B.H. Putney, B.D. Tapley, R.J. Eanes, J.C. Ries, B. E. Schutz, C.K. Shum, M.M. Watkins, S.M. Klosko, J.C. Chan, S.B. Luthcke, G.B. Patel, N.K. Pavlis, R.G. Williamson, R.H. Rapp, R. Biancle, and F. Noule, Gravity Model Development for TOPEX/POSEIDON: Joint Gravity Models 1 and 2, *J. Geophys. Res.*, 99, 24421–24447, 1994.

Nerem, R.S., F.J. Lerch, R. Salman, R. Trimmer, S. Kenyon, R.H. Rapp, N.K. Pavlis, S.M. Klosko, J.C. Chan, M.H. Torrance, Y.M. Wang, R.G., Williamson, E.C. Pavlis, Preliminary Results From the Joint GSFC/DMA Gravity Model Project, *Global Gravity Field and Its Temporal Variations*, IAG Symposia, Vol. 116, 92–110, Springer–Verlag, Berlin, 1996.

National Imagery and Mapping Agency, MADTRAN, Edition 1 (Version 4.2), 1997.

Pavlis, N.K., Modeling and estimation of a low degree geopotential model from terrestrial gravity data, *Rep. 386*, Dept. of Geod. Sci. and Surv., Ohio State Univ., Columbus, 1988.

Pavlis, N.K, Raytheon STX Corp., private communication, 1995.

Pavlis, N.K., J.C. Chan, and F.J. Lerch, Alternative Estimation Techniques for Global High-Degree Gravity Modeling, *Global Gravity Field and Its Temporal Variations*, IAG Symposia, 116, 111–120, Springer–Verlag, Berlin, 1996.

Rapp, R.H., Y.M. Wang, and N.K. Pavlis, The Ohio State 1991 geopotential and sea surface topography harmonic coefficient models, *Rep. 410*, Dept. of Geod. Sci. and Surv., The Ohio State Univ., Columbus, 1991.

Tscherning, C.C., and R.H. Rapp, Closed covariance expressions for gravity anomalies, geoid undulations, and deflections of the vertical implied by degree-variance models, *Rep. 208*, Dept. of Geod. Sci., Ohio State Univ., Columbus, 1974.

Uotila, U.A., Computation of Mean Anomalies of 1°x1° Blocks, *Rep. 95*, Dept. of Geod. Sci., Ohio State Univ., Columbus, 1967.

Yi, Y., and R.H. Rapp, The October 1990 1°x1° mean anomaly file including an analysis of gravity information from China, *Internal Rep.*, Dept. of Geod. Sci. and Surv., Ohio State Univ., Columbus, 1991.

4. THE ALTIMETRY-DERIVED GRAVITY ANOMALIES

In order to extend a spherical harmonic geopotential model to degree and order 360, a worldwide 30´x30´ mean gravity anomaly file was required. In the last 20 years, radar altimetry satellites have provided a means for estimating the gravity field over the oceans. These satellites map the shape of the ocean surface, from which the geoid can be inferred. Several methods are available for computing mean gravity anomalies from altimetry data. The altimetry-derived mean gravity anomaly data set made a major contribution to EGM96 by providing the necessary gravity information in nearly all the ocean areas between ±82° latitude.

From 1994 to 1996, the available altimetry improved in both quantity and quality, and continued progress is expected in the future. In 1994, the only GEOSAT Geodetic Mission (GM) data generally available were from the region south of 30° south latitude. However, work proceeded under the assumption that NIMA's request for the release of a complete set of GEOSAT-derived 30´x30´ mean gravity anomalies covering the latitude range of ±72° would be granted for use in developing EGM96. The release was approved, and in 1996 the remainder of the GEOSAT GM data was made available to the scientific community. As an aside, an improved version of the GEOSAT GM and Exact Repeat Mission (ERM) data was released in 1997 by the National Oceanic and Atmospheric Administration/National Oceanographic Data Center (NOAA/NODC). These improved data were reduced using more accurate (10–15 cm radial error) orbits and contain state-of-the-art tidal and atmospheric corrections computed by NASA GSFC.

The 30´x30´ mean gravity anomaly data set was pieced together from the GEOSAT and ERS–1 altimeter-derived gravity anomalies. The major source for the anomaly data were the GEOSAT GM data. The ERS–1 gravity anomalies, supplied by the Danish National Survey and Cadastre or Kort-og Matrikelstyrelsen (abbreviated KMS), made an important contribution by extending the coverage in the near-polar areas and a few near-shore areas, but had voids and were sparse in the Weddell Sea area near Antarctica. Tilo Schoene (of the Alfred Wegener Institute for Polar and Marine Research) supplied gravity anomalies for this region that were derived from a combination of GEOSAT and ERS–1 data [*Schoene*, 1996]. Comparisons with high-quality NIMA and Bundesanstalt für Geowissenschaften und Rohstoffe (BGR) shipborne gravity observations illustrate the quality and consistency of the global altimetry file. The comparisons with NIMA's marine gravity anomalies indicate that, in general, the GEOSAT anomalies are slightly better than the ERS–1 anomalies overall and significantly better in most high-frequency areas.

In this section, the main focus will be on the final altimetry data set provided to GSFC and used in EGM96. A detailed account of the NIMA GEOSAT processing is provided, including a discussion of the geoid height processing and the collocation process used to compute the gravity anomalies. NIMA was fortunate to have available very accurate marine survey derived anomalies in many parts of the oceans. Although the use and release of most of these marine data are restricted, they played an important role in studies. Comparisons of the marine and GEOSAT anomalies were carried out to test, refine, and verify the methodology and anomaly quality. The

marine data also were used to estimate the accuracy of the 30´ mean gravity anomalies obtained by averaging the KMS ERS–1 smaller size gravity anomalies.

4.1 GEOSAT

GEOSAT was launched on March 12, 1985, into an 800-kilometer, 108°-inclination orbit. The 3-day near-repeat ground track had a grid spacing of approximately 4 kilometers. The precision of the GEOSAT altimeter was 3.5 centimeters for a 2-meter significant wave height [*MacArthur, Marth, and Wall*, 1987]. The length of the primary, or Geodetic Mission, was 18 months, during which GEOSAT covered 200 million kilometers of ground track, producing 49 million data points at 2 points per second, distributed over the latitude range of ±72°. The Geodetic Mission ended when GEOSAT was maneuvered into the Exact Repeat Mission (ERM) 17-day repeating orbit on October 1, 1986. For a discussion of the GEOSAT mission, see *Jensen and Wooldridge* [1987] and *McConathy and Kilgus* [1987].

The Johns Hopkins University Applied Physics Laboratory (APL) satellite tracking facility downloaded the raw GEOSAT data and created a Sensor Data Record (SDR), which was sent to the Naval Surface Weapons Center (NSWC). NSWC incorporated Defense Mapping Agency (now part of NIMA) Doppler tracking data for orbit modeling and produced a Geophysical Data Record (GDR). The GDRs were sent to NIMA and to the Naval Oceanographic Office (NAVOCEANO) at Stennis Space Station, Bay St. Louis, MS, in weekly sets. The largest error source in the GDRs was radial orbit error. The error before adjustment was approximately 80 cm RMS, but could be as high as 2 or 3 m in local areas based on crossover statistics. The Schwiderski tide model, provided on the GDRs, was used to reduce the GEOSAT altimeter data.

NIMA has exploited altimetry data for its gravity products since the late 1970's. *Brace* [1977] discusses a GEOS–3 geoid, and *VanHee* [1987] describes the processes and results of NIMA's early GEOSAT processing. Many of the procedures now used are refinements of techniques described by *VanHee* [ibid.]. The emphasis in the next section will be on the GEOSAT processing in the years just prior to this project, during which NIMA made significant improvement in the quality of its GEOSAT GM processing strategies.

4.1.1 NIMA GEOSAT Processing, 1985–1994

NIMA's processing of the GEOSAT data consisted of identification of spurious data, radial orbit error reduction, and the generation of gravity products such as gravity anomalies. A least-squares adjustment using the differences at the intersection of the ascending and descending ground tracks, referred to as crossovers, is a common method of minimizing radial orbit error. The assumption is made that, with proper accounting for tidal contributions, the resulting sea surface height should be largely constant, consisting of geoidal and quasi-static dynamic ocean topography signals. NIMA's procedure used a control network, which consists of arcs that are more accurate but more widely spaced than the Geodetic Mission data being adjusted to it. Crossovers of both the GM arcs with the network and the GM arcs with other GM arcs were used. The network arcs are held fixed during the adjustment. The weight of the two types of

crossings is determined by their relative estimated accuracy. The processing performed during this period provided the foundation for the work done in support of the EGM96 project.

Initially, the weekly GEOSAT GM data sets were adjusted to a SEASAT network. Geophysicists at NAVOCEANO averaged and adjusted the data from SEASAT's 3 weeks of ERM data into a highly consistent network of uncertain longer wavelength accuracy. NIMA further modified the network by filling in sparsely covered areas and increasing the density of arcs in known trouble areas (see Figure 4.1.1–1). The GM data were adjusted to this enhanced SEASAT network, edited, and merged into a GEOSAT data base. After the adjustment, the spurious data stand out as being inconsistent with the surrounding data. The adjusted crossovers are used to identify such inconsistent data. The crossovers from the weekly sets are widely spaced so that only spikes that fell near a crossover or that were several degrees long could be identified.
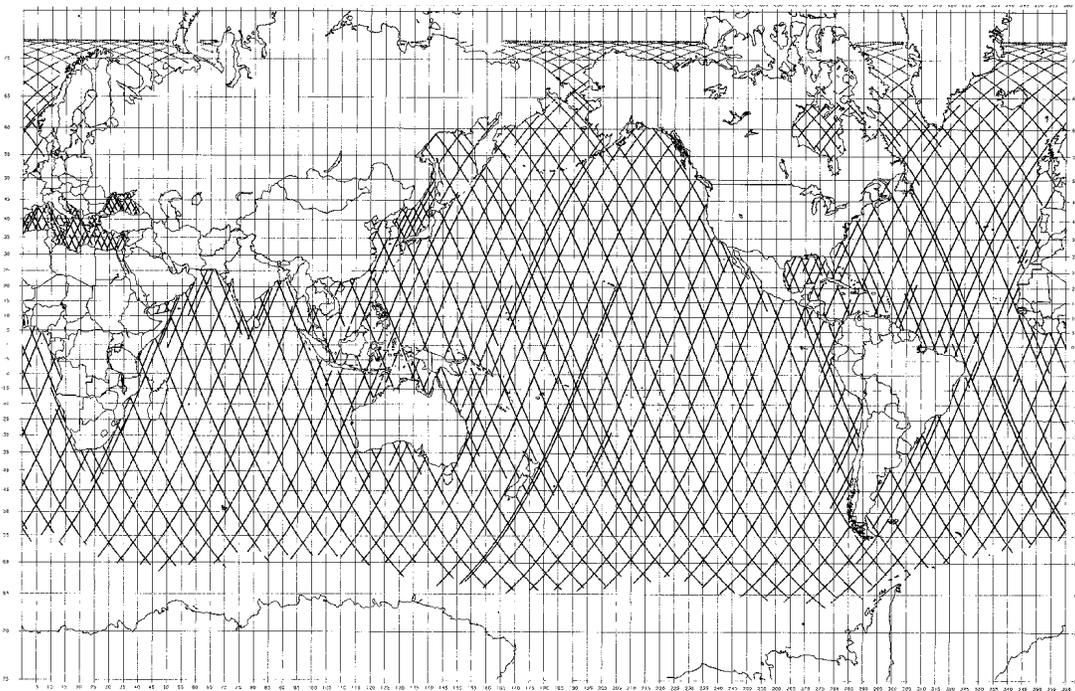
Figure 4.1.1–1. The SEASAT network.

Later, NIMA readjusted the entire GEOSAT GM data to a network developed by William E. Rankin at NAVOCEANO. This network was derived from the first year of the GEOSAT ERM data that were reduced with orbits computed by the NSWC in Dahlgren, VA (see Figure 4.1.1–2). The orbits had an initial estimated accuracy of 90 cm, compared to the estimated 3 m orbit accuracy of the initial ERM data [*Rankin*, *private communication*, 1997]. The resulting 244 revolutions, representing each distinct ground track, were then adjusted using the method of *Cloutier* [1983]. The arcs of this GEOSAT ERM network were much more closely spaced than the arcs of the SEASAT network. Crossover statistics showed that the ERM network was also

more self-consistent than the earlier SEASAT network. The GEOSAT network was derived from a year of ERM data instead of just 3 weeks' worth of data, and allowed the removal of periodic effects that had periods less than or equal to a year.
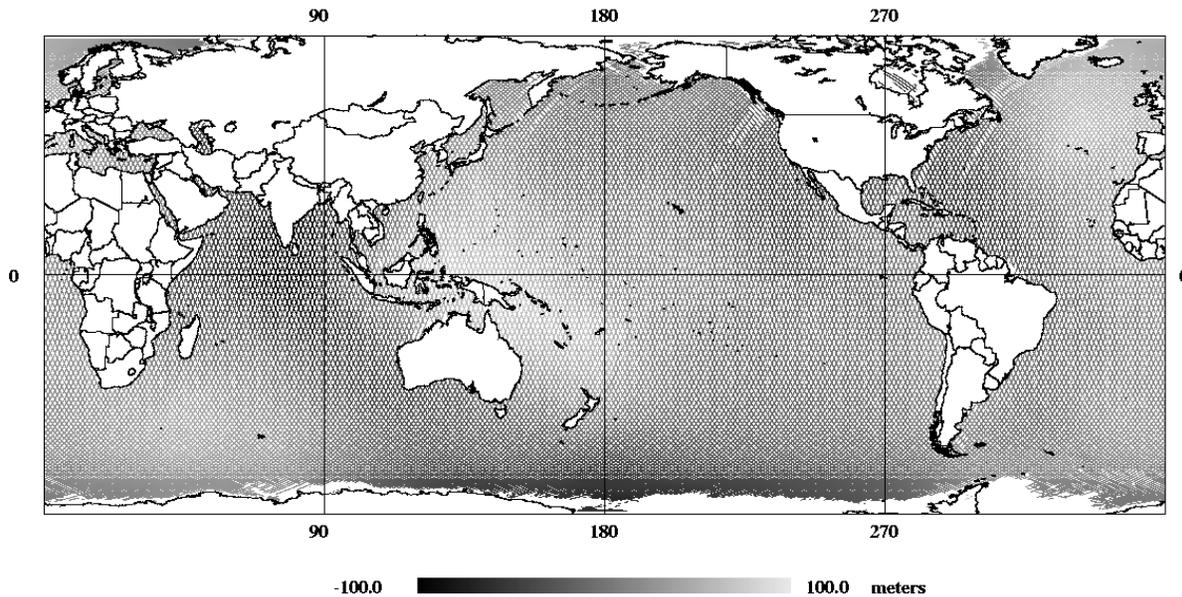
Figure 4.1.1–2. The GEOSAT ERM network.

NIMA first adjusted the GM data to this ERM network one arc at a time to remove the long wavelength error. A bias, bias and tilt, or bias, tilt, and parabolic model was applied depending on the length of the arc. These arc-adjusted GM data were then adjusted in diamond-shaped areas bounded by network arcs (see Figure 4.1.1–3) using a bias and tilt model. Automated crossover cell editing algorithms, developed by NIMA, were used to identify spurious data. The editing was a statistical filter. Crossovers whose adjusted difference were inconsistent with the other crossovers in the surrounding 1° or larger cell were omitted from the adjustment. The procedure was repeated until the solution converged. The set of crossovers deleted from the adjustment solution was used to generate edits that were applied to the point data. All the data from the entire GM mission that fell within the diamond-shaped adjustment area were used. The density of crossings along an arc was increased by about 75 times over the spacing of the crossings along an arc in the adjustment of the weekly sets to the SEASAT network. This density greatly improved the effectiveness of the crossover editing in identifying data inconsistencies. Only edited GEOSAT data were used to compute the NIMA products.

One-degree cell statistics of unadjusted or adjusted crossovers were used to provide a measure of the regional variation and consistency of the data. Before adjustment, radial orbit error was the dominate error source. Most cells had approximately a 1 m RMS, but in a few cells the RMS was 2 m. The adjustment of the data by weekly sets to the SEASAT network typically reduced the

cell RMS values to 13 cm. The readjustment of the GM data to the GEOSAT network by diamond-shaped areas further improved the typical RMS to about 7 cm. Before the readjustment, there was evidence of remaining orbital error; no such evidence was seen after the readjustment. See Figures 4.1.1–4 through 4.1.1–8.
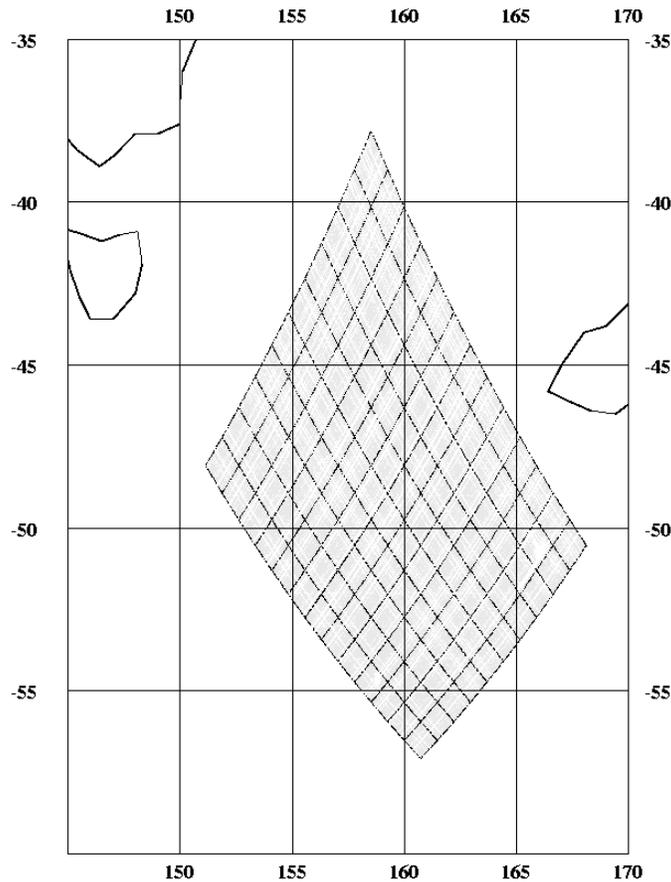
Figure 4.1.1–3. Adjustment area crossovers. Network x GM crossovers are black, GM x GM crossovers are gray.

Following the area adjustment, a file of 5´x5´ mean sea surface heights (Figure 4.1.1–9) was computed by averaging the readjusted GEOSAT data. These GEOSAT mean sea surface heights were used to compute a complete set of 5´x5´ GEOSAT mean free-air gravity anomalies. These anomalies were computed using an earlier version of the current Least Squares Collocation program and a set of autocovariance parameters for rough, moderate, and smooth areas. The autocovariance parameter values had been empirically derived from NIMA's highest quality marine data.
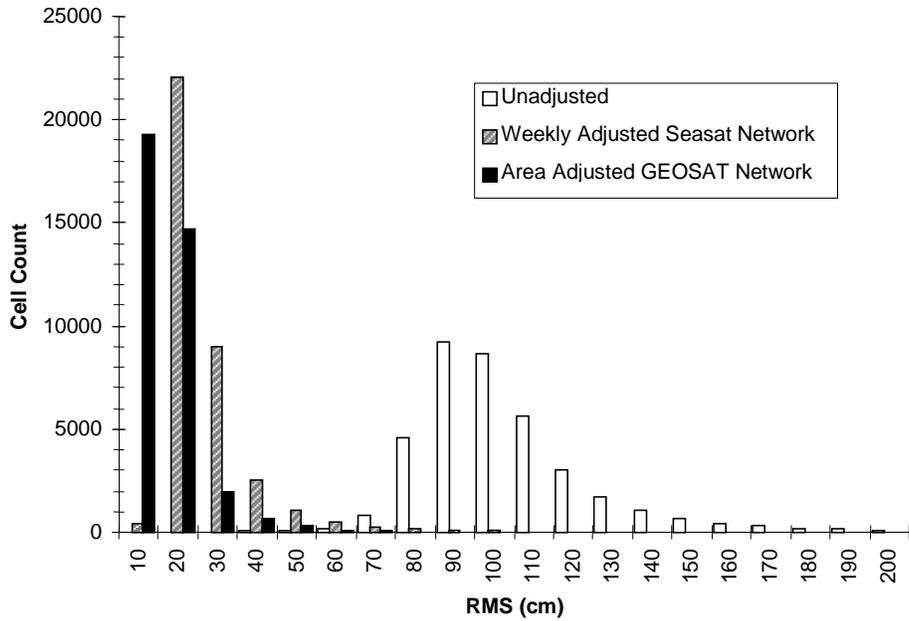
Figure 4.1.1–4. Distribution of 1° x 1° cell crossover statistics (10 cm bins).
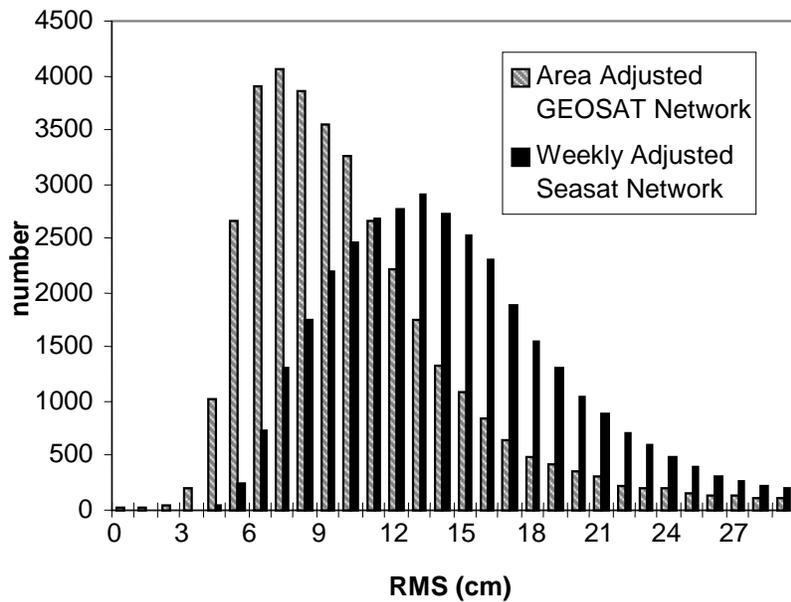
Figure 4.1.1–5. Distribution of 1° x 1° cell adjusted crossover statistics before and after the area adjustment of the GEOSAT GM data to the ERM network (1 cm bins).

0.0 ▰▰▰▰▰▰▰▰ 2.0 meters
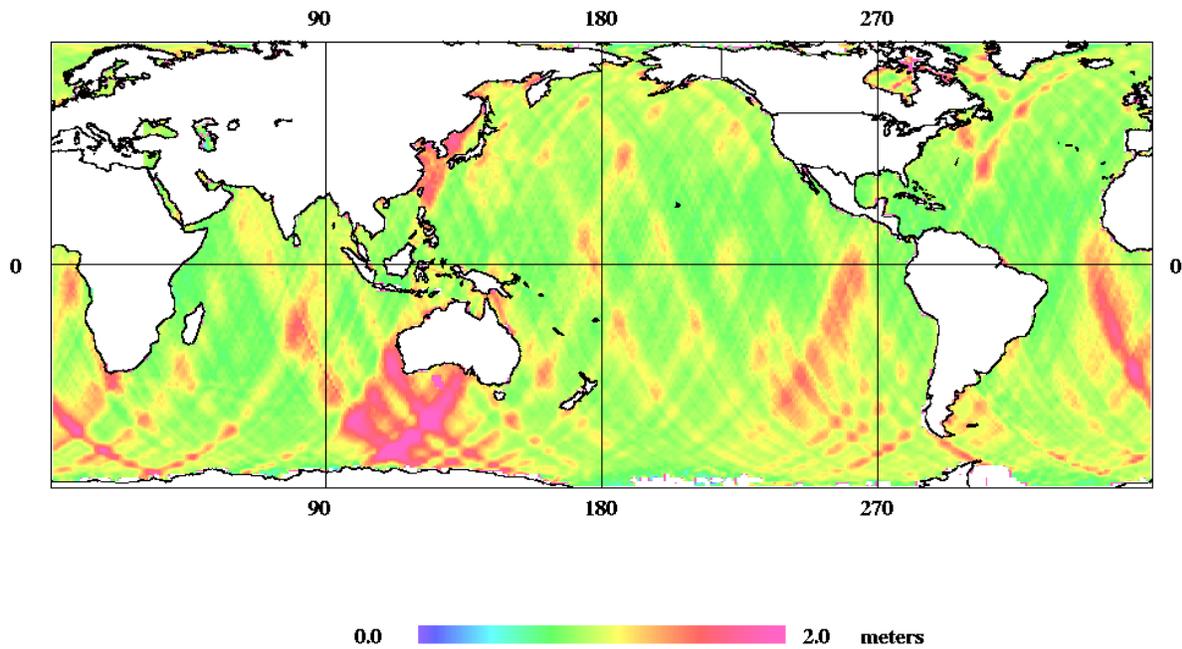
Figure 4.1.1–6. GEOSAT 1° cell unadjusted crossover RMS values.

0.0 ▰▰▰▰▰▰▰▰ 1.0 meters
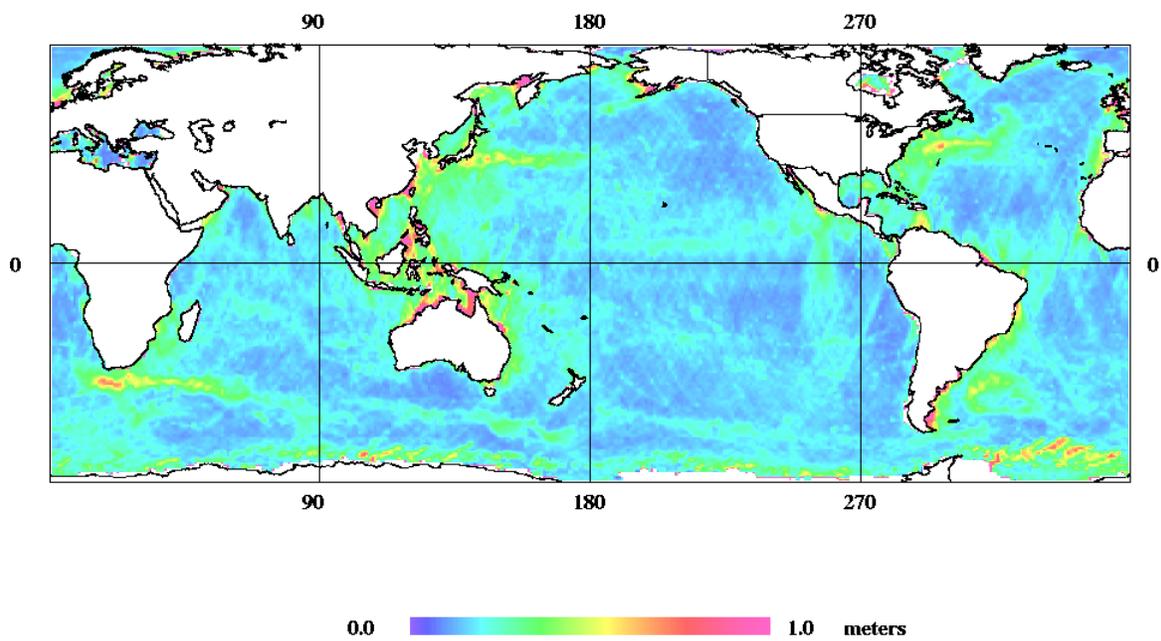
Figure 4.1.1–7. Crossover RMS after GEOSAT weekly sets were adjusted to the SEASAT network.
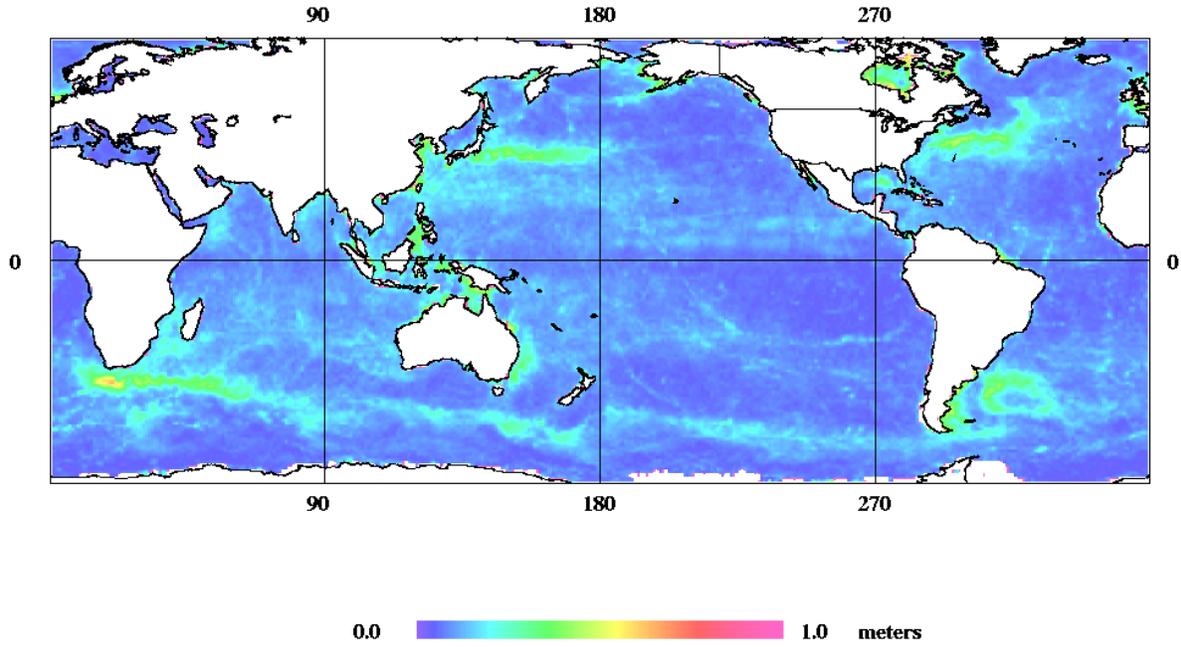
Figure 4.1.1–8. Crossover RMS values after GEOSAT diamond-shaped areas were adjusted to the GEOSAT ERM network.
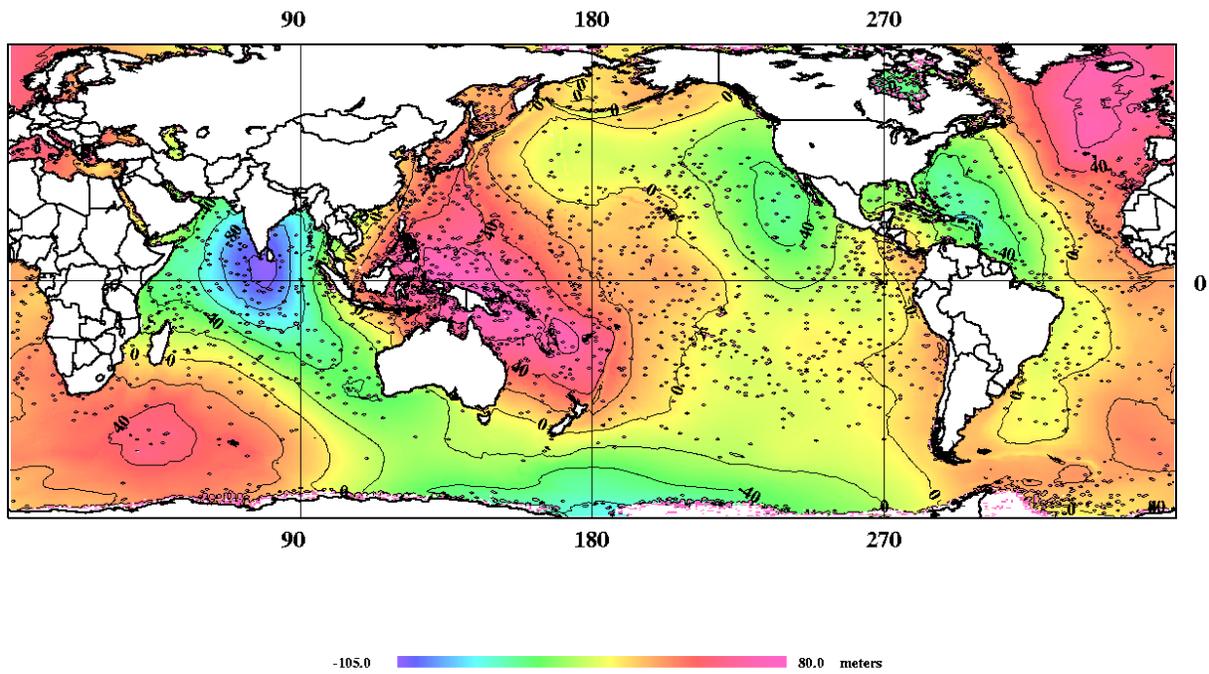
Figure 4.1.1–9. The 5´x5´ GEOSAT mean sea surface.

4.1.2 NIMA GEOSAT Processing, 1994–1996

Least Squares Collocation (LSC) was agreed upon by both the Altimetry and the Surface Gravity anomaly computation Working Groups as the preferred method to be used to compute both the land (surface) and water (altimetry) anomalies. Since the collocation procedure has already been discussed in detail in Section 3, the emphasis of this discussion will be on the computation of gravity anomalies from estimates of geoid undulations. As mentioned earlier, test studies using comparisons with high-quality marine mean gravity anomalies were used by the working groups to resolve issues and to verify and refine procedures.

NIMA's collocation procedure is a versatile, statistically based procedure that uses the correlation of one or more independent variables with an output variable. NIMA routinely uses geoid undulations, point gravity anomalies, or a combination of the two to predict mean gravity anomalies, mean geoid undulations, or gravity disturbance components. The computation is tuned to the local area by correlation parameters defining the relationship between the input and output variables. The LSC method has an advantage over existing FFT techniques because it provides an estimate of the accuracy of the computed value. Such estimates were needed for normal equation generation and weighting in the EGM96 solution. Using recommendations from the working groups and consulting with René Forsberg of KMS, Steve Kenyon revised NIMA's LSC program. The resulting collocation procedure devised to compute the GEOSAT 30´x30´ mean gravity anomalies differed in many respects over what had been used previously.

In the past, a global set of covariance parameters relating geoid undulations and gravity anomalies were used in all LSC computations. This was improved by empirically determining covariance parameters for smooth, rough, and moderate areas using marine anomalies. The NIMA collocation program computes the output values of 30´ mean gravity anomalies by 1° cells. The altimetry data from a 3°x3° computational area was used to compute the mean gravity anomalies within the inner 1°x1° cell. This overlap between adjacent cells provided for continuity across cell boundaries. To improve the procedure for the EGM96 project, a set of autocovariance parameters was calculated for each computational area by using the GEOSAT 5´x5´ mean gravity anomalies that NIMA had on hand in 1994. The *Forsberg* [1987] method was used to compute the C0 (variance) term, high- and low-frequency attenuation factors, and the correlation length (Figures 4.1.2–1 through 4.1.2–4). Each set of covariance parameters was stored in an individual file. The LSC program accessed the appropriate file to tune the calculation of each anomaly to its area. Therefore, the calculation of each set of four 30´ mean gravity anomalies within a 1° cell was easily tuned to its 3° computational area cap. The LSC program has a parameter to indicate the accuracy of the 5´x5´ residual geoid undulation data. In the past this had been set at 50 cm. This was set at 25 cm for all the 30´ mean gravity anomaly computations, regardless of the geographic location. Experience has shown that when computing point gravity anomalies, or small size mean gravity anomalies, a more realistic accuracy of 5 cm is appropriate in geographic areas of high variability.

These changes in the collocation procedure improved the resolution of the GEOSAT anomalies. Two ways NIMA has used to assess the quality of altimetry height data were to (1) compute gravity anomalies from the altimetry heights and compare them with high-quality, marine-
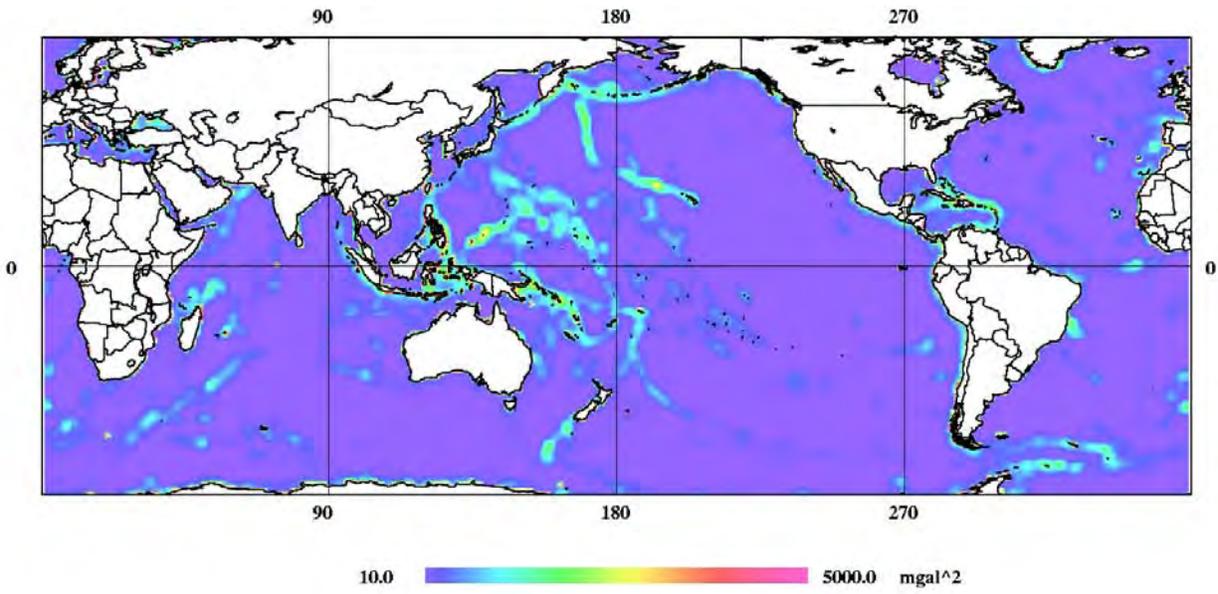
Figure 4.1.2–1. Covariance function variance terms (C0).
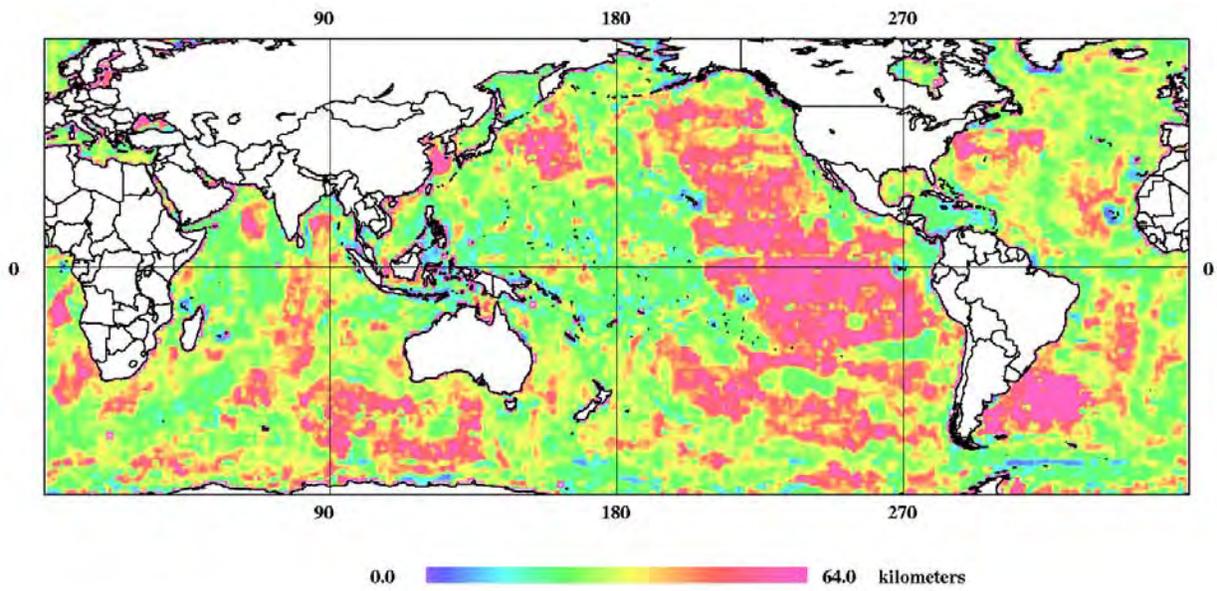
Figure 4.1.2–2. Covariance function high-frequency attenuation factors.
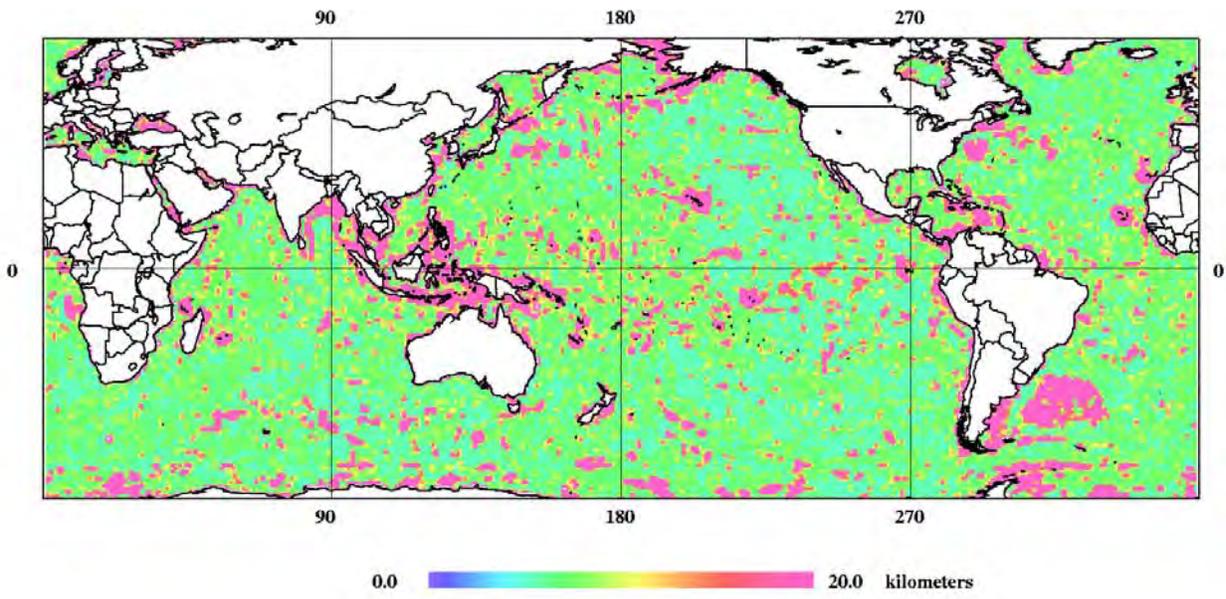
Figure 4.1.2–3. Covariance function low-frequency attenuation factors.
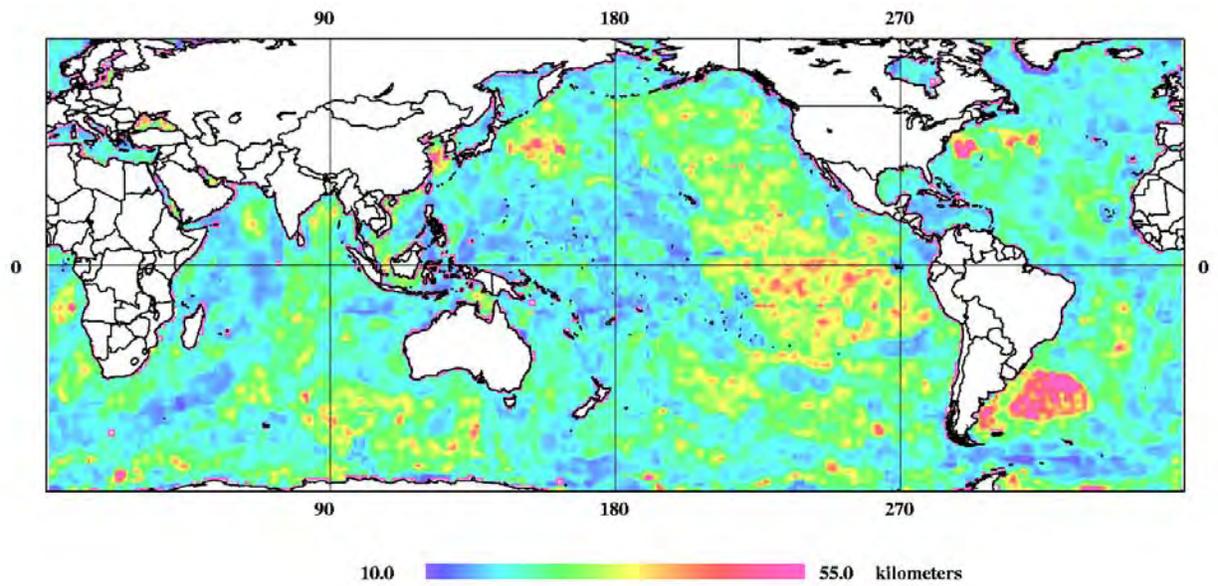
Figure 4.1.2–4. Covariance function correlation lengths.

4–11

derived anomalies where available and (2) compare the altimetry heights or anomalies with spherical harmonic derived values. Comparisons of type (1) indicated about 1 mGal improvement in the 30´ mean gravity anomalies when the rough, smooth, and moderate covariance parameters were replaced by the new set of computational area covariance parameters.

The use of anomalies computed from a combination of GEOSAT 5´x5´ mean sea surface heights and point gravity anomaly data was considered in near-shore and island areas. The quality of such combination anomalies are heavily dependent upon the quality, density, distribution, and consistency of the two types of data. Because EGM96 was to have unrestricted distribution, some of NIMA's holdings could not be used. With the available point gravity data, it turned out that the combination of altimetry with marine gravimetry was not the best approach based on comparisons with anomalies computed from nonreleasable high-quality data and on comparisons at the boundary with surface anomalies. In some cases, the best results were obtained by using only GEOSAT 5´x5´ residual geoid undulations in the collocation computation. In other cases, the best results were obtained by using terrain-corrected point gravity anomalies alone in the collocation computation. As a consequence, no combination anomalies were included in the computation of EGM96.

There was concern within the working group that NIMA's use of 5´x5´ area-mean values instead of point geoid undulations might be smoothing the data too much in high-frequency areas. Comparisons with high-quality 30´ mean gravity anomalies derived from shipborne survey data over trenches and sea mount chains showed that NIMA's GEOSAT anomalies were in closer agreement with survey data than the other altimetry sets available at the time. Over the center of these high-frequency features, the NIMA GEOSAT 30´ mean gravity anomalies were more than 20 mGal closer to the ship-derived 30´ mean gravity anomalies than the other data sets. Scattered sea mounts are more difficult to model with altimetry data; however, the NIMA GEOSAT anomalies also did well in those areas. The better performance of the GEOSAT data is the result of data density that is superior to that of ERS–1 and NIMA's concentration on improving GEOSAT data quality by adjustment and editing. At the 30´ resolution, the NIMA GEOSAT-derived anomalies computed from the 5´x5´ mean sea surface heights generally produce the smallest differences when compared with high-quality marine anomalies.

It should be noted that comparisons carried out by Dennis Manning of NIMA indicate that it is necessary to use point geoid undulation values instead of the 5´x5´ means to avoid smoothing when computing point gravity anomalies or small-size mean gravity anomalies. Also, the residual field should not be centered if the calculations are to be made using the 3°x3° computational areas. Centering the residual field for point gravity anomalies or mean gravity anomalies less than 15´ will result in discontinuities at the 1°x1° cell boundaries. An explanation of centering is given below.

The density of the altimetry data affects the quality of the anomalies computed from them. This is true whether point values or means are used. Comparisons of point gravity anomalies with marine gravity survey anomalies have identified instances where the ERS–1 anomalies recovered

more of an isolated sea mount's effect than did the GEOSAT anomalies. A close look revealed that the ERS–1 data were denser than NIMA's edited GEOSAT data in that area.

An altimetry mean sea surface such as the GEOSAT 5´x5´ mean sea surface (Figure 4.1.1–9) converges to the true "mean" sea surface as the number of measurements in each cell approaches infinity. The local rate of convergence is dependent on the regional temporal variability. The variability evident in the crossing points (Figures 4.1.1–5 and 4.1.1–8) was also present in the GEOSAT ERM sea surface heights (Figure 4.1.2–5). As expected, the regional variability was highly correlated with the known ocean currents. The meandering of the currents and eddies are examples of oceanographic effects that perturb the mean sea surface and create regional variability. The variability affects local confidence in the mean sea surface. In the discussion below, one must keep in mind that, while the overall RMS is 7 cm, the local RMS values are 10 to 40 cm in most ocean current areas. In the strong Gulf Stream current, the RMS can be as high as 55 cm. Off the southern tip of Africa, where currents collide, the RMS can reach 70 cm. Data density can suppress the time-dependent component of the Dynamic Ocean Topography (DOT). The long-term perturbation of the sea surface is the steady-state component of the DOT. A recent DOT model of the steady-state component was used to reduce the GEOSAT 5´x5´ mean sea surface to a closer approximation of the geoid.
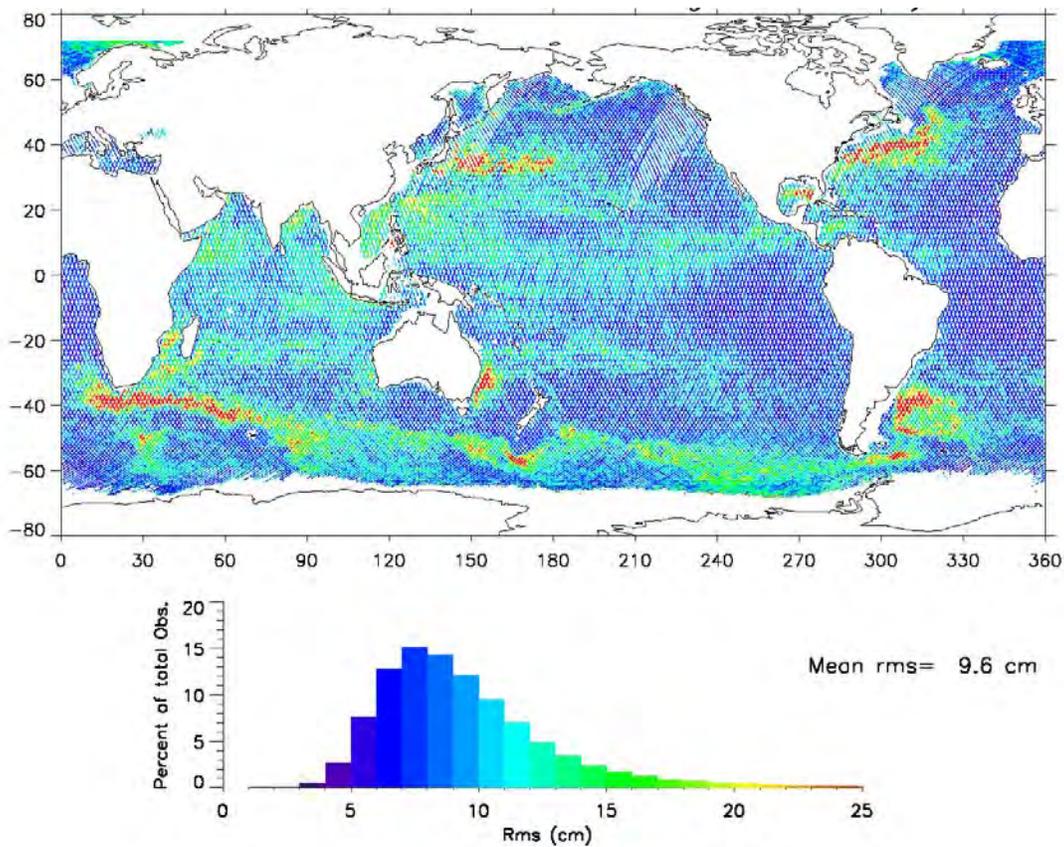
Figure 4.1.2–5. GEOSAT ERM sea surface height variability.
(Courtesy of B. Beckley of Raytheon STX)

Plots of the 1° cell crossover RMS values show that the variability of the ocean surface is geographically correlated with the known major currents. After the orbit readjustment, the overall variability in the current areas was reduced, but there was an even stronger contrast between the current areas and the surrounding cells, as illustrated in Figures 4.1.1–7 and 4.1.1–8.

Averaging of the dense GEOSAT point data was used to smooth out most of the sea surface height variability that was observed after the adjustment of the orbits. That is, even though there are considerable differences in the regional variability of the point data, the density of the point data allowed the determination of a much smoother 5´x5´ mean sea surface. Some improvement could still be made to the 5´ mean field by combining the GEOSAT data with other altimetry data such as ERS–1.

Consider the statistics of a sequence of n identically distributed, independent random variables from an underlying distribution of mean μ and variance σ^2. The Central Limit Theorem [*Hoel*, 1966; *Lindgren*, 1968] states that the limiting distribution of the arithmetic mean computed from the sum of the sequence is normal with mean μ and variance σ^2/n. This is so regardless of the normality of the underlying distribution function. Furthermore, the distribution function of the standardized sum is the standard normal distribution. As the number of random samples in the sequence increases, the better the limiting distribution function is approximated. If the underlying distribution function is normal, a good approximation is achieved for n as small as 5; even for a non-normal distribution, a good approximation is to be expected by n equal to 25 or greater.

The number of points per cell is a function of the cell size, the orbit inclination, and the along-track spacing. The size and shape of the cell and the slope of the track through the cell are latitude dependent. The width and area of a cell near ±72° are only 31 percent of one near the Equator. GEOSAT had an orbit inclination of 108° and an along-track spacing of two points per second of time. The average number of points per 5´x5´ GEOSAT mean was almost 10, but there was a very sharp dropoff in the average number of points per mean at about ±66° to about four points per mean. The number of points per mean increased sharply as ±72° was approached. There is another complication. Near the Equator, the 2 Hz along-track rate of the GEOSAT data usually has 3 points per arc within a 5´ cell. Near ±72°, only one point per arc is possible within a 5´ cell. When points in a cell are not all from different arcs, they can not be considered to be a random sample. The effect of having two or three points per arc within the cell on the mean surface can be estimated. The mean will still converge to μ, but more slowly. The variance estimate will also be underestimated. The number of arcs per cell rather than the number of points per cell is a better gauge of necessary density. The number of arcs per cell is barely adequate for a 5´ field. The addition of ERS–1 data would improve the GEOSAT 5´ field and is definitely required to support a 2´ field.

Currents and other nongravity forces displace the mean sea surface over a wide range of spatial and temporal scales. The difference between the mean sea surface and the geoid is referred to as the Dynamic Ocean Topography (DOT). A DOT spherical harmonic model (Figure 4.1.2–6) complete to degree and order 20, derived from TOPEX/POSEIDON (T/P) mission and ERS–1 altimetry data based on orbits determined using JGM–2 [*LaMance,* 1994], was used to remove the remaining systematic regional error from the 5´ GEOSAT mean sea surface heights under the

assumption that the largest portion of the DOT is relatively stationary over time. Notice the strong north–south effect across the Antarctic Circumpolar current. A 1° grid derived from the spherical harmonics and bilinear interpolation was used to estimate the DOT correction at each 5′ location. The DOT correction was subtracted from the mean sea surface to obtain an estimate of the geoid undulation. The application of this model made a significant improvement in the long and medium wavelength portion of the final file.
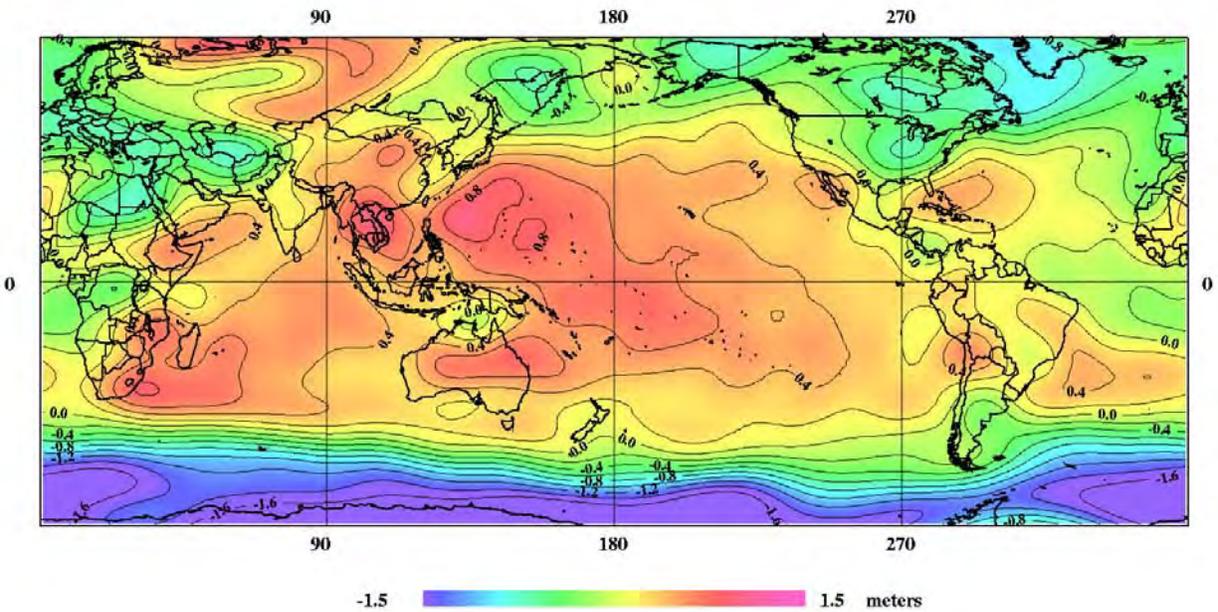
Figure 4.1.2–6. T/P and ERS–1 Dynamic Ocean Topography model to spherical harmonic degree 20.

Because of problems with systematic differences or tilts with altimetry data in the past, a number of tilt and correlation studies were carried out. R. Rapp [*private communication*, 1995] provided two BGR ship tracks (Figure 4.1.2–7) for studies that used the differences between marine gravity anomalies and altimetry-derived anomalies. Dennis Manning modified NIMA's 30′ mean gravity LSC procedure so that point gravity anomalies could be computed at the points along the BGR tracks. The estimate of the accuracy of the GEOSAT data used in the LSC was replaced with a more optimistic value, and no centering was done. In another comparison, 30′ mean gravity anomalies were selected from the GEOSAT file along lines of either constant latitude or longitude where NIMA's most accurate means are located. The GEOSAT point gravity anomalies agree well (±2–3 mGal) with the BGR data (see Figures 4.1.2–8 through 4.1.2–11), and the GEOSAT 30′ means agree well with NIMA's best marine data.
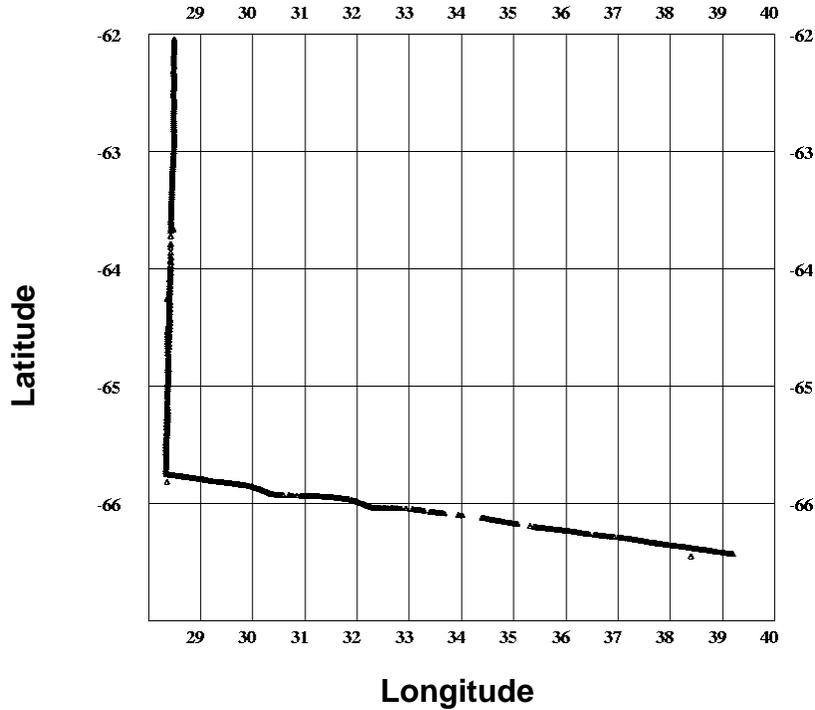
Figure 4.1.2–7. Bundesanstalt für Geowissenschaften und Rohstoffe (BGR) ship tracks north/south 1 and west/east 1 extracted from the ANT–VIII/6 cruise data.

Another DOT model, this one based on JGM–3, became available and was considered. BGR track North/South 1 ran across the slope of the difference between the two DOT models. Using a contour plot, differences between the two DOT models at the north and south ends of the 377 km track were estimated to be 7 and 18 cm, respectively. The GEOSAT 5´x5´ mean heights were reduced with each DOT model, and point gravity anomalies were computed at the BGR point locations, using the procedure devised for the bias and tilt studies. Results indicate close agreement (±2 mGal) between the two sets and the BGR point anomalies; however, the comparisons were inconclusive. The JGM–2 based model helped reduce the bias with respect to the BGR track more than the JGM–3 based model, but the latter provided a better reduction in the slope with respect to the BGR track. Since neither DOT model was clearly better, a decision was made to continue using the JGM–2 based DOT model.
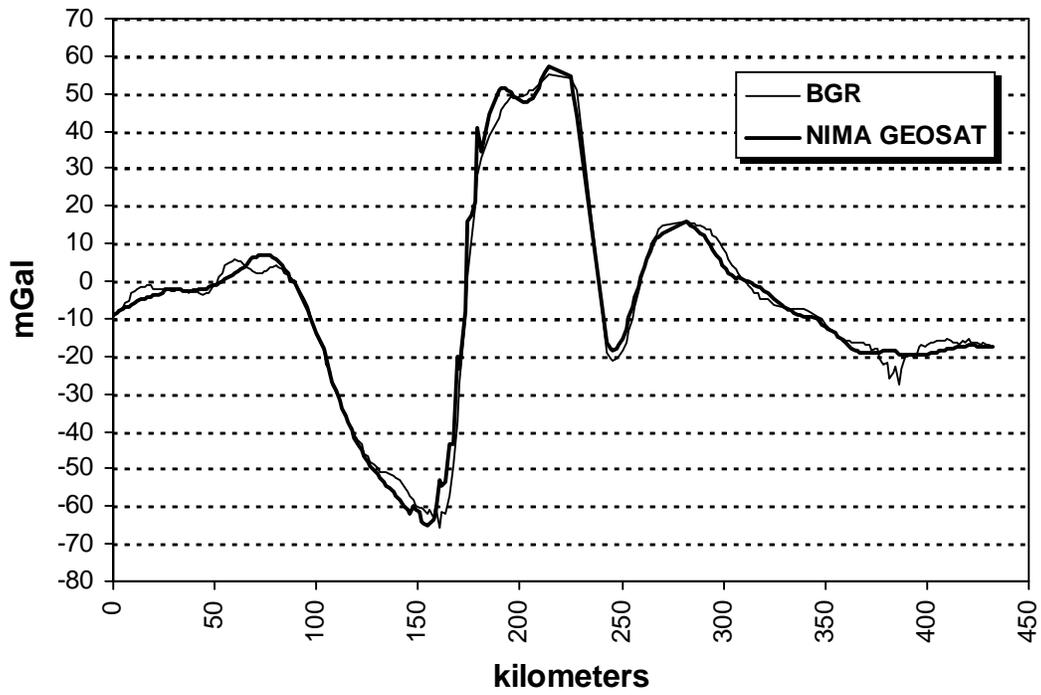
Figure 4.1.2–8. BGR and NIMA GEOSAT gravity anomalies, along BGR track west/east 1.
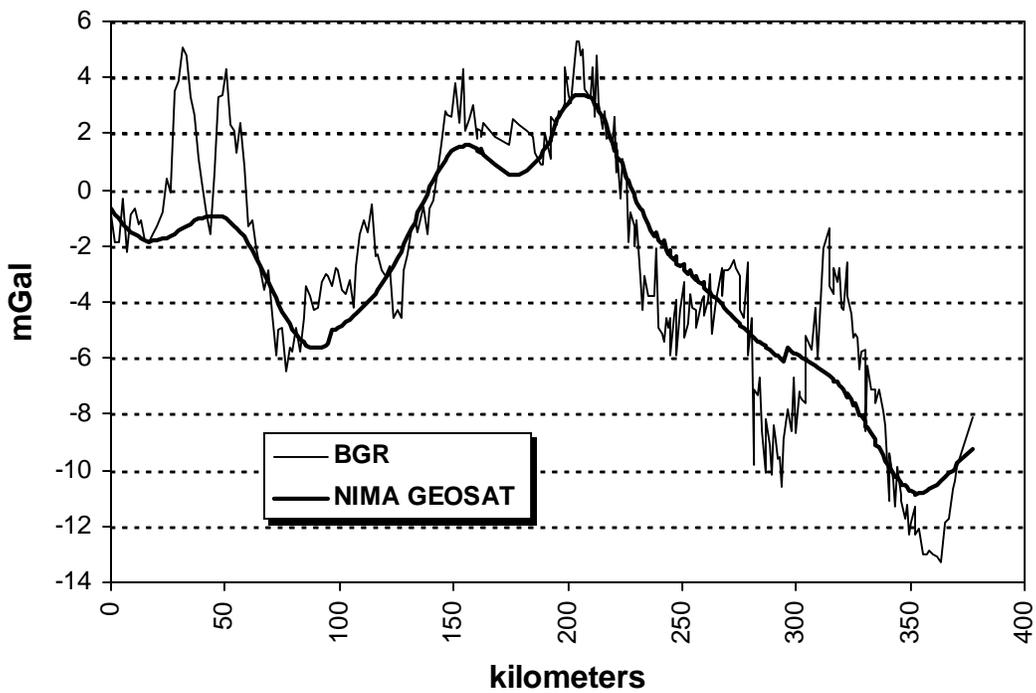
Figure 4.1.2–9. BGR and NIMA GEOSAT gravity anomalies, along BGR track north/south 1.
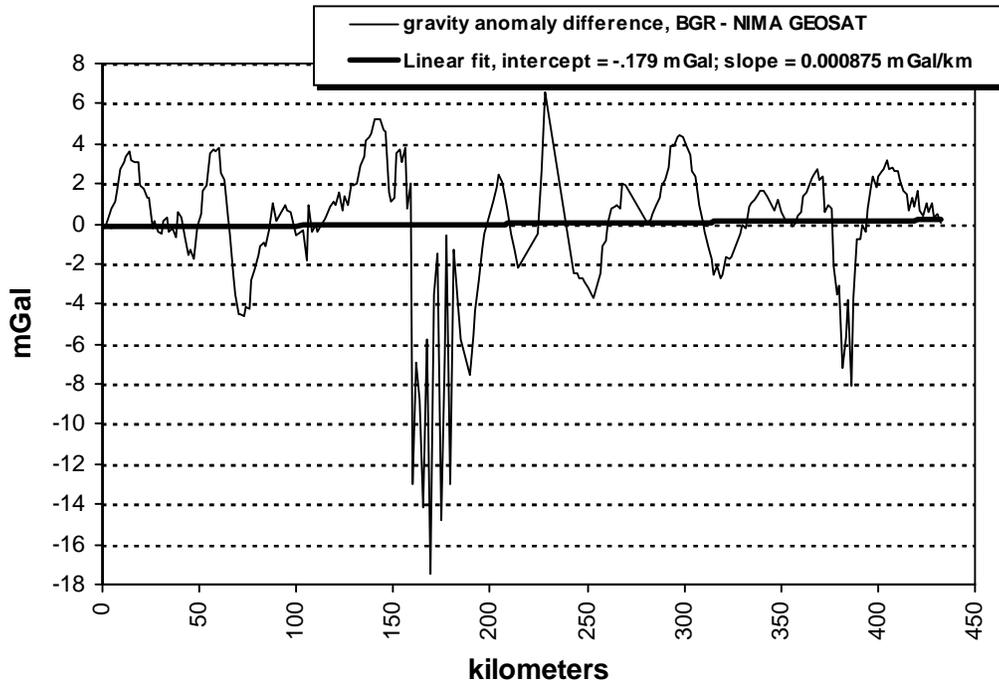
Figure 4.1.2–10. Differences between BGR and NIMA GEOSAT gravity anomalies, along BGR track west/east 1.
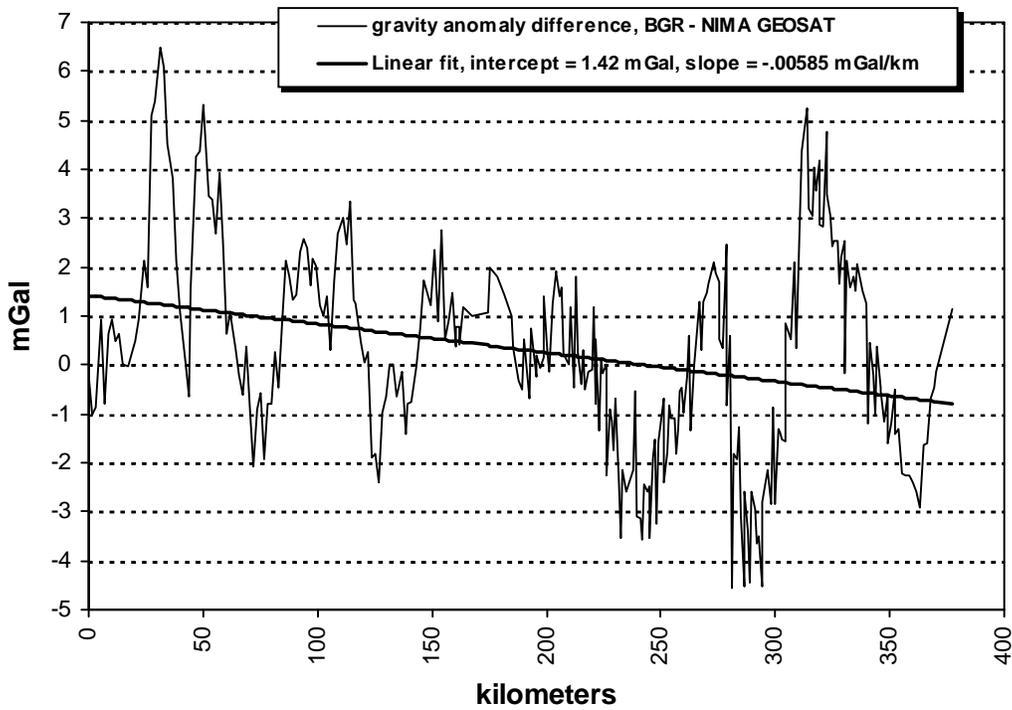
Figure 4.1.2–11. Differences between BGR and NIMA GEOSAT anomalies, along BGR track north/south 1.

The JGM–2/OSU91A geopotential model and the International Terrestrial Reference Frame 1991 (ITRF91) were adopted by the project so that all data processing would be consistent. JGM–2/OSU91A is a composite model where the OSU91A terms above degree and order 70 are used to extend the JGM–2 model (which is complete to degree and order 70) to degree and order 360. NIMA's official Earth Gravity Model was World Geodetic System 1984 (WGS84). The adoption of JGM–2/OSU91A for the project had two impacts on the computation of the GEOSAT anomalies: (1) The GEOSAT mean sea surface heights had to be transformed from WGS84 to ITRF91 and (2) the full 360x360 JGM–2/OSU91A model was used as the reference geopotential model in the remove and restore portion of the LSC procedure instead of the 70x70 portion of WGS84.

The GEOSAT mean sea surface heights were transformed from the WGS84 system to the ITRF91 system using a transformation of the type:

$$h_{ITRF91} = h_{WGS84} + \Delta x \cos \phi \cos \lambda + \Delta y \cos \phi \sin \lambda + \Delta z \sin \phi + B \qquad (4.1.2-1)$$

The Δx, Δy, and Δz indicate a translation of the coordinate system origin. B is a bias between the heights in the two reference frames. The differences from a comparison between the NIMA and OSU-supplied mean sea surface heights (referenced to ITRF90) were used to empirically determine a WGS84 to ITRF90 transformation using a weighted least squares adjustment. This transformation was then combined with an ITRF90 to ITRF91 transformation to obtain the WGS84 to ITRF91 transformation (in cm) that was applied to the GEOSAT sea surface heights.

$$h_{ITRF91} = h_{WGS84} - 40 \cos \phi \cos \lambda + 25 \cos \phi \sin \lambda - 2 \sin \phi + 88 \quad (\text{cm}) \qquad (4.1.2-2)$$

Figure 4.1.2–12 illustrates the WGS84 to ITRF91 transformation.
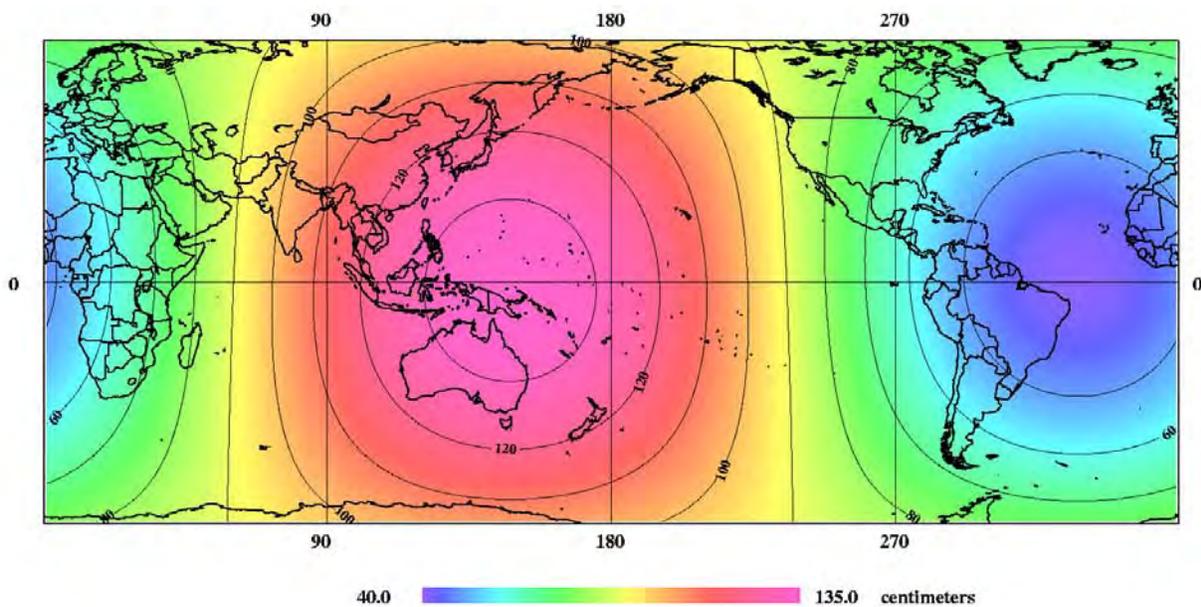
Figure 4.1.2–12. WGS84 to ITRF91 transformation for sea surface heights**.**

Later, as a verification, a set of stacked T/P data referenced to ITRF91 was obtained from OSU. Differences at the GEOSAT ERM network and the T/P stacked arc crossovers were computed and used in a weighted least squares adjustment to derive this transformation:

$$h_{ITRF91} = h_{WGS84} - 37 \cos \phi \cos \lambda + 24 \cos \phi \sin \lambda + 2 \sin \phi + 83 \text{ (cm)} \qquad (4.1.2\text{--}3)$$

The close agreement of the two solutions provided confidence in transformation (4.1.2–2). The Altimetry and Surface Gravity Working Groups decided not to recompute the anomalies using the transformation based on the crossovers (4.1.2–3). The effort and limited computer resources would instead be spent concentrating on improving the 30´ surface gravity anomaly predictions over land.

5´x5´ area-mean values of the geoid undulations generated from the JGM–2/OSU91A model were removed from the GEOSAT 5´x5´ mean geoid undulations to produce a residual mean file. The computational area or cap was selected from this file, for which the mean of the residuals was determined. The residuals were then "centered" by removing their mean from all the values. This was done to satisfy the conditions of the LSC process and to remove any bias in the data or model. After the collocation computation, an equivalent 30´x30´ mean gravity anomaly from JGM–2/OSU91A was restored to each residual mean gravity anomaly to produce the GEOSAT 30´x30´ mean gravity anomaly file.

Just as there had been concerns about possible biases and tilts in the GEOSAT geoid heights, there were also concerns that possible errors in the JGM–2/OSU91A model could be transferred to the resultant anomalies. Use of the full 360x360 model, as opposed to the 70x70 WGS84 model, might increase problems, especially since JGM–2/OSU91A only had GEOS–3 and SEASAT anomaly data to define the short-wavelength geoid in most oceanic areas (the GEOSAT Exact Repeat Mission data were limited to regions south of 60°S latitude). As NIMA knew of systematic differences between the GEOSAT and SEASAT data sets, these concerns remained even after the anomalies had been computed.

An analysis helped clarify the consequences of the changes in the remove and restore procedure. A nonzero residual field mean could be due to a bias in the altimetry file, the geopotential model, or both. The same is true of a tilt in the residual field. The centering corrects any bias in the residual geoid undulation field, satisfying the assumptions of the collocation procedure. However, if the bias error is in the model field, then the error in the model mean gravity anomaly restored is directly transferred to the final mean gravity anomaly. The centering does resolve biases in the altimetry geoid field when they exist, but the centering does not resolve any artificial tilt that might be introduced into the residual geoid undulation field by a locally poor-fitting model or by a tilt in the altimetry geoid undulation.

The analysis indicated that such a tilt actually introduces a small bias at each of the computational points. This would create a saw-toothed error in the mean gravity anomalies along the slope, the existence of which was verified. The error is so small with respect to changes in the anomaly field that it can not be discerned in the anomalies, although it can be seen in differences between anomaly sets where one set was derived from a residual field, with little or no slope, and

a residual field with a slope that is artificially imposed or imposed by a tilted geopotential field. Centering value plots (see Figure 4.1.2–13) indicate some of the few isolated areas where residual tilts exist. (See for example, the Gulf of Carpentaria and the Arafura Sea between New Guinea and Australia.) For most areas where this tilt type of error was likely, based on inspection of the centering value plots, free-air anomalies computed from ship and surface (land) point gravity anomalies were used in developing EGM96. The largest tilt in the geoid undulation residuals was in the Caspian Sea, where the GEOSAT anomalies were considered better than the alternatives and used in computing EGM96. Overall, tilts in the area-mean geoid undulation residual field are not considered to be a significant error source in the 30´ mean gravity anomalies used to develop EGM96.
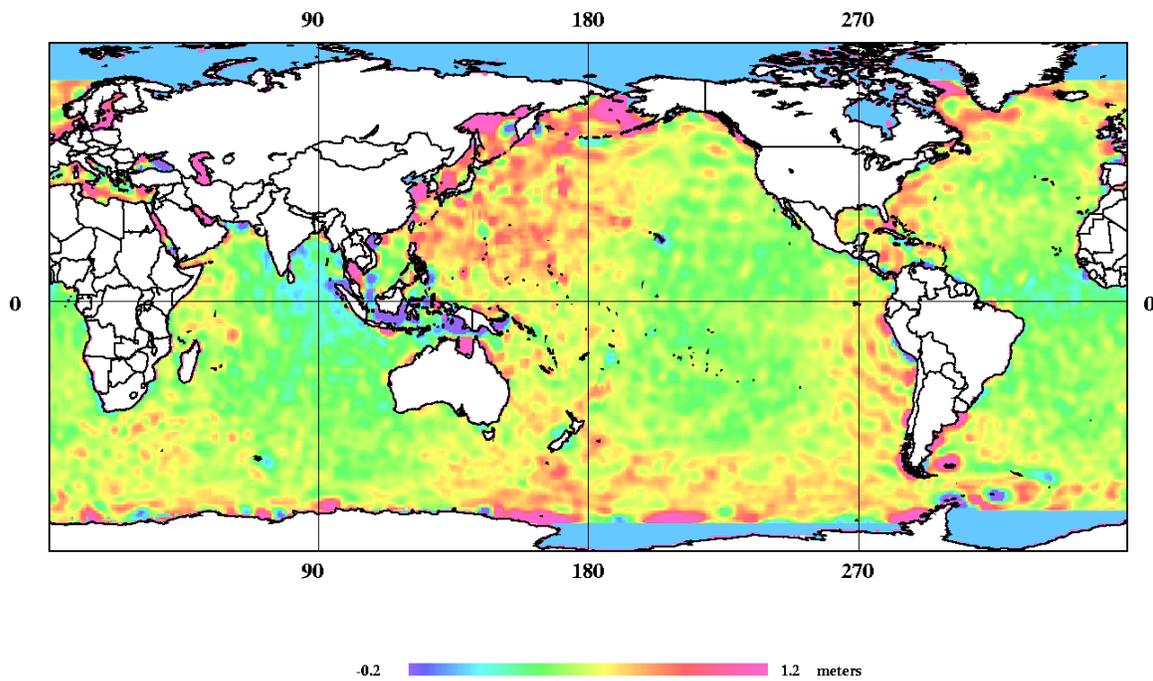
Figure 4.1.2–13. Centering values that reduced the computational area mean to zero**.**

A centering value (i.e., mean difference between altimetry and model values) is a problem only if the source of the bias is in the reference geopotential model, since the error in the model is transferred to the final anomaly. Of course, an improved geopotential model will reduce these errors. Mean gravity anomaly errors due to tilts in the residual field could be eliminated by centering the 3°x3° computational area for each 30´ subcell, instead of centering based on the entire computational area. Computation of deflection of the vertical components would be expected to be affected by tilts in the residual field.

Once the GEOSAT anomalies were computed, comparisons of the GEOSAT and other altimetry sets available at the time with high-quality ship-survey-derived gravity anomalies were made. The comparison results indicated that the altimetry-derived 30´x30´ anomalies were accurate to 2

to 3 mGal (Table 4.1.2–1). The NIMA, KMS, and NOAA anomalies give similar results when compared with the ship data, though the best results were obtained from the NIMA GEOSAT data.

Table 4.1.2–1. Comparison of 27610 altimeter-derived 30′ mean gravity anomalies and NIMA's ship observations.

Differences (mGal)	Mean	Std. Dev.	Range	
NIMA GEOSAT	0.4	2.3	-29.2	26.2
KMS ERS–1(168 days)	0.4	3.4	-57.0	61.5
NOAA (Multiple Sources)	0.4	3.1	-66.1	38.5
OSU (Multiple Sources)	1.5	4.5	-28.2	54.3

The GEOSAT data were the first of several altimetry-derived 30′x30′ mean gravity anomaly files provided to GSFC during the project. The next step was to evaluate the KMS ERS–1 anomalies to determine if they could be used to extend the GEOSAT coverage.

4.2   ERS–1

During the 2 168-day GM mission repeat cycles, ERS–1 generated 16 million altimetry points, distributed over the latitude range of ±81.5°, with a spacing of 8 km at the Equator. ERS–1, as compared to GEOSAT, was more accurately tracked and took advantage of better quality gravitational models in the generation of the orbital ephemerides. Consequently, the initial radial orbit error of ERS–1, based on crossovers, was approximately 22 cm, much lower than GEOSAT's 90 cm. However, after adjustment, the ERS–1 radial orbit accuracy was 10 cm [*Gruber, Massmann, and Reigber*, 1993], and the GEOSAT radial orbit accuracy was 7 cm.

Normally, in NIMA's LSC procedure, the four 30′ mean gravity anomalies in a 1° cell are computed from the 5′ mean geoid undulations within a 3°x3° computational cell centered on the cell of values being computed. Since there are no GEOSAT 5′ mean geoid undulations above its inclination limit in the range from 72° to 73° latitude, only six cells of data (as opposed to the normal nine cells) are available within the computational cell. With a third less data and with a lopsided distribution, the GEOSAT anomalies between 71° and 72° are of poorer quality than those computed from a full cap, which is reflected in the LSC accuracy estimates. Thus, ERS–1 anomalies were preferred in this latitude band.

It was important that there be no discontinuities at the boundary between the two altimeter data sources. A long boundary and possible discontinuities between GEOSAT and ERS–1 anomalies were avoided north of the FSU, Alaska, and Canada by using only ERS–1 anomalies. ERS–1 values were used above 70° in the Atlantic where a boundary between the GEOSAT and ERS–1 anomalies could not be avoided. *Andersen, Knudsen, and Tscherning* [1996] supplied 3.75′x3.75′ gravity anomalies that had been computed by FFT techniques from crossover-adjusted sea surface heights collected from ERS–1 during the first 168-day GM period. These KMS ERS–1 anomalies were averaged to 30′. The consistency of these two anomaly sets was

verified using comparisons with marine survey anomalies. The GEOSAT, ERS–1, and NIMA's best marine observations were compared in the North Atlantic; the results are presented in Table 4.2–1. The NIMA GEOSAT and KMS 168-day set of ERS–1 anomalies were consistent both with each other and with the marine observations. Therefore, the KMS anomalies were used to extend the coverage in the near-polar areas since ERS–1 has a wider latitude coverage than GEOSAT.

Table 4.2–1. Comparison of 1444 North Atlantic 30´ mean gravity anomalies ($60°< \phi < 70°$). Units are mGal.

Magnitude	Mean	Std. Dev.	Range	
ERS–1(168 day set)	21.0	18.0	-45.0	83.2
GEOSAT	21.2	17.9	-45.9	88.6
Marine Observations	22.1	17.7	-42.2	84.7
Differences				
ERS–1 - GEOSAT	-.1	3.3	-27.4	14.1
ERS–1 - Marine Observations	-1.0	3.1	-32.2	19.7
GEOSAT - Marine Observations	-.9	2.8	-22.4	29.2

Later KMS provided an improved set of ERS–1 anomalies. This set was derived from two 168-day GM periods rather than one, and used improved processing techniques. KMS [*Andersen, personal communication,* 1997], like NIMA, applied a crossover adjustment to the sea surface heights and used a similar editing and readjustment scheme. KMS used an FFT technique, whereas NIMA used LSC. The ERS–1 data were crossover adjusted and used to compute a smooth height field. Observations that differed greatly from this field were removed. The edited set was then readjusted and gridded. An additional covariance function for each track was introduced in the gridding procedure to help filter out sea surface variability. The new grid was used to compute a set of 3.75´x3.75´ gravity anomalies. These anomalies were then averaged to 30´ and used to replace the 168-day set. The result was a noticeable improvement in coverage and quality especially at the higher latitudes.

Schoene [1996] provided anomalies in the Weddell Sea. He used altimetry from two 3-day orbit and one 35-day orbit ERS–1 time periods as well as from the GEOSAT GM and ERM data. All geophysical corrections were applied. A collinear technique [*Van Gysen et al.*, 1992] was used to reduce the radial orbit error. Because of the severe ice conditions in this area, Schoene applied his newly developed outlier detection algorithm. Adjusted data were differentiated along descending and ascending tracks and interpolated to a 3.4 km uniform grid. *Sandwell's* [1992] Fourier technique was used to compute anomalies. These small size anomalies were averaged to obtain the 30´ mean gravity anomalies that were incorporated into the final altimetry file.

4.3 The Final Altimetry 30´ Mean Gravity Anomaly File

As new and better altimetry-derived anomalies became available, they were merged into the altimetry anomaly data set, extending the coverage and replacing less accurate values. The final altimetry-derived anomaly file was provided to GSFC in June 1996. Anomalies from the last KMS data set, provided in April 1996, and the Schoene file, obtained in May 1996, were included. The GEOSAT anomalies contained in this set were unchanged from the ones presented by *Trimmer and Manning* [1996]. Statistics of the final 30´ mean free-air altimetry-derived anomalies are given in Table 4.3–1. Figure 4.3–1 shows the geographic coverage of each source, while the resulting mean gravity anomalies and uncertainties are presented in Figures 4.3–2 and 4.3–3, respectively. Of the total of 158338 values, 139798 were supplied based on NIMA values, 16396 based on KMS values, and 2144 from T. Schoene. A uniform uncertainty of 3.5 mGal was assigned to the KMS and Schoene values. As an examination of the anomaly plots will reveal, the resulting anomaly values are visually continuous across the data boundaries.

Table 4.3–1. Statistical information of the final 30' mean altimeter-derived free-air anomalies (units are mGal).

Statistic	Value	
Number of values	158338	
Percentage of Earth's area	70.12	
Minimum value (φ,λ)	-300.28	(19.25°, 293.25°)
Maximum value (φ,λ)	328.02	(27.75°, 142.25°)
Mean value	-1.77	
RMS value	26.24	
Minimum σ	0.58	
Maximum σ	25.24	
RMS σ	1.84	
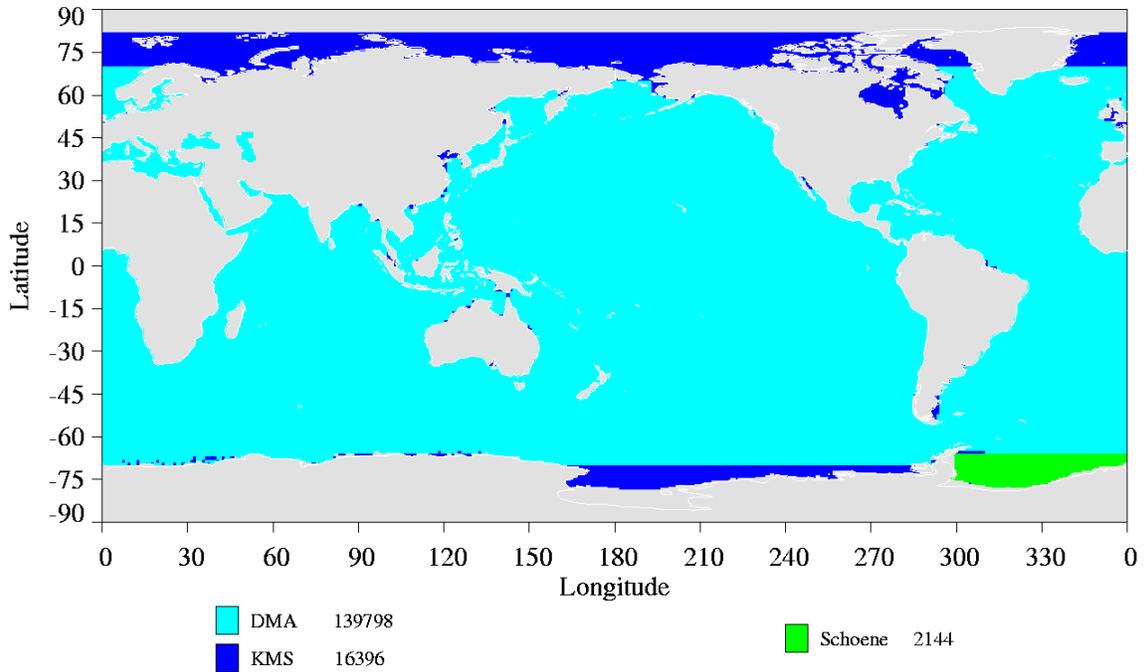
Figure 4.3–1. Sources of data for the final 30´ mean free-air altimetry-derived gravity anomalies.
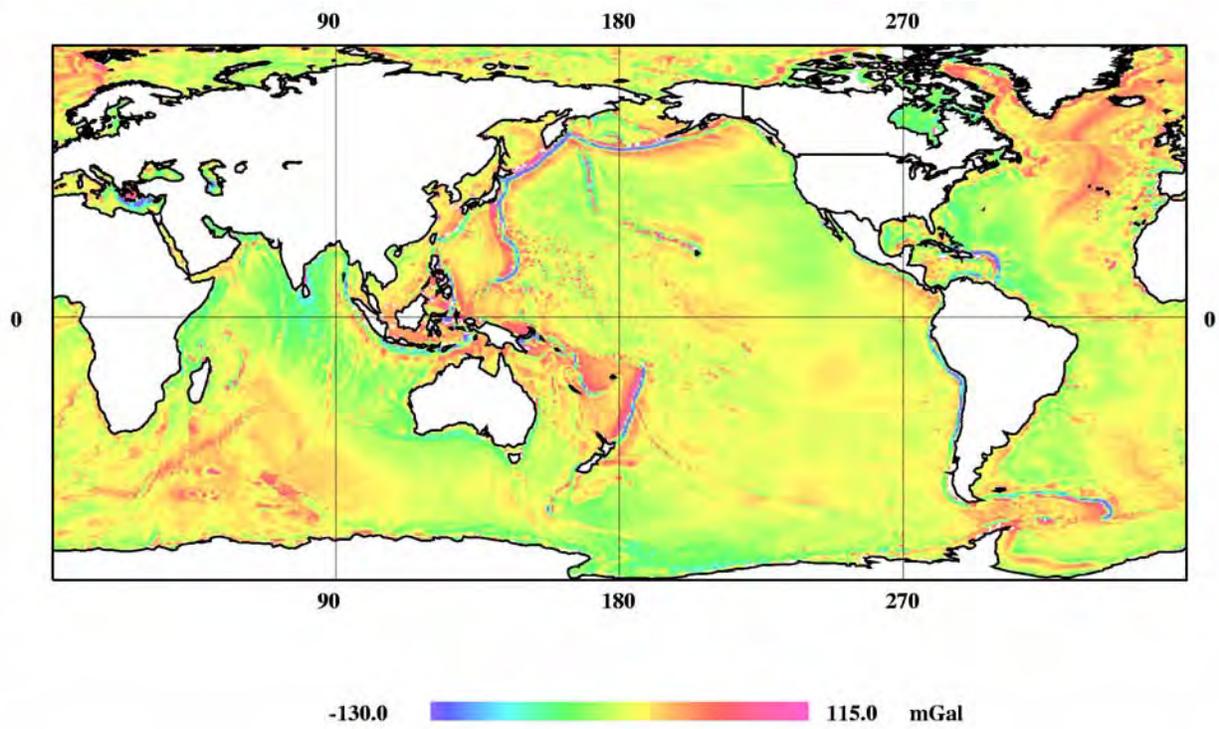
Figure 4.3–2. Final altimetry-derived 30´ mean free-air gravity anomalies.
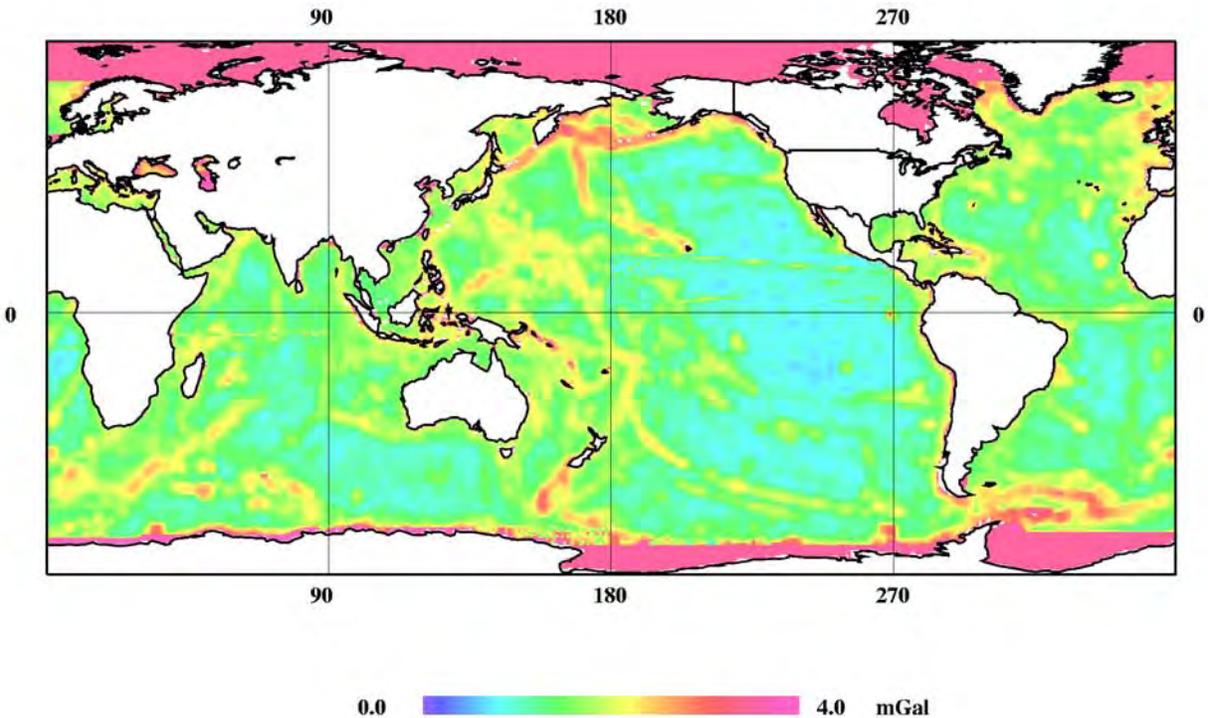
Figure 4.3–3. Estimated error of the final altimetry-derived 30´ mean free-air gravity anomalies.

4.4 Summary

A major goal of EGM96 was a global 30´ geoid with an associated accuracy of ±0.5 meters. This was considered a realistic goal based, in part, on the use of satellite altimetry-derived gravity anomalies. GEOSAT altimetry from the GM portion of its mission provided altimeter-derived 30´x30´ mean gravity anomalies for over 61 percent of the Earth's surface. NIMA's GEOSAT GM sea surface heights, which had been area adjusted to the NAVOCEANO GEOSAT ERM network, had a local relative consistency of 7 cm in most areas, as determined by crossover statistics.

NIMA used two approaches to assess the quality of altimetry sea surface height data: (1) Gravity anomalies were computed from the altimetry sea surface heights and compared with high-quality marine anomalies where available and (2) altimeter sea surface heights or anomalies were compared with spherical-harmonic-derived values. NIMA employed a DOT model, which reduced regional systematic errors in the GEOSAT heights and derived anomalies arising from geostrophic flow. Application of this DOT model provided a major improvement in the GEOSAT 5´x5´ mean sea surface height field, bringing it closer to a true geoid surface. The centering, which was part of the removal, and restoration of a full 360 degree and order JGM–

2/OSU91A model helped reduce any remaining bias or tilt. Tests confirmed that the adjustment of the GEOSAT GM data to the NAVOCEANO GEOSAT ERM network, the application of the DOT model, and the local centering of the residual field combined to reduce the long- to medium-wavelength errors.

GEOSAT was the major altimetry source for gravity anomaly prediction, comprising 88 percent of the altimetry values used for EGM96. The overall accuracy of the GEOSAT-derived 30´x30´ mean gravity anomalies based on comparisons with accurate marine-derived anomalies was 2.3 mGal RMS. The ERS–1 anomalies made an important contribution by extending and improving the coverage, especially in polar areas. The *Schoene* [1996] anomalies provided coverage in the Weddell Sea near Antarctica. By combining the NIMA, KMS, and Schoene sets, it was possible to maximize the coverage and improve the quality of the final set. This 30´x30´ mean gravity anomaly file, which covered about 70 percent of the Earth's surface, was the most accurate and complete altimetry file that NIMA could assemble at the time.

Richard H. Rapp of Ohio State University provided data sets, transformations, and verification of the WGS84 to ITRF91 sea surface height transformation. Rapp also identified and assisted in the acquisition of many data sets, including the Schoene anomalies, derived from a combination of ERS–1 and GEOSAT data, in the Weddell Sea. Forsberg, Tscherning, Andersen, and Knudsen of KMS contributed to the anomaly data sets by collaborating in the development of the collocation procedure and by providing ERS–1 anomalies. The similarity of methods is probably one reason that the NIMA GEOSAT anomalies and KMS ERS–1 anomalies are so consistent with each other. The NIMA GEOSAT anomalies and the KMS ERS–1 anomalies differ little when compared with NIMA's marine observations.

4.5   References

Andersen, O., P. Knudsen, and C.C. Tscherning, Investigation of Methods for Global Gravity Field Recovery from the Dense ERS–1 Geodetic Mission Altimetry, in *Global Gravity Field and Its Temporal Variations*, IAG Symposia, 116, 218–226, Springer–Verlag, Berlin, 1996.

Brace, K., Preliminary Ocean–Area Geoid From GEOS–III Satellite Radar Altimetry, NASA GEOS–III Investigations Final Meeting, New Orleans, LA, Nov. 18–19, 1977.

Cloutier, J., A technique for reducing low-frequency, time-dependent errors present in network-type surveys, *J. Geophys. Res.*, *88*, B1, 659–663, 1983.

Forsberg, R., A New Covariance Model for Inertial Gravimetry and Gradiometry, *J. Geophys. Res.*, *90*, No. B2, 1305–1310, 1987.

Gruber, T., F. Massmann, and C. Reigber, *ERS–1 D–PAF Products Manual*, GeoForschungs-Zentrum Potsdam, Potsdam, Germany, 1993.

Hoel, P., *Elementary Statistics*, John Wiley & Sons, Inc., New York, 1966.

Jensen, J., and F. Wooldridge, The Navy GEOSAT Mission: An Introduction, *Johns Hopkins APL Technical Digest, Vol. 8* (ISSN 0270–5214), JHU/APL, Laurel, MD, 1987.

LaMance, J., *Evaluation of Global Sea Surface Height Estimates From Combined ERS–1 and TOPEX Altimetry*, Ph.D. Thesis, University of Colorado, Boulder, CO, 1994.

Lindgren, B.W., *Statistical Theory*, The Macmillan Company, New York, 1968.

MacArthur, J., P. Marth, and J. Wall, The GEOSAT Radar Altimeter, *Johns Hopkins APL Technical Digest, Vol. 8*, ISSN 0270–5214, JHU/APL, Laurel, MD, 1987.

McConathy, D.R., and C.C. Kilgus, The Navy GEOSAT Mission: An Overview, *Johns Hopkins APL Technical Digest, Vol. 8*, ISSN 0270–5214, JHU/APL, Laurel, MD, 1987.

Sandwell, D., Antarctic Marine Gravity Field From High–Density Satellite Altimetry, *Geophys. J. Intl.*, *109*, 437–448, 1992.

Schoene, T., The gravity field in the Weddell Sea Antarctica, by radar altimetry from ERS–1 and GEOSAT, *Reports on Polar Research, 220/96*, Alfred Wegener Institute, Bremerhaven, Germany, 1996.

Trimmer, R., and D. Manning, The Altimetry Derived Gravity Anomalies to be Used in Computing the Joint DMA/NASA Earth Gravity Model, in *Global Gravity Field and Its Temporal Variations*, IAG Symposia, 116, 71–81, Springer–Verlag, Berlin, 1996.

Van Gysen, H., R. Coleman, R. Morrow, B. Hirsch, and C. Rizos, Analysis of Collinear Passes of Satellite Altimeter Data, *J. Geophys. Res.*, *97*, C2, 2265–2277, 1992.

VanHee, D., Preliminary Results from the Processing of a Limited Set of GEOSAT Radar Altimetry Data, *Johns Hopkins APL Technical Digest*, *Vol. 8*, ISSN 0270–5214, JHU/APL, Laurel, MD, 1987.

5. MODEL EVALUATION TECHNIQUES AND DATA

The interim and final project geopotential models were tested using a variety of techniques that assessed the models in terms of their performance on modeling satellite dynamics, and in how well they modeled the land or ocean geoids. The results of these tests guided the development of the final project models, for instance in selecting weights for a set of data, or validating the inclusion of a set of data in the solution. This section describes in detail the assumptions, methodology, theory, and data used in the tests to evaluate the satellite-only, low-degree combination, and high-degree geopotential models. These tests were used extensively during the various phases of the model development and in the final evaluation of the final project geopotential models.

The tests may be divided into three categories: (1) Orbital tests using arcs of satellite tracking data (principally SLR data), (2) tests using GPS/leveling, (3) tests using satellite altimetry and an independent model of the dynamic ocean topography (DOT) derived from an ocean circulation model, and (4) tests using altimetry-derived gravity anomalies.

The tests with satellite tracking data assess primarily the long-wavelength performance of a geopotential model, since satellite tracking data are most sensitive to the lower degrees (through $n = 40$, at most). The orbit tests were applied to all the components of the project geopotential models including the satellite-only models, the low-degree combination models (those that included satellite altimetry, surface gravity, and satellite tracking data), as well as the high-degree models developed via the block diagonal or the quadrature techniques. Orbit tests with SLR satellite tracking data are discussed in Sections 5.1.1 and 5.1.2. ERS–1 orbit tests, combining both SLR and altimetry, are described briefly in Section 5.1.3. Tests with dependent and independent tracking data sets from satellite users of NASA's Tracking and Data Relay Satellite System (TDRSS) are described in Section 5.1.4. The orbit performance of the models on TOPEX/POSEIDON (T/P) received special attention. Two sets of T/P tests were performed. Orbit residual tests, using the first generation precision orbit modeling, are described in Section 5.1.5. Orbit tests with the second generation precision orbit modeling, including the comparisons with the T/P reduced-dynamic orbits produced by the Jet Propulsion Laboratory (JPL), are described in Section 5.1.6.

Tests with GPS and leveling data involve a comparison of geoid undulations determined geometrically with the geoid undulations from a geopotential model. This test focuses on the land geoid in those specific regions where GPS and leveling data are available. The test is sensitive to mostly the short-wavelength components of the geopotential model, although the data also have sensitivity to the medium and longer wavelength components of the model. The GPS and leveling tests are directly sensitive to the quality of the surface gravity data included in the model for the region of the test. The GPS and leveling tests as performed at OSU are described in Section 5.2; those done at GSFC are described in Section 5.3.

Geoid undulation comparisons were also made using a global network of Doppler positioned stations. These tests also involve a comparison of a geometrically derived geoid undulation with a model-derived undulation. In this test, though, the station locations (ellipsoidal heights) are

determined from Doppler positioning rather than GPS positioning, and are located all over the globe, rather than in a single geographic region. This test is described in Section 5.4

DOT is the separation between the ocean surface and the geoid. The quality of the marine geoid of a geopotential model can be assessed by comparing the implied DOT derived from satellite altimeter data and the geopotential model with an independent estimate of the DOT obtained from an ocean circulation model. Section 5.5 discusses how the comparisons were implemented in the orthonormal domain at OSU using the POCM–4B ocean circulation model of *Semnter and Chervin* [*Stammer et al.*, 1996], and a 2-year T/P mean track. Section 5.6 discusses discrete comparisons performed at GSFC using POCM–4B and altimeter data from GEOSAT, ERS–1, and T/P. Section 5.7 discusses geopotential model comparisons along a discrete track of ERS–1 altimeter data from 65°S to 77.9 °S, after subtracting the DOT from POCM–4B.

Altimeter-derived gravity anomalies provide an independent means to test and evaluate satellite-only models. The 30' altimeter-derived gravity anomalies from the GEOSAT Geodetic Mission were used extensively to characterize the evolution in the satellite-only models, and the relative strengths of various sets of tracking data. The methodology of the comparisons and a description of the anomalies used are provided in Section 5.8

5.1   Orbit Test Description

5.1.1   SLR Satellite Test Set 1

As EGM96 was being developed, the interim gravity solutions were evaluated with SLR tracking data acquired on six satellites: LAGEOS, LAGEOS–2, Starlette, Ajisai, Stella, and GFZ–1. The first four were multiarc tests, in which both global parameters (in general stations, and polar motion) were adjusted along with the arc parameters to isolate geopotential contributions to the data fit. The last two tests involved reductions of a single arc of tracking data. The parameterization for these satellite orbit tests are summarized in Table 5.1.1–1. Of the test data described below, only the LAGEOS data are in the EGM96 solution.

5.1.2   SLR Satellite Test Set 2

After the completion of the EGM96 model, a new series of SLR satellite multiarc tests was developed to validate and verify the performance of EGM96S and EGM96. These multiarc tests involved data from 1995 and 1996 on Stella, LAGEOS, LAGEOS–2, and GFZ–1. All of these data were not included in EGM96. Note that, whereas the LAGEOS–1 and LAGEOS–2 SLR tests in set 1 were 30-day arcs, the new (set 2) tests were shorter: 10-day arcs for LAGEOS–1 and –2 and Stella; 3-day arcs for GFZ–1.

For this set of test data, the data reductions were done both with and without the adjustment of along-track, once-per-revolution empirical accelerations. These accelerations were adjusted every 5 days for the LAGEOS and Stella arcs, and once per arc for the GFZ–1 orbital tests. The adjustment of these once-per-revolution parameters removes sensitivity to errors in the zonal and resonance coefficients. Any change in the RMS of fit will then reflect the performance of other harmonic coefficients. The parameterization for these arcs is summarized in Table 5.1.2–1.

Table 5.1.1–1. SLR satellite orbit fit test arcs and parameterization (Set 1).

Satellite	Arcs	Arc Parameters Adjusted	Global Parameters Adjusted
LAGEOS	Three monthly arcs: Apr., May, June 1988 10433 observations	orbit states C_R along-track EA/15 days	all stations except GSFC, and latitude of Hawaii; 5-day pole ocean tides, SA, and SSA (2,0), and (3,0)
LAGEOS–2	Two monthly arcs: Nov., Dec. 1992 8636 observations	orbit states along-track acceleration, and 1-CPR EA/15 days	all stations except GSFC, and the latitude of Hawaii 5-day pole
Starlette	Eight 6-day arcs: Aug., Sept. 1988 6041 observations	orbital states C_R C_D/day	5-day pole
Ajisai	Eight 5-day arcs: Apr., May 1988 4893 observations	orbital states C_R C_D/day	5-day pole
Stella	One 10-day arc: epoch 960115 379 observations	orbital state C_D/day	None
GFZ–1	One 3-day arc: epoch 960115 195 observations	orbital state C_D/day	None

Key   1-CPR: 1-cycle-per-revolution, EA: empirical acceleration, CG: center of gravity

Table 5.1.2–1. SLR satellite orbit fit test arcs and parameterization (Set 2).

Satellite	Arcs	Arc Parameters Adjusted	Global Parameters Adjusted
LAGEOS	Five 10-day arcs, epochs: 951117, 960115, 960423, 960612, 960801 Total: 6935 observations	orbit states along-track EA/5 days	1-day pole
LAGEOS–2	Five 10-day arcs, epochs: 951117, 960115, 960423, 960612, 960801 Total: 4940 observations	orbit states along-track EA/5 days	1-day pole
Stella	Five 10-day arcs, epochs: 951117, 960115, 960423, 960612, 960801 Total: 2998 observations	orbital state C_D/day along-track EA/5 days	1-day pole
GFZ–1	Six 3-day arcs, epochs: 960804, 960807,960813, 960816, 960819, 960822, 960825 Total: 2590 observations	orbital state C_D/day along-track EA/5 days	None

5.1.3 ERS–1 Orbit Tests

The ERS–1 orbit test was a data reduction of SLR and altimeter data for a single arc, where this arc was one of the 29 ERS–1 arcs included in the EGM96 solution. This test is an independent test for the satellite-only and high-degree models, and a dependent test for the low-degree combination model. The test produced two results: The SLR and altimetry weighted RMS (WRMS) of fit. These values must be multiplied by factors of ~1.12 and 3.00, for the SLR and altimetry data types, respectively, to obtain the unweighted equivalents in centimeters. All modeling used in the orbit tests was identical to the data reduction processing for EGM96 (specific details on modeling used can be found in Section 7.1.4.3), except for the choice of geopotential and dynamic tides sets. The dynamic ocean topography model was not changed for the geopotential and tides tests. A single 5-day arc—starting on 931125—of ERS–1 cycle 17 was selected for the tests that had a data distribution typical of the arcs used in EGM96. The empirical 1-cycle-per-revolution (1-CPR) along-track acceleration terms, estimated over 12-hour periods, were used in the tests to accommodate the large drag modeling errors experienced on ERS–1.

5.1.4 TDRSS Orbit Tests

Several spacecraft tracked by the Tracking and Data Relay Satellite System (TDRSS) to support their operational orbit determination were used for model assessments. An overview of TDRSS can be found in Section 6.2.4, which details the orbit determination and handling of the 1994 Explorer Platform/Extreme Ultra-Violet Explorer (EP/EUVE) tracking data that were included in the development of the EGM96 models. The spacecraft used for the orbit tests were EP/EUVE, the Compton Gamma Ray Observatory (CGRO), the Earth Radiation Budget Satellite (ERBS), and the Rossi X-ray Timing Experiment (RXTE). These satellites are characterized by their low altitude (see Table 5.1.4–1) and, with the exception of ERBS, low inclination ($i < 30°$ orbits). These spacecraft are useful for evaluating geopotential models at altitudes and inclinations where traditional tracking data sources are weak. In these sequences of tests, the data from CGRO, ERBS, and RXTE are independent (i.e., the data were not included in EGM96). For EP/EUVE, the orbit tests included two sets of data: one that was included in EGM96 and one that was withheld.

Table 5.1.4–1. Orbit characteristics of the TDRSS-tracked satellites.

Spacecraft	CGRO	ERBS	EP/EUVE	RXTE
Altitude (km)	380	585	525	579
Inclination	28.5°	57°	28.4°	23°
Eccentricity	circular	circular	circular	circular

T/P, which is tracked by TDRSS as well as the extensive ground sources, was used to strengthen the orbit determination of the relay satellite orbits *Marshall et al.* [1995a]. The orbit tests utilized TDRSS tracking for three time periods. The first period was November 1–December 1, 1992,

which corresponds to T/P orbit repeat cycles 5 through 7. TDRSS tracking of EP/EUVE, ERBS, and CGRO from this time period was processed. These cycles have excellent T/P–TDRS data coverage for all of the TDRSS tracking data types, including one-way range-rate, two-way range-rate, and two-way range. As a consequence, superior TDRS orbit accuracies were obtained. Details of the T/P and TDRS modeling and estimated parameters are provided in Table 5.1.4–2. For each gravity model tested, a separate T/P SLR/DORIS solution is computed; then, in turn, a new set of TDRS orbits. This multistep process ensures consistency in the tests, even though the effects of geopotential changes on the geostationary TDRS orbits are small. The TDRSS orbits were then fixed in the user–spacecraft solutions, details of which are given in Table 5.1.4–3. All data arcs were 10 days long, with 5-day overlap periods. The data weights used for the TDRSS tracking of T/P were determined based on fits of the tracking data to the SLR/DORIS-determined precise T/P orbits. Consequently, these weights reflect both noise and structured residuals, of which the structured component is typically the largest.

Table 5.1.4–2. TDRS orbit determination parameter, modeling, and data specifics.

Modeling	TDRS	T/P
Dynamical parameters estimated	Epoch State Along-track constant and 1-CPR EA/day Cross-track 1-CPR EA/day,	Applied from Precise Orbit: Epoch State Along-track 1-CPR EA/day Cross-track 1-CPR EA/day C_D per 8 hours
Observational parameters estimated	Range bias/TDRSS for BRTS	Range bias/TDRSS USO clock bias/drift/accel TDRS–4 1-way range-rate measurement scale bias
Atmospheric Density	DTM [*Barlier et al.*, 1977]	

Nonconservative Force Models	TDRSS Macro Model for Solar and
	  Earth radiation
		T/P Macro Model for Solar & Earth
		  radiation, thermal, and drag [*Marshall
		  and Luthcke*, 1994a; 1994b]

Measurement corrections, with relativistic clock and wet & dry troposphere	Attitude and CG dependent TDRSS
	  antenna models
	Applied transponder delay range biases
	TDRS-to-BRTS ionosphere corrections
		Attitude- and CG-dependent TDRSS
		  high gain antenna
		TDRS-to-T/P ionosphere corrections

Station Coordinates[1]	transformed from WGS84 survey to ITRF90 [*Boucher and Altamimi*, 1991]	
Tracking @ 0.1 Hz 1-way range-rate 2-way range 2-way range-rate	Passes/day x length(min.) /TDRSS 10x4.5 via BRTS	Passes/day x length(min.) 5x35 5x35 5x35
Data Weights 1-way range-rate (mm/s) 2-way range (m) 2-way range-rate (mm/s)	 3.0	 1.0 2.0 0.5

Key: 1-CPR: 1-cycle-per-revolution, EA: empirical acceleration, CG: center of gravity, USO: ultra-stable oscillator
Notes: 1.   The technique used will result in the reference frame being in-between that of ITRF90 and that of
              TOPEX/POSEIDON.

Table 5.1.4–3. Modeling and parameterization used for TDRSS-user orbit determination tests.

Modeling	CGRO	ERBS	EP/EUVE	RXTE
Dynamical parameters estimated	Epoch State A-T&C-T 1-CPR EA/2 days C-T EA/2 days C_D/6 hrs	Epoch State A-T&C-T 1-CPR EA/arc C_D/8 hrs	Epoch State A-T&C-T 1-CPR EA/arc C_D/8 hrs	Epoch State A-T&C-T 1-CPR EA/arc C_D/8 hrs
Observational parameters estimated	range bias/TDRS	range bias/TDRS	range bias/TDRS USO bias, drift, accel (`92 only)	range bias/TDRS
Atmospheric Density	DTM [*Barlier et al.*, 1977]			
Nonconservative Force Models	CB – 46 m^2 15645.76 kg	CB – 4.7 m^2 2116.0 kg	CB – 16.3 m^2 3243.05 kg	CB – 20 m^2 3031.136 kg
Measurement corrections, with relativistic clock, wet&dry troposphere, and TDRS-to-user ionosphere	Attitude and antenna Range bias	2 m zenith antenna offset Range bias	Attitude and antenna Range bias	Range bias
Station Coordinates[1]	transformed from WGS84 survey to ITRF90 [*Boucher and Altamimi*, 1991]			
Tracking TDRSs @°W Longitude ('92/'94+)	4 @ 41° 3 @ 62° 5 @ 171°	4 @ 41° 5 @ 171/174.3°	4 @ 41° 6 @ 46° 5 @ 171/174.3°	4 @ 41° 5 @ 174.3°
Tracking @ 0.1 Hz 1-way range-rate 2-way range 2-way range-rate	Pass/day x length (min.) 5x13 6x13	Pass/day x length (min.) 8x9/9x9 7x9/9x9	Pass/day x length (min.) 5x20/ na 6x21/9x30 6x20/9x30	Pass/day x length (min.) 9x13 4x11
Data Weights 1-way range-rate (mm/s) 2-way range (m) 2-way range-rate (mm/s)	 1.0 0.5	 2.0/5.0 0.5/0.125	 1.0/na 2.0/10.0 0.5/0.25	 2.0 0.5

Key: 1-CPR: 1-cycle-per-revolution, EA: empirical acceleration, CG: center of gravity, USO: ultra-stable oscillator, A-T: Along-Track, C-T: Cross-Track, CB: Cannon Ball, na: not applicable

Notes: 1. The technique used will result in the reference frame being in-between that of ITRF90 and that of TOPEX/POSEIDON.

The second test period was from July 29–September 16, 1994 (T/P cycles 69–73), and involved the ERBS and EP/EUVE spacecraft. The EP/EUVE was heavily tracked during this period because of the preoperational test opportunity of the Second TDRSS Ground Terminal (STGT). The geopotential test solutions for this period included additional tracking observations beyond those used in the development of the satellite-only model (Section 6.2.3.4). Limited TDRSS tracking of T/P required the use of a simultaneous solution strategy to take advantage of the additional geometric constraints provided by the tracking of EP/EUVE and ERBS; this decision was also supported by results of analysis summarized in *Cox and Oza* [1994]. These solutions were 6–10 days in length, with the arc start and end times determined from the T/P cycle boundaries and TDRSS maneuvers. Overlap solutions were possible only for a portion of this period.

The third test period was from January 5–February 5, 1996 (T/P cycles 122–124). Intensive TDRSS tracking of T/P was provided so that the best possible TDRS orbits could be determined to support the STS–72 mission Shuttle Laser Altimeter. This provided excellent TDRS orbits to support processing of the tracking data for RXTE. The T/P-determined TDRSS orbits were then used to process the RXTE tracking data, using the same multistep procedure applied to the TDRSS data process for T/P cycles 5–7 in November 1992.

The complete set of TDRSS-based tests took advantage of improvements in the EP/EUVE orbit determination, such as the satellite-to-satellite ionospheric refraction corrections using a model based on the IRI–95 model of *Bilitza* [1996 and 1997], that were not available at the time that the normal equations were processed for the gravity model development. The test results include average RMS residuals and orbital position comparisons between adjacent arcs. For the 1992 and 1996 set of tests, the reported residual values reflect the weighted combination of three consecutive orbit solutions, and the two overlapping solutions, as illustrated in Figure 5.1.4–1 for T/P Cycles 5–7. The reported overlaps values reflect the average of the four 5–day overlap RMS position differences. For the 1994 tests, the average residuals reflect five consecutive solutions and two overlapping solutions, and the overlaps values reflect the average of four 5–day overlap RMS position differences for EP/EUVE. For ERBS, the average residuals reflect four consecutive solutions and one overlapping solution.
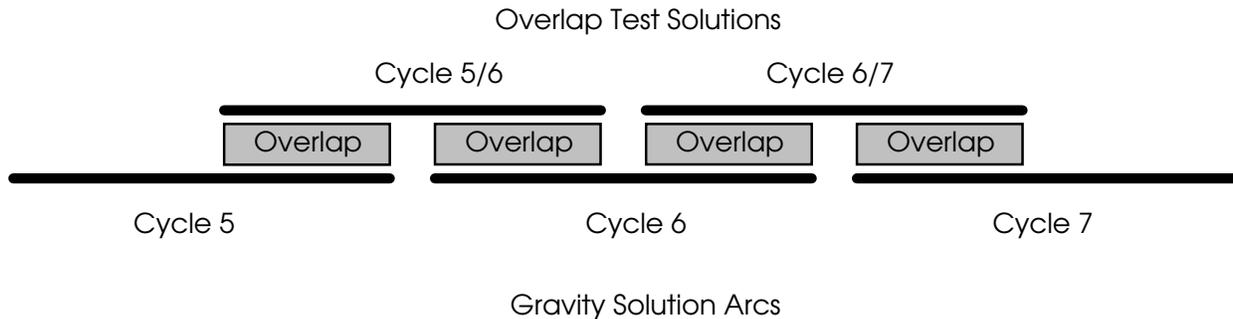
Figure 5.1.4–1. Relationship between TDRSS-based solution and overlap arcs for T/P cycles 5–7 in 1992.

5.1.5 TOPEX/POSEIDON First Generation Orbit Residual Tests

Orbit solutions using SLR and DORIS tracking data from T/P cycles 10, 19, 21, 46, and, in some cases, 69 through 73, were compared to JPL-supplied set of T/P reduced-dynamic ephemerides. The test solutions relied on the first-generation orbit parameterization, nonconservative force, and spacecraft attitude modeling discussed by *Marshall and Luthcke* [1994a and 1994b]. The parameterization for this set of T/P tests is summarized in Table 5.1.5–1. The stations used were the same as those produced with the JGM–2 gravitational solution [*Nerem et al*., 1994]. There are a number of SLR stations for which the applied data weight was not 1 m; a detailed list can

be found in Section 6.2.6.2, which describes the SLR data processing. Both the gravity field and tides were changed in these tests.

Table 5.1.5–1. Parameterization for the first-generation T/P orbit residual tests.

Gravity Field	Varied
Ocean Tides	Varied
Nonconservative Forces	GSFC *a priori* "box-wing" model
Empirical Parameters	1–CPR along-track acceleration (per day)
	1–CPR cross-track acceleration (per day)
	Constant along-track acceleration (per day)
Station Coordinates	CSR93L01/CSR94L01
	[*Boucher et al.*, 1993 and 1994]
Rotational Deformation	JGM–2 [*Nerem et al.*, 1994]
Data Weights	SLR: 1 m
	DORIS: 1 cm/s

5.1.6 TOPEX/POSEIDON Orbit Comparisons With JPL Reduced-Dynamic Solutions

The T/P reduced-dynamic tests arcs came from cycles 10, 19, 21, and 46. The parameterization for these orbit tests followed the second-generation orbit parameterization discussed by *Marshall et al.* [1995b], and is summarized in Table 5.1.6–1. This includes the augmented tide model derived from *Schrama and Ray* [1994] using T/P altimetry data, and a data-weighting scheme where the data uncertainty for the best, most common stations was 10 cm for the SLR data and 0.20 cm/s for the DORIS data. The SLR/DORIS orbits produced with each geopotential solution were compared with the GPS determined "reduced dynamic" orbits from JPL [*Bertiger et al.*, 1994]. These comparisons were made with the second generation of JPL-supplied reduced-dynamic orbits that had been computed using JGM–3 [*Haines et al.*, 1995; and *Guinn et al.,* 1995]. Unless otherwise noted, only the gravity field was changed in the tests. For instance, the new tidal solutions and new station sets were not applied, in order to evaluate the contribution due to gravity.

Table 5.1.6–1. Parameterization for the second-generation T/P orbit residual tests.

Gravity Field	Varied
Ocean Tides	*Schrama and Ray* [1994]; 35,000 terms; 15x15+
Nonconservative Forces	GSFC "box-wing," cycles 1–48
Empirical Parameters	1-CPR along-track (per day)
	1-CPR cross-track (per day)
	1 C_D per eight hours
Station Coordinates	CSR95L01[*Boucher et al.*, 1996]
Rotational Deformation	Space93 [*Gross*, 1993]
Data Weights	SLR: 10 cm
	DORIS: 0.20 cm/s

5.2 GPS/Leveling Tests

One method of geopotential model evaluation used in the past [e.g., *Rapp and Pavlis,* 1990] is through the comparison of geoid undulations, *N*, or geoid undulation differences, *ΔN*, implied by ellipsoidal (*h*) and orthometric heights (*H*), and as calculated from the geopotential model. The geometric geoid undulation, with respect to a defined reference ellipsoid, is:

$$N_{GE} = h_{GPS} - H_D \tag{5.2–1}$$

where H_D is the orthometric height of the point in some defined vertical datum. The undulation is given with respect to this datum and ellipsoid and so consequently will most probably be biased with respect to an ideal ellipsoid and ideal vertical datum reference surface (the geoid) [*Rapp, 1994; 1997a*].

If one assumes that a geoid undulation (N_{PC}) calculated from potential coefficients is given with respect to a reference frame with the same origin and alignment as the geometric undulations, one can directly compare the geometric and the gravimetric undulations, where:

$$DN = N_{GE} - N_{PC} = h_{GPS} - H_D - N_{PC} \tag{5.2–2}$$

A partial evaluation of the geopotential model can be obtained by considering the statistics of *DN* taken over a sufficiently large data set. In doing so, one needs to recognize the numerous error sources that enter into the calculation of *DN*.

In some cases, it is more appropriate to compare undulation differences between two points. The advantages of such a procedure is the reduction of long-wavelength errors (including a potentially significant bias in reference systems) in all parts of the system. In general, we write

$$\Delta N = N_2 - N_1 \tag{5.2–3}$$

When *N* is determined geometrically, we have:

$$\Delta N_{GE} = (h_2 - h_1) - (H_2 - H_1) \tag{5.2–4}$$

This value can be compared to the corresponding undulation difference calculated from the geopotential model with statistics of the differences computed over different geopotential models and different station sets. Relative differences, with respect to the distance between stations, can also be computed. Examples of such computations can be seen in *Rapp and Pavlis* [1990, Section 4.3].

In order to implement the procedures described herein, it is necessary to review the methods used in the calculation of geoid undulations from a set of potential coefficients.

5.2.1 Geoid Undulation Determination From a Potential Coefficient Model

The determination of a geoid undulation from a potential coefficient model has been thoroughly discussed [*Rapp,* 1971, 1997a], and only an abbreviated form will be presented here by way of an update to the discussion in *Rapp* [1997a, 1997b]. Consider point *P* on or above the surface of the Earth. The height of this point above the reference ellipsoid is *h*. Associated with point *P* is the

normal height H^*, the orthometric height H, the height anomaly ζ, and the geoid undulation N. These quantities are related [*Heiskanen and Moritz,* 1967, eq. 8–98] by:

$$h = H + N = H^* + \zeta \qquad (5.2.1–1)$$

We now introduce the disturbing potential, $T(r,\theta,\lambda)$ which is the difference between the true gravity potential (W) at point P and the gravity potential (U) implied by a rotating equipotential ellipsoid of revolution:

$$T(r,\theta,\lambda) = W(r,\theta,\lambda) - U(r,\theta) \qquad (5.2.1–2)$$

If W and U can be represented in a spherical harmonic series, then:

$$T(r,\theta,\lambda) = \frac{GM}{r} \sum_{n=2}^{\infty} \left(\frac{a}{r}\right)^n \sum_{m=-n}^{n} C_{nm} Y_{nm}(\theta,\lambda) \qquad (5.2.1–3)$$

The zero degree term in (5.2.1–3) has been set to zero assuming the equality of the actual mass of the Earth and the mass of the reference ellipsoid. In addition, the even zonal coefficients in (5.2.1–3) represent the difference between the coefficients of the actual and normal gravitational potentials.

Based on the generalization of Brun's formula, one has [*Heiskanen and Moritz,* 1967, eq. 2–178]:

$$\zeta_P = \frac{T_P - (W_0 - U_0)}{\gamma_P} \qquad (5.2.1–4)$$

where T_P is the disturbing potential at P. We let:

$$T_P = T_0 + T'_P \qquad (5.2.1–5)$$

where T_0 is the zero degree term of the disturbing potential and $T_p{}'$ is the disturbing potential excluding this term. We have:

$$T_0 = \frac{GM - GM_0}{r} \qquad (5.2.1–6)$$

where GM_0 is the geocentric gravitational constant of the reference ellipsoid and GM is the corresponding value of the Earth. Equation (5.2.1–4) can be rewritten as:

$$\zeta_P = \zeta_z + T'_P/\gamma_P \qquad (5.2.1–7)$$

where

$$\zeta_z = \frac{GM - GM_0}{r_P \gamma_P} - \frac{(W_0 - U_0)}{\gamma_P} \qquad (5.2.1–8)$$

The value of ζ_z can be determined only if estimates of GM and W_0 are known. This can be done with increasing accuracy with an uncertainty of approximately 10–15 cm today. In some applications, ζ_z is set to zero, which implies that the values of ζ refer to an ellipsoid where $GM = GM_0$ and $W_0 = U_0$.

To calculate geoid undulations, we use the following [*Heiskanen and Moritz,* 1967, eq. 8–100]:

$$N = \zeta + \frac{\overline{g} - \overline{\gamma}}{\overline{\gamma}} H \tag{5.2.1–9}$$

where $\overline{g}$ and $\overline{\gamma}$ are average values of actual gravity and normal gravity, respectively, between the geoid and point P (for $\overline{g}$) and between the ellipsoid and the equipotential surface corresponding to U_p (for $\overline{\gamma}$). *Heiskanen and Moritz* [*ibid.*, p. 327] show that:

$$\frac{\overline{g} - \overline{\gamma}}{\overline{\gamma}} H \approx \frac{\Delta g_B}{\overline{\gamma}} H \tag{5.2.1–10}$$

where Δg_B is the Bouguer anomaly. Then (5.2.1–9) becomes:

$$N = \zeta + \frac{\Delta g_B}{\overline{\gamma}} H \tag{5.2.1–11}$$

Using (5.2.1–11) and (5.2.1–7), we have:

$$N(\theta, \lambda) = \zeta_z + \frac{GM}{r_p \gamma_p} \sum_{n=2}^{M} \left(\frac{a}{r}\right)^n \sum_{m=-n}^{n} C_{nm} Y_{nm}(\theta, \lambda) + \frac{\Delta g_B(\theta, \lambda)}{\overline{\gamma}} H(\theta, \lambda) \tag{5.2.1–12}$$

where the maximum degree of expansion is taken as M. We designate the second term on the right-hand side of (5.2.1–12) as ζ^* so that the height anomaly term is given by:

$$\zeta(r, \theta, \lambda) = \zeta_z + \zeta^*(r, \theta, \lambda) \tag{5.2.1–13}$$

To conveniently determine ζ^*, we carry out an expansion from a point (r_E, θ, λ) on the ellipsoid. We write:

$$\zeta^*(r, \theta, \lambda) = \zeta^*(r_E, \theta, \lambda) + \frac{\partial \zeta^*}{\partial r} h + \frac{\partial \zeta^*}{\partial \gamma} \frac{\partial \gamma}{\partial r} h \tag{5.2.1–14}$$

where h is the height of the point above the ellipsoid. We write eq. (5.2.1–13) in the form:

$$\zeta(r, \theta, \lambda) = \zeta_z + \zeta^*(r_E, \theta, \lambda) + C_1(h, \theta, \lambda) + C_2(h, \theta, \lambda) \tag{5.2.1–15}$$

The C_1 term is calculated by differentiation of the spherical harmonic expansion of ζ^* given on the right-hand side of eq (5.2.1–12) with respect to r. We have:

$$C_1(h, \theta, \lambda) = -h \frac{GM}{r^2 \gamma} \sum_{n=2}^{M} (n+1) \left(\frac{a}{r}\right)^n \sum_{m=-n}^{n} C_{nm} Y_{nm}(\theta, \lambda) \tag{5.2.1–16}$$

To calculate the C_2 term, we first differentiate ζ^* with respect to γ

$$\frac{\partial \zeta^*}{\partial \gamma} = \frac{-h \zeta^*}{\gamma^2} \tag{5.2.1–17}$$

so that we now have:

$$C_2(h, \theta, \lambda) = \frac{-h\zeta^*}{\gamma^2} \frac{\partial \gamma}{\partial r} \qquad (5.2.1-18)$$

The value of normal gravity, on the surface of the ellipsoid, at a geodetic latitude ϕ is [*Moritz, 1992*]:

$$\gamma = \gamma_E \frac{1 + k \sin^2 \varphi}{\sqrt{1 - e^2 \sin^2 \varphi}} \qquad (5.2.1-19)$$

where γ_E is equatorial gravity and k is:

$$k = \frac{b\gamma_P}{a\gamma_E} - 1 \qquad (5.2.1-20)$$

where a and b are the semimajor and semiminor axes of the ellipsoid and γ_p is the value of gravity at the poles.

The gradient term in (5.2.1–18) is taken as the $\partial\gamma / \partial h$ term from *Heiskanen and Moritz* [1967, eq. 2–121]:

$$\frac{\partial \gamma}{\partial h} = -\frac{2\gamma_E}{a}\left(1 + f + m - 2f \sin^2 \varphi\right) \qquad (5.2.1-21)$$

where

$$m = \frac{\omega^2 a^2 b}{GM} \qquad (5.2.1-22)$$

For some calculations, to be noted later, the gradient term given by eq. (5.2.1–21) was approximated by the constant value of -.3086 mGal/m. We now express the geoid undulation from eq. (5.2.1–12) using the various correction term components:

$$N(\theta, \lambda) = \zeta_z + \zeta^*(r_E, \theta, \lambda) + C_1(h, \theta, \lambda) + C_2(h, \theta, \lambda) + C_3(H, \theta, \lambda) \qquad (5.2.1-23)$$

where C_3 comes from the third term on the right-hand side of eq. (5.2.1–12):

$$C_3(H, \theta, \lambda) = \frac{\Delta g_B(\theta, \lambda)}{\bar{\gamma}} H(\theta, \lambda) \qquad (5.2.1-24)$$

The $\bar{\gamma}$ term in this equation is the average value of normal gravity between the geoid and the point in question. It can be evaluated using the gradient term (5.2.1–24) given the normal value of gravity on the ellipsoid (5.2.1–19). We have:

$$\bar{\gamma} = \gamma + \frac{1}{2} \frac{\partial \gamma}{\partial h} H \qquad (5.2.1-25)$$

In some calculations, to be noted later, the $\bar{\gamma}$ value was taken as the γ value at the height of the point.

As described in *Rapp* [1997a], the process of calculating the three *C* terms given in (5.2.1–23) can be compressed to the evaluation of one spherical harmonic expansion of the sum of the three terms, which is designated $C(\theta,\lambda)$

$$C(\theta, \lambda) = C_1(h,\theta,\lambda) + C_2(h,\theta,\lambda) + C_3(H,\theta,\lambda) \tag{5.2.1–26}$$

In order to evaluate the C_3 term, one must calculate the Bouguer gravity anomaly. This can be done through the free-air gravity anomaly (Δg_{FA}) and the elevation. We have [*Heiskanen and Moritz*, 1967, eq. (3–18/19, 3–62)]:

$$\Delta g_B(\theta, \lambda) = \Delta g_{FA}(\theta, \lambda) - 2\pi\rho G \cdot H(\theta, \lambda) \tag{5.2.1–27}$$

where *G* is the gravitational constant and ρ is the density of the crust. Assuming a constant density of 2670 kg/m^3 (which is an average global estimate), eq. (5.2.1–27) becomes:

$$\Delta g_B(\theta, \lambda) = \Delta g_{FA}(\theta, \lambda) - 0.1119 \cdot H(\theta, \lambda) \tag{5.2.1–28}$$

Given the potential coefficients, the free-air anomaly is:

$$\Delta g_{FA}(r,\theta, \lambda) = \frac{GM}{r^2} \sum_{n=2}^{M} (n-1)\left(\frac{a}{r}\right)^n \sum_{m=-n}^{n} C_{nm}Y_{nm}(\theta, \lambda) \tag{5.2.1–29}$$

In order to evaluate the C_i term in eq (5.2.1–26), a set of elevations is needed. A global set of 5′x5′ elevations, JGP95E (see Section 2), was developed within this project. These values were first averaged into 30′x30′ cells and then expanded into a spherical harmonic expansion to degree 360 by *N. Pavlis* [1995, private communication]. These coefficients were then used to calculate 30′x30′ elevations (*H*) on a global basis. The procedure followed was consistent with the procedures used in the calculations of mean anomalies and mean ζ^* values.

We next consider the steps needed to evaluate the *C* values given a geopotential model that, in the cases here, is given to degree 360. One first creates a global set of 30′x30′ mean values of the following terms:

- ζ^*, the second term on the right-hand side of eq. (5.2.1–12), with *P* on the ellipsoid.

- $\dfrac{\partial \zeta^*}{\partial r}$, from eq. (5.2.1–16).

- Δg_{FA}, from eq. (5.2.1–29).

These values are now combined with the 30′x30′ elevation file to calculate the Bouguer anomaly, from eq. (5.2.1–27) and then the individual *C* terms in eq. (5.2.1–26). The result is a global set of *C* values. These quantities are now expanded into a spherical harmonic series to degree 360, including degree zero and degree one terms. This series representation of *C* can then be used to evaluate $C(\theta,\lambda)$ at a specific latitude and longitude. The calculation of this quantity will be affected by errors in the data as well as the neglect of terms in the expansion above degree 360. However, the magnitude of the various terms is fairly small except in areas of high elevation. Table 5.2.1–1 shows some statistics of the three *C* values based on the EGM96 model to be described later. The statistics are largely insensitive to the geopotential model used as can be seen by comparing the results in Table 5.2.1–1 with those of Table 1 of *Rapp* [1997a].

In summary, we used the geoid undulation calculation (eq. 5.2.1–23) along with the correction terms calculated for a specific geopotential model. For the GPS/leveling comparisons, the constant term, ζ_z will be ignored with its value, among other things, represented in the mean differences of *DN* (eq. 5.2–2). It should be noted that statistics will also be computed for the cases where the C terms are not calculated. This would correspond to the case where the geoid undulation is calculated in a classical way, ignoring topography, at a point on the ellipsoid.

Table 5.2.1–1. Statistics on the three *C* terms of equation (5.2.1–26). Units are cm.

	C_1	C_2	C_3	C
Mean	-0.3	0.0	-4.7	-5.0
Standard Deviation	±4.0	±0.6	±22.3	±23.8
Maximum	42.8	6.5	26.4	0.8
Minimum	-138.7	-7.4	-311.3	-361.9

5.2.2 The NGS GPS/Leveling Data

In 1995, a set of 1889 stations was made available by the National Geodetic Survey for use in the evaluation of the preliminary geopotential models. This data set is described in *Milbert* [1995]. The data set contained ellipsoid heights reported in the ITRF93 reference frame with the Helmert orthometric heights in the NAVD88 system. In addition, the ellipsoidal heights were given [*Milbert*, 1996, private communication] in the tide-free system [*Ekman*, 1989, or see Section 11.1]. The 1889 station set contained clusters of stations, resulting in overall undulation difference statistics that are not representative of the entire contiguous region of the U.S. A thinned set of stations having a more uniform distribution was created [*Zhang,* 1996, private communication], ensuring station separation of at least 25 km. A plot of this station set is shown in Figure 2 of *Rapp* [1997a]. Despite the improved distribution, this station set is not ideal given that a number of regions are still undersampled.

In April 1996, Milbert provided a new station set comprising 2497 stations. A thinned subset was created (using the same 25 km criterion as before) having 1156 stations. Figure 5.2.2–1 shows the distribution of the thinned subset.

As noted by *Smith and Milbert* [1997], the fairly good geographic station coverage in the U.S. enables the study of the GPS/leveling undulation results for nearly the entire country. One additional evaluation approach involves fitting a plane to the residuals and examining the resulting tilt and direction of the primary axis of the plane.

Consider the set of undulation difference residuals, *DN(φ,λ)* (see eq. 5.2–2), defined by the station set adopted for use. We fit a plane to these residuals as follows:

$$DN(\varphi, \lambda) = \Delta\varphi a + \cos\varphi\Delta\lambda b + c \qquad\qquad (5.2.2–1)$$

where $\Delta\phi = \phi - \phi_0$, $\Delta\lambda = \lambda - \lambda_0$ and ϕ_0, λ_0 are origin values taken as 37° (ϕ_0) and 263° (λ_0). The three parameters to be estimated from a least-squares adjustment are *a*, *b*, and *c*. We are

interested in the tilt of this plane with respect to some "horizontal" plane on which the residual would be random. In addition to the tilt we are interested in the direction of either the maximum tilt or minimum tilt. From eq. (5.2.2–1) the tilt in the north–south direction is "*a*" while the tilt in the east–west direction is "*b*." The units of tilt are distance/degree (or radian). It is more convenient to express the tilt in parts per million of the distance from the origins. If $\Delta\phi$ and $\Delta\lambda$ are given in degrees and *DN* is given in meters, the maximum tilt of the plane fitting the residuals is:

$$T = \sqrt{(a^2 + b^2)}\Big/0.111 \tag{5.2.2–2}$$

The azimuth, with respect to north at the origin point of the plane, would be:

$$A = \tan^{-1}(b/a) \tag{5.2.2–3}$$

Also of interest are the residuals after the plane fit has been carried out.

Ideally, one would like the value of *T* to be negligibly small. Values of *T* exist for a number of reasons: Errors in the leveling network causing errors in the orthometric heights; errors in the GPS positions and of special interest herein, long wavelength errors in the Earth's geopotential as seen through the geoid undulations computed from the potential coefficients. Ascribing the error contributions to each of these components is difficult, but two of the three sources are unchanged when different geopotential models are employed.
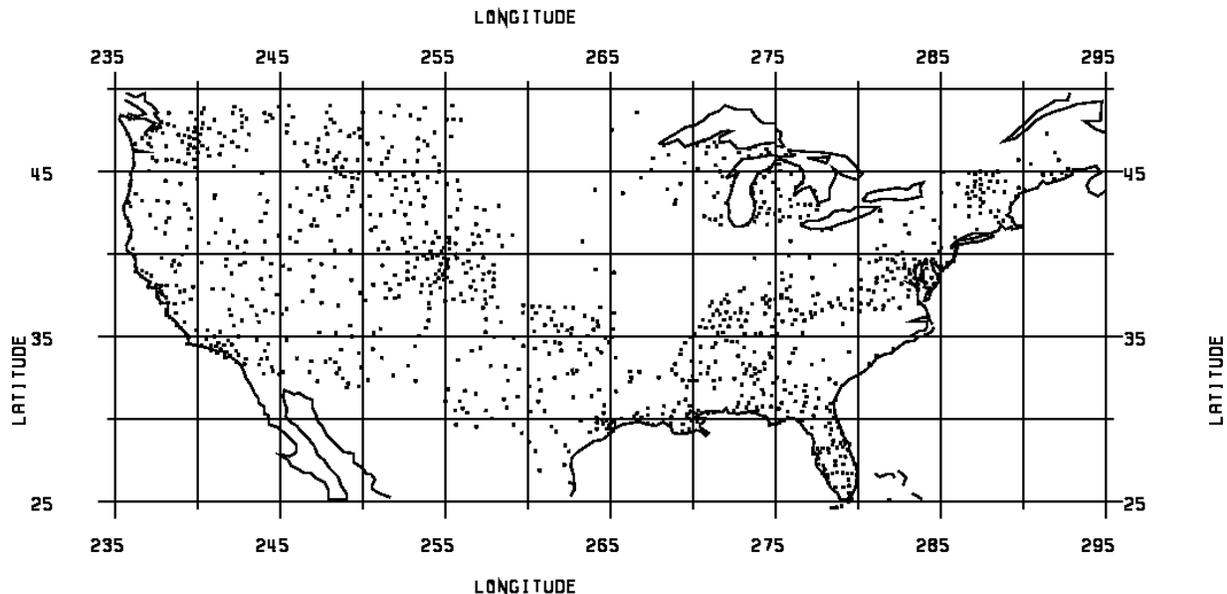
Figure 5.2.2–1. Thinned *Milbert* station set comprising 1156 stations.

5.3 GPS/Leveling Tests at GSFC

Technique

Comparisons of geopotential model-derived geoid undulations with values obtained from GPS positioning and leveling observations also were made routinely at GSFC, to test and evaluate geopotential models. When the comparisons are made in an "absolute" sense, the quantity of interest is the *DN* value defined in eq. (5.2–2). We compute the mean value of *DN* and its standard deviation for each traverse or network where GPS/leveling undulation values are available. One expects that successive improvements in the geopotential model should result in mean values of *DN* that stabilize around some constant value (representing primarily the datum bias between the geometric and the gravimetric estimates of the undulation). The standard deviations of *DN* should keep decreasing as the model's accuracy increases, and asymptotically approach the noise level of the GPS/leveling estimate (which, unfortunately, is not known in most cases). For "relative" comparisons, the differences between ΔN_{GE} defined in eq. (5.2–4) and the corresponding value ΔN_{PC}, which is computed from the geopotential model, are of interest. The standard deviation of these differences, and the average relative difference, are the statistics that we examine here. The average relative difference, in parts per million (ppm), is computed by averaging, over all the available baselines, the ratios:

$$\frac{\left|(\Delta N_{GE})_{ij} - (\Delta N_{PC})_{ij}\right|}{L_{ij}} \times 10^6 \tag{5.3–1}$$

where L_{ij} is the length of the baseline (or segment of the traverse) from point *i* to point *j*. The relative comparisons are particularly sensitive to the performance of the high-degree component of the geopotential model, since the long wavelength errors in the model (and in the geometrically defined undulations) are largely canceling out in this mode of differencing.

These general procedures have been used in previous geopotential model evaluations [e.g., *Rapp and Pavlis,* 1990]. The GPS/leveling comparisons made at GSFC differ (in terms of the technique) from those made at Ohio State, in the formulation used to compute a "geoid undulation" from the geopotential model coefficients. Specifically, for a point *P* (on the physical surface of the Earth) defined by its geocentric colatitude θ_P, longitude λ_P, and distance from the geocenter r_P (these coordinates are determined from the geodetic latitude, longitude, and height, provided by the GPS positioning), we computed the height anomaly ζ_P with respect to an ideal mean-Earth ellipsoid (ζ_Z was set to zero) by:

$$\zeta_P = \frac{GM}{r_P \gamma_p} \sum_{n=2}^{M} \left(\frac{a}{r_p}\right)^n \sum_{m=-n}^{n} \overline{C}_{nm} \overline{Y}_{nm}(\theta_P, \lambda_P) \tag{5.3–2}$$

where M is the maximum degree of the expansion. ζ_P was then directly compared to the geoid undulation or height anomaly that was provided by GPS and leveling. This approach is rigorously valid only if the GPS/leveling data provide height anomaly values (as is the case for the European and Scandinavian traverses that will be described next). If the GPS/leveling data provide geoid undulations, this approach is not precise enough for the level of accuracy that is

considered here. The more rigorous formulation of *Rapp* [1997a] has to be followed in this case to assess the performance of a particular geopotential model. This was not done at the time that test solutions were produced and evaluated at GSFC. However, when one compares the *relative* performance of different solutions, the approximate formulation is still capable of discriminating between different models.

Data

We have used GPS/leveling data from seven sources in our various tests. The first five sources were made available to GSFC by R.H. Rapp on 9/30/1992. These sources are also described in [*Rapp and Pavlis*, 1990] and [*Rapp and Kadir*, 1988]. They are:

1) The Australian traverse: 38 stations along the eastern coast of Australia in New South Wales [*Macleod et al.*, 1988]. The average length of each segment of the traverse is 39.4 km.

2) The Canadian traverse: we used 63 stations that form a traverse that starts near Yellowknife, and goes around the Great Slave Lake to Fort Smith. This is a subset of 83 stations in the Northwest Territories described by *Mainville and Véronneau* [1989]. The average segment length is 11.2 km.

3) The European traverse: this comprises 60 stations in a north–south direction extending from Norway to Austria [*Torge et al.*, 1989]. The average segment length is 49.7 km. The normal heights of the stations are provided, enabling the computation of height anomalies.

4) The Scandinavian traverse: this set is a section of the European traverse from southern Denmark to northern Norway. It consists of 46 stations with an average segment length of 46.1 km. As with the European traverse, normal heights are available for the stations.

5) The Tennessee network: 49 stations uniformly distributed across the State of Tennessee [*Rapp and Kadir*, 1988]. The 3–D positions were not tied to a geocentric system, so a large (~1.2 m) systematic bias exists between the geometrically derived undulation and a model value. To perform the relative comparisons, we selected, among all the possible pairs of stations, only those pairs whose baseline length is less than or equal to 65 km. This resulted in 101 baselines with an average length of 45.9 km that were used in the relative undulation difference tests.

The test data over these five areas were available and were used for testing and evaluation of models such as OSU89A/B, OSU91A, and the JGM series of models. During the course of the joint project, two additional sources of GPS/leveling information were made available to GSFC:

6) The NGS GPS/leveling data set: this was described in Section 5.2.2. We have variously made comparisons using the 1995 release of this set (1889 stations), the 1996 release (2497 stations), and the thinned versions of both releases, which were made available by R.H. Rapp.

7) The Canada (British Columbia) data set: a preliminary version of this data set is described in *Li and Sideris* [1994]. In April 1995, we received from *M. Véronneau* an updated version of this file, which contained 298 stations. The geometric coordinates of the stations were

obtained by a minimum constraint adjustment, holding the station 887006 in Penticton fixed at its ITRF92 (epoch 1988.0) coordinates [*Véronneau*, 1995, private communication]. The orthometric heights of the 298 stations were provided with respect to the CGD28 datum. For a subset of those (158 stations), the file also contained orthometric heights with respect to the NAVD88 datum. In our model evaluations, we have used the 298 station set with the CGD28 orthometric heights.

5.4 Geoid Undulation Tests Through Doppler-Positioned Stations

Sections 5.2 and 5.3 considered a comparison of geoid undulations implied by GPS and leveling data with geoid undulations from the geopotential models. A similar procedure using globally positioned Doppler tracking stations was described in *Rapp and Pavlis* [1990, Section 4.2] and *Rapp, Wang, and Pavlis* [1991]. In these tests, approximately 1800 stations were used with an editing criterion that any station for which the undulation difference, in absolute value, exceeded 4 m would be deleted. In these computations the ellipsoid heights, given within the Doppler reference frame (NWL 9D and NSWC 9Z–2) were transformed to an estimate of a geocentric system (IERS Terrestrial Reference Frame).

Early in the joint project, NIMA was asked to develop a test station set where the Doppler derived positions and the orthometric or normal heights were considered of high quality. Specifically, the following criteria [*Treiber*, *private communication*, 1995] were used to select the 875 stations provided for use in the joint project model evaluation:

1. The station must be surveyed to a local datum.

2. The position must have a satellite (NAVSTAR or GPS)-derived position and ellipsoid height.

3. The elevation of the position must be referenced to a local level datum (most often mean sea level).

4. The number of passes used in calculating the position must be greater than or equal to 30.

5. Elimination of as many duplicate and near-duplicate stations as possible, keeping the one with the best position accuracy and most number of passes.

6. The uncertainty of the satellite-derived X,Y,Z station components must each be less than 3 m.

The stations selected all were given originally in a reference frame (NSWC 9Z–2, NWL 9D, NWL 9C, or NWL 9B) associated with the Navy Navigation Satellite System. The ellipsoid heights in the original systems were converted by NIMA into heights with respect to a geocentric WGS84 ellipsoid using transformation parameters given in Table 2.2 (page 2–5) of *DMA* [1987].

For earlier geopotential models, statistics were calculated for *DN* after deleting stations in which the *DN* value (after transformation) exceeded 3 m. This procedure caused a different number of stations to be used with each geopotential model and made the comparison of the models through the standard deviations of the difference slightly misleading because of the different number of stations used. To avoid this problem, a test was performed with one of the preliminary models (PGS6907 to degree 70 supplemented by V037 from degree 71 to degree 360), and a file was created containing 850 stations where the *DN* file was (in an absolute sense) ≤4 m. Figure 5.4–1

shows the location of these stations. In the calculation of the N value from the potential coefficient model, eq. (5.2.1–12) was used setting ζ_z to zero and the Bouguer anomaly term to zero, with r being evaluated to a point on the ellipsoid. The correction terms for going from a height anomaly to a geoid undulation were not used because there was no specific identification available of the given height as an orthometric height (which would be required if the correction term was computed) or a normal height (which would cause no correction term to be applied).

Considering that the accuracy of the geometric "undulations" would be on the order of ±1 m (errors from Doppler h determination, transformation terms, orthometric or normal heights, horizontal and vertical datum issues), the neglect of the correction terms was reasonable. (In fact, a test was done with one geopotential model and the 850 stations with and without the correction terms described in Section 5.2.1. The standard deviation of the DN value differed only by 4 mm [out of 1.45 m], indicating that the errors in the data being used overwhelm any effects associated with the height anomaly/geoid undulation correction terms. In our case, it is not clear if we have geoid undulations or height anomalies for comparison purposes.) For tests to be reported in a later section (10.1.4), the 850 station set described here will be used without additional transformation and correction terms. The standard deviation of DN will be the criterion examined as the quality measure of the geopotential model.
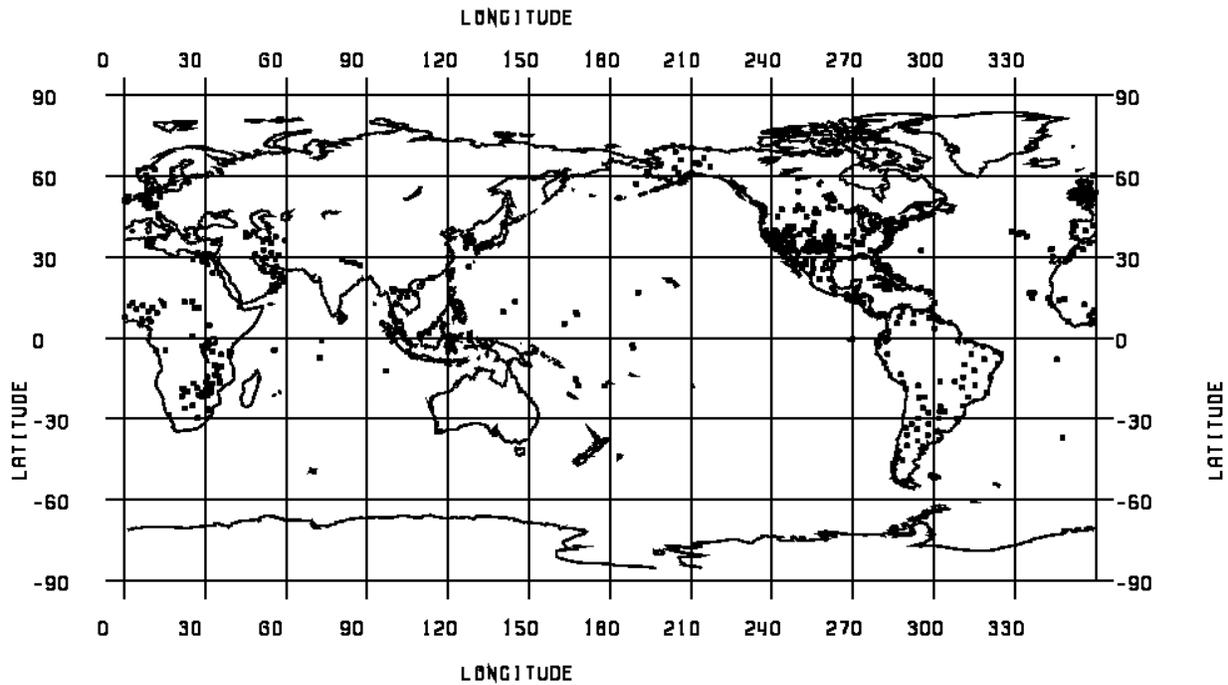
Figure 5.4–1. Distribution of Doppler stations.

5.5 Geoid Undulation Evaluation Using Dynamic Ocean Topography Comparisons With Orthonormal Functions

Dynamic Ocean Topography (DOT), ζ, is the separation between the ocean surface and the geoid. The value of ζ ranges from -220 cm (in the Antarctic region) to 70 cm (approximately) with a standard deviation of ±62 cm. Estimates of ζ can be obtained through global circulation models (GCMs) and from direct mapping of the ocean surface elevation using satellite altimeter data (e.g., TOPEX) and geoid undulation information from a geopotential model or a high-resolution geoid. In the case here, we are interested in comparing the GCM and sea surface height/geoid estimates of ζ over the long wavelengths, where the geoid undulation is believed to be known to sufficient accuracy to enable ζ, at specified wavelengths, to be accurately determined. In order to do this, the ζ estimates are first used to determine a spherical harmonic expansion to degree 24 using a least-squares estimation process with *a priori* weights on the coefficients to avoid large excursions in land areas where ζ is not defined. To carry out comparisons valid for the ocean areas of interest, the coefficients of the spherical harmonic expansions are converted to coefficients of an orthonormal (ON) expansion that are defined for a specific domain of the ocean. These ON expansions, from the GCM and the altimeter/geoid estimates of ζ, allow a comparison of the spectral components, by degree and cumulatively to a specified degree, to obtain an independent evaluation of the geoid undulation implied by a given geopotential model.

The procedure for the definition of the orthonormal functions associated with a defined ocean domain was developed in *Hwang* [1991, 1993]. The procedures developed by Hwang were initially implemented for TOPEX data by *Wang and Rapp* [1994]. Later studies by *Rapp, Zhang, and Yi* [1996] extended the comparisons to different geopotential models and a DOT data set obtained from an evaluation of 2 years of TOPEX data.

5.5.1 Basic Equations and Procedures for the DOT Estimations and Comparisons

The procedures implemented for this report are virtually identical to those described in *Rapp, Zhang, and Yi* [1996]. The spherical harmonic representation of ζ is given by the following:

$$\zeta(\theta, \lambda) = \sum_{n=0}^{k} \sum_{m=0}^{n} c_{nm} R_{nm}(\theta, \lambda) + s_{nm} S_{nm}(\theta, \lambda) \tag{5.5.1-1}$$

where θ is the geocentric colatitude and λ is longitude. R_{mm} and S_{mm} are the fully normalized spherical harmonics and c_{mm} and s_{mm} are the fully normalized spherical harmonic coefficients of the DOT, ζ. The maximum degree of the expansion is k. The orthonormal expansion, with orthonormal functions $O_{nm}(\theta, \lambda)$ and $Q_{nm}(\theta, \lambda)$ and orthonormal coefficients a_{mm}, b_{mm}, is:

$$\zeta(\theta, \lambda) = \sum_{n=0}^{k} \sum_{m=0}^{n} a_{nm} O_{nm}(\theta, \lambda) + b_{nm} Q_{nm}(\theta, \lambda) \tag{5.5.1-2}$$

The orthonormal functions are defined for a specific domain of the ocean, which, in our case, excludes the region to the north of $65°$N and to the south of $66°$S. In addition, the region of the Black, Caspian, Mediterranean, and Red Seas, Hudson Bay, and the shallow coastal regions were excluded, as were all land data. In addition, isolated islands, such as Bermuda and the Kerguelen Islands, also were excluded. With these functions, it is possible to determine the orthonormal coefficients after the spherical harmonic coefficients have been estimated for a specific estimate of DOT.

The least-squares determination of the spherical harmonic coefficients was carried out for estimates from GCMs and from TOPEX altimetric data and geoid undulation information. In the latter case, h is the sea surface height determined at a TOPEX normal point and N the geoid undulations at the corresponding point. All sea surface height data used are based on orbits computed using the JGM–3 geopotential model. Tidal corrections were made using the CSR 3.0 tide model [*Eanes and Bettadpur*, 1995]. The usual environmental corrections were made, including the inverted barometer correction where the reference pressure was the average pressure in the 10-day TOPEX cycle being processed. The corrected sea surface heights were reduced to a reference track. The DOT for a single point for cycle I after the aforementioned corrections would be:

$$\zeta_I(\theta, \lambda) = h_I(\theta, \lambda) - N(\theta, \lambda) \qquad (5.5.1–3)$$

In practice, a set of normal points are found that uniformly sample the denser 1-Hertz data. A mean value of $\zeta_I(\theta, \lambda)$ is formed by averaging 2 years of ζ_I values (TOPEX cycles 12 to 84). N was defined by the JGM–3 model to degree 70, augmented by the OSU91A model to degree 360. The total number of normal points used in this analysis after editing of significant outliers was 36115. (See *Wang and Rapp* [1994, Section 5.1] for more detailed editing information.)

Once the ζ values were determined, a least-squares adjustment was made to determine the spherical harmonic coefficients. In this calculation, zero values of ζ over land regions were introduced to help (along with a set of *a priori* degree variances) constrain the magnitude of the ζ coefficients and the ζ values in the land areas. (See *Rapp, Zhang, and Yi* [1996, p. 22587] for additional details.)

In order to efficiently process these data with numerous geopotential models, a procedure was developed to reduce the computational workload. The value of ζ at the normal points was calculated considering an undulation change from the JGM–3/OSU91A model to the model being evaluated. If ΔN is the undulation change, the revised ζ value for the geopotential model then would be

$$\zeta_i = \zeta_{JGM3/91A} - \Delta N \qquad (5.5.1–4)$$

where

$$\Delta N = N_i - N(JGM3/91A) \qquad (5.5.1–5)$$

This procedure eliminated the need to form normal points for each new model. However, it has a disadvantage in that the editing of the data was based on a geopotential model less accurate then the newer models being tested.

Once the spherical harmonic coefficients of ζ were estimated, they were converted to the orthonormal coefficients valid for the ocean domain described earlier. These coefficients were then compared to the ON coefficients of the DOT implied by (primarily) the Semtner/Chervin POCM–4B model described by *Stammer et al.* [1996]. The procedure used to evaluate the spherical harmonic coefficients was analogous to that used in the estimation using the TOPEX/geoid data. The specific procedures are described in *Rapp, Zhang, and Yi* [1996, pp. 22585–22587].

For example, if $a_{mm}(1)$, $b_{mm}(1)$ represent the ON coefficients from the TOPEX/geoid data, and $a_{mm}(2)$, $b_{mm}(2)$ represent the coefficients from the POCM–4B model, the DOT difference at degree n would be:

$$\Delta\zeta_n = \left[\sum_{m=0}^{n} \left(a_{nm(2)} - a_{nm(1)}\right)^2 + \left(b_{nm(2)} - b_{nm(1)}\right)^2 \right]^{1/2} \qquad (5.5.1–6)$$

The cumulative DOT difference from degree zero to degree k would be:

$$\Delta\zeta_k = \left[\sum_{n=0}^{k} \left(\Delta\zeta_n\right)^2 \right]^{1/2} \qquad (5.5.1–7)$$

The units of the quantities will be m or cm. Values of $\Delta\zeta_n$ and $\Delta\zeta_k$ for different k values will be given in subsequent sections. Geopotential models that yield smaller values of $\Delta\zeta$ will be considered the better geopotential models.

It should be also noted that considering an oceanwide estimate of $\Delta\zeta$ gives only a partial picture of the impact of new geopotential models. It is also helpful to construct maps of $\zeta(TOPEX/geoid)$ minus $\zeta(POCM–4B)$ to see the structure of the differences and where major and minor improvements have been made. Such plots were made for many of the geopotential models tested for the report. An example of such a plot using the geoid implied by JGM–3/OSU91A is given in Figure 5 of *Rapp, Zhang, and Yi* [1995].

5.5.2   Geoid Undulation Accuracy in the ON System

As seen from eq. (5.5.1–3), the geoid undulation plays a direct role in the determination of dynamic ocean topography. The accuracy of DOT determined from eq. (5.5.1–3) will be dependent on the accuracy of the geoid undulations implied by the geopotential model. The accuracy of geoid undulations can be considered in both the spatial and spectral domain. Given the error covariance matrix of the estimated potential coefficient set, the resulting geoid undulation commission errors can be calculated by error propagation. An example of such error estimates for the JGM–3 model to degree 70 can be found in *Tapley et al.* [1996, Plate 5]. It is also of interest to examine geoid undulation errors in the spectral domain, both in the spherical harmonic domain and in the orthonormal domain. The ON undulation accuracy is of importance when one considers the determination of DOT using the series representation described in Section 5.5.1.

An approximate equation to calculate geoid undulations from potential coefficients is a spherical approximation to the second term on the right-hand side of (5.2.1–12). We write:

$$N(\theta, \lambda) = R \sum_{n=2}^{M} \sum_{m=-n}^{n} C_{nm} Y_{nm}(\theta, \lambda) \qquad (5.5.2–1)$$

Let the standard deviation of each coefficient be $m(C_{mm})$. Assuming that the coefficients are independently estimated we have for the standard deviation at degree n:

$$m(N_n) = R \left[\sum_{m=-n}^{n} m^2 (C_{nm}) \right]^{1/2} \qquad (5.5.2–2)$$

The accuracy of $m(N_n)$ computed from this equation will reflect the accuracy in both land and sea areas. However, for the DOT studies one would like the accuracies in the ON system that reflects the domain in which the DOT is defined.

The determination of the error covariance matrix (or, in the simple case, coefficient accuracy) of the ON coefficients has been described by *Hwang* [1991, Section 7.5; 1993, Section 6]. In these calculations, an orthonormal system that is consistent with a potential coefficient system where the zero- and first-degree terms are zero must be used. This is designated system 3 (Z) by *Hwang*. Using this system and the ocean domain, the error covariance matrix of the geoid undulations on a grid, or as mean values, can be obtained in the ocean area. This covariance matrix can then be related to the standard deviations of the ON coefficients of the geoid undulations [*Hwang*, 1993, eq. (44)]. If $\overline{m}(a_{mm})$ and $\overline{m}(b_{mm})$ are the ON coefficient standard deviations of the ocean geoid undulation, the undulation accuracy at degree n is

$$\overline{m}(N_n) = \left\{ \sum_{m=0}^{n} \left[\overline{m}^2(a_{nm}) + \overline{m}^2(b_{nm}) \right] \right\}^{1/2} \qquad (5.5.2–3)$$

The cumulative undulation error in the ocean domain, to degree M, would be

$$\overline{m}(N) = \left[\sum_{n=2}^{M} \overline{m}^2(N_n) \right]^{1/2} \qquad (5.5.2–4)$$

In the calculations carried out here, the full error covariance matrix was not used. It is noted that the errors were propagated based only on the standard deviation of the potential coefficients, which were assumed to be independently estimated. Additional computations should be considered when the full error covariance matrix of the coefficients to degree 70 is used.

An example of the undulation accuracy by spherical harmonic and ON expansion for the JGM–3 potential coefficient model is seen in Table 1 of *Rapp, Zhang, and Yi* [1996]. Calculations for this report have been made by Zhang using the identical procedures described in *Rapp, Zhang, and Yi* [1996]. The results obtained are one way to assess the value of the geoid undulations in the calculation of dynamic ocean topography. Specific results will be given in Section 10.1.5.

5.5.3 Geostrophic Flow Determination and Comparison

The ζ values can be used to calculate the magnitude and direction of the "upper ocean geostrophic velocity" [e.g., *Tsaoussi and Koblinsky,* 1994, p. 24677] using the standard equations

$$u(\varphi, \lambda) = \frac{-g}{2R\omega \sin \varphi} \frac{\partial \zeta(\varphi, \lambda)}{\partial \varphi} \tag{5.5.3–1}$$

$$v(\varphi, \lambda) = \frac{g}{2R\omega \sin \varphi \cos \varphi} \frac{\partial \zeta(\varphi, \lambda)}{\partial \lambda} \tag{5.5.3–2}$$

where u is the east–west velocity component, v is the north–south component, R is a mean-Earth radius, g is an average value of gravity, and ω is the angular rate of rotation of the Earth. The $2\omega \sin\varphi$ term is the Coriolis parameter and $\phi = 90–\theta$.

The magnitude V and azimuth A of the total velocity vector, as used by *Engelis and Rapp* [1984], would be

$$V(\varphi, \lambda) = \left(u^2 + v^2\right)^{1/2} \tag{5.5.3–3}$$

$$A = \tan^{-1}(u/v) \tag{5.5.3–4}$$

Values of all quantities can be computed from the spherical harmonic expansion of ζ either from the altimeter/geoid process or from the ζ values of a global circulation models. The values of the differences between the estimates can also be computed. Examples of flow vector determination are shown in Plate 1 of *Rapp, Zhang, and Yi* [1996], with examples of geostrophic flow velocities and differences between various models given in Table 6 of that paper.

For computations to be reported later, the comparisons will be made using the ζ based on the newer geopotential model. The comparisons will be based on the use of a 2.5° grid of data in the oceans between 62.5°N and 62.5°S, excluding 10°N to 10°S, where, due to the Coriolis parameter, the calculation becomes undefined. Alternative procedures could be used for computations near the Equator, but they were not implemented for this report. Other areas excluded in these comparisons were Black, Caspian, Mediterranean, and Red Seas, Hudson Bay, and shallow coastal regions. In essence, the comparisons are made in the same region for which the ON domain is defined. Note that this procedure enables the differences to be computed up to a specified degree of the spherical harmonic expansion.

5.6 Discrete Comparisons With Undulations Implied by Altimeter Data and a Circulation Model

Technique

The main idea behind these comparisons was described by *Rapp and Pavlis* [1990, Section 4.4]. Satellite altimetry provides a range measurement from the spacecraft to the ocean surface. Knowledge of the satellite's orbit and of the DOT (ζ) enables one to estimate the geoid undulation (N_{alt}) at the subsatellite locations as:

$$N_{alt} = h - \zeta \tag{5.6–1}$$

where the sea surface height (h) is obtained as the difference of the satellite's ellipsoidal height minus the altimeter range measurement. h is corrected for instrument, media (ionosphere and troposphere), and geophysical effects (solid Earth and ocean tides). The altimetric estimates of the undulation, N_{alt}, obtained in this fashion can be compared to geoid undulation values obtained from a potential coefficient model, denoted N_{mod}.

N_{alt} is obviously contaminated by errors in the altimeter range (and its various corrections), in the satellite's radial orbit component and in the estimate of the DOT ζ. When TOPEX altimeter data are used to estimate N_{alt}, the radial orbit error contribution is significantly reduced (RMS radial orbit error at the ± 2 to 3 cm level [*Tapley et al.*, 1996]). Furthermore, through crossover adjustments one may adjust altimetric SSHs from other missions (e.g., GEOSAT, ERS–1) to the TOPEX-defined reference frame, and thus significantly improve the long wavelength accuracy of the SSHs from these missions, which originally were not supported by the same level of radial orbit accuracy as TOPEX. The DOT, which is needed in eq. (5.6–1), can be obtained from a global ocean circulation model. A model such as the POCM–4B, developed by *Semtner and Chervin* and described by *Stammer et al.* [1996], is a particularly desirable choice here for the estimation of ζ, since it is totally independent of any altimeter data (and of any *a priori* geoid knowledge).

In our comparisons, we (generally) examine the statistics associated with two variables of interest. The first is the difference:

$$\Delta_i = (N_{alt})_i - (N_{\text{mod}})_i = h_i - \zeta_i - (N_{\text{mod}})_i \tag{5.6–2}$$

between the altimetric and the model value of the geoid undulation, and the second is the residual geoid slope, defined by:

$$s_{ij} = \frac{[(N_{alt})_j - (N_{\text{mod}})_j] - [(N_{alt})_i - (N_{\text{mod}})_i]}{d_{ij}} \tag{5.6–3}$$

where d_{ij} is the distance between two subsatellite locations i and j. In some cases (e.g., the tests described in Section 8.5.5), the slope of the DOT was neglected when computing the residual geoid slope, and s_{ij} was obtained from:

$$s_{ij} \approx \frac{[h_j - (N_{\text{mod}})_j] - [h_i - (N_{\text{mod}})_i]}{d_{ij}} \tag{5.6–4}$$

When comparing the model undulation N_{mod} to the altimetric value N_{alt}, care should be taken with regard to the permanent tide system used. All the geopotential models developed in this study report the second-degree zonal coefficient in the tide-free (or nontidal) system. The altimetric undulations, however, are given in the mean tide system. Therefore, before comparisons between the two estimates were made, we always converted the model undulation to the mean tide system using [*Rapp and Pavlis*, 1990, eq. (70)]:

$$(N_{\text{mod}})_{mean} = (N_{\text{mod}})_{non-tidal} - 0.257 \cdot \left(\frac{3}{2} \cdot \sin^2 \varphi - \frac{1}{2} \right) \ \text{m} \tag{5.6–5}$$

where the model-implied undulation, in the nontidal system, was computed on the surface of the reference ellipsoid by:

$$(N_{\text{mod}})_{non-tidal} = \frac{GM}{r^e \gamma^e} \sum_{n=2}^{M} \left(\frac{a}{r^e}\right)^n \sum_{m=-n}^{n} \overline{C}_{nm} \overline{Y}_{nm}(\theta, \lambda) \tag{5.6–6}$$

where M is the maximum degree of the expansion. Notice that N_{mod} refers to an ideal mean-Earth ellipsoid, whose equatorial radius remains unspecified (the zero-degree undulation is set to zero). The mean value of Δ over the ocean represents the aggregate effect of (a) the difference between the ideal equatorial radius and the one used to define the altimetric SSHs, and (b) the TOPEX altimeter range bias (any relative bias between the TOPEX altimeter and those of GEOSAT or ERS–1 was absorbed in the crossover adjustment of the SSHs from these two missions to the TOPEX-defined sea surface).

As we will explain next, the altimetric values N_{alt} used in these comparisons were obtained from SSHs sampled at the nominal 1 Hz rate. N_{alt} is, therefore, quite rich in high-frequency content, and the statistics of Δ, and especially s, provide a sensitive indicator of the oceanic geoid accuracy of the models at the higher degrees (Δ is obviously testing the model over its entire bandwidth from $n = 2$ to M). For geopotential models derived without the use of "direct" altimetry (such as the Numerical Quadrature and the Block-Diagonal solutions of Chapter 8), there is justifiably little correlation between the geoid model error and the error of N_{alt}. Since the DOT model is independent of both, the standard deviation (σ_Δ) of the Δ values over the ocean represents (approximately):

$$\sigma_\Delta \approx \sqrt{G_c^2 + G_o^2 + O_c^2 + O_o^2 + A^2} \tag{5.6–7}$$

where G_c is the commission error of the model geoid ($n = 2$ to M), G_o is its omission error ($n = M + 1$ to ∞), O_c and O_o are the commission and omission errors of the ocean circulation model, respectively, and A is the total error of the altimetric SSH (comprising the noise of the altimeter itself, residual orbit error, and errors in the various corrections to the altimeter range measurement). Although O_c and O_o are not well known, eq. (5.6–7) may at least be used to provide an upper bound for a geopotential model's commission error. Over the ocean, G_c is not expected to exceed in an RMS sense σ_Δ. Furthermore, when the same altimeter data (and DOT model) are used to test different geopotential models (complete to the same degree M), changes in σ_Δ are dominated by changes in G_c. O_c, O_o, and A remain constant, while G_o may be affected only slightly (due to aliasing) to changes in the test model. The statistics of Δ (and s) are, therefore, suitable to discriminate between different geopotential solutions.

In our comparisons, the mean value of Δ and its standard deviation σ_Δ were computed as weighted estimates. The weights were computed as described by *Wang and Rapp* [1994, Section 2.3], to account for the increasing density of altimeter measurements as one approaches the latitudes corresponding to the satellite's inclination.

Data

Two pieces of information are required to evaluate eq. (5.6–1). The altimetric SSH, *h*, and the DOT, ζ. We describe next the origin of each.

SSH data from three altimeter missions were used. In every case, the data consisted of "mean" tracks generated by "stacking" the SSH values from successive repeat cycles over a fixed set of 1 Hz ground-track locations. This set is, of course, mission-dependent. We use mean tracks formed from TOPEX data, GEOSAT Exact Repeat Mission (ERM) data, and ERS–1 35-day repeat mission data (Phase C). The mean track from each mission provides for every 1 Hz subsatellite location a record with the following information: a) geodetic latitude, b) longitude, c) mean value of the SSH, d) standard deviation of the SSH (i.e., a measure of the sea surface variability at the particular location), and e) number of repeat cycles used to form the mean SSH. The last two fields can be used for editing purposes. For TOPEX, the mean track was generated by averaging data from cycles 9 through 82 (68 cycles in total, since we excluded data acquired by the POSEIDON altimeter). The average value of the SSH is not computed for a given location if fewer than five repeat cycles contribute valid estimates of the SSH for that location. The TOPEX SSHs are based on JGM–3 orbits. They refer to an ellipsoid of $a = 6378136.3$ m and $1/f = 298.257$. Their ocean tide corrections were computed from the *Schrama and Ray* [1994] model. The (static) inverted barometer correction was applied based on a constant (1013.3 mbar) reference pressure. Apart from the net instrument correction, provided on the TOPEX Geophysical Data Records, no additional altimeter range bias correction was applied to obtain the SSHs. The TOPEX mean track provides average SSH values for 593120 ground-track locations.

The mean tracks for GEOSAT and ERS–1 have been adjusted to the TOPEX-defined sea surface through a crossover adjustment described by *Wang and Nerem* [1995]. The first 42 cycles of GEOSAT's ERM were used, and provided a total of 950181 average values of the SSH. For ERS–1, cycles 1 through 18 from Phase C were used to produce a total of 1655723 average 1 Hz SSHs.

The model used to evaluate ζ was in the form of spherical harmonic coefficients, complete to degree and order 24. This expansion was developed by *Rapp et al.* [1996], through a least-squares fit to the output of POCM–4B, averaged over the time period from January 1, 1993, to December 31, 1994. It is the same spherical harmonic expansion of ζ, that is used in the comparisons described in Section 5.5.1. For some of our comparisons (e.g., Section 8.5.5), the DOT expansion was truncated to degree and order 14.

In order to maintain some correspondence in the comparisons described here with those described in Section 5.5.1, and also to ensure that the N_{alt} values used for the models' evaluation are based on the most accurate SSH estimates, we applied the following editing on the mean track data described above.

1) We exclude any subsatellite location falling within a 30´x30´ cell the mean elevation of which is $\geq$ -1000 m. This avoids shallow ocean areas where ocean tide corrections may be unreliable.

2) We exclude any SSH data in the Mediterranean, Caspian, Black, and Red Seas, in Hudson Bay, and in the Hudson Strait.

3) In the case of TOPEX, we considered only data within $-66° ≤ φ ≤ 65°$. In the case of ERS–1, we considered only data within $-72° ≤ φ ≤ 72°$, to avoid some spurious values obtained from altimeter returns over ice (and also to provide a comparable geographic coverage with that of GEOSAT).

Application of these editing criteria resulted in a TOPEX mean track with 520252 SSH values, a GEOSAT one with 839169 values, and an ERS–1 mean track with 1465425 values. These formed the test SSH data used in our various comparisons.

5.7 Undulation Comparisons Along an ERS–1 Track in the Antarctic Region

In September 1995, Tilo Schoene from the Alfred Wegener Institute for Polar and Marine Research, Department of Geology, in Bremerhaven, Germany, noted possible problems associated with the geoid undulations computed from the OSU91A geopotential model in the Weddell Sea region. The question arose because of comparisons of sea surface heights derived from ERS–1 altimeter data with the undulations of OSU91A. In plots prepared by Schoene considering data from 60°S to 77°S, the value of h-N was approximately -2 m from 60°S to 72°S, increasing to almost 8 m near 75°S. While the nearly constant difference of -2 m could be tentatively explained by the dynamic ocean topography in this area (see Figure 1, in *Rapp, Zhang, and Yi* [1996]), from 72°S to 77°S, there appeared to be a significant error in the OSU91A geoid undulations.

In October 1995, Schoene made available four tracks of sea surface heights based on ERS–1 altimeter data. The tracks contained points from 30°S to approximately 78°S, all tracks passing through the Weddell Sea. The four tracks were designated RR6008, RR6009, RR6023, and RR6037. Plots from each of these tracks showed a similar pattern: reasonable fits of the OSU91A undulations to sea surface heights between 60° S to 70° S followed by increasing differences that showed large differences near 75°S. The maximum difference of about 8m occurred on track RR6008. Thereby, this specific track was selected for use in the evaluation of the undulations from the new geopotential models. A subset (65°S to 78°S, 105 points) of sea surface heights from the original data set was selected for use in the evaluation process. In this case, the starting point was 65.0° S, 342.5° to 77.9°S, 316.0°. Since the agreement in the northern part of the track with OSU91A was fairly good, the 105 points were further divided into two segments: 50 points where the latitude was less than 72°S, and 55 points where the latitude was greater than 72°S.

The procedure implemented for the comparisons of undulation estimates is similar to that described in Section 5.6. The sea surface heights are converted to geoid undulations by applying a correction for dynamic ocean topography based on the POCM–4B DOT model. The resultant value is compared to the geoid undulation from the geopotential model and statistics of the differences on the two track segments computed. Specifically, we first compute

$$N(\text{ERS–1}) = h(\text{ERS–1}) - \zeta(\text{POCM–4B}) \tag{5.7–1}$$

Then, the difference is:

$$DN = N(\text{ERS–1}) - N(\text{geopotential model}) \tag{5.7–2}$$

5–28

The DOT values were computed from a degree 360 expansion of the POCM–4B DOT model. The determination of the model was carried out by *Zhang* [1996, private communication]. The estimation was made using a quadrature procedure where values of "DOT" on land were from the ocean DOT using an extrapolation with an exponential function so that values of DOT were continuous across the ocean–land interface. Although the expansion was made to degree 360, the spectral content at the higher degrees is probably not well determined. Tests were carried out with the value of ζ computed from an expansion just to degree 24; little change was found in the statistics of the differences. In addition, values of ζ from the POCM–4B model were not defined below 75°S, so that the extrapolation of values to 77°S creates a possible error. In attempt to retain the higher frequency information that might be in the expansion of the POCM–4B model, all statistics that will be given in Section 10.1.6 are based on using the degree 360 expansion. As an example of the results, we consider the use of the OSU91A model. In the north segment, the mean DN is -2.1 cm and the standard deviation is ±23.1 cm. For the south segment, the mean DN is 610.9 cm and the standard deviation of the difference is 274 cm. There is a clear distinction between the fits to the north and south segments on track RR6008.

5.8   Comparisons With Altimetry-Derived Anomalies

Technique

Altimetry-derived gravity anomalies provide an independent and accurate source of information that can be used to test and evaluate satellite-only gravitational models. Comparisons between altimetry-derived gravity anomalies and model-implied values have been described by *Marsh et al.* [1988] and *Marsh et al.* [1990].

We denote an area-mean value of the gravity anomaly obtained from satellite altimetry by $\overline{\Delta g}_{alt}$. This value was obtained here over equiangular 5° cells. In the present study, all the satellite-only models to be tested were complete to degree and order 70. Therefore, to enable a comparison over the same degree band, we filtered out of the 5° $\overline{\Delta g}_{alt}$ contribution from harmonics above degree 70. This was done using a preliminary high-degree (360) model. Thus, we formed the comparison quantity $\overline{\delta g}$, where:

$$\overline{\delta g} = \overline{\Delta g}_{alt} - \overline{\Delta g}_{hf} \tag{5.8–1}$$

where the high-frequency component $\overline{\Delta g}_{hf}$ is computed in terms of 5° area-mean values, on the surface of the reference ellipsoid, by:

$$\left(\overline{\Delta g}_{hf}\right)_{ij} = \frac{1}{\Delta\sigma_i} \frac{GM}{(r_i^e)^2} \sum_{n=71}^{360} (n-1)\left(\frac{a}{r_i^e}\right)^n \sum_{m=-n}^{n} \overline{C}_{nm} \cdot \overline{IY}_{nm}^{ij} \tag{5.8–2}$$

with *i* and *j* denoting the location of a 5° cell in our usual two-dimensional array that contains the global equiangular grid. $\overline{\delta g}$ could then be compared to a corresponding value obtained from the harmonic coefficients of a test model. The model-implied value $\overline{\Delta g}_{mod}$ was computed by:

$$\left(\overline{\Delta g}_{\text{mod}}\right)_{ij} = \frac{1}{\Delta\sigma_i} \frac{GM}{(r_i^e)^2} \sum_{n=2}^{M} (n-1)\left(\frac{a}{r_i^e}\right)^n \sum_{m=-n}^{n} \overline{C}_{nm} \cdot \overline{IY}_{nm}^{ij} \tag{5.8-3}$$

By varying the maximum degree of the summation M from 2 to 70 in eq. (5.8–3), one would form 69 global grids of model-implied values. Each such grid contained the test model's anomaly contribution up to that specific degree of summation. We denote these global sets of model-implied anomalies by $\overline{\Delta g}_{\text{mod}}^M$. We then formed, for each degree from 2 to 70, one global grid of the differences:

$$\left(d^M\right)_{ij} = \left(\overline{\delta g}\right)_{ij} - \left(\overline{\Delta g}_{\text{mod}}^M\right) \tag{5.8-4}$$

The statistics of d^M provide a measure of the accuracy of the satellite-only model as a function of degree M. We computed the area-weighted mean value and variance about the mean (i.e., the square of the standard deviation) of d^M, for every degree M from 2 to 70. For the special case of $M = 70$, we also identified the extreme differences and their geographic location.

A nonzero mean value of d^M (as M approaches 70) could represent very long wavelength errors that may be present in the altimetry-derived values. These errors could be associated with residual (mostly geographically correlated) orbit error, and/or very long wavelength errors in some of the corrections applied to the altimeter range data. However, changes in the mean value of d^M which are observed when different geopotential models are tested, indicate changes in the long wavelength parts of the corresponding models. The variance about the mean of d^M provides a measure of the accuracy of the satellite-only model and of its ability to capture the high(er) frequency content present in the altimetric anomalies $\overline{\delta g}$. Denoting this variance, at degree M, by v_M, one has:

$$v_M = SC_{2\to M}^2 + SO_{M+1\to 70}^2 + FC_{71\to 360}^2 + FO_{361\to\infty}^2 + E_{\overline{\Delta g}_{alt}}^2 \tag{5.8-5}$$

where

$SC_{2\to M}$ is the satellite-only model's gravity anomaly commission error ($n = 2$ to M),

$SO_{M+1\to 70}$ is the satellite-only model's gravity anomaly omission error ($n = M + 1$ to 70),

$FC_{71\to 360}$ is the high-degree model's gravity anomaly commission error ($n = 71$ to 360),

$FC_{361\to\infty}$ is the high-degree model's gravity anomaly omission error ($n = 361$ to ∞),

$E_{\overline{\Delta g}_{alt}}$ is the total (random and systematic) error in the altimetric 5° mean anomaly.

All of the above errors refer to 5° mean values. The sum of the last three terms on the right-hand side of eq. (5.8–5) is of the order of 1 mGal^2, for the altimetry-derived anomalies and the high-degree models used here. The value of v_M (which for current satellite-only models ranges approximately between 10 and 17 mGal^2 for $M = 70$), is, therefore, dominated by the contribution of the terms $SC_{2\to M}$ and $SO_{M+1\to 70}$. This is the desirable situation, since the test is meant to evaluate the satellite-only model. As M increases, $SC_{2\to M}$ increases while $SO_{M+1\to 70}$ decreases. However, due to the attenuation of the gravitational signal with altitude, present

satellite-only models contain limited gravitational information above degree ~40. Above this degree, their coefficient errors rapidly approach 100 percent of the expected coefficient magnitudes themselves. As a result of this, when v_M is plotted as a function of degree, it produces a characteristic L-shaped curve, with the "knee" around degree 40, above which v_M remains approximately constant. Obviously, improvements in the satellite-only solutions should always result in lowering the v_M curve as a whole, and the introduction of data with increased high-degree sensitivity should push the knee at ever higher degrees. Finally, a prerequisite for the validity of any satellite-only solution is that the v_M curve be monotonically decreasing as a function of degree. If this is not the case, the implication is that the model's omission error (mapped onto equiangular anomalies over the ocean) at some degree(s) is lower than the corresponding commission error, and this should normally not happen.

This type of comparison is of limited value for the evaluation of combination solutions. Such solutions contain altimetric information in the form of either "direct" tracking or altimetry-derived anomalies. Therefore, corresponding tests would not be based on independent data, and would only demonstrate the ability of the combination solution to fit the data that were used to develop it.

Data

To evaluate eq. (5.8–1) and thus form our comparison quantity $\overline{\delta g}$, we need two pieces of information. The altimetric 5° mean anomalies $\overline{\Delta g}_{alt}$ and a high-degree model to compute $\overline{\Delta g}_{hf}$. The 5° mean anomalies were formed here by averaging the altimetry-derived 30´ mean values received from NIMA on September 15, 1995 (henceforth this file is denoted ALT915). The ALT915 file was a preliminary version of the final 30´ altimetric anomaly data set that was used to develop EGM96. It contained a total of 156422 30´ mean anomalies. Of these, 141082 were estimates computed by NIMA using the GEOSAT Geodetic Mission data, and the least-squares collocation algorithm as described in Section 4. The rest of the values were estimates provided by KMS (14179 values), NOAA (1017 values), and *Laxon and McAdoo* (144 values). These covered primarily ocean areas outside GEOSAT's inclination, up to the inclination of ERS–1. Because the evaluation of the non-NIMA estimates was still ongoing at that time, we decided to form the 5° mean values using only the 141082 NIMA 30´ anomalies, whose quality had been tested and verified both by NIMA and through a number of preliminary combination solutions. 1602 5° mean values were computed as area-weighted averages of the 30´ values. Of these, 1163 values were based on 100 percent coverage (100 30´ values available within the 5° cell). During this averaging process, we also computed an estimate of the standard deviation of the 5° mean value. However, due to the lack of necessary information, this computation could not account for the error correlations that exist between the 30´ data, and provided optimistic results. We did not use this error estimate in any of our tests.

The preliminary Numerical Quadrature model designated V029 (see Table 8.5–1) was used to compute $\overline{\Delta g}_{hf}$. The merged 30´ anomaly file supporting this model used altimetric anomalies from the file ALT915; therefore, there is a consistency between the altimetric 5° mean values and the harmonics used to filter out their high-frequency content.

We imposed two selection criteria on the 5° $\overline{\Delta g}_{alt}$ values used in our geopotential model testing: (a) we use only anomalies from 5° cells whose mean elevation is less than -500 m and (b) we use only 5° mean values obtained from at least 90 30´ mean anomalies. As a result, 1248 5° mean values passed this editing and formed a "frozen" comparison data set used to evaluate the satellite-only models. The 1248 values cover 59.7 percent of the Earth's area. Table 5.8–1 provides relevant statistics of $\overline{\Delta g}_{alt}$, $\overline{\Delta g}_{hf}$, and $\overline{\delta g}$ for these 1248 5° mean values.

Table 5.8–1. Statistics of the 1248 altimetric 5° mean gravity anomaly data selected for the geopotential model comparisons. Mean, RMS, and standard deviation values are weighted by area. Units are mGal.

Statistic	$\overline{\Delta g}_{alt}$	$\overline{\Delta g}_{hf}$	$\overline{\delta g}$
Minimum value	-53.70	-14.55	-53.95
Maximum value	45.72	12.93	42.87
Mean value	-1.53	-0.03	-1.51
RMS value	13.74	1.75	13.64
S. Deviation value	13.66	1.75	13.56

5.9   References

Barlier, F., C. Berger, J.L. Falin, G. Kockarts, and G. Thuillier, A Thermospheric Model Based on Satellite Drag Data, Institut D'Aeronomic Spatiale de Belgique, *Aeronomica Acta*, 1977.

Bertiger, W.I., Y.E. Bar–Sever, E.J. Christensen, E.S. Davis, J.R. Guinn, B.J. Haines, R.W. Ibanez–Meier, J.R. Jee, S.M. Lichten, W.G. Melbourne, R.J. Muellerschoen, T.N. Munson, Y. Vigue, S.C. Wu, T.P. Yunck, B.E. Schutz, P.A.M. Abusali, H.J. Rim, M.M. Watkins, and P. Willis, GPS precise tracking of TOPEX/POSEIDON: Results and implications*, J. Geophys. Res*., *99*, C12, 24449–24464, Dec. 15, 1994.

Bilitza, D., Improving IRI for Better Ionospheric Predictions, 1996 Ionospheric Effects Symposium, May 1–9, 1996.

Bilitza, D., International Reference Ionosphere—Status 1995/96, to be published in *Space Research*, 1997.

Boucher, C., and Z. Altamimi, ITRF90 and other realizations of the IERS Terrestrial Reference System for 1990, IERS Tech. Note 9, Observatoire de Paris, December 1991.

Boucher, C., Z. Altamimi, and L. Duhem, ITRF92 and its associated velocity field, IERS Technical Note 15, Observatoire de Paris, October 1993.

Boucher, C., Z. Altamimi, and L. Duhem, Results and Analysis of the ITRF93, IERS Technical Note 18, Observatoire de Paris, October 1994.

Boucher, C., Z. Altamimi, M. Feissel, P. Sillard, Results and Analysis of the ITRF94, IERS Technical Note 20, Observatoire de Paris, March 1996.

Cox, C., and D. Oza, *Tracking and Data Relay Satellite (TDRS) Orbit Determination: Operations Concepts for Using Global Positioning System (GPS) Tracking and Alternative Approaches, 553–FDD–94/036/R0UD0*, Goddard Space Flight Center Mission Operations and Data Systems Directorate, 1994.

Defense Mapping Agency, Department of Defense World Geodetic System 1984, *DMA Technical Report 8350.2*, September 30, 1987.

Eanes, R., and S.V. Bettadpur, *The CSR 3.0 Global Ocean Tide Model, CSR–TM–95–06*, Center for Space Research, Univ. of Texas at Austin, 1995.

Ekman, M., Impacts of geodynamic phenomena on systems for height and gravity, *Bulletin Géodesique*, *63*(3), 281–296, 1989.

Engelis, T., and R.H. Rapp, Global ocean circulation patterns based on Seasat altimeter data and the GEM–L2 gravity field, *Mar. Geophys. Res.*, *7*, 55–67, 1984.

Gross, R.S., *A Combination of Earth Orientation Data: Space93, IERS Annual Report*, Observatoire de Paris, 1993.

Guinn, J., R. Muellerschoen, L. Cangahuala, D. Yuan, B. Haines, M. Watkins, and E.J. Christensen, TOPEX/POSEIDON Precision Orbit Determination Using Combined GPS, SLR, and DORIS, *International Association of Geodesy Symposia*, *GPS Trends in Precise Terrestrial, Airborne, and Space Applications, No.115*, Ed. by Beutler, Hein, Melbourne, and Seeber, Springer–Verlag, 1995.

Haines, B.J., E.J. Christensen, J.R. Guinn, R.A. Norman and J.A. Marshall, Observations of TOPEX/POSEIDON Orbit Errors Due to Gravitational and Tidal Modeling Errors Using the Global Positioning System, *International Association of Geodesy Symposia, GPS Trends in Precise Terrestrial, Airborne, and Space Applications, No.115*, Ed. by Beutler, Hein, Melbourne, and Seeber, Springer–Verlag, 1995.

Heiskanen, W.A., and H. Moritz, *Physical Geodesy*, W.H. Freeman and Co., San Francisco, 1967.

Hwang, C., Orthogonal Functions Over the Oceans and Application to the Determination of Orbit Error, Geoid and Sea Surface Topography From Satellite Altimetry, *Rep. 414*, Dept. of Geod. Sci. and Surv., Ohio State Univ., Columbus, OH, 1991.

Hwang, C., Spectral analysis using orthonormal functions with a case study on the sea surface topography, *Geophys. J. Int.*, *115*, 1148–1160, 1993.

Li, Y.C., and M.G. Sideris, Minimization and estimation of geoid undulation errors, *Bulletin Géodesique*, *68*, 201–219, 1994.

Macleod, R., A.H.W. Kearsley, and C. Rizos, G.P.S. surveys of mean sea level along the New South Wales coastline, *Aust. J. Geod. Photogramm. Surv.*, *49*, 39–53, 1988.

Mainville, A. and M. Véronneau, Orthometric heights using GPS, paper presented at CISM Meeting, Halifax, Geod. Surv. Div., Ottawa, Ont., 1989.

Marsh, J.G., F.J. Lerch, B.H. Putney, D.C. Christodoulidis, D.E. Smith, T.L. Felsentreger, B.V. Sanchez, S.M. Klosko, E.C. Pavlis, T.V. Martin, J.R. Robbins, R.G. Williamson, O.L. Colombo, D.D. Rowlands, W.F. Eddy, N.L. Chandler, K.E. Rachlin, G.B. Patel, S. Bhati, and D.S. Chinn, A new gravitational model for the Earth from satellite tracking data: GEM–T1, *J. Geophys. Res.*, *93*, 6169–6215, 1988.

Marsh, J.G., F.J. Lerch, B.H. Putney, T.L. Felsentreger, B.V. Sanchez, S.M. Klosko, G.B. Patel, J.R. Robbins, R.G. Williamson, T.E. Engelis, W.F. Eddy, N.L. Chandler, D.S. Chinn, S. Kapoor, K.E. Rachlin, L.E. Braatz, and E.C. Pavlis, The GEM–T2 Gravitational Model, *J. Geophys. Res.*, *95*, B13, 22043–22070, 1990.

Marshall, J.A., and S.B. Luthcke, Modeling Radiation Forces Acting on TOPEX/POSEIDON for Precision Orbit Determination, *J. Spacecraft and Rockets*, *31*, 1, 89–105, 1994a.

Marshall, J.A. and S.B. Luthcke, Radiative Force Model Performance for TOPEX/POSEIDON Orbit Determination, *J. Astro. Sci.*, *42*, 2, 229–246, April–June, 1994b.

Marshall, J.A., F.G. Lemoine, S.B. Luthcke, J.C. Chan, C.M. Cox, S.C. Rowton, R.G. Williamson, J.L. Wiser, Precision Orbit Determination and Gravity Field Improvement Derived from TDRSS, 46th International Astronautical Congress, IAF–95–A.1.05, Oslo, Norway, October 2–6, 1995a.

Marshall, J.A., N.P. Zelensky, S.M. Klosko, D.S. Chinn, S.B. Luthcke, K.E. Rachlin, R.G. Williamson, The temporal and spatial characteristics of TOPEX/POSEIDON radial orbit error, *J. Geophys. Res.*, *100*, C12, 25331–25352, 1995b.

Milbert, D.G., Improvement of a high resolution geoid height model in the United States by GPS height on NAVD88 benchmarks, in: New Geoids in the World, Balmino, G., F. Sansó (eds), International Association of Geodesy, *Bulletin d' Information*, *No. 77*, IGeS Bulletin No 4: 13–36, 1995.

Moritz, H., Geodetic Reference System 1980, *Bulletin Géodesique*, *66*, 2, 187–197, 1992.

Nerem, R.S., F.J. Lerch, J.A. Marshall, E.C. Pavlis, B.H. Putney, B.D. Tapley, R.J. Eanes, J.C. Ries, B. E. Schutz, C.K. Shum, M.M. Watkins, S.M. Klosko, J.C. Chan, S.B. Luthcke, G.B. Patel, N.K. Pavlis, R.G. Williamson, R.H. Rapp, R. Biancle, and F. Noule, Gravity Model Development for TOPEX/POSEIDON: Joint Gravity Models 1 and 2, *J. Geophys. Res.*, 24421–24447, 1994.

Pavlis, N.K, Raytheon STX Corp., private communication, 1995.

Rapp, R.H., Methods for the computation of geoid undulations from potential coefficients, *Bulletin Géodesique*, 101, 283–297, 1971.

Rapp, R.H., Separation between reference surfaces of selected vertical datums, *Bulletin Géodesique*, 69, 26–31, 1994.

Rapp, R.H., Use of potential coefficient models for geoid undulation determination using a spherical harmonic representation of the height anomaly/geoid undulations difference, *J. of Geodesy*, *71*, 5, 282–299, 1997a.

Rapp, R.H., Global models for the 1-cm geoid—present status and near term prospects, in Boundary Value Problems and the Modeling of the Earth's Gravity Field in View of the One Centimeter Geoid, Rummel and Sansó (eds.), Lecture Notes in Earth Science, Springer–Verlag, 1997b.

Rapp, R.H., and M. Kadir, A preliminary geoid for the State of Tennessee, *Surv. Mapp*., *48*, 251–260, 1988.

Rapp, R.H., and N.K. Pavlis, The development and analysis of geopotential coefficient models to spherical harmonic degree 360, *J. Geophys. Res*. 95, B13, 21885–21911, 1990.

Rapp, R.H., Y.M. Wang and N.K. Pavlis, The Ohio State 1991 geopotential and sea surface topography harmonic coefficient models, *Rep. 410*, Dept. of Geod. Sci. and Surv., Ohio State Univ., Columbus, 1991.

Rapp, R.H., C. Zhang, and Y. Yi, Analysis of dynamic ocean topography using TOPEX data and orthonormal functions, *J. Geophys. Res*., *101* (C10), 22583–22598, 1996.

Schrama, E.J.O. and R.D. Ray, A preliminary tidal analysis of TOPEX/POSEIDON altimetry, *J. Geophys. Res*., *99*, 24799–24808, 1994.

Smith, D.A. and D.G. Milbert, Evaluation of Preliminary Models of the Geopotential in the United States, *Intl. Geoid Service Bulletin*, 6, 1997.

Stammer, D., R. Tokmakian, A. Semtner, and C. Wunsch, How well does a $1/4°$ global circulation model simulate large scale oceanic observation?, *J. Geophys. Res*., *101*(C11), 25779–25812, 1996.

Tapley, B.D., M.M. Watkins, J.C. Ries, G.W. Davis, R.J. Eanes, S.R. Poole, H.J. Rim, B.E. Schutz, C.K. Shum, R.S. Nerem, F.J. Lerch, J.A. Marshall, S.M. Klosko, N.K. Pavlis, and R.G. Williamson, The Joint Gravity Model–3, *J. Geophys. Res*., *101* (B12*)*, 28029–28049, 1996.

Torge, W., T. Bašic′, H. Denker, J. Doliff, H.G. Wenzel, Long range geoid control through the European GPS traverse, *Deutsch Geod. Komm. Ser*., B, 290, 1989.

Tsaoussi, L., and C. Koblinsky, An error covariance model for sea surface topography and velocity derived from TOPEX/POSEIDON altimetry, *J. Geophys. Res*., *99,* C12, 24669–24684, 1994.

Wang, Y.M., and R.H. Rapp, Estimation of Sea Surface Dynamic Topography, Ocean Tides, and Secular Changes From TOPEX Altimeter Data, *Rep. 430*, Dept. of Geod. Sci. and Surv., Ohio State Univ., Columbus, OH, 1994.

Wang, Y.M., and R.S. Nerem, A mean sea surface and marine gravity anomalies from satellite altimeter data: preliminary results, *Eos Trans. AGU*, *76*, No. 46, 1995.

6. ESTIMATION OF THE GEOPOTENTIAL MODEL IMPLIED BY THE SATELLITE TRACKING DATA

6.1 Introduction

In this section we discuss the derivation of the satellite-only geopotential field model component of EGM96, known as EGM96S. EGM96S is a geopotential field solution to 70x70, determined solely by satellite tracking data, that draws on the heritage of gravity model development at the Goddard Space Flight Center (GSFC), from GEM–9 [*Lerch et al.*, 1979 and 1981] through JGM–1S and JGM–2S [*Nerem et al.*, 1994b]. The historical setting for the EGM96S satellite-only model gravity development is reviewed. Background information on geopotential recovery from satellite tracking data is provided. The satellite tracking data, the force modeling, and the reference frames used in this effort are described in detail.

6.1.1 History and Previous Models

Over the past two decades, the GSFC gravity model development efforts have wedded the desire for general geopotential modeling improvements with specific applications that were mission driven. While successive models provided improvements in global geoid accuracy, each of the fields was designed and evaluated on its ability to meet specific, mission-defined requirements, which generally emphasized advancing orbit accuracy as the most important goal. With the launch of GEOS–3 in 1975, precision orbit determination became a central concern of every geodetic and altimeter satellite mission. Exploitation of tracking and/or altimeter data required improved orbit knowledge and advanced understanding of a stable orbital reference frame. These requirements were incorporated into geopotential accuracy goals, and each of the successive GSFC efforts received direct mission funding support. This focus on orbit accuracy compelled several design decisions. For example, to achieve the highest possible orbit accuracy for TOPEX/POSEIDON (T/P), the JGM models significantly downweighted surface gravimetry when it was concluded that the inclusion of these data had a slight adverse effect on the T/P orbit accuracy.

The gravitational field and orbit accuracy improvements that were achieved have facilitated the assimilation of these data and their geodetic products into geophysical and oceanographic investigations. Table 6.1.1–1 summarizes the models that were developed and their associated mission goals. Meeting ever more stringent orbit accuracy goals, from multimeter to cm level, is the common theme that runs through 20 years of geopotential development effort from the GEM–9 through the JGM–2 models.

The objective of EGM96 was unencumbered by specific satellite mission goals; its goal was to advance the state of the art in global geopotential modeling for a broad range of mapping, navigation, ocean science, and geophysical applications. EGM96 afforded us the opportunity to adopt a more balanced approach to minimize data set incompatibilities (e.g., between surface gravimetry, satellite altimetry, and orbit data) and focus on achieving the best global model for a wide range of applications wherein orbit accuracy was no longer the overwhelming consideration. The improvements sought for EGM96 were:

- The use of new observational resources (both from tracking data and surface gravimetry).

- The review and reanalysis of the entire history of suitable tracking data.

- The improvement of the background force models in a complete reiteration of the JGM–2 model.

- The incorporation of altimeter data from recent missions such as ERS–1 and T/P.

The opportunity to form a collaborative partnership between the Defense Mapping Agency (DMA) of the Department of Defense (DoD) and NASA GSFC provided the impetus for the EGM96 development. (Subsequent to the release of EGM96, with a recent reorganization, DMA became the National Imagery and Mapping Agency [NIMA]). To achieve maximal global accuracy, the methodology for the JGM model development was thoroughly reviewed.

Table 6.1.1–1. History of geopotential models produced by the GSFC team.

Model	Maximum degree and order of contribution			Model Objectives
	Sat.	Surf. grav.	Alt.	
GEM–9	30			Support altimeter science goals of the GEOS–3 mission
GEM–10	30	22		[*Lerch et al.*, 1979 and 1981]
GEM–10B	36	36	36	
PGS–S3	36	36	36	Support altimeter science and orbit determination goals of
PGS–S4	36	36	36	the SEASAT mission [*Lerch et al.*, 1982]
GEM–L2	30	-	-	Support geodynamic science goals for SLR using LAGEOS (cm level site positioning and Earth orientation modeling) [*Lerch et al.*, 1985]
GEM–T1	36	-	-	Models to improve background force models and data
GEM–T2	36	-	-	Treatment to prepare for achieving T/P orbit modeling
GEM–T3	50	50	50	goals; utilized supercomputing capabilities for the first time [*Marsh et al.*, 1988, 1990; *Lerch et al.*, 1994]
JGM–1	70	70	70	Reiteration of GEM–T3: prelaunch T/P model [*Nerem et al.*, 1994b]
JGM–2	70	70	70	JGM–1 "tuned" with T/P SLR and DORIS tracking data [*Nerem et al.*, 1994b]

GEM: Goddard Earth Model developed by GSFC
JGM: Joint Gravity Model developed as a collaborative effort between GSFC, the University of Texas Center for Space Research (CSR), and the Centre National d'Etudes Spatiales (CNES), Toulouse, France.
DORIS: Détermination d'Orbite et Radiopositionnement Intégrés par Satellite

In overview, the additional observational resources that stimulated the collaboration between DMA and GSFC were:

a) **High-precision, dense, temporal tracking of several near-Earth satellites**: Near continuous tracking from the Tracking and Data Relay Satellite System (TDRSS) and continuous tracking from the Global Positioning System (GPS) provided significant advances in the information available for the satellite-only base model. EGM96 included TDRSS data from the Explorer

Platform/Extreme Ultra-Violet Explorer (EP/EUVE), and GPS data from EP/EUVE, GPS/MET, and T/P. The continuous tracking better resolves shorter period geopotential perturbations on the satellite orbit not well observed with traditional SLR or Doppler tracking. Lower altitude satellites, especially EP/EUVE, have higher sensitivity to geopotential signals because of reduced signal attenuation. The dense GPS and TDRSS tracking support the estimation of sufficient force model scaling parameters to mitigate atmospheric drag errors.

b) **New Satellite Laser Ranging missions:** LAGEOS–2, Stella, and GFZ–1 were launched in 1992 or later. These satellites expanded the SLR data available following the development of the JGM–2 model.

c) **Precise gravimetry:** Surface and airborne gravimetry data from many large continental regions were made available to NIMA. These regions included the former Soviet Union (FSU), China, and Greenland. Improved data were also available for Africa, Antarctica, and South America. The new data constituted a major advance over the surface gravimetry used in the JGM series of models and provided the opportunity to improve uniformly the short wavelength accuracy of the field over nearly the entire planet.

d) **Satellite altimetry:** The T/P data were not used in the JGM models. T/P provided dual-frequency altimeter data to correct for ionospheric path delay, 2 to 3 cm orbit accuracy, improved nonconservative force models to address the complex shape of this spacecraft, and significantly improved ocean tides to properly model this time-varying surface signal. Furthermore, the TOPEX altimeter data could be leveraged to provide upgraded information for the coincident ERS–1 altimeter mission, which acquired altimeter tracking to higher latitudes than that available from T/P. DMA also expressed a willingness to reiterate its gravity anomaly prediction efforts, which used the GEOSAT Geodetic Mission (GM) altimeter data set. These GM data provided a dense grid of information between $\pm 72^o$ latitude.

The combination of these data sets offered the prospects for global field improvement to reach the goal of ±50 cm geoid uncertainty for all locations on the Earth's surface. Because this goal represented the point geoid error, EGM96 needed to extend to at least degree and order 360 to minimize omission errors.

JGM–3 [*Tapley et al*., 1996] was a parallel effort, initiated by our colleagues at the University of Texas, to augment JGM–1 with several new data sets. This was accomplished through combining the JGM–1 coefficients/covariance matrix with observational information from T/P GPS, LAGEOS–2, Stella, and SPOT–2.

6.1.2 Background on Geopotential Recovery From Satellite Tracking Data

While a dedicated geopotential recovery mission has not yet reached orbit, a significant data set has been assembled that supports geopotential recovery. However, to understand the solution design used throughout the GEM, JGM, and EGM96 efforts and shed some insight into the significant changes incorporated into EGM96, let us review the strength of the geopotential signal contained in tracking data.

From linear orbit theory [*Kaula*, 1966], it can be shown that a given satellite samples the geopotential in a systematic and characteristic fashion. Satellites of geodetic interest are generally found in stable orbits and at altitudes largely above 700 km to alleviate atmospheric drag effects. For the purposes herein, we can assume that geodetic orbits have a fixed size, shape, and inclination. This stability gives rise to a systematic geographic sampling of the gravity field. Applying linear theory [*Kaula*, 1966], the gravitational field produces perturbations that are periodic at frequencies, Ψ :

$$\Psi = (n - 2p)\dot{\omega} + (n - 2p + q)\dot{M} + m(\dot{\Omega} - \dot{\Theta}) \qquad (6.1.2\text{--}1)$$

where:

n is the degree of the Stokes harmonic, $2 \le n \le N_{max}$

m is the order of the Stokes harmonic, $0 \le m \le n$

p is a subscript in the inclination function, $0 \le p \le n$

q is a subscript in the eccentricity function; here the limits of concern are: $-2 \le q \le 2$

$\dot{\omega}$ is the mean rate of precession of the argument of perigee

$\dot{\Omega}$ is the mean node rate

$\dot{M}$ is the mean anomalistic motion rate

$\dot{\Theta}$ is the mean rotation rate of the Earth.

Short-period perturbations are those whose frequencies Ψ are proportional to $\dot{M}$, the mean motion. Orbital resonance will occur when an integer multiple of the orbital period, $\dot{M} + \dot{\omega}$, beats against the rotation rate of the Earth (i.e., when $\Psi \approx 0$). Rearranging eq. (6.1.2–1), this produces

$$- q\dot{\omega} + (n - 2p + q)(\dot{M} + \dot{\omega}) + m(\dot{\Omega} - \dot{\Theta}) \approx 0 \qquad (6.1.2\text{--}2)$$

Neglecting the $-q\dot{\omega}$ term, which varies slowly compared to $\dot{M} + \dot{\omega}$, the harmonic orders for which resonance will occur are

$$m_r \approx k \frac{(\dot{M} + \dot{\omega})}{(\dot{\Omega} - \dot{\Theta})} \qquad (6.1.2\text{--}3)$$

where

$$k = (n - 2p + q)$$

Primary resonance occurs for $k = 1$, with terms of harmonic orders adjacent to the resonant orders (e.g. $m_r \pm 1$ and $m_r \pm 2$) being in near resonance. Although the effects of these resonances decrease with increasing k, secondary and tertiary resonances ($k = 2$ and 3, respectively) can have a important influence on orbits, especially those with exactly repeating ground tracks. For example, the order 43 resonance (a tertiary resonance) on GEOSAT has a significant influence on the orbit.

If $(n - 2p + q) = 0$, then Ψ will go through approximately m cycles per day; a class of perturbations referred to as "m-daily" terms. Any perturbation for which the perigee rate is the only term present

in eq. (6.1.2–1) (i.e., $n - 2p + q = 0$, and $m = 0$) is classified as a long-period perturbation, for which the period can be of the order of 50 days or more.

Long-period and resonant orbit perturbations will map into short-period radial perturbations that are proportional to $\dot{M} + \dot{\omega}$, the orbit period [*Rosborough*, 1986]. This is also the dominant frequency arising from nonconservative force model errors, which are discussed below. As a result, the treatment of the empirical 1-cycle per revolution (1-CPR) force model parameters, which are often used to accommodate unmodeled forces in the tracking data reduction, can have a large impact on the recovered gravity coefficients and their uncertainties in a geopotential model solution. This is particularly true for the resonant and zonal terms. Likewise, unmodeled forces acting at a frequency of y-CPR (such as a 2-CPR drag modeling error) can have a confounding effect on the ym_r order terms of the recovered geopotential harmonic coefficients.

Each of the perturbation families arise from terms of the same order. These perturbations give rise to "lumped" harmonics, which are the linear sum of the orbit's sensitivity to the coefficient values with an odd/even degree parity within each harmonic order at a given frequency [cf. *Wagner and Klosko*, 1975; *Rosborough*, 1986]. Coefficients of the same order are distinguishable from one another only by the higher degree term introducing unique short-period perturbations. These short-period perturbations are lumped with still higher degree terms of the same parity and order.

For the pre-1992 data sets used in JGM–1, all are capable of resolving long period zonal and strong resonance perturbations (which produce orbital perturbations that range in period from several days to near secular). However, only the strongest data are capable of sensing a significant subset of the *m*-daily perturbations, which are generally smaller in magnitude than the resonance and the long-period zonal effects. Given the rather sparse temporal tracking coverage provided by SLR and the high noise of TRANET/OPNET Doppler systems, none of the data available before 1992 could observe the large number of short-period orbital perturbations, which are generally much smaller than the *m*-daily perturbations. For example, Table 6.1.2–1 compares the major orbital perturbations arising from the (2,2) harmonic on both T/P and LAGEOS.

Poor short-period perturbation sensitivity is the major shortcoming of the pre-1992 data sets. For example, *Lerch et al.* [1991], showed that a well-tracked SLR satellite like Starlette is severely limited, even for the recovery of a complete 36x36 geopotential model; this is true although nearly every harmonic coefficient to 36x36 produces significant orbit perturbations. A typical SLR Starlette pass has a duration of 5 to 10 minutes. The international SLR network typically acquires 10 to 15 data passes per day from on this satellite. SLR provides tracking only over a small percentage (<10%) of Starlette's orbit. Such limited geometric sampling results in only one third or so of the 36x36 geopotential eigenvalues found in the Starlette normal equations being well determined (with eigenvalues having a range of 12 orders of magnitude between the best and worst resolved terms). There are too few well-observed lumped harmonics obtained from the temporal distribution of otherwise very accurate laser ranging data. This situation typifies the strength of the pre-1992 tracking data. Therefore, field recovery restricted to these data requires the maximal sampling of orbital inclinations and altitudes to provide unique lumped harmonics for the separation of terms.

Incorporation of data from high satellites in the solution permits small increases in visibility at the expense of increased signal attenuation. Starlette is one of the best SLR satellites for field resolution since it has a perigee height of 800 km and is somewhat eccentric. Although individually each SLR tracked orbit has similar rank deficiencies, in combination the SLR orbits complement one another and provide improved model definition. However, to separate and resolve all of the harmonics, we must have an extensive inclination sampling, which historically has relied on older and less accurate data, such as TRANET Doppler and even optical tracking. The GEM–T3, JGM–1, and JGM–2 efforts completely reviewed all of these historical data, and reanalyzed and recertified them in improved orbital solutions; their inclusion was still beneficial to the overall solution.

Table 6.1.2–1. Comparison of orbital perturbations arising from the (2,2) tesseral harmonic.

Satellite	Perturbation Frequency (cyc/day)	Classification	Estimated Magnitude of Perturbation (m)		
			Radial	Transverse	Normal
LAGEOS					
orbit freq = 6.39	10.77	short period	6	4	5
(cyc/day)	17.16	short period	3	5	0
	8.39	short period	11	16	0
	21.16	short period	11	15	0
	14.77	short period	18	15	8
	8.38	short period	4	6	0
	2.00	*m*-daily	0	190	53
	4.48	off-*m*-daily	22	31	0
TOPEX/POSEIDON					
orbit freq = 12.82	23.62	short period (2–CPR)	39	27	15
(cyc/day)	36.45	short period (3–CPR)	22	31	0
	49.27	short period	0	0	0
	14.84	short period	21	28	0
	40.48	short period	4	5	0
	27.66	short period	6	5	0
	14.84	short period	1	2	0
	2.02	*m*-daily	190	580	170
	10.81	off-*m*-daily	27	38	0
	10.80	off-*m*-daily	11	15	0

In contrast, all proposed dedicated geopotential missions are based on continuous, very precise tracking data that support resolution of the complete short-period orbit perturbation spectrum to some degree and order cutoff. This is an essential design feature that enables a single dedicated mission to resolve a complete banded harmonic geopotential model.

The post-1992 tracking data are significant in that, for the first time, high-quality near-continuous data were available that could directly observe the short-period perturbations. The three tracking systems that made this breakthrough were:

DORIS: Détermination d'Orbite et Radiopositionnement Intégrés par Satellite is a high-precision, dual-frequency, radiometric Doppler tracking system developed by France

[*Dorrer*, 1990; *Nerem et al*, 1994a]. These data are single-station, line-of-sight velocity measurements that, given satellite-to-station geometry, are dominated by an along-track velocity signal. Each station sees only, at most, about 15 percent of a low-altitude satellite orbit, but the near-global distribution of stations provides near-continuous coverage.

TDRSS: A high/low range and range-rate Tracking and Data Relay Satellite (TDRS) System used for communications and operational orbit determination by NASA as a replacement for the ground-based Unified S Band System. This system consists of several relay spacecraft in geostationary orbit over the Pacific and Atlantic oceans. With the high altitude of the TDRS satellites, these range-rate observations can provide a strong, direct radial mapping of the lower satellite within the TDRS field of view. Considerable value has been added to the these data by leveraging T/P tracking from SLR, DORIS, and TDRSS to permit significant advancements in the TDRS orbit positioning [*Marshall et al.*, 1996]. TDRSS obtains one-way (ground→TDRS→user or, more typically, user→TDRS→ground) and two-way (ground→TDRS→user→TDRS→ ground) average range-rate and range data. These data are highly suitable for geopotential recovery since the radial component of the orbit is less contaminated by nonconservative force modeling errors than the along-track component.

GPS: The DoD Global Positioning System is a constellation of 24 satellites in high Earth orbits. They provide continuous navigational coverage over the entire Earth [*Hoffman-Wellerhoff et al*., 1992], resulting in complete three-dimensional tracking coverage. The GPS tracking of low Earth-orbiting spacecraft is dense enough to support quasi-geometric reduced dynamic methods of orbit determination, as demonstrated with T/P [*Bertiger et al*., 1994; *Yunck et al*., 1994]. The dual-frequency signal allows for media refraction corrections to be measured directly for receivers that are so equipped. Data currently are available from a number of GPS-receiver-equipped missions: T/P, the EP/EUVE, and GPS/MET. Future missions such as JASON and CHAMP will track as many as 12 GPS satellites simultaneously in dual-frequency modes, using codeless receiver technology.

The DORIS data acquired on SPOT–2 and T/P were used in JGM–2 and JGM–3. The SPOT–2 DORIS data contribution to gravity model improvements are described in detail in *Nerem et al.* [1994a]. TDRSS and GPS analyses, new to the EGM96 effort, are discussed at length in Section 6.2 of this report.

SLR data from new satellite missions such as LAGEOS–2, Stella, and GFZ–1 (launched in 1992, 1993, and 1994) were included in EGM96. Newly available historic and modern TRANET data were used to strengthen the information at the lower and near-polar inclinations.

Section 6.2 discusses the satellite data complement of EGM96 in detail. A brief summary of the satellite data used in forming JGM–2 can be found in Section 6.2.1, whereas Section 6.2.7 presents a summary of these data and the specific data set included in this model.

6.1.3 EGM96 Force, Measurement, and Reference Frame Models

Several improvements over JGM–2/JGM–3 were sought in background force modeling and establishing an improved reference frame over the duration of the observations.

a) The background solid Earth and ocean tidal model was extended to enhance the recovery of resonant tidal effects that produce long-period orbit perturbations. For instance, a more complete frequency-dependent solid Earth tidal model was incorporated. This solid Earth tide model more completely modeled 22 tide lines whose Love numbers deviated from the default value of $k_2 = 0.30$. In addition, the dynamic ocean tidal terms that produce long-period orbit perturbations were adjusted. Model recovery in the presence of a more complete solid Earth tide model was now possible. Orbit modeling of ocean tidal effects was not implemented in the JGM series of models due to a coding error in the GEODYN orbit determination system. The JGM series adopted the resonant tides solution from GEM–T3, which was extended using a truncated Schwiderski background model of maximum degree 15, with a lower maximum degree for some of the tide constituents. (This tides set is referred to in this document as PGS4846X.) With the coding problem fixed and the reiteration of the JGM normal equations, an extensive resonant ocean tidal model was recovered in EGM96.

b) Improved dynamic polar motion modeling was implemented, accounting for the deformation of the Earth at the annual and the Chandler periods. The secular trend in the $C_{2,0}$ harmonic observed on various SLR missions [*Nerem and Klosko*, 1996; *Cheng et al.*, 1996] was forward modeled.

c) The reference frame improvements included extensive use of the International Terrestrial Reference Frame (ITRF) and International Earth Rotation Service (IERS) station network and Earth orientation results.

Table 6.1.3–1 summarizes the background force modeling, and Table 6.1.3–2 summarizes the reference frame and constants that were adopted for the EGM96 solution.

In order to meet the stringent orbit accuracy needed for altimeter missions, and to extract geopotential signals from tracking data, many improvements in nonconservative force and measurement modeling were implemented. For the most precise and continuous data, it is no longer adequate to treat nonspherical spacecraft as homogeneous spheres in the orbit determination process. Precise measurement modeling involves the definition of the location of the antenna phase center or laser retroflector with respect to the spacecraft center of mass. It implicitly requires the characterization of the spacecraft attitude as a function of time. The improvements in non-conservative force modeling involve the definition of the spacecraft shape as a series of flat plates oriented in space. Each plate possesses its own properties (area, specular and diffuse reflectivities, emissivity, and in some cases temperature), which are determined by the aggregate composition of the components on that side of the spacecraft. The nonconservative forces (atmospheric drag, solar radiation pressure, and planetary albedo and thermal emission) acting on each flat plate are computed independently and summed to calculate the overall acceleration on the spacecraft center of mass. T/P was the object of an intensive, multiyear effort to develop a sophisticated and computationally efficient algorithm to model the nonconservative forces acting on the spacecraft

[*Antresian*, 1992; *Antresian and Rosborough*, 1992; *Marshall and Luthcke*, 1994a, 1994b]. Complex satellite form models for use in precise orbit determination have also been developed for SPOT–2 [*Gitton*, 1991], ERS–1 [*Zhu and Reigber*, 1991], and the TDRS's [*Luthcke et al.*, 1997]. A detailed "box-wing" model also was tested, by *Olson* [1996], for the processing of the EP/EUVE GPS data (see also Section 6.2.3.3).

Table 6.1.3–1. Background force models adopted for EGM96. These models were used for all spacecraft, unless otherwise noted.

Description	Model	Comment
GM	398600.4415 x 10^9 m^3/s^2	
Geopotential	JGM–2 (70x70)	[*Nerem et al.*, 1994b]
Zonal Rates	$\overline{\dot{C}}_{2,0}$ = 1.162755 x 10^{-11}/y Epoch 1986.0	from multisatellite solution [*Nerem and Klosko*, 1996]
Rotational Deformation	$\overline{x}$ = 46 mas, $\dot{\overline{x}}$ = 3.3 mas/yr, Epoch: 1986.0 $\overline{y}$ = 294 mas, $\dot{\overline{y}}$ = 2.6 mas/yr	Same as JGM–2 [*ibid.*]; assumed $k_2 = k_S =$ 0.3, as required, in the closed formula Earth tide implementation
N-body	JPL DE200	Sun, Moon, all planets except Pluto
Solid Earth Tides	22 frequency-dependent terms assuming a FCN period of 430 days	IERS
Ocean Tides	JGM–2 (PGS4846X): Schwiderski background tide model including the dominant terms from 80 constituents with over 6000 terms. Resonant terms for the 12 major tide lines are adjusted simultaneously with the geopotential model. T/P-based model used to correct altimeter data.	Newer improved background models have been tested in orbit solutions. These are based on T/P derived tide models and eliminate significant omission errors by using nearly 30000 harmonic terms, which is achieved by using complete 15x15 (diurnal/semidiurnal), and 12x12 (long period) harmonic models of the 12 major tide lines.
Drag	DTM	[*Barlier et al.*, 1977]
Earth Albedo	Modeled	*Knocke et al.* [1988]
Tropospheric Refraction	Goad modifications to Hopfield	[*Goad*, 1974] Ground-to-space links only
Relativity	IERS standards	[*McCarthy*, 1989]

The development of a "box-wing" nonconservative force model requires considerable effort, and this model development was not pursued for other satellites, such as GPS/MET, HILAT, RADCAL, GEOSAT, and SEASAT. In some cases, the information needed to define the reflectivity and emissivity characteristics of the spacecraft surfaces is hard to come by—especially when many years have elapsed since the end of the flight mission. Thus for HILAT, RADCAL, GEOSAT, and SEASAT, only the offsets of the antennae phase centers (and laser retroflector in the

case of SEASAT) were accounted for. All of these spacecraft followed a gravity gradient stabilized attitude profile. For both EP/EUVE and GPS/MET, only the antenna offsets were modeled. Detailed satellite form modeling was not implemented for the processing of the GEOS–1, GEOS–2, GEOS–3, BE–C, D1–C, D1–D SLR data, and the Nova–1 and Oscar–14 Doppler tracking data. These data are older and less accurate than the more modern data available from other satellites. Finally, satellites such as LAGEOS, LAGEOS–2, Starlette, Ajisai, Stella, and GFZ–1, by design, are spherical and completely passive and require only the modeling of the offset of the point of the laser reflection from the center of mass. *Rubincam* [1988], *Rubincam et al.* [1997], and others have demonstrated that the acceleration history of LAGEOS can be at least partially explained by a thermal drag effect that is dependent on the satellite's spin history and thermal properties. A nominal model of the Yarkovsky thermal drag [*Rubincam*, 1988] was used in the processing of the LAGEOS SLR data. The determination of the tidal terms, as well as time-dependent terms in the geopotential, are sensitive to the accurate modeling of the nonconservative forces, even for satellites such as the LAGEOS's.

Table 6.1.3–2. Reference frame and constants adopted for EGM96.

Description	Model	Comment
Conventional Inertial System (CIS)	J2000 S.I. units	
Precession	1976 IAU	Under review by IAU
Nutation	1980 IAU + corrections	Under review by IAU
Planetary Ephemerides	JPL DE-200	
Polar Motion and UT1	IERS 90C04	
Plate Motion	NUVEL NNR, Epoch: July 1, 1986	w/ LAGEOS-derived supplemental values
$\overline{C}_{2,1}$ $\overline{S}_{2,1}$	$\overline{C}_{2,1}$ = -.1870x10^{-9} - 0.32x10^{-11}/yr $\overline{S}_{2,1}$ = 1.1953x10^{-9} + 1.62x10^{-11}/yr Epoch: 1986.0	Means consistent with IERS Rates consistent with IERS origin
Station Coordinates	JGM–2	Adjusted in the gravity solution. See Section 7.3.5
Constants Defining Reference Ellipsoid for Geometric and Dynamic Calculations	a_e = 6378136.3 m GM = 398600.4415 x 10^9 m^3/s^2 $(\overline{C}_{2,0})_{JGM-2}^{tide-free} = -484.1654767 \times 10^{-6}$ ω = 7292115x10^{-11} rad/s	These defining constants were used to evaluate the derived constants according to *Moritz* [1984]
Derived Ellipsoid Constants	$(J_2)_{NASA/DMA}^{zero} = -(\overline{C}_{2,0})_{JGM-2}^{tide-free}$ $\cdot \sqrt{5} - (-3.11080 \times 10^{-8} \cdot 0.3)$ 1/f = 298.256415099	$(J_2)_{NASA/DMA}^{zero}$ assumed k_2 = 0.3 In GEODYN, flattening is used only to calculate rectangular coordinates for the tracking stations when geodetic coordinates are given, in defining the subsatellite location for altimeter data, and in calculating the geodetic altitude for drag purposes

The residual nonconservative forces are largely accounted for through the adjustment of empirical accelerations [*Colombo*, 1984; *Tapley et al.*, 1994]. Nonetheless, nonconservative force mismodeling remains a major contributor to current orbit errors and is an area requiring further investigation.

6.1.4 Software Used and Method of Solution

As is the case for every GSFC gravity solution, the reduction and evaluation of all tracking data were accomplished using the GEODYN Precision Orbit Determination system [*Pavlis, D., et al.*, 1996]. GEODYN has been developed for over 30 years to process every precision orbit tracking data type ever supported by a NASA geodetic or altimeter mission. These data include:

- Satellite Laser Ranging (SLR).

- TRANET/OPNET one-way average range rate (satellite→ground).

- DORIS average range rate (ground→satellite).

- Radar (S-Band/C-Band) two-way and three-way range and range rate.

- Passive and active (i.e., flashing light) optical (right ascension/declination) observations.

- Satellite radar altimetry.

- GPS pseudo-range and single/double-differenced observations.

- Intersatellite range/range-rate data acquired by either the TDRSS constellation on various user satellites or the synchronous ATS–6 tracking of GEOS–3.

- Minitrack interferometric directional tracking.

While not germane to the discussion herein, GEODYN can also process the NASA and DoD tracking data from non-Earth missions and has supported GSFC geopotential modeling improvements for Mars, Venus, and the Moon [*Smith et al.*, 1993; *Nerem et al.*, 1993a; and *Lemoine et al.*, 1997].

GEODYN has undergone two major redesigns since its inception in the late 1960's. The first was a complete system redesign and rewrite in the early 1980's to support supercomputing and vectorization enhancements. Recently, the system has undergone additional changes to better exploit the multiprocessing capabilities found within the GSFC Cray J90 cluster. A review of the most extensive of these developments is found in *Marsh et al.* [1988].

SOLVE [*Ullman*, 1992] is designed as a companion program to GEODYN. It combines any number of normal equations produced by GEODYN (or any other normal equation generator) and inverts them to produce a least-squares solution. SOLVE can edit input matrices by parameter, shift the normal equations to a common set of *a priori* values, suppress parameters at a given value, and apply parameter constraints. SOLVE has supported the normal equation generation approach adopted by GSFC geopotential model development over the last 25 years, and also has been modified to exploit the multiprocessing capabilities of the Cray J90.

6.2   Satellite Data Processing Description

This section provides an overview of the data reduction methods and processing steps that are used to prepare the satellite tracking data for inclusion in the geopotential solutions. These steps, to first order, are similar for all types of data, although noisier data require more iterations and successive orbit reductions to identify and eliminate spurious observations. Systematic error sources can also plague observational data. The level of effort to identify systematic errors depends strongly on the type of data analyzed and the nature of these errors. The analysis and reduction of the tracking data are performed using GEODYN. The processing steps are:

a) **Observation reformatting and preprocessing:** It is often necessary, given the insufficiency or absence of models available at the time of earlier data acquisition, for value to be added to earlier data sets. For example, upgraded models are often employed beyond those released on the original altimeter Geophysical Data Records (e.g., improved ionospheric refraction and ocean tide models). Older range data are often recorded using an obsolete value for the speed of light. Some data lack important information such as correction values to reference the observations to the satellite center of mass. Nevertheless, these preprocessed data must be made consistent, and as accurate as possible, for current use recognizing the improvements in technology and modeling over time. This preprocessing step requires a continual review of the original data and the supporting models used at the time of their release. Keeping track of these upgrades and documenting elements of the preprocessors is necessary and part of the development of the historical data base.

Another common concern relates to data philosophy. Previously, it was customary to release "fully" corrected data, as distinct from the raw observations. Now, the reverse is true. GEODYN, therefore, was designed to use the raw observations and recommended corrections, which can be applied as needed for a given application. Even though GEODYN is designed with this latter approach, fully corrected data can still be processed. It is, therefore, necessary at times to build programs based on earlier correction algorithms to "uncorrect" the older data and separately report the correction values. This allows the correction algorithms to be upgraded when needed.

Over the last 30 years, satellite tracking observations have varied in format and in completeness of supporting modeling. To accommodate the wide range of formats, the first step in the GEODYN processing flow is uniform reformatting and blocking of the data. The Tracking Data Formatter (TDF) is the initial step in the GEODYN processing flow. TDF supports a wide range of standard formats, although it is occasionally necessary to preprocess and reformat data to a format acceptable for the TDF. Supported by user-specified options, TDF selects the data needed for a given orbit solution and reformats them into a blocked, compact form that allows vectorization (especially within a pass) of the data processing in GEODYN.

b) **Data validation and orbit assessment:** The reformatted data are reduced using a complete force model in the orbit determination process. When first processing data from a new satellite, experiments must be performed to evaluate the efficacy of different empirical force

modeling parameter adjustment schemes, so as to produce an accurate orbit and to isolate the gravitational effects for geopotential field improvement. Estimation of too many parameters risks decimating the geopotential signal, whereas estimation of too few leads to unacceptably large orbit errors.

These orbit reductions also are used to identify spurious observations, data biases, and, occasionally, when a new tracking network or station is being used, station positioning problems. GEODYN has automatic data editing schemes (a multiplier times the previous iteration's weighted RMS of fit being the most commonly employed approach), to assist in identification of bad data and allow for orbit convergence. Station coordinate problems are addressed in several ways; either through survey ties to well-known sites or through least-squares network adjustments using the tracking data.

It is also common to use ancillary analysis packages that take the postfit data residuals and evaluate them to quality control the final data set. These residual analysis packages employ various analysis approaches, for example using a Guier analysis [*Guier*, 1965] to help separate orbit from data errors.

As many runs as required are performed until the data set is "finalized" in the eyes of the orbit analyst. Optional data sets are generated and saved to eliminate (and document) deleted data. A final orbit is converged based on the accepted data.

c) **Normal equation generation:** The converged orbit is passed through the data set used in the final orbit processing step. Herein, the GEODYN setup contains an *a priori* uncertainty specified for all parameters to be adjusted. This is the superset of parameters of interest, and many are chosen for other investigative purposes beyond the final gravity solution. Numerical partial derivatives are computed relating each of the observations to the orbit and other parameter adjustments. Orbit error analysis tools (for example ERODYN [*Englar et al.*, 1978]) can use these normal equations to propagate parameter errors into both orbit errors and errors in other adjusting models, such as the gravity field, for supporting analyses.

The generation of these normal equations is by far the most computationally intensive part of data preparation for the geopotential solution. Typical matrices have in excess of 6000 parameters, while altimeter normal equations, with their need for dynamic ocean topography parameters, having 7500 or more parameters. Supercomputing and extensive use of vector and parallel processing architectures enabled the computation of the 2000 or so matrices used in the EGM96 solution. Storage of these matrices is an additional problem, with many individual normals approaching 400 Mbytes.

The SOLVE program [*Ullman*, 1992] is used for parameter selection and matrix inversion. To ease the manipulation of the vast array of information, we combine the normal equations at various processing levels to reduce the number required online for analysis or inclusion in the final solution.

d) **Solution development and testing:** The SOLVE program is used to:

- Sum all of the normal equations.

- Provide linear shifts of residual vectors to produce a consistent set of *a priori* parameters.

- Subselect the parameters for adjustment.

- Invert the matrix.

- Produce related error statistics, projections, and the complete error covariance (if requested).

The calibration of the solution using data subset testing [*Lerch et al*., 1991] requires the computation of a large number of separate solutions, especially in view of the large number of satellites and sets of tracking data. Each solution solves for not only the geopotential (5035 parameters for the static field through 70x70), but ocean tidal coefficients (112), pole position (~5000 parameters), and station location (~1500 parameters). In addition, the combination model solves for the coefficients of the dynamic ocean topography. The solution for such a large number of parameters is made possible through supercomputing and the use of vectorized codes.

The geopotential solutions are subjected to a variety of tests; some entail orbital solutions to evaluate orbit modeling improvements. Occasionally, testing will reveal a problem with an original data set or reduction, and normal equations will have to be recomputed after taking some remedial action to address the problem.

6.2.1 Data Employed in JGM–2 and Earlier GSFC Solutions

The JGM–1 and –2 solutions used data from 31 satellites, which are described in Table 6.1.2–1. These data extend back to many previous solutions in most cases and are documented in the GEM–T1, GEM–T2, GEM–T3, and JGM–1/2 papers found in the *Journal of Geophysical Research* [*Marsh et al.,* 1988; *Marsh et al.,* 1990; *Lerch et al.,* 1994; *Nerem et al.,* 1994b]. Here we present a brief summary of the tracking systems in order to place the tracking data used in EGM96 in their proper context.

The earliest satellite tracking systems were imprecise by today's standards. Camera images and Minitrack interferometric tracking yielded satellite single-point positioning of 10 to 100 m in precision. Although the observations themselves were somewhat imprecise, a large group of satellites having a diverse range of orbital characteristics were tracked by these systems. Therefore, these observations (especially those obtained on 20 or so different orbits by a globally deployed network of Baker–Nunn and MOTS cameras) have formed the basis for the earliest gravity modeling activities at GSFC and elsewhere and still are used to fill out the desired span of orbital inclinations needed for EGM96.

In the early and mid-1970's, radiometric tracking of considerably higher precision than that obtained by cameras became the routine method for locating and operating low-Earth orbiting NASA satellites. The main operational tracking network for NASA was the ground-based

Unified S Band Network. These radiometric tracking systems acquired tracking, and telemetry data for those satellites carrying transponders, and did so in all weather conditions, providing both range and range-rate observations.

Table 6.2.1–1. Orbital characteristics for satellites used in JGM–1 and JGM–2.

Satellite	a (km)	e	Inclination (°)	Perigee Height (km)	Mean Motion (rev/d)	Primary Resonant Period (d)	Data Type
ATS–6	41867	.0010	0.9	35781	1.01	92.8	SST
Peole	7006	.0162	15.0	515	14.82	2.1	L
Courier–1B	7469	.0174	28.3	989	13.46	3.8	O
Vanguard–2	8298	.1648	32.9	562	11.49	2.7	O
Vanguard–2RB	8496	.1832	32.9	562	11.09	294.3	O
DI–D	7622	.0842	39.5	589	13.05	8.4	O,L
DI–C	7341	.0526	40.0	587	13.81	2.5	O,L
BE–C	7507	.0252	41.2	902	13.35	5.6	O,L
Telstar–1	9669	.2421	44.8	951	9.13	14.9	O
Echo–1RB	7966	.0121	47.2	1501	12.21	11.9	O
Starlette	7331	.0200	49.8	785	13.83	2.8	L
Ajisai	7870	.0010	50.0	1487	12.43	3.2	L
Anna–1B	7501	.0070	51.5	1076	13.37	4.8	O
GEOS–1	8075	.0725	59.3	1108	11.96	7.0	O,L
ETALON–1	25501	.0007	64.9	19121	2.13	7.9	L
TOPEX/POSEIDON	7716	.0004	66.0	1342	12.80	3.2	O,L,Dp
Transit–4A	7322	.0079	66.8	806	13.85	3.5	O
Injun–1	7316	.0076	66.8	895	13.87	3.8	O
Secor–5	8151	.0801	69.2	1140	11.79	3.4	O
BE–B	7354	.0143	79.7	902	13.76	3.0	O
OGO–2	7341	.0739	87.4	425	13.79	3.8	O
OSCAR–14	7448	.0030	89.2	1042	13.50	2.2	Dp
OSCAR–7	7411	.0242	89.7	848	13.60	3.2	Dp
5BN–2	7462	.0058	90.0	1063	13.46	2.4	O
NOVA	7559	.0010	90.0	1123	13.20	6.3	Dp
Midas–4	9995	.0121	95.8	1505	8.69	3.0	O
SPOT–2	7208	.0015	98.7	840	14.17	6.2	Dp
GEOS–2	7711	.0308	105.8	1114	12.82	5.7	O,L
SEASAT	7171	.0010	108.0	812	14.29	3.1	O,L,R,A
GEOSAT	7169	.0010	108.0	754	14.30	3.0	Dp,A
LAGEOS	12273	.0010	109.9	5827	6.39	2.7	L
GEOS–3	7226	.0010	114.9	841	14.13	4.5	L,A,SST
OVI–2	8317	.1835	144.3	415	11.45	2.2	O

Key: L = Laser, Dp = TRANET/OPNET Doppler, O = Optical, D = DORIS, R = Radar, A = Altimetry, SST = sat-to-sat range rate

Laser systems, which are currently the most accurate ranging system, also have a long pedigree. These systems were first deployed in the late 1960's and were used for orbit determination on the BE–B, BE–C, GEOS–1, and GEOS–2 missions. By the early 1970's, the first international laser tracking campaign was organized, which produced 1 m level data on six satellites. The laser systems have evolved substantially, undergoing a nearly tenfold improvement in precision every 3 to 5 years from the middle 1970's through the early 1990's. This evolution typifies the progress that has been made in monitoring the motion of near-Earth satellites and has resulted in much

more stringent demands for geopotential models capable of exploiting these data to their cm accuracy level. The limitations associated with satellite laser ranging (SLR) include its dependence on clear weather, the small number of satellites that carry laser retroreflectors, and the limited number of ground stations in the SLR network. Nevertheless, these data are largely responsible for the great improvement seen in gravity models, especially after the 1975 launch of Starlette and the 1976 launch LAGEOS (see *Lerch et al.* [1993], which describes the contribution of SLR within GSFC geopotential solutions).

The parallel capability of the S Band and SLR networks provided tracking flexibility. The laser tracking capability supported high-precision orbit determination needs, whereas the S Band Network provided both tracking and operational telemetry and control capabilities for a large constellation of NASA satellites.

Concurrent with these developments, the US Navy (USN) developed a robust tracking network of its own, supported by ground beacons and spaceborne transponders. The TRANET Doppler network deployed a large number of global stations starting in the middle 1960's. This network supported precision orbit determination needs within the DoD. The dual-frequency TRANET network provided a large volume of 1 to 4 cm/s range-rate observations; recent data sets, with judicious editing, are capable of producing orbit solutions with RMS of fit of 0.6 to 0.8 cm/s.

The French space agency, Centre National d'Etudes Spatiales (CNES), has developed a radiometric tracking technology, DORIS, which is similar in principal to TRANET, but with the ground stations transmitting a dual-frequency signal that is captured by an onboard receiver. This technology, using solid-state electronics and higher frequencies, is capable of an order-of-magnitude improvement over TRANET noise characteristics. DORIS observations are also much cleaner and free of the residual ionospheric refraction effects (mostly third order) that plague the TRANET data.

A major difference between the JGM–1 and –2 solutions and EGM96 concerns the number of sets of data that were strongly weighted. In JGM–1 and –2, only four or five sets of satellite tracking data were highly weighted, including the SLR data from LAGEOS, Starlette, Ajisai; the DORIS data from SPOT–2; and the SLR and DORIS data from TOPEX/POSEIDON (only in JGM–2). The other data were used to condition the gravity models and to break the correlations between spherical harmonic coefficients that are sensed by these satellites as "lumped" perturbations. Especially given the incremental buildup to these solutions, and the earlier iteration of the model that produced GEM–T3, this process was both well understood, and largely a reiteration of earlier analyses.

EGM96 includes these older technologies, in addition to a significant array of new methods of satellite tracking that have been implemented from the 1980's onward. One of these is NASA's Tracking and Data Relay Satellite System (TDRSS), which provides tracking and satellite communication services. The US Department of Defense (DoD) has deployed the Global Positioning System (GPS), an active constellation of 24 satellites (with on-orbit spares), launched into 12-hour orbits in six orbital planes. GPS is the most robust of all tracking systems, providing 3–D navigational capability to any Earth-based or near-Earth orbiting observer. However, GPS is

incapable of providing telemetry services, requiring another communications system to retrieve the data.

The tracking technologies that supplied data to EGM96 span the entire history of the space program. The major strengths and weaknesses of these systems are briefly reviewed in Table 6.2.1–2. In EGM96, the number of strong data sets more than doubled. The new strong tracking data included the SLR tracking to LAGEOS–2 and Stella, and those obtained from TDRSS and GPS. The new data required that weighting strategies and field optimization approaches be thoroughly reinitialized. The remainder of Section 6.2 discusses these new developments.

Table 6.2.1.–2. A review of the tracking data types used in the JGM and EGM96 geopotential solutions.

Technology	Configuration, Observable Types	Precision	Typical Orbit Fit	Strengths	Weakness	Period of Use
Camera: Baker–Nunn MOTS SPEOPT	satellite image against stars, right ascension and declination; passive and/or active (i.e. ,spaceborne flashing lamp)	1–2 arcsec (10–20 m)	1–2 arcsec	first precision tracking systems	atmospheric shimmer star catalog errors passive data tracking limited to dawn/dusk geometry	1960–1974
Satellite Laser Ranging	2-way range, use restricted to satellites carrying retroreflectors	0.5 cm	2 cm (LAGEOS) 5 cm (Starlette)	most precise absolute range unbiased excellent optical refrac. modeling	clouds obstruct obs only 40–60% of passes acquired early network limited in distribution	1968+
Radiometric Ground-based	2-way range 2-way range-rate S band-> NASA -> active C-band-> DoD -> passive	1 m 0.3 cm/s	5 m 1 cm/s	first all-weather precision tracking system	single-frequency results in large ionospheric error meas. biases	1972+
TDRSS (NASA)	1-/2-way ground-TDRS-sat range/range-rate single-frequency S and K band links	1 m 0.4 mm/s	1.5 m 0.8 mm/s	excellent global coverage of user sats high precision	single-frequency transponder delay (range biases) TDRS orbit errors	1983+
OPNET/ TRANET (USN)	1-way sat-ground range-rate dual frequency (150 and 400 MHz)	0.2 cm/s	0.7 cm/s	good global network distribution	poor clocks large third-order ionospheric refraction errors 40% of data rejected	1965–1995, TRANET phasing out
DORIS (CNES)	1-way ground-sat range-rate dual frequency (401.25 and 2036.25 MHz)	0.4 mm/s	0.5 mm/s	high-precision, all weather excellent global coverage	sat tracks only one ground station at a time Note: the new DORIS system envisioned for the JASON mission will track two stations simultaneously. Additionally, the noise floor should be reduced to .1 mm/s	1992+
GPS (DoD)	pseudo-range/carrier phase (sat-to-sat)/(sat-to-ground)	1–2 cm	1–2 cm	3–D navigation of low satellites unsurpassed coverage	controlled by DoD some on-orbit receivers cannot cope with antispoofing future receivers will use codeless technology, and track up to 12+ satellites	1992+
Altimetry	2-way range (sat-ocean) both single- and dual-freq. altimeters flown	1–2 cm	7 cm	precise range to directly map ocean surface topography	limited by modeling of complex ocean surface signals	1975+

6.2.2 TOPEX/POSEIDON (T/P)

6.2.2.1 Analysis of the T/P GPS Tracking Data

The Global Positioning System (GPS) Demonstration Receiver (GPSDR) onboard the TOPEX/POSEIDON (T/P) spacecraft was the first geodetic-quality GPS receiver to be flown on a satellite as an experimental application of Precision Orbit Determination (POD) with GPS [*Melbourne et al*., 1994]. That this receiver shared the same qualities with those used on the ground for precise positioning meant that the data could be used for applications well beyond those of POD. This experiment provided the first precise (biased) range data set, with uniform distribution (within ±66° latitude). Simulation studies that considered the contribution of such data [*Pavlis*, 1991] indicated that a great deal of gravity information could be obtained, even when the tracked spacecraft was as complex and orbiting at such high altitude (1336 km) as T/P. Furthermore, the same data could be used to carry out an independent POD experiment in the dynamic mode to validate and compare the many tracking systems available on T/P (e.g., SLR, DORIS, GPS, and TDRSS). After some initial tests with a few isolated single-day data sets released by JPL during the initial 6–month verification phase of the mission, the data from complete T/P cycles started becoming available around mid-1993, beginning with cycles 10, 14, 15, 17, 18, and 19. These six cycles were preprocessed and reduced to normal equations to be included with the other data in EGM96. This section documents the processing of the T/P GPS tracking data during the development of EGM96.

Overview of GPS

GPS has now reached full operational status. The constellation consists of 24 satellites (with 3 on-orbit spares) in six orbital planes inclined at 55°. The constellation is designed to provide visibility to at least four satellites from most locations on the Earth, 24 hours a day. The GPS satellites transmit two L band carrier signals (L_1=1575.42 MHz; L_2=1227.6 MHz) that are modulated with coded information. In particular, the L_1 signal is modulated with the clear-acquisition (C/A) code, the precision (P) code, and a navigation message that is generated at the GPS Master Control Station in Colorado Springs and transmitted to the satellites. The L_2 carrier is modulated with the P–code and the navigation message. This navigation message carries various information that is of use to the GPS user, including the GPS ephemerides and clock information.

Following the notation used in *Hofmann–Wellenhof et al*. [1992], the fundamental GPS observations of code and carrier phase pseudo-ranges, respectively, can be written,

$$R = \rho + c\Delta\delta + \Delta^{\text{Iono}} + \Delta^{\text{Trop}} \qquad (6.2.2.1–1)$$

$$\lambda\Phi = \rho + c\Delta\delta - \Delta^{\text{Iono}} + \Delta^{\text{Trop}} + N \qquad (6.2.2.1–2)$$

where

ρ **is** the geometric range

$\Delta\delta$ is the difference between the satellite and receiver clock offsets from GPS time

Δ^{Iono} is the ionospheric effect

Δ^{Trop} is the tropospheric effect

N   is the phase ambiguity bias

λ is the carrier phase wavelength.

The receiver clock offset contribution is embedded in the term $\Delta\delta$. Since the satellite clock contribution is known from the navigation message, one can see that simultaneous observations to four satellites would be needed to accurately point position a receiver with a poor clock (four unknowns: X–, Y–, Z–position, and the receiver clock offset). Because the carrier phase observable has a much shorter wavelength than either of the code pseudo-ranges, it has a much higher precision than the codes. However, some means of determining the initial ambiguity must be employed. Additionally, the phase observable is subject to cycle slips (i.e., changes in the integer ambiguity), so care must be taken to correct for this when utilizing this observable.

Because the GPS signals are broadcast on two frequencies, and because the ionosphere is a dispersive medium, the user can correct for ionospheric effects using linear combinations of the observables specified by eqs. (6.2.2.1–1 and –2) [*Hofmann–Wellenhof et al*., 1992]. The benefit of this lies in the ability to form different combinations of the observables to achieve certain objectives. One huge advantage in having both frequencies is the ability to mostly eliminate the ionospheric refraction. Because the ionosphere is a dispersive medium at GPS frequencies, the signals propagate through the ionosphere at different speeds proportional to the square of the frequency. It is easy to show how linear combinations of the two different observables can be determined that are largely free of the ionospheric refraction.

Some systematic errors can be largely eliminated by appropriate combinations of the observables. If simultaneous observables are obtained between two receivers and a satellite, then differencing those observables eliminates first-order satellite clock errors. When those same receivers observe another satellite, two sets of single differences are formed. Forming double difference ranges (DDR) from the two sets of single differences results in the cancellation of all first-order satellite and receiver clock errors [*Leick*, 1990].

Description of the data sets

The analysis of GPS spacecraft tracking data involves two types of GPS data: that obtained onboard the "user" (tracked) spacecraft and that obtained at ground sites. In both cases, the receivers observe the same signals transmitted by the GPS constellation, and one-way measurements are involved. The observed code and carrier phase are affected by the instantaneous clock errors at either end of the measured link. The sampling rate and some of the required corrections are quite different for the spaceborne receivers, which act as roving stations with rapidly changing geometry with respect to the GPS constellation, unlike those fixed to the ground. These two sets, after they have been preprocessed individually to a certain degree (cycle slip repair, thinning/compression, ionospheric correction application), are used in a differencing process to form the DDR's which are the proxy data used in the final analysis for the computation of the orbits and normal equations. DDR's are used in preference to plain biased ranges so that the

effect of transmitter and receiver clock errors are implicitly canceled. In this indirect way, we form a biased range measurement of the baseline between the two receivers. Since the GPS s/c are used as stepping stones to form the DDR measurement, they are also part of the measurement process. The GPS orbits are not perfectly known, and the same DDR data can be used to differentially correct the orbits of both the user satellite and the GPS orbit constellation.

When we discuss the processing of the T/P GPSDR data, we cannot limit ourselves to the parameters related to the T/P spacecraft alone. We also need to describe the modeling used for the GPS spacecraft, since it is an integral part of the modeling geometry.

The T/P data were obtained directly from JPL (the principal investigators for the GPSDR), while the ground data were recovered from the International GPS Service (IGS) for Geodynamics archive on GSFC's Crustal Dynamics Data Information System (CDDIS) Distributed Archive Center (DAC) [*Noll*, 1993].

TOPEX/POSEIDON data

The T/P data were released in the form of daily, RINEX-formatted ASCII files [*Gurtner and Mader*, 1990]. A brief description of the slight modifications in the standard Version 2.0 RINEX format were documented in a JPL Interoffice Memorandum [*JPL–IOM 314.5–xxxx Draft*, 12–Mar–1992] and later as a "README" file by J. Rodney Jee. These data have undergone initial calibrations and compression to a 10-second sampling rate. One of the JPL preprocessing steps minimized Selective Availability (SA) effects by processing the data with the algorithm described in *Wu et al.* [1990]. Of the six T/P cycles that were released by JPL, cycles 14, 15, 17, and 18 were complete, with data covering all 10 days. Cycles 10 and 19 were short by a day. More detailed information is given in Table 6.2.2.1–1.

Table 6.2.2.1–1. Description of the six cycles of T/P GPSDR data obtained from JPL.

Cycle	Start/Stop Revolution	Start/Stop Dates	Remarks∗
10	1702–1822	92/12/22 – 92/12/30	Yaw ramp, rev. 1803
14	2205–2332	93/01/30 – 93/02/08	–
15	2332–2459	93/02/09 – 93/02/18	–
17	2586–2713	93/03/01 – 93/03/10	Yaw ramp, rev. 2664
18	2713–2840	93/03/11 – 93/03/20	Yaw flip/ramp, rev. 2730/2796
19	2852–2967	93/03/21 – 93/03/29	orbit maneuver, rev. 2965

∗Based on T/P Mission Operations Strategy Timeline Versions 1.6 (1/8/93, 3/8/93) and 1.2 (5/19/93)

The data preprocessing at GSFC operated initially on the individual daily files. It was only in the later stages of the project that the data were reduced in batches that spanned 8 or 9 days (hereafter referred to as the "long arc" method).

Ground–site data

In 1992 and 1993, the IGS was running only a pilot service. The network extent and operations were not yet standardized and were under continuous revision. The IGS network in use at the time is shown in Figure 6.2.2.1–1. IGS collects data at the standard sampling rate of 30 s and time-tags the data in GPS time (i.e., leap seconds are not accounted for). Except for the RINEX formatting, IGS applies no other corrections to the data. Although we retrieved all the ground data for the T/P cycles of interest, the analysis was restricted to those sites equipped with high-quality receivers (Rogues™) to make data preprocessing easier and to ensure uniform accuracy throughout the network.
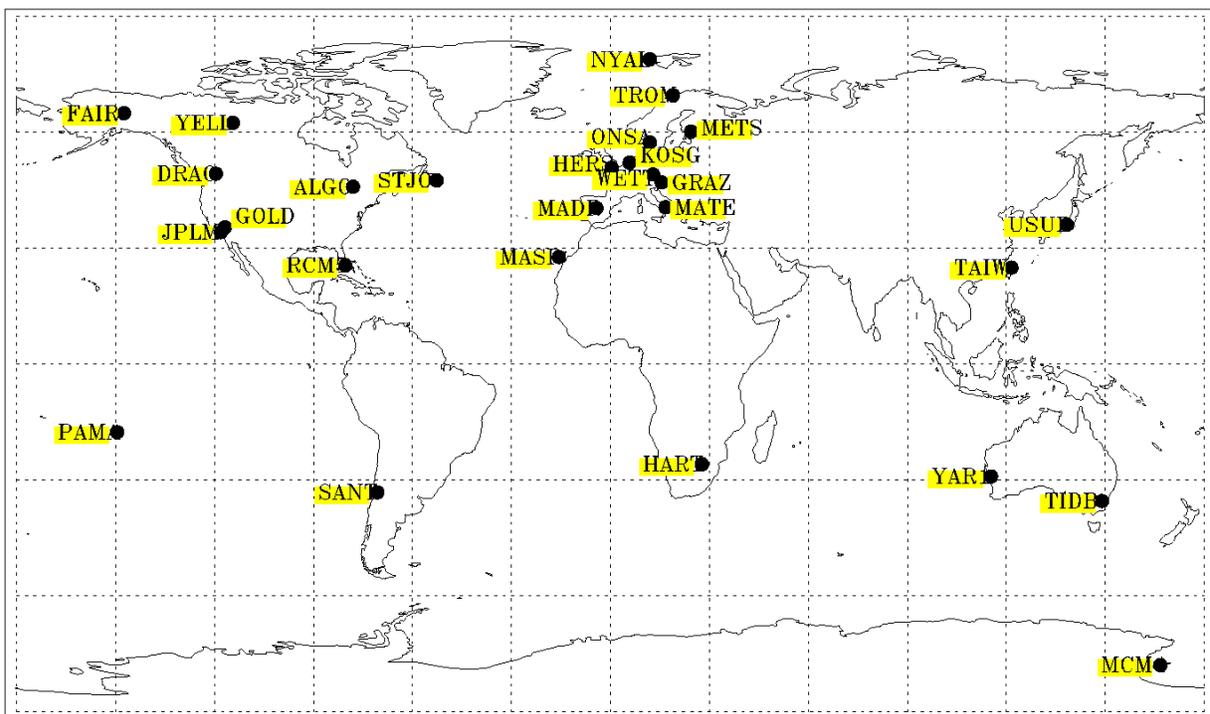
Figure 6.2.2.1–1. The International GPS Service for Geodynamics global tracking network.

Data preprocessing

While there was only one data set used to form the normal equations, the fact that it was constructed from two distinct subsets with different pedigrees requires that we begin our discussion of the preprocessing of these subsets separately. Once the first steps are covered, we present the details of their combination to form the set of DDR's.

T/P GPSDR data

The RINEX files were checked initially for blunders, for it was discovered that, in certain cases, the pseudo-range data contained spurious values. This step was deemed necessary because the pseudo-range data were used in the next step to identify and repair discontinuities in the phase data and to determine possible erratic behavior of the onboard clock. Most of these occurred at the initial or final stages of contact with a GPS spacecraft (i.e., while acquiring or dropping a GPS). All of these suspect entries were deleted. The resulting data were checked for any additional cycle-slips and T/P clock history based on the pseudo-ranges and broadcast GPS ephemerides and clocks.

The next step was to create data sets for each satellite separately so that they could later be combined with the ground data to form the DDR's. In doing so, we also combined the L_1 and L_2 carrier phase data in the so-called L_C, ionosphere-free combination. The phases were also converted to equivalent (biased) ranges. Selected days were sampled to determine the pattern of daily contacts with the GPS constellation. On the average, it seems that a "pass," defined as a continuous period of observations between T/P and one of the visible GPS spacecraft, lasted for about 45 minutes. The longer the passes, the fewer ambiguity constants need to be estimated, resulting in a stronger solution.

Every pass that was found free of cycle-slips ("phase-connected arc") was converted to approximate range data by forming a set of range-differences relative to the initial point and adding to that the corresponding pseudo-range at the same epoch. Since the data are eventually treated as biased range, this step is not strictly necessary. However, this helps to reduce the initial discrepancies to nearly negligible levels and thus speeds up the convergence process. This is of practical importance when the processing involves hundreds of thousands of observations daily.

Ground-site data

The initial criteria for accepting data from a ground site were uniform data quality and site locations resulting in a global network of reasonable extent. At the time, IGS had reached some 50 sites globally, most of them equipped with Rogue™ receivers. We decided to use the data from the stations whose geodetic and Cartesian coordinates appear in Appendix A. There are two entries for each site; the "higher" numbers correspond to the antenna phase center for the ionosphere-free frequency combination L_C. In some cases, the antenna phase center itself doubles as the reference mark, when there was no survey information available. In those cases, the two sets of coordinates are identical.

The raw RINEX files were first checked for blunders and then processed with an automatic editing procedure to identify and repair possible cycle-slips. The procedure that was followed is a locally implemented modified version of the algorithm described in [*Blewitt*, 1990]. The station clock behavior was checked on the basis of the available pseudo-ranges and, in general, no major problems were found. The product of the data editing process was a set of daily files, each containing data for a single station–GPS satellite combination. These were of the same form as the ones obtained from the T/P GPSDR editing process. The majority of the selected sites are in midlatitudes, and thus tracked the GPS spacecraft for several hours (3–6) daily. The statistics of

this step indicated that the majority of data losses occurred at sites closer to the poles, most likely associated with increased ionospheric activity.

Formation of the DDR's

The formation of the DDR's was accomplished in several steps. First an "inventory" of available data was created for each day based on the files with the clean ground-site and T/P GPSDR data. A three-dimensional catalog indicated when a certain site and T/P were observing the same GPS spacecraft so that a DDR between the site and T/P could be formed (Figure 6.2.2.1–2). Since the ground-site data were available at 30 s intervals, the DDR's were also formed at that rate despite the fact that the T/P data were available every 10 seconds. From this inventory, a daily scenario of DDR configurations was established, detailing the start and stop times when data for this configuration were to be double-differenced. At the same time, a data base was updated with the appropriate records required in GEODYN to account and solve for ambiguity and tropospheric refraction bias parameters. This stage was also used to eliminate "passes" of less than 15 minutes' duration.

E.C. PAVLIS EGS'95

GROUND - T/P DDRs
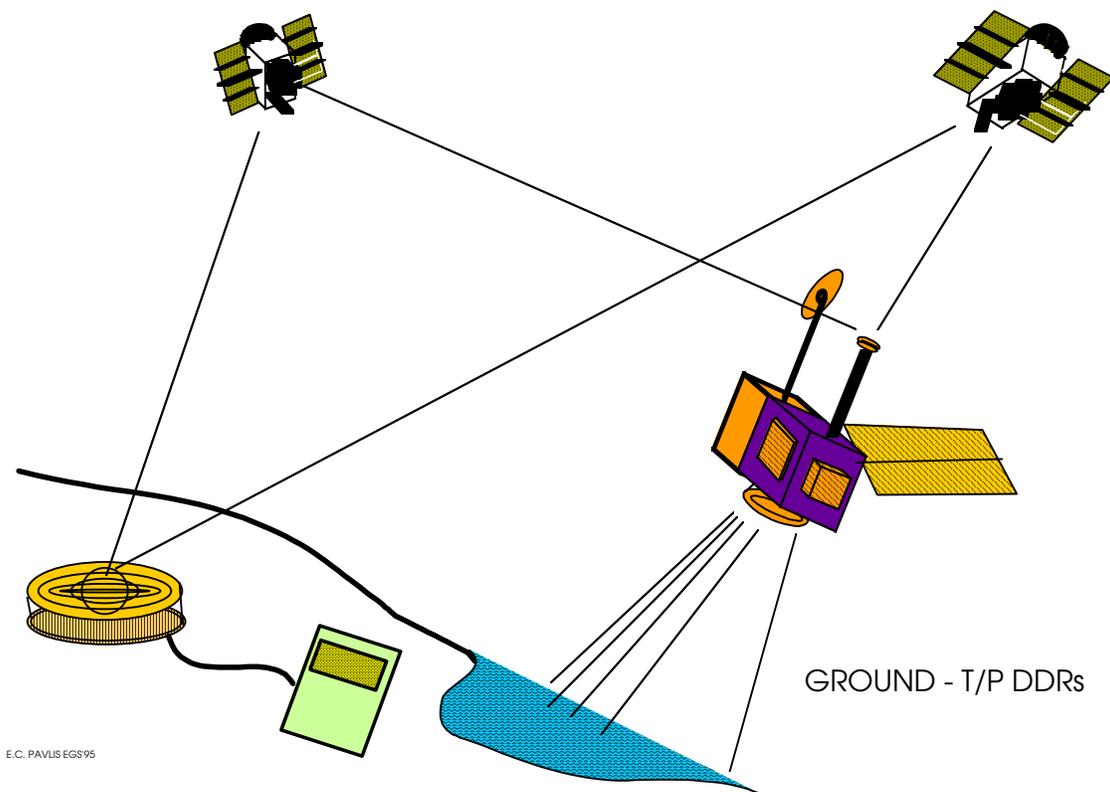
Figure 6.2.2.1–2. Definition of T/P and ground-site data double-difference combination.

In 1992 and early 1993, the ephemerides for the GPS spacecraft generated by various organizations were neither of the level of accuracy required in this effort nor very consistent with

our general modeling. Therefore, we processed the DDR tracking data to compute precise orbits for both T/P and the GPS constellation. To support this effort, we formed additional DDR's, which involved two ground-sites and two GPS spacecraft (Figure 6.2.2.1–3). These data were sampled at 6-minute intervals. Because of the high altitude and the slowly changing geometry with the ground sites of the GPS spacecraft, there is hardly any new information to be gained from a more frequent sampling. This was verified by differencing (GPS spacecraft) orbits produced with various sampling rates and comparing these differences to the expected accuracy of these orbits.

In the final step, the configuration scenarios were used to create input files compatible with GEODYN. Before any data reduction was performed, the data were edited for elevation cutoff in a set of preliminary reductions using initial conditions for the GPS spacecraft from the GPS "broadcast message" and the precise orbits produced at GSFC supporting the T/P project. This process eliminated a large number of observations at low elevation (below 15° for ground sites and 0° for T/P), which resulted in savings in processing time at the later stages. These daily files were eventually merged into "cycle" files containing all of the data in the corresponding T/P cycle.
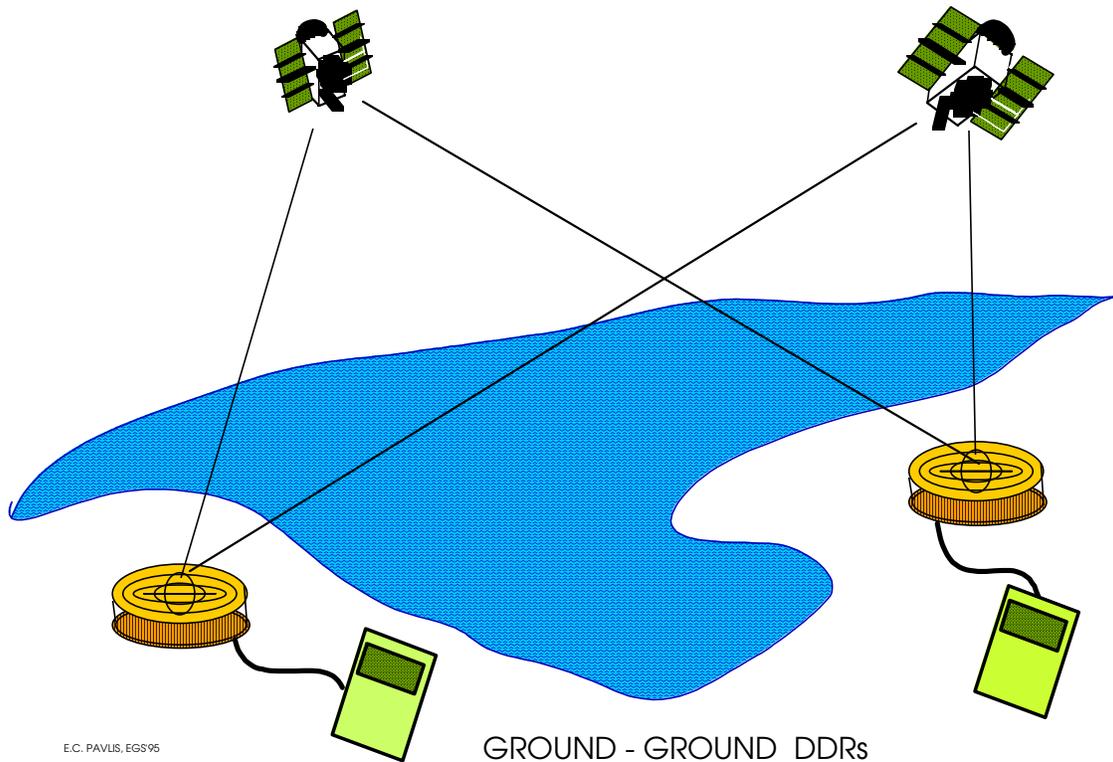
Figure 6.2.2.1–3. Definition of ground-site-to-ground-site data double-difference combination.

Data reduction

Initially, the GPS data were reduced in 1-day arcs, consistent with the prevailing style of the GPS ground-data analysis. Later, longer arc lengths were adopted, more consistent with the arc lengths used in the SLR/DORIS precise orbit analyses. Since the analysis of GPS DDR data from a space-borne receiver involves two types of orbits, those of the GPS spacecraft and that of the Low Earth Orbiter (LEO), we will discuss the models associated with each type separately, and refer to them as *arc models*, while the general models, which are independent of the spacecraft, will be discussed under *global models.*

Global models

The choice of the global models was based on the adopted standards for the reiteration of the JGM–2 normal equations in preparation for the new solution. In the case of the positions and velocities for the GPS ground sites, the only robust solution at the time was one from SIO [*Bock, 1993*], based on 16 months of tracking and incorporating the largest number of sites: 48 [*Boucher, Altamimi, and Duhem*, 1993]. These positions were given at an epoch—October 31, 1992—and for the reference mark at each site. Coordinates for the antennae phase centers for each site were constructed from the antennae height and type information file that was made available along with the marker coordinates. Tidal variations at the sites were described by the IERS series of ocean loading coefficients based on Schwiderski's tidal model. A tropospheric refraction bias was adjusted at each site at 4-hour intervals.

Arc models

TOPEX/POSEIDON. The geometric information relating the data to the center of mass of the spacecraft was obtained from various sources. Center of mass to center of figure reflect information in use by the precision orbit group at GSFC. Similarly, the surface description of the spacecraft that is required for the nonconservative force modeling and the attitude information also were obtained from the same group. The GPS antenna on T/P is a Dorne & Margolin type, with a choke ring attached to suppress excessive multipath. It had been precisely calibrated prior to launch, and these calibrated values were made available in the form of azimuth-elevation tables through a number of interoffice memoranda from JPL [335.9–92–016, 335.9–92–028, and 335.9.032–92]. Based on the values for L_1 and L_2 given in the last memorandum, we have incorporated corrections for the L_C frequency combination using:

$$L_C = L_1 + 1.546 (L_1 - L_2) \qquad (6.2.2.1–3)$$

The precise location of the antenna with respect to the center of mass of the spacecraft was also computed using eq. (6.2.2.1–3) and the offsets for L_1 and L_2 given in a JPL interoffice memorandum from *Joseph Guinn* [314.5–1665]. These are:

x = 2.1095

y = -0.4585

z = -4.5326

In the case of the ground sites, there were no reliable antenna phase center models available at the time, and, as these receivers are not in motion, it was considered safer to allow the changing geometry over time to average these effects than to apply a suspect model.

The force model used to describe the dynamics of the T/P orbit followed closely the first-generation precise orbit modeling described in *Marshal et al*. [1995b]. It allowed for a set of initial conditions per arc, an adopted drag coefficient, $C_D = 2.3$, an adopted solar radiation pressure scale factor, $C_R = 1.0$, and the following set of acceleration parameters adjusted on a daily basis:

a) constant along-track,

b) one-cycle-per-revolution (1-CPR) along-track, and

c) (1-CPR) cross-track.

In each of the cases b) and c), the amplitude of a sine and a cosine term are adjusted. Consistent with the altitude and sensitivity of the T/P orbit to gravitational perturbations, a stepsize of 30 seconds was used in the numerical integration of the equations of motion.

GPS spacecraft. During the period covered by the analyzed data set, both types of GPS spacecraft, Block I and II, were in operation, even though the majority were of the second type. The significance of this is threefold: Block I spacecraft are not affected by SA or AS, they have a different shape, size, and antenna location, and they follow a different attitude routine. We concerned ourselves with the second and third issues only. We have no reliable estimates for the size and mass of the various spacecraft types, so we have adopted two sets of values that seem to be used by most of the groups analyzing GPS data. For both Block I and II spacecraft, we set the cross-sectional area to 10 m^2. The mass of the Block I spacecraft is set to 450 kg, and for the IIs at 820 kg. Since the force modeling for the GPS spacecraft includes the adjustment of a C_R per arc, any error in the adopted area-to-mass ratio will be absorbed in the adjustment of C_R. The complicated attitude routine of the GPS spacecraft requires special modeling of nonconservative forces acting on the spacecraft. Simplified analytical models have been made available by *Fliegel and Gallini* [1991]—one for the Block I and one for the Block II spacecraft—and they are generally known as ROCK4 and ROCK42, respectively. The output of these models are the unscaled accelerations in the spacecraft body-fixed frame (SBF) in the X– and Z– directions. Due to misalignment errors in the Y–axis direction (along the solar panel axis of rotation), the accurate forward modeling of these accelerations is not possible. For that reason it is customary to adjust at least a constant acceleration in the Y–direction. This is commonly known as the Y–bias. In addition to the constant term, we also adjusted a 1-CPR term in the same direction, both on a daily basis.

In addition to different sizes, the two types of GPS spacecraft also have different antenna offsets. To relate the observed data (phases) to the spacecraft center of mass (the point to which the integrated orbits refer), we need precise vectors that connect the two. There is an ambiguity associated with the accuracy of these offsets, and, on occasion, one finds different values quoted for the same type of spacecraft. We have adopted here:

	Block I		Block II
X =	0.2100 m	X =	0.2794 m
Y =	0.0000	Y =	0.0000
Z =	0.8540	Z =	0.9519

The force model used in the computation of the GPS trajectories can be simplified immensely compared to what is needed for T/P or any other LEO. Due to software restrictions, we had to accept slightly more complicated modeling in exchange for a more efficient (vectorized) computational procedure. For GPS spacecraft, the gravity modeling was restricted to degree and order 18; 8 would have been enough, but the use of an ocean tide model that included terms up to degree 15 dictated this choice. Earth and ocean tides were modeled in the same fashion as for T/P, there was one C_R per arc, and no drag was modeled. The stepsize for the numerical integration was 360 seconds.

A summary of the initial reduction of the 1-day arcs is shown in Table 6.2.2.1–3. As explained earlier, the 1-day arc-length was initially used to rid the data of blunders and converge the orbits, not as a result of any sensitivity studies. While this process progressed, several significant modifications were implemented in GEODYN to allow efficient handling of the immense amount of data and large number of parameters associated with longer 10–day arcs spanning a full T/P cycle.

Table 6.2.2.1–3. Summary of initial reduction of the 58 daily arcs with T/P GPSDR and ground network DDR data.

Arc Epoch	T/P GPSDR	Ground Data	Total Accepted	RMS (m)
Cycle 10				
921222	11549	78553	90102	0.0107
921223	11999	85006	97005	0.0119
921224	12653	73119	85772	0.0125
921225	14352	80101	94453	0.0140
921226	12828	82781	95609	0.0126
921227	12978	97634	110612	0.0159
921228	11236	55126	66362	0.0162
921229	11228	86284	97512	0.0145
921230	12594	67018	79612	0.0150
Cycle 14				
930130	15145	37903	53048	0.0448
930131	14165	30748	44913	0.0203
930201	12244	31970	44214	0.0223
930202	11783	24208	35991	0.0249
930203	13294	39516	52810	0.0194
930204	12511	27659	40170	0.0215
930205	12775	25099	37874	0.0238
930206	18104	52323	70427	0.0234
930207	14502	32927	47429	0.0248
930208	16163	37004	53167	0.0283

Arc Epoch	T/P GPSDR	Ground Data	Total Accepted	RMS (m)
		Cycle 15		
930209	14830	51319	66149	0.0150
930210	14660	43504	58164	0.0158
930211	14304	33433	47737	0.0180
930212	15478	50816	66294	0.0160
930213	15160	46854	62014	0.0167
930214	17215	51724	68939	0.0143
930215	15639	46610	62249	0.0128
930216	13192	42056	55248	0.0125
930217	4796	42766	47562	0.0103
930218	3319	10726	14045	0.0108
		Cycle 17		
930301	14177	10351	24528	0.0613
930302	11686	40191	51877	0.0230
930303	14085	42596	56681	0.0263
930304	14969	10097	25066	0.0359
930305	12234	7854	20091	0.0369
930306	0	11330	11330	0.0170
930307	13624	7936	21560	0.0403
930308	11231	6789	18020	0.0249
930309	15162	8323	23485	0.0393
930310	12820	9097	21917	0.0392
		Cycle 18		
930311	9958	23469	33427	0.0135
930312	11511	22938	34449	0.0596
930313	14716	36773	51489	0.0241
930314	14082	41183	55265	0.0311
930315	7481	25753	33234	0.0212
930316	10514	35531	46045	0.0208
930317	6915	40074	46989	0.0189
930318	14976	55567	70543	0.0257
930319	16578	59866	76444	0.0187
930320	7852	12749	20601	0.0172
		Cycle 19		
930321	16374	13058	29432	0.0170
930322	13249	8024	21273	0.0158
930323	15153	14328	29481	0.0194
930324	14179	10963	25142	0.0183
930325	14172	10554	24726	0.0325
930326	14034	10658	24692	0.0235
930327	14417	11673	26090	0.0193
930328	12418	6017	18435	0.0295
930329	16679	10940	27619	0.0307

Despite software improvements, the reduction of the entire data set in terms of full cycles was impossible due to computer memory limitations. Thus, the DDR ground-site data had to be

eliminated. We performed a number of orbit comparisons (both for T/P as well as the GPS spacecraft) between trajectories computed on the basis of both types of data and on the basis of T/P DDR's alone. These tests indicated that the elimination of the ground-collected data caused no loss of accuracy. By doing so, we eliminated all the ambiguity unknowns that were involved in addition to the bookkeeping associated with an average additional 100000 observations on a daily basis! Once this was settled, the "long arcs" were formed by concatenating the 1-day arc results and performing a final convergence with a single set of initial conditions for each spacecraft per arc. The remainder of the force and measurement models were identical to those adopted for the 1-day arcs with the exception of the C_R factors for the GPS spacecraft: only one per arc per spacecraft was adjusted. Tests showed that a daily adjustment for C_R weakened the solution and did not change the recovered values. The results from this final reduction step are summarized in Table 6.2.2.1–4.

Table 6.2.2.1–4. Summary of final reduction of the six long arcs of T/P GPSDR double-differenced range data.

Arc	T/P DDR's	Spanned Dates	Length (days)	RMS (cm)
Cycle 10	114458	92/12/22 – 92/12/30	9	0.022
Cycle 14	110738	93/01/30 – 93/02/06	8	0.031
Cycle 15	123474	93/02/09 – 93/02/16	8	0.022
Cycle 17	89421	93/03/01 – 93/03/08	8	0.036
Cycle 18	93299	93/03/11 – 93/03/18	8	0.019
Cycle 19	112723	93/03/21 – 93/03/28	8	0.017
Totals	644113	–	–	0.025

Normal equations

Two sets of normal equations were formed: one for the 1-day arcs and one for the long arcs. Each set of normal equations included "*global*" and "*arc*" parameters. The global parameters are identical in context for each arc, but may differ in content. There are arcs, for example, when a different set of stations are tracking (some stations were not available for various reasons). The normal equations are extremely large due to the presence of nuisance arc parameters, such as the various biases (tropospheric, measurement/ambiguities).

An initial reduction of the individual normal equations eliminated these nuisance arc parameters. During this step, the empirical acceleration parameters were treated in several ways. For the 1-day arcs, the T/P constant along-track components of the empirical accelerations were adjusted, while the 1-CPR terms were linearly "shifted" to zero in SOLVE and suppressed (i.e., not estimated). This step allowed the gravity signal that had been accommodated by these parameters during the orbit reduction process to be channeled back into its rightful place: the gravity coefficients. For the long arcs, three different types of normal equations were produced to explore the amount of information that was lost when all or some of the empirical accelerations were allowed to adjust. One set was of the same type as that described for the 1-day arcs. This was the nominal set.

Variations to this approach included (a) one set in which all of the empirical accelerations were allowed to adjust freely and (b) one set in which only the along-track 1-CPR empirical accelerations were "shifted" to zero and suppressed. In the next step, these sets of normal equations were treated differently, depending on whether we dealt with the 1-day or the long arcs.

In the first case, the normals that belonged to the same T/P cycle were aggregated into a single combined set. These sets were then combined into a final set using equal weights for each cycle. The normal equations from the single-day arcs were used primarily in the preliminary solutions and to gauge the type of information that was gained when the long arcs were used in the solution. In the second (long arc) case, the set was already representative of a single T/P cycle, so the combined set of normal equations was formed simply by combining the six individual cycles. Since there were three different sets for the long arcs (dependent on the treatment of the empirical accelerations), there were also three different sets of combined normal equations.

It is important to clarify that, while the T/P GPSDR data were being processed to form normal equations, the treatment of the SLR and DORIS data from T/P was changed [*Marshall et al.*, 1995b]. This resulted in quite a different set of parameters describing the T/P orbit from the two sets of data (GPS vs. SLR/DORIS). A reformulation of the GPS normals was not possible due to both time and computer cost. That, of course, was unfortunate because it prohibited the combined use of the three data types to define the T/P orbit. For the six cycles where T/P GPSDR data were processed, two sets of initial conditions and arc parameters existed; one set was determined by the GPS data, and the other by the SLR and DORIS data. A combination of all these data is being pursued, especially in efforts to unify terrestrial reference frames across tracking technologies.

6.2.2.2 T/P SLR and DORIS Data Processing

This section presents the analysis procedures that were followed for the SLR and DORIS tracking data processing for T/P cycles 11 through 84. The data did not have to be analyzed for systematic effects, as that process had already been thoroughly performed by the GSFC T/P precision orbit determination (POD) process [*Marshall et al.*, 1995b]. The *a priori* for the normal equation formation was the set of models adopted for the second generation of the precision orbits [*Marshall et al.*, 1995b] including the JGM–3 gravity model, tracking site locations (referenced to an epoch of 930101), Earth-orientation parameters, and the improved T/P "macro model." The arc parameterization followed the standards of the second-generation precise orbit [*Marshall et al.*, 1995b]. The orbits were computed by combining the SLR and DORIS data, while adjusting atmospheric drag at 8-hour intervals, a daily constant along-track acceleration, and daily along- and cross-track 1-CPR accelerations.

The data uncertainties that were applied included a nominal .1 m for the SLR data, and .2 cm/s for the DORIS range-rate data. Some SLR sites were down-weighted to reflect their data quality. The relative ratio of the uncertainties between the various SLR tracking sites was the same as that implied by Table 6.2.6.2–1. However, the uncertainties applied for the stations listed in that table were 1/10th that listed, in keeping with the nominal T/P SLR data uncertainty, which was 1/10th of that applied to the other SLR-tracked satellites (see Section 6.2.6).

A summary of the T/P data spans and the fit statistics for the SLR and DORIS data is given in Table 6.2.2.2–1.

Normal Equation Processing

The normal equations were formed by passing the SLR/DORIS converged trajectory (including orbit state, coefficients of drag, and empirical acceleration parameters) through each of the data types separately. In this manner, the weights of the SLR, DORIS, and altimeter data (see Section 7.1) could be adjusted in SOLVE before addition of the separate normals to create the final T/P normal equations.

Table 6.2.2.2–1. Summary of TOPEX/POSEIDON 10–day solution statistics.

	SLR				DORIS	
Epoch	Number of Obs.	RMS (cm)	Number of Sites	Number of Obs.	RMS (cm)	Number of Sites
921231	1560	2.88	11	40730	0.0513	42
930110	2815	3.20	17	59384	0.0548	41
930120	3067	2.65	15	59134	0.0559	42
930129	4077	2.81	19	57545	0.0556	42
930208	2990	2.96	17	55287	0.0554	42
930218	3608	3.31	17	56776	0.0553	41
930228	4000	2.57	19	55573	0.0547	41
930310	5186	2.85	18	53754	0.0559	43
930320	3829	3.37	17	55142	0.0548	42
930330	5750	3.51	21	53422	0.0552	42
930409	4186	3.38	18	53842	0.0538	40
930419	6369	2.96	22	53995	0.0534	42
930429	4269	2.57	17	53066	0.0556	39
930509	5288	2.38	21	35569	0.0504	40
930519	3700	2.26	16	52145	0.0537	40
930528	2789	3.08	12	54796	0.0543	40
930607	3538	2.07	14	52391	0.0548	41
930617	4677	2.57	14	51555	0.0546	43
930627	4669	3.42	19	53457	0.0545	43
930707	5684	2.77	25	57360	0.0552	43
930717	6004	2.66	22	58047	0.0533	42
930727	8180	2.60	23	56074	0.0542	41
930807	4536	2.81	21	34783	0.0525	41
930816	6559	3.10	18	58220	0.0557	43
930826	5587	2.38	18	57263	0.0558	43
930905	4417	2.66	21	58885	0.0569	43
930915	5821	2.69	19	47170	0.0547	44
930924	4255	2.05	15	60836	0.0569	45
931004	4497	2.27	14	62095	0.0566	47
931014	3063	2.59	16	62694	0.0570	47
931024	3453	2.34	14	61387	0.0568	45
931103	3903	2.70	14	59056	0.0567	44
931113	3600	2.65	14	61031	0.0563	41
931123	3165	2.26	15	58213	0.0566	42
931203	2829	2.85	15	58829	0.0563	44

| Epoch | SLR | | | DORIS | | |
	Number of Obs.	RMS (cm)	Number of Sites	Number of Obs.	RMS (cm)	Number of Sites
931213	3887	2.99	18	57243	0.0565	44
931223	2832	2.74	15	57152	0/0553	42
940101	3689	2.46	19	60443	0.0545	42
940112	5288	3.24	21	56565	0.0553	43
940121	3675	2.62	16	58637	0.0557	44
940131	3857	2.40	16	60853	0.0558	44
940210	3828	2.42	17	59379	0.0555	41
940219	3187	2.74	16	62868	0.0557	42
940302	4254	3.21	18	56164	0.0547	45
940312	5444	3.23	20	58505	0.0540	43
940322	6583	3.31	22	57983	0.0546	45
940401	6272	2.66	20	61466	0.0545	44
940411	4704	2.72	17	61003	0.0551	44
940421	6431	3.06	20	63036	0.0549	44
940501	5169	2.96	21	62743	0.0543	44
940511	4542	2.67	16	61048	0.0550	45
940521	3032	2.51	12	62628	0.0550	45
940530	4534	2.20	13	62238	0.0549	44
940609	5049	2.58	17	33966	0.0559	45
940619	5514	2.81	20	60969	0.0549	45
940629	5591	3.19	21	62775	0.0549	45
940709	6534	2.03	19	62754	0.0544	45
940719	7088	2.13	20	45859	0.0525	45
940729	6915	2.03	21	62022	0.0548	47
940808	4905	2.25	20	59832	0.0771	45
940818	4649	2.49	18	57242	0.0555	44
940828	3996	1.93	19	58090	0.0562	44
940906	3697	2.09	19	58515	0.0547	43
940916	2813	1.86	12	59488	0.0545	44
940926	4178	2.56	17	60379	0.0548	43
941006	5945	2.55	19	58927	0.0546	44
941016	4979	2.71	19	56536	0.0537	44
941026	5125	2.68	20	55023	0.0547	44
941105	2779	2.07	19	56420	0.0532	46
941115	3613	2.76	19	56261	0.0539	44
941125	4627	2.92	17	56505	0.0534	44
941205	5243	2.11	19	54316	0.0552	43
941213	5511	2.86	17	62267	0.0542	45
941225	2152	1.79	13	54011	0.0533	45
Totals	334031			4191617		
Averages		2.66	17.7		0.0553	43.2

To form the normals that were used in the geopotential solutions, four steps were performed:

1. To ease the normal equation aggregation process for the two types of geopotential models, the 73 normal equation sets for each of the three tracking data types (SLR, DORIS, and altimetry; a total of 219 sets) were combined into four groups by tracking type. Two groups consisted of the individual years 1993 and 1994, while the other two were made up of the POSEIDON altimeter cycles and the T/P cycles 69 through 73 (see Table 6.2.2.2–1). The POSEIDON cycles had to be handled separately, since no POSEIDON altimeter data were

processed in EGM96. The cycle 69–73 grouping preserved the feasibility of combining the SLR/DORIS data with the TDRSS tracking of T/P and EP/EUVE (see Section 6.2.3.4), although, due to time limitations, we did not pursue this option. The result of this step was 11 sets of normal equations—4 each of SLR and DORIS data, and 3 altimetry sets.

2. The technology-dependent normals from the preceding step were added together to form a set of combined normal matrices for each tracking technology type, resulting in three sets of normal equations (SLR, DORIS, and, for the combination model, altimetry). At this step, some of the arc-dependent parameters that were not going to be adjusted in the gravity solution were eliminated from the normals to reduce their size. The coefficient of solar radiation pressure and constant along-track empirical acceleration term were fixed at their *a priori* values. A considerable amount of testing, through calibration analyses and external validation tests, such as comparisons with GPS traverses (cf. Sec 6.5.4), and orbit fits and overlap tests, was done to confirm the desirability of removing the 1-CPR acceleration parameters. In this case, the T/P "box-wing" model used in the construction of the normals was of sufficient quality to allow the nonconservative perturbations to be accommodated through the adjustment of the 8-hour interval coefficient of drag terms. Further, adjustment of the 1-CPR acceleration parameters removes a substantial portion of the unmodeled geopotential signal, so these 1-CPR parameters were forced to be zero.

3. The normal equations for each separate technology were further reduced by eliminating the effects of the remaining arc parameters, including the state vector and drag coefficients, via back substitution [*Ullman*, 1992], thereby leaving these terms free to be estimated in the gravity solution. The result was a set of normal equations for each separate technology containing the tracking site, Earth orientation, GM, gravity, and tide parameters. These normal equation sets were used to calibrate the individual tracking technology's contribution to the geopotential. Section 6.4.1.1 gives a more detailed discussion of the calibration process.

4. Once the weights for the SLR and DORIS normals were established, two sets of normal equations were generated. The normal equations for the different tracking technologies were first combined, then reduced in the same fashion as in Step 3, above. The first set included only the SLR and DORIS data used in the formation of the satellite-only model. The second included the altimetry data, in addition to the other two types, and was used in the formation of the low-degree comprehensive combination gravity solution (see Section 7 for details). The later normal equation set was reformed, as necessary, using the revised altimeter data weights that resulted from the calibration of the altimetry data.

6.2.3 Explorer Platform/Extreme Ultraviolet Explorer (EP/EUVE)

The Explorer Platform (EP) was launched on June 7, 1992, into a low-altitude (525 km), nearly circular orbit at an inclination of 28.4°. The primary science mission supports the Extreme Ultraviolet Explorer (EUVE), which is an astronomical payload intended to survey the sky and catalog sources in the extreme UV region. There are three scanning telescopes and a deep survey/spectrometer telescope onboard. Figure 6.2.3–1 depicts the Explorer Platform as equipped with the EUVE payload.
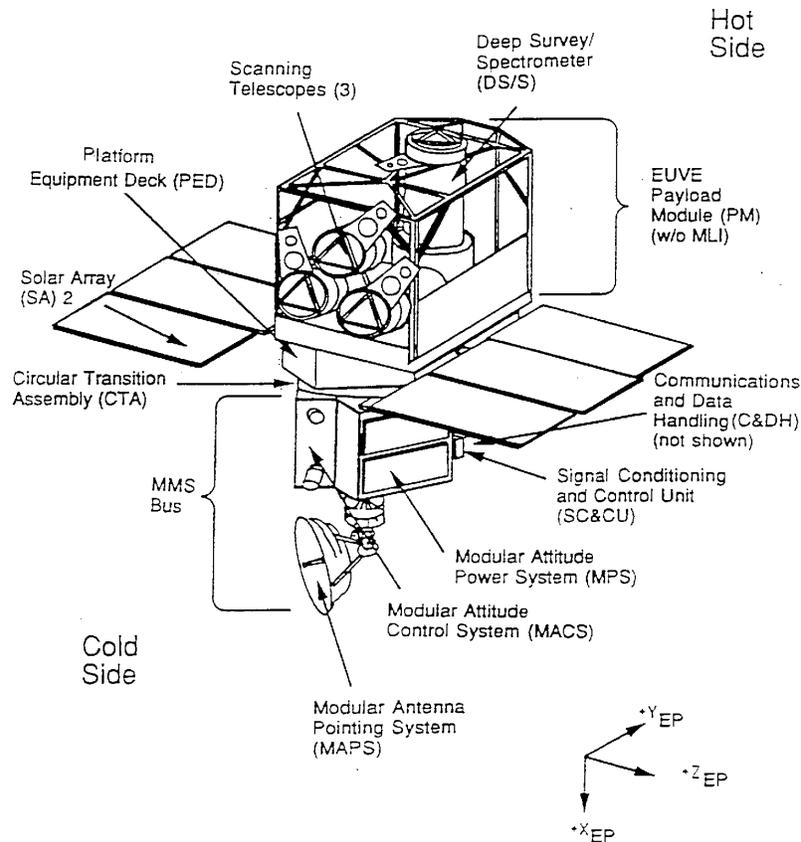
Figure 6.2.3–1. The Explorer Platform with the Extreme Ultraviolet Explorer payload.

Table 6.2.1–2 presents the orbital characteristics for the satellites from which tracking data were incorporated in JGM–1 and JGM–2. The satellites are listed in ascending order of orbital inclination. It is clear that there is a paucity of data at the lower inclinations. Additionally, the data that are present at or near the inclination of 28° are a limited set of low-accuracy optical data acquired in the mid-1960's. Further, the low altitude of the EP/EUVE orbit complemented the relatively few low-altitude satellites in the JGM models.. These satellite data provided the opportunity to make incremental improvements in both the static and time-varying components of the gravity field.

Including EP/EUVE data in the gravity model was a challenge. The benefit of the low altitude to the gravity sensitivity was offset by the large nonconservative force model errors. In addition, EP/EUVE was never intended to be a geodetic satellite. Its large, complex shape and its complicated attitude routines complicated both the force and the measurement modeling. Since routine operations only required orbits at the 100 m level, these concerns did not affect the routine spacecraft navigation, but had to be addressed to improve gravity field modeling.

TDRSS provided the operational data communications and navigation services. The TDRSS S band transponder onboard EP/EUVE was equipped with a high-gain parabolic antenna, an omni-directional antenna, and a relatively new feature—an Ultra Stable Oscillator (USO)—that allowed the use of precision one-way range-rate tracking in addition to the normal two-way tracking. The high-gain antenna, located on the X axis of spacecraft, provided nearly all communication and tracking services for the mission. As a result of the TDRSS Onboard Navigation System (TONS) experiment, and later testing for a new TDRSS ground terminal, a copious amount of TDRSS S band tracking data were available for EUVE.

The GPS receiver onboard EP was added as a secondary experiment. This "Explorer" receiver was donated by Motorola to NASA, and is primarily a single-frequency version of the Monarch™ receiver carried by TOPEX/POSEIDON. The Explorer is a 12-channel receiver capable of simultaneous operation on each channel. In an effort to ensure continuous visibility to the GPS satellites during the survey phase of the mission, EP was equipped with two omni-directional, body-mounted antennas. Although not shown, these antennas were mounted directly on opposite sides of the platform equipment deck. The Explorer operated on the GPS L_1 frequency, and was designed to provide both C/A– and P–code carrier phase and pseudorange measurements [*Dombrowski et al.*, 1991; *NASA GSFC*, 1989].

The following sections will describe the modeling of EP/EUVE and the processing of the GPS and TDRSS tracking data types.

6.2.3.1 EP/EUVE Attitude Considerations

The EUVE mission had two phases: A survey phase and a spectroscopy phase. The survey phase started after approximately 1 month of postlaunch checkout, and lasted for 6 months. During this phase, the spacecraft rotated slowly (3 revolutions per orbit) about a Sun-directed axis, allowing the scanning telescopes to map the entire sky in 6 months. Concurrently, the deep survey telescope pointed along the anti-Sun line, surveying the sky along the plane of the ecliptic. During the spectroscopy phase, the spacecraft directed the deep-survey/spectrometer at selected inertial sources. The 3200 kg EP/EUVE spacecraft used a three-axis stabilized, zero-momentum system with gyros and stellar references for its attitude control, and magnetic torquers to provide momentum management.

EUVE mission phases

The survey and spectroscopy phases were characterized by very different spacecraft attitude requirements. From an orbit determination (OD) perspective, it is not readily apparent which phase is the most desirable when trying to compute a precision orbit. In both cases, the spacecraft

nominally maintained its X axis in an inertial direction (see Figure 6.2.3–1). During the survey phase, the X axis was pointed toward the Sun, while the spacecraft slowly rotated about it. Later, during the spectroscopy phase, the spacecraft directed the X axis at some other celestial source, with no accompanying rotation, while the solar arrays were pointed at the Sun. The cyclical variation of the projected area onto the spacecraft velocity vector (important for drag) was significant during either phase. The additional rotation during the survey mode causes other perturbations that further complicated the OD.

Another consideration was antenna observability and the resulting continuous arc lengths that were available. While EP/EUVE was rotating, continuous GPS data passes of only 15–20 minutes were possible because the then currently tracked GPS satellites roll out of view. TDRSS, on the other hand, is relatively unaffected by the rolling since the high-gain antenna was located on the roll axis. Because the TDRSS antenna was on the Sunward side of the spacecraft during the survey phase, the tracking typically occurred only on the Sunward side of the orbit, although some also occurred toward the terminators. This, coupled with the approximately 2.5-meter phase center offset, presented a potential coordinate system origin error in TDRSS-based orbit solutions.

On the other hand, the spectroscopy phase offered the potential for relatively long continuous data arcs. Descriptions, provided by the Johnson Space Center (JSC), of spin down/up and slew intervals, roll reversal, and inertial mode for the first 1.5 years of the mission, were used to select the data periods. During the 6-month survey mode, there were several occasions when the anti-solar attitude was interrupted in order to point at various inertial targets. The length of time that EP/EUVE actually stayed pointing inertially at the sources varied greatly. In most cases, the length of time pointing at a single source was much less than a day. Since multiday data reduction runs were preferred, the abrupt changes in the spacecraft attitude would adversely affect the orbit modeling and gravity recovery if not properly accounted for.

Attitude data for 1994, when EP/EUVE supported TDRSS testing, was provided via the Mission Operations and Data Systems Directorate at GSFC. During this period, EP/EUVE was maneuvered much less frequently. As illustrated in Figure 6.2.3.1–1, attitude maneuvers occurred every 1–10 days; the spacecraft was reoriented and left in an inertially fixed attitude until the next maneuver, though on some occasions the attitude was constantly trimmed.

The GPS-based OD was generally restricted to periods when EP/EUVE was in survey mode. However, some periods were identified when the spacecraft was pointed at a celestial source for an extended amount of time, so OD was performed using the GPS data for these arcs as well. The TDRSS-based orbit determination was concentrated during the latter parts of the inertial spectroscopy phase, when the attitude was changed in frequently and dense tracking was available.

Quaternion data preprocessing

A preprocessing program to read the observed quaternion files and prepare these data for use in GEODYN was developed to support processing of the EP/EUVE GPS tracking data. Initial integrity checks were performed, and great effort was taken to ensure time-continuous,

nonduplicate data in the output. The 1-second sampled quaternions were not at integer time steps, which conflicted with the requirement that the attitude data be evenly spaced data in time for use in GEODYN. Software was developed to interpolate the input quaternions and output evenly spaced data at 5-second intervals. Additionally, the quaternion data must vary smoothly in time to avoid interpolation problems. Specifically, the sign of a quaternion is not significant; the same rotation sequence could be described by a quaternion set with opposite sign. Consequently, in order to interpolate the quaternions as a continuous function, the set had to be examined for rotations through 180 degrees and the quaternion signs changed appropriately.
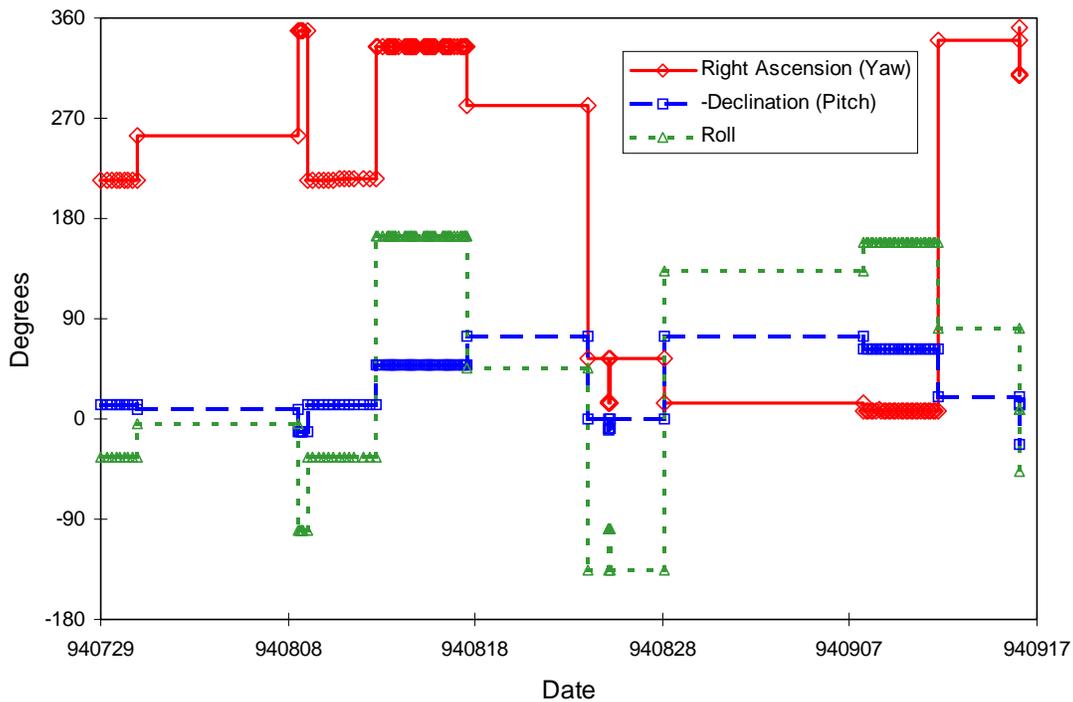
Figure 6.2.3.1–1. EP/EUVE commanded attitude, July 29–September 16, 1994.

The 50 days of dense TDRSS tracking from the 1994 period exceeded the 20 days of available observed quaternion data. Therefore, after appropriate verification against the telemetered data, a quaternion data set was generated using the commanded values. The maximum error incurred was well under a degree, as the EP/EUVE attitude control system maintained much finer pointing accuracy.

EP/EUVE attitude model

In GEODYN, antenna offsets within the spacecraft body fixed (SBF) frame may be specified, allowing a simple computation for the correction to the measurement. The quaternions can be

used in conjunction with this feature to supply the measurement model with precise information on the antenna location with respect to the SBF frame. In other words, at every measurement epoch, the quaternions are interpolated to supply a rotation of the SBF frame, and then the computed measurement is corrected by the vector amount of the antenna offset before being compared to the observed measurement. Orbit determination tests showed that including the quaternion set during the OD process improved the overall residual fit. Quaternion and GPS data availability was then an additional selection criterion.

One difficulty in modeling the measurement offsets and spacecraft attitude arose from the lack of specific geometric information pertaining to EP/EUVE. Various memoranda provided the locations of the GPS antennas on EP/EUVE. However, these memos did not explain the exact relationship to the available quaternion information. EP/EUVE has numerous SBF frames, each associated primarily with one of the onboard astronomical devices. Therefore, several assumptions were made to select the antenna offsets for the GEODYN modeling. In addition, no phase center information was available for the EP/EUVE antennae. However, we believe that the error introduced by not modeling the phase center variations was negligible when compared to the force modeling deficiencies and the uncertainties associated with the definition of the spacecraft reference frame.

6.2.3.2 Orbit Harmonic Analysis

Prior to the orbit determination analyses, we examined the predicted nonspherical gravity perturbations on the EP/EUVE orbit using the analytical method of *Kaula* [1966], as implemented by *Rosborough* [1986]. This technique evaluates the perturbations about the mean orbital plane that is considered to be a precessing ellipse. Linear orbit perturbation theory shows that EP/EUVE is in primary resonance with the order 15 terms, and in secondary resonance with the terms at order 30.

Results

The full spectrum of orbital perturbations produced by the geopotential coefficients was determined by mapping the linear orbit perturbations into the radial and transverse directions [*Rosborough*, 1986] for the EP/EUVE orbit. The mean elements and gravity model used for this analysis are listed in Table 6.2.3.2–1.

Although similar characteristics can be seen in all elemental perturbation spectra, Figure 6.2.3.2–1 illustrates the eccentricity perturbation spectrum for EP/EUVE. The furthest line to the left is the long period perturbation due to the odd zonals, and is at the frequency of the periapse rate (.03 cycles/day). The next three lines correspond to order 15 resonances (with frequencies of 0.1 to 0.2 cycles/day), while the fifth line from the left corresponds to an order 30 resonance (at a frequency of .27 cycles/day). The *m*–daily effects at 1, 2, and 3 cycles per day are quite evident, while other *m*–daily effects can be readily discerned up through order 13 or 14. The two spikes immediately surrounding the order 1 *m*–daily correspond to near resonances at order 14 and order 16. The most dominant short period perturbations are those at 15, 30 and 45 cycles per day, which correspond to one, two, and three times per orbit revolution.

Table 6.2.3.2–1. Parameters used in the EP/EUVE harmonic analysis.

Parameter	Value
semimajor axis (m)	6901136.3
inclination	28.43°
eccentricity	1.273355×10^{-3}
Earth radius (M)	6378137.0
GM (m^3/s^2)	$3.98600436 \times 10^{14}$
gravity model	JGM–2

Figures 6.2.3.2–2 and –3 depict the RMS of the radial orbit perturbations by degree and by order. As expected, the low degree and order terms dominate the perturbations. Figures 6.2.3.2–4 and –5, which illustrate the RMS of the transverse orbit perturbations by degree and by order, show the enhanced gravity field sensitivity derived from the along-track position perturbations. The transverse perturbations by coefficient degree diminish much less rapidly than the radial perturbations, since they include the enhanced sensitivity of the resonance orders. From *Kaula* [1966] and *Rosborough* [1986], we know that resonance produces large along-track perturbations. To model the EP/EUVE orbit to the level of 10 cm, a geopotential field complete to degree 70 and slightly greater than order 30 (the secondary resonance) is needed.
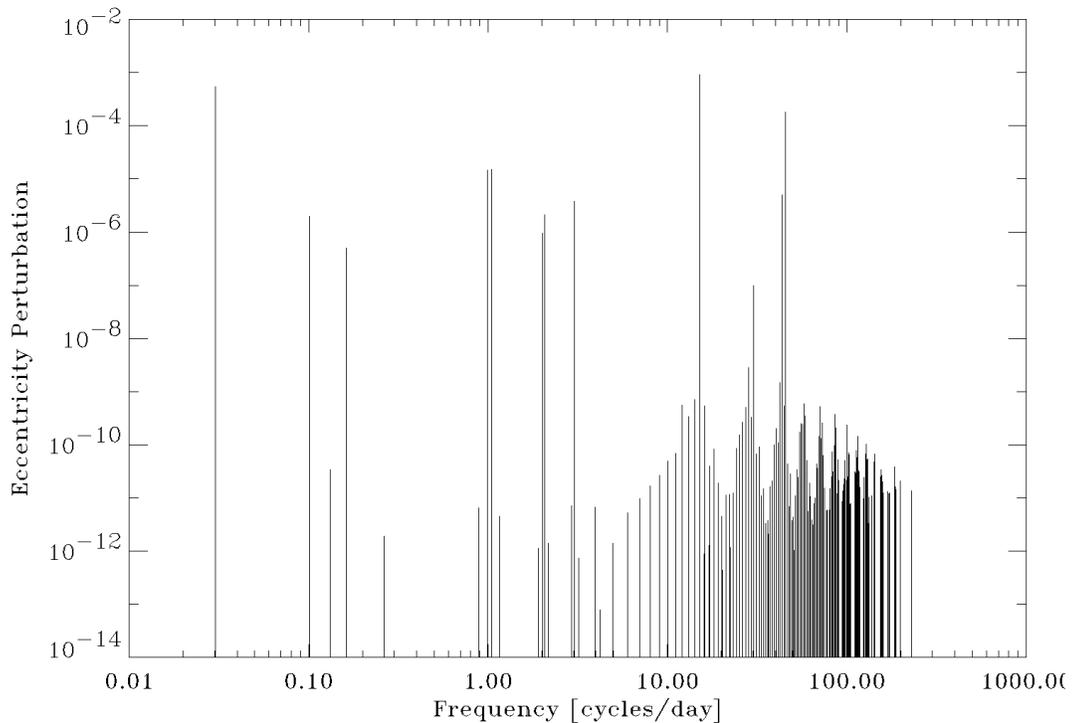
Figure 6.2.3.2–1. EP/EUVE orbit eccentricity perturbations spectrum (JGM–2).

6–39
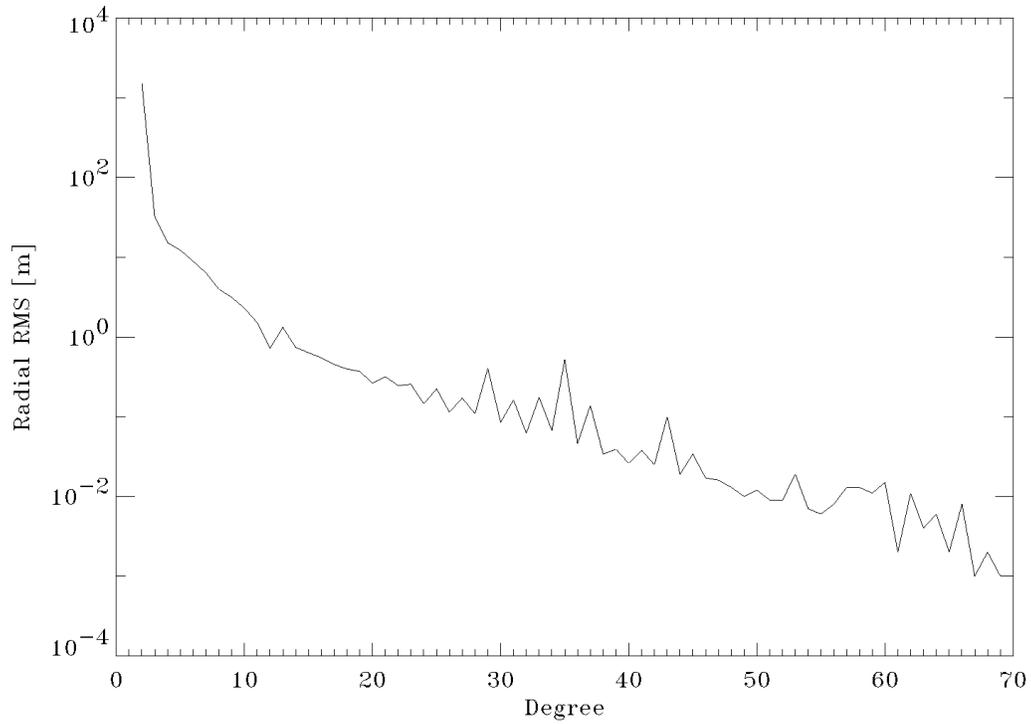
Figure 6.2.3.2–2. EP/EUVE RMS of radial orbit perturbations per coefficient degree (JGM–2).
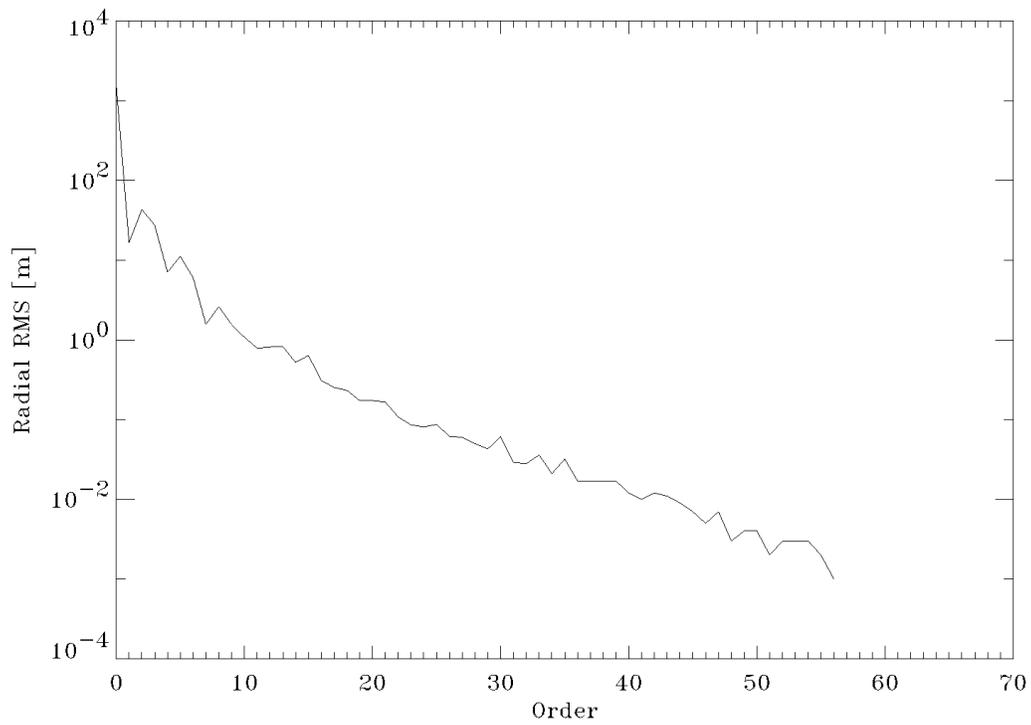
Figure 6.2.3.2–3. EP/EUVE RMS of radial orbit perturbations per coefficient order (JGM–2).

Figures 6.2.3.2–2 and –3 depict the RMS of the radial orbit perturbations for each degree and order, respectively. As expected, the low degree and order terms dominate the perturbations. Figures 6.2.3.2–4 and –5 are included for qualitative comparison to the radial RMS plots. These figures represent the RMS of the transverse orbit perturbations for each degree and order. Contrasting the equivalent radial plots, it is evident that the transverse position is significantly more sensitive to the extended gravity field. The transverse perturbations due to coefficient degree diminish with degree much less rapidly than the radial perturbations. Figure 6.2.3.1–5 also illustrates the increased sensitivity at the resonant orders of 15 and 30, which were absent from the radial plots. To model the EP/EUVE orbit to the level of 10 cm, a geopotential field complete to degree 70 and slightly greater than order 30 (the secondary resonance) is needed.

Using the analytical technique of *Rosborough* [1986], the JGM–2 calibrated error covariance was used to predict radial orbit errors at the EP/EUVE altitude (525 km) as a function of inclination (see Figure 6.2.3.2–6). For EP/EUVE inclination of 28.4°, the predicted radial orbit error due to geopotential effects is well over 1 m.
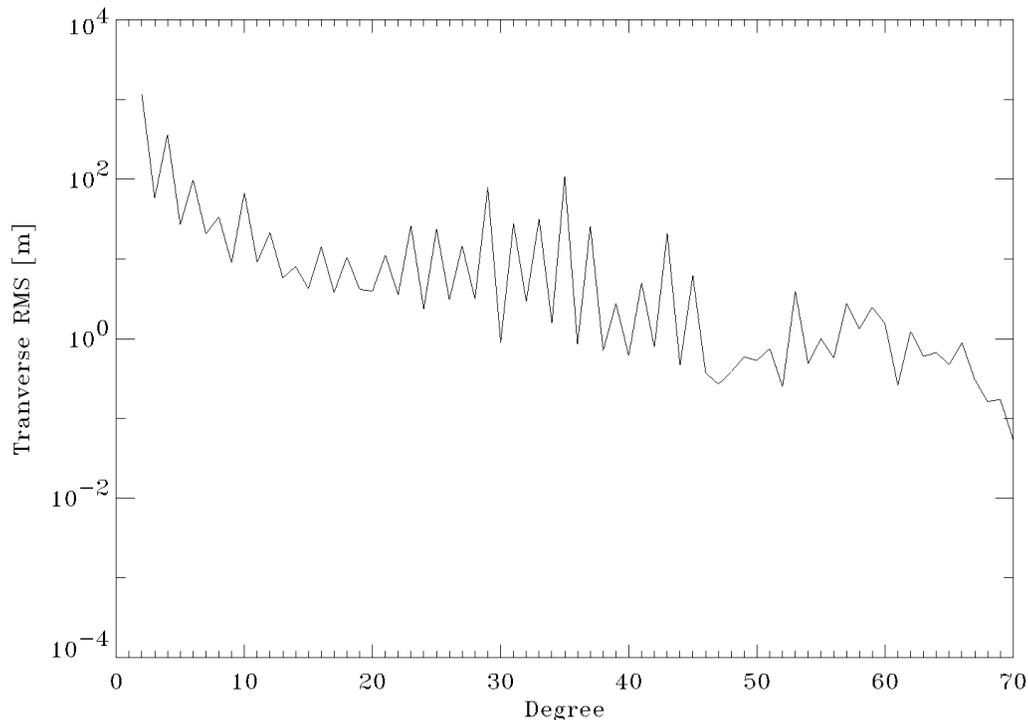
Figure 6.2.3.2–4. EP/EUVE RMS of transverse orbit perturbations per degree (JGM–2).
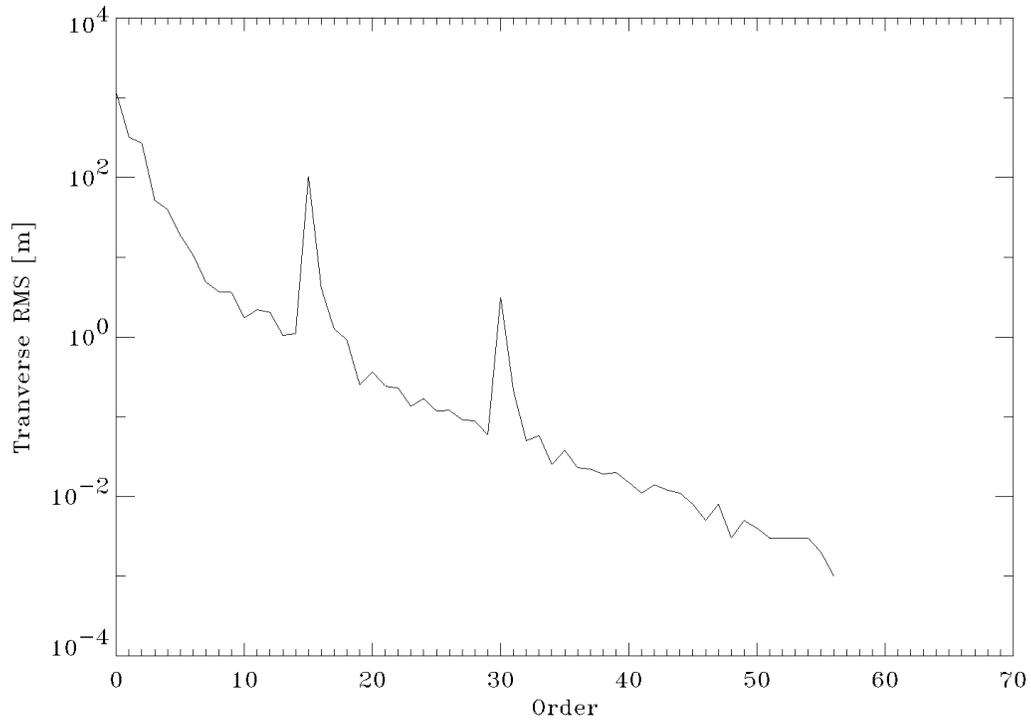
Figure 6.2.3.2–5. EP/EUVE RMS of transverse orbit perturbations per order (JGM–2).
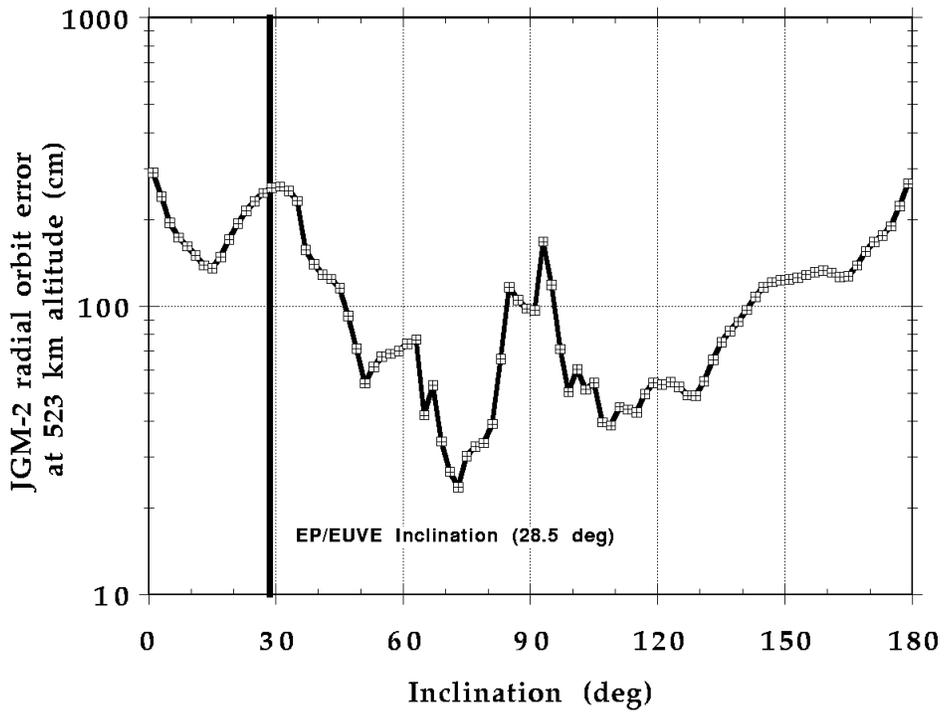
Figure 6.2.3.2–6. Predicted radial orbital errors at 523 km altitude (JGM–2).

6.2.3.3 GPS-Based EP/EUVE Orbit Determination

We present a brief overview of GPS with an emphasis on ground-data processing, then discuss in more detail the preprocessing and reduction of the EP/EUVE GPS tracking data. The seemingly abundant detail in this second part is justified since the described work is very specific to EP/EUVE and cannot be found in any other literature for reference.

Ground site data processing

The International GPS Service (IGS) is a worldwide effort for providing globally distributed GPS data and products from a dense network of tracking stations around the world. Over 100 fiducial sites gather data in a continuous mode. Of those, 70 sites are categorized as IGS Core Stations and are generally equipped with dual-frequency P–code receivers. Figure 6.2.3.3–1 shows the locations of the IGS Core Stations used in support of the EP/EUVE GPS data analysis.
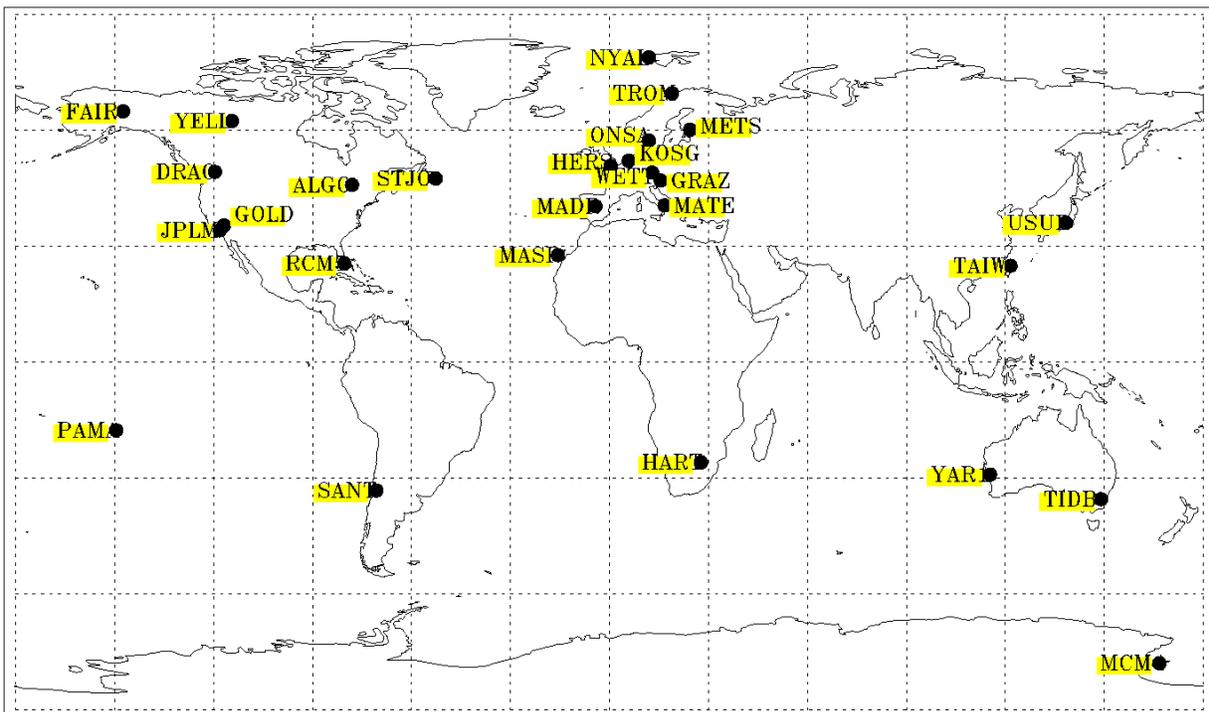
Figure 6.2.3.3–1. International GPS Service sites used in the EP/EUVE GPS data analysis.

The hierarchical flow of data is such that operational centers make their data available for nearby regional centers that then provide the data to one of three network centers. One of these network centers is the Crustal Dynamics Data Information System (CDDIS) Center at GSFC, and all data for this analysis were retrieved from there.

Rather than process all core sites, only those equipped with JPL Rogue receivers were incorporated into this study. The data used were from late 1992 and early 1993, amounting to approximately 25 to 30 stations. The decision for using the P–code Rogue data rests primarily on the fact that the cycle slip algorithm used for cleaning the GPS data from the ground sites is the TurboEdit Algorithm developed at JPL for its P–code receivers. A complete description of this algorithm may be found in *Blewitt* [1990].

EP/EUVE GPS Data Archiving

The EP/EUVE GPS data were transmitted from the spacecraft via a TDRS to the White Sands Ground Terminal (WSGT) in New Mexico. After transmission of the data to the operations centers at GSFC, where an initial integrity check was performed, the data were passed on to Johnson Space Center (JSC) for archival. All EP/EUVE GPS data used in the analysis were received from JSC. Each file received from JSC was simply a continuous binary stream of variable length, and did not necessarily constitute a particular time span or ensure data continuity with previous files or within the file. It was not uncommon to find small sections of data that, according to the time-tag, belonged in previous files or after the current file.

EP/EUVE attitude quaternions were also archived at JSC. As with the EP/EUVE GPS data, time-tag and continuity problems were also present in these data. The quaternions described the rotation from the J2000 inertial frame to the SBF frame.

EP/EUVE GPS Data Processing

Decoding of raw telemetry. A program was developed to decode the telemetry stream from the JSC files and write out the GPS data in the Receiver INdependent EXchange (RINEX) format. However, because the input data were nonuniform, the output files had to be checked for out-of-sequence or duplicate data. Additionally, more data integrity checks were performed. Parameters at the beginning and end of the data blocks were tested to verify that the blocks had realistic values. Pseudorange values were also tested to confirm realistic values, defined as ranges greater than (GPS altitude – EP/EUVE altitude), and less than (GPS altitude + Earth diameter + EP/EUVE altitude). If anything in the data block was suspect, the entire block was deleted and the search was continued for the next block. The result of this preprocessing was daily EP/EUVE RINEX files, as well as another file containing the onboard navigation solution and receiver clock offset histories for the day. The resulting RINEX files created were not "true" RINEX files, since, in order to conserve onboard memory, the pseudoranges, spacecraft ephemerides, and receiver clock corrections were recorded only every 10 seconds, whereas the carrier phase was stored every second.

Cycle slip flagging. The EP/EUVE RINEX files were then considered to be free of any anomalous data blocks, yet still contained possible cycle slips. Rather than attempt to fix cycle slips in the single-frequency carrier phase data, possible slips were flagged as a place to estimate a measurement bias. Two further steps were needed before the EP/EUVE data could be double-differenced with the IGS ground data: 1) Flag all possible cycle slips in the EP/EUVE data and 2)

move the EP/EUVE observables to a common physical epoch with the IGS sites so that the differencing could occur.

To look for possible slips, the difference in phase between two epochs was compared to the difference in range between two epochs. That is, assuming phase has been converted to the same unit of length as the pseudorange, we examined the difference

$$\Delta = (\Phi_{i+1} - \Phi_i) - (R_{i+1} - R_i) \qquad\qquad (6.2.3.3\text{–}1)$$

where

Φ_i = carrier phase at epoch i

R_i = pseudorange at epoch i.

Since the RINEX files contained 1-second phase values but only 10-second pseudorange values, 1/10th of the difference between successive pseudoranges was compared with the 1-second phase differences. In the absence of cycle slips and ionospheric effects, this difference would be expected to be within the bounds of the noise of the measurements and the linear interpolation assumptions. However, ionospheric effects were present, so some criteria had to be set in order to determine when a large Δ was indeed the result of a cycle slip rather than that of the ionosphere. Overall, the approach used was rather manual. Values for Δ were computed for several GPS satellites, and then referenced while plots of the arcs were examined. Cycle slips were usually obvious, so maximum values for Δ in the absence of a slip were determined. This was done for different days, and a value equivalent to 750 meters was selected. While this seems large for range changes due to ionosphere, it was apparent that considerable error resulted from the different sampling rates of the phase and pseudorange. The 1/10th approximation was not always valid since 1/10th the true range change (from the pseudorange) was not always close to the true range change represented in the consecutive 1-second carrier phase.

The data were then run through this "cleaning" process, and when large Δs were found, a flag was set. The initial ambiguity for the current arc was also adjusted in order to bring the value of Δ at the flagged location to zero, but this was only done to cause midarc ambiguities to have relatively small *a posteriori* values. Again, the goal here was not to fix cycle slips, but rather to flag their locations for estimation of measurement biases. Two possibilities exist for error in this approach: (1) Cycle slips were missed, resulting in increased errors, or (2) false cycle slips were flagged, causing the estimation of an unnecessary parameter and weakening the final solution somewhat. Of course, other editing tests were carried out with regard to outliers and resultant arc length.

EP/EUVE receiver clock offset. The measurements were then corrected for the EP/EUVE receiver clock offset from GPS time and made simultaneous with the ground station data so that double-differences could be formed. It was necessary to fit a polynomial to the 10-second data rate EP/EUVE clock offset data in order to correct the phase measurements every second. The dominate behavioral characteristic of the EP/EUVE clock offset data was a linear drift rate on the order of 70 milliseconds per day. Figure 6.2.3.3–2 illustrates the clock offset after the linear drift has been removed. Although EP/EUVE had the best available NASA onboard oscillator (the

USO), there were still significant fluctuations in the residuals, which do not compare favorably with the performance of the best ground-based clocks.
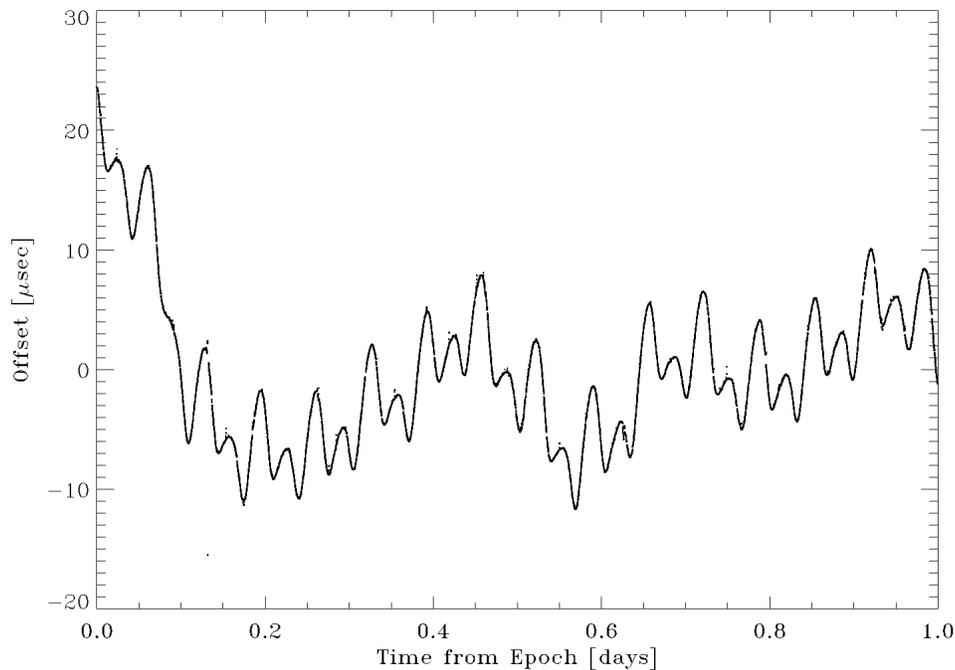
Figure 6.2.3.3–2. EP/EUVE telemetered GPS receiver clock offset with linear trend removed.

Following *Gold* [1994], quadratic fits to the telemetered EP/EUVE clock offset were initially computed daily. However, differencing the daily quadratic model with the original telemetered data showed differences that were negligible on some days but that translated into 600-km differences on other days. Instead, quadratics were fit to the nearest three telemetered offsets, and then evaluated where needed. The observables, as well as the epoch time-tag, were corrected to remove the error. For example, if the evaluated clock offset was Δt, then the time-tag was corrected by Δt, and the observables by cΔt (where c is the speed of light). This produced observables that were not on the integer second, nor separated by a constant integer second.

Achieving data simultaneity. *Wu et al.* [1990] present a data reduction scheme for minimizing Selective Availability (S/A) error on T/P GPS measurements that can be used to obtain simultaneity with the ground receivers. The EP/EUVE and T/P receivers are very similar, and part of that similarity lies in the 1-second sampling of the carrier phase data and the 10-second sampling of the pseudorange. *Wu et al.* [1990] show that for the T/P carrier phase data, a simple cubic interpolation over four 1-second phase points surrounding the desired new epoch is sufficient to maintain the T/P dynamics information. This approach takes advantage of the low pseudorange data noise achievable when smoothing over several minute intervals. However, proper smoothing requires that the satellite dynamics be removed. They propose that the carrier

phase be used as a dynamic model and subtracted from the pseudorange. Although it was not our desire to compress the data any further than was necessary, the scheme outlined was modified slightly and used to achieve simultaneity with ground data.

It was assumed that, although the EP/EUVE dynamics were even stronger than those of T/P, a cubic interpolation over four adjacent phase points would describe the orbit dynamics. Nothing further was done to obtain a phase value at the correct epoch. This approach could not be duplicated to obtain pseudorange values at the correct epoch because of the 10-second sampling. A polynomial would have to try to fit the EP/EUVE dynamics over 30 to 40 seconds (which translates to 300 km), and could not properly pick up the detailed dynamics over this interval. To achieve pseudorange simultaneity, the phase was subtracted from the pseudorange at every 10-second pseudorange point. The result should contain twice the ionospheric effect, noise from each of the observables, and the phase ambiguity bias. The pseudorange and carrier phase observations may be written as:

$$R = \rho + c\Delta\delta + \Delta^{Iono} + \varepsilon^R \qquad (6.2.3.3\text{--}2)$$

$$\Phi = \rho + c\Delta\delta - \Delta^{Iono} + \varepsilon^\Phi + N \qquad (6.2.3.3\text{--}3)$$

where ρ the geometric range, $\Delta\delta$ difference between the satellite and receiver clock offsets from GPS time that may remain, Δ^{Iono} is the ionospheric effect, ε stands for the measurement noise, and N is the phase ambiguity bias. Therefore at any epoch, i,

$$(R_i - \Phi_i) = 2\Delta_i^{Iono} + \varepsilon_i^R - \varepsilon_i^\Phi - N_i \qquad (6.2.3.3\text{--}4)$$

The time-tag corrected pseudorange observable, R_c, may now be computed by adding back in the satellite dynamics via the time-tag corrected phase observable, Φ_c. If there are no cycle slips, then $N_i = N_C$, and if we assume that the noise on the observations is random noise, and therefore epoch independent, then

$$R_c = \rho_c + c\Delta\delta_c + (2\Delta_i^{Iono} - \Delta_c^{Iono}) + \varepsilon^R \qquad (6.2.3.3\text{--}5)$$

The third term on the right-hand side of eq. (6.2.3.3–5) causes some concern. *Wu et al.* [1990] undoubtedly assumed that dual-frequency observations would be available, and their data reduction scheme would therefore be applied to an "ionosphere-free" combination. Consequently, the terms would be very small, and the difference negligible. The single-frequency EP/EUVE data, however, could have very sizable ionospheric effects, and the question then becomes whether

$$\Delta_i^{Iono} \overset{?}{\approx} \Delta_c^{Iono}$$

If these two terms are not nearly equal, then we will be adding (or subtracting) more of an ionospheric effect than this epoch should really have. Consider that the typical receiver clock offset that was applied to the data was on the order of a few seconds. The simultaneous time-tag we are trying to achieve is thus only a few seconds away. We are concerned with spatial, rather than temporal, changes in the ionosphere during these few seconds. EP/EUVE is moving at approximately 7.5 km/s, so the ionosphere that the signal traverses at the time-tag-corrected epoch is translated by only about 15 km from the ionosphere seen at epoch *i*. Assuming that,

spatially, the ionosphere at EP/EUVE altitude is correlated the same way as at Earth's surface, then these two ionospheric effects will be highly correlated [*Kelly*, 1989]. This was the assumption made, so eq. (6.2.3.3–5) becomes

$$R_c = \rho_c + c\Delta\delta_c + \Delta_c^{Iono*} + \varepsilon^R \qquad (6.2.3.3–6)$$

where the "*" denotes that this quantity is likely not identical to Δ_c^{Iono}.

Two GPS antennas. The EP/EUVE observables were now simultaneous with the ground site data, so double differences were formed. For all of the preprocessing, the two GPS antennas were treated separately throughout the entire double-difference procedure. If we denote the antennae as antenna A and antenna B, then the only double differences that were formed were when both EP/EUVE $\Leftrightarrow$ GPS links are from A, or from B. No differences are formed when one link was from A and one link from B. Since both antennas are connected to the same receiver, then technically, forming the hybrid double differences would enjoy the exact same benefits as the other double differences. This, in fact, was attempted, and the results will be discussed later.

Ionospheric correction. The ionospheric effect on GPS observables can cause the measured range to deviate from the true range by as much as 50 m, depending on the elevation angle. However, the observables available from the IGS sites to the GPS satellites occur on both L_1 and L_2 frequencies, thereby enabling the formation of the so-called "ionosphere-free" observable, L_c. The EP/EUVE observables, on the other hand, use only the single L_1 frequency. Forming the double differences with a LEO spacecraft does not reduce possible ionospheric effects, since the line of sight to a GPS satellite can be vastly different between the ground site and low-Earth orbits. With EP/EUVE at 525 km, ~40 percent of the ionosphere is above the spacecraft, so correcting the observables deserves some attention.

One possible means of correcting for the ionospheric path delay for single-frequency data is by forming the Differenced Range Versus Integrated Doppler (DRVID) [*MacDoran*, 1970]. Because the ionosphere is a dispersive medium, a group of signals of different frequencies (such as the modulated GPS carrier phase signals) will travel at a different velocity than the individual signals themselves. It turns out that this spread signal will experience a delay, which then has the effect of advancing the phase cycles. The total effect then is to increase the total delay experienced by the group, and decrease the total delay experienced by the phase,

$$\tau_g \cong \tau + \frac{kTEC}{f^2} \qquad (6.2.3.3–7)$$

$$\tau_\Phi \cong \tau - \frac{kTEC}{f^2} \qquad (6.2.3.3–8)$$

where τ represents the total delay of all nonionospheric effects, k is a constant (= 40.3), TEC is the total electron content along the line-of-sight path, and f is the frequency. If we consider that the total phase delay will actually also contain an ambiguity bias, then adding eqs. (6.2.3.3–7) and (–8) results in:

$$\frac{(\tau_g + \tau_\Phi)}{2} = \tau + bias \qquad (6.2.3.3–9)$$

An "ionosphere-free" (to first order) biased range observable with ~1/2 the noise of the pseudorange can, therefore, be created by adding the phase (in equivalent meters) to the pseudorange and dividing by two.

Gold [1994] applied the DRVID technique during his EP/EUVE analysis and showed definite orbit improvement. However, when this technique was attempted with GEODYN, a large mean difference in the orbit overlap differences was observed, primarily the cross-track component. In other words, overlap comparisons seemed to indicate that using the DRVID data type decreased the orbital precision. However, this mean appeared as a coordinate frame rotation and could be estimated and removed. Once removed, the overlaps showed better agreement than overlapping arcs determined from treating the carrier phase and pseudorange as separate measurements. Additionally, comparisons to high-quality, independent, JPL-generated EP/EUVE orbits indicated that the use of the DRVID data was preferred (assuming the JPL orbits are considered as truth). It was believed that the increased noise of the DRVID type (over that of the carrier phase) caused the problem in resolving the coordinate frame. Without it, however, the ionosphere effect in the single-frequency data resulted in poorer orbit quality. Because of the improvement in the orbit quality, and in the comparisons with the JPL orbits, the DRVID data were used in all subsequent EP/EUVE analysis.

Spatial Distribution of EP/EUVE GPS Data

The low inclination of EP/EUVE limited the ground coverage to $\pm 28.4°$ latitude. Furthermore, the unbalanced distribution of the operational IGS sites in 1992 and 1993 biased the coverage to the Northern Hemisphere, as shown in Figure 6.2.3.3–3.

Orbit Determination Methodology

Gold [1994] used JPL's GIPSY–OASIS II (GOA–II) software [*Webb and Zumberge*, 1995; *Lichten et al.*, 1995] to perform "precision" orbit determination for EP/EUVE, determining what were believed to be the most accurate EP/EUVE orbits that existed at that time. This conclusion was based in part on overlap analysis, because no other accurate source of EP/EUVE orbits was available. Orbit overlap comparisons are more of a test of orbit precision than orbit accuracy, and as such are only a partial indicator of accuracy. As a result of our GEODYN analysis, inter-software and interinstitutional comparisons became feasible. GOA–II software capabilities differ from those of GEODYN, most notably in the ability to model parameters stochastically and the ability to compute orbits using reduced dynamic techniques. OD methodology also differs, and this will be discussed further later.

The IGS ground data were combined in a double-difference mode (L_c observables), and processed in GEODYN to compute the GPS orbits. The purpose of doing this, rather than using the available orbits from either Scripps or JPL, was to create a globally consistent reference frame with what would be used in the EP/EUVE data reduction runs. In 1992 and early 1993, there were still problems in the overall techniques being used for GPS orbit computations. JPL, in particular, discovered that for some satellites during this period, its modeling was incorrect.

JPL also estimated polar motion and A1–UT1 rates stochastically, which resulted in reference frames that were different from the ITRF standard.
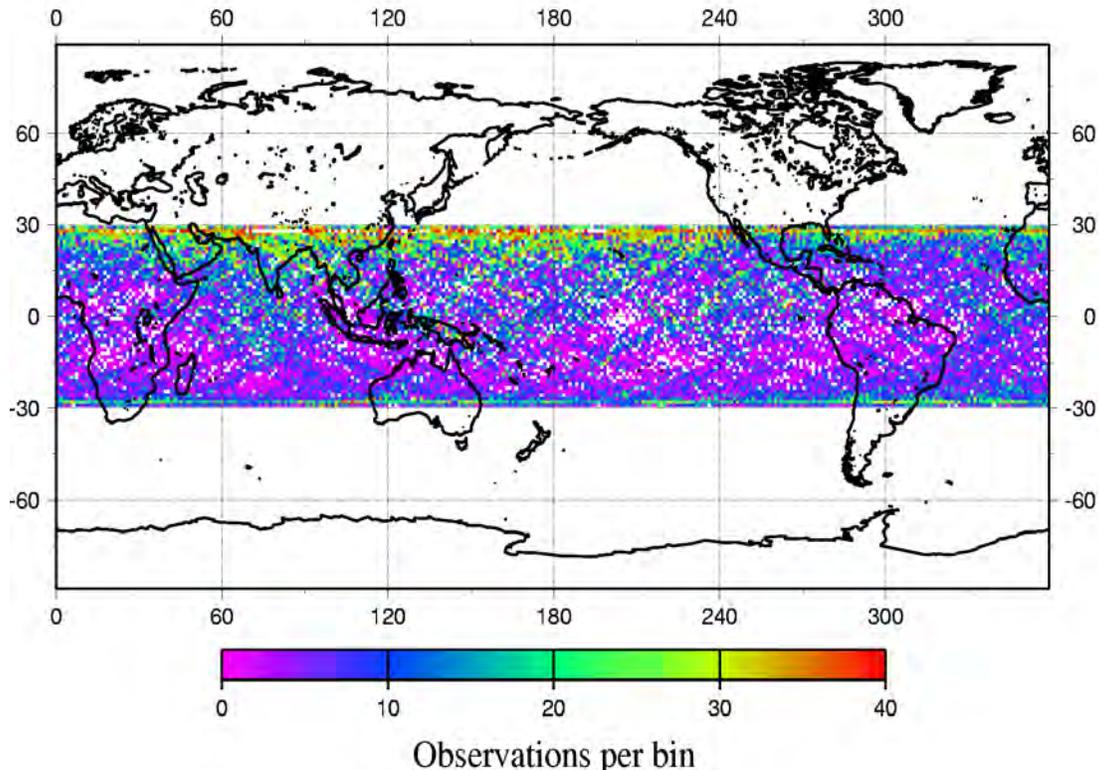
Figure 6.2.3.3–3. Spatial distribution of the EP/EUVE–IGS double-difference data, expressed as number of observations per 1° bins.

Rather than introducing known reference frame and modeling errors into the EP/EUVE data reduction runs, the GPS orbits were computed with GEODYN. The estimated parameters included the GPS state, solar radiation pressure coefficients, constant and one-cycle-per-revolution (1-CPR) empirical accelerations in the Y–bias direction, measurement biases for the phase ambiguities, and tropospheric scale biases for the Hopfield model on a half-hourly basis. Tests showed appreciable improvement in EP/EUVE orbit overlap tests when the tropospheric scale biases were estimated every half-hour instead of every 3 hours. The GPS orbits, including the tropospheric biases, were held fixed for the EP/EUVE data reduction runs. The preprocessed EP/EUVE data were then combined in a double-difference mode with the IGS L_c observables.

Force Modeling

We performed extensive tests to determine the force model parameterization that would yield the most accurate and consistent EP/EUVE orbits. Initially, the conclusions were based primarily on overlap analysis and comparisons to the orbits generated by *Gold* [1994]. As such, the first analyses proceeded with 30-hr arcs for September 15–16 and September 22–23, 1992. These

dates were chosen in order to replicate the work of *Gold* [1994], so that comparisons could be made to validate both sets of orbits. Unfortunately, only *Gold's* September 15–16 orbits were available, so the analysis was based on comparisons using only 2 days. Comparisons with TDRSS-based EP/EUVE orbits (see Section 6.2.3.4) gave additional insight that resulted in changes to the overall parameterization strategy.

Antenna offsets, solar radiation, and eclipsing. Before discussing orbit comparisons with external sources (e.g., JPL GPS or TDRSS), a summary of other tests will be given. Because of the uncertainty in the GPS antenna locations, GEODYN was used to estimate the antenna offsets and to observe the effect of perturbing the offset values. Not all coordinates of the antenna offset could be determined reliably using the EP/EUVE GPS data, and the estimated values varied tremendously depending on the arc of data selected. The changes in the orbit overlaps were examined but were inconclusive.

We formed hybrid double-difference range (DDR) observations, including data from both the GPS antennae on EP/EUVE, and solutions were attempted. The overlaps between two 30-hr arcs showed slight degradation over the arcs without the hybrid data type. Creating these DDR data increased the number of observations by approximately 15 percent, and previous analysis had shown that the amount of data available could make a significant difference in the results. Since the overlaps degraded with the use of the hybrid double differences, their use was not pursued in the EP/EUVE analysis. Nevertheless, these hybrid DDR data deserve future investigation.

The modeling of GPS satellites as they are transiting an Earth shadow boundary is incomplete. Therefore, we investigated the effects of excluding data from these satellites during the shadow boundary crossing and for up to 30 minutes afterwards. No appreciable effect was observed, so it was decided that these data would be left in all subsequent analyses.

Adjustment of the EP/EUVE solar radiation coefficient, C_R, was attempted with various combinations of other adjusted parameters. In all cases, this coefficient could never be resolved with any certainty. The lack of sensitivity was a probable consequence of the arcs being too short. Therefore, we adopted a nominal value of $C_R = 1.0$ in all EP/EUVE GPS-based analyses.

Initial force modeling. The EP/EUVE analyses were predicated on the assumption that excellent agreement with the JPL EP/EUVE orbits was the ultimate goal. The earliest analysis showed marked improvement as the number of estimated EP/EUVE drag coefficients, C_D, was increased. This improvement was not surprising given the variation of the projected cross-sectional area with respect to the velocity vector. We selected a parameterization frequency of 24 minutes, corresponding to approximately 1/4 of an orbital revolution. The resulting overlap agreement within the GEODYN-based orbits was excellent. A total position RMS of about 3.5 m on a 6-hour overlap of two 30-hour arcs was achieved for both September data sets. Agreement with the JPL orbits was also good; position differences were approximately 5 m RMS. However, frequent estimation of drag coefficients that provided this level of agreement almost certainly reduced the sensitivity to geopotential signals. Therefore, some other force model parameterization was sought that would maintain this good agreement, while yielding the fullest possible gravitational signal.

Simplified drag model. The estimation of a drag coefficient every quarter revolution effectively modeled the 1-CPR variations of the EP/EUVE projected cross-sectional area, albeit in a crude fashion. A more robust model of the spacecraft area variation was needed. The time-dependent variation of the spacecraft area could be effectively modeled by varying C_D. During the September data set, EP/EUVE was in survey mode, so we knew that the spacecraft was rotating about its X axis, which was pointed away from the Sun. A simplified drag model was developed based on predicted variations in the area, as mapped into C_D. It was assumed that the EP/EUVE solar arrays are fixed in the body system and orthogonal to the Sun during this phase of the mission. *Smith* [1996] verified that this was indeed a good assumption for this period. Further, the assumption was made that the variation in the direction to the Sun resulting from the location of EP/EUVE in its orbit was negligible. From the limited "mechanical" drawings at our disposal, EP/EUVE was treated as a rectangular box with two large flat plates, with the areas listed in Table 6.2.3.3–1.

Table 6.2.3.3–1. Estimated areas for EP/EUVE "box-wing" model.

Area Description	Area (m^2)
Long dimension area (along EP/EUVE X axis)	8.26
Short dimension area (orthogonal to EP/EUVE X axis)	4.13
Total panel area	17.50

The procedure took a nearly converged EP/EUVE velocity vector and the corresponding orbit period from a GEODYN data reduction as input. The velocity vector was rotated into the approximate EP/EUVE frame through the right ascension of the Sun in order to determine the angle from this vector to the X axis. This angle was then incremented through 360° to compute discrete projected areas, A_p, orthogonal to the velocity vector. Using a nominal value for the drag coefficient, C_{D0}, along with the average projected area over the arc, $\overline{A}$, discrete values for C_D were computed via

$$C_D = C_{D0} (A_{p /} \overline{A}) \qquad\qquad (6.2.3.3–10)$$

Tests indicated that applying a discrete value every 2.5 minutes, as determined in the above fashion, resulted in a drag model that was sufficiently smooth. Because the EP/EUVE velocity vector at epoch is a function of drag, this procedure is iterative, typically converging in two iterations when a nearly converged initial vector was used. However, the proper value for C_{D0} still had to be determined through overlap comparisons, both internally and with JPL orbits.

Empirical accelerations, both constant and 1-CPR, can be estimated while holding the drag model fixed. The result was that it was possible to maintain very good overlap agreement (both internally and with JPL) while applying the simplified drag model in conjunction with estimation of along-track constant and 1-CPR empirical accelerations. The drag model worked well for the September data, but gave degraded results for the analysis of data from later time periods.

Additionally, after September 1992, EP/EUVE was not necessarily maintained in survey mode, so a Sun-directed axis could not be determined.

Final force model parameterization. In order to select a definitive force model parameterization, the EP/EUVE data for the 3-day arcs in November 1992 were processed with various drag and empirical acceleration estimation strategies. A "box-wing" nonconservative force model was derived for EP/EUVE and included in the orbit tests. The RMS of fit of the two test arcs, as well as RMS position differences in their mutual 1-day overlap, were used as metrics to select the final force model parameterization. The GEODYN PANEL parameters describing the faces of the EP/EUVE box-wing model are summarized in Table 6.2.3.3–2. Nominal reflectivity values were assumed based on the properties of other spacecraft, such as T/P, that have a similar spacecraft bus.

Table 6.2.3.3–2. EP/EUVE "box-wing" model panel properties.

Panel	Area (m^2)	Vector Normal	Specular Reflectivity	Diffuse Reflectivity
1	4.13	1,0,0	.15	.6
2	4.13	-1,0,0	.15	.6
3	8.26	0, sin 30, cos 30	.15	.6
4	8.26	0, cos 30, -sin 30	.15	.6
5	8.26	0, -sin 30,-cos 30	.15	.6
6	8.26	0,-cos 30, sin 30	.15	.6
7	8.75	1,0,0	.1	.4
8	8.75	-1,0,0	.1	.4
9	8.75	1,0,0	.1	.4
10	8.75	-1,0,0	.1	.4

In all cases, the EP/EUVE state and measurement biases were estimated while the GPS orbits and troposphere biases were held fixed at the values determined from the reduction of the ground–ground double-difference data. The parameterization strategy and 1-day orbit overlap RMS differences (without reference frame solution removal) are presented in Table 6.2.3.3–3. Table 6.2.3.3–4 shows the residual RMS of fit and number of observations in each 3-day arc.

From Table 6.2.3.3–3, it is apparent that the simplified drag model is not suitable for the November data. Whereas the total position overlaps amounted to 3.5 m for the September data, the total overlap differences were 10.7 m for the November data. Frequent adjustment of the drag coefficient, one C_D every 24 minutes (labeled "24m C_D"), reduced the overlap differences to 4.5 m. The use of the box-wing model, coupled with less frequent estimation of the C_D and the estimation of daily 1-CPR along-track accelerations (labeled "panel"), degraded the overlap differences to 5.0 m. Estimation of the 1-CPR cross-track accelerations on a daily basis in addition to the 1-CPR along-track accelerations (labeled "panel3") reduced the overlaps from 5.0 to 2.1 m. Comparison of similar cases that differed only in the application of the box-wing model (e.g., "panel3" and "8h C_D") show that the box-wing model made no improvement when the 1-CPR accelerations were estimated. In terms of RMS of fit, all the box-wing and multiple C_D estimation schemes performed comparably. Estimation of the C_D values every 24 minutes

produced the smallest residuals—but at the cost of 4.5 m overlaps. This indicates that atmospheric density modeling errors exceeded the errors in modeling the projected surface area and drag characteristics of the spacecraft. Overall, the optimal strategy estimated the along- and cross-track 1-CPR empirical accelerations daily, in conjunction with a C_D every 4 hours. This is similar to the parameterization adopted for the TDRSS-based EP/EUVE orbit determination; however, the more continuous data coverage offered by the GPS tracking allowed for a more frequent parameterization.

Table 6.2.3.3–3. Overlap statistics from 3-day arcs in November 1992 for various EP/EUVE OD schemes. No rotations have been removed.

Arc Label	Description	Radial RMS (m)	Cross RMS (m)	Along RMS (m)	Total RMS (m)
DR	simple C_D model, Along-track 1-CPR/day, Along-track constant/day	2.81	4.40	9.28	10.65
24m C_D s	C_D /24 min.	0.59	4.01	1.92	4.48
panel	EP/EUVE Panel cards, Along-track 1-CPR/day, C_D /8 hrs	0.79	4.30	2.48	5.03
panel2	EP/EUVE Panel cards, Along/Cross-track, 1-CPR/day, C_D /8 hrs, Cross-track constant/day	0.46	1.16	1.89	2.27
panel3	EP/EUVE Panel cards, Along/Cross-track, 1-CPR/day, C_D /8 hrs,	0.45	0.91	1.85	2.11
8h C_D s	Along/Cross-track, 1-CPR/day, C_D/8 hrs,	0.44	0.91	1.87	2.13
panel4	EP/EUVE Panel cards, Along/Cross-track, 1-CPR/day, C_D /6 hrs,	0.38	0.88	1.76	2.00
6h C_D s	Along/Cross-track, 1-CPR/day, C_D /6 hrs,	0.38	0.88	1.76	2.00
panel5	EP/EUVE Panel cards, Along/Cross-track, 1-CPR/day, C_D /12 hrs,	0.56	0.79	4.62	4.72
4h C_Ds	Along/Cross-track, 1-CPR/day, C_D/4 hrs,	0.34	0.82	0.85	1.23

Table 6.2.3.3–4. Weighted residual RMS and number of observations for various parameterization schemes.

Arc	Arc 1		Arc 2	
Label	RMS (cm)	# of Obs	RMS (cm)	# of Obs
DR	62	26068	59	23938
24mCds	42	26068	39	23938
panel	48	26068	44	23939
panel2	45	26068	42	23939
panel3	45	26068	42	23939
8hCds	45	26068	42	23939
panel4	44	26068	42	23939
6hCds	43	26068	42	23939
panel5	46	26066	47	23934
4hCds	43	26068	42	23939

GPS EP/EUVE Arc Summary

The final GPS-based EP/EUVE-orbit-solution-specific force modeling and parameterization options are summarized in Table 6.2.3.3–5, and are in addition to or replace those listed in Tables 6.1.3–1 and –2. The solution statistics for the data included in the EGM96 development is given in Table 6.2.3.3–6. Two distinct classes of orbit fits are apparent: the first set with RMS of fit values in the 40–50 cm range, and the second with fits of 1–2 m. The source of the difference between these two sets is elusive, and has not been accounted for by attitude mode, arc length, or quality of data.

Table 6.2.3.3–5. Force model parameterization for GPS-based EP/EUVE OD.

Estimated Parameters	
Dynamical	Epoch State
	C_D/4 hrs
	Along/Cross-track 1-CPR/day
Observational	Phase Double-Difference ambiguities
Nonconservative Force Modeling	
Drag	Cannonball
Solar Radiation	Cannonball
Measurement Corrections	
Clocks (satellite and receiver)	Differenced out
Antenna Offsets	Attitude dependent
Troposphere Refraction	Goad modifications to Hopfield [*Goad*, 1974], plus 30-min. scale factors applied from GPS OD
Ionosphere Refraction	L_c on IGS-GPS, DRVID on EP/EUVE

Table 6.2.3.3–6. EP/EUVE orbit solution summary, using the JGM–2 geopotential model.

Epoch (YYMMDD)	Length (hrs)	Number of Observations	Weighted RMS (cm)	Attitude Mode	Internal Name
920915	57.5	10202	41.1	survey	wk6621
920918	23.7	7317	39.9	survey	wk6622
920922	95.1	29901	38.3	survey	wk6630
921103	120.0	41651	42.7	survey	wk6690
921222	18.3	11827	40.4	survey	wk6761
921227	88.1	16628	42.1	survey	wk6771
930314	56.0	26064	50.0	inertial	wk6881
930317	101.5	26003	49.8	inertial	wk6882
930323	20.8	10175	235.3	inertial	wk6891
930324	24.3	5282	145.5	survey	wk6892
930326	31.3	6973	272.7	survey	wk6893
930327	34.7	6248	469.2	survey	wk6894
930329	27.5	9036	1091.2	inertial	wk6901
Total	698.8	207307			

Orbit Overlap Analysis

Figure 6.2.3.3–4 shows an overlap comparison between two 30-hour arcs with 6 hours of common data for the September 15–16 data sets. The RMS overlap difference is 1.18 m radially, and 4.93 m in total position. The RMS radial difference is approximately equal to the predicted radial orbit error, which was found to be about 1 m for JGM–2 (see Figure 6.2.3.2–6). This indicates that the aliasing of the gravity errors in the initial state, and the time-variable errors in the force modeling, is not significantly larger than the geographically correlated radial orbit errors (which should cancel in the overlaps). Under the assumption that gravity modeling errors are the dominant source of error in the solutions, we should expect the effects of the aliasing of the gravity errors in the initial state to be approximately equal to or less than the predicted magnitude of the radial errors. The agreement between the radial overlap differences and the predicted radial orbit error demonstrated that the observed errors were consistent with the predictions for JGM–2.

Figure 6.2.3.3–5 presents a comparison between the September 15, 1992, GPS EP/EUVE orbits computed at GSFC and those determined by *Gold* [1994] at JPL. Large differences are present at the arc boundaries, and reference frame differences exist between the two orbits. To give a clearer indication of the true orbital agreement, statistics were computed only over the internal 20-hour overlap, after a frame rotation was estimated and removed via a Helmert transformation [*Hofman–Wellenhof et al.*, 1992]. The overlap is shown in Figure 6.2.3.3–6, for which the RMS difference is 1.09 m radially, and 4.50 m in total position. Figures 6.2.3.3–7 and –8 show the similar comparisons for the September 16 orbit solutions. The RMS difference of the central 20-hour portion (Figure 6.2.3.3–8) is 1.20 m radially, and 4.67 m in total RMS difference.

If we treat the reduced-dynamic JPL orbits as "truth" ephemerides, then the overlaps show that there is approximately 1.2 m of radial "error" in the GSFC dynamic solutions, in the absence of relative frame errors. This is in agreement with the predicted 1 m radial error caused by the errors in JGM–2. The internal consistency (precision) between the GSFC EP/EUVE orbits, indicated by the overlaps, indicates that we are modeling and converging to a consistent dynamic orbit. Moreover, the comparisons with the JPL "truth" orbits indicate that the accuracy of the solutions we converge to is comparable to the precision indicated by the overlaps. However, the uncertain knowledge of the cause of the entire difference between the two frames implied by the estimated Helmert transformations requires that we consider the accuracy of the solutions to be somewhat worse than the precision.
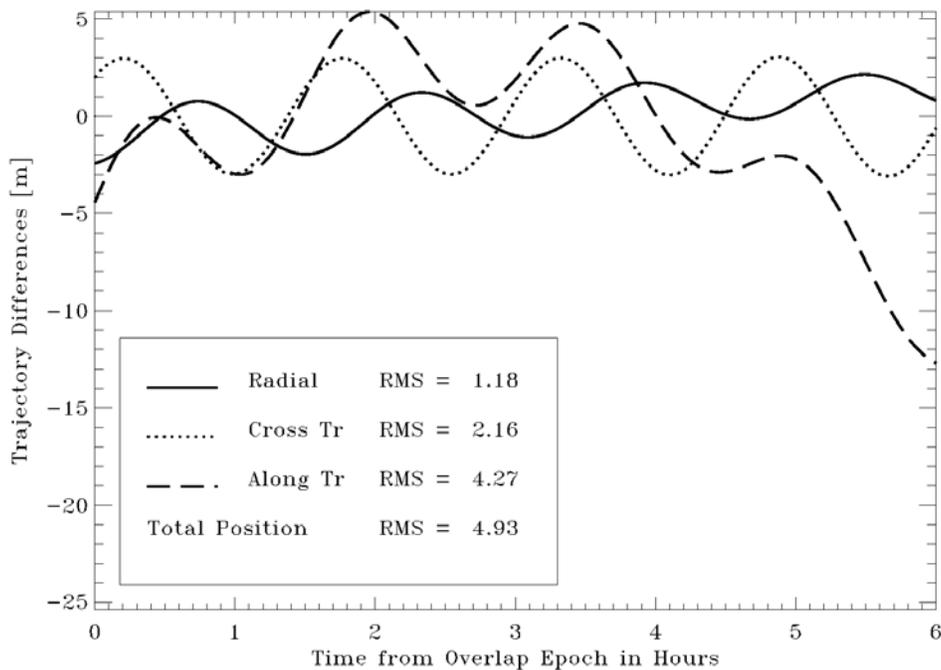
Figure 6.2.3.3–4. Overlap differences for GSFC GPS-based 30-hour EP/EUVE arcs (September 16 solution–September 15 solution). Solutions used DRVID and fully dynamic techniques.
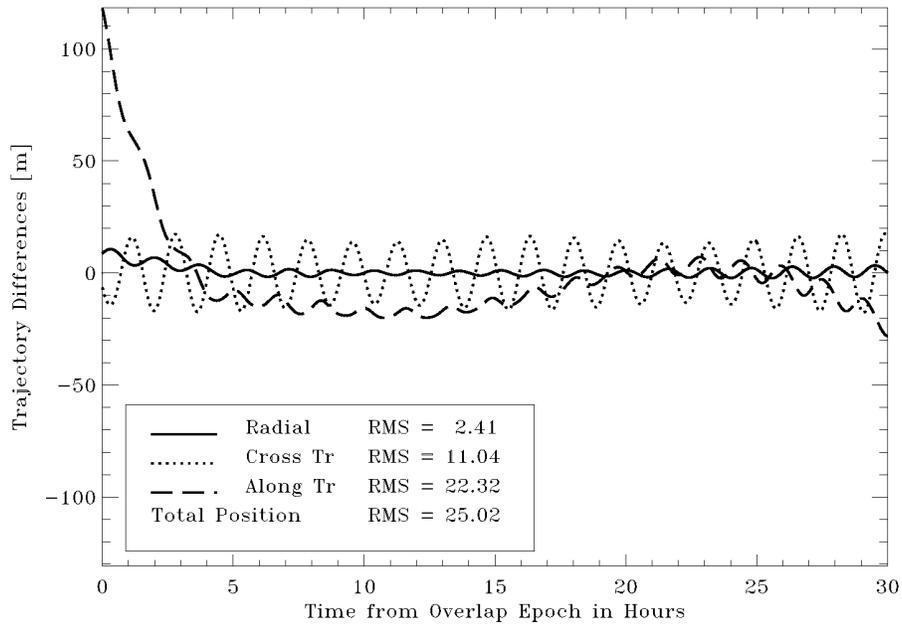
Figure 6.2.3.3–5. Difference between the JPL and GSFC GPS-based EP/EUVE orbit solutions for September 15, 1992. JPL orbit used reduced-dynamic techniques. The GSFC orbit used DRVID and fully dynamic techniques. Edge effects and frame rotations have not been removed.
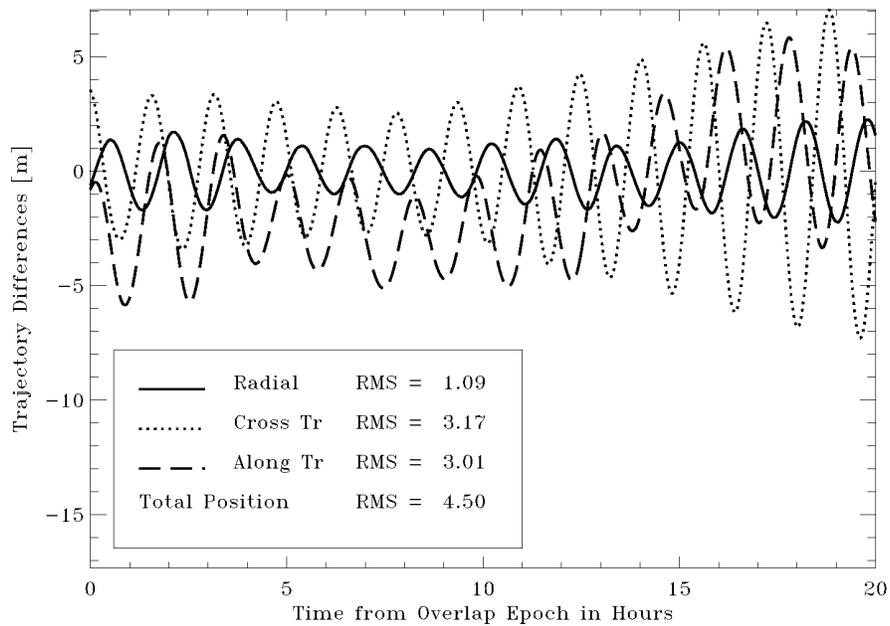
Figure 6.2.3.3–6. Difference between the JPL and GSFC GPS-based EP/EUVE orbit solutions for September 15, 1992, after removal of edge effects and frame rotations.
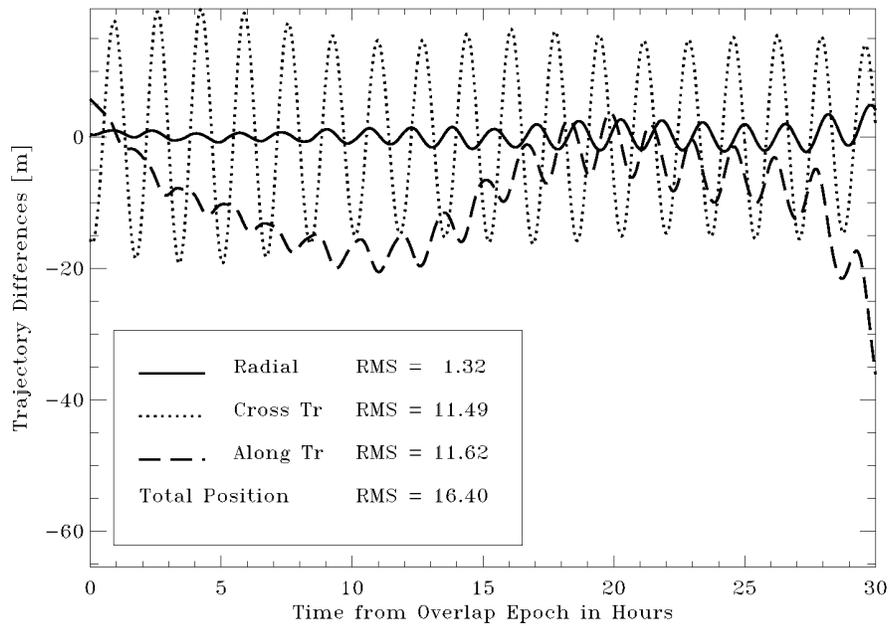
Figure 6.2.3.1–7. Difference between the JPL and GSFC GPS-based EP/EUVE orbit solutions for September 16, 1992. JPL orbit used reduced-dynamic techniques. GSFC orbit used DRVID and fully dynamic techniques. Edge effects and frame rotations have not been removed.
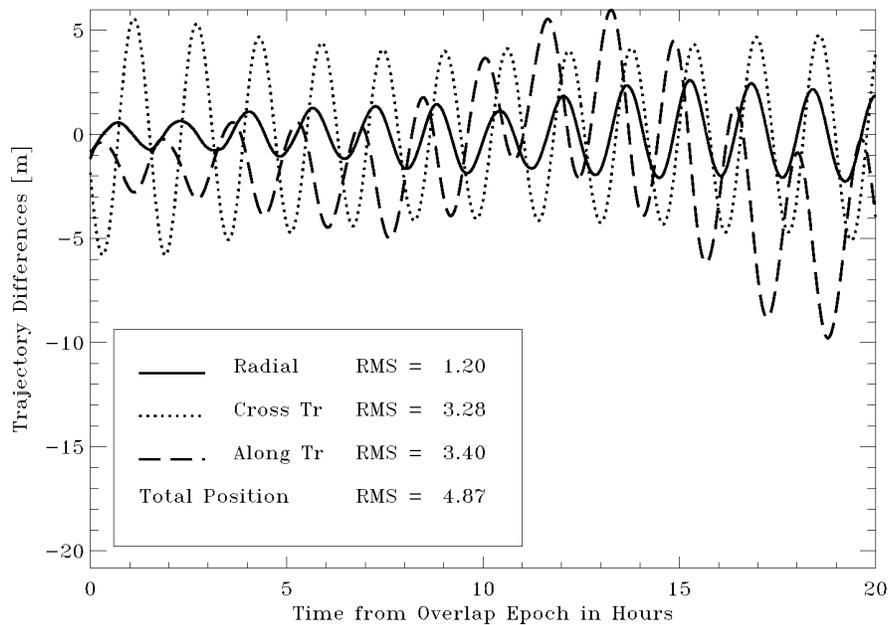
Figure 6.2.3.3–8. Difference between the JPL and GSFC GPS-based EP/EUVE orbit solutions for September 16, 1992, after removal of edge effects and frame rotations.

6.2.3.4 Processing of Tracking and Data Relay Satellite System (TDRSS) Data for EP/EUVE

Tracking and Data Relay Satellite (TDRS) System (TDRSS) tracking of EUVE from the period July 29 to September 16, 1994 (corresponding to T/P cycles 69–73), was processed to support the development of EGM96S. EP/EUVE was heavily tracked during this period as a preoperational test for the then-new Second TDRSS Ground Terminal (STGT). This dense tracking, combined with solar activity levels that were lower than the immediate postlaunch phase of the mission, made this period attractive from the viewpoint of performing precise orbit determination of the EP/EUVE spacecraft.

Overview of TDRSS

TDRSS is a constellation of six geosynchronous spacecraft that provide tracking and communication support to a host of Earth-orbiting spacecraft. A minimum of 85 percent tracking coverage is possible for users above 200 km altitude, based on user support requests [*Phung et al., 1980*]. Ground system support and communications are provided by two facilities located in White Sands, New Mexico. TDRSS can provide three types of user spacecraft telecommunication services: S band Single Access (SSA) by either of two high-gain antennas (HGA), Ku band Single Access (KSA), or S band Multiple Access (MA) via a phased antenna array on the face of the spacecraft. Figure 6.2.3.4–1 illustrates the layout of the antennas on each TDRS. These services may be provided in various modes and data rates, and can also provide range and range-rate tracking services in conjunction with the data traffic. Two-way (coherent) TDRSS S band tracking originates as a K band signal at the White Sands Ground Terminal (WSGT) or the Second TDRSS Ground Terminal, which is transmitted to the TDRS, then transmitted to and from the user spacecraft via S band, and finally transmitted back to WSGT via K band. If the user is equipped with a USO, useful one-way return (from the user to TDRS as S band, then from TDRS to ground as K band) or forward S band (ground to TDRS as K band, then to the user—which stores or uses the data onboard—as S band) range-rate tracking data may also be provided on a schedule complimentary to the two-way tracking. In most cases, the limitations are ground terminal constraints. Every TDRS has the capability to support higher data rates and formats assuming the ground terminal(s) are modified to accommodate these increased capacities.

The TDRS orbits are determined operationally using data from the Bilateration Ranging Transponder System (BRTS). This system consists of a set of TDRSS transponders located at fixed positions on the ground (two at WSGT, two at Ascension Island, one at American Samoa, and one at Alice Springs, Australia) that are tracked using the TDRSS S band range and range-rate tracking services; since the transponders are at known locations, the determination of the TDRS orbits is possible. BRTS tracking has a number of deficiencies: the range-rate signal is relatively small to these geostationary spacecraft, and the four BRTS ground transponders visible to each TDRS do not provide a robust tracking geometry. Furthermore, the S band signals between each TDRS and the BRTS transponders suffer from ionospheric refraction effects. TDRS's are treated operationally as homogeneous spheres when evaluating the force and

measurement models in the operational orbit determination process. Consequently, the operational TDRS trajectories are limited to 30–40 m total position accuracies [*Cox and Oza*, 1994]. These errors corrupt the TDRSS-tracked satellite ephemerides, and represent significant contributions to their orbit error budget.
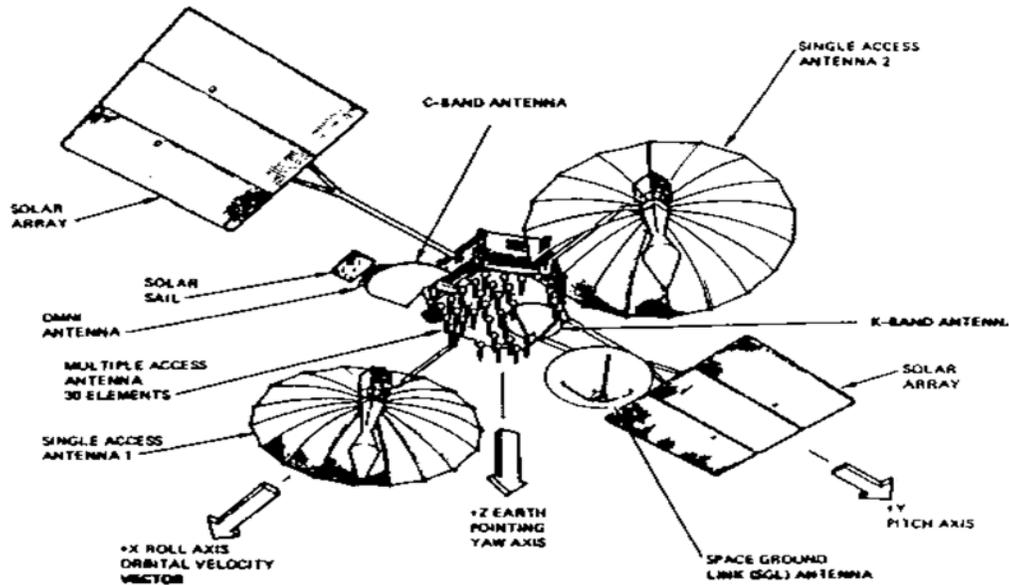
Figure 6.2.3.4–1. TDRS spacecraft.

The deficiencies in operational TDRSS orbit determination can be addressed largely by incorporating more detailed satellite force and measurement models and by exploiting the precise knowledge of the T/P spacecraft position. The T/P orbits on the mission geophysical data records routinely are produced with less than 3 cm radial and 10 cm total position root mean square (RMS) error over the 10-day orbit repeat period using Satellite Laser Ranging (SLR) and Doppler Orbitography and Radio Positioning Integrated by Satellite (DORIS) tracking data [*Tapley et al.,* 1994 and *Marshall et al.,* 1995b]. Consequently, these independent, SLR/DORIS-based, precise ephemerides can be used to create a "roving ground station," capitalizing on the extensive geometry of the link between each TDRS and T/P and the reduced ionospheric refraction effects associated with T/P orbit altitude of 1336 km [*Marshall et al.,* 1995a*, Marshall et al.,* 1996*,* and *Luthcke et al.,* 1997b]. The T/P orbit is held fixed and the TDRS orbits are determined from the one- and two-way range and range-rate TDRS-T/P tracking data in addition to the BRTS ranging and K band Tracking, Telemetry, and Control (TT&C) range data. TDRS orbits determined this way have uncertainties in the 1–2 m range and can then be used to perform orbit determination of any other spacecraft of interest. Figure 6.2.3.4–2 illustrates this process schematically.
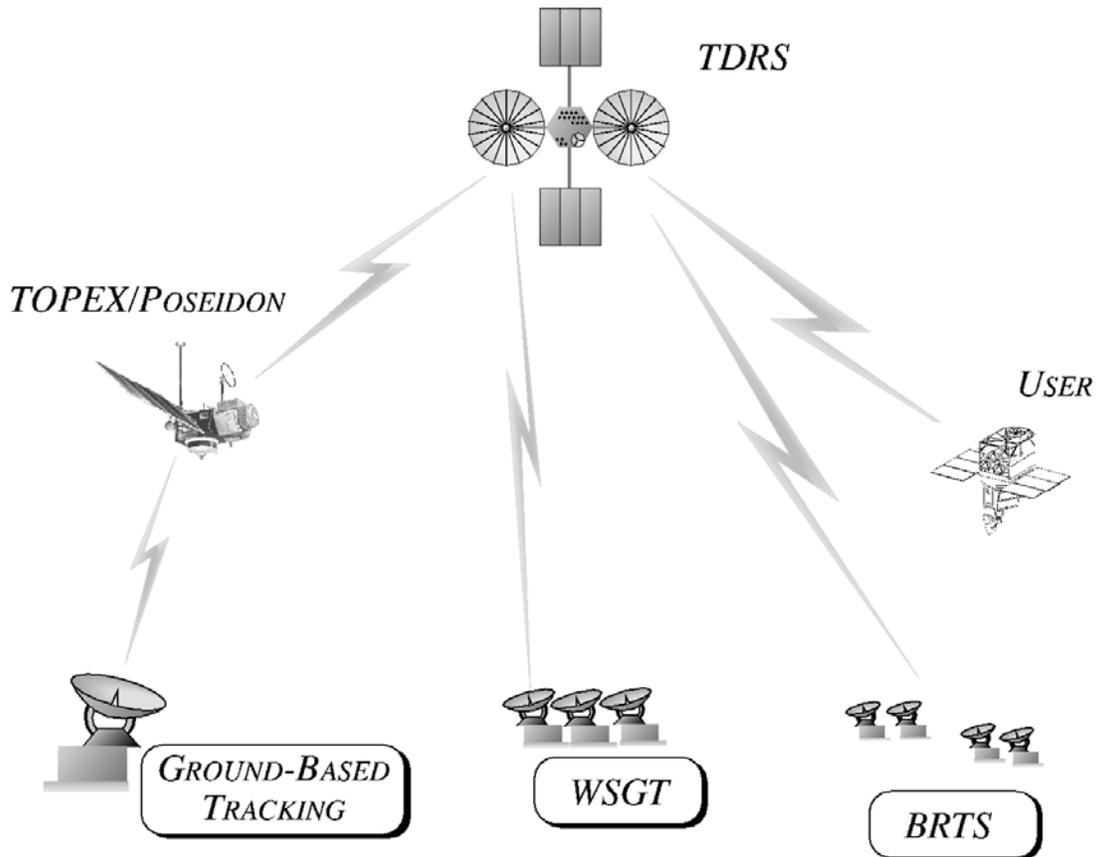
Figure 6.2.3.4–2. TDRSS orbit determination geometry.

EP/EUVE Tracking Coverage, Modeling, and Parameterization

Figure 6.2.3.4–3 illustrates the geographic distribution of the EP/EUVE tracking coverage provided during cycles 69 through 73, which consisted of two-way S band range and range-rate tracking. Despite the presence of a USO on EP/EUVE, one-way range-rate tracking was not available due to a transponder failure that occurred in March 1994. The two areas of tracking coverage provided are centered under each of the viewing TDRS spacecraft. Tracking over the central Pacific region was provided via TDRS–5, which was stationed at 174.3° West longitude, and the WSGT facility. Coverage over South America, the Atlantic Ocean, and Africa was provided by TDRS–4 at 41° West longitude (supported by WSGT), which shared the support coverage with TDRS–6 at 46° West longitude (supported by STGT). The 5° separation between the TDRS–4 and –6 resulted in the wider zone of coverage seen in the figure. The total coverage during this period represents approximately 60 percent longitudinal coverage. While this is less than the maximum possible using TDRSS, the areas of coverage provided a unique data set that complimented those of the other tracking technologies used in EGM96S.

Superior TDRS orbit accuracies are possible using the "roving ground station" technique [*Marshall et al.,* 1995a and 1996]; however, the limited TDRSS tracking of T/P during this period required the use of simultaneous user/TDRS orbit determination techniques to improve the TDRS orbits. TDRS–6 orbit solutions in particular would have been dominated by the BRTS data, and would have suffered accordingly. Consequently, a simultaneous TDRS–EP/EUVE solution strategy was chosen to capitalize on the additional geometric constraints provided by the tracking of EP/EUVE; this decision was also supported by results of analysis summarized in [*Cox and Oza,* 1994]. These TDRSS-based EP/EUVE solutions were 6 to 10 days in length, with the arc start and end times determined from the T/P cycle boundaries and TDRS maneuvers.
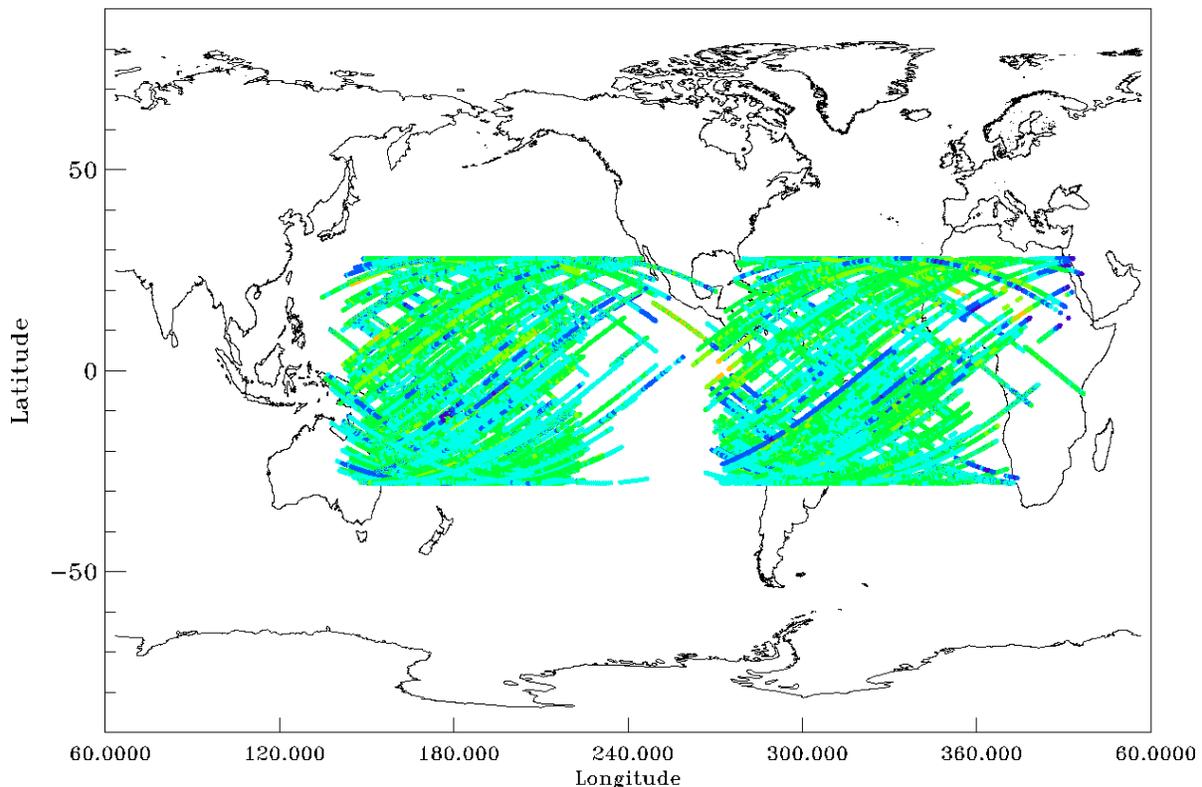
Figure 6.2.3.4–3. EP/EUVE TDRSS tracking coverage, July 29–September 16, 1994.

As a result of the GPS-based tests, which showed that use of the box-wing model made no impact on the residuals, a box-wing model was not used. Consequently, EP/EUVE was treated as a cannonball, with no modeling of the celestially targeted attitude for nonconservative force modeling purposes, although the attitude and antenna offsets were modeled. Comparatively dense TDRSS tracking of EP/EUVE during this period permitted the estimation of C_D values nominally every 8 hours. The constant area provided by the cannonball model, in conjunction

with the estimated C_D parameters, is sufficient to model the average effect of drag, although the 2-CPR variation in area is neglected.

Given the comprehensive analyses of the TDRSS tracking data performance and the positive orbit determination results realized through the use of T/P, an effort to better model the direct solar and Earth radiation accelerations on the TDRS was undertaken. Rather than treating the spacecraft as a homogeneous sphere, it is represented by a combination of 24 flat plates, inertially oriented to mimic the actual attitude [*Luthcke et al.*, 1997a]. These models are similar to the "macro-models" developed for T/P. The nonconservative forces acting on each plate are computed and vectorially summed to yield the aggregate acceleration on the center of mass. For each plate, a several parameters are modeled, including area, specular and diffuse reflectivity, and emissivity. However, the emissivity parameters are not used on TDRS because no thermal imbalance model is available.

Force modeling and solution parameterization details specific to the TDRSS-based orbit determination of EP/EUVE are summarized in Table 6.2.3.4–1; further specifics about the T/P nonconservative force modeling can be found in [*Antresian,* 1992; *Antresian and Rosborough,* 1992; and *Marshall and Luthcke*, 1994b]. Of note is the selection of data uncertainties. The relative data uncertainties between TDRSS data types (e.g., range and two-way range-rate) were determined using fits of the data to solutions based the two-way T/P range-rate data. These data were chosen as the basis for the relative weighting because of the coverage and because no data corrections had to be estimated. Once the data uncertainties were determined, the next step was to establish the relative weights between those used for the EP/EUVE and T/P spacecraft. In order to realize the most benefit from the use of T/P, the relative weighting between T/P and EP/EUVE was selected to allow the T/P data to dominate the TDRS solutions where EP/EUVE data were not available. The uncertainties used for T/P effectively reflect the combination of noise and systematic modeling errors in the data. The data uncertainties used for EP/EUVE were increased (i.e., the data were downweighted) with respect to those used for T/P; after a brief analysis, which is not presented here, increasing the data uncertainties by 5x was found to provide reasonable results.

During most periods, the TDRSS signals were received and transmitted by T/P and EP/EUVE using high-gain antennas (HGA). The T/P HGA is located on a boom on the zenith side of the spacecraft, requiring that the attitude history and antenna offsets be incorporated in the observation model in order to eliminate 1-CPR structure in the T/P residuals. The 2.5 m EP/EUVE high-gain TDRSS antenna offset was modeled, along with the commanded celestially targeted attitude. Details of the EP/EUVE attitude can be found in Section 6.2.3.1.

Antenna offsets were modeled for the TDRS spacecraft; this included offsets for the Single Access antennas, a nominal offset for the Multiple Access phased antenna array, and the K band space-to-ground-link antenna. Test runs showed that the EP/EUVE and BRTS ranging suffered from biases between the different S band tracking service types; these biases were having a detrimental effect on the EP/EUVE orbit determination. In an effort to correct for relative biases between the tracking service types, the Z-axis (nadir) component of the offsets were modified to correct for these differences. Consequently, the TDRS center of mass implied by the antenna

locations is not correct, potentially scaling the TDRS orbits, and contributing to a spurious estimation of the magnitude of GM in a gravity solution. The value of GM was estimated separately for the TDRSS-based EP/EUVE solutions within the EGM96S solution to prevent adverse effects on the scale of the solution. The recovered value of 398600.4365×10^9 m^3/s^2 is significantly less than the accepted value of 398600.4415×10^9 m^3/s^2 from *Ries et al.* [1992].

Table 6.2.3.4–1. Modeling and parameterization for the TDRSS-based EP/EUVE orbit determination.

Modeling	TDRS–4/5/6	TOPEX/POSEIDON	EP/EUVE
Dynamical parameters estimated	Epoch State Along-track constant and 1-CPR EA per day Cross-track 1-CPR EA/d, where significant 2-way T/P data exist	Applied from Precise Orbit: Epoch State Along-track 1-CPR EA/d Cross-track 1-CPR EA/d C_D per 8 hours	Epoch State Along/cross-track 1-CPR EA/arc C_D/8 hrs
Observational parameters estimated	Range bias/TDRS/arc for BRTS range	Range bias/TDRS/arc USO clock bias, drift, and acceleration TDRS–4 1-way range-rate scale bias	Range bias/TDRS/arc
Gravity	PGS5784 - a derivative of the IUGG satellite-only model described in Section 6.3.1		
Nonconservative Force Models Force Model	TDRS Macro Model for Solar and Earth radiation [*Marshall et al.*, 1995a]	T/P Macro Model for Solar, Earth, and radiation, and drag [*Marshall and Luthcke*, 1994a and 1994b]	Cannon ball 16.3 m^2 3243.05 Kg
Measurement corrections	Attitude- and CG-dependent TDRS antenna models Applied BRTS transponder delay range biases	Attitude- and CG-dependent TDRSS high-gain antenna Applied T/P transponder delay range bias	Attitude- and CG-dependent antenna model Applied transponder range bias
Station Complement Ground Terminal (TDRS) BRTS Transponders	WSGT (4,5), STGT (6) WHSJ, WH2J (4,5,6) ALSJ, AMSJ (5) ACNJ, AC2J (4,6)	WSGT (4,5)	WSGT (4,5), STGT (6)
Adjusted	No	No	No
Frame of Coordinates[1]	ITRF90 (from WGS84)	ITRF90 (from WGS84)	ITRF90 (from WGS84)
Tracking Data @ 1/10s 1-way range-rate 2-way range 2-way range-rate	Passes per day per TDRS: 10x4.5-min. via BRTS	Passes per day: 5x40-min. 1x40-min. 1x40-min.	Passes/day: 9x30-min. 9x30-min.
Data Weights 1-way range-rate 2-way range 2-way range-rate	 3 m	.10 mm/s 2 m .05 mm/s	 10 m .25 mm/s

Key: 1-CPR: one-cycle-per-revolution   EA: empircal acceleration
       CG: center of gravity   USO: ultrastable oscillator
Notes: 1.   The "roving ground station" technique will result in the reference frame being between that of ITRF90 and that of T/P

Bias estimation consisted of a range bias estimated for each TDRS as an aggregate over the solution arc for all BRTS ranging, and a similar bias was estimated for the user-service ranging to T/P and EP/EUVE. These estimated biases serve to accommodate uncorrected hardware equipment delays in the signal handling that occur between the ground equipment and the TDRS spacecraft, and are applied in addition to the modeled biases for each target transponder (BRTS and user). In actuality, these transponder biases should be modeled as transponder delays that affect all data types passing through a given transponder. However, GEODYN currently lacks the ability to model and estimate these delays for the TDRSS tracking types, so range biases were estimated by data type. Estimation by type resulted in separate biases for BRTS and the users; use of a combined bias for both BRTS and the users would add another constraint to the system, resulting in a stronger solution.

In addition to the range biases, clock biases, drift, and acceleration terms were estimated for the T/P USO. The estimation periods are broken at changes in the T/P attitude steering mode (i.e., a new period starts at each transition from sinusoidal to fixed yaw steering, or yaw flips). For unknown reasons, the T/P USO follows a linear drift only during periods of sinusoidal steering. During fixed yaw periods, the average drift rate is different, and exhibits an acceleration. Because the behavior is associated with the attitude mode, the drift and acceleration terms are split at yaw flips when one occurs during a solution arc. Modeling this change in behavior was absolutely necessary to determine the best possible TDRS orbits in support of the EP/EUVE orbit estimation.

As discussed in the preceding sections, the EP/EUVE inclination and altitude filled a critically undersampled altitude and inclination in the JGM series of geopotential models [*Nerem et al.,* 1994; and *Tapley et al.*, 1996]. In order to achieve the most accurate EUVE orbit solutions possible for inclusion in EGM96S, an updated gravity model derived from JGM–2S was used for the reduction of the tracking data. The PGS5785 gravity model was a satellite-only model that included a first-generation set of EP/EUVE normal equations, as well as other new and reprocessed data that were developed for the IUGG satellite-only model PGS5737 (see Section 6.3.1 for details on PGS5737).

Orbit Determination Results

The interim model PGS5784 substantially improved the EP/EUVE orbit determination. Data fits, along with the number of observations used in the generation of the EP/EUVE normal equation sets, are shown in Table 6.2.3.4–2. Normal equations for the T/P–TDRS or BRTS tracking were not included in EGM96S. The 2 years' worth of T/P tracking in the solution made this relatively short span of data redundant. BRTS tracking was not included in the solutions because of the poor sensitivity of the BRTS data to the effects of the geopotential on the high-altitude TDRS satellites.

Average TDRS RMS overlap values for the final reduction case are shown in Table 6.2.3.4–3. These overlap values are averages of 5-day ephemeris comparisons between the cycle 71 and 72 solutions and the 10-day cycle 72 overlap solution. These statistics reflect the precision in the orbit solutions and are not a direct measure of accuracy since both trajectories can share common

errors. However, when used in conjunction with the solution residual statistics, the overlaps can be used to qualitatively assess the overall solution quality. Given the lack of two-way TDRS–T/P data, the TDRS orbits are slightly degraded; previous analysis [*Marshall et al.,* 1995a] indicates that the total anticipated TDRS errors were approximately 10 to 15 m RMS with a precision of 7 to 10 m RMS. Conservatively assuming a 10 to 15 m TDRS positional uncertainty, the uncertainty imparted on the EP/EUVE orbit—based on the geometrical considerations of the TDRS altitude and the EP/EUVE altitude—is approximately 2.4 m. Comparison of the EP/EUVE range residuals to those for T/P imply an additional ~.8 m RMS of position error in range space. The two-way range-rate RMS residuals are ~.6 mm/s greater than T/P, which would correspond to an additional error of 0.9 meters RMS, if the cause were a constant radial displacement. Taking the error implied by the range-rate data (0.8 meters), and forming the root sum square with the implied range error (0.8 m), the frame uncertainty caused by TDRS position errors (2.4 m) yields an implied uncertainty of 2.7 m.

Table 6.2.3.4–2. T/P, EP/EUVE, and BRTS RMS Residuals for T/P cycles 69–73.

Cycle	TOPEX/POSEIDON			EP/EUVE			BRTS
	1-way RRT RMS (mm/s)	2-way RRT RMS (mm/s)	2-way RNG RMS (m)	Num. Obs. RRT RNG	2-way RRT RMS (mm/s)	2-way RNG RMS (m)	2-way RNG RMS (m)
69	0.80	0.58	0.91	11060	1.24		2.55
				11202		1.91	
70	1.07	0.55	1.11	8393	1.42		2.07
				12829		2.04	
71	1.09	0.64	1.10	15131	1.25		1.59
				16921		1.79	
72ovl[1]	1.05	0.49	1.51	17412	1.16		1.74
				19735		1.42	
72	0.95	0.61	1.20	19199	1.12		1.83
				19443		1.49	
73	0.82	0.42	0.71	10243	1.39		1.77
				27005		1.83	

1. This solution used for overlap testing only. TDRS maneuvers, and the resulting loss of EUVE tracking in the solutions, precluded meaningful overlaps of the other cycles.

Table 6.2.3.4–3. Average RMS overlap values for T/P cycles 71 and 72.

Spacecraft	Average Overlap (m)
EP/EUVE	1.8
TDRS–4	3.3
TDRS–5	5.3
TDRS–6	6.2

Normal Equations

To simplify the processing of the normal equations for the EP/EUVE tracking data, the TDRS orbits were constrained with a sigma of 0.5 m in position, $\sigma=.00005$ m/s in velocity, and $\sigma = 1\times10^{-8}$ for the general acceleration parameters. These constraints reproduced the uncertainty of the T/P and BRTS tracking defining the TDRS orbits, and eliminated the need for directly including a set of normal equations linking each TDRS to T/P and to the BRTS transponders. Range biases for EP/EUVE were estimated along with the orbit in the gravity solution. The WSGT, STGT, and BRTS transponder positions were not estimated due to the limited viewing geometry between the TDRS spacecraft and the ground sites, and the high correlations with the estimated range biases. As mention previously, a separate GM value was estimated in EGM96 for the TDRSS-based EP/EUVE data to account for scale errors. In addition to this, a separate set of harmonics, complete to degree and order 3, was estimated separately for this set of data. By doing this, any potential long-wavelength error or reference frame distortion in the TDRSS tracking and EP/EUVE orbit determination could be accommodated, while still permitting the nearly continuous data to provide maximal short-wavelength geopotential contributions. The maximum degree and order of 3 was chosen to accommodate possible distortions caused by combining data from the TDRS, each defining its own frame for the user, and the 140° separation between the nominal TDRS on-orbit locations. These approaches were tested experimentally in the overall data weight and calibration process.

6.2.4 GPS/MET

The Microlab–1 spacecraft was launched on April 3, 1995, on a Pegasus launch vehicle into a near-circular orbit at 740 km altitude and 70° inclination. The spacecraft carried a dual-frequency, eight-channel, TurboRogue™ GPS receiver to test limb sounding of the atmosphere using the Global Positioning System (GPS) [*Ware et al.*, 1996]. The purpose of this experiment was to track the GPS satellite signals as they traversed the ionosphere and troposphere. The perturbations in the phase of the GPS signals allow the development of inferred profiles of temperature and pressure with altitude. The GPS/MET experiment was designed to test the feasibility of sounding the atmosphere with the radio occultation technique using GPS, and to set the stage for future missions where such profiles might be used in routine weather forecasting and climatological studies. The objective of the GSFC analysis was to process the GPS/MET data with GEODYN, and assess their contribution toward improving models of the geopotential.

6.2.4.1 Spacecraft Description

A schematic of the Microlab–1 spacecraft is shown in Figure 6.2.4.1–1. The 74.8 kg spacecraft consisted of a cylindrical bus (1.04 m diameter x 0.38 m width), two solar arrays (diameter 0.97 m), and a gravity gradient boom with a tip mass to provide attitude stabilization. The attitude was controlled using three magnetic torque rods. Attitude sensors included six Sun sensors, two Earth sensors, and one magnetometer. Microlab–1 also carried a Trimble TANS Vector GPS receiver
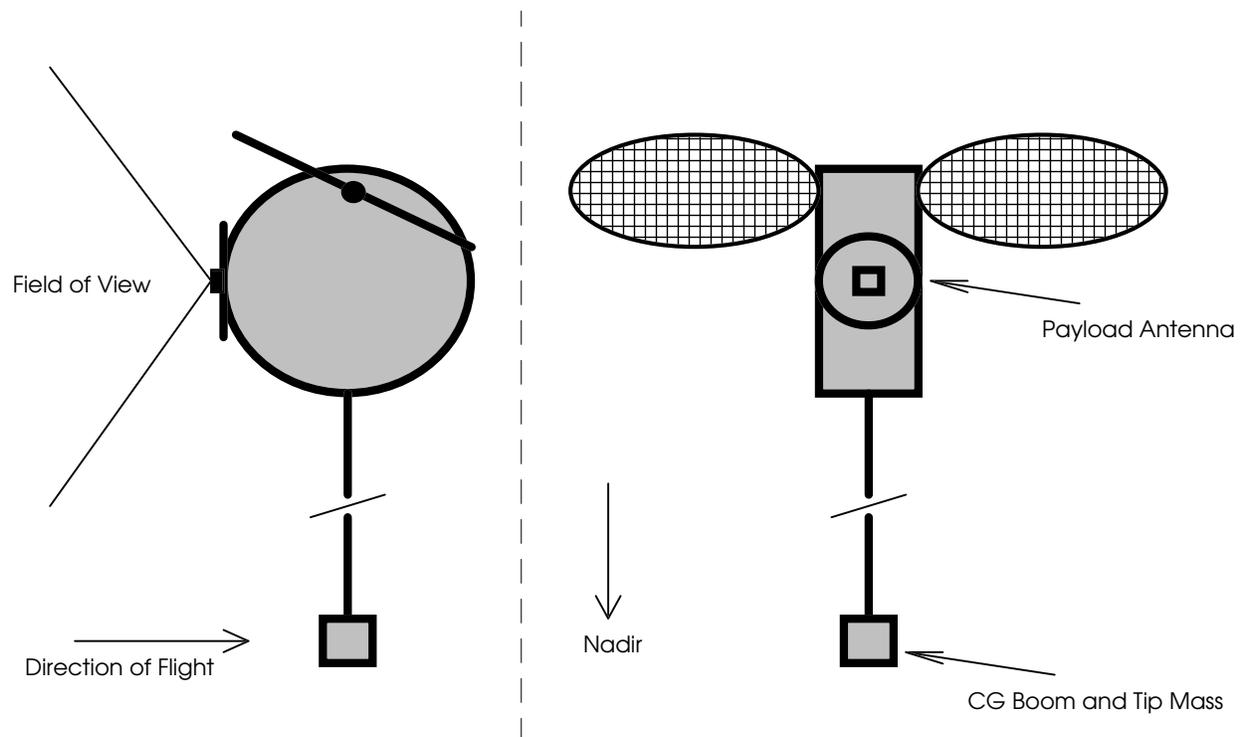
Figure 6.2.4.1–1. The Microlab–1 spacecraft.

for attitude determination. The GPS/MET antenna was mounted on the rear of the spacecraft 0.51 meters from the center of mass, in the antivelocity direction. Although the nominal mission plan was to observe setting occultations (by looking aft), the spacecraft could also be yawed 180° to see rising occultations.

6.2.4.2 Data Description

The data provided by University Corporation for Atmospheric Research (UCAR) consisted of phase and pseudorange observables, at both L1 and L2, at 10-second intervals in RINEX format. The time periods of greatest interest were those when antispoofing (A/S) was turned off in April–May, June–July, and October 1995. Although the TurboRogue was a codeless receiver, which allows tracking with A/S on, the periods when data were analyzed were those when A/S was turned off. The first such period occurred shortly after launch in April–May 1995, with subsequent 20-day periods in June–July and October 1995. The early data suffer from significant data gaps, which become less important later in the mission.

6.2.4.3 Data Processing Methodology and Modeling

The GPS/MET tracking data were processed as double differences with GEODYN [*Pavlis et al*, 1996], using a similar procedure as that described above in Sections 6.2.2 and 6.2.3. Although the GPS/MET receiver did acquire data at frequencies as high as 1 Hz to satisfy the requirements of the radio occultation experiment, the data were decimated to 30 seconds spacing to form double differences with IGS ground network data. Analysis of data at 30-second intervals are more than adequate for orbit determination purposes. Double differences were formed using a globally distributed network of ground stations. The Microcosm GPS Data Formatter (from Van Martin Systems, Inc.) was used to read the input RINEX data files, detect and, if possible, fix cycle slips using the Blewitt algorithm [*Blewitt*, 1990], and form the double differences. Where the cycle slip could not be repaired, a new ambiguity bias was created for that configuration of ground receiver, GPS/MET receiver, and two GPS satellites.

The first step was the determination of the GPS orbits. Double differences were formed with the ground stations and two GPS satellites. The weekly reports of the International GPS Service were scrutinized to ascertain which ground stations or GPS satellites might be anomalous, and these were excluded from both the GPS and GPS/MET orbit determination. The ranges on the ground side of the double difference were corrected for tropospheric refraction using the Hopfield model [*Hopfield*, 1971] using an approach that adjusted scale corrections every 3 hours for each of the ground stations. The GPS/MET tracking data were processed in arcs of 1 to 3 days' duration. Thus, in order to derive a dynamically consistent and continuous GPS orbit, the GPS orbits were determined over the same period as the GPS/MET tracking arc. Next, the newly determined GPS orbits were held fixed while determining the GPS/MET orbits. In addition, the troposphere parameters determined in the GPS OD were applied, but not adjusted, when the orbit of GPS/MET was computed. This approach was used to prevent the orbit errors from GPS/MET contaminating the GPS orbits. The orbit error on GPS/MET was dominated by the atmospheric drag mismodeling caused by the low altitude (740 km) of the spacecraft, the high area-to-mass ratio, and the complex shape.

The *a priori* force model on GPS/MET included the JGM–2 gravity field, with extended tides derived from GEM–T3 (PGS4846X). The station coordinates for the GPS sites were derived from ITRF94 [*Boucher et al.*, 1996]. Drag coefficients were adjusted every 8 hours, although, occasionally, data gaps required a less frequent determination. Data at less than –15° elevation with respect to the GPS/MET local horizontal were deleted in order to avoid ray paths traversing the atmosphere and/or regions where the first-order ionosphere correction based on the linear combination of the L1 and L2 frequencies might break down due to higher order ionospheric refraction contributions. Similarly, with respect to the ground stations, data at less than 20° elevation were also excluded from the solution in both the GPS and the GPS/MET orbit determination. In order to avoid unnecessary dilution of the solution through the estimation of an excessive number of phase ambiguity biases, double differences, including GPS/MET, belonging to configurations less than 8 minutes in length were eliminated from the solution. A similar constraint was applied in the GPS OD, with double differences from configurations lasting less than 45 minutes being excluded.

Two orbits were determined for GPS/MET. In the first step, drag coefficients and a single solar radiation pressure coefficient was adjusted along with the state of the GPS/MET spacecraft. In the second step, the converged value of solar radiation pressure coefficient (Cr) was held fixed, and empirical 1‑CPR terms were adjusted. Solar radiation pressure coefficients and empirical 1‑CPR accelerations cannot usually be adjusted simultaneously because of their high correlations. The use of the 1‑CPR terms has the advantage of drastically reducing the orbit error, as discussed below, at the potential cost of removing useful gravity field signal (primarily from the resonances and odd zonals).

6.2.4.4 GPS/MET Orbit Determination Results

Residual RMS of Fit and Groundtrack Coverage

The GPS/MET tracking data were processed in arcs that ranged in length from 15 to 57 hours. Figure 6.2.4.4–1 illustrates the groundtrack coverage of the complete set of data used in EGM96. The fit of the double-differenced data ranged from 0.05 to 0.13 meters RMS. Each arc included—of necessity—the adjustment of numerous ambiguity biases. The residuals display large systematic signals with peak-to-peak values of up to ± 0.50 meters (see Figure 6.2.4.4–2, which shows the data residuals for days 179 and 180 of 1995). The signature in the residuals is thought to be a manifestation of the attitude librations undergone by the GPS/MET spacecraft that were not included in the measurement model, even though the nominal offset of the antenna from the spacecraft center of mass was accounted for.

For the given values of cross-sectional area (2.0 m^2), and mass (74.8 kg), the solved-for values of the solar radiation pressure coefficient, Cr, were extremely stable. They usually ranged from 1.34 to 1.40, with occasional outliers. The 8-hour drag coefficients had values of 1 to 4. Only one set of along-track 1‑CPR accelerations was estimated per arc. The values of this parameter ranged from 2.0 to 12.0 x 10^{-9} m/s^2.
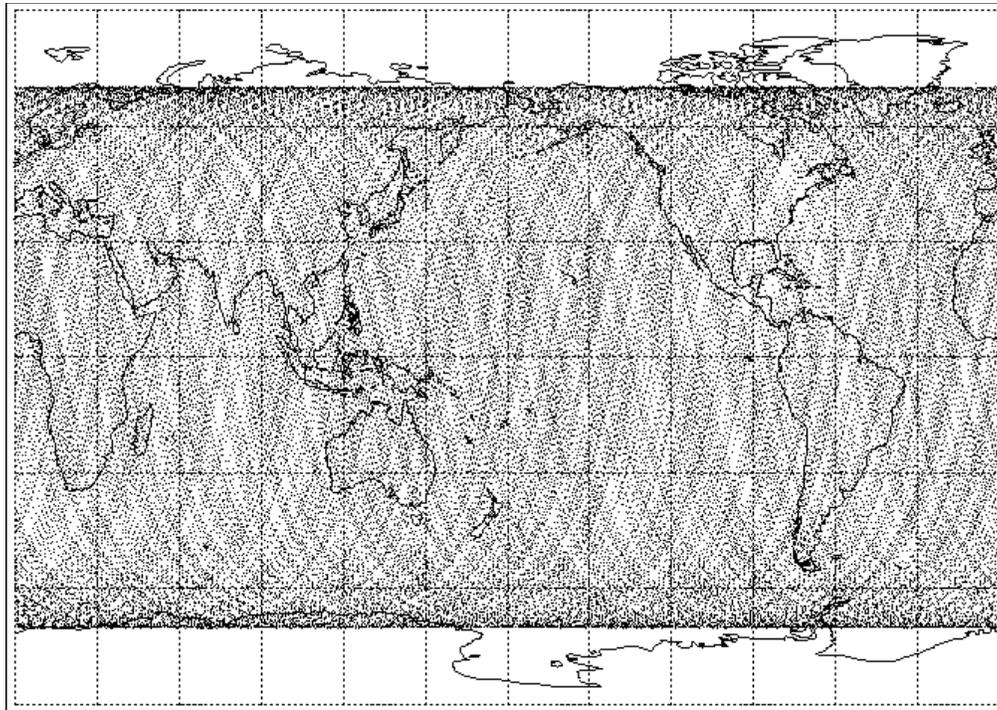
Figure 6.2.4.4–1. Ground tracks of GPS/MET data used in EGM96.
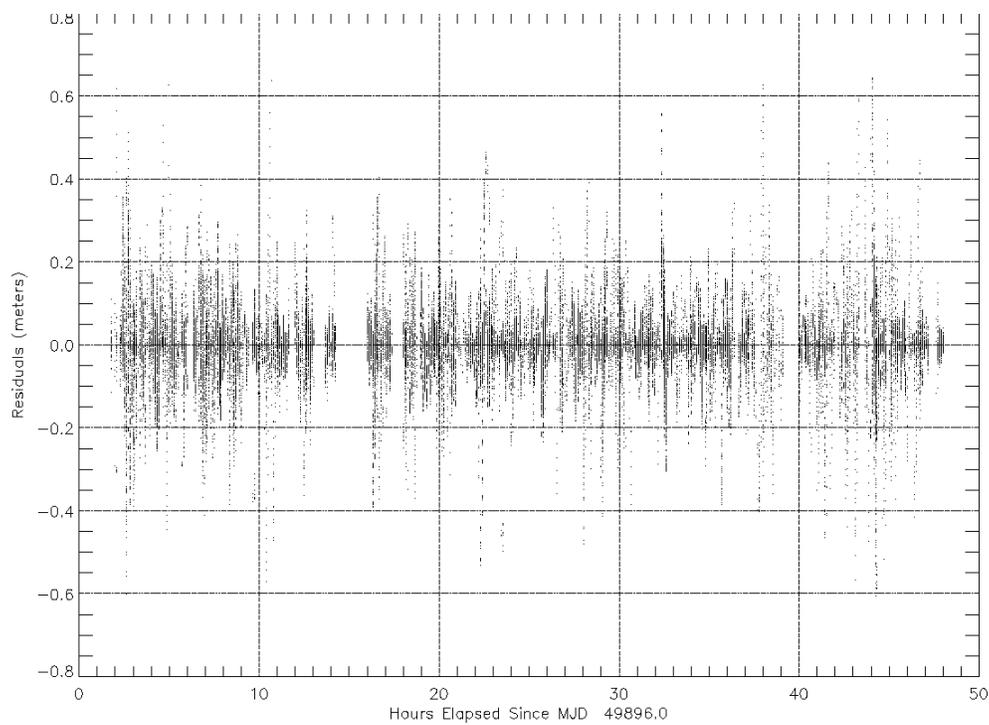
Figure 6.2.4.4–2. GPS/MET double difference phase residuals for days 179 and 180 of 1995.

6–72

Comparisons With UCAR and JPL Orbits

The GPS/MET orbits were compared with orbits produced both by JPL and by UCAR. Arcs from days 283 to 292 (October 11–19, 1995) were compared with the orbits produced by GEODYN. The reduced-dynamic technique [*Bertiger*, 1996], used by JPL, has been applied to TOPEX/POSEIDON (T/P) and other satellites [*Bertiger et al.*, 1994]. The orbits calculated by UCAR [*Schreiner*, 1996], using Microcosm, are obtained through analysis of double-differenced phase observables and, as we used, a fully dynamical orbit determination procedure. While the orbit determination techniques used by UCAR and GSFC were similar, there were some differences in the dynamical force models used. UCAR used JGM–3, for instance, while the GSFC orbits were computed with JGM–2. UCAR used a different polar motion series, whereas for the GSFC orbits, the polar motion was derived from the tables used for T/P in the production of the geophysical data records. The results are summarized in Tables 6.2.4.4–1 and 6.2.4.4–2. In general, the agreement between the GSFC and the UCAR/JPL orbits are of the order of 1 meter. The large difference between the JPL reduced-dynamic orbit and the GEODYN orbits on October 12, 1995, is due to a large data gap that causes the accuracy of the reduced dynamic procedure to degrade over that period of time. The differences with the UCAR orbits are smaller because of the similar orbit determination procedures and software.

Table 6.2.4.4–1. Comparisons of dynamic GSFC GPS/MET orbits to the reduced-dynamic orbits computed by JPL.

GSFC Arc	JPL Arc	No. of points in comparison	Total RMS Position Difference (m)
95_283–284	95_oct11	1622	1.19
95_285–286	95_oct12	1442	4.55
95_285–286	95_oct13	1622	0.40
95_287–288	95_oct14	1442	1.27
95_287–288	95_oct15	1622	1.79
95_290–292	95_oct17	562	0.90
95_290–292	95_oct18	1623	0.93
95_290–292	95_oct19	1622	0.92

Table 6.2.4.4–2. Comparisons of dynamic GSFC GPS/MET orbits to the dynamic orbits computed by UCAR.

GSFC Arc	UCAR Arc	No. of points in comparison	Total RMS Position Difference (m)
95_283–284	283	1440	0.93
95_283–284	284	1440	0.97
95_285–286	285	1440	0.52
95_285–286	286	1440	0.54
95_287–288	287	1440	0.82
95_287–288	288	1440	0.84
95_290–292	291	1440	0.79

| 95_290–292 | 292 | 1440 | 1.10 |

Analysis of GPS/MET Orbit Overlaps

As a test of internal consistency, orbit overlaps were computed for the GPS/MET for 2-day segments from days 283 to 288 of 1995. Each 2-day arc was then divided into two shorter segments of 27.3 to 30 hours. Then the subset arcs were compared with each other as well as with the 2-day "master" arc. The results are summarized in Table 6.2.4.4–3. One set of 1-CPR along-track acceleration parameters was adjusted in each arc, while drag coefficients were estimated for each 6- to 8-hour time span. The first and second sets of overlaps have a substantial amount of common data—27 or 30 hours out of a 48-hour arc. The third set of overlaps for each 2-day period contains a smaller amount of common data (12 hours out of 30 for days 283–284 and 285–286, and 6.66 hours out of 27.33 hours for the third test period from days 287–288). Of course, the overlaps that have the largest amount of common data show the smallest orbit differences. However, it is the third set of overlaps in each set that gives a better estimate of the orbit quality. These orbit overlaps range from 30 to 70 cm in total position difference. However, because of the large amount of common data, they are somewhat optimistic. They are consistent with the magnitude of the orbit differences with the JPL and UCAR orbits. These external and internal tests of GPS/MET orbits suggest that the overall orbit quality is about 1 meter, which, while not being of the same quality as the T/P orbit determination, is very good overall for geopotential recovery purposes. Further improvement will require that close attention be paid to accurate modeling of the shape and attitude of the spacecraft in both the measurement and the nonconservative force models.

Table 6.2.4.4–3. GPS/MET orbit overlap differences.

Data Span of Comparison	Length of Overlap (hrs)	RMS Orbit Overlap Differences (cm)			
		Radial	Along-track	Cross-track	Total
Day 283–284 (1995)					
2-day arc + 30-hr_arc_1	30	6	14	16	22
2-day arc + 30-hr_arc_2	30	5	16	31	35
30-hr_arc_1 + 30-hr_arc_2	12	8	24	47	53
Day 285-286 (1995)					
2-day arc + 30-hr_arc_1	30	0.3	1	4	4
2-day arc + 30-hr_arc_2	30	5	19	8	21
30-hr_arc_1 + 30-hr_arc_2	12	7	27	11	30
Day 287–288 (1995)					
2-day arc + 27-hr_arc_1	27.33	9	22	9	26
2-day arc + 27-hr_arc_2	27.33	13	47	14	50
27-hr_arc_1 + 27-hr_arc_2	6.66	25	61	21	70

6.2.5 Additional TRANET Doppler Data

The TRANET Doppler data used in JGM–1 and –2 were acquired on the GEOSAT Exact Repeat Mission (ERM), SEASAT, Nova–1, and Oscar–14 satellites. Additional satellite tracking data were obtained for the development of EGM96 included very early data from BE–C, D1–C, and D1–D and recent data from HILAT and RADCAL. These data were selected primarily because they added strength to the gravity solution by improving the distribution of orbit inclinations within EGM96. Data for BE–C, D1–C, and D1–D improved the low-inclination coverage (see Table 6.2.1–2). The D1–C and D1–D satellites were represented in prior geopotential field models by relatively sparse laser tracking from the first-generation laser tracking systems, which were predominantly in the Northern Hemisphere. The Doppler data provided a substantially greater data set with a significant augmentation in global coverage. The HILAT ($i = 82.0°$) and RADCAL ($i = 89.5°$) data improve the inclination coverage around the polar regions. These additional Doppler data were provided by DMA as part of this joint effort and were preprocessed at GSFC into the requisite GEODYN input format.

The TRANET Doppler observation is a two-frequency (150 and 400 MHz), line-of-sight (from satellite to ground), continuous average range-rate measurement [*Anderle,* 1986]. Because of the two oscillators involved and the strong atmospheric delay at these low frequencies, this type of Doppler data requires a relatively complex individual pass editing and bias estimation procedure. Each pass of Doppler data residuals is fit independently with a measurement model consisting of a constant, a tropospheric refraction scale factor, and an along-track timing bias. The fit process is iterated, employing an $n\sigma$ edit criterion. Each pass should fit to approximately the data noise value. Data with elevations below 5° are deleted, as are all data from passes whose elevations never exceed 10°. At least five good points per pass are required. A background noise floor is included in the solution RMS of fit to eliminate occasional overediting—this parameter has changed over time as the equipment has improved. In practice, both the noise floor estimate and the $n\sigma$ multiplier need to be experimentally determined in order to get satisfactory outlier editing. Tightening up on the edit criteria does not significantly affect which passes are accepted, and the recovered error model parameters are also not particularly affected. This front-end processing screens out a considerable amount of TRANET data. About 70 percent of the data passes the elevation cutoff criterion and a further 70 percent of the remaining data are kept in this local pass editing process. The selected data are subsequently analyzed for orbit and other parameters (in GEODYN) using a simple a $n\sigma$ editing criteria of four and adjusting a constant range-rate scale and a tropospheric scale bias on each pass. The nominal data sigma used is 1 cm/sec.

Much of the new data were taken by stations whose coordinates were not sufficiently well known in our reference frame. In almost all cases, local survey information to geodetic markers was not available. Thus, improved station positions were recovered from the data as a necessary first step, starting with the approximate locations supplied with the data, and using the same background modeling as for normal equation generation. The solution strategy was to adjust orbit parameters and station positions combining the same data arcs as would later be used for computing the normal equations.

6.2.5.1 The Early Doppler Data

Satellite Characteristics

BE–C, D1–C, and D1–D were geomagnetically stabilized, with widely separated high-frequency and low-frequency antennae. The magnetic stabilization is a two-axis system, with the privileged axis lining up with the local magnetic line of force. The magnetic damping inherent with this approach also rapidly reduces the satellite spin rate to approximately zero, so that only a simple angular offset about the privileged axis is required for full three-axis spacecraft positioning (This offset is an adjusted parameter—once per data arc). We used the geomagnetic stabilization model within GEODYN [*Safren*, 1975] to model the spacecraft attitude. We approximated the forms of these spacecraft using a flat plate box-wing model (conceptually similar to the model developed for TOPEX/POSEIDON [*Marshall and Luthcke*, 1994a, 1994b]). The box-wing model was deemed necessary to correct the observations to the spacecraft center of mass and to account for area variations in the radiation pressure and drag modeling. The effect of having widely separated high- and low-frequency antennas on the spacecraft was also modeled.

The individual spacecraft models were derived as well as possible given that we are operating at levels of accuracy undreamed of when the spacecraft were launched. In the case of BE–C, we were fortunate to have some old developments from the early 1970's San Andreas Fault Experiment, which provided the magnetic stabilization model. We also had available the "Design Data Sheets" for NASA S–66 from The Johns Hopkins University Applied Physics Laboratory (JHUAPL), Silver Spring, Maryland, from which we were able to establish the probable areas and dimensions for BE–C. For D1–C and D1–D, we were forced to rely on scaling from pictures (see *Husson and Banchereau* [1967], *Alouges* [1971] and *Caprara* [1987]). The actual Diademe spacecraft main body structure without solar panels is circularly symmetric about the privileged axis—the model approximates this structure as octagonal. The aggregate plate-specific properties reflectivities represent best guesses based on whatever could be gleaned about types of materials used.

The specific spacecraft models we have derived are provided in Tables 6.2.5.1–1 and 6.2.5.1–2. The coordinate system specifications is as follows: For **V** being the unit velocity vector and **R** being the unit position vector, **X** is along **V**, **Y** is **V**x**R**, and **Z** is **V**x(**V**x**R**) (positive downward toward Earth). The tables supply the outer normal vector, the plate area, and nominal specular, diffuse, and emissivity coefficients.

While all of the Doppler satellites we used are dual frequency in order to compensate for the ionospheric effect, the BE–C frequencies are 324/162 MHz, as compared to the 400/150 MHz of the other spacecraft. For D1–C and D1–D, the nominal antenna location is on the Z axis at about 0.3 m. For BE–C, the high- and low-frequency antennas are on separate solar panels on the +Y and –Y axes. Taking into account the frequencies, the equivalent ionosphere corrected phase center is at 3.628 m in Y and 0.3 m in Z.

Table 6.2.5.1–1. Satellite model for nonconservative forces: BE–C.

Panel	i_x	i_y	i_z	Area (m^2)	Specular Reflectivity	Diffuse Reflectivity	Emissivity (K)
1	1	0	0	0.072448	0.1250	0.5000	0.2800
2	0.707107	0.707107	0	0.072448	0.1250	0.5000	0.2800
3	0	1	0	0.072448	0.1250	0.5000	0.2800
4	-.707107	0.707107	0	0.072448	0.1250	0.5000	0.2800
5	-1	0	0	0.072448	0.1250	0.5000	0.2800
6	-.707107	-.707107	0	0.072448	0.1250	0.5000	0.2800
7	0	-1	0	0.072448	0.1250	0.5000	0.2800
8	0.707107	-.707107	0	0.072448	0.1250	0.5000	0.2800
9	0.707107	0	0.707107	0.028072	0.8000	0.1000	0.2800
10	0.5	0.5	0.707107	0.028072	0.8000	0.1000	0.2800
11	0	0.707107	0.707107	0.028072	0.8000	0.1000	0.2800
12	-.5	0.5	0.707107	0.028072	0.8000	0.1000	0.2800
13	-.707107	0	0.707107	0.028072	0.8000	0.1000	0.2800
14	-.5	-.5	0.707107	0.028072	0.8000	0.1000	0.2800
15	0	-.707107	0.707107	0.028072	0.8000	0.1000	0.2800
16	0.5	-.5	0.707107	0.028072	0.8000	0.1000	0.2800
17	0	0	1	0.021755	0.1250	0.5000	0.2800
18	0	0	-1	0.180556	0.1250	0.5000	0.2800
19	0	0.766044	0.642788	0.468128	0.0375	0.1500	0.8200
20	0	-.766044	-.642788	0.468128	0.0280	0.1120	0.9000
21	-.766044	0	0.642788	0.468128	0.0375	0.1500	0.8200
22	0.766044	0	-.642788	0.468128	0.0280	0.1120	0.9000
23	0	-.766044	0.642788	0.468128	0.0375	0.1500	0.8200
24	0	0.766044	-.642788	0.468128	0.0280	0.1120	0.9000
25	0.766044	0	0.642788	0.468128	0.0375	0.1500	0.8200
26	-.766044	0	-.642788	0.468128	0.0280	0.1120	0.9000

Data Processing

These early Doppler data (before 1969) were provided with a 4-second interval between data samples, and were obtained by counting a fixed number of cycles (the nominal counting interval is around 1 second). In the processing for EGM96, these data were aggregated into approximately 20-second spacing: the mean rate over each count interval is assumed to apply to the approximately 4-second interval from $[t_i+t_{i-1}]/2$ to $[t_{i+1}+t_i]/2$, and the now continuous Doppler are aggregated up to the desired nominal interval. This process is conceptually similar to the "normal point" approach used in satellite laser ranging analyses. If the mean rate over the actual count interval corresponded completely to the mean rate over the 4-second interval, a 5:1 reduction in apparent noise would be expected. Simply reducing the quantity of data being summed into the normal equations provides significant savings in computer time costs. Finally, the data were modeled as an average range rate, in contrast to earlier assumptions in Doppler processing of an instantaneous rate.

For editing these early Doppler data, an $n\sigma$ multiplier of 1.4 and a background noise floor of 2 cm/sec was found to produce the best results. Changing the multiplier from 3.5 to 1.4 changed the apparent noise from over 5 cm/sec to under 3 cm/sec with essentially the same passes of data being used.

Table 6.2.5.1–2. Satellite model for nonconservative forces: D1–C and D1–D.

Panel	i_x	i_y	i_z	Area (m^2)	Specular Reflectivity	Diffuse Reflectivity	Emissivity (K)
1	1	0	0	0.039270	0.1250	0.5000	0.2800
2	0.707107	0.707107	0	0.039270	0.1250	0.5000	0.2800
3	0	1	0	0.039270	0.1250	0.5000	0.2800
4	-.707107	0.707107	0	0.039270	0.1250	0.5000	0.2800
5	-1	0	0	0.039270	0.1250	0.5000	0.2800
6	-.707107	-.707107	0	0.039270	0.1250	0.5000	0.2800
7	0	-1	0	0.039270	0.1250	0.5000	0.2800
8	0.707107	-.707107	0	0.039270	0.1250	0.5000	0.2800
9	0	0	1	0.196350	0.1250	0.5000	0.2800
10	0	0	-1	0.196350	0.1250	0.5000	0.2800
11	0.707107	0	0.707107	0.088200	0.0375	0.1500	0.8200
12	-.707107	0	-.707107	0.088200	0.0280	0.1120	0.9000
13	0	0.707107	0.707107	0.088200	0.0375	0.1500	0.8200
14	0	-.707107	-.707107	0.088200	0.0280	0.1120	0.9000
15	-.707107	0	0.707107	0.088200	0.0375	0.1500	0.8200
16	0.707107	0	-.707107	0.088200	0.0280	0.1120	0.9000
17	0	-.707107	0.707107	0.088200	0.0375	0.1500	0.8200
18	0	0.707107	-.707107	0.088200	0.0280	0.1120	0.9000

The early Doppler sites had separate high-frequency and low-frequency antennae for 324/162 MHz and 400/150 MHz arranged in a rectangular array. This setup resulted in the effective electronic center for the ionosphere corrected 324/162 MHz data being different than the corresponding center for the 400/150 MHz data at the level of a few meters. Because of this, we had to compute separate station positions for BE–C and for D1–C and D1–D. Appendix A contains the station coordinate information; the 18 BE–C site numbers are of the form 41xxx, where xxx is the original Doppler site number and the 16 D1–C and D1–D station numbers are of the form 42xxx. In this process, the longitude of APLMND (41111 and 42111) in Scagsville, Maryland, was held fixed for the BE–C, D1–C and D1–D recovery. The nominal position for APLMND was derived from the laser site position in Greenbelt, Maryland (STALAS, 7063), using geodetic survey differences. Survey data for this site were made available by *M. Tanenbaum* [*NSWC, private communication,* 1995]. The satellite antenna center-of-mass offsets were also adjusted for each spacecraft.

Tables 6.2.5.1–3 through –5 describe the 3 arcs of BE–C, 10 arcs of D1–C, and 6 arcs of D1–D that comprised the normal equations used for EGM96. The somewhat higher fit statistics on D1–C, which are closer to 3 cm/sec than 2 cm/sec, are probably associated with the significantly higher orbit eccentricity (>0.08).

Table 6.2.5.1–3. Solution statistics for the BE–C Doppler data used in EGM96.

Arc Start/ Epoch	Arc End	Number of points	RMS (cm/s)	Number of Sites	Number of Passes	Argument of Perigee
650704	650710	5314	2.4241	15	307	44.0
650727	650802	4585	2.5260	17	281	159.6
650802	650808	4207	2.4337	17	276	190.9

Table 6.2.5.1–4. Solution statistics for the D1–C Doppler data used in EGM96.

Arc Start/ Epoch	Arc End	Number of points	RMS (cm/s)	Number of Sites	Number of Passes	Argument of Perigee
670224	670301	1551	2.9819	12	109	242.5
670301	670306	2240	2.4945	12	135	272.0
670306	670311	1875	2.8742	12	125	301.5
670311	670316	2356	2.6298	13	147	331.7
670316	670321	2313	2.4806	13	145	1.4
670321	670326	2206	3.0677	14	147	30.5
670326	670331	2069	2.8474	14	137	60.2
670331	670405	2811	2.9796	14	175	89.4
670405	670410	3738	2.7905	15	217	118.1
670410	670415	3378	2.5851	15	206	148.1

Table 6.2.5.1–5. Solution statistics for the D1–D Doppler data used in EGM96.

Arc Start/ Epoch	Arc End	Number of points	RMS (cm/s)	Number of Sites	Number of Passes	Argument of Perigee
670224	670301	2523	2.1639	12	148	183.5
670301	670306	3938	2.081	12	220	211
670306	670311	4120	2.2669	12	226	237.6
670311	670316	4143	2.21	14	229	264.7
670316	670321	2313	2.4806	13	145	1.4
670321	670326	2206	3.0677	14	147	30.5
670326	670331	4495	2.1364	15	254	345.5
670331	670406	5304	2.3071	14	303	12.9

6.2.5.2 The Modern Doppler Data

Satellite Characteristics

HILAT and RADCAL are gravity gradient, three-axis-stabilized spacecraft using the 400/150 MHz TRANET Doppler beacon. RADCAL is small, having a cross-sectional area of .3116 m^2 and mass of 90.72 kg. The nominal area of HILAT was not available (mass at launch was 113.736 kg), so the parameters for BE–C were used: A/M = 1.139/52.6 = 0.02 m^2/kg. Because

both drag and solar pressure coefficients are adjusted, this is not viewed as a problem. Unlike the early Doppler satellites, detailed spacecraft models were not deemed necessary. For HILAT, the effective antenna location is at –1.989 m in X, and 0.574 m in Z. For RADCAL, the effective antenna location is at –0.145 m in Z. These antenna locations were supplied by *M. Tanenbaum* [*NSWC, private communication,* 1995], and are the results of his computations for the effective phase centers from the actual spacecraft design specifications. Note that the actual antenna on HILAT may behave differently than assumed because the antenna actually consists of parallel double wires connected by a small conducting separator, whose measured dipole pattern departed substantially from the standard dipole model. As only amplitude measurements were taken in antenna testing—i.e., no phase measurements were taken—the real antenna phase center may vary. For RADCAL, there are four 400 MHz antennas on the top of the spacecraft in a "quad" pattern, and similarly four 150 MHz antennas on the bottom. This produces an effective 400 MHz antenna on top in the –Z direction and an effective 150 MHz antenna on the bottom in the +Z direction, which when combined give the effective negative Z phase center location (above the center of mass).

An additional complication with both spacecraft is attitude librations. For HILAT, the tracking data are in a period shortly after launch wherein attitude librations had not fully damped; in July 1983 the peak libration angle was declining from near 10° to around 7°; by October 1983, the peak libration variation was probably well below the 5° requirements (See *Potocki* [1984]). The attitude librations of RADCAL, reaching ±12° in pitch, are discussed in *Melvin et al*. [1996]. For both of these spacecraft, the variation in the attitude was unmodeled.

Data Processing

Modern Doppler data are continuous-count, integrated Doppler. The data were aggregated into approximately 20-second interval spacing when needed; this is a typical data rate for Doppler data. As in the early Doppler data, simply reducing the quantity of data being summed into the normal equations provides significant savings in computer time costs, and much less effort is required in relative data weighting with respect to the older data. The data type used is average range rate.

For editing these modern Doppler data, an $n\sigma$ multiplier of 1.4 was found to produce the best results, which is consistent with the early Doppler data processing. The background noise floor for HILAT was 0.15 cm/sec, and that for RADCAL was 0.2 cm/sec. For RADCAL, changing the multiplier from 3.0 to 1.4 changed the apparent noise from over 0.6 cm/sec to around .33 cm/sec with essentially the same passes of data being used; similar results were noted with HILAT.

Special station positioning treatment was not required on HILAT, for it was tracked by the same network as GEOSAT. We did a test station recovery so that any untoward station maintenance events would be uncovered. No problems were detected.

For RADCAL, station positioning was required, because the tracking network, the Western Test Range (WTR), was not previously encountered in the development of EGM96. One site was known to be identical with the prior GEOSAT time frame site—Thule, Greenland. Thule (as station 35508) is actually the same site and equipment as the earlier 557 site from GEOSAT. For the preliminary station recovery, the longitude of Thule was held fixed at the JGM–2 value. In

the gravity model recovery, the contributions of Thule as 557 (GEOSAT) and 35508 (RADCAL) were combined as a single site.

Tables 6.2.5.2–1 and –2 describe the 8 arcs of HILAT and the 36 arcs of RADCAL, which were formed into normal equations for EGM96, and which used these recovered station positions. The fit statistics on HILAT (0.3 to 0.5 cm/sec) are somewhat higher than those for RADCAL (0.3 to 0.4 cm/sec). Curiously, the earlier segment of HILAT is fitting better than the later, which is contrary to what we would expect if the attitude libration were a problem. The *a priori* RADCAL sites can be identified in Appendix A as site numbers of the form 35xxx.

Table 6.2.5.2–1. Solution statistics for HILAT Doppler data used in EGM96.

Arc Start/ Epoch	Arc End	Number of points	RMS (cm/s)	Number of Sites	Number of Passes	Argument of Perigee
830709	830716	2997	0.3166	16	211	223.3
830716	830722	2611	0.3301	16	185	206.6
830722	830728	2418	0.3752	15	175	181.0
831004	831009	2686	0.4109	17	188	350.0
831009	831014	2949	0.4712	17	214	343.6
831014	831020	3978	0.4091	17	284	314.9
831020	831026	3578	0.4100	18	262	300.8
831026	831101	3641	0.4275	17	262	281.0

Table 6.2.5.2–2. Solution statistics for the RADCAL Doppler data used in EGM96.

Arc Start/ Epoch	Arc End	Number of points	RMS (cm/s)	Number of Sites	Number of Passes	Argument of Perigee
940301	940306	1765	0.3543	11	196	178.1
940306	940311	1368	0.3574	11	151	164.8
940311	940316	1347	0.3549	11	141	150.3
940316	940321	1737	0.3370	11	190	133.8
940321	940326	1974	0.3500	12	218	115.4
940326	940331	2110	0.3656	12	223	96.1
940331	940405	2037	0.3452	12	210	77.9
940405	940410	2071	0.3636	12	217	61.8
940410	940415	2467	0.3729	12	243	47.7
940415	940420	2372	0.3988	12	231	34.7
940420	940425	2421	0.3634	12	229	22.1
940425	940430	2235	0.3579	12	218	8.8
940430	940505	2028	0.3891	11	198	354.1
940505	940510	2172	0.3271	11	198	337.4
940510	940515	2111	0.3785	11	199	318.4
940515	940520	2441	0.3445	11	222	297.9
940520	940525	2073	0.3184	11	196	277.8
940525	940530	2113	0.3425	12	214	259.2
940530	940604	2884	0.3429	12	239	242.2
940604	940609	2828	0.3167	12	246	226.0
940609	940614	2587	0.3489	13	234	209.4
940614	940619	2941	0.3453	13	268	191.6
940619	940624	3010	0.3484	13	266	172.4
940624	940629	2380	0.3894	12	229	153.2
940629	940704	2371	0.3596	12	218	135.6
940704	940709	2377	0.3536	13	224	120.4
940709	940714	2186	0.3604	11	214	107.4
940714	940719	2358	0.4180	14	224	95.7
940719	940724	2402	0.3944	14	241	84.7
940724	940729	2637	0.3928	14	262	73.8
940729	940803	2834	0.3511	14	265	62.2
940803	940808	2675	0.3807	14	258	49.1
940808	940813	2655	0.3618	14	247	33.8
940813	940818	2800	0.3565	14	253	15.8
940818	940823	2650	0.3586	13	251	355.7
940823	940828	2513	0.3463	14	239	335.5

6.2.6 Additional SLR Satellite Data Used in EGM96

EGM96 includes tracking data for the spherical satellite laser ranging (SLR) geodynamic research satellites LAGEOS, LAGEOS–2, Starlette, Stella, Ajisai, and GFZ–1. A subset of the SLR tracking data used in EGM96 for LAGEOS, Starlette, and Ajisai was used in JGM–2. The remaining spacecraft—LAGEOS–2, Stella, and GFZ–1—were introduced with the development of the EGM96 model. This section focuses on the newly processed SLR data; a summary of the data used in JGM–2 can be found in Section 6.2.1 and *Nerem et al.* [1994b]. The new SLR data included LAGEOS data from 1989–1992 and 1993–1994, data from 1993 and 1994 for LAGEOS–2, Ajisai, Starlette, and Stella, as well as the data for GFZ–1.

6.2.6.1 Summary of New Satellites

This section discusses the SLR satellites used in EGM96. For all the SLR satellites, the primary mission is to serve as a passive tracking target for terrestrial laser tracking stations. Data from the international network of laser tracking sites are used in scientific geodynamics research in gravity, tides, plate tectonics, and Earth rotation studies.

LAser GEOdynamics Satellite (LAGEOS)

LAGEOS is an aluminum brass core sphere with 426 laser corner cubes (422 fused silica glass, 4 germanium). LAGEOS was launched on a Delta launch vehicle on May 4, 1976 [*Cohen and Smith*, 1985].

LAser GEOdynamics Satellite–2 (LAGEOS–2)

LAGEOS–2 was built by the Italian Space Agency based on NASA's LAGEOS design of an aluminum brass core sphere with 426 corner cubes (422 fused silica glass, 4 germanium). The satellite was launched with an Italian booster, IRIS, carried onboard the Space Shuttle *Columbia* (STS–52) in October 1992.

Ajisai

The Ajisai satellite is a Japanese geodetic satellite that is covered with 120 sets of SLR cube-corner reflectors (1436 reflectors in all) in addition to 318 optical flats for reflecting sunlight. Ajisai's mission is to contribute to Japanese geodesy. The primary short-range objective for Ajisai is testing of NASDA's H–I launch vehicle, which successfully launched Ajisai on August 12, 1986. Long-range applications include a survey aimed at rectifying Japan's domestic geodetic network and general geodynamic research.

Starlette

The first of a new generation of artificial satellites for geodesy and geodynamics, Starlette was launched on February 6, 1975, by the French Centre National d'Etudes Spatiales (CNES), Groupe de Recherches de Géodésie Spatiale (GRGS) from the Guyana Space Center. Starlette is a sphere,

the center of which is made of a Uranium 238 alloy, and the skin is an aluminum and magnesium alloy, in which 60 laser corner cubes are embedded. The principal scientific objective for Starlette was the study of Earth and ocean tides. Since its launch, Starlette has made contributions to many areas of geodynamics, including gravity field modeling.

Stella

The French Centre National d'Etudes Spatiales (CNES) constructed the Stella satellite to be similar to the Starlette satellite. Stella was launched on an Ariane along with Spot–3 in 1993.

GeoForschungsZentrum–1 (GFZ–1)

GeoForschungsZentrum–1 (GFZ–1) is the first satellite mission designed and funded by the GeoForschungsZentrum Potsdam, Germany. The satellite was built in Russia, and the launch and space deployment were by the Russian RKK Energia organization. The satellite was launched from the *Mir* space station after being transported there from Russia on a PROGRESS cargo ship that was launched on April 9, 1995, and docked with the space station on April 11. The satellite will be utilized for high-resolution geodetic applications, especially geopotential recovery. At an altitude of 385 km, it is the lowest satellite tracked by the global SLR network. Because of the high slew rates needed to drive the SLR transmit/receive telescope, not all of the international network can track GFZ–1. For GFZ–1, typical tracking passes last 2.2 minutes, compared with 26 minutes for LAGEOS, and 5 minutes for Starlette. Although there was no preflight measurement of the center of mass, the value of 58.5±1 mm was theoretically determined postlaunch by two independent groups.

6.2.6.2 Tracking Coverage, Modeling, and Parameterization

The SLR normal point data were obtained from NASA's Crustal Dynamics Data Information System (CDDIS) [*Noll*, 1993]. These measurement data consist of round-trip travel time of a laser pulse from a tracking site to the cube-corner reflectors on the satellite. If normal points were not available, the full-rate, usually 5 Hz, SLR data were time averaged into normal points [*Gaignebet*, 1984]. These normal points and those obtained from CDDIS were validated for information content.

Initial data reductions were performed using GEODYN and the standard *a priori* force modeling (see Table 6.1.3–1). The *a priori* tracking site locations were those determined in the JGM–2 gravity solution. A deviation in the background force models was the use of the Jacchia 1971 atmospheric model [*Jacchia*, 1971] for drag calculations on Starlette, Ajisai, Stella, and GFZ–1. For the LAGEOS satellites, coefficients for general accelerations were adjusted in addition to the epoch state. Coefficients for the atmospheric drag perturbations were adjusted with the epoch state for the lower satellites. The nominal data uncertainty used for the SLR data was 1 m, but some of the SLR sites' lower quality data were down-weighted or eliminated from consideration. Table 6.2.6.2–1 lists the SLR sites for which the data uncertainty differed from the nominal 1 m.

Table 6.2.6.2–1. Stations for which the SLR data uncertainty was not the nominal 1 m.

number	name	(m)	number	name	(m)	number	name	(m)
118139018	Potsdam	2	751516048	Dionysos	4	759616018	Wettzell	4
186351018	Maidanak	10	751716018	Roumelli	4	760216018	Tromso	4
186454018	Maidanak	10	752516018	Xrisokalaria	4	781048018	Zimmerwald	4
186652018	Dunaovcy	10	752516028	Xrisokalaria	4	781138018	Borowiec	4
186753018	Evpatoria	10	752516038	Xrisokalaria	4	781138028	Borowiec	4
186859018	Komsomolsk	10	754116018	Matera	4	782445018	San Fernando	10
186960018	Balkhash	10	754216018	M. Generoso	4	783146018	Helwan	4
187349018	Simeiz	10	754316018	Noto	4	783728048	Shanghai	4
188444018	Riga	10	754416018	Lampedusa	4	783728058	Shanghai	4
189318018	Katzively	4	754516018	Punta Sa Menta	4	883316028	Kootwijk	4
195320018	Santiago	10	754516028	Punta Sa Menta	4	883316038	Kootwijk	4
723629018	Wuhan	10	754611028	Medicina	4	883316048	Kootwijk	4
723719018	Changchun	10	754616018	Medicina	4	883316058	Kootwijk	4
751016028	Askites	4	754862018	Cagliari	4	883316068	Kootwijk	4
751016038	Askites	4	755016018	Basovizza	4	883316078	Kootwijk	4
751216028	Katavia	4	755016028	Basovizza	4	883410018	Wettzell	4

The initial data reductions utilized an editing criterion of 3.5 times the weighted RMS of fit for the previous orbit iteration to eliminate data with large systematic errors. The measurement residuals from the initial orbit data reductions were analyzed to identify and eliminate passes and individual points that had obvious larger systematic errors. The identification of the anomalous data was done by performing a linear regression on each pass of measurement residuals and discarding passes whose absolute value of the range bias (mean) was greater than a few cm and/or whose absolute value of the timing bias (slope) was greater than a few tens of microseconds, and discarding individual observations that differed from the fitted line by more than a few cm. This edited data set was used to recompute the orbits and then form normal equations for satellite state, generalized acceleration parameters, geopotential coefficients, tides, tracking station positions and velocities, and the Earth orientation parameters. Except for GFZ–1, the solution arc epochs and length were chosen to be coincident with the T/P 10-day cycle definition (See Table 6.2.2.2–1). The GFZ–1 arcs are 3 days in length, chosen to somewhat optimize the number of passes within the 3-day span, given the sparse available data. Table 6.2.6.2–2 summarizes the satellite characteristics and parameterizations used for the SLR data incorporated into the EGM96 model.

The LAGEOS satellites, at an altitude of 1 Earth radius, are outside of the range of atmospheric models, so there was no drag modeled. The high altitude of these satellites results in potentially long tracking passes, as illustrated in Figures 6.2.6.2–1 and 6.2.6.2–2 for LAGEOS and LAGEOS–2, respectively. The unmodeled charged and neutral particle, and thermal drag forces on the LAGEOS [*Metris*, 1997] satellites were accommodated with two constant along-track, and two along-track once cycle per revolution (1-CPR, as a function of the argument of latitude) empirical acceleration sets per solution arc. The coefficient of solar radiation pressure was not adjusted in these computations, as these effects are highly correlated with the adjusted 1-CPR accelerations. A typical RMS of fit for these arcs is 2 to 3 cm (see Tables 6.2.6.2–3 to 6.2.6.2–5).

Table 6.2.6.2–2. SLR satellite modeling and parameterization in EGM96.

	LAGEOS 1989–92	LAGEOS 1993–94	LAGEOS-2	Ajisai	Starlette	Stella	GFZ–1
COSPAR ID	7603901		9207002	8606101	7501001	9306102	8601795
launch date	04-May-76		22-Oct-92	12-Aug-86	06-Feb-75	26-Sep-93	19-Apr-95
diameter (cm)	60		60	215	24	24	21.5
# laser corner cubes	426		426	1436	60	60	60
Average Altitude (km)	5895		5785	1492	953	795	350
inclination (deg)	109.9		52.0	50.0	49.8	98.6	51.7
eccentricity	0.0048		0.013	0.0011	0.021	0.0013	0.0013
period (min)	225		223	116	104	101	92
mass (kg)	406.965		406.965	685	47.25	47.25	20.63
arc length (days)	30	10	10	10	10	10	3
number of arcs	48	72	70	36	67	39	16
number of data points	218564	93194	851120	53698	39356	21366	5548
data noise (cm)	1.2	0.7	0.7	0.7	0.6	0.6	0.6
average points per arc	4553	1104	1216	1702	1009	548	358
average passes per arc	372	253	149	167	93	65	21
avg. num. sites per arc	18	15	16	15	14	15	7
Geophysical Modeling: See Table 6.1.3–2, with the following exceptions :							
Atmospheric Density				Jacchia 71	Jacchia 71	Jacchia 71	Jacchia 71
tracking station positions	JGM–2	JGM–2	JGM–2	JGM–2	JGM–2	JGM–2	JGM–2
Dynamical parameters adjusted in orbit determination and adjustment interval (days)							
solar radiation coefficient	fixed at 1.13	fixed at 1.13	fixed at 1.13	fixed at 1.13	fixed at 1.13	fixed at 1.13	fixed at 1.13
coefficient of drag	-	-	-	adjusted daily	adjusted daily	adjusted daily	adjusted daily
constant along-track EA	15	5	5	10	not adjusted	not adjusted	not adjusted
1–CPR along-track EA	15	5	5	10	not adjusted	not adjusted	not adjusted
Treatment of dynamical parameters in EGM96							
solar radiation coefficient	adjusted	adjusted	adjusted	adjusted	adjusted	adjusted	adjusted
coefficient of drag	-	-	-	adjusted daily	adjusted daily	adjusted daily	adjusted daily
constant along-track EA	adjusted	adjusted	adjusted	fixed at 0.0	fixed at 0.0	fixed at 0.0	fixed at 0.0
1–CPR along-track EA	fixed at 0.0	fixed at 0.0	fixed at 0.0	fixed at 0.0	fixed at 0.0	fixed at 0.0	fixed at 0.0

1–CPR: one cycle per revolution EA: Empirical Acceleration
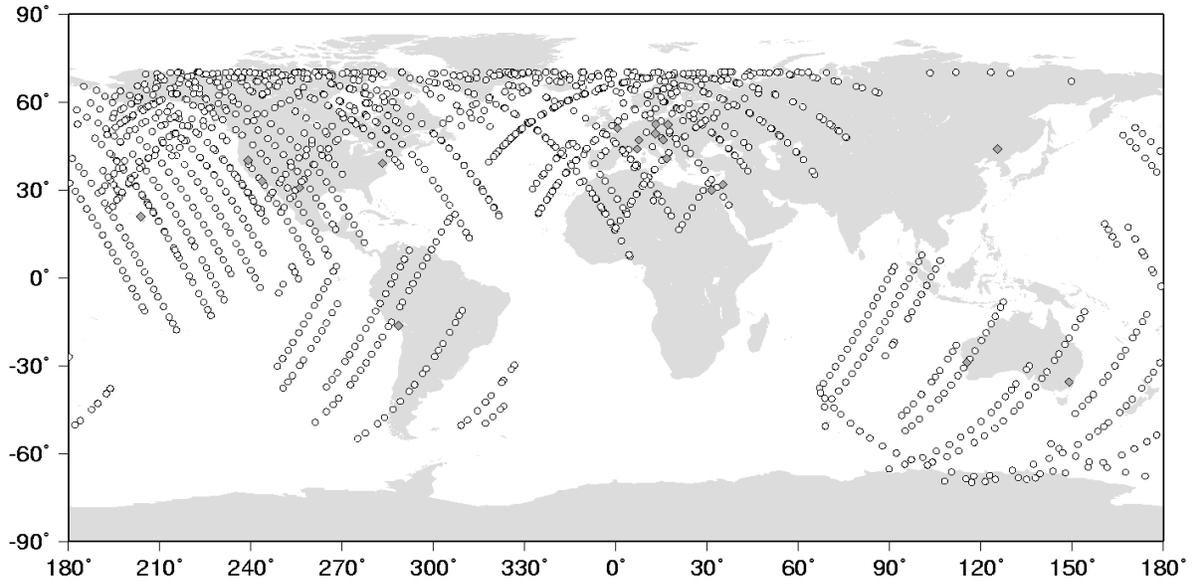
Figure 6.2.6.2–1. LAGEOS tracking coverage for solution epoch 930707.
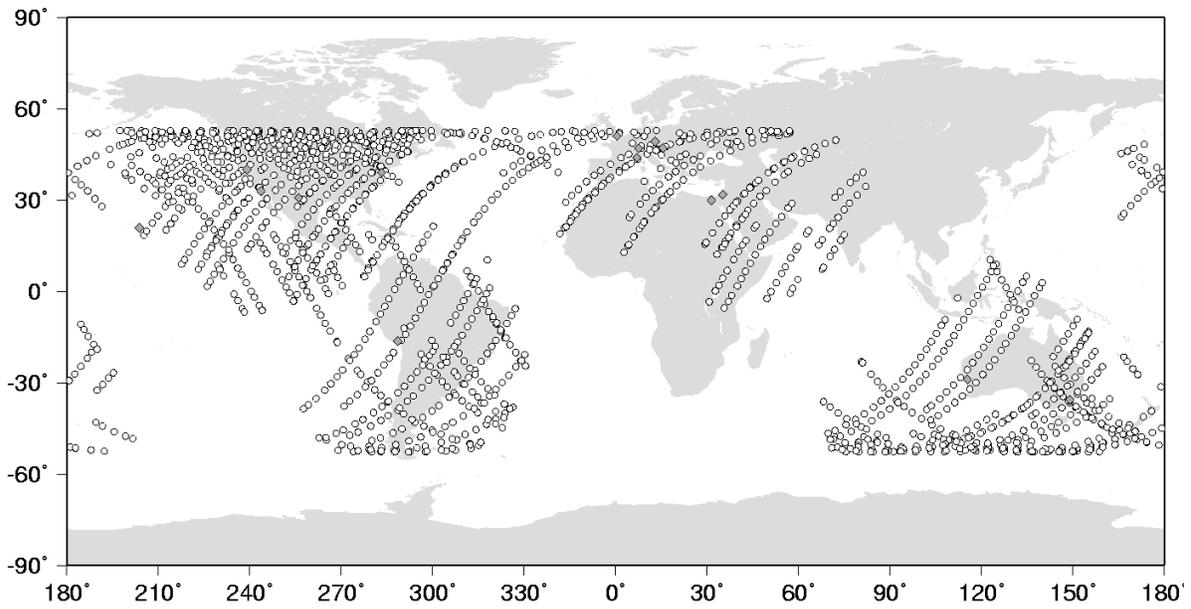
Figure 6.2.6.2–2. LAGEOS–2 tracking coverage for solution epoch 930707.

Table 6.2.6.2–3. Summary of LAGEOS 30-day solution statistics.

Epoch	Number of points	RMS (cm)	Number of Sites	Start	Number of points	RMS (cm)	Number of Sites
881231	6429	5.79	19	901231	4913	6.68	21
890130	5896	5.84	21	910130	4919	5.64	25
890301	5085	5.87	21	910301	2417	6.06	15
890331	4285	5.74	17	910331	2447	6.24	16
890430	5696	6.63	23	910430	2747	6.44	16
890530	4583	5.68	25	910530	3337	6.68	16
890629*	5353	5.93	24	910629*	3242	6.43	14
890803	4647	5.13	21	910803	4544	5.70	14
890902	4201	6.08	20	910902	5796	6.63	17
891002	6252	5.32	27	911002	6022	7.03	18
891101	6427	5.17	24	911101	4005	6.49	15
891201	4576	6.07	24	911201	4158	6.13	16
891231	5686	8.88	23	911231	4158	6.88	16
900130	5405	9.00	21	920130	4903	5.29	18
900301	5535	10.10	20	920229	3655	6.98	19
900331	2832	12.23	19	920330	4778	6.71	21
900430	5683	7.69	18	920429	4887	7.41	25
900530	3833	7.60	21	920529	2682	6.69	17
900629*	5088	7.83	19	920628*	4023	9.17	18
900803	4553	6.91	20	920802	4252	7.00	17
900902	4851	7.16	17	920901	4636	5.74	22
901002	5129	6.10	19	921001	5495	5.35	21
901101	5518	8.61	18	921031	3368	4.74	23
901201	2931	10.50	18	921130	2706	7.09	24

* 35 day arc length

Table 6.2.6.2–4. Summary of LAGEOS 10-day solution statistics.

Epoch	Number of points	RMS (cm)	Number of Sites	Start	Number of points	RMS (cm)	Number of Sites
921230	622	2.91	10	940102	1327	3.13	13
930109	809	3.15	12	940112	1532	2.87	12
930119	651	2.34	9	940121	985	2.45	11
930129	767	2.17	10	940131	1180	2.24	12
930208	1075	2.96	15	940210	785	2.14	12
930218	1113	2.73	14	940220	698	2.75	14
930228	1369	2.68	13	940302	1165	2.51	15
930310	1826	3.01	15	940312	963	2.52	13
930320	1131	2.73	14	940322	889	3.01	12
930330	1757	2.73	14	940401	1057	2.22	12
930408	1212	2.70	12	940411	833	2.15	9
930418	1481	2.96	15	940421	780	2.36	9
930428	1069	2.55	11	940501	862	2.25	11
930508	1194	2.49	13	940511	807	2.31	10
930518	1116	3.09	12	940521	629	2.55	9
930528	1237	2.52	15	940530	1172	2.08	12
930607	1098	2.12	15	940609	1061	2.21	10
930617	1168	2.43	13	940619	1004	3.01	12
930627	1574	2.26	14	940629	764	2.73	14
930707	1647	2.64	17	940709	1024	2.59	13
930717	1749	2.73	15	940719	934	2.17	16
930727	2028	2.71	16	940729	1187	2.47	16
930807	1973	2.18	17	940808	1050	2.29	14
930815	1787	2.41	17	940818	1089	1.89	13
930825	1995	2.21	17	940828	894	2.84	14
930904	1694	2.32	17	940906	1177	3.46	15
930914	2017	2.90	18	940916	846	3.69	15
930924	1504	2.37	16	940926	1377	3.58	15
931004	1324	1.85	12	941006	1607	2.84	14
931014	913	1.97	13	941016	1754	2.83	16
931024	717	2.20	11	941026	1554	2.25	15
931103	706	2.15	9	941105	973	2.78	13
931113	836	2.46	10	941115	1269	2.90	12
931122	881	3.70	9	941125	1400	3.08	14
931202	1179	3.05	11	941205	1486	2.72	14
931212	1138	2.56	14	941215	1369	2.66	14
931223	1069	3.11	13	941225	1057	2.99	11

Table 6.2.6.2–5. Summary of LAGEOS–2 solution statistics.

Epoch	Number of points	RMS (cm)	Number of Sites	Start	Number of points	RMS (cm)	Number of Sites
921230	725	2.42	7	940102	1085	2.76	10
930109	1094	2.31	13	940110	1173	2.10	11
930119	972	2.21	8	940121	784	2.80	9
930129	1323	2.20	13	940131	1014	2.08	13
930208	1566	2.43	14	940210	1088	2.03	13
930218	1243	2.29	13	940220	792	2.39	12
930228	1450	2.29	15	940302	1478	3.57	18
930310	1541	2.24	13	940312	1172	2.22	15
930320	1320	2.34	14	940322	1662	3.19	19
930330	1543	2.41	14	940331	1712	2.44	16
930408	981	2.16	14	940410	1419	2.81	13
930418	1646	2.25	12	940420	1675	2.64	15
930428	1411	2.21	10	940430	2266	2.09	19
930508	1415	1.79	12	940510	1407	2.49	16
930518	1356	1.76	7	940520	1118	3.21	17
930528	1002	1.94	8	940530	1310	2.16	19
930607	1554	1.83	11	940609	1134	1.93	14
930617	1536	2.45	13	940619	1384	3.11	16
930627	1578	2.04	14	940629	947	2.50	14
930707	1917	2.32	13	940709	857	3.13	13
930717	1557	2.32	13	940719	697	2.70	12
930727	1968	2.29	16	940729	866	2.02	13
930807	1768	2.38	17	940808	829	2.19	11
930815	1815	3.10	19	940818	1161	2.16	11
930825	1999	2.44	18	940828	963	1.74	11
930904	1738	2.75	17	940906	940	2.40	13
930914	2188	3.13	18	940916	685	3.39	13
930924	2085	3.25	18	940926	1288	3.15	17
931004	1291	1.98	11	941006	1690	2.19	15
931014	923	1.76	12	941016	1558	2.59	18
931024	935	2.58	12	941026	1601	2.52	19
931103	781	3.31	10	941105	1122	3.31	17
931113	781	2.89	11	941115	76	2.49	5
931122	758	2.56	8	941205	1624	2.31	16
931202	798	2.37	9	941215	1574	2.65	18
931212	1045	2.92	9	941225	982	2.94	13
931223	712	3.17	13				

Ajisai's altitude (1490 km) and spherical shape make modeling of the neutral particle drag relatively straightforward. However, this spacecraft is large and hollow; the high resulting area-to-mass ratio makes it subject to strong radiative and thermal imbalance perturbations. The Ajisai satellite solution parameterization included a daily adjustment of the coefficient of drag, one along-track constant acceleration, and one along-track 1-CPR acceleration set adjusted per 10-day solution arc. As with the LAGEOS satellites, the coefficient of solar radiation pressure was not adjusted. A typical RMS of fit for these arcs is 10 to 15 cm, as shown in Table 6.2.6.2–6.

The tracking coverage was not as globally distributed as that of the LAGEOS satellites, owing to the lower altitude of Ajisai. Figure 6.2.6.2–3 shows the coverage for a representative solution (930907), and illustrates the dearth of tracking over western Russia, China, India, and Africa.

Table 6.2.6.2–6. Solution Statistics for Ajisai.

Epoch	Number of points	RMS (cm)	Number of Sites	Epoch	Number of points	RMS (cm)	Number of Sites
921231	98	9.38	5	930707	1052	11.34	9
930110	782	10.63	15	930717	1125	12.32	9
930120	1304	9.70	10	930727	1363	11.74	11
930129	1274	8.98	14	930807	1557	38.13	13
930208	1762	11.10	17	930816	2455	39.51	17
930218	2367	12.02	17	930826	2532	9.66	16
930228	2070	12.31	15	930905	2209	14.44	15
930310	2923	35.59	15	930915	2458	11.92	16
930320	1029	31.36	12	930924	2540	11.80	17
930330	1559	14.25	17	931004	1578	12.28	11
930409	927	13.87	12	931014	1019	9.72	10
930419	1822	36.20	11	931024	1642	11.45	12
930429	957	11.77	10	931103	1685	14.64	14
930509	1572	12.90	14	931113	2190	19.26	14
930519	1838	47.16	13	931123	2779	16.29	15
930528	2115	65.38	18	931203	2558	31.58	17
930607	2276	63.22	20	931213	2776	35.69	15
930617	2186	50.23	17	931223	1802	33.66	14
930627	1551	42.98	14				

The 1993 SLR data to Starlette and Stella were reduced using similar parameterizations: A daily adjustment of the coefficient of drag and a fixed coefficient of solar radiation pressure. There was no adjustment of empirical acceleration parameters. However, partials for the coefficient of solar radiation pressure, two constant along-track accelerations, and two along-track 1-CPR acceleration sets were included per 10-day solution arc when the normal equations were formed. Figure 6.2.6–4 shows the Starlette tracking coverage for a representative solution. A typical RMS of fit for these solutions is 5 to 7 cm (Table 6.2.6.2–7). The RMS of fit for Stella is somewhat higher—11 to 18 cm (Table 6.2.6.2–8). Figure 6.2.6–5 shows the tracking coverage for Stella solution epoch 930707.
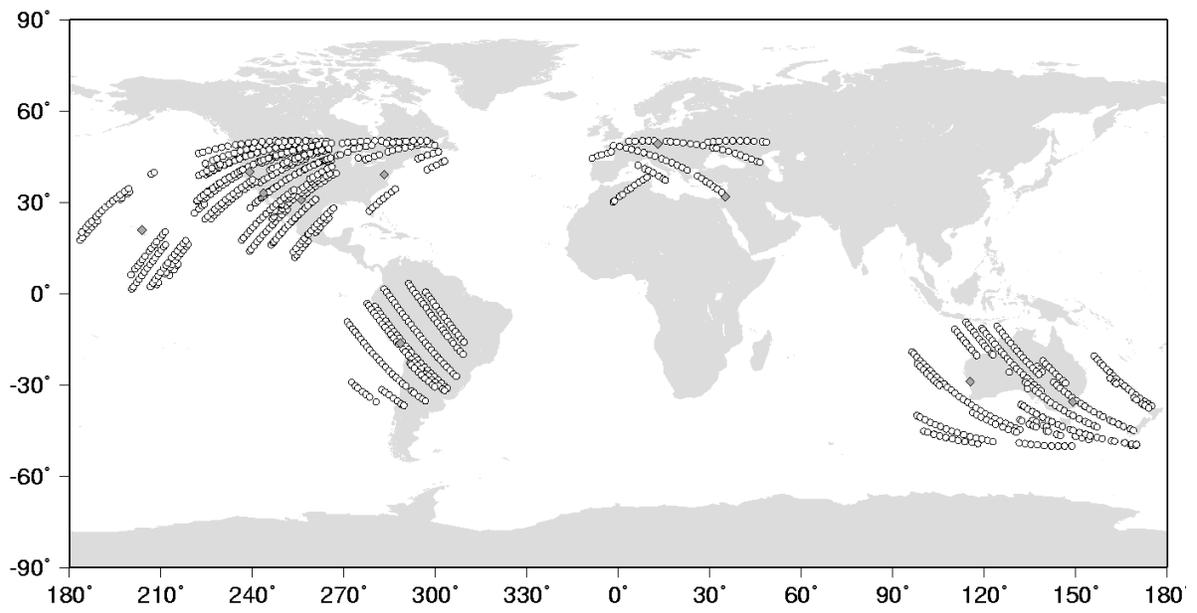
Figure 6.2.6.2–3. Ajisai tracking coverage for solution epoch 930707.
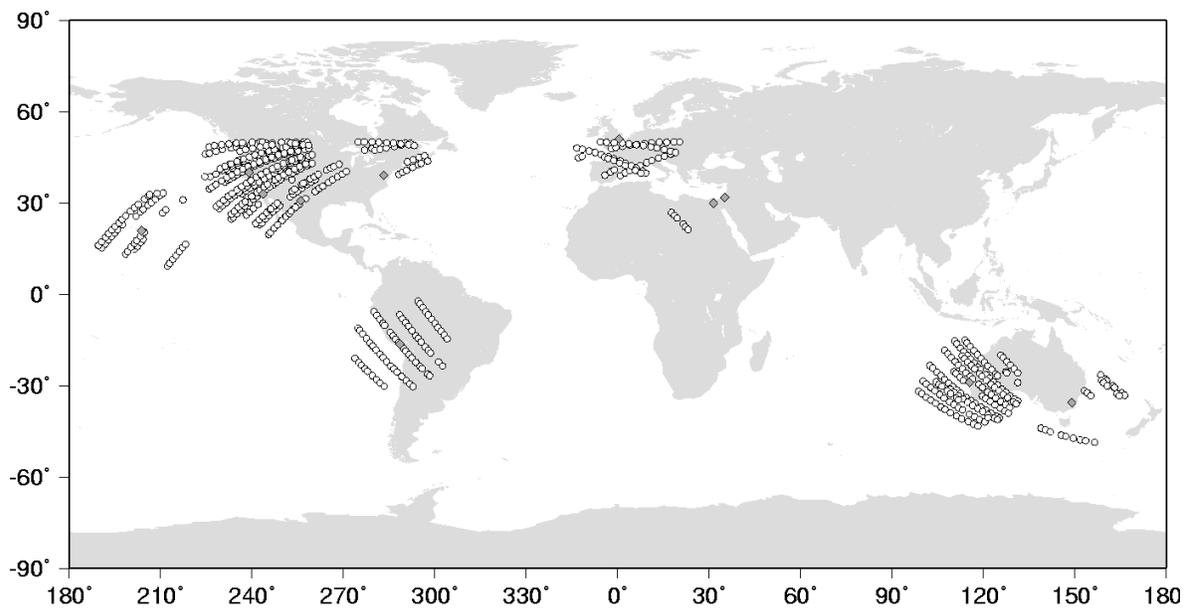
Figure 6.2.6.2–4. Starlette tracking coverage for solution epoch 930707.

Table 6.2.6.2–7. Solution statistics for Starlette.

Epoch	Number of points	RMS (cm)	Number of Sites
931004	995	9.75	14
931014	669	8.45	11
931024	849	11.90	14
931103	996	7.93	15
931113	818	12.49	17
931123	958	11.14	13
931203	777	9.28	14
931213	678	13.19	11
931223	361	10.60	10
940102	669	8.09	12
940112	1295	15.75	16
940121	900	16.96	15
940131	1072	14.24	13
940210	467	4.20	9
940220	747	10.99	9
940302	1232	8.90	15
940312	1291	9.02	14
940322	1459	13.86	19
940401	1241	14.85	19
940411	973	15.67	14
940421	930	16.74	12
940501	924	14.25	11
940511	791	14.78	11
940520	783	12.73	13
940530	1526	10.61	18
940609	1872	9.62	17
940619	1462	11.12	17
940629	704	10.09	14
940709	698	22.12	11
940719	556	21.09	12
940729	1110	12.44	17
940808	1066	10.16	16
940818	957	8.63	14
940828	1036	13.53	14
940906	1816	8.20	14
940916	1004	14.38	11
940926	1194	12.05	12
941006	1327	10.64	14
941016	1153	10.13	17

Table 6.2.6.2–8. Solution statistics for Stella.

Epoch	Number of points	RMS (cm)	Number of Sites
931004	528	13.11	15
931014	352	18.75	12
931024	578	18.86	15
931103	414	16.05	13
931113	482	15.41	16
931123	370	13.23	11
931203	482	18.32	11
931213	576	14.75	12
931223	384	12.40	13
940102	499	13.76	12
940112	575	15.11	12
940121	316	11.39	11
940131	327	9.79	9
940210	511	11.32	13
940220	454	14.72	13
940302	598	17.72	13
940312	777	14.36	16
940322	719	14.98	20
940401	462	13.72	15
940411	670	13.65	13
940421	957	13.91	17
940501	1011	12.23	18
940511	813	16.71	16
940520	621	13.61	15
940530	583	19.65	17
940609	417	14.10	15
940619	498	13.09	17
940629	480	14.57	17
940709	652	14.46	18
940719	545	13.22	17
940729	578	11.14	18
940808	528	16.60	17
940818	451	12.26	12
940828	450	13.27	15
940906	735	19.09	15
940916	471	14.80	13
940926	425	14.04	16
941006	680	12.54	16
941016	397	15.68	15
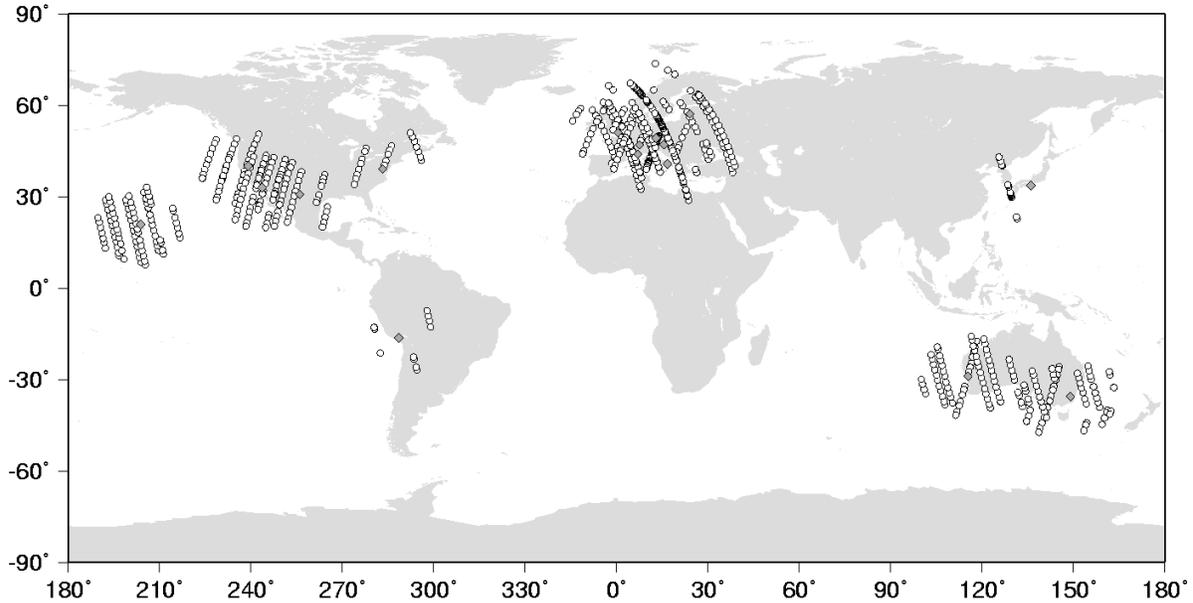
Figure 6.2.6.2–5. Stella tracking coverage for solution epoch 930707.

GFZ–1 orbits the Earth with a mean motion of 15.6 rev/day. The primary resonance with the 16th order terms have a period of 2.8 days. The 1995 SLR tracking of the GFZ–1 satellite was reduced in 3-day arcs to fully sample the beat period while still being short enough to minimize the growth of atmospheric drag perturbations. GFZ–1 was parameterized using an adjusted daily coefficient of drag and a fixed coefficient of solar radiation pressure. No estimation of empirical acceleration parameters was performed. A more frequent adjustment of atmospheric drag was not possible because of the sparse tracking (see Figure 6.2.6.2–6). When the normal equations were formed partials for the coefficient of solar radiation pressure, a constant along-track acceleration, and one along-track 1-CPR acceleration set were included for each 3-day solution arc. Solution statistics for the GFZ–1 data are given in Table 6.2.6.2–9.

Table 6.2.6.2–9. Solution statistics for GFZ–1.

Epoch	Number of points	RMS (cm)	Number of Sites
950420	229	117.26	7
950423	200	152.30	5
950605	169	22.56	3
950608	364	80.30	5
950611	324	147.60	9
950614	63	9.87	5
950617	279	149.35	9
950629	386	53.76	8
950709	213	85.11	6
950721	342	56.98	5
950725	399	106.69	7
950803	794	215.14	10
950806	385	51.23	6
950809	619	114.55	9
950812	391	77.38	9
950815	391	169.32	6
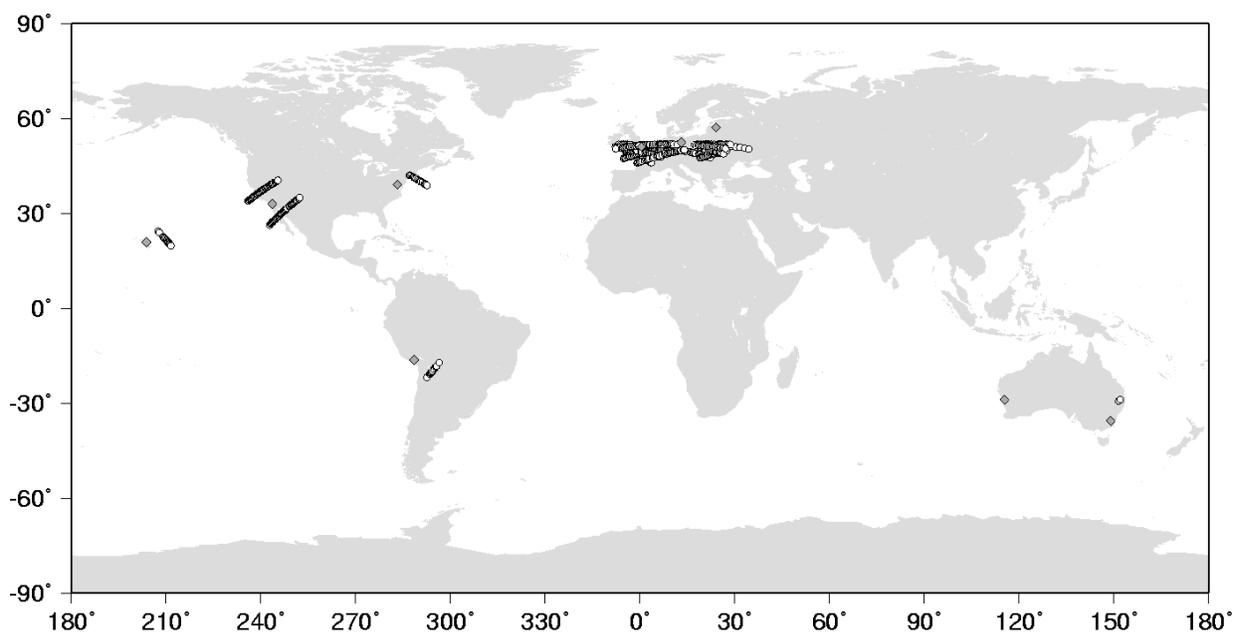
Figure 6.2.6.2–6. GFZ–1 tracking coverage for solution epoch 940102.

6.2.7 Summary of Satellite Tracking Data in EGM96S

A final summary of the tracking data used in the development of the EGM96S model is presented in Table 6.2.7–1. Comparison of the number of spacecraft included in the solution with those listed in Table 6.2.1–1 for the JGM–1 and –2 models shows a significant increase in number, with a corresponding increase in inclination coverage. In total, 10014956 observations were used in EGM96S, including the numerically significant contributions from DORIS (4612075 observations), SLR (2152920 observations), and GPS (1860298 observations).

Table 6.2.7–1. Summary of satellite tracking data included in EGM96S.

Satellite	a (km)	e	i (°)	Data Types	Number of Observations	Dates/ TOPEX/POSEIDON Cycles
ATS–6	41867	.0010	0.9	SST	See GEOS–3 ATS	
Peole	7006	.0160	15.0	Laser	4315	1971
Courier–1B	7469	.0160	28.3	optical	2470	
EP/EUVE	6895	.0013	28.5	TDRSS	151426	1994
				GPS	169596	1992–1993
Vanguard–2	8298	.1640	32.9	optical	1290	
Vanguard–2RB	8496	.1830	32.9	optical	681	
DI–D	7622	.0842	39.5	optical	6032	
				Laser	12160	1971
				Doppler	33483	1967
DI–C	7341	.0526	40.0	optical	2692	
				Laser	7680	1971
				Doppler	24537	1967
BE–C	7507	.0252	41.2	optical	7505	
				Laser	64786	1979–1982
				Doppler	14106	1965
Telstar–1	9669	.2430	44.8	optical	3946	
Echo–1RB	7966	.0120	47.2	optical	4468	
Starlette	7331	.0211	49.8	Laser	184740	1984–1986
					54766	1993–1994
Ajisai	7870	.0011	50.0	Laser	256307	1986–1987
					53698	1993
Anna–1B	7501	.0080	50.1	optical	4043	
GFZ–1	6728	.0013	51.7	Laser	5548	1995
LAGEOS–2	12163	.0132	52.0	Laser	93194	1993–1994
GEOS–1	8075	.0710	59.3	optical	60737	
				Laser	114261	1980
ETALON–1	25501	.0007	64.9	Laser	82918	1991
TOPEX/ POSEIDON	7716	.0004	66.0	Laser	334031	cycles 11–84
				DORIS	4191617	cycles 11–84
				GPS	644026	cycles 10,14,15,17,18,19

Satellite	a (km)	e	i (°)	Data Types	Number of Observations	Dates/ TOPEX/POSEIDON Cycles
Injun–1	7316	.0080	66.8	optical	3264	
Transit–4A	7322	.0080	66.8	optical	3831	
Secor–5	8151	.0790	69.2	optical	721	
GPS/MET	7128	.0011	70.0	GPS	1046676	1995
BE–B	7354	.0140	79.7	optical	1734	
HILAT	7178	.0045	82.0	Doppler	24858	1993
OGO–2	7341	.0750	87.4	optical	1204	
OSCAR–7	7440	.0020	89.2	optical	1851	
OSCAR–14	7448	.0030	89.2	Doppler	62227	1980
RADCAL	7193	.0105	89.5	Doppler	83930	1994
5BN–2	7462	.0060	90.0	optical	818	
NOVA–1	7559	.0010	90.0	Doppler	71767	1984
Midas–4	9995	.0110	95.8	optical	31749	
Stella	7173	.0013	98.6	Laser	21366	1993–1994
SPOT–2	7208	.0020	98.7	DORIS	420458	1990–1992
GEOS–2	7711	.0310	105.8	optical	61431	1975–1977
				Laser	18641	
GEOSAT	7169	.0010	108.0	Doppler	555663	Nov., Dec. 1986; Jan. 1987
SEASAT	7171	.0010	108.0	Laser	13145	
				Doppler	123516	
LAGEOS	12273	.0048	109.9	Laser	650870	1980–1992
					86897	1993–1994
GEOS–3	7226	.0010	114.9	SST ATS–6	27400	1975–1979
				SST period Laser	16935	1975–1979
				Laser	76662	1980
OVI–2	8317	.0180	144.3	optical	962	

SST: satellite-to-satellite

6.3   Satellite-Only Model Development

6.3.1 The IUGG Satellite-Only Solution, PGS5737

A satellite-only solution, PGS5737, was presented at the Boulder, CO, meeting of the International Union of Geodesy and Geophysics meeting (IUGG) in 1995. This model was a milestone, for it marked the first time a substantial portion of the reiterated normal equations and new data were included in a gravity solution after the 1992 release of JGM–2S. This interim model is summarized in this section. The salient new data and other characteristics of PGS5737 are summarized in Table 6.3.1–1. This model was used as a baseline for many of the subsequent satellite-only solutions leading to EGM96S.

Table 6.3.1–1. Summary of the IUGG satellite-only model PGS5737.

- Satellites and tracking data from JGM–2S
- 1989–1992 LAGEOS data
- 1993 SLR data from LAGEOS, LAGEOS–2, Starlette, Ajisai, and Stella
- 1994 SLR data from LAGEOS, LAGEOS–2, Starlette, and Stella
- Cycles 16–47 TOPEX/POSEIDON (T/P) SLR and DORIS data
- T/P GPS data (1-day arcs)
- EP/EUVE TDRSS data (preliminary version of normal equations)
- Two sets of SLR stations estimated:
    - one set for the SLR data from 1993 and 1994
    - one set for the SLR data from earlier years (pre-1992)
- 5-day pole position solved for the period from 1979.12.31 to 1994.12.31
- The *a priori* power law applied was:

$$\sigma_n = \frac{10^{-5}}{n^2} \frac{1}{\sqrt{2}}$$

(Kaula rule of thumb/$\sqrt{2}$), which is the same power law constraint applied in GEM–T2, JGM–1S, and JGM–2S.

At the time of PGS5737, an incompatibility existed between the reference frames for the SLR stations used in the gravity solutions. As Table 6.3.1–1 indicates, two sets of stations were adjusted: One set for all the SLR data from 1993 and 1994, and one set for all the earlier data. Specifically, the SLR data from 1993 and 1994 were converged with an *a priori* station set from CSR93L01 [*Boucher et al.*, 1994], with epoch at 1988.01.01, whereas the earlier data used the station set derived from the LAGEOS tectonic solution SL7.1 [*Smith et al.,* 1990] at epoch 1986.07.01 using NUVEL–1A [*DeMets et al.,* 1990] station velocities.

The TOPEX/POSEIDON (T/P) SLR/DORIS data were converged with the first-generation parameterization [*Marshall et al.*, 1995b], and included data through cycle 47. The T/P GPS data

included 1-day arcs from select periods between cycles 10 and 19. These arcs included both the ground–T/P–GPS–GPS double differences, as well as the ground–ground–GPS–GPS double-difference data to help constrain the determination of the GPS orbits. This solution also used a preliminary version of the EP/EUVE TDRSS data that was based on the original T/P precision orbit solutions and the *a priori* TDRS macro model [*Marshall et al.*, 1996]. These solutions used the T/P one-way and two-way range-rate, and the EP/EUVE two-way range-rate data to determine both the TDRS and EP/EUVE orbits. No range data (including BRTS) were used, and data editing was minimal. These normal equations included T/P TDRSS data as well as EP/EUVE TDRSS data. Drag coefficients were estimated every 12 hours (compared to every 8 hours with the final EP/EUVE TDRSS normal equations used in EGM96S). Overall, these data sets were less refined than those eventually used in EGM96S.

PGS5737 was evaluated using orbit fits with LAGEOS, LAGEOS–2, Ajisai, Starlette, Stella, and T/P. The SLR satellite fits are summarized in Table 6.3.1–2, based on the orbit tests described in Section 5.1. All the orbit tests show improvement for the new satellite-only model. The dramatic improvement in the fit of the Stella test arc is an artifact of how the 1-CPR acceleration parameters were treated on Spot–2 in JGM–2S. Spot–2 is in nearly the same orbit as Stella, and is sensitive to similar terms of the geopotential. The empirical 1-CPR acceleration parameters were adjusted in the orbit determination process for Spot–2, to remove residual nonconservative force mismodeling (Spot–2 is a complicated spacecraft with articulating solar arrays and other appendages with a large area-to-mass ratio). This adjustment effectively removed the odd zonal and resonance order signal from the SPOT–2 contribution to JGM–2S. If 1-CPR accelerations are not subsequently estimated for this orbit when using the JGM–2S model, the uncorrected error from the odd zonals and resonance terms would be significant. In the orbit tests for Stella, these parameters were not adjusted since Stella is a dense, small, cannonball-like satellite that is well modeled. In PGS5737, and EGM96S, the zonal information for the Sun-synchronous orbits (~98° inclination) is obtained from Stella's contribution correcting the shortcomings in JGM–2S, which was completed before Stella was launched.

Table 6.3.1–2. SLR orbit test (set-1) residuals for the satellite-only models JGM–2S and PGS5737.

Gravity	Tides	RMS of Fit (cm)				Single arc
		Multiple arc				
		LAGEOS[1]	LAGEOS–2[2]	Starlette	Ajisai	Stella
JGM–2S	PGS4846X	3.15	3.29	9.27	7.40	163.87
PGS5737	PGS5737	2.91	3.16	7.73	7.21	22.73

[1]Sa, Ssa tides adjusted as global parameters   [2]Sa, Ssa tides not adjusted

The results of RMS of fit tests with the T/P test arcs are summarized in Table 6.3.1–3. These tests used the first-generation orbit parameterization discussed by *Marshall et al.* [1995b]. Almost all the test arcs show an improvement in the fit to the SLR data. The DORIS data show

little change in the RMS of fit, since these data were already fitting close to their noise level in JGM–2S.

A test to assess the accuracy of the gravity anomalies predicted by satellite models provides an excellent means to assess the ability of the model to describe the longer wavelength geoid. The altimeter-derived 5°x5° mean anomalies from the GEOSAT Geodetic Mission, provided by NIMA, were used to compare JGM–2S with PGS5737 using the procedure outline in Section 5.8. Figure 6.3.1–1 summarizes the variance v_M about the mean difference by maximum degree of summation. At degree 70, the RMS variance is 16.35 mGal^2 for JGM–2S, and 13.39 mGal^2 with PGS5737, indicating a substantial improvement.

Table 6.3.1–3. T/P SLR and DORIS data RMS of fit using JGM–2S and PGS5737 and the first-generation T/P solution parameterization [*Marshall et al.*, 1995b]. PGS4846X tides used with JGM–2S, PGS5737 tides used with PGS5737.

Cycle	Epoch	SLR RMS (cm)		DORIS RMS (mm/s)	
		JGM–2S	PGS5737	JGM–2S	PGS5737
10	921221	4.16	3.81	0.583	0.584
14	930130	4.73	4.21	0.565	0.563
19	930330	4.97	4.40	0.559	0.557
21	930409	4.45	4.30	0.551	0.552
27	930607	3.32	3.03	0.554	0.556
33	930807	4.02	3.81	0.534	0.530
39	931004	3.48	3.19	0.575	0.578
46	931213	3.51	3.19	0.575	0.578
69	940729	4.40	3.25	0.560	0.551
70	940808	4.63	3.84	0.564	0.557
71	940818	3.84	3.82	0.561	0.558
72	940828	3.89	3.54	0.567	0.564
73	940906	3.79	3.23	0.554	0.550
Average		4.09	3.66	0.562	0.560

The JGM–2S and PGS5737 models were compared by calculating the RMS of the coefficient uncertainties (1σ) per degree for each model, and computing the ratio of these errors at each degree with PGS4846X and JGM–2S. The result is depicted in Figure 6.3.1–2. The absolute RMS errors per degree are read on the left scale for JGM–2S and PGS5737. They are shown for comparison with the Kaula power law spectrum and the error spectrum for PGS4846X. The ratio of the coefficient errors between PGS5737 and JGM–2S and JGM–2S and GEM–T3S is shown on the second Y axis. This illustration shows that the formal standard deviations of the PGS5737 coefficients have improved by up to a factor of three over JGM–2S for terms through degree 20. This is a substantial improvement over the gain between GEM–T3S and JGM–2S, which was only a factor of one to two. As will be shown later, the inclusion of the near-continuously tracked EP/EUVE caused most of the improvement in the low-degree terms.
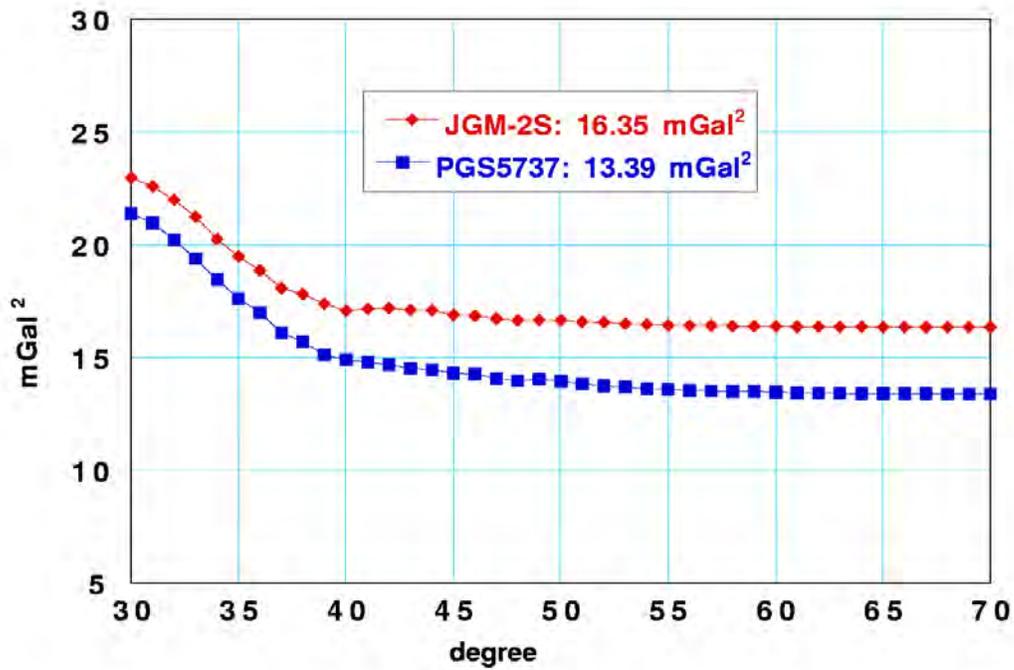
Figure 6.3.1–1. Variance about the mean difference between the GEOSAT altimeter-derived 5°x5° mean gravity anomalies and the JGM–2S and PGS5737 geopotential models, by maximum degree of summation.
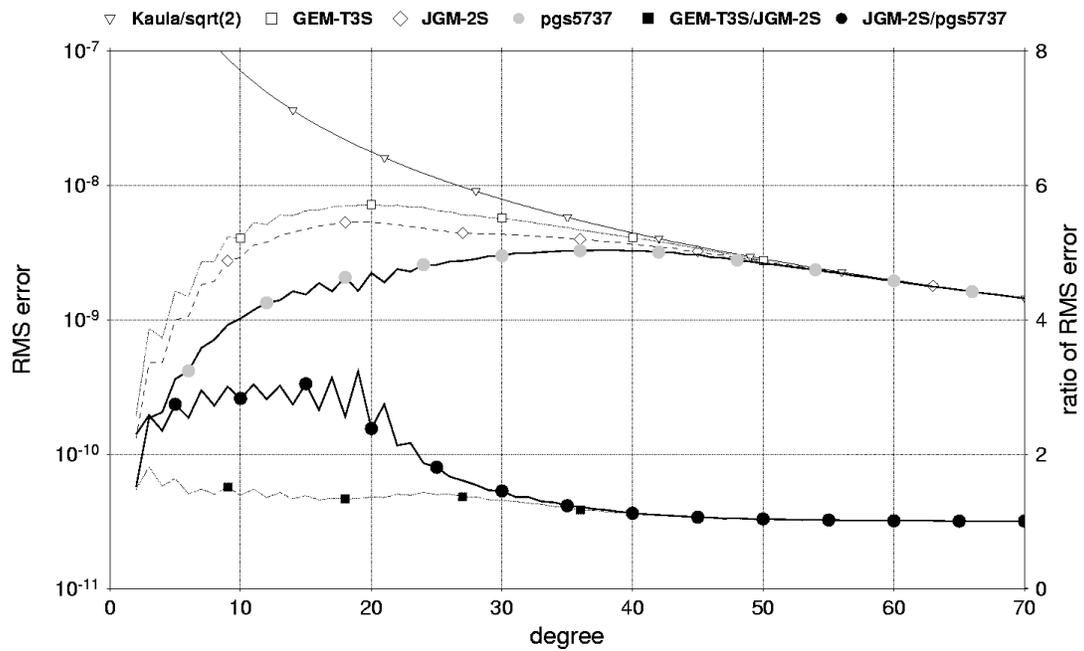
Figure 6.3.1–2. RMS error per degree per coefficient for model PGS5737. Comparison of coefficient uncertainties with JGM–2S shows strong formal error reduction at low orders.

PGS5737 represented an important update to JGM–2S and served as a baseline for further solutions, but highlights that much further work was needed. The new data from the TRANET-tracked satellites (HILAT, RADCAL, D1–D, D1–C, BE–C), as well as the GPS data from EP/EUVE and GPS/MET, still needed to be added to the solution. Furthermore, a global calibration of the normal equation weights was necessary to achieve an optimal modeling outcome with a calibrated error model.

6.3.2 *The Role of the* A Priori *Power Law Constraint*

An *a priori* constraint must be applied to the normal equations derived from the satellite tracking data in order to obtain a reasonable satellite-only gravity field solution. In unconstrained satellite-only solutions, the shorter wavelength terms are ill-determined and are recovered with excessive and unrealistic power. Furthermore, the solution uncertainties for these coefficients can be orders of magnitudes larger than the expected values of the coefficients themselves. Constraining them to zero with the application of a power law reduces their maximum errors to less than their expected value (See the GEM–T1 paper [*Marsh et al.*, 1988] for a complete discussion of this constraint method and its relationship to least squares collocation). In a combined solution including surface gravity and ocean altimetry, the shorter wavelength portion of the model does not need to be constrained. However, determining an optimal satellite model, which is the basis for the combined solutions, is a necessary first step.

Many years ago, *Kaula* [1963] pointed out that the power spectrum for Earth gravity coefficients followed the approximate power law $\sigma_n = 10^{-5}/n^2$. *Lerch et al.* [1991] showed that this power law actually overestimated the power in the harmonic coefficients, and that a better expression was $\sigma_n = 10^{-5}/\sqrt{2}n^2$. This was the form of the power law constraint applied in the PGS4846X, JGM–1S, JGM–2S, and PGS5737 models. While this constraint represents an improvement, it still underestimates the power in the harmonic coefficients for degrees 40 and higher when compared with a power spectrum derived from a quadrature solution. Since the satellite-only gravity model forms a foundation for the development of the high-degree models, it is imperative that the satellite-only model have the most realistic error spectrum possible. A new constraint was selected based on the spectrum of the geopotential coefficients from the quadrature solution V037, which was developed contemporaneously with PGS5737 based on the new 30´x30´ surface gravity data provided by NIMA. The new values of σ_n were used in subsequent solutions, from PGS6394 through EGM96S. These values are listed in Table 6.3.2–1, and compared with the $\sigma_n = 10^{-5}/\sqrt{2}n^2$ constraint in Figure 6.3.2–1.

The effect of the new constraint was tested on two satellite-only solutions: PGS6345 (with the $\sigma_n = 10^{-5}/\sqrt{2}n^2$ constraint) and PGS6348 (with the new constraint). These satellite-only solutions represented updates to PGS5737 that incorporated (a) the TRANET tracking of HILAT, RADCAL, D1–D, D1–C, and BE–C, (b) the GPS tracking of EP/EUVE and GPS/MET, and (c) a readjustment of the weights used in PGS5737. The coefficients of both fields were compared with the mean 5°x5° altimeter-derived anomalies from the GEOSAT Geodetic Mission. The variance about the mean at degree 70 was 11.05 mGal^2 for PGS6345 and 10.79 mGal^2 for PGS6348, showing an improvement of 0.26 mGal^2. The geoid error to 70x70 was computed from the full covariance of these satellite-only solutions, and was found to be 105 cm for

PGS6345 and 123 cm for PGS6348. Thus, the original $\sigma_n = 10^{-5}/\sqrt{2}n^2$ constraint causes the satellite-only solution to underestimate the geoid error by 15 percent.

Table 6.3.2–1. RMS of coefficients per degree from quadrature solution V037.

n	σ_n	n	σ_n	n	σ_n	n	σ_n
2	.12578E-05	20	.14714E-07	38	.52844E-08	56	.31743E-08
3	.11223E-05	21	.15096E-07	39	.53726E-08	57	.30541E-08
4	.50434E-06	22	.13505E-07	40	.47294E-08	58	.26457E-08
5	.35266E-06	23	.11827E-07	41	.48758E-08	59	.28290E-08
6	.25098E-06	24	.98631E-08	42	.47668E-08	60	.25853E-08
7	.19401E-06	25	.10549E-07	43	.44341E-08	61	.24429E-08
8	.11837E-06	26	.88223E-08	44	.41639E-08	62	.24999E-08
9	.98351E-07	27	.68110E-08	45	.42450E-08	63	.24003E-08
10	.77507E-07	28	.85066E-08	46	.43786E-08	64	.21588E-08
11	.54299E-07	29	.75938E-08	47	.41605E-08	65	.20863E-08
12	.30101E-07	30	.75732E-08	48	.37057E-08	66	.21956E-08
13	.46184E-07	31	.69961E-08	49	.33436E-08	67	.21675E-08
14	.27438E-07	32	.66633E-08	50	.36241E-08	68	.21057E-08
15	.25295E-07	33	.66756E-08	51	.32875E-08	69	.21244E-08
16	.23877E-07	34	.73554E-08	52	.32405E-08	70	.18057E-08
17	.19074E-07	35	.69657E-08	53	.35228E-08		
18	.19240E-07	36	.60043E-08	54	.32408E-08		
19	.16031E-07	37	.60134E-08	55	.29688E-08		

The difference in the gravity coefficients and the coefficient standard deviations between PGS6345 and PGS6348 are depicted in Figure 6.3.2–2. The differences in the coefficient standard deviations are largest above degree 30, and show that the change in the constraint has the largest effect at the higher degrees. However, because of the strong correlations between coefficients of the same order and odd/even degree parity (arising from the fact that these coefficients produce orbital perturbations at the same frequency [*Kaula*, 1966; *Rosborough*, 1986]), changes in coefficients can also occur at the lower degrees.

The results of orbit tests with these two satellite-only fields are shown in Table 6.3.2–2 for the SLR test satellites and in Table 6.3.2–3 for T/P. In both cases, there is little difference in the RMS of fit. This is as it should be, since the alteration of the constraint will leave the wavelengths to which these satellite tracking data are most sensitive relatively unchanged, and there are plenty of adjusting coefficients to satisfy the observed orbit perturbations. The constraint influences how this orbit information is distributed between coefficients of the same order. However, there is a hint that, for the lower orbiting satellites (Stella and Starlette), the application of the new constraint improves the RMS of fit.
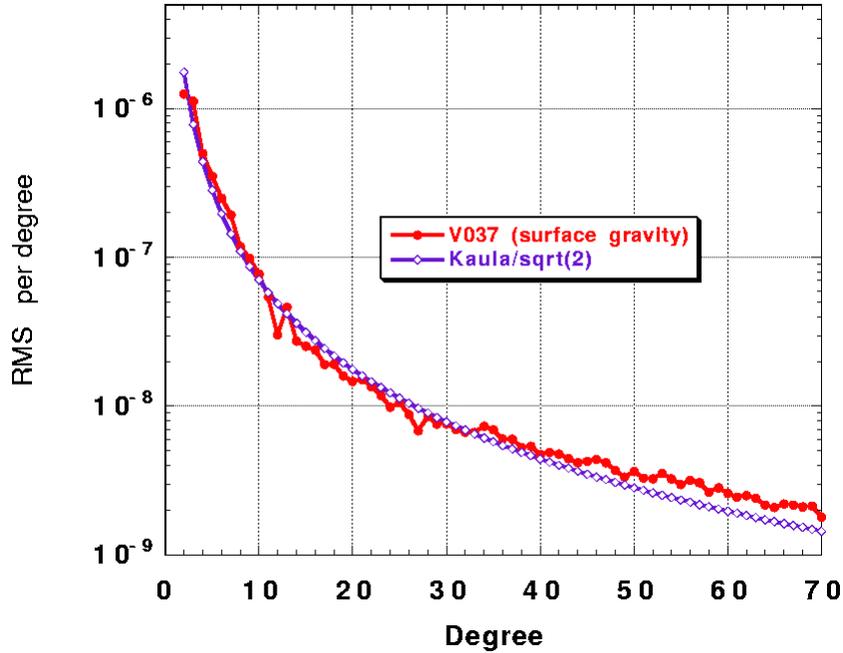
Figure 6.3.2–1. Comparison of two a priori power law constraints applied in satellite-only solutions: $\sigma_n = 10^{-5}/\sqrt{2}n^2$; V037 power spectrum (from quadrature solution using NIMA 30´x30´ surface gravity data).

all values are in units of 10^{-10}
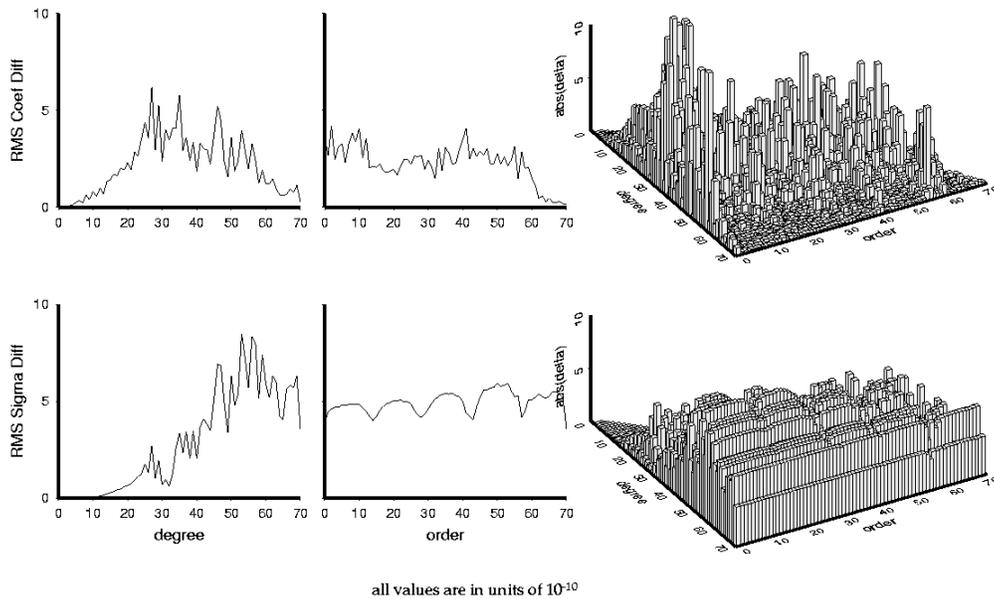
Figure 6.3.2–2. Gravity coefficient and standard deviation differences between two satellite-only models: PGS6345, using the $\sigma_n = 10^{-5}/\sqrt{2}n^2$ power law constraint, and PGS6348, using the new *a priori* power law constraint.

Table 6.3.2–2. SLR orbit test (set–1) residuals for the satellite-only models PGS6345 and PGS6348.

Gravity	Tides	RMS of Fit (cm)				
		Multiple arc				Single arc
		LAGEOS[1]	LAGEOS–2[2]	Starlette	Ajisai	Stella
PGS6345	PGS6345	2.91	3.15	7.75	7.14	18.53
PGS6348	PGS6348	2.91	3.17	7.71	7.14	18.37

[1]Sa, Ssa tides adjusted as global parameters   [2]Sa, Ssa tides not adjusted

Table 6.3.2–3. T/P SLR and DORIS data RMS of fit using PGS6345 and PGS6348, with their self-consistent tides solutions, and the first-generation T/P solution parameterization [*Marshall et al*., 1995b].

Cycle	Epoch	SLR RMS (cm)		DORIS RMS (mm/s)	
		PGS6345	PGS6348	PGS6345	PGS6348
10	921221	3.86	3.87	0.583	0.583
19	930330	4.17	4.18	0.555	0.555
21	930409	4.27	4.25	0.550	0.550
46	931213	3.48	3.49	0.574	0.574
69	940729	3.48	3.46	0.553	0.553
70	940808	3.98	3.95	0.559	0.558
71	940818	3.79	3.76	0.558	0.558
72	940828	3.61	3.60	0.564	0.564
73	940906	3.15	3.15	0.551	0.551
Average		3.75	3.75	0.561	0.561

6.3.3 The April 1996 Satellite-Only Model, PGS6394

Following PGS5737, the next milestone satellite-only solution was PGS6394. This solution incorporated all the new tracking data, including the new TRANET data (from RADCAL, HILAT, D1–D, D1–C, and BE–C), and the new GPS data (GPS/MET, EP/EUVE). In addition, the normal equations from T/P, consisting of 1-day arcs, were updated.. The new satellite-only field PGS6394 also included the new *a priori* constraint that was described in the preceding section. This satellite-only model formed the foundation for the high-degree models that were released to the International Evaluation Working Group (EGM–X02 to X05). The characteristics of PGS6394 are summarized in Table 6.3.3–1.

Some of the major analysis efforts that contributed to PGS6394 were:

a) The EP/EUVE TDRSS data were reprocessed after the IUGG using a post-IUGG satellite-only model (PGS5784).

b) New T/P GPS normal equations (1-day arcs)

Table 6.3.3–1. Summary of the PGS6394 satellite-only model.

- Satellites and tracking data from JGM–2S
- 1989–1992 LAGEOS data
- 1993 SLR data from LAGEOS, LAGEOS–2, Starlette, Ajisai, and Stella
- 1994 SLR data from LAGEOS, LAGEOS–2, Starlette, and Stella
- Cycles 16–47 T/P SLR and DORIS data
- T/P GPS data (1-day arcs: new version of normal equations)
- EP/EUVE TDRSS data (new version of normal equations)
- GPS Tracking from EP/EUVE and GPS/MET
- Two sets of SLR stations estimated:
  - one set for the SLR data from 1993 and 1994
  - one set for the SLR data from earlier years (pre-1992)
- 5-day pole position solved for the period from 1979.12.31 to 1994.12.31
- Power law constraint from surface gravity quadrature solution (V037)
- 5-day pole position solved for the period from 1979.12.31 to 1994.12.31

The results of satellite tracking data RMS of fit tests are summarized in Tables 6.3.3–2 and 6.3.3–3. The improvements in the satellite fits, which were originally obtained with the IUGG satellite-only model, PGS5737, appear to have been maintained in the new model, at least at the wavelengths and for the lumped coefficients to which these satellites are sensitive. An increase in the fit to the Stella test arc from 18.37 cm in PGS5737 to 19.39 cm is observed.

Table 6.3.3–2. SLR orbit test (set-1) residuals for the satellite-only models JGM–2S and PGS6394.

Gravity	Tides	RMS of Fit (cm)				
		Multiple arc				Single arc
		LAGEOS[1]	LAGEOS–2[2]	Starlette	Ajisai	Stella
JGM–2S	PGS4846X	3.15	3.29	9.27	7.40	163.87
PGS6394	PGS6394	2.92	3.15	7.70	7.15	19.39

[1]Sa, Ssa tides adjusted as global parameters   [2]Sa, Ssa tides not adjusted

The satellite-only model PGS6394 was a foundation for the combination model PGS6399, which included direct altimetry from T/P, GEOSAT, GEOS–3, and SEASAT, as well as surface gravity normals (to $N_{max} = 70$) constructed from the merged 30´x30´ surface gravity file, which excluded altimeter-derived anomalies.

Table 6.3.2–3. T/P SLR and DORIS data RMS of fit using JGM–2S and PGS6394 and the first-generation T/P solution parameterization [*Marshall et al.*, 1995b]. PGS4846X tides used with JGM–2S, PGS6394 tides used with PGS6394.

Cycle	Epoch	SLR RMS (cm)		DORIS RMS (mm/s)	
		JGM–2S	PGS6394	JGM–2S	PGS6394
10	921221	4.16	3.73	0.583	0.582
19	930330	4.97	4.18	0.559	0.555
21	930409	4.45	4.27	0.551	0.550
46	931213	3.51	3.47	0.572	0.574
69	940729	4.40	3.36	0.560	0.553
70	940808	4.63	3.95	0.564	0.552
71	940818	3.84	3.74	0.561	0.558
72	940828	3.89	3.60	0.567	0.564
73	940906	3.79	3.04	0.554	0.550
Average		4.18	3.70	0.563	0.560

6.3.4 Issues Leading to the Final Satellite-Only Model, EGM96S

While the PGS6394 satellite-only model appeared satisfactory, in terms of the RMS of fit for the various orbit tests and its performance when used as a foundation for high-degree quadrature models, there remained numerous outstanding issues:

a) The first set of issues concerned the data weight calibration and the need to optimize the model while ensuring realistic error estimates. We were concerned about the apparently optimistic satellite-only covariance, as measured by the degree of improvement over JGM–2S. The ratio of the RMS of the coefficient standard deviations per degree in JGM–2S and PGS6394 reaches a maximum of six at degree 10, and is above four from degrees 5 through 22 (see Figure 6.3.4–1).

Further, the weights of the new data had been selected incrementally, as each set was added to the solution. The satellite-only model had to be recalibrated to account for the interplay between the different sets of satellite tracking data in the presence of the new power law constraint.

b) A second outstanding issue affected all the GPS data, and was discovered only after the release of the combination model and the concomitant high-degree models. Because of an indexing problem that occurred during the creation of the normal equations, which included the GPS data from EP/EUVE, T/P, and GPS/MET, the partials for 74 of the S coefficients between degrees 19 and 21 were overwritten with those of time-variable gravity coefficients. The effect was to constrain the coefficients at their *a priori* values. Since the *a priori* values came from the combination model JGM–2, which used surface gravity and altimetry, these data sources were now getting into the satellite-only model (PGS6394) indirectly. Furthermore, the standard deviations for those specific S coefficients were minuscule compared to the standard deviations for the C coefficients at these same degrees. This

indexing error was unknown when the test models, based on the PGS6394 solution, were released to the international evaluation committee in April 1996.
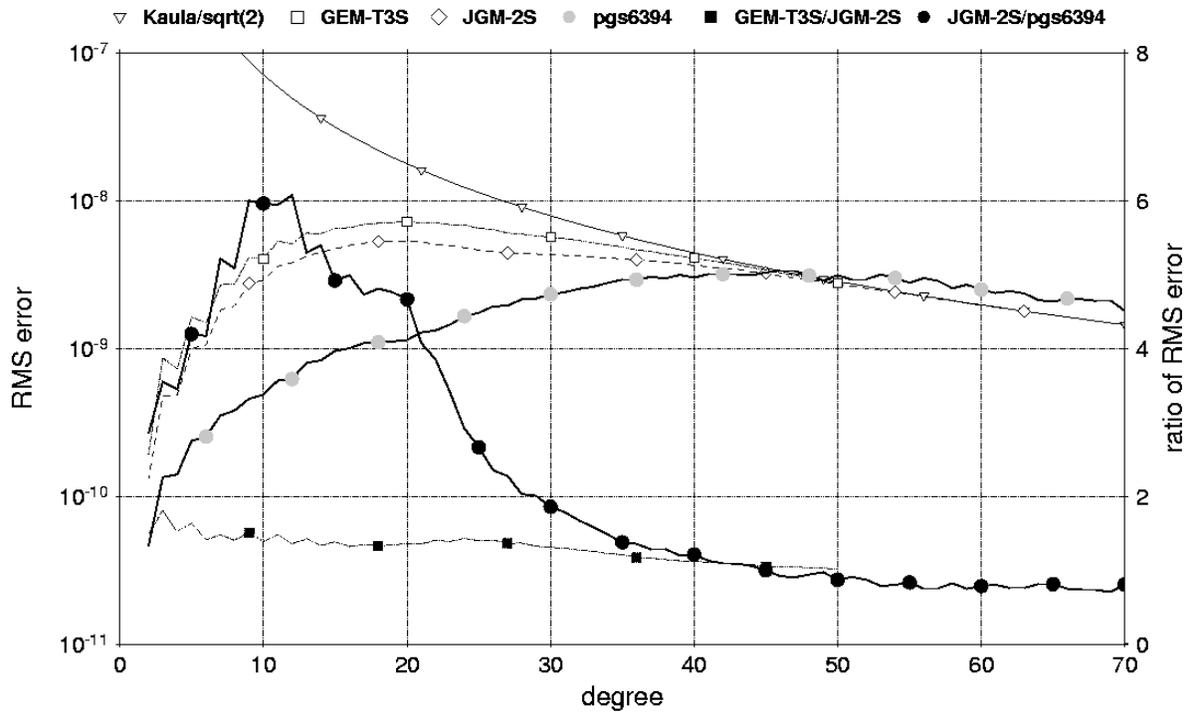
Figure 6.3.4–1. Ratio of the RMS coefficient error per degree for model PGS6394, compared with JGM–2S.

c) Later, it was also discovered that the Starlette data from 1983 produced groundtrack-like marks in the gravity anomaly error map derived from the full 70x70 covariance. The source of this problem was not understood, and since time precluded any reanalysis of these data prior to the scheduled completion of the model, the 1983 Starlette data were excluded from EGM96S and EGM96. Several years of Starlette remained in the solution to represent this important satellite.

d) Finally, there was an issue that concerned the altimetry used in the low-degree combination model. The T/P altimetry in PGS6399 was corrected for the high-degree geoid using OSU91A and relied upon a pre-T/P tide model (cf. *Schwiderski* [1980]) to remove the geometric effect of the tides in the altimeter data. The altimeter data normal equations had to be re-created to take advantage of a new T/P era tide model and improved high-degree geoid model corrections. In order to remain 100 percent consistent with the altimeter normals, the SLR and DORIS data normals were also re-created. For more details on the T/P altimetry reprocessing, see Section 7.3.2.

6.4   Final Satellite-Only Model Definition

As a result of the concerns raised in the development of the interim models described previously, the development of the final satellite-only model, EGM96S, included significant changes:

- The GPS normal equations were re-created, using a GEODYN load module that corrected the indexing error in the gravity field partials.

- TOPEX/POSEIDON (T/P) SLR/DORIS solutions were reconverged using the second-generation orbit parameterization [*Marshall et al.*, 1995b], including JGM–3 and the CSR93L01 station set. Cycles 11–84 (data from 1993 through 1994) were reprocessed. Though not germane to the satellite-only model, the corrections for the altimeter data now included the high-degree geoid correction from the quadrature model V058 (to degree 460), and the tide corrections from an updated version of the *Schrama and Ray* [1994] tide model.

- The SLR data from 1993 and 1994 were shifted to be consistent with the frame of the 1980–1992 data.

- The Starlette 1983 data were removed from the solution.

- The entire solution was calibrated after the new normal equations had been created. The calibrations for the satellites with continuous tracking (GPS and TDRSS) were studied in a parametric fashion (see Section 6.4.1). Other tests, such as those with the 5°x5° altimeter-derived anomalies, and GPS/leveling tests played a role in the selection of the weights of these satellites.

- The *a priori* GM value from *Ries et al.* [1992] was adopted to preserve the scale defined by SLR.

6.4.1   Weight Selection and Solution Calibration Procedure

The calibration procedure was described by *Lerch et al.* [1991] and has been applied in the development of previous Earth gravity solutions such as GEM–T2 [*Marsh et al.,* 1990] and JGM–1S and JGM–2S [*Nerem et al.*, 1994b]. This method adjusts the relative weights of the different sets of data in the solution in order to objectively obtain an optimum least-squares solution. The procedure, discussed in the next section, is designed to ensure that the final solution has a realistic covariance by requiring that the differences of the adjusted parameters between the master solution (containing all the data) and the subset solutions (each excluding a set of data) are commensurate with their corresponding uncorrelated error estimate differences.

In the development of EGM96S, all satellites and sets of data were calibrated at least once. That is, the calibration factors were examined, and a new master solution was constructed. Subsequently, the calibrations of important satellites such as T/P, Starlette, EP/EUVE, and GPS/MET were rechecked. The final solution accommodated two other considerations: (1) the 1990 and 1992 SPOT–2 data were calibrated separately and (2) the Starlette 1983 data were found to produce ground tracks in geographic maps of the projected gravity anomaly errors, and so were removed from the solution.

Prior to discussing the results of the calibrations, we will review the basis for the calibration procedures. To derive the gravity field solution, we solve a least-squares equation of the form:

$$\mathbf{Nx} = \mathbf{R} \tag{6.4.1-1}$$

which is the normal equation where $\mathbf{N}$ is the normal matrix, $\mathbf{x}$ is the vector of adjusted parameters, and $\mathbf{R}$ is the residual vector. $\mathbf{N}$ is the sum of the normal matrices from the individual sets of data, as well as the signal (or constraint) matrix, i.e.,

$$\mathbf{N} = \mathbf{K} + \mathbf{W}_1\mathbf{N}_1 + \mathbf{W}_2\mathbf{N}_2 + ... + \mathbf{W}_j\mathbf{N}_j \tag{6.4.1-2}$$

$$\mathbf{R} = \sum \mathbf{W}_j\mathbf{R}_j \tag{6.4.1-3}$$

where $\mathbf{K}$ is defined as

$$\mathbf{K} = \sum \frac{C_{nm}^2 + S_{nm}^2}{\sigma_n^2} \tag{6.4.1-4}$$

and represents the diagonal signal matrix (i.e., constraint matrix) that is introduced to achieve improved stability in the least-squares solution and prevent the high-degree terms from developing excessive power. Note that the constraint has the effect of both minimizing the signal and the noise in the satellite-only solution since the *a priori* value assumed for the coefficients is zero (see *Marsh et al.* [1988], which ties this method to least-squares collocation). The complete solution of eq. (6.4.1-1), including all the data and the *a priori* constraint matrix, is represented in the form:

$$\mathbf{X} = \left(\mathbf{K} + \sum \mathbf{W}_j\mathbf{N}_j\right)^{-1}\left(\sum \mathbf{W}_j\mathbf{R}_j\right) \tag{6.4.1-5}$$

A subset solution which does not include data set, t, is given as

$$\mathbf{X}_t = \left(\mathbf{K} + \sum_{j \neq t} \mathbf{W}_j\mathbf{N}_j\right)^{-1}\left(\sum_{j \neq t} \mathbf{W}_j\mathbf{R}_j\right) \tag{6.4.1-6}$$

and the covariance matrices for these two solutions is represented as

$$V(\mathbf{X}) = \left(\mathbf{K} + \sum \mathbf{W}_j\mathbf{N}_j\right)^{-1} \tag{6.4.1-7}$$

$$V(\mathbf{X}_t) = \left(\mathbf{K} + \sum_{j \neq t} \mathbf{W}_j\mathbf{N}_j\right)^{-1} \tag{6.4.1-8}$$

for the full and subset solutions, respectively. We are interested in the differences in the adjusted parameters due to data set t, and we assume that the difference between the subset and full solutions can be predicted by the two solution covariance matrices. So, we take the expected value of the difference between the solution vectors $\mathbf{X}$ and $\mathbf{X}_t$:

$$E(\mathbf{X}_t - \mathbf{X})(\mathbf{X}_t - \mathbf{X})^{\mathrm{T}} = V(\mathbf{X}_t) - V(\mathbf{X}) = V(\mathbf{X}_t - \mathbf{X}) \tag{6.4.1-9}$$

Finally, we introduce the calibration factor, k_t^2, for data set t. We also restrict the analysis to the adjusted geopotential coefficients and take the Trace [TR] of the difference of the covariance matrices, obtaining:

$$(\mathbf{X}_t - \mathbf{X})^2 = k_t^2 \, \text{TR}[V(\mathbf{X}_t - \mathbf{X})] = k_t^2 \left(\sigma_t^2 - \sigma^2\right) \tag{6.4.1–10}$$

where σ_t and σ are the coefficient uncertainties from the subset and master solutions. *The approximation procedure takes into account the standard deviations of the geopotential coefficients, but not the correlations in the gravity field covariance.* Calibration factors greater than unity indicate that the data excluded from the subset solution are overweighed, and that this set of data is changing the gravity coefficients by more than would be suggested by the covariance. It indicates an error covariance that is overly optimistic for the set of data being calibrated.

We use the following definition of the effective data uncertainty for data set t:

$$\hat{\sigma}_t = \frac{\sigma_r}{\sqrt{w_n w_a}} \tag{6.4.1–11}$$

where

    σ_r is the data uncertainty applied in the data reduction within GEODYN

    w_n is the weight scale factor applied within SOLVE to the normal equations used in a given gravity solution

    w_a is the weight scale factor applied within SOLVE during the aggregation of the individual normal equation sets from the data reduction. In most cases this scale factor is unity.

As a matter of convenient bookkeeping in the GEODYN/SOLVE environment, we generally refer to the scale value w_n in discussion of the *a priori* weight scale factor used in the calibration process (where it is relevant, both the final effective data uncertainty, $\hat{\sigma}$, and the normal equation weight scale factor, w_n, are reported). Correspondingly, the normal equation scale factor for the data set t are adjusted according to the following relation to correct the weighting:

$$w_n^* = \frac{w_n}{k_t^2} \tag{6.4.1–12}$$

where w_n^* is the new weight scale factor for this set of normal equations. This produces a final effective observation "noise" estimate of:

$$\hat{\sigma} = \frac{\sigma_r}{\sqrt{w_n^* w_a}} = k_t^2 \hat{\sigma}_t \tag{6.4.1–13}$$

As noted by *Marsh et al.* [1990] and *Lerch et al.* [1991], this quantity, $\hat{\sigma}$, is larger than that actual RMS of fit to the data or the "true" data noise assessment. This down-weighting of the data relative to its intrinsic noise is necessary in order to account for systematic sources of error that remain in the data or their processing, the fact that typical passes of tracking data contain

significant redundant information, and is vital in order to obtain a realistic error spectrum, as illustrated by comparison with independent measurements.

In addition to examining the global calibration factors, described by eq. (6.4.1–10), the calibrations by degree and order were examined in detail for each individual satellite. Close attention was paid to the behavior of the calibration factors to identify anomalies that might require further scrutiny.

The calibration factors by degree n are defined as:

$$k_{t_n}^2 = \frac{\sum_{m=0}^{n} (\mathbf{X}_t - \mathbf{X})^2}{\sum_{m=0}^{n} (\sigma_t^2 - \sigma^2)} \tag{6.4.1–14}$$

Likewise, the corresponding calibration factor over order m to maximum degree N_{max} is:

$$k_{t_m}^2 = \frac{\sum_{n=2}^{N_{\max}} (\mathbf{X}_t - \mathbf{X})^2}{\sum_{n=2}^{N_{\max}} (\sigma_t^2 - \sigma^2)} \tag{6.4.1–15}$$

The average calibration factor, $\bar{k}_t$, by degree, through a maximum degree N_{max}, and also by order can then be computed from the values derived above. These average calibration factors are the quantities reported in later sections.

Finally we remind the reader that the calibration process has been applied solely to the gravitational coefficients. Some evidence was observed that the calibration factors for the adjusted tide model constituents were different from those for the static gravity field. This is not surprising given that the tidal recovery is critically sensitive to the data's temporal distribution, whereas the geopotential model is far less so. Thus, data weights that might be optimum for determination of the static gravity field might not be the best for improving estimates of the tidal constituents. Some effort will be required in the future to explore this issue, which was not addressed in the development of the EGM96 solution.

6.4.2 Preliminary Calibration of Continuous Tracking Data Types

Special attention was paid to the selection of data weights for the GPS/MET and EP/EUVE spacecraft, which relied entirely on continuous space-based tracking. A parametric study was done for each of these satellites to determine the approximate appropriate weight, prior to the commencing the primary calibration of the full satellite-only model.

6.4.2.1 GPS/MET

The base model for the GPS/MET calibrations was PGS6474. This model was a derivative of PGS6394 that (1) correctly moved the frame of the 1993–1994 data to be consistent with the

earlier SLR data and (2) suppressed the C and S coefficients for degrees 19 through 21 in the GPS normal equations for T/P, GPS/MET, and EP/EUVE. The partials at these degrees were erroneous, as described in Section 6.3.3.

A number of factors were considered in the parametric weight study for GPS/MET. These included the impact of imposing a constraint within SOLVE on the GPS ambiguity biases and the effect of adjusting or not adjusting the 1-CPR empirical acceleration (EA) terms for GPS/MET. Analysis revealed that a constraint had to be imposed on the determination of the biases when the arc parameters were back substituted (i.e., estimated); otherwise, the gravity field contribution of GPS/MET was severely diminished. A summary of the GPS/MET test solutions is given in Table 6.4.2.1–1. Table 6.4.2.1–2 lists the variance, v_{70}, of the deviation about the mean for a maximum degree of summation, M, of 70 from the 5°x5° altimeter-derived gravity anomaly comparison test (described in Section 5.8), and the results of the GPS/leveling tests (described in Section 5.2) for the 5 area, British Columbia, and the USA/NGS test sets.

Table 6.4.2.1–1. Summary of GPS/MET gravity field calibration test solutions.

Model	Value of 1–CPR EA	bias uncertainty (m)	w_n	$\hat{\sigma}$ (m)
PGS6474	0.	0.01	0.05	4.47
PGS6496	Subset solution of PGS6474, No GPS/MET data.			
PGS6506	adjusted	0.01	0.05	4.47
PGS6512	0.	0.01	0.05	4.47
PGS6518	0.	none	0.05	4.47
PGS6519	0.	1.00	0.05	4.47
PGS6562	0.	0.01	0.01	10.00
PGS6561	0.	0.01	0.02	7.07
PGS6528	0.	0.01	0.10	3.16
PGS6527	0.	0.01	0.30	1.83
PGS6525	0.	0.01	0.50	1.41
PGS6529	0.	0.01	0.70	1.20
PGS6526	0.	0.01	1.00	1.00
PGS6563	0.	0.01	5.00	0.45
PGS6564	0.	0.01	10.00	0.32

1-CPR EA: one cycle-per-rev empirical accelerations

Figure 6.4.2.1–1 illustrates the differences in the geopotential coefficients and coefficient uncertainties due to adjustment of the 1-CPR EA terms on GPS/MET. The primary effect on the field is in the loss of zonal and resonance information when the terms are estimated. The anomaly test shows little difference in the high-degree information content, whether or not the acceleration terms are adjusted: the anomaly residuals at degree 70 are 9.85 mGal^2 when the 1-CPR terms are estimated (PGS6506) vs. 9.83 mGal^2 when they are held fixed at zero (PGS6512).

Table 6.4.2.1–2. Summary of altimeter-derived anomaly test variances, v_{70}, and GPS/leveling test standard deviations resulting from GPS/MET solutions using HDM180 for the high-degree field.

Gravity Model	w_n	$\hat{\sigma}$ (m)	v_{70} (mGal^2)	GPS/leveling Fit Standard Deviation (cm)		
				5 areas avg.	Brit. Columbia	USA/NGS
PGS6474	0.05	4.47	9.895	56.9	98.8	95.9
PGS6496	Subset solution		10.835	68.2	104.0	101.3
	No GPS/MET data.					
PGS6506	0.05	4.47	9.851	60.6	98.8	93.1
PGS6512	0.05	4.47	9.831	61.8	96.8	93.8
PGS6518	0.05	4.47	10.431	58.7	110.4	104.8
PGS6519	0.05	4.47	10.242	59.5	101.2	102.4
PGS6562	0.01	10.00	10.359	61.6	97.7	99.1
PGS6561	0.02	7.07	10.123	61.3	96.2	97.1
PGS6528	0.10	3.16	10.026	61.2	96.2	94.3
PGS6527	0.30	1.83	9.887	61.5	96.5	94.8
PGS6525	0.50	1.41	9.831	61.8	96.9	93.8
PGS6529	0.70	1.20	9.800	62.1	97.2	93.1
PGS6526	1.00	1.00	9.771	62.6	97.9	92.3
PGS6563	5.00	0.45	9.906	69.6	108.4	87.3
PGS6564	10.00	0.32	10.476	78.6	120.1	86.3

The application of a constraint on the ambiguity biases is essential to maximize the information content of the GPS/MET normal equations. With GPS/MET, there is an inordinate number of these ambiguity phase biases. For instance, during the 2-day arc from day 181 to 182, the GPS/MET data arc included 68149 double-difference observations. In addition to the satellite state and ancillary dynamic parameters, 4273 ambiguity biases (1 for every 16 observations) were determined. The location of the GPS/MET antenna (looking aft, facing the orbit horizon, rather than toward orbit zenith as with T/P) contributes to the number of passes. The GPS/MET data appear to be inordinately weakened by the large number of ambiguity biases. This weakness is substantiated by an examination of the gravity field solutions derived from normal equations where the biases were back substituted with no constraint (PGS6518), and with a relatively loose constraint of 1.0 m (PGS6519). Although the effective data uncertainty is constant, the noise in the high-degree portion of the solution increases when the biases are estimated. The 5°x5° anomaly comparison highlights this information loss with a variance of 10.43 mGals^2 for PGS6518 (no bias constraint) and 10.24 mGals^2 for PGS6519 (1 m bias constraint), compared to 9.83 mGals^2 for PGS6512 (0.01 m bias constraint). Increases in the standard deviation of the GPS and leveling fit tests for British Columbia and the USA/NGS are observed when the constraint on the biases is relaxed. For instance, the standard deviation of the USA/NGS GPS/leveling fit differences rises from 93 cm with a constraint of 0.01 m, and to 102–105 cm when the constraint is removed. These results are summarized in Table 6.4.2.1–2. Thus, in order to maximize the high-degree contribution of the GPS/MET data, a constraint was imposed on the phase ambiguity biases during the back substitution of the arc parameters in SOLVE (the

troposphere biases are determined separately using the direct ground-to-ground GPS data, and are independent of the GPS/MET tracking data).
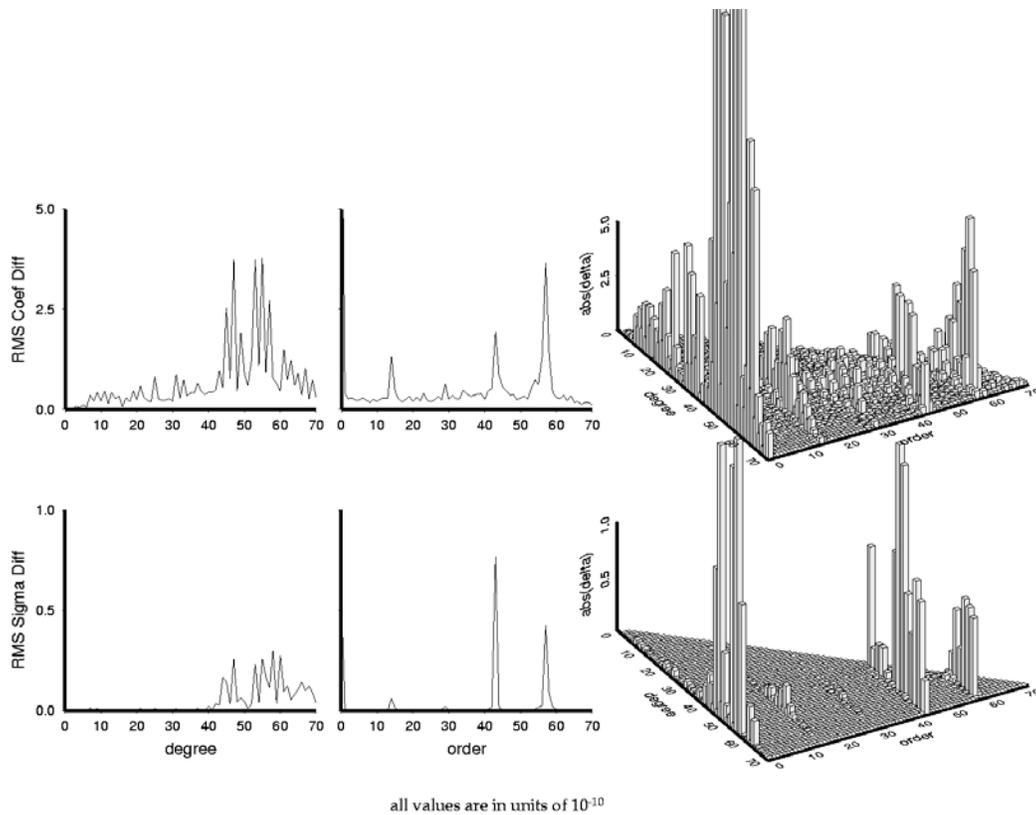
Figure 6.4.2.1–1. Effect of estimation of the GPS/MET 1–CPR empirical acceleration terms on the geopotential coefficients and their standard deviations (PGS6506 vs. PGS6512).

The calibration factors for the various GPS/MET solutions are listed in Table 6.4.2.1–3. The high calibration factors by degree are caused by the high calibration factors at $m = 0$. The calibration factors were reduced in later test solutions when the GM was fixed at the *a priori* value (it was globally adjusted in the PGS72XX series of satellite-only solutions and calibrations). The constraint on the phase ambiguity biases and the fixing of the GPS satellite orbits constrain the global scale of the solution, favoring the *a priori* GM value used in the GPS/MET orbit determination, 398600.4415×10^9 m^3/s^2. A comparison of the calibration factors by order and the corresponding variance values from the anomaly tests (Table 6.4.2.1–2) for the same fields shows that there is a broad plateau over which an effective data weight can be considered acceptable. Surprisingly, the data weight can change by a factor of 10 and bring about minimal changes in the calibration factors or the 5°x5° gravity anomaly comparisons. Therefore, these two tests alone cannot be used to select an appropriate data weight. An additional consideration

is the examination of the GPS/MET residuals, which indicate that significant systematic signals remain in the data at the decimeter level of fit. Based on the peak-to-peak signature in the residuals, a data weight of 1.4 or 1.5 m might be appropriate. A data weight of 4.47 m was selected, which allowed GPS/MET to contribute to the solution, but accommodated mismodeling of the attitude of the spacecraft. The lesson to be drawn from the GPS/MET calibration (and for the other continuous tracking types) is that the calibration procedures, in and of themselves, are insufficient to select a unique weight, and that other tests (GPS/leveling, the 5°x5° altimeter-derived anomaly comparison, and orbit residual tests) must also be considered.

Table 6.4.2.1–3. Summary of the GPS/MET calibrations against the PGS6496 subset solution.

Gravity Model	w_n	$\hat{\sigma}$ (m)	Average Calibration Factors $\overline{k}_t$		
			$n \leq 70$	$n \leq 20$	$m \leq 70$
PGS6562	0.01	10.00	0.810	0.990	0.537
PGS6561	0.02	7.07	0.891	1.103	0.666
PGS6528	0.10	3.16	0.935	1.206	0.707
PGS6527	0.30	1.83	1.017	1.422	0.765
PGS6525	0.50	1.41	1.052	1.515	0.790
PGS6529	0.70	1.20	1.072	1.562	0.807
PGS6526	1.00	1.00	1.088	1.594	0.825
PGS6563	5.00	0.45	1.151	1.571	0.951
PGS6564	10.00	0.32	1.236	1.586	1.066

6.4.2.2 EP/EUVE

TDRSS Data Calibration

The base model for the preliminary EP/EUVE TDRSS data calibrations was PGS6427, which was a derivative of the PGS6394 satellite-only gravity model without any TDRSS or GPS tracking of EP/EUVE. A variant of the normal equation set used in the primary calibration series (described in Section 6.4.3) was used for these test solutions, and had a scale factor $w_a = 2.75$ (as opposed to a value of one) applied to the range data during the aggregation of the normal equation sets. After these tests were performed, we decided that it was best to not up-weight the range data type, which is prone to significant systematic biases. Consequently, the relation between the normal equation weight scale factors and effective data uncertainties reported here will not be the same as those reported for the primary calibration series and the final satellite-only model.

A variety of different normal equation weight scale factors were compared, from 0.0003 to 30.0 (corresponding to data $\hat{\sigma} = 14.4$ cm/s and 348.2 m for $w_n = 0.0003$, and $\hat{\sigma} = 1.10$ cm/s and 0.05 m for $w_n = 30.0$). As with the GPS/MET data, the calibration factors are nonlinear and surprisingly insensitive to the weight changes; a factor of 10 change in the normal equation

weight scale factor does not lead to a corresponding expected change in the calibration factors. The preliminary calibration factors for the EP/EUVE TDRSS data are listed in Table 6.4.2.2–1. Obviously, values of w_n of 3 or higher are excessive, both in consideration of the approximate level of noise of the TDRSS data (approximately 1.0 m for range, and 0.1 cm/s for range rate), and the deterioration in the gravity model as indicated by the variance values, v_{70}, resulting from the 5°x5° altimeter-derived gravity anomaly comparison test. A more reasonable *a priori* normal equation scale factor would be 0.1 to 0.3; however, a final selection for the EP/EUVE TDRSS effective data uncertainty must also consider the presence of the EP/EUVE GPS data, which supplies similar information to the model.

Table 6.4.2.2–1. Summary of preliminary EP/EUVE TDRSS data calibration, 5°x5° altimeter-derived gravity anomaly test variance, v_{70}, and GPS/leveling test results.

Gravity Model	w_n	$\hat{\sigma}$ (m)/(cm/s)	Average Calibration Factors $\bar{k}_t$			v_{70} (mGal^2)
			$n \leq 70$	$n \leq 20$	$m \leq 70$	
PGS6427	*Baseline solution: derivative of PGS6394 with no EP/EUVE data*					11.460
PGS6959	0.0003	348.2/14.4	0.667	0.559	0.835	11.173
PGS6955	0.003	110.1/4.56	0.859	0.704	0.975	10.819
PGS6951	0.03	34.8/1.44	0.891	0.669	0.879	10.289
PGS6960	0.1	19.1/0.79	0.920	0.667	0.886	9.944
PGS6953	0.3	11.0/0.46	1.014	0.752	0.987	9.722
PGS6967	3.0	3.48/0.14	1.510	1.414	1.384	11.995
PGS6958	30.0	1.10/0.05	2.836	3.292	1.955	37.842

GPS Data Calibration

The base model for the preliminary EP/EUVE GPS tracking data calibrations was PGS6509, also a derivative of PGS6394 that included updated GPS/MET matrices where the n = 19 to 22 S coefficient partial derivatives were corrected, but still included the PGS6394-vintage T/P GPS matrix with the S coefficient partials problem (the problematic C/S terms were suppressed). Two matrices were tested: one with the 1-CPR empirical acceleration terms fixed at zero, and one with the 1-CPR terms adjusted. The calibration results are summarized in Table 6.4.2.2–2. Fixing the acceleration terms at zero improves the variance values from the 5°x5° altimeter-derived gravity anomaly comparisons, although the calibration factors increase for the same data weight. The GPS/leveling data that make up the five areas test, with the exception of some of the Australia data, and a small part of the USA/NGS data, lie outside the ground track of EP/EUVE. The deterioration of the NGS GPS/leveling test from 90–92 cm to 98 cm in the standard deviation for PGS6922 shows that the EP/EUVE GPS data are weighted too highly at $w_n = 0.500$. Thus, a w_n value of 0.125 seems to be a more appropriate starting point for the EP/EUVE GPS data in the calibration of the entire satellite-only model.

Table 6.4.2.2–2. Summary of preliminary EP/EUVE GPS data calibrations, 5°x5° altimeter-derived gravity anomaly test variance v_{70}, and GPS/leveling test results.

Gravity Model	1–CPR treatment	w_n	$\hat{\sigma}$ (m)	$\bar{k}_t$ $n \leq 70$	v_{70} (mGals^2)	GPS/leveling Fit Std. Dev. (cm) 5 areas	BC	USA/NGS
PGS6509	*Baseline, no EP/EUVE data*				11.559	53.3	91	97
PGS6920	adjusted	0.500	1.41	0.970	10.355	59.8	92	92
PGS6921	adjusted	0.125	2.83	0.802	10.309	60.1	94	90
PGS6937	fixed @ 0	0.063	3.98	0.887	10.305	59.9	94	92
PGS6931	fixed @ 0	0.125	2.83	0.923	10.248	60.4	95	93
PGS6922	fixed @ 0	0.500	1.41	1.073	10.279	61.8	96	98

6.4.3 Primary Calibration

The primary calibrations are summarized in Table 6.4.3–1, and the pre- and postcalibration data weights are listed in Table 6.4.3–2. The master solution for all these comparisons was PGS7200. This satellite-only solution was among the first to include all the new (corrected) GPS normal equations, the new EP/EUVE TDRSS normals, as well as the new T/P SLR and DORIS data. Following the primary series of calibrations, a new satellite-only model, PGS7240, was created that included the changes outlined in the primary calibration series. The postcalibration model PGS7240 was only an interim test solution, since other changes were introduced, as outlined in the subsequent sections.

PGS7200 subset solutions, complete to 70x70, were computed for each satellite and set of data using this master solution. In all cases, these satellite-only solutions used the same constraint matrix (derived from the quadrature solution V037, as discussed earlier) to condition the solution at the higher degrees. Some satellite orbits were represented by multiple data types, (i.e., SLR, DORIS, and GPS for T/P; TDRSS and GPS for EP/EUVE), or satellites with similar orbit geometry (i.e., SPOT–2 and Stella). In such cases, each set of data was calibrated individually against a subset with no data from that orbit, and then as a group including all types of data.

Most of the calibrations are less than unity, especially for the more recently launched satellites. The data from the older satellites (D1–D, D1–C, BE–C, Peole, and GEOS–2) have higher calibration factors. This is somewhat unexpected as the optical data for these spacecraft (excepting Peole, for which the optical data were not used) were not withheld from the subset solutions for practical reasons, and because of the high data uncertainties with which these data were applied (see Table 6.4.3–2). The presence of the orbit dynamics from the optical tracking should have resulted in some cancellation of the effects in the calibration process. Further, the *a priori* weights for these spacecraft data were the same as those used in JGM–2, yet these spacecraft represent a smaller relative contribution to the overall solution. Nonetheless, the weighting procedure suggests that these data should be down-weighted.

Table 6.4.3–1. Primary satellite tracking data calibration and 5°x5° altimeter-derived gravity anomaly test variance v_{70} results for EGM96S.

Master Model	Data Calibrated	Subset Model	Avg. Calibration Factor $\bar{k}_t$			v_{70} (mGal^2) of Master (M) or Subset (S)
			$n \leq 70$	$n \leq 20$	$m \leq 70$	
PGS7200	Master Solution					10.44 (M)
PGS7200	T/P (all)	PGS7201	0.725	0.633	0.747	10.62 (S)
PGS7201B	T/P SLR/DORIS	PGS7201	0.614	0.567	0.591	10.52 (M)
PGS7201A	T/P GPS	PGS7201	0.744	0.659	0.777	10.47 (M)
PGS7200	LAGEOS (all)	PGS7202	0.820	0.947	0.743	10.29 (S)
PGS7202B	LAGEOS (1980–92)	PGS7202	0.844	0.981	0.777	10.44 (M)
PGS7202A	LAGEOS (1993–94)	PGS7202	0.546	0.662	0.267	10.32 (M)
PGS7200	GPS/MET	PGS7203	1.139	1.859	0.648	11.39 (S)
PGS7200	EP/EUVE (all)	PGS7204	0.905	0.760	0.624	13.13 (S)
PGS7204A	EP/EUVE GPS	PGS7204	0.938	0.818	0.826	11.16 (M)
PGS7204B	EP/EUVE TDRSS	PGS7204	0.903	0.829	0.598	10.82 (M)
PGS7200	SPOT–2 and Stella	PGS7208	0.710	0.746	0.651	11.97 (S)
PGS7209	SPOT–2	PGS7208	0.704	0.754	0.633	10.43 (M)
PGS7205	Stella	PGS7208	0.722	0.767	0.547	11.49 (M)
PGS7200	Starlette (all)	PGS7206	0.842	0.800	0.727	11.54 (S)
PGS7206B	Starlette (1983–86)	PGS7206	0.836	0.770	0.756	10.52 (M)
PGS7206A	Starlette (1993–94)	PGS7206	0.798	0.806	0.671	10.64 (M)
PGS7200	LAGEOS–2	PGS7207	0.819	1.146	0.361	10.43 (S)
PGS7200	RADCAL and Nova–1	PGS7211	0.762	0.729	0.640	10.92 (S)
PGS7218	RADCAL	PGS7211	0.744	0.729	0.606	10.50 (M)
PGS7210	Nova–1	PGS7211	0.907	0.977	0.707	10.80 (M)
PGS7200	Ajisai (all)	PGS7213	0.735	0.880	0.550	10.40 (S)
PGS7213B	Ajisai (1986–87)	PGS7213	0.829	0.877	0.623	10.46 (M)
PGS7213A	Ajisai (1993–94)	PGS7213	0.751	0.880	0.469	10.41 (M)
PGS7200	HILAT	PGS7212	0.536	0.626	0.413	10.52 (S)
PGS7200	GFZ–1	PGS7214	0.527	0.422	0.521	10.46 (S)
PGS7200	GEOSAT and SEASAT	PGS7215	0.577	0.545	0.488	10.76 (S)
PGS7216	SEASAT	PGS7215	0.656	0.540	0.563	10.62 (M)
PGS7200	D1–D SLR/Doppler	PGS7219	1.664	2.127	1.153	10.59 (S)
PGS7200	D1–C SLR/Doppler	PGS7220	0.909	0.870	0.896	10.45 (S)
PGS7200	BE–C SLR/Doppler	PGS7221	1.096	0.883	1.020	10.61 (S)
PGS7200	Peole SLR	PGS7223	1.234	1.405	1.259	10.23 (S)
PGS7200	GEOS–3 SLR/Doppler	PGS7222	0.864	0.871	0.835	10.99 (S)
PGS7200	GEOS–2 SLR	PGS7224	0.971	1.078	0.506	10.44 (S)
PGS7200	D1–C and D1–D SLR/Doppler	PGS7230	1.362	1.881	1.037	10.63 (S)
PGS7230B	D1–D & D1–C SLR	PGS7230	1.382	1.886	1.020	10.50 (M)
PGS7230A	D1–D & D1–C Doppler	PGS7230	1.108	1.190	1.130	10.56 (M)

Table 6.4.3–2. Effective data uncertainties for the pre- (PGS7200) and postprimary (PGS7240) calibration satellite-only solutions.

Data	$\hat{\sigma}$ in PGS7200	$\hat{\sigma}$ in PGS7240
Ajisai 86–87	2.36 m	2.36 m
Ajisai 93–94	2.36 m	1.92 m
BE–C Doppler	5.35 cm/s	7.45 cm/s
BE–C SLR	2.18 m	3.02 m
D1–C Doppler	9.53 cm/s	12.91 cm/s
D1–C SLR	3.33 m	11.95 m
D1–D Doppler	9.53 cm/s	12.91 cm/s
D1–D SLR	8.16 m	11.95 m
EP/EUVE GPS	2.82 m	2.82 m
EP/EUVE TDRSS Doppler	0.79 cm/s	0.79 cm/s
EP/EUVE TDRSS Range	31.62 m	31.62 m
Etalon SLR	1.24 m	1.24 m
GEOS–1 SLR	5.00 m	5.00 m
GEOS–2 SLR	14.14 m	10.00 m
GEOS–3 ATS Doppler	0.81 cm/s	0.96 cm/s
GEOS–3 ATS period SLR	4.08 m	4.88 m
GEOS–3 SLR	1.58 m	1.83 m
GEOSAT Doppler	2.00 cm/s	1.63 cm/s
GFZ–1	10.0 m	7.07 m
GPS/MET	4.47 m	4.47 m
HILAT Doppler	2.53 cm/s	1.58 cm/s
LAGEOS SLR 80–92	1.12 m	1.12 m
LAGEOS SLR 93–94	1.00 m	0.63 m
LAGEOS–2	0.54 m	0.54 m
Nova	1.51 cm/s	1.83 cm/s
Optical	5.77 arcsec	5.77 arcsec
Oscar–14	10.00 cm/s	10.00 cm/s
Peole SLR	5.00 m	7.91 m
RADCAL Doppler	2.58 cm/s	2.24 cm/s
SEASAT Doppler	3.16 cm/s	2.58 cm/s
SEASAT SLR	7.07 m	5.77 m
SPOT–2 DORIS	0.71 cm/s	0.62 cm/s
Starlette SLR 83–86	1.69 m	1.69 m
Starlette SLR 93–94	1.13 m	1.13 m
Stella SLR	0.91 m	0.79 m
T/P DORIS	1.58 cm/s	1.58 cm/s
T/P GPS	0.35 m	0.35 m
T/P SLR	2.50 m	2.50 m

Strictly speaking, application of the calibration procedure described by *Lerch et al.* [1991] would require that many of the SLR, DORIS, GPS, and TDRSS sets of data be up-weighted. However, in order to avoid a satellite covariance that was too optimistic, the weights were adjusted to aim for a calibration factor of 0.8, rather than unity, thereby intentionally underweighting some of the satellite tracking data in the solution and producing a more pessimistic error covariance

The contribution of the EP/EUVE data is illustrated by examining the ratio of the RMS error per degree for the JGM–2S and the models used in the calibration of the EP/EUVE data: PGS7200,

PGS7204, PGS7204A, and PGS7204B (see Figure 6.4.3–1). The higher the ratio, the greater the level of predicted improvement over JGM–2S. For PGS7204, which included no EP/EUVE data, the errors are improved with respect to JGM–2S by a factor of 1.7 at degree 10, 1.3 at degree 20, and 1.1 at degree 30. For the master solution, PGS7200, which included all the EP/EUVE data, the corresponding factors of improvement are 3.6 at degree 10, 2.7 at degree 20, and 1.5 at degree 30. Individually, both the TDRSS and GPS produce virtually the same level of improvement (2.9 at degree 10, 2.2 at degree 20, and 1.4 at degree 30). However, at the normal equation weights used in this calibration set, the GPS data produce a slightly greater improvement (~.1) at the lower degrees than the TDRSS data does. Figure 6.4.3–1 also shows the reduction in strength in the new solutions, as compared to JGM–2S, for degrees above 40. This is the result of the more realistic satellite-only solution *a priori* constraint that was discussed in Section 6.3.2.
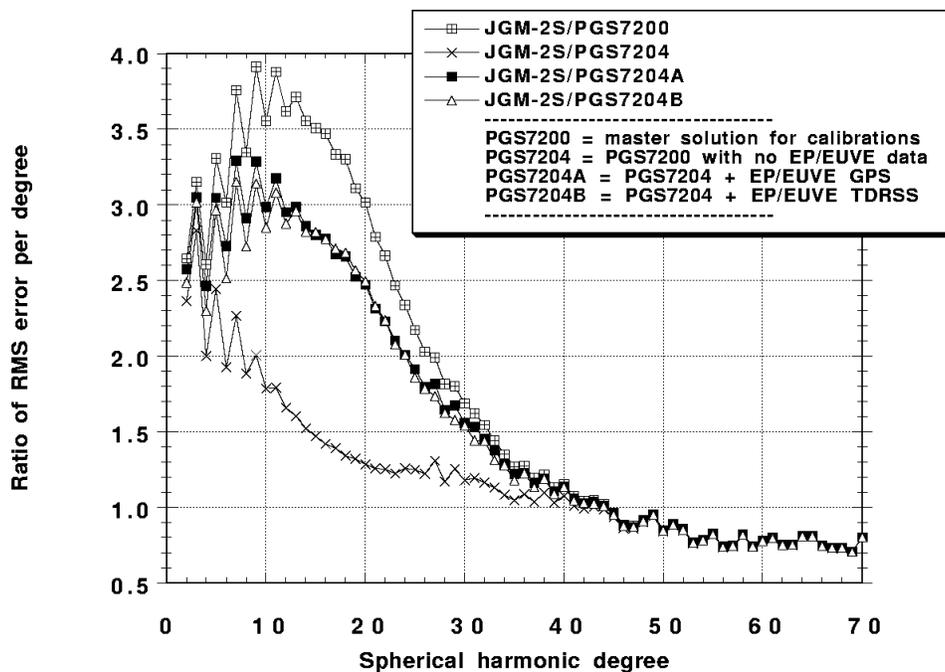
Figure 6.4.3–1. Ratio of RMS error per degree with JGM–2S for EP/EUVE calibration solutions.

The level of improvement seen at degree 10 when the TDRSS and GPS sets are combined is somewhat less than the RSS of the improvements for the individual contributions, showing that the contributions of these two data sets is largely uncorrelated. This occurs despite the fact that these two data sets represent the same orbit, and demonstrates the unique strengths of these two data types. The complementary nature of these two data types was also observed by *Rowlands et al.* [1997] for the TDRSS and GPS tracking of the Space Shuttle during the SLA–1 mission. The

low correlations also indicate that there may be added benefit from the inclusion of more EP/EUVE tracking of these types.

As a result of the primary calibrations, the following sets of data were up-weighted with respect to the weights determined incrementally in the PGS6394 class of models: LAGEOS (1993–94), Ajisai (1993–94), SPOT–2, Stella, GFZ–1, HILAT, RADCAL, GEOSAT, GEOS–2, and SEASAT. The weights of the following satellites were down-weighted as a result of these calibrations: Peole, D1–C, D1–D, GEOS–3, and Nova. In addition to the intentional down-weighting, these data receive less emphasis in EGM96 for another reason: their numerical contribution (number of observations) is unchanged since the JGM–2 solution, whereas the number of observations from the new SLR, DORIS, TDRSS, and GPS tracked satellites has increased substantially.

The coefficient differences from the calibrations illustrate the sensitivity of a particular satellite to the gravity field, in terms of which degrees and orders the data make the most contribution. These plots illustrate the calibration factors by degree and order, the coefficient differences between the master and the subset solution, as well as the differences in the coefficient uncertainties between the master and the subset. For instance, Figure 6.4.3–2, illustrating the EP/EUVE calibrations, shows that the spacecraft contributes strongly to the gravity field through approximately order 33, and then has no further sensitivity. This profile is a consequence of the satellite inclination (28.4°). Peole, which has a lower inclination (only 15°), contributes strongly only through order 15 (Figure 6.4.3–3). On the other hand, satellites that are polar in inclination (SPOT–2 and Stella; see Figure 6.4.3–4) contribute strongly at all degrees and orders. Starlette contributes powerfully, even though the satellite is tracked only by SLR (Figure 6.4.3–5). It still makes an important contribution to the gravity field even in the presence of the continuous tracking from satellites tracked by GPS, TDRSS, and DORIS. The incomplete orbit sampling from SLR is mitigated by the high quality of the data, the eccentricity of the orbit, the low perigee, and the relative ease with which the spacecraft can be modeled (cf. a cannonball). Other spacecraft that are at lower altitudes (such as EP/EUVE, GPS/MET, SPOT–2, GEOSAT, SEASAT) have complex shapes and sometimes sophisticated attitude histories that introduce difficulties and errors in the modeling of the nonconservative forces.

The calibration curves for T/P were of particular concern, especially since the spacecraft, by being tracked by four precise systems, contributes more than 40 percent of the total number of observations in the satellite-only solution. As illustrated in Figures 6.4.3–6 and –7, the calibrations for the SLR/DORIS, and GPS data sets are well behaved, and indicate that the data could in fact be up-weighted from their baseline weights in PGS7200.

A review of the variance values, v_{70}, from the comparisons of the geopotential model-derived gravity anomalies with the mean 5°x5° altimeter-derived anomalies from the GEOSAT Geodetic mission, given in Table 6.4.3–1, reveals which satellites contribute most strongly at the higher degrees to the satellite-only solution. The residual for the master solution with all the data, PGS7200, is 10.44 mGal^2. Those data, whose removal increase the variance by more than 0.5 mGal^2 include EP/EUVE (by 2.69 mGal^2), Starlette (by 1.10 mGal^2), SPOT–2 & Stella (by 1.53 mGal^2) and GEOS–3 (by 0.55 mGal^2). Removal of EP/EUVE from the solution increases the residual to 13.13 mGal^2! This makes EP/EUVE by far the most powerful satellite in the satellite-
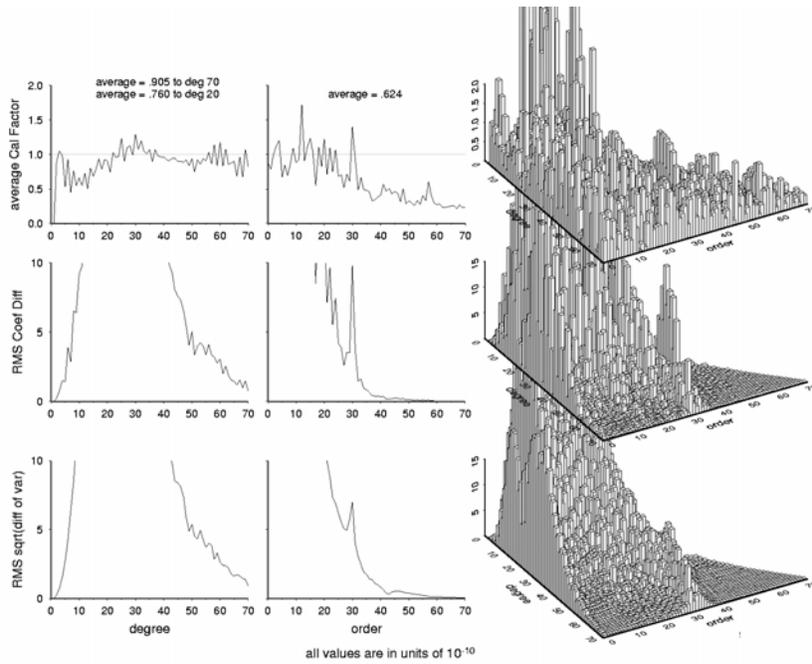
Figure 6.4.3–2. Effect of EP/EUVE GPS and TDRSS tracking on the primary calibration series gravity solution (PGS7200 vs. PGS7204).
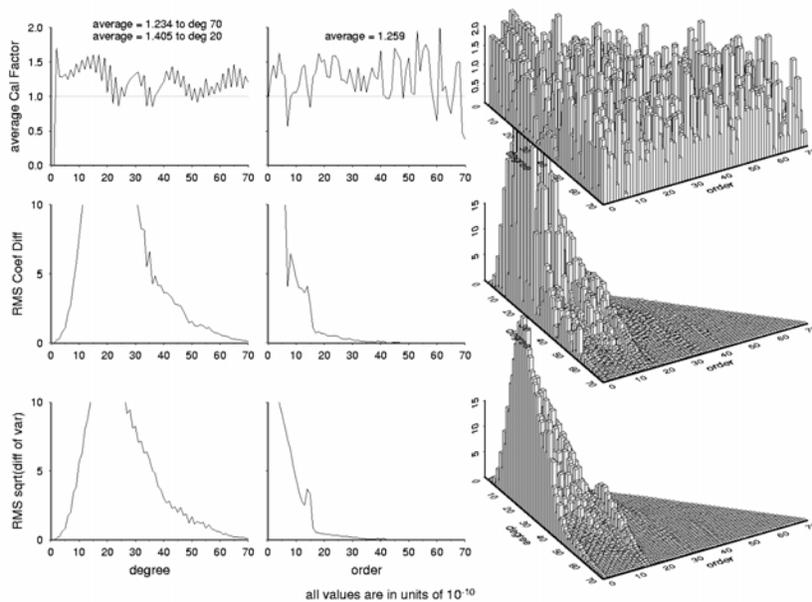
Figure 6.4.3–3. Effect of the Peole SLR tracking on the primary calibration series gravity solution (PGS7200 vs. PGS7223).
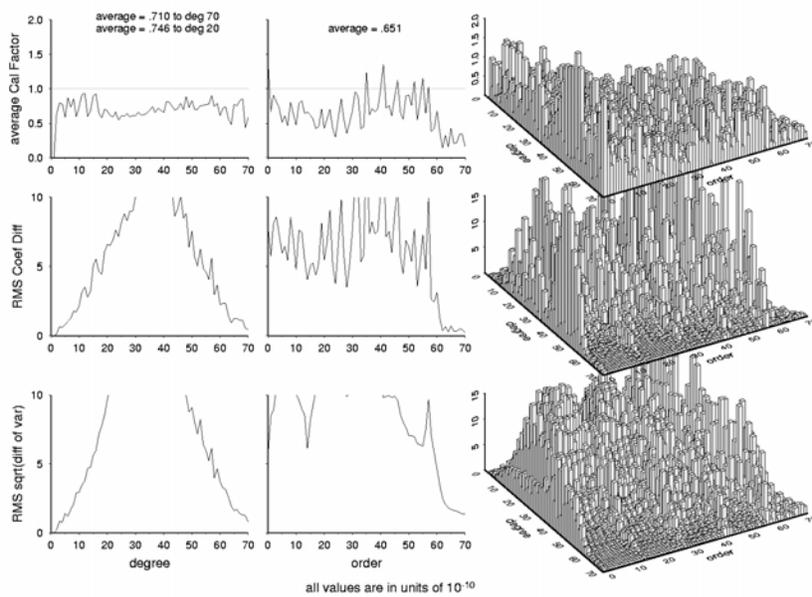
Figure 6.4.3–4. Effect of the polar orbiting SPOT–2 and Stella on the primary calibration series gravity solution (PGS7200 vs. PGS7223).
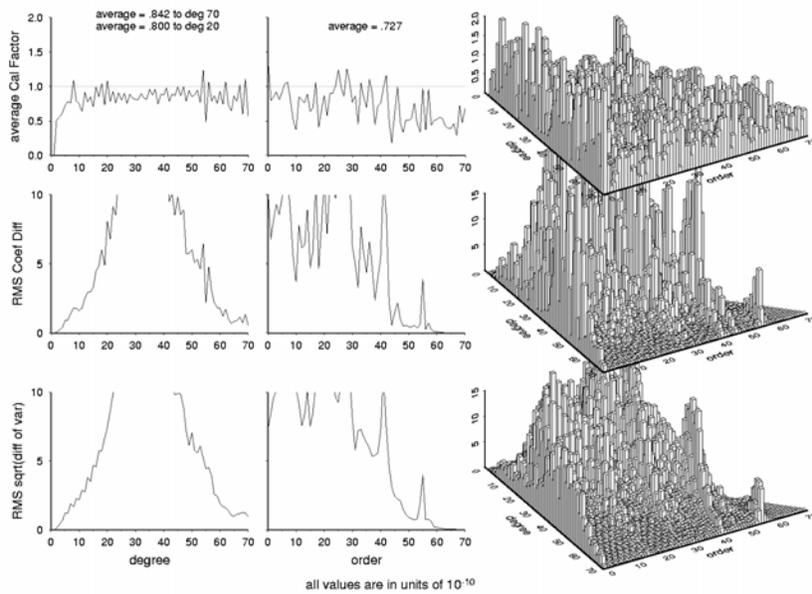
Figure 6.4.3–5. Effect of Starlette on the primary calibration series gravity solution (PGS7200 vs. PGS7206).
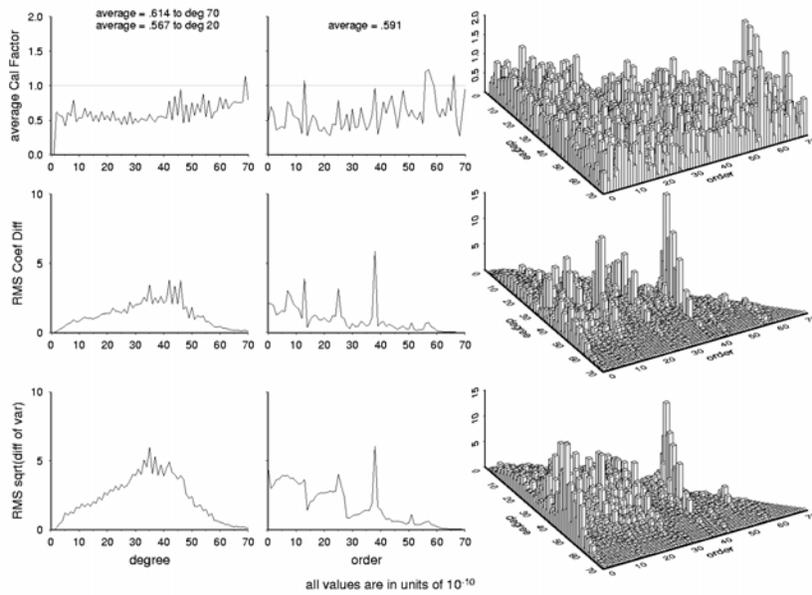
Figure 6.4.3–6. Effect of the T/P SLR and DORIS tracking on the primary calibration series gravity solution (PGS7201 vs. PGS7201B).
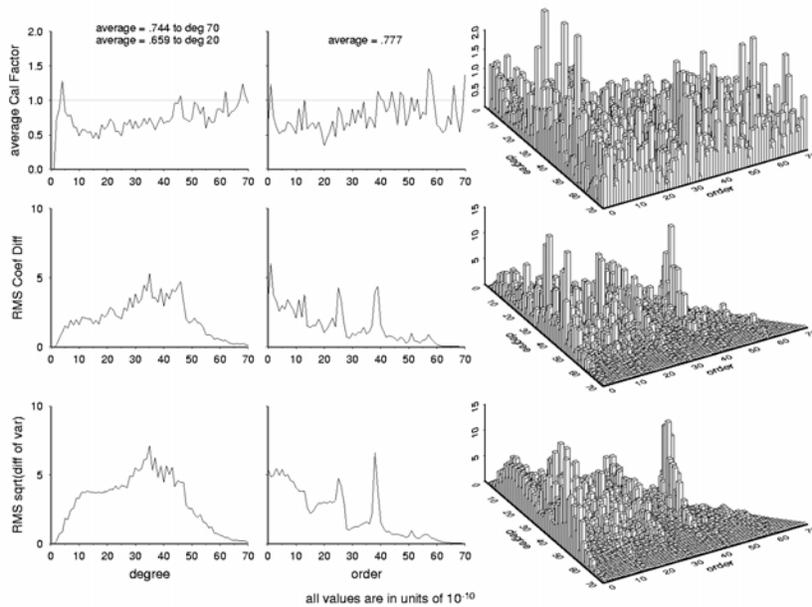
Figure 6.4.3–7. Effect of the T/P GPS tracking on the primary calibration series gravity solution (PGS7201 vs. PGS7201A).

only solution for resolving the shorter wavelength portions of the satellite-only model. The anomaly comparison also shows that the GPS and TDRSS data for EP/EUVE complement each other, since the anomaly comparison is lowest when both sets of data are included, rather than when either the GPS or TDRSS data are included individually (11.16 mGal^2 and 10.82 mGal^2). The complementary nature of these two data types was also observed by *Rowlands et al*. [1997] for the TDRSS and GPS tracking of the Space Shuttle during the SLA–1 mission. SPOT–2, Stella, Nova, and RADCAL are other examples of satellites located in similar orbits, whose data complement each other in the same fashion, as measured by the anomaly comparison with their respective subset solutions. The strength of GEOS–3 is interesting. In spite of the relative age of these data (EGM96 includes the GEOS–3 SLR data from approximately April 5, 1980, to November 26, 1980, and the GEOS–3 ATS from assorted arcs starting on April 27, 1975, through April 15, 1979), they continue to make an important contribution to the gravity solution. The unique contribution of GEOS–3 is undoubtedly due to both its altitude (~850 km) and retrograde inclination (114.9°; close to the mirror inclination of T/P). With the exception of the data from optically tracked satellites, EGM96 includes no tracking from satellites with inclinations greater than that of GEOS–3.

The D1–D and D1–C data weights were adjusted after the calibrations of the SLR and Doppler data were studied separately. The SLR data needed to be down-weighted by a greater amount than the Doppler data. Peole had a high calibration factor (1.405 for $n \leq 20$). In the JGM–2 type solutions and earlier, it uniquely provided tracking coverage at the low inclinations. In light of the new data from EP/EUVE, the importance of Peole in the solution has diminished.

The analysis of the gravity anomaly comparisons does point out some peculiarities. First, the removal of LAGEOS actually improves the anomaly comparison variance values (from 10.44 mGal^2 to 10.29 mGal^2). A similar phenomenon is observed with Ajisai (10.40 mGal^2) and LAGEOS–2 (10.43 mGal^2). One hypothesis is that these satellites act as important constraints on the low-degree field and general reference frame of the solution. Consequently, their removal from the solution implies an overfitting of the new data that is more sensitive to the higher degrees at the expense of the lower degrees.

6.4.4 Recalibration Activities

After the calibration of the satellite-only model and the adjustment of the weights that took place between the PGS7200 and PGS7240 solutions, a number of further issues were explored to optimize the final solution. These issues included:

1) The calibration and handling of GPS/MET, especially since the PGS7200 series of calibrations pointed out a problem at the low degrees and orders.

2) SPOT–2. The normal equations for 1990 and 1992 were calibrated separately and then added to the final solution.

3) The 1983 Starlette data. These data were excluded from the satellite-only model, and the calibrations for the 1984, 1986, and 1993–1994 data had to be reviewed.

4) LAGEOS and TOPEX/GPS. The weights of the TOPEX/GPS and LAGEOS (1980–1992) data were adjusted. The subset calibrations with PGS7200 and with PGS7240 both suggested these data could be slightly up-weighted.

5) GEOS–3. The contribution of GEOS–3 was scrutinized closely by examining the calibrations for the GEOS–3 ATS data and the GEOS–3 SLR data.

6) EP/EUVE. In light of the importance of this satellite, and the weight changes applied to the other strong sets of data (LAGEOS, T/P GPS, and GEOS–3), the calibrations were reexamined.

Numerous test solutions were generated to validate the data and test the performance of the solution at slightly different weights. In the interest of brevity, not all of these solutions will be discussed here. However, another milestone satellite-only model that was used as the basis of a number of tests, including the SPOT–2, Starlette, and GPS/MET recalibrations, was PGS7270K. This model was an interim between PGS7240 and EGM96S and included the following changes from PGS7240: T/P/GPS was up-weighted by reducing the data uncertainty from 0.35 m to 0.29 m, based on the PGS7200 and PGS7240 calibrations for that satellite. The weights of the T/P SLR and DORIS data were not changed in view of the large quantity of data already in the solution. Second, the weight of LAGEOS (1980–1992) was increased by changing the observation uncertainty $\hat{\sigma}$ from 1.25 m to 1.00 m. Finally, the 1983 Starlette data were removed from the solution.

6.4.4.1 GPS/MET: Further Calibrations

The calibrations for GPS/MET were repeated using PGS7270K; a summary of these calibrations is provided in Table 6.4.4.1–1. The up-weighting of the LAGEOS and T/P/GPS data reduced the influence of GPS/MET in the solution and improved that satellite's calibrations. In the PGS7200 calibration, the removal of GPS/MET causes a degradation of 0.95 mGal^2 in the variance of the altimeter-derived gravity anomaly comparison test, whereas in the PGS7270K satellite-only calibration, the removal of GPS/MET causes only a 0.82 mGal^2 degradation. Also, the calibrations at the low-degrees and orders show improvements without having altered the weight on the GPS/MET data (the calibrations for $n \leq 20$ is 1.859 for the PGS7200 solution and 1.064 for the PGS7270K solution). These results point out that, although GPS/MET contributes to the high-degree field, it is inconsistent at the low degrees with the other data in the solution. The reasons for this inconsistency may stem from a nonconservative force modeling or a measurement model error, for instance the known attitude librations of the GPS/MET spacecraft. The handling of the surface gravity data, which also contains valid high-degree information, but possible reference frame incompatibilities and inconsistencies at the lower degrees in the combination gravity solution, suggested a course of action for GPS/MET. In the case of the surface gravity data, a separate 5x5 harmonic field is adjusted. We tested the adjustment of a separate set of 5x5 coefficients on GPS/MET. As expected, the global calibration factors improve, although the price appears to be a slight (0.08 mGal^2) increase in the altimeter-derived gravity anomaly test residual variance. Since the long-wavelength incompatibilities have been removed, we may then experiment with up-weighting the data to amplify the high-degree

contribution of the data. Thus, as the normal equation scale factor is increased from $w_n = 0.05$ (data $\hat{\sigma} = 4.47$ m) to $w_n = 0.20$ (data $\hat{\sigma} = 2.24$ m), some gain in the anomaly comparison test is observed, with an improvement in the variances from 10.09 to 9.90 mGal^2. Finally, we verified that, in the context of a combination model, the up-weighting of GPS/MET and the separate adjustment of a 5x5 field improved the GPS/leveling calibrations (see Table 6.4.4.1–2). We stress that this method of handling GPS/MET is only an artifice to mitigate the long-wavelength inconsistencies inherent in the present set of normal equations. Further analyses are needed to examine improvements to both the orbit and attitude modeling of the spacecraft.

Table 6.4.4.1–1. Further GPS/MET calibration and 5°x5° altimeter-derived gravity anomaly test results.

Master Model	Data Calibrated	Subset Model	Avg. Calibration Factors $\bar{k}_t$			v_{70} (mGal^2) of Master (M) or Subset (S)
			$n \leq 70$	$n \leq 20$	$m \leq 70$	
PGS7200	Satellite-Only Model at Start of Primary Calibrations					10.44 (M)
PGS7200	GPS/MET $w_n = 0.05$	PGS7203	1.139	1.859	0.648	11.39 (S)
PGS7270K	New 2nd Generation, Post Calibration Satellite-Only Model					10.01 (M)
PGS7270K	GPS/MET $w_n = 0.05$	PGS7270L	0.979	1.064	0.695	10.83 (S)
PGS7270N	GPS/MET $w_n = 0.05$ Separate 5x5 adjusted on GPS/MET	PGS7270L	0.840	0.706	0.663	10.09 (M)
PGS7270T	GPS/MET $w_n = 0.10$ Separate 5x5 adjusted on GPS/MET	PGS7270L	0.834	0.670	0.705	9.99 (M)
PGS7270U	GPS/MET $w_n = 0.20$ Separate 5x5 adjusted on GPS/MET	PGS7270L	0.824	0.623	0.746	9.90 (M)

Table 6.4.4.1–2. GPS/leveling tests on combination models with GPS/MET up-weighting.

Model	Description	GPS/leveling Fit Standard Deviation (cm)		
		5 areas avg.	Brit. Columbia	USA/NGS
PGS7292[1]	GPS/MET $w_n = 0.05$ No separate 5x5 adjusted on GPS/MET	27.76	52.30	53.29
PGS7297[2]	GPS/MET $w_n = 0.20$ Separate 5x5 adjusted on GPS/MET	27.46	51.45	52.84

[1] Combination model based on PGS7270K satellite-only, plus Starlette 84–86 data, T/P/ERS–1 & GEOSAT altimetry, and surface gravity.

[2] New combination model based on PGS7292, with perturbation only on GPS/MET.

6.4.4.2 SPOT–2

A series of calibrations and orbit tests was performed on the 1990 and 1992 SPOT–2 data to evaluate the effect of the data from these two time periods on the interim gravity solutions. Since Stella shares the orbit with SPOT–2, the calibrations for that satellite were checked as a matter of course. A brief summary of the SPOT–2 data is given in Table 6.4.4.2–1.

Table 6.4.4.2–1. Summary of SPOT–2 DORIS data used in EGM96.

Data	Span (mm/dd-mm/dd)	No. of Obs.	No. Of Arcs	Combined RMS (mm/s)
1990	03/31–07/02	236967	22	0.67
1992	01/02–03/18	183491	10	0.67

The results of the calibration solutions are given in Table 6.4.4.2–2. When the 1-CPR acceleration terms are adjusted, the 1990 data exhibit lower calibration factors than the 1992 data. When the empirical acceleration terms are not adjusted, the calibration factors are highest for the 1990 data. This indicates that nonconservative force model errors—most likely the increased drag near solar maximum—are more severe than in 1992.

Table 6.4.4.2–2. Summary of SPOT–2 calibration and 5°x5° altimeter-derived gravity anomaly test results. A data uncertainty of 0.88 cm/s was used for the SPOT–2 data.

Master Model	Data Calibrated	Subset Model	Avg. Calibration Factors $\bar{k}_t$			v_{70} (mGal^2) of Master (M) or Subset (S)
			$n \leq 70$	$n \leq 20$	$m \leq 70$	
PGS7270K	*New 2nd Generation, Postcalibration Satellite-Only Solution*					10.01 (M)
PGS7270K	SPOT–2 and Stella	PGS7270V	0.776	0.844	0.703	11.58 (S)
PGS7270W	Stella	PGS7270V	0.778	0.817	0.591	11.12 (M)
PGS7270X3	1992 SPOT–2	PGS7270V	0.759	0.793	0.592	10.81 (M)
PGS7270X4	1990 SPOT–2	PGS7270V	0.684	0.685	0.561	10.72 (M)
PGS7270X5	1990 & 1992 SPOT–2	PGS7270V	0.719	0.742	0.610	10.59 (M)
PGS7270X6	1992 SPOT–2, 1–CPR fixed at 0	PGS7270V	0.772	0.869	0.606	10.70 (M)
PGS7270X7	1990 SPOT–2, 1–CPR fixed at 0	PGS7270V	0.852	0.980	0.641	10.78 (M)

The results of orbit tests for LAGEOS, LAGEOS–2, and Stella on these solutions are given in Table 6.4.4.2–3. For these solutions, the Stella data are independent. The adjustment of the 1-CPR terms in models PGS7270X3–X5 improves the Stella orbit solution by preventing the SPOT–2 nonconservative force modeling errors from creeping into the gravitational model. Further, these 1-CPR terms must be adjusted on SPOT–2, otherwise the gravity model for that orbit is degraded even beyond the nominal performance for the subset solution that excludes both

SPOT–2 and Stella data (see the results for PGS7270V). The LAGEOS and LAGEOS–2 RMS of fit show little change for any of these models, demonstrating that these satellites are not a good discriminator of performance for the Stella/SPOT–2/ERS–1 altitude and inclination.

Table 6.4.4.2–3. SLR orbit residual test results for SPOT–2 calibration. All geopotential models were evaluated using their self-consistent tides solution.

Model	Multiarc RMS of Fit (cm)		Single Arc RMS of Fit (cm)
	LAGEOS[1]	LAGEOS–2[2]	Stella
PGS7270V	3.16	3.21	80.06
PGS7270X3	3.17	3.22	44.51
PGS7270X4	3.16	3.22	46.09
PGS7270X5	3.16	3.23	40.79
PGS7270X6	3.14	3.25	98.06
PGS7270X7	3.16	3.24	108.52

[1]Sa, Ssa tides adjusted as global parameters   [2]Sa, Ssa tides not adjusted

Based on these results, the data for the individual years were combined into a single normal equation with scale factors of $w_n = 1.78$ for the 1990 data and $w_n = 1.44$ for the 1992 data. In the final EGM96S solution, the data were further up-weighted by a factor of two, resulting in $\hat{\sigma} = 0.53$ cm/s for the 1990 data and 0.58 cm/s for the 1992 data.

6.4.4.3 Starlette

After the Starlette 1983 data were found to be the cause of the anomalous groundtrack stripes over northern Mexico in the covariance error projection map of the gravity anomalies, these data were deleted from the solution. The characteristics of the "old" (1983–1986) Starlette data are summarized in Table 6.4.4.3–1. The removal of the 1983 data excluded 4 months of data and 21732 observations. Time constraints precluded a reanalysis of the 1983 data prior to the final development of the EGM96 solution.

Table 6.4.4.3–1. Characteristics of the 1983–1986 Starlette SLR data.

Year of Data	No. of Obs.	No. of Arcs	Data Span
1983	21732	25	09/02–12/31
1984	91951	73	01/02–12/30
1986	92879	73	01/04–12/30

The calibrations of the Starlette data were repeated after the removal of the 1983 data, and are summarized in Table 6.4.4.3–2. The effects on the calibrations of the increase in the Starlette weight were mitigated by the up-weighting of two other important solution data sets (T/P GPS and LAGEOS). The calibrations do not show any peculiarities with the 1983 Starlette data, so the anomalous stripes that appeared in the covariance error maps could not have been predicted. However, the calibrations do reveal that the solution is much less sensitive to the 1986 data as compared to the other Starlette data. The 1984/86 Starlette normal equation weight (1.032, or $\hat{\sigma}$ = 0.98 m) used in PGS7270J was adopted for EGM96.

Table 6.4.4.3–2. Summary of Starlette data calibration and 5°x5° altimeter-derived gravity anomaly variance test results.

Master Model	Data Calibrated	Subset Model	Avg. Calibration Factors $\bar{k}_t$			v_{70} (mGal^2) of Master (M) or Subset (S)
			$n \leq 70$	$n \leq 20$	$m \leq 70$	
Subset Solution, No Starlette Data		PGS7270E				11.48 (S)
PGS7270F	1983 Starlette $w_n = 1.2$ 1993–94 Starlette $w_n = 1.8$	PGS7270E	0.850	0.915	0.751	10.52 (M)
PGS7270G	1984 Starlette $w_n = 1.2$ 1993–94 Starlette $w_n = 1.8$	PGS7270E	0.891	0.928	0.768	10.45 (M)
PGS7270H	1986 Starlette $w_n = 1.2$ 1993–94 Starlette $w_n = 1.8$	PGS7270E	0.267	0.288	0.196	10.40 (M)
PGS7270J	1984/86 Starlette $w_n = 1.032$ 1993–94 Starlette $w_n = 1.8$	PGS7270E	0.892	0.890	0.781	10.32 (M)

6.4.4.4 EP/EUVE

The increase in weight on LAGEOS and T/P GPS resulted in slightly lower calibrations for the EP/EUVE data during the recalibration of these data, a summary of which is given in Table 6.4.4.4–1. For instance, in the joint calibration of all the data, the calibration factor by degree decreased from 0.905 in the PGS7200 calibration set to 0.877 with PGS7270K. Doubling the weight scale factor on the EP/EUVE GPS data (from $w_n = 0.125$ to $w_n = 0.250$) would be possible. However, the small gain of 0.05 mGal^2 in the altimeter anomaly comparison test residual variance is mitigated by a slight increase in the GPS/leveling comparisons (see Table 6.4.4.4–2) for the satellite-only model, an effect that is rendered negligible with the inclusion of the surface gravity and altimeter data types in the combination model.

As with GPS/MET data, adjusting a separate 4x4 set of harmonics for the EP/EUVE TDRSS data might be justified in terms of the strong geographical dependence of the tracking coverage (which strongly resembles a (2,2) or (3,3) surface harmonic), and certain long-wavelength errors associated with this data type. The calibrations for the TDRSS data improve slightly when this is done, although a slight degradation is observed in residual variance from the altimeter-derived

gravity anomaly comparisons. In the combination model a slight improvement in the GPS/leveling comparisons over the US is observed when this separate adjustment is performed (see Table 6.4.4.4–2).

Table 6.4.4.4–1. Summary of EP/EUVE calibration and 5°x5° altimeter-derived gravity anomaly test results.

Master Model	EP/EUVE Data Calibrated	Subset Model	Avg. Calibration Factors $\bar{k}_t$			v_{70} (mGal^2) of Master (M) or Subset (S)
			$n \leq 70$	$n \leq 20$	$m \leq 70$	
Subset Solution, No EP/EUVE Data		PGS7270P				12.682 (S)
PGS7270K	Master solution: TDRSS $w_n = 0.10$ GPS $w_n = 0.125$		0.877	0.704	0.612	10.014 (M)
PGS7298B	GPS $w_n = 0.125$	PGS7270P	0.903	0.760	0.770	10.704 (M)
PGS7298B1	GPS $w_n = 0.250$	PGS7270P	0.960	0.768	0.831	10.645 (M)
PGS7298A	TDRSS $w_n = 0.1$	PGS7270P	0.890	0.815	0.594	10.432 (M)
PGS7298A1	TDRSS $w_n = 0.1 + 4x4$ harmonic	PGS7270P	0.856	0.754	0.578	10.572 (M)

Table 6.4.4.4–2. GPS/leveling results for final EP/EUVE calibrations using HDM180 for the high-degree field.

	GPS/leveling comparisons standard deviation (cm)		
Model	5 areas	BC	USA/NGS
PGS7270K	60.5	84.5	101.3
PGS7270P	57.4	83.4	116.0
PGS7298A	59.8	83.8	104.0
PGS7298A1	58.6	83.2	105.9
PGS7298B	61.8	83.9	97.0
PGS7298B1	62.4	83.2	97.3

6.4.4.5 GEOS–3 Tests

Since the PGS7200-series calibrations demonstrated the value of the GEOS–3 data, we examined this satellite's contribution more closely. The subset solution used to calibrate the GEOS–3 SLR and GEOS–3 ATS data was based on the satellite-only model PGS7270K, which used the same normal equation weight ($w_n = 0.7$) as PGS7240. The results of the calibration are summarized in Table 6.4.4.5.–1. The tests with the altimeter-derived anomalies reveal that the GEOS–3 SLR data are stronger than the GEOS–3 ATS data. In addition, the calibrations show that the

PGS6394 weight on the GEOS–3 ATS data ($w_n = 2.6$; corresponding to data uncertainty of 2.53 m for the SLR data and 0.5 cm/s for the ATS data) was too high, justifying the decision to down-weight these data in the PGS7200 and later solutions. The calibrations for the GEOS–3 SLR data are high (from ~1.0 to ~1.1), when calculated by degree, and relatively insensitive to changes in the applied weight. By order, the high calibration factors occur at $m = 0$ to 2, and near the secondary resonance orders ($m = 28$, 43, and 59), as shown in Figure 6.4.4.5-1. No change in the weight of the GEOS–3 SLR data was applied in the final solution, EGM96S, as a result of these more detailed tests. GEOS–3 remains an important contributor to the gravity solution, and, in the future, some effort to scrutinize these data and enhance their value by improving stations, reference frames, or orbit solution parameterization would be worthwhile.

Table 6.4.4.5–1. Summary of GEOS–3 calibration and 5°x5° altimeter-derived gravity anomaly test results.

Master Model	GEOS–3 Data Calibrated	Subset Model	Avg. Calibration Factors $\overline{k}_t$			v_{70} (mGal^2) of Master (M) or Subset (S)
			$n \leq 70$	$n \leq 20$	$m \leq 70$	
Subset Solution, No GEOS–3 Data		PGS7270Q				10.566 (S)
PGS7270K	Master solution: SLR $w_n = 0.3$ ATS $w_n = 0.7$		1.050	0.949	0.872	10.014 (M)
PGS7270S	ATS $w_n = 0.7$	PGS7270Q	0.968	0.904	0.923	10.441 (M)
PGS7270T	ATS $w_n = 2.6$	PGS7270Q	1.324	1.101	1.429	10.634 (M)
PGS7270Z	SLR $w_n = 0.3$	PGS7270Q	1.076	1.037	0.863	9.988 (M)
PGS7270Z1	SLR $w_n = 0.4$	PGS7270Q	1.097	1.050	0.905	9.980 (M)
PGS7270Z2	SLR $w_n = 0.15$	PGS7270Q	1.064	1.029	0.839	10.000 (M)
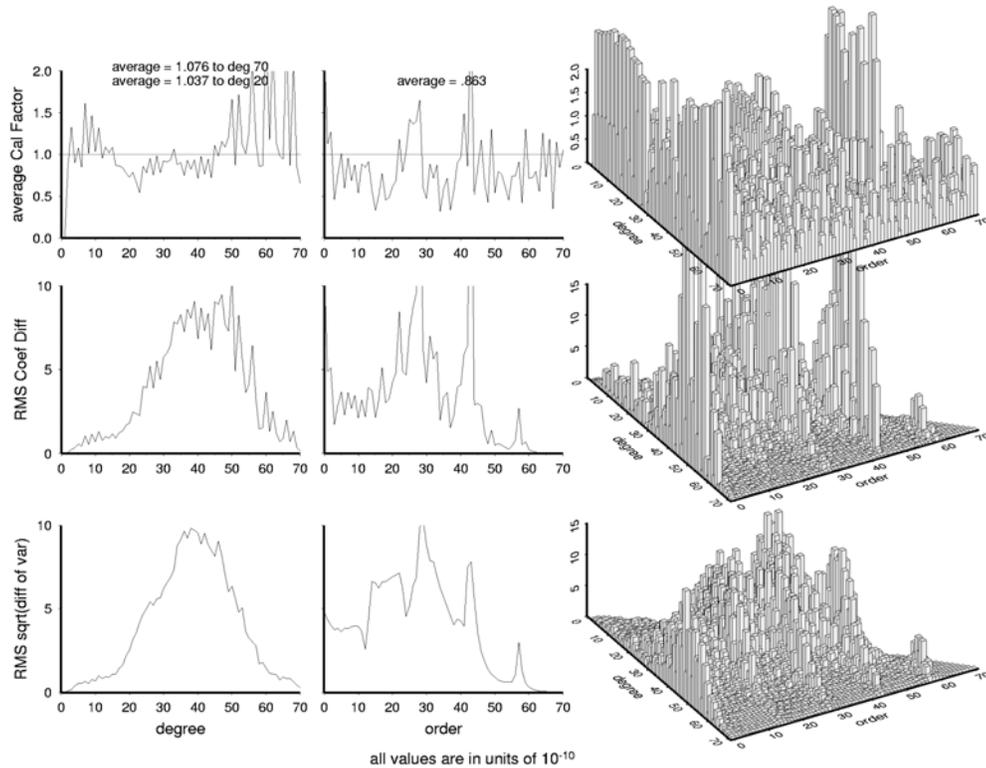
Figure 6.4.4.5–1. Effect of the GEOS–3 SLR tracking for $w_n = 0.3$ (PGS7270Q vs. PGS7270Z).

6.4.5 Independent Solution Calibrations

Prior to the start of the PGS7200 series of calibrations, the satellite-only solutions were tested by dividing the data into two sets: The first group essentially included the satellite data used in JGM–1S, and the second set used all the new data from 1993 and 1994, including SLR data, the entire TDRSS and GPS data sets, as well as all of the T/P tracking. The objective was to ascertain how globally consistent the "new" data were with the JGM–1S era data, and test how a drastic change in the weights of the GPS and TDRSS normal equations would affect the calibrations. Three solutions were computed, as summarized in Table 6.4.5–1: PGS6571, based on the JGM–1S data; PGS6572 using the normals for the 1993 and 1994 data, and PGS6573, with the weights on the GPS, TDRSS, and T/P SLR/DORIS data divided by two. In all three cases, the solutions were computed using the modified *a priori* constraint matrix described in Section 6.3.2.

Table 6.4.5–1. Description of independent calibrations solutions.

Model	Description
PGS6571	Satellite-only solution using data nominally included in JGM–1S. The appropriate normal equations and data weights from PGS7200 were used to make up the solution
PGS6572	Satellite-only solution using only the new data from 1993 onward, including SLR, DORIS, GPS, and TDRSS data types, in addition to all of the T/P tracking data. Normal equations from PGS7200 were used.
PGS6573	Same as PGS6572, but the normal equation weights on the GPS, TDRSS, and T/P data sets was divided by two.

Because the calibrations involve two completely independent solutions, the denominator in the definition of the calibration factors by degree n (eq. 6.4.1–14) must be modified [*Lerch et al.*, 1991] and becomes:

$$k_{t_n}^2 = \frac{\sum\limits_{m=0}^{n} (\mathbf{X}_t - \mathbf{X})^2}{\sum\limits_{m=0}^{n} (\sigma_t^2 + \sigma^2)} \tag{6.4.5–1}$$

The corresponding modification is also made to the denominator in the definition of the calibration factors by order m (eq. 6.4.1–15):

$$k_{t_m}^2 = \frac{\sum\limits_{n=2}^{N_{\max}} (\mathbf{X}_t - \mathbf{X})^2}{\sum\limits_{n=2}^{N_{\max}} (\sigma_t^2 + \sigma^2)} \tag{6.4.5–2}$$

The calibrations by degree and by order are depicted in Figures 6.4.5.8–1 and 6.4.5.8–2, and summarized in Table 6.4.5–2. In aggregate, these calibrations show that the "new" data (1993 onwards) are globally consistent with the "old" (JGM–1S era) data, both in terms of the recovered coefficients and the coefficient standard deviations. The low calibration factors indicate that one of the sets of data—we cannot determine which—is too pessimistically weighted. Reducing the weight of the new data by 50 percent alters the calibrations minimally.

Table 6.4.5–2. Independent calibration results.

Models Calibrated	Average Calibration Factors $\bar{k}_t$		
	$n \leq 70$	$n \leq 20$	$m \leq 70$
PGS6572 vs. PGS6571	0.508	0.890	0.332
PGS6573 vs. PGS6571	0.489	0.879	0.325

6.4.6 Final EGM96S Satellite Data Weights

The final satellite-only model, designated EGM96S, was constructed with the effective data uncertainties specified in Table 6.4.6–1. After the reconstruction of the GPS matrices, and the PGS7200 series of calibrations, the changes discussed in the preceding sections were applied. These include changes to the T/P GPS normals, the separate adjustment of a 5x5 harmonic coefficient set for GPS/MET, up-weighting of the GPS/MET data, a reduction of the effective data uncertainty on the EP/EUVE TDRSS data types, separate normal equation weighting of the 1990 and 1992 SPOT–2 data, and removal of 1983 Starlette data.

Table 6.4.6–1. Summary of EGM96S effective tracking data uncertainties.

Data	Uncertainty	Data	Uncertainty
Ajisai SLR 86–87	2.36 m	HILAT Doppler	1.58 cm/s
Ajisai SLR 93–94	1.92 m	LAGEOS SLR 80–92	1.00 m
BE–C Doppler	7.45 cm/s	LAGEOS SLR 93–94	0.63 m
BE–C SLR	3.02 m	LAGEOS–2 SLR	0.54 m
D1–C Doppler	12.91 cm/s	Nova Doppler	1.83 cm/s
D1–C SLR	11.95 m	Optical Satellites	5.77 arcsec
D1–D Doppler	12.91 cm/s	Oscar–14 Doppler	10.00 cm/s
D1–D SLR	11.95 m	Peole SLR	7.91 m
EP/EUVE GPS	2.82 m	RADCAL Doppler	2.24 cm/s
EP/EUVE TDRSS Doppler	0.91 cm/s	SEASAT Doppler	2.58 cm/s
EP/EUVE TDRSS Range	36.51 m	SEASAT SLR	5.77 m
Etalon SLR	1.24 m	SPOT–2 DORIS 1990	0.53 cm/s
GEOS–1 SLR	5.00 m	SPOT–2 DORIS 1992	0.59 cm/s
GEOS–2 SLR	10.00 m	Starlette SLR 84–86	0.98 m
GEOS–3 ATS Doppler	0.96 cm/s	Starlette SLR 93–94	0.75 m
GEOS–3 ATS period SLR	4.88 m	Stella SLR	0.79 m
GEOS–3 SLR	1.83 m	T/P DORIS	1.58 cm/s
GEOSAT Doppler	1.63 cm/s	T/P GPS	0.29 m
GFZ–1 SLR	7.07 m	T/P SLR	2.50 m
GPS/MET	2.24 m		

The SLR data uncertainties presented in Table 6.4.6–1 represent the nominal value that was applied to the majority of the tracking sites. However, there were several stations for which higher uncertainties were used. Table 6.2.6.2–1 lists all stations for which the SLR data uncertainty was not 1 m.

For the GPS, TDRSS, ATS, DORIS, and Doppler tracking data types, the values represent the actual uncertainty applied to all data of that type for that spacecraft. The final effective data uncertainty for the optical data does not include the effect of the cosine latitude scaling that was applied to the data uncertainty used in the reduction of the right ascension component of the tracking data.

6.4.7 GM *Issues*

Examination of the *GM* adjustments in the PGS7200 series of calibrations revealed that essentially two satellites were tightly constraining the estimated *GM* to the *a priori* value: GPS/MET and EP/EUVE GPS. For both satellites, the GPS satellite orbits were determined independently and then held fixed in the EP/EUVE GPS and GPS/MET orbit determination, effectively fixing the scale of the solution. In the case of GPS/MET, the handling of the ambiguity biases in the SOLVE back substitution also resulted in an additional *GM* constraint. Both of these processes unrealistically constrained *GM* and caused an overly optimistic solution formal standard deviation. A similar process can also affect the EP/EUVE TDRSS data; however the reduced number of relay spacecraft and the lightly constrained TDRS orbits preclude this from happening. The simultaneous adjustment of the GPS satellite orbits in the T/P orbit determination using the GPS data meant the T/P GPS data would not unduly constrain the *GM*.

The PGS7270K interim satellite-only solution was derived using satellite-specific *GM* estimation for EP/EUVE GPS, EP/EUVE TDRSS, and GPS/MET, while the remaining data (i.e., LAGEOS, T/P SLR/DORIS, TRANET, etc.) contributed to the global solution *GM*. The resulting global solution *GM* was 398600.44323 ± 0.00039 km^3/s^2, which exceeded the 1σ uncertainty limit of the largely LAGEOS-derived *a priori* value (398600.4415 ± 0.0008 km^3/s^2) adopted from *Ries et al.* [1992]. Thus, in the final solution for EGM96S and EGM96, the *GM* of the solution was held fixed at the *a priori* value, and was adjusted as satellite-specific parameters for the EP/EUVE GPS, EP/EUVE TDRSS, and GPS/MET matrices. The arc *GM* values from EGM96S for these satellites are listed in Table 6.4.7–1.

Table 6.4.7–1. Estimated GM values from EGM96S.

Satellite	Satellite-specific *GM* (km^3/s^2)
GPS/MET	$398600.44150 \pm 0.0000536$
EP/EUVE TDRSS	398600.43659 ± 0.0224
EP/EUVE GPS	$398600.44158 \pm 0.000127$

6.4.8 *Treatment of Tides in EGM96(S)*

As tracking precision has improved, the geopotential fields have increased in size and accuracy. A commensurate ability to model long-wavelength tidal signals for major tidal constituents [*Marsh et al.*, 1988, 1990; *Christodoulidis et al.*, 1988] has also evolved. Tide modeling for EGM96 reflects two distinct challenges;

a) To improve the long-wavelength tidal terms that are in near resonance, giving rise to sizable long-period perturbations. This, in turn, allows them to be estimated from tracking data;

b) To incorporate a large number of tidal coefficients spanning many tide lines, giving rise to a whole class of short-period orbital perturbations. Individually, these background tidal terms

are not recoverable, but, in aggregate, they are important for achieving current orbit accuracy goals.

For EGM96, the design of the background model was made on the basis of an orbital sensitivity analysis where terms having greater than a certain orbit perturbation cutoff were included. Omitted terms were restricted to contributing less than some tolerable RSS orbit error, thus balancing computational burden with model completeness.

6.4.8.1 Solid Earth Tide Modeling

The ocean tidal modeling and parameter recovery are made in the presence of a frequency-dependent model of the solid Earth tides. This model has undergone an upgrade since the issuance of the MERIT Standards [*Melbourne et al.*, 1983], which served as the background model for solid Earth tides employed in GEM–T3. This upgrade was adopted for EGM96. It accounts for additional frequency-dependent solid Earth Love numbers, based on an improved estimate of the Free Core Nutation resonance (from 507- to 430-day period), and was adopted as part of the T/P force modeling standards [*Zhu et al.*, 1990]. A comparison of solid Earth tide models is shown in Figure 6.4.8.1–1. The solid Earth tidal model is not adjusted, although it is unrealistically free of dissipation, because of our current uncertainty about the Earth's anelastic response at different periods of tidal forcing. However, each ocean tidal term that is estimated accommodates ocean, atmospheric, and solid Earth mass redistribution at its specific frequency as sensed by the precise tracking data.
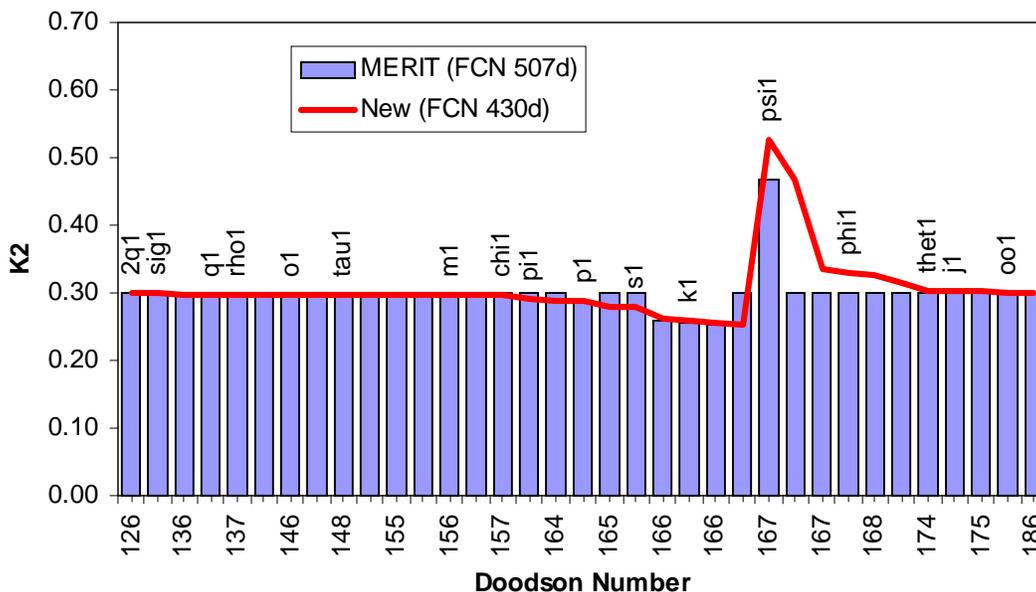
Figure 6.4.8.1–1. Difference in Solid Earth Love numbers between FCN periods of 507 and 430 days.

6.4.8.2 Background Ocean Tide Model: Elimination of Significant Omitted Terms

Because of the large number of background tidal terms required, an algorithm for efficiently computing all tides within a tidal family is used to reduce the computational burden. Based on the formulation developed by *Colombo* [*unpublished notes and private communication*, 1989], these expanded tidal constituents were used for EGM96.

The expanded model is an advancement over that given in [*Christodoulidis et al.*, 1988]. The new formulation computes the tidal accelerations within each family (e.g., the mainline and narrow band of smaller sideband tides) through the direct scaling of the accelerations due to the mainline. A summary of Colombo's development is presented below:

The formulation derived in [*Christodoulidis et al.*, 1988] shows the disturbing potential arising due to the ocean tides as:

$$U = 4\pi G r_e \rho_w \sum_{f} \sum_{lq} \frac{(1 + k_l')}{(2l + 1)} C_{lqf}^{\pm} \cdot \cos(\sigma_f(t) \pm q\lambda + \pi - m\frac{\pi}{2} + \varepsilon_{lqf}^{\pm}) P_{lq}(\phi) \qquad (6.4.8.2\text{–}1)$$

where:

G is the gravitational constant

r_e is the average radius of the Earth

ρ_w is the average density of sea water

k_l' is a load deformation coefficient

$C_{lqf}^{\pm}$ is the amplitude of the tidal term in the spherical harmonic expansion

$\varepsilon_{lqf}^{\pm}$ is the phase of the tidal term

$\sigma_f(t)$ is the astronomical phase at time, t

λ is the subsatellite longitude

m is the order of the tidal species, where $m = 0, 1, 2$ are the long period, diurnal, and semidiurnal tides, respectively

$P_{lq}(\Phi)$ is the Legendre function of degree l, and order q

l,q are the degree and order of the tidal harmonic

f ranges over all tidal constituents

$\pm$ arises in the decomposition of the Doodson tidal argument number to a set of subscripts following the development given in [*Christodoulidis et al.*, 1988].

A modified form of the above expression was introduced in tidal modeling within GEODYN for the EGM96:

$$U = 4\pi G r_e \rho_w \sum_f \left| \frac{V_f(t)}{\overline{V}_f} \right| \sum_{lq} \frac{(1 + k_l)}{(2l + 1)} \, C_{lqf}^{\pm} \cdot \cos(\sigma_f(t) \pm q\lambda + \pi - m\frac{\pi}{2} + \mathcal{E}_{lqf}^{\pm}) P_{lq}(\phi) \qquad (6.4.8.2\text{–}2)$$

where $V_f(t)$ and V_f are the osculating and mean values respectively of the Doodson Coefficient multiplied by the Doodson Constant.

Under the assumption that the admittance of the Earth is the same for all nearby frequencies within each tidal family, Colombo took this development a step further. By taking advantage of the slow modulation of the main line tides by their sidebands, the contribution to the tidal potential of the sidebands is evaluated through a linear scaling using tidal admittances. This permits efficient computational treatment of the sideband tides. This scaling is:

$$U = 4\pi G r_e \rho_w \sum_f \sum_{lq} \frac{(1 + k_l')}{(2l + 1)} \, C_{lqf}^{\pm} \cdot [A_f(t)\cos(\sigma_f(t) \pm q\lambda + \pi - m\frac{\pi}{2} + \mathcal{E}_{lqf}^{\pm}) +$$

$$B_f(t)\sin(\sigma_f(t) \pm q\lambda + \pi - m\frac{\pi}{2} + \mathcal{E}_{lqf}^{\pm})] \, P_{lq}(\phi) \qquad (6.4.8.2\text{–}3)$$

where:

$$A_f(t) = \sum_j \left| \frac{V_{fj}(t)}{\overline{V}_{fo}} \right| \cos(\sigma_{fj}(t) - \sigma_{fo}(t)) \qquad (6.4.8.2\text{–}4)$$

$$B_f(t) = -\sum_j \left| \frac{V_{fj}(t)}{\overline{V}_{fo}} \right| \sin(\sigma_{fj}(t) - \sigma_{fo}(t)) \qquad (6.4.8.2\text{–}5)$$

f_o represents the main tide line associated with f and j identifies the individual sideband lines. GEODYN contains an internal table that causes the evaluation of all important sideband tides for each constituent in the computation of the dynamic tidal accelerations. Table 6.4.8.2–1 gives the mainline Darwinian name, its Doodson number, and the sideband tides which are, within GEODYN, the defined tidal constituent families. Other tides that require modeling for orbit computations that lack significant sideband contributions are shown in Table 6.4.8.2–2.

Casotto [1989] used an analytical orbit theory to evaluate the ocean tidal perturbations on the T/P orbit. Casotto's goal was to achieve omission errors from the ocean tides being less than 1 cm RSS within T/P POD. On the basis of his study, a set of spherical harmonic coefficients for over 80 tide lines was identified as being T/P-sensitive. Many of these are sideband tides, and some are tides that result from the interaction of the third bodies with one another. These latter tides are implicitly modeled in the GEODYN formulation through our use of the osculating Keplerian elements of the perturbing bodies. We have used Table 7.2.1 from *Casotto* [1989] to map his recommendations into the tidal families shown in Tables 6.4.8.2–1 and 6.4.8.2–2. This represents the EGM96 background model.

Table 6.4.8.2–1. Tidal families modeled in GEODYN using scaling based on admittances.

Name	Mainline Doodson Numbers	Family Doodson Numbers
S_a	056.5545	056.5565
S_{sa}	057.5555	057.5535
M_m	065.4555	065.4755 065.6555 065.6655 065.6755 065.6855
M_f	075.5555	075.3355 075.3555 075.3655 075.3755 075.5655 075.5755 075.5855
M_{tm}	085.4555	085.2555 085.4655 085.4755
Q_1	135.6555	135.6355 135.6455 135.8555
O_1	145.5555	145.5455 145.7455 145.5255 145.7555 145.7655 145.7755 145.5355
M_1	155.6555	155.4455 155.4555 155.6455 155.6655 155.6755
P_1	163.5555	163.5575
K_1	165.5555	165.5355 165.5455 165.5655 165.5755
J_1	175.4555	175.4455 175.4655 175.4755 175.6555 175.6655
O_{o1}	185.5555	185.3555 185.3655 185.5655 185.5755 185.5855
$2N_2$	235.7555	235.7455
N_2	245.6555	245.6455
M_2	255.5555	255.7555 255.5455 255.7455 255.7755
L_2	265.4555	265.4455 265.6455 265.6555 265.6655 265.6755
S_2	273.5555	273.5575
K_2	275.5555	275.5455 275.5655 275.5755 255.7655 255.5355 255.5255

Table 6.4.2.2–2. Tides not having significant sideband terms.

Name	Doodson Number
S_{ta}	058.5545
π_1	162.5565
S_1	164.5545
ψ_1	166.5545
ϕ_1	167.5555
–	271.5575
R_2	274.5545
–	285.4555
–	295.5555

In our treatment of Casotto's recommendations, any coefficient requiring modeling in either the mainline or its sidebands was included in our model. We have tested Casotto's conclusions for the mainline and sideband tides and concur with his findings as reported in *Nerem et al.* [1993b]. The background ocean tide model adopted as *a priori* for EGM96 used harmonics obtained from the hydrographic analyses performed by *Schwiderski*. Later, we recommend additional upgrades to this background model based upon the T/P altimetry tidal solutions (if the user can accommodate the significant computational burden that is imposed.)

The ocean's mass is not uniformly distributed geographically. Thus, the ocean tides cause an apparent degree one time-dependent geopotential effects with respect to a terrestrial frame

attached to the Earth's crust. *Casotto* pointed out the most important of these degree-one terms that were used in the *a priori* ocean tidal model for EGM96.

We adopted Casotto's recommendations because there was no other alternative at the time. More recently, *Ray et al.* [1994] and *Brosche et al.* [1993] have produced theoretical models of the tidally coherent geocenter motions that agree well with the independent observations obtained by SLR data [cf. *Eanes and Watkins*, 1993]. With the implementation of purely kinematic diurnal and semidiurnal "apparent" geocenter motion models in GEODYN (i.e., the station network moves in time w.r.t. the origin of the orbital frame, while retaining its internal geometry), it is no longer recommended to explicitly model degree-one tidal geopotential terms. This recommendation is included in our upgraded EGM96-based ocean tidal model.

6.4.8.3 Design of the EGM96(S) Ocean Tidal Solution

Many tidal components, while being diurnal or semidiurnal on the Earth's surface (due to the Earth's rotation with respect to the Sun and Moon), give rise to long-period orbital perturbations (see Table 6.4.8.3–1). In EGM96, these tidal terms are adjusted simultaneously with the gravity model. The solid Earth tides are assumed to have a zero phase angle and are, therefore, assumed to be free of dissipation. Furthermore, the k_3 love number is set to zero as well. However, any residual phase due to anelastic properties of the solid Earth are accounted for in the adjusting subset of ocean terms. In EGM96, we have adjusted even and odd degree terms for each of the 12 major tidal frequencies. The resulting model accurately reflects the external tidal potential sensed by Earth-orbiting satellites arising from the tidal redistribution of mass in the integrated solid Earth–ocean–atmospheric systems.

Designing the EGM96 tidal solution was complicated by:

a) Strong, continuous GPS and TDRSS data sets that were of short overall duration. For SLR, there are many years of data included in the solution to support the separation of tidal signals into their respective constituents. For GPS and TDRSS, restricted data availability and the resources required to process these extremely large data sets into normal equations caused us to use shorter data segments. These data were excellent for recovery of the static geopotential. However, it is possible that, given their short duration, these data could alias the tidal solution.

b) Several strong satellite data sets were acquired on Sun-synchronous orbits since the GEM–T3 solution (e.g., Stella, SPOT–2). The perfect resonance with the dominant solar semidiurnal tide, S_2, and deep resonance with all solar tides, radiative and thermal forcing effects, could make these satellites unsuitable to contribute to the solar tidal solution.

c) Altimeter data sense both surface (direct/geometric) and orbital (dynamic) ocean tidal signals that were modeled using a state-of-the-art T/P-based tide model. These data were subsequently excluded from the global dynamic tidal solution as a result of a GEODYN limitation that did not allow isolation of the strictly dynamic contribution.

We remedied these potential deficiencies by allowing individual tidal solutions for specific satellites. In the case of the Sun-synchronous orbits, the satellite-specific adjustment was

restricted to the solar and K_1/K_2 tides. These data were, thereby, detrended for significant tidal signals while simultaneously being excluded from the global dynamic tidal solution. Table 6.4.8.3–2 describes those satellites that did not contribute to the global tides solution, including those for which satellite-specific tidal detrending was employed, and those for which the tides were excluded.

Table 6.4.8.3–1. Periods of the principal long-period orbit perturbations arising from ocean tides.

Name	S_a	S_{sa}	M_m	M_f	O_1	P_1	K_1	N_2	M_2	S_2	K_2
Period on Earth surface	1.0139 years	182.62 days	27.55 days	13.66 days	1.076 days	1.003 days	23.935 hours	12.658 hours	12.421 hours	12.000 hours	11.967 hours
Satellite:	Period (days)										
LAGEOS	same	same	same	same	13.8	221	1050	9.20	14.0	280	524
Starlette	same	same	same	same	11.9	60.8	91.0	7.61	10.5	36.4	45.5
GEOS 2	same	same	same	same	14.4	629	257	9.83	15.3	436	129
GEOS 3	same	same	same	same	15.2	482	132	10.6	17.2	104	66.2
BE–C	same	same	same	same	11.8	57.9	84.8	7.51	10.3	34.4	42.4
SEASAT	same	same	same	same	14.8	7130	178	10.2	16.1	174	89.0
Oscar–7	same	same	same	same	13.6	180	11700	9.12	13.6	177	5830
T/P	same	same	same	same	12.7	89	174	8.3	11.8	58.9	86.9
SPOT–2	same	same	same	same	14.2	364	366	9.6	14.8	$>2 \times 10^4$	183
GFZ–1	same	same	same	same	11.4	50.7	70.3	7.2	9.8	29.5	35.1
EP/EUVE	same	same	same	same	10.9	41.7	54.0	6.8	9.1	23.5	27.0
GPSMET	same	same	same	same	12.6	84.1	156	8.2	11.6	54.6	77.9
RADCAL	same	same	same	same	13.6	177	6341	9.1	13.6	173	3154
HILAT	same	same	same	same	13.2	125	393	8.7	12.8	94.6	196
LAGEOS–2	same	same	same	same	13.3	138	569	8.9	13.0	111	285
Ajisai	same	same	same	same	12.2	71.5	117	7.9	11.1	44.4	58.7

Table 6.4.8.3–2. Satellite-specific tidal solutions to detrend data for tidal signals. *These data do not contribute to the EGM96 global dynamic tidal solution.*

Satellite	Tidal Constituent	Method of Detrending
EP/EUVE GPS	S_a	separate (2,0) & (3,0)
GPS/MET	S_a	separate (2,0) & (3,0)
SPOT–2	S_a & S_{sa}	separate (2,0) & (3,0)
	S2	separate (2,2) & (3,2), no (4,2) to (7,2)
Stella	S_a & S_{sa}	separate (2,0) & (3,0)
	S_2	separate (2,2) & (3,2), no (4,2) to (7,2)
All Optical	all	Tide partials not included in the global solution or estimated separately
T/P GPS	all	separate tide model mirroring the global model

However, tests subsequent to the release of EGM96 showed that the following detrending was not really necessary. The only major problem in the tide model were for the computed S_a and S_{sa}

components. The problem was not improved or made worse by the inclusion or exclusion of the detrended tide signals.

6.4.8.4 EGM96S Adjusted Ocean Tides

In EGM96, 56 harmonic constituents (112 updated coefficients) representing the 13 major tidal constituents were selected. The selection of these tidal coefficients was based on their effect on the T/P orbit. Future analysis will have to be performed to address the issue of optimizing the estimated tides set to recover the signal sensed by the new compliment of low-latitude and low-inclination spacecraft. However, the present OD precision on these satellites of 25 cm to 3 meters may not support the requisite sensitivity. Table 6.4.8.4–1 lists the tide constituents that were adjusted.

Table 6.4.8.4–1. Summary of EGM96 adjusted ocean tides.

Main Line Constituent	Degree, Order of adjusted terms	Number of adjusted terms
S_a	(2,0) to (3,0)	2
S_{sa}	(2,0) to (3,0)	2
M_f	(2,0) to (5,0)	4
M_m	(2,0) to (3,0)	2
K_1	(2,1) to (6,1)	5
O_1	(2,1) to (6,1)	5
P_1	(2,1) to (5,1)	4
Q_1	(2,1) to (5,1)	4
K_2	(2,2) to (6,2)	5
M_2	(2,2) to (8,2)	7
S_2	(2,2) to (7,2)	6
N_2	(2,2) to (6,2)	5
T_2	(2,2) to (6,2)	5

6.4.8.5 EGM96S Ocean Tides

For completeness, the estimated tides from the EGM96S satellite-only solution are presented in Table 6.4.5.8–1, along with the GEM–T3S tides, which are provided for reference. GEM–T3 estimated a smaller set of tides than EGM96S. For terms that were estimated in EGM96S, but not in GEM–T3S, the value applied in GEM–T3S is shown without an uncertainty. A superficial comparison of the results will show significant differences in the S_a and S_{sa} 3,0 harmonic amplitudes. This may be a factor in the LAGEOS orbit tests results discussed in later sections.

As a reminder for the reader, this set of tides is not the final set of tides associated with EGM96. Rather, these tides are the result of the satellite-only model development. The final EGM96 are the result of the simultaneous solution with the low-degree combination model that is discussed in detail in Section 7 and evaluated in Section 10.

Table 6.4.8.5–1. Comparison of ocean tidal terms from GEM–T3S and EGM96S. GEM–T3S terms shown without an uncertainty were applied in that solution.

Tide Line			GEM-T3S				EGM96S			
	l	q	amplitude	σ (cm)	phase	σ (°)	amplitude	σ (cm)	phase	σ (°)
M_m	2	0	0.82	±0.31	262.1	±21.5	0.90	±0.12	262.8	±7.7
	3	0	0.98	0.82	35.4	47.8	0.21	0.25	38.7	68.0
S_a	2	0	2.70	0.40	26.3	8.9	2.47	0.17	38.7	4.1
	3	0	5.19	0.74	313.8	8.1	3.34	0.28	286.3	4.5
M_f	2	0	2.07	0.38	239.8	10.6	2.03	0.16	249.9	4.5
	3	0	0.37	0.94	334.0	140.8	0.38	0.30	271.9	46.1
	4	0	0.52	–	99.1	–	1.23	0.98	124.3	46.1
	5	0	0.48	–	239.7	–	0.62	0.48	163.2	44.0
S_{sa}	2	0	1.58	0.38	253.4	13.7	1.50	0.14	275.4	5.2
	3	0	0.56	0.72	50.3	74.1	1.68	0.23	93.0	8.3
K_1	2	1	2.78	0.17	325.0	3.6	2.83	0.12	320.6	2.2
	3	1	0.78	0.11	12.8	8.4	1.02	0.05	38.6	2.8
	4	1	2.39	0.21	256.6	5.1	2.36	0.09	256.9	2.3
	5	1	2.24	0.25	107.7	6.2	1.48	0.07	116.6	2.8
	6	1	0.17	–	275.5	–	0.17	0.33	346.6	111.7
O_1	2	1	2.71	0.16	314.8	3.4	2.73	0.08	314.9	1.7
	3	1	1.33	0.16	80.7	6.8	1.59	0.05	80.6	1.9
	4	1	1.89	0.21	281.2	6.3	1.75	0.10	275.7	3.2
	5	1	1.51	0.28	124.5	10.8	1.11	0.07	109.6	3.7
	6	1	0.18	–	284.2	–	0.33	0.28	306.3	48.4
P_1	2	1	0.94	0.18	314.7	11.0	0.99	0.09	316.4	4.9
	3	1	0.41	0.10	8.7	15.5	0.37	0.05	37.6	8.4
	4	1	0.88	0.22	255.6	14.1	0.74	0.07	260.7	5.5
	5	1	0.77	0.28	126.0	20.4	0.09	0.06	4.3	38.0
Q_1	2	1	0.53	–	313.7	–	0.59	0.08	322.1	8.0
	3	1	0.32	–	104.2	–	0.24	0.05	94.8	12.9
	4	1	0.29	–	288.1	–	0.41	0.08	277.6	11.3
	5	1	0.22	–	112.3	–	0.32	0.08	114.1	13.7
K_2	2	2	0.34	0.06	316.2	9.4	0.27	0.03	328.4	5.7
	3	2	0.19	0.04	187.3	10.0	0.15	0.02	195.0	6.0
	4	2	0.15	0.05	105.9	17.2	0.13	0.02	119.6	9.0
	5	2	0.06	0.03	94.6	28.5	0.06	0.01	23.3	11.2
	6	2	0.05	0.04	352.1	48.6	0.01	0.02	353.3	67.8
M_2	2	2	3.31	0.06	321.1	1.1	3.27	0.03	321.8	0.6
	3	2	0.26	0.07	154.9	14.4	0.31	0.02	171.9	3.5
	4	2	0.99	0.06	125.9	3.3	1.04	0.03	130.3	1.6
	5	2	0.31	0.04	13.6	6.8	0.29	0.01	10.2	2.4
	6	2	0.39	0.06	317.3	9.1	0.43	0.03	330.5	4.4
	7	2	0.09	–	199.2	–	0.14	0.01	197.5	5.6
	8	2	0.13	–	214.3	–	0.15	0.04	196.8	13.2
S_2	2	2	0.78	0.05	300.7	4.0	0.78	0.03	304.1	2.3
	3	2	0.28	0.05	223.7	9.3	0.23	0.02	212.7	4.8
	4	2	0.36	0.04	93.8	6.5	0.36	0.02	101.6	2.8
	5	2	0.16	0.04	21.5	14.6	0.15	0.01	33.8	4.8
	6	2	0.16	0.04	273.5	14.8	0.16	0.02	289.2	6.8
	7	2	0.04	–	142.6	–	0.05	0.01	19.3	13.2
N_2	2	2	0.70	0.08	334.1	6.2	0.64	0.03	335.0	3.0
	3	2	0.09	0.07	151.3	45.3	0.10	0.02	182.2	9.5
	4	2	0.24	0.06	140.7	14.7	0.25	0.02	145.2	5.8
	5	2	0.08	0.03	358.0	24.4	0.08	0.01	8.4	8.4
	6	2	0.08	0.05	354.9	36.8	0.07	0.02	12.9	14.9
T_2	2	2	0.04	0.06	324.6	80.8	0.05	0.03	301.5	33.6
	3	2	0.02	0.04	341.4	113.3	0.04	0.02	149.0	21.2
	4	2	0.05	0.05	134.8	61.9	0.02	0.02	143.2	68.6
	5	2	0.06	0.04	53.5	36.5	0.03	0.01	5.5	14.4
	6	2	0.04	0.04	176.7	68.2	0.03	0.02	280.1	37.7

6.5 Verification and Validation

Throughout the development of the satellite-only model, a series of orbit tests was performed to assess the overall performance of the intermediate models. Once EGM96S was completed, a more rigorous set of tests was performed. This section will discuss the testing of EGM96Snd evaluate its performance. The primary benchmark for the performance evaluation is JGM–2S, which was the preceding satellite-only model. In some cases, additional comparisons are also made with subsets of EGM96S to demonstrate the impact of certain satellites on the solution.

6.5.1 SLR and TDRSS Orbit Tests

Results of the SLR-based orbit tests for JGM–2S and EGM96S are shown in Table 6.5.1–1, and the ERS–1 tests are shown in Table 6.5.1–2. For these tests, the appropriate tide model has been used with each gravity field, with the exception of the EGM96S/PGS4846X combination. This is intended to minimize the error of omission caused by using a different tides set than the one that the model was developed with. JGM–2S used the PGS4846X tides, while EGM96S was evaluated using its simultaneously determined tide model. Compared to the predecessor satellite-only model, EGM96S gravity and tides solution is a significant overall improvement, especially for Starlette, Ajisai, Stella, GFZ–1, and ERS–1.

Table 6.5.1–1. SLR orbit test residuals for the satellite-only models (set-1).

Gravity	Tides	RMS of Fit (cm)						
		Multiple arc					Single arc	
		LAGEOS[1]	LAGEOS[2]	LAGEOS–2[1]	Starlette	Ajisai	Stella	GFZ–1
JGM–2S	PGS4846X	3.16	3.15	3.29	9.27	7.40	142.88	32.02
EGM96S	PGS4846X	3.09	3.09	3.17	9.37	7.38	11.70	7.09
EGM96S	EGM96S	3.42	2.91	3.25	7.85	7.16	11.63	7.61
PGS7316	PGS7316	3.46	2.90	3.26	7.85	7.14	11.75	8.06

[1] Sa, Ssa tides not adjusted   [2] Sa, Ssa tides adjusted as global parameters.

Table 6.5.1–2. ERS–1 single arc orbit test weighted RMS residuals. The altimetry data uncertainty is 3.0 m, and the SLR data uncertainty is ~1.12 m.

Gravity	Tides	Weighted RMS Residual	
		SLR	Altimetry
JGM–2S	PGS4846X	12.33	40.85
EGM96S	PGS4846X	7.45	32.97
EGM96S	EGM96S	7.45	32.97

Referring to Table 6.5.1–1, the effect of the Sa and Ssa tide estimation on the 30-day multiarc LAGEOS orbit tests is the only case where the JGM–2S significantly outperforms EGM96S

when their appropriate tides solutions are used. The LAGEOS RMS with no tidal adjustment is 3.16 cm with JGM–2S/PGS4846X vs. 3.42 cm with EGM96S/EGM96S. Yet, when the Sa and Ssa tides are adjusted, the RMS improves from 3.15 cm to 2.91 cm. In addition, a comparison of the test results using JGM–2S and EGM96S with the same tides (PGS4846X) shows a reduction in the RMS from 3.15–3.16 cm to 3.09 cm using the EGM96S geopotential model. The 10-day tests for LAGEOS, summarized in Table 6.5.1–3, show a maximum change of 0.3 mm, no matter which geopotential model (JGM–2S or EGM96S) or tide model (PGS4846X or EGM96S) is used. Thus, with the exception of the long-period Sa and Ssa tides, the EGM96S geopotential and tide solutions appear to be an improvement for LAGEOS.

The LAGEOS–2 test results confirm the improved performance of the EGM96S geopotential model. Using the PGS4846X tides model, the 30-day LAGEOS–2 tests results listed in Table 6.5.1–1 improve from 3.29 cm using the JGM–2S geopotential model to 3.17 cm with EGM96S. The 10-day tests listed in Table 6.5.1–2 show an even larger improvement—from 2.76 to 2.54 cm when the 1-CPR along-track empirical accelerations are estimated, with similar improvements when the 1-CPR terms are not adjusted. Further improvement also results using the EGM96S tide solution, where the RMS decreases from 3.76 cm with EGM96S/PGS4846X to 3.66 cm with EGM96S/EGM96S, when the 1-CPR terms are not adjusted. The longer 30-day multiarc tests degrade using the EGM96S tidal solution—the RMS increases from 3.17 cm with EGM96S/PGS4846X to 3.25 cm with EGM96S/EGM96S. However, the EGM96S geopotential and tides combination still outperforms the JGM–2S/PGS4846X combination.

The dichotomy between the tidal and geopotential solutions in the RMS of fit results also is apparent for both Starlette and Ajisai. The improvement on Starlette, for the multiarc test summarized in Table 6.5.1–1, is due to the EGM96S tidal solution, since the RMS improves from 9.37 cm with EGM96S/PGS4846X to 7.85 cm with EGM96S/EGM96S. Similarly, Ajisai improves the most when the EGM96S tide model is applied, from 7.38 cm with EGM96S/PGS4846X to 7.16 cm with EGM96S/EGM96S.

Table 6.5.1–3. Multiarc SLR orbit test residuals (set 2).

| Gravity Model | Tide Model | SLR Residual RMS (cm) | | | | | | | |
| | | LAGEOS | | LAGEOS–2 | | Stella | | GFZ–1 | |
		Adjust 1-CPR	No 1-CPR	Adjust 1-CPR	No 1-CPR	Adjust 1-CPR	No 1-CPR	Adjust 1-CPR	No 1-CPR
JGM–2S	PGS4846X	2.47	2.70	2.76	4.02	15.76	89.17	164.74	203.77
EGM96S	PGS4846X	2.50	2.72	2.54	3.76	5.32	11.58	102.64	111.48
EGM96S	EGM96S	2.49	2.68	2.55	3.66	5.24	10.31	102.71	111.20
PGS7316	PGS7316	2.48	2.67	2.56	3.67	5.23	10.36	104.41	113.31

In the single arc test results given in Table 6.5.1–1, the Stella and GFZ–1 results are extremely promising on the surface; in Stella's case they represent an improvement of more than 10x. However, the single-arc solutions used for these tests do not have much SLR tracking data. In the case of GFZ–1, the low orbit and sparse tracking resulted in only 195 observations over the 3-day

arc. While these tests are useful for a quick evaluation of the models, as was done for the development of EGM96S, for those two spacecraft it is best to look at the longer multiarc solutions (described in Section 5.1.2), given in Table 6.5.1–3. These results show less spectacular results for Stella, but significant improvements, nonetheless.

The effect of EP/EUVE on the EGM96S solution can be examined by comparison of the results for EGM96S and PGS7316, which is an EGM96S subset that excludes all of the EP/EUVE tracking data. The results from Tables 6.5.1–1 and –3 show only small differences for the LAGEOS, Starlette, and Ajisai tests, though the overall sense is that the inclusion of EP/EUVE had a very minor negative impact on the ability of EGM96S to fit the orbits of these satellites. However, the results for the lower altitude Stella and GFZ–1 indicate short-wavelength improvement, which the effects of attenuation obscure for the higher altitude satellite tests. At first inspection, the weak response of these tests is somewhat surprising given the large changes to the coefficients between the EGM96S and PGS7316 models, illustrated in Figure 6.5.1–1, and the results of the altimeter-derived gravity anomaly tests from the primary calibrations (discussed in Section 6.4.3) and for these models (cf. Section 6.5.3). The minimal change in the SLR satellite RMS of fit between PGS7316 and EGM96S leads to two conclusions: (1) The addition of the powerful EP/EUVE data has not really affected the modeling of the long-wavelength geopotential field as expressed by the lumped harmonics to which the SLR satellites are sensitive, and (2) the SLR residual test sets may not be the best tests to assess fully the contributions made by low-altitude, and low-inclination spacecraft such as EP/EUVE.

TDRSS tracking of several low-altitude and low-inclination satellites provides a powerful tool for both gravity model development and evaluation. TDRSS tracking of EP/EUVE in 1994 was included in the development of EGM96S, while more TDRSS data from ERBS, RXTE, CGRO, and EP/EUVE were available for testing. These new data sets provide an excellent independent test set (described in more detail in Section 5.1.4) to evaluate the performance of the final model. Tables 6.5.1–4 through 6.5.1–6 summarize the results of the TDRSS-based orbit tests for EGM96S and JGM–2S. As the TDRSS-based orbit tests included estimation of 1-CPR along- and cross-track accelerations, the performance assessment between models will be restricted primarily to the nonzonal and nonresonant contributions of the gravity model coefficients.

The best TDRSS orbit test results, in terms of both residuals and overlaps, for EP/EUVE and CGRO are obtained with the EGM96S model. This, of course, is the result of the addition of the 1994 EP/EUVE tracking data used for the results shown in Table 6.5.1–5. However, the improvement in the EP/EUVE overlaps for the 1994 test should be considered optimistic for two reasons. First, the simultaneous solution strategy that was used for the 1994 EP/EUVE test counts on minimal modeling errors for the user satellite to determine accurate TDRS orbits. In the case of JGM–2S, the gravity errors on EP/EUVE find their way into the TDRS orbits, resulting in large frame uncertainties and overlap differences. Second, that particular test is a dependent test, which should be expected to perform much better. However, some of the benefit derived from the EP/EUVE data is also evident in the RXTE results (Table 6.5.1–6). For that spacecraft, at a lower inclination of 23°, the performance of EGM96S is a tremendous improvement over that of JGM–2S.
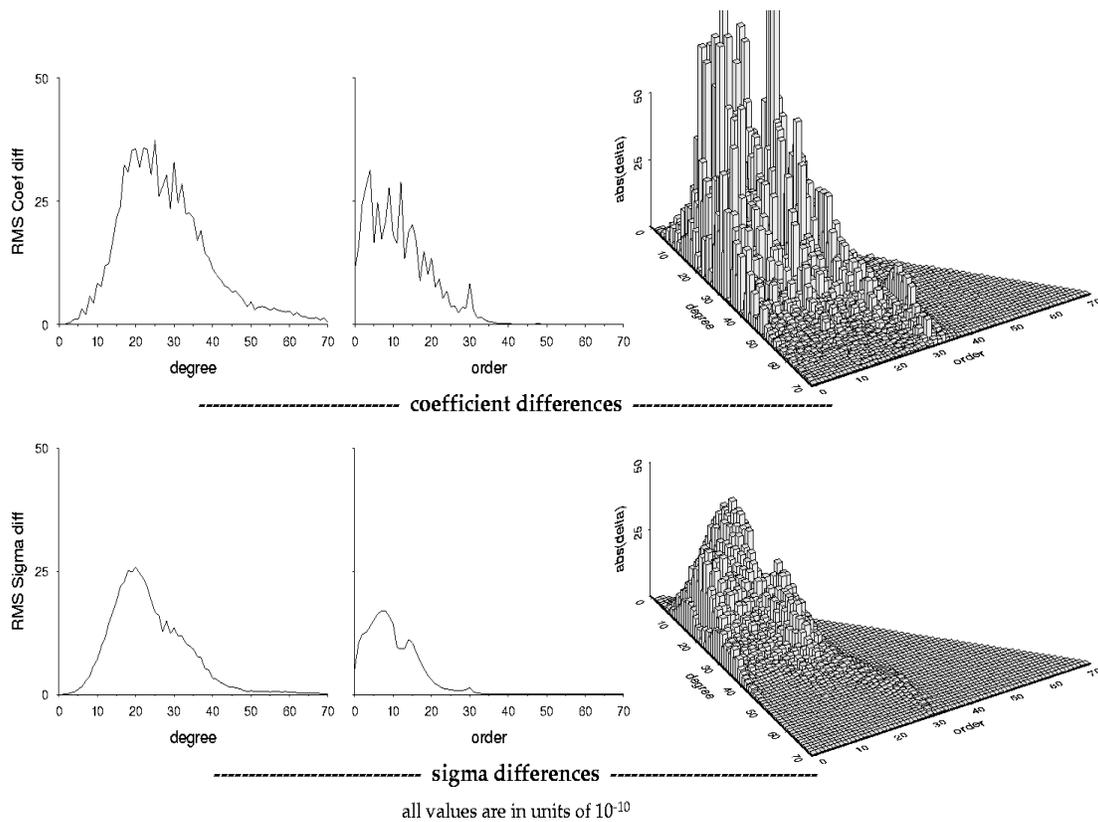
Figure **6.5.1–1.** The effect of EP/EUVE on the EGM96S gravity coefficients and uncertainties.

Table **6.5.1–4.** Average TDRSS-user orbit residuals and overlaps for 1992.

Spacecraft	Geopotential	Tides	1-way Range-Rate RMS (mm/s)	2-way Range-Rate RMS (mm/s)	2-way Range RMS (m)	Overlap Position RMS (m)
CGRO	JGM–2S	PGS4846X	–	8.16	9.22	40.00
	EGM96S	EGM96S	–	3.12	3.05	11.17
ERBS	JGM–2S	PGS4846X	–	1.20	2.19	2.31
	EGM96S	EGM96S	–	1.18	2.09	2.35
EUVE	JGM–2S	PGS4846X	13.90	10.16	10.74	14.76
	EGM96S	EGM96S	2.60	2.16	2.86	3.38

6.5.1–5. Average TDRSS-user orbit residuals and overlaps for 1994.

Spacecraft	Geopotential	Tides	1-way Range-Rate RMS (mm/s)	2-way Range-Rate RMS (mm/s)	2-way Range RMS (m)	Overlap Position RMS (m)
ERBS	JGM–2S	PGS4846X	–	1.23	2.71	3.16
	EGM96S	EGM96S	–	1.05	2.20	2.03
EUVE	JGM–2S	PGS4846X	–	9.56	10.09	26.62
	EGM96S	EGM96S	–	1.30	1.34	2.59

6.5.1–6. Average TDRSS-user orbit residuals and overlaps for 1996.

Spacecraft	Geopotential	Tides	1-way Range-Rate RMS (mm/s)	2-way Range-Rate RMS (mm/s)	2-way Range RMS (m)	Overlap Position RMS (m)
RXTE	JGM–2S	PGS4846X	–	4.50	7.35	6.43
	EGM96S	EGM96S	–	1.80	3.28	3.00

The only test that shows worse performance with EGM96S than with JGM–2S is the ERBS 1992 test set. In this case, there is an insignificant difference in the average RMS overlap, and the residuals are only numerically superior to JGM–2S. However, little improvement between these models should be observed in the ERBS tests as the inclination, 56°, is similar to a number of the spacecraft that were included in JGM–2S. Likewise, the radial orbit error projections for 525 km (cf. Section 6.5.5) show little improvement for this inclination.

Overall, EGM96S represents a significant improvement, as measured by both the both satellite orbit residual RMS of fit and solution overlap RMS differences, over the antecedent satellite-only model, JGM–2S. The improvements are greatest for low-altitude satellites such as ERS–1, EP/EUVE, RXTE, Stella, CGRO, and GFZ–1. The impact of the TDRSS and GPS tracking of EP/EUVE on EGM96S is particularly striking. Independent orbit tests run using RXTE and CGRO, both in orbit inclinations < 30°, show dramatic improvement in the orbit fits.

6.5.2   TOPEX/POSEIDON (T/P) Reduced-Dynamic Orbit Comparisons

Comparison of SLR/DORIS dynamic orbit solutions, using JGM–2S and EGM96S, to the reduced-dynamic GPS solutions provided by JPL indicates that an improvement in accuracy results from the use of the EGM96S. As stated previously in Section 5.1.6, these tests were performed using only the gravity model coefficients; the effects of tides were not studied. The use of EGM96S results in a 0.54 cm reduction in the average RMS radial position comparison and 1.92 cm in the average RMS total position difference (see Table 6.5.2–1). Assuming that the difference between the models is uncorrelated, and taking the difference in an RSS sense, the reduction in the average RMS radial difference is 1.72 cm.

The results are consistent, with the four test arcs showing uniform improvement associated with EGM96S. Overall, the RMS radial comparisons, and their RSS differences, are at the accuracy limits of the reduced-dynamic solutions [*Bertiger et al.,* 1994], meaning that (a) the significance of the improved comparisons with the reduced-dynamic solutions is ambiguous and (b) the EGM96S solutions are comparable to the reduced-dynamic orbits in accuracy. Despite these limitations, the implication is that there is a significant *accuracy* improvement associated with using the EGM96S gravity solution, as compared to JGM–2S, for T/P orbit determination.

Table 6.5.2–1. Comparison of second-generation T/P solutions produced by GSFC versus JPL-supplied GPS reduced-dynamic solutions.

Cycle	Gravity Model	SLR (cm)		DORIS (mm/s)		RMS Orbit Comparison (cm)			
		# pts	RMS	# pts	RMS	Radial	Cross	Along	Total
10	JGM–2S	2143	4.77	20286	0.580	2.80	6.31	11.21	13.16
	EGM96S		4.61		0.577	2.32	5.60	9.46	11.23
19	JGM–2S	3829	4.55	55142	0.552	3.65	4.99	10.05	11.80
	EGM96S		4.25		0.547	3.05	3.78	8.09	9.44
21	JGM–2S	4112	3.17	54260	0.540	3.17	5.71	7.92	10.26
	EGM96S		2.92		0.537	2.66	5.31	6.28	8.65
46	JGM–2S	4060	3.07	57865	0.564	2.46	5.72	7.17	9.50
	EGM96S		2.74		0.562	1.87	5.04	5.54	7.72
Average	JGM–2S	3536	3.89	46888	0.559	3.02	5.68	9.09	11.18
	EGM96S		3.63		0.556	2.48	4.93	7.34	9.26
	Difference		0.26		0.003	0.54	0.75	1.75	1.92

6.5.3 Altimeter-Derived Gravity Anomaly Tests

The 5°x5° area-mean altimeter-derived gravity anomaly test (described in Section 5.8) provides a measure of the accuracy of the satellite-only model and of its ability to capture the high(er) frequency content present in the altimetric anomalies. Table 6.5.3–1 shows the evolution of the gravity anomaly variance values from the JGM–2S solution to the present EGM96S model. There has been a steady improvement leading to the present. The new data incorporated in EGM96S resulted in a reduction of the variance from 16.35 mGal^2 for JGM–2S to 10.19 mGal^2 for EGM96S, which is a major gain for the satellite-only model. A significant portion of these gains results from the GPS and TDRSS tracking of EP/EUVE; exclusion of the all of the EP/EUVE data (model PGS7316) from the solution increases the variance by 2.57 mGal^2.

Comparison of the 5°x5° area-mean altimeter-derived gravity anomaly test results with the corresponding value predicted by the gravity model covariances over the oceans can be used to assess the overall calibration of the gravity solution covariance. Given that the error in the GEOSAT 5° gravity anomalies is small, then direct comparison of the standard deviation about the mean of the difference of the models with the GEOSAT gravity anomalies and the predicted uncertainty in the 5° gravity anomalies can be made. For these tests, we use the predicted values for the entire globe as opposed to prediction for the domain of the GEOSAT data. Evaluation of the predicted gravity anomaly errors over the entire globe and the oceanic portions of the Earth

show that the values are comparable (see Section 6.5.6.1 below), so this substitution should provide acceptable results. The ratio values, presented in the fifth column of Table 6.5.3–1, indicate that the JGM–2S model is well calibrated as the ratio is approximately unity. By comparison, the ratio for EGM96S, being less than unity, implies that the covariance is somewhat conservative (i.e., the predicted errors are higher than we observe). Elimination of the EP/EUVE data from the model results in an even more conservative result, indicating that the bulk of the data in the model is conservatively weighted, which is in agreement with the targeted calibration factors discussed in Section 6.4.3.

Table 6.5.3–1. Comparison of the variance about the mean of the difference between the 5°x5° GEOSAT altimeter-derived gravity anomalies and select satellite-only gravity models through EGM96S, compared to the predicted RMS 5° gravity anomaly errors for the globe resulting from the gravity solution covariances.

Gravity Model	Maximum Degree	GEOSAT v_{70} (mGal^2)	Predicted v_{70} (mGal^2)	$\delta\Delta g_{GEOSAT}^{70} / \sigma_{\Delta g}^{70}$
JGM–2S	70	16.35	17.06	0.98
PGS5737	70	13.39	10.66	1.12
PGS6394	70	10.38	10.68	0.99
EGM96S	70	10.19	11.68	0.93
PGS7316	70	12.76	15.72	0.90

6.5.4 GPS/Leveling Tests

The GPS/leveling test results for the USA/NGS and British Columbia sets show marked improvement of EGM96S over JGM–2S (see Table 6.5.4–1). While the standard deviation of fit is reduced in both areas, there is a dramatic reduction of 29.16 cm from the JGM–2S value for the NGS network.

Table 6.5.4–1. GPS/leveling test results for USA/NGS and Canada (BC). The HDM180 high-degree model used for all cases.

Model	Area	Mean (cm)	Std Dev (cm)	# Pts
JGM–2S	USA/NGS	−63.64	126.32	1873
	Canada (BC)	−24.52	92.39	298
EGM96S	USA/NGS	−112.75	97.16	1888
	Canada (BC)	−35.37	84.48	298

For the five-area test, summarized in Table 6.5.4–2, EGM96S shows an average improvement compared to JGM–2S. However, in Canada and Australia, the fits degraded. In the case of Australia, this degradation may be related to the large geoid changes caused by EP/EUVE over Indonesia and the Indian Ocean (see Section 6.5.5).

It should be noted that, during the development of EGM96, it was observed that a reduction of the GPS/leveling test standard deviation of fit in the satellite-only model did not necessarily translate into a comparable improvement in the test results for the companion combination model. This is a result of the weak signal from the satellite data occurring past degree and order ~40, and the strength of the surface gravity data. Consequently, the GPS/leveling results for a satellite-only model cannot be used directly to assess the performance of the complete combination model.

Table 6.5.4–2. GPS/leveling test results for the five areas.

Area	JGM–2S		EGM96S	
	Mean (cm)	Std Dev (cm)	Mean (cm)	Std Dev (cm)
Europe	124.33	82.83	64.90	65.24
Canada	−79.41	22.55	−76.16	39.97
Australia	−65.53	60.02	−91.36	98.01
Scandinavia	134.25	85.25	80.46	64.99
Tennessee	172.08	96.38	192.06	70.72
Average		67.64		64.89

6.5.5 Comparisons of EGM96S With JGM–2S

Figure 6.5.5–1 depicts the differences in the spectra of the RMS solution uncertainties (1σ) by degree. The factor of 3 to 4 reduction in the formal errors between EGM96S and JGM–2S for the lower degrees is the result of several changes. First, EGM96S includes 2.2 times more tracking data than JGM–2S. This could be expected to reduce the uncertainties by a factor of 1.5, provided the data weighting remained constant. Most of these additional data were from T/P and GPS/MET. Second, EGM96S includes the GPS and TDRSS data, which provide strong reductions in the uncertainties for the low-order terms and consequently in the RMS values by degree. Had a less conservative approach been adopted while weighting and calibrating the data, unrealistic peak reductions of over a factor of 6 would have resulted, as did occur for the PGS5737 (see Figure 6.3.1–2) and PGS6394 (Figure 6.3.4–1) satellite-only solutions.

The change in the Kaula-based constraint matrix is readily evident for $n > 43$. For coefficients approaching 100 percent uncertainty, the *a priori* power law dictates the magnitude of the resulting error estimate. If the power law is increased, the resulting error estimates for these terms will reflect this increase. This accounts for the larger reported errors in EGM96S over JGM–2S for the terms over $n = 43$.

A summary of the RMS geoid undulation and gravity anomaly differences between EGM96S and JGM–2S for different regions of the globe is given in Table 6.5.5–1 (the summary values are computed as an RMS of the 1° gridded point values in the region of interest, with zero meters elevation used to differentiate between land and water); Figure 6.5.5–2 illustrates the geoid height difference. The patterns in the figure are caused by the addition of EP/EUVE ($i = 28.4°$) data. This is evident by comparison of Figure 6.5.5–2 to Figure 6.5.5–3, which shows the geoid

undulation differences between EGM96S and the subset solution, PGS7316, which contains no EP/EUVE data. The summary of the comparisons between EGM96S and PGS7316 is given in Table 6.5.5–2. The distribution of the maximum changes over South America and Australia suggests a possible association with the TDRSS data. However, the presence of strong changes over East Africa, India, and Indonesia, where there is a dearth of older data, indicates that the GPS tracking of EP/EUVE is making a strong local contribution to the higher degree model in these regions. The gravity anomaly differences between EGM96S and JGM–2S are qualitatively similar to the geoid differences.
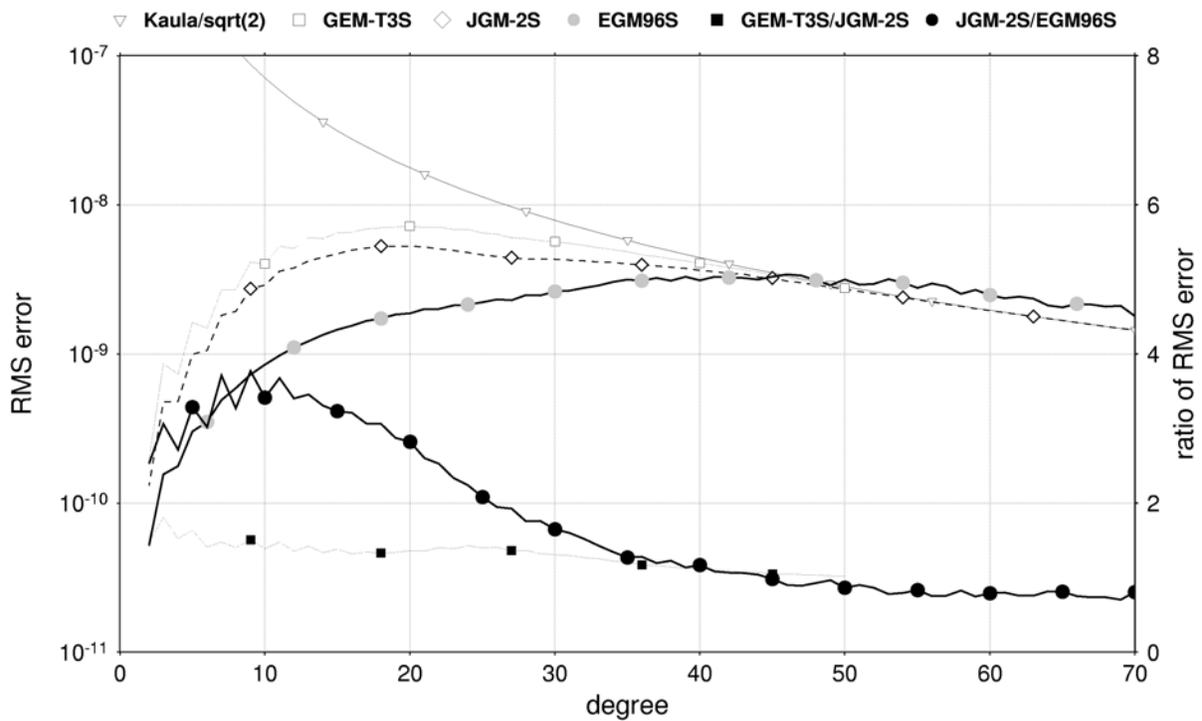
Figure 6.5.5–1. RMS error per degree per coefficient for EGM96S. Comparison of coefficient uncertainties with JGM–2S shows strong formal error reduction at low orders.

Table 6.5.5–1. RMS differences between EGM96S and JGM–2S. N_{max}=70.

	Global	Land		Water		
		All	USA	All	|lat|<67°	66°<|lat|<82°
Gravity Anomaly (mGal)	4.56	5.35	3.95	3.95	4.19	4.40
Geoid Undulation (m)	0.94	1.14	0.78	0.85	0.86	0.71
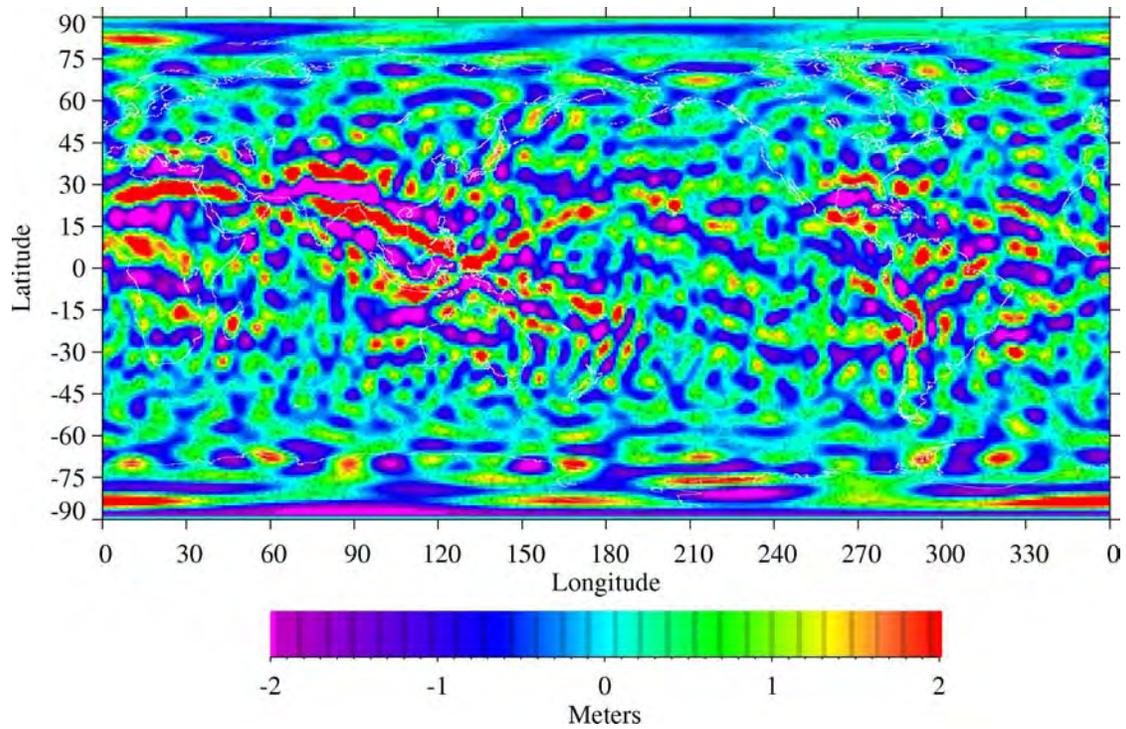
Figure 6.5.5–2. Geoid height difference, EGM96S–JGM–2S, for N_{max}=70. The range of the differences is –6.73 to 5.91 m.
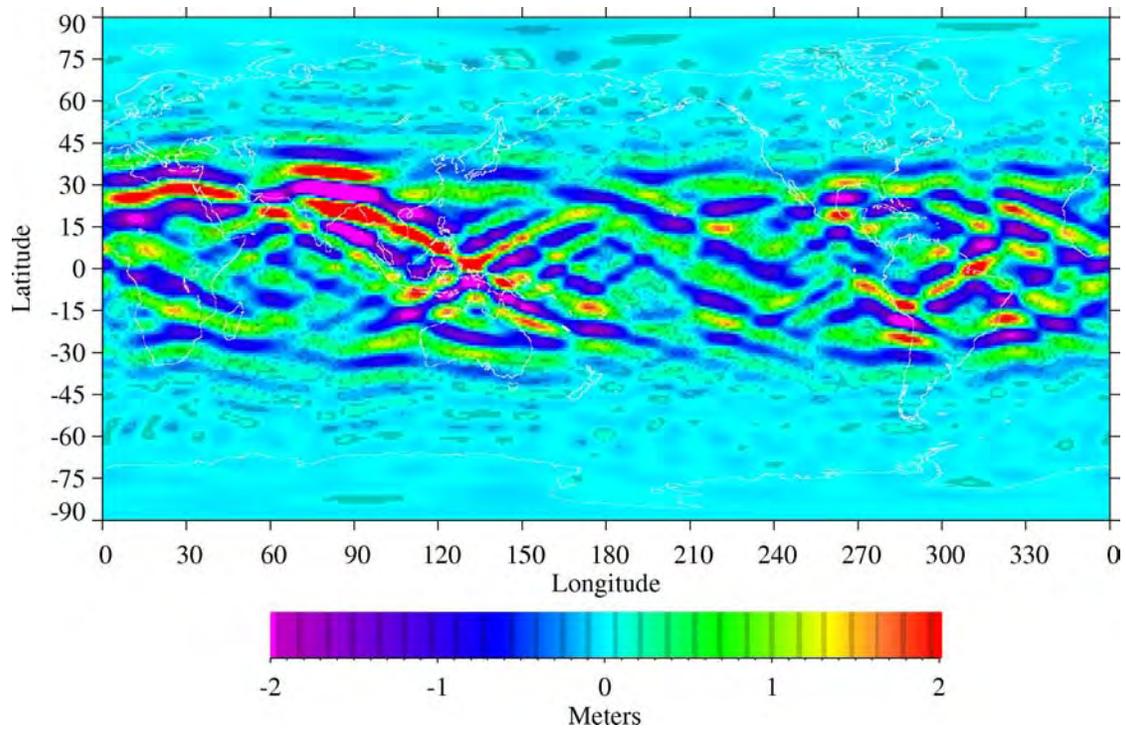
Figure 6.5.5–3. Geoid height changes caused by EP/EUVE. The sense of the difference is EGM96S minus the EGM96S subset solution that excludes all EP/EUVE data (PGS7316). The range of the differences is –5.97 to 5.85 m. N_{max}=70.

Table 6.5.5–2. RMS differences between EGM96S and the EGM96S subset solution that excludes all EP/EUVE data (PGS7316). N_{max}=70.

	Global	Land		Water		
		All	USA	All	$|lat|<67°$	$66°<|lat|<82°$
Gravity Anomaly (mGal)	2.84	3.41	1.99	2.58	2.66	0.20
Geoid Undulation (m)	0.67	0.83	0.42	0.59	0.61	0.03

6.5.6   Covariance Predictions

6.5.6.1 Geoid Undulation and Gravity Anomaly Error Prediction

Comparison of the predicted geoid height errors from JGM–2S (Figure 6.5.6.1–1) and EGM96S (Figure 6.5.6.1–2) shows remarkable improvement in the equatorial regions. Inclusion of 321022 GPS and TDRSS observations of EP/EUVE tracking has greatly reduced the formal predicted errors below 30° absolute latitude. A geographic breakdown of the predicted errors is given in Table 6.5.6.1–1. The impact of the entire compliment of GPS data—including EP/EUVE, T/P, and GPS/MET—is significant over all regions of the Earth. More striking is the effect of the EP/EUVE tracking; as illustrated in Figure 6.5.6.1–3, which depicts the RSS (i.e., uncorrelated) difference between EGM96S and the subset solution that contains no EP/EUVE data (PGS7316). The maximum improvement in the error estimates is 1.1 m. When the GPS data are excluded from EGM96S, and the TDRSS tracking of EP/EUVE is included, the global error increases from 1.19 m to 1.29 m. Elimination of the TDRSS data then increases the global error to 1.37 m. This demonstrates that the EP/EUVE tracking, whether it be GPS or TDRSS, is the predominant cause of improvement in the formal geoid height errors between JGM–2S and EGM96S.

Despite the greater longitudinal overflight sampling provided by the EP/EUVE GPS data, the normal point density of the TDRSS data used in EGM96S are denser by a factor of 1.5 (151426 observations over 220° longitude vs. 169596 observations over 360°). The relatively dense TDRSS tracking of the EP/EUVE satellite (see Figure 6.2.3.2–3) produces the relative minima in the EGM96S error in the equatorial region in the western Pacific and over South America and the Atlantic Ocean, which correspond to the two poorest modeled regions of JGM–2S. Detailed inspection of these regions shows the presence of isolated EP/EUVE ground tracks. The presence of these relative minima under the TDRS relay spacecraft fields of view shows the ability of the high–low satellite configuration to provide strong geopotential contributions via the direct mapping of the radial accelerations.
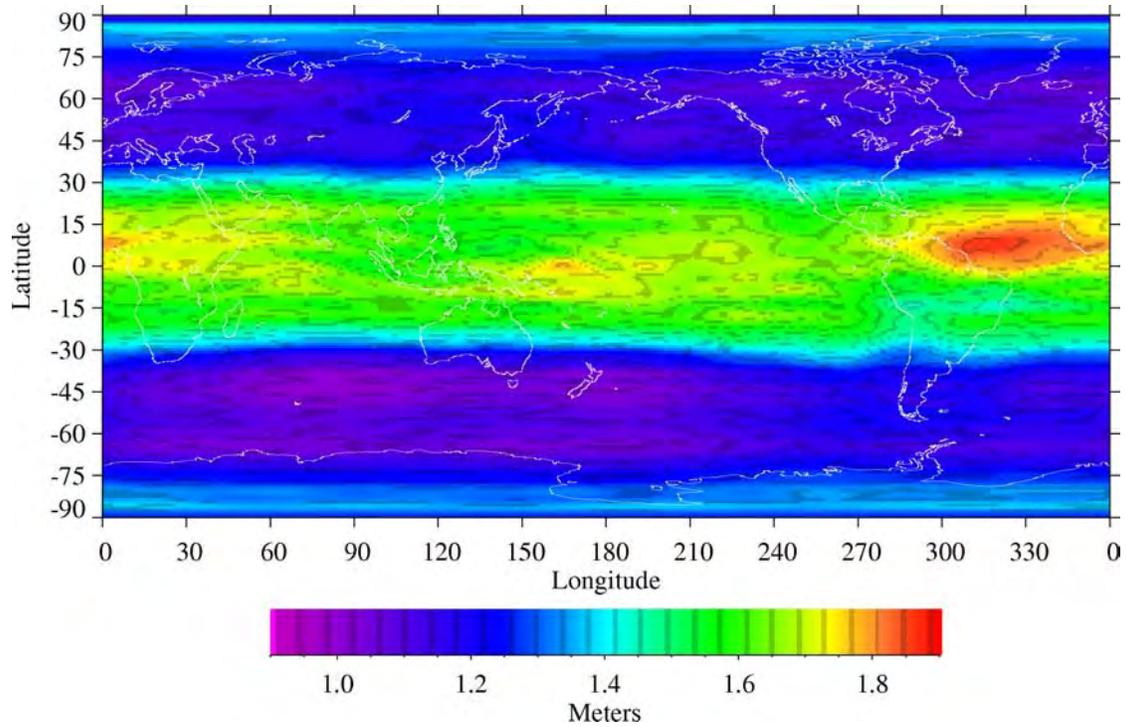
Figure 6.5.6.1–1. JGM–2S predicted geoid height error for N_{max}=70. The range of the errors is from 0.99 to 1.87 m.
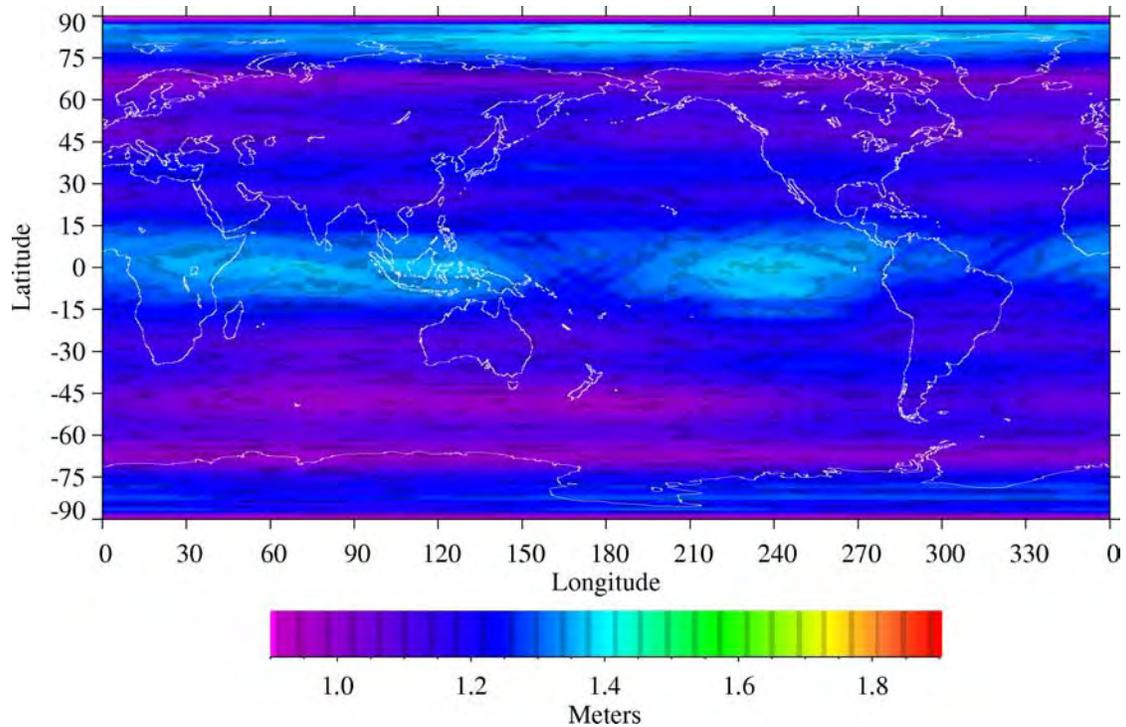
Figure 6.5.6.1–2. EGM96S predicted geoid height error for N_{max}=70. Color scale is the same as used for JGM–2S. The range of the errors is from 0.91 to 1.41 m.

Table 6.5.6.1–1. Predicted RMS geoid undulation error for N_{max}=70.

Geopotential	RMS Geoid Undulation Error (m)					
	Global	Land		Water		
		All	USA	All	|lat|<67	66<|lat|<82
JGM–2S	1.41	1.39	1.23	1.42	1.43	1.21
EGM96S	1.19	1.19	1.18	1.19	1.19	1.16
EGM96S–TDRSS	1.22	1.21	1.18	1.22	1.23	1.16
EGM96S–GPS	1.29	1.29	1.26	1.29	1.30	1.27
EGM96S–EP/EUVE	1.37	1.35	1.24	1.39	1.40	1.16
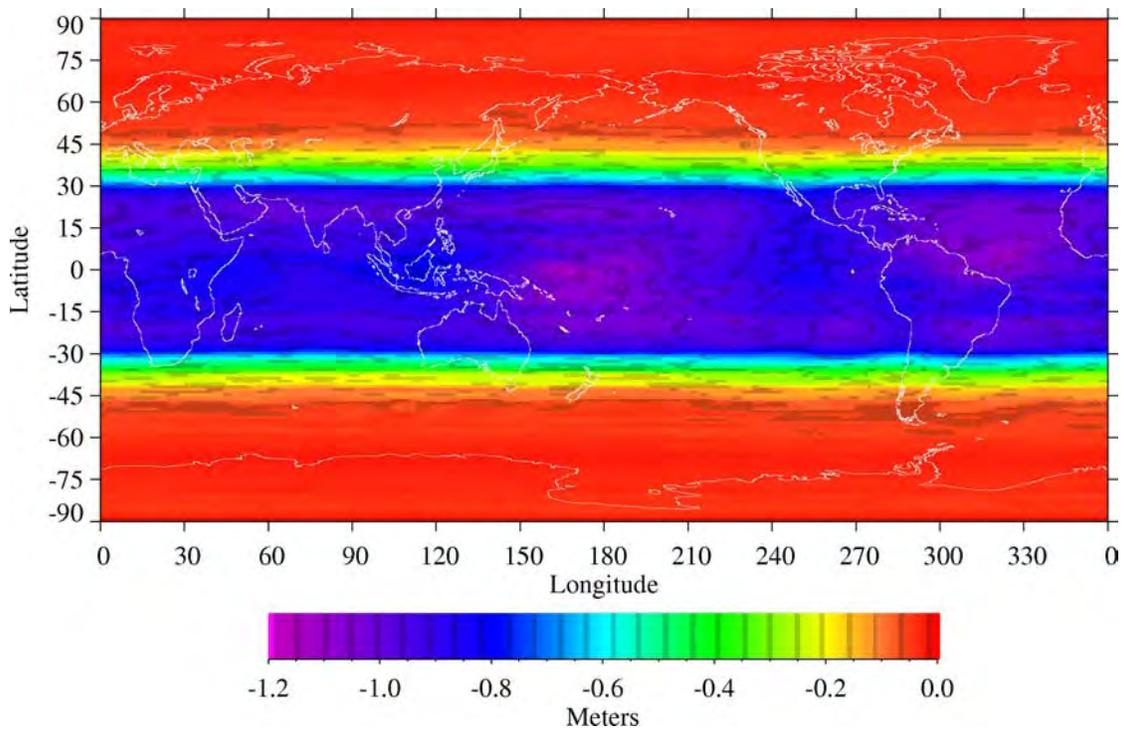
Figure 6.5.6.1–3. Uncorrelated difference in the geoid error prediction between EGM96S and the subset model that excludes all EP/EUVE data for N_{max}=70. The peak differences are -1.12 m (negative indicating that EGM96S has less error), with the largest difference in the projected error occurring underneath the ground track of EP/EUVE. At the higher latitudes (> 40°) change in the geoid height error is less than 0.05 m.

EGM96S does show some minor degradation compared to JGM–2S in the north polar region, particularly over the Beaufort Sea, while an improvement is seen over the South Pole. This asymmetrical north–south change in the poles was first noticed when the weighting of Spot–2 was altered. Between the changes in Spot–2 and the addition of the EP/EUVE data, the maximum predicted formal geoid height error of 1.4 m occurs over the North Pole in EGM96S. Comparison of the RMS values of the predicted geoid height error for the USA from Table 6.5.6.1–1 with the GPS/leveling results from Section 6.5.4 shows that the predicted error for EGM96S is greater than the standard deviation from the NGS leveling results, implying that the covariance is somewhat conservative. This can be contrasted with the projection for JGM–2S, where the GPS/leveling using the NGS network resulted in a standard deviation of 1.26 m (with a mean that deviates significantly from either EGM96S or JGM–3), which is higher than the formal predicted error of 1.22 m.

The change in the *a priori* constraint matrix used in EGM96S resulted in a significant increase in the global predicted anomaly error as compared to JGM–2S. Since the most substantial changes in the constraint matrix occurred in the high-degree field, direct comparison of the formal gravity anomaly errors predicted by the two models does not yield much insight in the relative performance of the models since the magnitude of the errors for degrees above 40 or so are dictated by the *a priori* power law constraint. The effect on different regions of the Earth is clearly seen in Table 6.5.6.1–2. Overall, the anomaly error estimates have increased from 8.3 to 8.8 mGal over the globe between JGM–2S and EGM96S. Elimination of the EP/EUVE tracking further increases the global error to 9.3 mGal. Comparison of Figures 6.5.6.1–3 and 6.5.6.1–4 shows that JGM–2S and EGM96S are comparable in the equatorial regions, demonstrating the power of the GPS and TDRSS tracking of EP/EUVE included in EGM96S. Likewise, the degradation over the poles indicates the relative paucity of satellite tracking over the poles.

As with the geoid height error, the changes in the modeling and weights used for Spot–2 have also had some effect on the predicted anomaly errors for the North Pole. Comparison of the polar regions between Figures 6.5.6.1–4 and 6.5.6.1–5 indicates that the errors for the North Polar regions in EGM96S are proportionately higher than the South Polar regions. In EGM96S, the maximum error of 10.11 mGal occurs at 203° E, 83° N over the Beaufort Sea, and the minimum of 7.98 mGal occurs at 179° E, 51° S off of New Zealand.

Table 6.5.6.1–2. Predicted RMS gravity anomaly error for N_{max}=70.

Geopotential	RMS Gravity Anomaly Error (mGal)					
	Global	Land		Water		
		All	USA	All	|lat|<67	66<|lat|<82
JGM–2S	8.30	8.29	8.07	8.31	8.31	8.18
EGM96S	8.83	8.85	8.92	8.82	8.80	9.00
EGM96S–TDRSS	8.91	8.91	8.93	8.91	8.89	9.00
EGM96S–GPS	9.27	9.30	9.32	9.26	9.24	9.00
EGM96S–EP/EUVE	9.28	9.24	9.07	9.29	9.30	9.00
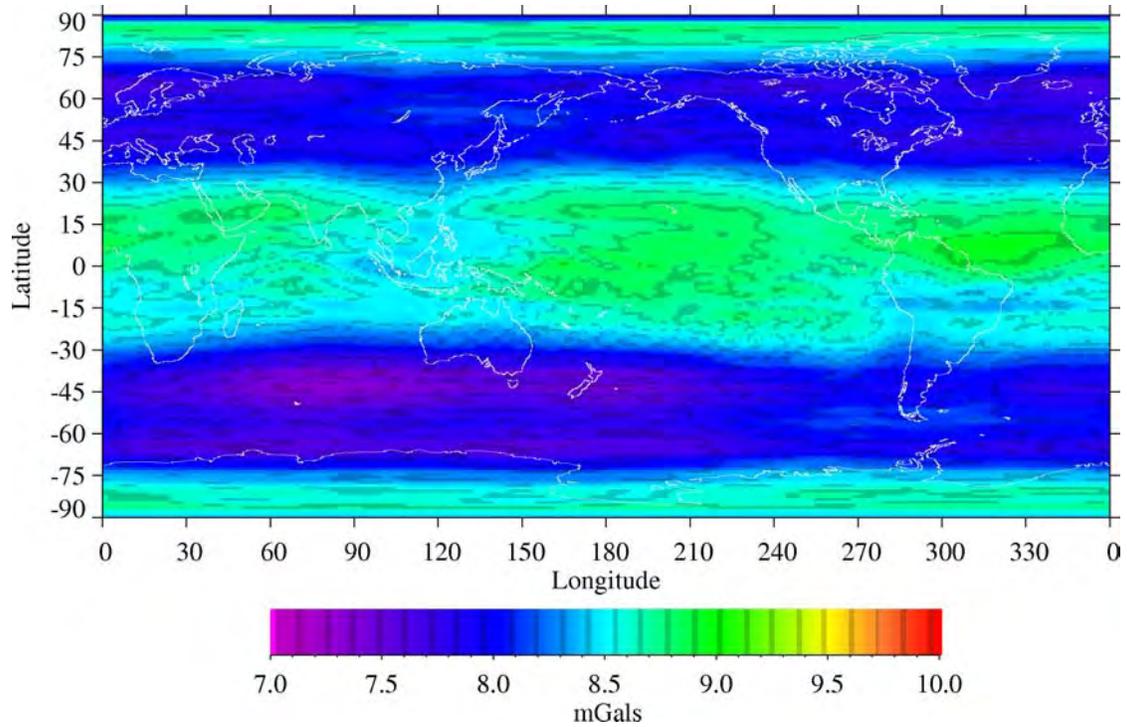
Figure 6.5.6.1–4. JGM–2S predicted gravity anomaly error for N_{max}=70. The minimum error is 7.32 mGal, and the maximum is 8.99 mGal.
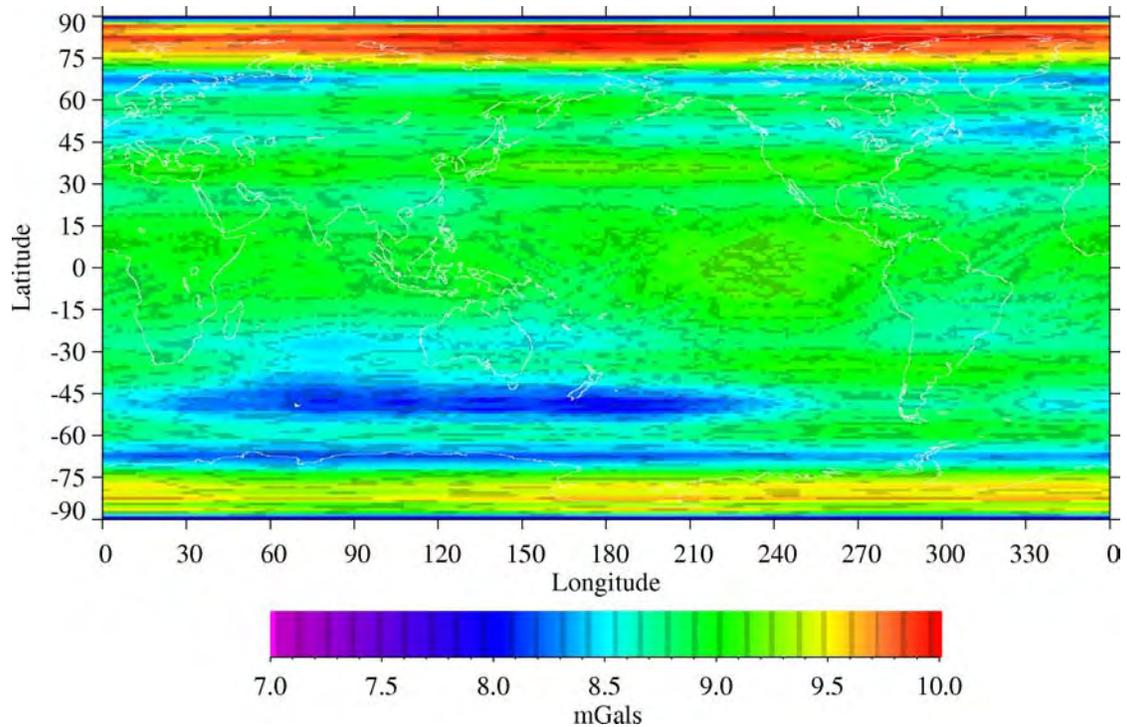
Figure 6.5.6.1–5. EGM96S predicted gravity anomaly error for N_{max}=70. The minimum error is 7.83 mGal, and the maximum is 10.11 mGal. The errors are larger with EGM96S than with JGM–2S, because of the application of a more realistic *a priori* power law constraint than the Kaula-based constraint used in JGM–2S.

6.5.6.2 Projected Radial Orbit Errors vs. Inclination

The radial orbit error was estimated for circular orbits at the altitudes of 525, 830, and 1336 km, using linear orbit perturbation theory and the gravity field error covariances using the method reported in *Rosborough* [1986]. Both JGM–2S and EGM96S were evaluated over a range of inclinations. Figures 6.5.6.2–1 through 6.5.6.2–4 depict the resulting RMS of the 1σ radial error estimate. Orbit perturbations longer than 10 days were excluded, and the analysis does not include the long-period perturbations due to the odd zonal coefficients.

The structure of the radial error versus inclination shows the weakness of JGM–2S at the under-sampled low inclinations ($i < 35°$). The poor behavior at these low inclinations is a consequence of the dearth of tracking data from satellites at low inclination used in the development of JGM–2S. In EGM96S, significant new data from the EP/EUVE satellite ($i = 28.4°$, altitude = 525 km) were included. EGM96S also shows an improvement, illustrated in Figure 6.2.6.2–3, at some polar inclinations ($82° < i < 93°$), which is likely the result of the addition of tracking data from the Doppler-tracked HILAT and RADCAL spacecraft. At the Sun-synchronous inclinations (~98°) of the Spot–2, Stella, and ERS–1 spacecraft, the change in the predicted error between JGM–2S and EGM96S is minimal because of the inclusion of the Spot–2, and early optical and Doppler satellite, tracking in both EGM96S and JGM–2S.

Figure 6.2.6.2–1 shows the predicted radial orbit error by inclination at an altitude of 525 km. At an inclination of 28.4°, the radial orbit error is predicted to be 9.12 m with JGM–2S, and 0.83 m with EGM96S, a reduction of 8.29 m, assuming the changes are correlated, and 9.08 m (the RSS sense difference) assuming that the changes are correlated. When this estimate is compared to the TDRSS orbit residual test results (Tables 6.5.1–4 and –5) for EP/EUVE using JGM–2S and EGM96S, good agreement is seen. The residuals of the strongly radial TDRSS range tracking of EP/EUVE improved by approximately 8 m with a corresponding improvement in the range-rate residuals. Direct comparison of the EP/EUVE solutions generated using JGM–2S with the solutions generated using EGM96S yields an average RMS difference in the radial component of 9.03 m, which, compared with the predicted reduction in the radial orbit error (8.29–9.08 m), suggests that the covariance improvement is reasonable and well calibrated..

At the T/P inclination of 66° and altitude of 1336 km (see Figure 6.2.6.2–4), the predicted radial orbit error is 2.93 cm with JGM–2S and 1.47 cm with EGM96S—a reduction of 1.46 cm, or 2.48 cm in an RSS sense. The results of the reduced-dynamic comparison tests using JGM–2S and EGM96S (see Section 6.5.2) yielded a 0.54 cm reduction in the average RMS radial position comparison (and 1.72 cm in an RSS sense), indicating that the projection of the EGM96S covariance on the T/P orbit is pessimistic.
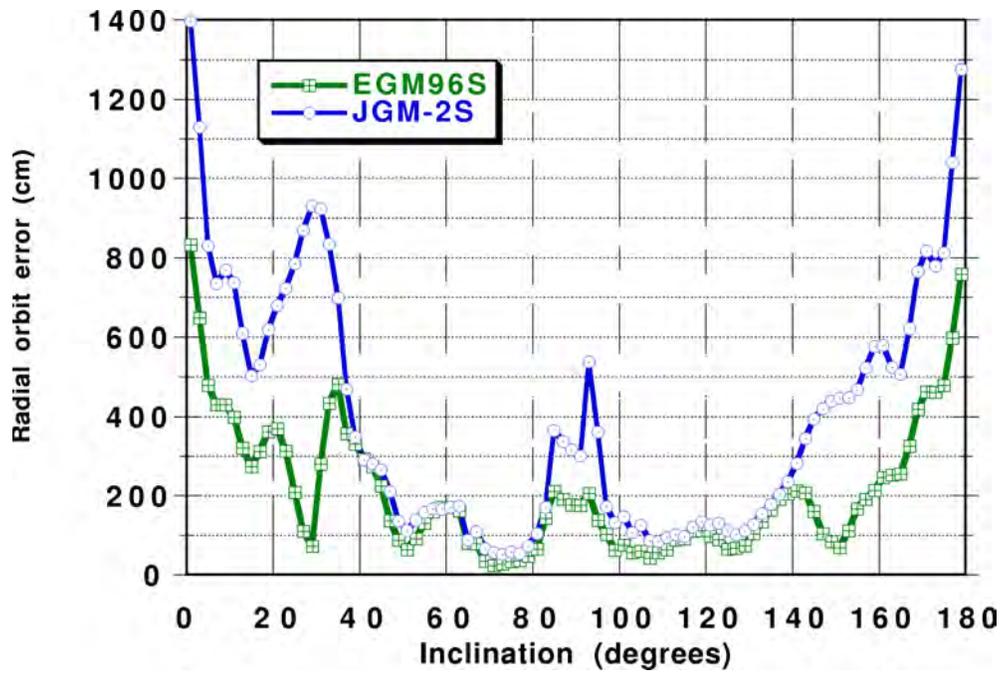
Figure 6.5.6.2–1. Projected radial orbit error for an altitude of 525 km.
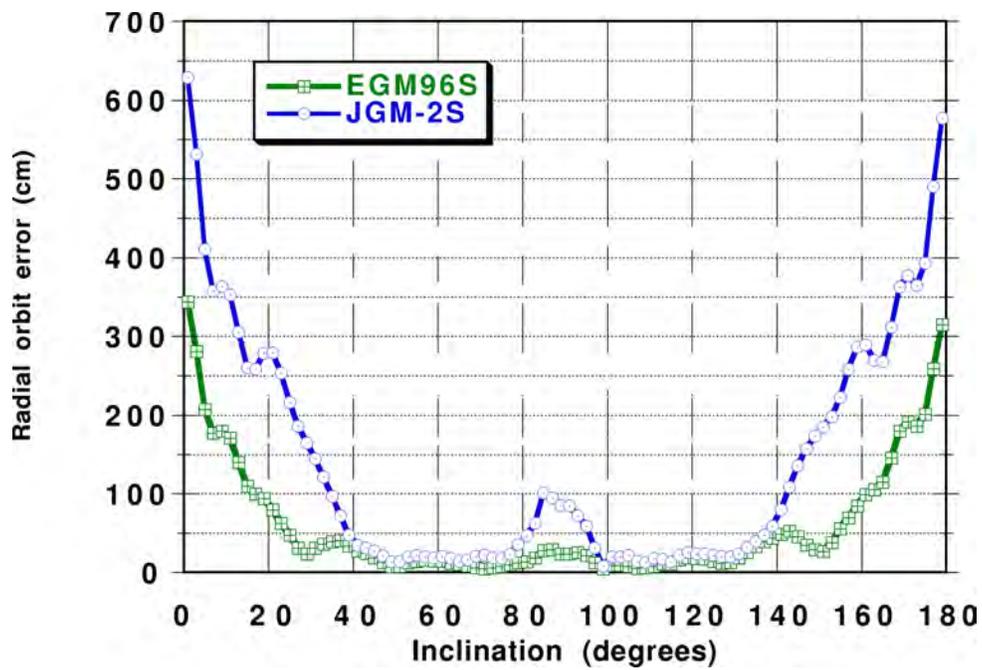
Figure 6.5.6.2–2. Projected radial orbit error for an altitude of 830 km.
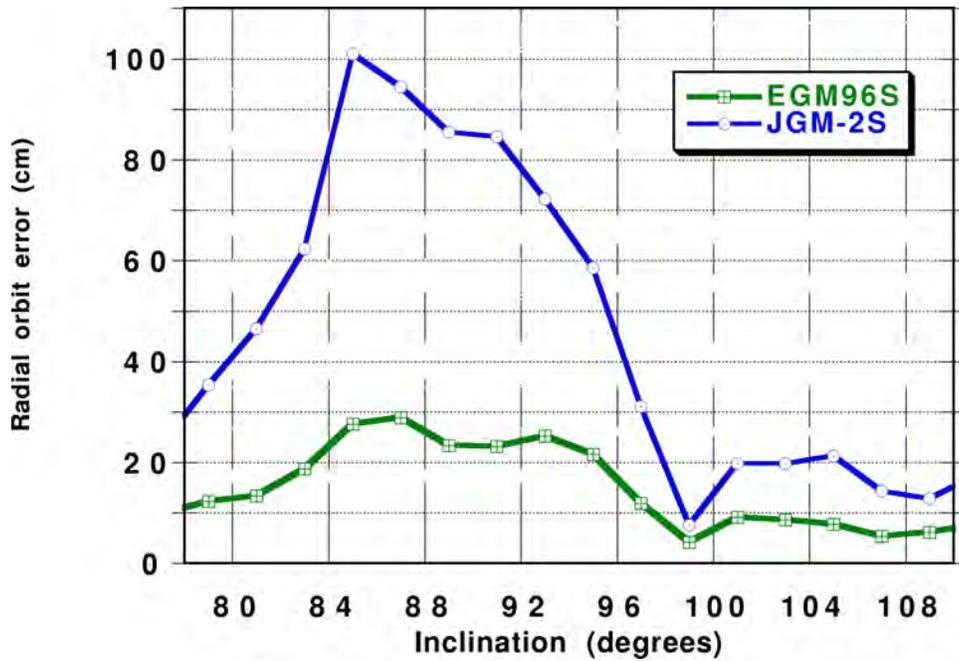
Figure 6.5.6.2–3. Projected radial orbit error at 830 km for polar inclinations.
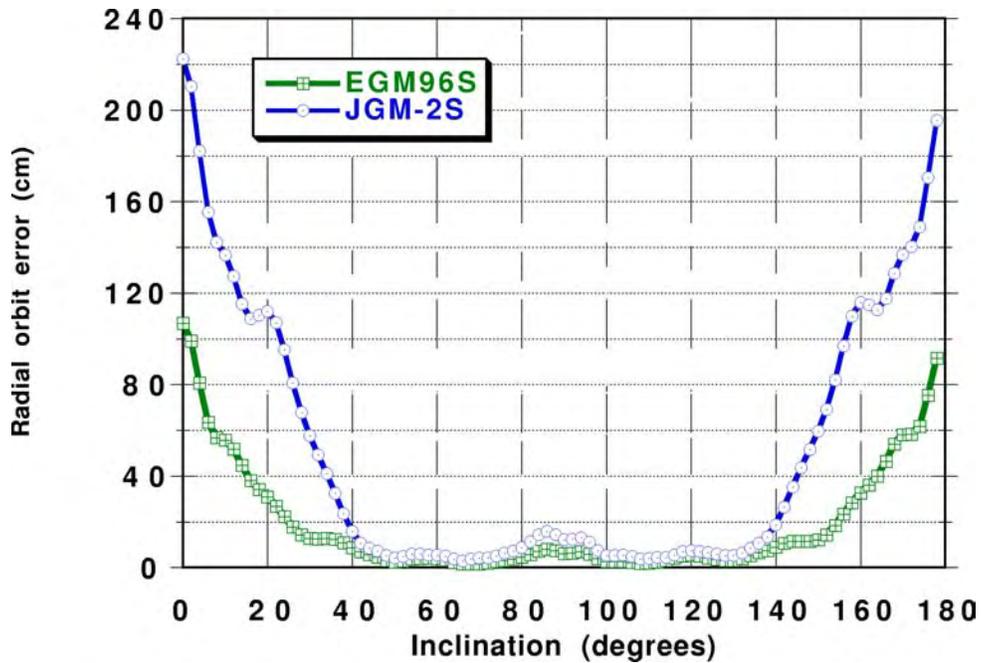
Figure 6.5.6.2–4. Projected radial orbit error for an altitude of 1336 km.

6.6　References

Alouges, A., "Passive Magnetic Stabilization," Ch. 4 in *French Space Technology*, Vol. 1, CNES, Paris, 1971.

Anderle, R.J., Doppler Satellite Measurements and Their Interpretation, in *Space Geodesy and Geodynamics*, Anderson, A.J, and A. Cazenave, eds., Academic Press, London, 1986.

Antresian, P.G., and G.W. Rosborough, "Prediction of Radiative Energy Forces on the TOPEX/POSEIDON Spacecraft," *J. Spacecraft and Rockets*, *29*, 1, 81–90, 1992.

Antresian, P.G., Precision Radiation Force Modeling for the TOPEX/Poseidon Mission, *PhD Thesis*, The University of Colorado, Boulder, 1992.

Barlier, F., C. Berger, J.L. Falin, G. Kockarts, and G. Thuillier, A Thermospheric Model Based on Satellite Drag Data, Institut d'Aeronimic Spatiale de Belgique, *Aeronomica Acta*, 1977.

Bertiger, W.I., Y.E. Bar–Sever, E.J. Christensen, E.S. Davis, J.R. Guinn, B.J. Haines, R.W. Ibanez–Meier, J.R. Jee, S.M. Lichten, W.G. Melbourne, R.J. Muellerschoen, T.N. Munson, Y. Vigue, S.C. Wu, T.P. Yunck, B.E. Schutz, P.A.M. Abusali, H.J. Rim, M.M. Watkins, and P. Willis, "GPS precise tracking of TOPEX/Poseidon: Results and implications, *J. Geophys. Res.*, *99*, C12, 24449–24464, Dec. 15, 1994.

Bertiger, W. I., personal communication, February 1996.

Bilitza, D., Improving IRI for Better Ionospheric Predictions, 1996 Ionospheric Effects Symposium, May 1–9, 1996.

Bilitza, D., International Reference Ionosphere—Status 1995/96, to be published in *Space Research*, 1997.

Blewitt, G., An automatic editing algorithm for GPS data, *Geophysical Research Letters*, *17*, 199–202, 1990.

Bock, Y., List of coordinates based on 16 months of PGGA analysis, Scripps Institute of Oceanography, IGS Electronic Mail Message 168, January 11, 1993.

Boucher, C., and Z. Altamimi, ITRF89 and other realizations of the IERS Terrestrial Reference System for 1989, IERS Tech. Note 6, Observatoire de Paris, April 1991.

Boucher, C., and Z. Altamimi, ITRF90 and other realizations of the IERS Terrestrial Reference System for 1990, IERS Tech. Note 9, Observatoire de Paris, December 1991.

Boucher, C., Z. Altamimi, L. Duhem, ITRF92 and its associated velocity field, IERS Technical Note 15, Observatoire de Paris, October 1993.

Boucher, C., Z. Altamimi, and L. Duhem, Results and Analysis of the ITRF93, IERS Technical Note 18, Observatoire de Paris, October 1994.

Boucher, C., Z. Altamimi, M. Geissel, P. Sillard, Results and Analysis of the ITRF94, IERS Technical Note 20, Observatoire de Paris, March 1996.

Brosche, P., J. Wünsch, J. Campbell, and H. Schuh, Ocean tides effects in universal time detected by VLBI, *Astron. Astrophys*., *245*, 676–682, 1991.

Caprara, G., *The Complete Encyclopedia of Space Satellites*, Portland House, N.Y., distributed by Crown Pub. Inc., ISBN 0–517–61776–5, June 1987.

Cartwright, D.E., and R.D. Ray, Oceanic Tides From Geosat Altimetry, *J. Geophys. Res*., *95*, C3, 3069–3090, 1990.

Cassotto S., Ocean tide models for TOPEX precise orbit determination, PhD dissertation, Center for Space Research, The University of Texas at Austin, 1989.

Christodoulidis, D.C., D.E. Smith, R.G. Williamson, and S.M. Klosko, "Observed Tidal Braking in the Earth/Moon/Sun System," *J. Geophys. Res*., *93*, B6, 6216–6236, 1988.

Cohen, S.C. and D.E. Smith, "LAGEOS Scientific Results: Introduction," *J. Geophys. Res*., *90*, 9217–9220, September 1985.

Colombo, O., "Altimetry, Orbits and Tides," NASA TM 86180, GSFC, November 1984

Cox, C., and D. Oza, Tracking and Data Relay Satellite (TDRS) Orbit Determination: Operations Concepts for Using Global Positioning System (GPS) Tracking and Alternative Approaches, Goddard Space Flight Center Mission Operations and Data Systems Directorate, 553–FDD–94/036/R0UD0, 1994.

DeMets, C., R.G. Gordon, D.F. Argus, and S. Stein, Current Plate Motions, *Geophys J. Intl*., *101*, 425–478, 1990.

Dombrowski, M., W. Denoon, G. Daelemans, G. Schauer, C. Woodall, and R. Kutz, Explorer Platform to Global Positioning System Receiver (GPSR), Interface Control Document (ICD), 408–EP–240–002, NASA GSFC, June 1991.

Dorrer, M., Le system DORIS, CNES Report, Cours Int. de Technol. Spatiale, Toulouse, France, 1990.

Eanes, R.J., and M.M. Watkins, The CSR93L01 Solution, in *IERS Annual Report for 1992*, Obs. de Paris, 1993.

Englar, T.S., R.H. Estes, D.C. Chin, G.A. Maslyar, "ERODYN Program Mathematical Description," BTS Contractor Report BTS–TR–78–69, September 1978.

Fliegel, H.F., T.E. Gallini, and E.R. Swift, Global Positioning System radiation force model for geodetic applications, *J. Geophys. Res., 97*, B1, 559–568, 1992.

Gaignebet, J. ed., Resolutions of Fifth International Workshop on Laser Ranging Instrumentation, Herstmonceux, England, September 1984.

Gitton, P., and J. Kneib, Influence of the surface forces on the orbit of the SPOT satellite, Internal report, Colorado Center for Astrodynamics Research, University of Colorado, Boulder, July 1990.

Goad, C.C., Wallops Island Tropospheric Refraction Study and Analysis, Wolf Report Number 004–74, July 12, 1974.

Gold, K.L., GPS Orbit Determination for the Extreme Ultraviolet Explorer, PhD Dissertation, Dept. of Aerospace Engineering Sciences, the University of Colorado, 1994.

Gross, R.S., A combination of Earth orientation data: Space93, IERS Annual Report, Observatoire de Paris, 1993.

Guier, W.H., "Satellite Geodesy," *APL Technical Digest, 4*, No. 3, pp. 2–12, 1965.

Gurtner, W., and G. Mader, Receiver independent exchange format version 2, *GPS bulletin, 2(3),* 1–11, 1990.

Hartmann, G.K. and R. Leitinger, "Range Errors Due to Ionospheric and Tropospheric Effects for Signal Frequencies Above 100 MHz," *Bull. Geod.*, *58*, pp. 109–136, 1984.

Hedin, A.E., MSIS–86 Thermospheric Model, *J. Geophys. Res.*, *92*, A5, 4649–4662, 1987.

Hofmann–Wellenhof, B., H. Lichtenegger, and J. Collins, *GPS Theory and Practice*, Springer–Verlag, Wien, New York, 1992.

Hopfield, H.S., Tropospheric effect on electromagnetically measured range: Prediction form surface weather data, *Radio Science*, *6*, 3, 357–367, 1971.

Husson, J.C., and A. Banchereau, "Les Satellites Geodesiques Français Diademe I et II: Contribution de l'Experience a la Navigation par Satellites," in Advanced Navigational Techniques, AGARD Conference Proceedings, No. 28, The Advisory Group for Aerospace Research and Development of NATO, 1967.

Jacchia, L.G., Revised Static Models of the Thermosphere and Exosphere With Empirical Temperature Profiles, Smithsonian Astrophysical Observatory Special Report No. 332, Cambridge, Massachusetts, May 1971.

Kaula, W. M., The investigation of the gravitational fields of the moon and planets with artificial satellites, *Advanced Space Technology*, *5*, 213–230, 1963.

Kaula, W. M., *Theory of satellite geodesy*, Blaisdell Publishing Co., Waltham, MA, 1966.

Kelly, M.C., *The Earth's Ionosphere*, Academic Press, New York, 1989.

Knocke, P.C., J.C. Ries, B.D. Tapley, Earth Radiation Pressure Effects on Satellites, *Proceedings of the AIAA/AAS Astrodynamics Conference*, 577–586, 1988.

Leick, A., *GPS Satellite Surveying*, John Wiley and Sons, New York, 1990.

Lemoine, F.G., D.E. Smith, M.T. Zuber, G.A. Neumann, and D.D. Rowlands, A 70th degree lunar gravity model (GLGM–2) from Clementine and other tracking data, *J. Geophys. Res., 102(E7),* 16339–16359, 1997.

Lerch, F.J., S.M. Klosko, R.E. Laubscher, and C.A. Wagner, Gravity Model Improvement Using Geos 3 (GEM 9 and 10), *J. Geophys. Res.*, *84*, B8, 3897–3915, 1979.

Lerch, F.J., B.H. Putney, C.A. Wagner, and S.M. Klosko, Goddard Earth Models for Oceanographic Applications (GEM 10B and 10C), *Marine Geodesy*, *5*, 2, 1981.

Lerch, F.J., S.M. Klosko, and G.B. Patel, Gravity Model Development From Lageos, *Geophys. Res. Letters*, *9*, (11), pp. 1263–1266, 1982.

Lerch, F.J., S.M. Klosko, C.A. Wagner, and G.B. Patel, On the Accuracy of Recent Goddard Gravity Models, *J. Geophys. Res.*, *90*, B11, 9312–9334, 1985.

Lerch, F.J., Optimum Data Weighting and Error Calibration for Estimation of Gravitational Parameters, NASA TM 100737, 1989.

Lerch, F.J., J.G. Marsh, S.M. Klosko, G.B. Patel, D.S. Chinn, E.C. Pavlis, and C.A. Wagner, An Improved Error Assessment for the GEM–T1 Gravitational Model, *J. Geophys. Res.*, *96*, 20023–20040, 1991.

Lerch, F.J., R.S. Nerem, B.H. Putney, S.M. Klosko, G.B. Patel, R.G. Williamson, H.B. Iz, J.C. Chan, E.C. Pavlis, Improvements in the Accuracy of Goddard Earth Models (GEM), Contributions of Space Geodesy to Geodynamics: Earth Dynamics/Geodynamics 24, AGU Monograph, D.E. Smith and D.L. Turcotte, eds., 1993.

Lerch, F.J., R.S. Nerem, B.H. Putney, T.L. Felsentreger, B.V. Sanchez, J.A. Marshall, S.M. Klosko, G.B. Patel, R.G. Williamson, D.S. Chinn, J.C. Chan, K.E. Rachlin, N.L. Chandler, J.J. McCarthy, S.B. Luthcke, N.K. Pavlis, D.E. Pavlis, J.W. Robbins, S. Kapoor, and E.C. Pavlis, Geopotential models from satellite tracking, altimeter, and surface gravity data: GEM–T3 and GEM–T3S, *J. Geophys. Res.*, *99*, 2815–2839, 1994.

Lichten, S., et al., Gipsy Oasis II: A high precision GPS data processing system and general satellite analysis tool, Technology 2005, NASA Technology Transfer Conference, Chicago, Illinois, Oct. 24–26, 1995.

Luthcke, S.B., J.A. Marshall, S.C. Rowton, K.E. Rachlin, C.M. Cox, and R.G. Williamson, Enhanced radiative force modeling of the tracking and data relay satellites, submitted to *J. Astro. Sci.*, March 1997a.

Luthcke, S.B., J.A. Marshall, C.M. Cox, F.G. Lemoine, D.D. Rowlands, R.G. Williamson, W.F. Eddy, T.R. Olson, D.E. Pavlis, and S.C. Rowton, Precision Orbit Determination Using TDRSS, submitted to *J. Astro. Sci.*, March 1997b.

MacDoran, P.F., A First Principles Derivation of Differenced Range Versus Integrated Doppler (DRVID) Charged Particle Calibration Method, JPL Space Programs Summary, 37–62, Vol. II, 1970.

Marsh, J.G., F.J. Lerch, B.H. Putney, D.C. Christodoulidis, D.E. Smith, T.L. Felsentreger, B.V. Sanchez, S.M. Klosko, E.C. Pavlis, T.V. Martin, J.R. Robbins, R.G. Williamson, O.L. Colombo, D.D. Rowlands, W.F. Eddy, N.L. Chandler, K.E. Rachlin, G.B. Patel, S. Bhati, and D.S. Chinn, A new gravitational model for the Earth from satellite tracking data: GEM–T1, *J. Geophys. Res.*, *93*, 6169–6215, 1988.

Marsh, J.G., F.J. Lerch, B.H. Putney, T.L. Felsentreger, B.V. Sanchez, S.M. Klosko, G.B. Patel, J.R. Robbins, R.G. Williamson, T.E. Engelis, W.F. Eddy, N.L. Chandler, D.S. Chinn, S. Kapoor, K.E. Rachlin, L.E. Braatz, and E.C. Pavlis, The GEM–T2 Gravitational Model, *J. Geophys. Res.*, *95*, B13, 22043–22070, 1990.

Marshall, J.A., and S.B. Luthcke, Modeling Radiation Forces Acting on TOPEX/POSEIDON for Precision Orbit Determination, *J. Spacecraft and Rockets*, *31*, 1, pp. 89–105, 1994a.

Marshall, J.A., and S.B. Luthcke, Radiative Force Model Performance for TOPEX/POSEIDON Orbit Determination, *J. Astro. Sci*., *42*, 2, 229–246, April–June, 1994b.

Marshall, J.A., F.G. Lemoine, S.B. Luthcke, J.C. Chan, C.M. Cox, S.C. Rowton, R.G. Williamson, J.L. Wiser, Precision Orbit Determination and Gravity Field Improvement Derived From TDRSS, 46th International Astronautical Congress, IAF–95–A.1.05, Oslo, Norway, October 2–6, 1995a.

Marshall, J.A., N.P. Zelensky, S.M. Klosko, D.S. Chinn, S.B. Luthcke, K.E. Rachlin, R.G. Williamson, The temporal and spatial characteristics of TOPEX/POSEIDON radial orbit error, *J. Geophys. Res.*, *100*, C12, 25331–25352, 1995b.

Marshall, J.A., F.J. Lerch, S.B. Luthcke, R.G. Williamson, and J.C. Chan, An assessment of TDRSS for Precision Orbit Determination, *J. Astro. Sci.*, *44*, 1, 115–127, January–March, 1996.

McCarthy, D.D. (ed.), IERS Standards 1989, IERS Technical Note 3, Observatoire de Paris, Paris, France, November 1989.

Melbourne, W., et al., Project MERIT Standards, Circ. 167, U.S. Naval Observatory, Washington, D.C., 1983.

Melbourne, W.G., E.S. Davis, T.P. Yunck, and B.D. Tapley, The GPS flight experiment on TOPEX/Poseidon, *Geophys. Res. Lett., 21 (19),* 2171–2174, 1994.

Melvin, P.J., L.M. Ward, and P. Axelrad, The analysis of GPS attitude data from a slowly rotation, symmetrical gravity gradient satellite, *J. Astro. Sci., 44*, 4, 515–540, Oct.–Dec., 1996.

Metris, G., D. Vokrouhlicky, J.C. Ries, and R.J. Eanes, "Nongravitational effects and the LAGEOS eccentricity excitations," *J. Geophys. Res*., *102*, 2711–2729, February 1997.

NASA GSFC, "Explorer Platform User's Guide," Configuration Management Officer, Fairchild Space Co., NASA GSFC, 408-EP-403-001, Revision A, August 1989.

Nerem, R.S., B.G. Bills, and J.B. McNamee, A High Resolution Gravity Model for Venus: GVM–1, *Geophys. Res. Let*., *20(7)*, 599–602, 1993a.

Nerem, R.S., B.H. Putney, J.A. Marshall, F.J. Lerch, E.C. Pavlis, S.M. Klosko, S.B. Luthcke, G.B. Patel, R.G. Williamson, and N.P. Zelensky, Expected orbit determination performance for the TOPEX/Poseidon mission, *IEEE Transactions on Geoscience and Remote Sensing*, *31*, 2, 1993b.

Nerem, R.S., F.J. Lerch, R.G. Williamson, S.M. Klosko, J.W. Robbins, and G.B. Patel, Gravity model improvement using the DORIS tracking system on the SPOT–2 satellite, *J. Geophys. Res., 99*, 2791–2813, 1994a.

Nerem, R.S., F.J. Lerch, J.A. Marshall, E.C. Pavlis, B.H. Putney, B.D. Tapley, R.J. Eanes, J.C. Ries, B. E. Schutz, C.K. Shum, M.M. Watkins, S.M. Klosko, J.C. Chan, S.B. Luthcke, G.B. Patel, N.K. Pavlis, R.G. Williamson, R.H. Rapp, R. Biancle, and F. Nouel, Gravity Model Development for TOPEX/POSEIDON: Joint Gravity Models 1 and 2, *J. Geophys. Res.*, 24421–24447, 1994b.

Noll, C.E., Data Archiving and Distribution for the Crustal Dynamics Project: The CDDIS, in *Contributions of Space Geodesy: Technology*, D.E. Smith and D.L. Turcotte (eds.), Geodynamics Series Vol. 25, AGU, 1993.

Olson, T.R., Geopotential improvement from Explorer platform single-frequency GPS tracking, PhD Thesis, 151 pp., University of Colorado, Boulder, 1996.

Pavlis, E.C., "Gravity Field Estimation From Future Space Missions: TOPEX/POSEIDON, Gravity Probe–B, and ARISTOTELES," presented at the XX General Assembly of the International Union of Geodesy and Geophysics, IAG Symposium No. 3, Vienna, Austria, August 11–24, 1991.

Pavlis, D., et al., GEODYN Operations Manual, 5 volumes, Hughes STX Corporation, 1996.

Phung, P.B., V.S. Guedeney, J. Teles, Tracking and Data Relay Satellite System (TDRSS) Range and Range-rate Tracking System Observation Measurement and Modeling, NASA Goddard Space Flight Center, X–572–80–26, September 1980.

Potocki, K.A., "The Hilat Spacecraft," *Johns Hopkins Technical Digest*, *5*, 2, 1984.

Ries, J.C., R.J. Eanes, C.K. Shum, and M.M. Watkins, Progress in the determination of the gravitational coefficient of the Earth, *Geophys. Res. Lett.*, *19(6),* 529–531, 1992.

Ray, R.D., B.F. Chao, B.V. Sanchez, and R.S. Nerem, Some geodetic applications of the new TOPEX/Poseidon oceanic tide models, abstract, *EOS Transactions*, American Geophysical Union, *75(44)*, 57, Fall Meeting Supplement, 1994.

Rosborough, G.W., *Satellite Orbit Perturbations Due to the Geopotential*, PhD Thesis, Center for Space Research, The University of Texas at Austin, January 1986.

Rowlands, D.D., S.B. Luthcke, J.A. Marshall, C.M. Cox, R.G. Williamson, and S.C. Rowton, Space Shuttle precision orbit determination in support of SLA–1 using TDRSS and GPS tracking data, *J. Astro. Sci.*, *45*, 1, Jan.–Mar. 1997.

Rubincam, D.P., Yarkovsky thermal drag on LAGEOS, *J. Geophys. Res.*, *93*, 13805–13810, 1988.

Rubincam, D.P., D.G. Currie, and J.W. Robbins, LAGEOS I once-per-revolution force due to solar heating, *J. Geophys. Res.*, *102*, 585–590, 1997.

Safren, H.G., Effect of a drag model using a variable projected area on the orbit of the Beacon–Explorer C Satellite, Goddard Space Flight Center, X–921–75–210, 1975.

Schrama, E.J.O, and R. Ray, A preliminary analysis of TOPEX/Poseidon altimeter measurements, *J. Geophys. Res.*, *99*, C12, 24799–24808, 1994.

Schreiner, W.S., personal communication, February 1996.

Smith, C., Center for Extreme Ultraviolet Astrophysics, University of California, Berkeley, private communications, April, 1996.

Smith, D.E., R. Kolenkiewicz, P.J. Dunn, J.W Robbins, M.H. Torrence, S.M. Klosko, R.G. Williamson, E.C. Pavlis, N.B. Douglas, S.K. Fricke, Tectonic motion and deformation from satellite laser ranging to LAGEOS, *J. Geophys. Res.*, 95, B13, 22013–22041, 1990.

Smith, D.E., F.J. Lerch, R.S. Nerem, M.T. Zuber, G.B. Patel, S.K. Fricke, and F.G. Lemoine, An improved gravity model for Mars: Goddard Mars Model 1, *J. Geophys. Res., 98(E11),* 20871–20889,1993.

Schwederski, E.W., On charting global ocean tides, *Rev. Geophys.*, 18, 243–268, 1980.

Tapley, B.D., J.C. Ries, G.W. Davies, R.J. Eanes, B.E. Schutz, C.K. Shum, M.M. Watkins, J.A. Marshall, R.S. Nerem, B.H. Putney, S.M. Klosko, S.B. Luthcke, D.E. Pavlis, R.G. Williamson, N.P. Zelensky, Precision orbit determination for TOPEX/POSEIDON, *J. Geophys. Res.*, 99, C12, 24383–24404, 1994b.

Tapley, B.D., M.M Watkins, J.C. Ries, G.W. Davis, R.J. Eanes, S.R. Poole, H.J. Rim, B.E. Schutz, C.K. Shum, R.S. Nerem, F.J. Lerch, J.A. Marshall, S.M. Klosko, N.K. Pavlis, and R.G. Williamson, The Joint Gravity Model–3, *J. Geophys. Res.*, *101 (B12)*, 28029–28049, 1996.

Ullman, R.E., SOLVE Program Mathematical Formulation, Hughes STX Report HSTX/G&G–9201, NASA Contract NAS–5–29393/503, January, 1992.

Wagner, C.A., and S.M. Klosko, Gravitational harmonics from shallow resonance orbits, *Celestial Mechanics*, 16, 1977.

Ware, R., M. Exner, D. Feng, M. Gorbunov, K. Hardy, B. Herman, Y. Kuo, T. Meehan W. Melbourne, C. Rocken, W. Schreiner, S. Sokolovskiy, F. Solheim, X. Zou, R. Anthes, S. Businger, and K. Trenberth, GPS Sounding of the Atmosphere from Low Earth Orbit: Preliminary Results, *Bull. of the American Meteorological Society*, 77, 1, 19–40, Jan. 1996.

Webb, F., and J. Zumberge, An introduction to Gipsy/Oasis II: Precision software for the analysis of data from the Global Positioning System, JPL Report D–11088, Jet Propulsion Laboratory, Pasadena, CA, July, 1995.

Wu, S.C., W.I. Bertiger, J.T. Wu, Minimizing Selective Availability Error on TOPEX GPS Measurements, AIAA/AAS 90–2942, 1990.

Yunck, T. P., S. C. Wu, J. T. Wu, and C. L. Thornton, Precise tracking of remote sensing satellites with the Global Positioning System, *IEEE Trans. Geosci. and Remote Sens*., 28(1), 108–116, 1990.

Yunck, T. P., W. I Bertiger, S. C. Wu, Y. Bar–Sever, E. J. Christensen, B. J. Haines, S. M. Lichten, R. J. Muellerschoen, Y. Vigue, and P. Willis, First assessment of GPS-based reduced dynamic orbit determination on TOPEX/POSEIDON, *Geophys. Res. Lett*., 21(7), 541–544, 1994.

Zhu, S.Y., E. Groten, and C.H. Reigber, Various aspects of numerical determination of nutation constants, II, An improved nutation series for the deformable Earth, *Astro. J., 99(3),* 1990.

Zhu, S.Y., and C.H. Reigber, The German PAF for ERS–1: ERS–1 standards used at D–PAF, ERS–D–STD–31101, Jan. 25, 1991.

7.   THE COMPREHENSIVE LOW-DEGREE COMBINATION MODEL

Satellite tracking data, surface gravimetry, and direct altimeter data provide unique and complementary information for the determination of the low-degree (through degree 70) geopotential model. The incorporation of all three sets of data into a single geopotential model is referred to as the *comprehensive* combination solution. This solution is one where parameters other than potential coefficients (dynamic ocean topography [DOT] and tidal coefficients, Earth-orientation parameters, station locations, etc.) are simultaneously estimated in the solution. In contrast, the combination solutions discussed in Section 8 involve only the geopotential coefficients. In this section, we discuss the derivation of the low-degree comprehensive combination model, where the normal equations from the satellite tracking data used in the development of the satellite-only model were combined with the direct altimeter data normal equations and surface gravity normals (which exclude the altimeter-derived anomalies and the contribution of the geopotential above degree 70).

Satellite tracking data provide the best and least ambiguous information for defining the longwavelength field through degree and order 40. However, because of the attenuation of the field sensitivity with altitude of the satellites included in the model, there is little signal from higher degree terms. The signal found from harmonics above degree 40 is largely confined to specific resonance orders. Therefore, while tracking data are essential, they yield large uncertainties for the middle and shorter wavelength portion of the field. These data, and their processing for inclusion in EGM96, are discussed at length in Section 6 of this report.

Surface gravimetry provides a second unique data resource for gravitational modeling. These data are almost completely complementary to the tracking data. They provide detailed and accurate shorter wavelength information of the local field where accurate surveys have been completed. Through the use of airborne mapping approaches and improved gravimetric system performance on dynamically moving platforms, these data are now available for remote regions like Greenland, portions of the Arctic, and limited sections of Antarctica, all of which generally lack ground-surveyed data. As detailed in Section 3 of this report, coverage over other continental regions was substantially improved. The current set of surface gravity data suffers from two deficiencies: First, available surface gravity data currently are sparse and of poorer quality over most of the Earth's oceans, and are completely void over many ocean areas of the Southern Hemisphere. Second, surface gravity data are affected by long-wavelength problems arising from instrument drift and inconsistencies in datum definitions—for example, across many political boundaries. Nevertheless, by providing short-wavelength information over the Earth's continents, the surface gravity data are a valuable asset.

The third resource that provides a large base of information for geopotential modeling solutions is spaceborne radar altimetry. The synoptic mapping of the ocean topography, given the general conformance of ocean surface to that of an equipotential surface, yields the most dense and most homogeneous data for field modeling applications. While these data are restricted for our purposes to the ocean and inland seas, they are replete with information that has allowed improved models of the gravity field, the ocean tides, and ocean circulation to be derived. For the

70x70 portion of the EGM96 geopotential, these data were processed as "tracking" data, and were used to define simultaneously the satellite orbit, the dynamic ocean topography (DOT), and the ocean geoid. Section 7.1 describes these data, our analysis approach, their preprocessing, and a description of mission-specific design considerations that were employed.

The altimeter data provide geopotential information extending to a resolution well beyond 360x360, provided nongravitational signals sensed by each range measurement are properly accounted for. Above degree 70, the gravity anomalies predicted from the GEOSAT Geodetic Mission (GM) mission are used to supply the ocean coverage in the model. The prediction of surface anomalies from the GEOSAT GM data was addressed in Section 4. Within EGM96, altimetry is included in two ways: (a) As direct tracking data in the low-degree comprehensive combination model and (b) through the prediction of surface gravity anomalies in the high-degree solutions. This approach optimizes the information content of the low-degree combination model and the high-degree quadrature and block-diagonal models.

When the normal equations from satellite tracking, surface gravimetry, and satellite radar altimetry are added together with appropriate relative weighting, a complete description of the Earth's gravity field can be derived. Nevertheless, while sufficient to yield a highly accurate model like EGM96, future geopotential satellite missions such as CHAMP and GRACE will significantly advance our current knowledge. The greatest gains are anticipated from these missions in the longest wavelengths of the field, where the patchwork of satellites currently included will be supplanted by continuous precise tracking data, allowing a much better resolution of the short-period orbital perturbations not well sensed by available tracking data, with the exception of GPS. However, beyond degree 90 to 120 (depending on mission configuration, orbital altitude, and duration), the surface gravimetry and altimeter information will be required to define the shorter wavelength field for the foreseeable future.

Section 7.1 summarizes the preprocessing and data reduction associated with the creation of the normal equations from direct altimeter data used in the PGS7337B (EGM96) combination solution. Section 7.2 reviews the derivation of the surface gravity normal equations, and Section 7.3 details the results associated with the development of the final combination model PGS7337B. The characteristics of the preliminary combination solutions developed for the IUGG in 1995 (PGS5741, see Section 6.3.1), and the preliminary combination solution PGS6399 that formed the low-degree component of EGM–X02, are also briefly reviewed.

7.1 Altimeter Data as a Satellite Tracking Observation

Satellite altimetry synoptically monitors the topography of sea surfaces. While satellite altimetry affords oceanwide (bounded by the satellite's inclination) coverage, it is limited in its broadest applications by the uncertainty in geoid models and their implied geoid slopes [*Martel and Wunsch,* 1993; *Wunsch*, 1996]. Accurate models of the gravitational field are required to separate marine geoid and oceanographic signals. GEOSAT was the first satellite to map the global large-scale variations of sea level on a long-term basis, providing data over a 5-year period. GEOSAT was followed by TOPEX/POSEIDON (T/P), which dramatically improved the basin scale monitoring of the ocean circulation through the achievement of 2–3 cm radial orbit accuracy and

direct measurements of the ionosphere and wet troposphere propagation delays. With the concurrent flight of the higher inclination European Space Agency's ERS–1 satellite, altimeter coverage extending to the high-latitude regions ($|\varphi| > 66°$) is also available. We have used altimeter data from these three satellites in EGM96.

Large-scale fluctuations in sea-surface topography are important indications of global change. Such variations include secular trends in the total mass or volume of the ocean [e.g., *Peltier*, 1988; *Douglas*, 1997]; interannual variations on a basin scale such as the anomalous undulations of the tropical thermocline caused by the El Niño Southern Oscillation [e.g., *Miller et al.,* 1988]; and hemispheric fluctuations on an annual and semiannual basis that are caused by the seasonal heating and cooling of the upper ocean [*Pattullo et al*., 1955; *Wyrtki and Leslie*, 1980]. The altimeter modeling in EGM96 attempts to accommodate the dominant time-varying DOT signals as well as the time-averaged (quasi-static) dynamic ocean topography, and provide for their separate solution so as not to alias the gravitational signal extracted from the altimeter data.

The dynamic topography signals at the annual and semiannual periods approach 15 and 5 cm respectively [cf. *Cheney et al.,* 1994; *Nerem et al.,* 1994a; *Stammer and Wunsch*, 1994], which is significantly larger than the geoid uncertainty at comparable wavelengths. As opposed to averaging these periodic effects (a consequence of their neglect), EGM96 provides for their direct recovery over a significant spatial bandwidth. Furthermore, through a comparison of the EGM96 solution to other investigations and predicted climatologies, we can verify the effective isolation of these time-dependent oceanographic effects and assess their elimination as a potential aliasing error source in the geopotential solution. The secular change in sea level is also accommodated through the frequent adjustment of arc-specific (i.e., every 5 days for the ERS–1 and every 10 days for T/P) altimeter range biases.

7.1.1 Mathematical Model

The simultaneous solution for the orbit and absolute dynamic topography employs a refinement of the methods described in *Marsh et al.* [1990] and *Nerem et al.* [1990]. Simultaneous solutions for the orbits, the gravitational fields, and the sea-surface dynamic topography surfaces have many advantages. The altimeter data provide valuable information on the shape of the ocean surface, which predominantly reflects the geoid at the shorter wavelengths. The altimeter data provide comparable spatial resolution over the oceans to the surface gravimetry data over the land areas.

Direct use of altimeter observations for defining the satellite ephemeris can yield a significant improvement in orbit accuracy for satellites such as GEOSAT and ERS–1. These data map the satellite's radial position over the ocean surface uniformly, and provide information that would otherwise be lacking given the large geographic gaps in ground-based tracking coverage over many of the ocean basins. The altimeter data are nearly continuous over the oceans, and complement the information provided by normal, but imprecise (in the case of the TRANET Doppler) or sparse (in the case of the SLR tracking) ground-based tracking data. Furthermore, laser ranging, and especially TRANET Doppler observations, are more sensitive to the satellite's

along-track position (where the velocity with respect to the station is dramatically changing over a pass) than to its radial position.

Unlike either GEOSAT or ERS–1, T/P is supported by an array of tracking systems that yield 2–3 cm radial orbit accuracy [*Bertiger et al.*, 1994; *Nouel et al.*, 1994; *Tapley et al.*, 1994; *Marshall et al.*, 1995] . In the case of T/P, the unmodeled long wavelength oceanographic signals could degrade the orbit accuracy if the altimeter data were allowed to significantly influence the orbit solutions. Precautions were taken to ensure that the nominal weight given to T/P altimetry was insufficient to significantly affect the orbit solution obtained from the SLR/DORIS data alone. These design considerations, along with those adopted for ERS–1 and GEOSAT and the results achieved are discussed in Section 7.1.2.

In GEODYN, the altimetric range observation is used to measure the instantaneous sea-surface height. The satellite measurement is given by:

$$h = h_{sat} - (r_{alt} + \Delta r_{alt} + h_\varepsilon + h_b) \qquad (7.1.1-1)$$

where:

h sea surface height above the reference ellipsoid defined at the subsatellite point normal to the ellipsoid

h_{sat} radial height of the satellite orbit defined as the distance from the center of mass of the satellite normal to the Earth's ellipsoid

r_{alt} the observed altimeter range corrected for instrument offsets from the sea surface to the satellite center of mass

Δr_{alt} instrument and environmental corrections, including EM bias

h_ε the instrument noise

h_b bias that results from the invariant instrument bias, its long period drift, and error in the knowledge of the Earth's semimajor axis for its reference ellipsoid (a_e).

The height of the nongravitationally forced variations in sea level, ζ, caused by the ocean circulation is given by:

$$\zeta = h - (h_{Nref} + h_{\Delta N}) - h_{Tg} - \zeta_t - \zeta_a \qquad (7.1.1-2)$$

where

h_{Nref} is the geoid height from a reference gravitational model geoid to some maximum degree and order

$h_{\Delta N}$ is the residual geoid height beyond this level of truncation

h_{Tg} are the geocentric body tides of the Earth

ζ_t are the ocean tides

ζ_a is the barotropic correction for the load of the atmosphere.

Table 7.1.1–1 describes the models employed for these terms in the PGS7337B (EGM96) combination solution. From equations (7.1.1–1) and (7.1.1–2), it is evident that isolation of the dynamic ocean topography (DOT), ζ, from the low-degree geoid, h_{Nref}, is highly dependent on models for the altimeter data corrections. The model employed to represent the static and periodic (with annual and semiannual terms) ζ is a truncated spherical harmonic expansion. This representation is:

$$\zeta_{total} = \overline{\zeta} + \zeta(t) \tag{7.1.1–3}$$

where $\overline{\zeta}$ is the quasi-static and $\zeta(t)$ is the time-varying portion of the dynamic ocean topography model. The static portion, $\overline{\zeta}$, is defined as

$$\overline{\zeta} = \sum_{n=0}^{20} \sum_{m=0}^{n} \sum_{a=1}^{2} \overline{\zeta}_{a_{nm}} S_{a_{nm}} \tag{7.1.1–4}$$

where

$$S_{a_{nm}} = P_{nm}(\sin\phi)\cos m\lambda \text{ for } a=1, \text{ and } S_{a_{nm}} = P_{nm}(\sin\phi)\sin m\lambda \text{ for } a=2.$$

Table 7.1.1–1. Models used to define the altimeter data corrections.

Correction	GEOSAT	T/P	ERS–1
h_{Nref}	JGM–3 [*Tapley et al.*, 1996], through 70x70. Model is adjusted in gravity solution.		
$h_{\Delta N}$	V058 (EGM–X04) from degree 71 through degree 460.		
ζ_t	Ocean Pathfinder tides derived from *Schrama and Ray* [1994] over ±66° latitude, and *Le Provost et al.* [1994] at the higher latitudes.		
h_{Tg}	MERIT standards [*Melbourne et al.,* 1983]		
ζ_a	Full correction based on the deviation from 1013.3 mbar ocean pressure		
$\Delta r_{alt\ (ionosphere)}$	IRI–95 *Bilitza et al.* [1996, 1997]	Direct dual-frequency correction [*Callahan*, 1994].	From GDRs (Bent model)
$\Delta r_{alt\ (troposphere)}$	Dry term from climatology Wet term from TOVS/SSMI values [*Emery et al.*, 1990]	Dry term from climatology Wet term from onboard radiometer.	Dry term from climatology Wet term from onboard radiometer.
$\Delta r_{alt\ (sea\ state)}$ including EM bias	Two percent of significant wave height $H_{1/3}$ in mm	Three-parameter model on GDR v. 5 dependent on $H_{1/3}$, wind speed (U), and U^2 [*Callahan*, 1994].	5.5 percent of $H_{1/3}$ in mm
Time Tag			$T_{True} = T_{alt} + 1.6$ msec [*Scharroo*, 1996a, 1996b]

TOVS: TIROS Operational Vertical Sounder   SMMI: Special Sensor Microwave Imager

The ζ coefficients represent average values over the timespan of the altimeter data. In

PGS7337B, the coefficients $\bar{\zeta}$ were determined through degree 20 for both T/P–ERS–1 and GEOSAT.

The time-varying component of the DOT, $\zeta(t)$, is given as:

$$\zeta(t) = \sum_{p=1}^{2} \sum_{n=0}^{10} \sum_{m=0}^{n} [(\zeta_{nmp}^{C} \cos m\lambda + \zeta_{nmp}^{S} \sin m\lambda) \cos \omega_p(t - t_0) +$$

$$(\zeta_{nmp}^{C} \cos m\lambda + \zeta_{nmp}^{S} \sin m\lambda) \sin \omega_p(t - t_0)] P_{nm}(\sin \phi) \quad , \quad (7.1.1\text{–}5)$$

where the index p represents the annual and semiannual periods, and ζ_{nmp}^{C} and ζ_{nmp}^{S} are the time-varying dynamic ocean topography coefficients estimated in EGM96. The term ω_p represents the frequency such that $\omega_p = 2\pi/T$, where T is the annual period of 365.2524 days or the semiannual period of 182.6262 days. The initial time t_0 is set to January 1.0 of a given year. The time-dependent annual and semiannual models of the DOT are solved for to degree and order 10.

Since altimeter data do not provide uniform coverage over the sphere, mathematical stabilization of the dynamic ocean topography solution is introduced for the static portion of the model. A form of least-squares collocation [*Moritz,* 1980] was used to control the power in the recovered coefficients. This approach reduces the modeling instability over the areas lacking data. A constraint was introduced into the solution that is based on a power law fit to the spherical harmonic degree variances obtained from the independently derived POCM–4B Ocean Circulation Model (OCM) developed by Semtner and Chervin as reported in *Stammer et al.* [1996] (see also *Semtner and Chervin*, 1992 and *Semtner*, 1995). The need for the application of this constraint is described in *Marsh et al.* [1990]. However, the linear form of the constraint given by (eq). 15 of *Marsh et al.* [ibid.] could not represent the variances beyond degree 10. The power law constraint that was applied in EGM96 took the form:

$$\sigma_{\zeta_{RMS}} = \frac{0.30775}{n^{1.4243}} \qquad (7.1.1\text{–}6)$$

where $\sigma_{\zeta_{RMS}}$ represents the RMS power of the static portion of the dynamic ocean topography $\bar{\zeta}$ per spherical harmonic degree (in m), and n represents the spherical harmonic degree. This relation was derived empirically from a spherical harmonic fit to degree 24 provided by *Rapp* [*personal communication*, 1996] of the output from the POCM–4B.

A constraint was also applied to the time-varying DOT coefficients $\zeta(t)$. Eq. (7.1.1–6) was rescaled by a factor of 0.8 such that

$$\sigma_{\zeta(t)_{RMS}} = \frac{0.24620}{n^{1.4243}} \qquad (7.1.1\text{–}7)$$

The selection of the rescaling factor was the result of several test solutions. The initial value was 0.1, which was successively relaxed by factors of two, the intent being to provide solution conditioning without unreasonably damping the estimated coefficients.

7.1.2 Orbit Reduction and Data Weighting Strategies Employed for Direct Use of Altimeter Data

The GEOSAT, T/P, and ERS–1 altimeter data had different characteristics and supporting tracking systems. The prime design considerations for inclusion of these data in the EGM96 solution are outlined in this section.

The SLR/DORIS tracking of T/P achieved orbits that had a radial RMS error of only 2–3 cm [*Tapley et al.*, 1994; *Marshall et al.*, 1995]. The altimeter data could not be allowed to affect significantly the determination of the T/P orbit. This meant that the altimeter data had to be downweighted with respect to the SLR and DORIS data. Orbit changes were restricted to being less than 1 cm RMS in the radial direction.

The weight of the ERS–1 altimeter data was determined with respect to T/P. Since the T/P and ERS–1 missions were concurrent, the T/P-defined ocean surface was used as a reference to strengthen the orbit recovery (described in detail below) of the sparsely tracked ERS–1 satellite. We estimated a joint DOT solution with both T/P and ERS–1, requiring that ERS–1 change the T/P-derived DOT solution by less than 2 cm RMS over ±66° latitude. The combined altimeter data sets extended the mapped ocean surface to ±82° latitude and improved both the geoid and DOT solutions over these previously unmapped high-latitude regions.

Two full years of T/P altimeter data from 1993 and 1994 were included in the EGM96 solution. POSEIDON data, from a separate altimeter instrument that operated 10 percent of the time, was not included in EGM96. The ERS–1 data were well distributed throughout 1993 and were part of the ERS–1 35-day repeating groundtrack mode of operation.

Altimeter data are a valuable source of data for improvement of the GEOSAT orbit. GEOSAT was tracked by TRANET Doppler systems, which are of high noise (0.2 cm/s) and suffer from a wide range of systematic error sources compared to more modern tracking systems (see Table 6.2.1–2). Having good radial orbit information at a third inclination was the motivation for inclusion of the GEOSAT altimeter data in EGM96. The GEOSAT altimetry normal point data used in EGM96 was originally created for the JGM series of models [*Nerem et al*., 1994b, and *Tapley et al*., 1996]. However, several changes were made to the altimeter range corrections values, as described in Section 7.1.1.

The combined T/P–ERS–1 tracking plus altimeter data sets, and those for GEOSAT, were independently calibrated against the surface gravimetry and satellite-only data sets to determine their relative weights. These altimeter and tracking data normal equations were then combined at this determined ratio of weights and recalibrated in combination to account for the possible redundancy of information provided by multiple altimeter systems.

7.1.3 Data Reduction of Altimeter Satellites

7.1.3.1 Data Editing Criteria

Significant care was paid to the data editing criteria applied to the altimeter data used in EGM96. Table 7.1.3.1–1 describes these criteria for the three sets of altimeter data used in EGM96. Data

over shallow water, defined as less than 200 m in depth for T/P and ERS–1, and 1000 m for GEOSAT, were eliminated to avoid larger tidal error and storm surge effects (see Figure 7.1.3.1–1). If the high-degree ($71 \leq n \leq 460$) geoid correction was greater than 3 meters, the data were not included. The motivation here was to eliminate data in regions of steep geoid changes (such as ocean trenches) that could otherwise corrupt the estimation of the large-scale dynamic ocean topography. Data outliers were found and removed by testing the implied sea surface height against a mean sea surface from an aggregation of missions. This "outlier test" was set to ±10 m for GEOSAT and ±3 m for T/P. ERS–1 used a slightly different test, where the limit was ±3 m through ±60° latitude, and 5.0 m above that region. Finally, other engineering and system performance metrics were applied in the selection of the altimeter data.

Table 7.1.3.1–1. Altimeter data selection criteria employed in EGM96.

Criteria	Comment	GEOSAT	T/P	ERS–1
"Bad Flags"	Data denoted as suspect on original GDR	applied (flag bit 0) (flag bit 2,4,5,6)	applied: (GEO_Bad 1,4,7) (Alt_Bad1 1,3,6)	applied: mispointing flag (Alt_Bad1 1,3,6)
σ_h	Estimated height uncertainty from GDR	$0.0 < \sigma_h \leq 0.10$ m	$0.0 < \sigma_h \leq 0.15$ m	$0.0 < \sigma_h \leq 0.5$ m
$H_{1/3}$	Significant wave height	$0.0 \leq H_{1/3} \leq 10.0$ m	$0.0 \leq H_{1/3} \leq 10.0$ m	$0.0 \leq H_{1/3} \leq 10.0$ m
$\sigma_{H1/3}$	Uncertainty for above	$0 \leq \sigma_{H1/3} \leq 1.0$ m	$0.0 \leq \sigma_{H1/3} \leq 1.0$ m	$0.0 \leq \sigma_{H1/3} \leq 1.0$ m
ζ_t	Ocean tides	$|\zeta_t| < 1.0$ m	$|\zeta_t| < 2.0$ m	$|\zeta_t| < 2.0$ m
σ_0	AGC/sigma–zero	$0.0 < \text{AGC} \leq 37.0$ dB $0.0 < \sigma_0 \leq 15.0$ dB	$0.0 < \sigma_0 \leq 25.0$ dB	σ_0 flag set
σ_{AGC}	Uncertainty of AGC	$\sigma_{AGC} < 0.25$ dB	not used	not used
$\Delta r_{alt \text{ (trop) dry}}$	Troposphere range delay: dry term	$2.0 \leq \Delta r_{alt} \leq 3.0$ m	$2.0 \leq \Delta r_{alt} \leq 3.0$ m	$2.0 \leq \Delta r_{alt} \leq 3.0$ m
$\Delta r_{alt \text{ (trop) wet}}$	Troposphere range delay: wet term	$0.0 < \Delta r_{alt} \leq 1.0$ m	$0.0 < \Delta r_{alt} \leq 1.0$ m	$0.0 < \Delta r_{alt} \leq 1.0$ m
$\Delta r_{alt \text{ (ion)}}$	Ionospheric range delay	$\Delta r_{alt} \leq 0.5$ m;	$\Delta r_{alt} \leq 0.5$ m; neg values set to 0	$\Delta r_{alt} \leq 0.5$ m
h_{Tq}	Solid Earth tides	$|h_{Tq}| < 1.0$ m	$|h_{Tq}| < 1.0$ m	$|h_{Tq}| < 1.0$ m
h	Implied sea-surface height is tested against "mean sea surface (mss)" from earlier aggregation of missions	$|h - h_{mss}| < 10.0$ m	$|h - h_{mss}| < 3.0$ m	$|h - h_{mss}| < 3.0$ m for $|\text{lat}| < 60°$ $|h - h_{mss}| < 5.0$ m for $|\text{lat}| \geq 60°$
Shallow sea mask	Test location against bathymetric grid	depth > 1000 m	depth > 200 m	bathymetry flag set
$h_{\Delta N}$	High-degree geoid contribution ($71 \leq n \leq 460$)	$|h_{\Delta N}| < 2.5$ m	$|h_{\Delta N}| < 3.0$ m	$|h_{\Delta N}| < 3.0$ m
Pointing error	attitude error in nadir looking direction	error < 1.3°	not used	not used
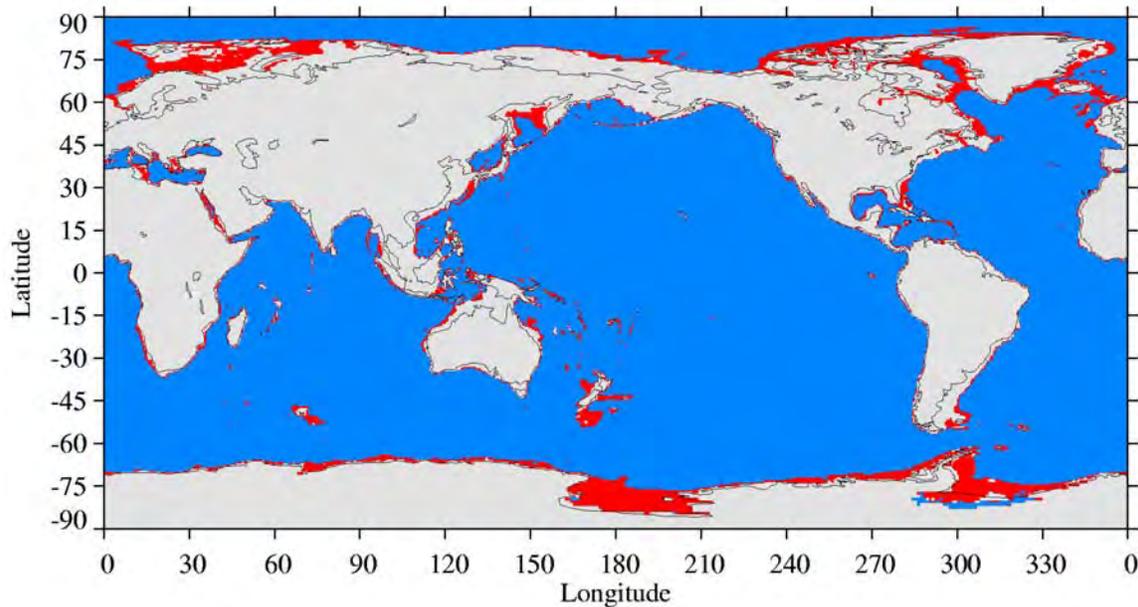
Figure 7.1.3.1–1. Depth-editing masks applied to the altimetry data. Depths between 200 and 1000 m are shown in red, and those greater than 1000 m are shown in blue. T/P and ERS–1 altimetry data were used for regions where the depth was greater than 200 m (the red and blue regions). For GEOSAT, only the altimetry data from regions where the depth was greater than 1000 m (the blue regions) were used.

Some geographic editing was performed to eliminate points for enclosed deep-water masses, which included the Caspian, Black, Aral, and Red Seas. Shallow areas such as the Hudson Bay are excluded by the shallow-sea mask. The rationale here was to eliminate points that did not share a common elevation surface with the world's oceans, as inclusion of such data would introduce errors into the recovered DOT solutions.

Due to time constraints, the GEOSAT altimeter data processing began with the normal points used in JGM–1 and JGM–2, rather than with the full-rate altimeter data from the Geophysical Data Records. The corrections for the tides, the ionosphere, and the high-degree geoid were replaced at this level, as summarized in Table 7.1.1–1.

7.1.3.2 Variable Data Weighting

An additional change in our treatment of the altimeter data from their incorporation in JGM–2 [*Nerem et al.*, 1994b] is the use of variable observation weighting based on likely sources of error that affect each point either as a function of geographic location, local meteorological conditions, and/or characteristics of regional ocean currents. Each of these effects contribute "noise" to the observations (here defined as signals that are not directly adjusted as part of the EGM96 recovery). For EGM96, each observation standard deviation was defined by:

$$\sigma^2 = 0.08^2 + 0.01\,h_{\Delta N}^2 + 0.08V^2 \text{ (meters)}^2 \qquad (7.1.3.2\text{–}1)$$

where:

σ is the observation standard deviation

V represents the RMS sea-surface variability obtained from collinear altimeter analyses [*Wang, private communication*, 1996]

$h_{\Delta N}$ is the modeled correction for the geoid (as described earlier) contribution from degree 71 to degree 460.

To prevent a severe downweighting of data in specific geographic regions, the observational uncertainties were bounded by the following limits:

$$0.08 \leq \sigma \leq 0.16 \qquad\qquad\qquad\qquad\qquad\qquad (7.1.3.2\text{–}2)$$

which limited the effective change of weight to be no more than a factor of 4 between observations. The final standard deviations that were applied were scaled by a factor of 10 such that $\sigma_w = 10\sigma$ to ease comparison of weighting against other data types.

7.1.3.3 Summary of Altimeter Data Used in EGM96

A summary of the altimeter data included in EGM96 is given in Table 7.1.3.3–1. A more detailed discussion of each of these altimeter and tracking data sets is presented in the following section.

Table 7.1.3.3–1. Summary of altimeter data utilized in EGM96.

Satellite	Time Span of Altimeter Data	Dynamic Ocean Topography	Observations
GEOSAT	November 1986 to January 1987	20x20 $\bar{\zeta}$	274812
T/P	January 1993 to January 1995 (Cycles 11–84). No POSEIDON data were used.	20x20 $\bar{\zeta}$ and 10x10 $\zeta(t)$, annual and semiannual terms	2892900
ERS–1	1993 Cycles 6, 8, 11, 14, and 17 of 35-day repeat	Coincident and solved simultaneously with T/P	542417

7.1.4 Orbit Reduction Results: Altimeter Normal Equations

7.1.4.1 GEOSAT

GEOSAT began its Exact Repeat Mission (ERM) phase on November 8, 1986, when the satellite completed maneuvers placing it into its 17-day repeat orbit. When developing the GEM–T1, –T2, and –T3, the TRANET Doppler tracking data from the first 3 months of the ERM period were made available to the T/P Project. This time period was selected for subsequent incorporation of the GEOSAT altimeter data in the JGM–1 and JGM–2 combination geopotential models. These same preprocessed normal point data, originally developed for the JGM models, were used in EGM96, although the modeled corrections were modified as discussed earlier.

Table 7.1.4.1–1 provides a summary of the arcs used to form the normal equations for GEOSAT. With 3 months of data, only one oceanographic season is sampled, and so only a static DOT model, $\bar{\zeta}$, was obtained from these data. Figure 7.1.4.1–1 shows the geographic coverage of the altimeter normal points.

Table 7.1.4.1–1. Summary of GEOSAT Doppler and altimeter normal point data.

| Epoch | Doppler | | Altimeter | | |
	number of points	RMS (cm/sec)	number of points	RMS (cm)	Estimated Bias (cm)
861108	16019	0.4645	19477	18.35	−18.9
861114	15437	0.4686	19432	18.96	−18.7
861120	15045	0.4914	20154	18.66	−17.5
861126	56850	0.5286	21125	18.51	−17.6
861202	58210	0.5066	20659	19.13	−16.5
861208	60379	0.5052	21340	18.52	−16.5
861214	58387	0.5109	21734	18.47	−17.3
861220	61308	0.5016	21827	18.90	−16.8
861226	59628	0.5006	21572	19.17	−16.8
870101	67633	0.5025	25213	19.29	−17.2
870108	67552	0.5082	22567	19.63	−17.6
870114	66752	0.4995	21243	19.02	−17.5
870120	47862	0.4966	18469	19.86	−17.3
Totals	651062		274812		
Averages		0.4988		18.96	−17.4
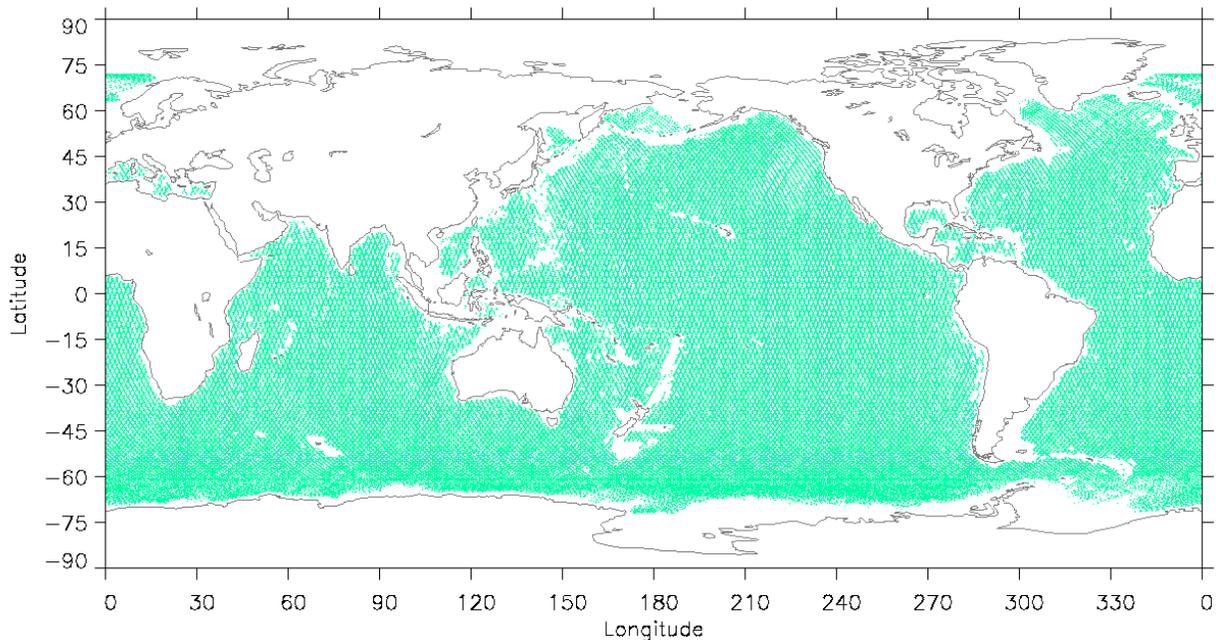
Figure 7.1.4.1–1. Geographic coverage of the GEOSAT altimeter normal point data used in the EGM96 solution.

7.1.4.2 TOPEX/POSEIDON

T/P was launched on August 10, 1992. This satellite is located in an orbit with ground track repeat cycle of 9.9 days. For the first nine or so cycles of the mission, verification and system assessment were ongoing, and it is believed that many of these first cycles had off-nadir pointing errors. Cycle 10, acquired over Christmas of 1992, had a data upset within the DORIS system, and many days of DORIS data were lost. Therefore, to eliminate any concern for these problems, the T/P data included in EGM96 started with Cycle 11 and ran for 2 years, through Cycle 84.

The T/P altimetry normal equations were formed using normal point data, as opposed to the full-rate 1 Hz data. Each normal point was created, after the observation editing process, for a 10-second interval by performing a linear fit to the observations within the interval. A number of restrictions were placed on the fitting process. First, a minimum of six observations was required per normal point interval, with a further restriction that the subintervals before and after the normal point time had to have a minimum of three points each, and that the maximum number of observations in the interval was 10. For points passing that test, iterative 3σ dynamic editing was performed on the residuals of the linear fit; if a point was edited, then the linear fit was recomputed, and the minimum number of observations was rechecked. Any normal point for which the RMS of the observations was greater than 0.5 m, or the along-track deflection implied by the linear fit to the undulation-corrected residual sea-surface height was greater than 10 seconds of arc, was discarded, and the interval selection process restarted. Finally, the time of the normal point was set to the nearest observation time to the middle of the interval, and a new "observation" record was created. Figure 7.1.4.2–1 depicts the geographic coverage of the T/P altimetry normal point data.
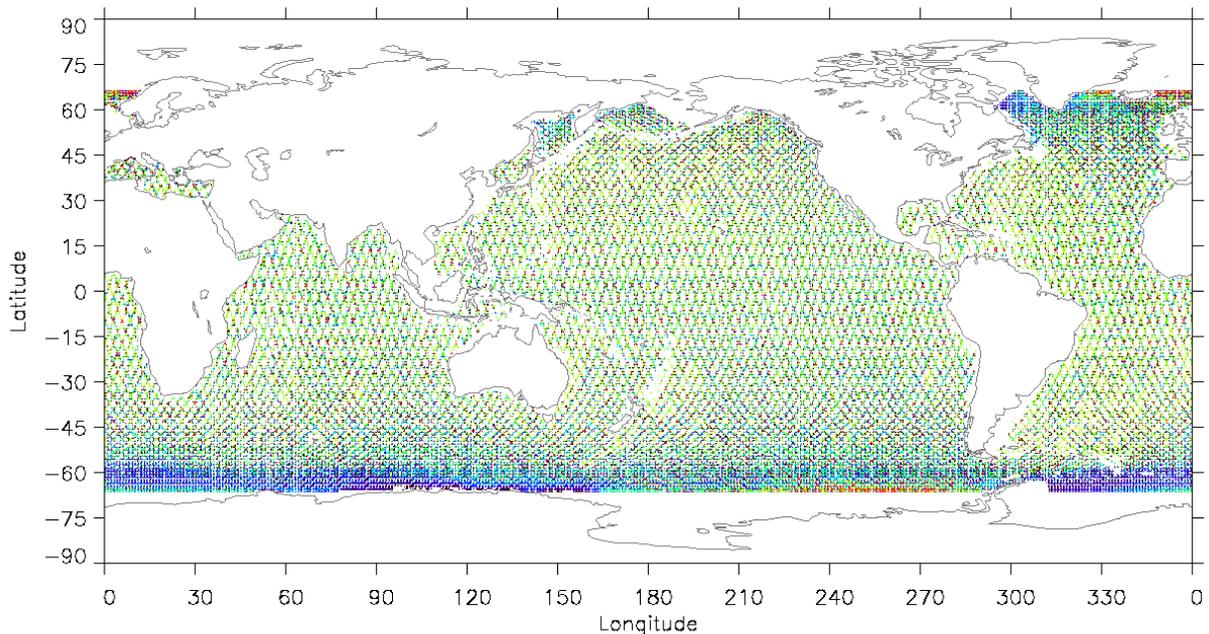
Figure 7.1.4.2–1. Geographic coverage of T/P altimeter normal points used in the EGM96 solution (excepting cycles 61,62,63 and 64).

The T/P altimetry normal equation sets were created by passing the same SLR/DORIS-based orbit solutions that were used in the development of the satellite-only gravity model (see Section 6.2.2.2) through the normal point data. Consequently, the dynamic modeling content of the altimetry normal equations matched those solutions. The altimetry measurement model was supplemented by the addition of an *a priori* T/P-derived DOT model. Also, biases were estimated for all the altimetry data in each solution arc. These biases accommodated the secular effects in sea level, and the long-term effects of the T/P clock drift correction error [*TOPEX Project, private communication*, 1996]. A summary of the altimetry residuals and statistics is presented in Table 7.1.4.2–1; the SLR and DORIS statistics have been repeated here from Table 6.2.2.2–1 for completeness.

Table 7.1.4.2–1. Summary of T/P SLR, DORIS, and altimeter data used in the normal equations. No altimetry data were used for cycles 12, 20, 31, 41, 55, 65, 79, and 83.

Cycle	Epoch	Laser number of points	Laser RMS (cm)	DORIS number of points	DORIS RMS (cm/sec)	Altimeter number of points	Altimeter RMS (cm)	Estimated bias (cm)
11	921231	1560	2.88	40730	0.0513	41126	18.7	−45.2
12	930110	2815	3.20	59384	0.0548		-	
13	930120	3067	2.65	59134	0.0559	41068	19.0	−45.7
14	930129	4077	2.81	57545	0.0556	39288	18.9	−45.0
15	930208	2990	2.96	55287	0.0554	41609	18.7	−45.2
16	930218	3608	3.31	56776	0.0553	37251	18.6	−44.8
17	930228	4000	2.57	55573	0.0547	47910	19.1	−46.1
18	930310	5186	2.85	53754	0.0559	47516	19.4	−45.8
19	930320	3829	3.37	55142	0.0548	47725	19.6	−46.3
20	930330	5750	3.51	53422	0.0552		Poseidon	
21	930409	4186	3.38	53842	0.0538	47377	19.6	−45.8
22	930419	6369	2.96	53995	0.0534	47128	19.6	−46.0
23	930429	4269	2.57	53066	0.0556	46459	19.4	−46.4
24	930509	5288	2.38	35569	0.0504	45661	19.5	−46.4
25	930519	3700	2.26	52145	0.0537	45591	19.9	−46.0
26	930528	2789	3.08	54796	0.0543	45056	19.7	−45.9
27	930607	3538	2.07	52391	0.0548	44598	19.7	−46.6
28	930617	4677	2.57	51555	0.0546	44360	19.6	−47.2
29	930627	4669	3.42	53457	0.0545	43414	19.7	−48.2
30	930707	5684	2.77	57360	0.0552	43379	19.9	−47.9
31	930717	6004	2.66	58047	0.0533		Poseidon	
32	930727	8180	2.60	56074	0.0542	43217	20.1	−46.4
33	930807	4536	2.81	34783	0.0525	37993	20.2	−46.9
34	930816	6559	3.10	58220	0.0557	42576	20.3	−47.0
35	930826	5587	2.38	57263	0.0558	42620	19.9	−47.7
36	930905	4417	2.66	58885	0.0569	42522	19.9	−48.1
37	930915	5821	2.69	47170	0.0547	38180	19.9	−48.2
38	930924	4255	2.05	60836	0.0569	42564	20.0	−47.1
39	931004	4497	2.27	62095	0.0566	42518	19.9	−47.2
40	931014	3063	2.59	62694	0.0570	42525	19.7	−46.6

		Laser		DORIS		Altimeter		
Cycle	Epoch	number of points	RMS (cm)	number of points	RMS (cm/sec)	number of points	RMS (cm)	Estimated bias (cm)
41	931024	3453	2.34	61387	0.0568		Poseidon	
42	931103	3903	2.70	59056	0.0567	42591	19.2	−47.3
43	931113	3600	2.65	61031	0.0563	43197	19.3	−45.9
44	931123	3165	2.26	58213	0.0566	42079	19.5	−46.0
45	931203	2829	2.85	58829	0.0563	44288	19.5	−46.2
46	931213	3887	2.99	57243	0.0565	45528	19.6	−46.7
47	931223	2832	2.74	57152	0.0553	45614	19.5	−46.6
48	940101	3689	2.46	60443	0.0545	47015	19.3	−46.1
49	940112	5288	3.24	56565	0.0553	47170	19.2	−45.7
50	940121	3675	2.62	58637	0.0557	47490	19.3	−45.8
51	940131	3857	2.40	60853	0.0558	47741	19.1	−45.5
52	940210	3828	2.42	59379	0.0555	47882	19.2	−45.3
53	940219	3187	2.74	62868	0.0557	47662	19.4	−45.3
54	940302	4254	3.21	56164	0.0547	47781	19.6	−46.4
55	940312	5444	3.23	58505	0.0540		Poseidon	
56	940322	6583	3.31	57983	0.0546	47595	19.4	−46.3
57	940401	6272	2.66	61466	0.0545	47137	19.4	−46.2
58	940411	4704	2.72	61003	0.0551	46901	19.4	−46.5
59	940421	6431	3.06	63036	0.0549	46022	19.9	−46.8
60	940501	5169	2.96	62743	0.0543	46144	19.6	−46.7
61	940511	4542	2.67	61048	0.0550	45898	19.6	−46.8
62	940521	3032	2.51	62628	0.0550	44916	19.5	−46.6
63	940530	4534	2.20	62238	0.0549	44847	19.6	−46.8
64	940609	5049	2.58	33966	0.0559	44251	19.9	−47.1
65	940619	5514	2.81	60969	0.0549		Poseidon	
66	940629	5591	3.19	62775	0.0549	43622	20.2	−48.0
67	940709	6534	2.03	62754	0.0544	43311	20.1	−47.3
68	940719	7088	2.13	45859	0.0525	42854	19.6	−47.6
69	940729	6915	2.03	62022	0.0548	42985	19.6	−48.3
70	940808	4905	2.25	59832	0.0771	42835	19.5	−48.1
71	940818	4649	2.49	57242	0.0555	42378	20.0	−48.8
72	940828	3996	1.93	58090	0.0562	42363	20.2	−48.6
73	940906	3697	2.09	58515	0.0547	41476	20.1	−48.6
74	940916	2813	1.86	59488	0.0545	27597	20.3	−47.3
75	940926	4178	2.56	60379	0.0548	38653	19.8	−47.4
76	941006	5945	2.55	58927	0.0546	41867	19.8	−47.7
77	941016	4979	2.71	56536	0.0537	42261	19.7	−48.7
78	941026	5125	2.68	55023	0.0547	42735	19.8	−48.4
79	941105	2779	2.07	56420	0.0532		Poseidon	
80	941115	3613	2.76	56261	0.0539	42683	19.8	−47.2
81	941125	4627	2.92	56505	0.0534	43690	19.4	−47.1
82	941205	5243	2.11	54316	0.0552	44580	19.5	−46.8
83	941213	5511	2.86	62267	0.0542		-	
84	941225	2152	1.79	54011	0.0533	46030	19.4	−47.8
Totals		334031		4191617		2892900		
Averages			2.66		0.0552		19.6	−46.8

7.1.4.3 ERS–1

ERS–1 has been flown in three mission configurations. Initially, the satellite had a 3-day repeating groundtrack. Subsequently, and for the data used in EGM96, the satellite was maneuvered into a 35-day repeat orbit. These data are, therefore, more than three times as geographically dense as those provided by T/P, and extend to ±82° latitude in some regions.

The actual coverage of the ERS–1 altimetry normal data used in EGM96 is presented in Figure 7.1.4.3–1. In several areas, the presence of sea ice, shallow water, or other editing criteria reduces the latitudinal coverage of the ERS–1 altimetry. For example, in the Ross Sea there is only a small amount of valid altimetry, from ERS–1 Cycle 8 (December 20, 1992–January 24, 1993), that is otherwise cut off from the altimetry over the Pacific Ocean. This isolated region of valid altimetry results from the opening of the interior of the seasonally ice-covered Ross Sea in the month of December. As the austral summer progresses, the mouth of the Ross Sea thaws, forming the connection with the Pacific Ocean [*Gloersen et al.*, 1992, Figure 4.1.16]. In the Arctic Ocean, the regions that are seasonally free of sea ice in the East Siberian and Laptev Seas north of Asia are generally shallower than 200 m, which resulted in the editing of the altimetry data in these regions. In contrast, the Norwegian and Barents Seas are relatively deep, so the altimetry data were retained [*Gloersen et al.*, Figure 3.1.15].
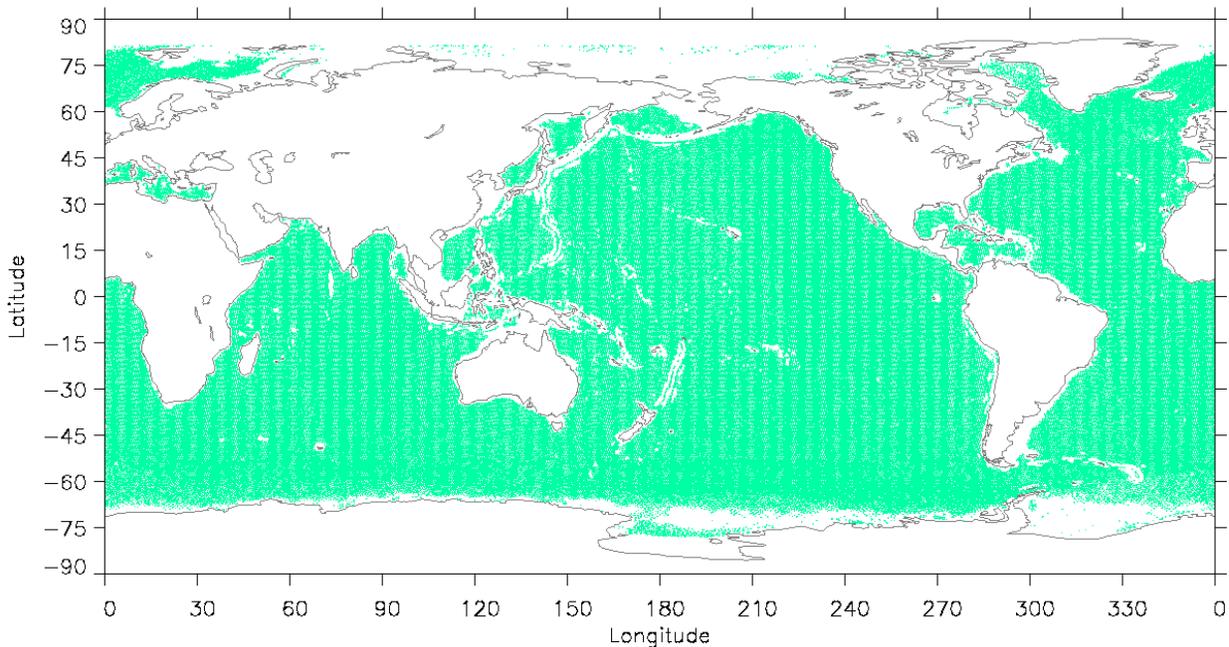
Figure 7.1.4.3–1. Geographic coverage of ERS–1 altimeter normal points used in the EGM96 solution.

With the loss of the prime tracking system, PRARE, almost immediately after launch, SLR was the only precision tracking system available to support ERS–1. In order to determine precise orbits for ERS–1, the use of the altimetry normal point data, in addition to the SLR data, was required. For that reason, ERS–1 was not included in the satellite-only model EGM96S. Therefore, a brief summary of the orbit determination is required. Table 7.1.4.3–1 summarizes the 5-day solution arc parameterization and the background modeling differences from the common background set given in Section 6.1.3. In general, every effort was made to ensure complete consistency with the modeling used for T/P, since both sets of data would be used to estimate a joint dynamic ocean topography solution.

The altimetry normal point data were formed in a similar manner as the T/P normal points, and used the editing criteria described in Section 7.1.3.1. A data uncertainty of 3 m was used for the altimetry normal points for the orbit determination only. Once the final orbit determination solution was available, the normal equations for the SLR and altimetry were generated separately, with the data uncertainty used on the altimetry corresponding to the values assigned for each point during the normal point generation according to the criteria described in Section 7.1.3.2.

Table 7.1.4.3–1. ERS–1 modeling and solution parameterization in EGM96.

Estimated Parameters (per 5-day solution)	
Dynamical	Epoch State
	C_D/12 hrs
	Along-track 1–CPR per 12 hours
Observational	One altimeter bias per 5-day arc
Geophysical Modeling—See Table 6.1.3–2, with the following exceptions:	
Gravity	JGM–3
Nonconservative Force Modeling	
Drag	Macro Model [*Zhu and Reigber*, 1991]
Solar Radiation	Macro Model [*Zhu and Reigber*, 1991]
Measurement Corrections	
Antenna Offsets	Attitude dependent
Dynamic Ocean Topography	T/P derived *a priori*

1-CPR: one cycle per revolution

Five 35-day cycles were chosen, which were distributed over the annual cycle. Each cycle was divided into 5-day solution arcs. Of the nominal 35 solution arcs, 6 were not used because of the presence of maneuvers (epochs 921021, 921215, 930104, 930404, 930419, and 931110), while an additional arc (930424) was not used in the gravity solution because of data retrieval difficulties. Table 7.1.4.3–2 provides an overview of the remaining 28 ERS–1 solutions arcs used in EGM96, and the orbit determination performance. The paucity of the SLR data notwithstanding, 15 cm RMS residuals were obtained for the SLR data.

Table 7.1.4.3–2. ERS–1 SLR and altimeter data used in the normal equations.

Cycle	Epoch	Laser		Altimeter		
		number of points	RMS (m)	number of points	RMS (m)	Estimated bias (cm)
6	921006	948	16.89	18639	24.57	−76.98
	921011	1377	12.45	19766	23.85	−76.54
	921016				maneuver	
	921021	640	21.81	19575	25.59	−75.85
	921026	640	21.81	19575	25.59	−75.85
	921031	740	14.23	19510	23.30	−78.51
	921105	1145	14.08	20016	24.05	−77.02
8	921215				maneuver	
	921220	931	13.57	20633	23.28	−74.62
	921225	362	4.48	20261	23.15	−73.97
	921230	377	11.01	20356	22.04	−73.63
	930104				maneuver	
	930109	699	7.97	20964	23.72	−71.93
	930114	1318	13.46	20760	23.12	−75.81
11	930330	666	13.65	20135	22.90	−75.28
	930404				maneuver	
	930409	768	14.24	16744	23.38	−73.78
	930414	1382	17.61	16665	23.13	−75.65
	930419				maneuver	
	930424	–	–	–	–	–
	930429	697	13.70	19747	23.07	−76.79
14	930713	2162	11.14	17717	22.33	−79.93
	930718	1988	10.63	19231	22.85	−77.18
	930723	2293	9.47	19694	24.09	−78.37
	930728	2551	13.59	19427	23.19	−77.86
	930802	2139	6.59	19637	23.33	−77.81
	930807	977	7.12	19494	23.86	−78.81
	930812	2599	10.47	19730	23.76	−79.47
17	931026	1555	19.76	17979	23.63	−76.77
	931031	1568	10.84	18692	22.32	−76.62
	931105	1272	13.43	19219	22.86	−77.46
	931110				maneuver	
	931115	1842	15.79	19587	23.21	−74.91
	931120	1550	12.57	18880	22.58	−78.42
	931125	1560	11.80	19082	27.04	−77.60
	Totals	37137		542417		
	Averages		12.64		23.51	−76.58

7.2 Use of Surface Gravity Data

7.2.1 Introduction

The estimation of a combination solution complete to degree and order 70 requires the processing of surface gravimetric data and the development of normal equations from these data. These normals are then combined with the satellite-only and altimeter-derived normals to estimate the 70x70 combination geopotential model. The development of surface gravity normals for the 70x70 portion of EGM96 followed closely the techniques described by *Pavlis* [1988], using the 1° gravity data described in Section 3. Since the 70x70 portion of EGM96 includes altimeter data in the form of "direct tracking," and the surface gravimetric data are introduced into the combination as a totally independent data type (i.e., no error correlations between the surface gravity, altimetry, and satellite tracking data are considered), the 70x70 surface gravity normals have to be developed based on gravimetric information independent of both the tracking and altimeter data. This requires the exclusion of any altimeter-derived anomalies from the file used to develop the 70x70 surface gravity normals. The requirement for independence from the tracking data is slightly violated because of the way that "fill-in" anomalies are computed. The specific details of the development of the surface gravity normals are described next.

7.2.2 Data Preprocessing

During the course of the joint project, several preliminary versions of the 1° surface free-air anomaly file were produced and released by NIMA. Although the following discussion applies equally well to any of these versions, the focus in the following sections is on the processing and the results obtained from the final 1° data set. This file is designated "nima.v091296.terr.deg01." Recall from Section 3 that the atmospheric correction has been applied already to the anomalies in this file. Therefore, the following systematic corrections need to be applied to the 1° mean free-air anomalies from this file before these are used to form normal equations for the gravitational potential coefficients [*Pavlis*, 1988]:

1) Ellipsoidal corrections (ε_h, ε_γ, ε_p)

   These correction terms and their numerical evaluation are described in [*Pavlis*, 1988] and [*Rapp and Pavlis*, 1990]. Here, their evaluation was made using the composite model JGM–**2** ($2 \leq n \leq 70$) [*Nerem et al.*, 1994b] augmented with OSU91A ($71 \leq n \leq 180$) [*Rapp et al.*, 1991]. The truncation at $n = 180$ is more than enough to capture the long wavelength information content of the terms. The correction terms were computed initially in the form of 30´x30´ mean values, so that they could be used for the correction of the 30´ data as discussed in Section 8. Simple arithmetic averaging of these 30´ values produced 1° means that were used here (denoted IE_h, IE_γ, IE_p).

2) Analytical continuation (g_1)

   The 1° anomaly data of file "nima.v091296.terr.deg01" are Molodensky free-air values referring to the physical surface of the Earth. The surface gravity normals can be formulated and developed treating the anomalies either as Molodensky free-air values, or as downward continued quantities (to the geoid). Besides the computational advantages of the latter

approach, tests reported by *Rapp et al.* [1991] have indicated that downward continuation tends to yield superior results as judged by comparisons to GPS/leveling-derived geoid heights. As explained in Section 8, three different techniques were implemented and tested for the computation of the analytical continuation terms. The adopted technique is the "gradient solution" to the analytical continuation problem [*Moritz*, 1980, p. 387]. Its implementation requires in principle very detailed gravity data, in lieu of which an approximate result can be obtained if the assumption of linear correlation between the free-air anomaly and the elevation is employed [see also *Wang*, 1988] and detailed elevation data are available. This was done here using the 5´x5´ mean elevations from JGP95E. The global computation of g_1 terms was made initially in terms of 5´x5´ values, using the 1D–FFT approach of *Haagmans et al.* [1993]. Simple arithmetic averaging of these 5´ values produced 1° means that were used here. It should be noted that, in the context of linear theory [*Moritz*, 1980, pp. 339–341], continuation to the geoid was considered equivalent to continuation to the reference ellipsoid. This particular aspect received some attention during the development stages of the project [*Jekeli,* 1995]. Additional theoretical investigation is needed in this area.

3) Removal of high-frequency anomaly contribution (δg^{hf})

The frequency content of the 1° mean anomalies is not restricted to the harmonics being solved for ($n \leq 70$). Rather, it is a function of data density and the roughness of the field, both of which vary considerably in a geographic sense. One way to reduce aliasing of the higher frequency content ($n > 70$) of the data into the estimated harmonics is to remove this component of the signal from the data prior to the normal equation formation [*Pavlis*, 1988]. This approach has been used in the development of surface gravity normals that were used in the OSU91A model [*Rapp et al.*, 1991] and the JGM–1, –2 [*Nerem et al.*, 1994b] and JGM–3 [*Tapley et al.*, 1996] models. The same approach was used here; δg^{hf} was evaluated in terms of 1°x1° mean values by:

$$\overline{\delta g}_{ij}^{hf} = \frac{1}{\Delta \sigma_i} \frac{GM}{(r_i^e)^2} \sum_{n=71}^{360} (n-1)\left(\frac{a}{r_i^e}\right)^n \sum_{m=-n}^{n} \overline{C}_{nm} \cdot \overline{IY}_{nm}^{ij} \qquad (7.2.2–1)$$

where the subscripts (i, j) identify the location of the 1°x1° cell in a two-dimensional array with $i = 0, 1, ..., 179$ and $j = 0, 1, ..., 359$. r_i^e is the length of the geocentric radius vector to the center of the (i, j)th cell and GM the geocentric gravitational constant. In addition:

$$\Delta \sigma_i = \Delta \lambda \int_{\theta_i}^{\theta_{i+1}} \sin \theta d\theta = \Delta \lambda \cdot (\cos \theta_i - \cos \theta_{i+1}) \qquad (7.2.2–2)$$

$$\overline{IY}_{nm}^{ij} = \int_{\theta_i}^{\theta_{i+1}} \overline{P}_{n|m|}(\cos \theta) \sin \theta d\theta \cdot \int_{\lambda_j}^{\lambda_{j+1}} \begin{Bmatrix} \cos m\lambda \\ \sin|m|\lambda \end{Bmatrix} d\lambda \quad \begin{matrix} \text{if } m \geq 0 \\ \text{if } m < 0 \end{matrix} \qquad (7.2.2–3)$$

where θ is geocentric colatitude, λ longitude and $\overline{P}_{nm}$ are the associated Legendre functions of the first kind of degree n and order m. *a* is the scaling parameter associated with the unitless fully normalized harmonic coefficients $\overline{C}_{nm}$. These coefficients were obtained from the quadrature solution V068, which is described in Sections 8.5 and 8.6. The terms δg^{hf} have

a minimum value of –187.4 mGal ($\varphi = 44.5°$, $\lambda = 150.5°$), a maximum of 290.9 mGal ($\varphi = 19.5°$, $\lambda = 204.5°$), and a global area-weighted RMS value of 17.4 mGal.

Jekeli [1996] reviewed the aliasing problem in spherical harmonic analyses. He showed that aliasing can be essentially eliminated if one uses mean values over spherical caps rather than over equiangular cells as is done here. Time and resources did not allow the implementation of his ideas (which would have required the reevaluation of all gravity anomaly predictions), and this possibility had to be left as an item for future work.

4) *Gravity anomaly estimates for unsurveyed areas* ($\overline{\Delta g}^{fi}$)

The file "nima.v091296.terr.deg01" contains 52271 1° mean anomalies covering 87.10 percent of the Earth (this file completely excludes geophysically predicted values). Surface gravity normals can be developed based on this incomplete file [*Pavlis*, 1988]. In such case, however, the 70x70 combination solution tends to exhibit unrealistic oscillations over the areas where surface gravity data are absent and the higher degree part of the field is poorly constrained (unsurveyed land areas or ocean areas not covered by "direct altimeter" data). To circumvent this problem, one can either impose an *a priori* constraint on the combination solution or fill in the areas void of actual gravity observations with some kind of synthetic values. The former approach has the disadvantage that the *a priori* constraint applies globally (not just over the empty areas) and "dampens" the overall power of the field at the higher degrees. This problem was identified in the GEM–T3 model [*Lerch et al.*, 1994]. *Pavlis and Rapp* [1990] proposed the evaluation of fill-in anomalies from the combination of information contained in the low-degree part of a satellite-only model, augmented with the information provided by a model of the topographic–isostatic potential. This approach has been followed in the development of OSU91A and JGM–1, –2 and –3 models. The same general approach is followed here, with specific modifications that are described next.

The file JGP95E was used to develop a spherical harmonic model of the topographic–isostatic potential implied by the Airy–Heiskanen isostatic hypothesis with a constant compensation depth of 30 km. This model is complete to degree and order 360; the detailed formulation used for its development can be found in *Pavlis and Rapp* [1990]. Figure 7.2.2–1 shows the anomaly degree variances implied by this model, along with the corresponding values from the satellite-only solution EGM96S and its error. Around degree 40, the signal variance of EGM96S dips below the noise. Therefore, it was decided to form a composite model with the harmonics of EGM96S from $n = 2$ to $n = 40$, augmented with the topographic–isostatic harmonic coefficients from $n = 41$ to $n = 360$ (the fact that around degree 40 all three curves of Figure 7.2.2–1 intersect is a fortunate coincidence—the spectrum of the composite model does not exhibit a step discontinuity at the cutoff degree). The coefficients of this model are denoted $\overline{C}_{nm}^{ti}$ and the 1°x1° fill-in mean anomalies are computed by:

$$\overline{\Delta g}_{ij}^{fi} = \frac{1}{\Delta \sigma_i} \frac{GM}{(r_i^e)^2} \sum_{n=2}^{70} (n-1) \left(\frac{a}{r_i^e} \right)^n \sum_{m=-n}^{n} \overline{C}_{nm}^{ti} \cdot \overline{IY}_{nm}^{ij} \qquad (7.2.2–4)$$

None of the systematic corrections previously considered applies to ($\overline{\Delta g}^{fi}$). The standard deviation associated with ($\overline{\Delta g}^{fi}$) was set to 18 mGal uniformly for all 1°x1° fill-in values.

This was based on the comparisons reported by *Pavlis and Rapp* [1990, p. 376]. The disadvantage of including the so-computed fill-in anomalies in the file used to form the surface gravity normals is that the independence from the satellite-only solution is now somewhat compromised. The $n \leq 40$ harmonics of EGM96S are used to provide part of the fill-in information. Given the limited area (about 13 percent of the Earth) and the low weight associated with $(\overline{\Delta g}^{\,fi})$, the current approach is considered preferable over the alternative *a priori* constraint.
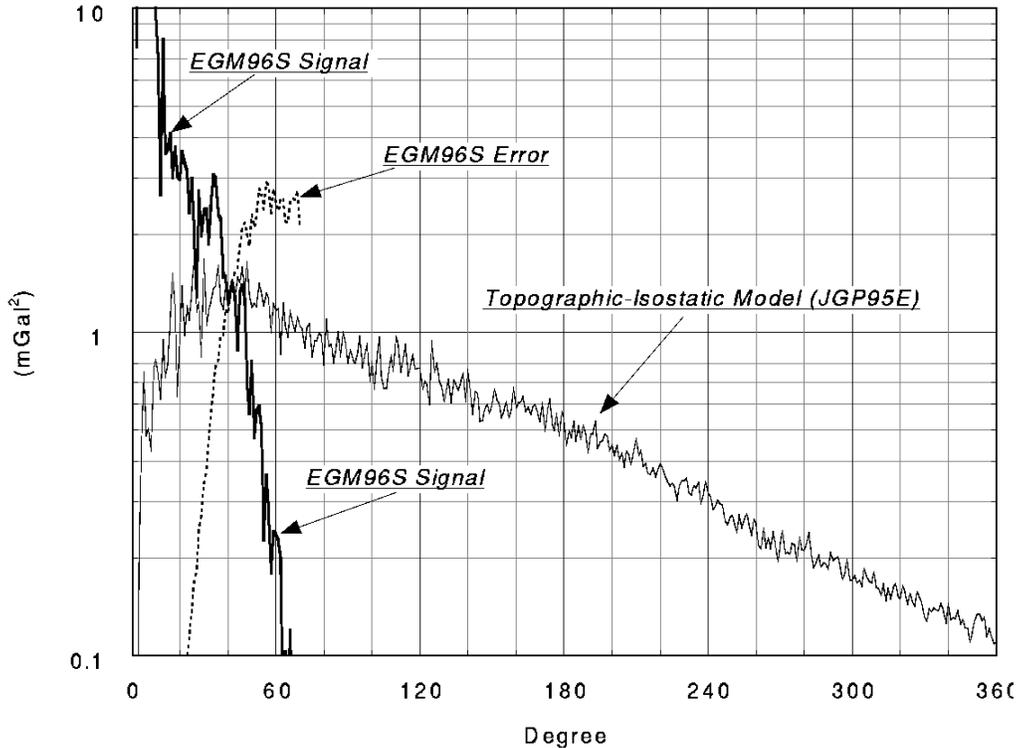
Figure 7.2.2–1. Gravity anomaly degree variances from the EGM96S model and from the topographic–isostatic model.

A complete file (100 percent coverage) of 1° mean values is now constructed as:

$$\overline{\delta g}_{ij} = \begin{cases} \overline{\Delta g}^{obs}_{ij} - \left(IE_h + IE_\gamma + IE_p\right)_{ij} + \left(\overline{g_1}\right)_{ij} - \left(\overline{\delta g}^{hf}\right)_{ij} & \text{observed value} \\ \overline{\Delta g}^{fi}_{ij} & \text{fill in value} \end{cases} \tag{7.2.2–5}$$

where $\overline{\Delta g}^{\,obs}_{ij}$ is the anomaly from file "nima.v091296.terr.deg01." To avoid some overly optimistic standard deviation estimates, the minimum standard deviation associated with $\overline{\Delta g}^{\,obs}_{ij}$ was set to 0.5 mGal. Statistics associated with this file are given in Table 7.2.2–1 (mean and RMS values are area-weighted estimates). Figure 7.2.2–2 shows the geographic distribution of observed and fill-in anomalies.

The combined file of observed and fill-in values is designated "dg60x60.mrgd.ti.v091896.ell" and possesses a mean value of –0.06 mGal, an RMS value of 20.36 mGal, and an RMS standard deviation of ±12.80 mGal. This file is used as input for the normal equation formation.

Table 7.2.2–1. Statistics of the 1°x1° mean anomalies used to form the $N_{max} = 70$ surface gravity normal equations (gravity anomaly units are mGal).

Statistic	Observed Anomalies	Fill-in Anomalies
Number of values	52271	12529
Percentage of Earth´s area	87.10	12.90
Minimum value (φ,λ)	–198.03 (–38.5°, 12.5°)	–51.68 (–73.5°, 195.5°)
Maximum value (φ,λ)	156.94 (–61.5°, 318.5°)	117.60 (–14.5°, 287.5°)
Mean value	–0.04	–0.20
RMS value	21.21	13.20
Minimum σ	0.50	18.00
Maximum σ	47.00	18.00
RMS σ	11.83	18.00
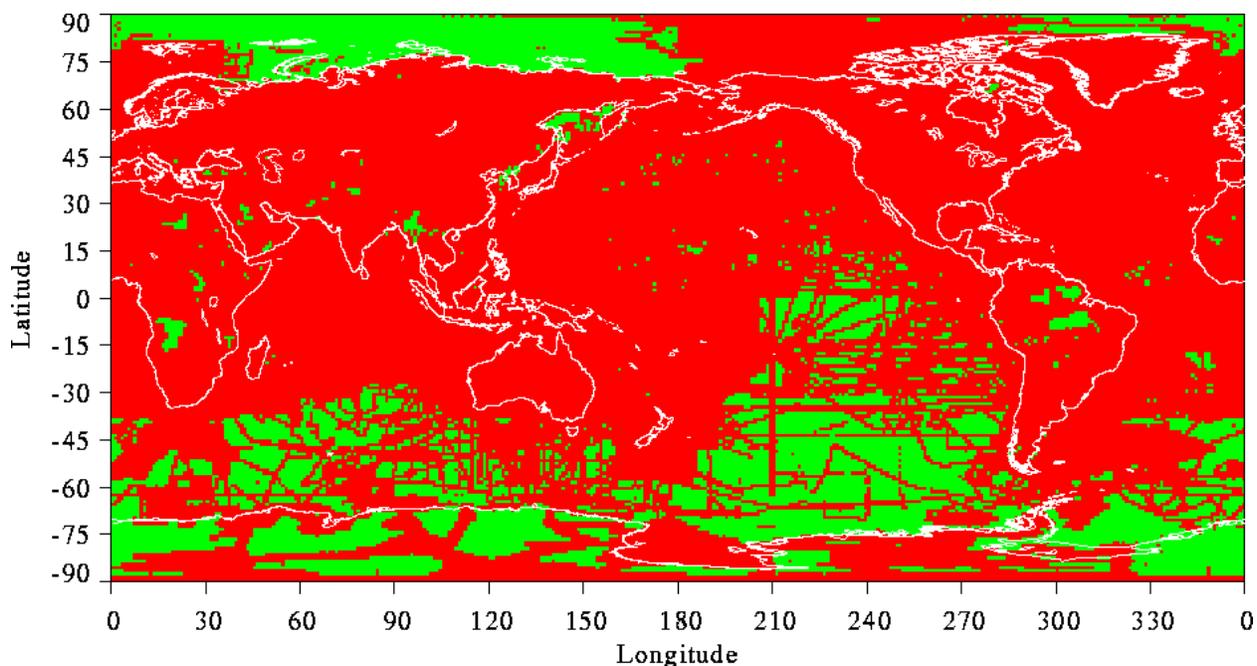
Figure 7.2.2–2. Geographic distribution of 52271 observed (dark) and 12529 fill-in (light) 1°x1° mean anomalies used to develop the surface gravity normal equations.

7.2.3 Normal Equations and Geopotential Coefficients From Surface Gravity Data

The anomaly data $\overline{\delta g}_{ij}$ defined in eq. (7.2.2–5) lead to observation equations for the gravitational coefficients of the form:

$$v_{ij} = \frac{1}{\Delta\sigma_i}\frac{GM}{(r_i^e)^2}\sum_{n=0}^{70}(n-1)\left(\frac{a}{r_i^e}\right)^n\sum_{m=-n}^{n}\overline{C}_{nm}^T\cdot\overline{IY}_{nm}^{ij}-\overline{\delta g}_{ij} \tag{7.2.3–1}$$

where v_{ij} is the residual associated with the observation $\overline{\delta g}_{ij}$ and $\overline{C}_{nm}^T$ identifies the (adjusted) coefficients obtained on the basis of the terrestrial gravity data alone (even zonal coefficients are remainders after subtraction of the coefficients of the normal potential). The degree summation in (7.2.3–1) starts from $n = 0$ (and excludes $n = 1$ terms); this is because the discrete 1° values give rise to covariances between $\overline{C}_{oo}^T$ and the rest of the coefficients. These covariances have to be accounted for when the normal equations are formed [*Pavlis*, 1988]. In vector-matrix form, eq. (7.2.3–1) reads:

$$\mathbf{V} = \mathbf{A}\cdot\hat{\mathbf{X}} - \mathbf{L_b} \tag{7.2.3–2}$$

where $\mathbf{A}$ is the design matrix, $\hat{\mathbf{X}}$ the vector containing $\overline{C}_{nm}^T$, $\mathbf{L_b}$ the vector of observations $\overline{\delta g}_{ij}$, and $\mathbf{V}$ the vector of residuals v_{ij}. Minimization of the (squared) weighted norm of residuals $\mathbf{V^TPV}$, subject to the condition (7.2.3–2), yields the normal equation system:

$$\mathbf{A^TPA}\cdot\hat{\mathbf{X}} = \mathbf{A^TPL_b} \tag{7.2.3–3}$$

where the weight matrix $\mathbf{P}$ is defined by:

$$\mathbf{P} = \sigma_o^2\,\Sigma_{Lb}^{-1} \tag{7.2.3–4}$$

with σ_o^2 being the *a priori* variance of unit weight (taken here to be 1) and Σ_{Lb} the error covariance matrix of the observations. The least-squares estimate of $\hat{\mathbf{X}}$ is given by:

$$\hat{\mathbf{X}} = \left(\mathbf{A^TPA}\right)^{-1}\mathbf{A^TPL_b} \tag{7.2.3–5}$$

The *a posteriori* variance of unit weight is:

$$\hat{\sigma}_o^2 = \frac{\mathbf{V^TPV}}{d.f.} \tag{7.2.3–6}$$

where *d.f.* are the degrees of freedom. The error covariance matrix of the estimates $\hat{\mathbf{X}}$ is:

$$\Sigma_{\hat{X}} = \hat{\sigma}_o^2\left(\mathbf{A}^T\mathbf{PA}\right)^{-1} \tag{7.2.3–7}$$

The proper combination of the surface gravity normal equations with the corresponding normals from the analysis of tracking and altimeter data depends critically on the reliability of the error covariance matrix Σ_{Lb}. This matrix should reflect the accuracy of the surface gravity data. The surface gravity data are accompanied by error estimates, but these are mostly measures of the data *precision*, rather than their *accuracy*. These estimates do not account for long wavelength systematic errors (e.g., vertical datum inconsistencies), which affect surface gravity data [*Heck*,

1990]. Systematic effects that are omitted in the mathematical model (7.2.3–1) result in a "true" Σ_{Lb} that is full. Estimating the appropriate correlations requires information about the gravity data that often is not available (e.g., the vertical datum to which each anomaly refers and the expected offsets between the various datums). Furthermore, considering a full Σ_{Lb} in the modeling exceeds current computational capabilities (for 1° data Σ_{Lb} would be a symmetric matrix of dimension 64800). To overcome these limitations, *Rapp and Cruz* [1986] implemented a modification of the error variances of the gravity anomaly data. The modification was based on the comparison of the coefficients and their formal errors as obtained from surface gravity data alone, with corresponding values from a satellite-only solution. Their technique is similar to the calibration technique of *Lerch* [1991]. This technique attempts to compensate for a colored (red) error spectrum, with a predominantly white error model with larger error variance. Its main disadvantage is that by rescaling the anomaly error variances and considering a diagonal Σ_{Lb}, one affects the propagated accuracy of $\overline{C}_{nm}^T$ over the entire bandwidth of the spectrum—not just the long wavelength portion of it. This tends to give too pessimistic error estimates for the higher degree coefficients, a problem that was already identified in the OSU89A/B models [*Rapp and Pavlis*, 1990]. Despite its limitations, this procedure has enabled meaningful low-degree (e.g., 36, 50, or 70) combination solutions with realistic error estimates to be developed, such as OSU91A, GEM–T3, and the JGM series of models. The same procedure was followed here. Denoting by σ_{ij}^{0} the original standard deviation and by σ_{ij}^{m} the modified one, we impose the condition:

$$\max(8,2\sigma_{ij}^{o}) \leq \sigma_{ij}^{m} \leq \min(16,2\sigma_{ij}^{o}) \tag{7.2.3–8}$$

The diagonal elements of Σ_{Lb} are then set to $(\sigma_{ij}^{m})^2$. The restriction of the range of σ_{ij}^{m} between 8 and 16 mGal is imposed so that a weight ratio of 4:1 is achieved between the best and worst data. The RMS modified standard deviation is 13.58 mGal, so the overall "strength" of the original data is fairly well preserved.

According to the above, normal equations were formed and the corresponding terrestrial-only solution $\overline{C}_{nm}^T$ was obtained (designated 'SG.v008'). Statistics related to this solution are given in Table 7.2.3–1. The geographic location of 9173 residuals exceeding in magnitude 7 mGal is shown in Figure 7.2.3–1. It is important to recognize that the residuals from the terrestrial-only solution are just a measure of the "goodness of fit" of $\overline{C}_{nm}^T$ to the input data. Any signal present in the data that cannot be accommodated by an $N_{max} = 70$ spherical harmonic expansion will manifest itself as a residual in this type of analysis. In Figure 7.2.3–1, large residuals over the ocean areas are also related to the filtering process. The solution V068, which was used to evaluate δg^{hf}, uses altimetry-derived anomalies over most of the ocean areas (see Section 8). The residuals observed in Figure 7.2.3–1 are (in part) a measure of the difference in the $n>70$ part of the spectrum between the altimetry-derived and the shipborne data. Over the majority of land areas where V068 uses data compatible to those used here, no large residuals are observed.

Since any signal or systematic error that can be described by the $N_{max} = 70$ expansion will be absorbed in $\overline{C}_{nm}^T$, thus leaving no residual trace, the quality of the surface gravity solution and the suitability of the weighting scheme employed have to be assessed through comparisons with independent estimates of the harmonic coefficients. To this end, SG.v008 was calibrated against

the satellite-only solution EGM96S in two ways: (a) As independent solutions and (b) by adding the surface gravity normals to those of EGM96S (without any *a priori* constraint) and performing a subset solution calibration [*Lerch*, 1991]. Figure 7.2.3–2 shows the calibration factors per degree from these two cases. Over all degrees, (a) yields a $\bar{k} = 1.056$ and (b) a $\bar{k} = 1.074$. Figure 7.2.3–2 shows that the two methods yield very similar results; some differences at the higher degrees may be related to the *a priori* constraint, which is present in (a) but absent from (b). Although the average calibration factors indicate that, in an overall sense, the surface gravity data are weighted appropriately, the large *k* values at the low degrees (indicating too high a weight for the surface gravity) are of concern. This is the part of the spectrum where surface gravity is most vulnerable to unmodeled systematics [*Laskowski*, 1983]. If introduced in the combination solution with too high weight, the long wavelength accuracy of the combined model may be degraded. On the other hand, since we have no way of variable (by degree) weighting, any downweighting of the surface gravity will affect also the shorter wavelengths where the calibration factors indicate that surface gravity is well weighted. Furthermore, downweighting the surface data causes the estimated uncertainties of the high-degree coefficients, which are highly dependent on this information, to be proportionately pessimistic. A compromise solution was implemented whereby we retain the current surface gravity weights but exclude from the combination solution any contribution from surface gravity for $n \leq 5$ (thus avoiding *k* values of 2.5 or higher). Implicitly, this method considers any signal recovered from surface gravity for $n \leq 5$ to be purely of nongravitational origin (this approach was also implemented in the JGM–1, –2, and –3 models' development). This is an extreme consideration. Future solutions can likely benefit from a more appropriate modeling of systematic errors in surface gravity data bases and from improved weighting techniques.

Table 7.2.3–1. Statistics of the terrestrial-only gravitational solution
(gravity anomaly units are mGal).

Statistic	Value
Number of observations	64800
Number of unknowns	5038
Degrees of freedom	59762
Minimum residual (φ,λ)	–107.16 (–61.5° , 318.5°)
Maximum residual (φ,λ)	173.89 (–38.5°, 12.5°)
Mean residual	–0.17
RMS residual	6.23
$\hat{\sigma}_o^2$	0.24
Number of $|\text{residual}| > 7$ mGal	9173
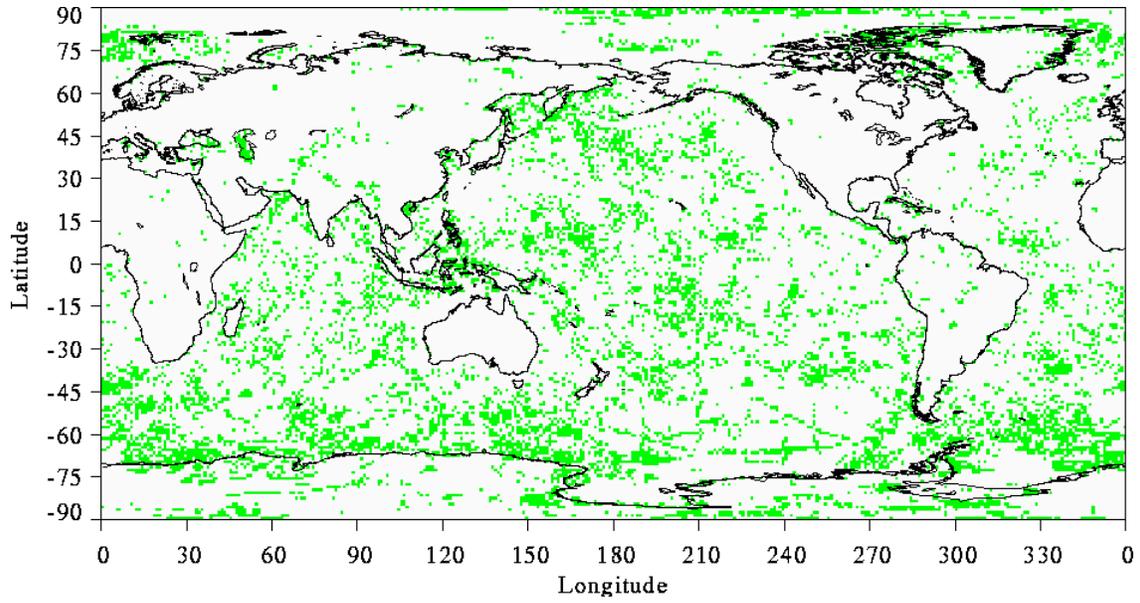
Figure 7.2.3–1. Geographic distribution of 9173 residuals from the surface-gravity-only solution SG.v008 that exceed 7 mGal in magnitude.

Independent Solutions: EGM96S vs. SG.v008 (solid line)

Subset Solutions: (EGM96S + SG.v008) vs. SG.v008 (dotted line)
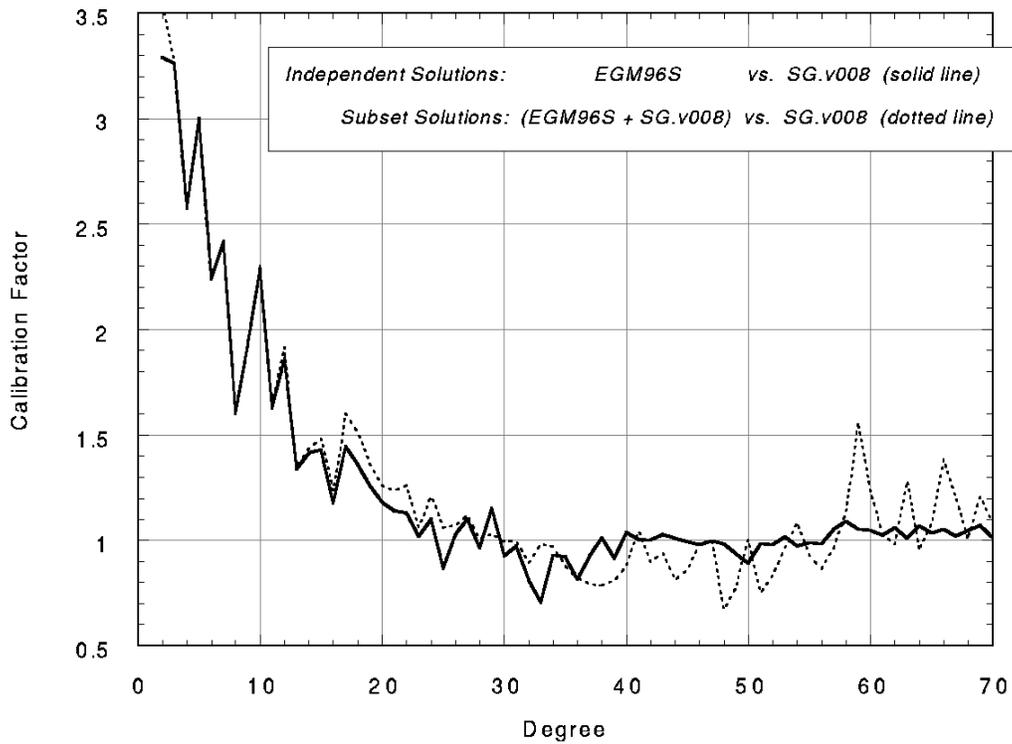
Figure 7.2.3–2. Calibration factors per degree from the independent and subset calibrations of the surface gravity solution.

7.3   Combination Model Development

7.3.1   The Preliminary Project Combination Models: A Summary

Two interim project combination models received heavy public exposure. These models include the PGS5741 combination model presented at the IUGG in Boulder, Colorado, in 1995, and the PGS6399 (EGM–X02 to degree 70), which became part of one of the models released to the Special Working Group (see Section 9) in April 1996. We summarize these models so that the development of the final combination model PGS7337B can be placed in its proper context.

7.3.1.1 The IUGG Combination Model: PGS5741

The IUGG combination model was based on the PGS5737 satellite-only model (discussed in Section 6.3.1). It included altimetry from TOPEX/POSEIDON (T/P), GEOSAT, SEASAT, and GEOS–3. Normal equations for 1°x1° surface gravity were also included based on the October 1990 OSU data base and received a normal equation scale factor of 0.25, corresponding to a downweighting of the surface gravity data by a factor of 4, as in JGM–1 and JGM–2. The altimeter data did not include the same corrections as the final project model PGS7337B. Specifically, they relied on OSU91A through degree 360 for the high-degree geoid correction ($h_{\Delta N}$ from eq. (7.1.1–2), and pre-T/P era tide models [i.e., *Schwiderski*, 1980, 1981] for the ocean tide correction (ζ_t from eq. [7.1.1–2]). The dynamic ocean topography (DOT) solutions for the static component $\bar{\zeta}$ were estimated through degree 15 for GEOSAT, SEASAT, and GEOS–3, and through degree 20 for T/P. A time variable, $\zeta(t)$, 10x10 solution was also made for T/P, which included annual and semiannual terms. Table 7.3.1.1–1 summarizes the altimetry data used in the PGS5741 solution. The constraint used to condition the solution was derived from *Marsh et al.* [1990].

Table 7.3.1.1–1. Summary of altimetry data included in the PGS5741 combination model.

Spacecraft	Period	Observations	$\hat{\sigma}$ (m)	$\bar{\zeta}$	$\zeta(t)$
T/P	Cycles 16–47	1844323	2.23	20x20	10x10
GEOSAT	November 1986–January 1987	277648	4.17	15x15	none
SEASAT	All Available	92499	3.53	15x15	none
GEOS–3	All Available	200862	5.77	15x15	none

7.3.1.2 The April 1996 Combination Model: PGS6399

The April 1996 combination model, PGS6399, was based on the PGS6394 satellite-only model, discussed in Section 6.3.3. Thus, the new combination model differed from PGS5741 in that new satellite tracking data normal equations had been added (from EP/EUVE GPS, GPS/MET, HILAT, RADCAL, D1–D, D1–C), and the EP/EUVE TDRSS normal equations had been

updated. The surface gravity normal equations now relied on the new 30'x30' data provided by NIMA, rather than using exclusively the data from the OSU October 1990 data base. In addition, the surface gravity data received their full weight ($w_n = 1.0$), and a separate set of 5x5 geopotential coefficients was adjusted for the surface gravity data. The direct altimeter data and the weights that were applied on these data were the same as in PGS5741 (see Table 7.3.1.1–1). The PGS6399 low-degree combination model was combined with the V058 quadrature solution through degree 360 to form the EGM–X02 solution, released for evaluation to the Special Working Group led by Professor Michael Sideris from the University of Calgary (see Section 9).

7.3.1.3 An Evaluation of the Preliminary Combination Models PGS5741 and PGS6399

We review briefly, in Table 7.3.1.3–1, the orbit tests that were performed using the SLR satellites. The results for the PGS5741 and PGS6399 models are compared with the results for JGM–2 and –3. The results for the final combination model, PGS7337B (discussed in detail in Section 10), are repeated here from Table 10.1.1.1–1. On these orbit tests, we see a mixture of results. Starlette has improved over the JGM–2 and –3, according to these tests, but Ajisai shows no change.

Table 7.3.1.3–1. SLR orbit test residuals using the preliminary combination models (set-1).

Gravity	Tides	RMS of Fit (cm)						
		Multiple arc					Single arc	
		LAGEOS[1]	LAGEOS[2]	LAGEOS–2[2]	Starlette	Ajisai	Stella	GFZ–1
JGM–2	PGS4846X	3.13	3.14	3.23	9.01	7.50	115.46	26.49
JGM–3	PGS4846X	3.08	3.10	3.16	8.97	7.46	23.13	26.23
PGS5741	PGS5741	3.14	2.89	3.31	8.02	7.51	17.91	16.36
PGS6399	PGS6399	3.24	2.92	3.31	7.93	7.57	23.00	10.81
PGS7337B	PGS7337B	3.19	2.87	3.38	7.92	7.34	10.26	11.38

[1] Sa, Ssa tides not adjusted   [2] Sa, Ssa tides adjusted as global parameters.

The ERS–1 SLR and altimetry test results for the preliminary models are summarized in Table 7.3.1.3–2. For this single arc of ERS–1 data, there has been an improvement in the fit to both the SLR data and the altimeter data. The ERS–1 data were not included in these preliminary models, so this arc is an independent test of their performance. Even for the later combination model, PGS6399, there was only a modest reduction in the weighted RMS (WRMS) of fit to the altimeter data (from 9.10 with JGM–3 to 8.52 with PGS6399), corresponding to an overall improvement in the modeling of the marine geoid of 8.85 cm (for a data uncertainty of 3 m).

Table 7.3.1.3–2. ERS–1 single-arc orbit test weighted RMS residuals for the preliminary combination models. The altimetry data uncertainty is 3.0 m, and the SLR data uncertainty is approximately 1.12 m.

Gravity Model	Tide Model	Weighted Residual	
		SLR	Altimetry
JGM–2	PGS4846X	10.54	8.97
JGM–3	PGS4846X	11.81	9.10
PGS5741	PGS5741	8.90	8.61
PGS6399	PGS6399	8.29	8.52
PGS7337B	PGS7337B	7.87	7.54

7.3.2 The Path to the Final Project Combination Model

After the creation of the PGS6399 (EGM–X02) combination model, it was apparent that the performance of the models over land areas was excellent, due to the inclusion of the new 30'x30' NIMA data, but that the performance over the oceans offered only a small improvement over JGM–3. For instance, Table 7.3.2–1 shows comparisons of project combination models using 2 years of T/P altimeter data, and the POCM–4B ocean circulation model from *Rapp* [1996] (these comparisons are discussed in detail for the final combination model in Section 10.1.5.1, and the methodology is reviewed in Section 5.5).

Table 7.3.2–1. Difference between dynamic ocean topography estimates, using 2 years of T/P data, from the combination models and the POCM–4B model.

Model	Comment	Cumulative RMS Difference to Degree n (cm)	
		$n = 14$	$n = 24$
OSU91A		15.5	16.7
JGM–3/OSU91A		12.4	13.8
V037	IUGG 1995 quadrature model	13.7	17.2
PGS5741/OSU91A	IUGG 1995 combination model with OSU91A for n>70	13.1	14.7
PGS5741/V037	IUGG 1995 combination model with V037 for n>70	11.8	13.4
JGM–3/V037	JGM–3 with V037 for n>70	12.6	14.2
V058 (to $n = 360$)	April 1996 quadrature model	13.0	16.7
PGS6399/V058	April 1996 combination and quadrature solution (released as EGM–X02)	12.1	13.8

The first observation is that the project combination models combined with the appropriate quadrature model (PGS5741 with V037, and PGS6399 with V058) are not really an improvement in the ocean domain over JGM–3 combined with OSU91A above degree 70. For instance, at degree 14, the cumulative RMS difference for JGM–3/OSU91A is 12.4 cm, while for PGS6399/V058 the cumulative RMS difference is 12.1 cm. This is not meant to imply that the

high-degree quadrature solutions are not an improvement since the cumulative difference at degree 14 is 15.5 cm with OSU91A and 13.0 cm with V058. It is the performance of the combination models over the oceans that is the issue.

As of April 1996, the normal equations for direct altimetry were more than 2 years old. These normal equations relied on OSU91A for the correction of the high-degree (beyond degree 70) geoid and the Schwiderski tide model to remove the geometric effect of the tides. A reiteration of the processing of the direct altimetry was essential in order to take advantage of the new project-derived high-degree geoid models, as well as the tide models based on T/P data. These new tide models, developed by many different groups and institutions, superseded the much earlier work of Schwiderski. To that end, the project embarked on a complete reprocessing of the altimetry including T/P, GEOSAT, and ERS–1. The details of the final reprocessing of the data are given in Section 7.1. Three important changes included (1) The use of the quadrature model V058 (EGM–X04) to degree 460 to correct for the high-degree geoid, (2) the use of the Ocean Pathfinder (T/P era) tides derived from *Schrama and Ray* [1994] and *Le Provost et al.* [1994], and (3) a shallow sea mask of 200 m, rather than 1000 m, on the T/P and ERS–1 data (justified because of the improvement in the tide models). In addition, the earlier versions of the GEOSAT altimeter data processing had relied on the ionosphere correction provided on the geophysical data records (GDR) [*Cheney et al.*, 1991] from *Klobuchar* [1987], whereas in this reiteration the newer IRI95 model [*Bilitiza et al.*, 1994] was used. The SEASAT altimeter data were omitted from the final combination solution since delivery of the final project combination model was set for September 1996, and the schedule did not permit a thorough validation of the reprocessing of these data.

The development of the final combination solution PGS7337B was a multistep process. Many interim solutions were developed to evaluate the quality of the dynamic ocean topography solutions, determine the relative weights of the ERS–1, T/P, and GEOSAT data, as well assess the performance of the models on land with GPS/leveling data. The significant milestones are summarized in the following sections.

7.3.2.1 Validation of the "New" T/P Normal Equations and Selection of the Degree of Truncation for the Dynamic Ocean Topography Solution

The first test solutions that included the new T/P altimeter data normal equations were PGS7271 and PGS7272. These models were based on the updated satellite-only model PGS7270D, discussed in Section 6, and the normal equations for the surface gravity that excluded the altimeter-derived gravity anomalies. The satellite-only model upon which these models were based had itself undergone considerable evolution since April 1996, since the new normal equations for the GPS and TDRSS data were included and a complete calibration of the satellite tracking data had been completed. The surface gravity normal equations were identical to those used in the April 1996 solutions with small changes made in some regions to add some new 30′x30′ gravity anomalies that had become available. The dynamic ocean topography comparisons from *Rapp* [*personal communications*, 1996] are presented in Table 7.3.2.1–1. At degree 14, the cumulative RMS difference has decreased from 12.1 cm with PGS6399/V058 to 9.9 cm, suggesting an improvement in the modeling of the marine geoid of 7.1 cm. This apparent

marine geoid improvement can be attributed to both the altimeter data reprocessing and the updated satellite-only model.

Table 7.3.2.1–1. Difference between dynamic ocean topography estimates, using 2 years of T/P data, from the PGS7271 and PGS7272 combination models and the POCM–4B model.

Model	Comment	Cumulative RMS Difference to Degree n (cm)	
		$n = 14$	$n = 24$
PGS7271/V037	$\bar{\zeta}$ solution to 30x30	9.9	11.7
PGS7272/V037	$\bar{\zeta}$ solution to 20x20	9.9	11.5

The results of the dynamic ocean topography tests shown in Table 7.3.2.1–1 do not distinguish between the degree of truncation of the model. The predicted geoid errors for these two models are summarized in Table 7.3.2.1–2 (the summary values are computed as an RMS of the 1° gridded point values in the region of interest, with zero meters elevation used to differentiate between land and water). The geoid over the oceans, in the region under the T/P ground track, is 12.7 cm with PGS7271, and 11.6 cm with PGS7272. So, not surprisingly, the geoid errors are larger when the DOT solution is truncated at a higher degree. The geoid error projections over the oceans decrease from 122 cm in the satellite-only model, PGS7270D, to 51 cm in PGS7275 (the satellite-only plus surface gravity solution, as subset of PGS7271 and PGS7272), to 13.6 in PGS7271 and 12.7 cm with PGS7272.

Table 7.3.2.1–2. Geoid undulation error projections from the full 70x70 covariances for the T/P altimeter test combination models (PGS7271 and PGS7272).

Geopotential	RMS Geoid Undulation Error (cm)					
	Global	Land		Water		
		All	USA	All	$|\varphi|<67$	$66<|\varphi|<82$
PGS7270D[1]	121.9	121.5	123.3	122.0	122.2	117.6
PGS7271	19.5	29.3	27.5	13.6	12.8	23.9
PGS7272	18.9	29.0	27.1	12.6	11.6	23.6
PGS7275[2]	46.9	34.3	31.3	51.1	52.3	27.8

1. satellite-only model   2. satellite plus surface gravity model

The paramount question is to what extent the separability between the geoid and the sea surface topography has been achieved. The separability between these quantities comes about in three ways: (1) Through the strength of the satellite-tracking data in the model, (2) through the application of a power law constraint that helps to condition the static portion of the dynamic ocean topography ($\bar{\zeta}$) solution in regions where it is not defined (cf. over land), and (3) through

the inclusion of marine gravimetry. The $\bar{\zeta}$ solutions in the JGM–2 model were only to degree and order 15 (albeit for satellites other than T/P). Even though the quality and strength of the satellite tracking data have improved with the addition of the new continuous (GPS and TDRSS) data sets, it was felt that doubling the maximum size from degree 15 to degree 30 would be unreasonable. The correlations between the geoid and the $\bar{\zeta}$ solutions were computed for both the PGS7271 and the PGS7272 solutions. The correlations were evaluated between the geoid and the 20x20 $\bar{\zeta}$ solution for PGS7272, and between the geoid and the 30´x30´ $\bar{\zeta}$ solution for PGS7271 on a 1°x1° grid. The average correlations of these gridded values were computed over the ocean domain of ±66° and ±28.5°. The results are presented in Table 7.3.2.1–3. The correlations will approach –1 as the degree of separability between the geoid and the $\bar{\zeta}$ solution decreases. The global correlations are higher for PGS7271 than PGS7272, supporting the assertion that estimation of terms higher than degree 20 is not justified for the current set of normal equations and combination solutions.

Table 7.3.2.1–3. Average correlations between the geoid and the T/P dynamic ocean topography solutions from combination solutions evaluated on a 1° x 1° grid over the ocean domain.

Gravity Model	Comment	Correlation $|\varphi| < 28.5°$	Correlation $|\varphi| < 66°$
PGS7271	$\bar{\zeta}$ solution to 30x30	−0.612	−0.595
PGS7272	$\bar{\zeta}$ solution to 20x20	−0.486	−0.431

Finally, the power spectrum of the dynamic ocean topography of the PGS7271 and PGS7272 solutions is compared with the geoid error from the PGS7271 solution in Figure 7.3.2.1–1. The RMS geoid error per degree intersects the dynamic topography signal at roughly degree 17 to 18, suggesting that truncation of the $\bar{\zeta}$ solution at degree 20 rather than degree 30 is preferable.

7.3.2.2 Calibration of the TOPEX/POSEIDON Altimeter Data

The PGS7271 and PGS7272 were calibrated with a subset solution that excluded the altimeter data (PGS7275). The calibrations for the PGS7272 model, as well as the RMS differences in the coefficients and coefficient standard deviations, are depicted in Figure 7.3.2.2–1. The average calibrations by degree and order are summarized in Table 7.3.2.2–1. The calibrations are less than unity, suggesting—as far as this test is concerned—that the altimeter data are conservatively weighted. However, as discussed in Section 6, the calibration method using subset solutions considers only the coefficient standard deviations and ignores the correlations in the covariance matrix, which may be significant for normal equations containing direct altimetry. The calibrations are with respect to an effective sigma of 2.23 m for the T/P altimeter data. For comparison, the T/P-DORIS data have an effective $\sigma = 1.58$ cm/s, and the T/P-SLR data have an effective $\sigma = 2.50$ m.
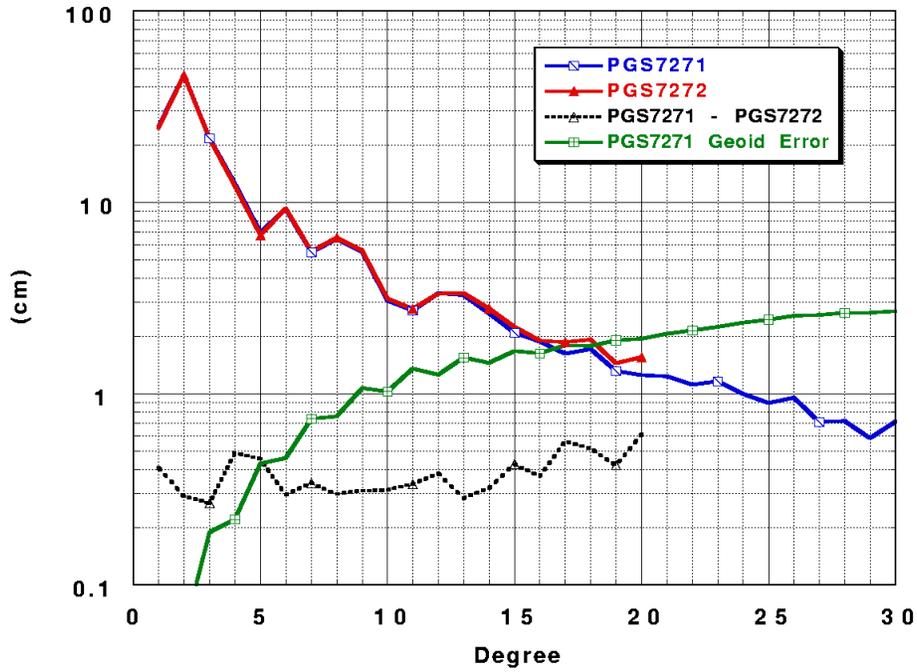
Figure 7.3.2.1–1. Comparison of the dynamic ocean topography power spectra from the PGS7271 and PGS7272 combination solutions, both containing T/P altimetry, with the RMS geoid error per degree for the PGS7271 solution.
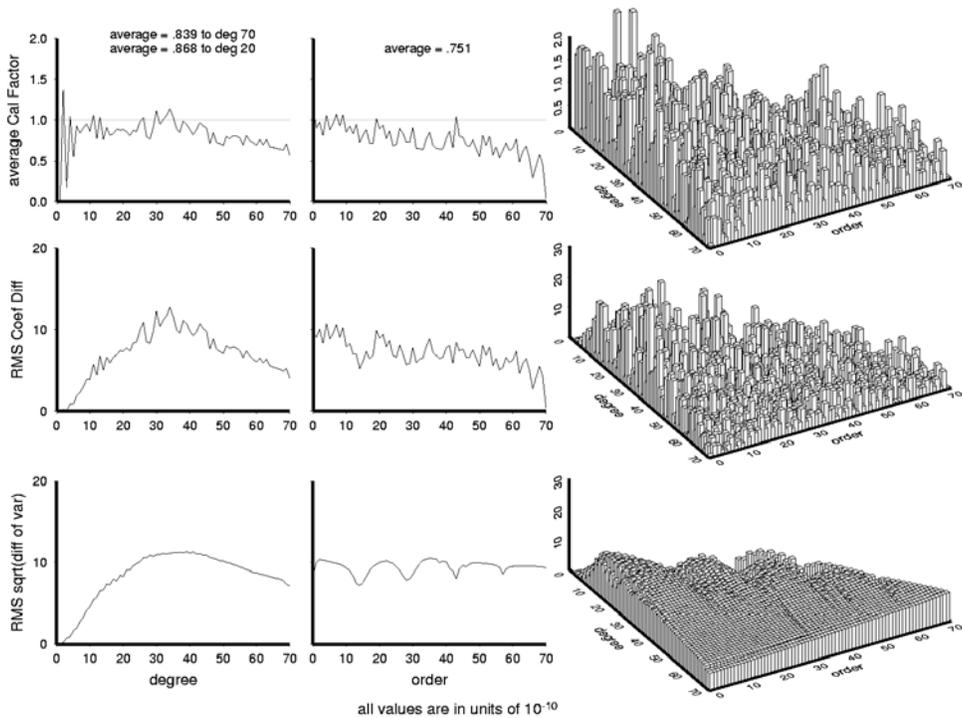
Figure 7.3.2.2–1. Calibration of the T/P altimeter data ($\sigma = 2.23$ m) with a subset solution (PGS7275) that includes only the surface gravity data and the satellite tracking data.

Table 7.3.2.2–1. Summary of T/P altimeter data calibrations ($\hat{\sigma} = 2.23$ m).

Gravity Model	Comment	Average Calibration Factors $\overline{k}_t$		
		$n \le 70$	$n \le 20$	$m \le 70$
PGS7271	$\overline{\zeta}$ solution to 30x30	0.826	0.852	0.744
PGS7272	$\overline{\zeta}$ solution to 20x20	0.839	0.868	0.751

7.3.2.3 Selection of the ERS–1 Altimeter Data Weights

Section 7.1.4.3 discussed the data weighting used in the ERS–1 orbit determination and the normal equation generation. To choose the appropriate weight for the ERS–1 SLR and altimeter data, three combination models were created. In this process, the nominal relative weighting between the SLR and altimeter data was preserved, while the weight of the entire combined set of ERS–1 normal equations was adjusted. For each test model, a complete joint T/P–ERS–1 DOT solution to 30x30 was computed, and compared with the T/P-only solution from PGS7271. The geoid differences over the latitudes of the T/P ground track, the changes in the static topography, $\overline{\zeta}$, for latitudes within ±66° were computed, and the calibration factors of the ERS–1 SLR and altimeter data with respect to the PGS7271 solution were examined. The primary design criterion was that the combination model $\overline{\zeta}$ solution determined using only the T/P altimetry data (from PGS7271) and that determined using both T/P and ERS–1 altimetry data should not differ by more than 2 cm RMS in the ocean areas between ±66° latitude.

Table 7.3.2.3–1 lists the results of several test solutions, all of which satisfied the design criterion. For a data weight $\hat{\sigma}$ of 4.13 m (PGS7277), the RMS $\overline{\zeta}$ difference was 0.64 cm, with only 0.75 cm RMS change in the geoid. The geoid changes differences between the T/P altimetry-only model, PGS7271, and the model including ERS–1, PGS7277, are depicted in Figure 7.3.2.3–1. ERS–1 alters the geoid (and $\overline{\zeta}$) determinations minimally where T/P altimeter data are present ($|\varphi| \le 66°$). In contrast, at the higher latitudes ($66° < |\varphi| < 82°$), the changes in the geoid were 7.38 cm RMS, with maxima of –59 cm (at 75° N 358°E) and 39 cm (at 72° N 11°E) occurring between Scandinavia and Greenland.

Table 7.3.2.3–1. RMS changes in the geoid and static portion of the dynamic ocean topography ($\overline{\zeta}$) between T/P–ERS–1 solutions and the T/P altimeter solution PGS7271.

Gravity Model	ERS–1 $\hat{\sigma}$ (m)		$\Delta\overline{\zeta}$ (cm)	Ocean Geoid Change (cm)		Total Geoid Change (cm)	
	SLR	Alt.	oceans ±66°	$|\varphi| < 66°$	$66° < |\varphi| < 82°$	$|\varphi| < 66°$	$66° < |\varphi| < 82°$
PGS7276	3.16	5.84	0.39	0.44	7.24	0.50	5.23
PGS7277A	2.58	4.77	0.52	0.61	8.81	0.71	6.47
PGS7277	2.23	4.13	0.64	0.75	10.01	0.87	7.38
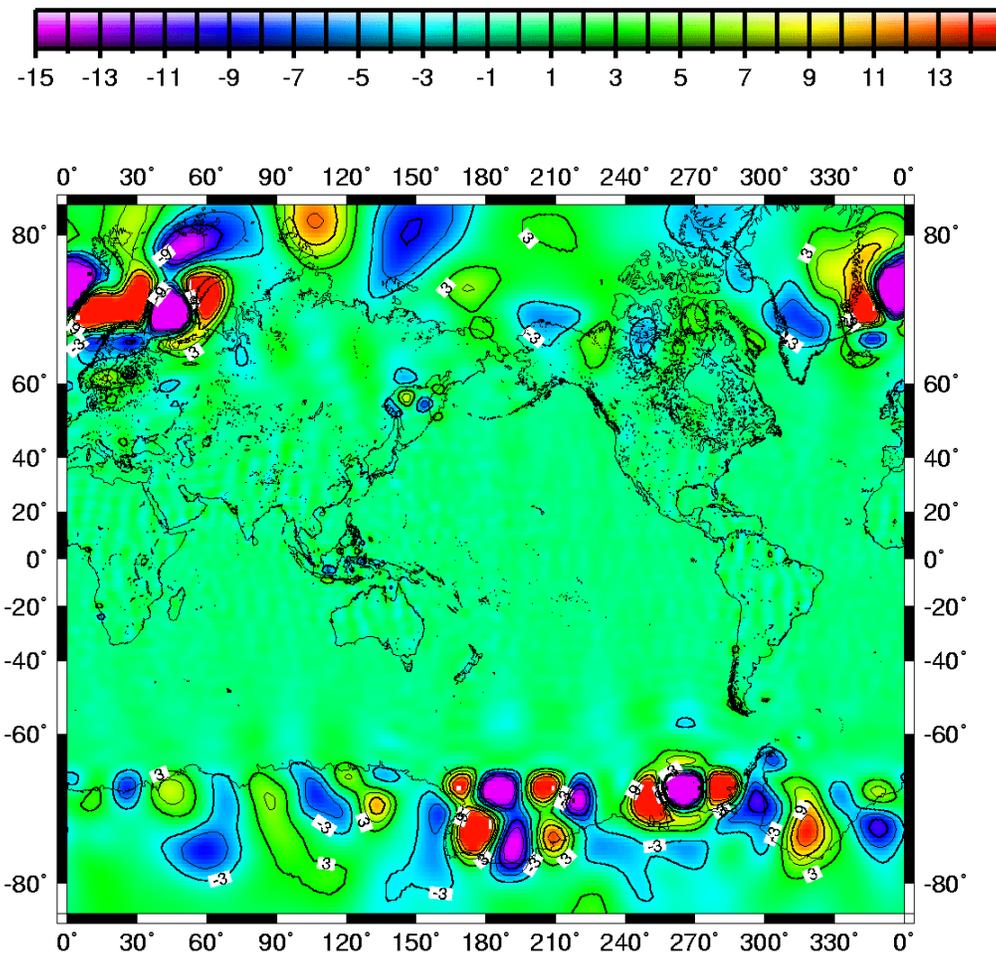
Figure 7.3.2.3–1. Geoid differences between the PGS7271 and PGS7277 combination models, illustrating the effect of combining the ERS–1 SLR and altimeter data with T/P. ERS–1 effective σ = 2.23 m for the SLR data, and 4.13 m for the altimeter data. ERS–1 is, thus, downweighted with respect to T/P, and alters the geoid and static DOT determinations minimally where T/P altimeter data are present (±66°), but has the intended influence outside of this region. Contour interval is 3 cm.

The calibration factors for these test models were also examined, with respect to the PGS7271 combination model, and are summarized in Table 7.3.2.3–2. The RMS changes in the coefficients, and coefficient standard deviations due to the addition of the ERS–1 data, are no more than $1\mathrm{x}10^{-10}$ (see Figure 7.3.2.3–2). The ERS–1 data weight seems high enough in the PGS7277 model to have a significant influence on the solution at the high latitudes, but conservative enough not to affect the solution where the T/P altimeter data are present. The PGS7277 data weights for ERS–1 were adopted for all subsequent combination models, including EGM96 (PGS7337B).

Table 7.3.2.3–2. Summary of ERS–1 vs. T/P calibrations.

Gravity Model	ERS–1 σ (m)		Average Calibration Factors $\bar{k}_t$		
	SLR	ALT	$n \le 70$	$n \le 20$	$m \le 70$
PGS7276	3.16	5.84	0.579	0.606	0.288
PGS7277A	2.58	4.77	0.625	0.669	0.345
PGS7277	2.23	4.13	0.656	0.713	0.375
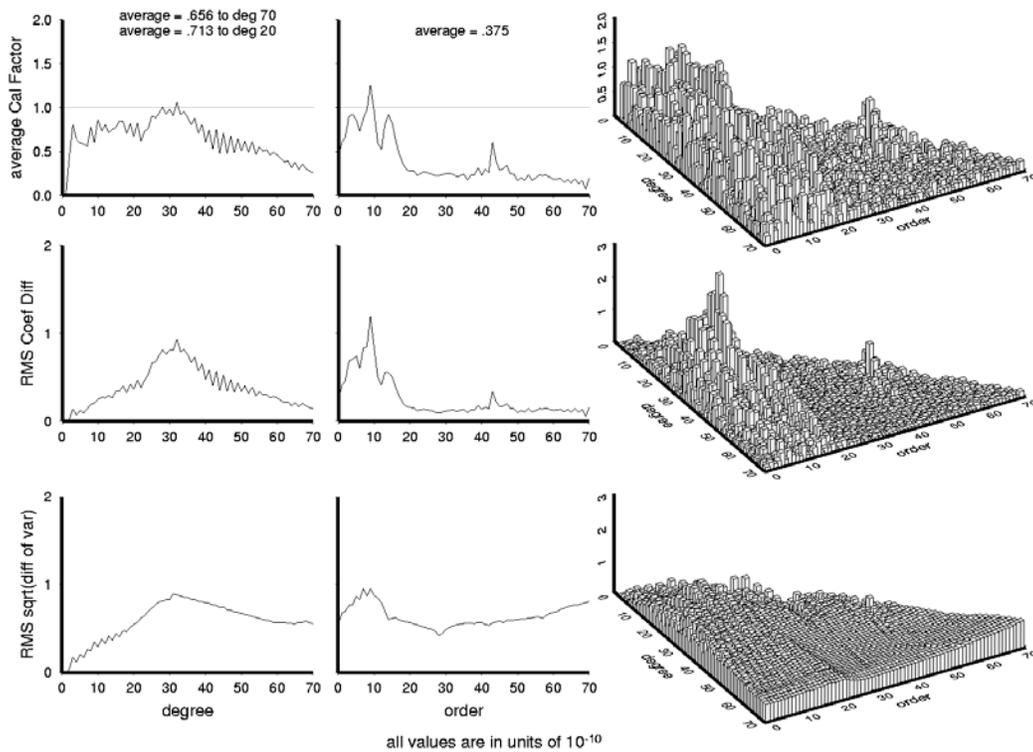
Figure 7.3.2.3–2. Calibration of the ERS–1 altimeter and SLR data with respect to a combination solution containing T/P altimetry (PGS7277 vs. PGS7271). The calibrations correspond to σ = 2.23 m for the ERS–1 SLR data, 4.13 m for the ERS–1 altimeter data, and 2.23 m for the T/P altimeter data.

7.3.2.4 Validation of the GEOSAT Altimeter Data

Two low-degree (70x70) combination solutions were created using the GEOSAT altimeter data normal equations, the surface gravity normal equations, and the direct satellite tracking data. For this preliminary assessment, no T/P altimeter data were included in the combination solution. In

PGS7278, the empirical GEOSAT 1-cycle-per-revolution (1-CPR) along-track accelerations were not adjusted, while they were adjusted in solution PGS7279. The calibrations, orbit fits, DOT solutions, GPS/leveling tests, and predicted errors were all examined for these two solutions. The initial weights selected for the GEOSAT data were $w_n = 0.72$ ($\sigma = 1.18$ cm/s) for the Doppler data, and $w_n = 0.23$ ($\sigma = 2.09$ m) for the altimeter data. These data weights represent an upweighting of the Doppler data over the satellite-only model, where the GEOSAT Doppler data had a σ of 1.63 cm/s. In addition, the data weights used in PGS7278 and PGS7279 represent a substantial upweighting of the GEOSAT data over those used in JGM–2 ($\sigma = 2.0$ cm/s and 3.53 m). This was justified in light of the improvements that had been made to the processing of the GEOSAT altimeter data, as documented in Section 7.1.

The calibrations for the GEOSAT altimeter data are summarized in Table 7.3.2.4–1 and depicted in Figure 7.3.2.4–1 for PGS7279. The calibration factors are less than unity, indicating a conservative weight for these data, although the calibrations are higher at the lower degrees.

Table 7.3.2.4–1. Summary of GEOSAT altimeter data calibrations.

Gravity Model	Comment	Average Calibration Factors $\bar{k}_t$		
		$n \leq 70$	$n \leq 20$	$m \leq 70$
PGS7278	No 1-CPR accelerations	0.815	0.930	0.699
PGS7279	1-CPR accelerations adjusted	0.819	0.932	0. 704

The predicted geoid error (see Table 7.3.2.4–2) in the ocean areas within ±66° latitude is almost twice that of the T/P altimetry-only combination model PGS7271. This is understandable given the limited amount of GEOSAT altimeter data included in the solution, compared to the 2 years of T/P data included in PGS7271 and PGS7272.

Table 7.3.2.4–2. Geoid undulation error projections from the full 70x70 covariances for the T/P (PGS7271) and GEOSAT (PGS7278) altimetry-only test solutions.

Geopotential	RMS Geoid Undulation Error (cm)					
	Global	Land		Water		
		All	USA	All	$|\varphi|<67$	$66<|\varphi|<82$
PGS7271	19.5	29.3	27.5	13.6	12.8	23.9
PGS7278	25.5	31.5	29.2	22.6	22.6	23.8

The static portion of the GEOSAT dynamic ocean topography solutions from the combination solutions were compared with the average sea surface predicted by the POCM–4B ocean circulation model. These comparisons were performed at GSFC, and involved computing the differences between two sets of spherical harmonic coefficients for each spherical harmonic

degree over the ocean areas. Those for POCM–4B came from a 24x24 spherical harmonic fit to the POCM–4B provided by *Rapp* [*private communication*, 1996]. In this particular test, the ocean areas were defined as those 1°x1° degree blocks where the depth, according to the JGP95E elevation model, was 1000 m or deeper for latitudes within ±66°. For simplicity, the cumulative $\bar{\zeta}$ differences were examined only at degree 14 and degree 20.
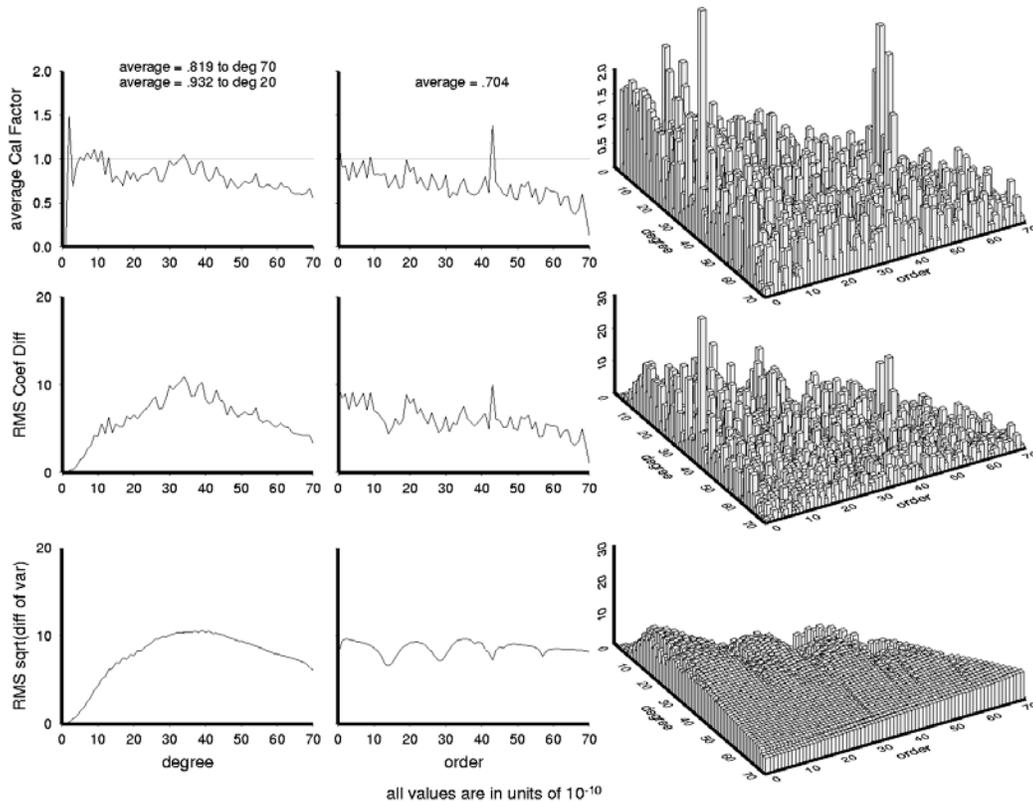
Figure 7.3.2.4–1. Calibration of the GEOSAT altimeter data with respect to a subset solution (PGS7275) containing only the surface gravity and satellite tracking data.

There is some inconsistency in comparing the dynamic ocean topography solution for GEOSAT with POCM–4B. The GEOSAT solution spans 74 days from November 1986 to January 1987, whereas the output from the POCM–4B model is valid over all of 1993 and 1994. In addition, the GEOSAT solution corresponds to the Northern Hemisphere winter, whereas the POCM–4B model output is a 2-year global average. Nevertheless, some useful information can be gleaned from these comparison. The same test was made with the recovered GEOSAT DOT coefficients from other combination models (JGM–2, PGS5741, and PGS6399) in order to place the current results in their proper context. The differences of the T/P DOT solution from PGS7272 with

POCM–4B are also shown for comparison purposes. These results are summarized in Table 7.3.2.4–3.

Comparing the DOT differences from the PGS7279 solution with the previous project solutions and with JGM–2 shows that substantial progress has been made. For instance, at degree 14, the cumulative differences with POCM–4B are now 14.09 cm, compared to 15.72 cm with JGM–2, and 14.75 cm with PGS6399, an RSS reduction of 7.0 cm from JGM–2 and 4.4 cm from PGS6399 (evaluation model EGM–X02).

Table 7.3.2.4–3. Dynamic ocean topography differences between a 24x24 spherical harmonic fit to POCM–4B, and the static portion of the dynamic ocean topography models from test combination solutions.

Solution	Satellite	Cumulative $\overline{\zeta}$ Differences to degree n, (RMS, cm)		C_{10} term of $\overline{\zeta}$ (cm)
		$n = 14$	$n = 20$	
PGS7272	T/P	12.86	13.67	14.66 ± 2.93
PGS7278	GEOSAT	20.45	20.88	2.34 ± 4.67
PGS7278	GEOSAT	13.40	14.01	PGS7272 degree 1 values used
PGS7279	GEOSAT	14.09	14.70	12.01 ± 4.68
PGS7279	GEOSAT	12.99	13.63	PGS7272 degree 1 values used
JGM–2	GEOSAT	15.72	na – 15x15 only	18.50 ± 9.21
PGS5741	GEOSAT	16.75	na – 15x15 only	15.38 ± 5.92
PGS6399	GEOSAT	14.75	na – 15x15 only	20.26 ± 5.74

It has been known from some time that a coordinate system offset exists between T/P and GEOSAT. To compare the DOT solutions without this reference frame offset, which can be taken to be largely a degree 1 effect, the comparisons with the PGS7278 and PGS7279 solutions were repeated by replacing the C_{10} terms of the GEOSAT DOT solutions, with the C_{10} terms from the T/P DOT solution of PGS7272. At degree 14, the cumulative DOT differences became 13.40 cm for PGS7278 and 12.99 cm for PGS7279, instead of 20.45 cm for PGS7278, and 14.09 cm for PGS7279.

The entire GEOSAT frame is ill defined for several reasons: (1) Only 74 days of GEOSAT Exact Repeat Mission (ERM) Doppler data are available to define the tracking station locations, which are determined simultaneously with the orbits, the DOT solution, and the geopotential, (2) Doppler tracking, particularly at the epoch of GEOSAT, is a weaker data type than satellite laser ranging, so the ability to determine the tracking stations, and thus the GEOSAT frame, will be affected, (3) the GEOSAT Doppler stations are connected tenuously to the frame of the SLR stations through survey ties between the GEOSAT Doppler stations and the Doppler stations that tracked SEASAT. SEASAT benefited from SLR tracking so that the SEASAT Doppler stations

are better determined than those of GEOSAT. These same SEASAT SLR stations can be directly linked to those that now track T/P. Thus, some inconsistency between the T/P and GEOSAT frames is understandable, and could be mitigated in future solutions through the adoption of better survey ties, or the addition of a longer time series of GEOSAT Doppler data to better determine the GEOSAT tracking station locations.

The other lesson that can be drawn from the results in Table 7.3.2.3–3 is that the adjustment of the 1-CPR along-track acceleration on the GEOSAT orbits removes an important bias in the GEOSAT ζ solution. Previous experience has shown that high correlations can exist between the empirical acceleration correction parameters and the degree 1 terms of $\overline{\zeta}$. In PGS7278, the orbit error, which has a predominant signature of once per revolution, has been mapped directly into the degree 1 terms of the DOT. However, even though these $\overline{\zeta}$ comparisons suggest it is imperative to adjust the once per revolution accelerations on GEOSAT, a case can be made for not adjusting them for two reasons: (1) The 1-CPR parameters were not adjusted in the satellite-only model; to adjust them in the combination model would introduce an inconsistency between the these two solutions and (2) adjustment of the 1-CPR parameters could remove beneficial geopotential signal.

In order to explore the effects of adjusting the 1-CPR terms on GEOSAT in the combination model, the GPS/leveling tests, summarized in Table 7.3.2.4–4, were examined for PGS7278 and PGS7279. The test results degrade on average over both the five areas and the U.S. with the adjustment of the 1-CPR empirical acceleration parameters on GEOSAT, although the British Columbia test shows a slight improvement. These GPS/leveling results point to some loss in geopotential signal between the PGS7278 and the PGS7279 models.

Table 7.3.2.4–4a. GPS/leveling tests for the GEOSAT test combination solutions using V058 for the high-degree (70<n≤360) field.

Gravity Model	GPS/leveling Comparison Standard Deviation (cm)		
	Five Areas Average	BC	USA/NGS
PGS7278	27.73	56.73	53.19
PGS7279	28.75	56.51	53.58

Table 7.3.2.4–4b. GPS/leveling tests for the GEOSAT test combination solutions using V058 for the high degree (70<n≤360) field: Detail for the five areas.

Gravity Model	GPS/leveling Comparison Standard Deviation (cm)				
	Europe	Canada	Australia	Scandinavia	Tennessee
PGS7278	35.70	27.45	26.17	25.21	21.93
PGS7279	36.66	28.90	26.39	24.64	24.57

7.3.2.5 Initial Calibration of the Altimeter Data

Once each set of altimeter data was validated individually, the three sets of data were combined into an individual solution. The altimeter data were then calibrated as a group against the subset solution containing only satellite tracking and surface gravity (PGS7275). The final group of calibration factors is shown in Table 7.3.2.5–1. The group calibration factor was 0.875 by degree, and on this basis the applied normal equation weights for the GEOSAT and T/P altimeter data were decreased by 15 percent. The group calibrations barely changed, and the predicted geoid error over the oceans increased only slightly from 11.6 to 12.0 cm RMS (see Table 7.3.2.4–2).

Table 7.3.2.5–1. Summary of altimeter data group calibrations.

Gravity Model	Altimeter Data weights	Average Calibration Factors $\bar{k}_t$		
		$n \leq 70$	$n \leq 20$	$m \leq 70$
PGS7285A	T/P: 2.23 m GEOSAT: 2.09 m ERS–1: 4.13 m	0.875	0.963	0.760
PGS7288	T/P: 2.50 m GEOSAT: 2.26 m ERS–1: 4.13 m	0.870	0.954	0.757

Table 7.3.2.5–2. Geoid error projections from the full 70x70 error covariances for the GEOSAT, T/P, ERS–1 test combination models.

Geopotential	Global	Land		Water		
		All	USA	All	$|\varphi|<67$	$66<|\varphi|<82$
PGS7285A	18.2	28.5	26.6	11.6	10.8	20.6
PGS7288	18.6	28.7	26.7	12.0	11.3	20.8

RMS Geoid Undulation Error (cm)

7.3.2.6 GPS/Leveling Tests With Combination Solutions

In the ordinary course of events, the procedure to derive a combination model solution would be to first develop the best possible satellite-only model and then add in the surface gravity and direct satellite altimetry. However, because of the unique demands of this project, it was important to understand the role of certain sets of satellite tracking data and ascertain their influence on the resulting combination model geoid solutions, as measured by the GPS/leveling tests. Along the course of the model development, the GPS/leveling tests for the PGS7285A and PGS7288 models showed a strong degradation in the standard deviation of the derived undulation differences over the US as compared to earlier combination solutions that used a significantly different satellite-only model base. Specifically, the standard deviation of the leveling test differences for PGS6399/V058 was 51.08 cm, while that for PGS7285A was 55.01

cm, and, for PGS7288, 54.81 (see Table 7.3.2.6–1). A detailed parametric study was suggested because of the role of the "old" (1983–1986) Starlette data in the solution. As discussed in Section 6, these data had been removed from the satellite-only and combination solutions when it was discovered that these data produced visible stripes in the geoid and gravity anomaly error maps. The problem was traced specifically to the 1983 data, and in the PGS7291 and later solutions, the 1984 and 1986 Starlette data were once again included. When these data were added back to the combination solutions, the standard deviation of the geoid undulation differences over the US with the NGS data was reduced from 55 cm to 53.14 cm. This means that a single set of satellite tracking data was responsible for an improvement in the modeling of the geoid over the United States of 14 cm. In order to elucidate the role of other satellite tracking data sets and how they might affect the GPS/leveling tests, changes to the weighting and handling of the satellite tracking data were tested in the combination model domain before being implemented in the final solution. The test solutions are described in Table 7.3.2.6–2, and the GPS/leveling tests are summarized for these test solutions are presented in Table 7.3.2.6–3.

Table 7.3.2.6–1. GPS/leveling tests for GEOSAT–T/P–ERS–1 test combination solutions using V058 for the high-degree ($70 < n \leq 360$) field.

Gravity Model	GPS/leveling Comparisons Standard Deviation (cm)		
	Five Areas Average	BC	USA/NGS
PGS6399	28.02	54.02	51.08
PGS7285A	28.72	55.75	55.01
PGS7288	28.48	56.01	54.81

Table 7.3.2.6–2. Combination model test solutions.

Model	Description
PGS7285A	Combination solution: without Starlette 84–86 data
PGS7292	Combination solution: PGS7270D satellite only + 84/86 Starlette
	Includes T/P–ERS–1 & GEOSAT altimetry and surface gravity
	T/P 1–CPR empirical acceleration parameters adjusted
PGS7292B	PGS7292 with 1–CPR terms on T/P/SLR/DORIS/ALT not adjusted.
PGS7293	PGS7292 with Spot–2 at $w_{n=}1.3$
PGS7294	PGS7293 with Spot–2 at $w_n = 3.9$
PGS7295	PGS7292 with EP/EUVE GPS at $w_n = 0.25$
PGS7296	PGS7292 with GEOS–3 ATS at $w_n = 2.6$
PGS7297	PGS7292 with GPS/MET at 0.20 + separately adjust 5x5 on GPS/MET
PGS7297A	PGS7297 with separate adjust of 4x4 on EP/EUVE TDRSS
PGS7297B	PGS7297 without Spot–2
PGS7297F	PGS7297 + adjust separate 3x3 harmonic on EP/EUVE TDRSS
PGS7297H	PGS7297F + downweight EP/EUVE TDRSS to $w_n = 0.075$ rather than $w_n = 0.100$

Aside from the Starlette 1984–1986 data, the changes to the weights of the other satellite data did not alter the US/NGS GPS/leveling comparisons by more than one cm. The adjustment of the 1-CPR terms on the T/P SLR/DORIS/altimeter data had no impact on the GPS/leveling comparisons (quite the opposite from GEOSAT). The parameterization for T/P adjusts a pair of along-track and a cross-track 1-CPR acceleration terms each day—a total of 40 per arc, or approximately 2800 over the full 74 cycles of data in the solution. The adjustment of so many parameters could seriously weaken the solution—and does, in fact, reduce the calibrations. Yet, since the GPS/leveling comparisons show no effect, we concluded that the geoid information measured in these tests must come from sources other than the T/P SLR/DORIS data. The GEOS–3 ATS data have been drastically downweighted since their inclusion in JGM–2, and the PGS7296 solution tested the impact of restoring these data to the earlier JGM–2 weight. This test was suggested by the PGS7200 calibrations, which showed that in the satellite-only model, GEOS–3 remained one of the strongest satellites in the solution, as measured by the change in the 5°x5° altimeter-derived anomaly comparisons. The largest change in the comparisons is brought about by the total exclusion of the Spot–2 data, but only on the five areas comparisons and the British Columbia test. Excluding Spot–2 from the solution solely on the basis of the GPS/leveling results would not be reasonable, since other evidence indicates that Spot–2 is beneficial to the solution. In conclusion, with the exception of the addition of the 1984–1986 Starlette data, it appears that GPS/leveling comparisons can be changed by less than 1 cm in the standard deviation, when the weights on various sets of satellite tracking data are changed in a combination model solution. In spite of the small changes, the experiments indicated that some of the changes, such as the adjustment of low-degree harmonics with the EP/EUVE TDRSS and GPS/MET data, and the upweighting of the GPS/MET data, were at least neutral if not even slightly beneficial to the overall solution, and the determination of an improved geoid model.

Table 7.3.2.6–3. GPS/Leveling results for combination test solutions using HDM180 for the high-degree ($70 < n \leq 360$) field.

Gravity	GPS/leveling Comparisons Standard Deviation(cm)		
Model	5 Areas Average	BC	USA/NGS
PGS7285A	28.13	55.39	54.95
PGS7292	27.76	52.30	53.11
PGS7292B	27.88	52.07	53.08
PGS7293	27.49	52.47	53.07
PGS7294	27.95	52.11	53.16
PGS7295	27.80	52.30	53.01
PGS7296	27.80	52.71	53.08
PGS7297	27.46	51.45	52.84
PGS7297A	27.48	51.59	52.59
PGS7297B	26.55	50.05	52.86
PGS7297F	27.58	51.45	52.69
PGS7297H	27.40	51.90	52.71

7.3.3 The Final Project Combination Solution

The final project combination solution was derived from the PGS7270K37 (EGM96S) satellite-only model, and took into account the weights in the altimeter data implemented in PGS7288. The changes to the satellite-only model in the final stages that had been suggested by the GPS/leveling tests on the combination models in the final stages included: (1) Inclusion of the Starlette 1984–1986 data and (2) adjustment of separate 5x5 and 3x3 harmonics on the GPS/MET and EP/EUVE TDRSS data to remove potential sources of long-wavelength error. The 1-CPR empirical acceleration parameters on GEOSAT were not adjusted, with the recognition that the degree 1 terms of the GEOSAT DOT solution would be affected. The PGS7337B combination solution, as had all previous combination solutions, adjusted a separate set of 5x5 harmonics for the surface gravity. In the subsequent sections, we describe the final project combination model (PGS7337B), which became the 70x70 portion of EGM96.

7.3.3.1 Geopotential Comparisons and Error Characteristics

As a first step in characterizing the PGS7337B solution, the cumulative geoid differences by degree with the JGM–3 model are shown in Figure 7.3.3.1–1. The cumulative geoid differences are shown over the entire globe, as well as only over land and ocean areas. The EGM96 model changes the geoid over land areas more than over the oceans. At degree 70, the standard deviation of the undulation differences is 82 cm over land and 20 cm over the oceans. The larger geoid differences over land are expected, since the surface gravity normal equations embedded in the JGM–3 solution were derived from the OSU October 1990 data base, whereas, in PGS7337B (EGM96), the surface gravity normal equations are based on the merged file containing the NIMA 30′x30′ anomalies. Up to degree 10, the JGM–3 and EGM96 geopotential models are highly correlated, and the standard deviation of the total geoid undulation difference between the two models is less than five cm. The total (to degree 70) geoid differences between JGM–3 and EGM96 are depicted in Figure 7.3.3.1–2. It is in the continental areas of Asia, Africa, and South America and the high-latitude regions that the geoid changes are the most substantial. The geoid changes are more subdued over the oceans and in the land areas where the surface gravity data were already of high quality in the JGM models (North America, Europe, Australia).

The RMS degree variance for the new combination model PGS7337B is illustrated in Figure 7.3.3.1–3 and compared with JGM–2 and JGM–3. The ratio of the RMS errors per degree between the combination models is shown in Figure 7.3.3.1–4. According to the formal errors from these combination solutions, JGM–3 improved on JGM–2 by factors of two to three below degree 10. The errors for the model PGS7337B are greater than JGM–3 through degree 6 (see Figure 7.3.3.1–4, where the ratio of JGM–3/PGS7337B is less than unity). Thereafter, the ratio of the formal errors between the two models is greater than unity, and between two and three through degree 70, suggesting an across-the-board improvement in the predicted errors between JGM–3 and PGS7337B. Part of the systematic reduction in the formal errors between the two models can be attributed to the handling of the surface gravity in the two models. In JGM–3 (and JGM–2), the surface gravity normal equations were downweighted by a factor of four with respect to their normal equation weights in PGS7337B. This downweighting of the surface

gravity in the JGM models was done because a degradation in the orbit fits was observed when the surface gravity normal equations received their full weight. This downweighting of the surface gravity was implemented since the primary design driver for those models were satellite orbit fits, where T/P was the primary concern. Thus, an improvement in the formal uncertainties by approximately a factor of two between JGM–3 and PGS7337B should be expected. Of course, other improvements will be expected given the new 30'x30' anomalies that contributed to the solution in many regions of the globe. Over the United States, where the surface gravity data were already of high quality prior to the creation of EGM96, this factor-of-two change in the formal geoid errors is directly observable. The formal geoid errors (to 70x70) in JGM–3 are 53.6 cm, compared to 25.9 cm in PGS7337B (see Table 7.3.3.1–1). The other major contributor to the change in the predicted errors is the large amount of T/P altimeter data present in PGS7337B (more than 2 million observations), but absent in JGM–3, which will scale the formal errors at all degrees. Over the ocean areas, the global geoid error to 70x70 is predicted to be 35.1 cm with JGM–3 and 11.1 cm with PGS7337B (EGM96).
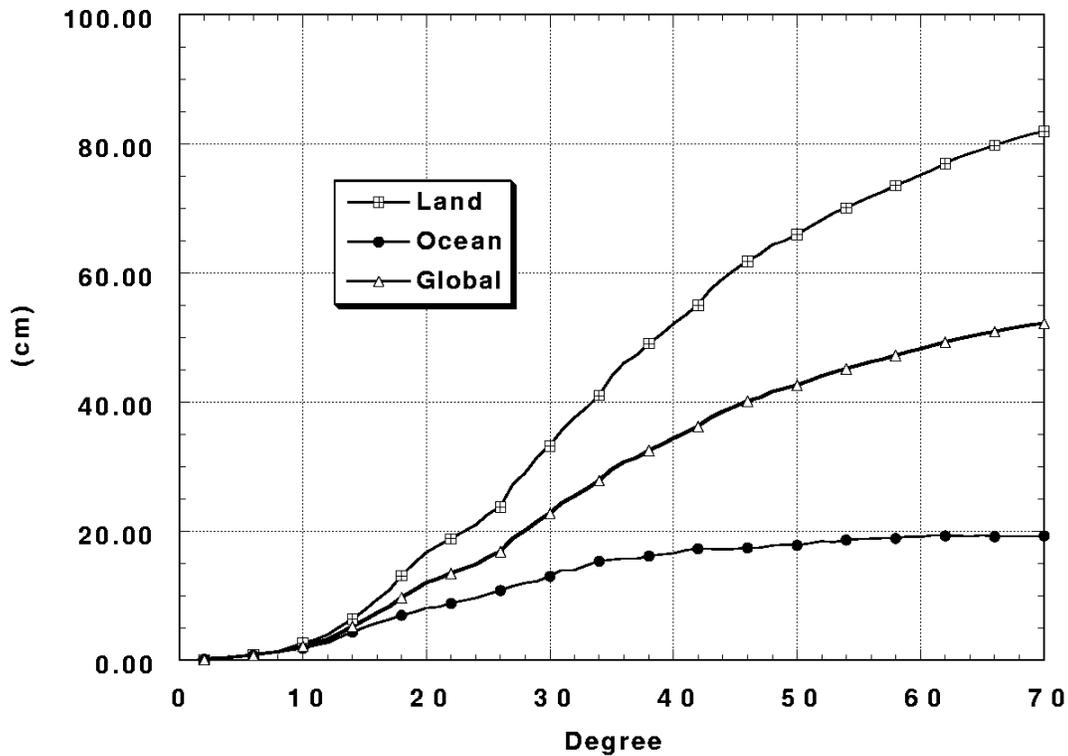
Figure 7.3.3.1–1. Standard deviation of the geoid undulation differences (cumulative to degree) between EGM96 and JGM–3 to degree 70. EGM96 changes the geoid over land in a global sense by 82 cm, and over the oceans by 20 cm.
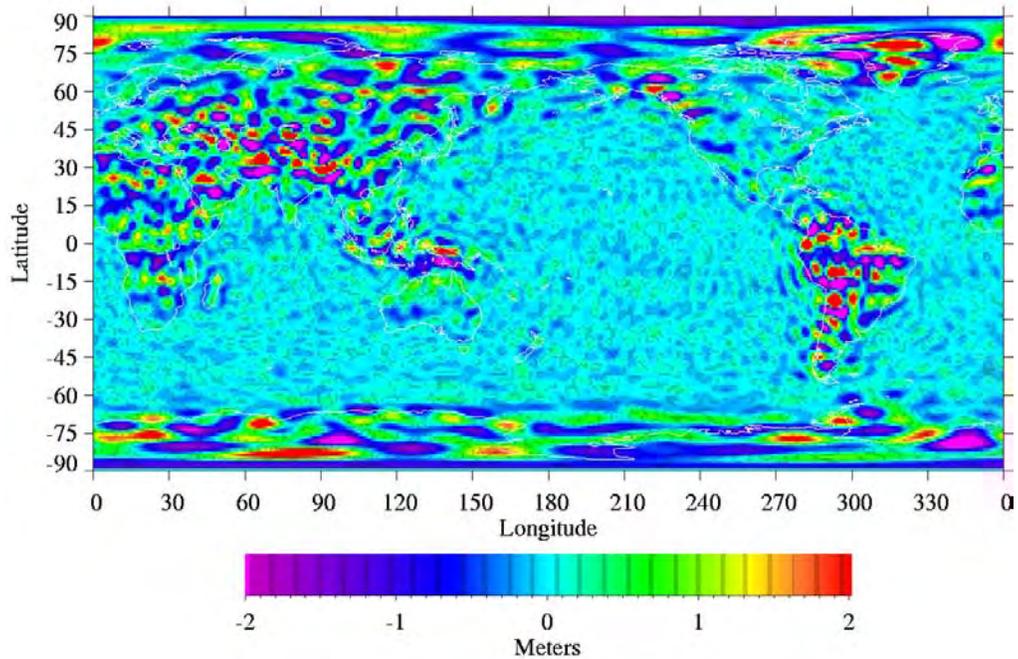
Figure 7.3.3.1–2. Geoid undulation differences between EGM96 (PGS7337B) and JGM–3 to 70x70. The geoid undulation differences over some land areas can exceed the colorbar scale of ±2 meters.
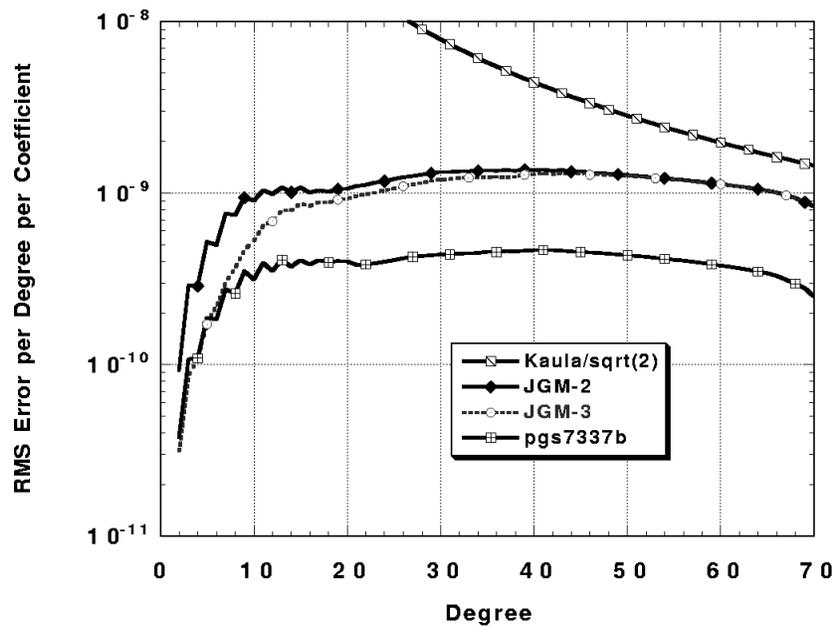
Figure 7.3.3.1–3. RMS error per degree per coefficient for the JGM–2, JGM–3, and PGS7337B combination model solutions.
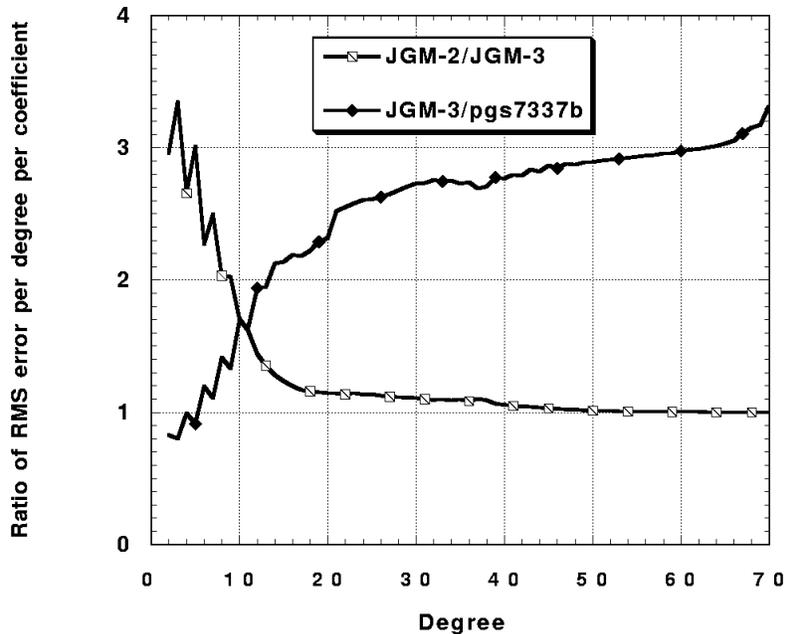
Figure 7.3.3.1–4. Ratio of the RMS error per coefficient per degree between JGM–2 and JGM–3, and between PGS7337B and JGM–3.

Table 7.3.3.1–1. Geoid undulation error projections from the full 70x70 error covariances for EGM96 and other combination models.

| Geopotential | RMS Geoid Undulation Error (cm) | | | | | |
| | Global | Land | | Water | | |
		All	USA	All	$\|\varphi\|<67$	$66<\|\varphi\|<82$
JGM–2	53.4	80.2	55.7	37.4	36.4	51.8
JGM–3	50.9	76.2	53.4	35.8	35.1	46.2
PGS7337B (EGM96)	18.1	28.0	25.9	11.8	11.1	20.7

The JGM–3 and PGS7337B (EGM96) geoid errors to 70x70 are compared on a global map in Figures 7.3.3.1–5a and 7.3.3.1–5b. The JGM–3 geoid error exceeds 1 meter over South America, southeast Asia, and portions of Africa. The maximum error in PGS7337B (EGM96) is 50 cm. In the PGS7337B solution, the errors presented reflect a combination of the T/P altimeter data distribution and the uncertainties assigned to the surface gravity data that were used. For instance, the geoid errors in the shallow seas (such as the Yellow Sea between Korea and Japan, and the Red Sea) as well as in the ocean areas north of 66°N and south of 66°S increase because of the lack of T/P altimeter data. Also, the maximum error of 50 cm occurs at 88°E 35°N, in western China. where the lower quality surface gravity data from the "China–B" set were assigned higher uncertainties. The Antarctic is, in general, a region lacking in surface gravity data, and this is reflected in the formal geoid (70x70) error estimates for that area of between 30 and 40 cm.
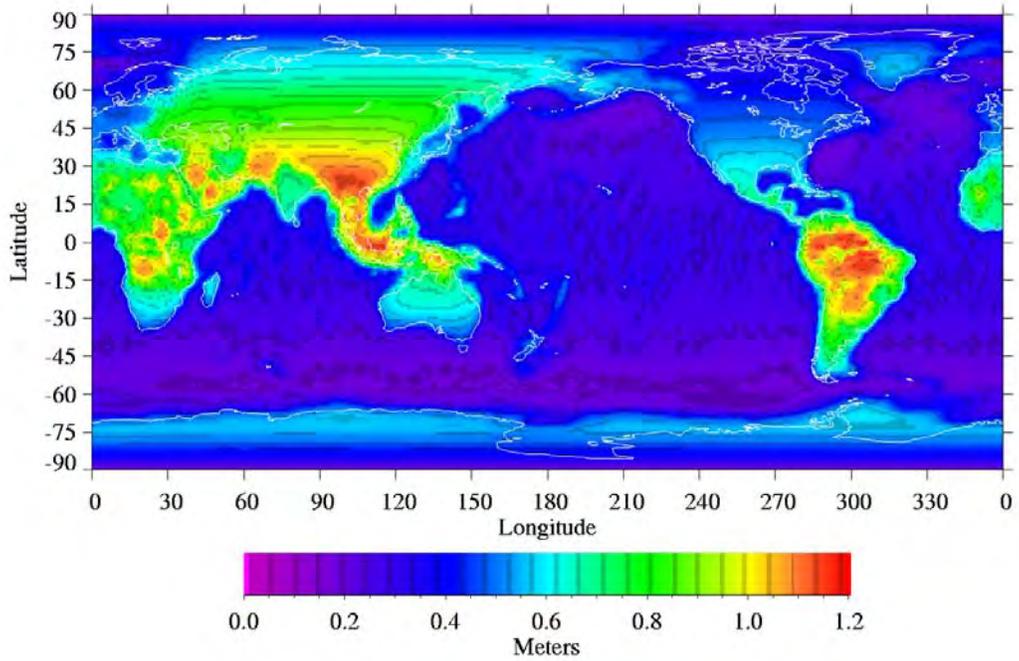
Figure 7.3.3.1–5a. JGM–3 Geoid errors to 70x70 from the full error covariance.
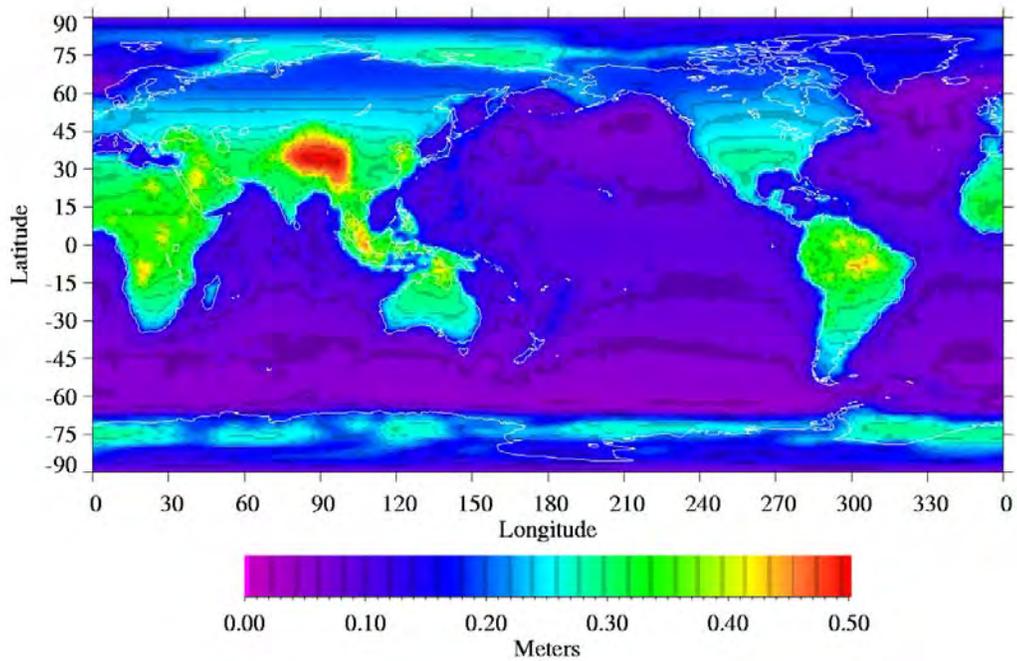
Figure 7.3.3.1–5b. Geoid errors to 70x70 from the full error covariance of the PGS7337B combination solution.

In other areas where the geoid errors in PGS7337B (EGM96) remain around 40 cm, such as central Brazil and Indonesia, programs are underway to improve the quality and density of the surface gravity data.

7.3.3.2 Evaluation of the DOT Solutions for the Final Combination Model PGS7337B

The static dynamic ocean topography, $\bar{\zeta}$, solutions for T/P and GEOSAT from the PGS7337B combination solution are presented in Figures 7.3.3.2–1 and 7.3.3.2–2. The two spherical harmonic $\bar{\zeta}$ solutions were compared with the 24x24 spherical harmonic representation of the previously mentioned POCM–4B model. As before with the GEOSAT altimetry test models, the comparisons were performed for GEOSAT with the full $\bar{\zeta}$ solution, and by substituting the C_{10} terms from the PGS7337B T/P–ERS–1 $\bar{\zeta}$ solution. The cumulative T/P–ERS–1 $\bar{\zeta}$ differences at degree 14, shown in Table 7.3.3.2–1, have improved over the PGS7272 combination test solution, with an RSS difference of 12.50 cm, compared to 12.86 cm with PGS7272 (see Table 7.3.2.4–3). Likewise, once the C_{10} terms of the GEOSAT dynamic ocean topography solution are replaced with those from the T/P DOT solution, the cumulative differences with the POCM–4B become 12.14 cm at degree 14, a decrease (and an improvement) over the GEOSAT-only test solution PGS7279 of 12.99 cm. It is interesting to note that, exclusive of the degree 1 terms, the GEOSAT $\bar{\zeta}$ solution from PGS7337B agrees better with POCM–4B than the PGS7337B $\bar{\zeta}$ solution. The improvement over the T/P- and GEOSAT-only altimeter solutions occur because (1) both sets of data combine synergistically and (2) the modifications to the satellite-only model, including the reintroduction of the Starlette 84–86 data, have strengthened the determination of the geoid, as evidenced by the results of the GPS/leveling tests over the United States.

The geographical error distribution based on the formal covariance of PGS7337B (EGM96) for the T/P–ERS–1 and GEOSAT $\bar{\zeta}$ solutions are depicted in Figures 7.3.3.2–3 and 7.3.3.2–4, respectively, which show the estimated errors for $|\varphi|{\leq}66°$, while Table 7.3.3.2–2 lists the RMS errors for latitudinal bands of ±28.5°, ±66°, and $66°{<}|\varphi|{<}82°$. For the T/P–ERS–1 solution, the RMS error over the ocean areas within $66°{<}|\varphi|{<}82°$ is 18.33 cm—almost three times the 6.45 cm RMS error in the latitudes within ±66°. The errors depicted in the figures increase toward the coasts because of the 200 m depth editing criteria in shallow seas, and because the spherical harmonic function that represents the $\bar{\zeta}$ model has no data to define it over land. For GEOSAT, the degree 1 terms of the T/P–ERS–1 dynamic ocean topography solution were substituted for the GEOSAT value. The RMS error for the GEOSAT $\bar{\zeta}$ over the T/P latitude domain is 10.18 cm, higher than that for T/P–ERS–1. This is the result of the lesser amount of GEOSAT altimetry data, which has a stronger impact than the marginally higher weight of the GEOSAT altimetry data in the solution, and is evident in the error gradient, which is much shallower than that for T/P–ERS–1, in the coastal regions.
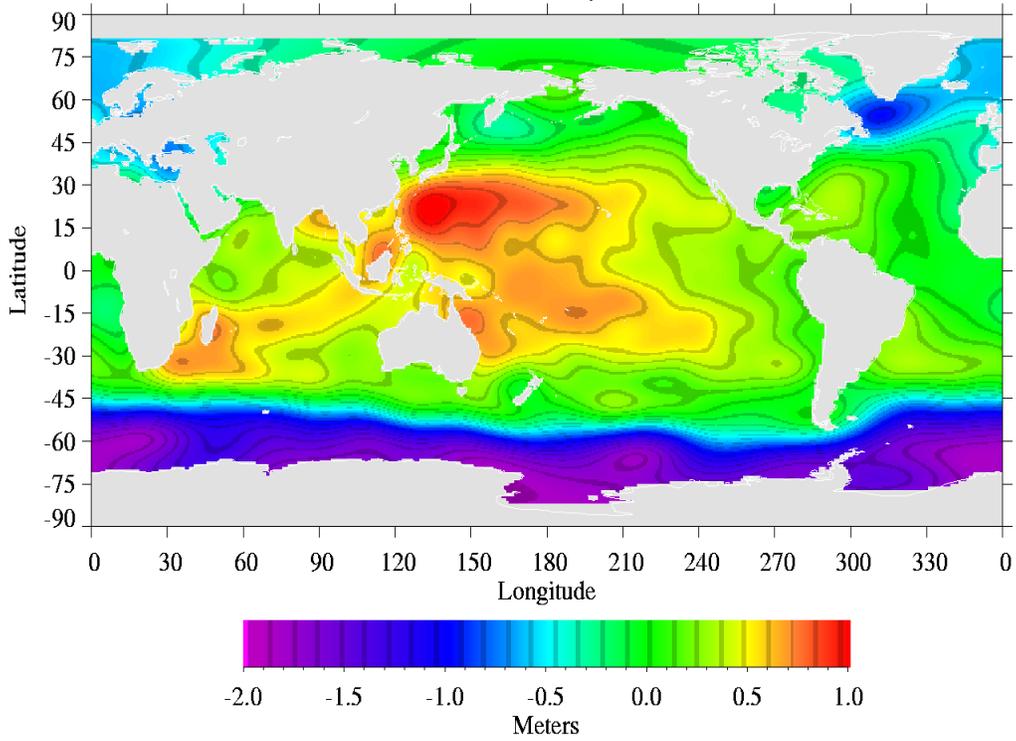
Figure 7.3.3.2–1. Dynamic ocean topography solution for T/P from the PGS7337B combination solution.
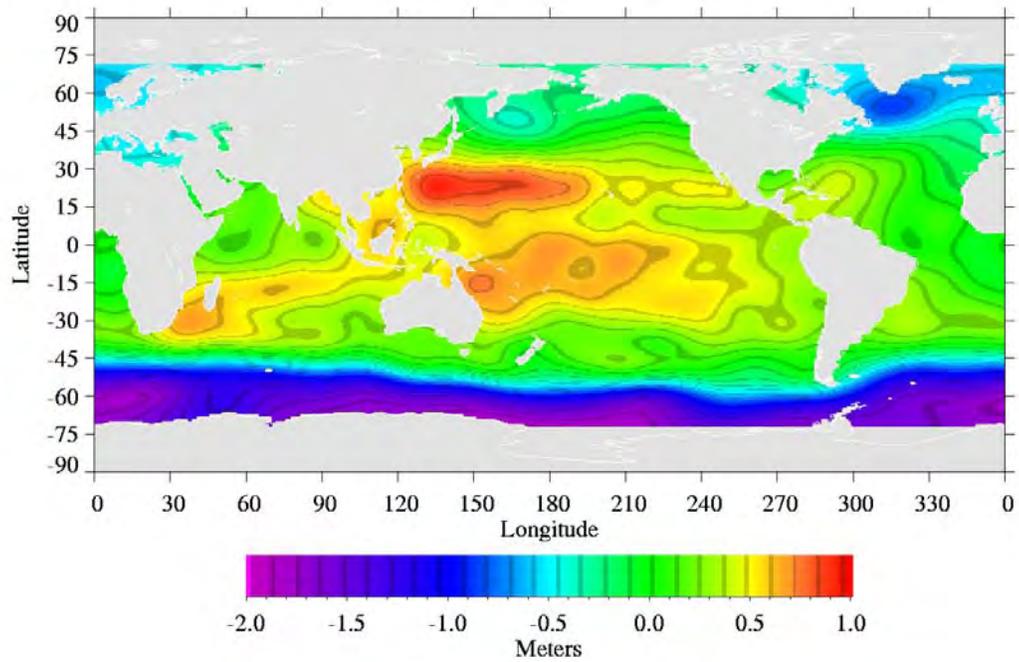
Figure 7.3.3.2–2. Dynamic ocean topography solution for GEOSAT, including the degree 1 terms, from the PGS7337B combination solution.

Table 7.3.3.2–1. Dynamic ocean topography differences between a 24x24 spherical harmonic fit to POCM–4B, and $\bar{\zeta}$ models from combination solutions.

Solution	Satellite	Cumulative $\bar{\zeta}$ differences to degree n (RMS, cm)		C_{10} term of $\bar{\zeta}$ (cm)
		$n = 14$	$n = 20$	
PGS7337B	T/P–ERS–1	12.50	13.26	16.05 ± 2.30
PGS7337B	GEOSAT	19.82	20.25	2.39 ± 4.53
PGS7337B	GEOSAT	12.14	12.80	–

In order to understand the change in the predicted errors for the DOT solutions, it is necessary to understand the change in the data weights applied to the altimeter data in each of the combination model solutions, as well as how much altimeter data were included in each model. The predicted errors will also reflect the strength of the geopotential determination, and how well the geopotential can be separated at the low degrees from the dynamic ocean topography. The GEOSAT altimeter data uncertainty in JGM–2 was 3.53 m (2.0 cm/s for the GEOSAT Doppler data), 4.17 m (1.2 cm/s for the Doppler) in PGS5741 and PGS6399, and 2.26 m (1.2 cm/s for the Doppler) in PGS7337B. Thus, even though the altimeter data were downweighted between JGM–2 and the interim project models (PGS5741 and PGS6399), the formal $\bar{\zeta}$ error improved.
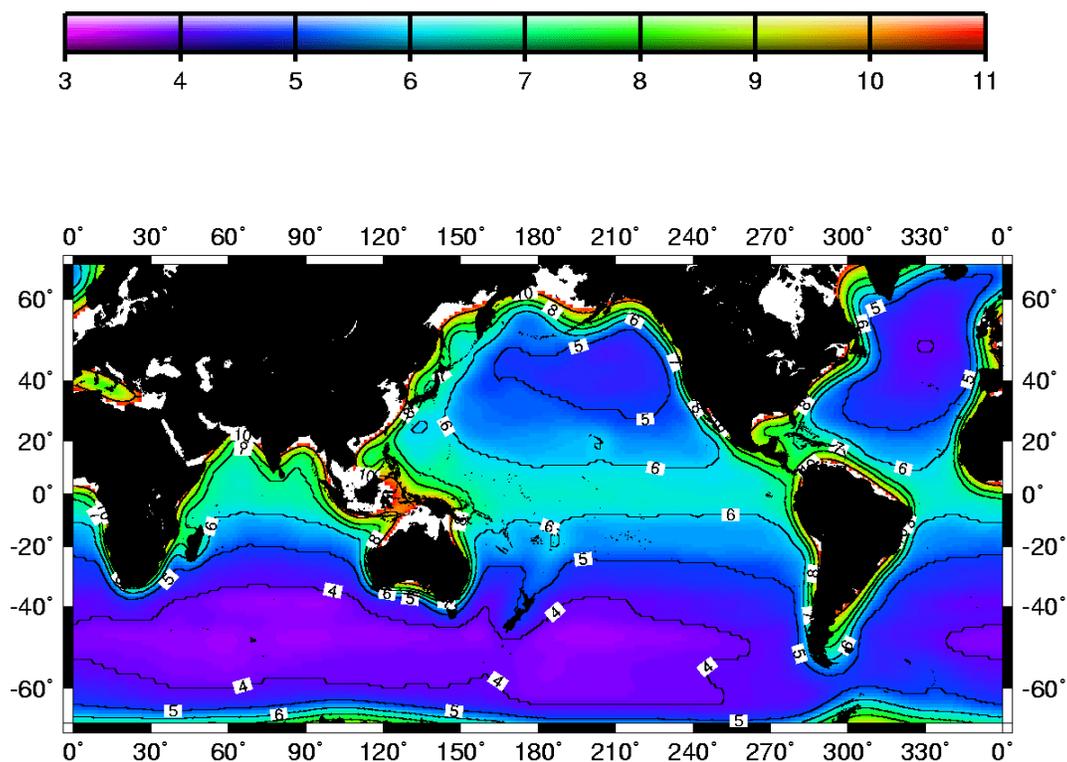
Figure 7.3.3.2–3. The T/P–ERS–1 dynamic ocean topography model ($N_{max} = 20$) error, predicted from the error covariance of the PGS7337B solution. Only the errors for ±66° are shown.
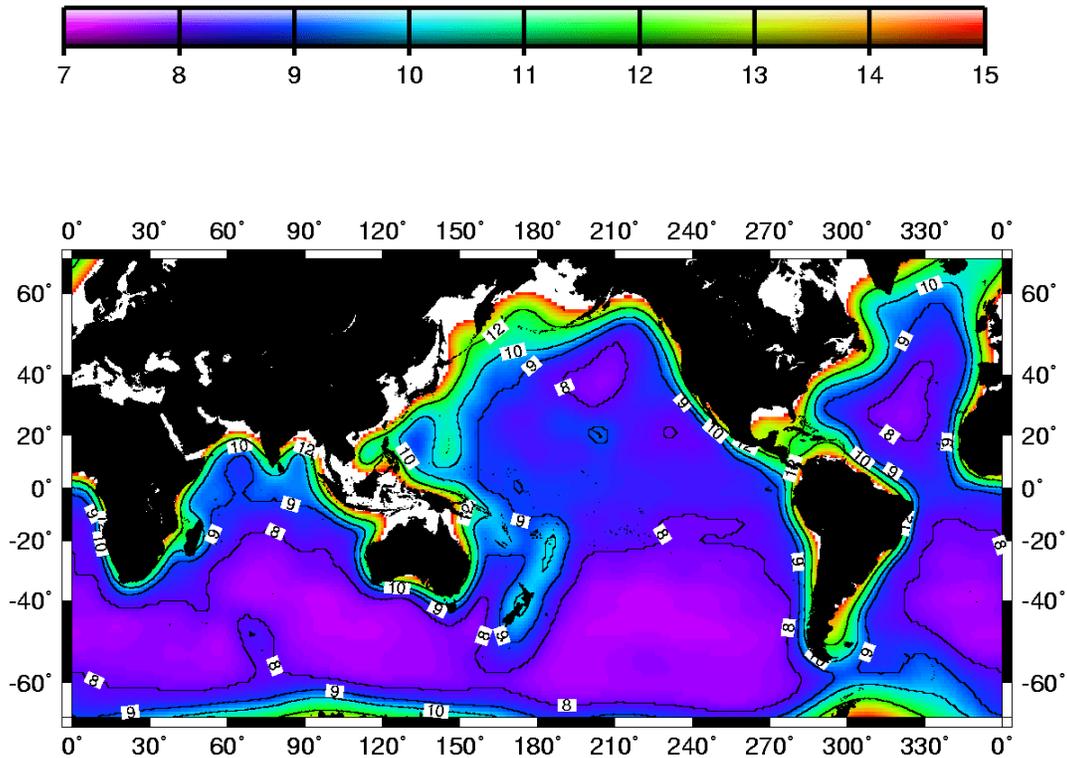
Figure 7.3.3.2–4. The GEOSAT dynamic ocean topography model error ($N_{max} = 20$), predicted from the error covariance of the PGS7337B solution. Ocean areas in white have errors >15 cm.

Table 7.3.3.2–2. Predicted RMS error of the dynamic ocean topography (ζ) models, from 1°x1° grids of the combination model covariances

Solution	Satellite	N_{max}	RMS ζ Error Over the Oceans (cm)			
			$|\varphi|<28.5°$	$|\varphi|<66°$	$66°<|\varphi|< 82°$	$|\varphi|<82°$
PGS5741	T/P	20	9.95	10.34	nv	nv
PGS6399 (EGM–X02)	T/P	20	8.25	9.03	nv	nv
PGS7337B	T/P–ERS–1	20	6.92	6.44	18.33	9.00
JGM–2	GEOSAT	15	17.45	17.86	nv	nv
PGS5741	GEOSAT	15	11.05	11.59	nv	nv
PGS6399 (EGM–X02)	GEOSAT	15	10.71	9.84	nv	nv
PGS7337B	GEOSAT	20	10.06	10.18	nv	nv

nv = ζ model not valid in these latitudes

The predicted dynamic ocean topography errors can be compared with the differences between the GEOSAT $\bar{\zeta}$ solution and POCM–4B for $|\varphi|\leq66°$. In the case of GEOSAT, at degree 20 the cumulative RMS difference for PGS7337B is 12.88 cm. The predicted $\bar{\zeta}$ solution error (from Table 7.3.3.2–2) is 10.18 cm for PGS7337B. Considering that the differences between the $\bar{\zeta}$ solution and the POCM–4B model must also include errors in POCM–4B, the predicted $\bar{\zeta}$

7–52

solution error and the RMS difference between POCM–4B and the PGS7337B GEOSAT $\overline{\zeta}$ solution are consistent if POCM–4B has errors of about 7.9 cm. If the POCM–4B errors are smaller than this, then the PGS7337B GEOSAT $\overline{\zeta}$ solution error is optimistic. Unfortunately formal covariance values are not available for POCM–4B, so this can only be used as a confirmation of the expectation that the POCM–4B error is substantially less than the PGS7337B GEOSAT $\overline{\zeta}$ solution errors.

The global correlations between the PGS7337B dynamic ocean topography solutions and the geoid were computed for GEOSAT and T/P–ERS–1, and are depicted in Figures 7.3.3.2–5 and 7.3.3.2–6, respectively; the statistics of these correlations are summarized in Table 7.3.3.2–3. The correlations for the T/P–ERS–1 solution are higher than for GEOSAT (average is –0.37 vs. –0.17 for T/P–ERS–1 within ±66°). In addition, for both DOT solutions, the geoid/DOT correlations are higher in the equatorial regions (where the altimeter track spacing is sparser) than at the higher latitudes. On balance, the correlations are higher for T/P than for GEOSAT because of the larger quantity of data and the higher weight applied to the T/P altimeter data. Both maps show a broad region of lower correlations in the southern Indian Ocean between 40°S and 60°S.

The amplitude and phase of the time variable dynamic ocean topography, $\zeta(t)$, solutions (to 10x10) from T/P–ERS–1 are shown in Figures 7.3.3.2–7 and 7.3.3.2–8. The peak amplitude of the annual variation from the EGM96 solution is 10.4 cm, while the corresponding peak signal in the semiannual amplitude is 7.1 cm. The EGM96 solutions for $\zeta(t)$ match in general appearance the $\zeta(t)$ solutions from *Knudsen* [1994] and *Nerem et al.* [1994a], although the peak amplitudes from these solutions are higher than in EGM96, and have more detail. The *Knudsen* [1994] solution was a spherical harmonic solution to 18x18, while the solution from *Nerem et al.* [1994a] was computed on a 1°x1° grid using altimeter data contained in a 3° radius from the grid point. In the region of the Kuroshio, off Japan, *Knudsen* [1994] reports that the peak amplitude of the annual variation is about 12 cm, whereas the corresponding peak in the EGM96 annual $\zeta(t)$ solution is about 8 cm. Similarly in the *Knudsen* [1994] solution, a peak appears in the annual $\zeta(t)$ east of the Horn of Africa near 60°E 10°N of 8 cm, whereas a peak of about 8 cm also appears in the EGM96 annual $\zeta(t)$. The amplitude of the annual and semiannual variations of the EGM96 time variable DOT may appear subdued in comparison with other T/P-derived solutions for the following reasons: (1) The EGM96 solution for $\zeta(t)$ was only to 10x10, (2) the constraint on the time-variable dynamic ocean topography may have overly minimized the power of the recovered terms, and (3) the possible correlation with the adjustment of an arc-by arc altimeter bias for all the altimeter data (see Section 7.3.3.3). The constraint on the time-variable dynamic topography was imposed after it was discovered that, in the T/P and ERS–1 test solutions (e.g., PGS7277) the amplitude of the annual and semiannual variations of the dynamic ocean topography attained unreasonable values in the high latitudes beyond the T/P altimeter data.
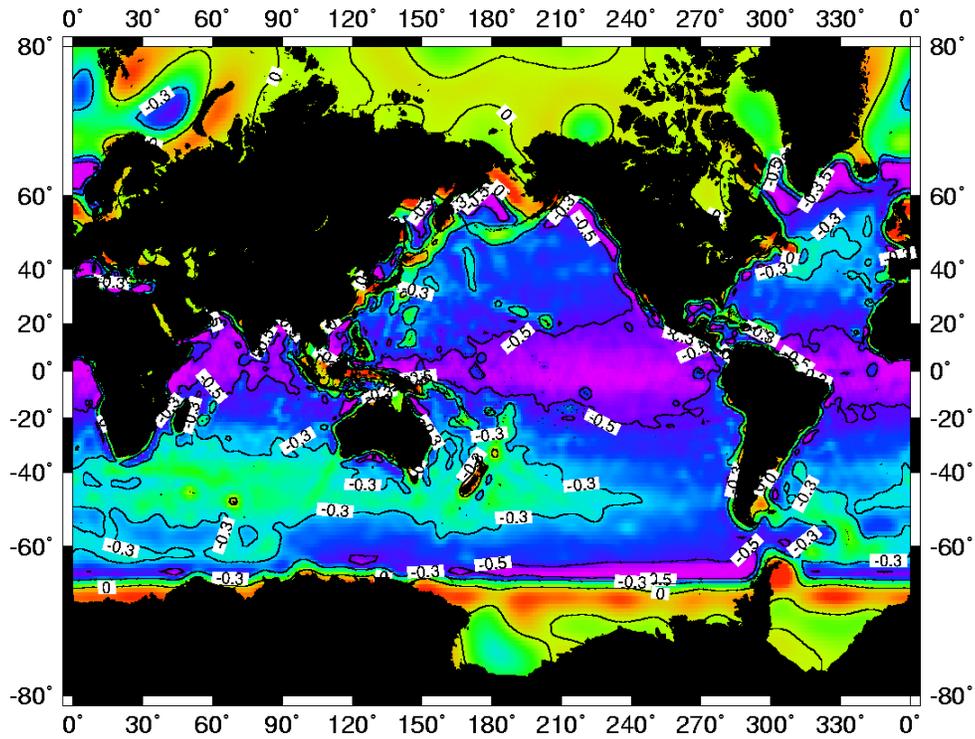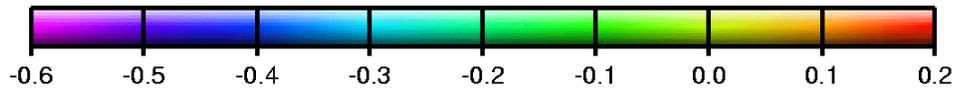
Figures 7.3.3.2–5. Global RMS correlations between the static T/P–ERS–1 dynamic ocean topography model (N_{max} = 20) from the PGS7337B solution and the geoid. Contour lines are at –0.5, –0.3, and 0.0 intervals.
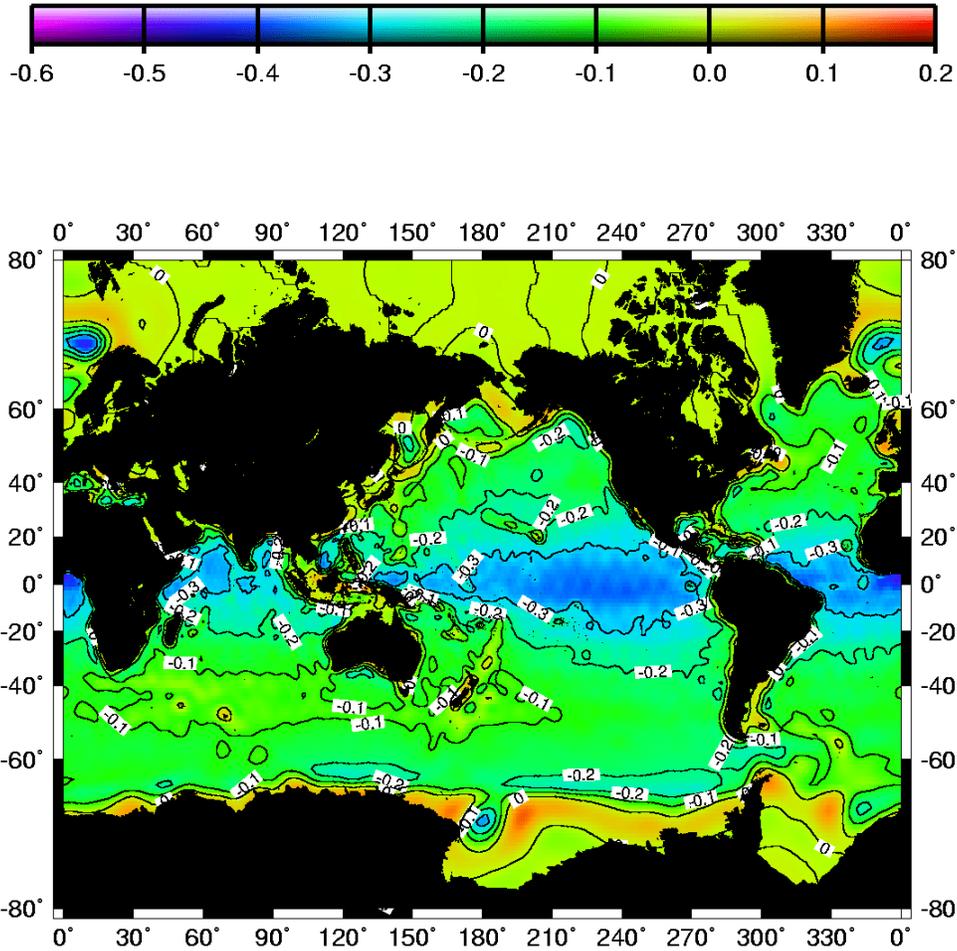
Figures 7.3.3.2–6. Global RMS correlations between the GEOSAT DOT model ($N_{max} = 20$) from the PGS7337B solution and the geoid. Contours are at –0.3, –0.2, –0.1, and 0.0 intervals.

Table 7.3.3.2–3. Predicted correlations between the geoid and the dynamic ocean topography models, from 1°x1° grids derived from the combination model covariances.

Solution	Satellite	N_{max}	RMS Correlation Over the Oceans (cm)		
			$|\varphi|<28.5°$	$|\varphi|<66°$	$66°<|\varphi|< 82°$
PGS5741	T/P	20	−0.437	−0.371	nv
PGS6399 (EGM−X02)	T/P	20	−0.306	−0.263	nv
PGS7337B	T/P−ERS−1	20	−0.438	−0.367	−0.022
JGM−2	GEOSAT	15	−0.183	−0.117	nv
PGS5741	GEOSAT	15	−0.270	−0.188	nv
PGS6399 (EGM−X02)	GEOSAT	15	−0.158	−0.110	nv
PGS7337B	GEOSAT	20	−0.231	−0.167	nv

nv = ζ model not valid in these latitudes
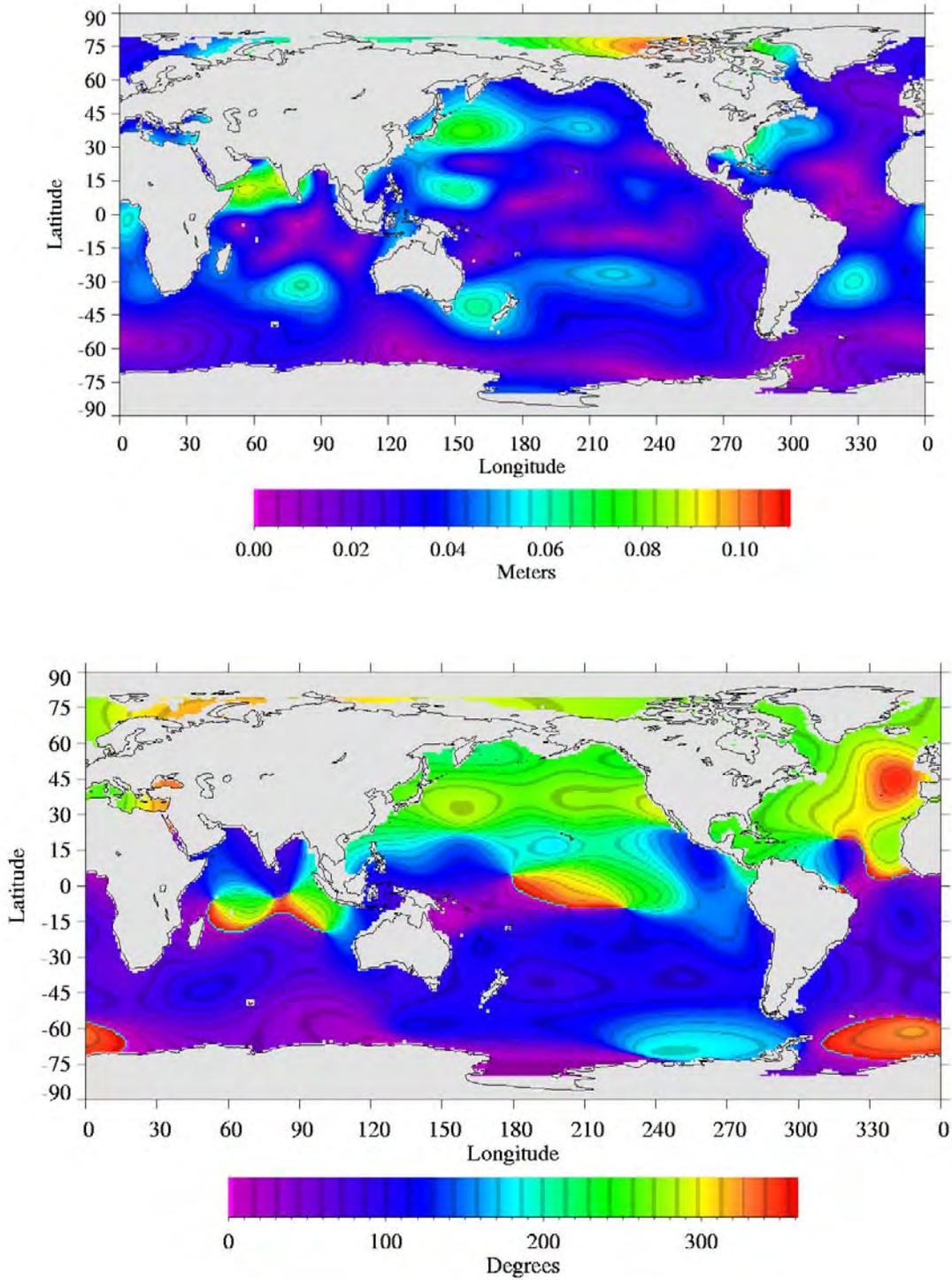
Figure 7.3.3.2–7. Amplitude and phase of the annual variation in the T/P dynamic ocean topography from the PGS7337B solution ($N_{max} = 10$). The phase is defined with respect to January 1.
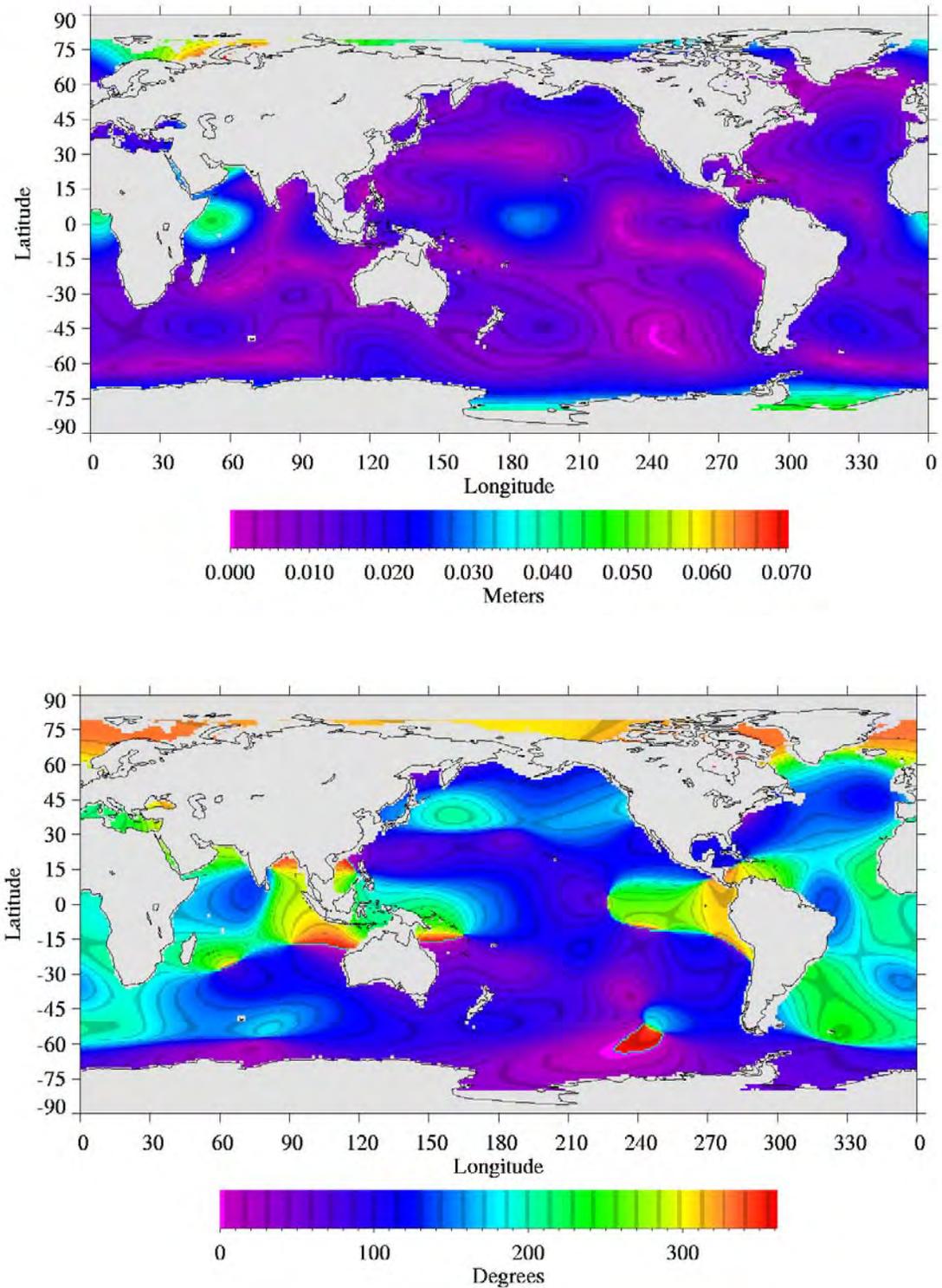
Figure 7.3.3.2–8. Amplitude and phase of the semiannual variation in the T/P dynamic ocean topography from the PGS7337B solution ($N_{max} = 10$). The phase is defined with respect to January 1.

7.3.3.3 The Altimeter Biases From the PGS7337B (EGM96) Solution

Altimeter biases were adjusted for each data arc during the creation of the normal equations, details of which were provided in Section 7.1. These biases were retained until the final gravity solution and adjusted as global parameters, along with the geopotential, tides, and other parameters. The altimeter biases from the PGS7337B combination solution are shown in Figures 7.3.3.3–1 for GEOSAT, 7.3.3.3–2 for T/P, and 7.3.3.3–3 for ERS–1. The 13 GEOSAT altimeter biases have a mean of –17.0 cm with a standard deviation of 0.28 cm. The 66 T/P altimeter biases have a mean of –47.7 cm with a standard deviation of 0.19 cm. The T/P altimeter biases show a strong annual variation with an amplitude of 2 to 2.5 cm. The ERS–1 altimeter bias has a mean of –77.0 cm with a standard deviation of 2.11 cm, and shows an annual variation similar to T/P. This annual variation in the T/P and ERS–1 biases has absorbed the effect of the degree zero term of the annual variation in the dynamic ocean topography (i.e., the mean change in sea level), which was not directly estimated in the EGM96 solution.
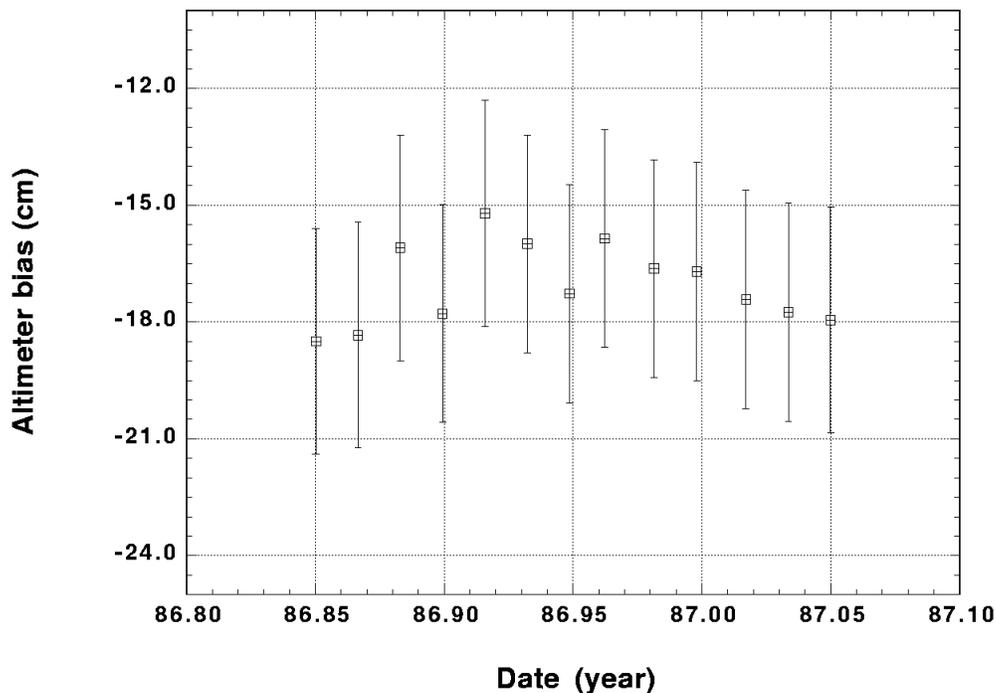
Figure 7.3.3.3–1. GEOSAT altimeter biases from the PGS7337B solution.
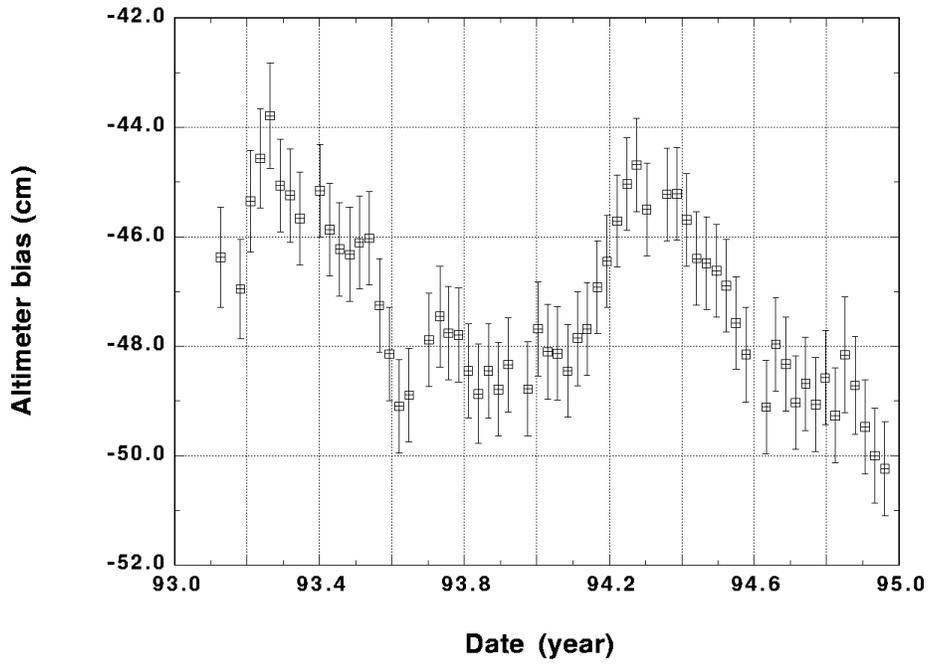
Figure 7.3.3.3–2. T/P altimeter biases from the PGS7337B solution.
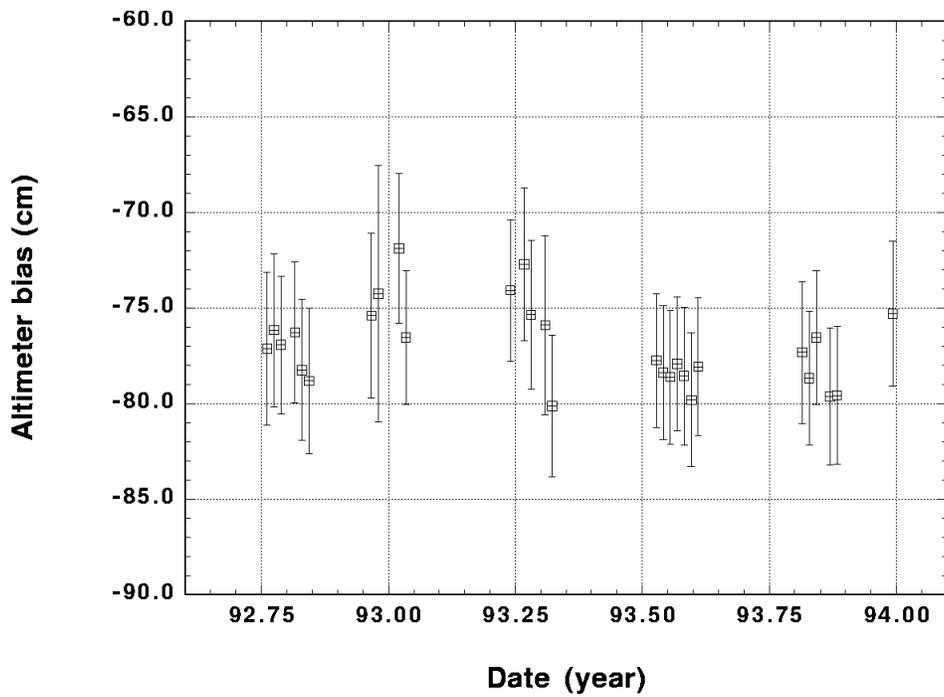
Figure 7.3.3.3–3. ERS–1 altimeter biases from the PGS7337B solution.

7–59

7.3.3.4 Final Testing of PGS7337B Variants

After the creation of the PGS7337B (EGM96) combination model, a number of variants were created in order to understand the performance sensitivity of the final combination solution. These permutations are listed in Table 7.3.3.4–1. The GPS/leveling tests with these final permutations are listed in Table 7.3.3.4–2. The PGS7337 solution verified that adjusting the once-per-revolution empirical acceleration parameters on GEOSAT resulted in a loss in geopotential signal. The NGS and British Columbia tests are neutral; however, the five-area average test shows a substantial improvement from 26.72 to 25.75 cm in PGS7337B. Three of the constituents (Europe, Canada, and Tennessee) of the five-area test (see Table 7.3.3.4–3) standard deviations are reduced by 0.9 cm, to 1.9 cm, when the one-cycle-per-revolution parameters are not adjusted. The strength of EP/EUVE in the solution is shown in PGS7337D by the degradation of the USA/NGS test from a standard deviation of 52.69 cm to 55.55 cm. The NGS test demonstrates that EP/EUVE contributes as strongly to the solution as the 1984 to 1986 data from Starlette. The removal of HILAT/RADCAL from the solution in PGS7337G has a negligible effect on the GPS/leveling tests. Downweighting of the altimetry has little effect on the US/NGS GPS/leveling test, but degrades the GPS/leveling comparisons over British Columbia and over the five areas by 0.6 and 0.75 cm in the standard deviation.

Table 7.3.3.4–1. Permutations of the PGS7337B combination solution.

Model	Description
PGS7337B	Final combination solution (EGM96)
PGS7337	PGS7337B with 1-CPR empirical accelerations adjusted on GEOSAT
PGS7337D	PGS7337B with all EP/EUVE (TDRSS and GPS) removed
PGS7337G	PGS7337B with HILAT and RADCAL removed
PGS7338	PGS7337 with altimetry downweighted by 50 percent
PGS7339	PGS7337B without GEOSAT altimetry

Table 7.3.3.4–2. GPS/Leveling results for PGS7337B permutations using HDM190 for the high-degree ($70<n\leq360$) field.

Gravity Model	GPS/leveling Comparisons Standard Deviation(cm)		
	5 Areas Average	BC	USA/NGS
PGS7337B	25.75	51.66	52.59
PGS7337	26.72	51.57	52.71
PGS7337D	25.65	52.19	55.55
PGS7337G	25.68	51.17	52.68
PGS7338	26.51	52.21	52.60
PGS7339	26.11	52.14	53.00

Table 7.3.3.4–3. GPS/Leveling results for PGS7337B permutations using HDM190 for the high-degree (70<n≤360) field: Detail for the five areas.

Gravity Model	GPS/leveling Comparisons Standard Deviation (cm)				
	Europe	Canada	Australia	Scandinavia	Tennessee
PGS7337B	31.57	27.35	27.95	19.07	21.04
PGS7337	32.47	29.28	27.40	19.47	22.68
PGS7337D	31.87	26.98	27.76	18.97	20.96
PGS7337G	31.40	26.52	27.79	19.06	22.19
PGS7338	32.76	28.13	27.40	19.77	22.42
PGS7339	32.28	27.47	27.63	20.36	21.01

The T/P–ERS–1 dynamic ocean topography solution from these PGS7337B derivative fields was compared with the POCM–4B ocean circulation model using the 24x24 spherical harmonic representation of the POCM–4B (see section 7.3.2.4). Removal of the GEOSAT altimeter data as in PGS7339 is undesirable since both the GPS/leveling comparisons (see Tables 7.3.3.4–2 and 7.3.3.4–3) as well as the $\bar{\zeta}$ vs. POCM–4B comparisons for T/P degrade (see Table 7.3.3.4–4). Downweighting of the altimeter data in PGS7338 has a negligible effect on the T/P DOT comparisons. Referring to Table 7.3.3.1–1, where the RMS errors from the 70x70 error covariance of the PGS7337B are tabulated, the RMS errors from the 70x70 error covariance of PGS7338 increase slightly (19.1 cm RMS over the globe compared to 18.1 cm; 28.65 cm RMS over land areas compared to 28.0 cm in PGS7337B; 13.5 cm over ocean areas compared to 11.8 cm in PGS7337B; and 12.9 cm over ocean areas ±66° compared to 11.1 cm in PGS7337B). The surprise is that a 50-percent change in the altimeter data weights should have so little impact on the predicted geoid errors to 70x70.

Table 7.3.3.4–4. Differences between a 24x24 spherical harmonic fit to POCM–4B, and the dynamic ocean topography ($\bar{\zeta}$) solutions from PGS7337B (EGM96) derivatives.

Solution	Satellite	Cumulative $\bar{\zeta}$ Differences to degree n, (RMS, cm)		C_{10} term of $\bar{\zeta}$ (cm)
		$n = 14$	$n = 20$	
PGS7337B	T/P–ERS–1	12.50	13.26	16.05 ± 2.30
PGS7337	T/P–ERS–1	12.54	13.32	15.95 ± 2.30
PGS7337D	T/P–ERS–1	13.15	13.91	15.17 ± 2.32
PGS7338	T/P–ERS–1	12.53	13.26	15.95 ± 2.43
PGS7339	T/P–ERS–1	12.66	13.46	15.77 ± 2.32

The dynamic ocean topography comparisons also demonstrate the strength of the EP/EUVE data. The T/P–ERS–1 $\bar{\zeta}$ vs. POCM–4B comparisons at degree 14 degrade from 12.50 cm to 13.15 cm with PGS7337D, for latitudes within ±66°. The combination model $\bar{\zeta}$ comparisons with the POCM–4B and PGS7337B and PGS7337D are illustrated in Figures 7.3.3.4–1 and 7.3.3.4–2. When EP/EUVE is excluded as in PGS7337D, the $\bar{\zeta}$ vs. POCM–4B differences increase substantially in the regions underneath the EP/EUVE track, most especially in the Indian Ocean and the waters off Indonesia. Differences which were 10 to 12 cm with PGS7337B are in excess of 20 cm with PGS7337D. The $\bar{\zeta}$ comparison can be repeated for the latitudes within ±28.5°. In this case, the cumulative dynamic ocean topography differences at degree 20 are 9.84 cm with PGS7337B, and 10.87 cm with PGS7337D, corresponding to a degradation in the ocean geoid over these latitudes of 4.62 cm.
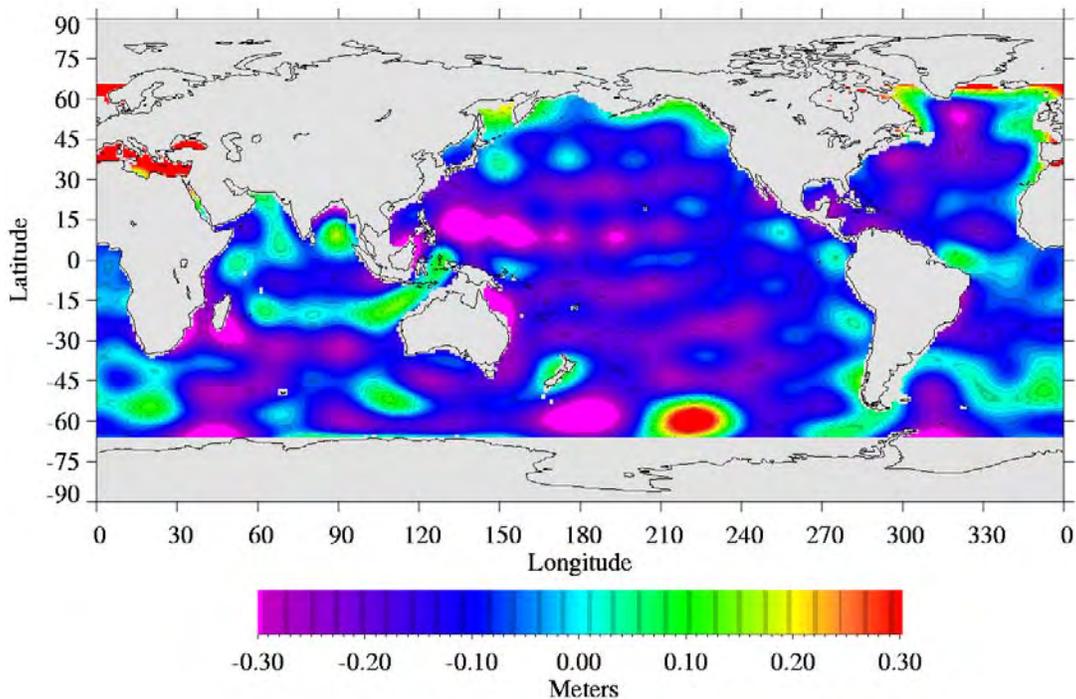
Figure 7.3.3.4–1. Differences between the T/P–ERS–1 dynamic ocean topography model (N_{max} = 20) from PGS7337B and the POCM–4B ocean circulation model.
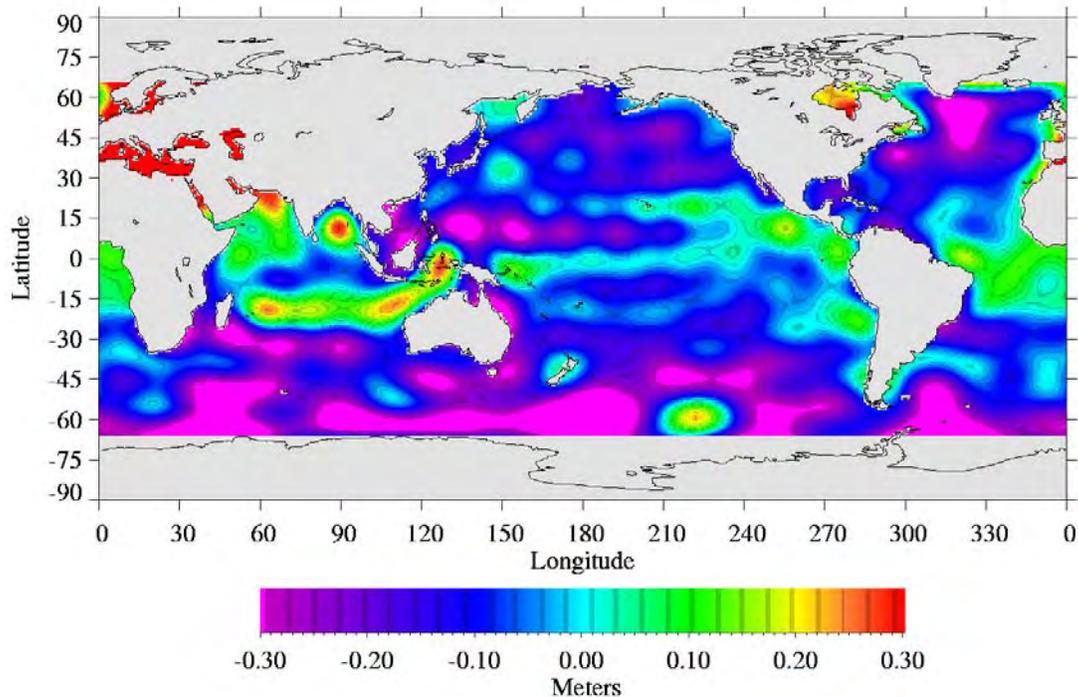
Figure 7.3.3.4–2. Differences between the T/P–ERS–1 dynamic ocean topography model (N_{max} = 20) from PGS7337D (a subset of PGS7337B with no EP/EUVE data) and the POCM–4B ocean circulation model. The EP/EUVE data contribute strongly to the marine geoid determination in the equatorial regions.

7.3.4 Tides

Table 7.3.4–1 compares the EGM96 tidal solution with PGS4846X, a model derived from the GEM–T3 tides solution using a truncated Schwiderski background model of maximum degree 15, with a lower maximum degree for some of the tide constituents. Generally, there is good agreement between the two models if the tidal amplitudes are over 1 cm. As with the satellite-only model solution, the S_a 3,0 tide term shows significant difference. However, the S_{sa} 3,0 term is now in much better agreement.

Table 7.3.4–2 presents a comparison of ocean tidal resonant terms from EGM96 and an update to the altimeter-derived oceanographic tides [*Schrama and Ray*, 1994; *Ray, private communication*, 1997]. Overall excellent agreement has been achieved in terms of both the amplitude and phase, providing a confirmation of the dynamic tides. The largest differences are in the S_2 2,2 and 4,2 tidal terms. In this case, the EGM96 solution includes the effect of the atmospheric tides, so some differences are anticipated and agree with atmospheric tidal predictions.

Table 7.3.4–1. Comparison of ocean tidal terms from the GEM–T3-derived tidal model PGS4846X and EGM96. PGS4846X uncertainties are from the GEM–T3 solution.

Tide Line	l	q	PGS4846X amplitude	σ (cm)	phase	σ (°)	EGM96 amplitude	σ (cm)	phase	σ (°)
M_m	2	0	0.84	±0.27	260.1	±18.6	0.90	±0.13	259.2	±7.9
	3	0	0.97	0.60	37.8	34.6	0.33	0.22	59.1	37.6
S_a	2	0	2.65	0.29	26.3	6.8	2.54	0.17	40.0	3.9
	3	0	5.17	0.52	313.9	5.8	2.59	0.26	290.2	5.5
M_f	2	0	2.05	0.28	240.4	7.8	2.05	0.16	240.0	4.4
	3	0	0.44	0.69	337.1	84.8	0.25	0.28	289.9	63.5
	4	0	0.52	–	99.1	–	1.42	0.88	124.4	35.7
	5	0	0.48	–	239.7	–	0.39	0.28	182.3	40.0
S_{sa}	2	0	1.61	0.30	255.9	10.8	1.48	0.14	275.6	5.2
	3	0	0.53	0.51	54.1	55.3	0.88	0.24	100.2	15.2
K_1	2	1	2.78	0.12	325.1	2.6	2.83	0.11	319.4	2.3
	3	1	0.79	0.09	13.6	6.9	0.95	0.05	33.5	2.8
	4	1	2.39	0.17	257.2	4.2	2.30	0.09	257.1	2.3
	5	1	2.23	0.20	107.8	4.9	1.92	0.06	114.0	1.8
	6	1	0.17	–	275.5	–	0.26	0.28	274.1	60.3
O_1	2	1	2.70	0.11	314.5	2.4	2.73	0.08	314.8	1.7
	3	1	1.37	0.13	79.5	5.6	1.57	0.05	83.7	1.6
	4	1	1.84	0.18	282.5	5.4	1.76	0.10	274.5	3.0
	5	1	1.59	0.18	121.6	6.6	1.21	0.06	115.2	3.0
	6	1	0.18	–	284.2	–	0.33	0.27	323.2	47.4
P_1	2	1	0.97	0.13	313.9	7.5	0.98	0.08	316.3	4.9
	3	1	0.38	0.09	6.5	14.5	0.27	0.05	30.0	10.4
	4	1	0.84	0.18	256.1	12.1	0.75	0.06	262.2	5.2
	5	1	0.76	0.20	122.9	14.3	0.47	0.06	114.5	7.5
Q_1	2	1	0.53	–	313.7	–	0.59	0.08	321.8	7.8
	3	1	0.32	–	104.2	–	0.20	0.05	98.3	14.8
	4	1	0.29	–	288.1	–	0.40	0.08	278.1	11.5
	5	1	0.22	–	112.3	–	0.26	0.07	126.5	15.7
K_2	2	2	0.34	0.04	315.9	6.6	0.27	0.03	327.5	5.5
	3	2	0.19	0.04	188.5	8.0	0.18	0.01	184.3	3.3
	4	2	0.15	0.04	105.5	14.1	0.13	0.02	120.8	8.7
	5	2	0.06	0.03	90.3	27.1	0.03	0.01	1.2	17.0
	6	2	0.04	0.04	358.3	50.0	0.04	0.02	329.3	61.0
M_2	2	2	3.31	0.04	321.1	0.7	3.27	0.03	321.9	0.6
	3	2	0.25	0.05	155.8	11.2	0.27	0.02	167.4	3.6
	4	2	0.98	0.04	125.8	2.3	1.05	0.03	130.0	1.6
	5	2	0.31	0.03	15.2	5.3	0.29	0.01	10.9	2.3
	6	2	0.39	0.04	317.2	6.4	0.44	0.03	329.3	4.3
	7	2	0.09	–	199.2	–	0.13	0.01	198.9	5.2
	8	2	0.13	–	214.3	–	0.16	0.03	193.0	12.1
S_2	2	2	0.78	0.02	301.0	2.9	0.76	0.03	304.1	2.3
	3	2	0.29	0.03	223.1	6.3	0.28	0.02	222.4	3.1
	4	2	0.36	0.04	94.0	2.3	0.38	0.02	102.3	2.7
	5	2	0.16	0.03	17.0	11.3	0.15	0.01	22.5	4.3
	6	2	0.17	0.04	276.8	13.3	0.15	0.02	287.0	6.7
	7	2	0.04	–	142.6	–	0.03	0.01	105.6	16.1
N_2	2	2	0.69	0.06	334.3	4.7	0.65	0.03	335.9	2.9
	3	2	0.10	0.05	152.2	30.0	0.08	0.01	169.4	11.1
	4	2	0.23	0.04	140.2	10.2	0.24	0.02	143.7	5.9
	5	2	0.08	0.03	354.5	23.0	0.08	0.01	0.6	6.8
	6	2	0.07	0.05	358.0	33.3	0.08	0.02	10.8	13.4
T_2	2	2	0.04	0.04	321.1	49.1	0.04	0.03	294.7	41.9
	3	2	0.02	0.03	340.9	30.0	0.02	0.01	328.2	36.2
	4	2	0.05	0.04	149.9	45.5	0.02	0.02	135.0	46.4
	5	2	0.06	0.03	57.0	25.5	0.04	0.01	29.1	11.7
	6	2	0.03	0.04	183.0	64.8	0.02	0.02	275.0	43.6

Table 7.3.4–2. Comparison of ocean tidal resonant terms: updated altimeter-derived model [*Schrama and Ray* 1994; *Ray, private communication*, 1997] vs. the EGM96 dynamic solution.

Tide Line			Altimetric				EGM96 Dynamic			
	l	*q*	amp.	σ (cm)	phase	σ (°)	amp.	σ (cm)	phase	σ (°)
K₁	2	1	3.00	–	317.57	–	2.83	±0.11	319.4	±2.3
	3	1	0.98	–	34.26	–	0.95	0.05	33.5	2.8
	4	1	2.08	–	254.10	–	2.30	0.09	257.1	2.3
O₁	2	1	2.59	–	313.91	–	2.73	0.08	314.8	1.7
	3	1	1.36	–	84.27	–	1.57	0.05	83.7	1.6
	4	1	1.51	–	279.96	–	1.76	0.10	274.5	3.0
M₂	2	2	3.23	–	320.62	–	3.27	0.03	321.9	0.6
	3	2	0.30	–	168.99	–	0.27	0.02	167.4	3.6
	4	2	1.06	–	130.20	–	1.05	0.03	130.0	1.6
S₂	2*	2*	1.24	–	318.09	–	0.76	0.03	304.1	2.3
	3	2	0.30	–	205.69	–	0.28	0.02	222.4	3.1
	4*	2*	0.37	–	106.46	–	0.38	0.02	102.3	2.7
N₂	2	2	0.70	–	330.49	–	0.65	0.03	335.9	2.9
	3	2	0.11	–	172.64	–	0.08	0.01	169.4	11.1
	4	2	0.24	–	141.35	–	0.24	0.02	143.7	5.9

* The EGM96 dynamic solution for these terms includes the S_2 atmospheric tide.

7.3.4.1 Orbit Tests

The assumption used in evaluating the tide model is that the satellites sense a tidal signal that is independent of, or at most weakly correlated with, the signal produced by the "static" gravity field. Thus, various orbit tests can be run by keeping the gravity field constant while varying the tide model. This assumption is justified as the correlations between gravity and tide parameters in the EGM96 are 0.2 or less. To test the quality of the computed ocean tide model for orbit applications, tests were made using selected SLR data sets, as described in Section 5.1.1. *One deviation from the standard LAGEOS tests is that the S_a and S_{sa} terms were not estimated; this will be discussed in more detail below.*

The orbit test results are given in Table 7.3.4.1–1. Comparison of test case one, which used the *a priori* PGS4846X tide model [*Lerch et al.*, 1992], with test case two show that the EGM96 tide model improves the Ajisai and Starlette RMS residual fits. However, for LAGEOS and LAGEOS–2 the opposite is true. One feature of the *a priori* GEM–T3 gravity/tide model, which gave heavy weight to the SLR data, is the very large—over 5 cm—value obtained for the $S_a(3,0)$ harmonic due to the contamination from LAGEOS's strong contributions, and the "LAGEOS Anomaly" [*Rubincam et al.*, 1997]. In short, the *a priori* tide model includes the effects of the unmodeled LAGEOS anomaly. The tides estimated, along with the EGM96 gravity solution, are less affected by the LAGEOS anomaly as a result of the additional data added from the newer satellites (i.e., T/P, EP/EUVE, GPS/MET, etc.) and the use of 1-CPR empirical acceleration estimation during certain time periods for LAGEOS. Consequently, LAGEOS orbit tests that do not compensate for the anomaly will show *worse* results with EGM96. In order to compensate

for this mismodeling, our past LAGEOS orbit tests allowed for the S_a and S_{sa} (2,0) and (3,0) terms to be adjusted. Doing this (as in case 3) reduced the LAGEOS fit 2.89 cm. Use of the *a priori* values for the S_a and S_{sa} (2,0) and (3,0) terms for all the satellites in the tests (case four) confirms this result, although with a deleterious effect on Ajisai and Starlette.

Table 7.3.4.1–1. Satellite orbit test (set-1) results using various ocean tide models with the EGM96 geopotential model.

Test	Tide Model	Multiarc RMS of Fit (cm)			
		Ajisai	LAGEOS	LAGEOS–2	Starlette
1	*a priori* (PGS4846X)	7.54	3.07	3.23	9.28
2	EGM96	7.34	3.18	3.38	7.92
3	adjust S_a & S_{sa} for LAGEOS		2.89		
4	using *a priori* S_a & S_{sa} for test	7.38	2.92	3.18	8.12
5	adjust S_2(2,2) & (4,2) for LAGEOS–2			3.09	
6	EGM96 adjustments with expanded model	7.23	3.07	3.34	7.80
7	above, using *a priori* S_a & S_{sa} for test	7.16	3.00	3.16	7.83
8	EGM96 with no detrending	7.37	3.25	3.47	7.99
9	above, using *a priori* S_a & S_{sa} for test	7.35	3.04	3.15	8.07
10	EGM96 with no detrending & yearly LAGEOS Sa & Ssa for '80–'94, LAGEOS–2 for '93–'94)	7.41	3.32	3.52	7.99
11	above, using '88 S_a & S_{sa} tides for test		3.05		
12	above, using *a priori* S_a & S_{sa} for test	7.37	3.03	3.14	8.06

The LAGEOS–2 tests show the same pattern as LAGEOS. The EGM96 tide models produce higher RMS fits for the test arcs as compared to the *a priori* tide model or the case where the *a priori* S_a and S_{sa} terms are used. A test case (five) was generated where S_2 tidal terms were estimated (LAGEOS–2 is in a different orbit than LAGEOS, with somewhat different sensitivity to the solar tides); the results of this test showed the best results seen to date for LAGEOS–2.

The modeling errors in the LAGEOS and LAGEOS–2 data did not seem to propagate significantly into the diurnal and semidiurnal tides, as the comparisons between the individual tide constituents of EGM96 and *Ray et al.* [1994] were quite good (see test case six). Combining the S_a and S_{sa} terms from the *a priori* with the expanded tide model (case seven), made an improvement on Ajisai, whereas the similar test using the nominal tides background model did not.

To evaluate the effect of the detrending in the EGM96 solution, a test model, PGS7337K, was generated that included all of the satellites in a single global tide model. The results of test case eight show that the orbit fits are almost as good as those resulting from the use of EGM96 for Ajisai and Starlette. We assume from these results that there was no need for "detrending" the S_2 (2,2) and (4,2) components for Spot–2 and Stella, or for all of the tide information from the T/P GPS data. However, the addition of the S_a and S_{sa} tide signals from the EP/EUVE GPS data, GPS/MET, Spot–2, and Stella made the orbit fits for LAGEOS and LAGEOS–2 somewhat

worse, as the results for test case nine, where S_a and S_{sa} were fixed to their *a priori* values, would imply.

The continued undesirable behavior of the LAGEOS and LAGEOS–2 orbit tests indicated that the primary cause was how the LAGEOS and LAGEOS–2 data are treated in the gravity/tides solution. Furthermore, all of the problems seem to be concentrated only in the Sa and Ssa components. Therefore, we attempted to separate out the LAGEOS anomaly and possible LAGEOS–2 anomaly from the tide model, while maintaining a global tide solution for all the other satellites. The LAGEOS and LAGEOS–2 Sa and Ssa tides were then estimated on a yearly basis in solution PGS7337M, resulting in 15 LAGEOS Sa components for (2,0), 2 LAGEOS–2 S_a components for (2,0), 15 S_{sa} components for (2,0), 2 LAGEOS–2 S_{sa} components for (2,0), etc. The values are presented in Table 7.3.4.1–2.

Table 7.3.4.1–2. LAGEOS and LAGEOS–2 yearly S_a/S_{sa} tide values and uncertainties from solution PGS7337M, compared to the EGM96 global tides solution for these terms.

S_a	2	0	Satellite	Year	Amplitude (cm)	σ (cm)	phase (°)	σ (°)
S_a	2	0	Global		2.6	±.18	43.52	±3.91
			LAGEOS	1980	2.54	1.52	359.02	44.03
				1981	4.35	4.76	16.66	54.98
				1982	1.75	5.03	79.05	168.78
				1983	2.33	3.93	15.85	101.38
				1984	1.39	3.57	19.63	142.83
				1985	2.78	3.81	50.97	78.84
				1986	2.3	2.74	32.83	72.03
				1987	2.71	2.93	55.62	61.39
				1988	1.38	3.30	71.59	132.58
				1989	2.68	3.88	56.44	82.43
				1990	3.35	3.43	34.46	60.32
				1991	1.77	3.78	25.21	123.85
				1992	3.23	2.87	8.92	52.25
				1993	3.06	2.18	25.24	41.40
				1994	1.12	1.66	358.67	89.10
			LAGEOS–2	1993	2.38	1.34	50.84	31.96
				1994	1.59	1.40	29.08	51.91
S_a	3	0	Global		2.31	.25	285.55	5.74
			LAGEOS	1980	7.74	2.98	306.56	21.11
				1981	7.13	3.13	307.11	25.15
				1982	9.54	3.65	346.17	18.64
				1983	7.37	2.97	295.61	21.81
				1984	6.39	1.87	312.26	16.80
				1985	6.82	2.19	332.34	18.27
				1986	10.16	1.95	286.99	10.11
				1987	6.33	1.30	272.65	10.47
				1988	6.15	2.28	331.94	20.98
				1989	19.11	75.60	79.6	256.79
				1990	11.42	69.44	242.31	368.40
				1991	54.64	78.75	262.04	91.06
				1992	35.86	58.64	270.71	110.10
				1993	9.83	3.48	295.56	19.81
				1994	22.66	3.88	281.84	10.36
			LAGEOS–2	1993	1.48	1.95	192.36	80.05

S_a	2	0	Satellite	Year	Amplitude (cm)	σ (cm)	phase (°)	σ (°)
				1994	2.33	2.42	99.26	46.97
S_{sa}	2	0	Global		1.8	.14	276.78	4.46
			LAGEOS	1980	2.84	2.41	227.45	48.38
				1981	2.22	3.83	268.17	96.50
				1982	4.46	4.51	266.48	58.77
				1983	2.39	3.94	285.87	95.18
				1984	1.62	3.51	337.61	126.37
				1985	1.73	2.79	267.59	91.91
				1986	1.13	1.99	272.46	106.69
				1987	2.23	2.83	245.06	73.92
				1988	1.6	3.51	303.64	125.76
				1989	1.35	3.86	220.95	164.79
				1990	1.61	2.97	284.35	99.05
				1991	1.69	3.47	249.28	119.60
				1992	0.5	3.41	221.76	397.05
				1993	0.76	2.07	341.27	151.57
				1994	1.38	2.23	305.03	92.99
			LAGEOS–2	1993	2.72	.95	271.77	19.98
				1994	2.71	1.14	276.17	23.77
S_{sa}	3	0	Global		0.85	.22	96.22	14.60
			LAGEOS	1980	1.38	2.75	304.38	114.60
				1981	1.24	2.40	2.65	103.62
				1982	0.41	3.46	112.52	455.80
				1983	0.77	2.94	220.28	218.11
				1984	0.3	1.72	114.3	337.10
				1985	0.79	1.97	68.47	149.50
				1986	2.73	2.01	32.74	41.92
				1987	0.92	1.62	128.32	101.40
				1988	2.4	2.10	23.45	53.15
				1989	25	54.50	117.19	121.65
				1990	10.66	36.10	187.93	171.09
				1991	6.67	54.90	302.11	481.58
				1992	7.77	49.61	299.69	378.30
				1993	0.55	3.54	141.02	365.36
				1994	8.29	3.87	166.85	27.88
			LAGEOS–2	1993	2.17	2.33	317.49	61.44
				1994	1.15	2.59	34.31	128.35

While not indicating a complete solution to the problem of the optimal tides estimation, the results of the orbit tests using PGS7337M are promising. Comparison of test case ten, which used the global tides solution, with case two shows that the results for the LAGEOS satellites are significantly worse, which is to be expected since the global solution should accommodate none of the S_a and S_{sa} effects of the LAGEOS anomaly. Unfortunately, the detrending of the LAGEOS tidal components had a slight negative impact on Ajisai, as based on the comparisons between cases eight and ten. Use of the S_a and S_{sa} terms estimated using LAGEOS (only) for 1988 restore the LAGEOS fit the 3.0 cm level, as does the use of the *a priori* S_a and S_{sa} values, confirming that the separately estimated tidal terms captured some unmodeled force acting on LAGEOS. As is also apparent from these tests, and the comparisons between test cases eight and nine, Ajisai benefits in a minor way from the LAGEOS derived S_a and S_{sa} values.

Starlette, which is probably the best satellite of the set to assess the tidal performance due to the comparatively high orbit eccentricity and low perigee height, shows the best overall results using

the estimated EGM96 tide parameters. This is true using either the nominal, Schwiderski-based, background tide model, or the expanded tide model. However the results of all the orbit tests indicate that the ideal tidal solution has yet to be reached.

It is important to note that the geopotential model calibration activity was focused on the static portion of the model. The tidal parameter calibration, when attempted using these data weights, is unsatisfactory. This indicates significant problems with the temporal sampling of the long-period tidal resonance effects. While satellite-specific adjustment of tidal parameters may improve this situation to a degree, this remains an outstanding issue awaiting further investigation and perhaps alternative solution approaches.

7.3.4.2 Expanded Background Ocean Tide Model: A Recommendation

The introduction of extensive time series of empirical acceleration adjustments as part of the orbit determination strategy provides a great degree of accommodation for errors made in modeling the long period tidal perturbations. It is, therefore, the background tidal model, giving rise to short-period orbit perturbations and containing both omission and commission errors, which was additionally scrutinized with the completion of the adjusted EGM96 tide terms. These short-period errors are not effectively abated within the orbit solution with the adjustment of empirical time dependent accelerations with the exception of those at the orbit frequency, when 1-CPR accelerations are adjusted.

The magnitude of the short-period orbit mismodeling is a function of the local error being made in the tidal modeling at the subsatellite point. These orbit errors will (a) be largest where the tide modeling is most in error; (b) be a function of the level of detail employed for ocean tidal modeling in the orbit process (i.e., defined by the cutoff for omitted terms), and (c) have the same aliasing period (for example, shown in Table 7.3.4.2–1 for T/P) for orbit errors as that of the tidal sampling itself. The theoretical basis for these perturbations are given in *Colombo* [1984].

Table 7.3.4.2–1. Tidal aliasing period for T/P.

Tidal Constituent	Period on Earth's Surface	Aliasing Period (Days) (to sample tidal cycle at fixed point on the Earth's surface)
Q_1: 135.6555	1.120 days	69.4 days
O_1: 145.5555	1.076 days	45.7 days
P_1: 163.5555	1.003 days	88.9 days
K_1: 165.5555	23.935 hours	173.2 days
9_1: 167.5535	23.805 hours	329.4 days
N_2: 245.6555	12.658 hours	49.5 days
M_2: 255.5555	12.421 hours	62.1 days
S_2: 273.5555	12.000 hours	58.7 days
K_2: 275.5555	11.967 hours	86.6 days

The expanded EGM96 background tide model has been developed and tested. These models include M_2, S_2, N_2, K_2, P_1, O_1, Q_1, and K_1 harmonic models complete to degree and order 15 from Schwiderski. Analysis associated with these improved tidal models will be discussed below to quantify the effect of background tidal omission and commission errors on SLR orbit modeling accuracy.

This expanded tide model consists of 3349 coefficients pairs. When taking into account the total number of mainline and sideband terms, this represents about 35000 different spherical harmonic terms and a significant computational burden. This expanded background model effectively eliminates all omission errors and should be used for achieving the highest possible orbital accuracy. Analysis performed by *Marshall et al.* [1995] shows significantly reduced tidal signature in the T/P POE's disagreement with the reduced dynamic trajectories.

Use of a more complete background model is recommended. Table 7.3.4.1–1, shows the results of using the EGM96 tidal adjustments with the expanded background model. One can see that further orbital improvements are forthcoming with its application, though this is at the cost of increased computation time.

7.3.5 Reference Frame Realization

The description of the gravitational potential model with a spherical harmonic series involves the geodetic coordinates of the point of computation. Therefore, it requires consistency between the reference frames used in the development of the model and at the time of evaluation. The Earth fixed reference frame for the EGM96 gravity model solution is defined by fixing the latitude and longitude of the Greenbelt, Maryland, SLR site, and the latitude of the Haleakela, Hawaii, site at the position used in JGM–2. The adjustment of SLR site positions with information from all of the SLR satellites ensures that the frames of these satellites will be the same. For satellites that use other tracking technologies, the connection to the SLR frame is achieved by one of three methods, in order of preference:

1. By use of local survey information relating the position of an SLR system with that of other technologies at some SLR sites.

2. Through orbital dynamics of a satellite that was tracked by multiple systems.

3. Through one common Earth orientation parameter (EOP) adjustment for all of the satellite data and fixing a longitude of a tracking site for that tracking system and satellite.

For the first-frame tie method, the local survey distances between the SLR system, and the other tracking technologies were fixed to link the frame from other technologies to the SLR. For example, Table 7.3.5–1 shows the local survey information that was used to link the Spot–2 DORIS frame with the LAGEOS SLR frame.

An example of the second type of frame tie—through satellite dynamics—is the simultaneous SLR and Doppler tracking of SEASAT. Because the SLR and Doppler data both contributed to the estimation of the SEASAT state vectors, the Doppler and SLR frames are linked together. This Doppler–SLR connection was exploited to link the modern Doppler tracking frame to the SLR frame. Table 7.3.5–2 shows the local survey tie information used in EGM96 to tie the

Doppler sites from SEASAT and GEOSAT together. The Doppler site at Thule, Greenland, brings the modern Doppler information (Hilat and Radcal) into the same frame as GEOSAT, and hence into the SLR frame through the common GEOSAT–SEASAT Doppler sites.

The constraint for the SLR position of Greenbelt and Hawaii defined the Earth-fixed frame for T/P. The T/P orbit dynamics, common to both tracking systems, constrained the locations of the T/P DORIS sites to be consistent with that of the SLR.

Table 7.3.5–1. Spot–2 DORIS and SLR local survey ties used in EGM96.

location	DORIS site	SLR site	ΔX (m)	ΔY (m)	ΔZ (m)
Huahine	4027	7061	−4.6635	8.8673	4.5090
Easter Island	4041	7061	−9.8646	3.5882	−5.1321
Arequipa	4046	7907	4.6540	−1.0900	3.8000

For some of the Doppler-tracked satellites, there were no tracking systems that were collocated with SLR. Additionally, the systems either were not located at a Doppler site that was used by GEOSAT or SEASAT, or local survey information to link the different Doppler systems was neither available nor reliable. This forced the Doppler to SLR frame tie to be achieved only through the common EOP adjustment. To remove the rank deficiency in the adjustment of EOP, satellite sate, and tracking sites, a longitude of one of the Doppler tracking sites was held fixed. Although the common adjustment of EOP allows the frame tie to the SLR to be achieved, this tie is somewhat weaker than the first two methods. An example of this type of constraint was the fixing of the longitude of Herndon, Virginia, for the Oscar satellite data.

Table 7.3.5–2. SEASAT–GEOSAT Doppler receiver local survey ties used in EGM96.

Location	SEASAT site	GEOSAT site	ΔX (m)	ΔY (m)	ΔZ (m)
Brussels	21	547	34.03	13.66	−23.22
Ottowa	128	564	0.81	−1.25	−0.90
Calgary	30414	563	−0.01	−0.02	0.03

Table 7.3.5–3 lists the satellites used in the gravity model solution, the tracking technology used, and the frame tie utilized in the EGM96 estimation.

Table 7.3.5–3. EGM96 satellite and tracking system frame definition.

Satellite	Tracking Type	Frame tie utilized
Ajisai	Laser	SLR frame: fix ϕ and λ of Greenbelt, MD, and ϕ of Haleakala , HI
BE–C	Laser	SLR frame: fix ϕ and λ of Greenbelt, MD, and ϕ of Haleakala , HI
	Doppler	fix λ of APL, MD (41111)
D1–C	Laser	fixed Earth Orientation
	Doppler	fix λ of APL, MD (41112 same site as D1–D)
D1–D	Laser	fixed Earth Orientation
	Doppler	fix λ of APL, MD (41112 same site as D1–C)
ERS–1	Laser	SLR frame same as T/P
ETALON–1	Laser	SLR frame: fix ϕ and λ of Greenbelt, MD, and ϕ of Haleakala , HI
EUVE	TDRSS	site positions unadjusted
	GPS	Earth Orientation and site positions unadjusted
GEOS–1	Laser	SLR frame: fix ϕ and λ of Greenbelt, MD, and ϕ of Haleakala , HI
GEOS–2	Laser	SLR frame: fix ϕ and λ of Greenbelt, MD, and ϕ of Haleakala , HI
GEOS–3	Laser	SLR frame: fix ϕ and λ of Greenbelt, MD, and ϕ of Haleakala , HI
	SST Doppler	dynamic tie to the SLR
GEOSAT	Doppler	Doppler tracking sites at Brussels, Ottowa, and Calgary tied to SEASAT sites (Table 7.3.5–2)
GFZ–1	Laser	SLR frame: fix ϕ and λ of Greenbelt, MD, and ϕ of Haleakala , HI
GPS/MET	GPS	site 55020898 common with T/P and EUVE
HILAT	Doppler	15 Doppler sites in common with GEOSAT
LAGEOS	Laser	SLR frame: fix ϕ and λ of Greenbelt, MD, and ϕ of Haleakala , HI
LAGEOS–2	Laser	SLR frame: fix ϕ and λ of Greenbelt, MD, and ϕ of Haleakala , HI
NOVA–1	Doppler	fix λ of 3711
optical (all)	optical	optical frame: fixed Earth Orientation
OSCAR–14	Doppler	fix λ of 60407
Peole	Laser	fixed Earth Orientation
	Doppler	
RADCAL	Doppler	Doppler site at Thule, Greenland (35508) tied to the Thule GEOSAT site (557)
SEASAT	Laser	SLR frame: fix ϕ and λ of Greenbelt, MD, and ϕ of Haleakala , HI
	Doppler	satellite dynamics constrain the Doppler sites to the SLR frame
Spot–2	DORIS	DORIS systems at Easter Island, Huahine, and Arequipa, Peru, are tied to the SLR systems at those sites (Table 7.4.3–3)
Starlette	Laser	SLR frame: fix ϕ and λ of Greenbelt, MD, and ϕ of Haleakala , HI
Stella	Laser	SLR frame: fix ϕ and λ of Greenbelt, MD, and ϕ of Haleakala , HI
T/P	Laser	SLR frame at epoch 930101, fix ϕ and λ of Greenbelt, MD, and ϕ of Haleakala , HI
	DORIS	satellite dynamics tie the T/P DORIS sites to the SLR frame
	GPS	five GPS sites fixed

A subtle frame issue arose in the aggregation of the normal equation for EGM96. The more recently analyzed SLR data (1993 through 1995) were analyzed in a frame that was not consistent with that of the earlier data. The frame used for the 1993 to 1995 SLR data was the T/P precise orbit determination (POD) frame. This frame was neither consistent in epoch position nor in time evolution with the JGM2 frame. The T/P POD frame (CSR93L01 [*Boucher et al.*, 1994]) had an epoch of January 1, 1988, and a tectonic velocity model from CSR93L01, whereas the other JGM–2 SLR data were in a frame that had an epoch of July 1, 1987, and used the NUVEL NNR–1 tectonic motion model [*DeMets et al.,* 1990] for all sites. To combine normals

for the recent SLR data in the CSR93L01 frame with the normal from the JGM–2 frame, the *a priori* positions and tectonic velocities for the CSR93L01 frame were transformed to that of the JGM–2 frame with the following algorithm:

Given the two frames JGM–2 ("*s*") and CSR93L01 ("*c*") with different epochs, epoch positions, and velocities, we define the following:

$$t_s^0 \neq t_c^0 \qquad\qquad \text{epoch}$$
$$\vec{X}_s(t_c^0) \neq \vec{X}_c(t_c^0) \qquad \text{epoch station position}$$
$$\dot{\vec{X}}_s \neq \dot{\vec{X}}_c \qquad\qquad \text{tectonic station velocity}$$

then the station position at time *t* for the *s* frame is

$$\vec{X}_s(t) = \vec{X}_s(t_s^0) + (t - t_s^0)\dot{\vec{X}}_s \qquad\qquad\qquad (7.3.5 -1)$$

and for the *c* frame,

$$\vec{X}_c(t) = \vec{X}_c(t_c^0) + (t - t_c^0)\dot{\vec{X}}_c \qquad\qquad\qquad (7.3.5 -2)$$

The first step in this transformation algorithm transformed the "c" frame to the "s" frame by applying the difference between the two different *a priori* values, using the SOLVE program [*Ullman*, 1992], to change the "right-hand side" of the normal equations set "c" *a priori* values to:

$$\vec{X}_s(t_c^0), \dot{\vec{X}}_s \qquad\qquad\qquad (7.3.5 -3)$$

This step changed the epoch position of the frame but not the epoch time.

The second step used the normal equations created in the first step in the SOLVE program for the EGM96 solution, but:

a. The right-hand side of the normal equations from step 1 was not allowed to change to compensate for different *a priori* values of station and tectonic velocity.

b. The unchanged station normal equations from the preceding step were combined with the "s" frame normals.

c. The unchanged station tectonic velocity normal equations from step a. above were removed; i.e., the site velocity normals were not combined with the "s" frame site velocity normals.

d. The SLR positions were adjusted; the SLR site velocity parameters were not adjusted.

The result was SLR station positions in EGM96 at epoch t_s^0 with tectonic velocity $\dot{\vec{X}}_s$.

7.3.5.1 The EGM96 Earth Orientation Parameters

EGM96 included solution for Earth-orientation parameters (EOP). The X– and Y– position of the pole (in milliarcseconds), and the recovered values for A1–UTC in seconds are shown in Figure 7.3.5.1–1. The figure also shows the excess length of day in milliseconds, calculated by forming a simple forward difference in the recovered A1–UTC series. The increased density of plotted values in 1993 and 1994 reflects the different EOP adjustment intervals in that time span. EOP were adjusted in 5-day intervals from 1980 through 1993, and 1-day intervals thereafter. These

adjustment intervals for EOP were chosen to correspond to the same intervals of the *a priori* series: the IERS 90C04 time series [IERS,1990].

The EOP solution differences from the *a priori* IERS 90C04 time series are shown in Figure 7.3.5.1–2. The recovered X-pole position in the EGM96 solution was offset by 6 mas bias from the *a priori* series 90C04, which has been removed from the top frame of Figure 7.3.5–2. The larger scatter in the differences for 1980 through the middle of 1983, particularly evident in the X- and Y-pole plots, is a result of the poorer quality SLR data from that time period. The SLR systems of the early 1980's were generally second generation, having noise of a few cm, and the number of systems worldwide was less than those deployed currently. Beginning in the middle of 1983, the SLR systems began a major upgrade resulting in data with increased precision and reduced systematic errors. Prior to the launch of T/P in 1992, the SLR systems were further upgraded to have precision of a few mm. Coupled with lengthened tracking schedules that allowed more data to be acquired, these better quality data allowed more frequent adjustment of the EOP in 1993 and 1994 within the EGM96 solution. The somewhat larger scatter shown in the figure for 1993 and 1994, when compared to 1990 through 1992, is due to the 5x more frequent adjustment interval. As the data used in the estimation have both better spatial and temporal coverage, and increased precision, the 1-day adjustment differences display a scatter that is a bit less than expected from the increased adjustment frequency. The slight slope apparent in the Y-pole plot is secular drift in the Y-pole position caused by the effect of the Laurentide postglacial rebound [*Peltier*, 1997].
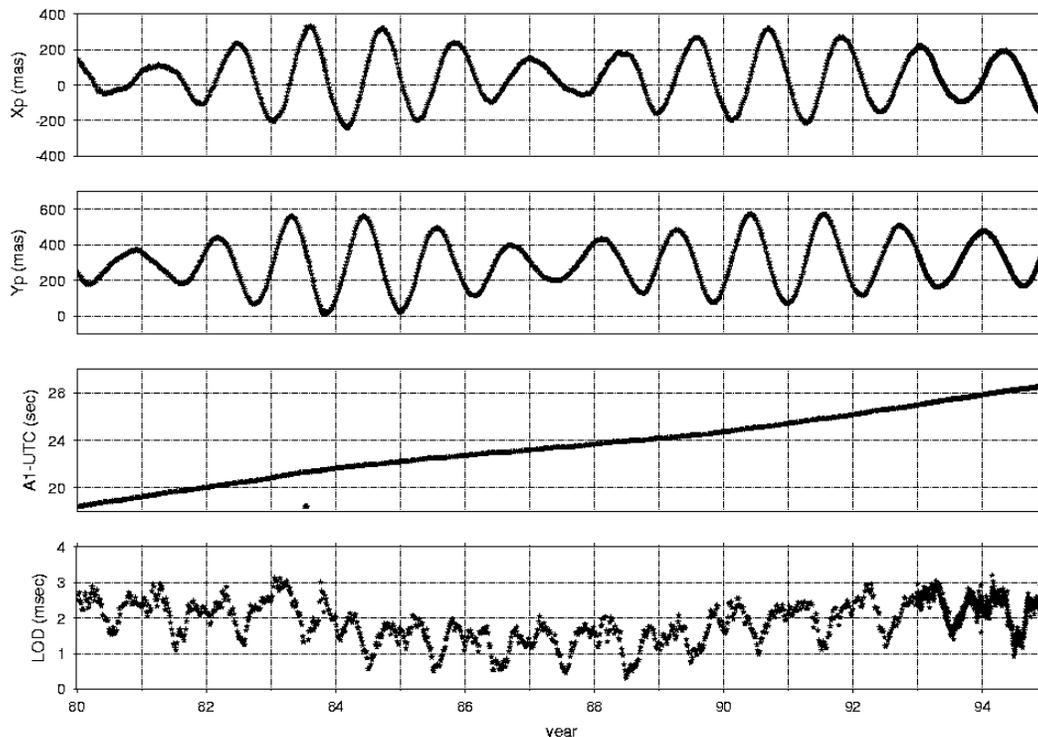
Figure 7.3.5.1–1. X-pole, Y-pole, A1–UTC, and Length of Day for EGM96.
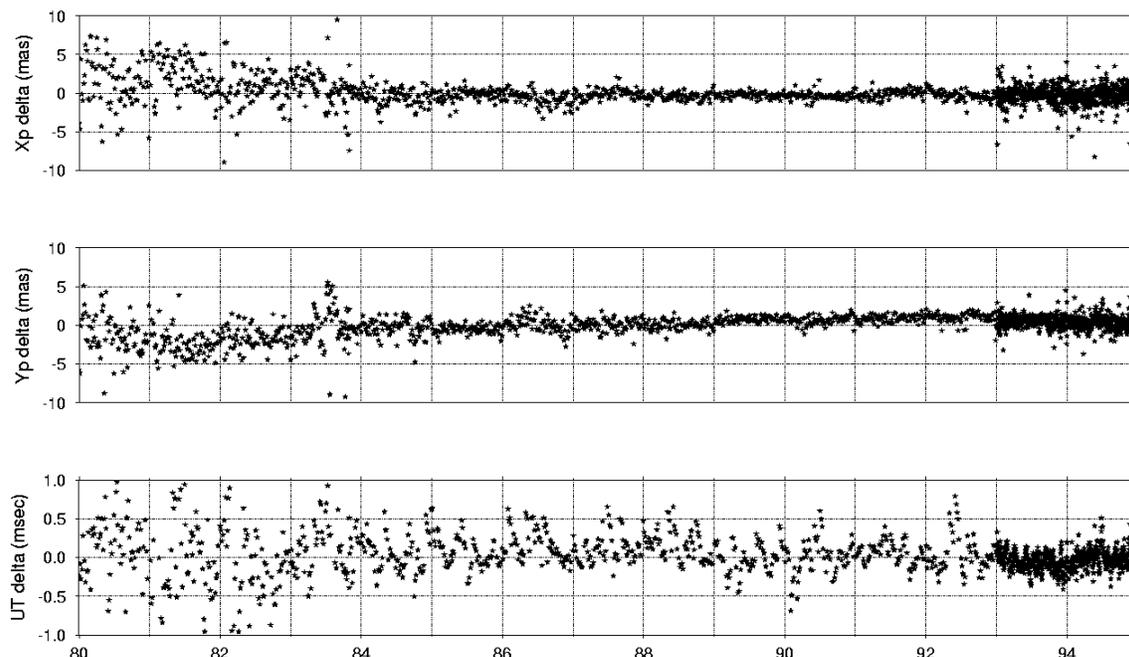
Figure 7.3.5.1–2. Difference of EGM96 EOP solution with the IERS 90C04 time series. A 6 mas bias has been removed from the ΔXp values.

7.3.5.2 The Relationship of the EGM96 Solution to ITRF94

In EGM96, the global frame is defined by the network of the SLR stations. This frame will have multiple realizations depending on the number and distribution of the stations included in the definition of the transformation. A comparison of the EGM96 frame with the International Terrestrial Reference Frame 1994 (ITRF94) frame was performed by using a seven-parameter similarity transformation between the two Cartesian. This similarity transformation takes the form [*McCarthy,* 1996]:

$$\begin{pmatrix} x_s \\ y_s \\ z_s \end{pmatrix} = \begin{pmatrix} x \\ y \\ z \end{pmatrix} + \begin{pmatrix} T1 \\ T2 \\ T3 \end{pmatrix} + \begin{pmatrix} D & -R3 & R2 \\ R3 & D & -R1 \\ -R2 & R1 & D \end{pmatrix} \begin{pmatrix} x \\ y \\ z \end{pmatrix} \qquad (7.3.5.1-1)$$

where the sense of the transformation is from (x, y, z) to (x_s, y_s, z_s); (T1, T2, T3) give the translation of the coordinate origin between the two frames; $R1$, $R2$, and $R3$ represent differential rotations expressed in radians around the axes (x_s, y_s, z_s); and D is the differential scale change. The criteria for computation of this transformation were (1) that the total position residual after application of the transformation be less than 10 cm, (2) that no duplicate stations be used at the same tracking site, and (3) uncertainty estimates on the station coordinates from both the IERS solution and the EGM96 solution were used to perform a weighted least-squares adjustment.

7–75

Between 18–24 stations satisfy these criteria. Solutions were tried using a base set of 24 stations, and permutations of this base set, omitting selected stations. A list of the EGM96 coordinates for the 24 base stations, along with their formal uncertainties, is provided in Table 7.3.5.2–1. To make the uncertainties commensurate with the ITRF94 values, the formal uncertainties were scaled by a factor of 0.5 for all the stations, except for the Greenbelt, MD, site. The latitude and longitude of this station were fixed in the comprehensive combination low degree geopotential solution, resulting in unrealistically small uncertainties. Therefore, an uncertainty of 0.5 cm was used for each of this site's Cartesian position components. In all cases, the comparisons used coordinates mapped to the epoch 930101. The EGM96 SLR station coordinates have an epoch 860701, and so were mapped to epoch 930101 using the tectonic motion model SL7.1 This velocity field should be used for mapping any of the station coordinates from EGM96 to an epoch other than 860701. Table 7.3.5.2–2 shows the result of the similarity transformation.

Table 7.3.5.2–1. List of sites used in similarity transformation from EGM96 to ITRF94 at epoch January 1, 1993.

Location	CDP site #	X (m)	Formal σ	Y (m)	Formal σ	Z (m)	Formal σ
McDonald, TX	7080	−1330021.108	± 0.012	−5328401.810	±0.010	3236480.850	±0.009
Yarragadee, Australia	7090	−2389006.647	0.010	5043329.383	0.008	−3078525.015	0.011
Easter Island	7097	−1884984.202	0.035	−5357608.164	0.027	−2892853.365	0.026
Greenbelt, MD	7105	1130719.648	0.001	−4831350.615	0.005	3994106.481	0.004
Quincy, CA	7109	−2517234.830	0.009	−4198556.117	0.010	4076569.741	0.007
Monument Peak, CA	7110	−2386278.155	0.009	−4802354.156	0.009	3444881.584	0.007
Platteville, CO	7112	−1240678.276	0.022	−4720463.372	0.022	4094480.628	0.015
Mazatlan, Mexico	7122	−1660089.477	0.015	−5619100.327	0.012	2511637.936	0.013
Huahine	7123	−5345867.168	0.024	−2958246.908	0.030	−1824623.998	0.026
Mt. Haleakala, HI	7210	−5466006.579	0.007	−2404427.473	0.013	2242187.825	0.002
Goldstone, CA	7265	−2356475.774	0.040	−4646618.236	0.034	3668424.777	0.031
Arequipa, Peru	7403	1942807.808	0.015	−5804069.781	0.008	−1796915.575	0.010
Askites, Greece	7510	4353444.996	0.043	2082666.210	0.049	4156506.597	0.035
Melengiclick, Turkey	7580	4247620.580	0.057	2778638.882	0.062	3851607.444	0.046
Yigilca, Turkey	7587	4117362.098	0.057	2517076.757	0.058	4157678.991	0.048
Grasse, France	7835	4581691.838	0.011	556159.287	0.013	4389359.298	0.013
Shanghai, China	7837	−2831087.645	0.045	4676203.467	0.043	3275172.908	0.040
Graz, Austria	7839	4194426.774	0.013	1162693.812	0.013	4647246.486	0.013
Herstmonceux, England	7840	4033463.906	0.010	23662.265	0.011	4924305.001	0.011
Orroral Valley, Australia	7843	−4446476.946	0.019	2678127.190	0.021	−3696251.318	0.017
Cabo San Lucas, Mexico	7882	−1997242.085	0.072	−5528041.089	0.061	2468355.427	0.062
Ensenada, Mexico	7883	−2406126.993	0.072	−4898368.198	0.067	3290336.760	0.051
Matera, Italy	7939	4641965.147	0.012	1393069.826	0.012	4133262.160	0.013
Wettzell, Germany	8834	4075577.118	0.021	931785.238	0.022	4801583.424	0.017

The origins of the EGM96 and ITRF94 frames coincide to within 1 cm, and there is a change scale of about 1.5 ± 0.4 ppb between EGM96 and ITRF94. The rotations seem robust and are little altered by the number of stations selected for the transformation. The rotations about X and

Y are most likely directly related to the constraints that were used to solve for the SLR station coordinates in the EGM96 solution—namely, that both the latitude and longitude of Greenbelt, as well as the latitude of Haleakala (Maui, Hawaii) were fixed at the JGM–2 values. These rotations are seen in the comparison of the EGM96 polar motion series to the *a priori* IERS series 90C04 (see Figure 7.3.5.2–2), where a constant offset of about 6 mas is observed in the X position of the Earth's rotation pole.

Table 7.3.5.2–2. Transformation parameters from EGM96 to ITRF94.

	T1 (ΔX) (mm)	T2 (ΔY) (mm)	T3 (ΔZ) (mm)	D (scale) (ppb)	R3 (Z–rot) (mas)	R2 (Y–rot) (mas)	R1 (X–rot) (mas)
	24 stations used						
Solution	1.43	3.62	–2.48	1.47	–7.59	6.19	0.14
Standard deviation	2.58	2.42	2.55	0.36	0.10	0.10	0.10
	22 stations used: Base set without 7882 and 7883						
Solution	1.49	3.66	–2.46	1.47	–7.59	6.20	0.14
Standard deviation	2.58	2.42	2.56	0.36	0.10	0.10	0.10
	21 stations used: Base set without 7882, 7883, and 7837						
Solution	1.35	4.29	–2.05	1.52	–7.59	6.18	0.12
Standard deviation	2.60	2.44	2.58	0.36	0.10	0.10	0.10
	18 stations used: Base set without 7510, 7580,7587, 7882, 7883, and 7837						
Solution	0.93	4.42	–2.35	1.52	–7.61	6.18	0.12
Standard deviation	2.62	2.46	2.62	0.37	0.10	0.10	0.10

The correlations between the similarity transformation parameters for the case of 24 SLR stations is shown in Table 7.3.5.2–3. The highest correlations for these parameters are 0.4. The detailed station-by-station difference statistics after application of the transformation are listed in Appendix E, for the 24 SLR station case. The residual RMS difference in position for all 24 stations after the transformation is applied is 28.5 mm in X, 28.2 mm in Y, and 20.5 mm in Z.

Table 7.3.5.2–3. Correlations between the similarity transformation parameters for base set of 24 SLR stations.

	T1	T2	T3	D	R3	R2	R1
T1, Δx	1.0	–0.065	–0.053	0.022	0.282	0.493	0.139
T2, Δy		1.0	0.068	0.268	–0.114	–0.053	–0.422
T3, Δz			1.0	–0.497	0.052	–0.057	–0.421
D, scale				1.0	–0.053	0.043	0.081
R3, Z-rot					1.0	–0.077	0.175
R2, Y-rot						1.0	0.158
R1, X-rot							1.0

7.3.5.3 The Relationship of the EGM96 Solution to WGS84

EGM96's heritage derives from the previously successful solutions JGM–1 and –2 that support the T/P project [*Nerem et al*., 1994b]. One of the constraints imposed by this fact is the adoption of a specific reference frame (heretofore refered to as the T/P frame), on the basis of which a large number of satellite tracking data were already reduced to normal equations. The T/P frame was, within the accuracy of its realization, identical to ITRF91. The joint project requires that the final product be referred to a current realization of the WGS84, designated WGS84(G730) [*Malys and Slater*, 1994]. One aspect of this investigation, therefore, is to gauge the differences between these two frames. The WGS84(G730) frame was based on a global GPS campaign in 1992 and has been shown [*ibid*.] to be indistinguishable from ITRF92 at the 10 cm level. The ITRF92 frame differs from ITRF91 at the 2 cm level, well within the accuracy of the two. This essentially leads to the conclusion that the reference frame realized by the EGM96 components (station positions, velocities, constants, gravity coefficients, etc.) and the WGS84(G730) frame are indistinguishable within their respective accuracy estimates.

Since IERS annually revises the definition of the ITRF, another aspect of the problem is how important are these changes in terms of changes in the computed geoid. Inspection of the history of transformation parameters between successive ITRF realizations from Table 3.1 of *McCarthy* [1996] leads to the conclusion that the changes are minor for all of the most recent years considering the accuracy of these frames. In other words, the ITRF is quite stable through time.

Various test transformations of the common sites' positions between the two frames showed only small variations, well below the accuracy of the results (see Section 7.3.5.2). To verify that these changes are indeed insignificant in the most important applications of EGM96, we used a preliminary set of transformation parameters, listed in Table 7.3.5.3–1, and proceeded to evaluate their effect on the computed geoid and a representative set of satellite orbits.

Table 7.3.5.3–1. Transformation parameters from EGM96 to ITRF94.

Parameter	Value Used
T_x	–0.12 mm
T_y	+5.08 mm
T_z	–1.81 mm
D	1.40 ppb
R_x	0.30 mas
R_y	6.10 mas
R_z	–7.60 mas

In addition to the coordinate system differences, the adopted values for *GM* and a_e (used in scaling the spherical harmonic series) are also different, albeit only slightly. We therefore had to further scale the coefficients of the spherical harmonic series to account for these differences:

$$GM_{\text{T/P}} = 398600.4415 \text{ km}^3\text{s}^{-2}$$

$$GM_{\text{WGS84}} = 398600.4418 \text{ km}^3\text{s}^{-2}$$

$$a_{e\ (\text{T/P})} = 6378136.300 \text{ m}$$

$$a_{e\ (\text{WGS84})} = 6378137.000 \text{ m}$$

Based on the invariance of the geopotential, we made the following correction to scale the C and S coefficients of the transformed EGM96 to produce a set fully compliant with WGS84(G730), designated here as EGM96W:

$$\{C, S\}_{\text{EGM96W}} = \{C, S\}_{\text{EGM96}} \frac{GM_{\text{T/P}}}{GM_{\text{EGM96W}}} \left(\frac{a_{e(\text{T/P})}}{a_{e(\text{EGM96W})}} \right)^n \qquad (7.3.5.3\text{–}1)$$

The application of the Helmert transformation parameters was effected in two ways: the rigorous procedure described in [*Goldstein*, 1984] and the much simpler method described in [*Kleusberg*, 1980]. The latter is valid for differentially small quantities and the parameters described in Table 7.3.5.3–1 certainly fall in that category. It is not surprising then that the two methods gave identical results. The coefficient set thus produced was used to perform geoid and orbital tests.

The geoid tests comprised maximum, minimum, and RMS difference computations for two global geoid grids, each computed with one of the above sets of coefficients including terms up to degree 360 (i.e., the complete model). Due to the introduction of nonzero degree 0 and 1 terms by the transformation procedure, two sets of statistics were computed: (a) When the degree 0 and 1 terms were included and (b) where we ignored them. The results were close in either case:

(a) Min = –5.3 mm, Max = 6.1 mm, RMS = 3.2 mm

(b) Min = –1.6 mm, Max = 1.0 mm, RMS = 0.7 mm

Given the accuracy of the model, these differences are of no consequence for any of the intended applications. The global distribution of the differences is shown in the Figures 7.3.5.3–1 and –2

As far as the orbital tests, one recognizes that a change in the GM value introduces a change in the initial conditions that can be resolved only by repeating the data reduction process to readjust them. The tests that were performed validated this fact in every case. Several satellite orbits were tested; however, the ones that carried the greatest weight in making a decision were those of the two LAGEOS satellites, Starlette, and Ajisai. The LAGEOS arcs were 30 days long, the Starlette arc 6 days, and the Ajisai 5 days. In all cases, the radial component differences (the largest amongst radial, cross, along), were at, or less than, 3 mm RMS. Furthermore, the values of these discrepancies are mostly due to the mean scale offset between the two orbits, which is entirely the result of the difference in GM values.

As a result of the above investigation and the geoid and orbital tests that were performed, it was concluded that the original EGM96 coefficients, and those transformed and scaled to comply with WGS84(G730), produced sufficiently comparable orbits and geoidal models so that adoption of the transformed set was not warranted.
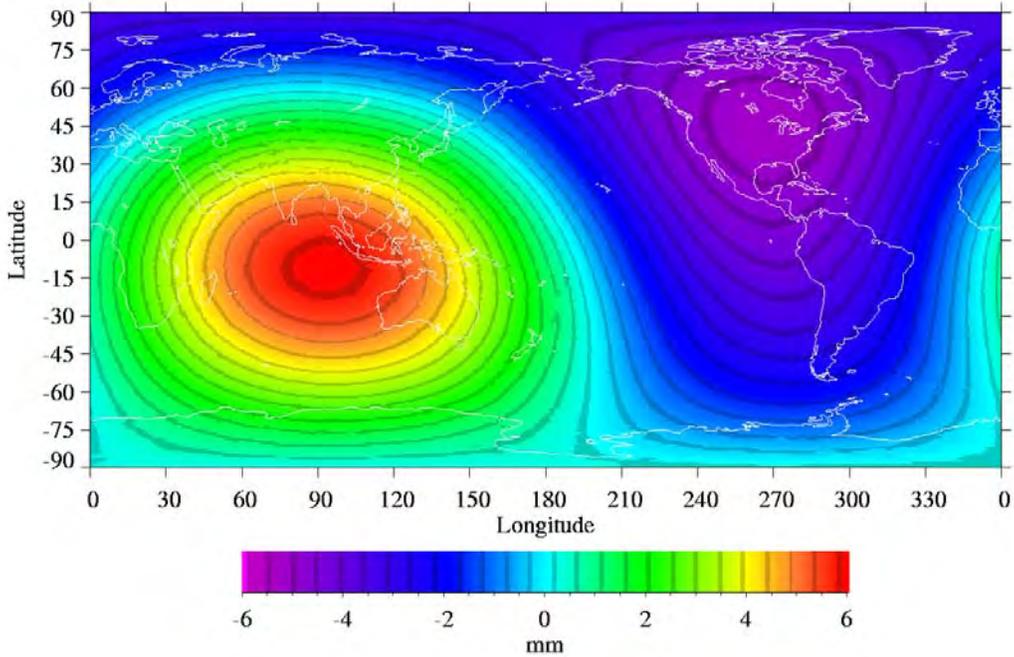
Figure 7.3.5.3–1. Geoid undulation difference introduced by the test transformation from the EGM96 solution frame to the WGS84(G730) frame. All terms (including degree 1) through degree 360 used.
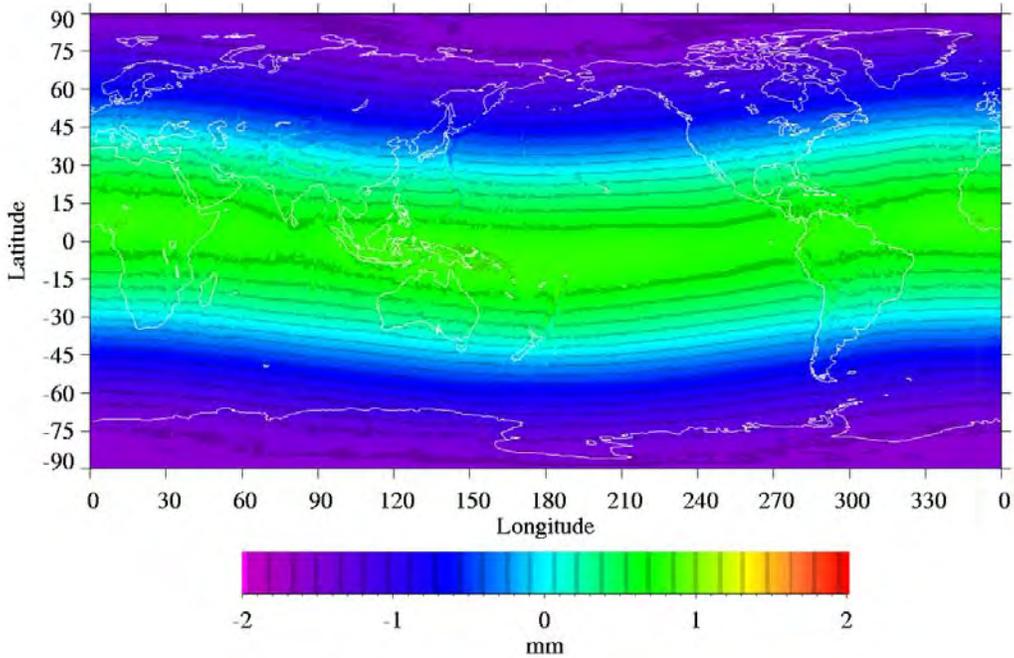
Figure 7.3.5.3–2. Geoid undulation difference introduced by the test transformation from the EGM96 solution frame to the WGS84(G730) frame. Terms from degrees 2 through 360 used.

7.4   Summary

Satellite tracking data, discussed in detail in Section 6, are sensitive primarily to the long-wavelength geopotential through degree 40. Altimeter data and surface gravity data provide complementary shorter wavelength information. These three data types were combined to form a low-degree (N_{max} = 70) *comprehensive* combination geopotential solution, PGS7337B. In addition to the geopotential, this comprehensive solution included estimates for 112 tidal coefficients, Earth orientation parameters, station locations, and spherical harmonic coefficients describing the dynamic ocean topography (DOT). The DOT solutions included a common 20x20 model of the static component for both T/P and ERS-1, a 20x20 static model for GEOSAT, and 10x10 models for the yearly and semiannual variations for the combination of T/P and ERS-1.

The combination solution included direct altimeter data from GEOSAT, T/P (excluding the POSEIDON data), and ERS–1, extending altimeter coverage to the high latitudes ($|\varphi| < 82°$). Altimeter normal point data were formed using a number of editing criteria, including a minimum depth criterion to eliminate inaccurate tidal corrections and storm surge effects (200 m for T/P and ERS–1, and 1000 m for GEOSAT), and a maximum high degree ($70 < n \le 460$) geoid contribution to eliminate regions of steep geoid gradients, such as ocean trenches. A variable data weighting scheme was used to assign the altimeter data uncertainty as a function of RMS sea surface variability and the high-degree geoid contribution. In total, 274812 GEOSAT Exact Repeat Mission observations (from November 1986 through January 1987), 2892900 T/P observations spanning two complete years (1993 and 1994), and 542417 ERS–1 observations sampling a complete year (1993), were used in the EGM96 solution.

The development of surface gravity normal equations for the low-degree portion of EGM96 used the 1° gravity data described in Section 3. Since the altimetry data were incorporated as direct satellite tracking data, the altimeter-derived anomalies were excluded from the file used to develop the surface gravity normals. Ellipsoidal corrections and an analytic downward continuation were applied. For regions lacking data coverage, "fill-in" anomalies were formed from the combination of EGM96S coefficients (to maximum degree 40), augmented with the information provided by a model of the topographic-isostatic potential (from degree 41 to 70). To reduce aliasing of the higher-frequency content ($n > 70$) of the actual data (i.e. no "fill-in"), this component of the signal was removed prior to the normal equation formation.

The development of the final combination solution was a multistep process. Many interim solutions were developed to evaluate the quality of the dynamic ocean topography solutions, determine the relative weights of the ERS–1, T/P, and GEOSAT data as well assess the performance of the models on the land with GPS/leveling data. Evaluation of the interim models showed that the power spectra of the T/P-derived dynamic ocean topography dipped below the spectrum of the geoid uncertainty at about degree 17. The GPS and TDRSS satellite tracking data from EP/EUVE improve significantly the marine geoid determination in the equatorial regions. Improved satellite tracking data, the large quantity of T/P altimetry data, as well as the incorporation of the surface gravity data at its full weight (unlike JGM–1,–2, and –3), decreased the predicted 70x70 global geoid undulation error from 50.9 cm for JGM–3 to 18.1 cm using EGM96.

7.5   References

Bertiger, W.I., Y.E. Bar–Sever, E.J. Christensen, E.S. Davis, J.R. Guinn, B.J. Haines, R.W. Ibanez–Meier, J.R. Jee, S.M. Lichten, W.G. Melbourne, R.J. Muellerschoen, T.N. Munson, Y. Vigue, S.C. Wu, T.P. Yunck, B.E. Schutz, P.A.M. Abusali, H.J. Rim, M.M. Watkins, and P. Willis, "GPS precise tracking of TOPEX/POSEIDON: Results and implications, *J. Geophys. Res.*, *99*, C12, 24449–24464, 1994.

Bilitza, D., Improving IRI for Better Ionospheric Predictions, 1996 Ionospheric Effects Symposium, 1–9 May, 1996.

Bilitza, D., International Reference Ionosphere—Status 1995/96, to be published in *Space Research*, 1997.

Boucher, C., Z. Altamimi, and L. Duhem, Results and Analysis of the ITRF93*, IERS Technical Note 18*, Observatoire de Paris, October, 1994.

Busalacchi, A.J., and J. Picaut, Seasonal variability from a model of the tropical Atlantic Ocean*, J. Phys. Oceanogr., 13*, 1564–1588, 1983.

Callahan, P.S., TOPEX/POSEIDON NASA GDR User's Handbook, *JPL Rep. D–8950, Rev. C,* Jet Propulsion Laboratory, Pasadena, California, 1993.

Cheney, R.E., N.S. Doyle, B.C. Douglas, R.W. Agreen, L. Miller, E.L. Timmerman and D.C. McAdoo, The Complete GEOSAT Altimeter GDR Handbook, *NOAA Manual NOS NGS 7,* U.S. Dept. of Commerce, NOAA/NOS, Rockville, MD, 1991.

Cheney, R., L. Miller, R. Agreen, N. Doyle, J. Lillibridge, TOPEX/POSEIDON: The 2-cm solution, *J. Geophys. Res., 99*, 24,555–24,564, 1994.

Colombo, O.L., "Altimetry, Orbits and Tides," NASA TM 86180, GSFC, November 1984.

Cartwright, D.E., and R.D. Ray, Oceanic Tides from GEOSAT Altimetry, *J. Geophys. Res*., 95, C3, 3069–3090, 1990.

Douglas, B.C., Global sea level rise: A redetermination, *Surveys in Geophysics, 18*, 2–3, 279–292, 1997.

Emery, W.J, G.H. Born, D.G. Baldwin, and C.L. Norris, Satellite-Derived Water Vapor Corrections for Geosat Altimetry, *J. Geophys. Res., 95,* C3, 2953–2964,1990.

Fu, L.L., J. Vasquez, and M.E. Parke, Seasonal variability of the Gulf Stream from satellite altimetry, *J. Geophys. Res, 92*, 749–754, 1987.

Fu, L.L., E.J. Christensen, C.A. Yamarone, M. Lefebvre, Y. Ménard, M. Dorrer, and P. Escudier, TOPEX/POSEIDON mission overview, *J. Geophys. Res., 99,* C12, 1994.

Gloersen, P., W.J. Campbell, D.J., Cavalieri, J.C. Comiso, C.L. Parkinson, and H.J. Zwally, Arctic and Antarctic Sea Ice, 1978–1987: Satellite Passive-Microwave Observations and Analysis, Scientific and Technical Information Program, NASA, NASA SP–511, Washington D.C., 1992.

Goldstein, J., The Effect of Coordinate System Rotations on Spherical Harmonic Expansions: A Numerical Method, *J. Geophys. Res., 89*, 4413–4418, 1984.

Haagmans, R., E. de Min and M. van Gelderen, Fast evaluation of convolution integrals on the sphere using 1D FFT, and a comparison with existing methods for Stokes' integral, *Manusc. Geod.*, *18*, 227–241, 1993.

Heck, B., An evaluation of some systematic error sources affecting terrestrial gravity anomalies, *Bull. Geod.*, *64*, 88–108, 1990.

IERS Annual Report for 1989, International Earth Rotation Service (IERS), Observatoire de Paris, July 1990.

Jekeli, C., On the analytical reduction of the surface gravity anomaly for harmonic analysis, presented at the meeting of Working Group I of the DMA/GSFC Joint Gravity and Geoid Improvement Project, Greenbelt, MD., 1995.

Jekeli, C., Spherical harmonic analysis, aliasing, and filtering, *J. Geod.*, *70*, 214–223, 1996.

Kleusberg, A., The Similarity Transformation of the Gravitational Potential, *manuscripta geodetica, 5*, No. 4, 241–256, 1980.

Klobuchar, J. A., Ionospheric time-delay algorithm for single-frequency GPS users, *IEEE Trans., Aerosp. Electron Syst., AES–23,* 325–331, 1987.

Knudsen, P., Global low harmonic degree models of the seasonal variability and residual ocean tides from TOPEX/POSEIDON altimeter data, *J. Geophys, Res., 99,* 24643–24655, 1994.

Laskowski, P., The effect of vertical datum inconsistencies on the determination of gravity related quantities, *Rep. 349*, Dept. of Geod. Sci. and Surv*.,* Ohio State Univ., Columbus, 1983.

Le Provost, C., M.L. Genco, F. Lyard, P. Vincent, and P. Canceil, Spectroscopy of the world ocean tides from a finite element hydrodynamic model, *J. Geophys. Res., 99,* 24777–24798, 1994.

Lerch, F.J., Optimum data weighting and error calibration for estimation of gravitational parameters, *Bull. Geod.*, 65, 44–52, 1991.

Lerch, F.J., R.S. Nerem, B.H. Putney, T.L. Felsentreger, B.V. Sanchez, J.A. Marshall, S.M. Klosko, G.B. Patel, R.G. Williamson, D.S. Chinn, J.C. Chan, K.E. Rachlin, N.L. Chandler, J.J. McCarthy, S.B. Luthcke, N.K. Pavlis, D.E. Pavlis, J.W. Robbins, S. Kapoor, and E.C. Pavlis, Geopotential models from satellite tracking, altimeter, and surface gravity data: GEM–T3 and GEM–T3S, *J. Geophys. Res.*, *99*, 2815–2839, 1994.

Levitus, S., Climatological Atlas of the World Ocean, *NOAA Prof. Paper 13*, 1982.

Malys, S., and J. Slater, *Maintenance and Enhancement of the World Geodetic System 1984*, ION GPS–94, Salt Lake City, UT, September 1994.

Marsh, J.G., F.J. Lerch, C.J. Koblinsky, S.M. Klosko, J.W. Robbins, R.G. Williamson, and G.B. Patel, Dynamic sea surface topography, gravity and improved orbit accuracies from the direct evaluation of Seasat altimeter data, *J. Geophys. Res., 95,* 13129–13150, 1990.

Marshall, J.A., N. Zelensky, S. Klosko, D. Chinn, S. Luthcke, K. Rachlin, E. Williamson, The temporal and spatial characteristics of TOPEX/POSEIDON, *J. Geophys. Res., 100*, 25331–25352, 1995.

Martel, F., and C. Wunsch, Combined Inversion of Hydrography, Current Meter Data and Altimetric Elevations for the North Atlantic Circulation, *Manuscr. Geod., 18*, 1993.

McCarthy, D.D., IERS Conventions (1996), *IERS Technical Note 21,* U.S. Naval Observatory, July 1996.

Miller, L., R.E. Cheney, and B.C. Douglas, GEOSAT altimeter observations of Kelvin waves and the 1986–87 El Niño, *Science, 239*, 52–54, 1988.

Mitchum, G., Comparison of TOPEX sea surface heights and tide gauge sea levels, *J. Geophys. Res., 99, C12*, 24541–24554, 1994.

Moritz, H., *Advanced Physical Geodesy*, Herbert Wichmann, Karlsruhe, Federal Republic of Germany, 1980.

Nerem, R.S., B.D. Tapley, and C.K. Shum, Determination of the ocean circulation using Geosat altimetry, *J. Geophys. Res., 95,* 3163–3179, 1990.

Nerem, R.S., E.J.O. Schrama, C.J. Koblinsky, and B.D. Beckley, A preliminary evaluation of ocean topography from the TOPEX/POSEIDON mission, *J. Geophys. Res., 99,* C12, 24565–24583, 1994a.

Nerem, R.S., F.J. Lerch, J.A. Marshall, E.C. Pavlis, B.H. Putney, B.D. Tapley, R.J. Eanes, J.C. Ries, B.E. Schutz, C.K. Shum, M.M. Watkins, S.M. Klosko, J.C. Chan, S.B. Luthcke, G.B. Patel, N.K. Pavlis, R.G. Williamson, R.H. Rapp, R. Biancle, and F. Nouel, Gravity Model Development for TOPEX/POSEIDON: Joint Gravity Models 1 and 2, *J. Geophys. Res.*, 24421–24447, 1994b.

Nouël, F., J.P. Berthias, M. Deleuze, A. Guitart, P. Laudet, A. Piuzzi, D. Pardines, C. Valorge, C. Dejoie, M.F. Susini, and D. Taburiau, Precise Centre National d'Etudes Spatiales orbits for TOPEX/POSEIDON: Is reaching 2 cm still a challenge?, *J. Geophys. Res.,* 99, 24405–24420, 1994.

Pattulo, J., W. Munk, R. Revelle, E. Strong, The seasonal oscillation in sea level, *J. Mar. Res, 14*, 88–155, 1955.

Pavlis, N.K., Modeling and estimation of a low degree geopotential model from terrestrial gravity data, *Rep.* 386, Dept. of Geod. Sci. and Surv., Ohio State Univ., Columbus, 1988.

Pavlis, N.K., and R.H. Rapp, The development of an isostatic gravitational model to degree 360 and its use in global gravity modelling, *Geophys. J. Int., 100*, 369–378, 1990.

Peltier, W.R., Global Sea Level and Earth Rotation, *Science*, *240*, 895–901, 1988.

Peltier, W.R., and X. Jiang, Glacial isostatic adjustment and Earth rotation: Refined constraints on the viscosity of the deepest mantle, *J. Geophys. Res., 101*, 3269–3290, 1997.

Rapp, R.H., and J.Y. Cruz, The representation of the Earth's gravitational potential in a spherical harmonic expansion to degree 250, *Rep. 372*, Dept. of Geod. Sci. and Surv., Ohio State Univ., Columbus, 1986.

Rapp, R.H., and N.K. Pavlis, The development and analysis of geopotential coefficient models to spherical harmonic degree 360, *J. Geophys. Res., 95*, 21885–21911, 1990.

Rapp, R.H., Y.M. Wang and N.K. Pavlis, The Ohio State 1991 geopotential and sea surface topography harmonic coefficient models, *Rep. 410*, Dept. of Geod. Sci. and Surv., Ohio State Univ., Columbus, 1991.

Ray, R.D., B.V. Sanchez, and D.E. Cartwright, Some extensions to the response method of tidal analysis applied to TOPEX/POSEIDON altimetry, abstract, *EOS Transactions*, American Geophysical Union, *75*, 16, 1994.

Ray, Richard D., Raytheon STX Corp., private communications, 1997.

Rubincam, D.P., D.G. Currie, J.W. Robbins, LAGEOS I once-per-revolution force due to solar heating, *J. Geophys. Res.*, *102*, B1, 585–590, 1997.

Sharroo, R., G. Mets, R. Visser, and B. Ambrosius, TOPEX-Class Orbits for the ERS Satellites, presented at the American Geophysical Union, 1996 Spring Meeting, Baltimore, MD, 20–24 May, 1996a.

Sharroo, R., Delft Institute for Earth-Oriented Space Research, private communication, 1996b.

Schrama, E.J.O., and R.D. Ray, A preliminary tidal analysis of TOPEX/POSEIDON altimetry, *J. Geophys. Res., 99*, 24,799–24,808, 1994.

Schwiderski, E.W., On charting global ocean tides, *Rev. Geophys. Space Phys., 18*, 243–268, 1980.

Schwiderski, E.W., *Global ocean tides: Atlas of ocean tidal charts and maps, Tech. Rep. 2–10*, Nav. Surface Weapons Cent., Dahlgren, Va., 1981.

Semtner, A.J., Modeling Ocean Circulation, *Science*, *269*, 1995.

Semtner, A.J., and R.M. Chervin, Ocean general circulation from a global eddy-resolving model, *J. Geophys Res, 97,* 1992.

Smith, D.E., R. Kolenkiewicz, P.J. Dunn, J.W Robbins, M.H. Torrence, S.M. Klosko, R.G. Williamson, E.C. Pavlis, N.B. Douglas, S.K. Fricke, Tectonic motion and deformation from satellite laser ranging to LAGEOS, *J. Geophys. Res.*, *95*, B13, 22013–22041, 1990.

Stammer, D., and C. Wunsch, Preliminary assessment of the accuracy and precision of TOPEX/POSEIDON altimeter data with respect to the large-scale ocean circulation, *J. Geophys. Res., 99, C12*, 24584–24604, 1994.

Tapley, B.D., J.C. Ries, G.W. Davies, R.J. Eanes, B.E. Schutz, C.K. Shum, M.M. Watkins, J.A. Marshall, R.S. Nerem, B.H. Putney, S.M. Klosko, S.B. Luthcke, D.E. Pavlis, R.G. Williamson, N.P. Zelensky, Precision orbit determination for TOPEX/POSEIDON, *J. Geophys. Res.,* 99, 24383–24404, 1994.

Tapley, B.D., M.M. Watkins, J.C. Ries, G.W. Davis, R.J. Eanes, S.R. Poole, H.J. Rim, B.E. Schutz, C.K. Shum, R.S. Nerem, F.J. Lerch, J.A. Marshall, S.M. Klosko, N.K. Pavlis, and R.G. Williamson, The Joint Gravity Model–3, *J. Geophys. Res.*, *101 (B12)*, 28029–28049, 1996.

TOPEX Project, private communication, 1996.

Ullman, R.E., SOLVE Program Mathematical Formulation, Hughes STX Report HSTX/G&G–9201, NASA Contract NAS–5–29393/503, January, 1992.

Wang, Y.M., Downward continuation of the free-air gravity anomalies to the ellipsoid using the gradient solution, Poisson's integral and terrain correction: Numerical comparison and the computations, *Rep. 393*, Dept. of Geod. Sci. and Surv., Ohio State Univ., Columbus, 1988.

Wang, Y.M., Raytheon STX Corp., private communication, 1996.

Wunsch, C., Requirements on marine geoid accuracy for significant improvement in knowledge of the ocean circulation, paper U21B–03, AGU, Spring Meeting, 1996.

Wyrtki, K., and W.G. Leslie, The mean annual variation of sea level in the Pacific Ocean, *Tech. Rep. HIG–80–5,* 159 pp., Inst. for Geophys, Univ. of Hawaii, Honolulu, 1980.

Zhu, S.Y., and C.H. Reigber, "The German PAF for ERS–1: ERS–1 Standards Used at D–PAF," ERS–D–STD–31101, January 25, 1991.

8. THE ESTIMATION OF THE HIGH-DEGREE GEOPOTENTIAL MODELS

8.1 Introduction

In theory, the estimation of a combination solution complete to degree and order 360 could be carried out as described in Section 7 for the 70x70 model (using 30´x30´ mean anomalies rather than 1°x1° values). This, however, would require the formation of complete normal equations for more than 130000 parameters to describe and model the gravitational signal present in the altimeter and the surface gravity data sets. This task is beyond our present computational capabilities, and, therefore, the problem has been partitioned into two pieces: (1) the rigorous accumulation of normal equations and the treatment of satellite altimeter data as "direct tracking" to define the solution up to a maximum degree (70) that is computationally manageable and (2) the determination of the coefficients beyond degree 70 and up to degree 360. In addition to reasons of computational feasibility, the maximum degree 70 enables the appropriate modeling of the gravitational signal contained in satellite tracking data (SLR, Doppler, DORIS, and GPS), given the attenuation of the gravitational signal with altitude. The key point that dictates application of different techniques for the estimation of the 70x70 combination and 360x360 solutions is the treatment of altimeter data. The need to solve simultaneously (with the geopotential coefficients) for orbit corrections and Dynamic Ocean Topography (DOT), coupled with the fact that altimetry is confined over the oceans and does not comply with any of the symmetry patterns that are discussed in Section 8.2.2, mandates the formation of complete sets of normal equations for "direct" altimetry. Because both the orbit errors and the DOT are of long wavelength nature, one is able to recover the higher degree coefficients from the analysis of global gravity anomaly data sets that employ altimeter-derived anomalies, without significant contamination from orbit errors or mismodeled DOT effects. These anomalies are formed based on the best available prior knowledge of orbits and DOT. *Rapp* [1993] discussed extensively the alternative uses of altimeter data in global gravity modeling and gave a detailed description of the analytical formulation underlying both estimation strategies. In this section, the development of the higher degree and order part of the EGM96 model will be discussed.

8.2 Alternative Estimation Techniques

Given a *complete global observation grid* of a functional of the field (e.g., Δg), certain symmetries of the grid's geometry and of the error properties of the data lead to highly efficient estimators for high-degree harmonic coefficient recovery. These techniques have been studied and advanced by *Colombo* [1981]. Estimators of this type are:

1. The (simple) Numerical Quadrature (NQ), i.e., the discrete counterpart of orthogonality relations.

2. Least-squares adjustment using Block-Diagonal (BD) normal equations.

3. Optimal Estimation (OE), which is a least-squares collocation type of technique.

Models that have been developed using the NQ approach include OSU86E/F [*Rapp and Cruz*, 1986a] and OSU89A/B [*Rapp and Pavlis*, 1990]. BD techniques of various sophistication have been used to develop GPM2 [*Wenzel*, 1985], DGFI–92A [*Gruber and Bosch*, 1992], and GFZ95A [*Gruber et al.*, 1996]. OE was used to develop the OSU86C/D models [*Rapp and Cruz*, 1986b].

The main advantage of these techniques is their extreme computational efficiency due to the sparseness of the normal (or covariance) matrices involved and the applicability of FFT algorithms. It must be emphasized, however, that these techniques pertain to the problem of *harmonic analysis*, which is only part of the problem of developing *combination* solutions. Once a complete grid of data is analyzed harmonically with any one of the above techniques, there is still an adjustment to be performed, which will combine the satellite-derived coefficients with those obtained from the analysis of the gridded data.

These harmonic analysis techniques are applicable only to grids of data of *uniform* type, and do not allow for data gaps or arbitrary data weights, if strict compliance with the anticipated sparseness patterns of normal or covariance matrices is expected. Therefore, data types such as altimetry treated as "direct tracking" cannot be incorporated within the combination solution in this manner. One may use altimeter-derived gravity anomalies, along with land values to form a complete anomaly grid that can be used in the above algorithms, as was done in the development of the OSU86 and OSU89 models. The same approach is followed here.

The three expansion techniques mentioned above and the accumulation of normal equations that was applied to define the 70x70 portion of the model (Section 7) can be used as parts of an iterative process: A complete grid of gravity anomalies is analyzed to define a high-degree model. The higher degree harmonics of this model are used to filter out the high-degree contribution of the field from surface gravity and "direct" altimetry data. A combination solution is performed that yields the lower degree harmonics, improved orbits of the altimeter satellites, and a model of the DOT. Using the DOT model and the improved orbits, one may iterate the prediction of altimeter-derived anomalies, which along with land data define an improved global anomaly grid. A new high-degree expansion can be obtained based on this global grid, and the whole process may be iterated. This has been the philosophy behind the development of OSU91A [*Rapp et al.*, 1991] and JGM–1 and –2 [*Nerem et al.*, 1994].

Here, two techniques were studied and implemented for the determination of the higher degree harmonic coefficients of EGM96: the NQ and the BD least-squares approach [*Pavlis et al.*, 1996]. In both cases, the data input to the estimators consisted of the satellite-only model EGM96S and its *complete* variance–covariance (or normal) matrix, and a complete global grid of 30´x30´ mean anomalies. The detailed implementation of these approaches is described next.

8.2.1 *The Numerical Quadrature Approach*

Given a complete set of mean gravity anomalies $\overline{\Delta g}_{ij}^{e}$ on an equiangular grid ($i = 0, ..., N–1$; $j = 0, ..., 2N–1$) on the reference ellipsoid, NQ estimates a set of *spherical* harmonic disturbing potential coefficients $\overline{C}_{nm}^{T}$ by:

$$\overline{C}_{nm}^{T} = \frac{1}{4\pi a\gamma} \sum_{i=0}^{N-1} r_i^e \sum_{k=0}^{s'} \frac{L_{nmk}}{\overline{S}_{n-2k,|m|}(b/E)} \frac{\overline{IP}_{n-2k,|m|}^{i}}{(n-2k-1)q_{n-2k}^{i}} \sum_{j=0}^{2N-1} \overline{\Delta g}_{ij}^{e} \begin{Bmatrix} IC \\ IS \end{Bmatrix}_m^{j} \begin{array}{l} \text{if } m \geq 0 \\ \text{if } m < 0 \end{array} \quad (8.2.1\text{--}1)$$

as it is derived in [*Rapp and Pavlis*, 1990]. In eq. (8.2.1–1), even-degree zonal coefficients are remainders after subtraction of the reference values implied by the normal ellipsoidal potential. *a* is a scaling parameter associated with the coefficients $\overline{C}_{nm}^{T}$ (usually the equatorial radius of the adopted mean-Earth ellipsoid), while

$$\gamma = GM/a^2 \tag{8.2.1--2}$$

where *GM* is the geocentric gravitational constant and

$$\overline{IP}_{n,|m|}^{i} = \int_{\delta_i}^{\delta_{i+1}} \overline{P}_{n|m|}(\cos\delta) \sin\delta\, d\delta \tag{8.2.1--3}$$

$$\begin{Bmatrix} IC \\ IS \end{Bmatrix}_m^{j} = \int_{\lambda_j}^{\lambda_{j+1}} \begin{Bmatrix} \cos m\lambda \\ \sin|m|\lambda \end{Bmatrix} d\lambda \quad \begin{array}{l} \text{if } m \geq 0 \\ \text{if } m < 0 \end{array} \tag{8.2.1--4}$$

where δ is reduced colatitude [*Heiskanen and Moritz*, 1967, Section 1–19], λ longitude, and r_i^e is the length of the geocentric radius vector to the center of the $(i, j)^{\text{th}}$ cell on the ellipsoid. The terms L_{nmk} and $\overline{S}_{n,|m|}(b/E)$ are necessary to yield the *spherical* harmonic coefficients $\overline{C}_{nm}^{T}$ from data that reside on an ellipsoidal boundary surface, according to the formulation of *Jekeli* [1988] and *Gleason* [1988] (*b* is the semiminor axis of the ellipsoid and $E = ae$ its linear eccentricity). $1/q_n^i$ are quadrature weights, whose precise definition will be considered in Section 8.5.

The estimation of the complete high-degree set of geopotential coefficients is performed as a two-step procedure [*Rapp and Pavlis*, 1990]. First, the global set of $\overline{\Delta g}_{ij}^{e}$ (after appropriate systematic corrections that are discussed in Section 8.3) provides, through eq. (8.2.1–1), a "terrestrial" estimate $\overline{C}_{nm}^{T}$ of those harmonic coefficients present in the satellite-only model. In addition, eq. (8.2.1–1) is used to propagate the error variances of $\overline{\Delta g}_{ij}^{e}$ to $\overline{C}_{nm}^{T}$ and form the full error covariance matrix cov[$\overline{C}_{nm}^{T}$]. Based on the harmonic coefficients of the satellite-only model $\overline{C}_{nm}^{S}$, and their associated error covariance matrix cov[$\overline{C}_{nm}^{S}$], and their "terrestrial" counterparts, a least-squares adjustment is used to estimate a unique set of coefficients (and its associated full variance–covariance matrix), essentially as a weighted average of the two independent estimates. The formulation of this adjustment process is described in full detail in [*Rapp and Pavlis*, 1990, Section 2.3]. This adjustment provides also a global set of adjusted gravity anomalies. In a second step, the adjusted gravity anomalies are input to eq. (8.2.1–1) to yield the complete set of harmonic coefficients up to the high degree (360). The error variances of these higher degree coefficients are obtained by quadratic addition of the propagated anomaly error and an estimate of the sampling error [*ibid.*, eqs. 50–53]. This general procedure was proposed originally by *Kaula* [1966] and has been used in several high-degree models developed at The Ohio State University [*Rapp*, 1981; *Rapp and Cruz*, 1986a; *Rapp and Pavlis*, 1990]. With the exception of the quadrature weight definition, the implementation of NQ in the EGM96 model development was identical to the one used in the development of the OSU89A/B models, and all the details of this approach can be found in [*Rapp and Pavlis*, 1990].

8.2.2 The Block-Diagonal Least-Squares Approach

Starting from the same set of $\overline{\Delta g}^e_{ij}$ as above, the estimation of the disturbing potential harmonic coefficients using least-squares is based on the mathematical model:

$$\overline{\Delta g}^e_{ij} = \overline{\Delta g}(r^e_i, \theta_i, \lambda_j) = \frac{1}{\Delta\sigma_i} \frac{GM}{(r^e_i)^2} \sum_{n=2}^{N_{max}} (n-1)\left(\frac{a}{r^e_i}\right)^n \sum_{m=-n}^{n} \overline{C}^T_{nm} \cdot \overline{IY}^{ij}_{nm} \qquad (8.2.2\text{--}1)$$

where:

$$\Delta\sigma_i = \Delta\lambda \int_{\theta_i}^{\theta_{i+1}} \sin\theta d\theta = \Delta\lambda \cdot (\cos\theta_i - \cos\theta_{i+1}) \qquad (8.2.2\text{--}2)$$

$$\overline{IY}^{ij}_{nm} = \int_{\theta_i}^{\theta_{i+1}} \overline{P}_{n|m|}(\cos\theta) \sin\theta d\theta \cdot \int_{\lambda_j}^{\lambda_{j+1}} \begin{Bmatrix} \cos m\lambda \\ \sin|m|\lambda \end{Bmatrix} d\lambda \quad \begin{matrix} \text{if } m \geq 0 \\ \text{if } m < 0 \end{matrix} \qquad (8.2.2\text{--}3)$$

θ is geocentric colatitude, N_{max} is the maximum degree of the expansion, and the rest of the notation is the same as that used in Section 8.2.1. Given the 30´x30´ merged gravity anomaly file that is described in Section 8.3, one can set up a system of observation equations and estimate the "terrestrial" coefficients $\overline{C}^T_{nm}$ following the same general procedure described in Section 7.2.3. The combination solution can be obtained by adding the normal equations from the analysis of satellite tracking data to the "terrestrial" normal equations. This general approach originally was proposed and studied by *Rapp* [1967].

It is obvious from the above that the formation (and inversion) of the full normal matrix in this approach is extremely demanding computationally for large values of N_{max}. The solution to N_{max} = 360 that we seek cannot be done using the full normal matrix, even with the most powerful supercomputers that are available at present. Nevertheless, the least-squares approach has certain advantages compared to the NQ method, as discussed in the next section. It was, therefore, considered appropriate to investigate the application of a technique that combines the computational efficiency of NQ with some of the advantages of least squares. The BD approximation of the full normal matrix formulation in least squares is such a technique. *Colombo* [1981] has shown that, if

a) The data reside on a surface of revolution (e.g., a rotational ellipsoid),

b) The grid is complete and the longitude increment constant,

c) The data weights are longitude independent, and

d) The data weights are symmetric with respect to the Equator,

then zero elements in the normal equations formed in the least-squares estimation will occur as prescribed by

$$[N]_{\overline{C}_{nm}\overline{C}_{rs}} = 0 \quad if \quad \{m \neq s\} or \{m = s \ and \ n - r = 2k + 1\} \qquad (8.2.2\text{--}4)$$

Note that in this notation the order subscript is a signed integer, whose sign identifies the type of coefficient (positive: Cosine, negative: Sine). If (d) does not hold true, then

$$[N]_{\overline{C}_{nm}\overline{C}_{rs}} = 0 \quad \textit{if} \ \ \{m \neq s\} \tag{8.2.2–5}$$

The sparseness patterns implied by equations (8.2.2–4 and –5) will be referred to as BD1 and BD2, respectively. In addition, a BD3 pattern will be considered, and is defined by:

$$[N]_{\overline{C}_{nm}\overline{C}_{rs}} = 0 \quad \textit{if} \ \ \{|m| \neq |s|\} \tag{8.2.2–6}$$

which admits nonzero off-diagonal elements across coefficients of different type within a given order. It is instructive to consider the computational efficiency implied by these patterns. Table 8.2.2–1 provides relevant statistics for a solution complete from degree and order 0 to degree and order 360, excluding degree 1 terms. Such a solution involves 130318 unknown coefficients, and the upper (or lower) triangular part of the (symmetric) full normal matrix has 8491455721 elements.

Table 8.2.2–1. Statistics related to an expansion to $N_{max} = 360$ using different sparseness patterns.

Statistic	Sparseness Pattern		
	BD1	BD2	BD3
Total number of nonzero elements	7905721	15746100	31362241
Percentage of full-matrix elements	0.09	0.19	0.37
Number of blocks	1440	721	361
No. of unknowns in largest block	181	360	718
No. of elements in largest block	16471	64980	258121

The enormous computational savings that can be inferred from Table 8.2.2–1 make the BD approximations very attractive estimation strategies. These savings, however, come at the expense of the rigor exercised in the development of the model. The real-world anomaly data to be analyzed (see Section 8.3) comply *only* with the conditions (a) and (b) above (in fact, to comply even with the (a) and (b) conditions, "fill-in" techniques and analytical continuation have to be employed, since the original 30´ file is neither complete nor residing on a surface of revolution). Furthermore, the normal equations of the satellite-only model do not conform with any such sparseness pattern (although off-diagonal elements corresponding to coefficients of different orders tend to be smaller than the elements within the same order). To test the consequences of using the BD approach, one may simply neglect elements in the normals from terrestrial and satellite tracking data that occupy the locations prescribed by equations (8.2.2–4) or (8.2.2–5) or (8.2.2–6), and then investigate if the omission of these terms is an approximation that can be tolerated, based on the quality of the resulting model. This can be assessed through comparisons with the NQ type of solution (provided, of course, that both techniques are applied to the same data). The numerical investigation of these questions is presented in Section 8.2.4.

8.2.3 Analytical Comparison of the Numerical Quadrature and the Least-Squares Approach

The analytical and numerical differences between the numerical quadrature (NQ) and the least-squares (LS) estimation techniques can be studied from both the *harmonic analysis* and the *combination solution* perspectives. Such studies have been reported by *Rapp* [1969, 1986], *Colombo* [1981], *Pavlis* [1988], and *Sneeuw* [1994]. A brief review of the conclusions reached by these investigations follows. Detailed derivations and analyses supporting these conclusions can be found in the cited references. NQ is used here to identify the *simple* quadratures formula with the "composite" set of quadrature weights proposed by *Colombo* [1981, page 76].

Harmonic Analysis

1. NQ determines each coefficient independently of all others (there is a small by-degree dependency if *spherical* coefficients are estimated from data on the ellipsoid). In contrast, LS estimates a correlated set of coefficients; thus, solutions to different maximum degrees will yield different values for the common harmonics. This will occur even if the input data are uncorrelated, and arises from the loss of orthogonality between the discrete (point or integrated) samples of the associated Legendre functions [*Pavlis*, 1988, Section 4.2.1]. Unlike them, the discrete (point and integrated) samples of (cos $m\lambda$ and sin $m\lambda$) preserve their orthogonality in the interval $[0,2\pi)$. It is this property along with the equatorial symmetry and the parity properties of Legendre functions that give rise to the sparseness pattern in eq. (8.2.2–4).

2. NQ cannot account for varying accuracies among the gravity anomaly data, while the LS estimator is capable of accounting for any (positive-definite) error covariance matrix associated with the input anomalies.

3. If L ($= \pi/\Delta\lambda$) denotes the Nyquist degree implied by the data sampling interval, the normal equations formed based on eq. (8.2.2–1) become singular if $N_{max} \geq L$ [*Colombo*, 1981]. From a global 30´x30´ anomaly file, one can estimate a complete set of coefficients to $N_{max} = 359$ using LS. Higher degree coefficients can be obtained as aliased estimates of those below L, as is also done in *Colombo's* [1981] development of NQ algorithms.

4. LS estimation can recover *exactly* a set of coefficients from synthetic noiseless data, provided the data are band limited and the Nyquist degree is not exceeded. Software developed for this study has been tested in the recovery of a coefficient set to $N_{max} = 359$, from synthetic 30´x30´ anomalies computed on the surface of the ellipsoid. The percentage difference between the "true" and recovered coefficients for all degrees up to 359 was 0.00 percent. The simple NQ technique is incapable of recovering the input coefficients, as *Rapp's* [1986] numerical experiments have demonstrated.

Combination Solution

1. In a combination solution adjustment that employs NQ for the harmonic analysis of the gravity anomalies, only those harmonics whose *degree* is less than or equal to the maximum degree present in the satellite-only model are adjusted. In contrast, if BD least-squares are

used for the harmonic analysis, then all coefficients whose *order* is less than or equal to the maximum order present in the satellite-only model are adjusted [see also *Colombo*, 1981, page 64].

2. In the case of NQ, the error estimates of the higher degree coefficients (beyond those participating in the combination solution adjustment) are obtained by quadratic addition of the propagated and sampling errors [*Rapp and Pavlis*, 1990, Section 2.3]. In BD least-squares, the error spectrum up to the high degree is obtained directly from the solution, without the need for empirical sampling error models, and with no dependence on any type of desmoothing factors. Furthermore, BD least-squares permits the computation of error covariances between certain harmonic coefficients.

3. The LS approach (regardless of the BD approximation employed) permits the use of *a priori* information to condition the solution at the higher degrees. This has specific advantages, especially with regard to the predicted error spectrum of the model at the higher degrees. The NQ technique (at least as it was formulated and applied by *Rapp and Pavlis* [1990]) does not permit the use of *a priori* information in the determination of the higher degree coefficients. To account for unmodeled systematic effects in the gravity anomaly data, *Rapp and Pavlis* [*ibid*.] modified (generally increased) the error estimates of the data. This permitted a meaningful low-degree combination to be developed, but produced a somewhat pessimistic error spectrum at the higher degrees [*ibid*., Figure 12].

4. In the case of *band-limited* data, one can show that the least-squares approach using *a priori* information is formally equivalent to least-squares collocation [*Moritz*, 1980, page 166; *Colombo*, 1981, Section 2.13]. In such case, the BD approaches discussed previously are the least-squares counterpart of the Optimal Estimation technique proposed by *Colombo* [*ibid*.].

5. The adjustment technique employed by *Rapp and Pavlis* [1990] combines two independent estimates of the gravitational potential coefficients by operating on their values and the normal matrices associated with them. The LS approach (again regardless of the BD approximation employed) operates just on the two sets of normal equations. If one wants to remove any *a priori* constraint from the combination solution, the adjustment technique of *Rapp and Pavlis* [*ibid*.] may become inapplicable. This is because satellite-only models developed to degree 70 or so create very poorly conditioned normal equations for the higher degree coefficients. These normal equations may actually be singular without the use of any *a priori* constraint. In such case, the vector $\overline{C}_{nm}^{S}$, which is required to set up equation (48) of *Rapp and Pavlis* [*ibid*.], is not available. The least-squares approach can be implemented, without any *a priori* constraint on the satellite-only model, regardless of any singularity of the satellite-only normals.

6. Finally, an important advantage of the BD structures discussed above is their correspondence to similar structures that result from the analysis of data from certain configurations of Satellite-to-Satellite Tracking (SST) and Satellite Gravity Gradiometry (SGG). These aspects have been recognized and studied by *Colombo* [1984, 1988]. *Schuh* [1996] provides a detailed study of the numerical solution strategies applicable to the analysis of such observables. SST or SGG data that may become available in the future could be used along

with surface gravimetric data in combination solutions to high degree, using BD approximations of the respective normal equations.

8.2.4 The Block-Diagonal Least-Squares Algorithm: Development and Preliminary Investigation

Three different approximations (BD1, BD2, and BD3) of the normal equations from terrestrial data may be attempted. BD1 provides the simplest structure, followed by BD2 and BD3 in increasing complexity. The merged anomaly file to be analyzed fulfills conditions (a) and (b) pertaining to the grid's geometry, but does not fulfill conditions (c) and (d) pertaining to the data weights. Since the data weights reflect accuracies of local gravimetric surveys, we cannot arbitrarily change them so that we can enforce compliance with either condition (c) or (d). Instead, we will simply ignore the elements in the normal equations that occupy the locations prescribed by equations (8.2.2–4) or (8.2.2–5) or (8.2.2–6), respectively. Because the data weights do not vary geographically in any simple analytic fashion, the effect of violating conditions (c) and/or (d) can only be studied numerically. To this end, preliminary investigations were started of the applicability of the different BD patterns before the joint project was initiated. These experiments led to the numerical approach that was finally implemented in the development of the high-degree part of EGM96. Our investigation was conducted independently from (and apparently in parallel with) similar studies reported by *Bosch* [1993] and, more recently, *Schuh* [1996]. A discussion of the steps that we took follows.

The starting point of our investigation was the analysis done by *Lerch, Pavlis, and Chan* [1993]. There, the 30´x30´ merged anomaly file that supported the development of the OSU91A model [*Rapp et al.*, 1991, Section 6.0], was used along with the JGM–1S satellite-only model [*Nerem et al.*, 1994] (and its covariance matrix) to test the applicability of the sparseness structures BD1 and BD2. JGM–1S is complete to degree and order 60. The weighting of the anomaly data was identical to the one used by *Rapp et al.* [ibid.]. Among several test solutions that were made, three are of interest here: an NQ solution that was done in an identical fashion to the OSU89A/B models, and two BD solutions following the BD1 and BD2 patterns, respectively. The important point here is that, in the BD1 and BD2 solutions, the JGM–1S error covariance matrix was truncated to the same BD structure as the one used in the corresponding terrestrial normal equations. Intercomparison of the resulting models showed relatively large differences between the BD-type of solutions and the NQ model, especially over the $n = 6$ to $n = 40$ degree range. Orbit fit tests are shown in Table 8.2.4–1. These tests indicated that the NQ model was superior to the BD-type of solutions. Especially the fits of Starlette and Ajisai (satellites sensitive to the degree range 6 to 40), are significantly degraded in the BD solutions as compared to the NQ.

The main conclusions of this preliminary study were:

1. The BD1 and BD2 truncations of either the satellite-only or the terrestrial normal equations (or both) create errors in the combination solution that cannot be tolerated.

2. Both BD1 and BD2 type of solutions yielded results far superior to the DGFI–92A model [*Gruber and Bosch*, 1992], whose performance (especially in orbit fits) was very poor. This

was rather encouraging, since it indicated that the BD techniques had the potential to produce comparable results to the NQ algorithm.

Table 8.2.4–1. SLR satellite orbit test (set-1) results (RMS of fit in cm) using some NQ and BD models N_{max} =70.

Model	LAGEOS	LAGEOS–2	Starlette	Ajisai
DGFI–92A	32.18	21.59	991.12	544.37
NQ	2.78	4.44	9.52	7.67
BD1	2.79	4.46	21.31	10.07
BD2	2.77	4.38	21.22	8.96

The next step was to investigate which of the two types of normal matrices (satellite-only or terrestrial) was affected the most by the BD approximations. To this end, we used the full normal matrices for both types of data for expansions to $N_{max} = 30$ and computed the relative magnitude of their off-diagonal elements:

$$r_{ij} = |n_{ij}| / \sqrt{n_{ii} \cdot n_{jj}} \tag{8.2.4–1}$$

When r_{ij} was plotted, it became apparent that the satellite-only normals contain many more elements of relatively large magnitude outside the blocks prescribed by BD1 or BD2 than the terrestrial normal equations [see also *Chan and Pavlis*, 1995, Figures 3, 4]. This implied that improvements in the quality of the combination solution could be expected if the BD approximations were removed from the satellite-only normals. In addition, to enhance the rigor in the terrestrial normals, we decided to adhere to the BD3 structure in all subsequent solutions, since this pattern is still well within our computational capabilities. In order to include in the least-squares adjustment the full satellite-only normals, and at the same time preserve the numerical efficiency, a rearrangement of the unknown coefficients has to be performed. This will be illustrated with a simplified example.

Consider for a moment that a "high degree" solution complete to $N_{max} = 6$ is to be developed, in a least-squares combination with a satellite-only model complete to $N_{sat} = 4$. The terrestrial normal equations involve 46 unknowns (complete set to $N_{max} = 6$, excluding n = 1 terms), while the satellite-only normals involve 22 unknowns. In all of our solutions, $\bar{C}_{00}, \bar{C}_{21}$ and $\bar{S}_{21}$ are included in the satellite-only normals. However, the values of these terms are fixed to the *a priori* adopted constants through the use of very small standard deviations. The unknown coefficients are ordered first by increasing order (m), then by type (C then S), and last by increasing degree (n). This is denoted ordering pattern "V" in [*Pavlis*, 1988, Table 3]. Adhering to the sparseness pattern BD3, the *terrestrial* normal equations take the form shown in Figure 8.2.4–1a, where gray areas indicate nonzero elements. This type of normal matrix can be set up and inverted very efficiently, thus providing the terrestrial estimates of the coefficients and their associated BD covariance matrix. In our analysis to $N_{max} = 359$, this matrix contains 360 diagonal blocks, the largest one having dimension 716x716 ($m = 1$), while the smallest has dimension 2x2 ($m = 359$).

Terrestrial Normals   **Combined Normals**

(a)   (b)

(c)   (d)

(e)   (f)
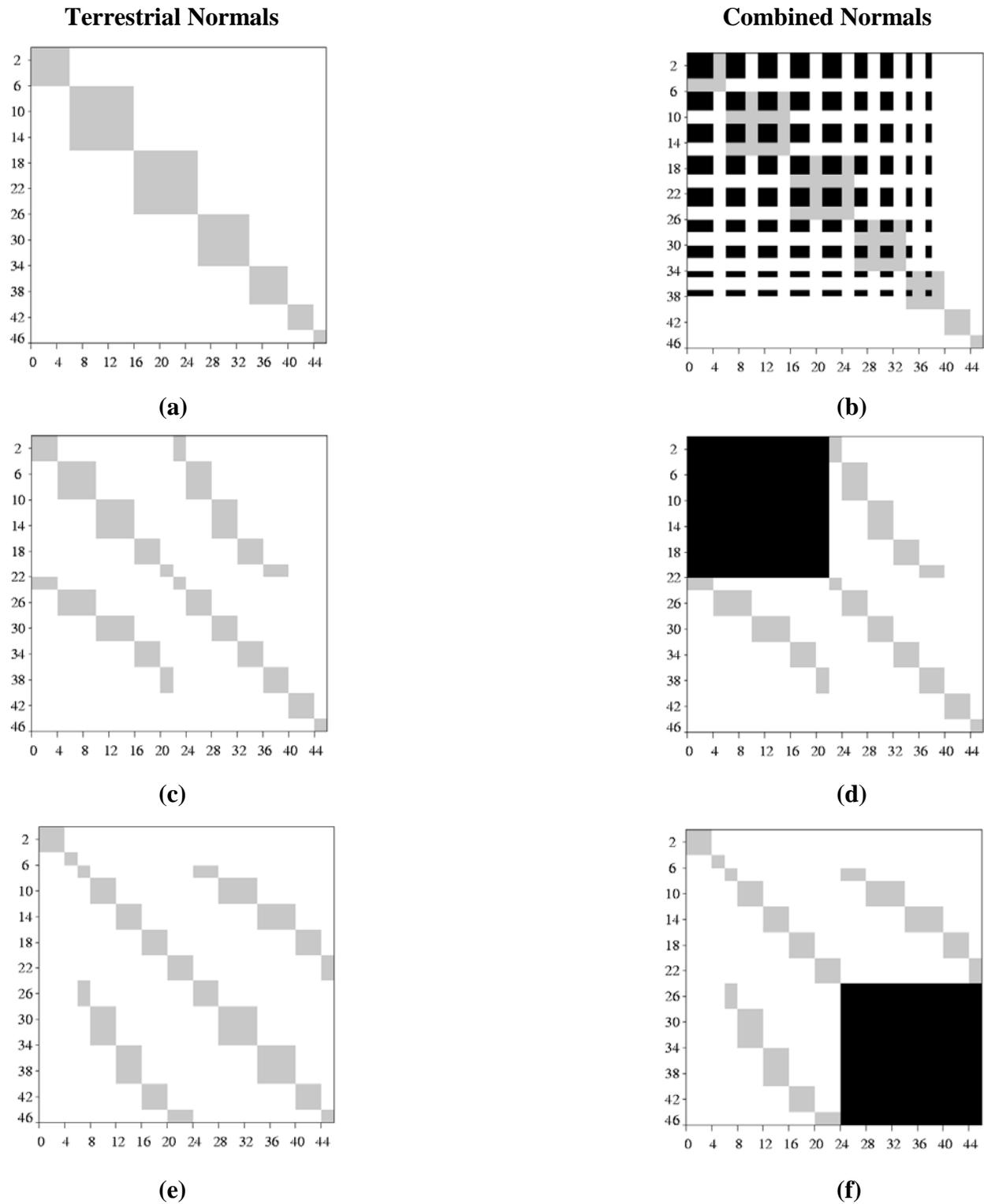
Figure 8.2.4–1. Structure of terrestrial and combined normal equations for different
orderings/groupings of unknown coefficients.

On a Cray J90 supercomputer, the formation of the terrestrial normals required 1,400 CPU seconds, and its inversion and computation of the solution 700 CPU seconds.

However, if one conforms with this ordering of unknowns, the *combined* (terrestrial plus satellite-only) normal equations take the form shown in Figure 8.2.4–1b. In this figure, black areas indicate the nonzero elements in the combined normals, which arise from the satellite-only normal equation contribution (overlaid on the structure of Figure 8.2.4–1a). It is obvious that the "V" type of ordering of unknowns creates a large (although sparse) block in the combined normals, which would have to be treated as a full matrix. In the real-world case, where the satellite-only model is complete to $N_{sat} = 70$, this block would be of dimension 45787x45787. To circumvent this problem, the unknowns have to be reordered so that the coefficients present in the satellite-only model are grouped together. There are several ways that this may be done, two of which are discussed next. Assuming that the satellite-only model is complete to degree and order N_{sat}, one may group the unknowns in three groups as:

Forward grouping	*Reverse grouping*
Group 1: $n \leq N_{sat}, m \leq N_{sat}$	Group 1: $n > N_{sat}, m > N_{sat}$
Group 2: $n > N_{sat}, m \leq N_{sat}$	Group 2: $n > N_{sat}, m \leq N_{sat}$
Group 3: $n > N_{sat}, m > N_{sat}$	Group 3: $n \leq N_{sat}, m \leq N_{sat}$

Inside each group, the coefficients are ordered following the same pattern V as before. For our simplified example, Figures 8.2.4–1c and 8.2.4–1d show the structure of terrestrial and combined normals, respectively, for the forward grouping, while Figures 8.2.4–1e and 8.2.4–1f do the same for the reverse grouping. *Bosch* [1993] studied the structure of the combined normal equations resulting from the forward grouping and proposed an algorithm for the solution of this system. In our investigation, we reorder the unknowns according to the reverse grouping. The difference between these two groupings appears irrelevant at first glance (and, in fact, the forward grouping is a more "natural" choice); however, as we will explain next, the structure of the normals in Figure 8.2.4–1f possesses a very significant advantage compared to 8.2.4–1d. It must be emphasized here that the reordering of the unknowns does not affect the values of the elements in either the satellite-only or the terrestrial normals; reordering simply rearranges rows and columns in these matrices. The terrestrial normals are originally formed according to pattern V, while the satellite-only normals according to pattern "I" of [*Pavlis*, 1988, Table 3].

The reverse grouping results in a partitioning of the combined normal equations into four nontrivial submatrices as shown in Figure 8.2.4–2 (upper triangular part of the symmetric matrix) for the simple example used before. G_{11} is a square block-diagonal matrix of purely "terrestrial" origin, and so is G_{22}. The rectangular submatrix G_{23} has the shape of a "wing." It consists of nonzero rectangular blocks, which have the same row partitioning as G_{22}. Notice that this wing arises also from the terrestrial normals alone; it is a consequence of the reordering of the unknowns, as can also be seen from Figure 8.2.4–1e. Finally, the block G_{33} is a full symmetric

matrix, containing both terrestrial and satellite-only contributions added together. According to this partitioning, we write the combined normal equations as:

$$
\begin{bmatrix} \mathbf{G_{11}} & \varnothing & \varnothing \\ \varnothing & \mathbf{G_{22}} & \mathbf{G_{23}} \\ \varnothing & \mathbf{G_{23}^T} & \mathbf{G_{33}} \end{bmatrix} \cdot \begin{bmatrix} \mathbf{\hat{X}_1} \\ \mathbf{\hat{X}_2} \\ \mathbf{\hat{X}_3} \end{bmatrix} = \begin{bmatrix} \mathbf{U_1} \\ \mathbf{U_2} \\ \mathbf{U_3} \end{bmatrix}
\tag{8.2.4–2}
$$

The parameters in $\mathbf{\hat{X}_1}$, $\mathbf{\hat{X}_2}$, and $\mathbf{\hat{X}_3}$ are the potential coefficients contained in groups 1, 2, and 3, respectively, according to the reverse grouping.

Figure 8.2.4–2. Partitioning of the combined normal equations arranged according to the reverse grouping.

$\mathbf{G_{11}}$ is a block-diagonal matrix, and its inversion does not pose any computational problem. In fact, since $\mathbf{G_{12}}$ and $\mathbf{G_{13}}$ are both zero matrices, the parameters $\mathbf{\hat{X}_1}$ are estimated solely on the basis of the terrestrial data; hence, their values (and associated error variances) are identical to those obtained from the inversion of the terrestrial normal equations. The subsystem

$$
\begin{bmatrix} \mathbf{G_{22}} & \mathbf{G_{23}} \\ \mathbf{G_{23}^T} & \mathbf{G_{33}} \end{bmatrix} \cdot \begin{bmatrix} \mathbf{\hat{X}_2} \\ \mathbf{\hat{X}_3} \end{bmatrix} = \begin{bmatrix} \mathbf{U_2} \\ \mathbf{U_3} \end{bmatrix}
\tag{8.2.4–3}
$$

is denoted

$$
\mathbf{G} \cdot \mathbf{Y} = \mathbf{R}
\tag{8.2.4–4}
$$

The solution of this system was performed according to the formulation of *Colombo* [1984, Section 3.8]. We denote by $\mathbf{L}$ the lower triangular Cholesky factor of $\mathbf{G}$, so that

$$\mathbf{G} = \mathbf{L} \cdot \mathbf{L}^{\mathbf{T}} \tag{8.2.4–5}$$

Partitioning $\mathbf{L}$ in the same way as $\mathbf{G}$ yields

$$\begin{bmatrix} \mathbf{L}_{22} & \varnothing \\ \mathbf{L}_{32} & \mathbf{L}_{33} \end{bmatrix} \cdot \begin{bmatrix} \mathbf{L}_{22}^{\mathbf{T}} & \mathbf{L}_{32}^{\mathbf{T}} \\ \varnothing & \mathbf{L}_{33}^{\mathbf{T}} \end{bmatrix} = \begin{bmatrix} \mathbf{G}_{22} & \mathbf{G}_{23} \\ \mathbf{G}_{23}^{\mathbf{T}} & \mathbf{G}_{33} \end{bmatrix} \tag{8.2.4–6}$$

Multiplication of the matrices in (8.2.4–6) yields:

$$\mathbf{L}_{22} \cdot \mathbf{L}_{22}^{\mathbf{T}} = \mathbf{G}_{22} \tag{8.2.4–7a}$$

$$\mathbf{L}_{22} \cdot \mathbf{L}_{32}^{\mathbf{T}} = \mathbf{G}_{23} \tag{8.2.4–7b}$$

$$\mathbf{L}_{33} \cdot \mathbf{L}_{33}^{\mathbf{T}} = \mathbf{G}_{33} - \mathbf{L}_{32} \cdot \mathbf{L}_{32}^{\mathbf{T}} \tag{8.2.4–7c}$$

Equation (8.2.4–7a) indicates that $\mathbf{L}_{22}$ is the Cholesky factor of $\mathbf{G}_{22}$. Since $\mathbf{G}_{22}$ is block-diagonal, its Cholesky factor is also block-diagonal, and the blocks of $\mathbf{L}_{22}$ are the Cholesky factors of the blocks of $\mathbf{G}_{22}$. Therefore, each block in $\mathbf{G}_{22}$ can be factored independently. Furthermore, the inverse of $\mathbf{L}_{22}$ is also a block-diagonal lower triangular matrix, and can be computed easily by inverting the individual blocks of $\mathbf{L}_{22}$. In the case of the expansion to $N_{max} = 359$ with a satellite-only model complete to degree and order 70, $\mathbf{G}_{22}$ consists of 71 blocks. The first one, corresponding to the zonal coefficients of $n > 70$, has dimension 289x289. All the other blocks have dimension 578x578, each corresponding to the tesseral coefficients of a given order $0 < m \le 70$, and of degree $70 < n \le 359$. With $\mathbf{L}_{22}$ and $\mathbf{L}_{22}^{-1}$ computed, eq. (8.2.4–7b) yields:

$$\mathbf{L}_{32}^{\mathbf{T}} = \mathbf{L}_{22}^{-1} \cdot \mathbf{G}_{23} \tag{8.2.4–8}$$

It is important to consider the structure of $\mathbf{L}_{32}^{\mathbf{T}}$. Since $\mathbf{L}_{22}^{-1}$ is a square block-diagonal lower triangular matrix, and since the rectangular matrix $\mathbf{G}_{23}$ consists of nonzero blocks, *of the same row partitioning* as $\mathbf{L}_{22}^{-1}$, their product (i.e., $\mathbf{L}_{32}^{\mathbf{T}}$) will have exactly the same structure as $\mathbf{G}_{23}$, and no additional nonzero elements than $\mathbf{G}_{23}$. This is the important advantage that the reverse grouping of the parameters has over the forward grouping. In the case of the forward grouping, the Cholesky factorization creates a dense (nonzero) area under the wing of Figure 8.2.4–1d. The key feature of the reverse grouping is that to the left of the wing one has a block-diagonal matrix that shares the row partitioning of the wing. The net effect is that the lower triangular part of $\mathbf{G}$ and the Cholesky factor of $\mathbf{G}$ have identical structure. This has been recognized also by *Schuh* [1996, page 25].

Finally, once $\mathbf{L}_{32}^{\mathbf{T}}$ has been computed, the right-hand side of eq. (8.2.4–7c) can be evaluated. The matrix $\mathbf{L}_{33}$ is obtained as the Cholesky factor of the full symmetric matrix $\mathbf{G}_{33} - \mathbf{L}_{32} \cdot \mathbf{L}_{32}^{\mathbf{T}}$. In our case, with the satellite-only model complete to degree and order 70, this full matrix has dimension 5038x5038 and poses no computational problem. With $\mathbf{L}_{22}$, $\mathbf{L}_{32}^{\mathbf{T}}$, and $\mathbf{L}_{33}$ computed, we now have the entire Cholesky factor of $\mathbf{G}$. The solution vector $\mathbf{Y}$ is obtained as follows. We have

$$\mathbf{G} \cdot \mathbf{Y} = (\mathbf{L} \cdot \mathbf{L}^{\mathbf{T}}) \, \mathbf{Y} = \mathbf{R} \tag{8.2.4–9}$$

and the transformation

$$\mathbf{L}^{\mathbf{T}} \cdot \mathbf{Y} = \mathbf{Z} \tag{8.2.4–10}$$

implies:

$$\mathbf{L} \cdot \mathbf{Z} = \mathbf{R} \tag{8.2.4–11}$$

$\mathbf{Z}$ is obtained using "forward substitution" in eq. (8.2.4–11), and then $\mathbf{Y}$ is computed through "back substitution" in (8.2.4–10).

In addition to the solution vector, one is also interested in the error variances and covariances of the estimated coefficients. This requires the inversion of the combined normals. The partitioning of eq. (8.2.4–2) is considered again, whereby it is obvious that the error covariance matrix corresponding to the $\hat{\mathbf{X}}_1$ group of parameters is given by $\mathbf{G}_{11}^{-1}$. This block-diagonal matrix can be computed easily by inverting the individual blocks of $\mathbf{G}_{11}$. The inversion of the matrix $\mathbf{G}$ of eq. (8.2.4–4) is more involved. We have

$$\mathbf{G}^{-1} = \left(\mathbf{L} \cdot \mathbf{L}^{\mathbf{T}} \right)^{-1} = \left(\mathbf{L}^{\mathbf{T}} \right)^{-1} \cdot \left(\mathbf{L}^{-1} \right) = \left(\mathbf{L}^{-1} \right)^{\mathbf{T}} \cdot \left(\mathbf{L}^{-1} \right) \tag{8.2.4–12}$$

Since $\mathbf{L}$ is lower triangular, $\mathbf{L}^{-1}$ is also lower triangular, and, according to the partition of (8.2.4–6), one has:

$$\mathbf{L} \cdot \mathbf{L}^{-1} = \mathbf{L} \cdot \tilde{\mathbf{L}} = \begin{bmatrix} \mathbf{L_{22}} & \varnothing \\ \mathbf{L_{32}} & \mathbf{L_{33}} \end{bmatrix} \cdot \begin{bmatrix} \tilde{\mathbf{L}}_{22} & \varnothing \\ \tilde{\mathbf{L}}_{32} & \tilde{\mathbf{L}}_{33} \end{bmatrix} = \begin{bmatrix} \mathbf{I} & \varnothing \\ \varnothing & \mathbf{I} \end{bmatrix} \tag{8.2.4–13}$$

where the inverse of $\mathbf{L}$ was denoted $\tilde{\mathbf{L}}$. Multiplication of the matrices in (8.2.4–13) yields:

$$\tilde{\mathbf{L}}_{22} = \mathbf{L}_{22}^{-1} \tag{8.2.4–14a}$$

$$\tilde{\mathbf{L}}_{33} = \mathbf{L}_{33}^{-1} \tag{8.2.4–14b}$$

$$\tilde{\mathbf{L}}_{32} = -\tilde{\mathbf{L}}_{33} \cdot \mathbf{L}_{32} \cdot \tilde{\mathbf{L}}_{22} \tag{8.2.4–14c}$$

As explained above, $\mathbf{L}_{22}$ is a block-diagonal lower triangular matrix, and its inverse can be computed easily. $\mathbf{L}_{33}$ is a lower triangular matrix, which in our case ($N_{sat} = 70$) has dimension 5038x5038, so its inversion poses no problem either. $\tilde{\mathbf{L}}_{32}$, however, creates a significant computational problem. Considering eq. (8.2.4–14c) and the structure of the matrices involved, it is easy to see that $\tilde{\mathbf{L}}_{32}$ is a rectangular matrix with nonzero elements below its main diagonal. In our case, with $N_{max} = 359$ and $N_{sat} = 70$, this matrix has dimension 5038x40749, and its computation (although possible) is extremely demanding. Moreover, even if we assume for a moment that $\tilde{\mathbf{L}}_{32}$ was available, the computation of $\mathbf{G}^{-1}$ (which is the matrix we ultimately want) requires additional effort. From eq. (8.2.4–12) we have:

$$\mathbf{G}^{-1} = \tilde{\mathbf{L}}^{\mathbf{T}} \cdot \tilde{\mathbf{L}} = \begin{bmatrix} \tilde{\mathbf{L}}_{22}^{\mathbf{T}} & \tilde{\mathbf{L}}_{32}^{\mathbf{T}} \\ \varnothing & \tilde{\mathbf{L}}_{33}^{\mathbf{T}} \end{bmatrix} \cdot \begin{bmatrix} \tilde{\mathbf{L}}_{22} & \varnothing \\ \tilde{\mathbf{L}}_{32} & \tilde{\mathbf{L}}_{33} \end{bmatrix} = \begin{bmatrix} \tilde{\mathbf{L}}_{22}^{\mathbf{T}} \cdot \tilde{\mathbf{L}}_{22} + \tilde{\mathbf{L}}_{32}^{\mathbf{T}} \cdot \tilde{\mathbf{L}}_{32} & \tilde{\mathbf{L}}_{32}^{\mathbf{T}} \cdot \tilde{\mathbf{L}}_{33} \\ \tilde{\mathbf{L}}_{33}^{\mathbf{T}} \cdot \tilde{\mathbf{L}}_{32} & \tilde{\mathbf{L}}_{33}^{\mathbf{T}} \cdot \tilde{\mathbf{L}}_{33} \end{bmatrix} \tag{8.2.4–15}$$

The term $\tilde{\mathbf{L}}_{32}^{\mathbf{T}} \cdot \tilde{\mathbf{L}}_{32}$ creates a full matrix, which, when added to $\tilde{\mathbf{L}}_{22}^{\mathbf{T}} \cdot \tilde{\mathbf{L}}_{22}$, destroys the block-diagonal structure of the latter. Also, $\hat{\mathbf{L}}_{32}^{\mathbf{T}} \cdot \tilde{\mathbf{L}}_{33}$ is a full matrix (and so is $\hat{\mathbf{L}}_{33}^{\mathbf{T}} \cdot \tilde{\mathbf{L}}_{33}$), thus making $\mathbf{G}^{-1}$ a huge (in our case, 45787x45787) full matrix whose only pattern is symmetry. Due to these complications, in this analysis we computed only:

1. The block-diagonal error covariance matrix $\mathbf{G}_{11}^{-1}$, corresponding to the $\hat{\mathbf{X}}_1$ parameter group.

2. The error variances of the $\hat{\mathbf{X}}_2$ group of parameters, i.e., the diagonal elements of the matrix $\tilde{\mathbf{L}}_{22}^{\mathbf{T}} \cdot \tilde{\mathbf{L}}_{22} + \tilde{\mathbf{L}}_{32}^{\mathbf{T}} \cdot \tilde{\mathbf{L}}_{32}$.

3. The full error covariance matrix $\tilde{\mathbf{L}}_{33}^{\mathbf{T}} \cdot \tilde{\mathbf{L}}_{33}$ corresponding to the $\hat{\mathbf{X}}_3$ parameter group.

Additional elements of $\mathbf{G}^{-1}$ may be computed using the Cholesky factor of $\mathbf{G}$ and solving linear systems of the type:

$$\mathbf{G} \cdot \mathbf{g}_{\mathbf{j}}^{\mathbf{I}} = \mathbf{e}_{\mathbf{j}} \qquad (8.2.4\text{–}16)$$

where $\mathbf{g}_{\mathbf{j}}^{\mathbf{I}}$ is the jth column of $\mathbf{G}^{-1}$ and $\mathbf{e}_{\mathbf{j}}$ is a vector whose jth element is 1 and all others 0 [*Colombo*, 1984, pp. 126–127]. The elements that we computed in (1), (2), and (3) above represent a "poor man's variance–covariance matrix," as *Colombo* [*ibid*.] puts it. Additional investigation and algorithm development is needed to improve this situation. It must be noted here that a more complete variance–covariance matrix for the high-degree model is required primarily to enable error propagation for various functionals of the field (gravity anomalies, geoid heights, etc.), with higher resolution. This implies that not only do we need efficient techniques to compute a better approximation of the full covariance, but also efficient techniques to propagate this matrix afterwards. As a continuation of the joint project, work is now underway to investigate these problems.

Software developed to implement the algorithm described above was tested and verified as follows. A satellite-only normal matrix was formed to $N_{sat} = 30$, and a terrestrial normal matrix to $N_{max} = 70$. The combined normal equations that adhere to the structure of Figure 8.2.4–2 were set up and inverted in two different ways: 1) "brute force" as if the matrix were full and 2) using the software developed to implement the above formulation and exploit the sparseness of the matrix. Per degree, the RMS coefficient differences ranged from 0.4×10^{-18} ($n = 2$) to 0.2×10^{-20} ($n = 70$). The corresponding values for the coefficient standard deviations were 0.4×10^{-19} ($n = 2$) to 0.1×10^{-20} ($n = 70$). Overall, the RMS coefficient difference between the two solutions was 0.5×10^{-20}, while the RMS standard deviation difference was 1.2×10^{-20}. These differences are approximately 10 orders of magnitude below the coefficient and standard deviation values themselves. They represent numerical noise and different roundoff errors present in the two solution methods.

The "$N_{max} = 70$, $N_{sat} = 30$" test scenario was also used to compare four types of solutions [*Chan and Pavlis*, 1995]:

1. Full satellite-only normals to $N_{sat} = 30$ and full terrestrial normals to $N_{max} = 70$ (optimal solution).

2. Full satellite-only normals to $N_{sat} = 30$ and full terrestrial normals to $N_{max} = 30$. Diagonal-only terms for the terrestrial normals from $n = 31$ to $N_{max} = 70$. This solution corresponds to an NQ type of adjustment.

3. Both satellite-only and terrestrial normals truncated according to the sparseness pattern of Figure 8.2.4–1a. This solution is denoted "BD3."

4. Full satellite-only normals to $N_{sat} = 30$, BD3 terrestrial normals to $N_{max} = 70$. Combined normals are according to the pattern of Figure 8.2.4–1f (or 8.2.4–2). This solution is denoted "BD3 plus wing."

The results from solutions (2), (3), and (4) were compared to those from (1), which is used here as a benchmark. This comparison clearly indicated that, in order to achieve the smallest differences with solution (1) over the lower portion (to $N_{max} = 30$) of the field, one has to use either the "BD3 plus wing" or the NQ type of adjustment. Solutions (2) and (4) performed equally well over this degree range, yielding coefficient differences with solution (1), which were at most about 20 percent of the corresponding coefficient standard deviations. Above degree 30, solutions (3) and (4) are identical (as expected), and their difference with respect to solution (1) are smaller than the difference (2)–(1). This is also expected since (2) approximates the terrestrial normals above degree 30 as a diagonal matrix. Additional details and plots related to these tests can be found in [*Chan and Pavlis*, 1995].

The development, verification, and experiments described above enabled the block-diagonal adjustment algorithm to be in place approximately by the time the joint project started. This algorithm was used to estimate the block-diagonal models, which will be described in Section 8.5.

8.3   The Merged 30´x30´ Mean Anomaly File

As explained in Section 8.2, the high-degree combination solutions are developed based on a satellite-only model (and its full error covariance matrix) and a complete global grid of 30´x30´ mean anomalies. The procedures followed to define this anomaly file are discussed here. This file is created by merging gravity anomaly information from:

1. Terrestrial (including airborne) 30´ $\overline{\Delta g}$ (Section 3.4).

2. Altimetry-derived 30´ $\overline{\Delta g}$ (Section 4).

3. Terrestrial 1° $\overline{\Delta g}$ (Section 3.5) converted to 30´ estimates by a "split up" process.

4. $\overline{\Delta g}$ implied by topographic–isostatic information (Section 2.5) and the low-degree part of the satellite-only model.

Since both the NQ and the BD estimators require complete coverage and cannot accommodate multiple and overlapping data for a given region, the philosophy underlying the merging process is to design an algorithm that will select a unique anomaly estimate for each 30´ cell on the ellipsoid, giving preference to the most reliable estimate [*Rapp and Pavlis*, 1990, Section 3.5]. The procedure used here for the merging is similar (but not identical) to the one used by *Rapp*

and Pavlis [*ibid*.]. During the course of the project, several preliminary versions of the terrestrial and altimetry-derived anomaly files were produced and released by NIMA. These were used to develop corresponding versions of the 30´ merged file. As test solutions progressed, analysis of the resulting models helped identify some problems in the data, which were investigated and subsequently corrected. The preliminary test models were also used to guide refinements in the merging procedure. Here we will not review all of the intermediate merged files and their development; rather, we will concentrate on the final merged file that supports the estimation of the high-degree portion of EGM96. Intermediate merged files will be mentioned where appropriate as they pertain to certain preliminary models.

Five files containing 30´ $\overline{\Delta g}$ were used in the merging process that produced the final merged anomaly file. These were based on:

A. **nima.v091296.terr.min30**   Terrestrial 30´ values from NIMA

B. **nima.v060796.alt.min30.dt2**   Altimetry 30´ values from NIMA

C. **osu.v072189.terr.min30_mod**   Terrestrial 30´ values from OSU

D. **nima.v091296.terr.deg01**   Terrestrial 1° values from NIMA

E. **egm96s.ti.f041t360_jgp95e.min30**   Composite topographic–isostatic 30´ values

Before the merging procedure, the data in file (D) were "split up" in order to define a 30´ counterpart of the 1° anomalies. This split-up process sets all four 30´ $\overline{\Delta g}$ within a 1° cell containing a valid 1° anomaly estimate, equal to the 1° $\overline{\Delta g}$ value. The standard deviation of each split-up 30´ $\overline{\Delta g}$ is set equal to two times the standard deviation of the corresponding 1° $\overline{\Delta g}$. This is the same procedure followed by *Rapp and Pavlis* [1990, page 21893]. The resulting 30´ split-up file will be denoted hereon as (D´).

Files (A) through (D´) (when overlaid) do not provide complete global coverage. As discussed in Section 7.2.2, we have defined a composite geopotential model consisting of the coefficients of EGM96S from $n = 2$ to $n = 40$, augmented by the topographic–isostatic coefficients implied by the JGP95E topographic data base (Section 2.5) from $n = 41$ to $n = 360$. These coefficients, denoted $\overline{C}_{nm}^{ti}$, are used to compute "fill in" anomalies ($\overline{\Delta g}^{fi}$) for areas devoid of any other estimate. These are computed in terms of 30´x30´ mean values on the surface of the reference ellipsoid using an equation similar to (7.2.2–4), but with the maximum degree of summation extending to 360.

Each fill-in 30´ anomaly was assigned a standard deviation equal to 36 mGal, a value based on comparisons reported by *Pavlis and Rapp* [1990].

During the merging process, two additional systematic corrections are applied to the anomaly data, so that the resulting merged file would be consistent with the theoretical formulation used. Considering the description of these data given in Sections 3 and 4, the two corrections are:

1) *Ellipsoidal corrections* IE_h, IE_γ, IE_p

   These are applicable to the anomalies of files (A), (C), and (D´). The altimetry-derived anomalies of file (B) do not require these corrections, since the least-squares collocation

prediction that estimated these values directly provides anomalies consistent with the boundary condition:

$$\Delta g = -\left(\frac{\partial T}{\partial r}\right) - \frac{2}{r} T \qquad (8.3-1)$$

where Δg in eq. (8.3–1) represents the magnitude of the radial projection of the gravity anomaly vector. *Jekeli* [*personal communication*, 1995] suggested this refinement to the procedure used during the development of OSU89A/B and OSU91A (where ellipsoidal corrections were also applied to the altimetry-derived values). (IE_h, IE_γ, IE_p) were computed as 30´ mean values, using the JGM–2/OSU91A model complete to degree and order 180. The details of such a computation can be found in [*Pavlis*, 1988, Sections 2.3.3, 2.3.4]. In terms of 30´ mean values, the total correction ($IE_h + IE_\gamma + IE_p$) computed here has an area-weighted RMS value of 109 µGal, and extreme values from –962 to +1326 µGal. Despite the small magnitude of these corrections, their long wavelength character can produce geoid undulation errors exceeding 80 cm [see *Pavlis*, 1988, Figures 42, 43], in geopotential solutions obtained from terrestrial data alone.

2) *Analytical continuation* (g_1)

The gravity anomalies in files (A) through (D´) represent Molodensky free-air values defined on the surface of the Earth. However, eqs. (8.2.1–1) and (8.2.2–1) both require gravity anomalies defined on the surface of the reference ellipsoid. The purpose of analytical downward continuation is to define a fictitious gravity anomaly field on the ellipsoid that, when upward continued, reproduces the surface and external field. The fictitious anomaly field on the ellipsoid does not define the actual gravity anomaly within the masses; it is just a mathematical creation that enables efficient formulas to be applied on the relatively simple surface of the reference ellipsoid. The potential coefficients obtained on the basis of the continued anomalies re-create the actual external potential of the Earth. Analytical continuation is an interesting topic with challenging mathematical, as well as numerical, aspects [*Moritz*, 1980]. Some aspects of the continuation problem were examined during the course of the project, as discussed in the next section. Here, we restrict the discussion on the actual procedure followed in the definition of the final merged 30´ file for EGM96. The g_1 terms were computed based on the same formulation used in the development of the OSU89A/B models [*Rapp and Pavlis*, 1990, Section 2.2.4]. Employing the assumption of linear correlation between the free-air anomaly and the elevation [see also *Wang*, 1988], 5´x5´ values of the g_1 term were computed based on the JGP95E mean elevations. The computation was made globally using the 1D FFT approach of *Haagmans et al.* [1993]. Simple arithmetic averaging of these 5´ values produced 30´ means. Within the context of *linear theory* [*Moritz*, 1980, pp. 339–341], continuation to the geoid was considered equivalent to continuation to the reference ellipsoid. Continuation corrections g_1 are applicable to the data of files (A), (B), (C), and (D´); however, over ocean areas, the value of g_1 is identically zero, according to the formulation used here. According to the above, the anomaly $\overline{\Delta g}^e$ is defined as:

$$\overline{\Delta g}^e = \begin{cases} \overline{\Delta g}^{obs} - (IE_h + IE_\gamma + IE_p) + g_1 & \text{file (A), (C), (D')} \\ \overline{\Delta g}^{obs} & \text{file (B)} \\ \overline{\Delta g}^{fi} & \text{file (E)} \end{cases} \qquad (8.3\text{--}2)$$

As was the case with the 1° terrestrial data (Section 7.2.2), the atmospheric correction was already applied to the anomalies of files (A), (C), and (D) (see Section 3.3.1). We now consider the merging procedure. First we define various geographic areas that are treated separately in the merging algorithm.

1) **Inland and Enclosed Seas:** These are ocean areas within the following "windows." Over these areas, a 30´ $\overline{\Delta g}$ from either file (A) or file (C), if available, is preferred over 30´ altimetric $\overline{\Delta g}$ from file (B).

   a. Canadian Arctic: $(68.0° < \varphi \le 77.0°, 182.0° \le \lambda < 236.0°)$

   b. Hudson Strait: $(57.5° < \varphi \le 64.0°, 290.0° \le \lambda < 296.0°)$

   c. Hudson Bay: $(50.0° < \varphi \le 65.0°, 265.0° \le \lambda < 285.0°)$

   d. Red Sea: $(12.5° < \varphi \le 30.0°, 30.0° \le \lambda < 45.0°)$

   e. Gulf of Aden: $(10.0° < \varphi \le 16.0°, 42.0° \le \lambda < 51.0°)$

   The geographic area covered by the union of these five areas is denoted "INLAND."

2) **Airborne Gravity Anomalies:** Whenever airborne anomalies are available, they are preferred over any other available value. This is done everywhere, *except* for the areas:

   a. Baffin Bay: $(\varphi \le 74.0°, 280.0° \le \lambda < 315.0°)$

   b. Denmark Strait: $(\varphi \le 74.0°, 315.0° \le \lambda)$

   Over these two areas, the airborne data "compete" with altimetry-derived anomalies, and the altimetric value is preferred, if it satisfies the depth criterion discussed below. The geographic area covered by all available airborne data minus the two regions above is denoted "AIR."

3) **Shallow Areas:** We define shallow areas to be those where the 30´ mean elevation from JGP95E is greater than or equal to –500 m *and* a 30´ $\overline{\Delta g}$ from file (A) exists. Over such areas, we try to avoid the use of altimetric anomalies, since these may be contaminated by unreliable ocean tide corrections [see also *Rapp and Pavlis*, 1990, Section 3.5]. However, preliminary tests indicated that certain shallow areas exist, where terrestrial data from file (A) are poor and should not be preferred over altimetry-derived anomalies [*Kenyon, personal communication*, 1996]. These are shallow areas falling within the "windows" identified below.

   a. Black Sea: $(40.0° < \varphi \le 50.0°, 27.5° \le \lambda < 45.0°)$

   b. Caspian Sea: $(35.0° < \varphi \le 50.0°, 45.0° \le \lambda < 55.0°)$

   c. Patagonia: $(-56.0° < \varphi \le -44.0°, 284.0° \le \lambda < 295.0°)$

   d. African Coast (W): $(-40.0° < \varphi \le 35.0°, -20.0° \le \lambda < 20.0°)$

8–19

e. African Coast (E): $(-40.0° < \varphi \le 10.0°, 20.0° \le \lambda < 60.0°)$

According to the above, "SHALLOW" areas are those where $\overline{H}_{30'} \ge -500$ m, a 30´ $\overline{\Delta g}$ from file (A) exists, *and* the area in question does not fall into one of the five windows above.

With the area identifications above in mind, the merging algorithm overlays anomaly data from the five files (A) through (E), sequentially following a "best last" philosophy. Namely:

1) Initialize the 30´ $\overline{\Delta g}$ of each cell using a fill-in value from file (E).

2) If a split-up $\overline{\Delta g}$ is available from file (D´), use the split-up value.

3) If an OSU 30´ $\overline{\Delta g}$ is available, use this value from file (C).

4) If a terrestrial 30´ $\overline{\Delta g}$ from NIMA is available, use this value from file (A).

5) If a 30´ altimetry-derived $\overline{\Delta g}$ is available, use this value from file (B), unless:

   a. the cell belongs to the region "INLAND," or

   b. the cell belongs to the region "AIR," or

   c. the cell belongs to the region "SHALLOW."

During this merging process, the minimum standard deviation of the 30´ mean anomalies was set to ±0.5 mGal, regardless of source, to avoid some overoptimistic accuracy estimates. Table 8.3–1 summarizes some statistics related to the anomalies selected from each of the files to create the final merged 30´ data set used to develop EGM96. Note that these statistics refer to the anomalies *before* the g_1 continuation terms are applied. The merged file so created has an overall mean value of –0.2 mGal, an RMS anomaly of 29.2 mGal, and an RMS anomaly standard deviation of ±7.1 mGal.

Table 8.3–1. Statistics of the 30´ mean anomaly data selected by the merging procedure. Mean and RMS values are weighted by area. Gravity anomaly units are mGal.

	File A NIMA terr.	File B NIMA alt.	File C OSU terr.	File D´ "Split-up"	File E "Fill-in"
Number of values	86740	146042	1064	6500	18854
Percentage of area	30.68	66.14	0.11	0.74	2.33
Minimum value	–214.4	–300.3	–153.6	–184.6	–170.3
Maximum value	399.5	328.0	301.7	263.6	170.3
Mean value	4.2	–2.4	8.6	9.4	0.8
RMS value	35.2	25.6	56.7	49.1	28.0
RMS stand. dev.	5.4	1.7	16.9	35.7	36.0

Comparison of the statistics given in Table 8.3–1 with corresponding statistics given in Table 19 of [*Rapp et al.*, 1991, page 61] demonstrates the significant improvements, in terms of both coverage and (at least formal) accuracy, brought about by the release of the new terrestrial and altimetry-derived 30´ mean anomalies from NIMA. Approximately 97 percent of the Earth's area is now covered by high-quality 30´ $\overline{\Delta g}$, while only 82 percent was covered with corresponding

data when the OSU91A model development took place. Figure 8.3–1 illustrates the geographic locations that anomalies from the five files occupy in the merged 30´ file. Subdivisions within each of the five files pertaining to method of evaluation or anomaly source (see Sections 3 and 4) are also identified in Figure 8.3–1. The merged 30´ file was designated **dg30x30.mrgd.v091796**.
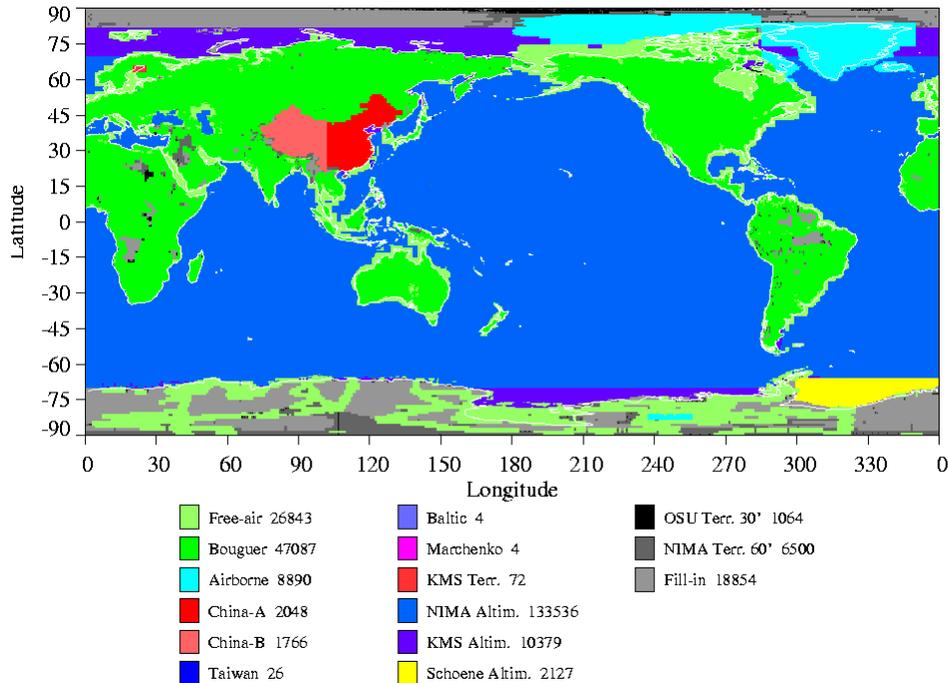
Figure 8.3–1. Identification of 30´ mean anomalies in the merged data file.

8.4 The Analytical Downward Continuation of Surface Gravity Anomalies to the Reference Ellipsoid

Gravitational potential coefficients may be estimated from gravity anomalies defined on the surface of the Earth, using Least Squares Adjustment (LSA) or Least Squares Collocation (LSC) techniques. The use of surface anomalies implies that the condition (a) of page 8–4 cannot be satisfied anymore. This substantially increases the computational effort required for the estimation of the potential coefficients, since it renders both the quadrature formulas and the block-diagonal approximation of normal equations inapplicable. Low degree "terrestrial" solutions employing surface gravity anomalies and the LSA technique have been developed by *Pavlis* [1988]. LSC solutions employing surface anomalies (which require the use of covariance functions that depend also on radial distances) have yet to be developed. To enable efficient estimation of the high-degree (360) potential coefficient model, we chose to implement the NQ (eq. (8.2.1-1)) and the BD least squares (eq. (8.2.2-1)) techniques. Both of these techniques require gravity anomalies defined on the surface of the reference ellipsoid. These anomalies must be such that they reproduce the actual gravitational potential of the Earth, on and outside its

surface. One of the methods widely used is analytical downward continuation of the Earth's external potential onto the reference ellipsoid (which can be partially or entirely within Earth's topographic masses) [*Wang*, 1988; *Rapp and Pavlis*, 1990; *Rapp et al.*, 1991]. Analytical downward continuation has a delicate theoretical aspect that is outside the scope of this document. For more details on analytical downward continuation, consult *Moritz* [1980], *Arnold* [1978, 1980], *Cook* [1967], *Levallois* [1973], *Morrison* [1969], *Sjöberg* [1977,1980], and *Wang* [1994, 1997].

The gravity anomaly on the reference ellipsoid can be defined in terms of the gravity anomaly on the Earth's surface by a Taylor's series expansion as:

$$\Delta g^* = \Delta g - \frac{\partial \Delta g}{\partial h} h + \frac{1}{2!} \frac{\partial^2 \Delta g}{\partial h^2} h^2 - ... \tag{8.4--1}$$

where Δg is the surface gravity anomaly, Δg^* is the gravity anomaly downward continued on to the ellipsoid, and h is the ellipsoidal height. Approximating the ellipsoidal height with the orthometric height H, and assuming a linear approximation, we have

$$\Delta g^* \approx \Delta g - \frac{\partial \Delta g}{\partial h} h \approx \Delta g - \frac{\partial \Delta g}{\partial H} H \tag{8.4--2}$$

We then define g_1 as:

$$g_1 = -\frac{\partial \Delta g}{\partial H} H \tag{8.4--3}$$

There are several ways to evaluate the vertical gradients of the gravity anomalies. One way is to use a spherical harmonic coefficient model [*Rapp*, 1984, p.20]. An alternative approach uses a surface integral [*Heiskanen and Moritz*, 1967, eq. (2-217)]:

$$\left(\frac{\partial \Delta g}{\partial H}\right)_P = -\frac{2}{R} \Delta g_P + \frac{R^2}{2\pi} \iint_{\sigma} \frac{\Delta g - \Delta g_P}{l_0^3} d\sigma \tag{8.4--4}$$

where l_0 is the distance between the computation point and the current point, and R is the mean radius of the Earth.

There are advantages and disadvantages of the two methods of evaluating the vertical gradients discussed above. Computation of the correction can be made in an iterative way using the existing geopotential models as an initial starting point. That is, the g_1 term can be computed from a currently available coefficient model, then applied to gravity anomalies being used in the development of a new coefficient model. The g_1 term can then be recomputed using the new coefficient model and applied to the gravity anomalies again. This process is then repeated until a final set of values is converged upon. The disadvantage of this method is that the vertical gradients are limited to the generally deficient high-frequency information content of the existing coefficient models. This limitation does not affect the vertical gradients computed using the surface integral method. Provided that the surface gravity free-air anomalies are given in a dense global grid, the vertical gradient of the gravity anomalies can be accurately computed. However, this method requires much more computational effort, and most important, it requires detailed

global gravity anomaly data that currently are not available to the public. In order to overcome this problem, a simple approximation of the free-air gravity anomalies can be made [*Uotila*, 1960; *Moritz*, 1980, p. 416]:

$$\Delta g = 2\pi G \rho H + C_1 \tag{8.4–5}$$

where

    C_1 = a constant

    G = Newton's gravitational constant

    ρ = the density of the Earth's topographic mass

Substituting (8.4–5) into (8.4–4), we obtain

$$(g_1)_P = \left(-H\frac{\partial \Delta g}{\partial H}\right)_P \approx -R^2 G H_P \iint_\sigma \frac{\rho H - (\rho H)_P}{l_0^3} d\sigma \tag{8.4–6}$$

Here we have ignored the first term in (8.4-4) because it is at least one order smaller than the integral. It becomes zero if the planar approximation is taken.

While global detailed gravity anomalies are difficult to obtain, detailed terrain models—which provide the orthometric heights—have been widely available (e.g., the JGP95E in 5´x5´ equal angular mean block values; see Section 2), making the approximate calculation of the g_1 terms straightforward.

In addition to the above-mentioned methods, Poisson's integral [*Heiskanen and Moritz*, 1967, p. 318] can be used to reduce the surface gravity anomalies to the ellipsoid. The surface gravity anomaly Δg and the analytically downward continued gravity anomaly Δg^* are related by the following equation [Heiskanen and Moritz, eq. 8-87]:

$$\Delta g_P^* = \frac{\Delta g_P}{t^2} - \frac{1-t^2}{4\pi}\iint_\sigma \frac{\Delta g^* - \Delta g_P^*}{D^3}d\sigma \tag{8.4–7}$$

where

$$t = \frac{R}{R + H_P}, \quad D = \frac{l}{R + H_P} \tag{8.4–8}$$

where l is the distance between the computation point, P, and the current point on the sphere σ. Solving (8.4–7) by iteration, we obtain

$$\begin{aligned}
\left(\Delta g_0^*\right)_P &= \frac{\Delta g_P}{t^2}\\
\left(\Delta g_1^*\right)_P &= \frac{\left(\Delta g_0^*\right)_P}{t^2} - \frac{1-t^2}{4\pi}\iint_\sigma \frac{\Delta g_0^* - (\Delta g_0^*)_P}{D^3}d\sigma
\end{aligned} \tag{8.4–9}$$

    ...

We define the difference between the reduced anomaly and the surface gravity anomaly by

$$G_1 = \Delta g^* - \Delta g \qquad (8.4\text{--}10)$$

We have dropped the subscript P for all quantities in eq. (8.4-10). Under linear approximation, these three methods are effectively identical. However, because different data are used in each method, differences in the results are expected.

8.4.1 Numerical Aspects of the Computation of the g_1 Term

The integral in eq. (8.4–6) has a strong singularity at the computation point. The integral exists if the orthometric height and the density of the Earth's topographic mass satisfy Leibniz's condition [*Mikhlin*, 1965]. In the numerical computations, we assume that Leibniz's condition is always satisfied, so that the integral exists. In order to remove this singularity and improve the computation accuracy, special attention must be paid to the integral in the innermost zone. This problem has been studied by several authors [*Hein*, 1977 and 1978; *Sünkel* 1977; *Wang*, 1987]. One method of evaluating the integral is to expand the function ρH into bicubic spline function; then the integration in the innermost zone can be computed analytically. Such a procedure has been developed [*Nöe*, 1980; *Wang*, 1987] under a planar approximation. However, as we show in the following, if the function ρH can be approximated by a bilinear function in the innermost zone, the contribution of the innermost zone is negligible.

We chose the computation point P as the origin of a two-dimensional coordinate system xPy, where x and y are the axes pointing north and east, respectively. Then the function ρH may be approximated by a bilinear function of x and y:

$$\rho H = a_0 + a_1 x + a_2 y \qquad (8.4.1\text{--}1)$$

where a_0, a_1, and a_2 are constants to be determined. Note that:

$$\begin{aligned} x &= l_0 \cos \alpha \\ y &= l_0 \sin \alpha \end{aligned} \qquad (8.4.1\text{--}2)$$

where l_0 is the distance between the computation point and current point; α is the angle between the l_0 and the x axis. If the data are given in equal angular blocks, we approximate the innermost zone by the area of a circle, $l_0 \le \varepsilon$, where ε is determined by [*Schwarz et al.*, 1990]:

$$\varepsilon = \sqrt{\delta / \pi} \qquad (8.4.1\text{--}3)$$

where δ is the area of the innermost block.

After the planar approximation, the contribution of the innermost zone is, then

$$-HR^2 G \int_0^\varepsilon \int_0^{2\pi} \frac{a_1 x + a_2 y}{l_0^3} dx dy = -HR^2 G \int_0^\varepsilon (a_1 + a_2) l_0^{-1} dl \int_0^{2\pi} (\cos \alpha + \sin \alpha) d\alpha = 0 \quad (8.4.1\text{--}4)$$

For a smooth function, the approximation of eq. (8.4.1–1) may be sufficient. Therefore, the contribution of the innermost zone is approximately zero. In the computation with highest accuracy, the contribution of the innermost zone can also be computed separately by using the procedure developed by *Wang* [1987].

If the elevation and density of the Earth's topographic mass are given in a regular grid, the vertical gradient of gravity anomaly can be computed by using the discrete form of eq. (8.4–6):

$$(g_1)_{ij} = -CH_{ij} \sum_{m=0}^{M} \sum_{n=0}^{N} \frac{(\rho H)_{mn} - (\rho H)_{ij}}{\sin^3 \dfrac{\psi_{ijmn}}{2}} \cos \phi_m \quad \begin{array}{l} i = 1,...M \\ j = 1,...N \end{array} \tag{8.4.1--5}$$

where

$$C = \frac{G}{8R} \Delta\phi\Delta\lambda \tag{8.4.1--6}$$

$$\sin^2(\frac{\psi_{ijmn}}{2}) = \sin^2(\frac{\phi_m - \phi_i}{2}) + \sin^2(\frac{\lambda_{mn} - \lambda_{ij}}{2}) \cos\phi_m \cos\phi_i \tag{8.4.1--7}$$

and m and n (and i and j as well) are the indices along the latitude and longitude directions.

We denote

$$f_{ijmn} = 1/\sin^3(\psi_{ijmn}/2) \tag{8.4.1--8}$$

and define

$$f_{ijmn}^* = \begin{cases} f_{ijmn} & if \quad i \neq m, j \neq n \\ 0 & if \quad i = m, j = n \end{cases} \tag{8.4.1--9}$$

Separating eq. (8.4.1–5) into two parts and ignoring the contribution of the innermost zone, we get

$$(g_1)_{ij} = g_{ij}' - g_{ij}'' \tag{8.4.1--10}$$

with

$$g_{ij}' = -CH_{ij} \sum_{m=0}^{M} \sum_{n=0}^{N} f_{ijmn}^*(\rho H)_{mn} \cos\phi_m \tag{8.4.1--11}$$

$$g_{ij}'' = -CH_{ij}(\rho H_{ij}) \sum_{m=0}^{M} \sum_{n=0}^{N} f_{ijmn}^* \cos\phi_m \tag{8.4.1--12}$$

Equations (8.4.1–11) and (8.4.1–12) can be evaluated using the method of 1D–FFT developed by *Haagmans et al.* [1993]:

$$g_{ij}' = -CH_{ij} F^{-1}\{ \sum_{m=0}^{M} F\{f_{mn}^*\} F\{(\rho H)_{nm}\} \cos\phi_m \} \tag{8.4.1--13}$$

$$g_{ij}'' = -CH_{ij}(\rho H)_{ij} F^{-1}\{ \sum_{m=0}^{M} F\{f_{mn}^*\} F\{1\} \cos\phi_m \} \tag{8.4.1--14}$$

where F is the 1D–FFT and F^{-1} is its inverse. Equations (8.4.1–13) and (8.4.1–14) calculate the g_1 term in latitude bands. In order to save computation time, the 1D–FFT of the product $(\rho H)_{mn}$ is

computed once and stored in a matrix. The time-consuming part is that the 1D–FFT of the kernel function f_{nm}^{*} has to be computed M times for every latitude band. This work can be reduced by 50 percent utilizing the symmetry of the sphere with respect to the Equator.

8.4.2 g_1 Term Comparisons in a Local Region

Jekeli [1995] computed the g_1 term using detailed gravity data (4 km x 4 km grid) in a region over the United States. These values were then compared with the g_1 terms computed from the coefficient model OSU91A and from using elevation data in the surface integral method. *Jekeli* [*ibid*.] concluded that the OSU91A coefficient model gives better reduction of the gravity data in the mountainous region tested. The RMS differences between the g_1 terms from the detailed gravity anomaly and OSU91A coefficient model was 1.37 mGal (30´x30´) in the western mountainous region, while the RMS value of the difference between the g_1 terms from the detailed gravity anomalies and those derived using the elevation data was 1.63 mGal. In the flat area, the g_1 values derived from the elevation data agreed slightly better with those from the detailed gravity anomaly (0.35 vs. 0.36 mGal). To verify Jekeli's findings, a series of tests was conducted. The 4 km x 4 km gravity anomalies over the test region ($35° \leq \phi \leq 49°$, $245° \leq \lambda \leq 268°$) were regridded into a 3´x3´ equal-angular grid. Four different methods, plus two variations, were then used in the computations:

s1   the g_1 term is defined by eq. (8.4–3). The coefficient model JGM–2/OSU91A was used to compute the gravity anomaly gradient.

s2   the G_1 term is defined by eq. (8.4–10), and is computed from the third iteration of Poisson's integral using a global (merged) 30´ mean gravity anomaly file.

s3   same as s2, except the data used were the 3´x3´ gravity anomalies. To stabilize the iteration, a 6´ moving average was applied.

s4   same as s3, but a 12´ moving average was applied.

s5   same as the first iteration of s3, but with no moving average applied.

s6   same as s5, but a 12´ moving average was applied.

Table 8.4.2–1 gives a statistical overview of the resultant correction terms (g_1 and G_1) for each method. Table 8.4.2–1 shows that all the maximum correction term values occur at the same location. The locations of the minimum values are slightly different for method s1 and s2, where different data were used. Clearly, s3 has the most power of the corrections. Method s5 is the first iteration of s3 without the 6´ moving average applied, and shows that the first iteration also provides the most power of the corrections. Comparison of s6 to s5 shows the effect of the 12´ moving average used to smooth the data, and that the effect is insignificant: the RMS decreased from 1.5 mGal to 1.4 while the extreme values decreased from 15.6 to 14.8 mGal. However, the smoothing is important for the computation of the Poisson iteration, as it stabilizes the iteration and reduces unexpected spikes, which are common when a solution is unstable. Table 8.4.2–2 shows statistics of the differences between the correction terms in the test region.

Table 8.4.2–1. Statistical overview of g_1 and G_1 terms in terms of 30´x30´ mean values. Units are mGal.

Method	s1	s2	s3	s4	s5	s6
Min. Value	−4.6	−3.6	−7.0	−4.4	−5.9	−4.6
ϕ min	43.25	42.75	44.25	44.257	44.25	44.25
λ min	251.75	250.25	250.25	250.25	250.25	250.25
Max. Value	10.1	12.7	20.2	17.2	15.6	14.8
ϕ max	44.25	44.25	44.25	44.25	44.25	44.25
λ max	252.75	252.75	252.75	252.75	252.75	252.75
Mean	0.1	0.1	0.3	0.2	0.1	0.1
RMS	1.1	1.2	1.9	1.6	1.5	1.4

The 30´ grid size of data used in method s2 is comparable with the resolution of the maximum degree and order of 360 in the coefficient model used in method s1, resulting in a high degree of similarity between the correction terms. Comparison of methods s3 and s5 shows that the second and third iterations of Poisson's integral contribute 0.5 mGal to the overall RMS difference, with an extreme value of 4.1 mGal. This level of difference may be below the error introduced by errors in the data. Therefore, the first iteration may be accurate enough for most g_1 term computations. The comparison between the results from s5 and s6 shows that the terms are not significantly changed when smoothing is applied. However, this small change enables a stable solution. This is especially important if a higher order of the iteration of Poisson's integral is needed.

Table 8.4.2–2. Absolute maximum/RMS differences, taken over the USA, of the continuation terms computed using six methods. Units are mGal..

Method	s1	s2	s3	s4	s5	s6
s1	----	4.8/0.6	10.9/1.2	8.6/0.9	7.0/0.9	6.3/0.8
s2		----	9.8/1.0	7.7/0.7	9.1/0.7	7.9/0.6
s3			----	2.7/0.4	4.1/0.5	4.9/0.6
s4				----	3.3/0.3	3.1/0.3
s5					----	1.2/0.2
s6						----

8.4.3 Global g_1 Term Computations and Comparisons

Three methods were used to evaluate the g_1 term: The numerical computation (1D–FFT) of the surface integral in equation (8.4–6) is denoted procedure "E." In this procedure, the 5´x5´ global elevation file, JGP95E, was used. The computation of the g_1 term from a coefficient model, defined as procedure "G," used the combined coefficient model JGM–2 ($2 \leq n \leq 70$)/OSU91A ($71 \leq n \leq 360$). Finally, Poisson iteration (eq. (8.4–9)) was used, here designated as procedure "P," with the merged 30´ gravity anomaly file data (1995).

The first global g_1 term computation, by *Wang* [1988], is similar to procedure E, and used the global 5´x5´ elevation file TUG87 [*Wieser*, 1987]. This procedure made the planar approximation of eq. (8.4–6) and used a two-dimensional FFT technique. The results were used in the OSU89B and OSU91A coefficient model development efforts. This procedure and procedure E differed in the numerical computation method used (2D– vs. 1D–FFT) and in the elevation data source file. In our comparisons it was found that the results of *Wang* [*ibid.*] were very close to those of procedure E. The g_1 term from both procedures have similar RMS values (2.38 vs. 2.49 mGal) and similar extreme values (45 vs. 52 mGal). It was also found that the results of *Wang* [*ibid.*] had a problem with step functions along the border of computation blocks (15°x30°) in the Antarctic region resulting from the insufficient border used in the 2D–FFT computations at that region. The results from *Wang* [*ibid.*] will not be used for our future gravity anomaly reductions, and will not be discussed further.

Table 8.4.3–1 shows the statistics of the g_1 terms computed from the above-mentioned procedures. All statistics were computed over land (i.e., where the elevation > 0 meter). A cosine weighting scheme was also used to compensate for the area change caused by the convergence of the meridians. All comparisons were made in 30´x30´ mean block values.

Table 8.4.3–1. Statistics of 30´ mean values of g_1 terms computed globally using three different procedures. Units are mGal.

Procedure	E	G	P
Number	46581	46581	46581
Mean	0.68	0.14	0.12
Std. Dev.	2.49	1.10	1.03
Minimum	−11.93	−13.84	−17.18
Maximum	51.56	22.60	23.95
$|\bullet| \geq 5$	1897	442	382
$|\bullet| \geq 5$ (% of total)	4.1	0.9	0.8

Table 8.4.3–1 shows that the procedure E has the most power. The standard deviation of the g_1 values produced by procedure E is more than twice that of either procedure G or P. This result is expected because the data used in procedure E have a much smaller grid size (5´) than procedure P, which used a 30´ grid. The resolution of the coefficient model JGM–2/OSU91A used in procedure G is about 55 km, approximately corresponding to a 30´ grid size, and produces results that are similar to those from procedure P. The numbers of points where the magnitude of the g_1 term is greater than 5 mGal for procedures G and P are 442 and 382, respectively. This is significantly less than the 1897 points that met this criterion from procedure E. A summary of the g_1 differences from these three different procedures is given in Table 8.4.3–2.

From Table 8.4.3–2, one can see that the difference of the g_1 terms from procedures E and G are significant. The RMS value of the differences is almost twice the RMS value of the g_1 term from procedure G. The differences of the g_1 terms from procedures G and P are relatively small. Figure 8.4.3–1 shows the g_1 term differences between procedures E and G. Large differences occur in mountainous regions, such as in the Andes mountain range in South America, western

United States, and western China. Because the differences are significant, it is important to know which procedure provides the more accurate g_1 term. This can be determined only by performing additional tests. If the assumption of the linear correlation between gravity anomalies and the elevation were plausible, then procedure E should provide much more information about the g_1 term than either procedure G or P. The residual gravity anomalies and the GPS/leveling tests (cf. Section 8.5.2) support this assumption. Clearly, these tests show that the g_1 terms from the procedure E, which made use of the digital terrain data, outperformed the g_1 terms from procedures G and P. This emphasizes the importance of the detailed digital elevation data for the g_1 term computations. To free ourselves from the linear correlation assumption, we have to have globally detailed gravity anomalies, which is currently unrealistic.

Table 8.4.3–2. Statistics of g_1 term differences in terms of 30´x30´ mean values. Units are mGal.

	E-G	P-G
Number	46581	46581
Mean	0.54	0.18
Std. Dev.	2.00	0.76
Minimum	−11.17	−17.18
Maximum	43.02	21.32
$|\bullet|\geq 5$	1448	179
$|\bullet|\geq 5$ (% of total)	3.1	0.4
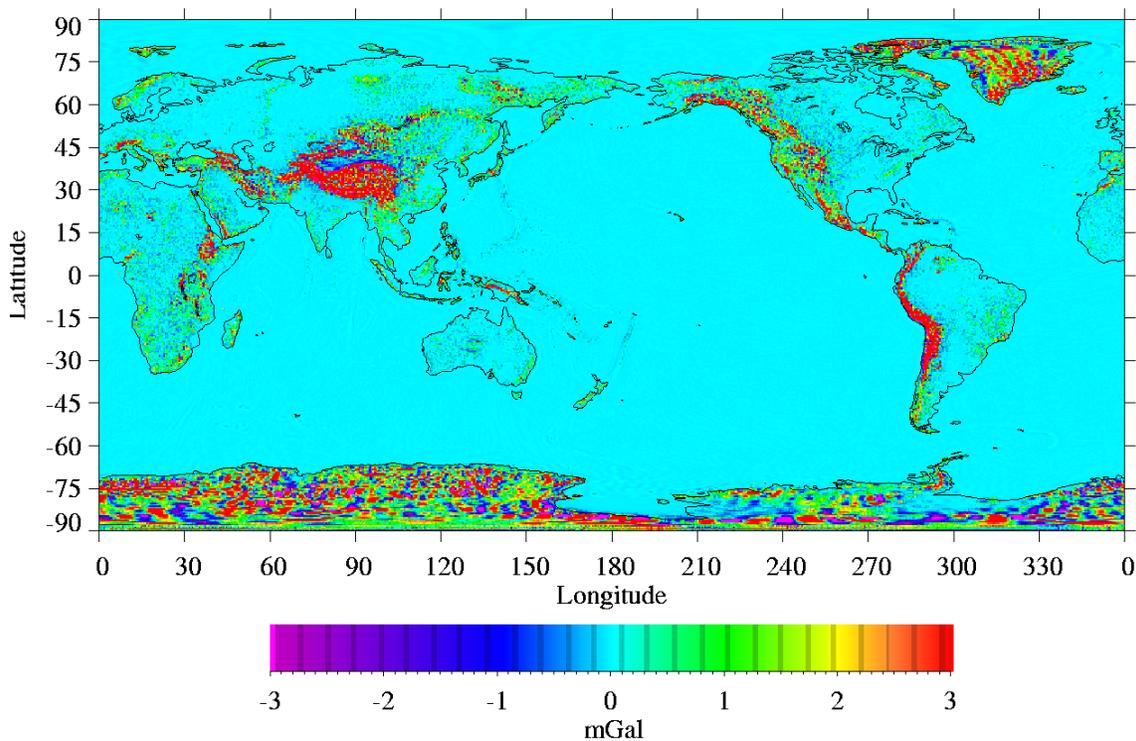
Figure 8.4.3–1. Difference in 30´ mean g_1 term values between the numerical computation of the surface integral (procedure "E") and the use of a coefficient model (procedure "G"). Differences are E–G.

8.5   Preliminary High-Degree Expansion Developments

Several preliminary high-degree expansions have been computed during the course of the joint project. These test solutions resulted from the gradual availability of improved satellite-only models, improved versions of the terrestrial and altimetry-derived anomaly files, and the need to investigate several aspects of the high-degree model development (analytical continuation terms, anomaly weighting procedures, and quadrature weights). Furthermore, test models had to be developed in two ways, one using the NQ approach and the other the BD approach, and the resulting solutions had to be compared against each other and against independent test data. The gravity anomaly weighting procedure and the analytical continuation technique are aspects of the high-degree model development common to both the NQ and the BD approaches. These aspects were investigated by developing several NQ test models. On the basis of these experiments, the adopted approaches were then applied to the BD models as well. The NQ type of solutions, being the easiest to develop, also provided an excellent way of testing new satellite-only models and merged anomaly files. For completeness, Table 8.5–1 lists all of the NQ test models that were developed during the course of the project (61 in all), and summarizes the "parameters" used in their development.

Table 8.5–1. High-degree expansions developed using the Numerical Quadrature (NQ) technique.

Model Name	Satellite-Only Model Used	Merged 30′ Δg File Used	g_1 Terms Used	Δg Weighting Scheme	Quadrature Weights Type
V001	PGS5606	DMA95	Elev. (JGP95A)	$\sigma = 10$ mGal	2
V002	PGS5606	DMA95	Elev. (JGP95A)	$\sigma = 15$ mGal	2
V003	PGS5606	DMA95	Elev. (JGP95A)	A	2
V004	PGS5606	DMA95	Elev. (JGP95A)	B	2
V005	PGS5606	DMA95	Elev. (JGP95A)	C	2
V006	PGS5606	DMA95	Elev. (JGP95A)	D	2
V007	JGM–2S	DMA95	Elev. (JGP95A)	A	2
V008	JGM–2S	DMA95	Elev. (JGP95A)	B	2
V009	PGS5606	OSU91	Elev. (TUG87)	A	2
V010	PGS5606	OSU91	Elev. (TUG87)	B	2
V011	PGS5676	DMA95	Elev. (JGP95A)	A	2
V012	PGS5676	DMA95	Elev. (JGP95A)	B	2
V013	PGS5712	DMA95 (b2)	Elev. (JGP95A)	A	2
V014	PGS5712	DMA95 (b2)	Elev. (JGP95A)	B	2
V015	PGS5712	DMA95 (b2)	Elev. (JGP95A)	$\sigma = 15$ mGal	2
V016	PGS5712	L91O95	Elev. (TUG87)	B	2
V017	PGS5734	DMA95 (b2)	Poisson's Integral	B	2
V018	PGS5734	DMA95 (c2)	Poisson's Integral	B	2
V019	PGS5734	DMA95 (b2)	Grad. (JGM2/91A)	B	2
V020	PGS5734	DMA95 (c2)	Grad. (JGM2/91A)	B	2
V022	PGS5734	DMA95 (c2)	Elev. (JGP95C)	B	2
V024	PGS5712	DMA95 (c2)	Poisson's Integral	B	2
V026	PGS5712	DMA95 (c2)	Grad. (JGM2/91A)	B	2
V028	PGS5712	DMA95 (c2)	Elev. (JGP95C)	B	2

Model Name	Satellite-Only Model Used	Merged 30′ Δg File Used	g₁ Terms Used	Δg Weighting Scheme	Quadrature Weights Type
V029	PGS5734	DMA95 (915)	Elev. (JGP95C)	B	2
V030	PGS5734	DMA95 (915A)	Elev. (JGP95C)	B	2
V031	PGS5973	V112095	Elev. (JGP95D)	$\sigma = 15$ mGal	2
V032	PGS5973	V112095	Grad. (V030)	$\sigma = 15$ mGal	2
V033	PGS5973	V112095	Elev. (JGP95D)	B	2
V034	PGS5973	V112095	Grad. (V030)	B	2
V036	PGS5973	DMA95 (915A)	Elev. (JGP95D)	B	2
V037	PGS5973	V112995	Elev. (JGP95D)	B	2
V039	PGS5734	DMA95 (915A)	Elev. (JGP95D)	B	2
V040	PGS5973	V112995	Elev. (JGP95D)	B	2
V041	PGS5973	V112995	Elev. (JGP95D)	B	3
V042	PGS5973	V112995	Elev. (JGP95D)	B	4
V043	PGS6345	V020896	Elev. (JGP95E)	B	3
V044	PGS6345	V020896	Elev. (JGP95E)	B	4
V045	PGS6345	V020896	Grad. (V030)	B	3
V046	PGS6345	V020896	Grad. (V030)	B	4
V047	PGS6345	V021596	Elev. (JGP95E)	B	3
V048	PGS6345	V021596	Elev. (JGP95E)	B	4
V049	PGS6345	V021596	Grad. (V030)	B	3
V050	PGS6345	V021596	Grad. (V030)	B	4
V051	PGS6348	V021596	Elev. (JGP95E)	B	3
V052	PGS6348	V021596	Elev. (JGP95E)	B	4
V053	PGS6366	V021596	Elev. (JGP95E)	B	3
V054	PGS6365	V021596	Elev. (JGP95E)	B	3
V055	PGS6376	V021596	Elev. (JGP95E)	B	3
V056	PGS6376	V021596	Elev. (JGP95E)	B	4
V057	PGS6394	V021596	Elev. (JGP95E)	B	3
V058	PGS6394	V021596	Elev. (JGP95E)	B	4
V059	PGS7270d	V021596	Elev. (JGP95E)	B	4
V060	PGS7270d	V072496	Elev. (JGP95E)	B	3
V061	PGS7270d	V072496	Elev. (JGP95E)	B	4
V062	PGS7270d	V072496	Grad. (V058_460)	B	3
V063	PGS7270d	V072496	Grad. (V058_460)	B	4
V064	PGS7270d	V072496 (15′)	Elev. (JGP95E)	B	4
V065	PGS7270h	V072496	Elev. (JGP95E)	B	4
V066	PGS7270k	V072496	Elev. (JGP95E)	B	4
V068	PGS7270k37	V091796	Elev. (JGP95E)	B	4

Certain "parameters" appearing on Table 8.5–1 require further explanation. Weighting scheme "$\sigma = 10$ mGal" or "$\sigma = 15$ mGal" implies that the weight was computed based on a constant standard deviation assigned to all 30′ $\overline{\Delta g}$ regardless of their origin or geographic location. The weighting schemes A, B, C, and D were devised by rescaling the original standard deviations σ_{ij}^{o} of the mean anomalies, and restricting the result to vary within a certain range, similar to the procedure described in Section 7.2. We have:

A: $\max(12,\ 2\sigma_{ij}^{o}) \le \sigma_{ij}^{m} \le \min(24,\ 2\sigma_{ij}^{o})$ (8.5–1)

B: $\max(14,\ 2\sigma_{ij}^{o}) \le \sigma_{ij}^{m} \le \min(27,\ 2\sigma_{ij}^{o})$ (8.5–2)

C: $\max(28,\ 2\sigma_{ij}^{o}) \le \sigma_{ij}^{m} \le \min(54,\ 2\sigma_{ij}^{o})$ (8.5–3)

D: $\quad \max(\ 6, \ 2\sigma_{ij}^{o}) \le \sigma_{ij}^{m} \le \min(12, \ 2\sigma_{ij}^{o})$ $\hspace{5cm}$ (8.5–4)

In the development of the OSU89A/B and OSU91A models, the weighting scheme B was implemented.

With L ($= \pi/\Delta\lambda$) denoting the Nyquist degree implied by the data sampling interval (here $L = 360$), four types of desmoothing factors q_n^i (see eq. 8.2.1–1) are considered here:

Type 1 (Pellinen) $q_n^i = \beta_n^i \qquad \forall \, n$ $\hspace{5cm}$ (8.5–5)

Type 2 (Colombo) $q_n^i = \begin{cases} \left(\beta_n^i\right)^2 & 0 \le n \le L/3 \\ \beta_n^i & L/3 < n \le L \\ 1 & L < n \end{cases}$ $\hspace{4cm}$ (8.5–6)

Type 3 $q_n^i = \begin{cases} \left(\beta_n^i\right)^2 & 0 \le n \le L/3 \\ \beta_n^i & L/3 < n \le L \\ \beta_L^i & L < n \end{cases}$ $\hspace{4cm}$ (8.5–7)

Type 4 $q_n^i = \begin{cases} \left(\beta_n^i\right)^2 & 0 \le n \le L/2 \\ \left(\beta_n^i\right)^{L/n} & L/2 < n \le L \\ \beta_L^i & L < n \end{cases}$ $\hspace{4cm}$ (8.5–8)

The Pellinen smoothing operators β_n^i are computed by [*Colombo*, 1981]:

$$\beta_n^i = \frac{1}{\left(1 - \cos\psi_0^i\right)} \frac{1}{(2n+1)} \left[P_{n-1}(\cos\psi_0^i) - P_{n+1}(\cos\psi_0^i)\right] \hspace{2cm} (8.5–9)$$

where ψ_0^i is the semiaperture of a spherical cap having the same area as the equiangular block on the ith latitude band. It is computed by [*Colombo*, 1981, p. 85]:

$$\psi_0^i = \cos^{-1}\left[\frac{\Delta\lambda}{2\pi}\left(\cos\delta_{i+1} - \cos\delta_i\right) + 1\right] \hspace{3cm} (8.5–10)$$

This formulation accounts for the latitude dependence of ψ_0^i and β_n^i, as discussed by [*Katsambalos*, 1979]. In the development of the OSU89A/B and OSU91A models, the desmoothing factors of type 2 were used, with β_n^i computed according to (8.5–9) and (8.5–10). The discontinuities of this type of composite q_n^i factors result in certain undesirable discontinuities of the estimated signal and error spectrum. The rationale behind the introduction of the types 3 and 4 composite q_n^i factors was simply to avoid such discontinuities. Type 3 differs from Colombo's suggestion *only* beyond the Nyquist degree; it is continuous at $n = L$. Type 4 differs from Colombo's suggestion after degree $n = L/3$; it is continuous for all degrees (Colombo's proposed factors have discontinuities at $n = L/3$ and $n = L$). The reciprocal values of the desmoothing factors (i.e., the quadrature weights $1/q_n^i$) are plotted in Figure 8.5–1, for $\psi_0 = 0.282°$, corresponding (approximately) to 30′ sampling interval.

With the above information in mind, we now discuss certain test models that guided the decision-making process that led to the procedures finally adopted for the development of the high-degree part of EGM96.
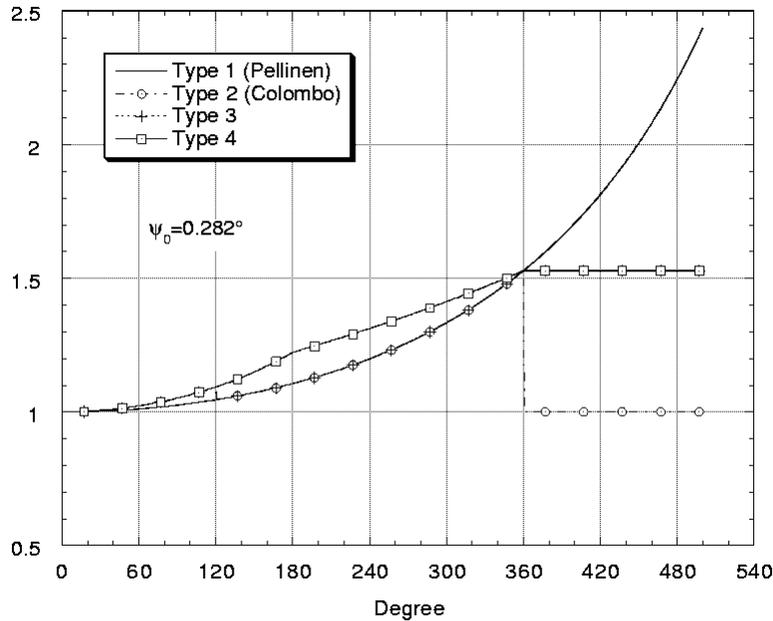
Figure 8.5–1. Quadrature weights ($1/q_n^i$) for 30´ area-mean values.

8.5.1 Gravity Anomaly Weighting Procedure

The standard deviations used to compute the weight associated with each individual 30´ $\overline{\Delta g}$ require careful consideration. The complication here stems primarily from our inability to consider error correlations that most probably exist between the anomaly estimates [*Weber and Wenzel*, 1982]. To compensate for the unmodeled error correlations, we follow the technique of *Rapp and Cruz* [1986b], whereby the original standard deviation associated with each anomaly in the merged file is rescaled and the result is restricted to vary within a preassigned range of values as described in equations (8.5–1) through (8.5–4). This restriction of the range of the modified standard deviations is needed to maintain a reasonable ratio of weights associated with the best versus worst data in the solution. If this restriction is omitted, exceedingly large weight ratios will be present in the adjustment, effectively enforcing all the residuals to concentrate on the areas of poorest gravity data, while leaving the data in well-surveyed areas unchanged (i.e., unaffected by the information contained in the satellite-only normals) [*ibid*., Section 6.1]. Based on the OSU89A/B and OSU91A experience, we tried to maintain an approximate 4:1 weight ratio in the four weighting schemes of equations (8.5–1) through (8.5–4) that were tested. Six test models, designated V001 to V006, were developed for this purpose. In addition to the four weighting schemes, the solutions V001 and V002 were made where the anomaly weights were assigned uniformly corresponding to 10 and 15 mGal standard deviations, respectively. The six

solutions were compared in terms of the magnitude and geographic distribution of the gravity anomaly residuals, and in terms of selected statistical indicators related to the least-squares adjustment. Recall here that the gravity anomaly residuals (v) indicate differences in the gravity anomaly signal sensed by the satellite-only model and that represented by the merged data, *over the degree range present in the satellite-only model* ($2 \leq n \leq 70$). The residual anomaly maps for the six solutions (not shown here) were examined, and it was verified that the same general geographic areas were associated with large (absolute) residual values, regardless of weighting algorithm. These areas included the polar caps, areas in South America, South-East Asia, parts of Africa, and parts of Alaska. All of these areas are known to lack high-quality gravity anomaly data. Particularly helpful in this type of comparison are the solutions with uniform weight. These can be used to verify that areas of large residuals are not "artificially" created by inappropriate downweighting of data. Visual inspection of the residual plots verified that this was not the case.

We now consider certain statistics related to the least-squares adjustments that produced the solutions V003, V004, V005, and V006. These are indicators of the internal consistency of the two sources of information participating in the adjustment (satellite-only model and merged 30´ $\overline{\Delta g}$). The results from the four test solutions are shown in Table 8.5.1–1, along with those for the final NQ model V068, which is included for future reference. $\hat{\sigma}_0^2$ is the *a posteriori* variance of unit weight (ideally equal to 1), and $\overline{k}$ is the average calibration factor over all degrees [see *Rapp and Pavlis*, 1990, p. 21898].

Table 8.5.1–1. Statistical information on four combination solutions using different weighting schemes and the final NQ model V068.

Model Name	V006	V003	V004	V005	V068
Std. Dev. range (mGal)	6–12	12–24	14–27	28–54	14–27
RMS Std. Dev. (mGal)	7.1	13.6	15.6	30.4	15.0
$\hat{\sigma}_0^2$	6.674	3.019	2.646	1.456	1.525
$\overline{k}$	1.254	1.205	1.191	1.083	0.995
RMS v (mGal)	3.06	3.35	3.39	4.19	2.16
Maximum $|v|$ (mGal)	32.4	46.3	48.2	75.0	33.8
No. of $|v| > 7$ mGal	13520	14707	15333	20704	4568
$n(N/S \approx 1)$	–(†)	295	280	185	285

(†) at degree 360 the Noise/Signal ratio for solution V006 is approximately 83%.

Table 8.5.1–1 shows also the harmonic degree at which the RMS anomaly signal equals the RMS anomaly error for each solution, denoted by $n(N/S \approx 1)$. The RMS error is computed as the quadratic sum of propagated plus sampling error [*ibid*., p. 21890]. From the table, one can see that as the weight of the anomaly data decreases, the maximum (absolute) and RMS residual increases (as expected, since decreasing weight implies more freedom for the anomaly data to adjust). The same is true, of course, for the number of residuals exceeding in magnitude 7 mGal. Examining the variation of $\hat{\sigma}_0^2$ one can deduce that the D weighting (range 6–12) is quite optimistic. The schemes B (14–27) or C (28–54) appear to be more reasonable choices, while

little difference is seen between A (12–24) and B schemes. The $\bar{k}$ value, which ideally should be 1, favors the 28–54 range; however, this weighting scheme implies that the signal spectrum dips below the noise around degree 185, which is totally unrealistic. The variation of the calibration factors per degree is shown in Figure 8.5.1–1 for the four weighting schemes. Of particular interest is this information at the lowest end of the spectrum, since this is the frequency band where the satellite-only model has strong observability (see also Figure 7.2.2–1), and the anomaly data are most vulnerable to unmodeled systematics. This figure also supports the conclusion that the 6–12 range (V006) is quite optimistic ($k > 1$), while the 28–54 (V005) is somewhat pessimistic ($k < 1$). The best candidates are the schemes A or B, and the distinction between these two is difficult. We decided to proceed with weighting scheme B (14–27), the same scheme used in the development of OSU89A/B and OSU91A models. The test models V013 (A) and V014 (B), which were developed later using an updated satellite-only model and a modified merged file, did not provide evidence favoring scheme A. The results pertaining to the final NQ model V068 (last column of Table 8.5.1–1) indicate that the weighting scheme chosen on the basis of these preliminary solutions is satisfactory ($\bar{k} = 0.995$). The large number of residuals exceeding 7 mGal that are seen in solutions V003, V004, V005, and V006, compared to the corresponding counts for V068, were due to a problem in the preliminary merged file related to Bouguer anomalies in the proximity of coastal areas. This problem was corrected in subsequent terrestrial anomaly estimations at NIMA.
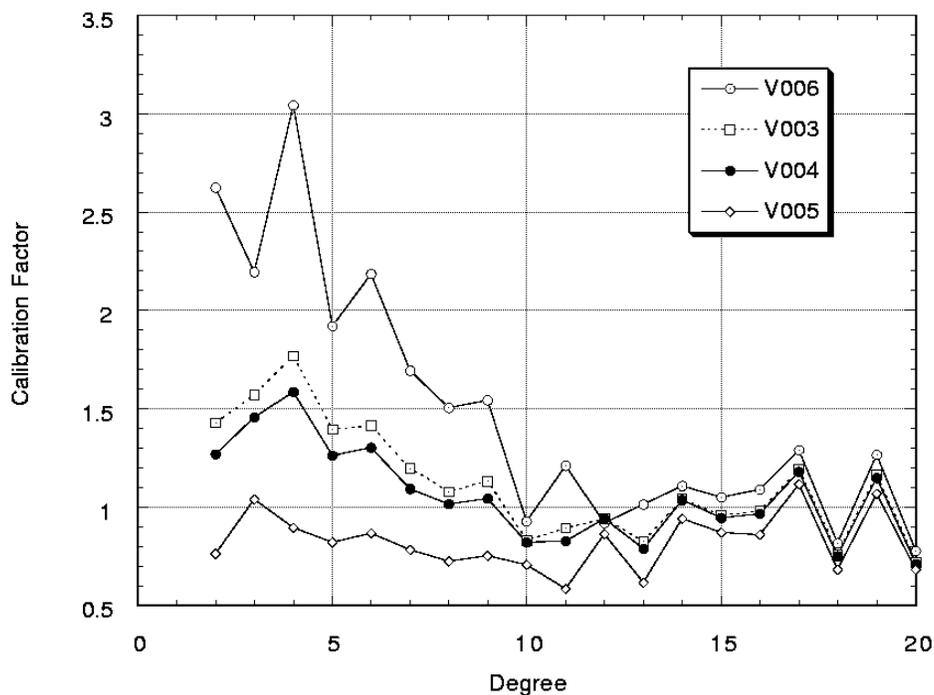
Figure 8.5.1–1. Calibration factors per degree corresponding to four anomaly weighting schemes.

In closing this section, we need to note that, although the weighting procedure used here enabled us to develop meaningful combination solutions, the more general problem of consideration of correlated errors in the global merged file remains an open question, which could not be addressed within the time limits of this investigation.

8.5.2 Analytical Continuation Techniques

In Section 8.4, three techniques were presented for the computation of analytical continuation corrections:

1) Poisson's integral *(P)*, where the continuation corrections are numerically evaluated by iterative solution of the integral equation (8.4–7). This equation is applied directly to the 30´ $\overline{\Delta g}$ of the merged file used to develop the high-degree expansion. This is necessitated by the lack of more detailed free-air anomaly data in a global sense (primarily over land areas).

2) Continuation based on the first-order gradient of the free-air anomaly *(G)* computed from a preexisting high-degree model ($N_{max} = 360$).

3) Continuation based on the first-order gradient of the free-air anomaly *(E)*, computed from a detailed Digital Elevation Model (DEM), under the assumption of linear correlation between the free-air anomaly and the elevation.

From a theoretical point of view, the first two approaches *(P)* and *(G)*, being free of the assumption of linear correlation between Δg_{FA} and *H*, are preferable. However, the gravity anomaly gradient that is required in order to analytically continue the surface data is a functional of high-frequency content. The 30´ mean anomaly data or the $N_{max} = 360$ model that are used in *(P)* and *(G)*, respectively, may be too smooth to capture the high-frequency character of the continuation corrections, especially over areas where the field has large gradients. From this perspective, the elevation-based g_1 terms may be preferable since they are based on 5´x5´ elevation data. On the other hand, as *Jekeli* [1995] pointed out, the elevation-based g_1 terms may produce false gradients over areas where the variation of free-air anomaly is not accompanied by corresponding elevation variations.

To evaluate the performance of these three techniques, test combination solutions were developed and their implied geoid undulations were compared against values obtained from GPS positioning and leveling data (see Section 5.3). The NQ solutions V018, V020, and V022 form one set of these tests, developed based on the PGS5734 satellite-only model, while the solutions V024, V026, and V028 form a corresponding set developed based on the PGS5712 satellite-only model. The results of the GPS/leveling tests for four areas are summarized in Table 8.5.2–1. These results indicate that a) there is little difference between the *(P)* and *(G)* continuation techniques and b) the elevation-based g_1 terms tend to produce geoid undulations that are in better agreement with the GPS/leveling-implied values over mountainous regions. This is especially evident from the comparisons over British Columbia, where the *(E)* technique yields standard deviation difference of 64–65 cm as compared to 72–73 cm difference obtained from *(G)* and *(P)*.

A concern related to the results of Table 8.5.2–1 was that the *(G)* type of continuation correction there was computed using the JGM–2/OSU91A composite model to degree 360. Because, at the time of the OSU91A model development, detailed and accurate data were not available over the area of British Columbia, the poor performance of the *(G)* approach over this area may be a reflection of the shortcomings of the JGM–2/OSU91A model over British Columbia and not of the continuation technique itself. To clarify this point, the test solutions V048 and V050 were made. In V050, the gradients were computed using a preliminary NQ model (V030), which incorporates the newly available surface anomaly data. Since the *(P)* and *(G)* approaches yield very similar results, only the *(E)* and *(G)* continuation terms were tested. The results are shown in Table 8.5.2–2, where comparisons over 1889 GPS/leveling benchmarks over the conterminous United States are also included. The results of Table 8.5.2–2 do not significantly alter the conclusions reached above. There is, however, a slight improvement seen over the U.S. test data set from the *(E)* to the *(G)* approach (53.1 versus 52.8 cm std. deviation difference). This may be because the U.S. test data set covers areas of both mild and steep gravity gradients, as opposed to the British Columbia one, which covers a mountainous area. Over British Columbia, the problem with the *(G)* type of continuation persists.

Table 8.5.2–1. Mean and standard deviation differences: GPS/leveling minus model-implied geoid undulations, for three different analytical continuation techniques. Units are cm, maximum degree is 360.

Area	Europe		Scandinavia		Australia		Canada (BC)	
No. of stations	60		46		38		298	
Model	Mean	S. Dev.	Mean	S. Dev.	Mean	S. Dev.	Mean	S. Dev.
V018 *(P)*	16	48	29	38	−53	31	−9	73
V020 *(G)*	16	48	29	38	−53	31	−9	72
V022 *(E)*	14	43	26	37	−54	31	−16	65
V024 *(P)*	16	48	30	38	−52	32	−10	73
V026 *(G)*	16	48	30	38	−53	32	−9	72
V028 *(E)*	14	44	26	37	−54	32	−16	64

Table 8.5.2–2. Mean and standard deviation differences: GPS/leveling minus model-implied geoid undulations, for two different analytical continuation techniques. Units are cm, maximum degree is 360.

Model	V048 *(E)*		V050 *(G)*	
Area / No. of stations	Mean	S. Dev.	Mean	S. Dev.
Europe / 60	10.1	31.1	12.2	36.1
Scandinavia / 46	14.7	22.9	18.1	25.6
Australia / 38	−89.1	27.7	−89.0	27.9
Canada (BC) / 298	−16.6	58.2	−11.0	66.1
USA / 1889	−102.6	53.1	−102.5	52.8

Apart from the GPS/leveling tests, the residual gravity anomaly maps were plotted for the different continuation approaches. These indicated that, over mountainous regions (e.g., the Rocky Mountains), the *(G)* or *(P)* types of continuation tend to produce larger residual anomalies than does the *(E)* approach. On the basis of these comparisons, we decided to implement the *(E)* type of continuation in subsequent solutions. We fully recognize, however, that additional study is required to clarify the behavior of different continuation techniques. GPS/leveling data over other areas of the globe could be helpful in this type of analysis.

8.5.3 Preliminary Block-Diagonal Solutions

We now turn our attention to some preliminary high-degree expansions of the BD type. We will first discuss the development of five BD models that were presented at the XXI General Assembly of the International Union of Geodesy and Geophysics in Boulder, Colorado, in July 1995 [*Pavlis et al.*, 1996]. These five models were developed based on the same merged 30´ $\overline{\Delta g}$ file DMA95(c2) (and the same anomaly weighting scheme) used to develop the V022 NQ expansion, the same analytical continuation corrections as in V022, and the same satellite-only model (PGS5734). Therefore, the performance of the two expansion techniques (NQ and BD) could be assessed by comparing the results of V022 with those obtained from the five BD models. The differences in the development of these models are summarized in Table 8.5.3–1. Reference values computed from the JGM–2 ($2 \le n \le 70$)/OSU91A ($70 < n \le 360$) model were introduced in the BD solutions to compensate for the omission of the cross-order off-diagonal terms in the surface gravity normals. This approach is similar to the technique of successive approximations used in the inversion of large systems, whereby one obtains an approximate solution by considering only diagonal terms, then improves this estimate by introducing off-diagonal terms and iterating the solution with appropriate updates of the right-hand-side vector.

Table 8.5.3–1. Description of five preliminary block-diagonal solutions.

Model Name	Ref. Field	"Wing"
HDM020	Ellipsoidal	yes
HDM028	JGM–2/OSU91A	yes
HDM033	Ellipsoidal	no
HDM031	JGM–2/OSU91A	no
HDM036 (†)	JGM–2/OSU91A	yes

(†) same solution as HDM028 but with 1/5 of Kaula's
rule added for $n > 70$.

The effect of reference values in the BD technique can be demonstrated analytically as follows. Consider the rigorous set of normal equations for the merged 30´ $\overline{\Delta g}$ data as:

$$\mathbf{N} \cdot \hat{\mathbf{X}} = \mathbf{U}$$

(8.5.3–1)

where $\hat{\mathbf{X}}$ represents the adjusted coefficients of the disturbing potential, i.e., remainders after subtraction of the even zonal harmonics of the normal ellipsoidal field. The BD3 truncated version of the normal system may be written as:

$$\tilde{\mathbf{N}} \cdot \hat{\hat{\mathbf{X}}} = \mathbf{U} \tag{8.5.3–2}$$

Notice that in both cases the right-hand-side vector is the same (and is computed rigorously). The difference in the estimates of the unknowns (rigorous minus BD3 approximation) is, therefore:

$$d\mathbf{X} = \hat{\mathbf{X}} - \hat{\hat{\mathbf{X}}} = (\mathbf{N}^{-1} - \tilde{\mathbf{N}}^{-1}) \cdot \mathbf{U} \tag{8.5.3–3}$$

Equation (8.5.3–3) indicates that the magnitude of $d\mathbf{X}$ can be reduced by reducing the magnitude of the term $(\mathbf{N}^{-1} - \tilde{\mathbf{N}}^{-1})$ (i.e., providing a better approximation of the normal matrix) or, for a given approximation of the normal matrix, by reducing the magnitude of $\mathbf{U}$. The magnitude of $\mathbf{U}$ can be reduced by modeling residual anomalies (after subtraction of a reference high-degree model), rather than the complete $30´\ \overline{\Delta g}$ values. So far, the introduction of a reference model is only a tool to enhance the numerical precision in the solution of the normal system and to compensate, to an extent, for the BD3 truncation of the normal matrix. This interpretation changes, if *a priori* constraints are introduced in the system (as was done in HDM036). The reference model, then, also carries stochastic information, and the solution becomes a band-limited counterpart of least-squares collocation.

To investigate the importance of the wing (which correlates low- and high-degree coefficients of the same order— see Figure 8.2.4–2), tests were made where the wing terms were deliberately set to zero (designated by "no" in Table 8.5.3–1). Recall that the existence of nonzero wing terms prevents the *a posteriori* error covariance matrix of the high-degree model from being strictly block-diagonal (and thus relatively easy to form and manipulate). The performance of the resulting solutions was assessed through tests with independent data. The most sensitive tests for the evaluation of the low-degree part of the models are orbit fits to SLR data, as shown in Table 8.5.3–2 (HDM036 gave practically identical results as HDM028).

Table 8.5.3–2. SLR orbit test residuals for some preliminary geopotential models (set 1, RMS of fit in cm).

Model Name	LAGEOS	LAGEOS–II	Starlette	Ajisai
PGS5734	2.91	3.16	7.73	7.21
V022	2.94	3.15	7.89	7.24
HDM020	2.96	3.16	8.37	7.39
HDM028	2.95	3.15	7.87	7.24
HDM033	2.94	3.15	8.09	7.26
HDM031	2.95	3.15	7.90	7.25

All models are truncated to maximum degree 70.

These results indicate that:

a) The use of the high-degree reference model is necessary in the BD technique (compare HDM020 vs. HDM028, or HDM033 vs. HDM031).

b) The presence of the wing improves slightly the orbit fit results (compare HDM028 vs. HDM031). However, the fact that this improvement is only marginal indicates that the wing passes information primarily from the low-degree harmonics to the high-degree ones (of a given order), and not the other way around. This behavior strongly depends on the relative weight of the surface gravimetric data with respect to the satellite information.

c) A *relative* comparison of the results of Table 8.5.3–2 to those of Table 8.2.4–1 is instructive. It demonstrates that the use of the full satellite-only normal matrix in the current BD solutions has alleviated the problems with the long- and medium-wavelength portions of the combination solution. These problems were manifested in the poor orbit fits to Starlette and Ajisai before. Now, these fits (HDM028) are equal to or better than the fits of the NQ model V022.

HDM028 and HDM036 should be considered the best candidate BD solutions in terms of the rigor exercised in their development. The performance of these models compared to the NQ solution V022 is now tested using independently derived geoid undulations from GPS positioning and leveling data (see Section 5.3). The results from absolute comparisons are shown in Table 8.5.3–3. Note here that in all BD models, the $n = 360$ harmonics (which cannot be estimated with the BD approach), are obtained from the corresponding NQ model V022. Over Europe, Scandinavia, and Australia, the BD models perform more poorly than the V022 NQ model. Over British Columbia and the U.S., the BD models are performing slightly better than the NQ model.

Table 8.5.3–3. Mean and standard deviation differences: GPS/leveling minus model-implied geoid undulations. Units are cm, maximum degree is 360. Number of stations per area is as in Table 8.5.2–2.

Model	V022		HDM028		HDM036	
Area	Mean	S. Dev.	Mean	S. Dev.	Mean	S. Dev.
Europe	14	43	14	47	14	47
Scandinavia	26	37	26	41	26	41
Australia	−54	31	−59	35	−59	34
Canada (BC)	−16	65	−15	63	−14	63
USA	−101	57	−102	56	−102	56

These comparisons can also be done in a relative sense, over segments of the GPS/leveling traverses [*Rapp and Pavlis*, 1990]. In this mode, the test is particularly sensitive to the performance of the higher degree part of each model, since long-wavelength model errors are canceling out, to a large extent, when undulation differences are taken. The results from these

tests over three GPS/leveling traverses are shown in Table 8.5.3–4, in terms of standard deviation of the undulation differences ΔN(model)–ΔN(GPS/leveling), and in parts per million (ppm) over the length of the traverse segments.

Over the three GPS/leveling traverses tested, the BD models perform more poorly than the NQ model. The comparisons in terms of ppm, particularly, indicate that the higher degree and order part of the BD models perform substantially more poorly than V022.

Table 8.5.3–4. Relative comparison between GPS/leveling and model-implied geoid undulation differences. Standard deviation units are cm, maximum degree is 360.

Area	Europe		Scandinavia		Australia	
No. of lines	59		45		37	
Aver. line length (km)	49.7		46.1		39.4	
Model	S. Dev.	ppm	S. Dev.	ppm	S. Dev.	ppm
V022	23	3.6	23	4.1	21	5.1
HDM028	26	4.2	27	4.7	24	5.6
HDM036	25	4.2	27	4.6	23	5.4

To investigate this problem further, the signal, difference, and error gravity anomaly degree variances were computed for models V022 and HDM036; these are plotted in Figure 8.5.3–1. The difference between the two solutions is roughly an order of magnitude smaller than the error variance of either model for the same degree. One should notice the excellent agreement between the error variances implied by the two models. This is rather remarkable since the error variances of V022, above degree 70, are computed (sampling error part) based on a semiempirical formula devised by Jekeli [*Colombo*, 1981]. The signal degree variances of HDM036 imply a rougher field above degree approximately 180, as compared to V022. A possible cause for this behavior may be aliasing. Power in the 30′ $\overline{\Delta g}$ data, corresponding to harmonics above degree 360, aliases to the lower degree harmonics being solved for in the BD type of solutions. The relative comparisons of Table 8.5.3–4 show that the use of an *a priori* constraint in HDM036 (which dampens slightly the higher degree part of the spectrum as compared to HDM028), tends to improve the comparisons with the GPS/leveling undulation differences.

The hypothesis that aliasing is the (main) cause of the increased power observed in the spectra of the BD solutions can be tested in a simulated (noiseless) data environment. To this end, 1°x1° $\overline{\Delta g}$ were formed from the composite JGM2/OSU91A model complete to degree and order 300, using *Colombo's* [1981] harmonic synthesis algorithm. The 1°x1° $\overline{\Delta g}$ were then used to recover the "true" JGM2/OSU91A coefficients in two different ways: a) using *Colombo's* [*ibid.*] harmonic analysis algorithm (recovery to N_{max} = 300) and b) using the BD least-squares technique that was implemented in the HDM028 development (recovery to N_{max} = 179). Recall that 1° sampling implies Nyquist degree 180. The anomaly degree variances implied by the difference between original and recovered coefficients for the two techniques are plotted in Figure 8.5.3–2. The BD approach is far superior to the NQ technique, in terms of the coefficient
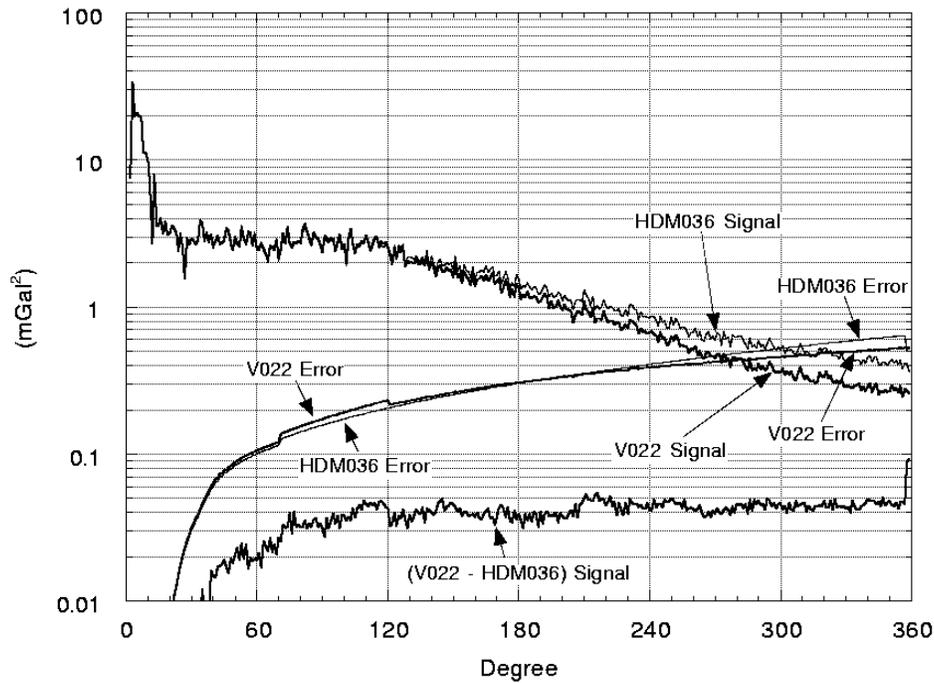
Figure 8.5.3–1. Gravity anomaly signal and error degree variance for solutions V022 and HDM036.
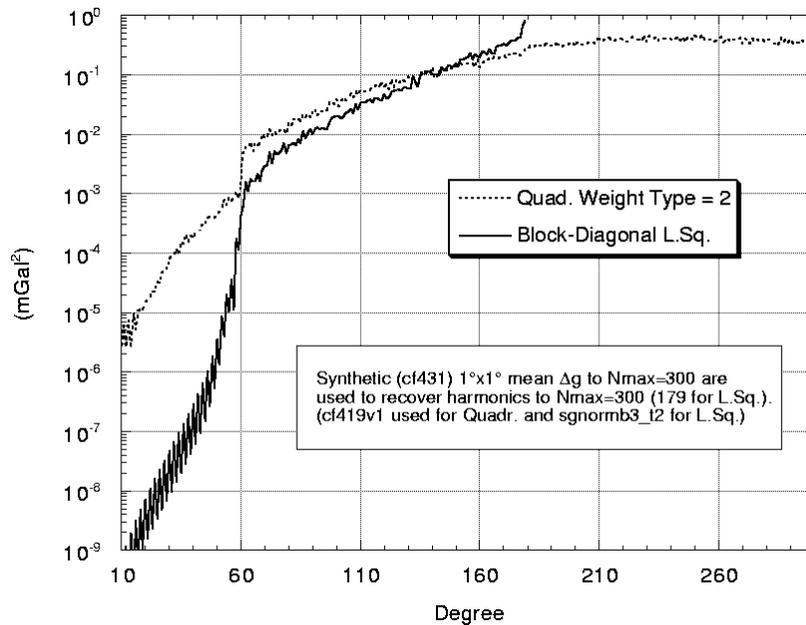
Figure 8.5.3–2. Gravity anomaly degree variances implied by the difference between the original and recovered harmonic coefficients.

recovery, up to approximately degree 60. Degree 60 is the "reflection" of degree 300, with respect to the Nyquist degree 180. At approximately degree 140, the BD technique results in larger difference degree variances than the NQ. The anomaly degree variances of the original JGM2/OSU91A coefficients and those recovered by the two techniques are shown in Figure 8.5.3–3. Notice that the "true" spectrum at the higher degrees lies somewhere between the BD and the NQ recovered ones. The behavior of the BD estimate of the spectrum is very similar to that observed with the real data analysis, and this provides additional evidence that aliasing was contaminating the higher degree harmonics obtained from BD least-squares in HDM028 and HDM036. The technique that was developed to reduce aliasing effects in the BD solutions is discussed in the next section.
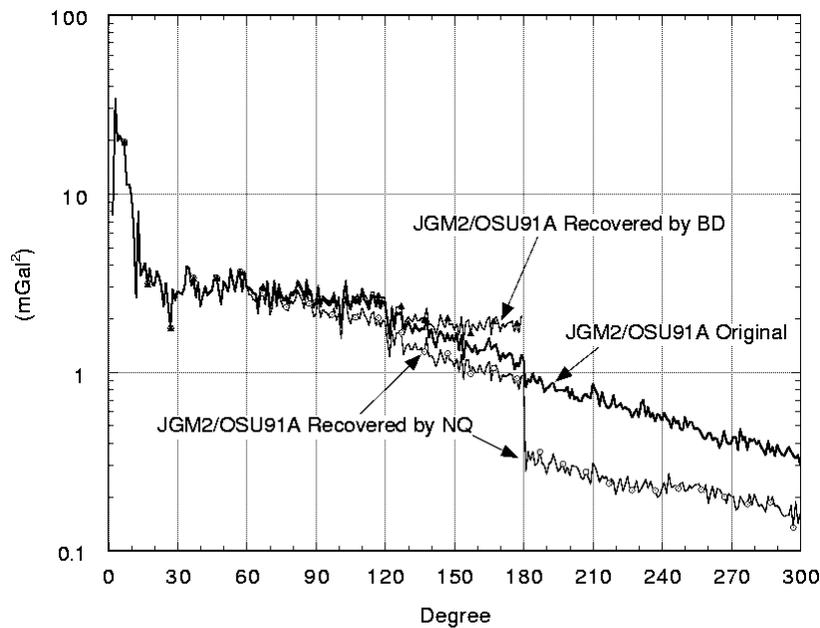
Figure 8.5.3–3. Gravity anomaly degree variances from the original and recovered harmonic coefficients.

8.5.4 Treatment of Aliasing Effects in Block-Diagonal Solutions

The aliasing problem encountered in the BD type of solutions may be addressed in a number of different ways. It must be recognized, first of all, that the frequency content of the 30′ $\overline{\Delta g}$ is most likely varying with geographic location. This is due to both the geographic variation in the roughness of the gravity signal and to the density and accuracy of detailed anomaly data that were used in the estimation of the 30′ mean values. The least-squares collocation prediction of the equiangular average values used here, viewed as a filter, has its own frequency response, which affects the frequency content of the predictions. *Jekeli* [1981] studied in detail the transfer function associated with various types of averaging operators.

To account for the fact that the data contain signal beyond the maximum degree estimable by least squares, L–1, (where L is the Nyquist degree), *Colombo* [1981, p. 50] suggested the modification of the error covariance matrix of the data. The new matrix is the sum of the noise contribution and the expected signal beyond the solved-for harmonics. The latter may be estimated, in a global average sense, based on a model of the anomaly degree variances, such as *Kaula's* rule or the model of *Tscherning and Rapp* [1974]. This approach was not implemented here. An alternative approach could be to simply split up the 30´ $\overline{\Delta g}$ in 15´ values, in the same way as was done with the 1° values as described in Section 8.3. This would allow the BD technique to be implemented beyond degree 359 (and out to degree 719), thus providing the means to accommodate any signal beyond $n = 359$ present in the 30´ data. This approach was tested. Unfortunately, the side effect of this technique is that the power of the harmonics below 360 is now significantly underestimated, and this forced us to reject this approach.

The aliasing effects in the BD solutions could be reduced if an estimate of the actual harmonic coefficients implied by the 30´ data for $n \geq L$ were available. These coefficients could be used to filter out of the 30´ data the contribution of degrees equal or higher than $L = 360$, making the reduced anomalies approximately band limited. The reduced anomalies could then be used as input to the BD estimator. An estimate of the higher degree coefficients can be obtained (free of any singularity problems) using the numerical quadrature algorithm of *Colombo* [1981]. To implement this approach, the problem that had to be overcome was the sharp discontinuity of the spectrum at the Nyquist degree, which can also be seen in Figure 8.5.3–3. This discontinuity is a consequence of the piecewise definition of desmoothing factors of type 2, as has been pointed out by *Rapp* [1981] and *Hajela* [1984]. Inspection of Figure 8.5.3–3 suggested that the spectral discontinuity could be significantly reduced if a constant value were assigned to the desmoothing factors for all degrees beyond L, equal to the desmoothing factor at $n = L$. This was the motivation behind the introduction of the type 3 desmoothing factors defined in eq. (8.5–7). This approach was devised here in an experimental fashion with no theoretical *a priori* justification. Taking this a step further, we decided to try the additional modification of the desmoothing factors that removes the discontinuity at $L/3$ as well, i.e., the desmoothing factors of type 4 as defined in eq. (8.5–8).

To summarize: In order to use BD least-squares (or even least squares with full matrices for this matter), one wants to have input data that are band limited to $N_{max} = 359$ (30´ $\overline{\Delta g}$ case). To filter out signal in the data beyond $n = 360$, one needs a model that extends beyond degree 360. Such a model may be obtained using NQ techniques with the alternative definitions (type 3 or 4) of the desmoothing factors. Obviously, if the 30´ $\overline{\Delta g}$ data do contain signal beyond 360, to make the most out of the data one would like to be able to recover this signal as best as it can be estimated. The harmonics beyond 360 thus will be useful not only for the filtering required to implement the BD approach. It must be noted here that *Colombo's* [1981] Optimal Estimation technique is another way that the harmonics beyond the Nyquist degree could be estimated. However, as discussed in [*Rapp and Cruz*, 1986b, Section 6.4], this approach tends to smooth excessively the recovered spectrum, when realistic error estimates are assigned to the gravity anomaly data. The NQ technique with the approximate (as opposed to optimal) quadrature weights offers a much simpler way of estimating the harmonic coefficients, free of this smoothing problem.

We consider now the NQ solutions extending to $N_{max} > L$. First, we need to determine the maximum degree to which it would be meaningful to expand these models. For this purpose, we used the empirical relationship of *Jekeli* [*Colombo*, 1981, p.78] as a guide. This relationship expresses the sampling error as a percentage of the signal, and is given in eq. (8.5.4–1). Note that this expression was developed for NQ estimators employing type 1 (Pellinen) desmoothing factors.

$$\frac{\sigma_n^{sampl.error}}{\sigma_n^{signal}} \times 100 = [(-16.19570 \cdot (n/L) + 30.34506) \cdot (n/L) + 40.29588] \cdot (n/L)^2 \qquad (8.5.4\text{–}1)$$

Figure 8.5.4–1 illustrates these percentages for both 1° and 30´ sampling. For the 30´ case at hand, a reasonable maximum degree is approximately 500. Note that eq. (8.5.4–1) considers sampling error *only*. In the real data case where measurement noise is also present, one should expect the maximum attainable degree to be less than what (8.5.4–1) predicts.
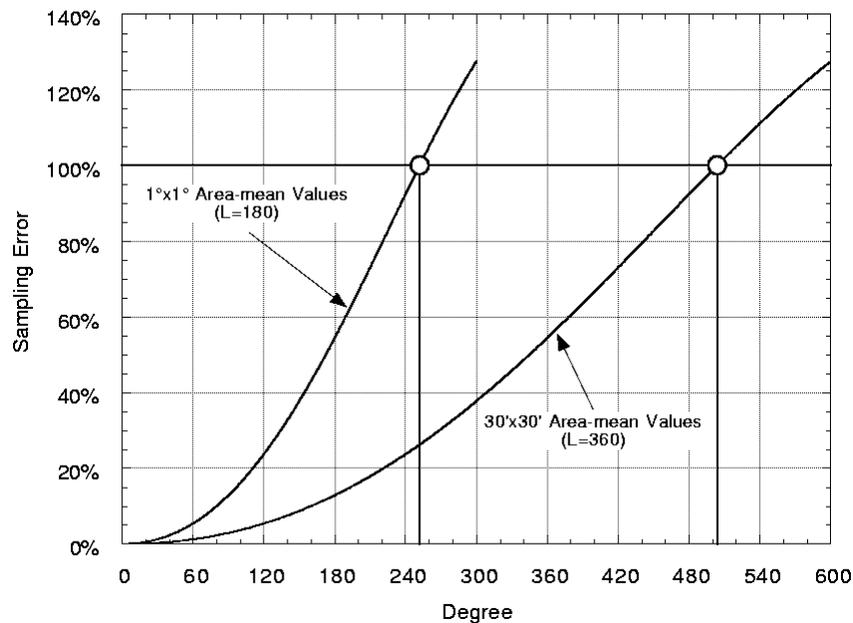
Figure 8.5.4–1. Sampling error as a percentage of the signal as implied by Jekeli's formula.

Based on the above considerations, three NQ models were developed complete to degree and order 500. These are V040, V041, and V042, using the quadrature weights of type 2, 3, and 4, respectively. Aside from the quadrature weights, these solutions were identical in every other aspect of their development (see Table 8.5–1). The gravity anomaly signal and error degree variances from these models are plotted in Figures 8.5.4–2a and b, respectively. As expected, from $n = 2$ to $n = 120$ ($L/3$), all three solutions are identical. From $n = 121$ to $n = 360$, the signal and error variances implied by V042 are slightly higher than the corresponding values for V040 or V041 (these two are identical). Finally, the signal variances from solutions V041 and V042 at the Nyquist degree $L = 360$ show only a small discontinuity as compared to V040. The
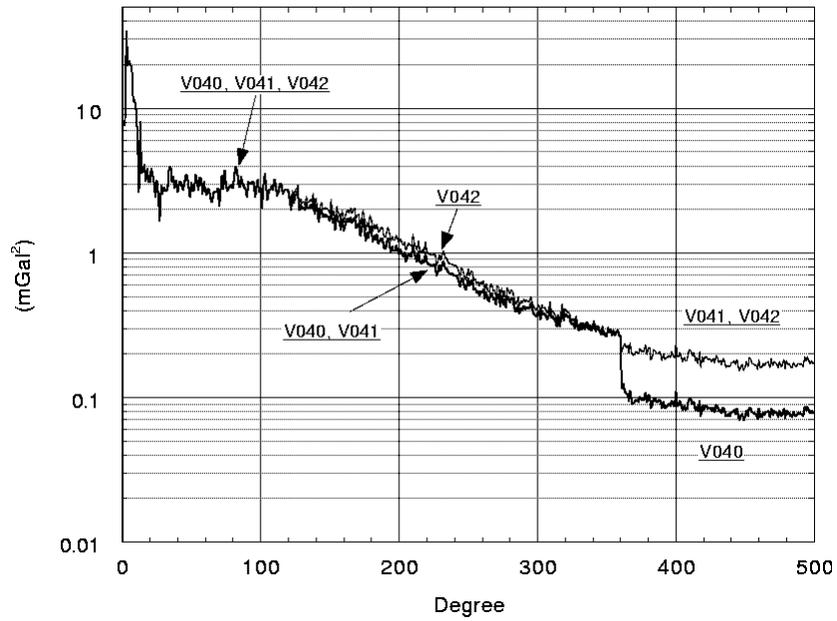
(a)
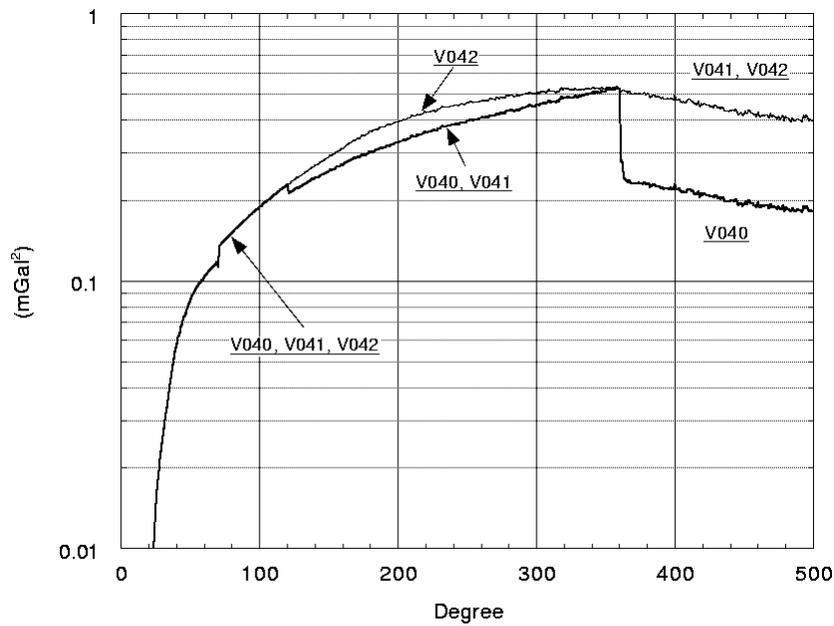
(b)

Figure 8.5.4–2. Gravity anomaly signal (a) and error degree variances (b) implied by three NQ solutions employing different quadrature weights.

discontinuity seen for V041 and V042 should be expected, given that we are trying to recover coefficients beyond $L = 360$, from 30´ $\overline{\Delta g}$ data. The validity of the recovered harmonics beyond $L = 360$ was checked using the GPS/leveling data over the U.S. and British Columbia. Careful examination of the curves of Figures 8.5.4–2a and b indicates that the signal and error spectra cross each other around degree $n = 280$. Previous experience with the OSU89A/B development has indicated that the error spectra from the NQ type of solutions tend to be too pessimistic at the higher degrees, and that valid signal beyond the degree where signal and error curves intersect does exist in these solutions (see *Rapp and Pavlis* [1990, Table 9, p. 21903]). To verify that this is also true here, the GPS/leveling tests were performed for different degrees of truncation, as shown in Tables 8.5.4–1 and 8.5.4–2 for two test areas. This was done for the three types of quadrature weights 2, 3, and 4.

Table 8.5.4–1. Standard deviation difference between GPS/leveling and model-implied undulations over the USA (1889 stations). Units are cm.

| Model | N_{max} | | | |
	280	360	440	500
V040	56.6	53.3	52.3	52.0
V041	56.6	53.3	52.1	51.8
V042	56.2	52.9	51.7	51.4

Table 8.5.4–2. Standard deviation difference between GPS/leveling and model-implied undulations over British Columbia (298 stations). Units are cm.

| Model | N_{max} | | | |
	280	360	440	500
V040	61.4	59.6	58.9	59.0
V041	61.4	59.6	59.0	59.1
V042	60.9	59.0	58.5	58.6

The main conclusions that can be drawn from these results are:

1) As in the OSU89A/B and OSU91A cases, here also the error spectra associated with the NQ models appear to be pessimistic at the higher degrees. The comparisons with the independent GPS/leveling data always improve when extending the models beyond $n = 280$ and out to $n = 360$.

2) Quadrature weights of type 4 always yield slightly better fits compared to the other two types of quadrature weights. This is true regardless of degree of truncation.

3) In both areas tested, extending the models beyond degree 360 and out to degree 440 improves the comparisons. This is a good indication that the coefficients beyond the Nyquist degree that were recovered do represent actual gravitational signal present in the anomaly data (at

least over the two areas tested, which in general are well-surveyed gravimetrically). Over the U.S., the results do improve even with the extension of the models to degree and order 500; this is not true, however, over British Columbia. Therefore, it is suspected that beyond some degree (close to 440) the recovered harmonic coefficients represent mainly a fit to noise.

These preliminary results concerning expansions beyond the Nyquist degree were encouraging. One needs to recall at this point that our objective here is *not* to produce gravitational models extending beyond degree 360. This exercise is meant to provide only the means of prefiltering the gravity anomaly data for contributions beyond degree 359, before these data are input to the BD algorithm. We are using the models beyond degree 360 only to reduce possible aliasing effects in the BD solutions. It is, therefore, important, before additional discussion is presented regarding models beyond degree 360, to demonstrate (or at least indicate) the effectiveness of this approach of prefiltering the anomaly data.

To this end, we now revisit the relative geoid undulation comparisons (Table 8.5.3–4) with the following test solutions: the NQ model V055 (see Table 8.5–1) and two BD models (HDM106 and HDM107). These three models were estimated using the same satellite-only model (PGS6376), the same merged 30′ $\overline{\Delta g}$ data file (V021596) (and weighting scheme), and the same analytical continuation terms. In HDM106, the V055 model to $N_{max} = 360$ was used as a reference (i.e., its contribution was removed from the $\overline{\Delta g}$ data before the BD adjustment), while in HDM107 the contribution of the harmonics of the V055 model to $N_{max} = 460$ was removed from the anomaly data before the BD adjustment (the choice of $N_{max} = 460$ will be discussed in the next section). We then repeated the relative undulation comparisons of Table 8.5.3–4 using these three models (since the models HDM106 and HDM107 are complete to $N_{max} = 359$ only, they were augmented by the V055 model coefficients of $n = 360$). The results are given in Table 8.5.4–3. One observes that the HDM107 results are always better than the HDM106, by about 0.5 ppm. The HDM107 results are only slightly worse than the results obtained from the NQ model V055. The two BD solutions HDM106 and HDM107 were also tested in terms of absolute geoid comparisons (such as those shown in Table 8.5.3–3). HDM107 was found to perform equal to or better than HDM106.

These results indicated that the prefiltering approach proposed and tested here is a viable technique to reduce the aliasing effects in the BD solutions. Therefore, we decided to pursue this approach further, as will be discussed in the next sections.

Table 8.5.4–3. Relative comparison between GPS/leveling and model-implied geoid undulation differences. Standard deviation units are cm, maximum degree is 360.

Area	Europe		Scandinavia		Australia	
No. of lines	59		45		37	
Aver. line length (km)	49.7		46.1		39.4	
Model	S. Dev.	ppm	S. Dev.	ppm	S. Dev.	ppm
V055	20	3.2	20	3.5	23	5.1
HDM106	22	3.8	23	4.1	27	5.8
HDM107	20	3.3	21	3.7	25	5.2

8.5.5 Numerical Quadrature Solutions Extending Beyond the Nyquist Degree

As was explained in the previous section, the objective of the joint project was the development of a gravitational model complete to degree 360. The expansions beyond this degree are to be viewed, therefore, strictly as an intermediary (and experimental) step, necessary to alleviate aliasing problems in the implementation of the BD technique. Note also that the coefficients of the NQ models up to degree 360 remain unchanged regardless of the degree of expansion beyond 360. Nevertheless, one still has to validate these higher degree NQ models and, in particular, to try and determine the highest possible degree of expansion that yields meaningful results.

Tailored geopotential models to degree 500 have been reported by *Li and Sideris* [1994]. The main idea behind these solutions [*Weber and Zomorrodian*, 1988] is quite different from the idea behind the expansions attempted here. In the former studies, an existing global geopotential model is tailored to regional gravity data of higher resolution and/or accuracy, and the tailoring may involve extensions of the model to a degree that is higher than the maximum degree of the original global solution (a discussion of the applications and shortcomings of tailored models can be found in [*Kearsley and Forsberg*, 1990]). Here, we attempt to expand the solutions to degrees higher than 360, based *only* on 30´ mean anomaly data. Obviously, depending on the accuracy and density of the gravity information based on which the $30´\ \overline{\Delta g}$ were estimated, the performance of the current models beyond degree 360 will vary geographically. This may be considered, to some extent, as "tailoring" of the global model to the geographic regions that have the best (highest resolution/accuracy) gravity data. But in that regard, every high-degree model is a tailored one, since the gravity data based upon which the models are developed vary geographically in both accuracy and density.

Numerical quadrature solutions developed after V030 (Table 8.5–1) were all expanded to $N_{max} = 500$. The majority of these models were of experimental purpose, and aided the design of the alternative quadrature weights defined in eqs. (8.5–7) and (8.5–8). We will not present here detailed results from these preliminary models. Rather, we will concentrate on some of the later solutions, which were based on improved versions of the satellite-only model and of the terrestrial data, and which received a considerable amount of scrutiny. It was recognized early on that determining precisely the maximum achievable degree of expansion would be a difficult task. Depending on the quality and density of gravity anomaly data and on the roughness of the field, one may reach different conclusions by performing tests with independent data over different geographic regions. Ideally, to determine this degree one must perform comparisons with *globally* available independent data that are sensitive to the higher degree part of the field. No such data set is available at present. Even if such data were available, they would have been used in the development of the models in the first place, thus rendering them dependent information. In the absence of such a global data set, the preliminary NQ solutions extending beyond degree 360 were evaluated considering their spectral characteristics (anomaly degree variances) and through the use of independent GPS/leveling data over land areas and satellite altimeter data over the ocean.

Spectral Considerations

Before any comparisons with independent data are to be performed, the validity of the recovered coefficients beyond degree 360 may be examined by considering the gravity anomaly degree variances that are implied by these coefficients. These considerations can assess only how reasonable the recovered harmonics appear to be. The recovered coefficients should imply anomaly degree variances that in general follow the decaying behavior "observed" up to degree 360. This type of check provides a necessary but not sufficient argument for the validity of the recovered coefficients.

A special harmonic expansion (designated V051ROS) was made using as input the merged 30´ $\overline{\Delta g}$ used to develop the test solution V051. V051ROS was developed using the type 3 quadrature weights. The original standard deviations of these (unadjusted) anomalies were also used to estimate the propagated error in the harmonic coefficients. These anomaly standard deviations are optimistic, since they do not account for unmodeled systematics as discussed in Section 8.5.1. However, unmodeled systematics are expected to be mostly of long-wavelength nature [*Laskowski*, 1983]. Therefore, the very-high-degree coefficient errors computed on the basis of these standard deviations are expected to be fairly representative of the quality of the expansion at these short wavelengths. Recall from Section 8.3 that about 96 percent of the Earth's area is covered by 30´ $\overline{\Delta g}$ estimated using least-squares collocation. These anomalies are accompanied by the error estimates obtained from the collocation prediction, and these errors are quite representative of the short wavelength inaccuracies present in the data.

The gravity anomaly signal and error degree variances implied by V051ROS are plotted in Figure 8.5.5–1. The signal degree variance discontinuity at the Nyquist degree (360) is similar to the one observed for the solutions V041 and V042 (Figure 8.5.4–2a), as expected. Examining in detail the spectral characteristics beyond $n = 360$, one observes that around degree 460 the signal curve dips below the noise curve. In addition, the signal curve appears to "flatten" beyond $n \approx 460$, which is an indication that the coefficients beyond $n \approx 460$ represent a fit to noise, rather than valid gravitational signal. Apart from the discontinuity at $n = 360$, the recovered spectrum up to degree 460 is not unreasonable. On the basis of these results, the use of the recovered harmonics beyond degree $n = 460$ cannot be justified. It now remains to be shown if the $n = 360$ to $n = 460$ part of the recovered spectrum contains valid information.
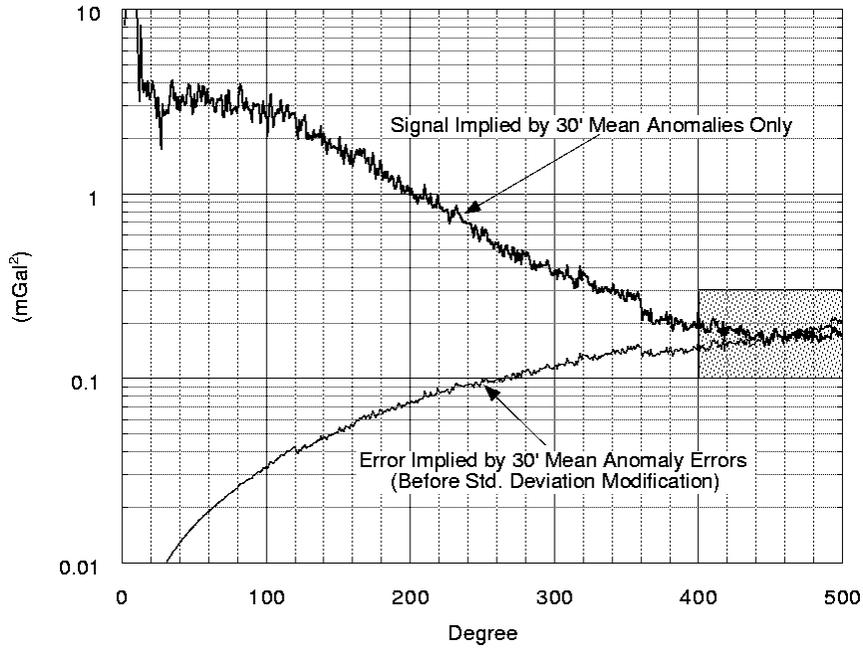
(a)
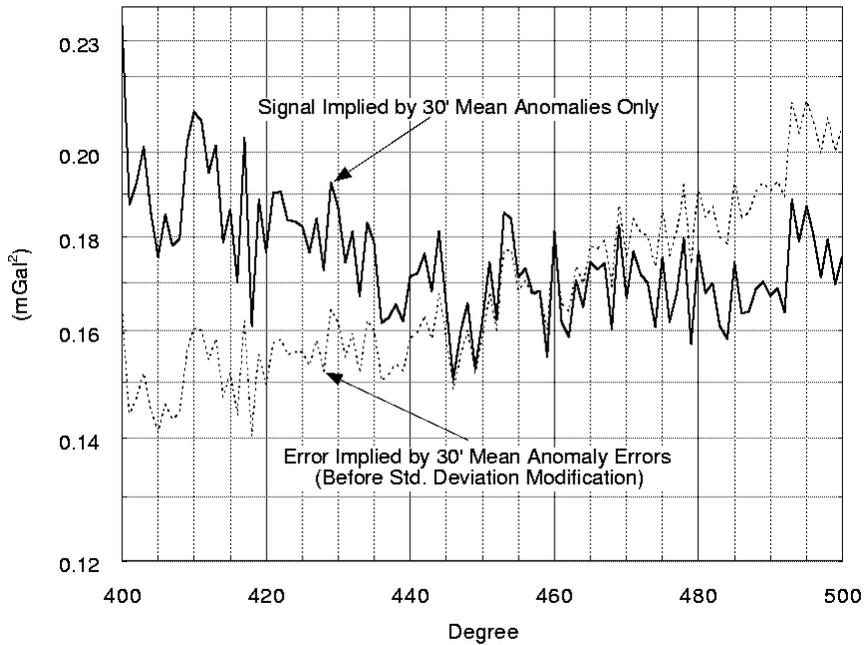
(b)

Figure 8.5.5–1. Gravity anomaly signal and error degree variances implied by the solution V051ROS.

Before we present comparisons with independent data in the next paragraphs, it is helpful to consider what should be expected from an expansion to degree 460. This may be estimated in a global RMS sense using existing degree variance models. We consider here the anomaly degree variances (c_n) implied by the following models:

1) Kaula's rule for the decay of the potential coefficient spectrum is $10^{-5}/n^2$, and implies anomaly degree variances given by:

$$c_n(\text{mGal}^2) = \frac{192}{n + 1.5} \qquad\qquad (8.5.5\text{–}1)$$

2) The model of *Tscherning and Rapp* [1974], defined by the analytical form:

$$c_n(\text{mGal}^2) = \frac{A(n-1)}{(n-2)(n+B)}\, s^{n+2} \quad \text{for } n > 2; \quad c_2 = 7.5 \ \text{mGal}^2 \qquad (8.5.5\text{–}2)$$

where $s = R_B^2/R^2$. R_B is the radius of the embedded (Bjerhammar) sphere and R ($= 6371$ km) is the radius of the mean-Earth sphere. The model (8.5.5–2) was computed using two different sets of parameters (A, B, s). The first was estimated by *Tscherning and Rapp* [ibid., page 22], and has the numerical values:

$$A = 425.28 \ \text{mGal}^2$$
$$B = 24 \qquad\qquad (8.5.5\text{–}3)$$
$$s = 0.999617$$

while the second, estimated by *Jekeli* [1978], has the numerical values:

$$A = 343.3408 \ \text{mGal}^2$$
$$B = 24 \qquad\qquad (8.5.5\text{–}4)$$
$$s = 0.9988961$$

3) The composite model described by *Jekeli and Upadhyay* [1990], which consists of the actual power spectrum (obtained from estimated harmonic coefficients) for degrees $n = 2$ to $n = 30$, and a sum of four reciprocal distance models for $n > 30$. In its original form, this model is defined by [*Jekeli*, private communication, 1992]:

$$c_n(\text{mGal}^2) = \begin{cases} \text{OSU81 model - implied values for } n = 2,...,30 \\[2ex] \left(\dfrac{n-1}{R}\right)^2 \displaystyle\sum_{i=1}^{4} \sigma_i^2 (1 - \rho_{oi})\rho_{oi}^n \qquad n > 30 \end{cases} \qquad (8.5.5\text{–}5)$$

The numerical values of the parameters are given in Table 8.5.5–1.

We should mention here that the c_n values implied by all of the above models are formally interpreted to refer to a mean-Earth radius R ($= 6371$ km). To be comparable, c_n values implied by the harmonic coefficients obtained from the models of this study have to be computed by [*Pavlis*, 1991, eq. 3.121]

$$c_n = \left(\frac{GM}{a^2}\right)^2 (n-1)^2 \left(\frac{a^2}{R^2}\right)^{n+2} \sum_{m=-n}^{n} (\overline{C}_{nm})^2 \qquad (8.5.5\text{--}6)$$

where, the adopted values by the joint project that scale the coefficients $\overline{C}_{nm}$ are:

$$GM = 3986004.415 \times 10^8 \text{ m}^3\text{s}^{-2}$$
$$a = 6378136.3 \text{ m} \qquad\qquad (8.5.5\text{--}7)$$

Table 8.5.5–1. Numerical values associated with the anomaly degree variance model of eq. (8.5.5–5).

i	σ_i^2 [m^4/s^4]	ρ_{0i}
1	0.4	0.99875
2	5	0.9962
3	70	0.989
4	780	0.968

Using the above equations, we have computed and plotted in Figure 8.5.5–2 the anomaly degree variances implied by the composite model JGM–2 ($n = 2$ to 70)/OSU91A ($n = 71$ to 360), as well as those implied by the four analytic degree variance models. For our purposes, we need to compute the expected global RMS contribution, from degrees $n = 361$ to $n = 460$, to various functionals of the disturbing potential, as implied by the different c_n models. Considering always values referring to the mean-Earth radius, the squared RMS contributions contained within the degree range $[n_1, n_2]$ are given by:

$$\text{Gravity Anomaly}: \quad \Delta g^2(n_1, n_2) = \sum_{n=n_1}^{n_2} c_n \qquad (8.5.5\text{--}8)$$

$$\text{Geoid Undulation}: \quad N^2(n_1, n_2) = \frac{R^2}{\gamma^2} \sum_{n=n_1}^{n_2} \frac{1}{(n-1)^2} c_n \qquad (8.5.5\text{--}9)$$

$$\text{Deflection of the Vertical (Total)}: \quad \theta^2(n_1, n_2) = \frac{1}{\gamma^2} \sum_{n=n_1}^{n_2} \frac{n(n+1)}{(n-1)^2} c_n \qquad (8.5.5\text{--}10)$$

The last equation can be obtained from eq. (7–38) of [*Heiskanen and Moritz*, 1967], considering that $Q_n(\psi_0 = 0) = 2/(n{-}1)$. A single component estimate (isotropic approximation) for the deflection of the vertical may be obtained by dividing the θ value by $\sqrt{2}$ (see also [*Wang and Rapp*, 1991]). Using eqs. (8.5.5–8, –9, and –10), we computed the contributions for the degree range [361, 460] as implied by the four analytic degree variance models ($\gamma = 9.7976$ ms^{-2} was used as an average value of gravity). The results are given in Table 8.5.5–2.
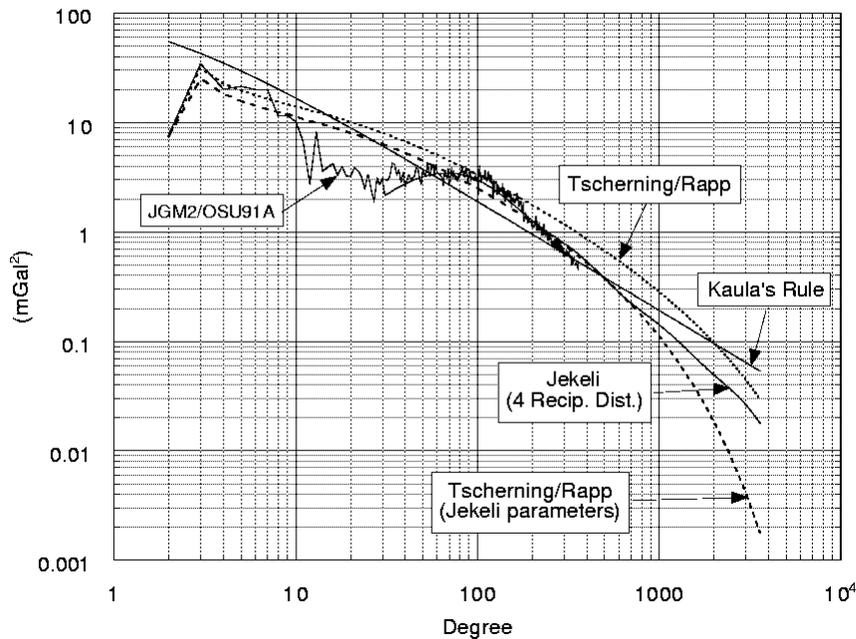
Figure 8.5.5–2. Anomaly degree variances.

Table 8.5.5–2. Global RMS expected contribution to the gravity anomaly, geoid undulation, and single-component deflection of the vertical, from the degree range [361, 460], as implied by 4 c_n models.

C_n Model	Δg (mGal)	N (cm)	$\theta/\sqrt{2}$ (arcsec)
Kaula	6.8	11.0	1.0
T/R	9.2	14.8	1.4
T/R (Jekeli)	7.1	11.5	1.1
Jekeli (4 R.D.)	7.2	11.6	1.1

Comparisons With GPS/Leveling Data

Although several preliminary solutions extending beyond degree 360 were variously tested against independent data, in this and the next paragraph we will concentrate on the evaluation of the higher degree coefficients of the NQ model V058. This was one of the later solutions and received a more thorough testing. Table 8.5.5–3 shows the results from the comparisons with GPS/leveling-derived undulations in five areas. Over the U.S., the set of 960 GPS/leveling stations is a thinned version of the 1889 station set. It was provided by R.H. Rapp, and is described in [*Rapp*, 1997] (see also Section 5.2.2). The V058-implied values have been computed with different degrees of truncation, in a fashion similar to that shown in Tables 8.5.4–1 and 8.5.4–2, to investigate the effect of higher degree terms in the model.

One may also compute the reduction or increase in the standard deviation of the differences, for a given degree range $[n_1, n_2]$, by:

$$\Delta\sigma = sign \cdot \sqrt{\left|\sigma_{n_1}^2 - \sigma_{n_2}^2\right|}; \quad sign = \frac{(n_1 - n_2)(\sigma_{n_1}^2 - \sigma_{n_2}^2)}{\left|(n_1 - n_2)(\sigma_{n_1}^2 - \sigma_{n_2}^2)\right|} \tag{8.5.5–11}$$

where a negative $\Delta\sigma$ value indicates improvement in the GPS/leveling comparisons when the model is extended from n_1 to n_2. These $\Delta\sigma$ values (in an absolute sense) are comparable to the global RMS estimates of the geoid undulation contribution computed based on eq. (8.5.5–9). The $\Delta\sigma$ values implied by the results of Table 8.5.5–3 and eq. (8.5.5–11) are given in Table 8.5.5–4.

Table 8.5.5–3. Mean and standard deviation difference: GPS/leveling minus V058 model-implied geoid undulations computed with different degrees of truncation (N_{max}). Units are cm.

Area	Europe		Scandinavia		Australia		USA		Canada (BC)	
No.	60		46		38		960		298	
N_{max}	Mean	S. Dev.	Mean	S. Dev.	Mean	S. Dev.	Mean	S. Dev.	Mean	S. Dev.
280	8.7	31.6	11.8	26.2	−83.6	24.9	−111.6	55.0	−20.0	58.9
360	9.4	30.3	13.0	21.9	−85.8	26.6	−111.2	52.3	−17.5	56.9
460	10.6	29.0	13.5	20.5	−84.6	25.3	−111.0	51.0	−14.9	56.4
500	10.6	29.5	13.8	21.1	−82.9	25.2	−111.0	50.8	−14.3	56.4

Table 8.5.5–4. GPS/leveling minus V058 model-implied geoid undulation differences. Reduction (–) or increase (+) in the standard deviation difference for three degree ranges (see text). Units are cm.

Degree Range	Europe	Scandinavia	Australia	USA	Canada (BC)
[281, 360]	−9.0	−14.4	+9.3	−17.0	−15.2
[361, 460]	−8.8	−7.7	−8.2	−11.6	−7.5
[461, 500]	+5.4	+5.0	−2.2	−4.5	0.0

The results shown in Tables 8.5.5–3 and 8.5.5–4 indicate that:

1) Truncation of the NQ solution V058 to degree 280 (as its error spectrum would imply) causes significant degradation in the GPS/leveling comparisons over most of the areas tested (the error spectrum of V058 is very similar to that of solution V022 shown in Figure 8.5.3–1). Notice, however, that this is not the case over the Australian traverse, whose behavior is rather intriguing.

2) Extending the model to degree 460 improves the GPS/leveling comparisons (over the $N_{max} = 360$ case), in *every* area tested. The improvement ranges from 7.5 cm to 11.6 cm. These values are in very good agreement with the expected global RMS geoid undulation

contribution for the degree range 361 to 460, given in Table 8.5.5–2, considering also that the recovered coefficients are subject to sampling error and measurement (propagated) noise.

3) Extending the model to degree 500 degraded the comparisons over Europe and Scandinavia, slightly improved the comparisons over Australia and the U.S., and had no impact in the British Columbia test. These mixed results tend to confirm the conclusion reached in the previous paragraph (which was based on the comparison of signal and error spectra): the extension of the model to degree 500 is not justifiable.

To enhance the sensitivity of the GPS/leveling tests to the higher degree and order portion of the model, we have also made comparisons in a relative sense, similar to those given in Table 8.5.3–4. These results are given in Table 8.5.5–5, and confirm once again the conclusions reached above. A similar type of comparison was performed with the data over the U.S. and British Columbia, which are not traverses but, rather, networks of stations. The relative differences were formed by pairing all the available stations. The results are not shown here; however, they support the same conclusions as those reached above.

Table 8.5.5–5. Relative comparison between GPS/leveling and V058 model-implied geoid undulation differences computed with different degrees of truncation (N_{max}). Standard deviation units are cm.

Area	Europe		Scandinavia		Australia	
No. of lines	59		45		37	
Aver. line length (km)	49.7		46.1		39.4	
N_{max}	S. Dev.	ppm	S. Dev.	ppm	S. Dev.	ppm
280	25	4.3	26	4.7	26	5.3
360	20	3.2	20	3.6	24	5.1
460	17	2.9	16	3.1	21	3.9
500	18	3.0	16	3.1	22	4.1

Comparisons With Ocean Altimeter Data

TOPEX altimeter data have been used here to test the effect of truncating the V058 model at different degrees and extending it beyond degree 360. TOPEX data were selected mainly because the excellent orbit accuracy (JGM–3 orbits) supporting this mission drastically reduces one of the error sources affecting geoid undulations estimated from altimeter measurements of the sea surface (RMS radial orbit error at the ±2 to 3 cm level [*Tapley et al.*, 1996]). Dynamic Ocean Topography (DOT) is the other main constituent necessary to estimate geoid undulations from altimetric Sea Surface Heights (SSHs). This signal is, in general, of long wavelength nature, with the exception of certain oceanic regions such as Western Boundary Current (WBC) regions, where significant short wavelength variations of the DOT are present. We form two test quantities, Δ and *s,* defined as:

$$\Delta_i = h_i - \varsigma_i - N_i \tag{8.5.5–12}$$

$$s_{ij} = \frac{(h_j - N_j) - (h_i - N_i)}{d_{ij}} \qquad\qquad (8.5.5{-}13)$$

where:

h_i is the TOPEX SSH at the ith location. This value represents a 2-year mean estimate computed by "stacking" the data from TOPEX cycles 9 through 82 along a master ground track. The sampling locations correspond to a nominal 1 Hz sampling rate.

ς is the DOT implied by the POCM–4B ocean circulation model of *Semtner and Chervin* described by *Stammer et al.* [1996]. ς was computed from a set of spherical harmonic coefficients complete to degree and order 14. These are a truncated set of the coefficients estimated by R.H. Rapp [*personal communication*, 1996].

N is the geoid undulation computed from the V058 model at various degrees of truncation.

s_{ij} is the residual along-track slope between the ith and jth locations.

d_{ij} is the distance between the ith and jth locations. s_{ij} was not computed if d_{ij} was larger than 11.6 km, which is the distance corresponding to a 2-second time separation between subsatellite points.

The quantity Δ_i is composed of errors in the TOPEX SSH and of commission and omission errors in the DOT and in the geoid undulation estimates. The TOPEX SSH is considered accurate at the ± 2 cm level for the 2-year mean track. At the very high degree and order range that is of concern here, the commission and omission errors of the geoid height are dominating, given that DOT is in general of long wavelength nature. Our computation of along-track slopes neglects the slopes of the DOT. DOT slopes can be significant over WBC regions [*Hwang*, 1997]. Over trench areas, however, the SSH slopes are dominated by the geoid slope contribution, and, therefore, s_{ij} is useful for comparisons such as those presented next. Statistics of the quantities Δ and s were computed over six areas sampled by TOPEX altimetry. The definition of these areas and related information are given in Table 8.5.5–6.

Table 8.5.5–6. Information related to the areas chosen for some comparisons with TOPEX altimetry.

Area	A0	A1	A2	A3	A4	A5
φ min	−66°	−62°	50°	−37°	10°	−50°
φ max	65°	−50°	60°	−15°	45°	−30°
λ min	0°	300°	160°	180°	140°	220°
λ max	360°	340°	210°	190°	150°	240°
No. of Δ	520252	8844	6259	3146	4650	6280
No. of s	519126	8786	6180	3121	4620	6255

In all test areas, the altimetric data were edited out if they fell into a 30´x30´ cell with elevation $H \geq -1000$ m. Area A0 also excludes data falling into the Mediterranean, Caspian, Black, and

Red Seas and into the Hudson Bay. Area A0 provides more or less "oceanwide" estimates of the statistics of interest. Area A1 is off the coast of Patagonia, A2 covers the Aleutian trench, A3 the Kermadec and Tonga trenches, and A4 the Mariana, Bonin, Japan, and Kuril trenches. The areas A1 through A4 cover regions of very steep geoid slopes, where the higher degree and order portion of the model is expected to have significant power. In contrast, area A5 covers a very smooth region of the geoid on the southwest Pacific basin. The statistics of the comparisons performed over these areas are given in Table 8.5.5–7.

These results confirm once again the conclusions reached based on the previous (GPS/leveling) tests. Namely:

1) Truncation of the NQ solution V058 to degree 280 degrades significantly the statistics for both quantities Δ and s. This is true for all the areas considered.

2) Extending the model to degree 460 improves the Δ and s comparisons in every area tested. The improvement ranges from 3.5 cm (A5) to 13.6 cm (A2) for Δ and 0.3 arcsec (A5) to 1.3 arcsec (A2) for s. These values have been computed using eq. (8.5.5–11). As expected, the improvement is minimal over the smooth area A5 and maximal over the area A2, which is one of the rougher areas tested. Oceanwide (i.e., over A0), the improvement is 7.5 cm and 0.6 arcsec for Δ and s, respectively. These values agree reasonably well with the expected global RMS geoid undulation and vertical deflection contribution for the degree range 361 to 460, given in Table 8.5.5–2.

3) Extending the model to degree 500 degraded the comparisons over all the areas tested, except for the very smooth region A5, where a negligible improvement is seen. This again indicates that the extension of the model to degree 500 is not justifiable.

Table 8.5.5–7. Standard deviation of the quantities Δ (cm) and s (arc seconds) over the six test areas, for different degrees of truncation (N_{max}) of the V058 model (see text).

Area	A0		A1		A2	
N_{max}	Δ	s	Δ	s	Δ	s
280	31.24	2.194	44.51	3.731	46.41	3.666
360	27.98	1.972	37.61	3.274	38.13	3.023
460	26.96	1.870	35.54	2.983	35.61	2.724
500	27.01	1.878	35.95	3.018	36.52	2.843

Area	A3		A4		A5	
N_{max}	Δ	s	Δ	s	Δ	s
280	43.12	2.959	49.17	3.612	16.79	1.609
360	32.64	2.581	41.73	3.123	15.84	1.544
460	30.92	2.422	39.90	3.008	15.45	1.506
500	31.02	2.429	40.60	3.103	15.43	1.501

In summary, from the spectral considerations, the GPS/leveling tests, and the TOPEX altimetry comparisons, a consistent picture emerges: the NQ models computed on the basis of the 30´

merged anomaly file available in this study and employing the alternative definition of quadrature weights of type 4 appear to be capable of recovering valid gravitational information up to degree and order 460. This conclusion should be accompanied by the caveat that over geographic regions with poor gravity anomaly data and rough geoid, the extension of the models to $n = 460$ may have a negative effect on the results. Over most of the ocean areas, however, where high-quality altimetry-derived anomalies are available, and over major portions of land (North America, Europe, Australia, former Soviet Union), where dense gravity anomaly data exist, the models to degree 460 appear to provide an improvement over the solutions to degree 360.

Based on these conclusions, we decided to use the V058 model to degree 460 to filter out of the altimeter range data the geoid contribution from $n = 71$ to $n = 460$ prior to the formation of normal equations, as explained in Section 7.1. Similarly, NQ models to degree 460 were used as reference in the processing of 30´ mean anomalies for the implementation of the BD algorithm. The procedure adopted for the development of the final BD model is discussed next.

8.5.6 *The Use of* A Priori *Constraints in Block-Diagonal Solutions*

Up to this point we have designed and tested a procedure for the development of combination high-degree expansions using the BD approach. This procedure requires an NQ model extending beyond the Nyquist degree implied by the gravity anomaly sampling interval. This NQ model is used as a reference in a "remove–compute–restore" fashion, and its dual function is to:

a) Compensate for the omission of cross-order off-diagonal terms in the BD3 approximation of the normal equations (see Section 8.5.3).

b) Reduce aliasing effects by prefiltering the 30´ $\overline{\Delta g}$ data for contributions beyond the Nyquist degree, so that the BD approach is applied to a gravity anomaly field that is approximately band-limited (see Section 8.5.4).

Several preliminary BD models were estimated following this procedure. Before we discuss some specific BD solutions however, we will address another issue related to the *a posteriori* error spectrum of the high-degree model. A problem that has been identified in earlier high-degree models (e.g., *Rapp and Pavlis* [1990]) is that the modification of the anomaly error estimates (see eq. 8.5–2), required to effectively combine the terrestrial and satellite information, has the side effect that it yields pessimistic estimates for the higher degree part of the model's error spectrum. We have discussed this problem in Section 7.2.3 and also demonstrated in the previous section that the truncation of models to the degree where the signal and error spectra intersect (currently $n \approx 280$) results in significant degradation of the comparisons with independent data. The BD algorithm offers the possibility to remedy (at least to some extent) this situation. This may be accomplished by introducing *a priori* information in the adjustment for the high-degree model. As we discussed in Section 8.5.3, this approach changes the interpretation of the role of the reference model in the BD technique and results in an estimation scheme that is the band-limited counterpart of least-squares collocation. The introduction of *a priori* constraints for the coefficients of degree *higher* than the maximum degree present in the satellite-only model modifies eq. (8.2.4–2) as follows:

$$\begin{bmatrix} \mathbf{G}_{11} + \mathbf{P}_{\mathbf{X1}} & \varnothing & \varnothing \\ \varnothing & \mathbf{G}_{22} + \mathbf{P}_{\mathbf{X2}} & \mathbf{G}_{23} \\ \varnothing & \mathbf{G}_{23}^{\mathrm{T}} & \mathbf{G}_{33} \end{bmatrix} \cdot \begin{bmatrix} d\hat{\mathbf{X}}_1 \\ d\hat{\mathbf{X}}_2 \\ d\hat{\mathbf{X}}_3 \end{bmatrix} = \begin{bmatrix} d\mathbf{U}_1 \\ d\mathbf{U}_2 \\ d\mathbf{U}_3 \end{bmatrix} \tag{8.5.6-1}$$

The unknown coefficients and the right-hand-side vector have been denoted by $d\hat{\mathbf{X}}$ and $d\mathbf{U}$, respectively, to emphasize that these vectors represent remainders with respect to the reference model used. $\mathbf{P}_{\mathbf{X1}}$ and $\mathbf{P}_{\mathbf{X2}}$ are diagonal matrices. In this analysis they were constructed so that their elements vary only as a function of the degree of the coefficient to which they correspond. For a coefficient of degree n, the corresponding diagonal element of either $\mathbf{P}_{\mathbf{X1}}$ or $\mathbf{P}_{\mathbf{X2}}$ was defined by:

$$\mathbf{P}_{\mathbf{X}}(n) = \frac{w}{[r(n)]^2} \tag{8.5.6-2}$$

where w is a (non-negative) weight factor and $r(n)$ is the RMS disturbing potential coefficient of degree n. $r(n)$ was evaluated by:

$$r(n) = \frac{\sqrt{c_n}}{\left(\dfrac{n-1}{R}\right) \cdot \left(\dfrac{GM}{a}\right) \cdot \left(\dfrac{a}{R}\right)^{n+1} \cdot \sqrt{(2n+1)}} \tag{8.5.6-3}$$

where the c_n values were obtained from the four reciprocal distance composite covariance model of eq. (8.5.5–5). GM and "a" were as defined in eq. (8.5.5–7) and $R = 6371$ km.

Several points related to the introduction of *a priori* information require some discussion. First of all, notice that we do not add anything to the diagonal block $\mathbf{G}_{33}$. This is because $\mathbf{G}_{33}$ contains the satellite-derived normal equations, and these already include the *a priori* constraint discussed in Section 6.3.2. From the estimation point of view, it is well known (e.g., *Uotila* [1986]) that (8.5.6–1) implies that $d\hat{\mathbf{X}}$ has an *a priori* value of zero, with variance equal to $(\mathbf{P}_{\mathbf{X}})^{-1}$. The magnitude of the elements of $\mathbf{P}_{\mathbf{X}}$ control how "freely" $d\hat{\mathbf{X}}$ will be allowed to adjust (larger $\mathbf{P}_{\mathbf{X}}$ would result in smaller norm for $d\hat{\mathbf{X}}$). The *a posteriori* variances of the unknowns $\hat{\mathbf{X}}$ can never exceed the variances implied by $(\mathbf{P}_{\mathbf{X}})^{-1}$. This is exactly the property that we want to exploit here in order to produce more optimistic error estimates for the high-degree coefficients of the BD model than those obtained from the NQ expansion. To assess accurately how pessimistic the NQ error spectrum is at the very high degrees is quite difficult. Based on the comparisons with independent data given in the previous section, we seek an *a priori* constraint $\mathbf{P}_{\mathbf{X}}$ that would imply signal-to-noise ratio values greater than 1 for all degrees up to $n = 360$.

The models that we intend to use here as reference were obtained from corresponding NQ solutions (i.e., NQ models obtained from the same satellite-only model and merged $30'$ $\overline{\Delta g}$ file as the BD solution under consideration). One could argue that our $\mathbf{P}_{\mathbf{X}}$ should be defined based on the *a posteriori* error spectrum of the NQ model used as reference. Examination of Figure 8.5.3–1, however, reveals that if we were to use the *a posteriori* error variances of the NQ model to define $\mathbf{P}_{\mathbf{X}}$, we would be overconstraining the BD solution (toward the NQ model), especially over the low- and medium-degree range, while at the higher end of the spectrum ($n>280$), the BD model and its predicted error spectrum would be left largely unaffected by the use of the constraint. This is the exact opposite of what we aim to accomplish with the use of the *a priori*

constraint. (There is an added complication with the use of the NQ errors as *a priori* constraint for the BD solution. The two solutions are highly correlated since they are derived based on the same data. Therefore, introducing the NQ model and its errors as independent *a priori* information in the BD adjustment makes little sense from an estimation point of view.) A suitable form of *a priori* constraint that leaves the low- and medium-wavelength part of the BD solution free to adjust, while providing an upper bound for the predicted errors at the very high degrees, can be obtained from a covariance model for the disturbing potential. This explains the choice made above in the definition of $\mathbf{P_X}$. The introduction of the weight factor w enables us to vary the influence of the *a priori* constraint in the BD combination adjustment (choosing $w = 0$, for example, removes the constraint altogether from the adjustment), while always preserving the spectral "shape" of the constraint that is contained in $r(n)$. What needs to be determined, therefore, is a suitable value of w, which satisfies the signal-to-noise ratio goal specified above. At the same time, w should be small enough to allow some freedom in the adjustment of the high-degree coefficients through the BD technique. We performed a number of experimental solutions to determine a suitable value for w. Table 8.5.6–1 lists the "parameters" associated with the development of selected BD high-degree expansions. Parameters common in all these expansions (and not shown in Table 8.5.6–1) are:

a) All the expansions listed in Table 8.5.6–1 use g_1 continuation terms computed from the elevations of the JGP95E data base, according to the third method discussed in Section 8.5.2.

b) All the expansions listed in Table 8.5.6–1 use the weighting scheme "B" defined in eq. (8.5–2).

c) The merged $30'$ $\overline{\Delta g}$ file designated V021596 was used for the development of all of the solutions in Table 8.5.6–1, except two: HDM180 was based on V072496 and HDM190 on V091796 (see also Table 8.5–1).

In order to enable the comparison of some of the above models to a common standard, we also consider here the spherical harmonic coefficients obtained from the *unadjusted* $30'$ $\overline{\Delta g}$ of the merged file V021596 (i.e., no combination with satellite model is performed here). Two such coefficient sets were computed, using the numerical quadrature expansion method: V051ROS using quadrature weights of type 3, and V052ROS using quadrature weights of type 4. The percentage difference P_n between two potential coefficient models, by degree, is defined as [*Rapp*, 1986, pp. 376–377]:

$$
P_n = \left[\frac{\displaystyle\sum_{m=0}^{n} \left(\Delta C_{nm}^2 + \Delta S_{nm}^2 \right)}{\displaystyle\sum_{m=0}^{n} \left(C_{nm}^2 + S_{nm}^2 \right)} \right]^{1/2} \times 100 \tag{8.5.6–4}
$$

Table 8.5.6–1. Selected high-degree expansions developed using the Block-Diagonal (BD) technique.

Model Name	Satellite-Only Model Used	Ref. Model / N_{max}	Constraint Weight w
HDM106	PGS6376	V055 / 360	0.0
HDM107	PGS6376	V055 / 460	0.0
HDM108	PGS6376	V055 / 460	0.2
HDM109	PGS6376	V055 / 460	0.5
HDM110	PGS6376	V055 / 460	0.7
HDM111	PGS6376	V055 / 460	1.0
HDM117	PGS6376	V056 / 460	0.0
HDM118	PGS6376	V056 / 460	0.2
HDM120	PGS6376	V056 / 460	0.7
HDM127	PGS6394	V056 / 460	0.0
HDM128	PGS6394	V056 / 460	0.2
HDM130	PGS6394	V056 / 460	0.7
HDM180	PGS7270K	V066 / 460	0.7
HDM190	PGS7270K37	V068 / 460	0.7

where ΔC and ΔS are the differences between the fully normalized potential coefficients. We first computed the percentage differences of the models HDM106, ..., HDM111 with respect to the expansion V051ROS. These are plotted in Figure 8.5.6–1. On the same figure, we show the percentage differences between the NQ model V055 and the expansion V051ROS. As we expect, up to degree 70 the observed differences are due to the inclusion of the satellite information in all the BD solutions (and the V055 model), which is absent from the V051ROS expansion. Also, the jump discontinuity at $n = 120$, which appears in all BD models but not in the V055 model, is due to the discontinuity of quadrature weights (type 3) at this degree. Note that the discontinuity in the signal spectra cancels out when V055 is compared to V051ROS, since both these NQ models were developed using the same quadrature weights (type 3). Beyond $n = 70$, the V055 and V051ROS models differ by about 3 to 4 percent. This demonstrates the fact that, in the NQ type of combination solution, the adjusted $\overline{\Delta g}$ (which define V055), are practically identical with the unadjusted ones (which define V051ROS), beyond the maximum degree present in the satellite-only model.

The percentage differences of the BD models are quite revealing. We know that, due to the presence of the "wing" in our normal equations, the influence of the satellite-only information will extend to coefficients beyond degree 70 and will affect all coefficients of order ≤ 70. Therefore, we expect higher percentage differences between these models and V051ROS than the differences seen with V055. However, the results for HDM106 show a P_n value exceeding 60 percent at degree $n = 359$. This is quite unrealistic—the satellite-only solution is not expected to have such a large influence at such high degrees. The curve of HDM107 shows that about half of the percentage difference seen in HDM106 at the higher degrees is due to aliasing. When the reference model is extended to $n = 460$ (for HDM107), the difference at $n = 359$ drops to about 34 percent. Notice also the "knee" appearing around degree 260; this degree is the "reflection" of the maximum degree of the reference model (460) with respect to the Nyquist degree (360). Recall from Table 8.5.6–1 that neither HDM106 nor HDM107 contains any *a priori* constraint.

The different behavior of the P_n values for these two models is due purely to the extension of the maximum degree of the reference model from 360 (HDM106) to 460 (HDM107). When the *a priori* constraint is introduced in the BD models, the P_n values above degree 70 reduce further. As expected, this reduction increases with increasing weight w of the constraint. From Figure 8.5.6–1, we also observe that there is little difference in the P_n curves for the w values of 0.5, 0.7 and 1.0.
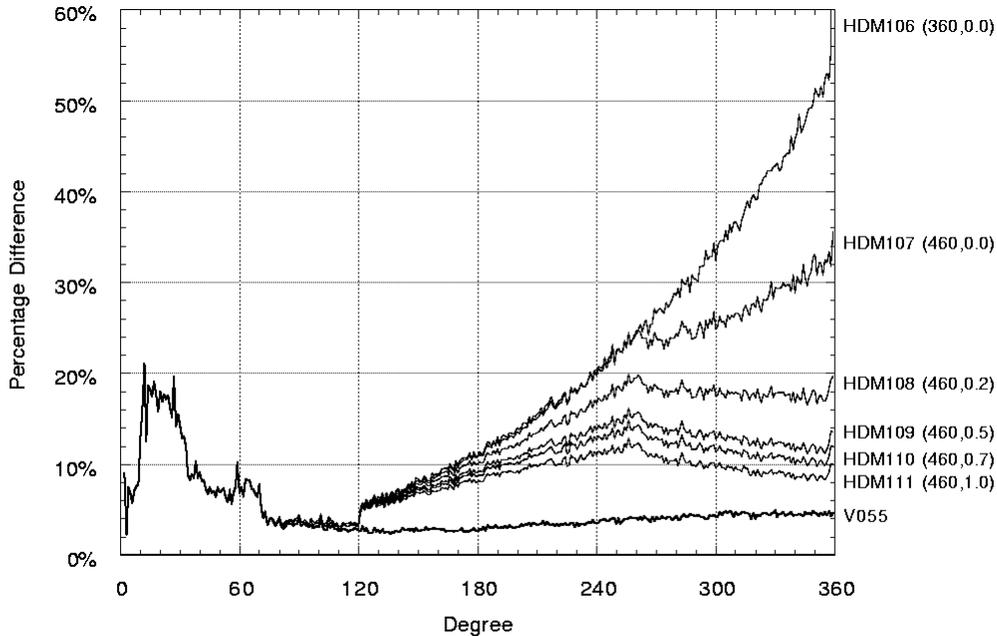
Figure 8.5.6–1. Percentage difference between harmonic coefficients obtained from several test combination solutions and those obtained from unadjusted 30′ mean anomalies (V051ROS). Parenthetical values show the maximum degree of the reference model used and the weight (w) of the *a priori* constraint.

We examine now the error spectra implied by the use of different w factors. Figure 8.5.6–2 shows the anomaly signal and error degree variances for some of the solutions under consideration. On the same figure, we have plotted the error degree variances implied by the *unmodified* anomaly standard deviations that accompany the data of file V021596 (this is the same error curve as the one plotted in Figure 8.5.5–1). We observe that with $w = 0.2$, the error variances of the NQ model V055 and those of HDM108 are practically the same (apart from the discontinuities associated with the V055 error spectrum at the cutoff degree of the satellite model $n = 70$, and at the jump of the quadrature weights $n = 120$). The smallest weight factor of those tested here, $w = 0.7$ (solution HDM110), satisfies our signal-to-noise ratio requirement.

The effect of the *a priori* constraint in the BD solutions was also tested using GPS and leveling-derived geoid heights. Table 8.5.6–2 shows the results from the comparisons over the U.S. and British Columbia. We observe that there is little sensitivity to the value of w used (among those

values that were tested). Notice also that all the BD models tested perform slightly better than the corresponding NQ solution V055. The models of Table 8.5.6–2 were also used to perform both absolute and relative geoid tests with the GPS/leveling traverses over Europe, Scandinavia, and Australia (similar to those shown in Tables 8.5.3–3 and 8.5.3–4). These tests (not shown here) did not indicate any significant sensitivity of the results to the value of w, either. On the basis of these comparisons, and considering also the error spectra shown in Figure 8.5.6–2, we decided to adopt the value of 0.7 for w.

Before concluding this section, we present the percentage differences of the models HDM127, HDM128, and HDM130 with respect to the expansion V052ROS. These are plotted in Figure 8.5.6–3 along with the percentage differences between the NQ model V058 and the expansion V052ROS. As expected (since V052ROS was developed using the quadrature weights of type 4), the curves corresponding to the BD solutions are now free of the jump discontinuity at $n = 120$. The solution HDM130, which used our preferred value of $w = 0.7$, shows above $n = 260$ a roughly constant difference with V052ROS of about 10 percent.
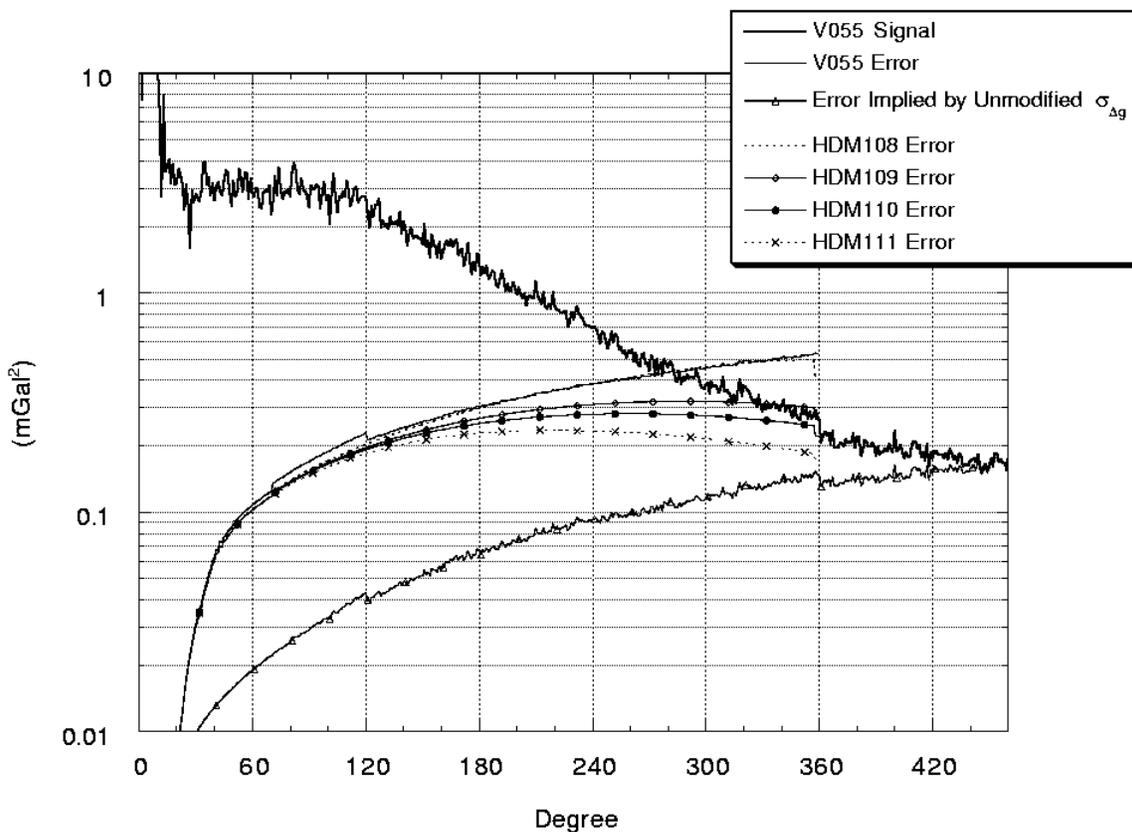
Figure 8.5.6–2. Gravity anomaly signal and error degree variances from various high-degree expansions (see text).

Table 8.5.6–2. Mean and standard deviation difference between GPS/leveling and model-implied geoid undulations, for different weight (*w*) of the *a priori* constraint. Units are cm, maximum degree is 360.

Area No. of stations		USA 1889		Canada (BC) 298	
Model	Weight *w*	Mean	S. Dev.	Mean	S. Dev.
V055	—	−100.2	55.7	−9.7	59.0
HDM106	0.0	−101.4	54.7	−8.7	58.5
HDM107	0.0	−101.3	54.7	−9.1	58.3
HDM108	0.2	−101.2	54.8	−9.1	58.2
HDM109	0.5	−101.1	54.9	−9.2	58.2
HDM110	0.7	−101.1	54.9	−9.2	58.2
HDM111	1.0	−101.0	55.0	−9.3	58.2

An interesting feature, present in both Figures 8.5.6–1 and 8.5.6–3, is the apparent "hump" of the P_n values near degree 60. One would expect that the influence of the satellite-only model (which is what the P_n values represent up to degree 70), would be decreasing in a roughly monotonic fashion after approximately degree 30 or 40. This is because the strength of the satellite-only information rapidly decreases after degree 40, due to the attenuation of the gravitational signal with altitude (see also Figure 7.2.2–1). The behavior of P_n around degree 60 is, therefore, somewhat surprising and counterintuitive. The exact reason for this behavior is not presently clear.
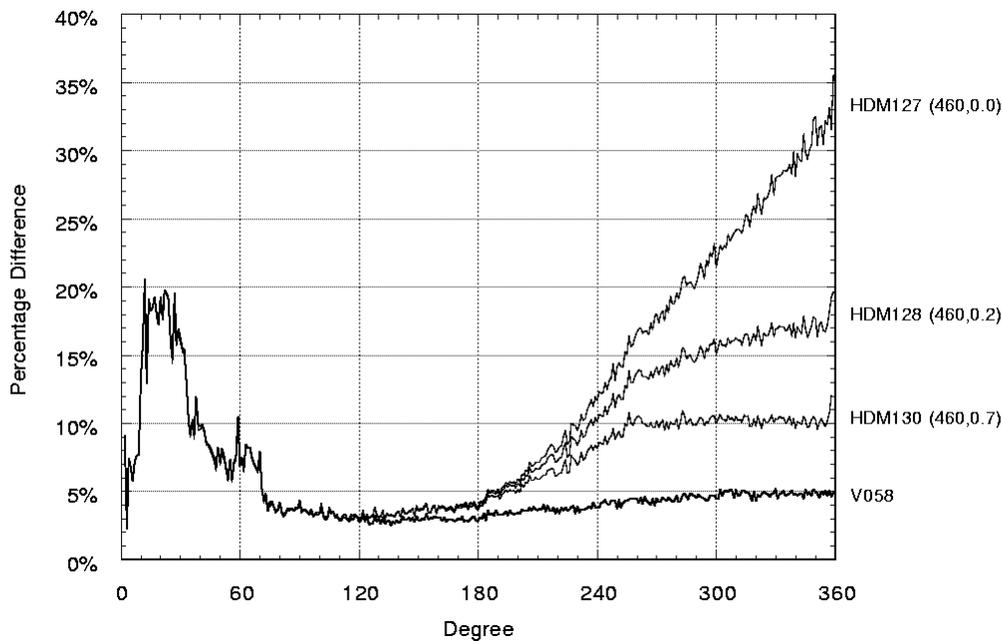
Figure 8.5.6–3. Percentage difference between harmonic coefficients obtained from four combination solutions and those obtained from unadjusted 30′ mean anomalies (V052ROS). Parenthetical values show the maximum degree of the reference model used and the weight (*w*) of the *a priori* constraint.

Finally, a few general comments concerning our use of the *a priori* constraint in the BD solutions are in order. One may criticize our approach as being an artificial way of modifying the error spectrum of the BD solution at the higher ($n > 120$—see Figure 8.5.6–2) degrees. This, to some extent, is true. In essence, we use the constraint to add "strength" back to the surface data at the higher degrees, which was inadvertently taken out of them by our modification (generally increase) of their standard deviations, coupled with the fact that we omit error correlations in forming our weight matrix. The modification of standard deviations was done to account for unmodeled long wavelength systematics in the anomaly data, and thus enable a meaningful low-degree combination solution. Our use of the constraint is a crude way of performing variable (by degree) weighting of gravity anomaly data. We fully recognize here that there is a need for additional study, in order to develop alternative ways of accounting for the long wavelength systematic errors that are still present in (near) global gravity anomaly data bases. Properly accounting for these systematics in our combination solution should eliminate the need for the modification of the anomaly standard deviations and, therefore, also the need for *a priori* constraints in the BD model development.

On the positive side, one should recognize that the BD approach developed and implemented here offers a competitive alternative to the Optimal Estimation (OE) approach proposed by *Colombo* [1981] and implemented by *Hajela* [1984] and *Rapp and Cruz* [1986b]. The present approach possesses two main advantages over the OE approach:

1) It enables the combination solution with the *complete* error covariance matrix of the satellite-only model *and* the high-degree expansion to be done in a single step. In the aforementioned studies, OE has been used only to analyze harmonically global grids of adjusted gravity anomalies. These grids were produced from combination solutions employing the simple NQ approach. To the author's knowledge, OE technique that simultaneously would adjust gravity anomalies and a satellite-only model with its complete error covariance matrix has not been attempted to date.

2) The present approach is free of the problems encountered by *Rapp and Cruz* [ibid.] in the estimation of a reliable error spectrum from the OE solution without excessively smoothing the corresponding signal spectrum.

These aspects, along with its computational efficiency, make the BD technique a preferable alternative to OE.

8.6 The Final Numerical Quadrature and Block-Diagonal High-Degree Models

The analytical formulation discussed in the previous sections, along with the various experimental solutions and their evaluation, led to the following procedure, which was adopted for the development of the final NQ and BD models high-degree models:

1) The final satellite-only model PGS7270K37 (EGM96S) and its complete error covariance matrix are combined with the merged $30'$ $\overline{\Delta g}$ file, designated V091796, to produce the final NQ model, designated V068 (and its associated error spectrum). V068 was originally

developed complete to degree and order 500, but (as explained in Section 8.5.5) only its part to $N_{max} = 460$ is used next.

2) The PGS7270K37 normal equations are "shifted" to the V068 model (to degree 70) as reference (see also [*Rapp et al.*, 1991, pp. 20–21]). All the parameters other than gravitational coefficients, present in the "shifted" PGS7270K37 normal equations, are back substituted.

3) The contribution from $N_{min} = 2$ to $N_{max} = 460$ is subtracted from the 30′ $\overline{\Delta g}$ of file V091796, using the V068 harmonic coefficients.

4) The "shifted" normal equations from (2) and the residual 30′ $\overline{\Delta g}$ from (3) are combined using the BD adjustment approach. The *a priori* constraint (8.5.6–2) is used here with $w = 0.7$. This adjustment yields the $d\hat{\mathbf{X}}$ vectors of equation (8.5.6–1) and the variance–covariance elements discussed in Section 8.2.4. Addition of the reference model V068 to $d\hat{\mathbf{X}}$ yields the final BD solution, designated HDM190. This model is complete from $N_{min} = 2$ to $N_{max} = 359$. We augment this model with the degree 360 coefficients from V068. The standard deviations of these coefficients were *not* taken from V068; they were set to a constant value for all 721 coefficients, this value being the RMS error per coefficient at $n = 359$ of the HDM190 model.

We should mention here that the above general procedure (with minor modifications) was also the one used in the development of the test solutions V058 and HDM130. These models were two of the four test solutions submitted for evaluation by the Special Working Group (SWG) chaired by M. Sideris. The feedback received from the SWG (Section 9) did not indicate any apparent shortcomings with the models developed based on this procedure. This was an additional reason for adopting it for the final high-degree model development.

8.6.1 Intercomparison of the V068 and HDM190 Models

Residual 30′ Mean Gravity Anomalies

The 30′ residual gravity anomalies obtained from the least-squares combination adjustments that produced V068 and HDM190 provide a measure of the difference between the gravity anomaly signal present in the 30′ merged $\overline{\Delta g}$ file, and the corresponding signal implied by the satellite-only model EGM96S. In the case of V068, the residual 30′ $\overline{\Delta g}$ are obtained from eq. (49b) of *Rapp and Pavlis* [1990, page 21889]. Since the V068 combination solution adjusts the "terrestrial" coefficients only up to the maximum degree present in EGM96S (70), one expects the residual $\overline{\Delta g}$ from this adjustment to reflect the differences in the two sources of information (satellite-only versus terrestrial) over the same range of degrees. In the case of HDM190, the residual $\overline{\Delta g}$ are computed by:

$$v_{\Delta g}^{ij} = \overline{\Delta g}_{adj}^{ij} - (\overline{\Delta g}_{obs}^{ij} - \overline{\Delta g}_{hf}^{ij}) \tag{8.6.1–1}$$

where $\overline{\Delta g}_{obs}^{ij}$ is the 30′ gravity anomaly from file V091796 *after* the application of g_1 continuation terms and:

$$\overline{\Delta g}_{adj}^{ij} = \frac{1}{\Delta\sigma_i}\frac{GM}{(r_i^e)^2}\sum_{n=2}^{359}(n-1)\left(\frac{a}{r_i^e}\right)^n\sum_{m=-n}^{n}\overline{C}_{nm}^{HDM190}\cdot\overline{IY}_{nm}^{ij}$$ (8.6.1–2)

$$\overline{\Delta g}_{hf}^{ij} = \frac{1}{\Delta\sigma_i}\frac{GM}{(r_i^e)^2}\sum_{n=360}^{460}(n-1)\left(\frac{a}{r_i^e}\right)^n\sum_{m=-n}^{n}\overline{C}_{nm}^{V068}\cdot\overline{IY}_{nm}^{ij}$$ (8.6.1–3)

since the BD adjustment is performed only up to degree 359, and since the higher frequency component (n = 360 to 460) of the data is prefiltered using V068, prior to the adjustment. In contrast to the NQ case (V068), the residuals from the BD adjustment reflect two things: 1) the effect of the satellite-only information on those "terrestrial" coefficients whose order is ≤70 and 2) the signal present in the input anomaly data that cannot be accommodated by a set of coefficients to N_{max} = 359. The latter arises from the fact that our prefiltering approach is not perfect. The 30´ data (at least locally) may contain signal beyond n = 460 (omission error), and at the same time our V068 estimate of the n = 360 to 460 contribution is not errorless (commission error). Therefore, one should expect the residuals from HDM190 to possess more high-frequency information than those from V068. Some statistics related to the 259200 30´ residual anomalies from V068 and HDM190 are given in Table 8.6.1–1. It is obvious from the standard deviation values of the two sets of residuals that HDM190 yields residuals with significantly more power than those from V068. In addition, both the extreme values and the number of (absolute) residuals exceeding 7 mGal are significantly larger for HDM190 than for V068.

Table 8.6.1–1. Statistics of the residual 30´ mean anomalies from the solutions V068 and HDM190. Gravity anomaly units are mGal.

Statistic	V068	HDM190
Minimum value (φ,λ)	−33.75 (2.25°, 116.25°)	−106.96 (−74.75°, 295.75°)
Maximum value (φ,λ)	30.36 (34.25°, 71.25°)	76.78 (85.25°, 346.25°)
Number of $|v|$ > 7 mGal	4568	21365
Mean value	−0.012	−0.012
Std. Deviation value	2.156	3.656

The geographic distribution of the residuals from V068 and HDM190 are shown in Figures 8.6.1–1 and 8.6.1–2, respectively. Comparative examination of these two figures indicates that:

a) In the residual anomaly maps from both solutions, the same *general* geographic regions are identified, where significant discrepancies exist between the "terrestrial" anomaly signal and the one implied by the satellite-only model. Such regions include western Canada and parts of Alaska, extended areas in South America (Brazil, Peru, Argentina), Central Asia (China, Mongolia), and South-East Asia (Indonesia and the Philippines), New Zealand, parts of Africa (Tanzania, Kenya, Sudan, Ethiopia), and the Middle East. Large residuals also exist over extended parts of Antarctica, the Arctic Ocean, and coastal regions of Greenland, as well as over the Balkans (especially Romania) and Eastern Turkey. All these areas are known to

lack high-quality and high-density gravity anomaly data. Despite the advances made by the joint project in the acquisition of gravity anomaly data, these residual maps indicate that significant work remains to be done in this area. Also, when examining such residual maps, one should always keep in mind that areas that are completely void of any gravity data (see Figure 8.3–1), and were filled in with topographic–isostatic anomalies may not appear to have large residuals. This is because the fill-in anomalies use the satellite-only model to degree 40; therefore, over long wavelengths, there will be little disagreement between the satellite-only model and these values.

b) A striking difference between Figures 8.6.1–1 and 8.6.1–2 is the large amount of high-frequency signatures present in 8.6.1–2 but absent from 8.6.1–1. This is particularly visible over oceanic areas. For example, the Emperor Seamount chain ($\varphi \approx 30°$ to $50°$, $\lambda \approx 170°$) and the South West Indian Ridge (south of Africa and Madagascar) produce a clear residual anomaly signature in Figure 8.6.1–2. Effects of this kind are also present over land areas in Figure 8.6.1–2. The Urals and the Rocky Mountains are two examples. The origin of these features is related to the frequency content of the data, to which the BD solution is sensitive, while the NQ solution is not. All of these areas are characterized by very high frequency anomaly signals. Our prefiltering approach has limited success in removing these signals, and what is left in the data (and cannot be represented by a degree 359 expansion) manifests itself as a residual. In effect, Figure 8.6.1–1 is a low-pass filtered version of Figure 8.6.1–2.

The different information content of the residuals from the NQ and the BD adjustments should not be interpreted as a shortcoming of the BD technique. In fact, a very localized outlier in the terrestrial data may have little influence in the 70x70 portion of the model and, thus, may leave a very small residual signature, which can pass unnoticed in a map such as in Figure 8.6.1–1. Such an outlier would probably be easier to identify in a map such as in Figure 8.6.1–2. In any event, the two types of adjustments have certain complementary properties, and, thus, it is useful to examine and compare results from both.

Spectral Comparisons

One may also compare the solutions V068 and HDM190 in a spectral sense. We use the following comparison variables, defined in [*Rapp*, 1986, pp. 376–377]:

1) The percentage difference P_n, by degree n, as defined in eq. (8.5.6–4), and the average percentage difference over a range of degrees $[n_1, n_2]$, given by:

$$P_{[n_1, n_2]} = \frac{\sum_{n=n_1}^{n_2} P_n}{(n_2 - n_1 + 1)} \qquad (8.6.1–4)$$
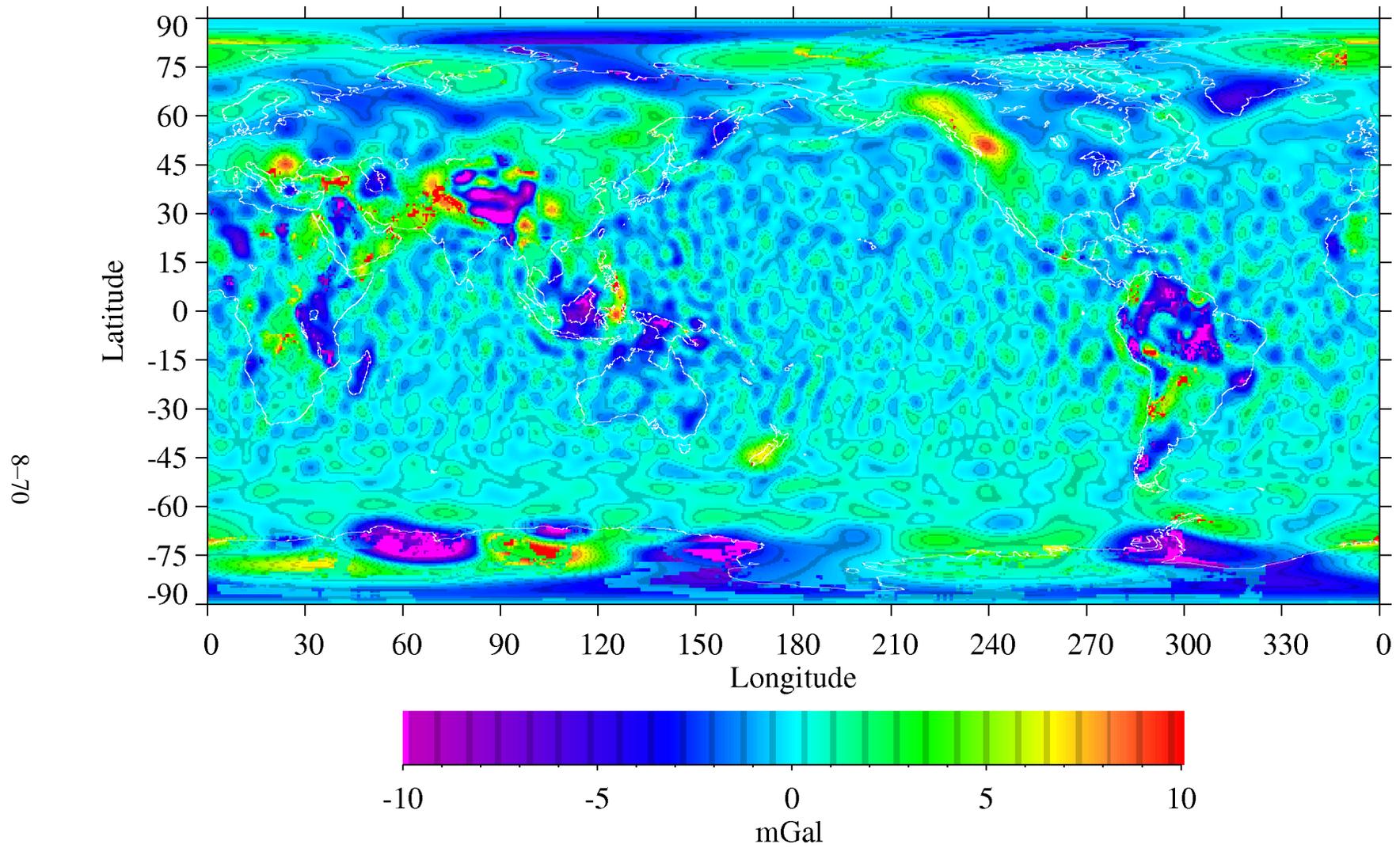
Figure 8.6.1–1. Residual 30´ mean gravity anomalies from the numerical quadrature solution V068.
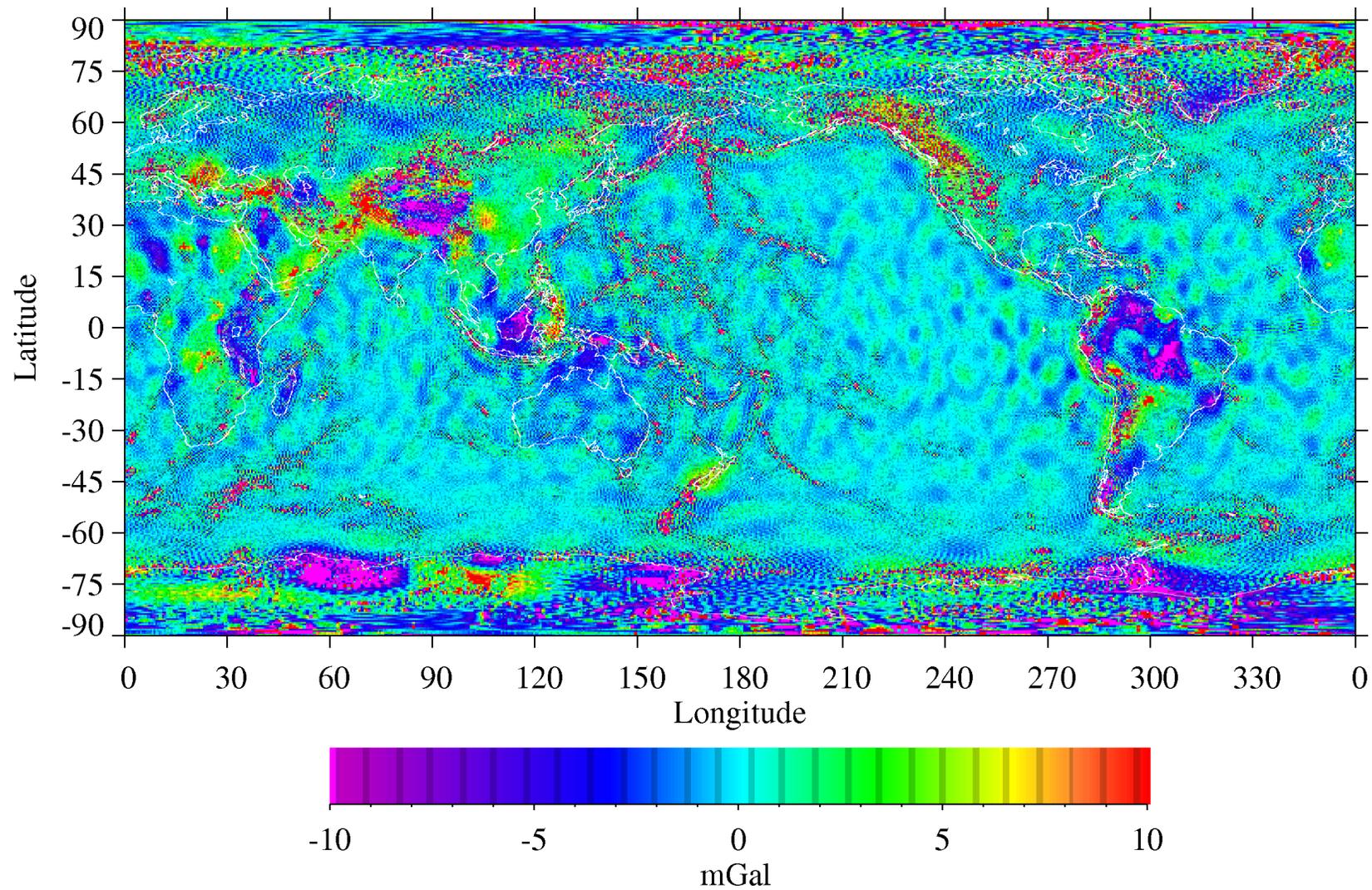
Figure 8.6.1–2. Residual 30´ mean gravity anomalies from the block diagonal solution HDM190.

2) The RMS geoid undulation difference, by degree n, given by:

$$\delta N_n = R \cdot \left[\sum_{m=0}^{n} \left(\Delta C_{nm}^2 + \Delta S_{nm}^2 \right) \right]^{1/2} \tag{8.6.1–5}$$

and the RMS undulation difference over a range of degrees $[n_1, n_2]$, given by:

$$\delta N_{[n_1, n_2]} = \left[\sum_{n=n_1}^{n_2} \delta N_n^2 \right]^{1/2} \tag{8.6.1–6}$$

3) The RMS gravity anomaly difference, by degree n, given by:

$$\delta g_n = \gamma (n-1) \cdot \left[\sum_{m=0}^{n} \left(\Delta C_{nm}^2 + \Delta S_{nm}^2 \right) \right]^{1/2} \tag{8.6.1–7}$$

and the RMS gravity anomaly difference over a range of degrees $[n_1, n_2]$, given by:

$$\delta g_{[n_1, n_2]} = \left[\sum_{n=n_1}^{n_2} \delta g_n^2 \right]^{1/2} \tag{8.6.1–8}$$

ΔC and ΔS always denote the differences between the fully normalized potential coefficients of the two models. Using the above equations and the scaling parameters $R = 6378136.3$ m and $\gamma = GM/a^2$, with GM and "a" as defined in eq. (8.5.5–7), we computed the numerical values of these comparison variables shown in Table 8.6.1–2.

Table 8.6.1–2. Comparison between high-degree models V068 and HDM190.

Degree range $[n_1, n_2]$	[2,359]	[71,359]
Average % difference	4.30	5.21
RMS undulation diff. (m)	0.03	0.02
RMS anomaly diff. (mGal)	0.83	0.82

The anomaly degree variances implied by V068, HDM190, their difference, and their respective errors are shown in Figure 8.6.1–3. It is obvious from Table 8.6.1–2 and Figure 8.6.1–3 that the two solutions V068 and HDM190 have very small differences, which are well below the predicted errors of either model. HDM190 has slightly higher power than V068 (especially over the degree range $n = 200$ to 320). The most prominent feature in Figure 8.6.1–3 is the higher error implied by V068, which is a result of the use of the *a priori* constraint in HDM190. One should also notice that the HDM190 error spectrum is continuous at degree 70 (the maximum degree of the satellite-only model), while V068 exhibits a (small) jump discontinuity at this degree. There is, however, a jump of about 0.03 mGal^2 in the HDM190 error spectrum from $n = 357$ to 358. This behavior was noticed in every BD solution made in this study. It is not clear

why this reduction in the predicted error appears in the BD solutions as one approaches the Nyquist degree.
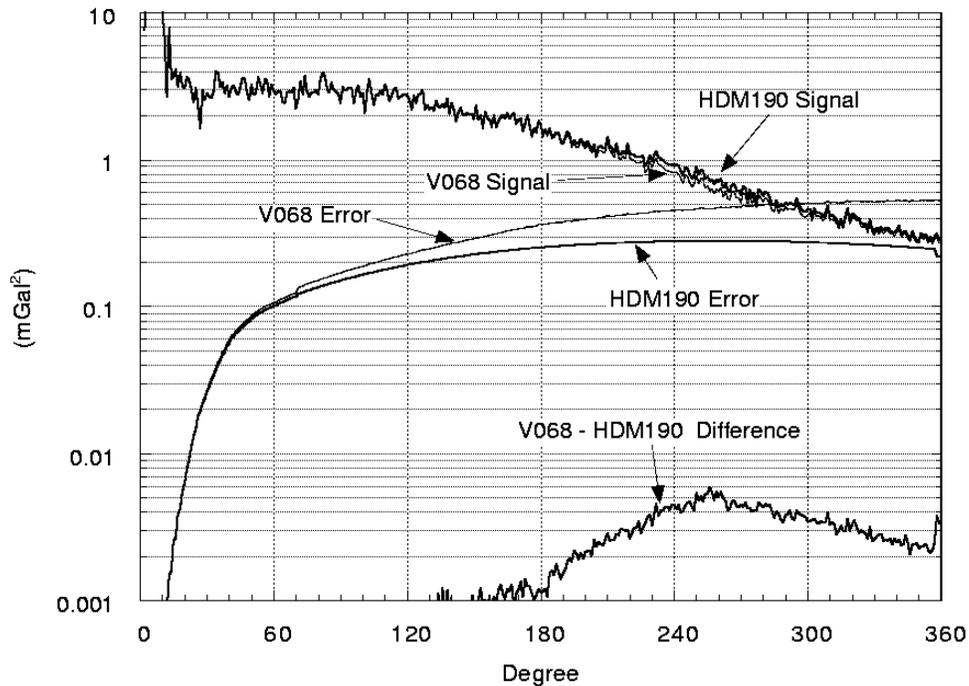
Figure 8.6.1–3. Gravity anomaly degree variances from solutions V068, HDM190, their difference, and their respective errors.

Table 8.6.1–3 provides the cumulative global RMS signal and formal error in gravity anomaly and geoid undulation (both point values), implied by the two models, over the degree range $n = 2$ to 359. These values have been computed using the same scaling parameters as in equations (8.6.1–5) and (8.6.1–7) above, so they formally refer to a sphere of radius $R = 6378136.3$ m. Since there is little difference between the two models over the long wavelength part of the spectrum, there is also little difference in the global RMS signal and error of the corresponding geoid undulations. The gravity anomaly, on the other hand, is sensitive to the higher degree differences in the models and their error spectra, and this is reflected in the predicted signal and most prominently in the predicted anomaly errors from the two models.

Table 8.6.1–3. Cumulative global RMS signal and formal error in gravity anomaly (mGal) and geoid undulation (m) implied by the high-degree models V068 and HDM190. Degree range is [2,359].

Model	Δg signal	Δg error	N signal	N error
V068	27.135	10.691	30.401	0.453
HDM190	27.368	8.553	30.401	0.410

The close agreement between the coefficients of the two high-degree models V068 and HDM190 is merely an indicator of the consistency in the results obtained with the two techniques, when both techniques were applied to the same input data. This agreement should not be interpreted as a measure of accuracy of either model. The two models are highly error correlated, and, furthermore, the use of V068 as reference for HDM190, coupled with the introduction of the *a priori* constraint in HDM190, makes the observed agreement an expected consequence of our design. It is, therefore, important to examine the differences between the models and try to assess which solution is preferable, depending on the criteria we adopt. Recall that neither V068 nor HDM190 incorporates altimetry in the form of "direct tracking." Only the low-degree combination model (PGS7337B) discussed in Section 7 possesses this advantage. Based also on the experience gained during the development of the OSU91A solution, we therefore anticipate that one of the two high-degree solutions presented here will be used to augment the 70x70 combination model, and thus define a "composite" high-degree expansion. Accordingly, our primary criterion to distinguish between V068 and HDM190 has to be the performance of each model at the higher (than 70) degrees. We also recognize here that, given the very close agreement between the two models (see Table 8.6.1–2), discriminating between them will be difficult. The complete evaluation (using comparisons with independent data) of the two high-degree expansions, by themselves and as complements to the 70x70 combination solution PGS7337B, will be discussed in Section 10. In the next paragraph we will set the stage for some of the comparisons discussed in Section 10.1.7.

Geoid Undulation Comparisons (Spectral–Geographic)

Geoid undulation differences between the two models V068 and HDM190, in the form of 30ʹ mean values, can be computed by:

$$\overline{\delta N}^{ij} = \frac{1}{\Delta\sigma_i}\frac{GM}{r_i^e\gamma_i^e}\sum_{n=2}^{M}\left(\frac{a}{r_i^e}\right)^n\sum_{m=-n}^{n}\Delta\overline{C}_{nm}\cdot\overline{IY}_{nm}^{ij} \qquad (8.6.1\text{–}9)$$

where γ_i^e is normal gravity on the surface of the reference ellipsoid (at the center of the *i*th latitude band), and the rest of the notation is as in eq. (8.6.1–2). To be precise, the $\overline{\delta N}$ values thus computed represent differences of (quasi) height anomalies (see also Section 5.2.1), but this distinction will be omitted here. One may vary the maximum degree of the summation *M*, from 2 to 359, and for each value of *M* produce a global 30ʹ grid of the undulation differences between the two models, up to this specific degree. The mean and standard deviation values of these differences can be computed then for subregions of the globe, for each degree *M* (notice here that the mean undulation difference between the models does not necessarily vanish when subregions of the globe are considered). This approach enables a geoid undulation comparison between the two models that possesses both spectral and geographic characteristics. Obviously, such comparisons can be performed also with functionals other than geoid heights (see Section 5.8).

In this manner we have computed the mean and standard deviation (RMS about the mean) of the $\overline{\delta N}$ values (V068 minus HDM190), for every degree from $n = 2$ to $n = 359$, for land areas, ocean areas and globally. A 30ʹ cell is considered here to be "oceanic" if its 30ʹ mean elevation

(JGP95E) is less than –1000 m. The standard deviation of the $\overline{\delta N}$ values is plotted in Figure 8.6.1–4. Apart from the very low degrees (n = 2 to 10), one observes that the standard deviation of the $\overline{\delta N}$ values is always higher over land than over ocean. One should recall here that the V068 coefficients beyond degree 70 are computed without any regard to the weight associated with each individual gravity anomaly (in effect, eq. [8.2.1–1] treats all the anomaly data as equally weighted). In contrast, each coefficient of the HDM190 model depends on the individual gravity anomaly weights. Therefore, one should expect the largest differences between the two models to occur over areas where the anomaly weights depart significantly from "uniformity." Such areas are primarily over land, since the altimetry-derived anomalies used over most of the ocean are assigned very similar weights according to the weighting scheme (8.5–2). Table 8.6.1–4 provides statistics associated with the $\overline{\delta N}$ values when the degree M in (8.6.1–9) becomes 359.
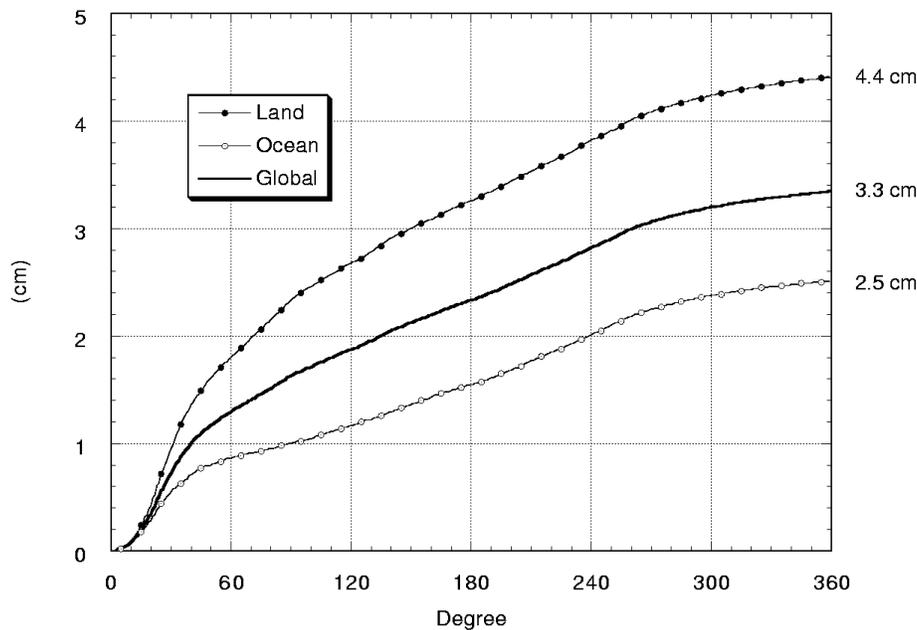
Figure 8.6.1–4. Standard deviation (RMS about the mean) of geoid undulation differences between V068 and HDM190, for different geographic regions, as a function of harmonic degree.

Table 8.6.1–4. Statistics of the geoid undulation differences (in terms of 30´ mean values), V068 minus HDM190. Maximum degree is 359, units are cm.

Statistic	Land	Ocean	Globally
Number	113668	145532	259200
% of Area	37.1	62.9	100.0
Minimum	–89.4	–37.3	–89.4
Maximum	59.4	49.3	59.4
Mean	–0.12	0.07	0.00
Std. Dev.	4.41	2.51	3.35

The geographic distribution of the 30′ mean values of the geoid undulation differences V068 minus HDM190, for $M = 359$, is shown in Figure 8.6.1–5. We distinguish two kinds of areas where large differences occur: (a) areas with significant variation in gravity anomaly weights and (b) areas with significant very high frequency geoid signals. A typical example of (a) is Antarctica, while the Aleutian trench provides a good example for (b). One should keep in perspective the fact that the observed undulation differences between V068 and HDM190 are about an order of magnitude smaller than the predicted undulation accuracy of either model. The differences of type (a) occur primarily over areas that are poorly surveyed, and lack independent test data that could be used to distinguish between the two models. For differences of type (b) however, occurring over ocean areas (e.g., trenches), one could use satellite altimeter data and a global circulation model in an attempt to distinguish between the models. Such comparisons were made both on an oceanwide basis, as well as over specific regions such as the Aleutian trench and the Mendocino Fracture Zone. These results will be discussed in Section 10.1.7.

8.7   Summary

This section presented the development of high-degree (360) combination gravitational models supporting the EGM96 solution (to be defined in Section 10). Two estimation techniques were considered: the (simple) Numerical Quadrature (NQ), and a Block-Diagonal Least-Squares approach (BD). The NQ approach followed the same method used by *Rapp and Pavlis* [1990] in the development of the OSU89A/B models. The only modification here was the introduction of a different type of quadrature weights, which avoid jump discontinuities. The BD adjustment technique was developed, verified, and implemented in various ways. The aliasing at the high degrees, to which the BD approach is susceptible, received particular attention in this investigation. To alleviate this problem, we devised and implemented an estimation strategy where the 30´ mean gravity anomalies are first used to define (through NQ) a solution extending beyond the Nyquist degree. This solution was originally developed to degree 500. However, comparisons with independent data suggested that valid gravitational signal did not exist beyond degree 460. Therefore, this model was used, up to degree 460, to prefilter from the gravity data any harmonic contribution beyond the solved-for degree (359), and these "band limited" anomalies were used as input to the BD algorithm. In addition, we introduced *a priori* constraints for the higher degree coefficients in an attempt to provide a more reliable propagated error spectrum for the higher degrees ($n > 200$) of the BD model.

The two estimation techniques were implemented based on exactly the same data: the satellite-only model EGM96S and its full error covariance matrix, and a complete global set of 30´ mean anomalies (obtained by merging terrestrial observations with altimetry-derived values and topographic-isostatic predictions). The results from the two approaches (NQ and BD) were thoroughly intercompared. From the analysis that we performed, we conclude that rather than abandoning the NQ in favor of the BD approach, or vice versa, one could achieve better results by applying the NQ first (to obtain a first estimate of the high-degree model), and then use the BD approach to refine this estimate and its propagated error. In that regard, the two approaches work hand in hand rather than in competition.
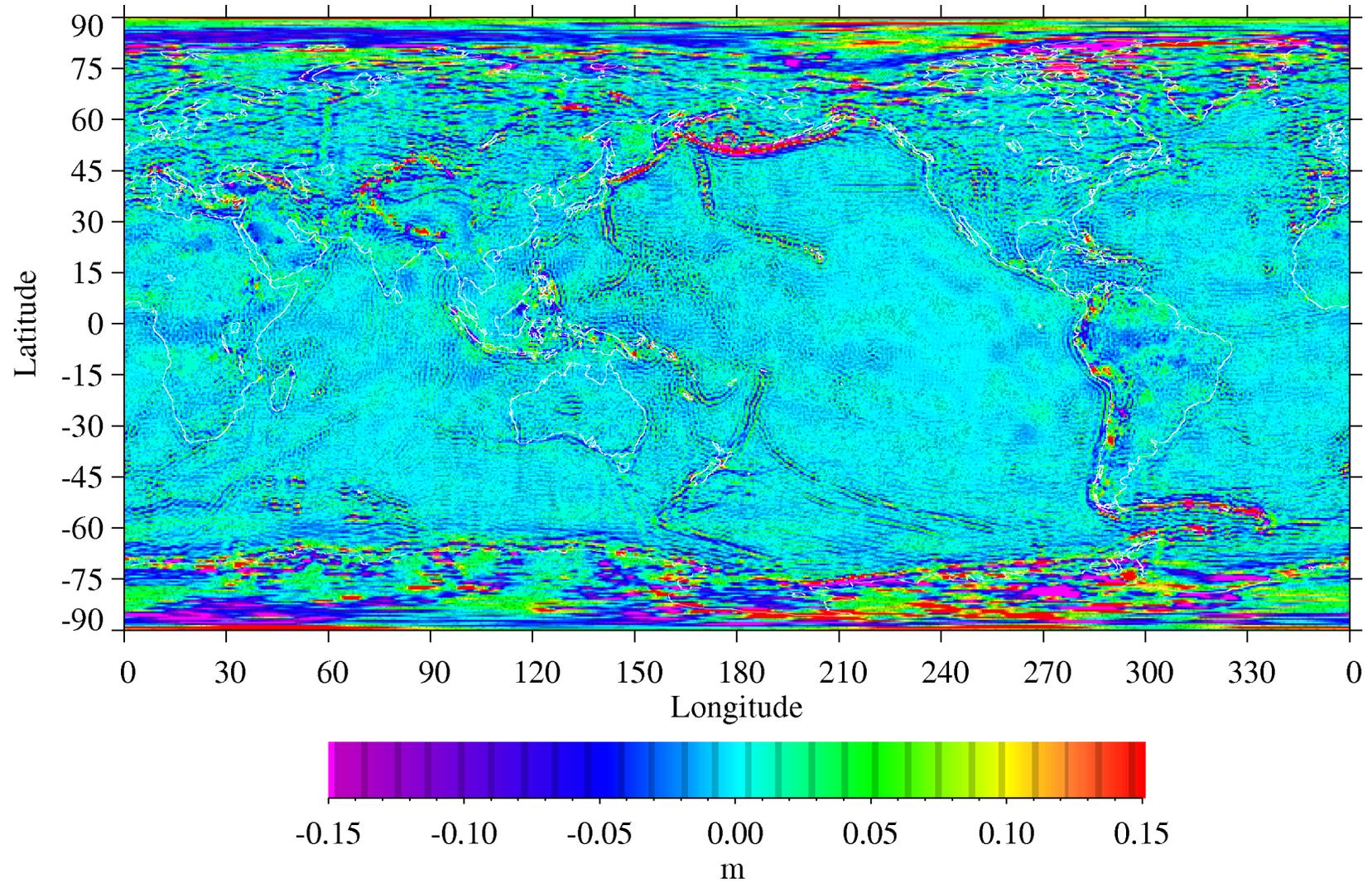
Figure 8.6.1–5. 30´ Mean values of geoid undulation differences for V068 minus HDM190. Maximum degree is 359.

This effort advanced our insight and understanding of several aspects of the high-degree model development. At the same time, several aspects of these solutions were identified where we fully recognize the need for additional study. Such study could not have been conducted within the limits and scope of the joint project. Areas needing further investigation include:

1) Gravity anomaly weighting and the consideration of long wavelength systematic errors associated with the gravity anomaly data.

2) Downward continuation techniques. This aspect becomes particularly important if one wishes in the future to extend the high-degree models beyond 360, and possibly to degree 720 through the use of 15´ mean anomalies. Additional theoretical and numerical study is required here.

3) Aliasing effects in least-squares estimation methods. Although we devised and implemented one possible treatment for these effects, we make no claim as to the optimality of our approach. The alternative approach proposed by *Jekeli* [1996], and the use of area-mean gravity anomaly data defined over spherical caps (rather than over equiangular cells as was the case here), deserve investigation and testing with both simulated and real data.

4) "Direct" altimetry. Is it possible to incorporate altimeter data in the form of "direct tracking" in the BD solution? This could circumvent the need for "cut and paste" approaches in the development of the 360 model. We recognize also that the use of error correlated data over the ocean (altimeter ranges and altimetry-derived gravity anomalies) would require particular attention to be paid to data weighting issues.

5) Error variance–covariance matrix for the high-degree solution. As noted in Section 8.2.4, we need to develop and verify efficient numerical algorithms for the formation and the subsequent propagation of some representative approximation of the complete variance–covariance matrix associated with the high-degree BD model.

Last, but certainly not least, one should recognize the need to further improve the accuracy and density of gravity anomaly data over several areas of the Earth. Although the 30´ merged anomaly file used here represents a significant improvement over the corresponding file used in the OSU91A model development, there are still many areas of the globe (especially the polar caps) where very limited gravity anomaly information exists. Airborne gravity surveys would hopefully provide significant improvements in the gravity coverage of certain remote regions of the globe in the (near) future.

8.8   References

Arnold, K., The spherical-harmonics expansion of the gravitational potential of the Earth in the external space and its convergence, *Gerlands Betri. Geophysik*, Leipzig, Vol. 87, No. 2, 1978.

Arnold, K., Picone's theorem and the convergence of the expansion in spherical harmonics of the gravitational potential of the Earth in the external space, *Bollettino di Geofisica Teorica ed Applicata*, 22, No. 86, 1980.

Bosch, W., A rigorous least squares combination of low and high degree spherical harmonics, presented at the IAG General Meeting, Beijing, People's Republic of China, 1993.

Chan, J.C., and N.K. Pavlis, An efficient algorithm for computing high degree gravity field models using "wing-block" diagonal technique, internal report HSTX/G&G–9501, Hughes STX Corporation, Greenbelt, MD, 1995.

Colombo, O.L., Numerical methods for harmonic analysis on the sphere, *Rep. 310*, Dept. of Geod. Sci. and Surv., Ohio State Univ., Columbus, 1981.

Colombo, O.L., The global mapping of gravity with two satellites, *Netherlands Geod. Comm., Publications on Geodesy, New Series*, Vol. 7, No. 3, Delft, 1984.

Colombo, O.L., High resolution analysis of satellite gradiometry, in *Progress in the Determination of the Earth's Gravity Field*, Extended Abstracts for the meeting held in Ft. Lauderdale, Florida, Sept. 13–16, 1988, edited by R.H. Rapp, *Rep. 397*, Dept. of Geod. Sci. and Surv., Ohio State Univ., Columbus, 1989.

Cook, A.H., The determination of the external gravity field of the Earth from observations of artificial satellites, *Geophys. J. R. Astron. Soc.*, *13*, 1967.

Gleason, D.M., Comparing ellipsoidal corrections to the transformation between the geopotential's spherical and ellipsoidal spectrums, *Manusc. Geod.*, *13*, 114–129, 1988.

Gruber, T., and W. Bosch, A new 360 gravity field model, presented at the XVII General Assembly of the European Geophysical Society, Edinburgh, Scotland, 1992.

Gruber, T., M. Anzenhofer, and M. Rentsch, The 1995 GFZ high resolution gravity model, in *Global Gravity Field and Its Temporal Variations*, edited by R.H. Rapp, A.A. Cazenave, and R.S. Nerem, International Association of Geodesy Symposia, No. 116, Springer–Verlag, Berlin Heidelberg, 1996.

Haagmans, R., E. de Min, and M. van Gelderen, Fast evaluation of convolution integrals on the sphere using 1D FFT, and a comparison with existing methods for Stokes' integral, *Manusc. Geod.*, *18*, 227–241, 1993.

Hajela, D.P., Optimal estimation of high degree gravity field from a global set of 1°x1° anomalies to degree and order 250, *Rep. 358*, Dept. of Geod. Sci. and Surv., Ohio State Univ., Columbus, 1984.

Hein, G., *Die Berechnung von anomalen verikalen Schweregradienten hoher Präzison*, Deutschen Geodätische Kommission bei der Bayerischen Akademie Der Wissenschaften, Reihe C, Heft Nr. 234, München, 1977.

Hein, G., Numerische Studien zur optimalen Wahl der Größe und Berechnungs-methode der Kernzone bei gravimetrischen Lotabweichungen, in *Beiträger zur physikalischen Geodäsie*, zusammengestellt von Erwin Groten, Deutschen Geodätische Kommission bei der Bayerischen Akademie Der Wissenschaften, Reihe B, Heft Nr. 233, München, 1978.

Heiskanen, W.A., and H. Moritz, *Physical Geodesy*, W.H. Freeman and Co., San Francisco, 1967.

Hwang, C., Analysis of some systematic errors affecting altimeter-derived sea surface gradient with application to geoid determination over Taiwan, *J. Geod.*, *71*, 113–130, 1997.

Jekeli, C., An investigation of two models for the degree variances of global covariance functions, *Rep. 275*, Dept. of Geod. Sci. and Surv., Ohio State Univ., Columbus, 1978.

Jekeli, C., Alternative methods to smooth the Earth's gravity field, *Rep. 327*, Dept. of Geod. Sci. and Surv., Ohio State Univ., Columbus, 1981.

Jekeli, C., The exact transformation between ellipsoidal and spherical harmonic expansions, *Manusc. Geod.*, *13*, 106–113, 1988.

Jekeli, C., On the analytical reduction of the surface gravity anomaly for harmonic analysis, presented at the meeting of Working Group I of the DMA/GSFC Joint Gravity and Geoid Improvement Project, Greenbelt, MD, 1995.

Jekeli, C., Spherical harmonic analysis, aliasing, and filtering, *J. Geod.*, 70, 214–223, 1996.

Jekeli, C., and T.N. Upadhyay, Gravity Estimation from STAGE, a satellite-to-satellite tracking mission, *J. Geophys. Res., 95*, 10973–10985, 1990.

Katsambalos, K.E., The effect of the smoothing operator on potential coefficient determinations, *Rep. 287*, Dept. of Geod. Sci. and Surv., Ohio State Univ., Columbus, 1979.

Kaula, W.M., Tests and combination of satellite determinations of the gravity field with gravimetry, *J. Geophys. Res.*, *71*, 5303–5314, 1966.

Kearsley, A.H.W., and R. Forsberg, Tailored geopotential models - applications and shortcomings, *Manusc. Geod.*, 15, 151–158, 1990.

Laskowski, P., The effect of vertical datum inconsistencies on the determination of gravity related quantities, *Rep. 349*, Dept. of Geod. Sci. and Surv., Ohio State Univ., Columbus, 1983.

Lerch, F.J., N.K. Pavlis, and J.C. Chan, High-degree gravitational modeling: quadrature formulæ versus a block-diagonal normal matrix inversion, presented at the XVIII General Assembly of the European Geophysical Society, Wiesbaden, Germany, 1993.

Levallois, J.J., General remark on the convergence of the expansion of the Earth potential in spherical harmonics, translated from French, DMAAC–TC–1915, St. Louis, MO, 1973.

Li, Y.C., and M.G. Sideris, Minimization and estimation of geoid undulation errors, *Bull. Geod., 68*, 201–219, 1994.

Mikhlin, S.G., *Multidimensional Singular Integrals and Integral Equations*, translated from Russian, Pergamon Press, Oxford, 1965.

Moritz, H., *Advanced Physical Geodesy*, Herbert Wichmann Verlag, Karlsruhe, Federal Republic of Germany, 1980.

Morrison, F., Validity of expansion of the potential near the surface of the Earth, presented at the IV Symposium on Mathematical Geodesy, Trieste, 1969.

Nerem, R.S., F.J. Lerch, J.A. Marshall, E.C. Pavlis, B.H. Putney, B.D. Tapley, R.J. Eanes, J.C. Ries, B. E. Schutz, C.K. Shum, M.M. Watkins, S.M. Klosko, J.C. Chan, S.B. Luthcke, G.B. Patel, N.K. Pavlis, R.G. Williamson, R.H. Rapp, R. Biancle, and F. Noule, Gravity model development for TOPEX/POSEIDON: Joint Gravity Models 1 and 2, *J. Geophys. Res.*, *99*, 24421–24447, 1994.

Nöe, H., Numerical investigations on the problem of Molodensky, Mitteilungen der Geodätischen Institute der Technischen Universität Graz, Folge 36, 1980.

Pavlis, N.K., Modeling and estimation of a low degree geopotential model from terrestrial gravity data, *Rep. 386*, Dept. of Geod. Sci. and Surv., Ohio State Univ., Columbus, 1988.

Pavlis, N.K., and R.H. Rapp, The development of an isostatic gravitational model to degree 360 and its use in global gravity modelling, *Geophys. J. Int.*, *100*, 369–378, 1990.

Pavlis, N.K., Estimation of geopotential differences over intercontinental locations using satellite and terrestrial measurements, *Rep. 409*, Dept. of Geod. Sci. and Surv., Ohio State Univ., Columbus, 1991.

Pavlis, N.K., J.C. Chan, and F. Lerch, Alternative estimation techniques for global high-degree gravity modeling, in *Global Gravity Field and Its Temporal Variations*, edited by R.H. Rapp, A.A. Cazenave, and R.S. Nerem, International Association of Geodesy Symposia, No. 116, Springer–Verlag, Berlin Heidelberg, 1996.

Rapp, R.H., The geopotential to (14, 14) from a combination of satellite and gravimetric data, presented at the XIV General Assembly of IUGG/IAG, Lucerne, Switzerland, 1967.

Rapp, R.H., Analytical and numerical differences between two methods for the combination of gravimetric and satellite data, *Bollettino di Geofisica Teorica ed Applicata*, *XI*, 108–118, 1969.

Rapp, R.H., The Earth's gravity field to degree and order 180 using Seasat altimeter data, terrestrial gravity data, and other data, *Rep. 322*, Dept. of Geod. Sci. and Surv., Ohio State Univ., Columbus, 1981.

Rapp, R.H., The determination of high degree potential coefficient expansions from the combination of satellite and terrestrial gravity information, *Rep. 361*, Dept. of Geod. Sci. and Surv., Ohio State Univ., Columbus, 1984.

Rapp, R.H., Global geopotential solutions, in *Mathematical and Numerical Techniques in Physical Geodesy*, edited by H. Sünkel, Springer–Verlag, Berlin Heidelberg, 1986.

Rapp, R.H., Use of altimeter data in estimating global gravity models, in *Satellite Altimetry in Geodesy and Oceanography*, edited by R. Rummel and F. Sansó, 373–417, Springer–Verlag, Berlin Heidelberg, 1993.

Rapp, R.H., Use of potential coefficient models for geoid undulation determinations using a spherical harmonic representation of the height anomaly/geoid undulation difference, *J. Geod.*, *71*, 282–289, 1997.

Rapp, R.H., and J.Y. Cruz, Spherical harmonic expansions of the Earth's gravitational potential to degree 360 using 30´ mean anomalies, *Rep. 376*, Dept. of Geod. Sci. and Surv., Ohio State Univ., Columbus, 1986a.

Rapp, R.H., and J.Y. Cruz, The representation of the Earth's gravitational potential in a spherical harmonic expansion to degree 250, *Rep. 372*, Dept. of Geod. Sci. and Surv., Ohio State Univ., Columbus, 1986b.

Rapp, R.H., and N.K. Pavlis, The development and analysis of geopotential coefficient models to spherical harmonic degree 360, *J. Geophys. Res., 95*, 21885–21911, 1990.

Rapp, R.H., Y.M. Wang and N.K. Pavlis, The Ohio State 1991 geopotential and sea surface topography harmonic coefficient models, *Rep. 410*, Dept. of Geod. Sci. and Surv., Ohio State Univ., Columbus, 1991.

Schuh, W.D., Tailored numerical solution strategies for the global determination of the Earth's gravity field, *Technical Report*, Inst. of Theor. Geod., Tech. Univ. of Graz, Austria, 1996.

Schwarz, K.P., M.G. Sideris, and R. Forsberg, The use of FFT techniques in physical geodesy, *Geophys. J. Int.*, *100*, 485–514, 1990.

Sjöberg, L., On the error of spherical harmonic developments of gravity at the surface of the Earth, *Rep. 257*, Dept. of Geod. Sci. and Surv., Ohio State Univ., Columbus, 1977.

Sjöberg, L., On the Convergence Problem for the Spherical Harmonic Expansion of the Geopotential at the Surface of the Earth, *Bulletino di Geofisica ed Science Affini*, Vol. 39, No. 3, 1980.

Sneeuw, N., Global spherical harmonic analysis by least-squares and numerical quadrature methods in historical perspective, *Geophys. J. Int.*, *118*, 707–716, 1994.

Stammer, D., R. Tokmakian, A. Semtner, and C. Wunsch, How well does a 1/4° global circulation model simulate large-scale oceanic observations?, *J. Geophys. Res., 101*, 25779–25811, 1996.

Sünkel, H., Die Darstellung geodätischer Integralformeln durch bikubische Spline-Funktionen, Mitteilungen der Geodätischen Institute der Technischen Universität Graz, Folge 28, 1977.

Tapley, B.D., M.M. Watkins, J.C. Ries, G.W. Davis, R.J. Eanes, S.R. Poole, H.J. Rim, B.E. Schutz, C.K. Shum, R.S. Nerem, F.J. Lerch, J.A. Marshall, S.M. Klosko, N.K. Pavlis, and R.G. Williamson, The Joint Gravity Model–3, *J. Geophys. Res.*, *101 (B12),* 28,029–28,049, 1996.

Tscherning, C.C., and R.H. Rapp, Closed covariance expressions for gravity anomalies, geoid undulations, and deflections of the vertical implied by anomaly degree variance models, *Rept. 208*, Dept. of Geod. Sci. and Surv., Ohio State Univ., Columbus, 1974.

Uotila, U.A., Investigations on the gravity field and shape of the Earth, Helsinki*, Publ. Isostat. Inst. Int. Assoc. Geod.*, No. 33, 1960.

Uotila, U.A., Notes on adjustment computations, Part I, Dept. of Geod. Sci. and Surv., Ohio State Univ., Columbus, 1986.

Wang, Y.M., Numerical aspects of the solution of Molodensky's problem by analytical continuation, *Manusc. Geod.*, *12*, 290–295, 1987.

Wang, Y.M., Downward continuation of the free-air gravity anomalies to the ellipsoid using the gradient solution, Poisson's integral and terrain correction—Numerical comparison and the computations, *Rep. 393*, Dept. of Geod. Sci. and Surv., Ohio State Univ., Columbus, 1988.

Wang, Y.M., On the error of analytical downward continuation under planar approximation, *Manusc. Geod.*, *20*, 34–45, 1994.

Wang, Y.M., On the error of analytical downward continuation of the Earth's external gravitational potential on and inside the Earth's surface, *J. Geod.*, *71*, 70–82, 1997.

Wang, Y.M., and R.H. Rapp, Geoid gradients for Geosat and TOPEX/Poseidon repeat ground tracks, *Rep. 408*, Dept. of Geod. Sci. and Surv., Ohio State Univ., Columbus, 1991.

Weber, G., and H.G. Wenzel, Estimation of error properties, in Validation of SEASAT–1 altimetry using ground truth in the North Sea region, *Deutsch Geod. Komm. Ser. B, 263*, 79–88, 1982.

Weber, G., and H. Zomorrodian, Regional geopotential model improvement for the Iranian geoid determination, *Bull. Geod., 62*, 125–141, 1988.

Wenzel, H.G., Hochauflösende Kugelfunktionsmodelle für das Gravitationspotential der Erde, *Wiss. Arb. 137*, Fachrichtung Vermess. der Univ. Hanover, Hanover, Federal Republic of Germany, 1985.

Wieser, M., The Global Digital Elevation Terrain Model TUG87, Internal Report on Set-up, Origin and Characteristics, Institute of Mathematical Geodesy, Technical University of Graz, Austria, July 1987.

9. THE PRELIMINARY GEOPOTENTIAL MODELS AND THEIR EVALUATION BY THE SWG

9.1 Background

As noted in Section 1, a key element of the joint project was the help obtained in the testing of various geopotential models by the Special Working Group (SWG) of the International Geoid Service, whose chairman is Michael Sideris. In December 1995, it became clear that the estimation of the test geopotential models would be delayed for a variety of reasons. It was felt that the work of the SWG could be made more efficient if a pretest model could be used by the SWG to validate file transmission procedures and software that would be used by members of the SWG to evaluate the near final models. To this end, a model, designated EGM–X01, was placed on a server at GSFC; members of the SWG were notified of details of the file format, constants, etc., by an E–mail message dated December 8, 1995, from N. Pavlis to M. Sideris. This model was a degree 360 model estimated using early satellite models and early surface gravity data sets. The project did not view this model as a candidate final model because of the preliminary nature of the data used in the estimation process. On the other hand, EGM–X01 was able to serve as an able precursor to the models provided later for detail evaluations.

Through the early months of 1996, additional computations were carried out and new data sets became available. In addition, discussions within the project clarified the types of solution that could be candidates for the final model. In April 1996, at a meeting of the joint project team, four models were selected, out of numerous models available, for testing by the SWG. The selected models were representative of distinctly different ways in which the degree 360 model could be estimated. In addition, a degree 360 model was made available that was a blending of the JGM–3 model [*Tapley et al*., 1996] and the OSU91A model ($71 \leq n \leq 360$). This model was considered the state-of-the-art geopotential model prior to the project model development. The five models were then placed on an appropriate server with a message from N. Pavlis to M. Sideris, dated April 10, 1996, providing data set names and formats.

At the time of the joint project decision, the satellite model was designated PGS6394. This model was used to create a low-degree combination (with surface gravity data) geopotential model designated PGS6399. This solution was complete to degree 70 and needed to be augmented by a high-degree set from degree 71 to 360.

To obtain this higher degree set of coefficients, two quadrature type solutions were completed using the PGS6394 model, terrestrial gravity data, and altimeter-derived anomalies for the ocean areas. A quadrature procedure had been developed for the OSU91A model estimation for degrees 51 to 360. These solutions, which used the currently available data and the same quadrature weights as OSU91A, were used to determine a model designated V057 (see Table 8.5–1). An alternative set of weights was developed by N. Pavlis, avoiding some of the disadvantages of the earlier systems. The application of these weights, with the same data as used for the V057 model, yielded the V058 model complete to degree 360 (see Table 8.5–1). (The various quadrature weights are described in Section 8.5) Another type of technique, a block diagonal solution

procedure, was implemented by N. Pavlis to have a simultaneous solution of all possible coefficients (see Section 8.2.2). In this solution, coefficients are formally estimated through degree 359. No coefficients are estimated at degree 360, so that such coefficients must be taken from a quadrature solution (see Section 8.2). Using the same data with the quadrature solutions, a block diagonal solution, HDM130, was estimated. To complete the solution, the degree 360 coefficients of the V058 model were incorporated into the HDM130 model.

With the above as background, the following models were designed for evaluation by the SWG:

SWG Designation	Internal Designation
EGM–X02	PGS6399 ($2 \leq n \leq 70$)/V058 ($71 \leq n \leq 360$)
EGM–X03	V057
EGM–X04	V058
EGM–X05	HDM130

The specific procedure used in the estimation of the EGM–XXX model was not given to the SWG to avoid possible biases due to analyst expectations.

9.2   Results

After the delivery of the preliminary geopotential models to the SWG, the joint project efforts continued in processing new data, improving weighting procedures, etc.. Starting in June 1996, reports from various members of the SWG were received by Sideris and made available to all members of the SWG and the participants of the joint project. In August 1996, the members of the joint project team met to discuss the implication of the SWG reports and the plan for the computations that would lead to the final model, to be designated EGM96. The individual reports were needed to see if clear preferences were seen between the X02 to X05 models, and to see if any model had superior or inferior characteristics. In reading the general comments of the papers available in early August, one typically would find little preference between the models. When there was a preference, it was generally for X02 or X05. One of the items noticed was the improved comparisons found with the X05 model using deflection of the vertical data. This seemed to indicate that the block diagonal procedure was yielding better high-frequency information than the quadrature-based procedures. This had been seen earlier by the project when looking at sea-surface undulations implied by the geopotential models. On the other hand, satellite data residuals were slightly better with the X02 model, which was a blended ($2 \leq n \leq 70$, $71 \leq n \leq 360$) model. Other project tests with dynamic ocean topography had indicated better agreement in GCM ζ values and TOPEX/geoid ζ values for the X02 model.

The preliminary conclusion made by the project was that the final model would most probably be the blended model, with the high-degree part ($71 \leq n \leq 360$) coming from a block diagonal solution supplemented by quadrature-derived coefficients at degree 360. It was also concluded that solutions should be continued with the quadrature weights used in the X04 model for evaluation by the project at the final stages of model selection.

In late September 1996, M. Sideris presented an oral summary of the results of the SWG. A later paper summarized the results [*Sideris*, 1997]. Based on the results presented in this paper, one also sees a preference for the X02 or X05 model. The complete reports of the SWG, with results for the final (EGM96) model, can be found in *Bulletin No. 6 of the International Geoid Service*, 1997.

9.3   References

Sideris, M., International tests of the new GSFC/DMA geopotential models, in Gravity, Geoid and Marine Geodesy, International Symposium, Tokyo, September 30–October 5, 1996, Segawa, Fujimoto, and Okubo (ed.), International Association of Geodesy Symposia, Vol. 117, Springer–Verlag, 1997

Tapley, B.D., M.M. Watkins, J.C. Ries, G.W. Davis, R.J. Eanes, S.R. Poole, H.J. Rim, B.E. Schutz, C.K. Shum, R.S. Nerem, F.J. Lerch, J.A. Marshall, S.M. Klosko, N.K. Pavlis, and R.G. Williamson, The Joint Gravity Model–3, *J. Geophys. Res.*, *101 (B12)*, 28029–28049, 1996.

10.   THE SELECTION OF THE EGM96 GEOPOTENTIAL MODEL

The final models were evaluated with a number of criteria, including their performance on orbit, GPS/leveling, and dynamic ocean topography tests, as well as by the characteristics of their error spectra. Experience with earlier high-degree models had demonstrated that the "optimum" solution would be one that included direct altimetry since the direct altimetric ranges are so valuable for defining the details in the ocean geoid. Recall that the altimetry enters the candidate solutions in two separate ways. The low-degree (to 70x70) combination solution (PGS7337B) includes only direct altimetry, whereas the high-degree quadrature (V068) and block-diagonal (HDM190) models include the 30´x30´ altimeter-derived anomalies. The two altimeter data types were not included simultaneously in the combination or high-degree solutions since to do so would likely result in an overoptimistic ocean geoid error spectrum. Thus, the final solution was expected to be a blended solution, either PGS7337B/V068 or PGS7337B/HDM190. Nevertheless, the validation of the combination, quadrature, and block-diagonal solutions required that all three solutions (PGS7337B, V068, HDM190) as well as the two blended solutions be intercompared. This process of comparison would characterize the relative performance of each of the models and identify if any anomalies had occurred in their derivation.

10.1 Evaluation of Selected Models

The models were evaluated using a variety of techniques, including GPS/leveling, dynamic ocean topography (DOT, or ζ) comparisons, and orbit tests. Whereas in testing the satellite-only model, we are most interested in the satellite orbit tests, as well as the tests with the altimeter-derived anomalies, in the selection of the final model, we are most interested in its performance in geoid tests, as tested by GPS/leveling comparisons over land, and through tests involving the dynamic ocean topography over the oceans. In addition, the model must have satisfactory performance in the orbit domain. An additional consideration was the characteristics of the solution error spectra, which are discussed in further detail in Section 10.3. Thus, the development of EGM96 was subjected to fundamentally different constraints than the JGM series of gravity models. In JGM–1 and JGM–2, the paramount consideration was the orbit performance, particularly for TOPEX/POSEIDON (T/P). In fact, to that end, the surface gravity data normal equations used in these solutions were downweighted by a factor of four, in order to obtain more satisfactory orbit fits [*Nerem et al.*, 1994].

The orbit performance of EGM96 is reviewed in Section 10.1.1. In these orbit tests, the performance of the high-degree models (V068, and HDM190) and the combination model (PGS7337B) is tested through degree 70. In general, the satellite tracking data are not sensitive to wavelengths shorter than those at degree 70, so it makes no sense to carry out evaluations to a higher degree.

The GPS/leveling tests performed at Ohio State University and at GSFC are summarized in sections 10.1.2 and 10.1.3. The tests with the dynamic ocean topography are summarized in Section 10.1.5. The need for selecting a blended solution is discussed in Section 10.2. The characteristics of the error spectra of EGM96 are reviewed in Section 10.3.

10.1.1 Orbit Evaluations

10.1.1.1 Orbit Evaluations Using SLR Data

The SLR satellite tests for the candidate final models, V068, HDM190, and PGS7337B, are summarized in Tables 10.1.1.1–1 to –3. They are compared with OSU91A for the high-degree models, and JGM–2 and JGM–3 for the combination model PGS7337B. Table 10.1.1.1–1 lists the test results for the first set of SLR satellite tests (see Section 5.1.1 for details), including the 30-day multiarc tests on LAGEOS and LAGEOS–2. Table 10.1.1.1–2 summarizes the tests using the second set of SLR multiarc tests, which are 10 days in length (explained in Section 5.1.2). Results for the single ERS–1 test, described in Section 5.1.3, are listed in Table 10.1.1.1–3. In reviewing these test results, it is important to understand that the geopotential models are tested using three effective filters: the satellite orbit itself, the arc length of the test, and whether empirical one-cycle-per-revolution (1-CPR) acceleration parameters were adjusted. Each satellite, by virtue of its semimajor axis, eccentricity, and inclination, is uniquely sensitive to certain sets of geopotential coefficients. The arc length will determine the sensitivity to the long-period and resonance perturbations for each satellite, effectively acting as a high-pass filter in frequency space. The adjustment of empirical 1-CPR acceleration parameters will efficiently filter out any signals that have a 1-CPR signature. For most spacecraft, these empirical accelerations will reduce the contribution of zonal and resonance geopotential terms. The adjustment of other parameters (Sa, Ssa tides or solar radiation pressure coefficients, for instance) can also affect the test results.

A prime objective of the project was to develop a simultaneous solution for the geopotential coefficients and the tides. Such a simultaneous solution is possible only with the low-degree combination model (PGS7337B) and the satellite-only model (PGS7270K37 or EGM96S). The last time the tides were adjusted simultaneously with gravity in the history of the Goddard Earth Models was with GEM–T3. Because of an error in their normal equation partials, the JGM series of models adopted the resonant tides solution from GEM–T3, which was extended using a truncated Schwiderski background model of maximum degree 15, with a lower maximum degree for some of the tide constituents [*Nerem et al*., 1994]. (This tides set is referred to in this document as PGS4846X.) As a result, PGS4846X is the tide model that should be used for JGM–2 and JGM–3. The combination model PGS7337B is best tested with the PGS7337B tide model, although we also show results with the PGS4846X tide model to illuminate some characteristics of the solution performance. Since the V068 and HDM190 high-degree models are derived from EGM96S, they are most consistent with the EGM96S tide model solution. OSU91A was derived from GEM–T2, so the PGS4846X tides are most consistent with that high-degree model. For convenience, throughout this section we will refer to comparisons with a geopotential model and tide model solution as "geopotential solution/tide solution," or, for example, JGM–3/PGS4846X for JGM–3 tests with the PGS4846X tide model, or V068/EGM96S for V068 tests with the EGM96S tide model.

Table 10.1.1.1–1. SLR orbit test residuals for the candidate models (set-1).

Gravity	Tides	RMS of Fit (cm)						
		Multiple arc					Single arc	
		LAGEOS[1]	LAGEOS[2]	LAGEOS–2[1]	Starlette	Ajisai	Stella	GFZ–1
EGM96S	EGM96S	3.42	2.91	3.25	7.85	7.16	11.63	7.61
V068	EGM96S	3.45	2.90	3.42	7.86	7.14	6.56	11.55
HDM190	EGM96S	3.45	2.91	3.42	7.86	7.13	7.57	11.77
OSU91A	PGS4846X	3.31	3.22	3.40	11.85	8.79	224.11	51.46
JGM–2	PGS4846X	3.13	3.14	3.23	9.01	7.50	115.46	26.49
JGM–3	PGS4846X	3.08	3.10	3.16	8.97	7.46	23.13	26.23
PGS7337B	PGS4846X	3.08	3.11	3.23	9.28	7.54	9.67	11.72
PGS7337B	PGS4846X	3.08	3.11	3.23	9.28	7.54	9.67	11.72
V068	PGS7337B	3.21	2.87	3.42	7.97	7.34	6.38	36.88
HDM190	PGS7337B	3.21	2.87	3.43	7.97	7.34	7.16	36.88
PGS7337B	PGS7337B	3.19	2.87	3.38	7.92	7.34	10.26	11.38

[1,3] Sa, Ssa tides not adjusted   [2] Sa, Ssa tides adjusted as global parameters.

For LAGEOS, LAGEOS–2, Starlette, and Ajisai, we need to distinguish between the apparent change in performance due to the new geopotential models (i.e., PGS7337B), and the change in performance with the new tide model (PGS7337B). Referring to Table 10.1.1.1–1, for LAGEOS, the RMS of fit changes little between JGM–3/PGS4846X (3.10 cm) and PGS7337B/PGS4846X (3.11 cm), when the Sa/Ssa tides are adjusted, and does not change at all when the tides are not adjusted. This indicates that, for LAGEOS, the JGM–3 and PGS7337B *gravity* models are comparable. However, when the PGS7337B general tides are used and the Sa and Ssa tides are estimated, the RMS of fit improves from 3.11 cm to 2.87 cm. In contrast, a degradation is observed with PGS7337B gravity and PGS7337B tides when the Sa/Ssa tides are not adjusted— the RMS increases from 3.08 cm to 3.19 cm for JGM–3/PGS4846X and PGS7337B/PGS7337B, respectively. This implies that, with the exception of force modeling errors that can be aliased by the Sa and Ssa tidal terms, the PGS7337B tides are an improvement for LAGEOS in the same fashion as the EGM96S tides were shown to be in Section 6.5.1.

From Table 10.1.1.1–2, the RMS of fit for the 10-day LAGEOS multiarc tests does not change significantly from JGM–2 to JGM–3 to PGS7337B, whether or not the 1-CPR empirical accelerations are adjusted, illustrating that these three gravity models have comparable performance when shorter period tidal and geopotential perturbations are considered. An understandable improvement occurs on the LAGEOS fits between OSU91A and both high-degree models, V068 and HDM190 (0.5 cm for the 10-day multiarcs), since the base model for the new models is EGM96S rather than GEM–T2. Taken together, these results suggest that PGS7337B neither improves nor degrades the modeling of the geopotential coefficients as sensed by LAGEOS, but that the tidal solution, with the exception of the long-period tides, appears to be an improvement over PGS4846X.

For LAGEOS–2, the 30-day multiarc test degrades from 3.16 cm with JGM–3/PGS4846X to 3.38 cm with PGS7337B/PGS7337B. With PGS7337B/PGS4846X the fit is 3.23 cm. As discussed in Section 7.3.3.1 (see Table 7.3.3.1–1), when the S2 (2,2) and S2(4,2) tide terms in the multiarc test are adjusted, the fit on LAGEOS–2 becomes 3.09 cm. Examination of the 10-day LAGEOS–2 multiarc tests (Table 10.1.1.1–2) shows that an improvement of 0.2 to 0.4 cm in the RMS of fit is noted from JGM–2/PGS4846X to the subsequent models (JGM–3/PGS4846X, PGS7337B/PGS4846X). The most plausible reason for this improvement is the inclusion of the new LAGEOS–2 SLR data in the JGM–3 and PGS7337B solutions. Some subtleties are apparent when the 1-CPR empirical accelerations are not adjusted on the 10-day arcs. The RMS of fit of the 10-day LAGEOS–2 arcs decreases from 3.71 cm with JGM–3/PGS4846X to 3.41 cm with PGS7337B/PGS7337B. Virtually no change over JGM–3/PGS4846X (the RMS is 3.71 cm) is seen with PGS7337B/PGS4846X (the RMS is 3.74 cm). Thus, as with LAGEOS, the SLR tests on LAGEOS–2 suggest no change in the geopotential as sensed by LAGEOS–2 (over JGM–3), an improvement in the shorter period tides, but not necessarily the longer period tides to which the 30-day arcs are more sensitive.

Table 10.1.1.1–2. Multiarc SLR orbit tests on the candidate geopotential models (set–2).

Gravity Model	Tide Model	SLR Residual RMS (cm)							
		LAGEOS		LAGEOS–2		Stella		GFZ–1	
		Adjust 1-CPR	No 1-CPR	Adjust 1-CPR	No 1-CPR	Adjust 1-CPR	No 1-CPR	Adjust 1-CPR	No 1-CPR
EGM96S	EGM96S	2.49	2.68	2.55	3.66	5.24	10.31	102.71	111.20
V068	EGM96S	2.51	2.70	2.55	3.64	5.09	5.90	67.78	76.37
HDM190	EGM96S	2.51	2.70	2.55	3.64	5.09	6.12	67.81	76.42
OSU91A	PGS4846X	3.04	3.24	2.79	4.08	85.15	143.75	90.27	127.81
JGM–2	PGS4846X	2.50	2.72	2.72	4.06	13.44	72.85	83.07	91.02
JGM–3	PGS4846X	2.52	2.74	2.52	3.71	8.39	14.61	78.32	87.39
PGS7337B	PGS4846X	2.51	2.74	2.54	3.74	5.07	9.10	62.05	68.55
V068	PGS7337B	2.52	2.71	2.56	3.42	5.07	6.07	67.77	76.17
HDM190	PGS7337B	2.52	2.71	2.56	3.42	5.08	6.56	67.79	76.22
PGS7337B	PGS7337B	2.51	2.70	2.56	3.41	4.97	7.31	62.24	68.52

The tests on Starlette (Table 10.1.1.1–1) indicate a substantial improvement over JGM–3/PGS4846X from 8.97 cm to 7.92 cm with PGS7337B/PGS7337B. With the "old" PGS4846X tides and the new geopotential model PGS7337B, the Starlette fits actually degrade with respect to JGM–3/PGS4846X to 9.28 cm. Thus, the conclusion from this orbit test is that the improvement on Starlette is due to the adjustment of the tide model. This supposition may be verified by applying JGM–3 with the "new" tide model PGS7337B. In this case, the RMS of fit on the Starlette multiarc test for JGM–3/PGS7337B is 7.85 cm.

The satellite-only model (EGM96S) and the high-degree models (V068, HDM190) yield the best orbit fits for Ajisai, with fits of 7.13 to 7.16 cm when the self-consistent EGM96S tides are used. This compares to a fit on the same test with JGM–2S/PGS4846X on Ajisai of 7.40 cm. The

combination models all experience a degradation in the Ajisai orbit fit relative to the satellite-only models, JGM–2S and EGM96S. For instance, using JGM–3/PGS4846X the RMS is 7.46 cm, and with PGS7337B/PGS4846X the RMS is 7.54 cm. Use of both the PGS7337B tides and PGS7337B gravity improves the Ajisai fit to 7.34 cm, but this still represents a degradation with respect to the satellite-only model EGM96S, where the fit is 7.16 cm. This degradation must be caused by the addition of the direct altimeter data, since the high-degree surface gravity solutions and EGM96S perform so much better on this satellite orbit test. Further investigation of this phenomenon is needed.

The Stella orbit tests suggest a substantial improvement for PGS7337B. The RMS of fit for the multiarc improves from 8.39 cm with JGM–3/PGS4846X to 5.07 cm with PGS7337B/PGS4846X. When the 1-CPR empirical accelerations are not adjusted using the same models, the improvement is more dramatic, from 14.61 to 9.10 cm. Stella prefers the new PGS7337B tide model, since the multiarc RMS decreases to 7.31 cm with using the PGS7337B tides. These Stella multiarc test results suggest that PGS7337B has improved all portions of the geopotential as sensed by Stella, including the zonal, resonance, and other geopotential terms.

GFZ–1 shows improvement over JGM–3/PGS4846X, where the multiarc RMS decrease from 78.32 cm to 62.05 cm with PGS7337B/PGS4846X (see Table 10.1.1.1–2). The new tide model has minimal impact on the GFZ–1 multiarc tests, and the RMS fit remains about 62 cm. The GFZ–1 orbit fits remain high with the new geopotential models. GFZ–1 has strong sensitivity to terms beyond degree 70, especially in the resonance orders. The modeling for this satellite would certainly benefit from the incorporation of additional data, and the adjustment of coefficients at least at the satellite's resonance orders, beyond degree 70.

The ERS–1 SLR and altimetry residual test results are summarized in Table 10.1.1.1–3. It is important to realize that this is a single-arc test, and that the dynamic ocean topography (DOT) model was not changed between the various geopotential solutions (recall from Section 7.1, that the DOT is derived from a T/P altimetry solution). The SLR fit improves significantly between the JGM models and PGS7337B when the PGS4846X tides are used, and parallels the Stella test results. The RMS of fit to the altimetry data has likewise improved: The weighted RMS decreases from 9.10 with JGM–3 to 7.54 with PGS7337B, indicating an (RSS) improvement of 5.1 (about 15.3 cm), in the modeling of the geopotential over the oceans.

Table 10.1.1.1–3. ERS–1 single-arc orbit test weighted RMS residuals. The altimetry data uncertainty is 3.0 m, and the SLR data uncertainty is ~1.12 m.

Gravity Model	Tide Model	Weighted Residual	
		SLR	Altimetry
EGM96S	EGM96S	7.45	32.97
V068	EGM96S	7.60	9.20
HDM190	EGM96S	7.66	9.18
JGM–2	PGS4846X	10.54	8.97
JGM–3	PGS4846X	11.81	9.10
PGS7337B	PGS4846X	7.88	7.54
PGS7337B	PGS7337B	7.87	7.54

The high-degree models (OSU91A, V068, HDM190) perform extremely well on the satellite orbit tests. There is a substantial improvement in the Starlette fits (Table 10.1.1.1–1) between OSU91A and HDM190—from 11.85 cm to 7.86 cm—although this improvement may be ascribed in part to the new tide model EGM96S. OSU91A does not do well on Stella (with an RMS fit of 143.75 cm for the Stella multiarc test without 1-CPR estimation, and 5.09 cm on the same test with V068). The poor performance of Stella with OSU91A is no surprise, since the satellite-only model from which OSU91A was derived, GEM–T2, contained no data from either Spot–2 or Stella. The multiarc orbit fits on LAGEOS–2 using new high-degree models V068 and HDM190 are comparable to those using the satellite-only model EGM96S; they are a bit worse, when the 1-CPR accelerations are not estimated, than those using PGS7337B with its tide solution. The V068 and HDM190 models perform better on GFZ–1 when 1-CPR terms are adjusted (the fits are 67.8 cm) than EGM96S (with a fit of 103 cm), but somewhat worse than with PGS7337B where the fit is 62 cm. The high-degree models should perform better for GFZ–1 than the satellite-only model as they include high-frequency data that the satellite-only model lacks. While GFZ–1 was included in the satellite-only model, the amount and distribution of the tracking were relatively sparse. The combination model PGS7337B has improved zonal and resonance terms compared to either V068 or HDM190 since the RMS of fit when 1-CPR terms are not adjusted is 76.4 cm for the high-degree models and 68.5 cm with PGS7337B.

The single-arc ERS–1 test shows that the SLR fit for HDM190/EGM96S (WRMS = 7.66) is superior to the PGS7337B combination model (7.87), yet the fit to the altimeter data is worse with both high-degree models (9.18 with HDM190/EGM96S vs. 7.54 with PGS7337B/ PGS7337B, or a RSS degradation of 5.2 cm.) The direct altimeter data present in the combination model provide important ocean geoid information that simply is not present in the high-degree models V068 and HDM190. This subject is discussed in greater detail in Section 10.1.6.

On balance, the combination model PGS7337B appears to provide better orbit fits than JGM–3, and is certainly an improvement over JGM–2. However, there exist important tradeoffs regarding the addition of the altimeter data to the solution and in the behavior of the long-period tides. For satellites such as Starlette, Ajisai, and Stella, use of both the new tide model as well as the new combination model yields the most improvement. The high-degree models V068 and HDM190 perform satisfactorily on all orbit tests, with performance commensurate with or superior to the parent satellite-only model, EGM96S, and in some cases the combination solution. The best fit to the ERS–1 direct altimeter data is obtained with the combination model, PGS7337B.

10.1.1.2 Orbit Tests With TOPEX/POSEIDON

Comparison of SLR/DORIS-based T/P dynamic orbit solutions using the JGM and PGS7337B models to the reduced-dynamic GPS solutions provided by JPL may indicate a slight degradation of accuracy between JGM–3 and PGS7337B. As stated in Section 5.1.6, these tests were performed using only the gravity model coefficients; the effects of tides were not studied. Of the four repeat cycles used in the test, two of the SLR fits remain essentially unchanged, and two

degrade by 0.1 to 0.2 cm RMS. The DORIS fits are of little value here, essentially representing the noise level of the data. The radial component of the reduced-dynamic comparisons degrades by 0.1 to 0.2 cm on all four test arcs from JGM–3 to PGS7337B. In an RSS sense, there is a difference of 0.5 cm in the average radial RMS values. *Bertiger et al.* [1994] concluded that the reduced-dynamic orbits are accurate to better than 3 cm, with radial precision of 1 cm RMS or less (as assessed by 30–hr solution overlaps). The observed radial differences with the reduced-dynamic orbits between JGM–3 and PGS7337B in these tests are somewhat less than the published accuracy *and* precision limits of the reduced-dynamic solutions. Therefore, caution must be exercised in interpreting these results.

The predicted radial orbit error, based on the geopotential solution covariances, through order 11 for T/P is 1.77 cm for JGM–2, 0.48 cm for JGM–3, and 0.74 cm for PGS7337B. In contrast, when all orders are considered, the total radial orbit error is 2.21 cm for JGM–2, 1.05 cm for JGM–3 and 0.88 cm for PGS7337B (see Section 10.4). The differences with the JPL reduced-dynamic orbits and the SLR fits show an improvement with respect to JGM–2, but a slight degradation compared with JGM–3. The results are in accord with the covariance predictions, especially considering that GPS and SLR data will be most sensitive to the orbit performance at the lower degrees and orders. It is important to bear in mind that two other factors may also influence these tests. The reduced-dynamic orbits themselves are dependent on the underlying dynamical model, so the JGM–3-based reduced-dynamic orbit tests may slightly favor JGM–3. No reduced-dynamic comparisons for T/P are available with PGS7337B, but the authors hope that they can become available in the future. In addition, the nonconservative force model, in particular the "macromodel" derived by *Marshall and Luthcke* [1994], was based on JGM–2-era T/P orbits that still had (relatively speaking) substantial orbit error, so that a retuning of the macromodel using improved orbits from either JGM–3 or PGS7337B would be desirable.

Table 10.1.1.2–1. Comparison of T/P solutions versus JPL-supplied GPS-based reduced dynamic solutions. SLR fits in cm, DORIS fits in mm/s.

Cycle	Gravity Model	SLR (cm)		DORIS (mm/s)		RMS Orbit Comparison (cm)			
		# pts	RMS	# pts	RMS	Radial	Cross	Along	Total
10	JGM–2	2143	4.58	20286	0.580	3.02	6.85	11.89	14.05
	JGM–3		4.60		0.577	2.18	6.45	8.97	11.27
	PGS7337B		4.58		0.577	2.31	6.51	9.22	11.52
19	JGM–2	3829	4.42	55142	0.551	3.71	5.17	10.51	12.29
	JGM–3		4.24		0.546	3.00	3.52	7.66	8.95
	PGS7337B		4.29		0.547	2.97	4.18	7.79	9.32
21	JGM–2	4112	3.05	54260	0.539	3.20	5.40	7.93	10.12
	JGM–3		2.86		0.537	2.46	5.03	5.86	8.10
	PGS7337B		3.05		0.537	2.60	5.16	6.16	8.44
46	JGM–2	4060	3.00	57865	0.565	2.48	6.76	7.80	10.62
	JGM–3		2.73		0.563	1.74	4.53	5.11	7.04
	PGS7337B		2.80		0.562	1.96	5.58	5.54	8.10
Average	JGM–2	3536	3.76	46888	0.559	3.10	6.05	9.53	11.77
	JGM–3		3.61		0.556	2.35	4.88	6.90	8.84
	PGS7337B		3.68		0.556	2.46	5.36	7.18	9.35

10.1.1.3 Results of TDRSS Orbit Tests

Results of the TDRSS-based orbit tests are presented in Tables 10.1.1.3–1, –2, and –3 for the 1992, 1994, and 1996 periods, respectively. To summarize in advance, the overall best results achieved used the PGS7337B (i.e., EGM96 to maximum degree 70) gravity and tide model. The ERBS results show that, for this orbit altitude (575 km) and inclination (57°), there is little difference between the gravity models when 1-CPR accelerations are estimated. This result is expected, as all the models in question have a comparable tracking compliment of spacecraft with inclinations above 45°. For the lower inclination satellites (CGRO, EP/EUVE, and RXTE), the improvements seen using PGS7337B are in agreement with the covariance predictions, which show a dramatic reduction in orbit error for inclinations near that of the EP/EUVE data included in the solution (see Section 10.4). This is particularly true for the dependent EP/EUVE test from the 1994 period, but the improvement is also seen in the independent test (1992 period) using EP/EUVE.

10.1.1.3–1. Average TDRSS-user orbit residuals and overlaps for 1992.

Spacecraft	Geopotential	Tides	1-way Range-Rate RMS (mm/s)	2-way Range-Rate RMS (mm/s)	2-way Range RMS (m)	Overlap Position RMS (m)
CGRO	PGS7337B	PGS7337B	–	2.98	2.89	9.59
	JGM–2	PGS4846X	–	3.43	3.80	9.10
	JGM–3	PGS4846X	–	3.41	3.69	11.03
ERBS	PGS7337B	PGS7337B	–	0.94	1.91	1.72
	JGM–2	PGS4846X	–	1.03	2.00	1.84
	JGM–3	PGS4846X	–	1.05	1.99	1.81
EP/EUVE	PGS7337B	PGS7337B	2.55	2.12	2.76	3.21
	JGM–2	PGS4846X	3.89	3.40	4.18	4.56
	JGM–3	PGS4846X	4.23	3.72	4.50	5.68

10.1.1.3–2. Average TDRSS-user orbit residuals and overlaps for 1994.

Spacecraft	Geopotential	Tides	1-way Range-Rate RMS (mm/s)	2-way Range-Rate RMS (mm/s)	2-way Range RMS (m)	Overlap Position RMS (m)
ERBS	PGS7337B	PGS7337B	–	0.84	2.03	1.59
	JGM–2	PGS4846X	–	0.91	2.11	1.86
	JGM–3	PGS4846X	–	0.89	2.10	1.89
EP/EUVE	PGS7337B	PGS7337B	–	1.28	1.29	2.02
	JGM–2	PGS4846X	–	2.80	3.14	6.44
	JGM–3	PGS4846X	–	3.08	3.23	9.10

10.1.1.3–3. Average TDRSS-user orbit residuals and overlaps for 1996.

Spacecraft	Geopotential	Tides	1-way Range-Rate RMS (mm/s)	2-way Range-Rate RMS (mm/s)	2-way Range RMS (m)	Overlap Position RMS (m)
RXTE	PGS7337B	PGS7337B	–	0.99	1.81	1.38
	JGM–2	PGS4846X	–	1.93	3.29	2.79
	JGM–3	PGS4846X	–	1.55	3.00	2.61

A curious feature of these results is that the JGM–2 model outperforms JGM–3 for all of the EP/EUVE results and the CGRO overlaps, but not for RXTE. With the exception of the inclination, the only significant difference between the EP/EUVE tests and the RXTE tests is the relative amount of range versus range-rate data. The majority of the RXTE tracking is supplied by the TDRSS ranging services as a result of onboard limitations; however, this should not unduly influence the orbit tests for this satellite.

10.1.1.4 Evaluation of PGS7337B Using Reduced-Dynamic Orbits From the STS–72 Shuttle Laser Altimeter (SLA) Mission

The JGM–3 and PGS7337B geopotential models were evaluated by processing TDRSS and GPS tracking data from the Space Shuttle STS–72 Mission using a reduced-dynamic technique. The application of the reduced dynamic method with GEODYN is described by *Rowlands et al.* [1997]. This comparison spans the period from January 16, 1996, at 14:00 to January 17, 1996, at 00:00 hours, and corresponds to STS–72 SLA observation period seven. For STS–72, the Space Shuttle was located in an orbit at about 300 km altitude and at an inclination of 28.5 degrees. The arc was 10 hours long, or a little over 6.5 revs of STS–72. The orbit solutions use a combination of TDRSS closed-loop range-rate and GPS double-difference phase observations. The characteristics of the GPS receiver are described in *Rowlands et al.* [1997].

A total of 1764 TDRSS observations and 3762 GPS observations was used. A reduced-dynamic solution technique was employed for the estimation of 1-CPR along- and cross-track empirical accelerations every quarter revolution, or every 22.5 minutes. During this arc, the Shuttle does periodic attitude maintenance maneuvers so that the estimated empirical accelerations will absorb not only force model error, but the effects of these thrusting events. The weight given to the constraint equation to tie period number i to period number j was:

$$W_T = W_{T0} \cdot \text{EXP}[-4.605 \cdot (i-j)] \qquad (10.1.1.4\text{–}1)$$

where

$W_{T0} = 5 \times 10^{-7}$ for along-track 1–CPR empirical accelerations

$W_{T0} = 5 \times 10^{-6}$ for cross-track 1–CPR empirical accelerations

In addition, the weights given to the constraints for the four accelerations at the beginning and end of the arc were increased by a factor of 4 and 16, to prevent end effects from contaminating

the solution. A single drag coefficient was also estimated, along with antenna offsets for both TDRSS and GPS.

The TDRSS and GPS residuals show essentially no difference when using either JGM–3 or PGS7337B (0.004% difference), a consequence of the reduced-dynamic procedure, which allows the data to be processed essentially down to the noise. The overlap test results show a 6.3 percent improvement when using PGS7337B. The overlap orbit differences were computed from three 5-hour arcs that overlap by 2.5 hours. The results are listed in Table 10.1.1.4–1.

Reduction in the amplitude of the recovered 1-CPR empirical accelerations was observed when using PGS7337B (see Table 10.1.1.4–2). The average along-track amplitude was reduced by 31 percent, while the average cross-track amplitude was reduced by 22 percent. The reduction in the magnitude of the empirical accelerations is an indirect indication of improvement with the PGS7337B gravity model, even in light of the thrusting events experienced by the Shuttle over this arc. Overall, the 10-hour reduced-dynamic orbits differ by only 1.54 m in total position RMS and 0.64 m in radial position RMS.

Table 10.1.1.4–1. RMS orbit overlaps differences for STS–72 from reduced-dynamic orbit tests.

Gravity	Average RMS Difference (m)			
Model	Total Position	Radial	Cross-track	Along-track
JGM–3	2.35	0.83	1.71	1.34
PGS7337B	2.20	0.75	1.37	1.55
% Change[†]	–6.3	–9.5	–20.0	15.41

[†] negative value is an improvement using PGS7337B

Table 10.1.1.4–2. Amplitude of STS–72 along-track and cross-track accelerations from reduced-dynamic orbit determination.

Gravity	Along-Track Amplitude (m/s^2)		Cross-Track Amplitude (m/s^2)	
Model	Mean	Std. Dev.	Mean	Std. Dev.
JGM–3	7.5×10^{-7}	6.4×10^{-7}	3.6×10^{-6}	1.6×10^{-6}
PGS7337B	5.2×10^{-7}	3.3×10^{-7}	2.8×10^{-6}	1.6×10^{-6}
% Change[†]	–31%	–48%	–22%	0%

[†] negative value is an improvement using PGS7337B

10.1.2 Evaluation of Candidate Models via GPS/Leveling Data at Ohio State

The procedures to be used in the evaluation of geopotential models through GPS/leveling data were described in Section 5.2. The data to be used involve 1156 stations thinned from a larger (2497) station set made available by the National Geodetic Survey as described by *Smith and*

Milbert [1997a] and shown in Figure 5.2.2–1. These data have been used to calculate mean differences, standard deviation, tilts, and data residuals for many of the models developed by the joint project. Only results from the near-final models and a few selected nonproject models will be given here.

In the initial stage of research leading to the correction terms described in Section 5.2.1, with first results given in *Rapp* [1997a], certain procedures were followed that were improved upon toward the completion of the model development. To be consistent with previous calculations, the original techniques were followed consistently in all model testing. The upgraded procedures were applied only after the final model had been selected.

There were four differences between the original implementation of the correction term calculation and the final procedure:

1. Eq. (5.2.1–21) was used for the theoretical free-air gravity gradient in the upgraded calculations. In the original calculations, the gradient was approximated by the constant value of –0.3086 mGal/m.

2. Eq. (5.2.1–25) was used to calculate the average value of normal gravity between the ellipsoid and the point in the upgraded calculations. In the original calculations, the average value was taken (incorrectly) at the elevation of the point.

3. Eq. (5.2.1–19) was used to calculate the normal value of gravity at a specified latitude in the upgraded calculation. In the original calculation, the value of normal gravity was computed using a series expansion to terms in $\sin^2\phi$.

4. The original calculations were based on the constants (*a*, *GM*) of the project. In the final computation, the WGS84 enhanced system of constants was used.

The changes noted above have impact on the order of 2 cm on mean differences and 5 mm on standard deviations. Calculations made with the upgraded procedure will be designated by an * after the model designation.

The geopotential models to be reported on will include the OSU91A model, JGM–3 ($n \leq 70$)/HDM180 ($70 < n \leq 360$), the TEG–3 model [*Tapley et al.*, 1997] ($n \leq 70$)/HDM180 ($70 < n \leq 360$), the blended preliminary model EGM–X02, HDM190, V068, and PGS7337B ($n \leq 70$)/HDM190 ($70 < n \leq 360$) (EGM96). The HDM180 model was a block-diagonal solution prior to the HDM190 model. No differences with the use of HDM190 would be expected. The other models are described in Section 8. The mean differences and standard deviation of the differences, with and without the C correction term, are given in Table 10.1.2–1.

One notes the significant reduction in the standard deviation when the C correction term is applied. The OSU91A model has the poorest fit and the TEG–3/HDM180 model yields the smallest standard deviations when the correction term procedures are used. Little differences are seen in the last five models listed in the table.

The mean difference given in the table is dependent on the equatorial radius (6378137.0 m) of the ellipsoid used for the determination of the ellipsoidal heights, and the separation of the

NAVD88 origin reference surface and the geoid. As such, no specific conclusion on a best model can be inferred from the examination of the mean differences given in Table 10.1.2–1.

Table 10.1.2–1. Geoid undulation differences, GPS/leveling minus geopotential model, based on 1156 stations of the thinned NGS station set.

	No Correction		With Corrections	
Model	Mean Diff. (cm)	Std. Dev. (cm)	Mean Diff. (cm)	Std. Dev. (cm)
OSU91A	−97. 5	61.5	−84.9	54.7
JGM–3/HDM180	−105.1	55.5	−92.5	43.7
TEG–3/HDM180	−103.7	52.2	−91.0	40.9
EGM–X02	−112.8	52.0	−100.6	42.3
V068	−108.8	52.2	−96.1	43.5
HDM190	−108.6	52.1	−96.0	43.3
PGS7337B/HDM190	−111.8	52.1	−99.1	42.4
PGS7337B/HDM190*	−111.8	52.1	−101.0	42.9

* with updated correction term

The second type of calculation that can be carried out with these data is the bias, tilt, direction and fit of a plane to the undulation residual (*DN*), as described in Section 5.2.2. The results for these quantities are given in Table 10.1.2–2.

The magnitude of the tilt and the standard deviation of the residual fit to the plane are significantly reduced when the correction term is used. The tilt is the smallest with the TEG–3/HDM180 model, although fit is about 13 percent poorer (30.6 vs. 27.1 cm) than the PGS7337B/HDM190 model. The problem with the interpretation of the tilt value is that there are numerous sources of tilt in the data that go into the computation.

Additional information can be found by examining the geographic distribution in the United States of the DN residuals. Such plots have been constructed for a variety of the geopotential models examined in this study. The procedure in making such plots is to take the residual values at each data point and construct a 2°x2° gridded set of values using a least-squares collocation procedure. The accuracy of the grid will be better in areas in which the data points are dense. In areas lacking data (see Figure 5.2.2–1), the collocation estimates are simply smoothed extrapolation from the given data. An example of a residual plot for the EGM96 (PGS7337B/HDM190) model based on the updated correction procedure is shown in Figure 10.1.2–1. Note the tilt across the country, in a northwest–southeast direction, from Florida to the northwest tier of States. From Table 10.1.2–2 one sees that the tilt of these residuals is 0.409 ppm, which is approximately 170 cm across the country (from Maine to Seattle, WA). *Smith and Milbert* [1997b] have shown that the tilt is essentially negligible when a geoid is calculated using selected gravity and terrain data. However, *Smith and Milbert* [*ibid.*] note that "care should be taken . . . in interpreting the small magnitude of the tilt in the high resolution models" and proceed to explain why in the case of the calculation in the United States. (It should be noted that

the low tilt found in *Smith and Milbert* was based on the original unthinned, 2497-station data set and could be biased by clusters of stations.)

Considering the results from Tables 10.1.2–1 and –2, the model that gives the smallest standard deviation is the TEG–3/HDM180 model. This fact is (probably) associated with the smaller tilt seen with the model, as can be seen from Table 10.1.2–2. In this case, however, the residuals about the plane fit are higher with the TEG–3/HDM180 model than with the other (V068, HDM190, PGS7337B/HDM190 = EGM96) models.

Table 10.1.2–2. Determination of planar fit to the undulation residuals of the 1156 stations of the thinned NGS station set

| Model | No Correction | | | With Correction | | |
	Tilt (ppm)	Azimuth (°)	Std. Dev. (cm)	Tilt (ppm)	Azimuth (°)	Std. Dev. (cm)
OSU91A	.359	329	49.2	.303	336	46.9
JGM–3/HDM180	.381	336	42.9	.330	344	34.4
TEG–3/HDM180	.346	336	37.0	.280	341	30.6
EGM–X02	.410	335	35.1	.360	342	29.5
V068	.471	338	30.6	.422	344	26.7
HDM190	.457	338	30.6	.420	345	27.0
PGS7337B/HDM190	.455	338	32.6	.406	345	27.1
PGS7337B/HDM190*	.455	338	32.6	.409	344	26.9

*with updated correction term
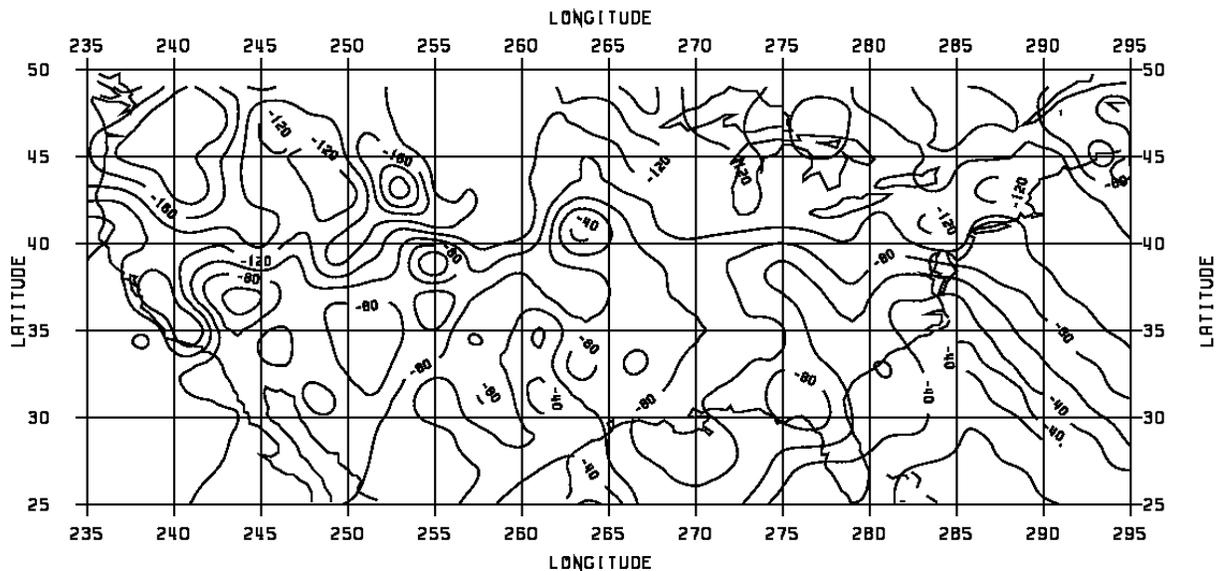
Figure 10.1.2–1. Geographic distribution in the United States of the geoid undulation residuals for the EGM96 model, based on a least-squares collocation fit to a 2°x2° gridded set of residuals.

10–13

10.1.3 GSFC GPS/Leveling Tests of Candidate Final Models

The GSFC GPS/leveling tests are summarized in Tables 10.1.3–1 and 10.1.3–2, and are compared with the results for JGM–3 augmented with OSU91A (these tests are described in Section 5.3). In the comparison between the two high-degree models, the block-diagonal model slightly outperforms the quadrature model. The blended solutions, however, are superior over British Columbia (51.7 cm for PGS7337B/HDM190 compared with 56.3 cm standard deviation for HDM190, for example), and over the five areas. A minimal degradation occurs in the USA/NGS test when each high-degree model is blended with the combination model. The dramatic difference over British Columbia seen with the blended solutions, and to a smaller extent over four of the five areas (Europe, Canada, Australia, and Scandinavia), may be ascribed to the role direct altimetry is playing in the combination solution. Direct altimetry not only provides direct sensitivity to the geoid below the subspacecraft point (once the sea surface topography has been estimated) but through the orbit the direct altimetry has indirect sensitivity to the geopotential over land. For coastal and near-coastal areas (such as British Columbia), this indirect sensitivity may play a role in improving the GPS/leveling results. It would be interesting to test this hypothesis over other areas with more high-quality GPS/leveling data.

Table 10.1.3–1. GSFC GPS/leveling tests for candidate models: US and British Columbia.

Model	USA/NGS			CANADA (BC)		
	Mean (cm)	Std. Dev (cm)	No. of Pts	Mean	Std. Dev (cm)	No. of Pts
JGM–3/OSU91A	−94.96	56.15	1889	−23.57	94.71	297
V068	−101.17	52.65	1889	−12.34	56.64	298
HDM190	−101.47	52.28	1889	−11.83	56.28	298
PGS7337B/V068	−104.57	52.74	1889	−22.37	51.93	298
PGS7337B/HDM190	−104.86	52.59	1889	−21.92	51.66	298

Table 10.1.3–2. GSFC GPS/leveling tests for candidate models: five areas test. Units are cm.

Area (No of Pts)	Europe (60)		Canada (63)		Australia (38)		Scandinavia (46)		Tennessee (49)		Avg.
Model	mean	σ	mean	σ	mean	σ	mean	σ	mean	σ	σ
JGM–3/OSU91A	13.38	46.64	23.59	27.75	−55.35	25.55	21.57	47.55	148.70	18.95	33.72
V068	13.05	32.36	26.83	28.20	−91.82	30.02	20.96	22.17	117.50	21.57	27.03
HDM190	12.99	32.65	26.92	27.58	−93.18	30.64	20.97	21.72	118.51	20.23	26.76
PGS7337B/V068	7.47	31.46	30.86	27.91	−78.46	27.28	18.55	19.39	121.44	22.59	26.10
PGS7337B/HDM190	7.80	31.57	30.77	27.35	−79.50	27.95	18.88	19.07	122.38	21.14	25.75

10.1.4 Evaluation of Candidate Models via Doppler Positioned Stations

Section 5.4 gave a description of the 850-station data set to be used in an undulation comparison. Table 10.1.4–1 presents the mean difference standard deviation and extreme difference for selected geopotential models.

Table 10.1.4–1. Statistics of geoid undulation differences, geometric minus geopotential model, for 850 Doppler positioned data set.

Model	Mean Diff. (cm)	Std. Dev. (cm)	Max. Diff. (cm)
OSU91A	−15	158	676
JGM–3/HDM180	−26	154	614
TEG–3/HDM180	−24	153	603
EGM–X02	−27	144	410
V068	−25	145	392
HDM190	−25	145	391
PGS7337B/HDM190	−27	145	412

The results given in Table 10.1.4–1 show little variation in the standard deviation for the last four models. All represent a small (9 percent) improvement over the results from OSU91A. Because of the errors involved with the ellipsoidal and orthometric heights of the Doppler stations, the comparisons given in this table are not a sensitive indicator of which geopotential models are better than others. However, the comparisons do provide a sense of confidence that a model has not downgraded the undulation determination, relative to the other models, in the regions represented by the 850 stations.

10.1.5 Evaluation of Geopotential Models via Ocean Circulation Model Comparisons

10.1.5.1 Dynamic Ocean Topography

The evaluation of DOT from T/P altimeter data and geoid undulations and the comparison to estimates from global circulation models has been described in Section 5.5.1. In this section, we describe specific results for several geopotential models and two sets of dynamic topography estimates.

The first set of comparisons will be with the POCM–4B DOT data set. The root mean square differences, computed with the coefficients of the orthonormal expansion using eq. (5.5.1–7), are given in Table 10.1.5.1–1. The maximum degree n is taken as 14 to be consistent with the optimum degree described in *Rapp, Zhang, and Yi* [1996, p. 22588] and also degree 18, which will be argued in subsequent discussion to be the most reasonable maximum degree when using the EGM96 geopotential model. Degree 24 is the maximum degree of the expansions made in the computation so that values are given for that degree also.

Table 10.1.5.1–1. Difference between dynamic ocean topography estimates using 2 years of T/P data and various geoid undulation models and that from the POCM–4B GCM model.

Geoid	Cumulative RMS Difference (cm) to Degree (n)		
Model	14	18	24
OSU91A	15.5	16.1	16.7
JGM–3/HDM180	12.6	13.4	14.2
TEG–3/HDM180	11.7	12.4	13.1
EGM–X02	12.1	13.2	13.8
V068	11.0	12.4	13.8
HDM190	11.1	12.4	13.9
PGS7337B/HDM190	9.6	10.5	11.2

For the sake of brevity, consider the differences to degree 18. Recall that these differences apply to the ocean region between 65°N and 66°S, excluding selected regions defined in Section 5.5–1. A significant improvement took place from OSU91A to JGM–3/+. The TEG–3 model [*Tapley et al*., 1997] also shows improvement (smaller difference) over JGM–3. The EGM–X02 model was just slightly improved from JGM–3 model. The V068 and HDM190 models give essentially the same fit, while the blended model gives a significantly improved fit.

Figure 10.1.5.1–1 shows the DOT differences with respect to the POCM–4B model taken to degree 18. The top panel shows the differences with the JGM–3/HDM180 model, while the bottom panel shows the differences using the EGM96 model. The new model yields significantly reduced differences in the Banda Sea area and in several regions in the Antarctic Circum-Polar Current, specifically between 50°S to 65°S and 170°E to 235°E. Other areas of improvement are near 10°S by 350°E, 50°N by 160°E, 5°N by 70°E, etc.. Clearly, areas of significance (e.g., 30 cm) remain, but the improvement is encouraging. The improvement is due to the improvement in the long wavelength gravity field that can be associated with the new satellite tracking data, the appropriate use of satellite altimetry data, and the incorporation of new 1°x1° surface gravity data in the low degree ($n \leq 70$) combination model.

Figure 10.1.5.1–2 shows information related to dynamic ocean topography in the Banda Sea area based on spherical harmonic expansions to degree 18. The top plot represents the POCM–4B model; the middle plot the difference between the DOT from TOPEX/JGM–3/HDM180 and POCM–4B; the bottom panel is the DOT difference based on the EGM96 model. A similar type of plot is shown in Figure 6 of *Rapp, Zhang, and Yi* [1996]. From the middle plot one sees differences that reach –80 cm near 9°S, 130°E. At the same location in the bottom panel, the difference is –2 cm. Not all regions show such improvement. For example, at 5°N, 122°E, the difference in the middle panel is –42 cm, while it is –14 cm in the lower panel. However, in general, there is a substantial reduction in DOT differences in this region when the EGM96 model is used.

Comparison with dynamic topography estimates from other models has also been carried out, although the emphasis has been on comparison to the POCM–4B model because of previous indications that the model did give DOT estimates that agree somewhat better with

TOPEX/geoid estimates than alternate models. For these additional models, we chose the POP(96) model developed at the Los Alamos National Laboratory [*Malone*, 1996, *private communication*, *Fu and Smith*, 1996] and the Levitus DOT based on hydrographic data over an extended time period. The POP(96) model was used in *Rapp, Zhang, and Yi* [1996] with a degree 24 spherical harmonic expansion carried out in a procedure virtually identical to that used for POCM–4B. A comparison of POCM–4B and POP(96) through spherical harmonic and orthonormal expansions is found in *Rapp, Zhang, and Yi* [1996, p. 22585, also Figure 2]. This model is based on a computer simulation of three-dimensional ocean circulation with realistic bottom topography and windstress fields [*Fu and Smith*, 1996]. An expansion of the Levitus DOT in a way consistent with that done for the POCM–4B and POP(96) models was carried out. The results of the comparison are given in Table 10.1.5.1–2.

(a)

(b)
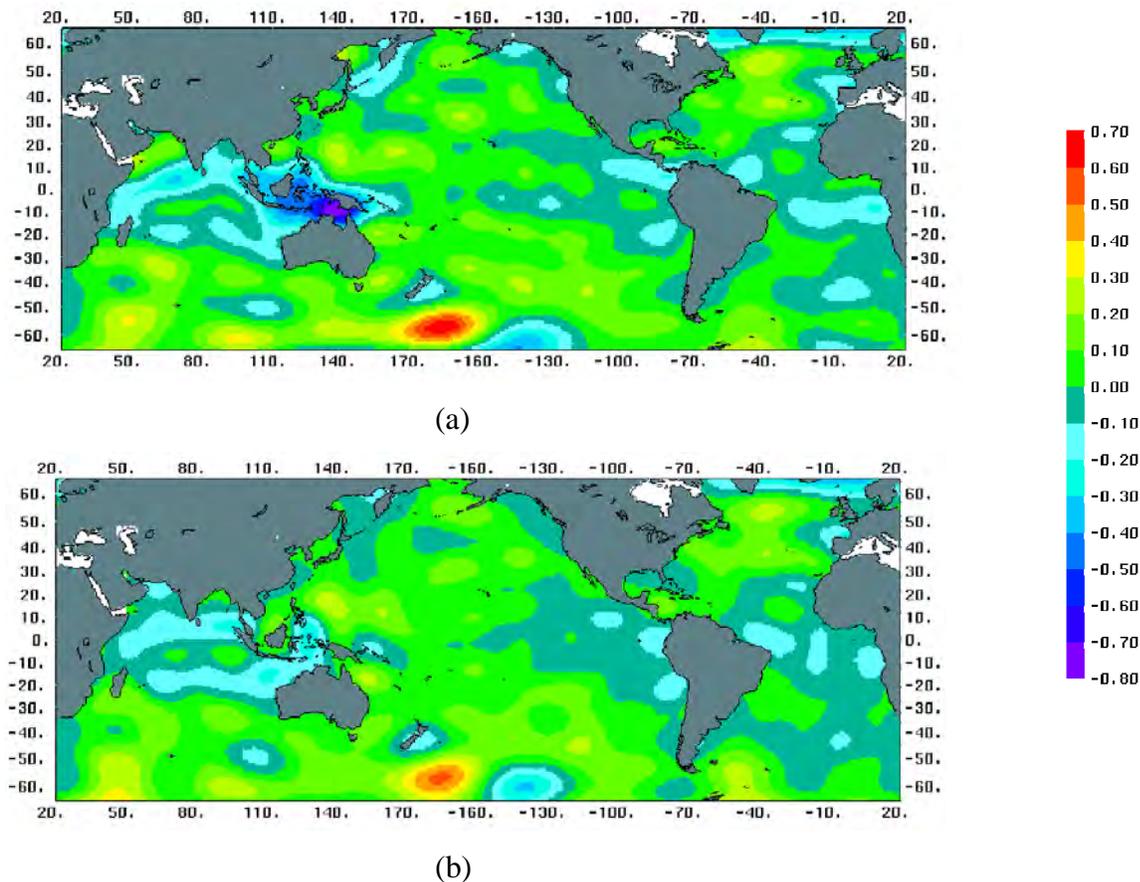
Figure 10.1.5.1–1. Dynamic ocean topography differences, T/P minus POCM–4B, based on spherical harmonic expansions to degree 18. The geoid undulation from JGM–3/HDM180 is used in (a), while the geoid undulation from EGM96 is used in (b). Units are meters.
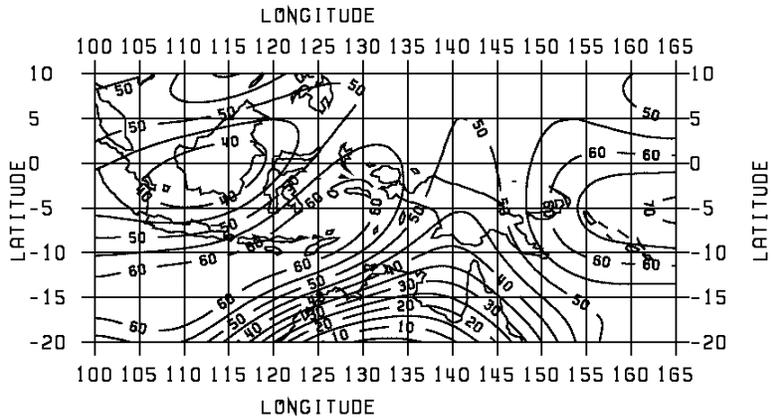
(a)
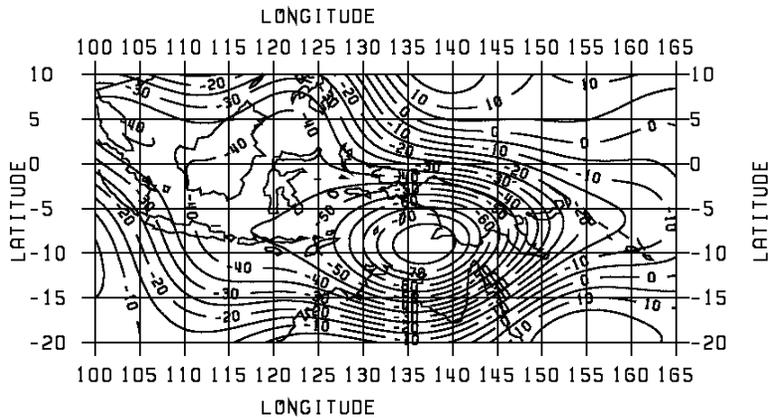
(b)
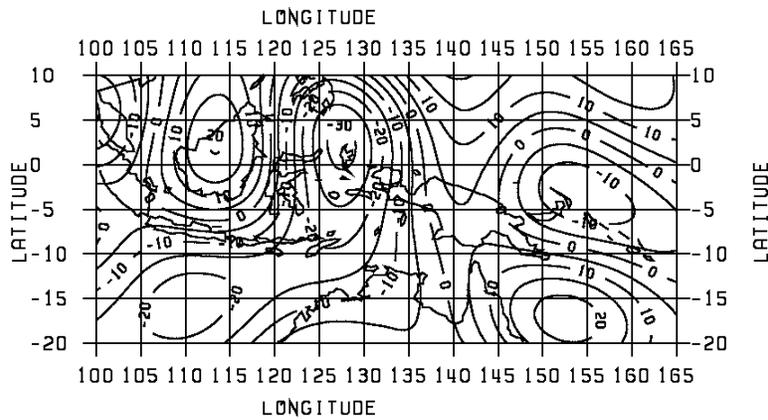
(c)

Figure 10.1.5.1–2. Dynamic ocean topography in the Banda Sea, based on expansions to degree 18: (a) from POCM–4B, (b) difference T/P (JGM–3/HDM180)–POCM–4B, (c) difference T/P (EGM96)–POCM–4B.

10–18

Considering the results in Table 10.1.5.1–2, we see a clear improvement in the comparisons when EGM96 is used with any of the DOT models. In addition, POCM–4B model yields slightly better agreement with the T/P DOT estimate than the POP(96) model, a result also reported in *Rapp, Zhang, and Yi* [1996].

An updated (1994) version of the Levitus DOT was also analyzed in August 1996, with the estimate of DOT provided by *C. Wagner* [1996, *private communication*]. These new data were referenced to a 1000 m (approximately) depth so that the comparisons with TOPEX/geoid data were significantly poorer (±28 cm v. ±14 cm) than those reported in Table 10.1.5.1–2, where the reference depth for the *Levitus* [1982] solution was approximately 2250 m (actually 2250 dB).

To understand the contribution of the lower depths of the ocean to DOT determinations, an expansion of the Levitus data at the 1050 dB level was made and compared to the expansion of the data reference to the 2250 dB level. To degree 18, the difference was ±10.9 cm. Plots of the difference between the two DOT estimates showed that much of the difference occurred south of 40°S.

Table 10.1.5.1–2. Difference between dynamic ocean topography using 2 years of T/P data with two geopotential models and three ocean-data-based models, to degree 18.

Geopotential Model	Dynamic Ocean Topography Model		
	POCM–4B RMS (cm)	POP(96) RMS (cm)	Levitus (1982) RMS (cm)
JGM–3/HDM180	13.4	14.4	14.7
EGM96	10.5	11.8	13.7

10.1.5.2 Current Velocity Comparisons

Section 5.5.3 of this report described the determination of "upper ocean geostrophic velocity" using dynamic ocean topography information. As can be seen from eqs. (5.5.3–1 and –2), the determination of the u and v velocity components depends on the slope of the DOT. Consequently, comparisons of velocity information between the TOPEX/geoid and a circulation model (e.g., POCM–4B) reveal somewhat different information than the DOT comparison. These type of comparisons have been described in *Rapp, Zhang, and Yi* [1996, p. 22590, also Table 6]. A similar procedure was followed in the evaluations for this report. The spherical harmonic expansions of the DOT for the TOPEX/geoid were differenced with the representation of the DOT from the POCM–4B model. This $\Delta\zeta$ representation was then used to calculate the Δu and Δv velocity components on a 2.5° x 2.5° grid. Statistics were calculated for all ocean data points from 62.5°N to 62.5°S excluding points near the Equator (10°N to 10°S). The velocity differences are given in Table 10.1.5.2–1 when JGM–3/HDM180 and the EGM96 geopotential model are used.

Table 10.1.5.2–1. Statistics of geostrophic flow velocity differences of T/P geoid vs. POCM–4B to degree 18.

	JGM–3/HDM180 (cm/s)	EGM96 (cm/s)
RMS u	±3.0	±2.2
Max u	8	11
Min u	−21	−16
RMS v	±1.9	±1.5
Max v	16	13
Min v	−19	−11
RMS V	±3.7	±2.7
Max V	24	20

One clearly sees from this table the approximately 30 percent reduction in the velocity differences when the EGM96 model is used instead of JGM–3/HDM180. In addition, most of the extreme differences are also reduced.

Note that the velocity difference calculations were not carried out with all the models developed as part of the project. The dynamic ocean topography comparisons were considered one of the primary evaluation tools in the model development, and so comparisons of DOT were made with most of the models. The velocity comparisons were then made for the final model (EGM96) and for the JGM–3 model augmented by the next-to-last high-degree component based on a block-diagonal/quadrature solution.

10.1.5.3 A Few Comments on the GCM Comparisons

The evaluation of geopotential models via the altimeter/geoid undulation dynamic ocean topography comparisons is just one step in the overall model evaluation. In doing such evaluation, there is a presumption that the global circulation model (or hydrographic data) is sufficiently accurate that the comparisons carried out convey meaningful information. As demonstrated in *Rapp, Zhang, and Yi* [1996] and in this report, improved DOT comparisons are found with geopotential models that also perform better in other evaluation tests. Nevertheless, one must be cautious in these GCM comparisons because there are errors in the DOT determinations that are difficult to quantify. The errors in a GCM may be measured in terms of DOT estimates, sea-surface height variability on different time scales, sea-surface slopes, eddy kinetic energy, etc.. An evaluation of the POCM–4B model using T/P data and hydrographic data has been described by *Stammer et al.* [1996]. This paper notes "that a present state of the art global OGCM simulates many aspects of the large scale general circulation surprisingly well." The authors also indicate, however, that "there are substantial problems where . . . the most prominent model failure is the general tendency towards a too weak model circulation on all scales."

A comparison of the POP global circulation model with information obtained from T/P data is described by *Fu and Smith* [1996]. These authors note "that the sea level variance produced by

the model is generally less than the observation by a factor of 2 primarily in the eddy-rich regions." By itself this would not be a problem in the evaluation of geopotential models because such computation considers average DOT values over 1, 2, or more years. However, if eddy generated by a model are not constant in time or are in the wrong geographic location, problems in the comparisons could exist depending on the updated scales over which the comparisons take place. Discussion and results by *Smith* [1996] demonstrate that the POCM–4B DOT has eddies incorrectly located in the Gulf Stream region. Comparisons of DOT in such local regions with altimeter/geoid information would be difficult to interpret considering the numerous sources of error. For the spatial resolution (1100 km) considered in this paper, high-frequency spatial errors in the POCM–4B model most probably have little impact. As the accuracy improves in our geoid undulations, allowing us to extend the comparisons to higher degrees of expansion, it will be even more important to discuss the accuracy of a GCM.

Finally, one needs to consider how new GCMs will be developed and if such models could still be used in the evaluation of geopotential models. *Stammer et al.* [1996] describe the development of the Semtner–Chervin-type model, such as POCM–4B. They point out some problems related to temporal aspects of the model. They suggest that altimeter-derived sea-surface height data can be assimilated into the GCM estimation so that the resultant model will be more representative of the real world ocean, in terms of heat content, salinity, variability, etc.. The use of such an improved model for the evaluation of geopotential models using DOT and velocity comparisons will depend on the use of geoid undulation information in the GCM estimation process with the incorporation of the altimeter data.

10.1.5.4 Geoid Undulation Accuracy and the Highest Degree for Which the Determination of Dynamic Ocean Topography Appears Reasonable

We next turn to the geoid undulation accuracy in the ocean domain and its comparison with the magnitude of the dynamic ocean topography. A discussion of this nature may be found in *Rapp, Zhang, and Yi* [1996, p. 22585; Figure 3] and *Tapley et al*. [1996, Plate 8] for the JGM–3 geopotential model. Section 5.5.2 of this report describes the undulation accuracy calculation in the ocean domain using orthonormal functions. For the study here, only the standard deviations of the coefficients of the EGM96 model were considered, as was the case when the JGM–3 results were reported in *Rapp, Zhang, and Yi* [1996]. The undulation accuracy, by degree, for the JGM–3 model and EGM96, to degree 23, are given in Table 10.1.5.4–1. The values for JGM–3 are identical to the values given in Table 1 of *Rapp, Zhang, and Yi* [1996]. The standard deviations of the EGM96 geoid undulations are smaller than those of JGM–3 by a factor of about 2 or 3 above degree 8. The cumulative geoid undulation standard deviations for EGM96 to degree 10, 15, 18, and 20 are as follows: ±2.2 cm, ±3.8 cm, ±4.6 cm, and ±5.1 cm. To degree 20, the cumulative geoid undulation standard deviation for the JGM–3 model, in the ocean domain, is ±10.9 cm. The standard deviations of the EGM96 and JGM–3 model are plotted in Figure 10.1.5.4–1. The significant apparent improvement is dependent on the formal error calibration of the low-degree combination geopotential model, which is discussed in Section 7.

Table 10.1.5.4–1. Geoid undulation accuracy in ocean domain and DOT comparisons with the POCM–4B.

Degree	Geoid Undulation Accuracy in Ocean Domain		POCM–4B vs. T/P EGM96	
	JGM–3 (cm)	EGM–96 (cm)	Difference RMS (cm)	Correlation Coefficient
2	0.3	0.2	±3.6	1.00
3	0.4	0.3	4.2	0.99
4	0.6	0.4	3.0	0.99
5	0.8	0.6	2.3	0.98
6	1.0	0.7	1.5	0.89
7	1.3	0.8	3.0	0.89
8	1.5	0.9	1.9	0.95
9	1.9	1.1	2.4	0.92
10	2.1	1.1	1.9	0.84
11	2.4	1.3	2.1	0.69
12	2.7	1.3	2.3	0.58
13	2.9	1.4	2.5	0.67
14	3.1	1.4	2.1	0.77
15	3.3	1.5	2.0	0.61
16	3.4	1.5	2.0	0.29
17	3.5	1.5	2.4	0.25
18	3.6	1.5	2.2	0.44
19	3.7	1.5	1.9	0.22
20	3.6	1.5	2.1	0.28
21	3.6	1.4	1.9	0.12
22	3.3	1.3	1.7	0.03
23	3.0	1.2	1.4	0.24

Also shown in Table 10.1.5.4–1 is the root mean square difference between the dynamic ocean topography implied by POCM–4B and by the T/P altimeter data using the geoid undulation from the EGM96 model, and the correlation coefficients, by degree, between the two DOT estimates. The results can be compared to corresponding values for the JGM–3 model given in Table 5 of *Rapp, Zhang, and Yi* [1996]. The difference values are plotted in Figure 10.1.5.4–1. As would be expected from the cumulative values given in Table 10.1.5.1–1, the degree differences are somewhat smaller with the EGM96 model than when the JGM–3 model is used. The improvement is most significant below degree 18.

Also plotted in Figure 10.1.5.4–1 is the square root of the DOT power in the ocean domain. In previous discussions, one has been interested in the degree at which the curve intersects with the undulation standard deviation, as this is an approximate indication of when the signal-to-noise ratio is one. In such an estimation, one ignores the error in the DOT power. One sees that the undulation standard deviation is close to the DOT magnitude at degree 17 and becomes greater than it at degree 22. One notes, however, that the difference between DOT from TOPEX/EGM96 and POCM–4B is almost equal to the signal of POCM–4B at degree 16 and exceeds it after that. (When JGM–3 was used in this type of analysis, the corresponding degree was 12 (*Rapp, Zhang, and Yi* [1996, Figure 3].)
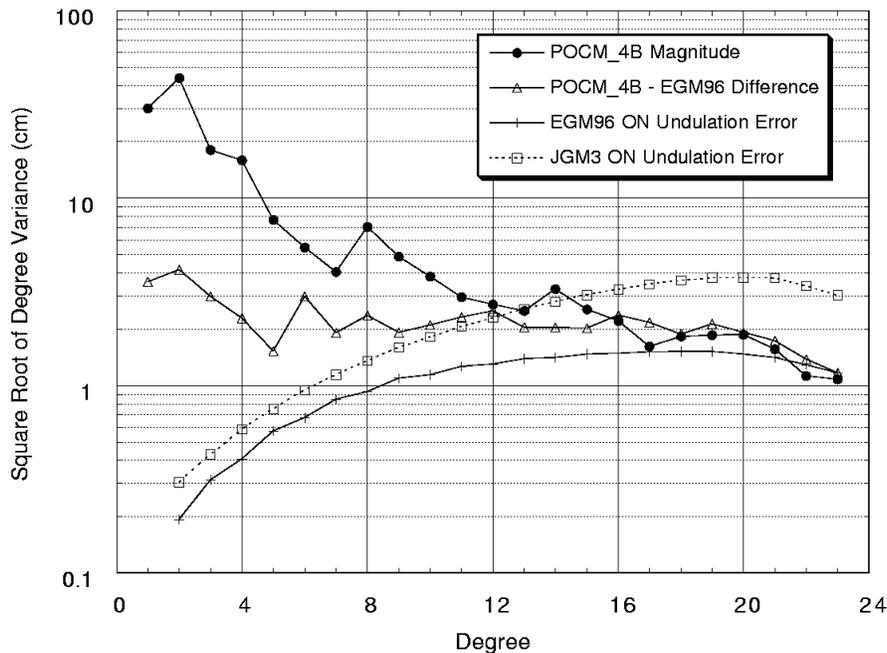
Figure 10.1.5.4–1. The standard deviations of the EGM96 and JGM–3 models.

A final item to consider are the degree correlation coefficients given in Table 10.1.5.4–1. At the lower degrees, the correlation is over 0.9. As the degree increases, the correlations decrease to about 0.5 at degree 15. The correlation then falls at degrees 16 and 17, increases again (to 0.44) at degree 18, and then falls again.

From the discussion one needs to estimate the maximum degree for which DOT estimation should be made using the EGM96 model. The picture is not as clear as it was for the JGM–3 model when degree 14 was recommended. In the EGM96, a maximum degree might be 21 based on signal to noise (of the undulation) being 1, or degree 16 when the DOT difference is equal to the signal, or degree 15 where the correlation remains above 0.5. Considering this information, it is suggested that the maximum degree for which DOT can be reliably estimated using the EGM96 model is 18. The primary motivation for this value lies in the moderate (0.44) correlation that exists between the T/P EGM96 and POCM–4B DOT estimates. This selection of degree 18 is the reason that cumulative values in previous sections dealing with the DOT comparisons have given values to degree 18.

Fu and Smith [1996] suggest a simple procedure to calculate the cumulative error in the DOT from a GCM assuming the altimeter sea-surface height data contributes ±2 cm to the system errors. The error in the GCM would be:

$$A = (B^2 - C^2 - D^2)^{1/2}$$
(10.1.5.4–1)

where:

A   is the cumulative error in the GCM model;

B   is the root mean square cumulative difference between the GCM DOT estimate and that of the altimeter/geoid analysis;

C   is the cumulative geoid undulation standard deviation;

D   is the altimetric system error.

At degree 18, the value of *B* is ±10.5 cm, the value of *C* is 4.6 cm, and with $D = ±2$ cm, the value of *A* is ±9.2 cm. The value will vary by degree.

10.1.6 Comparisons With an ERS–1 Profile in the Antarctic Region

Section 5.7 described a comparison of geoid undulations defined on an ERS–1 track in the Weddell Sea region. The track is divided into north and south segments, where the south segment extends to 77°S. Statistics on the comparisons for the two segments are given in Table 10.1.6–1.

Table 10.1.6–1. Comparison of geoid undulations implied by an ERS–1 35-day track (6008) in the Weddell Sea with that computed from geopotential models.

Model	Part A: 65.0°S to 72.0°S				Part B: 72.0°S to 77.9°S			
	Mean Diff. (cm)	Std. Dev. (cm)	RMS Diff. (cm)	Abs. Max (cm)	Mean Diff. (cm)	Std. Dev. (cm)	RMS Diff. (cm)	Abs. Max (cm)
OSU91A	−2	23	23	103	611	274	669	961
JGM–3/HDM180	−3	28	28	141	187	149	240	377
TEG–3/HDM180	6	23	24	80	141	104	175	292
EGM–X02	0	18	18	91	198	169	261	468
V068	−16	25	30	141	105	85	135	274
HDM190	−17	26	31	146	101	76	126	250
PGS7337B/HDM190*	10	32	34	105	131	134	187	281

*EGM96

In considering the standard deviations for Part A, one sees that the minimum standard deviation (±18 cm) was achieved with the EGM–X02 model. The final model adopted (EGM96) shows the poorest fit of the models shown for Part A. For Part B, the EGM–X02 model gives the poorest fit, excluding OSU91A. The best fits are with the V068 and HDM190 models. The EGM96 results are better than those obtained with JGM–3 but poorer than most of the other contemporary models.

The evaluation of geopotential models using this ERS–1 track is problematic, as reliable estimates of dynamic ocean topography are lacking in the south part of the track and ice is a possible source of error in the derived sea-surface height. The editing of altimeter data that are used in the geopotential model development can also affect how well a model will yield geoid undulations that fit these data. ERS–1 data are an excellent source of information in this region, and care needs to be taken in the incorporation of such data in the geopotential model estimation.

10.1.7 Discrete Comparisons With Geoid Undulations Implied by Altimeter Data and an Ocean Circulation Model

We present here the results from the comparisons of model geoid undulations to undulations implied by altimetric Sea Surface Heights (SSHs) and the DOT implied by the POCM–4B ocean circulation model. These comparisons were made according to the formulation presented in Section 5.6. We consider the following models: The composite model JGM–3/OSU91A, which represents the state of the art in oceanic geoid modeling prior to the joint project work; the NQ solution V068; and the BD solution HDM190 (both of these models were developed without the benefit of "direct" tracking altimetry). A composite model was formed by augmenting the 70x70 comprehensive solution PGS7337B with the HDM190 coefficients ($n = 71$ to 359) and with V068 providing the $n = 360$ coefficients. This composite model is designated "C" here. Table 10.1.7–1 summarizes the results from these comparisons (the SSH data selection criteria and the total number of SSH values used from each mission are given in Section 5.6).

Table 10.1.7–1. Statistics of geoid undulation differences: altimetry/POCM–4B minus model-implied values. Maximum degree of POCM–4B DOT coefficients is 24, maximum degree of all geopotential models is 360. Units are cm.

Mission	T/P		GEOSAT		ERS–1	
Model	Mean	S. Dev.	Mean	S. Dev.	Mean	S. Dev.
JGM–3/OSU91A	51.8	28.8	51.8	29.6	51.3	29.2
V068	52.6	25.8	52.8	26.8	52.3	26.5
HDM190	52.7	25.7	52.9	26.7	52.3	26.4
C	52.9	21.0	53.1	22.8	52.6	22.1

From Table 10.1.7–1 one observes that:

1) All of the models developed within the joint project perform significantly better than the JGM–3/OSU91A model, as judged by the standard deviation of the undulation differences.

2) It is worth noting that both V068 and HDM190 outperform JGM–3/OSU91A, although these two models do not incorporate "direct" altimeter data, while JGM–3 does. This demonstrates the progress made in the satellite-only solution (EGM96S), upon which V068 and HDM190 were developed, and the progress made in the estimation of the altimetry-derived anomalies, which support the oceanic geoid determination that is achieved by V068 and HDM190.

3) HDM190 always performs slightly better than V068, although the difference between these two models is very small.

4) The contribution of "direct" altimetry becomes clear when the results from the composite model C are compared to the results from V068 or HDM190. Model C further reduces the standard deviation of the geoid undulation differences by about 4 to 4.5 cm.

5) One should also notice the excellent agreement between the mean differences computed on the basis of the three different solutions (V068, HDM190, and C) across the three different missions. The mean difference represents (primarily) the aggregate effect of the T/P altimeter bias and of the difference between the adopted (6378136.3 m) and the ideal values of the semimajor axis of the reference ellipsoid.

The geographic distribution of the residual SSHs (see eq. [5.6–2]) was plotted for all three missions and all four geopotential models listed in Table 10.1.7–1. We have chosen to show here the residuals obtained from the ERS–1 data comparisons (because they produce the densest ground track), in Figures 10.1.7–1a through 10.1.7–1d (the residuals plotted in these figures are *centered*, i.e., the mean difference has been subtracted from the plotted values). The plots corresponding to the other two missions showed very similar patterns and are not presented here. The impact of "direct" altimetry is evident from a comparison of Figure 10.1.7–1d to either 10.1.7–1b or 10.1.7–1c. Several medium-wavelength features are present in 10.1.7–1b and 10.1.7–1c, which are largely removed in 10.1.7–1d. Figures 10.1.7–1a and 10.1.7–1d correspond to models developed using "direct" altimetry. The improvement achieved with solution C as compared to JGM–3/OSU91A is evident from the comparison of these two figures. This is also clearly visible when the histograms of the two sets of residuals are compared.

Figures 10.1.7–1a and 10.1.7–1d show that there are certain geographic regions where relatively large residual SSHs persist. Two such areas exist in the south Pacific Ocean, around ($\varphi \approx$ –55°, $\lambda \approx$ 180°) and ($\varphi \approx$ –55°, $\lambda \approx$ 220°). Significant residual SSHs are also present in the northern Atlantic region between Greenland and Scandinavia. One should always keep in mind that since POCM–4B is not errorless, some of these discrepancies may indicate problems of the circulation model rather than of the geopotential solution. Considering the discussion in Section 5.6 (see eq. [5.6–7]), the results presented here indicate that the commission error of the solution C, up to degree 360, is not expected to exceed ±22 cm, in an oceanwide RMS sense. If one accepts an estimate of ±10 cm for the total error (commission plus omission) of the circulation model, and an estimate of ±2 cm for the error of the altimetric SSHs (mean tracks) (see also Section 10.1.5.4), then the total (commission plus omission) RMS error in oceanic geoid undulations (point values) from solution C is estimated based on the present comparisons to be approximately ±19 cm.

In Section 8.6.1, we discussed the close agreement between the high-degree solutions V068 and HDM190. Comparisons of geoid undulations implied by altimetric SSHs and the POCM–4B circulation model to the undulations implied by the two geopotential models offer a possibility of discriminating between V068 and HDM190. On an oceanwide basis, Table 10.1.7–1 indicates that HDM190 is a slightly preferable solution. We investigated this issue further by performing comparisons over two areas where V068 and HDM190 produced geoid undulations that were visibly different in Figure 8.6.1–5. The two areas selected cover the Aleutian Trench and the Mendocino Fracture Zone (FZ). The specific limits of these two areas are defined as:
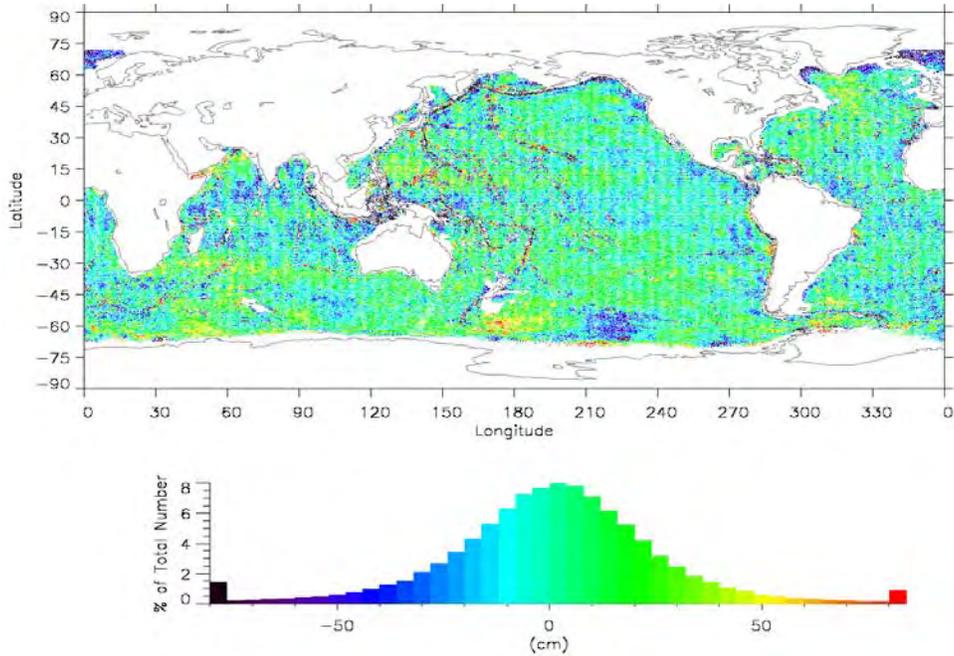
(a)
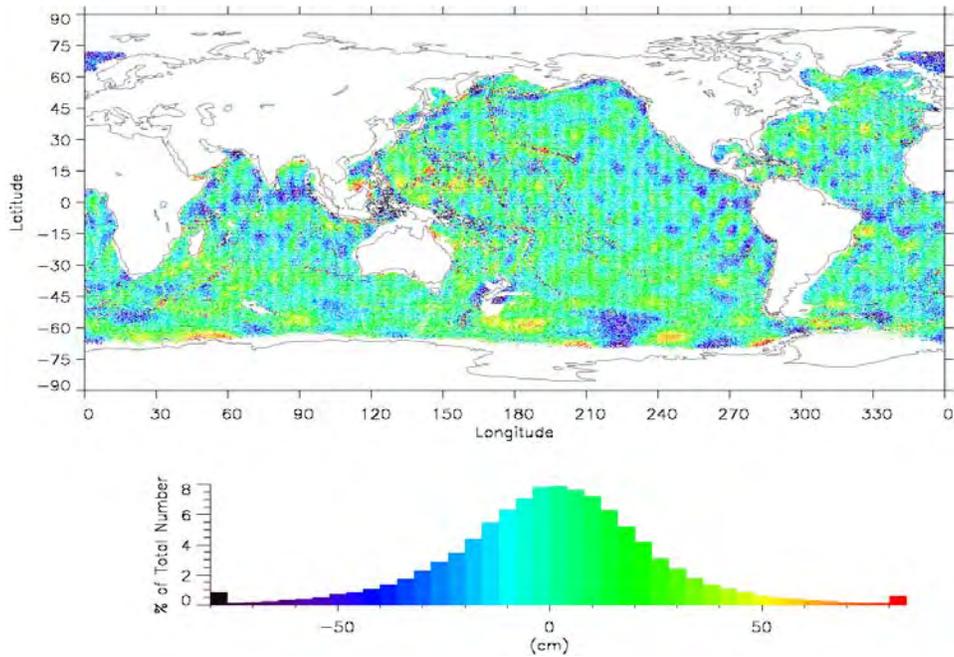
(b)

Figure 10.1.7–1. Geographic distribution of the residual SSH obtained from ERS–1 altimetry/POCM–4B minus geopotential model-derived geoid undulations: (a) JGM–3/OSU91A, (b) V068, (c) HDM190, and (d) EGM96. Maximum degree of all geopotential models is 360, maximum degree of POCM–4B is 24.
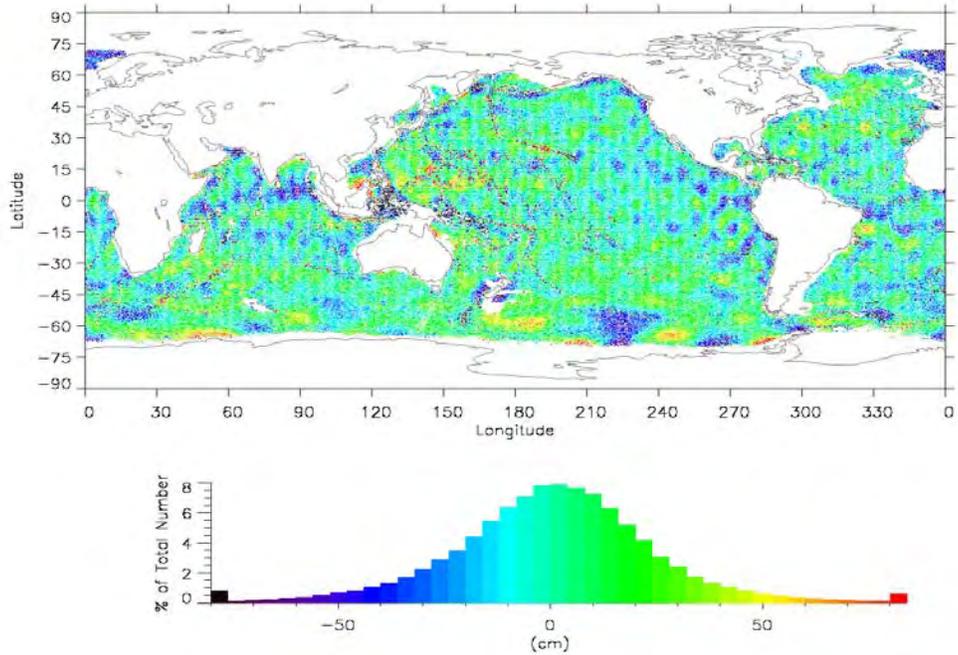
(c)
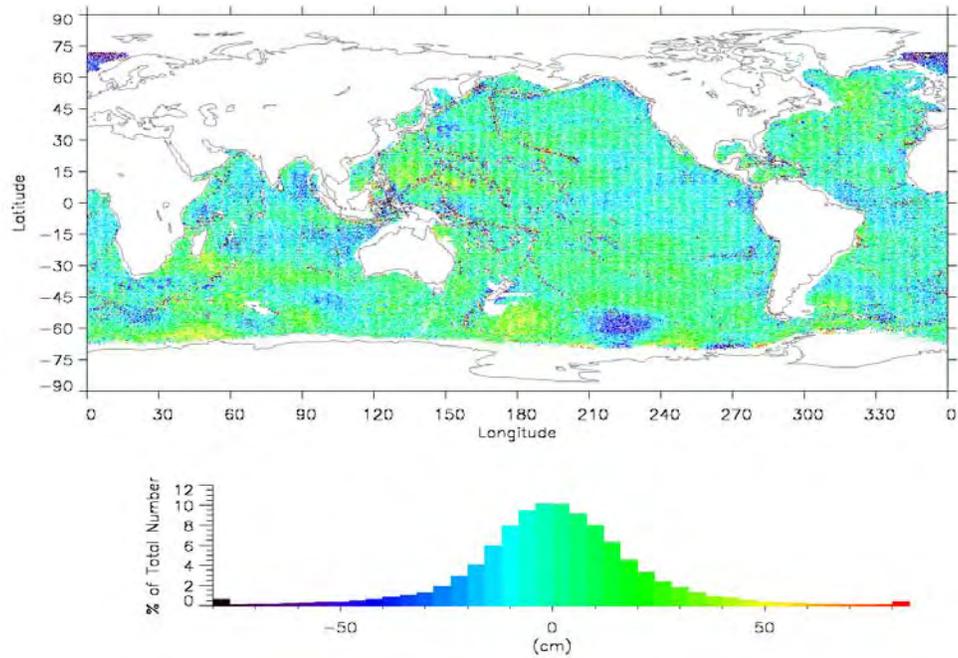
(d)

Figure 10.1.7–1. Geographic distribution of the residual SSH obtained from ERS–1 altimetry/POCM–4B minus geopotential model-derived geoid undulations: (a) JGM–3/OSU91A, (b) V068, (c) HDM190, and (d) EGM96. Maximum degree of all geopotential models is 360, maximum degree of POCM–4B is 24.

Aleutian Trench: $50° < \varphi < 60°, 160° < \lambda < 210°$

Mendocino FZ: $39.5° < \varphi < 40.5°, 210° < \lambda < 235°$

Over the Aleutian Trench area, 16200 SSHs and 15950 along-track SSH slopes were used, while 1175 SSHs and 1103 SSH slopes were used over the Mendocino FZ, in the comparisons summarized in Table 10.1.7–2.

Table 10.1.7–2. Standard deviation of geoid undulation differences (altimetry/POCM–4B minus the model-implied values) and RMS residual along-track SSH slope, over two ocean areas. Maximum degree of POCM–4B DOT coefficients is 24, maximum degree of the geopotential models is 360.

Area	Aleutian Trench		Mendocino FZ	
Model	S. Dev. (cm)	Res. Slope (")	S. Dev. (cm)	Res. Slope (")
V068	39.9	3.34	23.0	3.22
HDM190	37.3	3.25	22.2	3.19

Table 10.1.7–2 indicates that in both areas the HDM190 model is in closer agreement with the information obtained from altimetry/POCM–4B than is the V068 solution. Comparisons of residual along-track SSH slopes were also made on an oceanwide basis, for V068 and HDM190. For TOPEX, GEOSAT, and ERS–1, the residual SSH slopes obtained from V068 were (1.973´´, 2.265´´, 2.394´´) while for HDM190 the corresponding values were (1.968´´, 2.259´´, 2.389´´). The number of slope values used from each mission were (519126, 833866, 1457164). Although the difference between the V068 and the HDM190 results is small, HDM190 consistently performs better than V068. This provides a good indication that the high-degree coefficients of HDM190 are slightly more accurate than the corresponding coefficients of V068.

10.2 The Definition of the EGM96 High-Degree Geopotential Model

The data analysis and the preliminary model development and evaluation activities that were discussed in the previous sections have yielded three combination geopotential solutions that are candidates for the definition of EGM96. These are:

1) PGS7337B: a comprehensive combination solution complete to degree 70, which incorporates altimetry in the form of "direct" tracking.

2) V068: a numerical quadrature combination solution complete to degree 360.

3) HDM190: a block-diagonal combination solution complete to degree 359.

The primary goal of the joint project is to develop a combination solution complete to degree 360. Of the three candidate models above, only V068 is capable of meeting this goal on its own. To define EGM96 to degree 360, one has to consider the relative performance of the three solutions, over the common part of their bandwidth, as well as the performance of models that

can be formed by "cutting and pasting" different solutions together. Some of the pertinent results are summarized next.

The results of the orbit residual tests reported in Section 10.1.1 (e.g., Tables 10.1.1.1–1 and –2) indicate that the comprehensive solution PGS7337B (when accompanied by the corresponding tide model PGS7337B), yields the best orbit modeling capability, for most of the SLR satellites tested. However, both V068 and HDM190 demonstrate orbit modeling performance that is quite comparable to that of PGS7337B.

The GPS/leveling tests performed at Ohio State University (e.g., Table 10.1.2–1) indicate that the composite model PGS7337B/HDM190 outperforms both the V068 and HDM190 solutions. Of the two high-degree models, HDM190 was found to perform slightly better. In addition, the tilt values (Table 10.1.2–2) over the U.S. are smaller for the composite model PGS7337B/HDM190 than for V068 or HDM190. The GPS/leveling tests performed at GSFC (see Tables 10.1.3–1 and 10.1.3–2), support also the PGS7337B/HDM190 choice.

The evaluation of the candidate models via comparisons with altimeter data and Ocean Circulation Model information provides a very clear distinction between the candidate solutions. The absence of "direct" altimetry from V068 and HDM190 is evident from the results of both the OrthoNormal (ON) spectral comparisons discussed in Section 10.1.5 (Table 10.1.5.1–1) and the discrete evaluations discussed in Section 10.1.7 (Table 10.1.7–1). These tests demonstrate that, in order to ensure the highest oceanic geoid accuracy, one needs to incorporate altimetry as "direct" tracking into the current combination solutions. Since PGS7337B is the only candidate model that includes "direct" altimetry, the degree 70 portion of EGM96 is defined by the coefficients of PGS7337B. The results of Section 10.1.7 also indicate that the higher degree coefficients of HDM190 are slightly better than the corresponding coefficients of V068. The $n = 71$ to 359 coefficients of EGM96 are obtained, therefore, from HDM190, while V068 contributes the $n = 360$ coefficients of EGM96.

Up to degree 70, EGM96 is accompanied by a full error covariance matrix, which is obtained as part of the development of PGS7337B. From degree 71 to degree 359, the EGM96 coefficients are accompanied by their error variances, obtained from the development of HDM190. The $n = 360$ EGM96 coefficients were all assigned an equal value for their error variance. This value is obtained from the RMS error per degree per coefficient, for the $n = 359$ coefficients of HDM190. The error estimates of the coefficients of V068 are not used.

Apart from the tests and evaluations performed by the EGM96 developing team, the independent evaluations of test models conducted by the SWG (see Section 9) also provided feedback that overall supports the particular manner in which EGM96 is defined.

The cut and paste approach that we use here to define EGM96 (which is similar to the approach used in the OSU91A definition) has the disadvantage that it results in a discontinuous error spectrum for the 360 model (at $n = 70$), as is discussed next. This approach is necessitated primarily by the computational load associated with the processing of "direct" altimetry. Data from upcoming geopotential mapping missions such as GRACE may alleviate the need for such piecewise definitions of the high-degree model. This may become possible, since such missions

promise to enable highly accurate global gravity field mapping, independent of satellite altimetry (at least in the form of "direct" tracking).

10.3 Spectral Estimates of Gravimetric Signals and Their Associated Errors

In this section we present and discuss the spectral information implied by the EGM96 model for the signal and error of various functionals of the disturbing potential (e.g., gravity anomalies, geoid undulations, geoid undulation differences). These spectral estimates are also compared to corresponding values implied by other geopotential models such as OSU91A and JGM–3.

One can compute degree variances from potential coefficients and their associated errors, referring to spheres of various radii. However, when such degree variances (or corresponding RMS quantities) are compared to values obtained from comparisons with data residing on the surface of the Earth, one needs to refer the spectral estimates to a sphere of radius equal to that of the mean-Earth ($R = 6371$ km). In this section, all of the computations of spectral quantities are made referring to the mean-Earth sphere, according to formulas that are given next.

10.3.1 Gravity Anomaly Signal and Error Spectra

The potential coefficients (and their associated errors) of JGM–3, HDM190, and EGM96 are consistent with scaling values:

$$GM = 3986004.415 \times 10^8 \text{ m}^3\text{s}^{-2}$$
$$a = 6378136.3 \text{ m}$$
(10.3.1–1)

The OSU91A coefficients and errors are consistent with the following scaling values [*Rapp et al.*, 1991, p. 10]:

$$GM' = 3986004.36 \times 10^8 \text{ m}^3\text{s}^{-2}$$
$$a' = 6378137. \text{ m}$$
(10.3.1–2)

We have accounted appropriately for this different scaling, so that the results presented here are directly comparable. The (point value) gravity anomaly signal degree variances (c_n), referring to the mean-Earth sphere, are given by [*Pavlis*, 1991, eq. (3.121)]:

$$c_n = \left(\frac{GM}{a^2} \right)^2 (n-1)^2 \left(\frac{a^2}{R^2} \right)^{n+2} \sum_{m=-n}^{n} \left(\overline{C}_{nm} \right)^2$$
(10.3.1–3)

Similarly, the gravity anomaly error degree variances are:

$$\varepsilon c_n = \left(\frac{GM}{a^2} \right)^2 (n-1)^2 \left(\frac{a^2}{R^2} \right)^{n+2} \sum_{m=-n}^{n} \left(\varepsilon \overline{C}_{nm} \right)^2$$
(10.3.1–4)

where $\varepsilon \overline{C}_{nm}$ are the estimated standard deviations of the potential coefficients. The anomaly degree variances of the difference between two models can be computed using eq. (10.3.1–3), with $\Delta \overline{C}_{nm}$ in place of $\overline{C}_{nm}$. Using the above equations, we computed the degree variances of the

anomaly signal and error implied by OSU91A, JGM–3, HDM190, and EGM96. Figure 10.3.1–1 shows some of the resulting curves, for the degree range 2 to 360, while Figure 10.3.1–2 focuses on the lower part of the spectrum ($n = 2$ to 120) for added clarity. The cumulative global RMS gravity anomaly signal and error implied by these four geopotential models is given in Table 10.3.1–1, for selected degrees of expansion. Notice that the error spectrum of OSU91A plotted in Figure 10.3.1–1 is based on the formal standard deviations of the OSU91A potential coefficients, while the values tabulated in Table 10.3.1–1 *for n > 260* were computed by replacing the (pessimistic) formal errors of this model, by the RMS anomaly signal itself. This procedure was suggested by [*Rapp et al.*, 1991, p. 64].
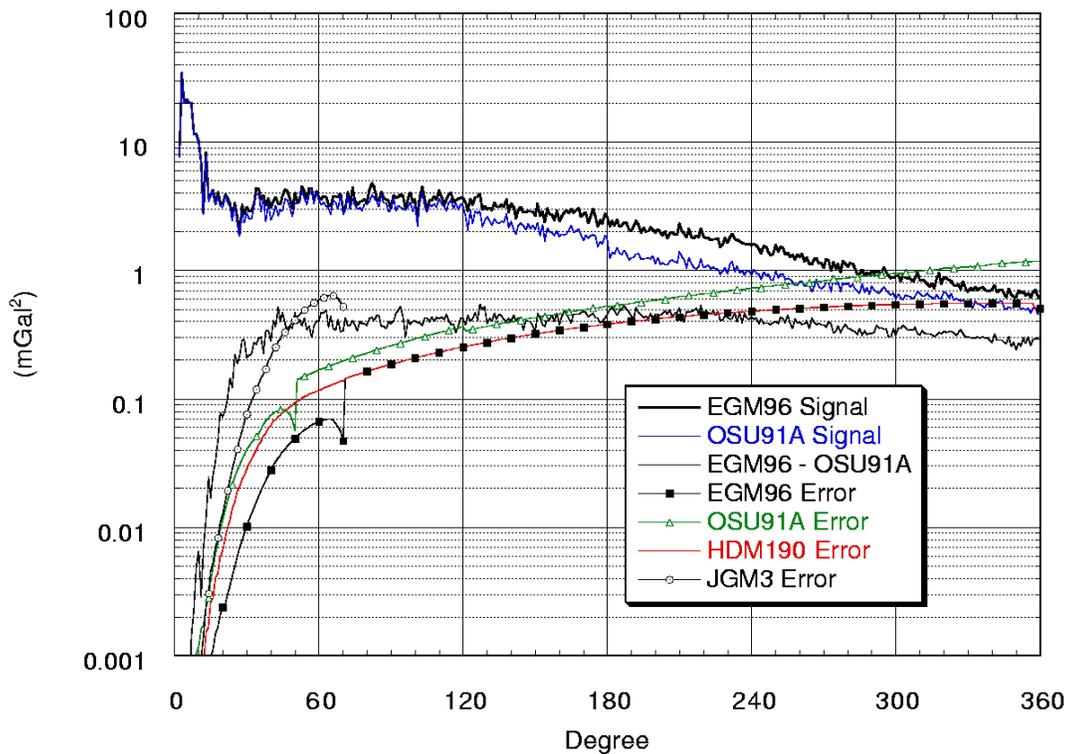
Figure 10.3.1–1. Gravity anomaly signal, differences, and error degree variances implied by some geopotential models. Values refer to $R = 6371$ km.

Several observations and remarks can be made by examining Figures 10.3.1–1 and 10.3.1–2 and the results of Table 10.3.1–1. Considering the signal spectra of OSU91A and EGM96, one observes that EGM96 implies significantly more power for the gravity anomaly than OSU91A, especially above degree $n \approx 120$. The two main factors that contribute to produce the observed behavior are:
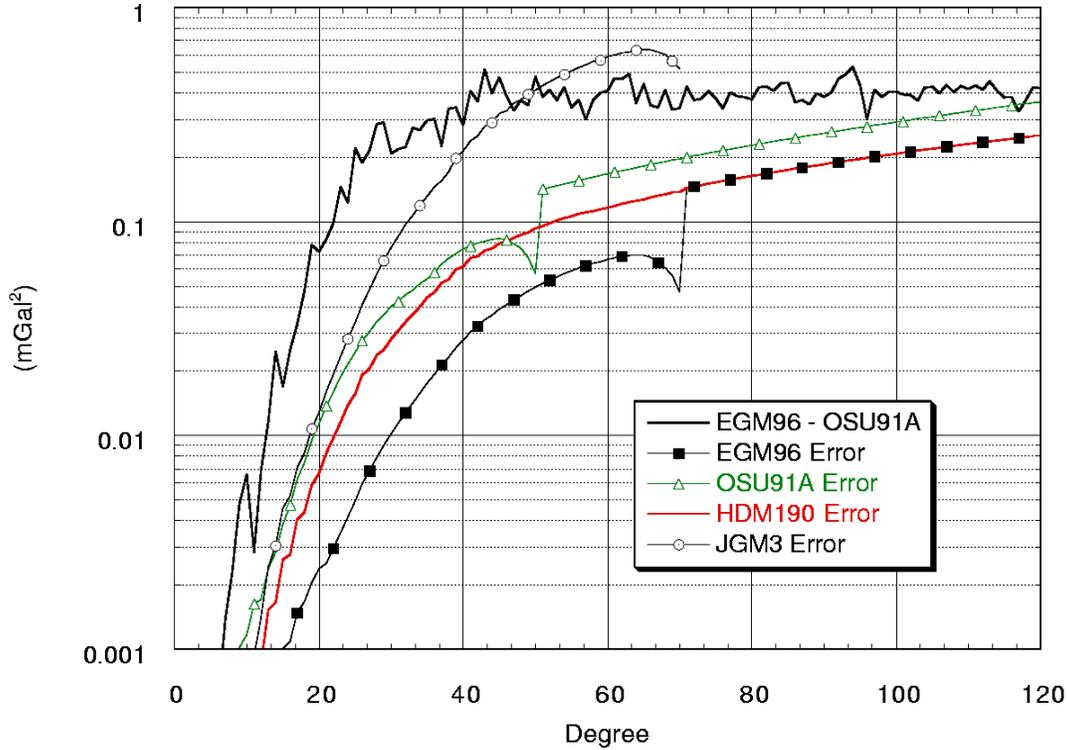
Figure 10.3.1–2. Gravity anomaly signal, differences, and error degree variances implied by some geopotential models, over the degree range 2 through 120. Values refer to $R = 6371$ km.

Table 10.3.1–1. Cumulative global RMS gravity anomaly signal and error (mGal) implied by four geopotential models for selected degrees of expansion.

	OSU91A		JGM–3		HDM190		EGM96	
Degree	Signal	Error	Signal	Error	Signal	Error	Signal	Error
36	15.662	0.785	15.823	1.071	15.829	0.663	15.853	0.401
50	16.960	1.286	17.197	2.263	17.272	1.209	17.364	0.810
70	18.876	2.242	19.099	4.036	19.135	1.951	19.394	1.375
120	22.752	4.350	—	—	23.415	3.700	23.628	3.431
180	25.417	6.687	—	—	26.893	5.731	27.079	5.561
360	28.224	12.683	—	—	30.906	11.074	31.067	10.987

1) The gravity anomaly merged file used here (see Table 8.3–1) contains significantly more terrestrial 30´ mean values, with more power, than the corresponding file used in the OSU91A model development [*Rapp et al.*, 1991, Table 19]. Also, the altimeter-derived 30´ mean anomalies used in EGM96 are somewhat "rougher" than those used in OSU91A. Furthermore, in EGM96, only ~3 percent of the Earth's area requires split-up and fill-in values, compared to ~18 percent in OSU91A. Split-up values originate from 1° data and,

therefore, are smoother than corresponding 30´ mean values. Also, the topographic–isostatic coefficients used to compute the higher (than $n = 36$ or 40) part of the fill-in values imply a smoother gravity anomaly spectrum than what is actually "observed" (compare Figures 7.2.2–1 and 10.3.1–1). The lack of available 30´ mean anomaly estimates based on actual gravity observations, which necessitated the use of more split-up and fill-in values when OSU91A was developed, may also be responsible for a small (but noticeable) "step" in the OSU91A signal spectrum at $n = 180$.

2) The BD technique used to estimate the higher degree coefficients ($n = 71$ to 359) of EGM96, estimates a somewhat rougher field than the NQ technique (see also Figure 8.6.1–3). There is also a very small "step" in the OSU91A signal spectrum at $n = 120$, which may be attributed to the quadrature weights of Type 2 that were used in its development.

One should also notice that EGM96 yields a more powerful spectrum compared to OSU91A, over the entire degree range 2 to 360. The fact that even at the lower degrees one observes more power in EGM96 can be partially attributed to the rougher spectrum estimated in the satellite-only solution (EGM96S), as a consequence of the SST data from GPS and TDRSS to lower altitude spacecraft. These data were not available in the GEM–T2 solution, upon which OSU91A is based. The removal of *a priori* constraints from the estimation of the 70x70 portion of EGM96 (in contrast to OSU91A) also contributes to the added power. Over the degree range 2 to 360, the global RMS (point) gravity anomaly difference between EGM96 and OSU91A is ±11.4 mGal, while over the degree range 2 to 70 it is ±4.1 mGal.

We consider now the error spectra associated with the various models. As expected, the HDM190 and the EGM96 errors are identical (by construction) above $n = 70$. HDM190 produces a practically continuous error spectrum (apart of a very small "step" at $n = 70$ and another at $n = 357$) over its entire degree range 2 to 360. In contrast, the cut and paste approach used to define EGM96 produces the undesirable discontinuity at $n = 70$. A similar problem is present in the OSU91A error spectrum at degree 50, which was the maximum degree in the GEM–T2 model.

Below degree 70, the apparent improvement observed when comparing the OSU91A versus the EGM96 errors is due to the more accurate satellite-only model (EGM96S versus GEM–T2), the more accurate and complete terrestrial anomaly data, and the T/P "direct" altimeter data (and their relative weighting). Above degree 70, the differences observed in the error spectra of EGM96 and OSU91A are in part due to the improved 30´ anomaly data in EGM96 and to the use of *a priori* constraints in the development of HDM190. Notice also that the quadrature weights of Type 2, used in OSU91A, produce a small "step" in its error spectrum at $n = 120$.

The difference between the EGM96 and the HDM190 error spectra below degree 70 reflects the different treatment of altimetry ("direct" tracking versus 30´ mean anomalies). This difference is a function of both the gravitational information content of the two forms of data *and* of the relative weights with which these data enter into the respective solutions.

The significant difference observed between the error spectra of JGM–3 and EGM96 requires careful examination, especially in view of its implications regarding geoid undulation accuracy,

as we will discuss in the next section. Three different components comprise each of these two models:

(a) A satellite-only solution.

(b) Surface gravity normal equations.

(c) Normal equations from "direct" altimetry.

The JGM–3 model [*Tapley et al.*, 1996] was developed by sequential addition of satellite-tracking data into the JGM–1 combination solution [*Nerem et al.*, 1994]. This means that there exists no satellite-only model, separately developed, that supports JGM–3 (i.e., JGM–3S was never developed). This also means that one cannot directly compare the satellite-only portion of JGM–3 to EGM96S to assess what part of the observed (formal) improvement in EGM96 is to be attributed to the additional satellite tracking data, or their different weighting as compared to the tracking data (and weighting) used in JGM–3. As far as differences in the (b) and (c) components of the two models, JGM–3 contains the *exact* same surface gravity information (with the same weighting) as was used in JGM–1 (and JGM–2). In JGM–1, the surface gravity normal equations were downweighted by a factor of 4 with respect to their weight used in OSU91A. The weighting of surface gravity data in OSU91A is similar to their weighting in EGM96. Therefore, the surface gravity information in JGM–3 is downweighted by a factor of 4 (approximately) with respect to EGM96. Although the gravity data used in JGM–3 originate from the older OSU October 1990 data base, their downweighting applied in JGM–3 is disproportionately low with respect to their quality. This surface gravity downweighting is certainly a major contributing factor to the pessimistic error spectrum that JGM–3 predicts at the higher degrees ($n > 25$). In addition, JGM–3 contains *exactly* the same "direct" altimeter data as JGM–1, and therefore does not benefit from the wealth of T/P altimetry which was used in EGM96. Although the weights assigned to "direct" altimeter data in EGM96 may require some further calibration, they are not expected to change so much as to explain the large differences in the two error spectra.

The relative weighting questions discussed here reflect mainly two things: First, the fact that relative weighting and model error calibration remain to be two of the most critical and difficult aspects of combination solution developments, and second, the different philosophies and optimization strategies that underlie the development of various gravitational models. JGM–1, –2, and –3 were models developed with the primary goal to support the highest possible accuracy in orbit determination applications, particularly for T/P. OSU91A and EGM96, on the other hand, have put at least equal emphasis on geoid modeling performance. Downweighting of surface gravimetric data in JGM–1, –2, and –3 was found to improve slightly the orbit fit results obtained from these models. In EGM96, such downweighting was not found to be necessary or beneficial to the model's performance, and therefore was not applied.

10.3.2 Geoid Undulation Error Estimates

Degree variances for the commission error of point values of geoid undulations, referring to the mean-Earth sphere, are computed by:

$$\varepsilon N_n^2 = \left(\frac{GM}{a\gamma}\right)^2 \left(\frac{a^2}{R^2}\right)^{n+1} \sum_{m=-n}^{n} \left(\varepsilon \overline{C}_{nm}\right)^2 \tag{10.3.2–1}$$

Global RMS estimates are then evaluated as the square root of the corresponding degree variances. Table 10.3.2–1 presents the results by degree and cumulatively, for selected degrees, for the OSU91A, JGM–3, HDM190, and EGM96 models. For OSU91A, the signal variances were used again for $n > 260$, instead of the pessimistic error variances of this model.

The results of Table 10.3.2–1 imply that the formal cumulative RMS commission error of the composite model JGM–3 ($n = 2$ to 70) / OSU91A ($n = 71$ to 360), up to degree 360 is ±69.4 cm. One is also interested in the omission error of these models, representing the expected RMS undulation signal above degree 360. An estimate of this may be obtained based on some anomaly degree variance model. The *Tscherning and Rapp*, [1974] model, evaluated using *Jekeli's* [1978] parameters, yields a global RMS point undulation signal above degree 360 of ±16.7 cm. The total RMS error in point geoid undulation, from a given model, can be computed by quadratic summation of the commission and omission errors.

Table 10.3.2–1. Global RMS geoid undulation commission error (cm) implied by four geopotential models. Values are given by degree ("At *n*") and cumulatively ("To *n*"), for selected spherical harmonic degrees.

Degree	OSU91A		JGM–3		HDM190		EGM96	
n	At *n*	To *n*	At *n*	To *n*	At *n*	To *n*	At *n*	To *n*
2	0.18	0.18	0.04	0.04	0.06	0.06	0.05	0.05
6	1.3	2.2	0.5	0.7	0.5	0.8	0.4	0.6
10	2.5	5.1	1.6	2.5	1.4	2.4	0.9	1.8
20	3.6	10.8	3.9	10.1	2.8	7.8	1.7	4.9
30	4.5	17.2	6.2	19.2	3.8	13.3	2.3	7.9
50	3.2	25.8	8.5	39.3	4	22.5	2.9	14.6
70	4.2	32.7	6.8	53.8	3.5	28.1	2.0	19.0
75	4.0	34.0	—	—	3.4	29.2	3.4	20.6
100	3.5	38.8	—	—	3	33.2	3.0	26.0
120	3.3	41.7	—	—	2.7	35.6	2.7	29.0
180	2.6	47.3	—	—	2.2	40.4	2.2	34.7
360	1.2	54.7	—	—	1.3	46.9	1.3	42.1

One should keep in mind that these estimates are *global* RMS values. The actual geoid undulation errors of the models have significant geographic variations. Such information can be represented only through the rigorous propagation of their associated error covariance matrices. Unfortunately, this is possible only for the commission error of the models up to degree 70 (50 in the case of OSU91A), since complete covariance matrices above this degree are not presently available. The omission error estimates are also global RMS values and cannot express the inhomogeneity and anisotropy of the field. Nevertheless, the total RMS geoid undulation error values are useful overall metrics of the expected accuracy from different solutions. These values

were computed here for the JGM–3/OSU91A composite model, and for the HDM190 and EGM96 models. The results are given in Table 10.3.2–2.

Table 10.3.2–2. Global RMS geoid undulation total (commission plus omission) error (cm) implied by three geopotential models and the [*Tscherning and Rapp*, 1974] anomaly degree variance model with *Jekeli's* [1978] parameters. Half the value of the expected total error is also listed for easy reference.

Model	Total Error	Half of Total Error
JGM–3/OSU91A	71.4	35.7
HDM190	49.8	24.9
EGM96	45.3	22.6

Over the ocean, due to the availability of satellite altimetry, the undulation errors of the models are considerably less than their global RMS values. A reasonable "rule of thumb" that may be used to estimate the total undulation error over the ocean is one half of its corresponding global RMS value. Up to degree 70, this rule of thumb closely approximates the ratio of oceanwide to global commission errors that are computed through rigorous error covariance propagation. A similar approximation was made by *Rapp* [1997b] to assess the errors implied by OSU91A over various geographic regions. If this approximation is accepted, then the values in the last column of Table 10.3.2–2 may be compared to the results of Table 10.1.7–1. The expected total RMS errors of HDM190 and EGM96 are in very good agreement with the RMS differences obtained from the oceanwide discrete comparisons with altimetric SSHs and the POCM–4B DOT. Notice that the results from HDM190 imply a total error for the POCM–4B model between ± 6 and ± 10 cm. In addition, according to the above results, the EGM96 errors appear to be very slightly pessimistic (although the discrepancy is probably well within the accuracy of our assumed rule of thumb). JGM–3/OSU91A, on the other hand, predicts too large undulation errors, compared to its observed performance. This type of reasoning, although subject to the approximations made above, does provide some additional evidence supporting the reliability of the error estimates of EGM96 and the assertion that the JGM–3 errors are pessimistic.

10.3.3 Error Estimates of Geoid Undulation Differences

It is also of interest to compute the expected errors of geoid undulation differences. Based on the formulation developed by *Christodoulidis* [1976], the commission error variance of the undulation difference (computed solely on the basis of the geopotential model) between two points P and Q, is given by:

$$C_{PQ}^2 = 2 \cdot \left(\frac{R}{\gamma} \right)^2 \sum_{n=2}^{M} \frac{1}{(n-1)^2} \varepsilon c_n \left(\frac{a^2}{R^2} \right)^{n+2} \left[1 - P_n(\cos \psi_{PQ}) \right] \qquad (10.3.3\text{--}1)$$

while the omission (or truncation) error is given by:

$$T_{PQ}^2 = 2 \cdot \left(\frac{R}{\gamma}\right)^2 \sum_{n=M+1}^{\infty} \frac{1}{(n-1)^2} c_n \left(\frac{a^2}{R^2}\right)^{n+2} [1 - P_n(\cos \psi_{PQ})] \qquad (10.3.3-2)$$

where M is the maximum degree of the model and ψ_{PQ} is the angular separation (spherical distance) between the two points (see also [*Rapp et al.*, 1991, p.71]).

This formulation provides estimates for the global RMS geoid undulation difference error for the station pair *PQ*, if this were to be subjected to all possible rotations on the sphere. In the numerical implementation of these equations, we used the same anomaly degree variance model (to estimate the truncation error), as in Section 10.3.2. The results obtained for OSU91A and EGM96 are shown in Table 10.3.3–1 for selected values of the station separation. These results may be compared to the relative undulation differences that were found in the GPS/leveling and model undulation comparisons discussed, e.g., in Section 8.5.5. One observes then that the predicted errors for corresponding station separations are significantly larger than the observed differences. This behavior was also encountered with the OSU91A model [*Rapp et al.*, 1991, p.72]. It is not clear why the error predictions for undulation differences (which for short distances are most sensitive to the high-degree error spectrum of the model) are so pessimistic. One possible reason may be the fact that the present formulation does not account for the error correlations among the model coefficients. A rigorous propagation of the model's error covariance matrix may shed some light on this problem, although such an approach would then be limited by the relatively low degree (70) up to which this matrix is available.

Table 10.3.3–1. Global RMS error in geoid undulation differences implied by the OSU91A and the EGM96 geopotential models, as a function of station separation.

			OSU91A			EGM96		
Linear Separ. (km)	Angular Separ. (°)	Trunc. Error (cm)	Comm. Error (cm)	Total Error (cm)	Relative Error (ppm)	Comm. Error (cm)	Total Error (cm)	Relative Error (ppm)
10	0.1	10.3	9.2	13.8	13.8	8.0	13.0	13.0
20	0.2	17.9	18.1	25.5	12.7	15.7	23.8	11.9
30	0.3	22.7	26.6	35.0	11.7	23.0	32.3	10.8
40	0.4	25.3	34.4	42.7	10.7	29.6	39.0	9.7
50	0.4	26.2	41.3	48.9	9.8	35.5	44.1	8.8
70	0.6	24.8	52.4	57.9	8.3	44.6	51.1	7.3
90	0.8	22.6	59.6	63.7	7.1	50.3	55.2	6.1
100	0.9	22.1	62.0	65.8	6.6	52.1	56.6	5.7
200	1.8	23.1	71.8	75.4	3.8	58.8	63.2	3.2
300	2.7	23.4	75.7	79.3	2.6	60.0	64.4	2.1
10000	89.9	23.5	77.4	80.9	0.08	59.5	64.0	0.06

10.4 Radial Orbit Error Predictions From the Geopotential Solution Error Covariances

In this section, we review the radial orbit error vs. inclination, as predicted by the gravity field covariances from JGM–2, JGM–3, and PGS7337B, for satellites in near-circular orbits at 525 km, 830 km, and 1336 km altitude. The radial orbit error is also decomposed by order for the orbits of GEOSAT, ERS–1, T/P, EP/EUVE, HILAT, RADCAL, Starlette, and Ajisai. The mapping of the radial orbit error from the gravity field error covariances [*Rosborough,* 1986] assumes a 10-day cutoff in the period of the orbit perturbations, except for Starlette, where a 25-day cutoff was used.

The radial orbit error versus inclination for near-circular orbits at the T/P altitude (1336 km) is shown in Figure 10.4–1. At the T/P inclination of 66°, the radial orbit error has decreased from 2.2 cm with JGM–2, to 1.1 cm with JGM–3, to 0.9 cm with EGM96. Between 40° and 140° inclination, the radial orbit error is below 10 cm for all three gravity models. Although the largest reductions in the radial orbit error at this altitude have occurred at the lower inclinations (below 40°), the gravity models remain weaker at these lower inclinations.

At 830 km altitude, the radial orbit error reaches a maximum of 141 cm at 1° inclination, and a minimum of 5.3 cm at 99° inclination with JGM–2. The inclusion of data from Spot–2 (and Stella for JGM–3 and PGS7337B) in these models is the reason for the minimum in the radial orbit error at this inclination and altitude. With JGM–3 the error is 105 cm at 1° inclination, and 3.5 cm at an inclination of 99°. For PGS7337B (EGM96), the error reaches only 63 cm at $i = 1°$, and 2.5 cm at $i = 99°$ (see Figure 10.4–2). At the lower inclinations ($i < 40°$), the EP/EUVE data begin to have an influence, even at an altitude of 830 km. A subset solution of PGS7337B was created that excluded the EP/EUVE data. This model (PGS7337D) predicts that at 29° inclination, the EP/EUVE TDRSS and GPS data reduce the radial orbit error from 24.2 cm to 10.3 cm with PGS7337B (EGM96). Another feature of the PGS7337B model is the dramatic decrease in the radial orbit error at the polar inclinations of 85° to 95°. For JGM–2 and JGM–3, the radial error reaches 56.2 and 44.7 cm at i = 85°. With PGS7337B (EGM96), the "hump" in the radial orbit error at 830 km at the polar inclinations has nearly vanished. The reduction is due in part to the addition of TRANET data from HILAT (altitude of 800 km and inclination of 82°) and RADCAL (altitude of 815 km and inclination of 89.5°) in PGS7337B. Without these data, the radial orbit error at 830 km altitude and 85° inclination would increase from 12.0 cm to 28.9 cm (see Figure 10.4–3). The HILAT and RADCAL data strongly benefit the PGS7337B solution between 85° and 93° inclination, reducing the predicted radial orbit error by 5 to 16 cm.

At 525 km altitude, the predicted radial orbit error is dramatically reduced over JGM–2 and JGM–3, especially at the low inclinations ($i < 40°$). At an inclination of 29°, the radial orbit error is 257 cm with JGM–2, 244 cm with JGM–3, and 24 cm with PGS7337B. Without the EP/EUVE data in the solution, the radial orbit error at this inclination would increase to 98 cm (see Figure 10.4–4). EP/EUVE also reduces the predicted radial orbit error at adjacent inclinations. At the RXTE inclination (23°) the radial orbit error is 53 cm with PGS7337B and 84 cm with PGS7337D, where the EP/EUVE data were excluded. Likewise, at the Tropical
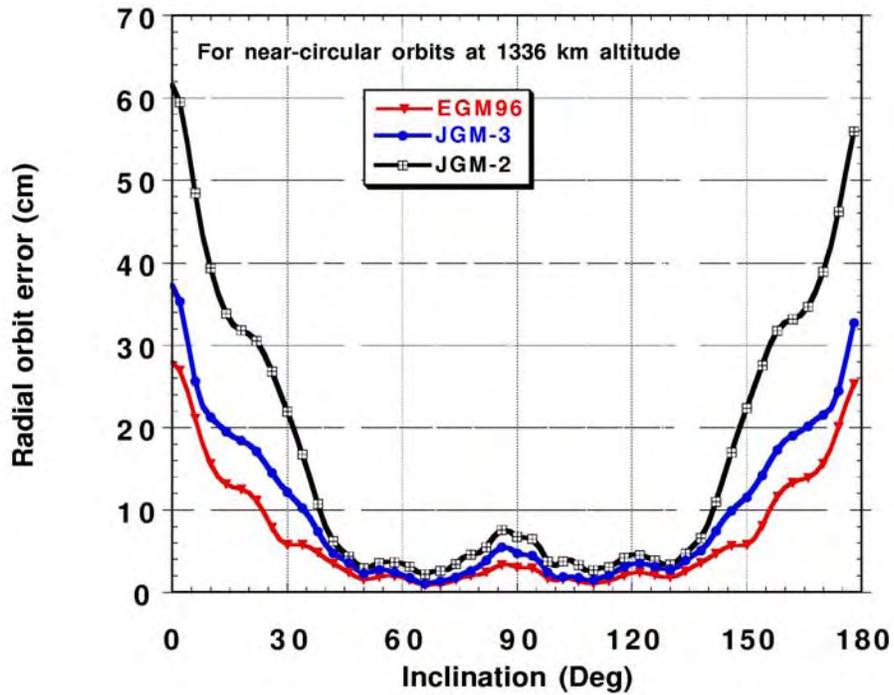
Figure 10.4–1. Radial orbit error vs. inclination for near-circular orbits at the TOPEX altitude (1336 km).
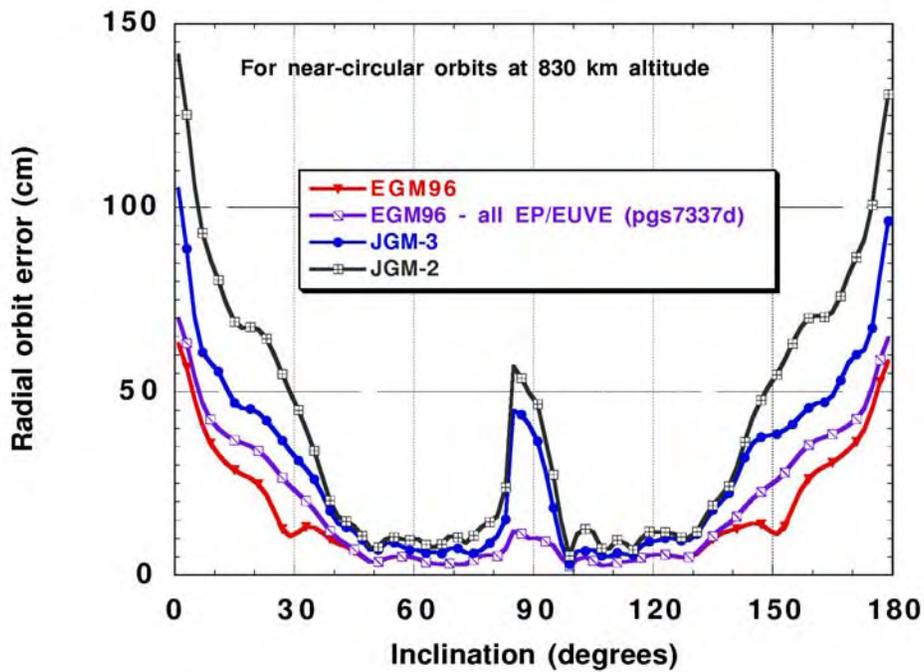
Figure 10.4–2. Radial orbit error vs. inclination for near-circular orbits at 830 km altitude.
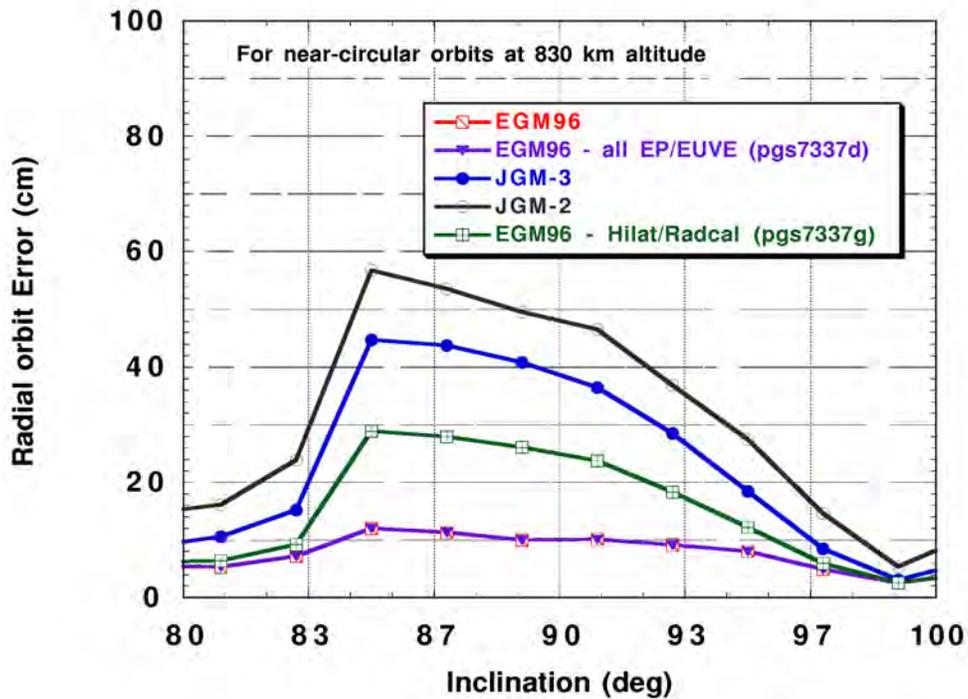
Figure 10.4–3. Radial orbit error for near-circular orbits at 830 km altitude at polar inclinations. The HILAT and RADCAL data in EGM96 improve the radial orbit error between $i = 85°$ and $i = 93°$ by 5 to 16 cm, as compared with PGS7337G, a subset solution of EGM96 that excludes these data.

Rainfall Measurement Mission (TRMM) inclination (35°) the radial orbit error is 73 cm with PGS7337B and 102 cm with PGS7337D, compared to 224 cm with JGM–3.

The radial orbit error from the gravity field error covariances was also calculated as a function of harmonic order. For T/P (see Figure 10.4–5), the radial orbit error for EGM96 is an improvement over JGM–2, but not JGM–3 for the lower orders, through order 11. At order 1, the radial orbit error for EGM96 is larger than with JGM–3 by approximately 1.5 mm. The increase in radial orbit error at the low orders is compensated by the reduction in the error for $m > 12$, and especially at the resonant orders, so that the overall error for T/P decreases from 1.1 cm with JGM–3 to 0.9 cm with EGM96. The SLR fits will be more sensitive to the modeling at the lower orders, and they do show a slight increase with EGM96 (see Table 10.1.1.2–1). Thus, the change of SLR fits on T/P are consistent with the predictions of the error covariances between JGM–2, JGM–3, and EGM96. In a root-sum-of-the-squares (RSS) sense, between orders 1 and 12, radial orbit error is 2.9 mm higher with EGM96 than with JGM–3. However, over all orders, the radial orbit error is predicted to be 10.5 mm with JGM–3 and 8.8 mm with EGM96. In understanding the difference in performance for TOPEX, it is important to bear in mind that JGM–3 and EGM96 had different design considerations. JGM–3 was created by adding T/P SLR/DORIS and T/P GPS data (weighted at 13 cm) to the JGM–1 covariance (in addition to other DORIS and SLR tracking data). Thus, JGM–3 is a solution highly tuned toward T/P. In EGM96, the T/P GPS

data did not receive as much weight (29 cm was applied in the solution), and orbit fits on a single satellite were not the single design driver. In addition, because of the vast quantities of other data, the contribution of T/P in the solution was proportionately downweighted. Nevertheless, further reductions in the radial orbit error are needed, however challenging that may be, in order to satisfy the goal of computing orbits accurate to 1 cm for Jason (the successor to T/P, scheduled for launch in the year 2000).
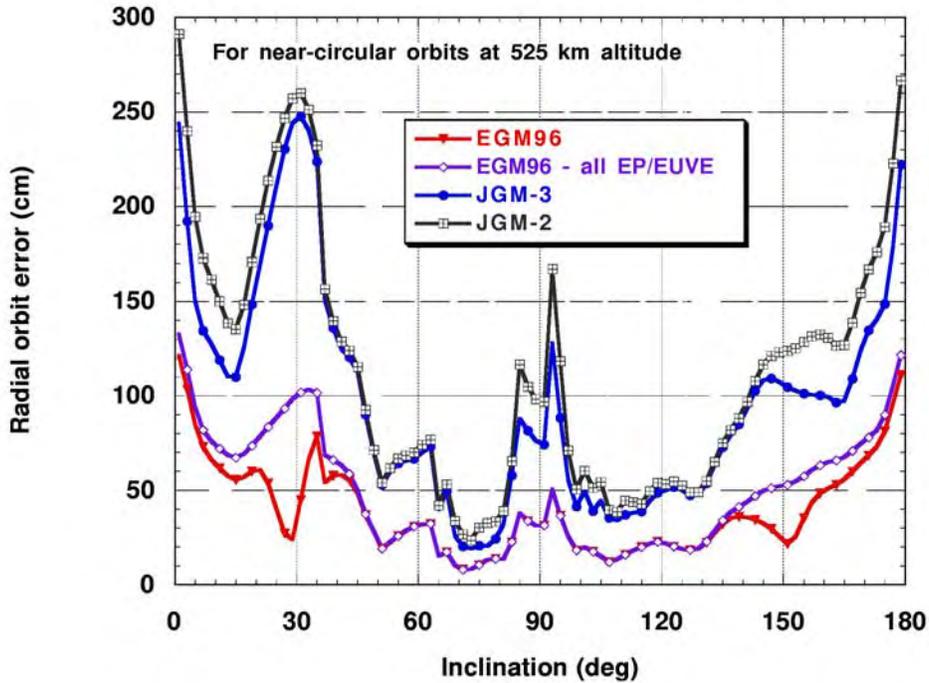
Figure 10.4–4. Radial orbit error v. inclination for near-circular orbits at the EP/EUVE altitude (525 km).

The predicted radial orbit error for GEOSAT decreases from 6.5 cm with JGM–2, to 5.0 cm with JGM–3, to 2.6 cm with EGM96 (see Figure 10.4–6). The improvement for GEOSAT may be attributed to: (1) the upweighting of the GEOSAT data in the solution, (2) the change in the parameterization for the empirical once per revolution acceleration terms (adjusted in JGM–2, but not adjusted in EGM96), and (3) the change in the applied weight for the surface gravity (see Section 7). The largest error remains at order 1, and is still 1.4 cm in EGM96. The large order 1 error is caused by poor modeling of the m-daily terms for this orbit and the uncertainty in the reference system for GEOSAT (coordinate system errors typically appear in the order 1 terms).
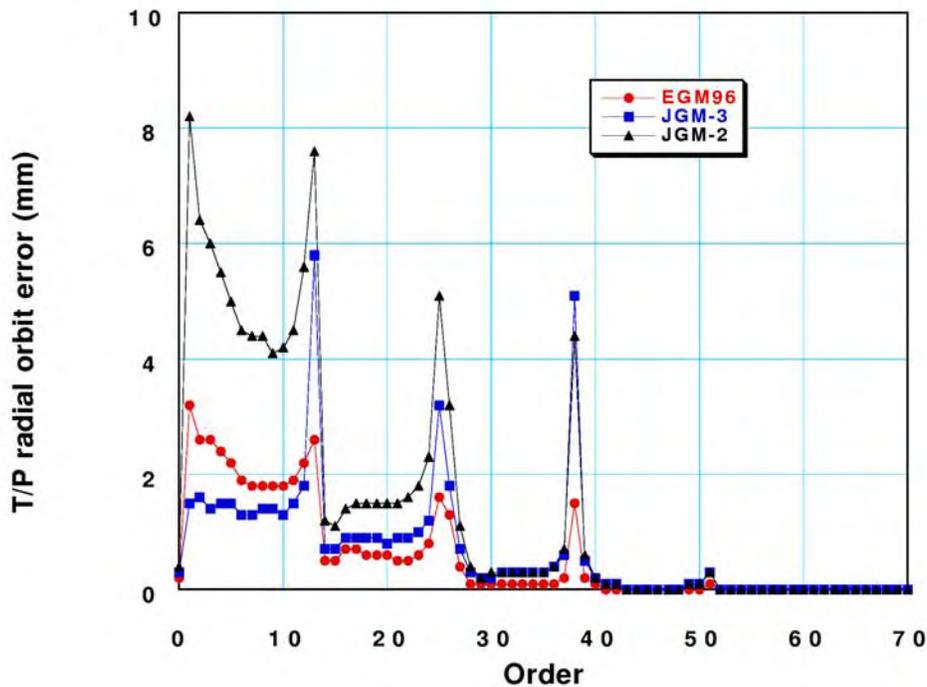
Figure 10.4–5. Radial orbit error vs. harmonic order for TOPEX/POSEIDON from JGM–2, JGM–3, and EGM96.

The radial orbit error vs. harmonic order is shown in Figure 10.4–7 for ERS–1. The total radial orbit error is predicted to be 6.1 cm with JGM–2, 3.7 cm with JGM–3, and 2.9 cm with EGM96. At order 1, JGM–3 has an error of 8.2 mm compared to 9.1 mm for EGM96. At the low orders ($m = 2$ to $m = 10$) both JGM–3 and EGM96 have comparable errors. At the higher orders, the predicted radial orbit error is improved for EGM96 compared to JGM–3 due to the presence of the ERS–1 altimeter data in the solution. Because of the limited SLR tracking available for this satellite, altimeter data are essential in order to produce a balanced, high-quality orbit for this satellite. The altimeter data contribute directly to the radial orbit improvement at the higher orders.

The predicted improvement of modeling for the EP/EUVE orbit has already been described. It is worthwhile to determine how the GPS and TDRSS tracking of EP/EUVE contribute to the predicted improvement in the orbit modeling in the presence of the other data in the EGM96 solution. The radial orbit error for EP/EUVE is shown in Figure 10.4–8 for EGM96, and PGS7337D, a subset solution of EGM96 that excluded all the EP/EUVE data. Without the EP/EUVE tracking, the largest error occurs at the primary resonance order ($m = 15$) and at the low orders. The predicted radial orbit error is 30.5 cm at order one with PGS7337D, compared to 7.4 cm with EGM96. Similarly, at order 15 (the primary resonance), the radial orbit error is 84.4 cm in PGS7337D, and 10.4 cm in EGM96. The continuous tracking from GPS and TDRSS contribute by better resolving the resonance and *m*-daily perturbations for this orbit.
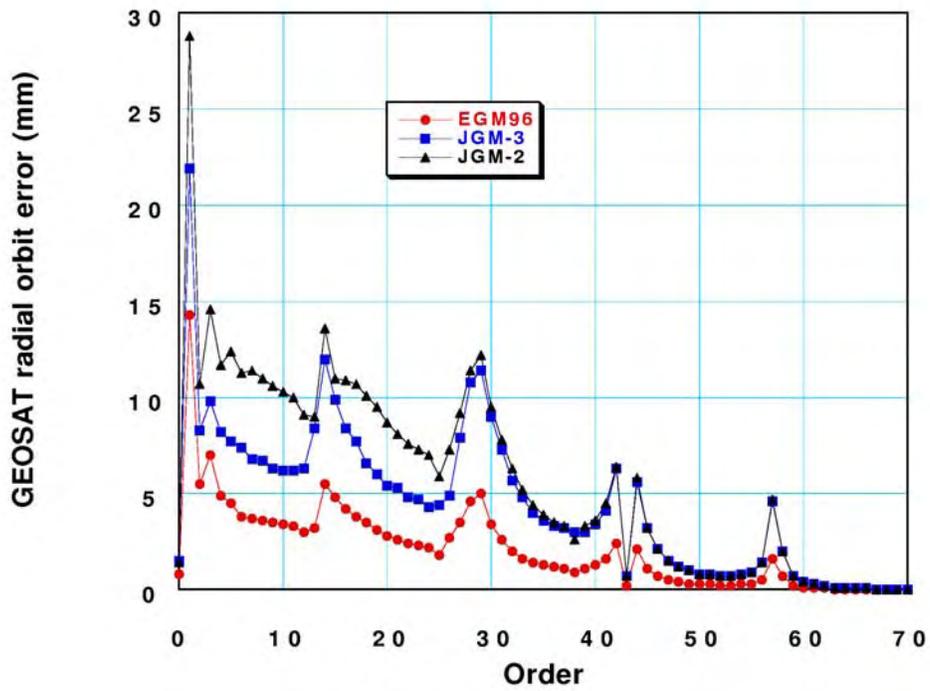
Figure 10.4–6. Radial orbit error vs. harmonic order for GEOSAT from JGM–2, JGM–3, and EGM96.
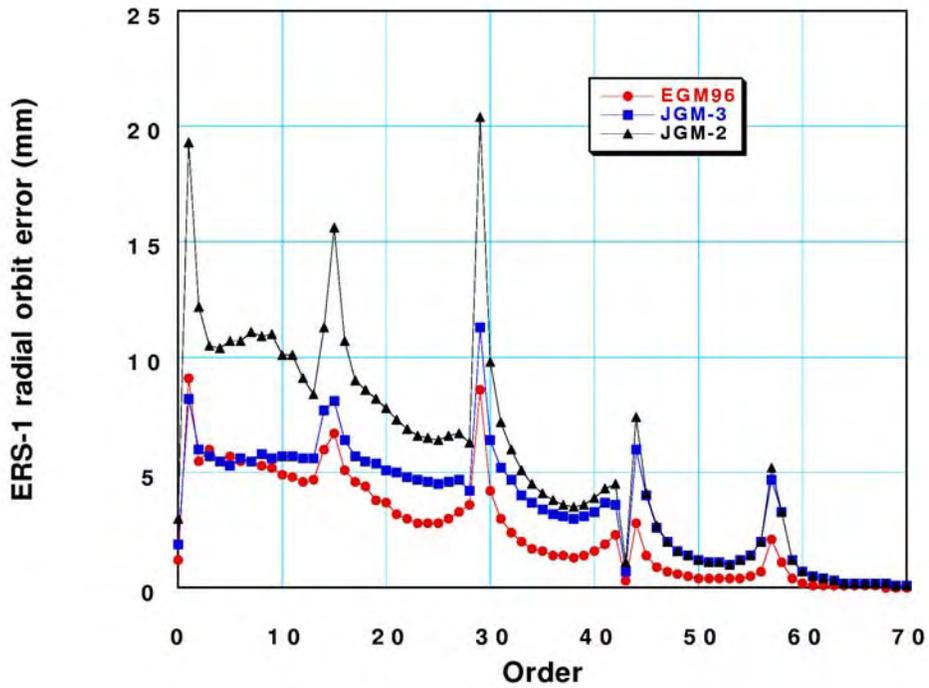
Figure 10.4–7. Radial orbit error vs. harmonic order for ERS–1 from JGM–2, JGM–3, and EGM96.

The radial orbit errors for the HILAT and RADCAL spacecraft are depicted in Figures 10.4–9 and 10.4–10. In both JGM–2 and JGM–3, the largest errors occur at or near the $k = 1$ ($m = 15$) or $k = 2$ and 3 ($m = 28$ and $m = 42$) resonances. The primary contribution of the TRANET data for these satellites (24858 observations for HILAT, and 83930 observations for RADCAL) has been to tune the resonance coefficients for these orbits.
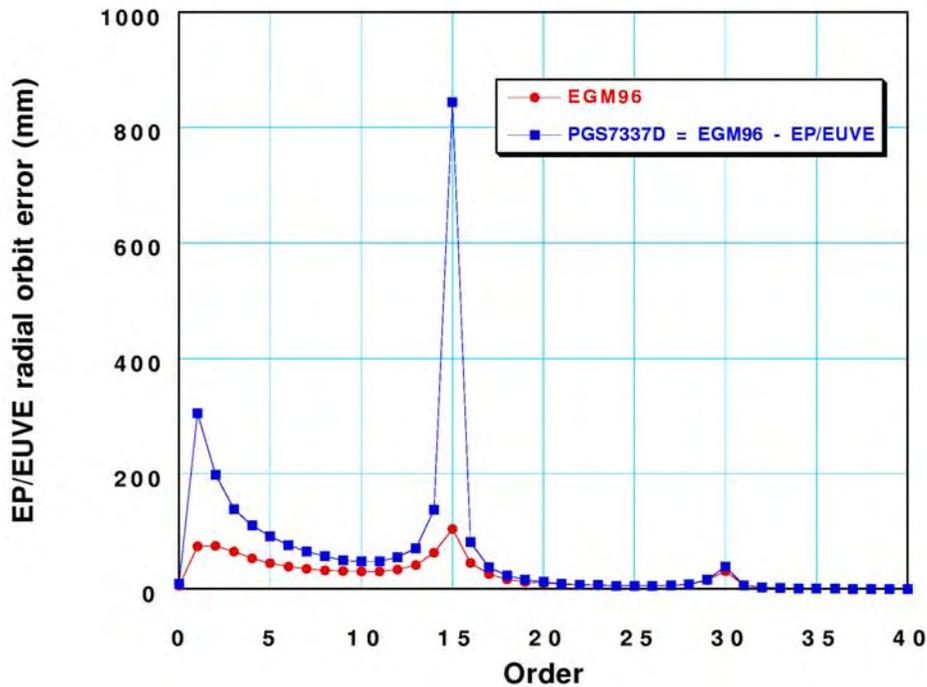
Figure 10.4–8. Radial orbit error vs. harmonic order for EP/EUVE from EGM96, and PGS7337D, a subset solution of EGM96 that excludes all EUVE data. The continuous tracking from GPS and TDRSS allow the EP/EUVE resonance and m-daily perturbations to be recovered in EGM96.

The predicted radial orbit error for two important geodetic satellites is shown in Figures 10.4–11 and 10.4–12 for Starlette and Ajisai. In the case of Starlette, the radial orbit error projections assume a near-circular orbit with an altitude of 960 km (49.8°inclination), so the radial orbit error predictions apply to a satellite in a near-circular orbit, rather than the slightly eccentric Starlette orbit. Nevertheless, the orbit error predictions serve as a useful gauge of the predicted performance of the gravity field models.

Regardless of the gravity field model (JGM–2, JGM–3, or EGM96), the radial orbit error as a function of harmonic order has the same behavior: a peak at orders 1–3, followed by an almost monotonic decay at the higher orders. The total radial orbit error is 5.2 cm with JGM–2, 4.5 cm

with JGM–3, and 2.5 cm with EGM96. Using EGM96, the $k = 3$ ($m = 41$) resonance contributes 3 mm of radial orbit error, and 4.2 cm of along-track error (out of a total along-track error of 11.9 cm).

The eccentricity of the actual Starlette orbit used in the development of EGM96, and the quality of the SLR tracking data, result in minimal predicted errors for the resonance orders, as compared to the other spacecraft which are predominantly in circular orbits. The $k = 1$ ($m = 13/14$) resonance on Starlette, which has a period of approximately 14 days, is well determined from the present data. The $k = 2$ ($m = 27/28$) and $k = 3$ ($m = 41$) resonance errors on Starlette are evident, but are not the dominant sources of radial orbit error. This is in contrast to the errors predicted for altitudes and inclinations corresponding to the tracking data used in EGM96 that came from satellites in circular orbits (cf. GEOSAT and ERS–1). For such cases the dominant errors occur at order 1 and at the resonance orders.
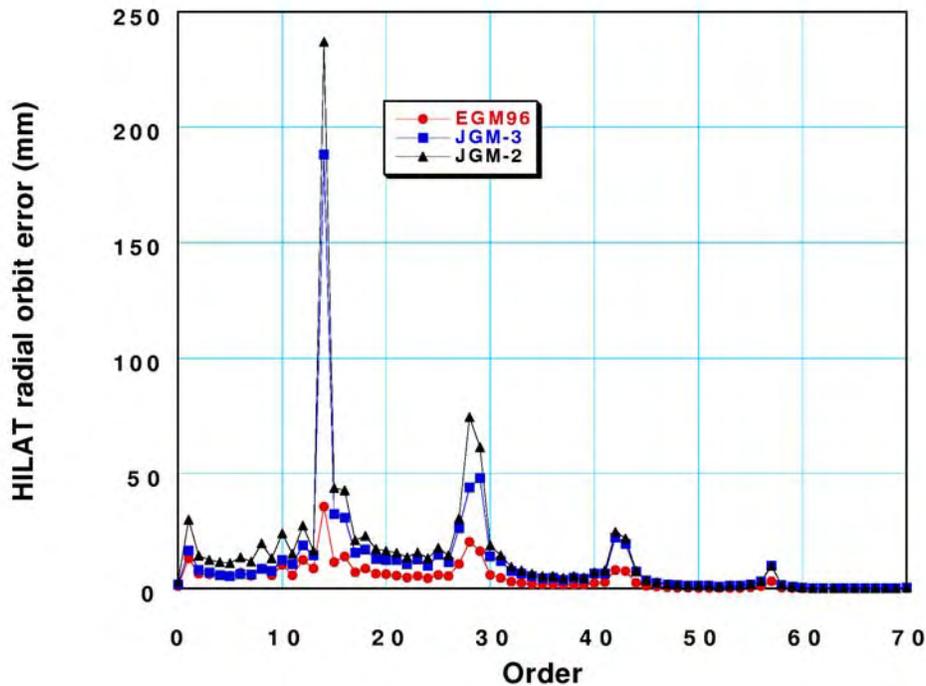
Figure 10.4–9. Radial orbit error vs. harmonic order for HILAT from JGM–2, JGM–3, and EGM96.
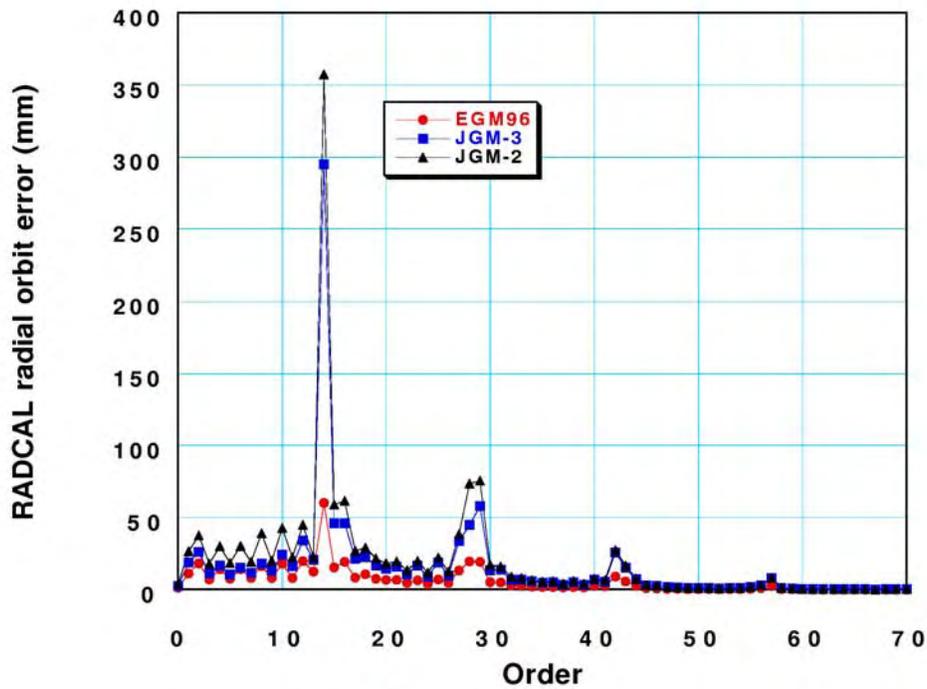
Figure 10.4–10. Radial orbit error vs. harmonic order for RADCAL from JGM–2, JGM–3, and EGM96.
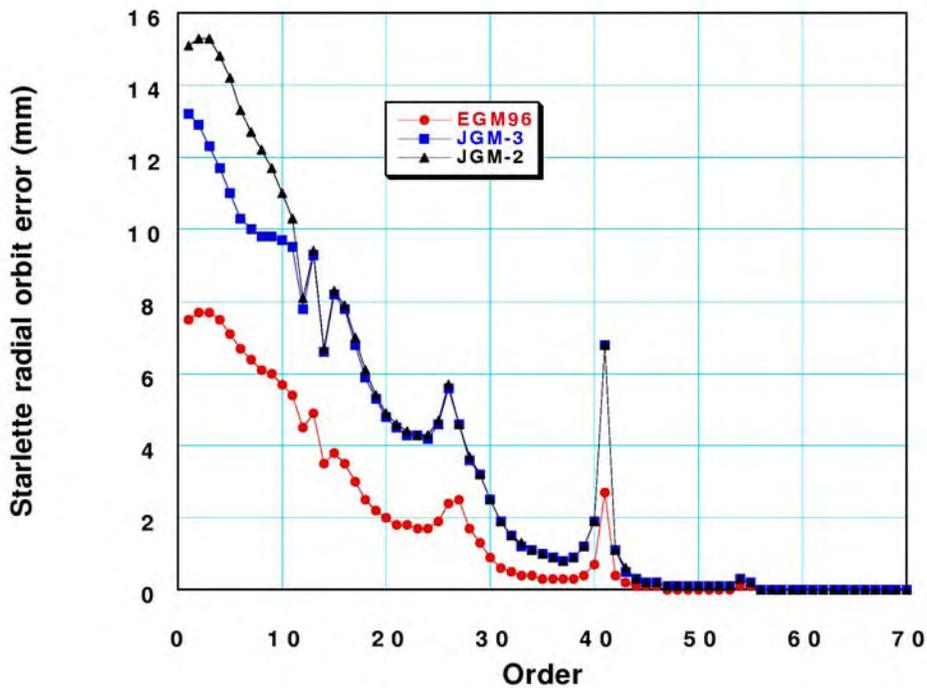
Figure 10.4–11. Radial orbit error vs. harmonic order for Starlette from JGM–2, JGM–3, and EGM96. A cutoff of 25 days in the orbit element perturbations was assumed, in order to capture the $k = 3$ ($m = 41$) resonance.

10–47

The low orders and the $k = 1$ ($m = 12$) resonance are the dominant source of error on the Ajisai orbit. The $k = 1$ ($m = 12$) resonance on Ajisai has a period of 3.1 to 3.2 days, so that it is surprising that the current set of data (arcs of 4 to 5 days for the "old" Ajisai data, and 10 days for the 1993–1994 Ajisai data) has failed to resolve this perturbation adequately.
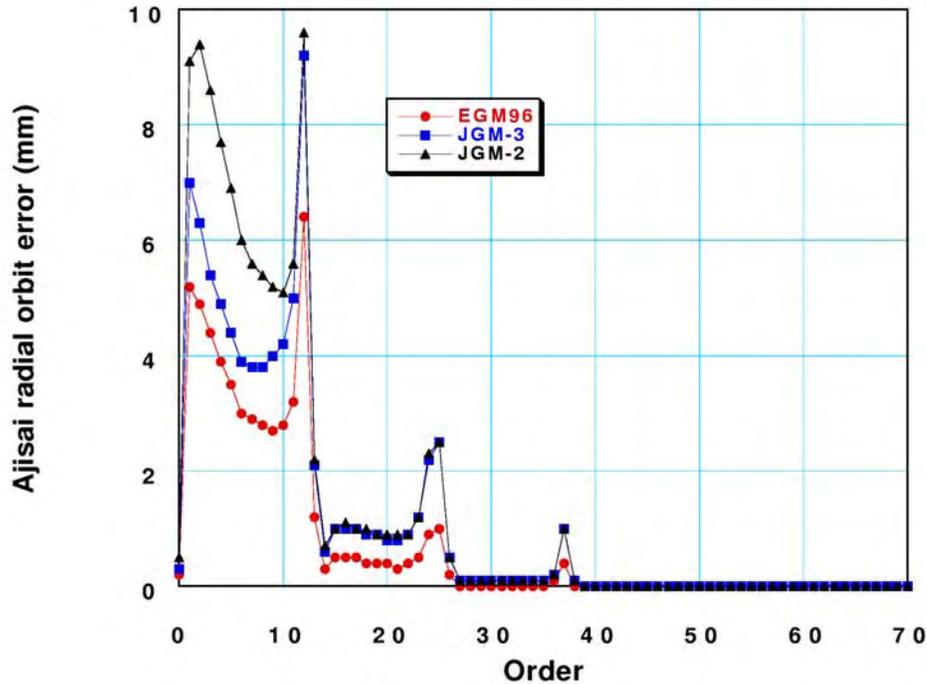
Figure 10.4–12. Radial orbit error vs. harmonic order for Ajisai from JGM–2, JGM–3, and EGM96.

10.5 REFERENCES

Bertiger, W.I., Y.E. Bar–Sever, E.J. Christensen, E.S. Davis, J.R. Guinn, B.J. Haines, R.W. Ibanez–Meier, J.R. Jee, S.M. Lichten, W.G. Melbourne, R.J. Muellerschoen, T.N. Munson, Y. Vigue, S.C. Wu, T.P. Yunck, B.E. Schutz, P.A.M. Abusali, H.J. Rim, M.M. Watkins, and P. Willis, "GPS precise tracking of TOPEX/POSEIDON: Results and implications, *J. Geophys. Res.*, *99*, C12, 24449–24464, Dec. 15, 1994.

Christodoulidis, D., On the Realization of a 10 cm Relative Oceanic Geoid, *Report No. 247*, Dept. of Geod. Sci. and Surv., The Ohio State University, Columbus, 1976.

Fu, L, R. Smith, Global Ocean Circulation from Satellite Altimetry and High Resolution Computer Simulation, Bulletin, *American Meteorological Society*, *77(11), 2625–2636, 1996.

Jekeli, C., An investigation of two models for the degree variances of global covariance functions, *Rep. 275*, Dept. of Geod. Sci. and Surv., Ohio State Univ., Columbus, 1978.

Levitus, S., Climatological Atlas of the World Ocean, *NOAA Professional Paper 13*, U.S. Dept. of Commerce, Rockville, MD, 1982.

Levitus, S., R. Burgett and T. Boyer, *World Ocean Atlas 1994*, NOAA Atlas NESDIS, U.S. Dept. of Commerce, Washington, DC, 1994.

Marshall, J.A., and S.B. Luthcke, Radiative Force Model Performance for TOPEX/POSEIDON Orbit Determination, *J. Astro. Sci.*, *42*, 2, 229–246, April–June 1994.

Nerem, R.S., F.J. Lerch, J.A. Marshall, E.C. Pavlis, B.H. Putney, B.D. Tapley, R.J. Eanes, J.C. Ries, B.E. Schutz, C.K. Shum, M.M. Watkins, S.M. Klosko, J.C. Chan, S.B. Luthcke, G.B. Patel, N.K. Pavlis, R.G. Williamson, R.H. Rapp, R. Biancle, and F. Noule, Gravity Model Development for TOPEX/POSEIDON: Joint Gravity Models 1 and 2, *J. Geophys. Res.*, 24421–24447, 1994b.

Pavlis, N.K., Estimation of geopotential differences over intercontinental locations using satellite and terrestrial measurements, *Rep. 409*, Dept. of Geod. Sci. and Surv., Ohio State Univ., Columbus, 1991.

Rapp, R.H., Y.M. Wang, and N.K. Pavlis, The Ohio State 1991 geopotential and sea surface topography harmonic coefficient models, *Rep. 410*, Dept. of Geod. Sci. and Surv., Ohio State Univ., Columbus, 1991.

Rapp, R.H., C. Zhang, Y. Yi, Analysis of dynamic ocean topography using T/P data and orthonormal functions, *J. Geophys. Res.*, *101(C10)*, 22583–22598, 1996.

Rapp, R.H., Use of potential coefficient models for geoid undulation determination using a spherical harmonic representation of the height anomaly/geoid undulations difference, *J. of Geodesy*, *71*, 5, 282–299, 1997a.

Rapp, R.H., Global models for the 1–cm geoid—Present status and near term prospects, in *Boundary Value Problems and the Modeling of the Earth's Gravity Field in View of the One Centimeter Geoid*, Rummel and Sansó (eds.), Lecture Notes in Earth Science, Springer–Verlag, 1997b.

Rowlands, D.D., S.B. Luthcke, J.A. Marshall, C.M. Cox, R.G. Williamson, and S.C. Rowton, Space Shuttle precision orbit determination in support of SLA–1 using TDRSS and GPS tracking data, *J. Astro. Sci.*, *45*, 1, Jan.–Mar., 1997.

Smith, D.A., and D.G. Milbert, Evaluation of preliminary models of the geopotential in the United States, in *Bulletin of the International Geoid Service*, 1997a.

Smith, D.A., and D.G. Milbert, Evaluation of the EGM96 model of the geopotential in the United States, in *Bulletin of the International Geoid Service*, 1997b.

Smith, D., On the improvement of gravimetric geoid undulations and oceanographic dynamic topography through a combination with satellite altimetry and the application of a modified Kalman filter algorithm, *Rep. 436*, Dept. of Geod. Sci. and Surv., The Ohio State University, Columbus, 1996.

Stammer, D., R. Tokmakian, A. Semtner, and C. Wunsch, How well does a 1/4° global circulation model simulate large-scale oceanic observations?, *J. Geophys. Res*., *101(C10),* 25779–25811, 1996.

Tapley, B.D., C.K. Shum, J.C. Ries, S.R. Poole, P.A.M. Abusali, S.V. Bettadpur, R.J. Eanes, M.C. Kim, and B.E. Shulz, The TEG–3 geopotential model, in Gravity, Geoid and Marine Geodesy, International Symposium, Tokyo, September 30–October 5, 1996, Segawa, Fujimoto, and Okubo (ed.), International Association of Geodesy Symposia, Vol. 117, Springer–Verlag, 1997.

Tapley, B.D., M.M Watkins, J.C. Ries, G.W. Davis, R.J. Eanes, S.R. Poole, H.J. Rim, B.E. Schutz, C.K. Shum, R.S. Nerem, F.J. Lerch, J.A. Marshall, S.M. Klosko, N.K. Pavlis, and R.G. Williamson, The Joint Gravity Model–3, *J. Geophys. Res*., *101 (B12),* 28029–28049, 1996.

Tscherning, C.C., and R.H. Rapp, Closed covariance expressions for gravity anomalies, geoid undulations, and deflections of the vertical implied by anomaly degree variance models*, Rep. 208,* Dept. of Geod. Sci. and Surv., Ohio State Univ., Columbus, 1974.

11.   THE EGM96 GEOID UNDULATION WITH RESPECT TO THE WGS84 ELLIPSOID

The geoid is an equipotential surface of the Earth's gravity field that is closely associated with the mean ocean surface. "Closely associated" can be defined in a number of ways [*Rapp*, 1995]. A working concept is that the mean difference between a geoid and the mean ocean surface should be zero. Deviations between the mean ocean surface and the geoid represent (primarily) mean Dynamic Ocean Topography (DOT). The standard deviation of the DOT is approximately ±62 cm, with extreme values from about 80 cm to about –213 cm, the latter in the Antarctic Circumpolar Regions (e.g., 66°S, 356°E). Plots of the DOT can be seen in numerous papers and reports as well as in sections 7 and 10 of this report.

The geoid undulation is the separation between the geoid and an ellipsoid whose surface is equipotential. The ellipsoid is defined by four quantities: a (equatorial radius), f (inverse flattening), ω (angular velocity), and GM (geocentric gravitational constant). Alternate quantities are possible. For example, the second-degree zonal harmonic, J_2, is a primary quantity in the definition of *The Geodetic Reference System*, 1980 [*Moritz*, 1992].

11.1 Permanent Tide Considerations

The definition of the geoid is complicated by the permanent deformation of the Earth caused by the presence of the Sun and the Moon. Consideration of these permanent tidal effects has led to the definition of three types of geoids and three types of reference ellipsoids [*Ekman*, 1989, 1995; *Rapp et al.*, 1991; *Bursa*, 1995a]. The three geoids are described as follows:

1. **Tide-free (or nontidal)**—This geoid would exist for a tide-free Earth with all (direct and indirect) effects of the Sun and Moon removed.

2. **Mean**—This geoid would exist in the presence of the Sun and the Moon (or, equivalently, if no permanent tidal effects are removed).

3. **Zero**—This geoid would exist if the permanent direct effects of the Sun and Moon are removed, but the indirect effect component related to the elastic deformation of the Earth is retained.

Conceptually, one would have analogous definitions of an ellipsoid that would be associated with the corresponding type of geoid. We could have a tide-free ellipsoid, a mean-tide ellipsoid, or a zero-tide ellipsoid. There will be a different equatorial radius and flattening associated with each type of ellipsoid.

If one considers a reference ellipsoid fixed by a definition of a and f, one will have different geoid undulations depending on the type of geoid undulation (tide free, mean, zero) that is being studied. Equations to convert from one system to another may be found in *Ekman* [1989], *Rapp* [1994], etc.. Let N_m be the mean geoid undulation, N_n the nontidal one, and N_z be the zero geoid undulation. Then we have [*Ekman*, 1989]:

$$N_m - N_z = 9.9 - 29.6 \sin^2\phi \quad \text{cm} \tag{11.1–1}$$

$$N_z - N_n = k \ (9.9 - 29.6 \sin^2\phi) \ \ \text{cm} \tag{11.1-2}$$

$$N_m - N_n = (1+k) \ (9.9 - 29.6 \sin^2\phi) \ \ \text{cm} \tag{11.1-3}$$

where k is a Love number usually taken as 0.3.

The issue in the determination of the undulations for the EGM96 model is, then, in what tide system are such undulations to be given. In the case that the geoid undulations are to be used with satellite altimeter data for the determination (e.g.) of dynamic ocean topography (see eq. 5.5.1–3), the undulations must be given in a system consistent with that used for the determination of the sea surface height. This is normally the mean tide system, so that geoid undulation (N_m) in the mean tide system is used. For other applications, the situation is not as clear.

At the 1983 IAG General Assembly in Hamburg, a resolution (16) was passed that states, in part "...the indirect effect due to the permanent yielding of the Earth be not removed." This recommendation suggests that the appropriate geoid to consider is the zero geoid with the corresponding zero geoid undulation of interest.

Also pertinent to the discussions are the conventions used in the reporting of station positions on the surface of the Earth determined from satellite (e.g., GPS) positioning procedures considering permanent tide issues. Recommendations can be found in the procedures conceptually adopted as part of the International Earth Rotation Service (IERS). These procedures are described in the *IERS Conventions* [1996] [*McCarthy*, 1996]. The effect of permanent deformation is described in Section 7, p. 65. In this case, the total permanent deformation is removed in the initial tidal correction, followed by the restitution of the indirect effect: "The restitution of the indirect effect of the permanent tide is done to be consistent with the XVIII IAG General Assembly Resolution 16; ..."

An important application of the geoid undulation will be the determination of the orthometric height (H) of a point from the ellipsoidal height (h). From eq. (5.2.1–1) we have:

$$H = h - N \tag{11.1-4}$$

The H value will be given with respect to the geoid whose undulations, with respect to a specific ellipsoid, are given by N. It is now clear that h and N must be given in a consistent tide system. Although IAG Resolution 16 recommends a zero-tide system, an informal survey of several groups involved with position determination indicated that position (and clearly heights) were being reported in a tide-free system. Although the difference between heights in a tide-free and zero-tide system are on the order of 10 cm, it is important for consistency purposes that h and N be given in the same system. Consequently, a decision was reached by the joint project that the preferred tide system would be the tide-free system and that the geoid undulations will be for the tide-free geoid.

11.2 The Determination of the Zero Degree Term (ζ_z)

We now determine the value of ζ_z defined by eq. (5.2.1–8). As written, the value of ζ_z will be dependent on latitude through the variation of r and γ. However, this variation is sufficiently small that mean values can be taken. One then rewrites (5.2.1–8) as follows:

$$\zeta_z = \frac{GM - GM_0}{r\gamma} - \frac{(W_0 - U_0)}{\gamma} \qquad (11.2–1)$$

where r and γ are regarded as mean values over the ellipsoid. Based on the WGS84 ellipsoid, we have [*Defense Mapping Agency*, 1991, Tables 3.1 and 3.2]:

$$r = 6371007 \quad \text{m}$$
$$\gamma = 9.797645 \quad \text{ms}^{-2} \qquad (11.2–2)$$

We next need to consider the determination of GM, GM_0, W_0, U_0. The value of GM_0 will be that adopted for the updated GM of the WGS84 ellipsoid. This value is $3.986004418 \times 10^{14}$ m^{3}s^{-2}, which is identical to that given in the *IERS Numerical Standards* [*McCarthy*, 1996, Table 4.1]. The best estimate of GM can be taken as the same value based on the recommendations of the IAG Special Commission SC3, *Fundamental Constants* [*Bursa*, 1995b, p. 381]. With this situation, the first term in eq. (11.2–1) is zero.

In order to calculate the second term on the right side of (11.2–1), one first needs to adopt or determine the ideal potential on the surface of the geoid followed by the determination of U_0 based on the parameters of the enhanced WGS84 ellipsoid. We start with the adoption of the following estimate of W_0 from *Bursa* [1995b, eq. (39)]:

$$W_0 = 62\ 636\ 856.88 \ \text{m}^2\text{s}^{-2} \qquad (11.2–3)$$

This value is consistent with a set of a and f values given in a consistent tide system. In the tide-free system in which we have chosen to work, we have [*Bursa et al.*, 1995b, eq. (24) and (27)]:

$$a = 6378136.46 \ \text{m} \qquad (11.2–4)$$

$$f = 1/298.25765 \qquad (11.2–5)$$

For determination of U_0 the parameters of the enhanced WGS84 ellipsoid are:

$$a = 6378137.00 \ \text{m} \qquad (11.2–6)$$

$$f = 1/298.257223563 \qquad (11.2–7)$$

$$GM = 3.986004418 \times 10^{14} \ \text{m}^3 \ \text{s}^{-2} \qquad (11.2–8)$$

$$\omega = 7292115 \times 10^{-11} \ \text{sec}^{-2} \qquad (11.2–9)$$

The value of ω is the mean angular velocity of the Earth. Using these four values, the corresponding U_0 value on the surface of the ellipsoid can be calculated [*Heiskanen and Moritz*, 1967, eq. (2–61)]; one finds:

$$U_0 = 62\ 636\ 851.71 \ \text{m}^3\text{s}^{-2} \qquad (11.2–10)$$

Using the values of W_0 and U_0 in eq. (11.2–1) yields:

$$\zeta_z = -52.8 \text{ cm},\quad\quad\quad\quad\quad\quad\quad\quad\quad\quad\quad\quad\quad\quad\quad\quad\quad\quad\quad (11.2\text{--}11)$$

which will be rounded to –53 cm for actual computation.

An alternative procedure is to calculate the zero-degree term based on the first of eq. (2–200) in *Heiskanen and Moritz* [1967, p.111]. One has:

$$\zeta_z = \delta a - \frac{1}{3} a \delta f \quad\quad\quad\quad\quad\quad\quad\quad\quad\quad\quad\quad\quad\quad\quad\quad\quad (11.2\text{--}12)$$

where δa and δf are the differences, ideal minus reference value, for the equatorial radius and flattening. Using the a values from (11.2–4) and (11.2–6) and the flattening values from (11.2–5) and (11.2–7), one finds from (11.2–12) a value of ζ_z equal to –52.9 cm, which agrees, within the accuracy of the spherical approximation of (11.2–12) with the value given by (11.2–11).

In summary, we adopt the following value of ζ_z:

$$\zeta_z = -53 \text{ cm} \quad\quad\quad\quad\quad\quad\quad\quad\quad\quad\quad\quad\quad\quad\quad\quad\quad\quad\quad (11.2\text{--}13)$$

The use of this value in the undulation computation enables the undulation to refer to the WGS84 ellipsoid defined by the parameters in eqs. (11.2–6 to –9). One must recognize that this calculation is subject to numerous error sources, primarily in the determination of the ideal equatorial radius. It would not be unreasonable to attach a standard deviation of ±10 cm to the ζ_z value given in (11.2–13).

11.3 The Coordinate Origin Issue for Undulation Calculation

The geoid undulation calculated from eq. (5.2.1–12) refers to a coordinate system the origin of which is at the center of mass of the Earth. This is because the summation shown starts from degree two, implicitly forcing the degree one terms to be zero.

In practice, the location of the center of mass, as well as the alignment of the axes of the reference frame, is defined by the system in which the geopotential model, station coordinates, etc., are estimated. The system used for the model development is described in Section 7.3.5, where it is shown that the effective reference frame in which EGM96 was estimated was practically equivalent to the reference frame, WGS84 (G873), implemented as the current (November 1996) operational WGS84 reference frame [*Malys*, 1996]. This frame is considered to be coincident with the ITRF94 to better than 2 cm.

In summary, the geoid undulations, as computed with the procedures described in this section, will refer to the WGS84 ellipsoid, whose origin is at the center of mass of Earth, as defined by WGS84 (G873)/ITRF94, and whose axes are aligned with the indicated reference frames.

11.4 The Calculation of the Geoid Undulation Values

The calculation of the geoid undulation takes place using eq. (5.2.1–23/26):

$$N(\theta, \lambda) = \zeta_z + \zeta^*(r_E, \theta, \lambda) + C(\theta, \lambda) \quad\quad\quad\quad\quad\quad\quad\quad\quad (11.4\text{--}1)$$

where $\zeta_z = -0.53$ m, $C(\theta, \lambda)$ is the sum of three corrections terms and $\zeta^*(r_E, \theta, \lambda)$ is:

$$\zeta^*(r_E, \theta, \lambda) = \frac{GM}{r_E \gamma_E} \sum_{n=2}^{360} \left(\frac{a}{r_E} \right)^n \sum_{m=-n}^{n} C_{nm} Y_{nm}(\theta, \lambda) \qquad (11.4\text{–}2)$$

where the subscript E indicates an evaluation for a point on the ellipsoid at a geocentric latitude corresponding to $90^o - \theta^o$. The even-degree zonal value of C_{nm} represents the difference between the EGM96 coefficient and the reference values computed for the WGS84 ellipsoid with the constants defined by eq. (11.2–6 to –9). The values calculated are those of the even zonal coefficients (J_{2n}) in a representation of the potential as defined by the equation below (2–91) in *Heiskanen and Moritz* [1967, p. 73]. These coefficients are related to the $C_{2n,0}$ coefficients of (11.4–2), as follows:

$$C_{2n,0}(ref) = -J_{2n}/\sqrt{(2n+1)} \qquad (11.4\text{–}3)$$

The value of J_{2n} were computed using eq. (2–92) of *Heiskanen and Moritz* [1967, p.73] using subroutine GRS written by *N. Pavlis* [*private communication*]. One has:

$J_2 = 0.1082\ 6298\ 2131 \times 10^{-2}$

$J_4 = -0.2370\ 9112\ 0053 \times 10^{-5}$

$J_6 = 0.6083\ 4649\ 8882 \times 10^{-8}$ (11.4–4)

$J_8 = -0.1426\ 8108\ 7920 \times 10^{-10}$

$J_{10} = 0.1214\ 3927\ 5882 \times 10^{-13}$

The value of N can be computed in two ways. The first procedure is to calculate a grid of ζ^* and C values using efficient software for rapid calculation of gridded values using high-degree spherical harmonic expansions. Adding the ζ^*, C, and ζ_z values yields the gridded values. The grid interval selected by NIMA for this calculation was $0.25° \times 0.25°$ ($15´ \times 15´$). Values can be interpolated to an arbitrary point using a spline interpolation procedure to assure 1- to 2-cm interpolation precision. The grid of values for the EGM96 geoid undulation with respect to the WGS84 can be found at the following NIMA Web site:

<div align="center">http://164.214.2.59/geospatial/products/GandG/wgs-84/geos.html</div>

An alternative procedure to the gridding process is the calculation of the N value at a specified location. This procedure requires the evaluation of two spherical harmonic expansions (one for ζ^* and one for C) followed by the addition of ζ_z according to eq. (11.4–1). This procedure has been implemented by a modification of the program described by *Rapp* [1982]. The two major changes were: 1) the deletion of all computations except those related to the ζ (equivalent to the geoid undulation computation in the reference) and 2) the incorporation of the calculation of $C(\theta, \lambda)$ given the spherical harmonic representation of the correction term. The modified program is called F477NONLY and has also been placed on the Web site noted above. Also included are the EGM96 coefficients and the coefficients of the correction term C based on the EGM96 coefficients.

Whether one uses the gridded values to interpolate the undulation or the point calculation using the software provided, the result should be the same within 1 or 2 cm. The value will be the

geoid undulation, in the tide-free system with respect to the WGS84 ellipsoid, implied by the EGM96 geopotential model.

11.5 References

Bursa, M., Primary and Derived Parameters of Common Relevance of Astronomy, Geodesy, and Geodynamics, *Earth, Moon, and Planets, 69*, 51–63, 1995a.

Bursa, M., *Report of Special Commission SC3, Fundamental Constants*, Travoux de L'Association Internationale de Geodesie, Reports Generaux et Rapports Technique, IAG, 140 rue de Grenelle, 75700 Paris, 1995b.

Defense Mapping Agency, Department of Defense World Geodetic System 1984, *DMA Technical Report 8350.2*, Second Edition, September 1, 1991.

Ekman, M., Impacts of Geodynamic Phenomena on Systems for Height and Gravity, *Bulletin Geodesique, 63(3)*, 281–296, 1989.

Ekman, M., What Is the Geoid? in *Coordinate Systems, GPS, and the Geoid*, M. Vermeer (ed.), *Reports of the Finnish Geodetic Institute, 95*:4, 49–51, 1995.

Heiskanen, W., and H. Moritz, *Physical Geodesy*, W.H. Freeman and Co., San Francisco, 1967.

Malys, S., *The WGS84 Reference Frame*, National Imagery and Mapping Agency, November 7, 1996.

McCarthy, D., IERS Conventions (1996), *IERS Technical Note 21*, Observatoire de Paris, 1996.

Moritz, H., Geodetic Reference System 1980, *Bulletin Geodesique, 66(2)*, 187–192, 1992.

Rapp, R.H., A FORTRAN Program for the Computation of Gravimetric Quantities From High Degree Spherical Harmonic Expansions, *Rep. 334*, Dept. of Geod. Sci. and Surv., Ohio State Univ., Columbus, 1982.

Rapp, R.H., Global Geoid Determination, in *Geoid and Its Geophysical Interpretation*, Vaniček, and Christou (eds.), CRC Press, Boca Raton, FL, 1994.

Rapp, R.H., Equational Radius Estimates From TOPEX Altimeter Data, Festchrift Erwin Groten, Institute of Geodesy and Navigation, University FAF, Munich, 1995.

Rapp, R.H., R.S. Nerem, C.K. Shum, S.M. Klosko, and R.G. Williamson, *Consideration of Permanent Tidal Deformation in the Orbit Determination and Data Analysis for the Topex/Poseidon Mission*, NASA TM 100775, Goddard Space Flight Center, Greenbelt, MD, 1991.

12. SUMMARY

12.1 EGM96 Solution Achievements

In this report we have described the derivation of the EGM96 geopotential model, including the estimation of the 30´x30´ anomalies, the processing of the satellite tracking data, and the direct altimeter data. The solution methodologies are described in detail for both the low-degree combination model, and the high-degree models. The creation and testing of the intermediate and final solutions are also described. The final solution blends a low degree (to degree 70) combination model (obtained from combining satellite tracking data, surface gravity data, and direct altimeter measurements) which is based on the most complete and rigorous modeling and estimation techniques, with high-degree models (beyond degree 70 to degree 360) that exploit symmetry properties associated with the potential coefficient estimation from regularly gridded 30´x30´ mean gravity anomaly data.

The development of the EGM96 geopotential model was a major undertaking which challenged our current technical and computational capabilities. The three year cooperative effort combined the insights, resources, and data available within NASA and NIMA, and involved more than two dozen participants. The major technical objectives were achieved and an improved high degree gravitational model was delivered to the science, mapping, and navigation communities. Major advancements in gravitational field modeling achieved with EGM96 included: (a) the incorporation of new surface gravity data, satellite-tracking data and altimeter data into a 360x360 geopotential solution, (b) improved model accuracy, (c) the development of important solution by-products including a global topographic model used in reduction of the surface gravity data and the simultaneous estimation of a tidal solution along with the geopotential coefficients, (d) design, testing, and implementation of the block-diagonal method for development of the high-degree solutions.

An important aspect in the development of the EGM96 model was the multiple set of criteria used to test the interim and final project geopotential models. A variety of techniques were used to assess the performance of the models including satellite tracking data fits, GPS/leveling geoid undulation comparisons, dynamic ocean typography comparisons with ocean circulation models, comparisons to altimeter-derived gravity anomalies, and other land and ocean geoid tests. The extensive testing assured not only that the model provided good orbit fits, but that it also performed well for a variety of terrestrial and oceanic applications.

From the early design stages of EGM96 it was recognized that a large amount of new surface gravity data were becoming available due to changes in the international political landscape. A major effort was undertaken by NIMA to process these data and to form 30´x30´ mean anomaly estimates. The 30´ mean values were estimated using a uniformly consistent and rigorous approach (least squares collocation). This was true for all continental areas where detailed gravimetry was available, as well as for those areas covered by airborne gravity surveys. Over most of the Earth's oceans 30´ mean gravity anomalies were estimated using satellite radar altimeter data acquired by the US Navy's GEOSAT satellite during its Geodetic Mission. Mean

gravity anomalies derived from ERS-1 altimeter data were used in ocean areas not covered by GEOSAT.

Surface Gravity Data

EGM96, through its incorporation of newly available surface gravimetry has significantly improved continental geoid modeling. The new data include contributions over most of Asia and the former Soviet Union, airborne gravity surveys over polar regions including Greenland, surveyed data from South America, Africa, and North America, as well as improvements to the data sets provided by many countries. These data enhancements have all increased the short wavelength global geoid accuracy of the resulting model. Of importance is the progress which was achieved in eliminating a significant level of inconsistency between the geopotential signal sensed by satellite tracking versus terrestrial anomaly data. Earlier combination solutions "required" (given model design considerations) the strong downweighting of surface gravimetry (for example in JGM–2 and JGM–3). EGM96 gave much higher weight to the surface information, yet still performs well on orbital and ocean geoid modeling applications. The more effective use of this unique information resulted in a model which has more realistic error estimates, especially at higher degrees, and spectral error characteristics which are less discontinuous at the degree 70 boundary than earlier "cut and paste" models such as JGM–3/OSU91A. At degree 70, comprehensive solution approaches were abandoned in favor of more computationally efficient block-diagonal and quadrature techniques. Since the surface gravity data are no longer downweighted, stronger information comes from surface gravimetric sources to define the middle degree terms in the model. It is this part of the field ($n \geq 40$) where satellite tracking information falls off significantly because of the attenuation in the field sensitivity experienced on satellites now used for geodetic purposes.

Satellite-to-Satellite Tracking Data

EGM96 used several new data types to great advantage. The range and range-rate tracking of low Earth orbiting user satellites by the TDRSS geostationary constellation, and the complete 3-D positioning of similar spacecraft achieved using the constellation of 24 GPS satellites, provided precise data not available in previous models. The TDRSS and GPS tracking acquired on the low altitude (525 km), low inclination (28.5°), EP/EUVE satellite provided a large geopotential modeling improvement in the equatorial regions. While only three satellites tracked by these systems were used in EGM96 (TOPEX/POSEIDON, EP/EUVE, and GPS/MET), these data represent a sizable fraction of the observational data used in EGM96. By providing nearly continuous tracking, these data are sensitive to many of the short period orbit perturbations which are not well sensed by conventional, discontinuous tracking data types (like SLR and ground based Doppler). They improved the separation of harmonic terms in the satellite-only EGM96S model, and provided complementary information to the surface gravimetry and altimeter data sets in the middle degrees of the model.

Altimeter Data

EGM96 incorporated altimeter data in two distinct forms: (1) as 30'x30' mean altimeter-derived anomalies in the high-degree models, and (2) as direct tracking data in the low-degree (to degree 70) combination model.

The 30´x30´ mean altimeter-derived anomalies used in the development of EGM96 were obtained from GEOSAT and ERS–1. The major source for these anomaly data was the GEOSAT Geodetic Mission altimeter data, where the oceanic gravity anomalies were produced using a rigorous least squares collocation process. The Danish National Survey and Cadastre or Kort-og Matrikelstyrelsen (KMS) contributed to the anomaly data sets by collaborating in the development of the collocation procedure and by providing ERS–1 gravity anomalies [*Andersen et al.*, 1996; *Forsberg*, 1987]. The ERS-1 data made an important contribution by extending the coverage in the near-polar areas and a few near-shore areas. Tilo Schoene (of the Alfred Wegener Institute for Polar and Marine Research, Bremerhaven, Germany) provided gravity anomaly values for the Weddell Sea area near Antarctica. These data were derived from a combination of GEOSAT and ERS–1 altimetry [*Schoene*, 1996].

In addition, altimeter data from GEOSAT, TOPEX/POSEIDON, and ERS–1 were used as direct tracking information in the low degree ($n \leq 70$) combination model, improving both the orbit accuracies of ERS–1 and ocean surface mapping from these systems. Concurrent altimeter data provided by TOPEX and ERS–1 were used to define a consistent dynamic ocean topography (DOT), extending to the high latitudes, where two years of data allowed simultaneous solution for a mean dynamic topography model augmented by both annual and semi-annual terms.

Conventional Tracking Data

Data from conventional tracking, including observations acquired by SLR, TRANET, and DORIS systems were upgraded for inclusion in EGM96. Of special interest was the addition of data from several new laser (LAGEOS–2, Stella, GFZ–1) and Doppler (HILAT and RADCAL) tracked satellites. These data added strength to the solution and filled several important inclination and altitude gaps in the JGM–2S satellite orbit distribution.

Improved Model Accuracy

EGM96 represents a significant model improvement over recent available models such as JGM–2 and JGM–3. This improvement is seen at the lowest degrees, in improved orbital fits to precise SLR data sets and in the improved modeling of the ocean geoid for ocean circulation studies. Through the middle and high degrees, the uncertainty improvements are more than a factor of two over both JGM–2 and OSU91A, which are its major predecessors. Results of the calibration of the satellite-only model foundation and tests of the combination model covariance indicate that the predicted uncertainties are well calibrated and represent reasonable, if somewhat conservative error predictions. Most striking is the elimination of areas with large geoid uncertainties, which was seen in earlier models where accurate surface gravity information was lacking, for instance over large sections of Asia, Africa, and South America.

EGM96 Solution By-Products

Important ancillary products were developed contemporaneously with the EGM96 solution. Along the static geopotential, the combination component of the solution to 70x70 included estimates of dynamic tide parameters, dynamic ocean topography solutions to 20x20 for TOPEX/ERS–1 and GEOSAT, station coordinates, and a pole position time series.

In addition, for the accurate evaluation of 30' mean anomalies and associated terrain reductions, a 5´x5´ global topographic model (JGP95E) was developed. The JGP95E model used previously unavailable terrestrial data as well as topographic information obtained from satellite altimeter measurements acquired over Antarctica.

EGM96 provided an improved dynamic tide model for orbital applications. A select subset of tidal terms, representing the resonant portion of the tidal spectra for the major tide lines, was estimated simultaneously with the static geopotential harmonics. These tidal parameters improve the modeling of lower altitude orbits, provide GSFC's first estimates for the Q_1 tide line, and fully exploited the capability of simultaneously modeling the complete tidal family (mainline and sideband tide lines) to eliminate much of the aliasing arising from lack of sideband modeling in earlier recovery efforts.

Advances in Solution Design and Methodology

A new method of developing high-degree geopotential solutions was designed, tested, and implemented. The block-diagonal technique is computationally efficient, yet allows the preservation of the most important correlative effects found within the high degree model and permits a much smoother transition at degree 70 between solution methodologies.

Improved *a priori* constraint models of the expected power in the gravitational field and dynamic ocean topography models were used. The *a priori* power law constraint used in the satellite-only geopotential solutions was derived from the coefficients of a quadrature combination solution. The Kaula-type power law constraint used in previous models, such as JGM–1S and JGM–2S, underestimated the power and consequently the predicted error at the higher degrees of the satellite-only solutions. A power law fit to the spherical harmonic spectrum of the POCM–4B ocean circulation model was used to better condition the solutions for dynamic ocean topography for solutions that included direct altimetry.

The prediction of gravity anomalies from altimetry was advanced through the incorporation of dynamic ocean topography modeling and improvements in covariance functions. Fitting the GEOSAT GM mean sea surface to that of TOPEX removed a large part of the long wavelength errors in the altimeter-derived gravity anomalies.

Structural and procedural changes in the GEODYN and SOLVE programs were implemented to improve computational efficiencies and eliminate "bottlenecks" in the development of the 70x70 satellite-only and combination model portions of EGM96. These modifications included changes to improve the I/O for the manipulation of numerous large matrices, and recoding to take advantage of multiple processors on the CRAY J932 supercomputer.

International Cooperation

Another key element of the joint project was the contribution made during the testing of various geopotential models by the Special Working Group of the International Geoid Service, chaired by Michael Sideris. Their testing [*Sideris*, 1997], performed independently, and with out knowledge of the make up of the models provided to them, yielded valuable information that helped to determine the best estimation and solution development strategy for EGM96. The international cooperation that occurred during the EGM96 project represents a first in the development of a major geopotential model.

12.2 Future Challenges

The process of finalizing EGM96, calibrating its errors, and determining the optimal data weights for its diverse sets of data, revealed many areas for future investigation. In some cases, clear deficiencies in current methodologies, or understanding of model properties, were discovered. While EGM96 represents a major milestone, significant efforts are still needed to take full advantage of existing data, and to prepare for future gravity missions. Some of the most important subjects which need to be studied include improved calibration techniques, improved methods for ocean tidal recovery, alternative representations of the dynamic ocean topography, as well as the incorporation of new satellite tracking data and new surface gravity data into future solutions.

Improved Calibration Techniques

Our objective calibration techniques produced unexpected results when applied to the strong data obtained from the continuous tracking of low Earth orbiting satellites by either the GPS or the TDRSS constellations. The non-linear behavior of the deduced calibration factors, described in Section 6.4, which was the basis for the determination of the data weights, is a concern. It both forced us to adopt weights which could not be objectively determined, and to rely on performance metrics against independent data (e.g. tests against altimeter-derived gravity anomalies and GPS/leveling traverses), to determine final weights. While we have several ideas about the cause of this behavior, improved calibration methods are needed as additional data sources like these come to be dominant within geopotential solutions. Indeed, continuous tracking data geometries will be the basis for the upcoming CHAMP and GRACE geopotential missions.

Improved Methods for Ocean Tidal Recovery

Unlike the static geopotential, the recovery of dynamic tidal terms is critically dependent on the nature of the tidal resonances experienced by a given satellite, and the temporal distribution of the data included in the recovery. Our calibration methods, which focused on the static geopotential model, yielded poor calibration results for the tidal terms. There are additional challenges with tidal recovery:

- Some of the strong satellites (e.g. SPOT–2, Stella) are sun-synchronous with perfect resonances with the dominant semi-diurnal solar tides (S_2 constituents) and deep resonances with all other solar tides.

- Many thermal and radiational signals can alias solar tidal effects, for example, the LAGEOS "anomaly" has a large corrupting effect on the 3rd degree component of the S_a tides.

- For satellites sensing short period gravity effects, short period tides will also be sensed. It is unclear how many terms from which specific tidal families need to be adjusted to accommodate errors in the part of the ocean tide models.

Alternative tidal recovery strategies need to be investigated. Recovery of larger tide models should also be considered.

Alternative Representation of the Dynamic Ocean Topography

The dynamic ocean topography models recovered as part of EGM96 are represented as spherical harmonics. This representation has certain limitations. First, by being global, it requires definition of the dynamic ocean topography over the continents which is both meaningless, and subject to poor behavior given the non-existence of information over these regions. Secondly, at the ocean/land boundaries, given that the altimeter mapped ocean surface abruptly ends at this interface, it is common to see the implied flow deduced from the dynamic ocean topography going into or out of land. Alternative representations are free of many of these shortcomings. Consideration is being given to using orthonormal functions, defined only over the ocean surface for dynamic ocean topography representation. This includes use of: (1) height functions [*Sanchez et al*., 1997], (2) Empirical Orthogonal Functions (EOF) [*Rapp et al.,* 1996; *Hwang*, 1991], and/or (3) Proudman functions [*Rao et al.*, 1987; *Sanchez and Pavlis*, 1995] to improve the separation of geoidal and dynamic ocean topography signals, and improve the modeling characteristics.

Additional Tracking Data

There are a number of sources of additional tracking data which were not included in EGM96. These include TDRSS tracking of CGRO, RXTE, and ERBS [*Luthcke et al.*, 1998]. In addition, the TDRSS constellation will provide data for future missions in unique orbits and inclinations, such as the TRMM mission (350 km altitude, 35° inclination) which was launched on November 27, 1997, from Tanegashima, Japan. GPS data from other satellite missions, such as OERSTED and the GEOSAT Follow-On (launched on February 10, 1998) will become available in the near future, even prior to the launch of CHAMP.

Surface Gravity Data

Despite the significant advances made in terms of both the coverage and the accuracy of terrestrial/airborne gravity data for EGM96, many geographic regions are still poorly surveyed (e.g. western China), have very sparse data (e.g. Antarctica), or are completely void of terrestrial anomaly data. Continuation of the collection efforts in these areas will definitely yield future model improvements. Future work is needed to identify problems in model performance over

certain regions that have been noted in the literature for instance over the Foxe Basin, Ungava Bay, and Lake Superior (cf. *Sansò*, [1997]). Not only the gravity data availability, but also their modeling and weighting within combination solutions require additional study. Analytical continuation techniques require more careful examination both from a theoretical and computational standpoint.

Long wavelength systematic errors in terrestrial gravity anomaly data bases require special consideration in the analysis of surface gravity data. It is becoming more evident that a better approach is needed to account for these systematics and preserve the strengths of these unique data over significant bandwidths of the model.

Finally, despite the significant advances in terrestrial gravity anomaly information over land areas, the marine surface gravimetry has not been significantly upgraded or re-examined for EGM96 since the development of The Ohio State University database in 1990. A major effort will be required to improve the quality and coverage of the marine gravimetry for future gravity solutions. Release of additional marine gravimetric holdings would improve this situation and provide additional information for the needed separation of dynamic ocean topography and ocean geoid signals from their aggregate effect sensed by satellite radar altimeter data.

Therefore, while EGM96 has reached several milestones, efforts continue to improve the model for both specialized and multi-purpose applications. In preparation for the CHAMP and GRACE dedicated geopotential missions, better modeling of the ocean geoid to more fully exploit the 3–4 cm accuracy achieved with synoptic TOPEX/POSEIDON altimetry is needed to continue improving our understanding of ocean circulation and also to baseline temporal geopotential effects. We look forward to challenging activities in gravitational field modeling in the years ahead.

12.3 References

Andersen, O., P. Knudsen, and C.C. Tscherning, Investigation of Methods for Global Gravity Field Recovery from the Dense ERS–1 Geodetic Mission Altimetry, in *Global Gravity Field and Its Temporal Variations*, IAG Symposia, 116, 218–226, Springer–Verlag, Berlin, 1996.

Forsberg, R., A New Covariance Model for Inertial, Gravimetry and Gradiometry, *J. Geophys. Res.*, 90, B2, 1305–1310, 1987.

Hwang, C., Orthogonal Functions Over the Oceans and Application to the Determination of Orbit Error, Geoid and Sea Surface Topography From Satellite Altimetry, *Rep. 414*, Dept. of Geod. Sci. and Surv., Ohio State Univ., Columbus, OH, 1991.

Luthcke, S.B., J.A. Marshall, C.M. Cox, F.G. Lemoine, D.D. Rowlands, R.G. Williamson, D.E. Pavlis, T.R. Olson, W.F. Eddy, S.C. Rowton, Precision Orbit Determination Using TDRSS, *J. Astro. Sci.,* in review, 1998.

Rao, D.B., S.D. Steenrod, and B.V. Sanchez, A method of calculating the total flow from a given sea surface topography, NASA Tech. Memo. TM–87799, Goddard Space Flight Center, 1987.

Rapp, R.H., C. Zhang, and Y. Yi, Analysis of Dynamic Ocean Topography Using TOPEX data and Orthonormal Functions, *J. Geophys. Res., 101*, C10, 22583–22598, 1996.

Sanchez, B.V., and N.K. Pavlis, Estimation of main tidal constituents from TOPEX altimetry using Proudman function expansion, *J. Geophys. Res., 100*, C12, 25229–25248, 1995.

Sanchez, B.V., W.J. Cunningham, and N.K. Pavlis, The Calculation of the Dynamic Sea Surface Topography and the Associated Flow Field From Altimetry Data: A Characteristic Function Method, *J. Phys. Ocean., 27*, 7, July, 1997.

Sansò, F., The Earth Gravity Model EGM96: Testing Procedures at IGeS, in *International Geoid Service Bulletin No. 6*, Politecnico di Milano, Milano, Italy, 1997.

Sideris, M., International tests of the new GSFC/DMA geopotential models, in Gravity, Geoid and Marine Geodesy, International Symposium, Tokyo, September 30–October 5, 1996, Segawa, Fujimoto, and Okubo (ed.), International Association of Geodesy Symposia, Vol. 117, Springer–Verlag, 1997.

Schoene, T, The gravity field in the Weddell Sea Antarctica, by radar altimetry from ERS–1 and GEOSAT, Reports on Polar Research, 220/96, Alfred Wegener Institute, Bremerhaven, 1996.

ACKNOWLEDGMENTS

Appendixes

A.   EGM96 *A PRIORI* STATION COORDINATES

The following table lists the *a priori* station locations used in the processing of the satellite tracking data. The epoch date applies to the tectonic velocity model used for that station (see Section 7.3.5). A range indicates that no tectonic model was used; the station locations being valid for dates within the range. Only a subset of these stations positions were estimated in the EGM96 comprehensive solution, the resulting *a posteriori* locations for those stations are given in Appendix B.

Station Name	Station Number	X m	Y m	Z m	Epoch yymmdd	Satellite/Tracking Technology
AC2J	410	6119570.4590	-1570186.9700	-872798.6560	94	TDRSS BRTS
ACN722	41722	6118462.3833	-1571566.1520	-878452.0200	870101	BE–C
ACNJ	403	6119570.4590	-1570186.9700	-872798.6560	94	TDRSS BRTS
ACSDOP	10068	6119383.0922	-1571424.9883	-871693.0729	780904	SEASAT
AGASSI	9050	1489750.4890	-4467466.2090	4287308.2280	60-69	Optical
ALGONQUIN	7410	918213.1730	-4346066.5472	4561957.6873	860701	SLR
ALGONQUIN	54010401	918129.6360	-4346071.2360	4561977.8210	921031	T/P GPS
ALGONQUIN	54010402	918129.6523	-4346071.3138	4561977.9031	921031	EP/EUVE T/P GPS
ALSJ	404	-4049082.1510	4210177.2990	-2554089.2730	94	TDRSS BRTS
ALTDOP	127	-3850348.7809	397635.0358	5052350.5284	780904	SEASAT
AMERICAN SOMOA	7096	-6100047.5355	-996197.8448	-1568973.4192	860701	SLR
AMSJ	405	-6100064.7960	-996801.2400	-1568551.3970	94	TDRSS BRTS
AMSTERDAM	4008	1086061.5265	4927963.1145	-3887828.4788	900601	DORIS SPOT–2
ANCDOP	114	-2656163.6653	-1544374.9123	5570653.4940	780904	SEASAT
ANCH14	41014	-2656157.6509	-1544452.1173	5571220.4500	870101	BE–C
ANCH55	556	-2656165.7023	-1544374.5571	5570653.3967	870101	HILAT GEOSAT
ANCHOR	60414	-2656161.7594	-1544376.3971	5570662.6250	801015	OSCAR–14
ANKARA	7589	4121934.4151	2652189.6601	4069034.8862	860701	SLR
AREQUIPA	4046	1942796.4203	-5804077.7599	-1796919.3062	900601	DORIS SPOT–2
AREQUIPA	7403	1942808.6840	-5804069.7914	-1796914.5712	860701	SLR
AREQUIPA	9007	1942791.4160	-5804077.1750	-1796919.7410	60-69	Optical
ARIZON	35037	-1939535.2243	-4843753.3367	3659822.5356	870101	GEOSAT
ARLIT	4035	5992632.2465	775892.2630	2035862.1301	900601	DORIS SPOT–2
ASCENSION	35000	6119381.0484	-1571426.5754	-871692.7935	870101	GEOSAT
ASKITES	7510	4353443.5757	2082667.6951	4156507.3230	860701	SLR
ASUNCI	35013	3090627.2345	-4872485.0474	-2709329.6792	870101	GEOSAT
ATHENG	9051	4606873.0250	2029751.4770	3903550.7510	60-69	Optical
AUST56	561	-740301.8191	-5457074.8177	3207238.5557	870101	HILAT GEOSAT
BADARY	4883	-838277.3606	3865777.0644	4987626.6478	900601	DORIS SPOT–2
BAHRAI	35012	3633912.5234	4425268.9070	2799868.5119	870101	GEOSAT
BAIRES	3791	2745490.8402	-4483592.7946	-3599089.4183	840601	NOVA–1
Baker-Nunn camera	9021	-1936777.8194	-5077708.5295	3331919.9484	60-69	Optical
Baker-Nunn camera	9028	4903766.4576	3965217.1307	963863.5554	60-69	Optical
BALKHASH	1869	1255422.5012	4265647.6987	4557736.7009	860701	SLR
BANGK2	35028	-1133939.8291	6092551.7563	1503386.8034	870101	GEOSAT
BAR GIYYORA	7530	4443964.1110	3121946.2511	3334694.9604	860701	SLR
BDADOP	30967	2293704.2617	-4883225.0207	3390590.1435	780904	SEASAT
BERMD	7039	2308232.9710	-4873591.6230	3394571.5460	60-69	Optical
BERMUDA	7067	2308537.3501	-4874080.0923	3393629.4479	860701	SLR
BGKDOP	30800	-1139091.1860	6089771.3864	1510701.8067	780904	SEASAT
BOLOGNA	7546	4461398.5825	919568.3161	4449511.2710	860701	SLR
BOROWIEC	7811	3738331.5061	1148247.7609	5021816.2241	860701	SLR
BPOIN	1021	1118043.4030	-4876309.0770	3942967.4810	60-69	Optical
BRUSSE	547	4027868.0946	307028.8973	4919513.9471	870101	HILAT GEOSAT
BSEDOP	116	4004965.4861	-96567.3683	4946540.0408	780904	SEASAT
BSI546	546	4004966.7133	-96567.6002	4946539.3700	870101	HILAT
CABO SAN LUCAS	7882	-1997245.6586	-5528039.1113	2468356.9098	860701	SLR
CAGLIARI	7545	4893397.1340	772674.8368	4004141.8403	860701	SLR
CALDOP	30414	-1659602.2862	-3676726.3280	4925494.0388	780904	SEASAT
CALGAR	563	-1659602.2787	-3676726.2360	4925494.2472	870101	GEOSAT
CALGRY	60125	-1659601.6003	-3676759.3159	4925484.0893	801015	OSCAR–14

Station Name	Station Number	X m	Y m	Z m	Epoch yymmdd	Satellite/Tracking Technology
CAMBRI	35011	-594792.4023	-2201200.7615	5936676.4774	870101	GEOSAT
CANBERRA	3101	-4446485.0577	2678131.3171	-3696270.6598	840601	NOVA–1
CANBERRA	7843	-4446479.8294	2678127.0800	-3696247.8612	860701	SLR
CARVN	7079	-2328604.2210	5299345.0060	-2669677.9820	60-69	Optical
CERRO TOLOLO	7401	1815517.1985	-5213465.9441	-3187999.5367	860701	SLR
CHANGCHUN	7237	-2674386.6214	3757189.3163	4391508.4636	860701	SLR
CHICHIJIMA	7844	-4491073.8935	3481526.9762	2887390.6379	860701	SLR
CNIDOP	30970	5384988.1922	-1576480.2513	3023839.8978	780904	SEASAT
COLBA	7037	-191272.1890	-4967271.4900	3983262.9130	60-69	Optical
COLDLK	9114	-1264844.0880	-3466892.6000	5185463.2890	60-69	Optical
COLDLK	9424	-1264826.4690	-3466886.9990	5185464.8310	60-69	Optical
COLEG	1033	-2299247.7130	-1445699.0890	5751816.9140	60-69	Optical
COLOMBO	4885	1113279.1666	6233646.2384	760276.2744	900601	DORIS SPOT–2
COMRIV	9031	1693804.4010	-4112337.4800	-4556643.6110	60-69	Optical
CURAC	9009	2251841.5530	-5816912.3720	1327168.2550	60-69	Optical
CYPRUS	35006	4349913.5199	2904399.4362	3638100.6898	870101	GEOSAT
DAKAR	4018	5886437.4553	-1848461.6505	1611441.2410	900601	DORIS SPOT–2
DAKLAS	7820	5886263.3136	-1845682.0616	1615247.2371	710601	Peole
DELFTH	8009	3923405.9510	299902.7530	5002981.3490	60-69	Optical
DENVER	35027	-1252439.3410	-4752041.3687	4054730.8537	870101	GEOSAT
DENVR	7045	-1240461.4510	-4760226.5280	4048986.4910	60-69	Optical
DGCDOP	30939	1915630.3838	6030276.5583	-801046.8810	780904	SEASAT
DIEGO	35010	1915629.5050	6030276.0501	-801047.2690	870101	GEOSAT
DIONYSOS	3041	4595219.4967	2039461.6128	3912623.6788	840601	NOVA–1
DIONYSOS	4047	4595215.4061	2039475.4603	3912614.7880	900601	DORIS SPOT–2
DIONYSOS	7515	4595215.1498	2039436.7778	3912630.2377	860701	SLR
DIONYSOS	7930	4595228.0844	2039443.8757	3912614.0119	710601	DI–C DI–C SLR
DIONYSOS	7940	4595216.7240	2039465.4022	3912616.0723	860701	SLR
DIYARBAKIR	7575	3848634.0083	3251760.7607	3898911.2948	860701	SLR
DJCB10	4103	4612392.3294	4218387.1646	1267105.1251	900601	DORIS SPOT–2
DJIBOUTI	4025	4583119.7172	4250952.0067	1266247.2807	900601	DORIS SPOT–2
DJIBOUTI	67120	4583115.2504	4250958.8709	1266254.9859	801015	OSCAR–14
DODAIR	9025	-3910446.7900	3376353.1640	3729219.3350	60-69	Optical
EASDOP	30730	-1888661.2205	-5355672.5472	-2893875.7077	780904	SEASAT
EASTER ISLAND	4041	-1884994.6149	-5357604.6153	-2892858.5944	900601	DORIS SPOT–2
EASTER ISLAND	7097	-1884977.9003	-5357609.7920	-2892854.2688	860701	SLR
EDINB	7036	-828471.2380	-5657448.7200	2816818.4410	60-69	Optical
EDWAFB	9113	-2450006.2278	-4624424.1895	3635042.7149	60-69	Opticall
EDWAFB	9425	-2449989.3750	-4624423.4660	3635032.6060	60-69	Optical
EDWRDS	35504	-2459944.9075	-4624307.0697	3628701.8500	870101	RADCAL
EFFELS	3141	4029171.6660	490750.7087	4904016.4812	840601	NOVA–1
EGLIN	35512	335711.5275	-5491154.4301	3216412.1600	870101	RADCAL
ENSENADA	7883	-2406129.7553	-4898365.8029	3290338.3291	860701	SLR
FAIRBANKS	4888	-2282502.6907	-1453416.6838	5756694.5698	900601	DORIS SPOT–2
FAIRBANKS	54040800	-2281621.3270	-1453595.7800	5756962.0230	921031	T/P GPS
FAIRBANKS	54040801	-2281621.3684	-1453595.8066	5756962.1279	921031	EP/EUVE T/P GPS
FLAGSTAFF	7891	-1923977.9733	-4850871.6062	3658574.1411	860701	SLR
FLODOP	641	4522403.6462	898003.7084	4392486.2340	780904	SEASAT
FLORES	4053	4221385.6376	-2549305.6531	4031508.8487	900601	DORIS SPOT–2
FORT DAVIS	3171	-1324205.3645	-5332056.7167	3232053.2930	840601	NOVA–1
FORT DAVIS	7080	-1330022.2827	-5328401.7128	3236480.5530	860701	SLR
FRENCH	591	3850660.2641	-5052187.8819	571067.1426	870101	GEOSAT
FTMYR	1022	807878.4110	-5651974.1440	2833506.0550	60-69	Optical
GFORK	1034	-521692.0340	-4242042.1720	4718727.7300	60-69	Optical
GOLDSTONE	4010	-2356503.6612	-4646583.9169	3668453.2602	900601	DORIS SPOT–2
GOLDSTONE	7288	-2356495.3702	-4646607.6926	3668425.8330	860701	SLR
GOLDSTONE	54040572	-2353614.0837	-4641385.4050	3676976.4619	921031	EP/EUVE T/P GPS
GRAND TURK	7068	1920481.8328	-5619478.4749	2318915.0429	860701	SLR
GRASSE	3721	4588035.4180	556435.2740	4381673.9269	840601	NOVA–1
GRASSE	7835	4581690.8695	556160.3679	4389360.1815	860701	SLR
GRAZ	7839	4194425.4902	1162694.8622	4647247.3761	860701	SLR
GRAZ	51100101	4194424.0520	1162702.5270	4647245.2630	921031	T/P GPS
GRAZ	51100102	4194425.4095	1162702.9033	4647246.7767	921031	EP/EUVE T/P GPS
GREECE	9091	4595165.2990	2039471.8610	3912663.4420	60-69	Optical
GRISSM	35040	327216.1032	-4835520.6707	4132670.7646	870101	GEOSAT
GSFCN	7077	1130078.6090	-4833034.5370	3992259.0350	60-69	Optical
GUAM	553	-5059776.6567	3591206.9500	1472786.8045	870101	HILAT GEOSAT

A-2

Station Name	Station Number	X m	Y m	Z m	Epoch yymmdd	Satellite/Tracking Technology
GUAM	7060	-5068950.6333	3584108.1362	1458769.7363	710601	Peole DI–C DI–C
GWMDOP	23	-5059775.0024	3591208.8964	1472788.9775	780904	SEASAT
HARTEBEESTHOEK	4019	5084641.4515	2670349.5971	-2768497.6605	900601	DORIS SPOT–2
HARTEBEESTHOEK	7501	5085401.1925	2668329.8107	-2768689.0329	860701	SLR
HARTEBEESTHOEK	53030201	5084625.1240	2670366.5890	-2768494.1940	921031	T/P GPS
HARTEBEESTHOEK	53030202	5084632.8935	2670370.6693	-2768498.4522	921031	EP/EUVE T/P GPS
HAULAS	7809	4578357.5216	457966.1109	4403174.0340	710601	DI–C DI—D
HAUTEP	8015	4578329.5530	457991.6640	4403198.0400	60-69	Optical
HAW100	41100	-5504174.5210	-2224152.5139	2325315.4800	870101	BE–C
HAW100	42100	-5504166.9590	-2224152.9153	2325304.7800	870101	DI–C–DI–D
HAWAI0	35007	-5511591.9671	-2226881.5663	2304026.0578	870101	GEOSAT
HAWAII	35507	-5509020.1219	-2230933.7789	2306265.9500	870101	RADCAL
HAWAIIAN VOLCA	4901	-5467477.6571	-2516164.1844	2107723.9797	900601	DORIS SPOT–2
HAYSTA	3161	1492398.5442	-4457294.0563	4296828.3966	840601	NOVA–1
HELSIK	9435	2884536.6870	1342144.0430	5509527.7090	60-69	Optical
HELWAN	7831	4728281.8282	2879671.5104	3156895.9406	860701	SLR
HERM57	570	3981776.5968	-89252.9306	4965288.9972	870101	GEOSAT
HERN55	550	1090142.0132	-4842521.9588	3991979.4107	870101	HILAT GEOSAT
HERN69	30690	1090120.8361	-4842525.4351	3991975.9027	870101	GEOSAT
HERNDN	60407	1090147.1080	-4842522.9097	3991985.2747	801015	OSCAR–14
HERSTM	3131	4033589.4675	24240.3066	4924219.7396	840601	NOVA–1
HERSTMONCEUX	7840	4033462.7122	23663.3892	4924305.9580	860701	SLR
HERSTMONCEUX	51321206	4033470.3020	23672.7160	4924301.1580	921031	T/P GPS
HERSTMONCEUX	51321207	4033470.4286	23672.7164	4924301.3137	921031	EP/EUVE T/P GPS
HILL	35509	-1804425.8835	-4461066.5668	4174196.2400	870101	RADCAL
HOBART	55011695	-3950184.0990	2522364.5980	-4311588.6210	921031	T/P GPS
HOBART	55011696	-3950184.0988	2522364.5976	-4311588.6214	921031	EP/EUVE T/P GPS
HONDOP	30188	-5511607.4154	-2226973.7729	2303883.9296	780904	SEASAT
HUAHINE	3111	-5345895.4182	-2958231.6082	-1824588.6959	840601	NOVA–1
HUAHINE	4027	-5345873.0283	-2958239.4610	-1824624.3011	900601	DORIS SPOT–2
HUAHINE	7123	-5345870.8596	-2958241.5206	-1824621.9093	860701	SLR
IDAHO	35036	-1738443.3640	-4295177.4130	4370317.4975	870101	GEOSAT
ILE DES PETREL	4042	-1941059.9461	1628659.3530	-5833613.5178	900601	DORIS SPOT–2
ISIGAKI	7307	-3265748.3194	4810004.1436	2614266.3516	860701	SLR
JAMAC	7076	1384174.8460	-5905664.5470	1966547.3080	60-69	Optical
JOBUR	1031	5084791.2370	2670405.7710	-2768142.2320	60-69	Optical
JOHNST	9117	-6007419.7090	-1111871.0386	1825753.9626	60-69	Optical DI–C
JOHNST	9427	-6007406.6360	-1111885.5460	1825752.7590	60-69	Optical
JUBC4	7074	976299.5400	-5601381.5700	2880254.9170	60-69	Optical
JUM24	7071	976288.6650	-5601391.2880	2880239.3620	60-69	Optical
JUM40	7072	976292.4350	-5601385.1490	2880250.3930	60-69	Optical
JUPC1	7073	976298.9260	-5601384.3410	2880248.4470	60-69	Optical
JUPGEO	9049	976297.3980	-5601389.3820	2880237.6830	60-69	Optical
JUPTR	9010	976307.4630	-5601387.4030	2880242.9600	60-69	Optical
KAENA	35514	-5512517.0712	-2197413.1117	2330518.8500	870101	RADCAL
KARITSA	7520	4596041.4459	1733478.2050	4055721.5852	860701	SLR
KATAVIA	7512	4573398.6970	2409323.6492	3723882.4539	860701	SLR
KATZIVELY	1893	3785943.5362	2550781.9952	4439462.0751	860701	SLR
KAUAI	4886	-5543974.5370	-2054589.9188	2387488.2812	900601	DORIS SPOT–2
KERGUE	567	1406287.5835	3918141.2653	-4816207.1821	870101	GEOSAT
KERGUELEN	4009	1405826.2968	3918281.8016	-4816204.3496	900601	DORIS SPOT–2
KINS02	35026	6136058.1434	1673472.8308	-482833.7137	870101	GEOSAT
KITAB	4882	1945025.1664	4556708.7963	4004235.7801	900601	DORIS SPOT–2
KOKEE_PARK	54042403	-5543838.0890	-2054587.5120	2387809.5650	921031	T/P GPS
KOKEE_PARK	54042404	-5543838.1702	-2054587.5418	2387809.5997	921031	EP/EUVE T/P GPS
KOMSOMOLSK	1868	-2948531.2953	2774305.2673	4912296.6314	860701	SLR
KOOTWIJK	8833	3899209.3752	396717.9747	5015093.0673	860701	SLR
KOOTWIJK	51350402	3899225.3380	396731.7740	5015078.2990	921031	T/P GPS
KOOTWIJK	51350403	3899225.4018	396731.7805	5015078.3815	921031	EP/EUVE T/P GPS
KOUROU	4016	3854715.1178	-5049977.7811	564747.2163	900601	DORIS SPOT–2
KWADJA	35505	-6160871.2927	1339996.5831	960765.0900	870101	RADCAL
KWAJALEIN ATOL	7092	-6143445.6311	1364705.8517	1034165.6915	860701	SLR
KWJDOP	10214	-6160996.3522	1339618.7841	960421.6883	780904	SEASAT
LA REUNION	4012	3364093.7674	4907945.3412	-2293482.6445	900601	DORIS SPOT–2
LAJDOP	30966	4432069.5835	-2268090.8198	3973465.6821	780904	SEASAT
LAMPEDUSA	7544	5072830.6500	1130887.6440	3684838.3756	860701	SLR
LASC02	35021	-1556213.6359	-5169448.5417	3387240.9826	870101	GEOSAT

Station Name	Station Number	X m	Y m	Z m	Epoch yymmdd	Satellite/Tracking Technology
LASC55	552	-1556211.7109	-5169449.0134	3387240.9948	870101	HILAT GEOSAT
LCR103	41103	-1556212.6533	-5169467.5797	3387270.7100	870101	BE–C
LCR103	42103	-1556211.8290	-5169464.8658	3387259.6100	870101	DI–C DI–D
LCR551	551	-1556211.8862	-5169450.6281	3387237.7800	870101	HILAT
LIBREVILLE	4013	6287388.6911	1071574.0764	39146.6377	900601	DORIS SPOT–2
MADRID	3061	4849193.9738	-360300.7531	4114932.3599	840601	NOVA–1
MADRID	51340787	4849202.5300	-360329.1630	4114912.9960	921031	T/P GPS
MADRID	51340788	4849202.5302	-360329.1626	4114912.9965	921031	EP/EUVE T/P GPS
MAHDOP	20	3602879.7363	5238221.2088	-515933.0560	780904	SEASAT
MAHE S	558	3602878.4361	5238221.1286	-515933.1584	870101	HILAT GEOSAT
MAIDANAK1	1863	1953260.2955	4588931.4119	3966826.0403	860701	SLR
MAIDANAK2	1864	1953288.2077	4588986.4271	3966762.2148	860701	SLR
MALVRN	8011	3920169.1760	-134712.8660	5012731.4410	60-69	Optical
MALVRN	9080	3920172.6250	-134728.0380	5012741.9180	60-69	Optical
MANILLE	4884	-3184357.6874	5291042.2170	1590419.4008	900601	DORIS SPOT–2
MARION ISLAND	4022	3448405.4997	2680356.1582	-4632640.7597	900601	DORIS SPOT–2
MASPALOMAS	53130300	5439189.1830	-1522054.8150	2953464.1310	921031	T/P GPS
MASPALOMAS	53130301	5439189.2873	-1522054.8445	2953464.1875	921031	EP/EUVE T/P GPS
MATERA	7939	4641964.0018	1393070.7531	4133263.1097	860701	SLR
MATERA	51273408	4641949.9004	1393045.2860	4133287.3294	921031	EP/EUVE T/P GPS
MAUI	7210	-5466007.6261	-2404422.6710	2242190.3342	860701	SLR
MAZATLAN	7122	-1660090.5095	-5619100.1270	2511637.7096	860701	SLR
MC MURDO	19	-1310715.7522	310468.5886	-6213364.3942	780904	SEASAT
MC MURDO	562	-1310719.0880	310473.0647	-6213363.2240	870101	HILAT GEOSAT
MC MURDO	56600194	-1310696.4040	310469.2610	-6213368.4790	921031	T/P GPS
MC MURDO	56600195	-1310696.4044	310469.2610	-6213368.4794	921031	EP/EUVE T/P GPS
MELENGICLICK	7580	4247619.0430	2778640.3320	3851608.0832	860701	SLR
METSAHOVI	4006	2890641.5607	1310310.5280	5513964.6277	900601	DORIS SPOT–2
METSAHOVI	51050388	2892571.0160	1311843.2980	5512634.0320	921031	T/P GPS
METSAHOVI	51050389	2892571.0162	1311843.2983	5512634.0324	921031	EP/EUVE T/P GPS
MHE717	41717	3602898.1319	5238251.2710	-515923.4300	870101	BE–C
MHE717	42717	3602901.3890	5238259.8616	-515929.1600	870101	DI–C DI–D
MISAWA	27	-3857197.7214	3108654.0898	4004045.8810	780904	SEASAT
MIZUSA	548	-3857196.8218	3108663.9914	4004050.9227	870101	HILAT GEOSAT
MOJAV	1030	-2357227.9720	-4646326.3870	3668316.3200	60-69	Optical
MONUMENT PEAK	7110	-2386280.9535	-4802352.1922	3444882.3784	860701	SLR
MONUMENT PEAK	7220	-2386295.2400	-4802345.3138	3444881.7819	860701	SLR
MSADOP	60027	-3857198.3599	3108656.9611	4004060.7961	801015	OSCAR–14
MT GENEROSO	7590	4390308.8519	696753.4804	4560836.7094	860701	SLR
MT HOPKINS	7921	-1936760.4038	-5077707.0939	3331922.7750	710601	DI–C DI–C SLR
MT HOPKINS	7921	-1936761.5848	-5077707.1434	3331922.0182	860701	SLR
MUDONI	8030	4205643.4530	163740.5740	4776553.4940	60-69	Optical
NANI TAL	9006	1018204.4175	5471111.1326	3109627.5016	60-69	Optical
NAPDOP	30448	-4923686.5069	270902.4325	-4031780.1104	780904	SEASAT
NAS MS	35039	130023.6947	-5379944.8847	3412091.2767	870101	GEOSAT
NATAL	7929	5186467.5812	-3653856.8589	-654320.9996	860701	SLR
NATAL	7929	5186467.7762	-3653856.3952	-654322.0366	710601	DI–C DI–C SLR
NATALB	9029	5186466.8500	-3653855.8320	-654322.3470	60-69	Optical
NEVADA	35038	-2369577.2872	-4327796.2390	4030076.8853	870101	GEOSAT
NEWFL	1032	2602768.2050	-3419144.3830	4697652.4940	60-69	Optical
NICEFR	8019	4579480.4390	586616.3290	4386423.4740	60-69	Optical
NMXDOP	113	-1556215.7432	-5169448.9373	3387242.1120	780904	SEASAT
NOTO	7543	4934529.0706	1321133.0993	3806522.5885	860701	SLR
NOUMEA	4036	-5739993.7234	1387548.5102	-2402085.3964	900601	DORIS SPOT–2
NY-ALESUND	4020	1202794.4505	254163.1717	6237609.1790	900601	DORIS SPOT–2
NY-ALESUND	51031700	1202431.3670	252626.7560	6237770.8340	921031	T/P GPS
NY-ALESUND	51031701	1202431.7219	252626.8302	6237772.6865	921031	EP/EUVE T/P GPS
OLFAN	9002	5056123.8840	2716518.5770	-2775768.9270	60-69	Optical
ONSALA	51040203	3370658.7530	711876.9950	5349786.8380	921031	T/P GPS
ONSALA	51040204	3370659.2724	711877.1044	5349787.6679	921031	EP/EUVE T/P GPS
OOMER	1024	-3977276.4680	3725648.2560	-3302977.2310	60-69	Optical
ORGAN	9001	-1535736.2680	-5166995.2570	3401048.3860	60-69	Optical
ORORL	1038	-4447486.9900	2677163.2440	-3695051.0990	60-69	Optical
ORRORL	67143	-4446452.6995	2678226.7411	-3696181.9326	801015	OSCAR–14
OSLONR	9115	3121282.5450	592652.3680	5512725.6120	60-69	Optical
OSLONR	9426	3121282.5450	592652.3680	5512725.6120	60-69	Optical
OTTAWA	128	1091452.1660	-4351289.4372	4518698.9501	780904	SEASAT

A-4

Station Name	Station Number	X m	Y m	Z m	Epoch yymmdd	Satellite/Tracking Technology
OTTAWA	564	1091453.1519	-4351290.7217	4518698.3403	870101	GEOSAT
OTTAWA	4048	1107623.8191	-4347253.8859	4518738.1809	900601	DORIS SPOT–2
OTTDOP	60128	1091456.5252	-4351286.9129	4518709.3597	801015	OSCAR–14
OWENS VALLEY	7853	-2410423.1090	-4477799.7734	3838689.9486	860701	SLR
PAMATAI	568	-5245203.4933	-3080478.4719	-1912829.9854	870101	GEOSAT
PAMATAI	67118	-5245201.2197	-3080482.7856	-1912812.8259	801015	OSCAR–14
PAMATAI	59220102	-5245195.1530	-3080472.1760	-1912825.6000	921031	T/P GPS
PAMATAI	59220103	-5245202.0745	-3080476.2416	-1912828.1418	921031	EP/EUVE T/P GPS
PARISD	3711	4201865.6873	177900.2966	4779213.3927	840601	NOVA–1
PASADENA	7896	-2493214.5563	-4655226.8569	3565576.3869	860701	SLR
PASADENA	54040005	-2493304.0660	-4655215.5300	3565497.3340	921031	T/P GPS
PASADENA	54040006	-2493304.1027	-4655215.5975	3565497.3860	921031	EP/EUVE T/P GPS
PATRIC	35515	918334.4121	-5548262.8113	2998909.3600	870101	RADCAL
PATRICK AFB	7069	917957.6958	-5548370.4334	2998776.7914	860701	SLR
PENCHU	3831	4052451.4621	1417630.1884	4701420.5744	840601	NOVA–1
PENTICTON	54010501	-2059164.5970	-3621108.3910	4814432.4380	921031	T/P GPS
PENTICTON	54010502	-2059164.6339	-3621108.4566	4814432.5254	921031	EP/EUVE T/P GPS
PERDOP	30968	-2353567.2425	4877206.9610	-3358325.8875	780904	SEASAT
PILLAR	35511	-2722178.5360	-4273170.7091	3861377.1000	870101	RADCAL
PINYON	54040701	-2369510.3640	-4761207.1860	3511396.1310	921031	T/P GPS
PINYON	54040702	-2369511.0476	-4761208.5610	3511397.1514	921031	EP/EUVE T/P GPS
PLATTE	3181	-1240642.5322	-4720485.2892	4094472.7782	840601	NOVA–1
PLATTEVILLE	7112	-1240679.3710	-4720463.6548	4094480.0377	860701	SLR
POKAFL	35503	-2268114.8969	-1448575.1754	5763731.0800	870101	RADCAL
PORT MORESBY	4055	-5288462.5919	3410034.8339	-1038802.7864	900601	DORIS SPOT–2
POTSDA	3121	3800592.5258	881915.4429	5028912.7059	840601	NOVA–1
POTSDAM	7836	3800638.5281	881983.4673	5028832.3690	860701	SLR
PRET55	554	5051977.3550	2725642.1746	-2774467.4272	870101	HILAT GEOSAT
PRETOR	67122	5067176.8811	2736607.5720	-2735027.2676	801015	OSCAR–14
PRT115	41115	5052004.3666	2725664.9079	-2774469.9800	870101	BE–C
PRT115	42115	5052014.3058	2725660.0317	-2774470.4900	870101	DI–C DI–D
PRTDOP	105	5051977.2545	2725639.9926	-2774467.7157	780904	SEASAT
PTMUGU	35506	-2574980.3274	-4615965.3962	3557715.0700	870101	RADCAL
PURIO	7040	2465070.5950	-5534916.6120	1985523.4730	60-69	Optical
PURPLE MOUNTAI	4045	-2608501.6251	4739980.6239	3366883.0635	900601	DORIS SPOT–2
QUIDOP	30121	1280855.9903	-6250960.0956	-10813.9440	780904	SEASAT
QUINCY	7109	-2517236.5422	-4198555.6290	4076569.2081	860701	SLR
QUITO	35022	1272867.5798	-6252770.3271	-23798.1977	870101	GEOSAT
RAPID	35029	-1038825.7846	-4464429.5247	4421682.7643	870101	GEOSAT
REYKJAVIK	4887	2585528.5453	-1044368.0215	5717158.8531	900601	DORIS SPOT–2
RICHMOND	4023	961079.9589	-5673576.1255	2741639.1979	900601	DORIS SPOT–2
RICHMOND	7295	961317.9319	-5674091.0706	2740489.7402	860701	SLR
RICHMOND	54049986	961319.0200	-5674090.9380	2740489.5280	921031	T/P GPS
RICHMOND	54049987	961319.0339	-5674091.0212	2740489.5687	921031	EP/EUVE T/P GPS
RIGA	1884	3183894.5245	1421498.2760	5322804.1825	860701	SLR
RIGA	9431	3183884.9110	1421484.3450	5322809.3760	60-69	Optical
RIGRND	3811	1429892.1158	-3495345.9055	-5122704.9889	840601	NOVA–1
RIO GRANDE	4017	1429849.7107	-3495346.2646	-5122723.2874	900601	DORIS SPOT–2
ROSMA	1042	647530.1870	-5177927.4920	3656709.1560	60-69	Optical
ROSMN	1037	647536.2270	-5177927.0920	3656710.4560	60-69	Optical
ROTHERA	4903	909378.0161	-2264934.4436	-5872957.0953	900601	DORIS SPOT–2
ROUMELLI	7517	4728693.4475	2174374.8234	3674573.6841	860701	SLR
S POLE	35001	-357.2083	246.9022	-6359557.0478	870101	GEOSAT
S00013	41013	-3779672.7658	3024728.1724	4139014.6900	870101	BE–C
S00013	42013	-3779737.6557	3024790.2920	4139060.8800	870101	DI–C DI–D
S00092	41092	-741633.9027	-5462238.2142	3198151.8500	870101	BE–C
S00106	41106	4005472.5586	-71748.9102	4946769.1700	870101	BE–C
S00106	42106	4005478.9247	-71754.5817	4946705.1500	870101	DI–C DI–D
S00111	41111	1122662.9002	-4823065.8035	4006488.0200	870101	BE–C
S00111	42111	1122662.4727	-4823063.1674	4006475.4300	870101	DI–C DI–D
S00200	41200	-2572048.0000	-4618401.2420	3556656.9260	870101	BE–C
S00403	42403	1122654.1750	-4823049.8630	4006464.4810	870101	DI–C
S00726	41726	-5367639.7203	3437957.3901	-226695.7600	870101	BE–C
S00729	42729	5142557.0549	-1566198.2185	3421742.2200	870101	DI–C
S00737	41737	-2348787.6687	-4652661.3767	3665945.1900	870101	BE–C
S00738	41738	-2127828.7251	-3785854.8991	4656075.8400	870101	BE–C
S00750	42750	-308280.8154	-4971541.3494	3970700.2700	870101	DI–C DI–D

Station Name	Station Number	X m	Y m	Z m	Epoch yymmdd	Satellite/Tracking Technology
S00810	42810	-5076834.9271	449286.2351	-3821955.1300	870101	DI–C DI–D
SAFLAS	7804	5105608.8229	-555260.6843	3769641.8628	710601	Optical
SAINTE-HELENE	4043	6104828.2371	-605837.7237	-1740706.8009	900601	DORIS SPOT–2
SAKHALINS	4881	-3465325.6624	2638267.0412	4644082.3881	900601	DORIS SPOT–2
SAMOA	60424	-6100053.6242	-997196.6187	-1568301.0799	801015	OSCAR–14
SAN DIEGO	7035	-2428829.4546	-4799752.3421	3417268.1093	860701	SLR
SAN FERNANDO	7824	5105472.9615	-555109.1443	3769893.3374	860701	SLR
SAN FR	590	5105461.7800	-555123.0415	3769894.8236	870101	GEOSAT
SAN MI	559	-3088049.2016	5333055.3892	1638819.2097	870101	HILAT GEOSAT
SANFER	68804	5105462.3115	-555116.1370	3769899.3783	801015	OSCAR–14
SANJ55	555	4083914.9754	-4209795.6869	-2499118.2191	870101	HILAT GEOSAT
SANJOS	67116	4084894.5785	-4209292.3553	-2498402.0561	801015	OSCAR–14
SANTIA	35025	1769924.4731	-5044552.7595	-3468251.7121	870101	GEOSAT
SANTIAGO CHILE	1028	1769719.3140	-5044614.9790	-3468253.3220	60-69	Optical
SANTIAGO CHILE	4038	1776346.2534	-5026544.3204	-3491183.8135	900601	DORIS SPOT–2
SANTIAGO CHILE	7400	1769699.6891	-5044613.4332	-3468259.3286	860701	SLR
SANTIAGO CHILE	67190	1776343.7729	-5026525.9446	-3491210.3971	801015	OSCAR–14
SANTIAGO CHILE	54170502	1769693.0220	-5044573.8000	-3468321.2970	921031	T/P GPS
SANTIAGO CHILE	54170503	1769693.0477	-5044573.8733	-3468321.3478	921031	EP/EUVE T/P GPS
SANTIAGO DE CU	1953	1474548.2815	-5811242.2759	2168945.4730	860701	SLR
SGN812	42812	4901636.7987	1305826.4767	3853646.8600	870101	DI–C DI–D
SHANGHAI	7837	-2831089.5022	4676203.1510	3275171.7583	860701	SLR
SHEMYA	35018	-3850346.7265	397633.3049	5052352.7003	870101	GEOSAT
SHIDOP	30123	6104421.3597	-611086.8184	-1740834.3107	780904	SEASAT
SHRAZ	9008	3376878.5850	4403998.7390	3136264.8090	60-69	Optical
SIGA50	4050	2189056.6415	-2235050.3736	-5539571.1576	900601	DORIS SPOT–2
SIGONE	35024	4901702.7823	1306297.9816	3853347.0489	870101	GEOSAT
SIMEIS	1873	3783901.1260	2551406.2643	4441258.1615	860701	SLR
SIMOSATO	3091	-3822376.4756	3699348.4306	3507574.8765	840601	NOVA–1
SIMOSATO	7838	-3822386.8080	3699362.8169	3507571.6552	860701	SLR
SIO1	54046000	-2455521.6680	-4767213.4330	3441654.8930	921031	T/P GPS
SIO1	54046001	-2455522.3781	-4767214.8116	3441655.8948	921031	EP/EUVE T/P GPS
SIOUX	35017	-523526.2993	-4687704.9586	4279311.3506	870101	GEOSAT
SJEDOP	8	4083912.1851	-4209798.4102	-2499118.6601	780904	SEASAT
SJEDOP	41008	4083934.0294	-4209821.1838	-2499132.7800	870101	BE–C
SJEDOP	42008	4083929.4964	-4209833.1574	-2499141.4900	870101	DI–C DI–D
SMG011	41011	-3088067.5348	5333084.3780	1638824.5900	870101	BE–C
SMG121	42121	-3088066.7402	5333092.5085	1638830.4800	870101	DI–C DI–D
SMGDOP	22	-3088046.5285	5333054.4982	1638820.6017	780904	SEASAT
SMTH12	41012	-3942263.0440	3468869.8525	-3608220.5400	870101	BE–C
SMTH41	60412	-3942246.5899	3468857.6862	-3608185.6861	801015	OSCAR–14
SMTH54	545	-3942244.2616	3468867.3886	-3608187.3351	870101	HILAT GEOSAT
SOCORRO ISLAND	4040	-2160928.0479	-5642987.4971	2034688.0783	900601	DORIS SPOT–2
SOCORRO ISLAND	4904	-2160725.0619	-5643017.7041	2034836.6338	900601	DORIS SPOT–2
SPAIN	9004	5105597.1270	-555217.1930	3769669.3600	60-69	Optical
ST HEL	35004	6104421.1477	-611085.7243	-1740834.3496	870101	GEOSAT
ST. JOHNS	54010100	2612631.3860	-3426807.0120	4686757.7650	921031	T/P GPS
ST. JOHNS	54010101	2612631.4522	-3426807.0989	4686757.8849	921031	EP/EUVE T/P GPS
ST2K	762	-1538987.0100	-5158453.2640	3412123.7900	94	TDRSS K band
ST3K	763	-1538992.1600	-5158470.5450	3412095.5120	94	TDRSS K band
STFDOP	112	-3942239.9155	3468860.6367	-3608198.0577	780904	SEASAT
STFDOP	42112	-3942259.0155	3468890.4438	-3608217.8100	870101	DI–C DI–D
STGK	761	-1538981.8470	-5158435.9590	3412152.0330	94	TDRSS K band
STODOP	30280	1743938.7467	-5022695.3563	-3512039.7188	780904	SEASAT
SUDBR	7075	692633.4030	-4347065.1170	4600486.8220	60-69	Optical
TAFDOP	24	-6100052.8595	-997191.2338	-1568313.4533	780904	SEASAT
TAFU56	560	-6100052.2476	-997197.6262	-1568313.6858	870101	HILAT GEOSAT
TAIPEI	52360100	-3024781.8950	4928936.9390	2681234.5460	921031	T/P GPS
TAIPEI	52360101	-3024782.7367	4928938.3098	2681235.2966	921031	EP/EUVE T/P GPS
TANAN	1043	4091868.6110	4434292.8650	-2064729.0580	60-69	Optical
TEXDOP	192	-740292.7343	-5457076.5957	3207236.8154	780904	SEASAT
TFN117	42117	-6100055.1567	-997184.4336	-1568467.2300	870101	DI–C DI–D
TFNA17	41017	-6100046.7409	-997200.8304	-1568469.3500	870101	BE–C
THULE	557	539848.9988	-1388562.3503	6180979.9849	870101	HILAT GEOSAT
THULE	35508	539849.0276	-1388561.9910	6180980.6200	870101	RADCAL
TIDBINBILLA	55010382	-4460996.1550	2682557.2220	-3674444.0600	921031	T/P GPS
TIDBINBILLA	55010383	-4460996.1553	2682557.2216	-3674444.0598	921031	EP/EUVE T/P GPS

Station Name	Station Number	X m	Y m	Z m	Epoch yymmdd	Satellite/Tracking Technology
TOKYO	9005	-3946701.0990	3366279.0930	3698835.7630	60-69	Optical
TONOPA	35510	-2272636.8270	-4507725.5575	3887868.5500	870101	RADCAL
TOULOUSE	4002	4628047.7950	119670.2331	4372787.4200	900601	DORIS SPOT–2
TOWN	55012695	-5041024.8480	3296980.2340	-2090553.3580	921031	T/P GPS
TOWN	55012696	-5041024.8485	3296980.2345	-2090553.3582	921031	EP/EUVE T/P GPS
TRIESTE	7550	4336737.4302	1071272.9526	4537911.8018	860701	SLR
TRISTAN DA CUN	4005	4978462.6980	-1086620.8900	-3823205.8480	900601	DORIS SPOT–2
TROMSO	4054	2102915.8107	721600.8904	5958200.5841	900601	DORIS SPOT–2
TROMSO	7602	2102904.4486	721602.2093	5958201.2303	860701	SLR
TROMSO	51030202	2102940.4470	721569.3530	5958192.1280	921031	T/P GPS
TROMSO	51030203	2102941.2602	721569.6324	5958194.4470	921031	EP/EUVE T/P GPS
TULDOP	118	539847.1362	-1388563.5608	6180979.8494	780904	SEASAT
TVE725	41725	-5035501.9019	3305618.2029	-2090236.8900	870101	BE–C
TVEDOP	30793	-5037685.7676	3301870.1081	-2090783.5547	780904	SEASAT
UCCLE	21	4027834.1423	307015.1066	4919537.0430	780904	SEASAT
UCLDOP	60021	4027832.2211	307019.6695	4919547.3028	801015	OSCAR–14
UKIAH	65170	-2713390.4069	-4144629.8555	4004321.0899	801015	OSCAR–14
UKIDOP	51960	-2713391.3773	-4144614.9871	4004299.6580	780904	SEASAT
ULASK	1036	-2282347.3240	-1452637.5000	5756905.1070	60-69	Optical
UNDAK	7034	-521692.0830	-4242042.5710	4718728.1760	60-69	Optical
USUDA	52172996	-3855263.0760	3427432.5350	3741020.4770	921031	T/P GPS
USUDA	52172997	-3855263.0763	3427432.5346	3741020.4769	921031	EP/EUVE T/P GPS
UZHGOR	9432	3907417.1510	1602443.8530	4763918.6440	60-69	Optical
VANDEN	35501	-2666947.0064	-4519838.3130	3612814.2900	870101	RADCAL
VANDENB/HARVES	54050000	-2686069.0140	-4527084.6020	3589502.1460	921031	T/P GPS
VANDENB/HARVES	54050001	-2686069.0140	-4527084.6020	3589502.1460	880101	EP/EUVE T/P GPS
VERNAL	7892	-1631486.1332	-4589133.9865	4106749.0397	860701	SLR
VILDO	9011	2280590.6930	-4914577.9440	-3355404.5010	60-69	Optical
VILLA DOLORES	9012	-5466059.6015	-2404292.2531	2242187.5109	60-69	Optical
VIRDOP	107	1090140.2873	-4842525.2604	3991974.6238	780904	SEASAT
WALLIS	4037	-6195393.7552	-413728.1303	-1454075.1797	900601	DORIS SPOT–2
WALLOP	35502	1263672.9995	-4875755.2848	3899751.9600	870101	RADCAL
WALMOT	7078	1261602.9930	-4881348.5680	3893440.2170	60-69	Optical
WASHINGTON	7043	1130731.5610	-4831323.5830	3994136.7680	60-69	Optical
WASHINGTON	7050	1130671.0675	-4831364.7332	3994105.4177	710601	DI–C DI–C SLR
WASHINGTON	7105	1130718.3591	-4831350.7074	3994106.7168	860701	SLR
WELL	55020897	-4780648.8030	436507.1660	-4185440.3900	921031	T/P GPS
WELL	55020898	-4780648.8030	436507.1658	-4185440.3904	921031	EP/EUVE T/P GPS
WESTFORD	7091	1492452.2012	-4457278.8673	4296816.2402	860701	SLR
WETTZELL	443	4075575.5765	931796.8756	4801583.8000	870101	HILAT
WETTZELL	549	4075575.4422	931796.9152	4801583.9195	870101	GEOSAT
WETTZELL	8834	4075575.8591	931786.2861	4801584.2787	860701	SLR
WETTZELL	60643	4075532.7175	931827.0848	4801618.8348	801015	OSCAR–14
WETTZELL	51420180	4075578.6669	931852.6525	4801569.9829	921031	EP/EUVE T/P GPS
WH2J	402	-1539599.2400	-5160545.8710	3408686.6130	94	TDRSS BRTS
WH2K	162	-1539390.3260	-5160968.1170	3408177.1720	94	TDRSS K band
WH3K	163	-1539394.9960	-5160983.8220	3408151.4530	94	TDRSS K band
WHSJ	401	-1539599.2400	-5160545.8710	3408686.6130	94	TDRSS BRTS
WHSK	161	-1539385.6410	-5160952.4110	3408202.8790	94	TDRSS K band
WHTSND	35513	-1529940.3884	-5171206.9248	3396640.1000	870101	RADCAL
WICHIT	35015	-783475.8033	-5236534.7266	3544673.8053	870101	GEOSAT
WNKFL	1035	3983120.0580	-48495.4330	4964717.0900	60-69	Optical
WOOMER	9003	-3983793.8390	3743090.8620	-3275530.6420	60-69	Optical
WOOMERA	9023	-3977781.8349	3725112.1640	-3303003.5081	60-69	Optical
WUHAN	7236	-2266557.5587	5009078.9147	3222265.2312	860701	SLR
XRISOKALARIA	7525	4745948.3462	1905707.3918	3799169.7957	860701	SLR
YARRAGADEE	7090	-2389010.1726	5043330.0284	-3078521.2447	860701	SLR
YARRAGADEE	55010703	-2389025.4730	5043316.8560	-3078531.0280	921031	T/P GPS
YARRAGADEE	55010704	-2389025.5000	5043316.9135	-3078531.0633	921031	EP/EUVE T/P GPS
YELLOWKNIFE	4051	-1224423.6561	-2689227.3625	5633645.2559	900601	DORIS SPOT–2
YELLOWKNIFE	54012702	-1224452.3720	-2689216.0910	5633638.3230	921031	T/P GPS
YELLOWKNIFE	54012703	-1224452.3943	-2689216.1399	5633638.4266	921031	EP/EUVE T/P GPS
YIGILCA	7587	4117360.5769	2517078.1458	4157679.6571	860701	SLR
YOZGAT	7585	4029729.1652	2802094.5583	4062068.5672	860701	SLR
YUMA	7894	-2196779.0845	-4887337.0800	3448424.5065	860701	SLR
ZIMMERWALD	7810	4331282.8479	567550.8855	4633140.5063	860701	SLR
ZIMMERWALD	8010	4331311.5580	567536.9340	4633125.6350	60-69	Optical

B.   EGM96 *A POSTERIORI* STATION COORDINATES

The following table lists the *a posteriori* station locations estimated in the EGM96 comprehensive solution. The epoch date applies to the tectonic velocity model used for that station (see Section 7.3.5). A range indicates that no tectonic model was used; the station locations being valid for dates within the range.

Station Name	Station Number	X m	Y m	Z m	σX m	σY m	σZ m	Epoch yymmdd	Satellite/Tracking Technology
ACN722	41722	6118463.4751	-1571566.3720	-878452.0749	2.6400	3.9200	3.4200	870101	BE–C
ACSDOP	10068	6119383.1598	-1571425.2136	-871692.9081	.4220	.5770	.3270	780904	SEASAT
AGASSI	9050	1489744.2933	-4467485.1630	4287308.3962	11.8000	14.3000	12.0000	60-69	Optical
ALGONQUIN	7410	918213.1444	-4346066.5882	4561957.6160	.0375	.0422	.0305	860701	SLR
ALGONQUIN	54010402	918129.6657	-4346071.3773	4561977.9704	.0202	.0949	.1000	921031	EP/EUVE T/P GPS
ALTDOP	127	-3850348.6168	397635.0432	5052350.7100	.2250	.2660	.2350	780904	SEASAT
AMERICAN SOMOA	7096	-6100047.5115	-996197.8201	-1568973.3541	.0463	.0605	.0590	860701	SLR
AMSTERDAM	4008	1086061.6048	4927963.1183	-3887828.2889	.1010	.0628	.0809	900601	DORIS SPOT–2
ANCDOP	114	-2656163.5004	-1544374.7196	5570653.8116	.2410	.2280	.2330	780904	SEASAT
ANCH14	41014	-2656150.9564	-1544464.0675	5571220.4741	45.7000	76.8000	10.0000	870101	BE–C
ANCH55	556	-2656165.8226	-1544374.5755	5570653.0387	.1180	.1640	.1090	870101	HILAT GEOSAT
ANCHOR	60414	-2656162.4455	-1544377.5876	5570657.7027	2.7400	2.8800	14.5000	801015	OSCAR–14
ANKARA	7589	4121934.5242	2652189.5731	4069034.7671	.0752	.0738	.0478	860701	SLR
AREQUIPA	4046	1942796.3744	-5804077.8014	-1796919.2674	.0147	.0080	.0103	900601	DORIS SPOT–2
AREQUIPA	7403	1942808.6336	-5804069.8089	-1796914.5982	.0147	.0080	.0103	860701	SLR
AREQUIPA	9007	1942782.9917	-5804089.2496	-1796919.4547	3.3400	2.8100	3.1500	60-69	Optical
ARIZON	35037	-1939535.3510	-4843753.5323	3659821.9409	.2900	.1540	.1370	870101	GEOSAT
ARLIT	4035	5992632.2967	775891.9734	2035862.3374	.0918	.1470	.0841	900601	DORIS SPOT–2
ASCENS	35000	6119380.8890	-1571426.7956	-871693.2464	.1830	.3870	.1590	870101	GEOSAT
ASKITES	7510	4353443.6345	2082667.6757	4156507.2846	.0430	.0486	.0353	860701	SLR
ASUNCI	35013	3090627.0763	-4872485.4701	-2709330.2790	.3000	.2130	.1440	870101	GEOSAT
ATHENG	9051	4606876.5679	2029745.2039	3903563.9147	19.0000	19.0000	21.6000	60-69	Optical
AUST56	561	-740301.9335	-5457074.8715	3207238.0946	.3270	.1230	.1380	870101	HILAT GEOSAT
BADARY	4883	-838277.2642	3865776.9436	4987626.7702	.1400	.0836	.0979	900601	DORIS SPOT–2
BAHRAI	35012	3633912.9804	4425269.0718	2799868.3203	.2740	.2320	.1450	870101	GEOSAT
BAIRES	3791	2745491.0223	-4483593.0902	-3599089.1670	1.5800	1.0500	1.6900	840601	NOVA–1
Baker-Nunn camera	9021	-1936773.6671	-5077710.2952	3331920.6732	5.8500	5.9000	6.4800	60-69	Optical
Baker-Nunn camera	9028	4903764.6240	3965218.9665	963863.8449	4.1500	4.4000	4.3300	60-69	Optical
BANGK2	35028	-1133939.5398	6092552.0825	1503386.5486	.3620	.1370	.1490	870101	GEOSAT
BAR GIYYORA	7530	4443964.2134	3121946.2598	3334694.9451	.0356	.0383	.0375	860701	SLR
BDADOP	30967	2293704.0845	-4883225.2042	3390590.5575	.3630	.2980	.2560	780904	SEASAT
BERMD	7039	2308223.0414	-4873597.2108	3394576.3464	4.0300	4.1900	4.7700	60-69	Optical
BERMUDA	7067	2308537.2821	-4874080.0147	3393629.4839	.1570	.1540	.1560	860701	SLR
BGKDOP	30800	-1139091.0898	6089771.4193	1510702.2396	.5280	.3980	.3030	780904	SEASAT
BOLOGNA	7546	4461398.7024	919568.2495	4449511.1807	.2770	.3760	.2970	860701	SLR
BOROWIEC	7811	3738331.9267	1148247.6737	5021816.1858	.0766	.0671	.0500	860701	SLR
BPOIN	1021	1118032.3854	-4876314.1608	3942971.4738	6.4600	6.8800	7.6100	60-69	Optical
BRUSSE	547	4027868.2500	307028.7648	4919513.6484	.1010	.2290	.1210	870101	HILAT GEOSAT
BSEDOP	116	4004966.0302	-96567.0781	4946540.1936	.2670	.3230	.2710	780904	SEASAT
BSI546	546	4004966.4757	-96567.3765	4946538.5084	.2480	.5140	.2780	870101	HILAT
CABO SAN LUCAS	7882	-1997245.6924	-5528039.1049	2468356.9411	.0715	.0610	.0623	860701	SLR
CAGLIARI	7545	4893397.1830	772674.8207	4004141.7973	.0541	.0669	.0467	860701	SLR
CALDOP	30414	-1659602.3934	-3676726.2671	4925493.8605	.2010	.1290	.1190	780904	SEASAT
CALGAR	563	-1659602.4034	-3676726.2871	4925493.8905	.2010	.1290	.1190	870101	GEOSAT
CALGRY	60125	-1659602.0961	-3676760.5419	4925478.9337	3.9000	3.4300	15.4000	801015	OSCAR–14
CAMBRI	35011	-594792.5914	-2201201.0564	5936676.2773	.1400	.1010	.1060	870101	GEOSAT
CANBERRA	3101	-4446484.4702	2678131.6869	-3696270.7900	.8530	1.3000	1.6400	840601	NOVA–1
CANBERRA	7843	-4446479.8884	2678127.1216	-3696247.8516	.0186	.0212	.0171	860701	SLR
CARVN	7079	-2328588.4916	5299362.6714	-2669655.2682	7.5500	7.9200	7.4200	60-69	Optical
CERRO TOLOLO	7401	1815517.0497	-5213465.2949	-3187998.6160	.0840	.0653	.0586	860701	SLR
CHANGCHUN	7237	-2674386.2577	3757189.4615	4391508.5975	.1020	.1140	.0839	860701	SLR
CHICHIJIMA	7844	-4491073.7860	3481527.0364	2887390.7518	.2800	.4070	.6560	860701	SLR
CNIDOP	30970	5384988.6354	-1576479.7674	3023840.1854	.6310	.7840	.5260	780904	SEASAT
COLBA	7037	-191282.1954	-4967273.2390	3983264.1917	3.4600	3.1600	3.8700	60-69	Optical
COLDLK	9114	-1264832.5969	-3466882.5986	5185480.8099	14.0000	16.4000	15.7000	60-69	Optical
COLDLK	9424	-1264836.4457	-3466889.9659	5185465.5903	11.0000	14.5000	12.5000	60-69	Optical

B–1

Station Name	Station Number	X m	Y m	Z m	σX m	σY m	σZ m	Epoch yymmdd	Satellite/Tracking Technology
COLEG	1033	-2299248.2644	-1445692.3834	5751811.3041	24.5000	28.3000	23.0000	60-69	Optical
COLOMBO	4885	1113279.2407	6233646.2119	760276.5153	.1740	.0944	.1000	900601	DORIS SPOT–2
COMRIV	9031	1693804.1841	-4112343.2746	-4556643.0200	4.5200	5.2900	4.3100	60-69	Optical
CURAC	9009	2251836.7479	-5816920.4248	1327173.2079	3.4600	3.2400	3.4200	60-69	Optical
CYPRUS	35006	4349913.8879	2904399.3277	3638100.3838	.2290	.2950	.1680	870101	GEOSAT
DAKAR	4018	5886437.4092	-1848461.7580	1611441.4207	.0676	.1120	.0673	900601	DORIS SPOT–2
DAKLAS	7820	5886270.1613	-1845673.0333	1615250.6403	2.1100	4.8900	3.3700	710601	Peole D1–D
DELFTH	8009	3923406.3116	299896.7061	5002983.7341	9.3000	7.4700	8.8600	60-69	Optical
DENVER	35027	-1252439.6754	-4752041.1942	4054730.1272	.2780	.1200	.1280	870101	GEOSAT
DENVR	7045	-1240468.7689	-4760222.7007	4048989.3206	3.5800	3.5900	4.1000	60-69	Optical
DGCDOP	30939	1915630.3015	6030277.1296	-801046.5813	.4480	.3570	.2600	780904	SEASAT
DIEGO	35010	1915629.8870	6030276.1759	-801047.5209	.4580	.3000	.2330	870101	GEOSAT
DIONYSOS	3041	4595219.4478	2039461.4750	3912623.4575	.6360	1.2400	1.5900	840601	NOVA–1
DIONYSOS	4047	4595215.2560	2039614.9579	3912614.9579	.1130	.1410	.0954	900601	DORIS SPOT–2
DIONYSOS	7515	4595215.2255	2039436.7553	3912630.1808	.0416	.0468	.0346	860701	SLR
DIONYSOS	7930	4595219.3031	2039455.8732	3912617.8426	4.5300	4.5900	6.3100	710601	D1–C D1–D
DIYARBAKIR	7575	3848634.0317	3251760.7450	3898911.2444	.0769	.0758	.0659	860701	SLR
DJCB10	4103	4612392.2850	4218387.0752	1267105.4435	.1450	.1510	.1040	900601	DORIS SPOT–2
DJIBOUTI	4025	4583119.7242	4250951.8905	1266247.5694	.1110	.1180	.0921	900601	DORIS SPOT–2
DJIBOUTI	67120	4583114.6051	4250959.4971	1266247.9789	4.7500	5.0000	18.5000	801015	OSCAR–14
DODAIR	9025	-3910445.4222	3376360.6395	3729224.3305	15.6000	26.4000	16.1000	60-69	Optical
EASDOP	30730	-1888661.3807	-5355672.1870	-2893875.7726	.5090	.3920	.3390	780904	SEASAT
EASTER ISLAND	4041	-1884994.6552	-5357604.6919	-2892858.5687	.0346	.0268	.0257	900601	DORIS SPOT–2
EASTER ISLAND	7097	-1884978.0549	-5357609.8562	-2892854.2309	.0346	.0268	.0257	860701	SLR
EDINB	7036	-828485.0155	-5657449.9170	2816821.9753	3.9000	3.5800	4.3900	60-69	Optical
EDWAFB	9113	-2450004.5819	-4624425.0064	3635043.0446	6.4500	6.7200	7.2000	60-69	Optical D1–C
EDWAFB	9425	-2450010.7423	-4624424.4174	3635040.9575	6.2000	6.1300	6.7600	60-69	Optical
EDWRDS	35504	-2459945.5184	-4624307.2619	3628701.4729	.7690	.4740	.3730	870101	RADCAL
EFFELS	3141	4029171.6197	490750.6888	4904016.4309	.3410	1.0900	1.4800	840601	NOVA–1
EGLIN	35512	335711.2238	-5491154.5203	3216411.4656	1.7800	.8890	.8640	870101	RADCAL
ENSENADA	7883	-2406129.7373	-4898365.7683	3290338.3593	.0723	.0668	.0506	860701	SLR
FAIRBANKS	4888	-2282502.7782	-1453416.9884	5756694.6288	.0695	.0832	.0671	900601	DORIS SPOT–2
FAIRBANKS	54040801	-2281621.4963	-1453595.7681	5756962.0198	.1050	.1090	.1520	921031	EP/EUVE T/P GPS
FLAGSTAFF	7891	-1923977.9238	-4850871.5857	3658574.1655	.1210	.1170	.0948	860701	SLR
FLODOP	641	4522404.2806	898003.3843	4392486.3478	1.5300	1.5600	1.3400	780904	SEASAT
FLORES	4053	4221385.4816	-2549305.8185	4031509.0589	.0753	.0869	.0580	900601	DORIS SPOT–2
FORT DAVIS	3171	-1324205.4309	-5332056.4859	3232053.3957	1.6800	.7030	1.7100	840601	NOVA–1
FORT DAVIS	7080	-1330022.2668	-5328401.7155	3236480.5307	.0121	.0095	.0094	860701	SLR
FRENCH	591	3850658.4894	-5052186.6305	571066.1472	6.0000	4.5700	2.7500	870101	GEOSAT
FTMYR	1022	807866.3531	-5651977.7664	2833509.6709	3.4300	2.9700	3.6600	60-69	Optical
GFORK	1034	-521699.9925	-4242044.0401	4718729.7535	4.7700	4.8000	5.4700	60-69	Optical
GOLDSTONE	4010	-2356503.8508	-4646583.9232	3668453.2654	.0913	.0636	.0492	900601	DORIS SPOT–2
GOLDSTONE	7288	-2356495.3546	-4646607.6658	3668425.8521	.0395	.0340	.0311	860701	SLR
GOLDSTONE	54040572	-2353614.1246	-4641385.4857	3676976.5262	.0801	.1580	.1260	921031	EP/EUVE T/P GPS
GRAND TURK	7068	1920481.6969	-5619478.2541	2318915.1311	.1970	.1530	.2040	860701	SLR
GRASSE	3721	4588035.2559	556435.2264	4381673.8640	.5510	1.4900	1.5700	840601	NOVA–1
GRASSE	7835	4581690.9207	556160.3542	4389360.1145	.0112	.0126	.0127	860701	SLR
GRAZ	7839	4194425.5585	1162694.8869	4647247.3079	.0128	.0128	.0131	860701	SLR
GRAZ	51100102	4194425.4683	1162703.0470	4647246.8292	.1280	.1060	.1290	921031	EP/EUVE T/P GPS
GREECE	9091	4595172.0579	2039471.7927	3912666.4395	4.1200	4.1600	4.7600	60-69	Optical
GRISSM	35040	327216.1182	-4835521.0289	4132670.6575	.2900	.1120	.1350	870101	GEOSAT
GSFCN	7077	1130067.4026	-4833037.2017	3992262.8805	5.4800	6.0800	6.4400	60-69	Optical
GUAM	553	-5059776.5385	3591207.2601	1472786.4909	.2400	.3100	.1440	870101	HILAT GEOSAT
GUAM	7060	-5068958.7922	3584096.4487	1458770.0910	2.5000	3.5300	1.7200	710601	Peole D1–C D1–D
GWMDOP	23	-5059774.7433	3591209.0408	1472788.9142	.4400	.5540	.3390	780904	SEASAT
HARTEBEESTHOEK	4019	5084641.5795	2670349.4330	-2768497.4126	.0670	.0981	.0781	900601	DORIS SPOT–2
HARTEBEESTHOEK	7501	5085401.1347	2668329.7001	-2768689.1718	.0338	.0425	.0415	860701	SLR
HARTEBEESTHOEK	53030202	5084633.4329	2670370.8129	-2768498.3258	.2390	.1910	.1640	921031	EP/EUVE T/P GPS
HAULAS	7809	4578356.0394	457976.4310	4403174.7701	.9620	3.1600	2.2000	710601	D1–C D1–D
HAUTEP	8015	4578335.8020	457984.5267	4403200.5210	4.7900	4.6400	5.5800	60-69	Optical
HAW100	41100	-5504174.5281	-2224152.9299	2325315.8335	4.3000	4.7600	4.6400	870101	BE–C
HAW100	42100	-5504167.5025	-2224153.9174	2325304.3244	2.5100	3.1600	3.1700	870101	D1–C D1–D
HAWAI0	35007	-5511592.2328	-2226881.4293	2304025.7112	.1840	.3410	.1550	870101	GEOSAT
HAWAII	35507	-5509020.6060	-2230933.0912	2306265.4461	.7880	1.2700	.5950	870101	RADCAL
HAWAIIAN VOLCA	4901	-5467477.1384	-2516164.9134	2107723.9336	1.5100	1.7100	.6690	900601	DORIS SPOT–2
HAYSTA	3161	1492398.5290	-4457293.7567	4296828.5057	1.2200	.5240	1.5600	840601	NOVA–1
HELSIK	9435	2884540.3331	1342141.8103	5509530.9328	12.3000	10.0000	10.6000	60-69	Optical
HELWAN	7831	4728281.9235	2879671.4785	3156895.9068	.0635	.0593	.0550	860701	SLR
HERM57	570	3981776.7327	-89253.1052	4965288.6498	.1010	.2400	.1280	870101	GEOSAT

B-2

Station Name	Station Number	X m	Y m	Z m	σX m	σY m	σZ m	Epoch yymmdd	Satellite/Tracking Technology
HERN55	550	1090141.9461	-4842522.0589	3991979.0079	.2920	.1260	.1350	870101	HILAT GEOSAT
HERN69	30690	1090120.7438	-4842525.5509	3991975.5091	.3000	.1370	.1440	870101	GEOSAT
HERNDN	60407	1090147.2592	-4842523.5814	3991979.6780	.7190	3.1900	16.6000	801015	OSCAR–14
HERSTM	3131	4033589.4160	24240.1448	4924219.6991	.3330	1.1200	1.4800	840601	NOVA–1
HERSTMONCEUX	7840	4033462.7857	23663.3738	4924305.9071	.0100	.0112	.0110	860701	SLR
HERSTMONCEUX	51321207	4033470.5058	23672.8520	4924301.3809	.1560	.1160	.1710	921031	EP/EUVE T/P GPS
HILL	35509	-1804426.4100	-4461066.7184	4174195.8556	.8050	.4050	.3800	870101	RADCAL
HONDOP	30188	-5511607.3131	-2226973.8076	2303884.4403	.3290	.4260	.2730	780904	SEASAT
HUAHINE	3111	-5345895.4121	-2958230.9542	-1824588.9887	1.0700	1.7500	1.8000	840601	NOVA–1
HUAHINE	4027	-5345873.1372	-2958239.3769	-1824624.2717	.0244	.0299	.0259	900601	DORIS SPOT–2
HUAHINE	7123	-5345870.8765	-2958241.5256	-1824621.8748	.0244	.0299	.0259	860701	SLR
IDAHO	35036	-1738443.5222	-4295177.6663	4370317.3025	.2580	.1440	.1330	870101	GEOSAT
ILE DES PETREL	4042	-1941059.8170	1628659.4059	-5833613.4940	.0524	.0531	.0510	900601	DORIS SPOT–2
ISIGAKI	7307	-3265748.4471	4810004.0458	2614266.3739	.3390	.1940	.2200	860701	SLR
JAMAC	7076	1384165.1662	-5905665.7466	1966548.1598	4.9800	4.8700	5.5100	60-69	Optical
JOBUR	1031	5084796.3883	2670402.9401	-2768137.9496	4.2200	4.3800	4.1400	60-69	Optical
JOHNST	9117	-6007419.5252	-1111873.4683	1825754.2601	8.4700	7.4200	8.7300	60-69	Optical–D1–Cisa
JOHNST	9427	-6007404.0824	-1111875.3300	1825755.4108	10.3000	10.3000	10.4000	60-69	Optical
JUBC4	7074	976293.1772	-5601381.3384	2880255.8013	11.9000	12.5000	13.2000	60-69	Optical
JUM24	7071	976281.9435	-5601401.9453	2880229.2753	11.0000	11.4000	12.1000	60-69	Optical
JUM40	7072	976278.7097	-5601392.0482	2880247.0213	6.9300	7.5100	7.7400	60-69	Optical
JUPC1	7073	976294.8141	-5601382.8150	2880246.5376	15.0000	15.8000	13.1000	60-69	Optical
JUPGEO	9049	976290.5463	-5601412.2460	2880253.1342	22.3000	25.3000	21.1000	60-69	Optical
JUPTR	9010	976294.3156	-5601402.6859	2880243.3633	2.9500	2.2000	2.9900	60-69	Optical
KAENA	35514	-5512517.4986	-2197412.6704	2330518.8471	.5790	1.1800	.4810	870101	RADCAL
KARITSA	7520	4596041.4869	1733478.1727	4055721.5474	.0660	.0755	.0509	860701	SLR
KATAVIA	7512	4573398.7822	2409323.6359	3723882.3962	.0409	.0483	.0373	860701	SLR
KATZIVELY	1893	3785943.6636	2550782.0915	4439461.6173	.3370	.2930	.5940	860701	SLR
KAUAI	4886	-5543974.5257	-2054590.2088	2387488.2007	.1020	.1520	.0723	900601	DORIS SPOT–2
KERGUE	567	1406287.8923	3918141.2297	-4816207.4603	.2710	.1700	.1680	870101	GEOSAT
KERGUELEN	4009	1405826.4182	3918281.8054	-4816204.1581	.0872	.0615	.0753	900601	DORIS SPOT–2
KINS02	35026	6136058.5205	1673472.4807	-482834.1528	.1860	.3930	.1700	870101	GEOSAT
KITAB	4882	1945025.1021	4556708.6856	4004235.8696	.1280	.0860	.0910	900601	DORIS SPOT–2
KOKEE_PARK	54042404	-5543838.2191	-2054587.6558	2387809.5586	.2690	.2140	.1590	921031	EP/EUVE T/P GPS
KOOTWIJK	8833	3899209.4976	396717.9913	5015092.9982	.0628	.0618	.0446	860701	SLR
KOOTWIJK	51350403	3899225.4601	396731.9344	5015078.4355	.1210	.1000	.1280	921031	EP/EUVE T/P GPS
KOUROU	4016	3854715.0474	-5049977.8625	564747.3219	.0928	.0802	.0537	900601	DORIS SPOT–2
KWADJA	35505	-6160871.0731	1339997.2248	960764.7329	.4150	1.0300	.3990	870101	RADCAL
KWAJALEIN ATOL	7092	-6143445.6048	1364705.8438	1034165.7649	.0446	.0633	.0668	860701	SLR
KWJDOP	10214	-6160996.0555	1339619.2783	960422.1441	.4130	.5940	.3190	780904	SEASAT
LA REUNION	4012	3364094.0211	4907945.3050	-2293482.4585	.0955	.0779	.0837	900601	DORIS SPOT–2
LAJDOP	30966	4432069.7057	-2268090.9068	3973465.8106	.2800	.3230	.2460	780904	SEASAT
LAMPEDUSA	7544	5072830.7554	1130887.5052	3684838.3021	.0502	.0616	.0459	860701	SLR
LASC02	35021	-1556213.9969	-5169448.7373	3387240.4443	.3190	.1510	.1460	870101	GEOSAT
LASC55	552	-1556211.8579	-5169449.0434	3387240.4816	.3090	.1430	.1360	870101	HILAT GEOSAT
LCR103	41103	-1556212.6777	-5169468.6340	3387270.8601	3.2900	3.7100	4.3200	870101	BE–C
LCR103	42103	-1556211.7892	-5169465.8509	3387259.2684	2.3000	2.5600	3.1700	870101	d1c–d1d
LCR551	551	-1556211.3244	-5169451.3532	3387236.5391	.7600	.4090	.3260	870101	HILAT
LIBREVILLE	4013	6287388.7284	1071573.8598	39146.8826	.0728	.1280	.0806	900601	DORIS SPOT–2
MADRID	3061	4849193.9875	-360301.2760	4114932.3391	.3650	1.3200	1.5700	840601	NOVA–1
MADRID	51340788	4849202.6877	-360329.0282	4114913.1404	.2240	.1320	.1830	921031	EP/EUVE T/P GPS
MAHDOP	20	3602880.2300	5238221.3182	-515932.9391	.5140	.4750	.3220	780904	SEASAT
MAHE S	558	3602878.7374	5238220.9507	-515933.5156	.3210	.2410	.1480	870101	HILAT GEOSAT
MALVRN	8011	3920175.7798	-134728.9708	5012740.1571	11.4000	7.9400	9.9600	60-69	Optical
MALVRN	9080	3920170.7640	-134729.5383	5012743.3957	16.0000	13.7000	21.4000	60-69	Optical
MANILLE	4884	-3184357.4938	5291042.2125	1590419.6014	.1730	.1330	.0992	900601	DORIS SPOT–2
MARION ISLAND	4022	3448405.5847	2680356.2010	-4632640.5391	.0668	.0822	.0717	900601	DORIS SPOT–2
MASPALOMAS	53130301	5439189.2609	-1522054.7601	2953464.2781	.2920	.1710	.1750	921031	EP/EUVE T/P GPS
MATERA	7939	4641964.0614	1393070.7500	4133263.0623	.0118	.0124	.0133	860701	SLR
MATERA	51273408	4641950.0076	1393045.4063	4133287.4306	.1230	.1080	.1210	921031	EP/EUVE T/P GPS
MAUI	7210	-5466007.6673	-2404422.6354	2242190.3428	.0069	.0129	.0021	860701	SLR
MAZATLAN	7122	-1660090.5096	-5619100.1158	2511637.7273	.0153	.0116	.0128	860701	SLR
MC MURDO	19	-1310715.6322	310469.3480	-6213363.9784	.7800	.5450	1.3400	780904	SEASAT
MC MURDO	562	-1310719.1367	310473.2955	-6213363.3846	.1280	.1290	.1970	870101	HILAT GEOSAT
MC MURDO	56600195	-1310696.2472	310468.9987	-6213368.2505	.1350	.1110	.2460	921031	EP/EUVE T/P GPS
MELENGICLICK	7580	4247619.0985	2778640.2951	3851608.0541	.0572	.0617	.0465	860701	SLR
METSAHOVI	4006	2890641.4313	1310310.3777	5513964.8024	.0678	.0829	.0679	900601	DORIS SPOT–2
METSAHOVI	51050389	2892571.0354	1311843.4674	5512633.9808	.1230	.1030	.1450	921031	EP/EUVE T/P GPS
MHE717	41717	3602898.6990	5238252.1396	-515923.1012	5.1600	5.5600	5.1800	870101	BE–C

B-3

Station Name	Station Number	X m	Y m	Z m	σX m	σY m	σZ m	Epoch yymmdd	Satellite/Tracking Technology
MHE717	42717	3602901.8121	5238258.9853	-515929.8574	3.9000	3.2400	3.7900	870101	D1–C D1–D
MISAWA	27	-3857196.8665	3108654.5494	4004045.8349	.9040	1.3200	.9540	780904	SEASAT
MIZUSA	548	-3857196.6833	3108664.1682	4004050.6139	.2100	.2410	.1370	870101	HILAT GEOSAT
MOJAV	1030	-2357237.7816	-4646322.1652	3668318.4583	3.0900	2.7600	3.4500	60-69	Optical
MONUMENT PEAK	7110	-2386280.9363	-4802352.1739	3444882.4140	.0093	.0088	.0071	860701	SLR
MONUMENT PEAK	7220	-2386295.2228	-4802345.2955	3444881.8175	.0093	.0088	.0071	860701	SLR
MSADOP	60027	-3857199.9359	3108657.9853	4004054.7957	3.6300	3.7500	16.5000	801015	OSCAR–14
MT GENEROSO	7590	4390308.8941	696753.4817	4560836.6590	.0736	.0859	.0557	860701	SLR
MT HOPKINS	7921	-1936761.5081	-5077707.1348	3331922.0871	.0540	.0520	.0510	860701	SLR
MT HOPKINS	7921	-1936764.0644	-5077702.9761	3331920.0967	2.3400	2.4100	2.0900	710601	D1–C D1–D
MUDONI	8030	4205640.9397	163735.4894	4776552.1264	11.1000	8.5500	10.6000	60-69	Optical
NANI TAL	9006	1018202.2682	5471111.4230	3109627.7288	3.0200	2.2000	2.9700	60-69	Optical D1–D
NAPDOP	30448	-4923686.5209	270902.6831	-4031779.8006	.2570	.3460	.2420	780904	SEASAT
NAS MS	35039	130023.4933	-5379945.1312	3412090.8810	.6340	.4300	.3960	870101	GEOSAT
NATAL	7929	5186466.9817	-3653860.9295	-654325.9854	5.4100	7.3300	4.4700	710601	D1–C D1–D
NATAL	7929	5186467.5888	-3653856.8610	-654321.1357	.0233	.0260	.0291	860701	SLR
NATALB	9029	5186470.3011	-3653872.4033	-654324.3034	5.8000	6.1400	5.7700	60-69	Optical
NEVADA	35038	-2369577.4795	-4327796.1978	4030076.1819	.2620	.1690	.1340	870101	GEOSAT
NEWFL	1032	2602761.0782	-3419147.2447	4697658.5644	9.3100	10.6000	9.7000	60-69	Optical
NICEFR	8019	4579480.9472	586622.2254	4386422.0266	4.1800	4.1500	4.8000	60-69	Optical
NOTO	7543	4934529.1562	1321132.9466	3806522.4332	.0049	.0046	.0034	860701	SLR
NOUMEA	4036	-5739993.6792	1387548.5686	-2402085.4040	.0666	.1190	.0749	900601	DORIS SPOT–2
NY-ALESUND	4020	1202794.2926	254163.0307	6237609.2750	.0466	.0479	.0425	900601	DORIS SPOT–2
NY-ALESUND	51031701	1202431.6329	252626.9676	6237772.3728	.1980	.1770	.4490	921031	EP/EUVE T/P GPS
OLFAN	9002	5056136.8710	2716518.2653	-2775760.9557	2.4700	2.9800	2.7700	60-69	Optical
ONSALA	51040204	3370659.2954	711877.3174	5349787.6989	.1520	.1290	.1830	921031	EP/EUVE T/P GPS
OOMER	1024	-3977272.0235	3725658.1528	-3302977.5101	7.6000	8.0200	7.5600	60-69	Optical
ORGAN	9001	-1535750.2581	-5167002.7872	3401049.2437	2.7900	2.0400	2.8200	60-69	Optical
ORORL	1038	-4447483.3776	2677176.2847	-3695048.6409	5.2100	5.4700	5.0100	60-69	Optical
ORRORL	67143	-4446452.8344	2678225.1034	-3696187.8279	5.0200	5.9100	16.9000	801015	OSCAR–14
OSLONR	9115	3121281.4688	592640.3531	5512716.2780	13.4000	11.5000	13.3000	60-69	Optical
OSLONR	9426	3121261.7887	592652.2613	5512714.0371	36.2000	29.4000	32.7000	60-69	Optical
OTTAWA	128	1091452.2043	-4351289.5920	4518698.9223	.2540	.1290	.1340	780904	SEASAT
OTTAWA	564	1091453.0143	-4351290.8420	4518698.0223	.2540	.1290	.1340	870101	GEOSAT
OTTAWA	4048	1107623.6464	-4347253.9763	4518738.2513	.0878	.0511	.0500	900601	DORIS SPOT–2
OTTDOP	60128	1091456.9303	-4351287.8865	4518703.7433	4.3000	3.4400	16.0000	801015	OSCAR–14
OWENS VALLEY	7853	-2410423.0599	-4477799.7545	3838689.9654	.0310	.0296	.0256	860701	SLR
PAMATAI	568	-5245203.5268	-3080478.1319	-1912830.5079	.2230	.3330	.1520	870101	GEOSAT
PAMATAI	67118	-5245200.6164	-3080484.2102	-1912818.7498	3.8800	5.4500	18.2000	801015	OSCAR–14
PAMATAI	59220103	-5245202.0318	-3080476.5309	-1912827.9221	.4910	.4430	.2140	921031	EP/EUVE T/P GPS
PARISD	3711	4201865.5516	177900.2909	4779213.4075	.5810	.0246	1.5700	840601	NOVA–1
PASADENA	7896	-2493214.5240	-4655226.8053	3565576.4181	.0854	.0908	.0688	860701	SLR
PASADENA	54040006	-2493304.1675	-4655215.6722	3565497.4332	.0945	.1330	.0936	921031	EP/EUVE T/P GPS
PATRIC	35515	918333.6316	-5548262.6322	2998908.9347	1.8400	1.1400	.8520	870101	RADCAL
PATRICK AFB	7069	917957.7442	-5548370.3775	2998776.8269	.0631	.0438	.0530	860701	SLR
PENCHU	3831	4052451.5033	1417630.0049	4701420.5793	.5170	1.1100	1.5100	840601	NOVA–1
PENTICTON	54010502	-2059164.6854	-3621108.4605	4814432.4899	.0816	.1160	.0975	921031	EP/EUVE T/P GPS
PERDOP	30968	-2353566.5774	4877207.4351	-3358325.7827	.3740	.3150	.2610	780904	SEASAT
PILLAR	35511	-2722179.0119	-4273170.7994	3861376.7059	.7450	.5370	.3780	870101	RADCAL
PLATTE	3181	-1240642.6553	-4720485.1016	4094472.8407	1.3300	.4990	1.5800	840601	NOVA–1
PLATTEVILLE	7112	-1240679.3246	-4720463.6102	4094480.0404	.0221	.0215	.0154	860701	SLR
POKAFL	35503	-2268115.1988	-1448575.1953	5763730.7374	.3200	.4780	.3090	870101	RADCAL
PORT MORESBY	4055	-5288462.6015	3410034.9217	-1038802.7033	.0818	.1030	.0780	900601	DORIS SPOT–2
POTSDA	3121	3800592.5333	881915.3846	5028912.7060	.3890	1.0400	1.4600	840601	NOVA–1
POTSDAM	7836	3800638.6841	881983.2511	5028832.2026	.0201	.0200	.0196	860701	SLR
PRET55	554	5051977.4548	2725641.8539	-2774467.7767	.2030	.3200	.1520	870101	HILAT GEOSAT
PRETOR	67122	5067174.8783	2736607.9359	-2735033.9119	3.4000	4.6100	17.6000	801015	OSCAR–14
PRT115	41115	5052003.6826	2725665.2301	-2774470.6812	2.9700	3.6800	3.7400	870101	BE–C
PRT115	42115	5052015.1106	2725659.4385	-2774472.1961	2.9100	3.2100	3.2300	870101	D1–C D1–D
PRTDOP	105	5051977.0641	2725639.5744	-2774467.7266	.3480	.3910	.2700	780904	SEASAT
PTMUGU	35506	-2574980.8644	-4615965.5824	3557714.6360	.7830	.5040	.3840	870101	RADCAL
PURIO	7040	2465062.4891	-5534920.3871	1985524.5992	4.1800	4.3500	4.8300	60-69	Optical
PURPLE MOUNTAI	4045	-2608501.6588	4739980.5237	3366883.1901	.0978	.0733	.0794	900601	DORIS SPOT–2
QUIDOP	30121	1280855.7432	-6250960.3151	-10813.5144	.5190	.3970	.2900	780904	SEASAT
QUINCY	7109	-2517236.5188	-4198555.6052	4076569.2286	.0088	.0099	.0069	860701	SLR
QUITO	35022	1272867.4641	-6252770.6437	-23798.7053	.3780	.1520	.1580	870101	GEOSAT
RAPID	35029	-1038825.8945	-4464429.6743	4421682.4132	.2670	.1200	.1320	870101	GEOSAT
REYKJAVIK	4887	2585528.5214	-1044368.2054	5717158.9183	.0773	.0949	.0762	900601	DORIS SPOT–2
RICHMOND	4023	961079.7629	-5673576.2697	2741639.2832	.1030	.0581	.0468	900601	DORIS SPOT–2

Station Name	Station Number	X m	Y m	Z m	σX m	σY m	σZ m	Epoch yymmdd	Satellite/Tracking Technology
RICHMOND	7295	961317.9709	-5674091.0825	2740489.7350	.0634	.0444	.0579	860701	SLR
RICHMOND	54049987	961319.1897	-5674091.0705	2740489.7008	.1380	.2280	.1320	921031	EP/EUVE T/P GPS
RIGA	1884	3183894.7907	1421498.0757	5322803.7037	.0653	.0689	.0575	860701	SLR
RIGA	9431	3183887.4783	1421485.4680	5322807.0968	11.2000	7.2500	8.0800	60-69	Optical
RIGRND	3811	1429892.4042	-3495346.3030	-5122704.8090	1.3300	.8290	1.5700	840601	NOVA–1
RIO GRANDE	4017	1429849.7536	-3495346.3298	-5122723.2177	.0729	.0539	.0497	900601	DORIS SPOT–2
ROSMA	1042	647521.8816	-5177927.5160	3656711.6016	4.3800	4.3400	4.8800	60-69	Optical
ROSMN	1037	647527.3072	-5177925.3011	3656711.5072	3.7000	3.3800	3.9800	60-69	Optical
ROTHERA	4903	909377.9388	-2264934.4917	-5872956.9877	.0977	.0802	.0908	900601	DORIS SPOT–2
ROUMELLI	7517	4728693.5156	2174374.8107	3674573.6374	.0368	.0433	.0358	860701	SLR
S00013	41013	-3779672.2018	3024727.0870	4139015.3351	2.6800	2.6100	4.5900	870101	BE–C
S00013	42013	-3779740.6397	3024790.7772	4139059.5747	7.2200	8.4500	15.1000	870101	D1–C D1–D
S00092	41092	-741633.3074	-5462237.7872	3198151.9955	3.0900	3.7100	3.7000	870101	BE–C
S00106	41106	4005471.6732	-71748.2928	4946779.4737	12.5000	10.9000	63.2000	870101	BE–C
S00106	42106	4005478.0877	-71754.2743	4946704.3765	4.3200	3.6600	15.2000	870101	D1–C D1–D
S00111	41111	1122663.1768	-4823066.9919	4006487.7611	.5750	2.4700	3.8400	870101	BE–C
S00111	42111	1122662.5715	-4823063.5917	4006475.1180	.4820	2.0700	3.6300	870101	D1–C D1–D
S00726	41726	-5367640.0505	3437957.5657	-226694.4282	5.8100	5.6400	5.3200	870101	BE–C
S00729	42729	5142555.9368	-1566196.5420	3421744.5702	11.0000	6.4000	9.2500	870101	D1–C
S00737	41737	-2348787.4101	-4652662.2433	3665945.6143	2.7000	2.8200	3.7300	870101	BE–C
S00738	41738	-2127828.8079	-3785855.3559	4656077.3780	2.9400	3.2100	9.7000	870101	BE–C
S00750	42750	-308280.7127	-4971544.2150	3970699.1877	2.6000	3.0200	5.0000	870101	D1–C D1–D
S00810	42810	-5076835.2338	449286.5371	-3821955.2948	4.1200	4.1000	5.2800	870101	D1–C D1–D
SAFLAS	7804	5105609.3668	-555248.8966	3769644.0185	1.3400	3.4700	2.0900	710601	D1–C D1–D
SAINTE-HELENE	4043	6104828.2242	-605837.7944	-1740706.7131	.0693	.1270	.0750	900601	DORIS SPOT–2
SAKHALINS	4881	-3465325.6494	2638266.9147	4644082.5188	.0881	.1110	.0793	900601	DORIS SPOT–2
SAMOA	60424	-6100053.0740	-997196.9286	-1568307.4091	2.4000	5.1800	18.4000	801015	OSCAR–14
SAN DIEGO	7035	-2428829.4024	-4799752.2627	3417268.1537	.0454	.0423	.0402	860701	SLR
SAN FERNANDO	7824	5105473.3523	-555109.3633	3769893.2629	.7970	.5010	.4000	860701	SLR
SAN FR	590	5105461.8339	-555123.3493	3769894.5687	.6700	1.0400	.7210	870101	GEOSAT
SAN MI	559	-3088048.9255	5333055.5561	1638818.8505	.3310	.2170	.1480	870101	HILAT GEOSAT
SANFER	68804	5105462.9900	-555115.5410	3769893.5178	3.1400	4.4200	16.7000	801015	OSCAR–14
SANJ55	555	4083914.7504	-4209795.8418	-2499118.6835	.2690	.2600	.1410	870101	HILAT GEOSAT
SANJOS	67116	4084894.5179	-4209291.2768	-2498407.5133	5.7600	5.8000	18.0000	801015	OSCAR–14
SANTIA	35025	1769924.4138	-5044552.9670	-3468252.4250	.3080	.1540	.1410	870101	GEOSAT
SANTIAGO CHILE	1028	1769714.3585	-5044613.3607	-3468250.3849	4.5400	4.9100	4.8000	60-69	Optical
SANTIAGO CHILE	4038	1776346.2162	-5026544.3817	-3491183.7344	.1010	.0668	.0529	900601	DORIS SPOT–2
SANTIAGO CHILE	7400	1769699.6072	-5044613.4392	-3468259.3585	.1250	.0824	.1030	860701	SLR
SANTIAGO CHILE	67190	1776344.7219	-5026525.4839	-3491215.0916	5.0300	3.7200	17.1000	801015	OSCAR–14
SANTIAGO CHILE	54170503	1769693.4668	-5044574.4523	-3468321.0603	.1690	.1580	.1210	921031	EP/EUVE T/P GPS
SANTIAGO DE CU	1953	1474548.3018	-5811242.1916	2168945.3754	.0803	.0618	.0805	860701	SLR
SGN812	42812	4901635.1038	1305827.7019	3853649.6493	3.5000	3.2800	5.1700	870101	d1c–d1d
SHANGHAI	7837	-2831089.5047	4676203.0012	3275171.9720	.0446	.0433	.0399	860701	SLR
SHEMYA	35018	-3850346.8781	397633.3172	5052352.4996	.1020	.2320	.1250	870101	GEOSAT
SHIDOP	30123	6104421.7321	-611086.2489	-1740834.0291	.4120	.5310	.3180	780904	SEASAT
SHRAZ	9008	3376887.2754	4403998.9323	3136267.7633	3.4800	3.3900	4.0700	60-69	Optical
SIGA50	4050	2189057.0209	-2235050.2216	-5539571.1117	.4550	.4760	.3630	900601	DORIS SPOT–2
SIGONE	35024	4901703.3717	1306297.7729	3853346.9306	.1320	.2930	.1380	870101	GEOSAT
SIMEIS	1873	3783901.3489	2551406.2725	4441257.9512	.1640	.1330	.1790	860701	SLR
SIMOSATO	7838	-3822386.7544	3699362.8507	3507571.6902	.0173	.0171	.0155	860701	SLR
SIMSAT	3091	-3822376.0851	3699389.1895	3507574.9136	1.0100	1.0400	1.6300	840601	NOVA–1
SIOUX	35017	-523526.4205	-4687705.2034	4279310.8583	.2770	.1080	.1310	870101	GEOSAT
SJEDOP	8	4083912.4581	-4209799.1743	-2499118.1970	.4850	.4910	.3360	780904	SEASAT
SJEDOP	41008	4083935.0975	-4209819.9010	-2499132.7014	3.8900	3.7000	3.9000	870101	BE–C
SJEDOP	42008	4083929.7784	-4209834.4118	-2499141.8753	3.3900	3.4600	3.4300	870101	D1–C D1–D
SMG011	41011	-3088068.7025	5333084.4648	1638824.8154	4.1900	4.3700	4.4400	870101	BE–C
SMG121	42121	-3088066.6670	5333092.3392	1638830.6079	3.5000	3.3300	3.9300	870101	D1–C D1–D
SMGDOP	22	-3088046.2344	5333054.9983	1638820.4834	.8200	.6000	.4800	780904	SEASAT
SMTH12	41012	-3942263.4779	3468869.6673	-3608220.1981	2.9500	3.0500	2.9900	870101	BE–C
SMTH41	60412	-3942246.3819	3468857.1464	-3608191.5197	3.6500	3.7500	16.9000	801015	OSCAR–14
SMTH54	545	-3942244.1221	3468867.5163	-3608187.6566	.2270	.2490	.1370	870101	HILAT GEOSAT
SOCORRO ISLAND	4040	-2160928.2044	-5642987.5191	2034688.1162	.1120	.0739	.0519	900601	DORIS SPOT–2
SOCORRO ISLAND	4904	-2160725.0918	-5643017.7365	2034836.6465	.2830	.1870	.1150	900601	DORIS SPOT–2
SPAIN	9004	5105600.2832	-555225.3822	3769676.6886	2.0500	2.7800	2.8100	60-69	Optical
ST HEL	35004	6104421.4267	-611085.9989	-1740834.8205	.1390	.3710	.1520	870101	GEOSAT
ST. JOHNS	54010101	2612631.4046	-3426807.0724	4686757.9386	.0968	.1250	.1250	921031	EP/EUVE T/P GPS
STFDOP	112	-3942239.7179	3468860.9325	-3608198.0559	.3220	.3420	.2590	780904	SEASAT
STFDOP	42112	-3942259.8818	3468891.8325	-3608217.6635	3.1800	3.2100	3.2800	870101	D1–C D1–D
STODOP	30280	1743938.7204	-5022695.9511	-3512039.3262	.3980	.2960	.2710	780904	SEASAT

Station Name	Station Number	X m	Y m	Z m	σX m	σY m	σZ m	Epoch yymmdd	Satellite/Tracking Technology
SUDBR	7075	692623.3224	-4347062.8532	4600488.1691	5.0500	5.2800	5.7600	60-69	Optical
TAFDOP	24	-6100052.6443	-997191.9535	-1568313.1559	.4420	.5790	.3470	780904	SEASAT
TAFU56	560	-6100052.2585	-997197.2863	-1568314.1007	.1380	.3700	.1450	870101	HILAT GEOSAT
TAIPEI	52360101	-3024782.6341	4928938.5072	2681235.0764	.2090	.2310	.1410	921031	EP/EUVE T/P GPS
TANAN	1043	4091879.8550	4434290.0302	-2064723.4802	7.0500	6.5100	6.7400	60-69	Optical
TEXDOP	192	-740292.3255	-5457076.2461	3207237.3457	.5340	.3920	.3490	780904	SEASAT
TFN117	42117	-6100055.9308	-997184.1107	-1568468.3071	3.3200	4.0700	3.9400	870101	D1–C D1–D
TFNA17	41017	-6100046.9110	-997203.4999	-1568470.0813	3.6900	4.7200	4.3800	870101	BE–C
THULE	557	539848.9278	-1388562.5089	6180979.5100	.1130	.0916	.1540	870101	HILAT GEOSAT
THULE	35508	539848.9566	-1388562.1496	6180980.1451	.1130	.0916	.1540	870101	RADCAL
TIDBINBILLA	55010383	-4460996.2163	2682557.0557	-3674444.0961	.1800	.1450	.1230	921031	EP/EUVE T/P GPS
TOKYO	9005	-3946699.8176	3366289.3601	3698835.4876	3.6400	3.7500	4.1700	60-69	Optical
TONOPA	35510	-2272637.3443	-4507725.8061	3887868.1522	1.0000	.7190	.5490	870101	RADCAL
TOULOUSE	4002	4628047.7073	119669.9950	4372787.6251	.0528	.0994	.0673	900601	DORIS SPOT–2
TRIESTE	7550	4336737.5053	1071272.9006	4537911.7508	.1380	.1720	.1040	860701	SLR
TRISTAN DA CUN	4005	4978463.0308	-1086620.9822	-3823205.8583	.1000	.1640	.0906	900601	DORIS SPOT–2
TROMSO	4054	2102915.7057	721600.7309	5958200.7242	.0709	.0816	.0752	900601	DORIS SPOT–2
TROMSO	7602	2102904.5012	721602.2541	5958201.1802	.1830	.1420	.1060	860701	SLR
TROMSO	51030203	2102941.2605	721569.8068	5958194.3784	.1320	.1150	.1920	921031	EP/EUVE T/P GPS
TULDOP	118	539846.9581	-1388563.3073	6180980.0556	.3160	.4290	.6540	780904	SEASAT
TVE725	41017	-5035503.2931	3305618.0871	-2090236.6455	4.4100	5.1500	5.1200	870101	BE–C
TVEDOP	30793	-5037685.6286	3301870.2027	-2090783.3095	.3780	.4410	.2840	780904	SEASAT
UCCLE	21	4027834.2200	307015.1048	4919536.8684	.1010	.2290	.1210	780904	SEASAT
UCLDOP	60021	4027832.8668	307020.3266	4919541.8964	3.1100	3.6800	15.4000	801015	OSCAR–14
UKIAH	65170	-2713391.0673	-4144631.1755	4004315.6169	3.9700	3.5100	16.5000	801015	OSCAR–14
UKIDOP	51960	-2713391.0252	-4144615.0052	4004299.8999	.3190	.2940	.2480	780904	SEASAT
ULASK	1036	-2282346.2908	-1452639.6132	5756902.0487	3.9800	4.0900	5.7000	60-69	Optical
UNDAK	7034	-521698.5993	-4242042.5789	4718726.4077	4.7500	5.4100	5.3900	60-69	Optical
USUDA	52172997	-3855263.1314	3427432.4727	3741020.2059	.1480	.1480	.1140	921031	EP/EUVE T/P GPS
UZHGOR	9432	3907425.3821	1602443.5478	4763918.6100	7.8700	7.2500	8.5400	60-69	Optical
VANDEN	35501	-2666947.6431	-4519838.4657	3612813.9463	.7910	.5430	.3980	870101	RADCAL
VANDENB/HARVES	54050001	-2686069.1772	-4527084.5421	3589502.2682	.1780	.2440	.1660	880101	EP/EUVE T/P GPS
VERNAL	7892	-1631486.1026	-4589133.9503	4106749.0614	.1010	.1070	.0670	860701	SLR
VILDO	9011	2280592.1725	-4914583.4188	-3355401.9614	3.3000	2.8300	3.1200	60-69	Optical
VILLA DOLORES	9012	-5466058.6093	-2404294.3631	2242187.7883	2.2600	2.8600	2.8100	60-69	Optical
VIRDOP	107	1090140.6371	-4842525.3431	3991974.9826	.4680	.3790	.3380	780904	SEASAT
WALLIS	4037	-6195393.6780	-413728.3066	-1454075.2209	.0584	.1150	.0654	900601	DORIS SPOT–2
WALLOP	35502	1263672.4932	-4875755.4113	3899751.3401	.8390	.3790	.3920	870101	RADCAL
WALMOT	7078	1261590.4875	-4881342.2427	3893442.8700	7.5700	8.8700	9.6200	60-69	Optical
WASHINGTON	7043	1130714.6445	-4831326.0937	3994140.2487	7.1300	7.5400	7.5600	60-69	Optical
WASHINGTON	7050	1130681.2169	-4831362.0173	3994106.4579	3.3300	.9520	1.7400	710601	D1–C D1–D
WASHINGTON	7105	1130718.3539	-4831350.7163	3994106.7229	.0012	.0046	.0039	860701	SLR
WESTFORD	7091	1492452.2470	-4457278.8652	4296816.2253	.0367	.0324	.0268	860701	SLR
WETTZELL	443	4075575.3321	931797.3197	4801583.1291	.4030	.7910	.4050	870101	HILAT
WETTZELL	549	4075575.5954	931796.7083	4801583.5872	.1410	.2680	.1520	870101	GEOSAT
WETTZELL	8834	4075575.9243	931786.2759	4801584.2308	.0208	.0224	.0169	860701	SLR
WETTZELL	60643	4075533.1861	931827.7754	4801613.3239	3.1800	3.8700	15.4000	801015	OSCAR–14
WETTZELL	51420180	4075578.7397	931852.7958	4801570.0734	.1520	.1200	.1580	921031	EP/EUVE T/P GPS
WHTSND	35513	-1529941.0328	-5171206.8094	3396639.5968	1.2400	.6590	.6220	870101	RADCAL
WICHIT	35015	-783475.9586	-5236534.8067	3544673.4189	.3100	.1180	.1370	870101	GEOSAT
WNKFL	1035	3983117.3370	-48500.1105	4964715.6142	5.1100	4.6400	5.4700	60-69	Optical
WOOMER	9003	-3983793.1470	3743101.3545	-3275532.4308	3.7800	3.8300	4.1500	60-69	Optical
WOOMERA	9023	-3977782.9785	3725110.7626	-3303003.5650	2.8200	2.8200	2.7300	60-69	Optical
WUHAN	7236	-2266557.3998	5009079.0463	3222265.4517	.1100	.1010	.1090	860701	SLR
XRISOKALARIA	7525	4745948.4169	1905707.3830	3799169.7370	.0458	.0499	.0391	860701	SLR
YARRAGADEE	7090	-2389010.1759	5043330.0402	-3078521.2241	.0099	.0076	.0110	860701	SLR
YARRAGADEE	55010704	-2389025.4996	5043316.9126	-3078531.0626	.0679	.1430	.0881	921031	EP/EUVE T/P GPS
YELLOWKNIFE	4051	-1224423.8417	-2689227.3989	5633645.3027	.0618	.0495	.0419	900601	DORIS SPOT–2
YELLOWKNIFE	54012703	-1224452.5284	-2689216.1843	5633638.4823	.1150	.1510	.1910	921031	EP/EUVE T/P GPS
YIGILCA	7587	4117360.6242	2517078.1619	4157679.5970	.0572	.0575	.0483	860701	SLR
YOZGAT	7585	4029729.2448	2802094.5531	4062068.4968	.0927	.0921	.0662	860701	SLR
YUMA	7894	-2196779.0597	-4887337.0687	3448424.5198	.1280	.1200	.1180	860701	SLR
ZIMMERWALD	7810	4331282.9104	567550.8646	4633140.4648	.0197	.0209	.0168	860701	SLR
ZIMMERWALD	8010	4331311.9489	567528.7460	4633131.1773	6.1700	6.3200	6.7200	60-69	Optical

C. EGM96 GRAVITATIONAL COEFFICIENTS AND THEIR UNCERTAINTIES

The following table contains the fully normalized [*Heiskanen and Moritz*, 1967, Sect. 1-14], unitless, potential coefficients from EGM96, complete through degree and order 20. $\overline{C}_{2,0}$ is in the tide-free system. $\overline{C}_{2,0}$, $\overline{C}_{2,1}$, and $\overline{S}_{2,1}$ refer to Epoch 1986.0. The following rates were applied in the estimation of EGM96: $\dot{\overline{C}}_{2,0}$ = 1.162755E-11/yr, $\dot{\overline{C}}_{2,1}$ = -.32E-11/yr, and $\dot{\overline{S}}_{2,1}$ = 1.62E-11/yr.

n	m	$\overline{C}_{n,m}$	$\overline{S}_{n,m}$	$\sigma(\overline{C}_{n,m})$	$\sigma(\overline{S}_{n,m})$
2	0	-4.84165371736E-04		3.5610635E-11	
2	1	-1.86987635955E-10	1.19528012031E-09	1.0000000E-30	1.0000000E-30
2	2	2.43914352398E-06	-1.40016683654E-06	5.3739154E-11	5.4353269E-11
3	0	9.57254173792E-07		1.8094237E-11	
3	1	2.02998882184E-06	2.48513158716E-07	1.3965165E-10	1.3645882E-10
3	2	9.04627768605E-07	-6.19025944205E-07	1.0962329E-10	1.1182866E-10
3	3	7.21072657057E-07	1.41435626958E-06	9.5156281E-11	9.3285090E-11
4	0	5.39873863789E-07		1.0423678E-10	
4	1	-5.36321616971E-07	-4.73440265853E-07	8.5674404E-11	8.2408489E-11
4	2	3.50694105785E-07	6.62671572540E-07	1.6000186E-10	1.6390576E-10
4	3	9.90771803829E-07	-2.00928369177E-07	8.4657802E-11	8.2662506E-11
4	4	-1.88560802735E-07	3.08853169333E-07	8.7315359E-11	8.7852819E-11
5	0	6.85323475630E-08		5.4383090E-11	
5	1	-6.21012128528E-08	-9.44226127525E-08	2.7996887E-10	2.8082882E-10
5	2	6.52438297612E-07	-3.23349612668E-07	2.3747375E-10	2.4356998E-10
5	3	-4.51955406071E-07	-2.14847190624E-07	1.7111636E-10	1.6810647E-10
5	4	-2.95301647654E-07	4.96658876769E-08	1.1981266E-10	1.1849793E-10
5	5	1.74971983203E-07	-6.69384278219E-07	1.1642563E-10	1.1590031E-10
6	0	-1.49957994714E-07		1.4497863E-10	
6	1	-7.60879384947E-08	2.62890545501E-08	2.2415138E-10	2.1957296E-10
6	2	4.81732442832E-08	-3.73728201347E-07	2.7697363E-10	2.8105811E-10
6	3	5.71730990516E-08	9.02694517163E-09	1.9432407E-10	1.8682712E-10
6	4	-8.62142660109E-08	-4.71408154267E-07	1.5229150E-10	1.5328004E-10
6	5	-2.67133325490E-07	-5.36488432483E-07	8.9838470E-11	8.7820905E-11
6	6	9.67616121092E-09	-2.37192006935E-07	1.1332010E-10	1.1518036E-10
7	0	9.09789371450E-08		1.3919821E-10	
7	1	2.79872910488E-07	9.54336911867E-08	4.3500231E-10	4.2584820E-10
7	2	3.29743816488E-07	9.30667596042E-08	3.9034671E-10	3.9858085E-10
7	3	2.50398657706E-07	-2.17198608738E-07	3.2646930E-10	3.1799577E-10
7	4	-2.75114355257E-07	-1.23800392323E-07	2.3251698E-10	2.2964717E-10
7	5	1.93765507243E-09	1.77377719872E-08	1.6792139E-10	1.7201828E-10
7	6	-3.58856860645E-07	1.51789817739E-07	8.9799183E-11	8.9575785E-11
7	7	1.09185148045E-09	2.44415707993E-08	1.3599934E-10	1.3564720E-10
8	0	4.96711667324E-08		2.2663861E-10	
8	1	2.33422047893E-08	5.90060493411E-08	4.0634230E-10	3.9490843E-10
8	2	8.02978722615E-08	6.54175425859E-08	3.6512930E-10	3.6825158E-10
8	3	-1.91877757009E-08	-8.63454445021E-08	2.9352566E-10	2.8069012E-10
8	4	-2.44600105471E-07	7.00233016934E-08	2.5244455E-10	2.6262799E-10

n	m	$\overline{C}_{n,m}$	$\overline{S}_{n,m}$	$\sigma(\overline{C}_{n,m})$	$\sigma(\overline{S}_{n,m})$
8	5	-2.55352403037E-08	8.91462164788E-08	2.0021311E-10	1.9479275E-10
8	6	-6.57361610961E-08	3.09238461807E-07	1.6673572E-10	1.6680807E-10
8	7	6.72811580072E-08	7.47440473633E-08	9.4505589E-11	9.5246237E-11
8	8	-1.24092493016E-07	1.20533165603E-07	1.5695393E-10	1.5769999E-10
9	0	2.76714300853E-08		2.2214648E-10	
9	1	1.43387502749E-07	2.16834947618E-08	5.8335018E-10	5.5609313E-10
9	2	2.22288318564E-08	-3.22196647116E-08	4.8353378E-10	4.8392082E-10
9	3	-1.60811502143E-07	-7.42287409462E-08	4.6594220E-10	4.5810990E-10
9	4	-9.00179225336E-09	1.94666779475E-08	3.6909229E-10	3.6635390E-10
9	5	-1.66165092924E-08	-5.41113191483E-08	2.9221604E-10	3.0036229E-10
9	6	6.26941938248E-08	2.22903525945E-07	2.2052623E-10	2.2142953E-10
9	7	-1.18366323475E-07	-9.65152667886E-08	1.8155999E-10	1.8063564E-10
9	8	1.88436022794E-07	-3.08566220421E-09	1.3135894E-10	1.3157891E-10
9	9	-4.77475386132E-08	9.66412847714E-08	1.8551471E-10	1.8432444E-10
10	0	5.26222488569E-08		3.0890035E-10	
10	1	8.35115775652E-08	-1.31314331796E-07	5.2560148E-10	5.0053305E-10
10	2	-9.42413882081E-08	-5.15791657390E-08	4.4292785E-10	4.4624108E-10
10	3	-6.89895048176E-09	-1.53768828694E-07	3.7051454E-10	3.6174988E-10
10	4	-8.40764549716E-08	-7.92806255331E-08	3.1088626E-10	3.2213352E-10
10	5	-4.93395938185E-08	-5.05370221897E-08	3.2221821E-10	3.2202850E-10
10	6	-3.75885236598E-08	-7.95667053872E-08	2.8294160E-10	2.7566976E-10
10	7	8.11460540925E-09	-3.36629641314E-09	1.8704768E-10	1.8901334E-10
10	8	4.04927981694E-08	-9.18705975922E-08	1.8275291E-10	1.8362644E-10
10	9	1.25491334939E-07	-3.76516222392E-08	9.0465977E-11	9.0959794E-11
10	10	1.00538634409E-07	-2.40148449520E-08	1.5964045E-10	1.5956547E-10
11	0	-5.09613707522E-08		3.4552145E-10	
11	1	1.51687209933E-08	-2.68604146166E-08	6.4201268E-10	6.1048276E-10
11	2	1.86309749878E-08	-9.90693862047E-08	5.7068253E-10	5.7276720E-10
11	3	-3.09871239854E-08	-1.48131804260E-07	5.0157135E-10	4.9518511E-10
11	4	-3.89580205051E-08	-6.36666511980E-08	4.8810597E-10	4.9707446E-10
11	5	3.77848029452E-08	4.94736238169E-08	3.8720715E-10	3.9094668E-10
11	6	-1.18676592395E-09	3.44769584593E-08	3.4564774E-10	3.4776352E-10
11	7	4.11565188074E-09	-8.98252808977E-08	2.9198446E-10	2.9066089E-10
11	8	-5.98410841300E-09	2.43989612237E-08	2.1462767E-10	2.1335842E-10
11	9	-3.14231072723E-08	4.17731829829E-08	1.9485030E-10	1.9528860E-10
11	10	-5.21882681927E-08	-1.83364561788E-08	1.2830605E-10	1.2848978E-10
11	11	4.60344448746E-08	-6.96662308185E-08	1.9818678E-10	1.9713732E-10
12	0	3.77252636558E-08		4.3588608E-10	
12	1	-5.40654977836E-08	-4.35675748979E-08	5.4452693E-10	5.1580423E-10
12	2	1.42979642253E-08	3.20975937619E-08	5.3272875E-10	5.4168090E-10
12	3	3.93995876403E-08	2.44264863505E-08	4.5756501E-10	4.4928026E-10
12	4	-6.86908127934E-08	4.15081109011E-09	3.7303817E-10	3.9051408E-10
12	5	3.09411128730E-08	7.82536279033E-09	3.3134311E-10	3.3356660E-10
12	6	3.41523275208E-09	3.91765484449E-08	4.1142705E-10	4.0153046E-10
12	7	-1.86909958587E-08	3.56131849382E-08	3.3782181E-10	3.3541151E-10
12	8	-2.53769398865E-08	1.69361024629E-08	2.5681411E-10	2.5872950E-10
12	9	4.22880630662E-08	2.52692598301E-08	1.6406791E-10	1.6446989E-10
12	10	-6.17619654902E-09	3.08375794212E-08	1.6918996E-10	1.6790941E-10
12	11	1.12502994122E-08	-6.37946501558E-09	6.7006102E-11	6.6840672E-11
12	12	-2.49532607390E-09	-1.11780601900E-08	1.2164740E-10	1.2112058E-10

n	m	$\overline{C}_{n,m}$	$\overline{S}_{n,m}$	$\sigma(\overline{C}_{n,m})$	$\sigma(\overline{S}_{n,m})$
13	0	4.22982206413E-08		4.8735174E-10	
13	1	-5.13569699124E-08	3.90510386685E-08	5.7337833E-10	5.4235587E-10
13	2	5.59217667099E-08	-6.27337565381E-08	6.2482536E-10	6.2901869E-10
13	3	-2.19360927945E-08	9.74829362237E-08	5.3388870E-10	5.2773007E-10
13	4	-3.13762599666E-09	-1.19627874492E-08	5.4039679E-10	5.4783125E-10
13	5	5.90049394905E-08	6.64975958036E-08	4.7950608E-10	4.8088793E-10
13	6	-3.59038073075E-08	-6.57280613686E-09	4.0896517E-10	4.0884469E-10
13	7	2.53002147087E-09	-6.21470822331E-09	3.9155909E-10	3.9410761E-10
13	8	-9.83150822695E-09	-1.04740222825E-08	3.5854029E-10	3.5240648E-10
13	9	2.47325771791E-08	4.52870369936E-08	2.6046428E-10	2.6319103E-10
13	10	4.10324653930E-08	-3.68121029480E-08	1.8490873E-10	1.8422246E-10
13	11	-4.43869677399E-08	-4.76507804288E-09	1.8376153E-10	1.8244164E-10
13	12	-3.12622200222E-08	8.78405809267E-08	6.1371381E-11	6.1572440E-11
13	13	-6.12759553199E-08	6.85261488594E-08	1.4093183E-10	1.4043508E-10
14	0	-2.42786502921E-08		5.4599206E-10	
14	1	-1.86968616381E-08	2.94747542249E-08	5.1130059E-10	4.8389874E-10
14	2	-3.67789379502E-08	-5.16779392055E-09	5.4973862E-10	5.6994964E-10
14	3	3.58875097333E-08	2.04618827833E-08	4.9957192E-10	4.9552362E-10
14	4	1.83865617792E-09	-2.26780613566E-08	4.6147419E-10	4.9345647E-10
14	5	2.87344273542E-08	-1.63882249728E-08	3.9151067E-10	3.9536505E-10
14	6	-1.94810485574E-08	2.47831272781E-09	3.9714930E-10	3.8064240E-10
14	7	3.75003839415E-08	-4.17291319429E-09	4.3406164E-10	4.2974545E-10
14	8	-3.50946485865E-08	-1.53515265203E-08	4.2197834E-10	4.2204868E-10
14	9	3.20284939341E-08	2.88804922064E-08	2.7047158E-10	2.6799755E-10
14	10	3.90329180008E-08	-1.44308452469E-09	2.1493467E-10	2.1309132E-10
14	11	1.53970516502E-08	-3.90548173245E-08	1.1626513E-10	1.1585650E-10
14	12	8.40829163869E-09	-3.11327189117E-08	1.0883382E-10	1.0845404E-10
14	13	3.22147043964E-08	4.51897224960E-08	2.9804138E-11	2.9985311E-11
14	14	-5.18980794309E-08	-4.81506636748E-09	3.2054988E-11	3.2450504E-11
15	0	1.47910068708E-09		5.3683772E-10	
15	1	1.00817268177E-08	1.09773066324E-08	5.2974731E-10	5.0086796E-10
15	2	-2.13942673775E-08	-3.08914875777E-08	6.0403581E-10	6.1012404E-10
15	3	5.21392929041E-08	1.72892926103E-08	5.8231646E-10	5.5913415E-10
15	4	-4.08150084078E-08	6.50174707794E-09	5.2298193E-10	5.3982246E-10
15	5	1.24935723108E-08	8.08375563996E-09	5.5310203E-10	5.5318757E-10
15	6	3.31211643896E-08	-3.68246004304E-08	4.6497321E-10	4.7095028E-10
15	7	5.96210699259E-08	5.31841171879E-09	4.1280301E-10	4.1673871E-10
15	8	-3.22428691498E-08	2.21523579587E-08	4.1946092E-10	4.1393325E-10
15	9	1.28788268085E-08	3.75629820829E-08	3.8464822E-10	3.8605019E-10
15	10	1.04688722521E-08	1.47222147015E-08	2.9362674E-10	2.9535457E-10
15	11	-1.11675061934E-09	1.80996198432E-08	1.9651296E-10	1.9498687E-10
15	12	-3.23962134415E-08	1.55243104746E-08	9.8639991E-11	9.8725357E-11
15	13	-2.83933019117E-08	-4.22066791103E-09	1.2015236E-10	1.1969380E-10
15	14	5.19168859330E-09	-2.43752739666E-08	3.1187284E-11	3.1381782E-11
15	15	-1.90930538322E-08	-4.71139421558E-09	4.8306488E-11	4.7133713E-11
16	0	-3.15322986722E-09		5.3130421E-10	
16	1	2.58360856231E-08	3.25447560859E-08	5.2980947E-10	5.0249031E-10
16	2	-2.33671404512E-08	2.88799363439E-08	5.1389747E-10	5.4074935E-10
16	3	-3.36019429391E-08	-2.20418988010E-08	4.8485480E-10	4.8575056E-10
16	4	4.02316284314E-08	4.83837716909E-08	5.3085070E-10	5.6684012E-10

n	m	$\overline{C}_{n,m}$	$\overline{S}_{n,m}$	$\sigma(\overline{C}_{n,m})$	$\sigma(\overline{S}_{n,m})$
16	5	-1.29501939245E-08	-3.19458578129E-09	5.0235685E-10	4.9883081E-10
16	6	1.40239252323E-08	-3.50760208303E-08	4.3608217E-10	4.2561981E-10
16	7	-7.08412635136E-09	-8.81581561131E-09	4.1560133E-10	4.1334452E-10
16	8	-2.09018868094E-08	5.00527390530E-09	4.6375155E-10	4.6442894E-10
16	9	-2.18588720643E-08	-3.95012419994E-08	4.2203404E-10	4.2207754E-10
16	10	-1.17529900814E-08	1.14211582961E-08	3.3663249E-10	3.3627437E-10
16	11	1.87574042592E-08	-3.03161919925E-09	1.7642883E-10	1.7706550E-10
16	12	1.95400194038E-08	6.66983574071E-09	1.2893049E-10	1.2847491E-10
16	13	1.38196369576E-08	1.02778499508E-09	4.9645374E-11	4.9771036E-11
16	14	-1.93182168856E-08	-3.86174893776E-08	3.1733130E-11	3.2124180E-11
16	15	-1.45149060142E-08	-3.27443078739E-08	3.8814590E-11	3.9089765E-11
16	16	-3.79671710746E-08	3.02155372655E-09	1.7759112E-10	1.7693092E-10
17	0	1.97605066395E-08		4.5595926E-10	
17	1	-2.54177575118E-08	-3.06630529689E-08	6.1168597E-10	6.0590338E-10
17	2	-1.95988656721E-08	6.49265893410E-09	5.0202766E-10	5.1481373E-10
17	3	5.64123066224E-09	6.78327095529E-09	6.3292562E-10	5.9927568E-10
17	4	7.07457075637E-09	2.49437600834E-08	5.0206810E-10	5.2913860E-10
17	5	-1.54987006052E-08	6.60021551851E-09	5.6101689E-10	5.5070220E-10
17	6	-1.18194012847E-08	-2.89770975177E-08	5.4939081E-10	5.4334128E-10
17	7	2.42149702381E-08	-4.22222973697E-09	4.5746637E-10	4.5401208E-10
17	8	3.88442097559E-08	3.58904095943E-09	4.3511790E-10	4.2576205E-10
17	9	3.81356493231E-09	-2.81466943714E-08	4.1146573E-10	4.1119523E-10
17	10	-3.88216085542E-09	1.81328176508E-08	3.9641987E-10	4.0000371E-10
17	11	-1.57356600363E-08	1.06560649404E-08	2.9773487E-10	2.9741388E-10
17	12	2.88013010655E-08	2.03450136084E-08	1.4784485E-10	1.4706358E-10
17	13	1.65503425731E-08	2.04667531435E-08	1.1998713E-10	1.1955420E-10
17	14	-1.41983872649E-08	1.14948025244E-08	4.9034053E-11	5.0069006E-11
17	15	5.42100361657E-09	5.32610369811E-09	4.5617974E-11	4.4691651E-11
17	16	-3.01992205043E-08	3.65331918531E-09	7.1252579E-11	7.0742716E-11
17	17	-3.43086856041E-08	-1.98523455381E-08	2.0333152E-10	2.0282665E-10
18	0	5.08691038332E-09		4.6789230E-10	
18	1	7.21098449649E-09	-3.88714473013E-08	5.2798106E-10	5.0885673E-10
18	2	1.40631771205E-08	1.00093396253E-08	5.0681599E-10	5.4650317E-10
18	3	-5.07232520873E-09	-4.90865931335E-09	5.4681971E-10	5.4400738E-10
18	4	5.48759308217E-08	-1.35267117720E-09	4.9090676E-10	5.2102762E-10
18	5	5.48710485555E-09	2.64338629459E-08	5.8920322E-10	5.8703487E-10
18	6	1.46570755271E-08	-1.36438019951E-08	5.2538248E-10	5.1113456E-10
18	7	6.75812328417E-09	6.88577494235E-09	4.5391343E-10	4.4506212E-10
18	8	3.07619845144E-08	4.17827734107E-09	4.5250150E-10	4.5442385E-10
18	9	-1.88470601880E-08	3.68302736953E-08	4.4309926E-10	4.4072646E-10
18	10	5.27535358934E-09	-4.66091535881E-09	4.3962755E-10	4.3706812E-10
18	11	-7.29628518960E-09	1.95215208020E-09	3.0269058E-10	3.0532107E-10
18	12	-2.97449412422E-08	-1.64497878395E-08	1.7926913E-10	1.7863254E-10
18	13	-6.27919717152E-09	-3.48383939938E-08	6.2153473E-11	6.2044245E-11
18	14	-8.15605336410E-09	-1.28636585027E-08	4.5358449E-11	4.6080793E-11
18	15	-4.05003412879E-08	-2.02684998021E-08	7.5716039E-11	7.6852783E-11
18	16	1.04141042028E-08	6.61468817624E-09	1.5974982E-10	1.5840268E-10
18	17	3.58771586841E-09	4.48065587564E-09	1.0867064E-10	1.0857707E-10
18	18	3.12351953717E-09	-1.09906032543E-08	2.8770747E-10	2.8596208E-10
19	0	-3.25780965394E-09		3.9880617E-10	

n	m	$\overline{C}_{n,m}$	$\overline{S}_{n,m}$	$\sigma(\overline{C}_{n,m})$	$\sigma(\overline{S}_{n,m})$
19	1	-7.59903885319E-09	1.26835472605E-09	5.5285072E-10	5.5819254E-10
19	2	3.53541528655E-08	-1.31346303514E-09	5.3996618E-10	5.6700245E-10
19	3	-9.74103607309E-09	1.50662259043E-09	5.7760045E-10	5.4562054E-10
19	4	1.57039009057E-08	-7.61677383811E-09	5.5266991E-10	5.9527084E-10
19	5	1.09629213379E-08	2.83172176438E-08	5.4725130E-10	5.2424864E-10
19	6	-4.08745178658E-09	1.86219430719E-08	5.4648203E-10	5.3804795E-10
19	7	4.78275337044E-09	-7.17283455900E-09	5.5134865E-10	5.4439979E-10
19	8	2.94908364280E-08	-9.93037002883E-09	4.4281042E-10	4.2972762E-10
19	9	3.07961427159E-09	6.94110477214E-09	4.1895916E-10	4.1630624E-10
19	10	-3.38415069043E-08	-7.37981767136E-09	4.1590690E-10	4.1338509E-10
19	11	1.60443652916E-08	9.96673453483E-09	3.6350417E-10	3.6418173E-10
19	12	-2.47106581581E-09	9.16852310642E-09	2.6437342E-10	2.6193982E-10
19	13	-7.44717379980E-09	-2.82584466742E-08	1.3571784E-10	1.3572279E-10
19	14	-4.70502589215E-09	-1.29526697983E-08	6.0064446E-11	6.0016480E-11
19	15	-1.76580549771E-08	-1.40350990039E-08	6.9036188E-11	6.7819564E-11
19	16	-2.16950096188E-08	-7.24534721567E-09	1.2086256E-10	1.2099640E-10
19	17	2.90444936079E-08	-1.53456531070E-08	1.7867126E-10	1.7929347E-10
19	18	3.48382199593E-08	-9.54146344917E-09	1.1549444E-10	1.1520432E-10
19	19	-2.57349349430E-09	4.83151822363E-09	2.9444927E-10	2.9634084E-10
20	0	2.22384610651E-08		4.6908617E-10	
20	1	5.16303125218E-09	6.69626726966E-09	4.5465090E-10	4.4522409E-10
20	2	1.98831128238E-08	1.75183843257E-08	5.3799405E-10	5.7729565E-10
20	3	-3.62601436785E-09	3.79590724141E-08	5.2764671E-10	5.2364203E-10
20	4	2.42238118652E-09	-2.11057611874E-08	5.3778329E-10	5.7080135E-10
20	5	-1.07042562564E-08	-7.71860083169E-09	5.5963913E-10	5.5066230E-10
20	6	1.10474837570E-08	-2.17720365898E-09	5.8502067E-10	5.6422287E-10
20	7	-2.10090282728E-08	-2.23491503969E-11	5.4119158E-10	5.2526828E-10
20	8	4.42419185637E-09	1.83035804593E-09	4.4722111E-10	4.4959414E-10
20	9	1.78846216942E-08	-6.63940865358E-09	4.4435385E-10	4.4772500E-10
20	10	-3.25394919988E-08	-5.12308873621E-09	4.3477963E-10	4.3629438E-10
20	11	1.38992707697E-08	-1.87706454942E-08	3.7824380E-10	3.8409415E-10
20	12	-6.35750600750E-09	1.80260853103E-08	2.8133033E-10	2.7918368E-10
20	13	2.75222725997E-08	6.90887077588E-09	9.9129615E-11	9.8552906E-11
20	14	1.15841169405E-08	-1.43176160143E-08	8.9023003E-11	9.0791190E-11
20	15	-2.60130744291E-08	-7.84379672413E-10	9.8594967E-11	1.0072429E-10
20	16	-1.24137147118E-08	-2.77500443628E-10	1.9230790E-10	1.9182381E-10
20	17	4.36909667960E-09	-1.37420446198E-08	1.9107891E-10	1.8937308E-10
20	18	1.51842883022E-08	-8.08429903142E-10	2.5237894E-10	2.5083660E-10
20	19	-3.14942002852E-09	1.06505202245E-08	1.7603753E-10	1.7721403E-10
20	20	4.01448327968E-09	-1.20450644785E-08	3.6744902E-10	3.6712141E-10

D.   EGM96 DYMANIC OCEAN TOPOGRAPHY COEFFICIENTS

Fully-normalized [*Heiskanen and Moritz*, 1967, Sect. 1-14] spherical harmonic coefficients of the Dynamic Ocean Topography in meters. The $\overline{C}_{2,0}$ values are in accordance with the recommendations of *Rapp et al*., [1991], as far as the permanent tide is concerned.

		TOPEX/POSEIDON and ERS–1				GEOSAT			
n	m	$\overline{C}_{n,m}$	$\overline{S}_{n,m}$	$\sigma(\overline{C}_{n,m})$	$\sigma(\overline{S}_{n,m})$	$\overline{C}_{n,m}$	$\overline{S}_{n,m}$	$\sigma(\overline{C}_{n,m})$	$\sigma(\overline{S}_{n,m})$
1	0	1.604709E-01		2.30E-02		2.392316E-02		4.53E-02	
1	1	-1.954346E-01	3.578986E-02	1.12E-02	1.58E-02	-1.679383E-01	8.186385E-03	1.90E-02	2.36E-02
2	0	-4.485608E-01		1.83E-02		-4.742153E-01		2.72E-02	
2	1	-5.572492E-02	1.483034E-02	9.96E-03	2.17E-02	-4.203759E-02	3.291309E-02	1.46E-02	2.87E-02
2	2	-2.209697E-02	-6.024443E-03	1.20E-02	1.12E-02	-3.817433E-02	-7.694695E-03	1.52E-02	1.52E-02
3	0	2.039577E-01		1.63E-02		1.913298E-01		2.33E-02	
3	1	-3.193309E-02	-5.105885E-02	1.09E-02	2.06E-02	-9.702405E-03	-1.946472E-02	1.46E-02	2.70E-02
3	2	6.562541E-04	-4.676271E-02	1.55E-02	1.15E-02	-1.670869E-02	-3.750277E-02	1.92E-02	1.61E-02
3	3	-2.610762E-02	-6.358613E-03	9.87E-03	1.09E-02	-2.168615E-02	3.042352E-03	1.34E-02	1.44E-02
4	0	-9.957892E-02		1.63E-02		-1.185085E-01		2.12E-02	
4	1	2.132078E-02	2.896921E-02	1.10E-02	1.57E-02	3.284643E-02	4.004700E-02	1.43E-02	2.06E-02
4	2	-2.284936E-02	2.143247E-03	1.57E-02	1.19E-02	-3.063320E-02	9.297914E-03	1.88E-02	1.56E-02
4	3	1.839340E-02	-2.676830E-02	1.06E-02	1.16E-02	1.751636E-02	-2.473942E-02	1.38E-02	1.44E-02
4	4	-1.864002E-02	-9.051651E-03	8.17E-03	1.04E-02	-1.268463E-02	-4.684023E-03	1.09E-02	1.30E-02
5	0	5.206220E-02		1.55E-02		4.004461E-02		1.87E-02	
5	1	-1.605488E-02	-1.048211E-02	9.64E-03	1.35E-02	-7.194118E-03	-1.194824E-02	1.26E-02	1.71E-02
5	2	1.133166E-02	2.808492E-02	1.32E-02	1.11E-02	3.966237E-03	2.755754E-02	1.57E-02	1.38E-02
5	3	5.690535E-03	-6.710072E-03	1.06E-02	1.20E-02	3.901948E-03	1.411427E-03	1.33E-02	1.39E-02
5	4	1.451076E-02	8.849084E-03	9.71E-03	9.06E-03	8.910538E-03	5.072241E-03	1.23E-02	1.16E-02
5	5	-4.654186E-03	5.429068E-03	8.33E-03	8.75E-03	-4.165423E-03	2.676984E-03	1.09E-02	1.10E-02
6	0	7.554166E-02		1.31E-02		7.077846E-02		1.54E-02	
6	1	-2.284519E-02	6.392970E-03	1.03E-02	1.26E-02	-1.922419E-02	-9.521897E-04	1.25E-02	1.49E-02
6	2	-2.230880E-02	1.870814E-02	1.05E-02	9.38E-03	-1.546387E-02	2.021150E-02	1.25E-02	1.17E-02
6	3	7.983477E-03	-3.307910E-02	9.89E-03	1.10E-02	1.426339E-02	-2.349178E-02	1.18E-02	1.24E-02
6	4	-5.132369E-03	-1.023330E-02	9.13E-03	9.26E-03	-7.818197E-03	-8.915781E-03	1.09E-02	1.13E-02
6	5	2.203678E-02	1.335907E-02	8.19E-03	8.20E-03	8.719474E-03	-1.454360E-03	1.04E-02	1.02E-02
6	6	-4.609631E-03	-1.001425E-04	8.41E-03	7.05E-03	-2.976657E-03	-8.518592E-03	1.04E-02	9.29E-03
7	0	-4.894897E-02		1.14E-02		-3.101673E-02		1.31E-02	
7	1	1.213518E-02	1.058129E-02	9.78E-03	1.14E-02	2.448248E-02	1.551598E-02	1.15E-02	1.30E-02
7	2	4.623517E-03	2.522492E-03	9.53E-03	8.89E-03	9.868357E-03	-1.323278E-03	1.10E-02	1.08E-02
7	3	6.477541E-03	9.164064E-03	8.57E-03	9.03E-03	8.292376E-03	5.324554E-03	1.02E-02	1.04E-02
7	4	-4.299915E-03	-9.669627E-03	8.76E-03	8.76E-03	-5.510875E-03	-3.716133E-03	1.01E-02	1.02E-02
7	5	1.044389E-02	3.734892E-03	7.85E-03	7.68E-03	6.725990E-03	-3.631856E-03	9.61E-03	9.39E-03
7	6	1.133551E-02	7.422554E-03	7.34E-03	7.28E-03	1.051263E-02	7.239155E-04	9.26E-03	9.16E-03
7	7	4.523126E-03	-8.901479E-03	7.53E-03	6.60E-03	2.090699E-03	-5.990029E-03	9.32E-03	8.55E-03
8	0	1.119485E-02		1.00E-02		1.460824E-02		1.13E-02	
8	1	-5.234208E-02	-2.681098E-02	8.76E-03	1.01E-02	-5.242907E-02	-2.466056E-02	1.01E-02	1.14E-02
8	2	-4.519246E-03	8.586636E-04	8.60E-03	8.38E-03	-1.489757E-03	9.491556E-04	9.80E-03	9.92E-03
8	3	1.989674E-02	1.524358E-03	7.68E-03	7.84E-03	1.675640E-02	1.215150E-04	9.05E-03	9.07E-03
8	4	1.735643E-02	7.518630E-03	7.63E-03	7.67E-03	1.416886E-02	1.028794E-02	8.82E-03	8.98E-03
8	5	-4.243776E-03	2.219930E-03	7.36E-03	7.42E-03	-3.783313E-03	-4.131097E-03	8.64E-03	8.74E-03

		TOPEX/POSEIDON and ERS–1				GEOSAT			
n	m	$\overline{C}_{n,m}$	$\overline{S}_{n,m}$	$\sigma(\overline{C}_{n,m})$	$\sigma(\overline{S}_{n,m})$	$\overline{C}_{n,m}$	$\overline{S}_{n,m}$	$\sigma(\overline{C}_{n,m})$	$\sigma(\overline{S}_{n,m})$
8	6	-5.426846E-03	1.022059E-03	6.80E-03	6.78E-03	-2.115521E-03	1.273560E-03	8.45E-03	8.20E-03
8	7	-4.256712E-03	4.746315E-04	6.91E-03	6.27E-03	-2.337646E-03	-2.786397E-03	8.48E-03	8.03E-03
8	8	1.356110E-04	-7.333417E-04	6.69E-03	6.18E-03	-2.399562E-03	-2.167179E-03	8.23E-03	7.97E-03
9	0	-3.002781E-02		8.71E-03		-2.636659E-02		9.73E-03	
9	1	2.971576E-02	1.013624E-02	8.16E-03	9.27E-03	2.891069E-02	8.581752E-03	9.19E-03	1.01E-02
9	2	4.719951E-03	-1.784737E-02	7.96E-03	7.88E-03	4.336630E-03	-1.625802E-02	8.91E-03	9.06E-03
9	3	-1.246354E-02	1.807515E-02	7.23E-03	7.26E-03	-1.503108E-02	1.493993E-02	8.37E-03	8.29E-03
9	4	1.760592E-03	-6.163950E-03	6.79E-03	6.93E-03	2.002386E-03	2.660457E-03	7.88E-03	8.00E-03
9	5	8.522354E-04	-1.175363E-02	6.82E-03	6.69E-03	4.167833E-03	-1.158189E-02	7.91E-03	7.85E-03
9	6	-1.318131E-03	-2.028934E-03	6.47E-03	6.31E-03	-6.474889E-04	1.864212E-03	7.67E-03	7.53E-03
9	7	-1.456526E-03	-8.402741E-03	6.20E-03	5.91E-03	-9.702969E-04	-9.446115E-03	7.54E-03	7.41E-03
9	8	-3.380855E-03	7.789211E-03	5.99E-03	5.95E-03	3.373640E-03	3.232767E-03	7.43E-03	7.49E-03
9	9	-1.777017E-04	-2.180967E-03	5.85E-03	5.85E-03	2.290201E-04	-7.672403E-04	7.36E-03	7.33E-03
10	0	-2.232930E-03		7.78E-03		-2.424569E-03		8.52E-03	
10	1	1.125822E-02	-1.007074E-02	7.23E-03	8.24E-03	1.529334E-02	-1.022353E-02	8.19E-03	8.92E-03
10	2	8.205547E-03	4.532399E-04	7.36E-03	7.25E-03	3.578494E-03	1.615055E-03	8.11E-03	8.20E-03
10	3	-2.608458E-04	-2.088651E-03	6.55E-03	6.60E-03	-3.100703E-03	-3.252328E-03	7.64E-03	7.52E-03
10	4	2.246509E-03	-5.450779E-03	6.10E-03	6.24E-03	5.267939E-03	-1.016209E-02	7.12E-03	7.21E-03
10	5	-3.667203E-03	-1.391779E-02	6.10E-03	6.04E-03	-2.702055E-03	-5.925477E-03	7.10E-03	7.05E-03
10	6	2.236519E-03	-8.114012E-03	6.01E-03	5.93E-03	1.621427E-03	-2.312510E-03	7.01E-03	6.96E-03
10	7	-1.871469E-03	-5.086154E-04	5.67E-03	5.55E-03	-7.682183E-04	9.710256E-04	6.80E-03	6.74E-03
10	8	2.155862E-03	3.227206E-03	5.65E-03	5.41E-03	3.060625E-03	7.259568E-05	6.83E-03	6.75E-03
10	9	-5.594664E-03	1.132412E-02	5.61E-03	5.26E-03	-6.106896E-03	7.166201E-03	6.96E-03	6.65E-03
10	10	1.928004E-03	1.757481E-04	5.19E-03	5.46E-03	4.329765E-03	3.425746E-03	6.61E-03	6.78E-03
11	0	9.033268E-03		6.88E-03		1.455916E-02		7.54E-03	
11	1	-1.680516E-02	-8.373003E-04	6.84E-03	7.62E-03	-1.045351E-02	2.195882E-03	7.54E-03	8.06E-03
11	2	-4.054688E-03	-4.453929E-03	6.84E-03	6.86E-03	-2.632034E-03	-3.020044E-03	7.41E-03	7.61E-03
11	3	-9.257278E-03	1.942852E-03	6.33E-03	6.31E-03	-2.640234E-03	5.537360E-04	7.17E-03	6.99E-03
11	4	5.082716E-03	1.110162E-02	5.86E-03	5.91E-03	1.842193E-03	5.510921E-03	6.72E-03	6.75E-03
11	5	3.138955E-03	-8.833864E-03	5.62E-03	5.62E-03	3.003924E-03	-5.823475E-03	6.47E-03	6.44E-03
11	6	-2.403188E-03	-4.983184E-03	5.51E-03	5.45E-03	-3.949320E-03	-4.480285E-03	6.41E-03	6.40E-03
11	7	8.725834E-05	3.996231E-04	5.37E-03	5.26E-03	-1.890565E-03	-8.139835E-04	6.35E-03	6.24E-03
11	8	8.616524E-04	1.923868E-03	5.12E-03	4.93E-03	6.784540E-04	-1.107606E-03	6.20E-03	6.07E-03
11	9	1.310866E-03	5.252988E-03	5.14E-03	4.94E-03	4.004445E-03	2.773998E-03	6.31E-03	6.11E-03
11	10	-1.938206E-03	6.247899E-04	4.81E-03	5.06E-03	-1.025561E-04	6.462955E-04	6.08E-03	6.30E-03
11	11	-7.165234E-04	2.486272E-03	4.78E-03	4.94E-03	-2.745384E-03	1.570932E-03	6.06E-03	6.16E-03
12	0	-1.200853E-02		6.29E-03		-9.456946E-03		6.82E-03	
12	1	1.723774E-02	1.725213E-02	6.09E-03	6.75E-03	1.386634E-02	1.235960E-02	6.77E-03	7.15E-03
12	2	-4.685421E-03	-7.615664E-04	6.26E-03	6.30E-03	-3.282982E-03	-2.322578E-03	6.76E-03	6.92E-03
12	3	-1.088491E-02	3.482889E-04	5.86E-03	5.84E-03	-4.039679E-03	-1.558012E-03	6.61E-03	6.46E-03
12	4	2.332111E-03	-1.913051E-03	5.30E-03	5.41E-03	-1.140663E-03	-3.353620E-03	6.11E-03	6.19E-03
12	5	6.271224E-03	2.141141E-03	5.10E-03	5.11E-03	3.965770E-03	6.293405E-03	5.93E-03	5.93E-03
12	6	4.521880E-03	-1.432125E-03	5.14E-03	5.07E-03	5.122506E-04	-2.522764E-03	5.89E-03	5.86E-03
12	7	-2.383804E-04	6.201749E-03	5.00E-03	4.91E-03	-1.148666E-04	4.658821E-03	5.85E-03	5.78E-03
12	8	-3.581748E-03	-1.893073E-03	4.86E-03	4.68E-03	-3.460059E-03	-1.820354E-03	5.76E-03	5.65E-03
12	9	-5.829201E-03	3.705931E-03	4.56E-03	4.52E-03	-3.892956E-03	1.219690E-03	5.65E-03	5.57E-03
12	10	-2.437513E-03	-9.008714E-04	4.59E-03	4.68E-03	-3.389709E-03	-4.454238E-03	5.72E-03	5.74E-03
12	11	4.908815E-04	1.539959E-03	4.44E-03	4.61E-03	-1.425427E-03	-1.347674E-03	5.68E-03	5.77E-03
12	12	1.587672E-03	-1.649137E-03	4.43E-03	4.40E-03	1.600567E-03	5.040105E-04	5.64E-03	5.58E-03
13	0	1.005194E-02		5.79E-03		6.868918E-03		6.24E-03	

		TOPEX/POSEIDON and ERS–1				GEOSAT			
n	m	$\overline{C}_{n,m}$	$\overline{S}_{n,m}$	$\sigma(\overline{C}_{n,m})$	$\sigma(\overline{S}_{n,m})$	$\overline{C}_{n,m}$	$\overline{S}_{n,m}$	$\sigma(\overline{C}_{n,m})$	$\sigma(\overline{S}_{n,m})$
13	1	-1.834422E-02	-1.050562E-02	5.65E-03	6.12E-03	-1.828747E-02	-1.320173E-02	6.20E-03	6.47E-03
13	2	-6.705321E-03	4.464235E-03	5.91E-03	5.96E-03	-4.267036E-03	4.486075E-03	6.28E-03	6.38E-03
13	3	-1.188351E-03	-1.104523E-02	5.56E-03	5.53E-03	1.790939E-03	-7.585905E-03	6.16E-03	6.05E-03
13	4	-3.421208E-03	4.330437E-03	5.22E-03	5.30E-03	-1.782054E-03	4.255156E-03	5.84E-03	5.87E-03
13	5	-8.414124E-03	2.817162E-03	4.92E-03	4.93E-03	-7.058413E-03	1.512985E-03	5.61E-03	5.60E-03
13	6	-5.807650E-03	2.928623E-03	4.74E-03	4.71E-03	-2.786546E-03	3.156739E-03	5.44E-03	5.45E-03
13	7	-4.071349E-03	-1.014433E-02	4.69E-03	4.59E-03	-3.179801E-03	-7.057593E-03	5.39E-03	5.37E-03
13	8	7.870262E-04	1.728822E-03	4.56E-03	4.51E-03	3.861602E-04	1.359698E-03	5.40E-03	5.34E-03
13	9	5.288858E-04	-1.502741E-03	4.31E-03	4.33E-03	2.991205E-03	-1.099031E-03	5.23E-03	5.23E-03
13	10	2.061050E-03	1.482271E-03	4.14E-03	4.17E-03	2.239104E-03	-6.754853E-04	5.18E-03	5.21E-03
13	11	9.854614E-04	-3.714751E-03	4.19E-03	4.27E-03	2.181231E-03	-3.442183E-03	5.25E-03	5.28E-03
13	12	-1.299271E-03	1.506260E-03	4.14E-03	4.08E-03	-1.981349E-03	1.213530E-03	5.25E-03	5.23E-03
13	13	3.329500E-03	6.705752E-05	4.02E-03	4.05E-03	9.668643E-04	1.561444E-04	5.14E-03	5.21E-03
14	0	-3.356773E-03		5.43E-03		-4.339972E-03		5.79E-03	
14	1	1.493405E-04	1.078219E-02	5.04E-03	5.55E-03	1.403190E-03	9.417646E-03	5.58E-03	5.88E-03
14	2	4.372656E-03	-4.337817E-03	5.37E-03	5.44E-03	8.156469E-03	-2.961010E-04	5.74E-03	5.82E-03
14	3	-5.385558E-03	1.052977E-03	5.18E-03	5.16E-03	-2.014438E-03	2.951846E-03	5.67E-03	5.62E-03
14	4	-6.784718E-03	-7.078420E-04	4.81E-03	4.90E-03	-2.642855E-03	-2.338677E-03	5.41E-03	5.44E-03
14	5	9.893087E-03	6.260376E-03	4.51E-03	4.54E-03	7.752984E-03	2.549991E-03	5.19E-03	5.18E-03
14	6	1.117494E-02	-5.151022E-03	4.39E-03	4.35E-03	8.295406E-03	-5.114919E-03	5.06E-03	5.04E-03
14	7	-5.377607E-03	-1.788494E-03	4.42E-03	4.34E-03	-1.412876E-03	-2.738985E-04	5.05E-03	5.03E-03
14	8	1.525173E-04	1.745906E-03	4.38E-03	4.28E-03	-1.595600E-03	5.415859E-04	5.04E-03	4.97E-03
14	9	-9.280498E-04	-5.284562E-03	4.10E-03	4.05E-03	-1.640550E-03	-4.007644E-03	4.91E-03	4.89E-03
14	10	6.073853E-04	4.970609E-03	3.90E-03	3.96E-03	1.029881E-03	4.773284E-04	4.82E-03	4.85E-03
14	11	1.498257E-03	3.296685E-03	3.81E-03	3.83E-03	7.123888E-04	-7.886540E-04	4.82E-03	4.81E-03
14	12	1.267148E-03	2.279558E-03	3.92E-03	3.89E-03	8.071546E-05	6.301761E-05	4.91E-03	4.91E-03
14	13	2.233491E-03	1.800364E-03	3.75E-03	3.89E-03	1.301083E-03	-1.312363E-03	4.86E-03	4.94E-03
14	14	-2.602402E-03	1.228412E-03	3.67E-03	3.69E-03	2.370069E-03	7.944851E-04	4.81E-03	4.82E-03
15	0	2.782286E-03		4.99E-03		-1.323237E-03		5.33E-03	
15	1	5.533023E-03	-1.545940E-03	4.65E-03	5.09E-03	9.350024E-03	1.082889E-03	5.10E-03	5.39E-03
15	2	-1.719431E-03	4.265442E-03	5.02E-03	5.09E-03	-7.338269E-04	2.140043E-03	5.34E-03	5.38E-03
15	3	6.744319E-03	-7.521090E-04	4.93E-03	4.87E-03	6.976214E-03	-1.504975E-03	5.29E-03	5.22E-03
15	4	4.666376E-03	-3.182924E-04	4.64E-03	4.69E-03	1.648383E-03	-7.510173E-04	5.12E-03	5.13E-03
15	5	-1.083482E-02	-1.060911E-03	4.46E-03	4.46E-03	-8.537373E-03	-1.854985E-03	4.96E-03	4.94E-03
15	6	-1.088702E-04	3.695017E-04	4.24E-03	4.23E-03	-1.231614E-03	1.503850E-03	4.80E-03	4.79E-03
15	7	-6.284026E-03	-7.563025E-03	4.07E-03	4.03E-03	-1.936194E-03	-4.533945E-03	4.68E-03	4.67E-03
15	8	2.139174E-03	6.842496E-04	4.06E-03	3.99E-03	1.558317E-03	2.204357E-03	4.69E-03	4.65E-03
15	9	8.468712E-05	3.057572E-03	3.94E-03	3.96E-03	-7.047974E-04	2.453976E-03	4.64E-03	4.62E-03
15	10	7.458316E-04	3.591978E-03	3.75E-03	3.77E-03	6.042250E-04	1.988949E-03	4.54E-03	4.58E-03
15	11	-9.531866E-04	2.536023E-03	3.61E-03	3.58E-03	4.009073E-04	4.956540E-04	4.51E-03	4.46E-03
15	12	-6.161134E-03	-1.369593E-03	3.51E-03	3.50E-03	-3.031042E-03	-1.614757E-03	4.49E-03	4.51E-03
15	13	-9.787570E-04	-2.915622E-03	3.52E-03	3.63E-03	3.995255E-04	-1.743536E-03	4.51E-03	4.57E-03
15	14	-8.682887E-04	1.777182E-03	3.56E-03	3.49E-03	5.540141E-04	1.665265E-03	4.54E-03	4.53E-03
15	15	-7.172564E-04	-1.794007E-03	3.40E-03	3.47E-03	6.816744E-04	-3.261188E-04	4.45E-03	4.50E-03
16	0	-2.917771E-04		4.57E-03		4.460571E-03		4.91E-03	
16	1	-1.100124E-02	-6.434365E-03	4.38E-03	4.73E-03	-6.524458E-03	-5.933519E-03	4.75E-03	5.00E-03
16	2	-1.672294E-03	-2.996234E-05	4.51E-03	4.54E-03	-2.352159E-03	-2.919773E-03	4.87E-03	4.87E-03
16	3	2.943228E-03	1.240331E-03	4.50E-03	4.49E-03	-2.804455E-03	2.986749E-05	4.86E-03	4.82E-03
16	4	-8.445582E-03	3.449711E-03	4.39E-03	4.43E-03	-6.602811E-03	1.963311E-03	4.78E-03	4.80E-03
16	5	3.196140E-03	3.238585E-03	4.12E-03	4.12E-03	4.432282E-03	8.656704E-04	4.62E-03	4.59E-03

n	m	$\overline{C}_{n,m}$	$\overline{S}_{n,m}$	$\sigma(\overline{C}_{n,m})$	$\sigma(\overline{S}_{n,m})$	$\overline{C}_{n,m}$	$\overline{S}_{n,m}$	$\sigma(\overline{C}_{n,m})$	$\sigma(\overline{S}_{n,m})$
			TOPEX/POSEIDON and ERS–1				GEOSAT		
16	6	3.137679E-04	1.108075E-03	3.98E-03	3.95E-03	2.496746E-04	3.437292E-04	4.49E-03	4.47E-03
16	7	-5.317920E-04	1.586993E-03	3.82E-03	3.75E-03	-2.708447E-04	3.062003E-03	4.38E-03	4.38E-03
16	8	-1.501610E-04	-2.439052E-03	3.88E-03	3.83E-03	-1.096165E-03	-1.982046E-03	4.40E-03	4.38E-03
16	9	-1.954907E-03	-1.628313E-03	3.74E-03	3.74E-03	-2.236299E-03	-9.510606E-04	4.36E-03	4.34E-03
16	10	-2.098073E-03	1.072196E-03	3.59E-03	3.59E-03	-2.016680E-03	8.965902E-04	4.28E-03	4.29E-03
16	11	-7.403756E-04	3.680741E-04	3.36E-03	3.37E-03	-5.504352E-05	1.030181E-03	4.23E-03	4.20E-03
16	12	1.858821E-04	1.409885E-03	3.25E-03	3.25E-03	1.287948E-04	1.064619E-03	4.18E-03	4.19E-03
16	13	-2.959113E-03	-1.739831E-03	3.21E-03	3.27E-03	-7.593017E-04	-4.052472E-04	4.20E-03	4.23E-03
16	14	1.807184E-03	-1.314425E-03	3.27E-03	3.23E-03	-2.610982E-03	9.242184E-05	4.31E-03	4.31E-03
16	15	-3.228986E-03	-1.409263E-03	3.19E-03	3.27E-03	-2.674789E-04	-6.469804E-04	4.28E-03	4.30E-03
16	16	1.449520E-03	-7.552637E-04	3.24E-03	3.20E-03	6.659955E-04	5.621313E-04	4.23E-03	4.21E-03
17	0	1.116231E-03		4.06E-03		-4.777012E-04		4.48E-03	
17	1	2.381863E-03	7.299718E-03	4.21E-03	4.46E-03	1.090654E-03	3.442144E-03	4.48E-03	4.67E-03
17	2	2.393240E-03	4.101545E-04	4.09E-03	4.11E-03	2.902646E-03	6.491432E-05	4.47E-03	4.49E-03
17	3	-3.806094E-04	3.726424E-03	4.35E-03	4.36E-03	-1.627579E-04	1.906565E-03	4.58E-03	4.55E-03
17	4	4.650857E-03	-5.024782E-03	4.03E-03	4.04E-03	5.398401E-03	-3.297388E-03	4.42E-03	4.44E-03
17	5	-4.154829E-03	1.747046E-03	4.01E-03	4.00E-03	-2.629254E-03	1.811158E-03	4.39E-03	4.35E-03
17	6	-1.275929E-03	-4.683031E-03	3.84E-03	3.85E-03	-2.631165E-03	-3.181258E-03	4.27E-03	4.25E-03
17	7	9.459171E-04	-6.010596E-04	3.67E-03	3.62E-03	1.466341E-03	4.347897E-05	4.14E-03	4.13E-03
17	8	-2.251918E-03	4.187715E-03	3.59E-03	3.56E-03	-1.839530E-03	7.250840E-04	4.11E-03	4.10E-03
17	9	1.187483E-03	6.422257E-03	3.47E-03	3.46E-03	1.828210E-04	2.896210E-03	4.06E-03	4.05E-03
17	10	4.841400E-03	-5.276345E-03	3.43E-03	3.44E-03	2.698925E-03	-1.228873E-03	4.05E-03	4.06E-03
17	11	2.746647E-04	-1.601087E-03	3.25E-03	3.23E-03	-1.731565E-03	-2.433310E-03	3.98E-03	3.97E-03
17	12	-7.014731E-04	-6.238196E-03	2.99E-03	3.02E-03	-1.024967E-03	-2.372569E-03	3.91E-03	3.92E-03
17	13	7.231830E-04	3.929736E-05	2.92E-03	2.98E-03	2.613441E-04	-1.240842E-04	3.89E-03	3.92E-03
17	14	-1.471435E-03	-2.142348E-03	2.99E-03	2.96E-03	5.191028E-04	-6.679532E-04	3.94E-03	3.95E-03
17	15	-1.540119E-03	6.224006E-04	2.95E-03	3.00E-03	-4.645262E-04	1.450705E-04	3.95E-03	3.96E-03
17	16	-1.251075E-03	-2.275447E-03	2.97E-03	2.87E-03	-1.314174E-03	-1.695615E-05	3.98E-03	3.91E-03
17	17	-1.034736E-03	3.814480E-04	2.91E-03	2.90E-03	-9.965784E-05	-4.170234E-04	3.91E-03	3.92E-03
18	0	3.756237E-03		3.73E-03		6.627187E-04		4.16E-03	
18	1	-2.620568E-03	-7.819799E-03	3.82E-03	4.07E-03	-1.368499E-03	-3.013201E-03	4.14E-03	4.30E-03
18	2	-6.104252E-03	2.947173E-03	3.86E-03	3.88E-03	-3.015698E-03	3.430323E-03	4.18E-03	4.21E-03
18	3	5.852088E-03	5.949392E-04	3.95E-03	3.95E-03	2.614233E-03	-1.072738E-03	4.22E-03	4.19E-03
18	4	-6.665388E-03	4.040958E-03	3.83E-03	3.85E-03	-2.319546E-03	6.824395E-04	4.15E-03	4.16E-03
18	5	-1.831296E-03	-3.170234E-03	3.84E-03	3.83E-03	-2.358910E-04	-1.283926E-03	4.15E-03	4.12E-03
18	6	3.107841E-03	6.522532E-03	3.61E-03	3.58E-03	2.163631E-03	5.250886E-03	4.02E-03	3.98E-03
18	7	4.813263E-04	2.035795E-03	3.49E-03	3.45E-03	-8.058278E-05	1.750001E-03	3.92E-03	3.92E-03
18	8	3.364327E-04	8.626000E-04	3.40E-03	3.39E-03	-5.595379E-04	-7.263289E-04	3.87E-03	3.86E-03
18	9	-1.400082E-03	-3.437621E-03	3.32E-03	3.29E-03	-1.587419E-03	-2.813601E-03	3.84E-03	3.82E-03
18	10	-4.255496E-04	-2.688300E-04	3.31E-03	3.30E-03	-1.247206E-03	7.039873E-04	3.81E-03	3.82E-03
18	11	3.459424E-03	-7.201619E-05	3.00E-03	3.01E-03	4.726711E-04	2.991546E-04	3.74E-03	3.75E-03
18	12	2.033473E-03	9.383069E-05	2.82E-03	2.83E-03	1.691415E-03	1.164587E-03	3.67E-03	3.67E-03
18	13	-8.067962E-05	-1.017682E-03	2.71E-03	2.71E-03	-8.159117E-05	-5.915232E-04	3.66E-03	3.67E-03
18	14	-1.146312E-03	2.386049E-03	2.67E-03	2.67E-03	-1.550134E-03	4.910869E-04	3.66E-03	3.66E-03
18	15	-8.004478E-04	-2.151266E-03	2.71E-03	2.71E-03	-7.547340E-04	-3.745798E-04	3.75E-03	3.74E-03
18	16	1.164481E-03	-5.881003E-04	2.77E-03	2.72E-03	-2.513270E-04	5.820506E-04	3.77E-03	3.75E-03
18	17	-6.223352E-04	-3.119553E-04	2.71E-03	2.72E-03	2.228127E-04	-1.680506E-04	3.71E-03	3.73E-03
18	18	-4.144397E-04	-1.258891E-03	2.83E-03	2.86E-03	-8.913538E-05	-1.166791E-03	3.72E-03	3.73E-03
19	0	-2.828289E-03		3.47E-03		-4.086032E-03		3.86E-03	
19	1	-4.335921E-03	1.574664E-03	3.56E-03	3.77E-03	-6.257698E-04	2.406075E-03	3.83E-03	3.96E-03

D–4

		TOPEX/POSEIDON and ERS–1				GEOSAT			
n	m	$\overline{C}_{n,m}$	$\overline{S}_{n,m}$	$\sigma(\overline{C}_{n,m})$	$\sigma(\overline{S}_{n,m})$	$\overline{C}_{n,m}$	$\overline{S}_{n,m}$	$\sigma(\overline{C}_{n,m})$	$\sigma(\overline{S}_{n,m})$
19	2	2.262980E-03	-7.122826E-04	3.76E-03	3.79E-03	8.983082E-04	-4.846144E-04	3.93E-03	3.96E-03
19	3	-5.710616E-03	-1.072110E-04	3.64E-03	3.62E-03	-2.202847E-03	1.106145E-05	3.90E-03	3.86E-03
19	4	2.930939E-03	-8.869524E-04	3.76E-03	3.79E-03	2.185807E-03	1.624818E-03	3.91E-03	3.93E-03
19	5	3.867036E-04	5.916199E-04	3.56E-03	3.55E-03	1.585983E-03	1.743710E-04	3.85E-03	3.83E-03
19	6	-1.160989E-03	-2.352925E-03	3.52E-03	3.50E-03	-8.961354E-04	-2.907189E-04	3.81E-03	3.79E-03
19	7	2.002806E-04	-1.845517E-03	3.42E-03	3.40E-03	9.582351E-04	-1.121892E-03	3.74E-03	3.73E-03
19	8	-1.492591E-04	-2.698986E-03	3.19E-03	3.16E-03	8.257242E-04	-2.202576E-03	3.64E-03	3.63E-03
19	9	7.462759E-04	3.730682E-03	3.15E-03	3.11E-03	2.968882E-04	3.010958E-03	3.62E-03	3.61E-03
19	10	3.949678E-03	2.339901E-03	3.03E-03	3.02E-03	1.681860E-03	2.462672E-03	3.56E-03	3.58E-03
19	11	2.585905E-03	1.075216E-03	2.93E-03	2.92E-03	7.578263E-04	1.394886E-04	3.54E-03	3.55E-03
19	12	1.840139E-03	-4.453725E-04	2.69E-03	2.70E-03	5.491922E-04	-8.737266E-04	3.48E-03	3.48E-03
19	13	-2.538516E-03	1.656087E-04	2.54E-03	2.55E-03	-5.322050E-04	6.282374E-06	3.44E-03	3.45E-03
19	14	-1.443535E-03	-1.554156E-03	2.48E-03	2.49E-03	-7.544513E-04	-1.279158E-03	3.44E-03	3.44E-03
19	15	-1.438951E-03	-2.647966E-03	2.53E-03	2.50E-03	-5.292518E-04	-1.022953E-03	3.46E-03	3.45E-03
19	16	-4.662194E-04	-1.516295E-03	2.63E-03	2.57E-03	1.228865E-04	-2.000662E-04	3.51E-03	3.49E-03
19	17	2.261546E-03	1.838579E-03	2.62E-03	2.64E-03	9.228836E-04	1.554565E-03	3.52E-03	3.53E-03
19	18	-1.079303E-03	-1.790807E-03	2.60E-03	2.60E-03	-1.259830E-03	-1.509605E-03	3.51E-03	3.51E-03
19	19	1.186660E-03	2.663172E-03	2.73E-03	2.72E-03	1.050988E-03	1.429825E-03	3.52E-03	3.52E-03
20	0	3.528256E-03		3.25E-03		3.088584E-03		3.60E-03	
20	1	4.524304E-03	6.829858E-04	3.24E-03	3.45E-03	3.133471E-03	3.313281E-04	3.56E-03	3.69E-03
20	2	2.338058E-03	7.485462E-05	3.48E-03	3.51E-03	-3.820898E-04	-2.215505E-03	3.64E-03	3.67E-03
20	3	6.302372E-04	9.235329E-04	3.40E-03	3.36E-03	1.692395E-03	7.106482E-04	3.65E-03	3.60E-03
20	4	2.589213E-03	-4.367592E-03	3.47E-03	3.48E-03	3.250154E-03	-1.758163E-03	3.63E-03	3.65E-03
20	5	3.229241E-04	-1.116250E-03	3.38E-03	3.36E-03	-1.303363E-03	-1.911487E-03	3.61E-03	3.58E-03
20	6	-1.936664E-03	1.045128E-03	3.35E-03	3.33E-03	-1.196985E-03	-7.435871E-04	3.57E-03	3.56E-03
20	7	5.561261E-04	2.109187E-03	3.13E-03	3.10E-03	-1.887013E-04	1.337745E-03	3.47E-03	3.46E-03
20	8	7.498945E-04	3.741507E-03	2.98E-03	2.97E-03	6.136080E-04	1.428426E-03	3.40E-03	3.39E-03
20	9	-2.851082E-03	-1.311181E-03	2.85E-03	2.85E-03	-8.496649E-04	-1.697886E-03	3.34E-03	3.34E-03
20	10	3.563674E-04	-3.173694E-03	2.79E-03	2.78E-03	-9.806221E-04	-2.775846E-04	3.31E-03	3.32E-03
20	11	-3.787773E-03	-2.451577E-03	2.68E-03	2.67E-03	-6.514156E-04	-1.041147E-04	3.28E-03	3.29E-03
20	12	8.133315E-04	8.416077E-04	2.38E-03	2.40E-03	-6.539811E-04	1.923356E-03	3.23E-03	3.23E-03
20	13	2.486965E-03	-2.297807E-03	2.23E-03	2.23E-03	1.557117E-03	-2.762863E-04	3.21E-03	3.21E-03
20	14	-6.032922E-04	1.774678E-03	2.16E-03	2.16E-03	4.449968E-04	8.450457E-04	3.21E-03	3.21E-03
20	15	4.205749E-03	-1.862896E-04	2.22E-03	2.23E-03	2.462484E-03	2.577659E-04	3.24E-03	3.24E-03
20	16	2.435526E-03	7.541919E-04	2.37E-03	2.35E-03	6.304321E-04	6.858218E-04	3.29E-03	3.28E-03
20	17	3.876075E-03	-2.376141E-03	2.42E-03	2.43E-03	1.660664E-03	-3.128631E-04	3.35E-03	3.35E-03
20	18	-4.170596E-04	-4.497282E-05	2.51E-03	2.50E-03	-9.344392E-04	-7.992956E-04	3.35E-03	3.36E-03
20	19	1.845629E-03	2.535670E-03	2.38E-03	2.38E-03	-3.759097E-04	6.225971E-04	3.31E-03	3.31E-03
20	20	-1.815014E-03	-1.131462E-04	2.66E-03	2.65E-03	-3.955619E-04	-1.799926E-04	3.36E-03	3.36E-03

E.   EGM96 AND ITRF94 SITE POSITION DIFFERENCES

EGM96 SLR site positions differenced with ITRF94 positions at Epoch 930101 after a seven parameter transformation is applied. All differences are in mm. The sense of the difference is EGM96 minus ITRF94.

Location	CDP site #	Δx (mm)	Δy (mm)	Δz (mm)	Δ lat. (mm)	Δ long. (mm)	Δ height (mm)	total Δ (mm)
McDonald, TX	7080	2.1	7.4	-15.4	-9.4	0.3	-14.5	17.2
Yarragadee, Australia	7090	4.7	12.1	3.4	7.4	-9.4	6.2	13.4
Easter Island	7097	-102.3	-19.0	37.5	57.3	-90.1	29.1	110.6
Greenbelt, MD	7105	-5.6	2.3	5.3	6.3	-4.9	0.6	8.0
Quincy, CA	7109	-8.5	-1.8	12.8	6.0	-6.4	12.8	15.5
Monument Peak, CA	7110	-0.9	-1.4	17.4	13.8	-0.2	10.9	17.5
Platteville, CO	7112	-12.6	19.1	10.9	18.3	-17.0	-4.7	25.4
Mazatlan, Mexico	7122	-6.5	-49.3	-20.1	-38.2	7.8	37.1	53.7
Huahine	7123	66.9	-88.3	-0.2	-4.7	109.6	-15.1	110.8
Mt. Haleakala, HI	7210	-2.3	3.4	-23.7	-22.5	-4.0	-7.7	24.0
Goldstone, CA	7265	-15.9	30.8	33.6	39.3	-28.1	2.9	48.3
Arequipa, Peru	7403	-3.4	19.3	-13.4	-18.5	2.9	-14.8	23.8
Askites, Greece	7510	5.9	6.7	5.9	-0.9	3.5	10.1	10.7
Melengiclick, Turkey	7580	37.5	-56.2	12.3	9.4	-67.5	8.0	68.7
Yigilca, Turkey	7587	7.2	-9.2	16.6	11.7	-11.6	11.9	20.3
Grasse, France	7835	18.9	8.5	0.6	-13.3	6.1	14.7	20.7
Shanghia, China	7837	-0.5	-41.7	-42.0	-17.7	22.0	-52.0	59.2
Graz, Austria	7839	-1.4	-8.0	-13.6	-6.7	-7.4	-12.3	15.8
Herstmonceux, England	7840	8.6	-5.0	-4.1	-9.2	-5.1	2.2	10.7
Orroral Valley, Australia	7843	26.3	-31.1	44.4	13.6	13.1	-57.2	60.2
Cabo San Lucas, Mexico	7882	-13.8	-19.9	0.7	-8.5	-6.2	21.9	24.3
Ensenada, Mexico	7883	-13.4	9.8	5.1	5.9	-16.4	0.2	17.4
Matera, Italy	7939	-9.4	24.2	12.9	11.1	25.8	6.9	29.0
Wettzell, Germany	8834	-12.4	0.9	-25.5	-7.6	3.6	-27.1	28.4

REPORT DOCUMENTATION PAGE

Public reporting burden for this collection of information is estimated to average 1 hour per response, including the time for reviewing instructions, searching existing data sources, gathering and maintaining the data needed, and completing and reviewing the collection of information. Send comments regarding this burden estimate or any other aspect of this collection of information, including suggestions for reducing this burden, to Washington Headquarters Services, Directorate for Information Operations and Reports, 1215 Jefferson Davis Highway, Suite 1204, Arlington, VA 22202-4302, and to the Office of Management and Budget, Paperwork Reduction Project (0704-0188), Washington, DC 20503.

1. AGENCY USE ONLY (Leave blank)	2. REPORT DATE	3. REPORT TYPE AND DATES COVERED
	July 1998	Technical Paper

4. TITLE AND SUBTITLE

The Development of the Joint NASA GSFC and the National Imagery and Mapping Agency (NIMA) Geopotential Model EGM96

5. FUNDING NUMBERS

Code 926

6. AUTHOR(S)

F.G. Lemoine, S.C. Kenyon, J.K. Factor, R.G. Trimmer, N.K. Pavlis, D.S. Chinn, C.M. Cox, S.M. Klosko, S.B. Luthcke, M.H. Torrence, Y.M. Wang, R.G. Williamson, E.C. Pavlis, R.H. Rapp, and T.R. Olson

7. PERFORMING ORGANIZATION NAME(S) AND ADDRESS (ES)

Goddard Space Flight Center
Greenbelt, Maryland 20771

8. PEFORMING ORGANIZATION REPORT NUMBER

98B00052

9. SPONSORING / MONITORING AGENCY NAME(S) AND ADDRESS (ES)

National Aeronautics and Space Administration
Washington, DC 20546-0001

10. SPONSORING / MONITORING AGENCY REPORT NUMBER

NASA/TP—1998–206861

11. SUPPLEMENTARY NOTES F.G. Lemoine, NASA–GSFC, Greenbelt, MD;S.C. Kenyon, J.K. Factor, and R.G. Trimmer, NIMA, St. Louis, MO; N.K. Pavlis, D.S. Chinn, C.M. Cox, S.M. Klosko, S.B. Luthcke, M.H. Torrence, Y.M. Wang, and R.G. Williamson, Hughes STX Corp., Lanham, MD; E.C. Pavlis, NASA–GSFC, Greenbelt, MD and Dept. of Astronomy, Univ. of MD, College Park, MD; R.H. Rapp, Dept. of Civil and Environmental Engineering and Geodetic Science, The Ohio State University, Columbus, OH; T.R. Olson, Colorado Center for Astrodynamics Research, University of Colorado, Boulder, CO

12a. DISTRIBUTION / AVAILABILITY STATEMENT

Unclassified–Unlimited
Subject Category: 43
Report available from the NASA Center for AeroSpace Information,
7121 Standard Drive, Hanover, MD 21076-1320. (301) 621-0390.

12b. DISTRIBUTION CODE

13. ABSTRACT (Maximum 200 words)

The NASA Goddard Space Flight Center (GSFC), the National Imagery and Mapping Agency (NIMA), and The Ohio State University (OSU) have collaborated to develop an improved spherical harmonic model of the Earth's gravitational potential to degree 360. The new model, Earth Gravitational Model 1996 (EGM96), incorporates improved surface gravity data, altimeter-derived gravity anomalies from ERS–1 and from the GEOSAT Geodetic Mission (GM), extensive satellite tracking data—including new data from Satellite Laser Ranging (SLR), the Global Postioning System (GPS), NASA's Tracking and Data Relay Satellite System (TDRSS), the French DORIS system, and the US Navy TRANET Doppler tracking system—as well as direct altimeter ranges from TOPEX/POSEIDON (T/P), ERS-1, and GEOSAT. The final solution blends a low-degree combination model to degree 70, a block-diagonal solution from degree 71 to 359, and a quadrature solution at degree 360. The model was used to compute geoid undulations accurate to better than one meter (with the exception of areas void of dense and accurate surface gravity data) and realize WGS84 as a true three-dimensional reference system. Additional results from the EGM96 solution include models of the dynamic ocean topography to degree 20 from T/P and ERS–1 together, and GEOSAT separately, and improved orbit determination for Earth-orbiting satellites.

14. SUBJECT TERMS
Gravity, Geopotential Solutions, geoid, High Degree Spherical Harmonic Models, Orbit Calculations, Surface Gravimetry, Altimetry, Dynamic Ocean Topography, GPS/Leveling, TOPEX/POSEIDON, ERS–1, GEOSAT, SLR, DORIS, GPS, TDRSS, TRANET

15. NUMBER OF PAGES
575

16. PRICE CODE

17. SECURITY CLASSIFICATION OF REPORT	18. SECURITY CLASSIFICATION OF THIS PAGE	19. SECURITY CLASSIFICATION OF ABSTRACT	20. LIMITATION OF ABSTRACT
Unclassified	Unclassified	Unclassified	UL